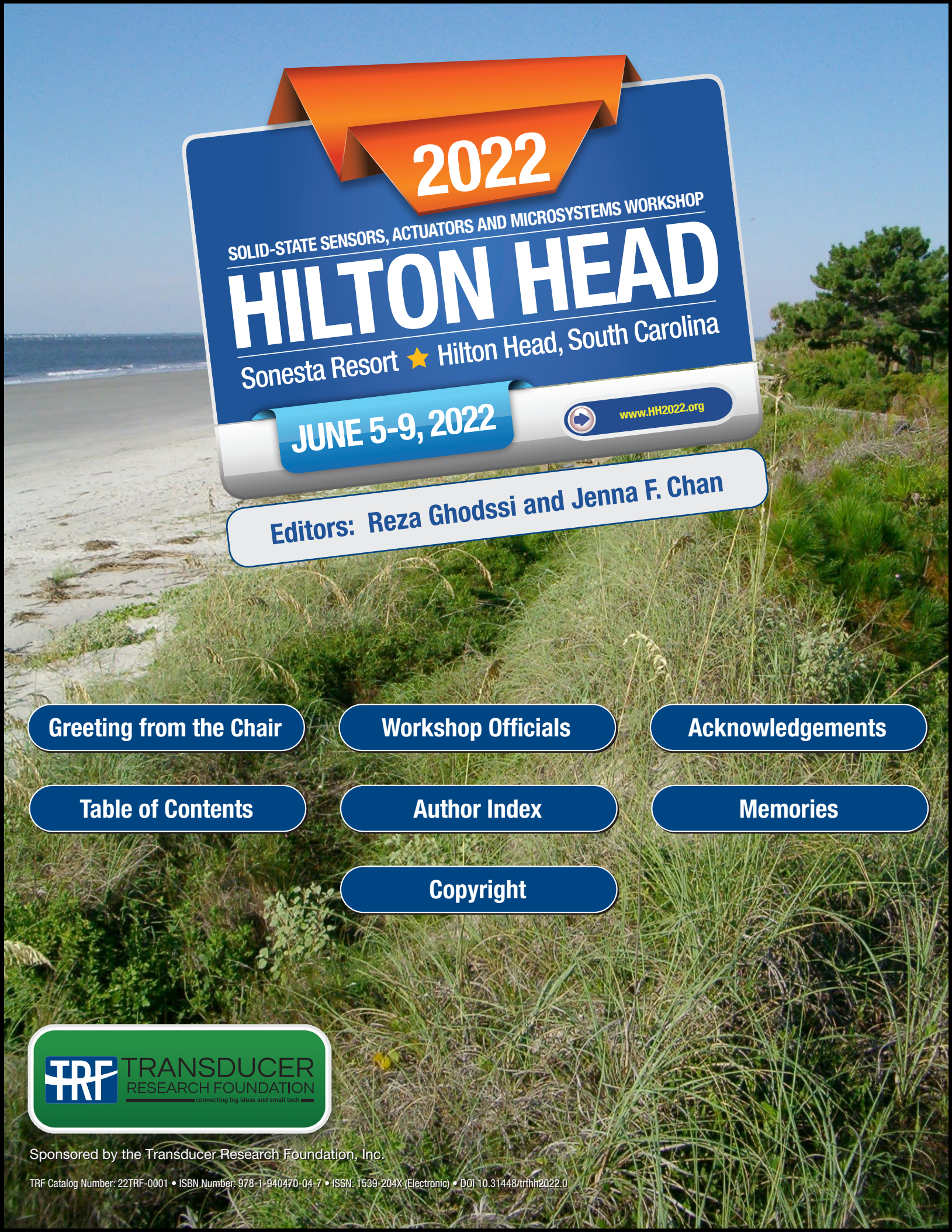

Sponsored by the Transducer Research Foundation, Inc.

TRF Catalog Number: 22TRF-0001 • ISBN Number: 978-1-940470-04-7 • ISSN: 1539-204X (Electronic) • DOI 10.31448/trfhh2022.0

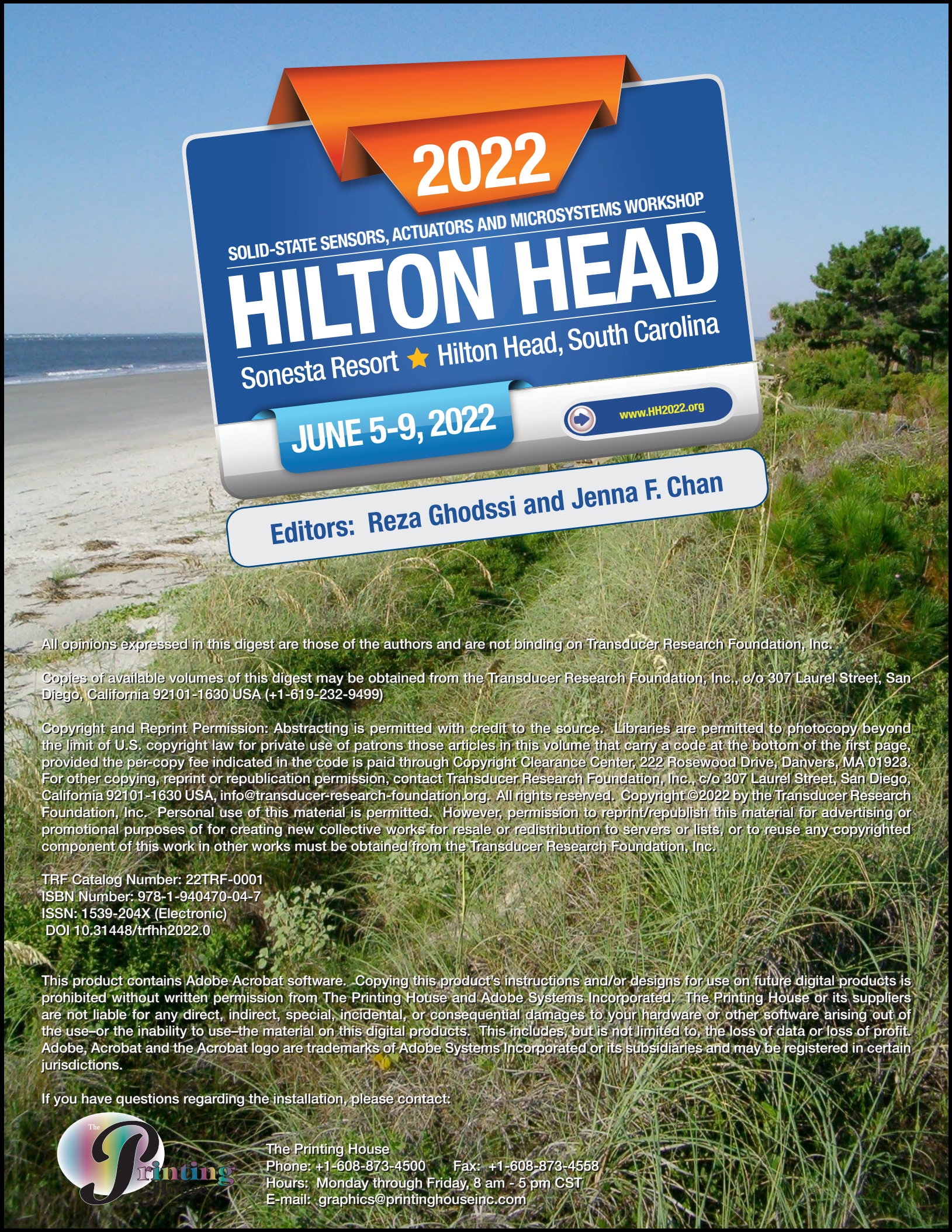

All opinions expressed in this digest are those of the authors and are not binding on Transducer Research Foundation, Inc.

Copies of available volumes of this digest may be obtained from the Transducer Research Foundation, Inc., c/o 307 Laurel Street, San Diego, California 92101-1630 USA (+1-619-232-9499)

Copyright and Reprint Permission: Abstracting is permitted with credit to the source. Libraries are permitted to photocopy beyond the limit of U.S. copyright law for private use of patrons those articles in this volume that carry a code at the bottom of the first page, provided the per-copy fee indicated in the code is paid through Copyright Clearance Center, 222 Rosewood Drive, Danvers, MA 01923. For other copying, reprint or republication permission, contact Transducer Research Foundation, Inc., c/o 307 Laurel Street, San Diego, California 92101-1630 USA, info@transducer-research-foundation.org. All rights reserved. Copyright ©2022 by the Transducer Research Foundation, Inc. Personal use of this material is permitted. However, permission to reprint/republish this material for advertising or promotional purposes of for creating new collective works for resale or redistribution to servers or lists, or to reuse any copyrighted component of this work in other works must be obtained from the Transducer Research Foundation, Inc.

TRF Catalog Number: 22TRF-0001
ISBN Number: 978-1-940470-04-7
ISSN: 1539-204X (Electronic)
DOI 10.31448/trfhh2022.0

This product contains Adobe Acrobat software. Copying this product's instructions and/or designs for use on future digital products is prohibited without written permission from The Printing House and Adobe Systems Incorporated. The Printing House or its suppliers are not liable for any direct, indirect, special, incidental, or consequential damages to your hardware or other software arising out of the use–or the inability to use–the material on this digital products. This includes, but is not limited to, the loss of data or loss of profit. Adobe, Acrobat and the Acrobat logo are trademarks of Adobe Systems Incorporated or its subsidiaries and may be registered in certain jurisdictions.

If you have questions regarding the installation, please contact:

The Printing House
Phone: +1-608-873-4500 Fax: +1-608-873-4558
Hours: Monday through Friday, 8 am - 5 pm CST
E-mail: graphics@printinghouseinc.com

GREETINGS FROM THE GENERAL CHAIR

Dear colleagues and friends, we are FINALLY here! It is a joy and thrill to see you ALL again **in person** since we met the last time in 2018. Welcome to the 2022 Solid-State Sensors, Actuators, and Microsystems Workshop; the twentieth in the biennial series of regional meetings that alternate with the International Transducers Conference. Since its inception in 1984, the Workshop's goal has been to provide a forum for presenting new ideas and leading-edge research achievements in a setting that facilitates an exchange of ideas and community building. We have always cared deeply about mentoring the students and young researchers in our MEMS community and more than ever, we are committed to continuing on that front by emphasizing and practicing diversity, equity, and inclusion.

The Hilton Head Workshop has historically been a regional meeting restricted to professionals living in North or South America as well as past attendees of previous Hilton Head Workshops. Beginning in 2020, the meeting opened to international colleagues beyond the Americas while maintaining the strong networking that this meeting always provides to our community. Hilton Head 2020 was unfortunately canceled due to the COVID-19 pandemic, and interestingly (but perhaps not coincidentally), its theme focused on healthcare grand challenges. Given the events of the past two years and in consideration of future science and technology directions, HH 2022's workshop theme continues the great work in this direction. Our focus is on "Preparation and Prevention: Tackling our Grand Challenges," which we hope will inspire our community, encourage new collaborations and ideas, and explore the potential for MicroElectroMechanical Systems (MEMS) to impact a variety of global issues and grand challenges.

Our Technical Program Committee (TPC) Chair, Dr. Jenna Chan, has done an outstanding job assembling and leading an expert program committee supporting the Workshop's goals. For the first time, the Hilton Head TPC has representatives from all key regions in America (North, Central, and South). Sunday starts with an all-day lecture series and panel (led by Dr. Ryan Sochol) highlighting the commercialization of human health and wellbeing provided by microsystems technologies. Throughout the week, daily featured keynote speakers are prominent, internationally known researchers and visionaries who will bring breadth and depth to our discussion of challenges and opportunities for MEMS and allied technologies. In addition, the program includes invited speakers from within and adjacent to the MEMS community, who will address important causes and grand challenges using novel, creative technologies, devices, and systems. On Tuesday afternoon, we are offering two special sessions on Early Career Faculty Development (led by Dr. Svetlana Tatic-Lucic) and "Sensorization Journey" (led by Drs. Tim Brosnihan and Paul Carey). The former, which targets senior graduate students, postdocs, and junior faculty members, will offer relevant guidance and advice for new faculty as well as those who aspire to become faculty members. The latter will address topics including students moving to industry (emerging leaders panel), prototypes moving to production (lab-to-fab journey), and sensors moving to new markets (smart cities).

All papers were selected on the basis of high-quality content and leading-edge contribution. Those deemed of broader interest to attendees were designated as oral and those of special interest as poster. The "shotgun" format is used to inform the attendees of the content of the upcoming poster session of the day. Late News Oral and Poster selection, which occurred in mid-March, brings the latest research to attendees. In addition, we again have something new and exciting planned for the period formally known as the "Rump Session," led by Dr. Chris Roberts. A tremendous "thank you" goes to Dr. Jenna Chan and the Technical Program Committee for putting together the technical content of the Workshop, which required studying, debating, ranking, and selecting from 192 submitted quality abstracts

Dr. Behraad Bahreyni, HH2022 awards committee chair, has done a fantastic job creating opportunities to recognize excellence at all levels, from the outstanding research presented at HH2022 to the long-standing contributions of members of our technical community. Best Paper and Best Poster awards will be given to the strongest technical works presented at the conference. Those with an entrepreneurial mindset can test their ideas through our new Bench-to-Market award. We also will recognize the lifelong contributions of leaders in our community through three new prestigious named

awards: the Mark Shannon Grand Challenges Award, the Denice Denton Mentorship Award, and the Wen Ko Technical Leadership Award.

We have a record in fundraising for this year's meeting! Dr. Swaminathan Rajaraman, Chair of the Commercial Development Committee, has worked tirelessly to create commercial support and exhibition contributions for this meeting. Special thanks also go to the Transducer Research Foundation, National Science Foundation, Army Research Lab, and our academic institutions such as the University of Maryland, University of Central Florida, and the University of Florida for their travel grant support for keynote and invited speakers, as well as presenting graduate student authors and postdoctoral associates. The involvement of these institutions and the financial support of the exhibitors and corporate sponsors are valuable and essential features of the 2022 Hilton Head Workshop, and I am most thankful to have had these outstanding government and academic institutions and industries participate in the workshop.

Sara Stearns, Shirley Galloway, and their team at Preferred Meeting Management, Inc., above all, deserve special recognition and thanks for all their hard work and superb organization in pulling this meeting together and for making it run so smoothly. The work they do "behind the scenes" over the two years of preparation to make this meeting special is exceptional; our community and our meeting have been the beneficiary of their excellence and commitment.

Finally, when the Hilton Head 2020 Workshop was canceled, on May 31, 2020 I wrote a letter and sent it to our community. At the end of that letter, I noted the following "I cannot wait for us to meet again in that lovely pavilion at the Sonesta Resort Hotel (if it will still be named Sonesta!?) on Hilton Head Island", June 2022. Once again, we will greet one another with big smiles and hugs and talk about our recent experiences, especially the ones we will have encountered during this devastating period. We'll also talk about how determined we all are to change the world for the better so that the next generation of MEMS students, faculty, scientists, and entrepreneurs will be better prepared to address future grand challenges." Well, I believe most of us shared that sentiment and have certainly come a long way since the pandemic started in 2020. Your personal commitment and the dedication of our community have helped us to reunite again "in person" at this historic conference. This meeting belongs to all of you; thank you for your enthusiastic participation. My best wishes for a memorable gathering in Hilton Head Island this June 2022.

Reza Ghodssi, Ph.D.
General Chair, Hilton Head 2022
TRF President-elect

Workshop Officials

Conference Chairs

General Chair Reza Ghodssi, University of Maryland, College Park, USA

Program Chair Jenna F. Chan, DEVCOM Army Research Laboratory, USA

Commercial Development Committee

Swaminathan Rajaraman (Chair)
University of Central Florida, USA

Katharine K. Cline, USA

Reza Ghodssi
University of Maryland, College Park, USA

Dave Monk
NXP Semiconductors, USA

Hananeh Esmailbeigi
University of Illinois, Chicago, USA

Angad Singh
Endotronix, USA

Jason Weigold
MEMStaff, USA

Early Career Faculty Development Session Committee

Svetlana Tatic-Lucic (Chair)
Lehigh University, USA

Benjamin Griffin
DARPA, USA

Jenica Patterson
National Institutes of Health, USA

Stephen Senturia
Massachusetts Institute of Technology, Emeritus, USA

Usha Varshney
National Science Foundation, USA

Community Engagement Committee

Ryan Sochol (Chair)
University of Maryland, USA

Daniela Diaz-Alonso
CIDESI, MEXICO

Kris Dorsey
Northeastern University, USA

Kari Moran
Naval Info. Warfare Center Pacific, USA

Roozbeh Tabrizian
University of Florida, USA

Sunday Short Course Program

Ryan Sochol (Chair)
University of Maryland, USA

Adrienne Higa
Berkeley Lights, USA

Vishnu Jayaprakash
AgZen, USA

Nazly Pirmoradi
PARC, a Xerox Company, USA

Juan Santiago
Stanford University, USA

Kedar Shah
Verily, USA

Vanessa Tolosa
Meta, USA

John Waldeisen
Entrepreneur, USA

Pae Wu
IndieBio and SOSV, USA

Awards Committee

Behraad Bahreyni (Chair)
Simon Fraser University, CANADA

Azadeh Ansari
Georgia Institute of Technology, USA

Tianhong Cui
Microsystems & Nanoengineering/
Springer Nature, USA

Kevin Daniels
University of Maryland, USA

Gymama Slaughter
Old Dominion University, USA

Jacopo Iannacci
Fondazione Bruno Kessler, ITALY

Amit Lal
Cornell University, USA

Local Organizing Committee

Azadeh Ansari (Chair)
Georgia Institute of Technology, USA

Farrokh Ayazi
Georgia Institute of Technology, USA

Oliver Brand
Georgia Institute of Technology, USA

Nima Ghalichechian
Georgia Institute of Technology, USA

Rump Session Committee

Robert "Chris" Roberts (Chair)
University of Texas, El Paso, USA

Vikrant Gokhale
Naval Research Laboratory, USA

Matteo Rinaldi
Northeastern University, USA

Christian Zorman
Case Western Reserve University, USA

Graduate Student Committee

Elizabeth Schell (Chair)
University of Pennsylvania, USA

Nicholas Bousse
Stanford University, USA

Ashley Chapin
University of Maryland, USA

Jinjing Han
University of Maryland, USA

Brianna Thielen
University of Southern California, USA

Technical Program Committee

Vladimir Aksyuk
NIST, USA

Azadeh Ansari
Georgia Institute of Technology, USA

Sina Askari
ECS/DARPA, USA

Alba Avila
University at Los Andes, Colombia, COLOMBIA

Behraad Bahreyni
Simon Fraser University, CANADA

Raji Baskaran
Manifolds Lab, USA

Technical Program Committee (continued)

Luke Beardslee
Emory University and
Georgia Institute of Technology, USA

Sarah Bedair
Army Research Laboratory, USA

Jenna Chan
DEVCOM Army Research Laboratory, USA

Hengky Chandrahalim
Air Force Institute of Technology, USA

Kevin Daniels
University of Maryland, USA

Daniela Diaz-Alonso
CIDESI, MEXICO

Kris Dorsey
Northeastern University, USA

Nima Ghalichechian
Georgia Institute of Technology, USA

Vikrant Gokhale
Naval Research Laboratory, USA

Juliet Gopinath
University of Colorado, Boulder, USA

Allyson Hartzell
Philips Innovation Services, USA

Matthew Hopcroft
University of California, Santa Barbara,
USA

Kirsten Kaplan
Facebook, USA

Amit Lal
Cornell University, USA

Carol Livermore
Northeastern University, USA

Yipeng Lu
Qualcomm, USA

Kari Moran
Naval Info. Warfare Center Pacific, USA

Spyridon Pavlidis
North Carolina State University, USA

Swami Rajaraman
University of Central Florida, USA

Chris Roberts
University of Texas in El Paso, USA

Ashwin Samarao
AEye, Inc., USA

Gymama Slaughter
Old Dominion University, USA

Logan Sorenson
HRL Laboratories, USA

Roozbeh Tabrizian
University of Florida, USA

Jennifer Talley
Air Force Research Laboratory, USA

Transducer Research Foundation

Officers

President
Thomas W. Kenny
Stanford University, USA

Vice-President
Antonio J. Ricco
NASA Ames Research Center and
Stanford University, USA

President-Elect
Reza Ghodssi
University of Maryland, USA

Treasurer
David Monk
NXP Semiconductor, USA

Vice-President
Kimberly Foster
Tulane University, USA

Directors

Michelle Bourke
Lam Research, CANADA

Jürgen Brugger
École Polytechnique Fédérale de Lausanne (EPFL), SWITZERLAND

Jenna F. Chan
DEVCOM Army Research Laboratory, USA

Amy E. Duwel
STR, USA

Alissa M. Fitzgerald
AMFitzgerald, USA

Kimberly Foster
Tulane University, USA

Luc Fréchette
Université de Sherbrooke, Québec, CANADA

Claudia Gärtner
microfluidic ChipShop GmbH, GERMANY

Reza Ghodssi
University of Maryland, USA

Amy E. Herr
University of California, Berkeley, USA

Thomas W. Kenny
Stanford University, USA

Nicole Kerness
Rheonix, Inc., USA

Tina Lamers
Aptiv, USA

Ellis Meng
University of Southern California, USA

David Monk
NXP Semiconductor, USA

Directors (continued)

Khalil Najafi
University of Michigan, USA

Mina Rais-Zadeh
University of Michigan and
NASA Jet Propulsion Laboratory, USA

Swaminathan Rajaraman
University of Central Florida, USA

Antonio J. Ricco
NASA Ames Research Center and
Stanford University, USA

Yuji Suzuki
University of Tokyo, JAPAN

James Walker
KBSO Patent Law, USA

Executive Director

Katharine K. Cline, USA

Emeritus Trustees

Mark Allen, University of Pennsylvania, USA
Luc Bousse
Joseph Giachino
G. Benjamin Hocker
Roger Howe, Stanford University, USA
Wen Ko
Mehran Mehregany, Case Western Reserve University, USA
Richard Muller, University of California at Berkeley, USA
Kurt Petersen, Silicon Valley Band of Angels, USA
Martin A. Schmidt, Massachusetts Institute of Technology, USA
Stephen Senturia
Leland "Chip" Spangler, Aspen Microsystems, USA
Kensall D. Wise

Acknowledgements

Special acknowledgement to the Transducer Research Foundation, Inc. for their educational grant funding support of this Workshop.

TRANSDUCER RESEARCH FOUNDATION
connecting big ideas and small tech

Exhibitors and Benefactors

We gratefully acknowledge the support of this Workshop from the following companies and institutions as of the printing of May 6, 2022:

A.M. Fitzgerald & Associates LLC

Analog Devices

CMC Microsystems

Coventor, A Lam Research Company

DEVCOM Army Research Laboratory

ENDOTRONIX

Evatec

Geegah Inc.

Heidelberg Instruments Inc.

i-ROM GmbH

IEEE Sensors Council

InvenSense, a TDK Group Company

KLA Corporation

Knowles Corporation

KP-MEMS

Lam Research Corporation

LioniX International

Lyncee Tec SA

MDPI - Actuators Journal

MEMS and Nanotechnology Exchange

MEMStaff Inc.

Microsystems & Nanoengineering/ Springer Nature

Microtech Ventures

National Nanotechnology Coordinated Infrastructure (NNCI)

NSF - National Science Foundation

NXP

Polytec, Inc.

Primordia BioSystems

Rogue Valley Microdevices Inc.

Sensors

Silex Microsystems

SiTime

SoftMEMS

Sumitomo Precision Products Co., Ltd.

Teledyne MEMS

University of Central Florida - College of Engineering and Computer Science

University of Florida - Interdisciplinary Microsystems Group

University of Maryland - A. James Clark School of Engineering

TRF – Hilton Head Memories

by Joseph M. Giachino

I read the Hilton Head notice announcing the awards in honor of Denice Denton, Wen Ko and Mark Shannon and it made me realize how rapidly time has passed. In my judgment the honors are well deserved and long overdue. I knew Wen and Denice very well and only knew of Mark by reputation. A sobering thought for me is that Mark was born the year I entered college.

This notice made me realize that most of the people now attending the Hilton Head Workshop have little knowledge how or why the workshop came about. So here is my take on the three why's of the workshop. Why a workshop? Why Hilton Head? Why TRF? These are the recollections of a very senior citizen.

WHY A WORKSHOP

A conference called TRANDUCERS was established in the 1970s. This conference was the place to present work concerning solid-state sensors, and later, actuators. The idea was that the conference should be held every two years in a different geographic area (Europe, Asia, Americas). This meant that the Americas would only host this meeting every six years. While at that time the field was small, a meeting every six years seemed inadequate to meet the community's needs in the Americas. Steve Senturia attempted to get a Gordon Conference on Microsensors to fill the void, but the application was turned down. That news was met with a determination to "do it ourselves."

Ken Wise initiated a meeting to address the best way to fill this void. To my recollection, the big meeting to discuss what to do was held in Michigan and the people present were:

Ken Wise – University of Michigan
Wen Ko – Case Western Reserve University
Dave Eddy – General Motors
Ben Hocker – Honeywell
Tom Poteat – Bell Labs
Steve Senturia – Massachusetts Institute of Technology
Joe Giachino – Ford

I am sure I left some out so check with Ken and Ben. I know Scott Chang–General Motors was supporting the Transaction printing.

The result reached at this meeting was that there should be a North America meeting every two years, in the even years when there was no Americas TRANSDUCERS meeting.

The format of the meeting was fashioned after the Gordon Conferences. There is a limit on the attendees, and in theory participants are invited to attend. The workshop concept led the group to limit attendees to persons based in North and South America. The format was to have only one session, with all in attendance, each day—rather than parallel sessions. Lunches that would allow people to talk and exchange ideas were included in the program. There was a free afternoon to allow participants time to explore.

The meeting also included a "rump" session, where refreshments were served and a very free flow of comments was encouraged. Several rump session comments have stuck in my memory

over the years: “Single crystal bigots” and “I agree with Professor Senturia.” I do not know whether any of our current Hilton Head Workshop attendees have any idea as to what these quotes refer!

WHY HILTON HEAD

The group decided the workshop would work best in a resort-type location with a casual, laid-back atmosphere to encourage people to informally interact. There were many suggestions for the venue including Mackinac Island, Mich., and Sandusky, Ohio.

Tom Poteat suggested Hilton Head, S.C. None of the other attendees knew of Hilton Head. Tom had grown up in the area and filled us in on the history and status. Hilton Head is a barrier island and in the early days was a place locals took their pigs to spend the winter. The pigs could forage for food, and they could not leave the island. I do not know how much of that is fact and how much is folklore. In the 1960s, developers began turning the island into an upscale resort community. The group was concerned about how accessible the island was to people coming from around the country. Tom let us know that the island was easily reached from Savannah and that there was even a small airport on the island, with shuttle service, if one did not want to drive.

What made the group decide on Hilton Head? Note that members of the group all had been previously involved in conference management and understood the effort involved in the tasks required for a successful meeting. So, when Tom said “If you select Hilton Head, I will be the local arrangements chair,” the group selected Hilton Head. After the first workshop, the suggestion was made that, like many IEEE meetings, the location should alternate between east coast and west coast. The suggestion was made that the meeting be held in Monterey, California. The group agreed that was a good location and the question was asked, “Who would like to be local arrangements chair for Monterey”? As there were no volunteers, thus was born the Hilton Head Workshop.

WHY TRF

The original plan was to have the IEEE Electron Device Society (EDS) sponsor the workshop, and the first two workshops indeed were sponsored by EDS. Note that this workshop was valuable to EDS because the profit from the year’s first workshop made EDS conferences profitable for that year.

The workshop committee had contacted the European and Asian groups concerning limiting attendance to the Americas. No group objected; in fact, the Europeans started EUORSENSORS based on the model of limiting attendance to Europeans. The EDS professional staff had no objection as all parties were in concert. However, an EDS member in a position of authority did object. This member was adamant that IEEE meetings had to be open to any and all IEEE members. It was further stated that if the workshop did not abide by these rules, there would be no IEEE support.

The workshop committee wanted to continue the successful workshop formula. As this could not be done under the auspicious of the IEEE, the Transducer Research Foundation (TRF) became the sponsor.

Wen Ko had, prior to the IEEE sponsorship of the first workshop, established TRF as an Ohio nonprofit. This was done as the model for this type of workshop was new and the committee

was not certain that EDS would approve of the concept. The committee wanted IEEE financial and technical (archiving, administrative) support to better serve the sensor community. When IEEE did not support our efforts, the TRF Board went out on its own.

Before we hired Katharine Cline's firm (Preferred Meeting Management, Inc.) in 1999, we ran the workshop by ourselves. This included a website, printing the proceedings, administration and all the mundane items that need to be done. Here are some examples that come to mind:

The TRF Board agreed that if there was any shortfall in revenue, the Board as individuals would make up the difference. To the relief of all, this has never been necessary.

The proceedings from the early meetings were printed by General Motors and delivered to Hilton Head by Dave Eddy. The one exception is when Dave was injured in an accident, and he had Mike Putty deliver the proceedings.

Tom Poteat negotiated with the hotel and had one keg of beer donated to the rump session. We worked with the hotel to allow us to buy our own wine, and it was served at the banquet and rump session. The hotel only charged a corkage fee, which reduced the expense.

We sold extra proceedings for cash—no credit cards or digital wallets, just plain money. To reduce the risk of having loose cash around, the monies were used to buy the wine.

Creating a Community

From the outset, the Workshop was devoted to creating a community of co-workers, including students. The founders take considerable pride in how that original intent has matured to the point where presentations by students, especially at our poster session, are many of the highlights of our program. As a "networking" event, the Hilton Head Workshop cannot be beat. It is the best!

Table of Contents

Scroll to the title and select a **Blue** link to open a paper. After viewing the paper, use the bookmarks to the left to return to the beginning of the Table of Contents.

Sunday, June 5

10:30 am - 12:00 pm **Short Course Morning – Translating Innovation**
Networking and Presentations

1:00 pm - 3:30 pm **Short Course Afternoon – Translating Innovation**
Panel Discussions

6:00 pm - 9:00 pm **Registration and Welcome Reception**

Monday, June 6

7:00 am **Breakfast**

7:45 am **Welcome**
TRF President - Thomas W. Kenny, *Stanford University*
Workshop Chair - Reza Ghodssi, *University of Maryland*
Program Chair - Jenna Chan, *DEVCOM Army Research Laboratory*

Plenary Speaker I

Session Chair: Swami Rajaraman, *University of Central Florida, USA*

8:15 am **MICROSENSOR MEASUREMENT OF EVOKED COMPOUND ACTION POTENTIALS IMPROVES SPINAL CORD STIMULATION CLINICAL EFFECTIVENESS AND LONG TERM EFFICACY** **1**
Lawrence Poree
University of California, San Francisco, USA

Session 1: Point-of-Use Sensing Systems

Session Chairs: Daniela Diaz-Alonso, *CIDESI, MEXICO*
Gymama Slaughter, *Old Dominion University, USA*

8:55 am **A PASSIVE WIRELESS DIFFERENTIAL SENSOR FOR IN-SITU EARLY DETECTION OF PERIPROSTHETIC JOINT INFECTION** **5**
Jiaxin Jiang, Krithika Sureshkumar, Chandrashekhar Choudhary, Tristan Kerkes, H. Claude Sagi, Chia-Ying Lin, Michael T. Archdeacon, and Tao Li
University of Cincinnati, USA

9:15 am **SALIVA-BASED SARS-COV-2 SELF-TESTING WITH RT-LAMP IN A MOBILE DEVICE (SLIDE)** **9**
Zifan Tang, Jiarui Cui, Aneesh Kshirsagar, Tianyi Liu, and Weihua Guan
Pennsylvania State University, USA

9:35 am **EARLY DETECTION OF SIMULATED HERBIVORE ATTACKS IN SORGHUM FIELDS THROUGH THE DEPLOYMENT OF VERY-LOW-POWER GAS SENSOR NETWORK** **13**
Shakir-ul Haque Khan[1], Sayali Tope[1], Mohit Karkhanis[1], Bryan Hatasaka[1], Seungbeom Noh[1], Rana Dalpati[1], Ashrafuzzaman Bulbul[1], Ravi V. Mural[2], Aishwaryadev Banerjee[1], Kyeongheon Kim[3], James C. Schnable[2], Mingyue Ji[1], Carlos Mastrangelo[1], Ling Zang[1], and Hanseup Kim[1]
[1]University of Utah, USA, [2]University of Nebraska, Lincoln, USA, and [3]Gyeongsang National University, KOREA

9:55 am **MULTIPLEXING AND INCREASING THE THROUGHPUT OF "ROLOSENSE ASSAY" UTILIZING COST-EFFECTIVE WIFI IMAGING AND DISPOSABLE MICROFLUIDICS CHIPS FOR SARS-COV-2 DETECTION** **17**
Jorge Manrique Castro[1], Frank Sommerhage[2], Selma Piranej[3], David DeRoo[2], Khalid Salaita[3], and Swaminathan Rajaraman[1,2]
[1]University of Central Florida, USA, [2]Primordia Biosystems, USA, and [3]Emory University, USA

10:15 am **Break and Tabletop Inspection**

10:44 am **Wen Ko Technical Leadership Award Announcement**

Invited Speaker I

Session Chair: Raji Baskaran, *Manifolds Lab, USA*

10:45 am **PERSONALIZED MEDICINE FOR OFTEN OVERLOOKED POPULATIONS BY USING TEXTILE-BASED SENSORS** **21**
Alicia Chong Rodriguez
Bloomer Tech, USA

Session 2: Next-Generation Design and Prototyping

Session Chairs: Alba Avila, *University at Los Andes, Colombia, USA*
Kris Dorsey, *Northeastern University, USA*

11:15 am **RAPID PROTOTYPING OF 3D PRINTED MEMS ARRAYS ON FLEXIBLE SUBSTRATES** **23**
Regan Kubicek, Sukjun Kim, and Sarah Bergbreiter
Carnegie Mellon University, USA

11:35 am **A HYBRID 3D MICRO-NANOPRINTING APPROACH FOR BIOMEDICAL MICROINJECTION NEEDLE ARRAYS** **27**
Sunandita Sarker[1], Adira Colton[1], Ziteng Wen[1], Xin Xu[1], Piotr Walczak[2], Miroslaw Janowski[2], Yajie Liang[2], and Ryan D. Sochol[1]
[1]University of Maryland, College Park, USA, and [2]University of Maryland, School of Medicine, USA

11:55 am **TOWARDS A CMOS INTEGRATED PIEZOELECTRIC MEMS PROCESS DESIGN KIT** **31**
Benyamin Davaji[1,2], Justin Kuo[1,3], Matteo Rinaldi[2], and Amit Lal[1,3]
[1]Cornell University, USA, [2]Northeastern University, USA, and [3]Geegah LLC, USA

12:15 pm **Poster Preview – Session 1**
Session Chairs:
Nima Ghalichechian, *Georgia Institute of Technology, USA*
Kirsten Kaplan, *Facebook, USA*

12:45 pm - 2:15 pm **Networking Lunch**

2:15 pm **Poster Session 1**
Contributed and Late News
See page 13 for listing of poster presentations

4:45 pm **End of Day**

Tuesday, June 7

7:30 am **Breakfast**

8:10 am **Announcements**

Plenary Speaker II

Session Chair: Vladimir Aksyuk, *National Institute of Standards and Technology (NIST), USA*

8:15 am **SENSORS THAT MAKE COMMUNITY SENSE** **34.1**
Mina Sartipi
University of Tennessee, Chattanooga, USA

Session 3: Acoustic Devices and Microsystems

Session Chair: Azadeh Ansari, *Georgia Institute of Technology, USA*

8:55 am **PERIOD TRIPLING STATES AND NON-MONOTONIC ENERGY DISSIPATION IN COUPLED MEMS RESONATORS** **35**
Mingkang Wang[1,2], Diego J. Perez-Morelo[1,2], Daniel Lopez[3,1], and Vladimir A. Aksyuk[1]
[1]National Institute of Standards and Technology (NIST), USA, [2]University of Maryland, USA, and [3]Pennsylvania State University, USA

9:15 am **HETEROGENEOUS INTEGRATION FOR HYBRID ACOUSTIC DEVICES: GAN/CU/YIG MAGNETOELASTIC HBARS** **39**
Vikrant J. Gokhale[1], Brian P. Downey[1], Pallavi Dhagat[2], Albrecht Jander[2], Shawn Mack[1], D. Scott Katzer[1], Jason A. Roussos[1], and David J. Meyer[1]
[1]US Naval Research Laboratory, USA and [2]Oregon State University, USA

9:35 am **UNDERWATER ACOUSTIC TWEEZERS CAPABLE OF TRAPPING LARGE AND HEAVY PARTICLES** **43**
Kianoush Sadeghian Esfahani, Yongkui Tang, Jaehoon Lee, Matin Barekatain, and Eun S. Kim
University of Southern California, Los Angeles, USA

9:55 am **Break and Tabletop Inspection**

10:24 am **Denice Denton Mentorship Award Announcement**

Invited Speaker II

Session Chair: Kari Moran, *Naval Info. Warfare Center Pacific, USA*

10:25 am **ADDRESSING THE GRAND CHALLENGES OF CLIMATE CHANGE** **47**
Leslie Field
Bright Ice Initiative, Inc., SmallTech Consulting, LLC and Stanford University, USA

Session 4: High-FOM Resonators

Session Chairs: Hengky Chandrahalim, *Air Force Institute of Technology, USA*
Logan Sorenson, *HRL Laboratories, USA*

10:55 am **HIGHEST FIGURE OF MERIT MICROACOUSTIC RESONATORS FOR MID-BAND 6G SPECTRUM** **48**
Gabriel Giribaldi, Michele Pirro, Meruyert Assylbekova, Luca Colombo, and Matteo Rinaldi
Northeastern University, USA

11:15 am **X-BAND FERROELECTRIC-ON-SI FIN BULK ACOUSTIC RESONATORS (FOS-FINBAR) WITH $f.Q$ OF 0.8×10^{13}** **52**
Faysal Hakim and Roozbeh Tabrizian
University of Florida, USA

11:35 am **POWER HANDLING CHALLENGES OF HIGH K_T^2 ALSCN LAMB WAVE RESONATORS** **56**
Mingyo Park, Yue Zheng, and Azadeh Ansari
Georgia Institute of Technology, USA

11:55 pm **Networking Lunch**
1:30 pm

Early Career Faculty Development Session

Chair: Svetlana Tatic-Lucic, *Lehigh University, USA*

2:00 pm -
4:00 pm Benjamin Griffin[1], Jenica Patterson[2], Stephen Senturia[3], and Usha Varshney[4]
[1]Defense Advanced Research Projects Agency (DARPA), USA,
[2]National Institutes of Health (NIH), USA,
[3]Massachusetts Institute of Technology, Emeritus, USA and
[4]National Science Foundation (NSF), USA,

2:00 pm - 4:00 pm **MSIG Industry Session: Sensorization Journey**
Savannah Jr. Ballroom

2:00 pm - 7:00 pm **Recreational Activities**

6:00 pm - 7:00 pm **Graduate Student Networking Event**

7:00 pm - 10:00 pm **Banquet**

Wednesday, June 8

7:30 am **Breakfast**

8:10 am **Announcements**

Plenary Speaker III

Session Chair: Juliet Gopinath, *University of Colorado, Boulder, USA*

8:15 am **MANUFACTURING NEXT-GENERATION MICROELECTRONICS** **60**
Carl E. McCants
Defense Advanced Research Projects Agency (DARPA), USA

Session 5: Physical and Environmental Sensors

Session Chairs: Sina Askari, *ECS/DARPA, USA*
Vikrant Gokhale, *Naval Research Laboratory, USA*

8:55 am **A MEMS MICROVALVE FOR THE SPACECRAFT ATMOSPHERE MONITOR (SAM) INSTRUMENT** **63**
Cecile Jung-Kubiak, Risaku Toda, Abhijit Shevade, M. Bulut Coskun, Sofia Rahiminejad, Matthew Dickie, Cliff Frez, John Gill, and Mina Rais-Zadeh
California Institute of Technology, USA

9:15 am **EXPLOITING NONLINEAR PROPERTIES OF VO_2 IN A MMWAVE ANTENNA-COUPLED SENSOR** **67**
Shangyi Chen[1], Mark Lust[2], and Nima Ghalichechian[3]
[1]University of Pennsylvania, USA, [2]Ohio State University, USA, and [3]Georgia Institute of Technology, USA

9:35 am **KILOVOLT PYROELECTRIC VOLTAGE GENERATION AND ELECTROSTATIC ACTUATION WITH FLUIDIC HEATING** **71**
Di Ni, Ved Gund, Landon Ivy, and Amit Lal
Cornell University, USA

9:55 am **A HIGH-Q SOLID DISK BAW GYROSCOPE IN MONOCRYSTALLINE 4H SILICON-CARBIDE WITH SUB-PPM AS-BORN FREQUENCY SPLIT** **75**
Zhenming Liu, Ardalan Lotfi, Michael P. Hardin, and Farrokh Ayazi
Georgia Institute of Technology, USA

10:15 am **Break and Tabletop Inspection**

10:44 am **Mark Shannon Grand Challenges Award Announcement**

Invited Speaker III

Session Chair: Jennifer Talley, *Air Force Research Laboratory, USA*

10:45 am **BIOLOGY-INSPIRED INTELLIGENCE IN THE DESIGN, CONTROL, AND POWER SYSTEMS OF INSECT-SIZED FLYING ROBOTS** **79**
Sawyer B. Fuller
University of Washington, Seattle, USA

Session 6: Ingestible and Implantable Microsystems 1

Session Chairs: Luke Beardslee, *Emory University and Georgia Institute of Technology, USA*
Spyridon Pavlidis, *North Carolina State University, USA*

11:15 am **MINIATURIZED CAPSULE SYSTEM FOR HYDROGEN SULFIDE DETECTION IN THE GASTROINTESTINAL TRACT** **81**
Justin M. Stine, Santiago Botasini, Luke A. Beardslee, Joshua A. Levy, and Reza Ghodssi
University of Maryland, College Park, USA

11:35 am **BIOPOWER-IN-GUT: AN INGESTIBLE BACTERIA-POWERED BATTERY CAPSULE** **85**
Maryam Rezaie, Zahra Rafiee, and Seokheun Choi
State University of New York, Binghamton, USA

11:55 am **MONITORING OF PHYSIOLOGICAL FLOW WITH A MICROFABRICATED ELECTROCHEMICAL PARYLENE FLOW SENSOR** **89**
Xuechun Wang[1], Trevor Hudson[1], Kee Scholten[1], Elliot Myong[1], J. Gordon McComb[2], and Ellis Meng[1]
[1]University of Southern California, Los Angeles, USA and [2]Children's Hospital Los Angeles, USA

12:15 pm **Poster Preview – Session 2**
Session Chair: Behraad Bahreyni, *Simon Fraser University, USA*

1:00 pm - 2:30 pm **Networking Lunch**

2:30 pm **Poster Session 2**
Contributed and Late News
See page 21 for listing of poster presentations

5:00 pm - **Free Time**

6:30 pm **Poster Session 3 and Reception**
Commercial and Open Posters
See page 29 for listing of poster presentations

8:00 pm - 10:00 pm **Rump Session**
Chair: Robert “Chris” Roberts, *University of Texas, El Paso, USA*

Thursday, June 9

7:30 am **Breakfast**

8:10 am **Announcements**

Plenary Speaker IV

Session Chair: Amit Lal, *Cornell University, USA*

8:15 am **PROBING THE LIFE IN BUBBLES – NANOPLASMONIC QUANTIFICATION OF PATHOGEN-DERIVED EXTRACELLULAR VESICLES IN BLOOD** **93**
Tony Y. Hu
Tulane University, USA

Session 7: Ingestible and Implantable Microsystems 2

Session Chairs: Kevin Daniels, *University of Maryland, USA*
Carol Livermore, *Northeastern University, USA*

8:55 am **PASSIVE 3D-PRINTED FULLY ELASTIC PILL FOR SAMPLING OF GUT MICROBIOME** **96**
Ruben Del-Rio-Ruiz, Cihan Asci, Rachel Owyeung, Giovanni Widmer, and Sameer Sonkusale
Tufts University, USA

9:15 am **BIOMIMETIC ANCHORING SYSTEM FOR SUSTAINED AND LOCALIZED GASTROINTESTINAL DRUG DELIVERY** **100**
Joshua A. Levy, Michael A. Straker, Luke A. Beardslee, and Reza Ghodssi
University of Maryland, College Park, USA

9:35 am **NON-INVASIVE SMART CAPSULE FOR CONTINUOUS MONITORING OF INFLAMMATORY BOWEL DISEASE** **104**
Sachin Kadian, Vidhya Selvamani, Sina Nejati, and Rahim Rahimi
Purdue University, USA

REMOVED

9:55 am **Break and Tabletop Inspection**

Invited Speaker IV

Session Chair: Roozbeh Tabrizian, *University of Florida, USA*

10:25 am **DIAMOND QUANTUM SENSORS** **107**
Victor Acosta
University of New Mexico, USA

Session 8: Late News

Session Chair: Yipeng Lu, *Qualcomm, USA*

10:55 am **GIANT NON-RECIPROCITY THROUGH FREQUENCY MODULATION OF A TWO DEGREE-OF-FREEDOM MICROMECHANICAL RESONATOR** **108**
James M.L. Miller[1], Jianing Zhao[1], Chae Hyuck Ahn[2], Eldwin J. Ng[2], Vu Hong[2], Yushi Yang[2], Nicholas E. Bousse[2], Thomas W. Kenny[2], and Gaurav Bahl[1]
[1]University of Illinois, Urbana-Champaign, USA and [2]Stanford University, USA

11:15 am **PCB-BOT: THE FIRST STEPS OF A 4 MG LEGGED MICROROBOT** **110**
Sukjun Kim, Regan Kubicek, and Sarah Bergbreiter
Carnegie Mellon University, USA

11:35 am **SCALABLE FABRICATION OF ACTIVE NANOGAPS WITH SUB-NANOMETER TUNABILITY FOR NANOSCALE SENSORS AND ACTUATORS** **112**
Weikun Zhu, Peter F. Satterthwaite, and Farnaz Niroui
Massachusetts Institute of Technology, USA

11:55 am **TRF Celebrations**

12:10 pm **Award Ceremony**
Chair: Behraad Bahreyni, *Simon Fraser University, USA*

12:45 pm - 2:15 pm **Networking Lunch**

2:15 pm **Workshop Adjourns**

Poster Presentations - Session 1

Contributed and Late News Posters

Monday, June 6 2:15 pm – 4:45 pm

Chemical or Biological Sensors, Actuators or Systems

MP-01 **A STRETCHABLE NEURAL INTERFACE FOR VAGUS NERVE STIMULATION: FABRICATION AND ELECTROCHEMICAL CHARACTERIZATION** **114**
Jongcheon Lim[1], Matthew P. Ward[1,2], John B. Furness[3], Luis C. Populin[4], and Hyowon Lee[1]
[1]Purdue University, USA, [2]Indiana University School of Medicine, USA, [3]University of Melbourne, AUSTRALIA, and [4]University of Wisconsin, Madison, USA

MP-02 **AN EQUIPMENT-FREE PAPERTRONIC SENSING SYSTEM FOR POINT-OF-CARE MONITORING OF ANTIMICROBIAL SUSCEPTIBILITY** **118**
Zahra Rafiee, Maryam Rezaie, Olya Noruz Shamsian, and Seokheun Choi
State University of New York, Binghamton, USA

MP-03 **CMOS-NANOWELL BASED HYBRID SMART BANDAGE FOR LONG TERM MONITORING OF WOUND HEALING VIA CYTOKINE QUANTIFICATION IN-SITU** **122**
Chengjie Zhu[1], Pengfei Xie[2], Ryan Thorpe[1], Jesus Maldonado[1], Suneel Kumar[2], Aaron Mazzeo[2], Mehdi Javanmard[2], Francois Berthiaume[2], and Kaushik Sengupta[1]
[1]Princeton University, USA and [2]Rutgers University, USA

MP-04 **DROPBLOT DESIGN INTEGRATES DROPLET MICROFLUIDICS WITH SINGLE-CELL ELECTROPHORESIS FOR TARGETED PROTEOMICS** **126**
Yang Liu and Amy E. Herr
University of California, Berkeley, USA

MP-05 **FIELD-DEPLOYABLE MICROFLUIDIC IMMUNOASSAY DEVICE FOR PROTEIN DETECTION** **130**
Gihoon Choi, Betty Mangadu, Yooli K. Light, and Robert J. Meagher
Sandia National Laboratories, USA

MP-06 **HYDROGEL ACTUATED MICRONEEDLE (HAM) WOUND PATCH** **134**
Rebecca Campbell[1], Jun Ying Tan[2], Alanis Santiago[1], Jungkwun Kim[2], and Albert Kim[1]
[1]Temple University, USA and [2]Kansas State University, USA

MP-07 **UV-BASED, IN-SITU, LOW POWER, WIRELESS SOIL CARBON MEASUREMENT SYSTEM** **138**
Steven Tran, Rabiul Hasan, Ashrafuzzaman Bulbul, Seungbeom Noh, Carlos Mastrangelo, and Hanseup Kim
University of Utah, USA

MP-08 **LEAF-MOUNTED MICRONEEDLE-BASED MULTISENSORY PLATFORM FOR MULTIPLEXED MONITORING OF PHYTOHORMONES IN LIVE PLANTS** **142**
Nafize I. Hossain and Shawana Tabassum
University of Texas, Tyler, USA

MP-09 **POLYMER AND STAINLESS STEEL-BASED 3D MICROELECTRODE ARRAYS (3D MEAS), WITH PENTA-MODAL SENSING CAPABILITIES FOR THE INVESTIGATION OF ELECTROGNIC CELLS** **146**
Charles M. Didier[1], Julia Freitas Orrico[1], Omar S. Cepeda-Torres[1,2], Aliyah Baksh[1], Jorge Manrique Castro[1], and Swaminathan Rajaraman[1]
[1]University of Central Florida, USA and [2]Polytechnic University of Puerto Rico, PUERTO RICO

MP-10 **PROGRAMMABLE MAGNETIC ROBOT (PROMAGBOT) FOR AUTOMATED NUCLEIC ACID EXTRACTION AT THE POINT OF NEED** **150**
Anthony J. Politza, Tianyi Liu, and Weihua Guan
Pennsylvania State University, USA

MP-11 **3D-PRINTED CAPSULE FOR SAMPLING LOWER DIGESTIVE TRACT MICROBIOTA** **154**
Sina Nejati, Sophie E. Schoenbrunner, Eric J. Balog, and Rahim Rahimi
Purdue University, USA

REMOVED

MP-12 **SOFT INJECTABLES USING SMART THREADS FOR DOSE-CONTROLLED DRUG DELIVERY** **158**
Mossab K. Alsaedi, Riddha Das, Hojatollah Rezaei Nejad, Atul Sharma, and Sameer Sonkusale
Tufts University, USA

MP-13 **TOWARDS DETERMINISTIC LATERAL DISPLACEMENT-BASED CONTINUOUS-FLOW MICROFLUIDIC PARTICLE REACTORS *VIA* DIRECT LASER WRITING** **161**
Adira Colton[1], Olivia M. Young[1], Talha Razaulla[2], Roseanne Warren[2], and Ryan D. Sochol[1]
[1]University of Maryland, College Park, USA and [2]University of Utah, Salt Lake City, USA

MP-14 **UTILIZATION OF VARYING TRANSIENT RESPONSE TIMES IN GRAVIMETRIC AND IMPEDIMETRIC MULTIVARIATE GAS SENSOR WITH SINGLE POLYMERIC SENSING FILM FOR ENHANCED SELECTIVITY** **165**
Steven A. Schwartz[1], Luke A. Beardslee[1,2,3], and Oliver Brand[1]
[1]Georgia Institute of Technology, USA, [2]Naval Submarine Medical Research Laboratory, USA, and [3]Emory University, USA

Physical Sensors, Actuators, or Systems

MP-15 **A 7 GHZ ACOUSTICALLY COUPLED FILTER WITH INTRINSIC SWITCHABILITY USING FERROELECTRIC SCANDIUM-ALUMINUM NITRIDE** **169**
Sushant Rassay, Dicheng Mo, and Roozbeh Tabrizian
University of Florida, USA

MP-16 **A FLEXIBLE ORIGAMI OPTO-ELECTRO ARRAY FOR IN VIVO OPTOGENETIC STIMULATION AND ELECTROPHYSIOLOGY RECORDINGS FROM DORSAL ROOT GANGLION** **173**
Yan Gong, Liu Xiang, and Wen Li
Michigan State University, USA

MP-17 **A $SC_{0.28}AL_{0.72}N$ LAMINATED BULK ACOUSTIC WAVE RESONATOR WITH SELF-OVEN-CONTROLLED SWITCHABILITY** **175**
Shaurya Dabas, Dicheng Mo, Sushant Rassay, and Roozbeh Tabrizian
University of Florida, USA

MP-18 **AN ACCURATE TEMPERATURE REGULATING SCHEME BASED ON A RESISTOR WITH TAILORED NONLINEARITY FOR EVAPORATIVE DRUG DELIVERY** **179**
Frank Goldschmidtboeing[1], Mohammadreza Saberi[1], Timo Gerach[1], Luca Conrad[1], Eiko Hager[1], Uttunga Shinde[1], Muhannad Ghanam[1], Uwe Pelz[1], Niklas Romming[2], Lasse Cornils[2], Jan Jaklin[2], Marc Kessler[2], and Peter Woias[1]
[1]University of Freiburg, GERMANY and
[2]Hauni Maschienenbau GmbH, GERMANY

MP-19 **LASER-INDUCED GRAPHENE PRESSURE SENSORS MANUFACTURED VIA INKJET PCB PRINTER** **183**
Landon Ivy[1], Ved Gund[1], Benyamin Davaji[1,2], Carlos Ospina[3], Di Ni[1], Peter Doerschuk[1], and Amit Lal[1]
[1]Cornell University, USA, [2]Northeastern University, USA, and [3]BotFactory Inc., USA

MP-21 **ETCH-HOLE FREE, LARGE GAP WAFER SCALE ENCAPSULATION PROCESS FOR MICROELECTROMECHANICAL RESONATORS** **187**
Gabrielle D. Vukasin[1], Nicholas E. Bousse[2], Anne L. Alter[3], and Thomas W. Kenny[2]
[1]Bosch LLC, USA, [2]Stanford University, USA, and [3]Apple, USA

MP-22 **IMPACT OF ASPECT RATIO ON VOLTAGE GAIN OF QUARTZ TRAPPED-ENERGY RESONATORS** **191**
Mary E. Galanko Klemash[1], Dylan Bruno[2], Tobias M. Kiebala[2], Ryan Rudy[1], Victor Farm-Guoo Tseng[1], and Sarah S. Bedair[1]
[1]Army Research Laboratory, USA and [2]Rochester Institute of Technology, USA

MP-23 **LARGE TILT-ANGLE PHOTOTHERMAL OPTICAL BEAM STEERING USING MICROPATTERNED CNT-BASED INFRARED ABSORBER ON MULTILAYER THIN FILM STRUCTURES** **195**
Harris J. Hall[1], Sean A. McDaniel[1], Fahima Ouchen[1,2], Jose L. Figueroa[1,2], David Torres[1], Piyush J. Shah[1,3], Emily M. Heckman[1], and LaVern Starman[1]
[1]Air Force Research Laboratory, USA, [2]KBR, Inc., USA, and [3]Apex Microdevices, USA

MP-24 **LOW POWER 38.4 MHZ MEMS BASED REFRENCE CLOCK FOR QUARTZ REPLACEMENT WITH LESS THAN 30 PPM FREQUENCY STABILITY** **199**
Sarah Shahraini[1], Timo Huusari[1], Somnath Kundu[1], Hao Luo[1], Parvin Akhkandi[2], Yasaman Majd[2], Eduardo Alban[1], Brent Carlton[1], Ruth Vidana Morales[1], Jason Mix[1], Reza Abdolvand[2], Mohamed Abdelmoneum[1], and Nasser Kurd[1]
[1]Intel, USA and [2]University of Central Florida, USA

MP-25 **MAGNETOHYDRODYNAMIC PROPULSION FOR MICROROBOTS** **202**
Ethan Leong and Camilo Velez
University of California, Irvine, USA

MP-26 **MICRO ENERGY HARVESTER USING ACOUSTICALLY RESONATING BUBBLE FOR BIOMEDICAL IMPLANTATION** **206**
Wenbo Li, Anthony Mercader, and Sung Kwon Cho
University of Pittsburgh, USA

MP-27 **ON THE GEOMETRY DESIGN OF ALN LAMB WAVE RESONATORS WITH PREDEFINED SHALLOW RELEASE CAVITIES** **210**
Tzu-Hsuan Hsu[1], Guan-Lin Wu[1], Yan-Ming Huang[1], Yens Ho[2], Yung-Hsiang Chen[2], Yelehanka Pradeep[3], Rakesh Chand[3], and Ming-Huang Li[1]
[1]National Tsing Hua University, TAIWAN, [2]Vanguard International Semiconductor Corporation, TAIWAN, and [3]Vanguard International Semiconductor Corporation Singapore PTE. Ltd., SINGAPORE

MP-28 **REALIZING THE WORLD'S SMALLEST GRAVIMETRIC SELF-RESETTING PARTICULATE MATTER SENSOR USING MEMS** **214**
Navpreet Singh[1], Mohannad Y. Elsayed[2], and Mourad N. El-Gamal[1]
[1]McGill University, CANADA and [2]MEMS Vision International Inc., CANADA

MP-29 **RECONFIGURABLE ARCHITECTURE EXTENDING BANDWIDTH LIMITS OF MICRO-ACOUSTIC RF FILTERS** **218**
Giuseppe Michetti and Matteo Rinaldi
Northeastern University, USA

MP-30 **TEMPERATURE-STABLE THIN-FILM LITHIUM TANTALITE-ON-SILICON RESONATORS** **222**
Yasaman Majd, Hamideh Kermani, and Reza Abdolvand
University of Central Florida, USA

MP-31 **ULTRASONIC AIR-BORNE PROPULSION THROUGH SYNTHETIC JETS** **226**
Hai Liu, Akash Roy, Yongkui Tang, Matin Barekatain, and Eun Sok Kim
University of Southern California, Los Angeles, USA

MP-32 **WIRELESS AND STAND-ALONE SUBMARINE PROPELLER BASED ON ACOUSTIC PROPULSION** **230**
Jaehoon Lee and Eun Sok Kim
University of Southern California, Los Angeles, USA

Technology, Materials, Packaging, and CAD

MP-33 **A FULLY STERILE, COST-EFFECTIVE, RAPIDLY ASSEMBLED, 3D PRINTER FOR BIOPRINTING OF ELECTROGENIC CELL CONSTRUCTS TO DEFINE FUNCTIONAL LAYERS AND ENHANCE SENSITIVITY OF CELL-BASED BIOSENSORS** **234**
Cacie Hart, Frank Sommerhage, and Swaminathan Rajaraman
University of Central Florida, USA

MP-34 **A ZINC MICRO/NANO CONDUCTIVE PASTE FOR PAPER-BASED FLEXIBLE BIOELECTRONICS** **238**
Amin Zareei, V[illegible] Kadian, and Rahim Rahimi
Purdue University, USA

REMOVED

MP-35 **CONTROLLABLE STATIC BREATH-FIGURE PROCESSES TO FORM ORDERED 3-D MICROSTRUCTURES ON POLYDIMETHYLSILOXANE WITHOUT LITHOGRAPHY AND MOLDING** **242**
Junce Cheng and Tingyi “Leo” Liu
University of Massachusetts, USA

MP-36 **MRI COMPATIBLE MULTIFUNCTIONAL CARBON NANOFIBER NEURAL PROBE** **246**
Ziqi Jia, Paritosh Rustogi, Jack W. Judy, and Yong-Kyu "YK" Yoon
University of Florida, USA

MP-37 **NON-HERMETIC PACKAGING FOR FLEXIBLE MEDICAL IMPLANTS BASED ON MULTI-STACK PARYLENE C/PDMS BILAYER THIN FILMS** **250**
Hao Chong[1,2], Steve J.A. Majerus[2], Kath M. Bogie[1,2], and Christian A. Zorman[1,2]
[1]Case Western Reserve University, USA and
[2]Louis Stokes Cleveland Veterans Affairs Medical Center, USA

MP-38 **PDMS MICROSTRUCTURES 3D-NANOPRINTED INSIDE UNCOATED, ENCLOSED PDMS-ON-GLASS MICROCHANNELS *VIA IN SITU* DIRECT LASER WRITING** **254**
Xin Xu, Olivia M. Young, Adira Colton, and Ryan D. Sochol
University of Maryland, College Park, USA

MP-39 **ROOM TEMPERATURE SEAL-RING AU-TO-AU BONDING HERMETICITY AND RELIABILITY TESTING** **258**
Amrid Amnache[1], Paul Gond-Charton[2], and Luc G. Fréchette[1]
[1]Université de Sherbrooke, CANADA and [2]Teledyne Dalsa Semiconductor, CANADA

MP-40 **STABLE, ELECTRON-BEAM SUBLIMATED, NANOSTRUCTURED SILICON DIOXIDE ON POLYCARBONATE AND STAINLESS-STEEL AS A BIOADHERENT DIELECTRIC TOWARDS NEURAL MICROPHYSIOLOGICAL SYSTEMS** **262**
Charles M. Didier[1], David Fox[1], Aliyah Baksh[1], Kevin Pollard[2], Nisha Iyer[3], Alexander Bosak[2], Yuen Yee Li Sip[1], Julia Freitas Orrico[1], Randolph Ashton[3], Michael J. Moore[2], Lei Zhai[1], and Swaminathan Rajaraman[1]
[1]University of Central Florida, USA, [2]Tulane University, USA, and [3]University of Wisconsin, USA

MP-41 **ULTRA-RAPID MICROFABRICATION OF HOLLOW-WELL MICRONEEDLES BY DIFFRACTION ULTRAVIOLET (UV) LITHOGRAPHY** **266**
Yuankai Li[1], Jun Ying Tan[1], Rebecca Campbell[2], Won Min Park[1], Albert Kim[2], and Jungkwun "JK" Kim[1]
[1]Kansas State University, USA and [2]Temple University, USA

Late News - Chemical or Biological Sensors, Actuators or Systems

MP-42 **A WEARABLE SYSTEM FOR ELECTROCHEMICAL SENSING OF SEROTONIN IN CRAYFISH** **270**
Jinjing Han, Justin M. Stine, Ashley A. Chapin, Tawen Ho, Norma Pena-Flores, Jens Herberholz, and Reza Ghodssi
University of Maryland, USA

MP-43 **GAS-PERMEABLE POLYDIMETHYLSILOXANE-ON-SILICON MEMBRANES FOR EXTRACORPOREAL MEMBRANE OXYGENATION** **272**
Benjamin Chui, David Blauvelt, Francisco Baltazar, Tariq Haniff, Jarrett Moyer, Nicholas Higgins, Peter Oishi, and Shuvo Roy
University of California, San Francisco, USA

MP-44 **IN-SITU SAMPLE PROCESSING AND ELECTROENZYMATIC SENSING FOR RELIABLE DEHYDROGENASE-BASED WEARABLE BIOMARKER MONITORING** **274**
Xuanbing Cheng, Jialun Zhu, Shuyu Lin, Sarah Forman, and Sam Emaminejad
University of California, Los Angeles, USA

MP-45 **MONITORING BIOCHEMICAL REACTIONS USING MICROSPHERICAL GLASS SHELL WHISPERING GALLERY MODE RESONATORS** **276**
Vedant Sumaria[1], Rosemary Smith[2], and Srinivas Tadigadapa[1]
[1]Northeastern University, USA and [2]University of Maine, USA

Late News - Physical Sensors, Actuators, or Systems

MP-46 **DESIGN AND EXPERIMENTAL VALIDATION OF A PIEZOELECTRIC RESONANT MEMS PHASE COMPARATOR** **278**
Mathieu Gratuze and Frédéric Nabki
École de Technologie Supérieure, CANADA

MP-47 **SIMULTANEOUS MOISTURE AND SALINITY MONITORING IN SOILS USING SPLIT RING RESONATOR (SRR) BASED SCANNING FREQUENCY TRANSMITTORY (SFT)** **280**
Sunghyun Hwang[1], William N. Carr[2], and Yong-Kyu Yoon[1]
[1]University of Florida, USA and [2]NeptuneSensor, USA

Late News - Technology, Materials, Packaging, and CAD

MP-48 **3-D PRINTED REDOX-ACTIVE ORGANIC ELECTRODES TO BRIDGE ACROSS BIOLOGY AND ELECTRONICS** **282**
Anwar Elhadad and Seokheun Choi
State University of New York, Binghamton, USA

MP-49 **ADDITIVE BATCH MICROFABRICATION OF 3D METAL ELECTROSTATIC SWITCHES TOWARDS 3D PRINTED METAL MEMS** **284**
Bhushan Lohani[1], Sheikh D. Hossain[1], Thomas Starke[2], and Robert C. Roberts[1]
[1]University of Texas, El Paso, USA and [2]3D Microprint GmbH, GERMANY

MP-50 **REGION-TARGETED BILAYER COATING TECHNOLOGY FOR INGESTIBLE DEVICES AND SYSTEMS** **286**
Michael A. Straker, Joshua A. Levy, Justin M. Stine, Vivian Borbash, Luke A. Beardslee, and Reza Ghodssi
University of Maryland, USA

Poster Presentations - Session 2

Contributed and Late News

Wednesday, June 8 2:30 pm – 5:00 pm

Chemical or Biological Sensors, Actuators or Systems

WP-01 **A SWEAT-BASED SELF-CHARGING POWER SYSTEM: INTEGRATION OF MICROBIAL ENERGY HARVESTING AND STORING DEVICES** **288**
Yang Gao and Seokheun Choi
State University of New York, Binghamton, USA

WP-02 **CHARACTERIZATION OF APTAMER FUNCTIONALIZED GOLD ELECTRODES FOR HISTONE DETECTION** **292**
Hayley Richardson[1], Jeffrey Barahona[1], Gavin Carter[1], Francis J. Miller Jr.[2,3,4], Edgar Lobaton[1], and Spyridon Pavlidis[1]
[1]North Carolina State University, USA, [2]Duke University, USA, [3]Wake Forest University, USA, and [4]Salisbury Veterans Affairs Medical Center, USA

WP-03 **DIRECT LASER WRITING OF TRIANGULAR-WALLED MICROARRAYS ONTO GLASS DIFFUSERS TO ENABLE CONTROLLED REFLECTIVITY UNDER ADAPTIVE OPTICS OPHTHALMIC IMAGING SYSTEMS** **296**
Ian Rosenthal[1,2], Lucas Garcia-O'Donnell[1], Brian Ngoh[1], Zhuolin Liu[2], Daniel X. Hammer[2], Anant Agrawal[2], and Ryan D. Sochol[1]
[1]University of Maryland, College Park, USA and [2]U.S. Food and Drug Administration, USA

WP-04 **EXPLORING MICROSPHERICAL GLASS SHELL RESONATORS FOR VOLATILE ORGANIC COMPOUNDS SENSING** **300**
Jiayuan Zhang, Vedant Sumaria, and Srinivas Tadigadapa
Northeastern University, USA

WP-05 **FLUID FORCES MODULATE CYTOKINE STIMULI FOR PERIPHERAL BLOOD MONONUCLEAR CELL ADHESION TO ENDOTHELIAL CELLS** **304**
Prashanth Sundaram, Manjusha Kulkarni, Emily Bowman,
Janelle Gabrielle, Nicholas Funderburg, and Shaurya Prakash
Ohio State University, USA

WP-06 **IN VITRO TRI-CULTURE BLOOD-BRAIN BARRIER (BBB) MODEL ENABLING DIRECT INTERCELLULAR CONTACT AT A SUSPENDED LAYER** **306**
Seungbeom Noh, Kenneth L. Monson, Vladimir Hlady, and Hanseup Kim
University of Utah, USA

WP-07 **IN-SOIL BIODEGRADABLE ZN-AIR BATTERIES** **310**
Jingwen Zhang and Mark G. Allen
University of Pennsylvania, USA

WP-08 **PAPER BASED MICROFLUIDICS INTEGRATED ELECTROCHEMICAL SENSOR FOR RAPID AND LOW-COST DETECTION OF ANALGESICS** **314**
Akshay Krishnakum[illegible] Amin Zaeeri,
Ulisses Alberto Heredia Rivera, and Rahim Rahimi
Purdue University, USA

REMOVED

WP-10 **SELF-POWERED SWEAT ION SENSOR WITH LONG DURATION ELECTROCHEMICAL POTENTIAL** **318**
Jorge A. Rodríguez and Daniela Diaz-Alonso
Center for Engineering and Industrial Development, MEXICO

WP-11 **A WIRELESS PAPER BASED SMART SENSOR FOR MEAT FRESHNESS MONITORING** **320**
Sarath Gopalakrish[illegible] Rahim Rahimi
Purdue University, USA

REMOVED

WP-12 **STRETCHABLE GLUCOSE SENSOR VIA CONJUGATED POLYMER CONFORMALLY-COATED CNT ELECTRODES PARTIALLY EMBEDDED IN PDMS** **324**
Anthony Palumbo[1], Chenguang Zhao[1], Hongjun Wang[1], Kalle Levon[2], and Eui-Hyeok Yang[2]
[1]Stevens Institute of Technology, USA and [2]New York University, USA

WP-13 **TOWARDS SINGLE-CELL PROTEOFORM PROFILING: ON-CHIP ISOELECTRIC FOCUSING IN IMMOBILIZED pH GRADIENT GELS** **328**
Gabriela Lomeli[1] and Amy E. Herr[1,2]
[1]University of California, Berkeley, USA and [2]Chan Zuckerberg Biohub, USA

Physical Sensors, Actuators, or Systems

WP-14 **3D MICROPRINTING OF MULTI-ACTUATOR SOFT ROBOTS ONTO 3D-PRINTED MICROFLUIDIC DEVICES *VIA EX SITU* DIRECT LASER WRITING** **332**
Oliva M. Young[1], Chen-Yu Chen[1], Xin Xu[1], William E. Bentley[1], Mark D. Fuge[1],
Axel Krieger[2], Paige Mass[3], Joshua P. Kanter[3], Laura Olivieri[3], and Ryan D. Sochol[1]
[1]University of Maryland, College Park, USA, [2]Johns Hopkins University, USA, and [3]Children's National Hospital & George Washington University, USA

WP-15 **A 9.4 GHZ INTRINSICALLY SWITCHABLE LAMB-WAVE RESONATOR USING ATOMIC-LAYER-DEPOSITED FERROELECTRIC HAFNIA-ZIRCONIA** **336**
Troy Tharpe and Roozbeh Tabrizian
University of Florida, USA

WP-16 **A MICROTIP EQUIPPED BIDIRECTIONAL MICROROBOT FOR NAVIGATING ON AND PENETRATING A LEAF SURFACE** **340**
Tony H. Wang, Dea Gyu Kim, Zhijian Hao, and Azadeh Ansari
Georgia Institute of Technology, USA

WP-17 **A SEMI-ANALYTICAL MODELING OF COUPLED PIEZOELECTRIC RESONATORS BASED ON SUPPORT TRANSDUCER TOPOLOGY** **344**
Chin-Yu Chang[1], Gayathri Pillai[2], and Sheng-Shian Li[1]
[1]National Tsing Hua University, TAIWAN and [2]Indian Institute of Science, INDIA

WP-18 **AN OUT-OF-PLANE WIDE BANDWIDTH MICRO-G FM ACCELEROMETER WITH DIFFERENTIAL OUTPUT** **348**
Seungyong Shin[1], Tanya Chauhan[1], Justin Matthews[1], Haoran Wen[2], and Farrokh Ayazi[1,2]
[1]Georgia Institute of Technology, USA and [2]StethX Microsystems, USA

WP-19 **DEVELOPMENT OF A SCALABLE SOFT FINGER GRIPPER FOR SOFT ROBOTS** **352**
Armin Jamali, Robert Knoerlein, Frank Goldschmidtboeing, and Peter Woias
University of Freiburg, GERMANY

WP-20 **ENHANCEMENT OF Q AND K^2 IN $AL_{0.8}SC_{0.2}N$/GAN/SAPPHIRE SURFACE ACOUSTIC WAVE RESONATORS USING SEMICONDUCTOR GROUND CONTACT** **356**
Yue Zheng[1], Jialin Wang[1], Mingyo Park[1], Ping Wang[2], Ding Wang[2], Zetian Mi[2], and Azadeh Ansari[1]
[1]Georgia Institute of Technology, USA and [2]University of Michigan, USA

WP-21 **GENERATION AND CONTROL OF INTERNAL FLOWS IN A SESSILE DROPLET BY SUBSTRATE OSCILLATION** **360**
Tianyi Zhang, Peng Zhou, Terrence Simon, and Tianhong Cui
University of Minnesota, USA

WP-22 **IN-SITU ULTRASONIC IMAGING OF PRINTED ELECTRONICS INK DEPOSITION AND CURING** **364**
Anuj Baskota[1], Landon Ivy[2], Carlos Ospina[3], Justin Kuo[1], Juneho Hwang[2], Ved Gund[2], Benyamin Davaji[2,4], Peter Doerschuk[2], and Amit Lal[1,2]
[1]Geegah Inc, USA, [2]Cornell University, USA, [3]BotFactory Inc., USA, and [4]Northeastern University, USA

WP-23 **LITHIUM NIOBATE ON SILICON LAMB MODE ACOUSTOELECTRIC WAVEGUIDE WITH 5.5 DB SUSTAINED TERMINAL GAIN** **368**
Hakhamanesh Mansoorzare and Reza Abdolvand
University of Central Florida, USA

WP-24 **WIRELESS PH SENSOR FOR SPOILAGE DETECTION MANUFACTURED IN ONE-STEP LASER ETCHING PROCESS** **372**
Jose Waimin, Sarath [illegible] and Rahim Rahimi
Purdue University, USA

REMOVED

WP-25 **MEMS RESONATOR MATCHING NETWORK FOR HIGH-SENSITIVTY SCALN PMUT-BASED ULTRASOUND RECEIVERS** **376**
Bernard Herrera Soukup, Pietro Simeoni, Gabriel Giribaldi, Luca Colombo, and Matteo Rinaldi
Northeastern University, USA

WP-26 **MODE LOCALIZATION AND TUNABLE OVERLAP IN A CLOSED-CHAIN MICROMECHANICAL RESONATOR ARRAY** **379**
Joon Hyong Cho[1,2], Michael A. Cullinan[2], and Jason J. Gorman[1]
[1]National Institute of Standards and Technology (NIST), USA and [2]University of Texas, Austin, USA

WP-27 **PHYSICALLY FLEXIBLE MULTI-LAYER LIQUID METAL-BASED BAND-PASS METASURFACE** **383**
Arkadeep Mitra[1], Kevin Xu[2], Jun H. Choi[2], and Jeong-Bong Lee[1]
[1]University of Texas, Dallas, USA and [2]University at Buffalo, USA

WP-28 **PIEZORESISTIVE MICRO-PILLAR SENSOR FOR IN-PLANE FORCE SENSING FOR BIOLOGICAL APPLICATIONS** **387**
Isha Lodhi[1], Durga Gajula[1], Devin K. Brown[1], Wilbur A. Lam[1,2,3], David R. Myers[1,2,3], and Oliver Brand[1]
[1]Georgia Institute of Technology, USA, [2]Emory University, USA, and [3]Children's Healthcare of Atlanta, USA

WP-30 **ULTRA-LOW NOISE, HIGH-SENSITIVITY MEMS ACCELEROMETER FOR SATELLITE GRAVIMETRY** **391**
Inês S. Garcia[1,2], Abdelrahman M. Elhawash[1], Jorge Cabral[2], Tiago Hormigo[3], João T. da Encarnação[4,5], Filipe S. Alves[1,2], and Rosana A. Dias[1]
[1]International Iberian Nanotechnology Laboratory (INL), PORTUGAL, [2]University of Minho, PORTUGAL, [3]Spin.Works S.A., PORTUGAL, [4]Delft University of Technology, NETHERLANDS, and [5]University of Texas, Austin, USA

WP-31 **WAFER-LEVEL HIGH-ASPECT-RATIO DEEP REACTIVE ION ETCHING OF 4H-SILICON CARBIDE ON INSULATOR SUBSTRATES** **395**
Ardalan Lotfi[1], Micheal P. Hardin[1], Zhenming Liu[1], Alex Wood[2], Chris Bolton[2], Kevin Riddell[2], Huma Ashraf[2], Joanne Carpenter[2], and Farrokh Ayazi[1]
[1]Georgia Institute of Technology, USA and [2]SPTS Technologies – A KLA Company, UK

WP-32 **ZERO-POWER MULTI-THRESHOLD TEMPERATURE SENSOR BASED ON SHAPE MEMORY ALLOY ANTENNA** **399**
Wenxin Zeng, Wei Wang, and Sameer Sonkusale
Tufts University, USA

Technology, Materials, Packaging, and CAD

WP-33 **A MODULAR MICROFABRICATION APPROACH WITH MULTI-LAYER MICROPILLAR 3D INTERCONNECTS, UTILIZING DLP 3D PRINTING TOWARDS 3D MICROELECTRODE ARRAYS AND COMPLEX MICROSYSTEMS** **403**
Charles M. Didier, Avra Kundu, and Swaminathan Rajaraman
University of Central Florida, USA

WP-34 **CONSTANT PHASE ELEMENT (CPE) MODELING AND ANALYSIS OF MULTI-MATERIAL, MICRO-BULLET SHAPED, HIGH-THROUGHPUT 3D MICROELECTRODES FOR *IN-VITRO* ELECTROPHYSIOLOGICAL APPLICATIONS** **407**
Jorge Manrique Castro and Swaminathan Rajaraman
University of Central Florida, USA

WP-35 **MECHANICAL SENSING TOWARDS 3D-PRINTED WEARABLES** **411**
Sonia F. Roberts[1], Jack Forman[2], Hiroshi Ishii[2], and Kristen L. Dorsey[1,2]
[1]Northeastern University, USA and [2]Massachusetts Institute of Technology, USA

WP-36 **MULTIFUNCTIONAL 3D PRINTED $BATIO_3$ PLATONIC SOLIDS PACKAGING FOR IMPLANTABLE MICRODEVICES** **415**
Sayemul Islam[1], Sumnoon Ahmed[1], Alanis I. Santiago[1], Michael Domic[1], Jungkwun Kim[2], Seung H. Song[3], and Albert Kim[1]
[1]Temple University, USA, [2]Kansas State University, USA, and [3]Sookmyung Women's University, KOREA

WP-37 **PAPERTRONICS: FULLY PAPER-INTEGRATED RESISTOR, CAPACITOR, AND TRANSISTOR CIRCUITS** **419**
Mya Landers, Anwar Elhadad, and Seokheun Choi
State University of New York, Binghamton, USA

WP-38 **PIEZOELECTRIC PAPER: LARGE-SCALE COMPATIBLE MANUFACTURING PROCESS AND SENSOR DEMONSTRATION** **423**
Kanagasubbulakshmi Sankaralingam, Ninweh Nina Jeorge, Sajana Sumanasinghe, Anindya L. Roy, Konrad Walus, and Boris Stoeber
University of British Columbia, CANADA

WP-39 **SCALABLE AND VERSATILE FABRICATION OF OPAL STRUCTURES WITH SLOPE SELF-ASSEMBLY AND CAPILLARY PEELING FOR MICRODEVICES AND SENSORS** **427**
Carlos D. Díaz-Marín[1], Diane Li[1], Samantha Cheung[1], Cameron Kilpatrick[2], Rishabh Shetty[1], Geoffrey Vaartstra[1], Ashwin Gopinath[1], and Evelyn N. Wang[1]
[1]Massachusetts Institute of Technology, USA and [2]Stanford University, USA

WP-40 **ULTRA FLEXIBLE MACROPOROUS MICRONEEDLES FOR SUSTAINED DELIVERY OF (2R,6R)-HYDROXYNORKETAMINE** **431**
Riddha Das[1], Aydin Sadeqi[1], Caroline A. Browne[2], Irwin Lucki[2], and Sameer Sonkusale[1]
[1]Tufts University, USA and [2]Uniformed Services University of Health Sciences, USA

Late News - Chemical or Biological Sensors, Actuators or Systems

WP-41 **A MOLECULAR IMPRINTED POLYMER (MIP)-BASED NT-PROBNP SENSING ELECTRODE USING LG9 PEPTIDES FOR HEART FAILURE MONITORING** **434**
Liang-Kai Wanf[1], Chih-Hung Lin[1], Yu-Ting Cheng[1], Hsiao-En Tsai[2], and Chih-Kuo Lee[2]
[1]National Yang Ming Chiao Tung University, TAIWAN and [2]National Taiwan University Hospital Hsin-Chu Branch, TAIWAN

WP-42 **HEAVY METAL SENSING IN VEGETABLE AND SOIL SOLUTIONS USING CARBON FIBER ELECTRODE** **436**
G M Hasan Ul Banna[1], James Siegenthaler[2], Romilly Benedict[1], Wei Zhang[1], and Wen Li[1,2]
[1]Michigan State University, USA and [2]Fraunhofer USA Center Midwest, USA

WP-43 **RAPID COST-EFFECTIVE PLOTTER CUT STENCIL MASKS FOR THE DEPOSITION OF ORGANIC AND INORGANIC MATERIALS AND THE CREATION OF A NEW ANTIBIOTIC DIFFUSION TEST FOR MINIMAL LETHAL CONCENTRATION DETECTION** **438**
Andre Childs, Jorge Pereira, Aliyah Baksh, Charles M. Didier, Edwin Davidson, Swadeshmukul Santra, and Swaminathan Rajaraman
University of Central Florida, USA

WP-44 **SCALING EFFECTS OF INKJET MICROFABRICATED 3D GOLD ELECTROCHEMICAL SENSORS FOR AQUEOUS LEAD DETECTION** **440**
Annatoma Arif, Bertha J. Chavez, Sheikh D. Hossain, and Robert C. Roberts
University of Texas, El Paso, USA

WP-45 **SMART ELECTROPALATOGRAPHY THIN-FILM FLIXIBLE PRESSURE SENSOR ARRAY FOR LINGUISTIC AND MEDICAL APPLICATIONS** **442**
Saeyeong Jeon, Ziqi Jia, Sunghyun Hwang, Suk-il Choi, Jiho Han, and Yong-Kyu Yoon
University of Florida, USA

WP-46 **THEORETICAL AND EXPERIMENTAL VALIDATION ON THE TUNING CAPABILITY OF A PERCOLATION-BASED GAS SENSOR** **444**
Farhan Sadik Sium, Shakir ul Khan, Seungbeom Noh, and Hanseup Kim
University of Utah, USA

Late News - Physical Sensors, Actuators, or Systems

WP-47 **A 17.3 GHZ ATOMIC-LAYERED HZO SOLIDLY MOUNTED RESONATOR: TOWARDS CMOS-BEOL MM-WAVE FREQUENCY CONTROL** **446**
Troy Tharpe, Shaurya Dabas, Dicheng Mo, and Roozbeh Tabrizian
University of Florida, USA

WP-48 **CO-RESONANT CANTILEVERS FOR MATERIALS RESEARCH AND SENSOR APPLICATIONS** **448**
Julia Körner
Leibniz University Hannover, GERMANY

WP-49 **FOCUSING OF A RELATIVISTIC ELECTRON BEAM WITH A MICROFABRICATED QUADRUPOLE MAGNET** **450**
Benjamin A Pound, Sophie Crisp, Alexander Ody, Pietro Musumeci, James Rosenzweig, and Robert Candler
University of California, Los Angeles, USA

WP-50 **INCREASING ELECTRORHEOLOGICAL RESPONSE IN HYDRAULIC ACTUATORS VIA SCALABLE MICROPATTERNED ELECTRODES** **452**
Chastity M. Kelly[1], Ashkan Ghanavati[1], Peter G. Kelly[2], and Carol Livermore[1]
[1]Northeastern University, USA and [2]Markforged, Inc, USA

Poster Presentations - Session 3

Commercial, Invited Open Posters, and Open Posters
Wednesday, June 8 6:30 pm – 7:30 pm

Invited Open Posters

WIOP-01 **AUTOMOTIVE MEMS ACCELEROMETER DESIGN VERIFICATION USING NONLINEAR COMPACT MODELING** **454**
Shaikh Md Rubayiat Tousif[1], Brian Van Dyk[2], and Aaron Geisberger[1]
[1]NXP Semiconductors Inc., USA and [2]Coventor, Inc., A Lam Research Company, USA

WIOP-02 **EXPLORE MEMS SWITCH FOR HIGH POWER AC/DC APPLICATIONS** **456**
Xu Zhu, Jim Terazawa, Chris Nassar, Michael Comstock, and Chris F. Keimel
Menlo Microsystems, Inc, USA

WIOP-03 **HYDROGEN GETTERS FOR MICROELECTRONICS PACAKING RELIABILITY IMPROVEMENT** **458**
Hua Xia, Jeffery Vriens, and David DeWire
Hermetic Solutions Group, LLC, USA

WIOP-04 **LOW-POWER MULTI-ELEMENT GAS SENSOR MANUFACTURED BY MICROCHANNEL PARTICLE DEPOSITION**
Serhii Mytnyk, Victoria Shalabaeva, Thomas Russell, and Marnix Rebergen
Mesoline, NETHERLANDS

Commercial Posters

WCP-01 **ENRICHING LIVES WITH PERFORMANCE SENSING**
Stephen F. Bart[1], Nishit Goel[2], Leonardo Baldasarre[3], Ilya Gurin[1], and Peter Hartwell[1]
[1]TDK - Invensense, USA, [2]TDK - Invensense, ITALY, and [3]TDK - Invensense, INDIA

WCP-02 **CUSTOMIZED MEMS SOLUTIONS FROM PROTOTYPE TO PRODUCTION VOLUMES**
James Walker[1], Arne Leinse[2], and Douwe Geuzebroek[2]
[1]LioniX International, USA and [2]LioniX International, NETHERLANDS

WCP-03 **EXPANDING THE WORLD OF MEMS THROUGH FLAT PANEL FABS**
Kimberly L. Harrison and Alissa M. Fitzgerald
A.M. Fitzgerald & Associates, LLC, USA

WCP-04 **FULL OPTICAL CHARACTERIZATION OF MEMS REAL-TIME DYNAMICS AND 3D TOPOGRAPHY**
David F. Oliver[1], Eric Lawrence[1], Marcus Winter[2], Markus Heilig[2], and Heinrich Steger[2]
[1]Polytec, Inc., USA and [2]Polytech GmbH, GERMANY

WCP-05 **FULL-FIELD VIBRATION MODE SHAPE AND TRANSIENT ANALYSIS BY 4D DIGITAL HOLOGRAPHIC MICROSCOPE (DHM®)**
Shenqi Xie, Frank Liu, and Yves Emery
Lyncée Tec, SWITZERLAND

WCP-06 **IMPROVING YOUR UNDERSTANDING OF ADVANCED MEMS DESIGN PROBLEMS: FASTER DESIGN AND SIMULATION FOR BETTER RELIABILITY, MANUFACTURING AND PERFORMANCE**
Christopher Welham[1], Arnaud Parent[1], Brian Van Dyk[2], and Hideyuki Maekoba[3]
[1]Coventor, A Lam Research Company, FRANCE, [2]Coventor, A Lam Research Company, USA, and [3]Coventor, A Lam Research Company, JAPAN

WCP-07 **LOWERING BARRIERS TO MICROSYSTEMS INNOVATION**
Andrew Fung, Qader Qureshi, and Gord Harling
CMC Microsystems, CANADA

WCP-08 **MASKLESS LITHOGRAPHY**
Rick Trevino
Heidelberg Instruments Inc., USA

WCP-09 **NATIONAL NANOTECHNOLOGY COORDINATED INFRASTRUCTURE (NNCI)**
Oliver Brand, David S. Gottfried, and Paul J. Joseph
Georgia Institute of Technology, USA

WCP-10 PDKS (PROCESS DESIGN KITS) FOR PIEZO-ELECTRIC MEMS FABRICATION PROCESSES INCLUDING MANUFACTURING VARIATIONS IN DEVICE DESIGNS
Mary Ann Maher
SoftMEMS LLC, USA

WCP-11 REDUCED ORDER MODELING FOR MEMS
Philipp Jan Mehner, David Kriebel, and Jan Edgar Mehner
I-ROM GmbH, GERMANY

WCP-12 SILICON MATTERS - IMPORTANCE OF SILICON SPECS WHEN GROWING THERMAL OXIDE
Cat Nylund and Kat Anaya
Rogue Valley Microdevices, USA

WCP-13 VARIOUS PZT THIN FILMS FOR MEMS ACTUATORS, SENSORS, AND TRANSDUCERS
Hiroshi Miyajima[1], Mario Kiuchi[1], Yukitaka Yamaguchi[1], Takashi Ikeda[2], and Gen Matsuoka[1]
[1]Sumitomo Precision Products, Co., Ltd., JAPAN and [2]Silicon Sensing Products, Ltd., JAPAN

WCP-14 ELECTROPHYSIOLOGY ENABLED BIOSENSORS
Frank Sommerhage[1], David W. DeRoo[1], and Swami Rajaraman[2]
[1]Primordia Biosystems, USA and [2]University of Central Florida, USA

WCP-15 THERE'S NOT MUCH ROOM LEFT AT THE BOTTOM - NANOPOWER MOTION SENSING USING THE ADXL367
Tzeno Galchev
Analog Devices, Inc., USA

MICROSENSOR MEASUREMENT OF EVOKED COMPOUND ACTION POTENTIALS IMPROVES SPINAL CORD STIMULATION CLINICAL EFFECTIVENESS AND LONG TERM EFFICACY

Lawrence Poree
University of California, San Francisco, USA

INTRODUCTION:

Evoked compound action potential (ECAP) recording provides an objective measure of spinal cord (SC) activation during SCS and can assist in programing of the SCS system. Real-time ECAP-controlled Closed-Loop SCS, in which the stimulation output is automatically adjusted to significant improvement in an open-label study.

OBJECTIVE:

This double-blind randomized controlled trial (RCT) was conducted to compare the safety and efficacy of real-time ECAP-controlled closed-loop stimulation (investigational group) with open-loop (fixed output) stimulation (OL, control) to treat chronic back and leg pain.

METHODS:

134 subjects were enrolled and randomized after trial leads were implanted. The target ECAP amplitude was recorded on the same lead as the stimulating electrode was set in the clinic and maintained either manually by the patient (OL) or by a computer controlled feedback closed-loop control (CL) mechanism (Fig 2). The primary endpoint evaluated ≥50% reduction in overall back and leg pain measured by the Visual Analog Scale (VAS). Opioid usage and other patient-reported outcomes (PROs) including emotional/physical functioning, sleep quality, and quality of life were also collected. Additionally, objective neurophysiological data, including SC activation and time spent in the therapeutic range, were collected.

RESULTS:

Herein the Evoke Study Group reports the 24-month outcomes from this ongoing RCT. The proportion of implanted subjects with ≥50% overall back and leg pain reduction at 24 months was statistically superior in the EVOKE Closed-loop (CL) vs. Open-loop (OL) group (84.0% vs. 65.9% subjects, respectively; p=0.040) (Fig 3). Long-term improvements in all other PROs, including POMS, ODI, PSQI, EQ-5D-5L, and SF-12, were also demonstrated. In addition, the patient/physician identified target ECAP amplitude during programming was the same for both groups, however, the OL group was unable to maintain this ECAP target in the outpatient setting (Fig. 4). The most frequent level of SC activation was three times greater for CL (median ECAP Amplitude: 22.5µV CL vs. 7.5µV OL).

SC activation was better maintained within the therapeutic range with EVOKE CL (median: 93.9% CL vs. 46.1% OL). There were no differences in the safety profiles between treatment groups, and the type, nature, and severity of adverse events were similar to other SCS studies.

CONCLUSION:

In this ongoing study, ECAP-controlled closed-loop spinal cord stimulation provided statistically superior pain relief and greater improvement in all other measures compared with the open-loop group at 3,6, 12 and 24 months. This significant improvement in clinical outcomes is consistent with the CL group being able to better maintain the targeted spinal cord activation level as measured by stability in the ECAP amplitudes.

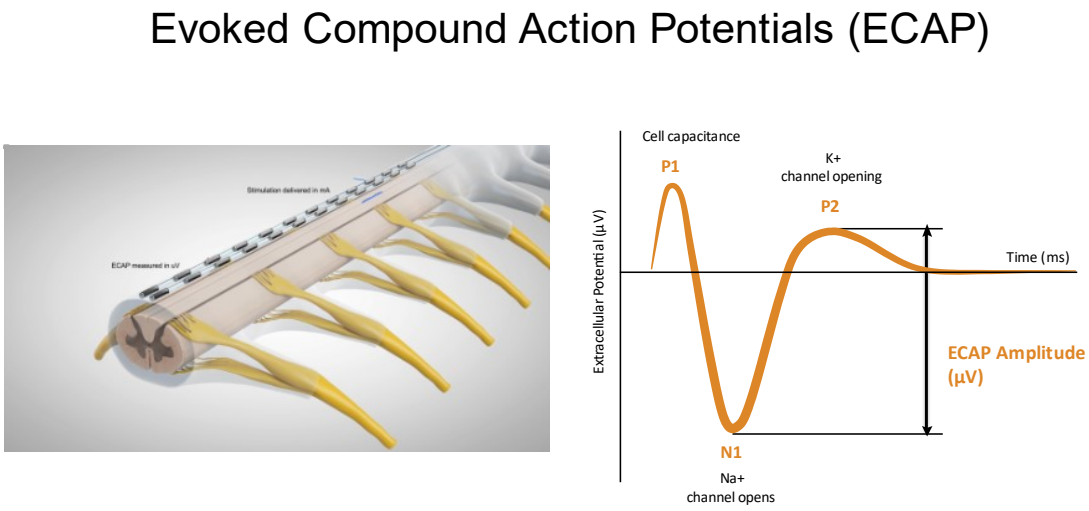

Figure 1.SCS leads with stimulating and recording capabilities used to measure ECAP potentials.

Copyright retained by Authors

Solid-State Sensors, Actuators, and Microsystems Workshop
Hilton Head Island, South Carolina, June 5-9, 2022

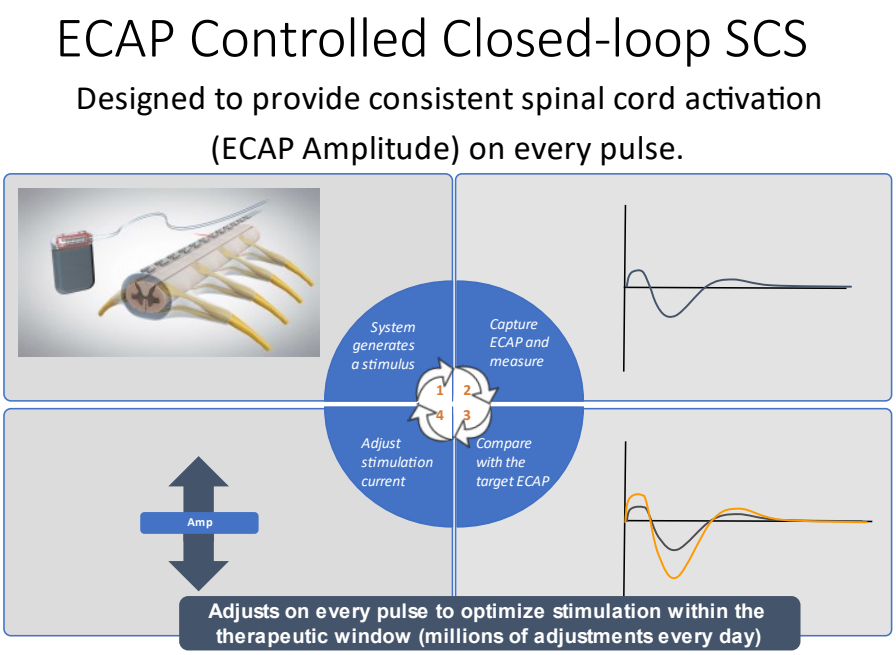

Figure 2: Computer controlled ECAP controlled closed-loop SCS automatically adjusts current output to maintain a constant ECAP amplitude.

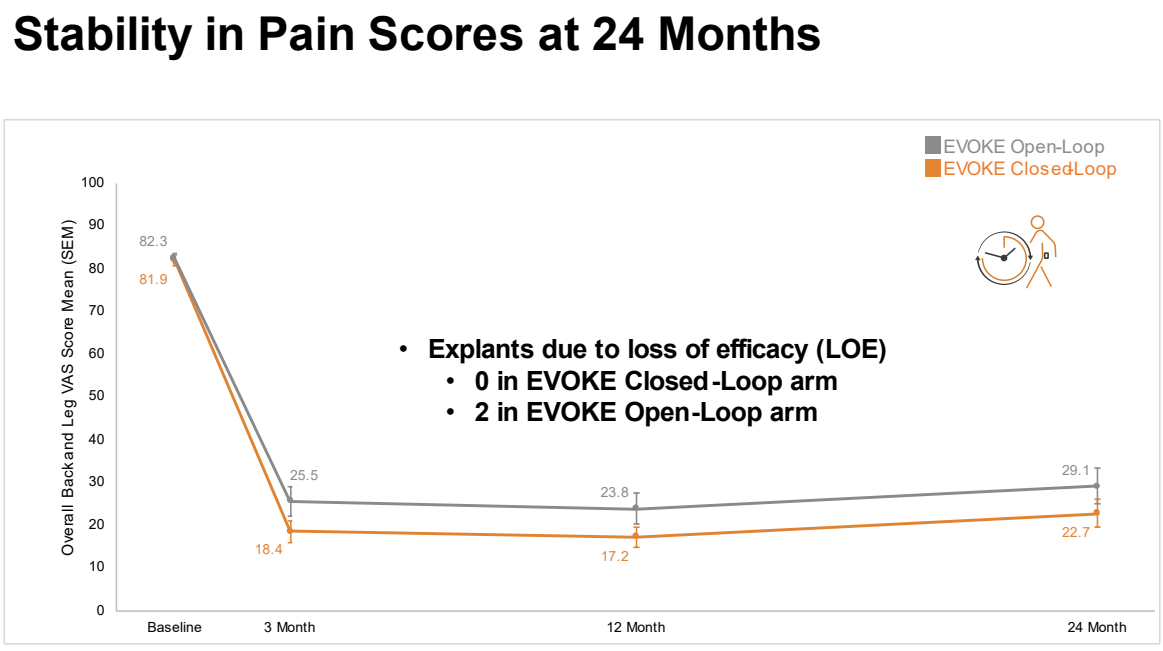

Figure 3: Both Open-loop and Closed-loop reduce pain scores with CL showing superiority

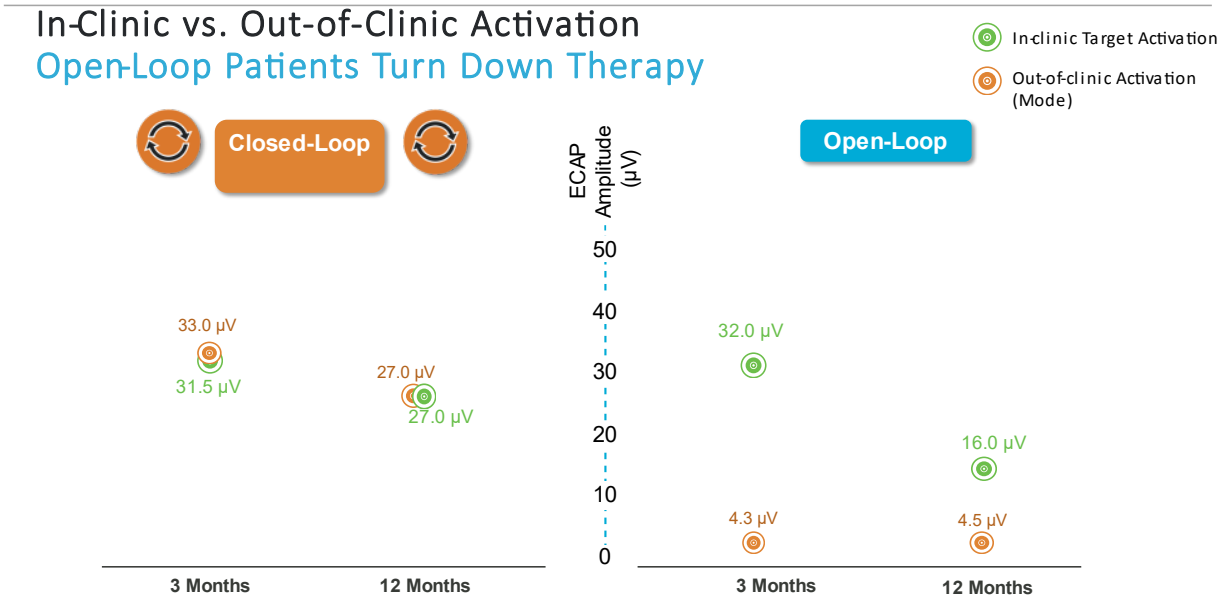

Figure 4: Closed-loop but not Open-loop group was able to maintain the target ECAP level in the clinic and well as in the out clinic environment.

page left blank intentionally

A PASSIVE WIRELESS DIFFERENTIAL SENSOR FOR IN-SITU EARLY DETECTION OF PERIPROSTHETIC JOINT INFECTION

Jiaxin Jiang[1], Krithika Sureshkumar[1], Chandrashekhar Choudhary[1], Tristan Kerkes[1], H. Claude Sagi[2], Chia-Ying Lin[2], Michael T. Archdeacon[2], and Tao Li[1#]*

[1]Department of Electrical Engineering and Computer Science, University of Cincinnati, USA

[2]Department of Orthopaedic Surgery, University of Cincinnati, USA

ABSTRACT

This paper reports, for the first time, an implantable, passive wireless biosensor for *in situ* early detection of periprosthetic joint infection utilizing the magnetoelastic (ME) transduction mechanism combined with antibody-functionalization to target specific types of bacteria. A novel differential sensor configuration is introduced to distinguish the effects of target bacteria from variations caused by the surrounding medium. Differential operation of the sensor was successfully tested for mass detection in various media (air, water, standard 5cSt fluid, and paraffin oil), demonstrating effective elimination of medium effect by subtracting reference sensor outputs. A triangular geometry is adopted for the sensor design, replacing traditional rectangular shapes used in ME immunosensors to enhance the mass sensitivity and facilitate early infection detection. *In vitro* tests for proof of concept were carried out using single sensors in both rectangular and triangular shapes in *E. coli* suspension and PBS control solution, and successfully demonstrated a 2.63× improvement in mass sensitivity for the triangular sensors.

KEYWORDS

Magnetoelastic sensor, implantable device, resonant sensor, bacteria detection, mass loading, viscosity

INTRODUCTION

With an aging population, the increased number of total knee arthroplasty surgeries has been accompanied by a commensurate increase in revision surgeries – a large proportion of which are directly attributable to periprosthetic joint infection (PJI) [1]. The socioeconomic burden associated with PJI is not insignificant, with an estimated cost of up to $50k/patient and $250 million/year in the US [2]. To date, there is not one unanimously accepted approach for the diagnosis of PJI. Earlier studies have reported serum biomarkers and reduction in viscosity of microbial culture of synovial fluids as criteria to evaluate the infection progression [3-4]. However, the time required for these factors to reach levels sufficient for diagnosis is associated with further accumulation of pathogen and worsening infection. A wireless miniature biosensor that can enable real-time, *in vivo* detection of target bacteria, particularly during the early stages of infection (e.g. 48-72 hours after surgery), is thus highly desirable. Presently there is only limited research reported in this area. A hydrogel has been investigated for antigen sensitivity, intended to be integrated with an LC circuit for use as a wireless sensor for early detection of surgical site infection [5].

Magnetoelastic (ME) transduction has been employed in a broad range of sensing applications such as stress/strain measurements [6-7], pH sensing [8], cell growth monitoring [9], metal ion detection [10], and immunoassay for pathogens [11-12] and biomarkers [13]. With inherent passive wireless characteristics, ME sensors are highly suitable for implantable applications such as integration with orthopedic implants to monitor possible structural failures [14] and with biliary stents to monitor sludge accumulation and restenosis [15].

This paper reports an implantable, passive wireless biosensor for integration with a knee arthroplasty implant for *in situ* early detection of PJI. The sensor uses the ME transduction mechanism to enable passive wireless interrogation without the need for an antenna or local power source. Antibodies are immobilized on the sensor to target specific types of bacteria. Compared with existing ME immunosensors, a novel differential sensor configuration is used to distinguish the effects of target bacteria from variations caused by the surrounding medium. To enhance mass sensitivity and facilitate early infection detection, a triangular geometry is adopted for the sensor design, replacing traditional rectangular shapes used in ME immunosensors. *In vitro* tests for proof of concept have been performed for *Escherichia coli* (*E. coli)* detection and the measurement results are reported.

DEVICE DESIGN

The concept of the ME biosensor for *in situ* early detection of PJI is illustrated in Fig. 1. The wireless miniature ME biosensor is functionalized with antibodies targeting specific types of bacteria and mounted in a biocompatible package for integration into a recess on the prosthetic knee joint. The package, which has anchors to suspend the sensor inside, can prevent physical interference from tissue surrounding the implant area while allowing exchange of fluid through perforations on the package lid. The sensor is wirelessly interrogated using external coils that are interfaced with an external unit for sensor excitation and signal readout.

The working principle of the sensor for bacteria detection is shown in Fig. 2. A time-varying magnetic field from a transmit coil excites the ME sensor to produce a longitudinal vibration, which generates a magnetic flux with a resonance frequency that varies with changes in the mass and medium in contact with the sensor

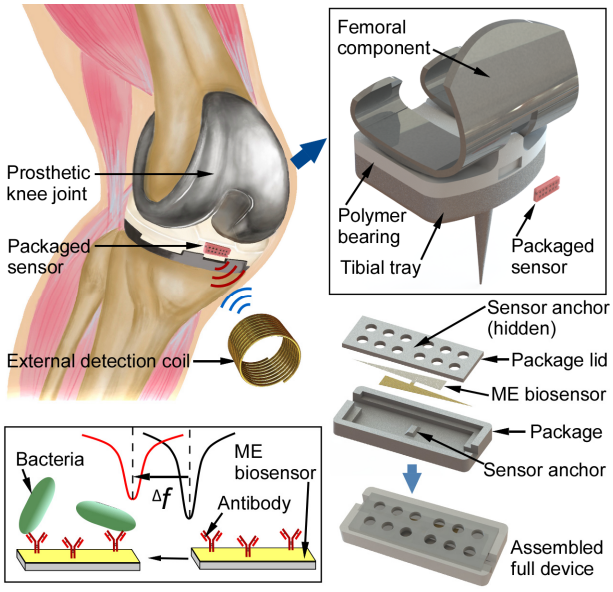

Figure 1: Device concept diagram of wireless biosensor for early PJI detection.

978-1-940470-04-7/HH2022/$25©2022TRF
DOI 10.31438/trf.hh2022.1

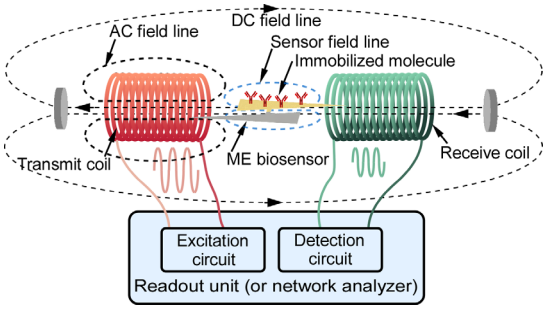

Figure 2: Schematic diagram showing detection and wireless readout methods of differential ME biosensor for bacteria detection. Network analyzer was used as readout unit for proof-of-concept experiments.

[16]. This flux can be detected wirelessly with a receive coil to measure the resonance frequency. Alternatively, a single coil can be used for both excitation and readout using signal reflection.

When a small amount of mass Δm is applied on the ME sensor of an initial mass M, the resonance frequency shift Δf can be derived from relationships given in [17] as

$$\Delta f = -\frac{\Delta m}{4LM}\sqrt{\frac{E}{\rho(1-\upsilon^2)}} \quad (1)$$

where L is the length of the sensor, E, ρ and υ are the Young's modulus, density and Poisson's ratio of the ME material, respectively.

ME sensors have been used as wireless high-performance immunosensors for *in vitro* applications, typically in an aqueous medium [11-13,18]. Changes in the medium properties and conditions such as temperature, density, viscosity, and pH, can cause significant changes in the resonance frequency of the ME immunosensors; therefore, these parameters are usually controlled carefully to maintain the sensor performance for immunoassay under *in vitro* conditions. However, for the targeted *in vivo* application, the properties of the surrounding body fluid, particularly the viscosity and density, can change at any time. To eliminate the effect of the surrounding medium, a novel differential sensor consisting of two ME sensors is utilized: one with, and the other without functionalized antibodies. The element without functionalization is used as a reference. When target bacteria are present in the medium and become bound to the antibodies, mass loading is applied only to the sensing element and any common mode changes such as those of the medium properties are eliminated by subtracting the outputs of the sensing and reference elements.

Mass sensitivity is defined as the frequency shift caused by a unit amount of mass loading. Higher mass sensitivity is desirable to provide a larger frequency shift for a given amount of mass loading, which is particularly important for the detection of bacteria during early stages of infection when the bacteria concentration is relatively low. It has been shown previously that the geometry of a ME sensor can affect its magnetic domain distribution; geometries with sharp corners can result in small magnetic domains, leading to stronger vibration and higher sensitivity [19]. As one of the methods investigated for mass sensitivity enhancement, triangular geometry is selected for the sensor design instead of the traditional rectangular geometry that has been commonly used for ME immunosensors.

The geometric design of the differential ME sensor is shown in Fig. 3, along with simulation results obtained using the COMSOL® Multiphysics software. A length difference of 0.6 mm between the sensing and reference elements is used to help separate the resonance frequency peaks of the two elements during signal readout. A spatial separation of 0.6 mm is also used to reduce the magnetic flux coupling between the two elements while keeping the

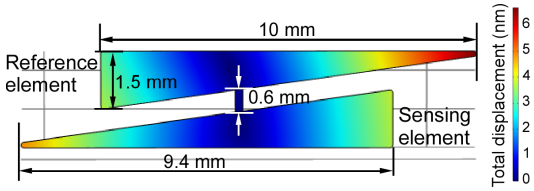

Figure 3: COMSOL® Multiphysics simulation of differential sensor configuration. Smaller displacement is observed for sensing element due to mass loading.

structure compact. A joint anchor that connects the two elements is placed at the 2/5 position from the base of each triangle where it is close to the null vibration point of the geometry. The simulation results shown in Fig. 3 along with others helped verify the differential sensor design as well as the improvement in mass sensitivity using the triangular geometry.

DEVICE FABRICATION

Ribbons of amorphous metallic glass (Metglas® 2826MB, $Fe_{45}Ni_{45}Mo_7B_3$ alloy from Metglas Inc.) were used as the ME material for sensor fabrication. The differential ME sensors were fabricated using an in-house high precision micro electro-discharge machine (Smaltec® EM203 µEDM). A 50 nm thick Cr layer followed by an 80 nm thick Au layer was then deposited on the sensing element of the differential sensors using e-beam evaporation with the reference element protected from deposition using photoresist. The Au surface provides a critical biocompatible layer for antibody immobilization while Cr serves as an adhesion layer with a larger-than-usual thickness to accommodate the surface roughness of the ME material.

Surface functionalization was performed by forming a self-assembled monolayer (SAM) on the Au surface using cysteamine (CYSTE) and then immobilizing antibodies on the SAM using crosslinking agents of N-(3-Dimethylaminopropyl)-N'-ethylcarbodiimide (EDC) and N-hydroxysulfosuccinimide (Sulfo-NHS) [20]. For this work, lyophilized cells of strain K12 *E. coli*, Sulfo-NHS, and bovine serum albumin (BSA) were purchased from Sigma Aldrich; CYSTE (98%), rabbit anti-*E. coli* polyclonal antibody, goat anti-rabbit antibody conjugated with Alexa Fluo® 488, and EDC were acquired from Fisher Scientific.

The functionalization procedure began with thorough cleaning

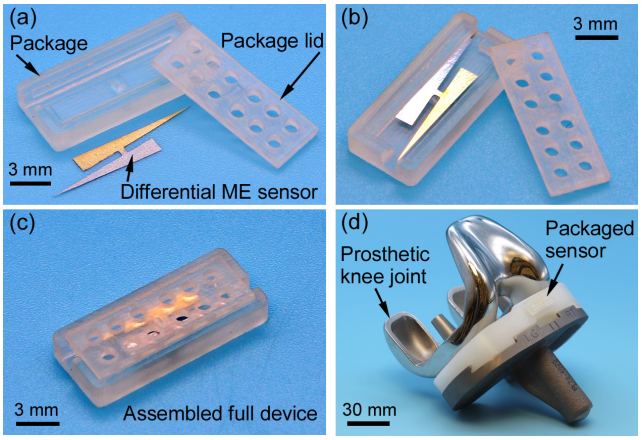

Figure 4: (a) Differential ME sensor (Metglas 2826MB) and package components (3D printed from VisiJet M3 resin); (b) sensor integrated on anchor inside package; (c) fully assembled device; (d) packaged device attached to prosthetic knee joint for demonstration of an intended integration site.

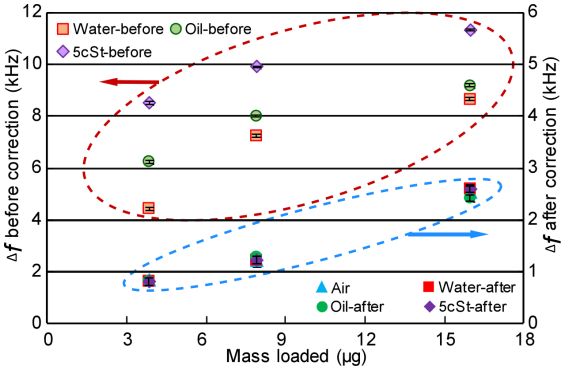

Figure 5: Measurement results showing characterization of differential ME biosensor for mass detection (ink coating) in different media and the effectiveness of eliminating medium effect on sensor response. The same mass loading generated different frequency shifts in various media before correction, which were effectively eliminated by subtracting reference element outputs. (Error bars too small to see. N=5)

of the ME sensors in an ultrasonic cleaner with a sequential use of acetone, IPA and DI water. The sensors were then immersed in a 20 mM CYSTE solution for 24 h to deposit the SAM. Anti-*E. coli* antibodies (2 μg/mL) were activated in a solution containing 0.01 mM EDC and 0.02 mM Sulfo-NHS for 2 h at 37°C. After washing with phosphate buffered saline (PBS, pH 7.4) to remove CYSTE molecules that did not adhere well, the ME sensors were soaked in the activated antibody solution to immobilize the antibodies on the sensors. Loosely bonded antibodies were removed by washing with PBS. To prevent non-specific binding during bacterial detection, the antibody-coated biosensors were further treated with a 1% w/w BSA solution for 30 min, rinsed with PBS to remove unbound BSA, and then dried under a nitrogen stream to make it ready for testing.

The package with perforated lid for the ME sensor was made by 3D printing from a biocompatible resin (VisiJet® M3). As shown in Fig. 4, two anchors in the package, one on the lid and the other on the inside bottom surface of the package, are used to clamp the differential sensor in the joint area, thus suspending it to prevent interference of the sensor vibration or blockage of the sensor functional surface. The packaged sensor can then be integrated in a recess formed on the prosthetic knee joint.

EXPERIMENTAL RESULTS

For all sensor experiments described below, two 40-turn coils of a 3/4 inch diameter made from 28 AWG magnet wire were used as the transmit and receive coils, respectively. A network analyzer (Keysight® E5061B) was connected to the two coils for sensor interrogation. The power of the excitation output from the network analyzer was 5 dBm and the received signal was processed by the network analyzer to generate the frequency response and thus the resonance frequency of the ME sensors.

Experiments were performed to verify the differential operation of the ME sensor and its capability to effectively eliminate the effect of varying medium properties. For these tests, mass loading was applied by coating multiple layers of ink on the sensing element of the differential sensors. The sensors were first tested in air to generate the baseline response and then tested in three different media (water, standard 5 cSt fluid, and paraffin oil) to emulate the impact of varying density and viscosity of the medium. The reference element outputs were scaled to correct for the frequency difference caused by the length mismatch in the sensor design, and then subtracted from the sensing element outputs to cancel the

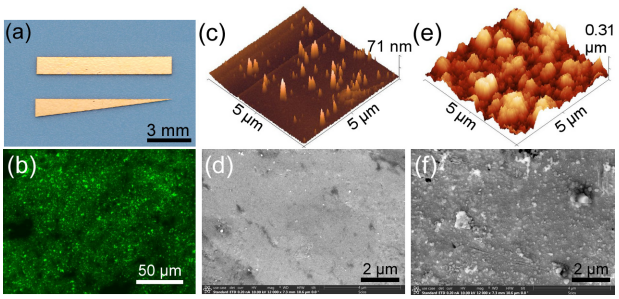

Figure 6: ME biosensor functionalization. (a) Photos of ME biosensors used for in vitro tests; (b) fluorescence microscopic image after antibody immobilization; (c) AFM and (d) SEM images of bare gold surface; (e) AFM and (f) SEM images after antibody immobilization.

medium effect. As demonstrated by the measurement results in Fig. 5, the same mass loading generated different frequency shifts in various media before correction (data points inside the red dashed circle). This can lead to serious discrepancy when interpreting the frequency response caused by mass loading. By subtracting the scaled outputs from the reference element in each medium, the medium effect was effectively eliminated (data points inside the blue dashed circle), demonstrating the validity of the differential sensor mechanism.

Imaging techniques including scanning electron microscope (SEM), atomic force microscope (AFM) and fluorescence microscope were used to verify the efficacy of surface functionalization on the ME sensor. As shown in Fig. 6 (c-d) and (e-f), the surface roughness of the sensor increased from 3.2 nm Ra on the bare gold surface to 62.7 nm after antibody immobilization. A secondary fluorescent antibody (goat anti-rabbit antibody conjugated with Alexa Fluo 488) was used to check the coverage of the primary antibody on the ME sensor using the Olympus IX81 microscope. The solution with the secondary antibody was diluted to a concentration of 4 μg/mL with PBS and then incubated with the functionalized ME biosensors. The fluorescent image in Fig. 6(b) verified the successful immobilization of the primary antibody on the sensor with satisfactory coverage.

In vitro tests were carried out for proof of concept for the detection of *E. coli* using single sensors. Both rectangular and right-angle triangular sensors with dimensions of 10 mm (L) × 1.5 mm (W) × 30 μm (T) were tested to demonstrate the improvement in sensitivity. Each ME sensor was first tested in 1 mL PBS solution for 30 minutes as control. Then 10 μL of *E. coli* suspension was added to the PBS solution and the resonance frequency was monitored for 50 min using a LabView program developed for data recording from the network analyzer. The concentration of the *E. coli* suspension was 8×10^6 cfu/mL determined by plate count. The test was repeated using 5 sensors and the results were averaged (N=5).

The *in vitro* test results for *E. coli* detection are plotted in Fig. 7. The control data was stable with a negligible frequency shift of <10 Hz. An average frequency shift of 97 Hz was obtained for the rectangular sensors during the testing period and 129 Hz for the triangular sensors. By estimating the number of *E. coli* cells attached to the sensor surfaces and assuming the mass of one *E. coli* cell to be 1 pg, the mass sensitivity can be calculated as 63 Hz/μg for the rectangular sensors and 166 Hz/μg for the triangular sensors. An improvement of 2.63× in mass sensitivity was observed for the triangular geometry compared to the traditional rectangular geometry.

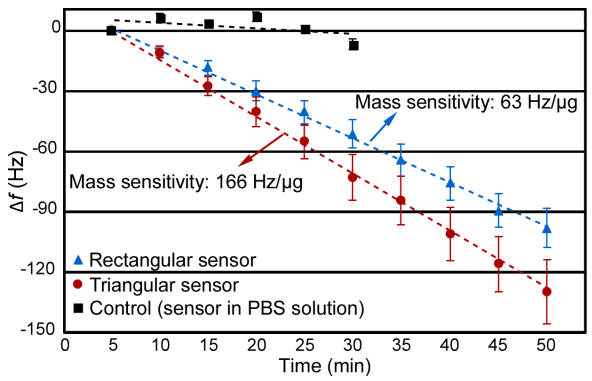

Figure 7: In-vitro test results for E. coli detection. Each sensor was tested in PBS solution for 30 min as control, then in E. coli suspension (8×10^6 cfu/ml determined by plate count) for 50 min. Data averaged from readings of 5 sensors (N=5). Error bar shows standard error. An improvement of 2.63× in mass sensitivity was observed for using the triangular geometry compared to the traditional rectangular geometry.

CONCLUSIONS

An implantable wireless biosensor for *in situ* early detection of PJI has been designed based on the ME transduction mechanism to enable passive wireless operation. The sensor can be functionalized to target specific types of bacteria that are known to be present during the early stages of PJI. A novel differential sensor configuration for distinguishing the effects of bacteria binding from variations caused by the surrounding medium was validated with experiments in emulated media. Triangular geometry was shown to enhance the mass sensitivity of the sensor over the traditional rectangular geometry. *In vitro* tests successfully demonstrated the capability of the sensor for detection of *E. coli* bacteria. Future works will focus on further improvement and characterization of sensor performance and integration, the capability to simultaneously target multiple types of bacteria, and evaluation of sensor characteristics for the *in vivo* environment.

ACKNOWLEDGEMENTS

This work was supported in part by internal funding at the University of Cincinnati. Facilities used for this work include the Mantei Research Center Cleanroom at the University of Cincinnati.

REFERENCES

[1] J. Gao, D. Xing, S. Dong, and J. Lin, "The primary total knee arthroplasty: A global analysis," *J. Orthopaedic Surgery and Research*, 15(190), 2020.

[2] C.R. Arciola, D. Campoccia, and L. Montanaro, "Implant infections: adhesion, biofilm formation and immune evasion," *Nature Rev. Microbiol.*, 16, 397-409, 2018.

[3] J. Fu, M. Ni, W. Chai, X. Li, L. Hao, and J. Chen, "Synovial Fluid Viscosity Test is Promising for the Diagnosis of Periprosthetic Joint Infection," *J. Anthroplasty*, 34(6), 1197-1200, 2019.

[4] J. Parvizi, T.L. Tan, K. Goswami, C. Higuera, C.D. Valle, A.F. Chen, and N. Shohat, "The 2018 Definition of Periprosthetic Hip and Knee Infection: An Evidence-Based and Validated Criteria," *J. Arthroplasty*, 33(5), 1309-1314.e2, 2018.

[5] E.A. Capogna, D.J. Munoz-Pinto, M.S. Hahn, and E.H. Ledet, "Identifying a crosslink density relationship of acrylamide hydrogels to be used with passive sensors for detecting periprosthetic infection," *41st Annual Northeast Biomedical Engineering Conference*, Troy, NY, USA, 2015.

[6] L. Liu, S. Zhang, Y. Qu, J. Zhou, F. Yang, R. Liu, and L. Liao, "Stress Monitoring of Prestressed Steel Strand Based on Magnetoelastic Effect Under Weak Magnetic Field Considering Material Strain," *Progress in Electromagnetics Research C*, 104, 157-170, 2020.

[7] L. Ren, K. Yu, and Y. Tan, "Wireless and Passive Magnetoelastic-Based Sensor for Force Monitoring of Artificial Bone," *IEEE Sensors Journal*, 19(6), 2096-2104, 2019.

[8] K.G. Ong, E.L. Tan, C.A. Grimes, and R. Shao, "Removal of Temperature and Earth's Field Effects of a Magnetoelastic pH Sensor," *IEEE Sensors Journal*, 8(4), 341-346, 2008.

[9] S. Shekhar, S.S. Karipott, R.E. Guldberg, and K.G. Ong, "Magnetoelastic sensors for real-time tracking of cell growth," *Biotechnology and Bioengineering*, 118(6), 2380-2385, 2021.

[10] X. Guo, S. Sang, A. Jian, S. Gao, Q. Duan, J. Ji, Q. Zhang, and W. Zhang, "A bovine serum albumin-coated magnetoelastic biosensor for the wireless detection of heavy metal ions," *Sensors and Actuators B: Chemical*, 256, 318-324, 2018.

[11] X. Huang, S. Sang, Z. Yuan, Q. Duan, X. Guo, H. Zhang, and C. Zhao, "A wireless biosensing microfluidic-chip based on resonating 'μ-diver'," *ACS Sens.*, 6(11), 3933-3939, 2021.

[12] L.V. Beltrami, M. Beltrami, M. Roesch-Ely, S.R. Kunst, F.P. Missell, E.J. Birriel, and C.D.F. Malfatti, "Magnetoelastic sensors with hybrid films for bacteria detection in milk," *J. Food Eng.,* 212, 18-28, 2017.

[13] R. Liu, X. Guo, J. Wang, J. Guo, Y. Zhang, W. Zhang, and S. Sang, "High sensitivity detection of human serum albumin using a novel magnetoelastic immunosensor," *Journal of Materials Science*, 54, 9679-9688, 2019.

[14] D.E. Mouzakis, D. Dimogianopoulos, and D. Giannikas, "Contact-Free Magnetoelastic Smart Microsensors with Stochastic Noise Filtering for Diagnosing Orthopedic Implant Failures," *IEEE Transactions on Industrial Electronics*, 56(4), 1092-1100, 2009.

[15] V. Pepakayala, J. Stein, and Y. Gianchandani, "Resonant magnetoelastic microstructures for wireless actuation of liquid flow on 3D surfaces and use in glaucoma drainage implants," *Microsystems & Nanoengineering*, 1, 15032, 2015.

[16] C.A. Grimes, S.C. Roy, S. Rani, and Q. Cai, "Theory, Instrumentation and Applications of Magnetoelastic Resonance Sensors: A review," *Sensors*, 11(3), 2809-2844, 2011.

[17] W. Shen, L. Mathison, V. Petrenko, and B. Chin, "Design and characterization of a magnetoelastic sensor for the detection of biological agents," *Journal of Physics D: Applied Physics*, 43(1), 015004, 2009.

[18] X. Huang, S. Sang, Z. Yuan, Q. Duan, X. Guo, H. Zhang, and C. Zhao, "Magnetoelastic Immunosensor via Antibody Immobilization for the Specific Detection of Lysozymes," *ACS Sens.*, 6(11), 3933-3939, 2021.

[19] P.G. Saiz, D. Gandia, A. Lasheras, A. Sagasti, I. Quintana, M. L. Fdez-Gubieda, J. Gutiérrez, M.I. Arriortua, and A.C. Lopes, "Enhanced mass sensitivity in novel magnetoelastic resonators geometries for advanced detection systems," *Sensors and Actuators: Chemical*, 296, 126612, 2019.

[20] M.D. Pozza, A.L. Possan, M. Roesch-Ely, and F.P. Missell, "Magneto-elastic biosensors: Influence of different thiols on pathogen capture efficiency," *Materials Science and Engineering C*, 75, 629-636, 2017.

CONTACT

*J. Jiang, tel: +1(513)208-3047; jiangj8@mail.uc.edu
#T. Li, tel: +1(513)556-3508; litao@uc.edu

SALIVA-BASED SARS-COV-2 SELF-TESTING WITH RT-LAMP IN A MOBILE DEVICE (SLIDE)

Zifan Tang, Jiarui Cui, Aneesh Kshirsagar, Tianyi Liu and Weihua Guan
The Pennsylvania State University, University Park, Pennsylvania, USA

ABSTRACT

We developed a fully integrated SARS-CoV-2 nucleic acid testing (NAT) device using a self-collected saliva sample. This platform consists of a ready-to-use reagents cartridge, an easy-to-use smartphone interface, and an ultra-compact and less-expensive analyzer. Our system automatically handled the complexity of heat-inactivated sample preparation, pressure-driven sample dispensing, real-time RT-LAMP reaction and detection, and data processing, storage, and upload. With a turnaround time of ~45 minutes, our reverse transcription loop-mediated isothermal amplification (RT-LAMP) achieved the limit of detection (LoD) of 5 virus particles/μl in the saliva sample. We believe our self-testing platform will have an ongoing benefit for COVID-19 control and fighting future pandemics.

KEYWORDS

SARS-CoV-2; POCT; Self-testing; RT-LAMP

INTRODUCTION

Coronavirus disease 2019 (COVID-19) became a worldwide pandemic in early 2020[1], and it was rapidly announced as a public health emergency of international concern by the World Health Organization (WHO)[2, 3]. As of March 2022, there are more than 400 million confirmed cases, and 6 million deaths of SARS-CoV-2 reported globally[3]. A lot of effort has been made into vaccine development, and it has been distributed in communities[4]. However, due to the fast mutation nature of the RNA virus and so many asymptomatic cases, all countries still face an unmet need to achieve a rapid, sensitive and reliable way to tackle the global and urgent problem. To reopen the communities and recover the economy, implementing routine level screening of healthy individuals should be a solution to minimize the risk of spreading. So far, nucleic acid amplification test (NAAT), such as RT-PCR, is the gold-standard technique due to its high sensitivity and specificity [5-8]. However, laboratory-based NAAT requires highly trained personnel, dedicated facilities, and instrumentations. Typically, results can be done within 2 hours, but many counties usually delay up to 7 days due to lack of facilities. Postponing obtaining molecular testing results will increase the virus spread. To alleviate these bottlenecks, we developed a fully integrated SARS-CoV-2 nucleic acid testing (NAT) device. SLIDE platform consists of a ready-to-use reagents cartridge, an easy-to-use smartphone interface, and an ultra-compact and less-expensive analyzer. It automatically handled the complexity of heat-inactivated sample preparation, pressure-driven sample dispensing, and real-time RT-LAMP reaction and detection, and data processing, storage, and upload. With a turnaround time of ~45 minutes, we achieved a limit of detection (LoD) of 5 virion/μl of a saliva sample. We believe our SLIDE self-testing platform will have an ongoing benefit for COVID-19 control and fighting future pandemics.

RESULTS & DISCUSSION

Overall Design and Module Validations

Overall Design. The overall design of the SLIDE analyzer is shown in **Figure 1a**. It consists of five seamlessly integrated modules controlled by a microcontroller unit (MCU): an optical module for fluorescence excitation and detection, two thermal modules, a piezo micro pump module, a connectivity module, and a power module. **Figure 1 b** shows a photograph of the assembled SLIDE analyzer and the smartphone interface.

Optical Module. The optical module consists of three independent excitation and detection units. Each unit has a LED excitation source (λ=470 nm) and a CMOS color sensor for real-time fluorescence monitoring. The excitation and the detection were arranged to be perpendicular to each other to minimize the excitation interference on the fluorescence signal。 To characterize the quantification ability of the optical module, we tested different calcein concentrations from 0 to 25 μM and measured the fluorescence intensity for 10 minutes. **Figure 1c** showed the mean and standard deviation of the relative fluorescence unit (RFU) as a function of the calcein concentration. A linear fit with R^2= 0.98 confirmed the quantitative capability of the optical module.

Micro pump Module. The sample dispensing and mixing is accomplished on the cartridge using a micro piezo pump. The volumetric rate of the micro piezo pump is controlled by the frequency and the driving voltage (fixed at 140V in our case). To characterize the micro pump, we tested the volumetric rate at different frequencies. As expected, the volumetric rate increased linearly with the operation frequency (R^2= 0.99, **Figure 1d**). This relationship provides us with the capability to modulate the liquid flow rate on the cartridge through programming the operation frequency.

Power Module. A rechargeable 1300 mAh Lithium polymer battery (14.43 Wh) was used to power our analyzer. To estimate the power consumption for each run, we used a power meter to characterize the voltage, current, and power during a complete cycle of the test. **Figure 1e** shows a 20 minutes segment of the measurement result. Before reaching the target temperature, the heaters continuously work at a high current (1.7 A for 95 °C and 2.2 A for 65 °C). After reaching the target temperature, the heater starts to change states between on and off to maintain the temperature. The total energy consumed is 3.02 Wh in each 45 minutes test, and we can perform four tests before recharging.

Thermal Module. We designed two independent thermal modules. One is for heat- inactivating the saliva and performing the thermal lysis at 95°C. The other is for controlling the temperature of the RT-LAMP reaction at 65°C. **Figure 1f** shows the temperature profile of the 95 °C thermal modules. The heating block reached 95 °C after 2.05 min of operation, while the saliva in the cartridge took 5.02 min. This delay is due to the non-ideal thermal coupling and the different specific heat capacity between the heating block and the cartridge. Nevertheless, the saliva can be sufficiently lysed at 95°C for 5 min within 10 mins from a cold start. For the heating module controlling the RT-LAMP reaction, we observed that the mean and the standard deviation of the temperature in the master mix solution is 64°C and 0.38°C, respectively (**Figure 2g)**.

Connectivity Module. A smartphone app was developed to assist the user in conducting the test. The SLDIE analyzer and the smartphone communicated through Bluetooth LE protocol. The app could provide test instructions, acquire data, and make positive and negative calls for easy interpretation of the test results. The app could also save the test results into a spreadsheet, which could be

978-1-940470-04-7/HH2022/$25©2022TRF
DOI 10.31438/trf.hh2022.2

Solid-State Sensors, Actuators, and Microsystems Workshop
Hilton Head Island, South Carolina, June 5-9, 2022

saved on the local smartphone or uploaded to cloud-based storage (Google Drive).

Automated Saliva Processing on The Cartridge

The cartridge was fabricated from polymethyl methacrylate (PMMA) using a laser cutting machine. It consists of three layers: top-loading layer, middle microchannel layer, and bottom covering layer (**Figure 2a),** and all pieces were bonded layer by layer using an adhesive solvent. It features a saliva collection chamber (250 µl) for loading and heat-inactivate the collected saliva, three trapping chambers for metering 10 µl of a processed saliva sample, and three reaction chambers with preloaded RT-LAMP master mix (30 µl), and a waste chamber for collecting the remaining saliva sample. Microchannels connect all these chambers, and the flow through the channels is controlled by micro pump and valves.

Over the past decade, numerous elegant designs have been demonstrated to control the liquid transfer in microfluidic systems using different types of valves. The wax valve has become popular in microfluidic due to its straightforward mechanism. The operation of a wax valve is based on the principle that the paraffin wax goes through a phase change from solid to liquid or liquid to solid as the wax temperature increases and decreases. Since our system involves the thermal module for the assay reaction, the wax valve naturally became the most straightforward choice to convert thermal energy into mechanical motion for flow control. Two paraffin wax valves are involved in each unit. Paraffin wax valve 1 locates between the trapping chambers and the reaction chambers. It separates the trapping chamber and the reaction chamber to block the flow during the sample trapping process to ensure only 10 µl of sample is transferred. Paraffin wax valve 2 locates in the middle of the releasing channel, which connects to atmospheric pressure. There are two purposes for this design. 1) Paraffin wax valve 2 serves as a liquid resistance to ensure no single unit can directly connect to the atmospheric pressure. This is a really important step to maintain consistency and repeatability among the three units. 2) It also prevents the amplicons from escaping to the environment to cause contamination issues.

Here, we use one unit as an example to illustrate working mechanisms (**Figure 2b).** First, the Saliva sample is heat-inactivated at 95°C for 5 minutes in the collection chamber. Then the saliva is pushed along the microchannel to the waste chamber, which is connected to atmospheric pressure. Along these microchannels, three 10 µl heat-inactivated saliva is taken by the trapping chambers for the following step reaction**.** Since the microfluidic channel of the PMMA layer is cut by a laser and the channel walls are hydrophobic, the trapping chamber can be filled without bubbles. The average trapping volume is 10.25 ±0.27 µl. The difference between the three chambers was less than 2.5%. Next, the heating block temperature was increased to 65 °C to open the paraffin wax valves 1 and 2. Part of the saliva will automatically flow into the reaction chamber by gravity. The rest of the saliva will be pushed by the following 30 pressure pulses at 1Hz with 10% duty at 5.6 ml/min. These pulses can help the saliva sample well mix with the RT-LAMP master mix. **Figure 2c** shows one example of the automatic sample dispensing processes.

Self-testing workflow

The overall workflow from sample collection to analysis using our SLIDE device is shown **Figure 3.** This test needs a ready-to-use reagents cartridge, a 3D printed portable ultra-compact analyzer, and an easy-to-use smartphone interface. First, the saliva sample is acquired from the patient. With the help of the saliva collection aids, the patient would self-collect ~120 µL of clean saliva into a cartridge. Next, the user can tighten the screw cap to completely seal the cartridge and then connect the cartridge with the piezo pump through Luer-lock compatible inlet port. After inserting the cartridge into the analyzer, users need to connect a smartphone to the SLIDE analyzer through Bluetooth and initiate the test. This process takes < 2 min hands-on time and is the only manual testing step. Next, the SLIDE analyzer automatically handles other complexities, including heat-inactivated sample preparation, the pressure-driven sample dispensing, real-time RT-LAMP reaction and detection, and data processing, storage, and upload. Briefly, the virus in the saliva sample is inactivated and lysed at 95°C for 5 minutes. Next, the 10 µl processed saliva will be automatically transferred into the reaction chamber and mixed with a preloaded RT-LAMP master mix by a fined-tuned sequence and parameter combination of microfluid design, piezo pump pressure, wax valve. The reaction will then be initiated on the device and held at 65 °C for 30 min for LAMP amplification. In the reaction, SARS-CoV-2 RNA is transcribed into DNA and amplified to billion copies of amplicons, producing fluorescent signals for detection. The LED excitation module shines through the cartridge during the amplification, and the fluorescence is detected by photodiodes secured perpendicular to the LED excitation module. The real-time amplification curve is displayed on the phone screen. Two possible decisions will be made based on the build-in voting algorithm: If more than or equal to 2 assays shows a sharp RUF increase, it is identified as positive. Otherwise, it is determined as negative. At the end of the test, users can upload their personal information, raw data, and results to the cloud. The whole process takes about 45 min with no user intervention.

Performance Evaluation with Mock Saliva Sample

After validating all the subsystems, we set out the experiment to test the performance of the SLIDE instrument for the automatic process of the sample preparation, amplification, detection, and result analysis. Here, we used a previously validated SARS-CoV-2 RT-LAMP primer set[9] against the highly conserved N region with a modified fluorescent concentration of SYTO9 (**Figure 4a).** We formed mock SARS-CoV-2 positive samples by spiking the healthy saliva sample with different concentrations of heat-inactivated SARS-CoV-2 virus particles. The final concentration of the mock sample ranges from 1 to 10^4 virion/µl.

Firstly, we manually validated the sample preparation and RT-LAMP reaction throughout the whole process. We heat-inactivated all the spiked saliva samples in the heating block for 5 min at 95°C. Next, 10 µl of the inactivated sample was taken by pipette and transferred into the 30 µl of the RT-LAMP master mix. After mixing the reagents with a vortex mixer, the reactions were performed using a benchtop PCR machine. Triplicate mock samples were performed at each concentration. 3/3 samples with the concertation higher than 5 virion/µl showed RFU values sharp increase, while no sample with 1 virion/µl showed sharp changes in RFU. The LoD is about 5 virion/µl (50 virion/reaction), which is on par with our previous RT-LAMP assay validation with purified RNA sample [9].

Same sample sets were performed, and similar results were obtained using the SLIDE device with the automatic process. To further evaluate the analytical sensitivity of the test, we tested more samples at low concentrations from 1 to 10 virion/µl using a SLIDE analyzer. 9/9 samples with the concertation of 10 virion/µl showed positive. 8/9 samples with 5 virion/µl and 3/9 with 5 virion/µl showed positive, respectively. The threshold to classify an amplification curve as positive or negative was 50 RFU. These validate this automatic process does not negatively affect the RNA quality and quantity for downstream detection. To estimate the LoD of the test, we fitted a logistic curve for the hit rates at different virion concentrations. The hit rate is defined as the number of

amplified samples over all tested samples. The LoD is estimated to be 6.5 virion/ µl (65 virion/reaction) at the 95% confidence level. This LoD is comparable with the LoD(6–12 copies/µL) using FDA-proved qRT-PCR assays with the same heat-inactivated saliva sample preparation method[10]. **Figure 4b** shows the inversely proportional relationship between the time to positive and virus particle concentration. As expected, the standard deviation among the times to positive increases as the virus particle concentration decreases in both manual and automatic results. The time to positive in the SLIDE instrument seems slightly slower than in the PCR machine. Due to the similar LoD in the two methods, the RNA quality and quantity should be the same after sample preparation. Therefore, we think this delay came from the different thermal coupling efficiency in these two systems and dynamic range differences in the optical detectors.

Saliva Clinical Sample

Two clinical saliva samples (one known positive and one known negative) were obtained through an approved institutional review board (IRB). All the samples were coded to remove information associated with patient identifiers. The RT-PCR performed the initial diagnosis as the reference method to benchmark our SLIDE. The amplification curves (raw data) are shown in **Figure 4b c&d.** The threshold to classify an amplification curve as positive or negative was set at 50 RFU based on the NTC sample. In 30 minutes, all of the chambers in the positive sample showed sharp RFU increases and stabilized at the value above the threshold, while no obvious RFU changes were observed in the negative sample. Based on the voting system for result making: more than or equal to 2 out of three amplified assay is identified as positive, otherwise is determined as negative. The pre-identified positive and negative samples by RT-PCR were also determined as positive and negative by our SLIDE device.

CONCLUSION

This paper demonstrates a fully integrated system for rapid (<45 min) self-testing for the SARS-CoV-2 virus from saliva samples. This fully portable approach can detect the virus rapidly without needing an RNA extraction kit and pipetting steps. All other complexities are handled automatically by the SLIDE analyzer, including heat-inactivated sample preparation, the pressure-driven sample dispensing and mixing real-time RT-LAMP reaction and detection, and data processing, storage, and upload. Our automatic system shows a great quantitative agreement with the manual process using a benchtop PCR machine (outside the cartridge). The analytical sensitivity (Limit of detection) against SARS-CoV-2 virus particle spiked saliva sample is 5 virion/µl. With these two clinical saliva samples, our device shows 100% agreement with the RT-PCR method. The promising results of the present study could likely be extended for use with saliva samples for noninvasive, portable, rapid, and scalable self-testing for COVID-19. Considering the limited reagent lifetime at room temperature, we will address the challenge of storing and transporting the liquid phase on the microfluidic reagent with reagent lyophilization in the future study.

ACKNOWLEDGEMENTS

This work is supported by the National Science Foundation under Grant No. 1902503, No. 1912410, and the National Institutes of Health under Grant No. R61AI147419.

REFERENCES

[1] H. Harapan *et al.*, "Coronavirus disease 2019 (COVID-19): A literature review," *Journal of infection and public health,* 2020.

[2] N. Zhu *et al.*, "A novel coronavirus from patients with pneumonia in China, 2019," *New England journal of medicine,* 2020.

[3] "World Health Organization (WHO). ," *WHO coronavirus-2019 https://www.who.int/emergencies/diseases/novel-coronavirus-2019*.

[4] J. S. Tregoning, K. E. Flight, S. L. Higham, Z. Wang, and B. F. Pierce, "Progress of the COVID-19 vaccine effort: viruses, vaccines and variants versus efficacy, effectiveness and escape," *Nature Reviews Immunology,* vol. 21, no. 10, pp. 626-636, 2021.

[5] J. F.-W. Chan *et al.*, "Improved molecular diagnosis of COVID-19 by the novel, highly sensitive and specific COVID-19-RdRp/Hel real-time reverse transcription-PCR assay validated in vitro and with clinical specimens," *Journal of clinical microbiology,* vol. 58, no. 5, pp. e00310-20, 2020.

[6] M. Nagura-Ikeda *et al.*, "Clinical evaluation of self-collected saliva by quantitative reverse transcription-PCR (RT-qPCR), direct RT-qPCR, reverse transcription–loop-mediated isothermal amplification, and a rapid antigen test to diagnose COVID-19," *Journal of Clinical Microbiology,* vol. 58, no. 9, pp. e01438-20., 2020.

[7] A. Tahamtan and A. Ardebili, "Real-time RT-PCR in COVID-19 detection: issues affecting the results," *Expert review of molecular diagnostics,* vol. 20, no. 5, pp. 453-454, 2020.

[8] C. B. Vogels *et al.*, "Analytical sensitivity and efficiency comparisons of SARS-CoV-2 RT–qPCR primer–probe sets," *Nature microbiology,* vol. 5, no. 10, pp. 1299-1305, 2020.

[9] Z. Tang *et al.*, "Rapid detection of novel coronavirus SARS-CoV-2 by RT-LAMP coupled solid-state nanopores," *Biosensors and Bioelectronics,* vol. 197, p. 113759, 2022.

[10] C. B. Vogels *et al.*, "SalivaDirect: A simplified and flexible platform to enhance SARS-CoV-2 testing capacity," *Med,* vol. 2, no. 3, pp. 263-280. e6, 2021.

CONTACT

*Weihua Guan, tel: +1-814-867-5748; wzg111@psu.edu

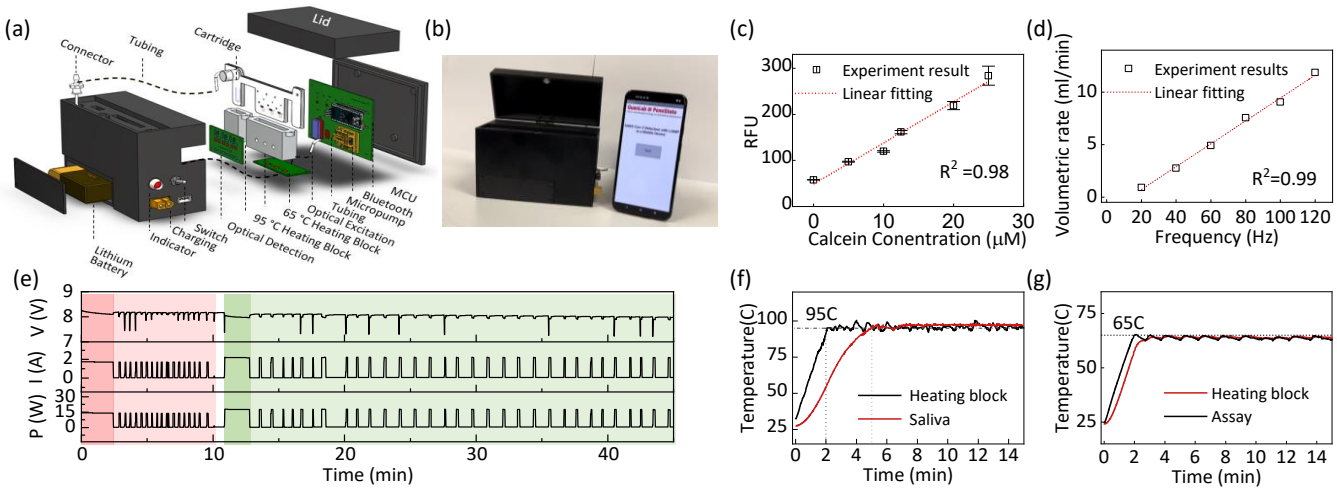

Figure 1*: SLIDE Instrument design and validation. (A) Schematic of the SLIDE device showing components in an exploded view. (B) Photograph of the SLIDE analyzer and the smartphone interface. (C) Characterization of the optical sensor (D) The temperature profile of the heating block and the liquid (saliva/assay) for 95°C virus heat inactivation and 65°C RT-LAMP reaction. (E) Characterization of the piezo pump frequency with the flowrate*

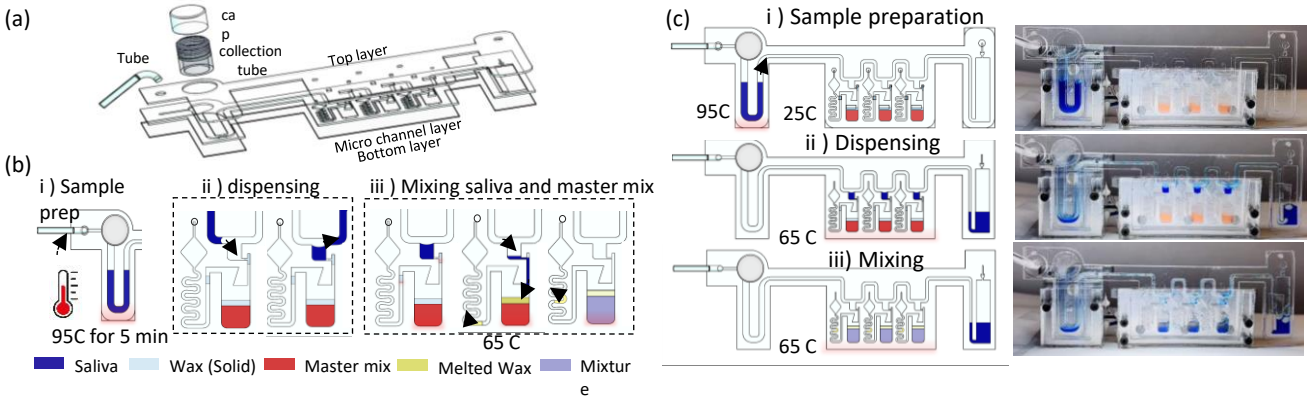

Figure 2. Illustration for the automated sample preparation dispensing and mixing on cartridges enabled by micropump.

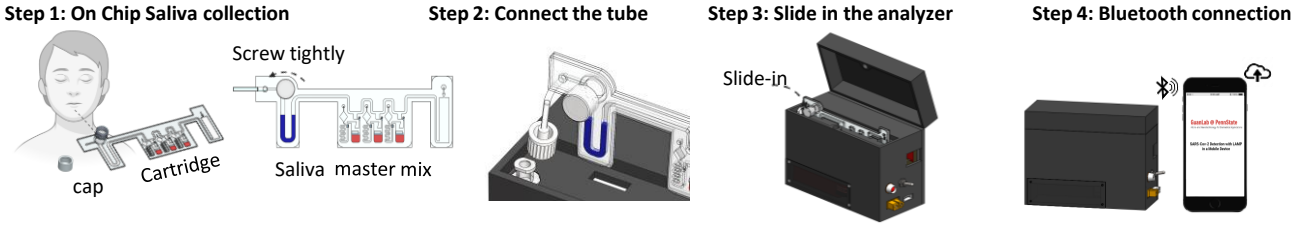

Figure 3. Overall operation workflow of SARS-CoV-2 SLIDE device. . The user self-collects 120 μL of saliva into the cartridge tube. After collection, the sealed cartridge is then inserted into the analyzer . The analyzer is connected to a smart phone through Bluetooth.

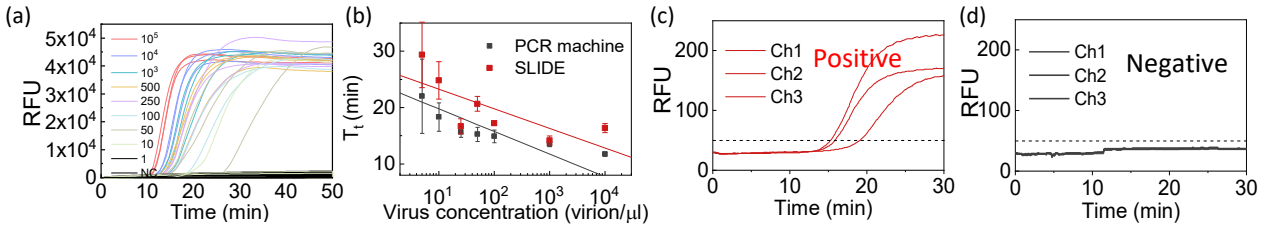

Figure 4: (a) RT-LAMP assay validation. (b) The inversely proportional relationship between the time to positive and virus particle concentration showed in both methods (PCR machine and SLIDE device. (c-d) Validation of the SLIDE automation system using saliva clinical samples.

EARLY DETECTION OF SIMULATED HERBIVORE ATTACKS IN SORGHUM FIELDS THROUGH THE DEPLOYMENT OF VERY-LOW-POWER GAS SENSOR NETWORK

Shakir-ul Haque Khan[1], Sayali Tope[1], Mohit Karkhanis[1], Bryan Hataska[1], Seungbeom Noh[1], Rana Dalapati[2], Ashrafuzzaman Bulbul[1], Ravi V Mural[3], Aishwaryadev Banerjee[1], Kyeongheon Kim[4], James C. Schnable[3], Mingyue Ji[1], Carlos Mastrangelo[1], Ling Zang[2] and Hanseup Kim[1]

[1]Electrical and Computer Engineering, University of Utah, Salt Lake City, UT 8411

[2]Materials Science and Engineering, University of Utah, Salt Lake City, UT 84112

[3]Department of Agronomy and Horticulture, University of Nebraska, Lincoln, NE 685

[4]Department of Convergence Electronic Engineering, Gyeongsang National University, South Korea, 52828

ABSTRACT

This *paper reports a novel method of detecting simulated herbivore attacks (mechanical damages) on a plant by sensing emitted gas, which was enabled by developing and deploying a very-low-power gas sensor network in an actual sorghum farm. When a group of nearby sorghum leaves were cut (simulating herbivore attacks), the damaged plants started emitting a unique volatile organic compound (VOC) marker, hexanal, ultimately increasing its concentration up to 60 ppm in 62 minutes within an area of less than 1.0 m diameter from the cut point. The emitted hexanal was detected by a near-zero-power (<100 pW) gas sensor that utilized a nanogap structure to provide normally-dormant (thus minimal power consumption) but continuously sensing capability for hexanal. When the near-zero-power gas sensor detected the target gas in concentrations above a pre-set threshold (29 ppm), it connected an internal switch to flow power and wake up the rest of the circuitry including a micro-controller, a display module and a wireless module, ultimately sending an alert through the wireless network to a central station. This result demonstrated the first, within our knowledge, gas sensor network and actual field demonstration of early (stimulated) herbivore attacks.*

KEYWORDS

low power, gas-sensor, prototype, field-deployment, herbivore- attack-simulation

INTRODUCTION

Herbivores cause significant degrees of physical damages to the stems and leaves of crops, resulting in a yield loss of about 20% to 40% every year globally [1]. And such damages can be even higher for some particular crops [2,3]. Thus, early detection is a key to reduce such a loss as well as associated issues including the overuse of harmful agrochemicals and resultant contamination of crops, soils and water [4,5].

The gold standard pest detection method is currently a manual scouting [6,7], often involving trapping pests or visually checking, that is time-consuming, expensive, and difficult to cover a large area. Emerging technologies are satellite- or drone-based imaging [8-10] that, however, held a resolution issue due to line-of-sight limitation; acoustic sound detection [11,12] that, however, cannot detect larvae or insects that do not produce significant levels of sound; and on-spot gas sample collection through a micro gas chromatography system [13,14] that, however, is not practically long-term field-deployable yet.

To address the limitations of existing methods, we tried to establish a closed-loop communication between plants and humans by developing a very-low-power, thus field-deployable (long-term sustaining), on-spot and real-time gas sensors and their wireless network, as described in Fig. 1. Recent literature reported that when herbivores attacked plants, the plants produced particular gas molecules to attract birds that can remove the herbivores as a natural defense mechanism. We hypothesized that if one could also sense the emitted gas molecules on-spot and early, one could utilize the detection to trigger earlier human interventions resulting in the enhancement of crop yields and energy efficiency in farming.

This paper reports the first time, within our knowledge, the

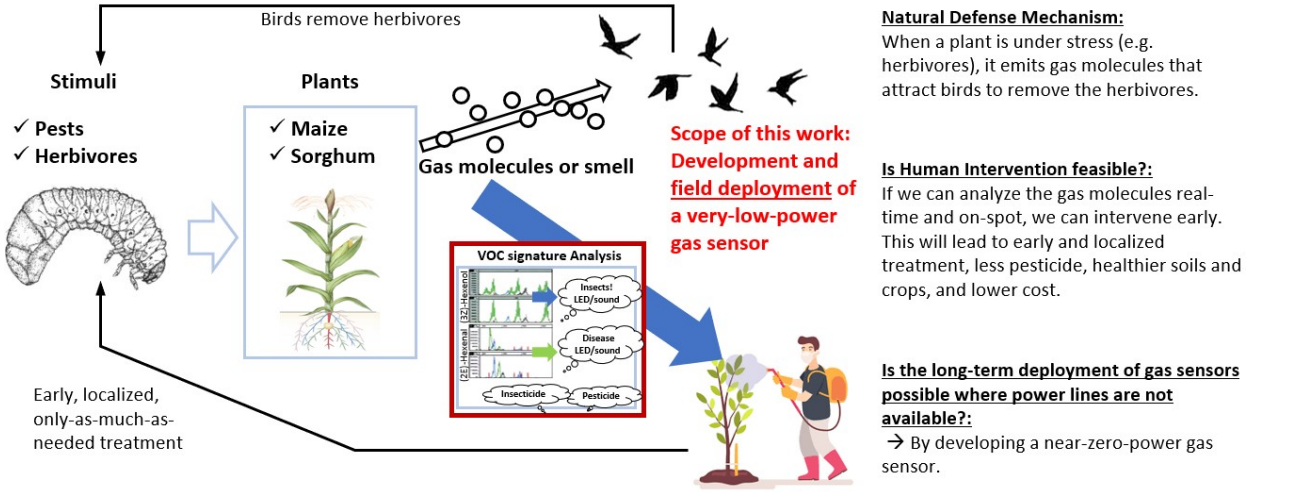

Figure 1. *The concept of this work: the detection capability of gas markers, which are released from plants when the plants are damaged, can be enabled by developing and deploying a very-low-power gas sensor network. Based on the measurement results, this work showed a promise of utilizing the developed gas sensor system for early pest treatment through human intervention.*

978-1-940470-04-7/HH2022/$25©2022TRF
DOI 10.31438/trf.hh2022.3

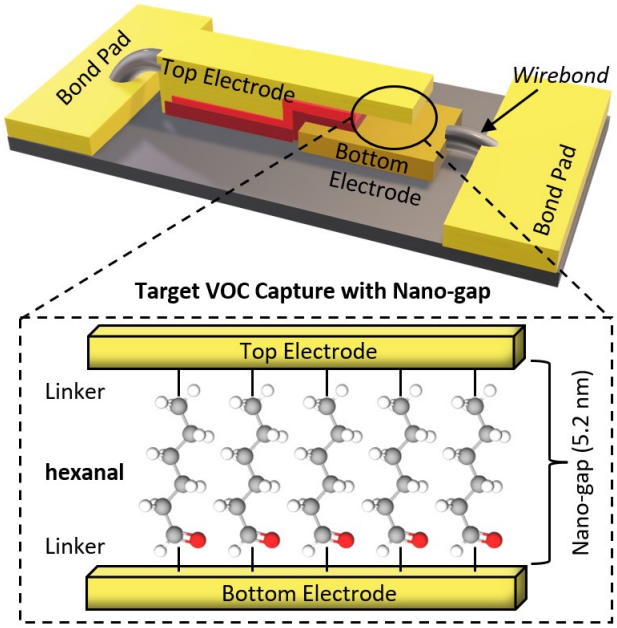

Figure 2. *(Top) Fabricated sensor chip, wire-bonded on both sides for integration to a circuit (Bottom) Capture of the target VOC within the nano-gap leading to current flow or sensor wake-up output.*

successful development and deployment of a very-low-power gas sensor network in an actual sorghum farm. This paper reports the operation principle, testing methodology and preliminary measurement results both in laboratory and in an actual sorghum field.

STRUCTURES AND OPERATION PRINCIPLE

The manufactured prototype (G1) was comprised of a nano-gap gas sensor, interface electronics (a transimpedance amplifier and a comparator), a microcontroller unit (MCU), a LED screen and a LoRa wireless module, as shown in Fig.3. The nano-gap sensor generated an electrical current upon capture of a target VOC. The generated current was then converted into a voltage signal by the transimpedance amplifier, and then the voltage signal was compared to a reference voltage by the comparator. If the voltage signal exceeded the reference value, the comparator turned on the MCU that subsequently activated both the LED screen display and the wireless alerting modules, allowing them to display

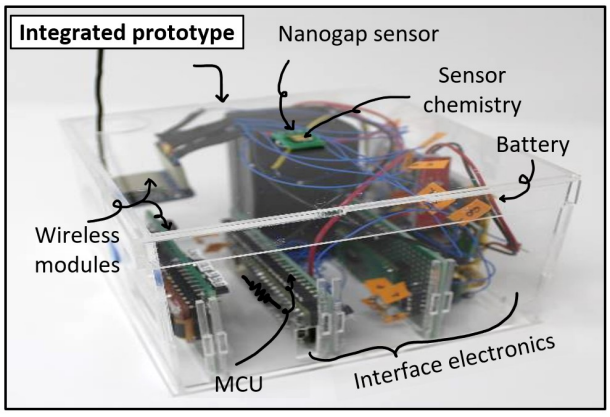

Figure 3. *Integrated prototype (G1) (10 × 10 × 7 cm³) that was deployed in sorghum field.*

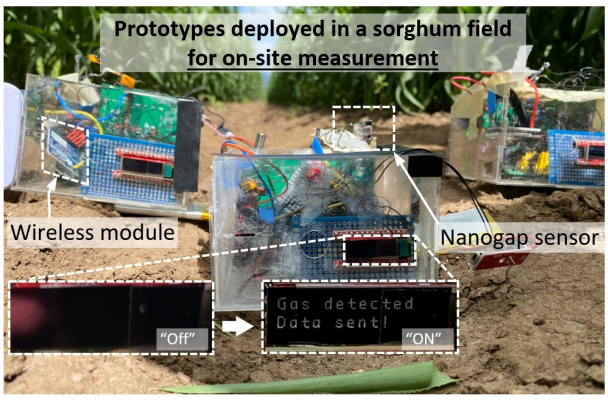

Prototypes	Temp. (ºC)	RH (%)	Wind speed (mph)	Distance from plant (m)	Height (cm)
× 4	*25*	*25*	*11*	*<1*	*10*

Figure 4. *Deployed prototypes in a sorghum farm for field testing. Each prototype included a nanogap sensor, a wireless module, a display and electronics. Four different prototypes were deployed with 3 being control and 1 equipped with a working sensor.*

or transmit data respectively.

The manufactured prototype normally remained in a power-conserving mode until being awoken up by the target gas detection when it actively consumed power for wireless alerting. Such a wake up was initiated by a nanogap-based wake-up gas sensor, of which the operation principle was reported previously [15]. Briefly, the nanogap-based sensor operated by utilizing a ~5.2 nm gap coated with a molecular probe or linker molecule to capture a target (hexanal in this case) resulting in a switch-like action in electrical current, as described in Fig. 2. Note that for the target gas for plant damage detection, sampling and analysis of gases from the ambient air near the sorghum plants before and after the damages were performed. The standard GC-MS measurement results, in comparison to the NIST database [16], clearly confirmed that hexanal was actively emitted from the damaged sorghum plants.

EXPERIMENTAL PROCEDURE

In-Lab Testing

In-lab tests were performed on the fabricated nano-gap sensor to determine (1) the lowest concentration of hexanal it can detect (estimated limit of detection), (2) the repeatability of the sensor response and (3) the possibility of interference from other gases during detection (selectivity), all prior to field deployment. For the limit of detection test the target concentration was reduced down to 50.00 ppm starting from 1418.44 ppm while the sensor response ratio being recorded. For the repeatability testing, the sensor was exposed to target gas in ~15,000 ppm for 45 minutes and alternatively to ambient air for 10 to 60 minutes in consecutive cycles, allowing it to be turned "on" the "off" until no further response was observed (the sensor remained off). For the selectivity tests the sensor was exposed to various types of gases including IPA, pentane, acetone and indole, all of which were known gases existing in sorghum fields.

For the In-lab tests, a flow setup was utilized which mainly consisted of multiple mass flow controllers that determined flow rates of either the target gas or a carrier gas (N_2) and thus manipulated the final concentrations. During the exposure, the output resistance of the sensor was monitored at a biasing voltage of 0.7 V over time for a period of 45 minutes. The utilized target gas, hexanal, for in-lab testing was commercially available.

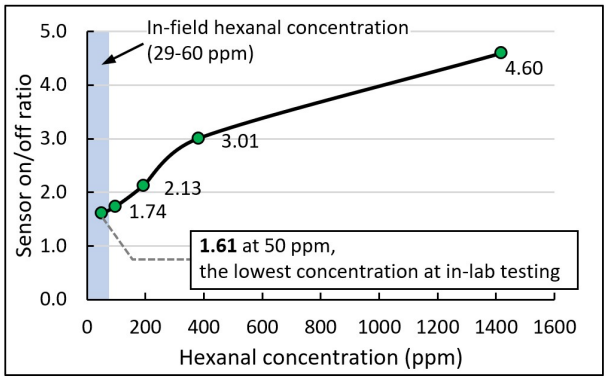

Figure 5. *Sensor on/off ratio with increasing concentration of hexanal. The lowest tested and detected concentration was 50 ppm that was within the on-field hexanal concentrations.*

Field Testing

The field testing was performed to demonstrate the detection capability of the integrated prototype in response to hexanal released by damaged plants in an actual farm, as shown in Fig. 4. Tests were performed in a sorghum field in Lincoln, Nebraska with four different 4 prototypes deployed over 5 hours. Sorghum plant leaves were instantly cut up within 30 cm away from the prototypes. Field temperature was recorded to be 25 ºC and relative humidity was 25%. From the prototype, a wireless gateway station was placed at a 5-m away position, although it could be wireless tethered up to 70 m. When triggered, the gateway station sent an alert message to a database that could be accessed from any computers connected to internet.

RESULTS

In-lab Testing: Limit of Detection

The lowest concentration of commercial hexanal detected with a microfabricated nano-gap sensor, in the lab, was measured as 50.00 ppm with the output current response ratio of 1.61, as shown in Fig.5. Indeed 50 ppm was the lowest limit that our testing set-up could provide. The sensor woke up to a range of hexanal concentrations above 50.00 ppm up to 1,418.44 ppm, as shown in Fig. 5. When the sensor was awoken, the response ratios were 1.61 times for 50.00 ppm, 1.74 for 97.04 ppm, 2.13 for 192.8 ppm, 3.01 for 380.95 ppm and finally 4.6 times for 1418.44 ppm of commercial hexanal. The sensor overall demonstrated an increasing trend of the response ratios with increasing concentrations (in ppm) of hexanal.

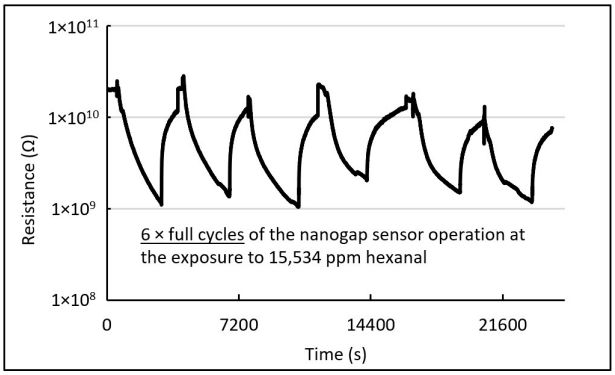

Figure 6. *Repeatable response to hexanal exposure was observed from the nano-gap sensor with 6 full cycles of sensor on and off obtained.*

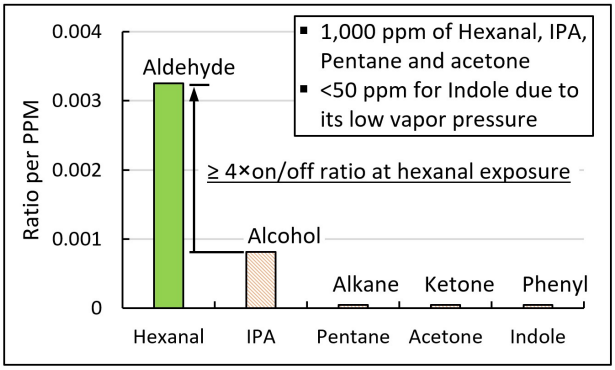

Figure 7. *Selectivity of the hexanal response was demonstrated against 4 other gas types belonging to alcohol, alkane, ketone and phenyl groups.*

In-Lab Testing: Repeatability

Measurement results from the in-lab testing showed that the sensor was repeatable to 6 times when exposed to a hexanal concentration of 15,534 pm (saturation concentration), as shown in Fig. 6. Note that the saturation concentration was utilized assuming the worst case. It was believed that the repeatability would increase further at the exposure to a lower concentration of a target gas. After the 6th cycle, the sensor did not respond to any further hexanal exposure. The sensor demonstrated the ability to recover naturally, once the test chamber was purged of hexanal indicative of the reversible nature of the target capture mechanism. The results indicated that the developed sensor prototype deployed in the field would be able to respond at least 6 times to damaged plants.

In-Lab Testing: Determining Sensor Selectivity

The sensor response was demonstrated to be selective by at least 4.06 times per unit ppm when compared to a list of pre-selected gases. The list of gases the sensor was exposed included alcohol, ketone, alkane, phenyls and hexanal, all of which have the possibility of being present in a farm (Fig. 7). Sensor response ratio per unit concentration (ratio per unit ppm) was calculated by dividing the on/off ratio with the concentration of gas exposure. The response to hexanal was 0.0035 ratio/ppm compared to the 2nd highest response to alcohol (IPA) at 0.0008 ratio/ppm. Sensor response ratios for other different groups were negligible with gases from the alkane (pentane), ketone (acetone) and phenyl (indole) functional groups generating no response. Concentrations of all the target gases were 1000 ppm except for indole which had a considerably low vapor pressure of 0.0122 mmHg. This response pattern indicated that the nano-gap sensor could be deployed in-field without any significant interference from false signals from other gases present.

Field Testing: Simulating Pest Damage to Plants

The sensor integrated prototype detected hexanal released from mechanically damaged or leaves cut with clippers 3.5 hours after deployment (Fig. 8). Until the sensor response was obtained, sorghum leaves were continuously cut with leaves belonging to around 80 plants damaged at the moment of detection. Upon detection the prototype displayed a gas detected message on the LED and triggered the LoRa module to send a wireless signal via the gateway, which was observed from 1415 km away. After 1.5 hours the prototype was removed from the field at which point the LED message disappeared indicating sensor recovery in the absence of hexanal. During the testing only the prototype that had

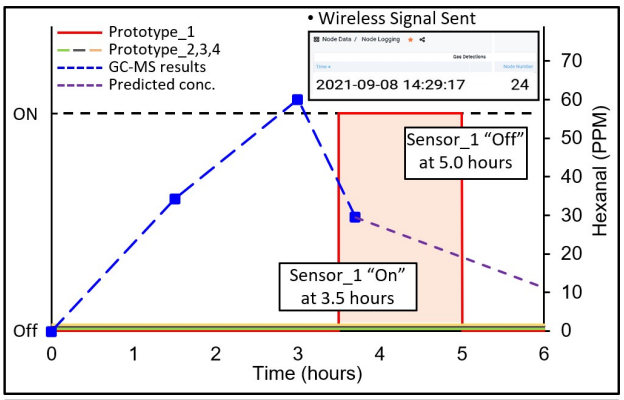

Detection Time (hours)	Recovery Time (hours)	Concentration (ppm)	Plants Damage	Wireless Signal Distance (km)
3.5	*1.5*	*29~60*	*× 80*	*1415*

Figure 8. *G1 Prototype field testing results: (Top) Time line of sensor response with prototype triggered at 3.5 (Bottom) Summary of the results obtained from field testing.*

a working sensor triggered while the three other controls that were deployed remained off. This test demonstrated that the sensor was indeed capable of detecting actual hexanal emitted from plants as was theorized from our in-lab commercial hexanal testing.

Field collection of air samples and post-analysis in the standard GC-MS proved the presence of hexanal which was found to be continuously increasing from 29 ppm and to 60 ppm. The accumulation of the hexanal around the prototype during the cutting caused the concentration of hexanal to build up allowing the nano-gap sensor to wake-up the rest of the circuit once a threshold concentration (29 ppm $\leq C_{threshold} <$ 60 ppm) was reached.

CONCLUSION

This paper reported a novel method of detecting simulated herbivore attacks on plant through sensing biomarker gases including demonstration of a low power gas sensor network in an actual sorghum farm. The gas sensor network was developed and deployed to implement the method. Damages done to the sorghum plants triggered the plants to release hexanal with the concentration reaching 60 ppm in 62 minutes. The gas sensor was able to detect this emitted hexanal within an area of less than 1 m diameter from the cut point once the concentration crossed the threshold of 29 ppm and consumed less than 100 pW of an operation power. Detecting the actual hexanal by the sensor, waking up the circuit and alerting through a wireless network to a central station were successfully performed in the field.

ACKNOWLEDGEMENTS

This research work was generously supported by the cooperative agreement of DE-AR0001064 of the ARPAE OPEN 2018 program (Program Manager: Dr. David Babson). Previously, it was also supported by the cooperative agreement of HR0011-15-2-0049 of the DARPA NZERO program (Program Managers: Drs. Roy Olsson and Benjamin Griffin). Microfabrication was performed at the Utah Nanofabrication Facility at the University of Utah.

REFERENCES

[1]. Chaya, D. T. X. A. M. (2019, March 25). *Climate Change-Caused Plant Pest Epidemic*. Food Tank.

[2]. "Studies in Agricultural Economics No.113" Research Institute of Agricultural Economics Committee on Agricultural Economics, Hungarian Academy of Sciences, 2011.

[3]. Wielgoss, A., Clough, Y., Fiala, B., Rumede, A., & Tscharntke, T. (2012). A minor pest reduces yield losses by a major pest: plant-mediated herbivore interactions in Indonesian cacao. *Journal of Applied Ecology*, *49*(2), 465–473.

[4]. Present Aspects and Effects of Pesticides on Health and the Environment. (2021). *International Journal of Pharmaceutical Research*, *13*(02).

[5]. Hassaan, M. A., & el Nemr, A. (2020). Pesticides pollution: Classifications, human health impact, extraction and treatment techniques. *The Egyptian Journal of Aquatic Research*, *46*(3), 207–220.

[6]. Beck, N., Herman, T., & Cameron, P. (1992). Scouting for lepidopteran pests in commercial cabbage fields. *Proceedings of the New Zealand Plant Protection Conference*, *45*, 31–34.

[7]. Reagan, T. E., & Mulcahy, M. M. (2019). Interaction of Cultural, Biological, and Varietal Controls for Management of Stalk Borers in Louisiana Sugarcane. *Insects*, *10*(9), 305.

[8]. Adedeji, A. A., Ekramirad, N., Rady, A., Hamidisepehr, A., Donohue, K. D., Villanueva, R. T., Parrish, C. A., & Li, M. (2020b). Non-Destructive Technologies for Detecting Insect Infestation in Fruits and Vegetables under Postharvest Conditions: A Critical Review. *Foods*, *9*(7), 927.

[9]. Gao, D., Sun, Q., Hu, B., & Zhang, S. (2020). A Framework for Agricultural Pest and Disease Monitoring Based on Internet-of-Things and Unmanned Aerial Vehicles. *Sensors*, *20*(5), 1487.

[10]. Sári-Barnácz, F., Szalai, M., Kun, M., Iványi, D., Chaddadi, M., Barnácz, F., & Kiss, J. (2021). 24. Satellite-based spectral indices for monitoring *Helicoverpa armigera* damage in maize. *Precision Agriculture '21*.

[11]. Prince, P., Hill, A., Piña Covarrubias, E., Doncaster, P., Snaddon, J., & Rogers, A. (2019b). Deploying Acoustic Detection Algorithms on Low-Cost, Open-Source Acoustic Sensors for Environmental Monitoring. *Sensors*, *19*(3), 553.

[12]. Escola, J. P. L., Guido, R. C., da Silva, I. N., Cardoso, A. M., Maccagnan, D. H. B., & Dezotti, A. K. (2020). Automated acoustic detection of a cicadid pest in coffee plantations. *Computers and Electronics in Agriculture*, *169*, 105215.

[13]. Levi-Zada, A., Nestel, D., Fefer, D., Nemni-Lavy, E., Deloya-Kahane, I., & David, M. (2012). Analyzing Diurnal and Age-Related Pheromone Emission of the Olive Fruit Fly, Bactrocera oleae by Sequential SPME-GCMS Analysis. *Journal of Chemical Ecology*, *38*(8), 1036–1041.

[14]. Jackels, S. C., Marshall, E. E., Omaiye, A. G., Gianan, R. L., Lee, F. T., & Jackels, C. F. (2014). GCMS Investigation of Volatile Compounds in Green Coffee Affected by Potato Taste Defect and the *Antestia* Bug. *Journal of Agricultural and Food Chemistry*, *62*(42), 10222–10229.

[15]. Banerjee, A., Khan, et al. Molecular bridge-mediated ultralow-power gas sensing. *Microsystems & Nanoengineering*, *7*(1).

[16]. Khan, S. U. H., Tope, S, et al. (2021b). Development of a Gas Sensor for Green Leaf Volatile Detection. *2021 21st International Conference on Solid-State Sensors, Actuators and Microsystems (Transducers)*.

CONTACT

*H. Kim, tel: +1-801-587-9497; hanseup.kim@utah.edu

MULTIPLEXING AND INCREASING THE THROUGHPUT OF "ROLOSENSE ASSAY" UTILIZING COST-EFFECTIVE WIFI IMAGING AND DISPOSABLE MICROFLUIDICS CHIPS FOR SARS-COV-2 DETECTION

Jorge Manrique Castro[1†], *Frank Sommerhage*[2†], *Selma Piranej*[3], *David DeRoo*[2], *Khalid Salaita*[3], *and Swaminathan Rajaraman*[1,2]

[1]University of Central Florida, Orlando FL, USA, [2]Primordia Biosystems, Orlando FL, USA, and [3]Emory University, Atlanta GA, USA

[†] Equally Contributing Authors

ABSTRACT

We present the development of a wireless, standalone device and disposable microfluidics chips that rapidly generate parallel SARS-CoV-2 readouts for selected variants directly using a nasal or saliva sample, based on the Rolosense Assay (RA) [1]. The SARS-CoV-2 test kit consists of a WiFi readout module, a microfluidic chip, and a sample collection/processing sub-system. Here, we focus on the fabrication and characterization of the microfluidic chip to multiplex RA for economic, disposable, and simultaneous detection of up to six different viruses or variants in a single test and data collection using a commercially available, WiFi-capable, and camera-integrated device (Figure 1).

KEYWORDS

Rolosense Assay, High-Throughput (HT), Microfluidics, Multiplexing, Microchannels, Microfabrication.

INTRODUCTION

Microfluidics platforms are being developed and deployed all around us in a variety of ways, starting from single purpose, disposable chips to analyze specific biological samples **[2]**, integrated into a broader system as the initially proposed Micro Total Analysis System (μTAS) for running chemistry on a chip **[3]** or into fully microfluidic-integrated-chip biosensors for organs modeling as demonstrated recently by Ding et al. **[4]**.

In terms of technological development, microfluidics platforms for biomedical applications are moving away from traditional soft lithographic techniques and instead using other novel and cost-effective approaches. For instance, 3D printing based microfluidic chips have been deployed towards bacterial detection **[5]**, and protein purification **[6]**. Additionally, double-sided adhesives based microfluidic fabrication strategies are being developed for microphysiological systems **[7]**. These newer microfabrication strategies are being implemented using novel designs, materials selection and operating at the limits of common microfabrication techniques. One recent review article that illustrates this expansion is from Ingber detailing the approaches to the expansion of microfluidics into more complex platforms as such as human organs-on-chips and personalized medicine **[8]** that allow drug development and disease modeling more efficiently.

Microfluidics are also playing a role in addressing challenges caused by recent global health events. With the advent of the coronavirus disease (COVID-19) and its rapid propagation around the world with multiple, and highly contagious variants, clinical testing of individuals remains not dynamic enough to prevent the spread of rapidly evolving viral targets such as SARS-CoV-2. Several tests both laboratory, and in-home/POC have been deployed to combat the pandemic **[9]**. In contrast to most state-of-the art tests involving microscopy and off-chip assays **[10]**, the Rolosense Assay (RA) does not require complex fluorescence, colorimetric read-outs, nor does the biological sample require exhaustive reverse transcription and DNA amplification as in Polymerase Chain Reaction (PCR) testing.

Single purpose RA requires a nasal swab or saliva sample inserted into a point-of-care (POC) solution detection platform for whole virion detection via DNA motors coated with virus binding ligands. The motors are 5 μm spheres which exhibit motion in the absence of virus and stall in the presence of virus. Microfluidics can increase the throughput of the sample collection chip to run parallel testing. A portable and easy-to-use version of the POC device could be made available over the counter for in-home use. This portable reader with reliable optical readout and wireless functionality can be reused with consumable, disposable microfluidic chips.

In this work, we propose an ***in-home/POC solution*** for ***high-throughput, multiplexed and low-cost RA*** utilizing microfluidics to detect multiple different viruses and/or different variants of viruses (e.g., original COVID-19, Delta, or Omicron variants) in parallel without electrical crosstalk **[11]**, which is eliminated due to optical

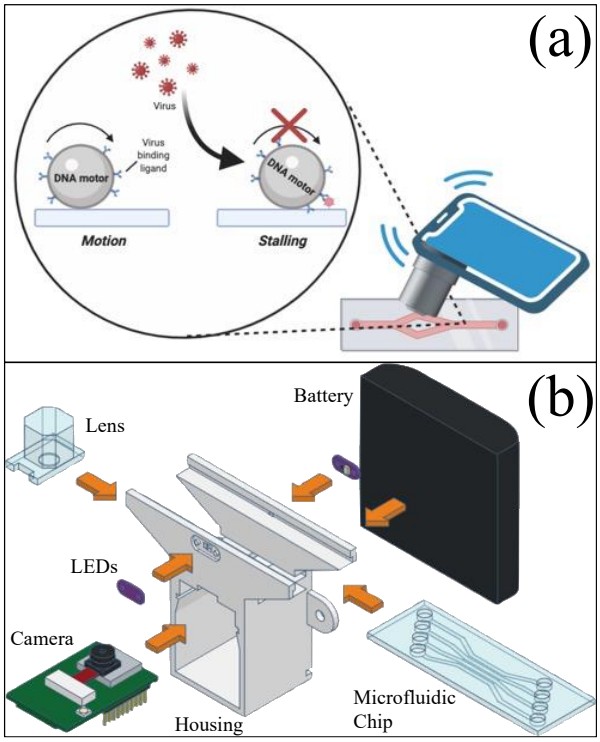

Figure 1. *(a): Traditional Rolosense Assay (RA) set up using a microscope and a cell phone camera. (b): Schematic of the optimized SARS-CoV-2 detection kit, showcasing both cost effective WiFi and disposable microfluidics transmitting RA results wirelessly to the patient phone to visualize optical results in real time, and run post processing virus detection by analyzing the motion of motorized particles, which is the principle of RA.*

978-1-940470-04-7/HH2022/$25©2022TRF
DOI 10.31438/trf.hh2022.4

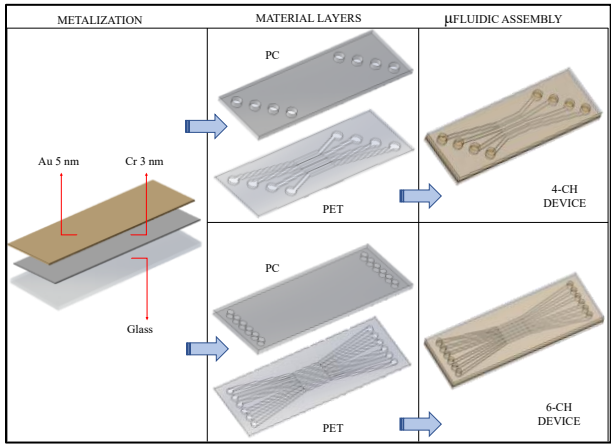

***Figure 2**. Multilayered microfluidic chip microfabrication and assembly. Integration from left to right - metallization: Chromium at 3 nm followed by Gold at 5 nm E-beam deposition on top of the glass substrate. Surface roughness characterization was performed on the top-most layer (Table I). Material Layers: Microfabricated intermediate layers of PET (plotter cut double-side adhesive) and micromilled PC. Surface profile characterization was performed to ports and channels (Table II). Microfluidic Assembly: Integrated chip by bonding all the layers together. Flow and leaking tests were performed successfully.*

detection principle. This assay optimization follows a simple multi-step procedure: sample collection (nasal swab), incubation (chip ports), sample loading/flowing (microchannels) and readout (detection kit + mobile phone).

MATERIALS AND METHODS

Traditional RA requires expensive optical microscope setup to capture images of the motion of 5 µm spheres (DNA motors) with high degree of precision **[12]**, whereas our approach utilizes standard magnification, low-resolution cameras, and sub-pixel motion detection along with WiFi-readiness/data transmission to a central data storage location for tracking the motion of spheres that can additionally be utilized in variant-outbreak detection in a multichannel microfluidic chip.

The WiFi readout module, as depicted in **Figure 1**, is contained in a 3D printed cartridge (Tronxy 820m) and integrates LEDs, basic optics (SuperEyes Lens) and two-core board-level microprocessor electronics (ESP32-CAM module), featuring a two-megapixel camera (OV2640) and an SD card reader. Assay multiplexing is achieved utilizing "Makerspace Microfabrication" technologies **[13]** to develop multilayered, four (4-CH) and six (6-CH) channel microfluidic devices (**Figures 2 & 3**).

Microfluidics devices were designed in CAD software (Solidworks, Dassault Systèmes) in a three-layer system. The top layer, a Polycarbonate (PC) sheet (75x25x1.5 mm) was machined with a specialized tabletop milling tool (Quick Circuit J5, T-Tech). This layer contains four inlet/outlet well ports set (4 mm diameter) or six inlet/outlet well ports set (2 mm diameter) for 4-CH and 6-CH devices respectively. Two different milling bits were implemented to identify the best quality cutting along the device edges and ports. For the 4-CH, a T2 milling bit was used, whereas for the 6-CH a finer T4 bit was used. The middle layer, microchannels were created using precision plotter cutting (Cameo 4, Silhouette) of Polyethylene Terephthalate (PET)-based double-sided adhesive (RTS3851-17, Medco) of size 75x25x0.15 mm, with good optical clarity. The structural composition (construction) of the double side

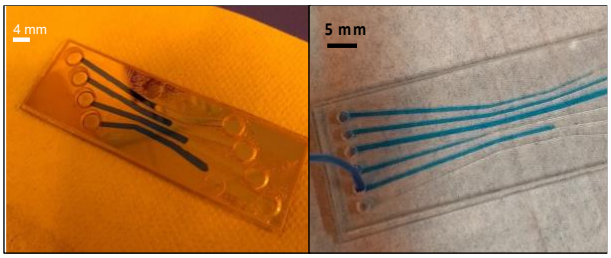

***Figure 3**. Optical images of fully integrated microfluidic chips under flow and leaking tests. Left: 4-CH device Right: 6-CH device. Microfluidic channel widths are between ~1-1.5 mm.*

adhesive is as follows: release film/adhesive/1.0 mil polyester/adhesive/release film. Lastly, the bottom layer comprises a glass substrate that was coated using E-beam evaporator (TC2000, Temescal) with Cr/Au layer (3 nm/5nm thickness) to serve as the microchannel functionalized surface where the RA **[1]** is conducted. All three layers were bonded (**Figures 2 & 3**) and the chip was fully characterized using the portable kit by mimicking RA (**Figures 4 & 5**) with 5 µm microbeads acting as the motors.

Optical characterization of the microfluidic devices (4-CH and 6-CH) was carried out using the WiFi readout module, hosting a browser-based web interface. High-resolution images were saved on an SD card in the ESP-32 CAM module and ported to the web interface. This visualization can be performed by any portable or fixed device with WiFi capability (e.g., smartphones, laptops, desktops, tables, etc.). Particle tracking analysis on captured high-resolution images was performed using motion tracking (Fiji Image J) that identified particles moving in the channels and distances covered. Data was visualized using a custom program (Octave) and scripted python code, comparing particles featuring active RA motors to particles merely moving based on Brownian motion **[14]**.

Physical characterization was performed by measuring surface roughness on channels and ports on 200, 500 and 1000 µm areas, and the dimensions of microchannels width and ports diameter, using laser confocal microscopy (VK-X3000, Keyence) as depicted in **Figures 6 & 7**. This characterization provided information about the accuracy/error of the instruments used in this development process from the design up to the fully assembled devices.

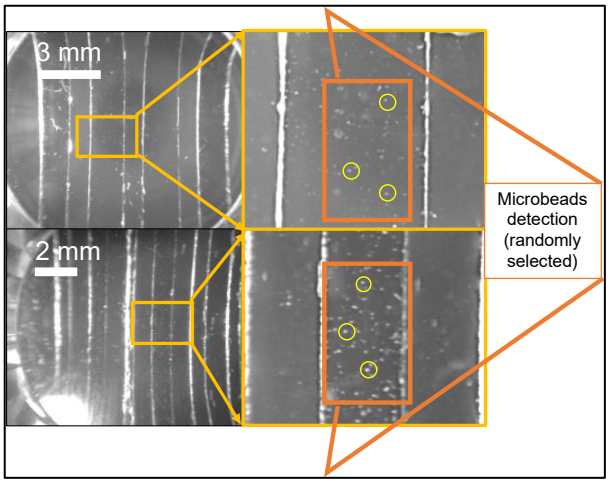

***Figure 4**. Optical micrographs of both 4-CH (top) and 6-CH (bottom) devices with RA being performed in our system. Optical micrographs on the right depict detection of individual 5µm microspheres/microbeads in the images captured by the ESP CAM module.*

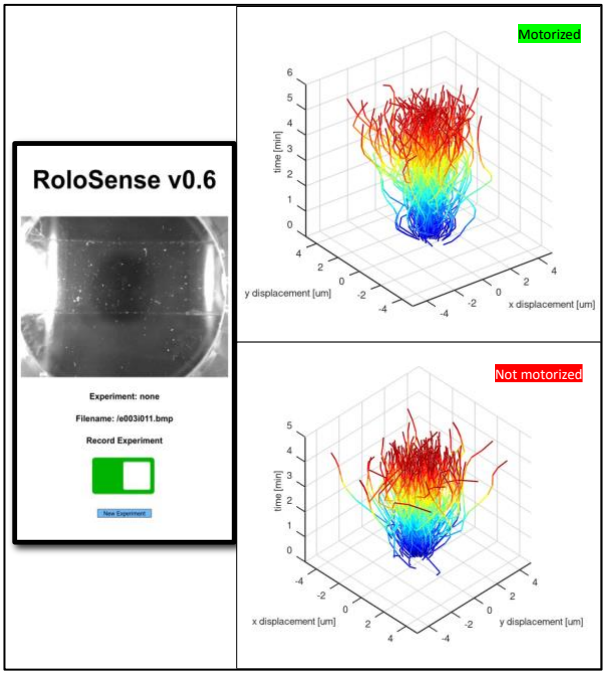

***Figure 5**. Optimized RA results presented as displacement trajectories of the 5 µm spheres in motorized and not motorized conditions in microchannels.*

***Table 1**. Rolosense Assay substrate specification sheet for the 6-channel device after metal deposition and surface characterization.*

ROLOSENSE ASSAY DISPOSABLE MICROFLUIDIC CHIP				
Structure and Materials	Multilayered device: Layer 1: Glass Substrate Layer 2: 3 nm Cr Layer 3: 5 nm Au Layer 4: Microchannels. Double side adhesive PET Layer 5: Ports. PC			
Characterized Material	Cr_3nm/Au_5nm coating			
Version	6-CH			
Instrument used for characterization	3D Surface Profiler			
Instrument used for deposition	E-Beam Evaporator			
Ports. Area under test (µm²)	1000 (n=6)			
Channels. Area under test (µm²)		200 (n=3)	500 (n=6)	1000 (n=3)
Surface Roughness Sa (µm)	0.085	0.034	0.046	0.022

***Table 2.** Microfabrication process specification sheet for PC and PET materials along with Micromilling and Plotter Cutting techniques for the 4 and 6 channels devices.*

ROLOSENSE ASSAY DISPOSABLE MICROFLUIDIC CHIP						
Structure and Materials	Multilayered device: Layer 1: Glass Substrate Layer 2: 3 nm Cr Layer 3: 5 nm Au Layer 4: Microchannels. Double side adhesive PET Layer 5: Ports. PC					
Characterized Material	PC		PET			
Version	4-CH	6-CH	4-CH	6-CH		
Instrument	Micromilling Tool		Cutting Plotter			
Instrument tools	Milling Bit T2	Milling Bit T4	Blade 1			
Settings	Feed rate 20 mm/s Depth of cut 2.2 mm RPM 60k		Force 33 Speed 3 Passes 2 Depth 4			
Port Diameter by design (mm)	4	2	4	2.5	2	1.4
Port Diameter by fabrication (mm)	5.238 (n=4)	2.873 (n=6)	3.834 (n=4)	2.528 (n=6)	1.882 (n=6)	1.409 (n=6)
Channel Width by design (mm)			1.5	1		
Channel Width by fabrication (mm)			1.535 (n=4)	1.118 (n=6)		
Error for Ports (%)	30	43	2.33	1.12	5.9	0.64
Error for Channels (%)			7.73	11.8		

RESULTS AND DISCUSSIONS

Visibility of 5 µm spheres was successfully demonstrated utilizing the wireless kit when implemented on both types of chips. **Figure 4-top** and **bottom** depict beads in the 4-CH chip and 6-CH chip, respectively. Microbeads were identified as bright spots in obtained images. The diameters of microbeads ranged from 4 to 6 pixels, based on background brightness and overall contrast.

Results for sub-pixel motion tracking in an x/y coordinate system representing the microchannel surface is shown in **Figure 5** for motorized and non-motorized particles. Time is represented on the z-axis as well as color (blue = start and red = end of tracking). Data analysis of a subsection of the ***entire frame detected 556 potential 5 µm RA motor spheres and the motion of 227 spheres was successfully tracked for up to 15 minutes.*** Each microparticle's position was normalized and the displacement plotted in superposition. The ***test-spheres traveled between 1 and 4 µm*** under the influence of Brownian motion (**Figures 4 & 5 bottom**).

Surface roughness characterization was performed on the 6-CH chip as a representative of the RA chips used. Design to device errors are observed for the ports which is expected, though the microchannels themselves ***exhibit acceptable (~10%) error*** due to the small displacements between the channel's walls during the mechanical bonding process of the double side adhesive to the metalized substrate.

For the optimal performance of the RA, a flat surface is desired to enhance the chemical-to-mechanical energy exchange of the DNA-motors. An average ***surface roughness of 46.7 nm*** was

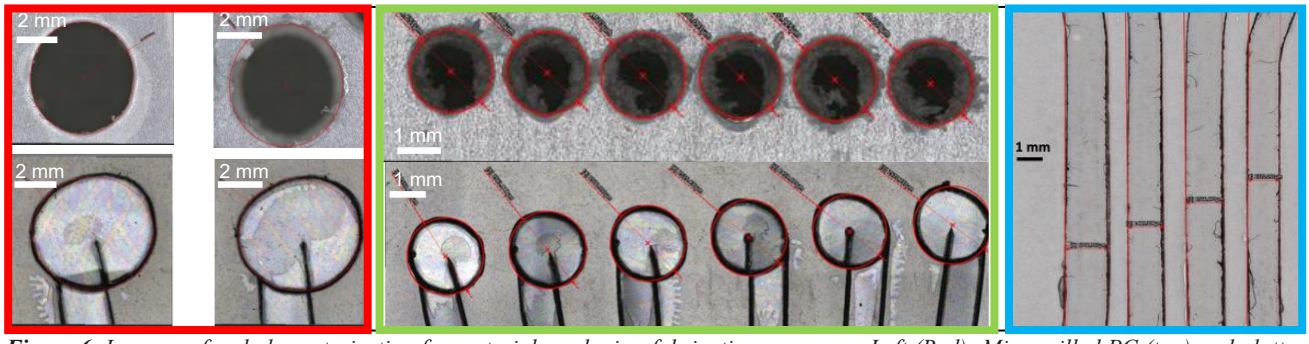

***Figure 6**. Laser confocal characterization for materials and microfabrication processes. Left (Red): Micromilled PC (top) and plotter cut PET (bottom) port diameter measurements for the 4-CH device. Center (Green): Similar measurements for the 6-CH device. Right (Blue): Plotter cut PET channel width measurements for the 4-CH device. All the dimensions and process conditions for 4-CH and 6-CH devices are presented in Table II. Cutting plotter technique revealed to have less error compared to the micromilling approach for the fabrication of ports (~2.5% vs ~36.5%) in both, 4-CH and 6-CH devices. The high error obtained for the micromilling approach, was due to the tapered shape of the milling bit.*

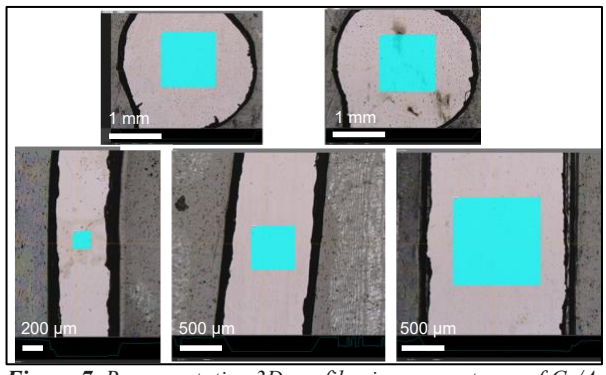

***Figure** 7. Representative 3D profiler image captures of Cr/Au layer surface roughness characterization for the 6-CH device. Ports on top with 1 mm² and channels at bottom with 200 and 500 µm² as evaluation area. Table I (above) presents the roughness value for each case.*

obtained for the 6-CH device, measured at ports and channels over 3 different areas (200, 500 and 1000 µm²) which is excellent for 5µm motor spheres (**Figure 7**). Surface roughness, materials, and microfabrication process specifications for the microfluidics are summarized in **Tables 1 and 2**.

CONCLUSIONS

Combining micromilling along with precise cutting plotter allowed to optimize the microfabrication process for a disposable microfluidic chip. This represents a step forward the multiplexing for detection of several strains of SARS-CoV-2, and paves the way to address incoming challenges with new variants. As the core kit functionality does not depend on the analyzed virus, one-step reagent modification might take place on the surface and motors functionalization to switch from one virus to another.

Cutting plotter provided an acceptable error between design and actual device requirements. This error was mostly due to the manual steps during the bonding process in the multilayered chip. On the other hand, milling tool requires more optimization by using specific purpose bits (e.g., drilling bits) in order to reduce the error on this tool. Its high deviation was caused by the tapered shape of the milling bits, that provided different values for inlet and outlet diameters on the actual ports.

ACKNOWLEDGEMENTS

Authors acknowledge support from the grants NIH U01AA029345-01, Florida High Tech Corridor Match Grants, NSF DMR 1905947, and NSF MSN 2004126.

REFERENCES

[1] K. Yehl *et al.*, "High-speed DNA-based rolling motors powered by RNase H," *Nature Nanotechnology,* vol. 11, no. 2, pp. 184-190, 2016/02/01 2016, doi: 10.1038/nnano.2015.259.

[2] N. Azim, N. Castaneda, A. Diaz, H. Kang, and S. Rajaraman, *MULTI-MODAL MICROELECTRODE ARRAYS FOR THE INVESTIGATION OF PROTEIN ACTIN'S ELECTRO-MECHANOSENSING MECHANISMS TOWARD NEURODEGENERATIVE DISEASE MODELS ON A CHIP*. 2018, pp. 253-256.

[3] A. Manz, N. Graber, and H. M. Widmer, "Miniaturized total chemical analysis systems: A novel concept for chemical sensing," *Sensors and Actuators B: Chemical,* vol. 1, no. 1, pp. 244-248, 1990/01/01/ 1990, doi: https://doi.org/10.1016/0925-4005(90)80209-I.

[4] S. Ding, H. Zhang, and X. Wang, "Microfluidic-Chip-Integrated Biosensors for Lung Disease Models," *Biosensors,* vol. 11, no. 11, 2021, doi: 10.3390/bios11110456.

[5] A. Kundu, T. Ausaf, P. Rajasekaran, and S. Rajaraman, "Multimodal Microfluidic Biosensor With Interdigitated Electrodes (IDE) And Microelectrode Array (MEA) For Bacterial Detection And Identification," in *2019 20th International Conference on Solid-State Sensors, Actuators and Microsystems & Eurosensors XXXIII (TRANSDUCERS & EUROSENSORS XXXIII)*, 23-27 June 2019 2019, pp. 1199-1202, doi: 10.1109/TRANSDUCERS.2019.8808696.

[6] T. Habib, C. Brämer, C. Heuer, J. Ebbecke, S. Beutel, and J. Bahnemann, "3D-Printed microfluidic device for protein purification in batch chromatography," *Lab on a Chip,* 10.1039/D1LC01127H vol. 22, no. 5, pp. 986-993, 2022, doi: 10.1039/D1LC01127H.

[7] S. Hosic *et al.*, "Rapid Prototyping of Multilayer Microphysiological Systems," *ACS Biomaterials Science & Engineering,* vol. 7, no. 7, pp. 2949-2963, 2021/07/12 2021, doi: 10.1021/acsbiomaterials.0c00190.

[8] D. E. Ingber, "Human organs-on-chips for disease modelling, drug development and personalized medicine," *Nature Reviews Genetics,* 2022/03/25 2022, doi: 10.1038/s41576-022-00466-9.

[9] H. Safiabadi Tali Seyed *et al.*, "Tools and Techniques for Severe Acute Respiratory Syndrome Coronavirus 2 (SARS-CoV-2)/COVID-19 Detection," *Clinical Microbiology Reviews,* vol. 34, no. 3, pp. e00228-20, doi: 10.1128/CMR.00228-20.

[10] S. Fuchs, S. Johansson, A. Ø. Tjell, G. Werr, T. Mayr, and M. Tenje, "In-Line Analysis of Organ-on-Chip Systems with Sensors: Integration, Fabrication, Challenges, and Potential," *ACS Biomaterials Science & Engineering,* vol. 7, no. 7, pp. 2926-2948, 2021/07/12 2021, doi: 10.1021/acsbiomaterials.0c01110.

[11] J. Fu, L. Wu, Y. Qiao, J. Tu, and Z. Lu, "Microfluidic Systems Applied in Solid-State Nanopore Sensors," *Micromachines,* vol. 11, no. 3, 2020, doi: 10.3390/mi11030332.

[12] A. Bazrafshan *et al.*, "DNA Gold Nanoparticle Motors Demonstrate Processive Motion with Bursts of Speed Up to 50 nm Per Second," *ACS Nano,* vol. 15, no. 5, pp. 8427-8438, 2021/05/25 2021, doi: 10.1021/acsnano.0c10658.

[13] A. Kundu, T. Ausaf, and S. Rajaraman, "3D Printing, Ink Casting and Micromachined Lamination (3D PICLµM): A Makerspace Approach to the Fabrication of Biological Microdevices," (in eng), *Micromachines,* vol. 9, no. 2, p. 85, 2018, doi: 10.3390/mi9020085.

[14] S. Piranej, A. Bazrafshan, and K. Salaita, "Chemical-to-mechanical molecular computation using DNA-based motors with onboard logic," *Nature Nanotechnology,* 2022/03/28 2022, doi: 10.1038/s41565-022-01080-w.

CONTACT

*Swaminathan Rajaraman, tel: +1-407-823-4339; swaminathan.rajaraman@ucf.edu

PERSONALIZED MEDICINE FOR OFTEN OVERLOOKED POPULATIONS BY USING TEXTILE-BASED SENSORS

Alicia Chong Rodriguez
Bloomer Health Tech., Inc., Boston, Massachusetts, USA

ABSTRACT

Understanding the performance of medical devices in all individuals triggered the FDA to launch the CRDH Health of Women Program earlier this year [1]. There is a danger that machine learning and AI could perpetuate the problem of suboptimal performance in women in healthcare as it has in other industries [2].

Women who present with symptoms consistent with an Acute Coronary Syndrome (ACS) or stroke are often under-diagnosed and under-represented in clinical trials. Moreover, there are data to suggest that women with cardiovascular disease have worse outcomes, poorer prognoses, and higher mortality rates than men.

Optimizing the performance of medical devices in women's bodies has been an unmet need identified in the last 30 years of studies in the field of sex-differences in cardiology. Determining the risk of future adverse cardiovascular events, as well as early detection and improving treatment and procedures for women who have previously suffered an ACS is therefore a problem of paramount importance in the field of cardiovascular medicine.

Remote patient monitoring offers unique opportunities for both female patients and clinicians to improve patient outcomes and deal with information gaps on female cardiac health. We have developed an augmented garment (AG) wireless monitor that records vital-sign information through textile sensors and can be integrated in a form factor such as a bra to enable long-term wear. It has the capability to record electrocardiographic (ECG) data that can be monitored in real-time via Bluetooth as it saves long-term continuous information and uploads to a secure server without the need to manually download the acquired data or connect the AG via wires. We aim to contribute to women's health research by generating sex-specific tools in the growing field of machine learning in healthcare.

KEYWORDS

ECG, women's heart health, sex disparities, artificial intelligence, remote patient monitoring wearables, garments

INTRODUCTION

Participation of Women in Clinical Studies

Historically, women have been underrepresented in clinical trials and, as a result, data derived from a predominantly male population are commonly and perhaps inappropriately extrapolated for clinical use in women [3]. Therefore, in 1993 the National Institutes of Health (NIH) of the United States mandated that women and minorities be included in any government-funded health research [4], a decision made due to the alarming lack of knowledge around women's health and the rising number of deaths from cardiovascular diseases (CVDs), the leading cause of death worldwide [5]. Even though it has led to new discoveries, inequities still exist. More recently, studies have demonstrated inadequate compliance with the NIH guidelines [4].

There has been little improvement in either the enrollment of women in trials or the use of sex-specific analyses [3]. Women constitute fewer than 30% of clinical trials for cardiovascular diseases and only half of scientific publications include analyses of the results according to the participants sex [6]. Therefore, data used for clinical decision-making, drug development and medical device design has been primarily made from clinical trials of cohorts composed mainly of men.

Trends and Wearables

Current trends show a rising adoption of wearable devices already in the market that are internet-connected wireless monitoring sensors which can non-invasively sense, collect, and even process different types of body-related data, e.g., electrical, thermal, and optical signals generated by the human body [6]. Success of remote health monitoring systems crucially depends on the integration, design and usability of the personal health monitoring systems [7]. Wearables come in different form factors ranging from smart glasses worn on the face; fitness trackers or smartwatches worn on the wrist, upper arm, and chest; jewelry with embedded chips like rings and necklaces; devices clipped to, snapped or embedded into clothing; to sensor patches and tattoos attached to the skin [7]. Of all the wearable devices available today, wristbands have higher market penetration and adoption rate than other wearable devices [8], although their mainstream acceptance has been challenging [9]. Better and more adaptable designs are expected for the growth of this segment.

In the design of remote-patient monitoring devices, we need to begin to acknowledge the users' needs beyond just "functionality" [9]. There has been a lot of prior work aiming to improve the existing Holter monitor [10] [11] [12][13]. Differences include handheld monitors, sticky patches that adhere directly to the chest without the need of wires and diverse form factors of the plastic casing of a traditional monitor with long wires (Figure 1).

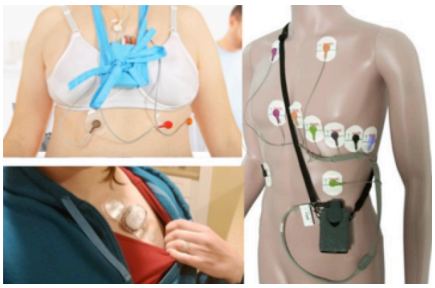

Figure 1: Examples of remote patient monitors.

These monitors are limited and have only incremental changes that prohibit wear longer than 30 days. Additionally similar sticky sensors that could be incorrectly placed impacts their performance in the chest area which makes them less effective and reproducible for long-term analysis [13]. The potential of using AI for non-invasive digital biomarkers through collecting comfortably high performing, validated health data, that detects or diagnoses diseases and provides the user, physician or caregiver information to improve health outcomes could be category-changing and reduce burden and increase women's participation and research efforts.

Motivation

According to the American Heart Association, nearly 44.4% of women age 20 and older in the U.S have some form of

Copyright retained by Authors

cardiovascular disease, about 9.1 million have coronary heart disease (CHD), 3.0 million women are living today with a history of myocardial infarction (MI) [14]. Accumulated knowledge of heart health in men is not necessarily applicable to women, making it more difficult to diagnose and treat women's heart problems effectively.

Recognizing that men and women differ in the diagnosis and outcomes of cardiovascular diseases has led to research interest and the recognition that there are crucial gaps negatively impacting women with heart disease [7]. It is a rising problem that has affected many families and the Go Red for Women campaign has raised awareness and thousands of real stories per year all over the U.S.

This clear need amongst the affected population for more tools, data, analyses and conception of devices designed for accelerating data collection on women and increasing recruitment, adherence, information and knowledge to mitigate these incremental and alarming gaps constitute the motivation behind this work.

PURPOSE

Taking knowledge from the lab into the real-world and building a startup is the topic of this talk. Increasing the knowledge of sex differences and special features in female physiology can help establish new promising predictors for morbidity and mortality as well as treatment and disease management.

Bloomer Tech is generating novel digital biomarkers and transforming women's health. It has scaled the production of its category-changing, textile-sensor technology to collect large amounts of health data from women, an asset that is in high demand and hard to access. The bra form factor and patented sensors enable physiological measurement and ease of use, having great potential for use in the primary care setting, decentralized clinical trials, or as a direct consumer device.

Figure 2. Bloomer Augmented Garment (AG) Platform

ACKNOWLEDGEMENTS

The author would like to thank her team at Bloomer Health Tech., Inc. for their contribution building a field that needs better solutions to improve the outcomes of women.

REFERENCES

[1] E. Fassbender, "FDA puts spotlight on health of women: workshop kicks off new CDRH program", *AAOS Now,* 16-18 (2013).

[2] R.B. Parikh, S. Teeple, and A.S. Navathe, "Addressing bias in artificial intelligence in health care", *JAMA*, 322(24), 2377-2378 (2019), https://doi.org/10.1001/jama.2019.18058.

[3] B. Stanberry, "Telemedicine: barriers and opportunities in the 21st century", *Journal of Internal Medicine,* 247, 615-628 (2000).

[4] V. Regitz-Zagrosek, "Sex and gender differences in symptoms of myocardial ischemia", *European Heart Journal*, 32(24), 3064-3066 (2011), https://doi.org/10.1093/eurheartj/ehr272.

[5] K. Ramasubbu, H. Gurm, and D. Litaker. "Gender Bias in Clinical Trials: Do Double Standards Still Apply?" *Journal of Women's Health & Gender-Based Medicine*, 10(8), 757-764 (2004), https://doi.org/10.1089/15246090152636514.

[6] A. Mosenia, S. Sur-Kolay, A. Raghunathan and N. K. Jha, "Wearable Medical Sensor-Based System Design: A Survey", *IEEE Transactions on Multi-Scale Computing Systems*, 3(2), 124-138 (2017), https://doi.org/10.1109/TMSCS.2017.2675888.

[7] E. Jovanov, "Wireless Technology and System Integration in Body Area Networks for m-Health Applications," *IEEE Engineering in Medicine and Biology 27th Annual Conference*, Shanghai (2005), pp. 7158-7160. https://doi.org/10.1109/IEMBS.2005.1616158.

[8] V. Dibia, "An Affective, Normative and Functional Approach to Designing User Experiences for Wearables*", Normative and Functional Approach to Designing User Experiences for Wearables* (July 14, 2015), http://dx.doi.org/10.2139/ssrn.2630715.

[9] C.S. Miner, D.M. Chan, and C.S. Campbell, "Digital Jewelry: Wearable Technology for Everyday Life", *CHI Extended Abstracts on Human Factors in Computing* Systems, 45-46 (2001).

[10] J. Penders, B. Gyselinckx, R. Vullers, M. De Nil, V.S. Nimmala, J. van de Molengraft, F. Yaziciglu, T. Torfs, V. Leonov, P. Merken, and C. Van Hoof, "Human++: From Technology to Emerging Health Monitoring Concepts", *IEEE 5th International Summer School and Symposium on Medical Devices and Biosensors*, Hong Kong (2008) pp. 94-98.

[11] https://www.gobio.com/brand/lifewatch/

[12] https://vitalconnect.com

[13] M. K. Delano, "A long term wearable electrocardiogram (ECG) measurement system", Doctoral dissertation, Massachusetts Institute of Technology, 2012.

[14] C.W. Tsao, A.W. Aday, Z.I. Almarzooq, A. Alonso, A.Z. Beaton, M.S. Bittencourt, A.K. Boehme, A.E. Buxton, A.P. Carson, Y. Commodore-Mensah, M.S. Elkind, K.R. Evenson, C. Eze-Nliam, J.F. Ferguson, G. Generoso, J.E. Ho, R. Kalani, S.S. Khan, B.M. Kissela, K.L. Knutson, D.A. Levine, T.T. Lewis, J. Liu, M.S. Loop, J. Ma, M.E. Mussolino, S.D. Navaneethan, A.M. Perak, R. Poudel, M. Rezk-Hanna, G.A. Roth, E.B. Schroeder, S.H. Shah, E.L. Thacker, L.B. VanWagner, S.S. Virani, J.H. Voecks, N-Y. Wang, K. Yaffe, and S.S. Martin on behalf of the American Heart Association Council on Epidemiology and Prevention Statistics Committee and Stroke Statistics Subcommittee, "Heart Disease and Stroke Statistics—2022 Update: A Report From the American Heart Association", *Circulation*, *145*(8), (2022), https://doi.org/10.1161/CIR.0000000000001052.

CONTACT

A. Chong Rodriguez, heart@bloomertech.com

RAPID PROTOTYPING OF 3D PRINTED MEMS ARRAYS ON FLEXIBLE SUBSTRATES

Regan Kubicek, Sukjun Kim, and Sarah Bergbreiter*
Department of Mechanical Engineering, Carnegie Mellon University, Pittsburgh, PA, USA

ABSTRACT

This paper presents the first 3D printed MEMS sensor arrays on flexible substrates. A novel fabrication method integrates direct 3D printing on flexible substrates with metal deposition and laser ablation to rapidly prototype arrays of 3D MEMS devices in a couple of hours instead of days using conventional methods. A secondary contribution introduces a novel bio-inspired MEMS strain sensor that closes a switch at a designed strain threshold, providing a low-latency digital indicator for when a particular strain has been reached.

KEYWORDS

Sensor Arrays, 3D Printing, MEMS, Flexible Electronics, Bio-inspired, Two-Photon Polymerization (TPP)

INTRODUCTION

Fabricating MEMS devices on flexible substrates enables compliant, lightweight device integration essential to applications from flexible displays [1] to health monitoring [2]. Sensing 'skins' composed of MEMS sensor arrays on flexible substrates are particularly appealing for numerous robotic applications from humanoids [3] to UAVs [4]. However, creating flexible sensor arrays similar to those found in biological systems like our own skin involves numerous engineering challenges. While larger (> 1 cm) flexible sensor arrays have become more common [5], microscale MEMS sensors are typically limited to rigid silicon wafers to take advantage of standard microfabrication processes. In addition, traditional MEMS sensor arrays typically require significant design and fabrication time from days to months.

Some of these challenges have previously been tackled using transfer printing – an approach designed to transfer MEMS devices fabricated on a rigid donor substrate to a flexible receiver substrate through bonding [6]. While this solves the problem of putting MEMS on a flexible substrate, transfer printing still has fabrication limitations, misalignment challenges, and requires significant cleanroom time to fabricate the MEMS devices [7]. Rapid prototyping through 3D printing could provide benefits, including increased design complexity and a reduction in fabrication time. Polymer 3D structures with microscale features have previously been printed on flexible polyethylene terephthalate (PET) sheets using two-photon polymerization (TPP) [8, 9]. In addition, electrical functionality has been added to TPP-printed structures using metal sputtering to fabricate 3D MEMS actuators, but these were limited to rigid substrates [10].

This work builds on these previous techniques to rapidly fabricate MEMS sensor arrays on a highly flexible substrate. We take advantage of rapid prototyping by using the two-photon polymerization process and extend its utility through the design of new processes to print complex structures (including long overhangs without supports) directly onto 50 µm thin PET sheets. Sputtered metal is used to provide electrical conductivity to the sensors similar to the approach used in [10], but in this work, laser ablation of deposited metal is demonstrated as an alternative approach to chemical etching or shadow masking to achieve electrical isolation. This rapid prototyping process enables MEMS devices to be directly printed on flexible substrates, drastically decreasing fabrication time, and reducing cost, while also presenting 3D devices that are not achievable or challenging to achieve with traditional 2D processes.

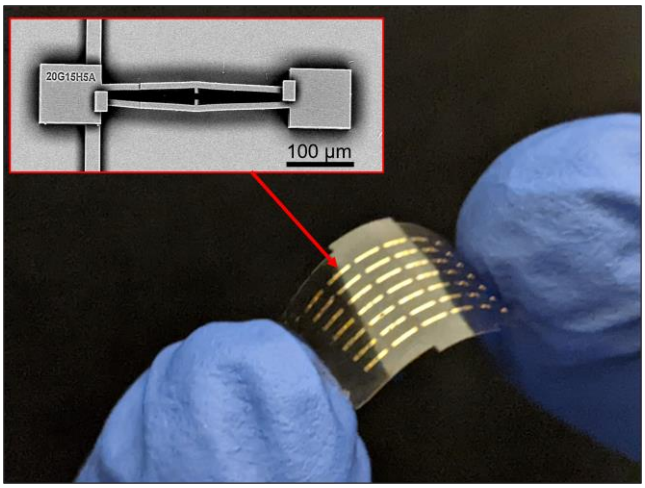

Figure 1. Flexible 42 sensor array directly 3D printed on 50µm thick PET. One example of the bio-inspired MEMS strain switch sensor is shown in the inset.

To demonstrate this novel fabrication process, we also present a new strain sensor inspired by mechanosensors found on the wings of the hawkmoth *Manduca Sexta* called campaniform sensilla [11, 12]. Campaniform sensilla are different from most engineered sensors in that they do not provide a continuous analog signal but instead send neural spikes in response to particular strain stimuli [13]. In previous work, we presented a macro scale strain sensor that outputs a discrete analog signal [14]. This work extends this idea and dramatically reduces the size of the sensor to enable both higher density arrays as well as greater substrate compliance (Figure 1). The result is a strain sensor that activates at a particular strain threshold, acting as a switch. When combined with a simple voltage divider, the contact switch provides a large enough change in voltage to be captured by a digital input on a microcontroller.

FABRICATION

This fabrication process in this work combines two-photon polymerization, metal sputtering, and laser ablation to facilitate rapid prototyping of 3D MEMS on flexible substrates. Structures are

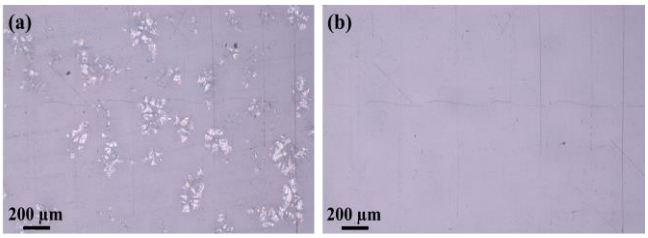

Figure 2. PET adhered to glass slide with Crystalbond 555 (a) Rapid cooling creates artifacts in the Crystalbond which can cause interface finding issues. (b) Slow cooling of Crystalbond provides an optically clear sample that is ideal for automatically finding the interface.

978-1-940470-04-7/HH2022/$25©2022TRF
DOI 10.31438/trf.hh2022.5

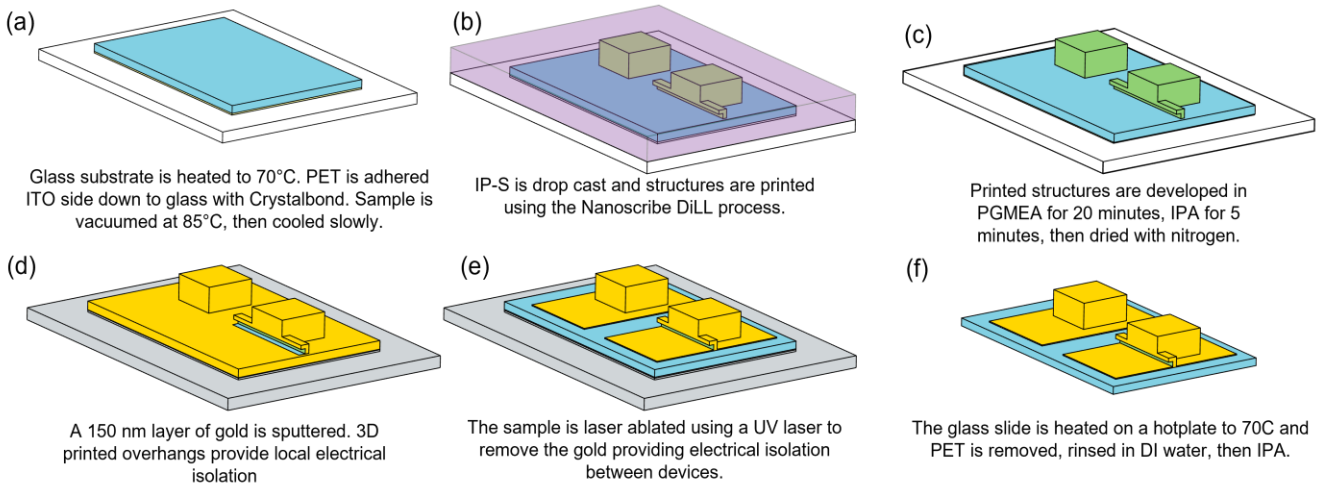

Figure 3: A rapid fabrication process produces flexible MEMS from concept to device in hours. Note the electrical isolation in (e) using 3D overhanging structures and laser etching. Overhangs provide local electrical isolation and laser etching provides global electrical isolation.

directly printed on PET using TPP with a Nanoscribe Photonic Professional GT+ (Nanoscribe Gmbh). In the first step of the fabrication process, an ITO-coated PET sheet is cut to shape using an LPKF U4 laser. During this process, fiducials are added for alignment during printing and for final laser ablation. The substrate used in the fabrication process is an off-the-shelf 300 Ω/sq, 50µm thick Indium Tin Oxide (ITO) coated PET (Sheldahl). The ITO is not used for its conductivity but instead provides a refractive index contrast to the adhesive layer which is required for interface finding in TPP.

One challenge in handling flexible substrates using existing tools is keeping the substrate flat during processing. To accomplish this, Crystalbond 555 is used as an adhesion layer to bond the substrate flat during the fabrication process. A 25mm x 25mm x 0.7 mm silica glass slide is cleaned with IPA and placed on a hotplate at 70°C. Crystalbond 555 is applied to the glass slide, and the PET is placed ITO side down, allowing the capillary forces to pull it uniformly on the glass. The prepared slide is then placed in a vacuum oven at 85°C with a gauge pressure of 25 inHg for 30 minutes to remove air bubbles trapped under the PET. Trapped bubbles can cause interface finding issues during printing and deformations in the substrate while under a high vacuum during subsequent sputtering.

The sample is placed back on a hotplate at 60°C and covered with a petri dish. The hotplate is turned off and left to cool for 20 minutes to room temperature. This slow cooling is a crucial step that prevents artifacts from forming in the Crystalbond, leaving an optically clear layer under the PET that is ideal for interface finding during the 3D printing process (Figure 2). Automatically finding an interface is a critical step in printing using TPP. A weak interface signal can result in structures printed too deep or above the substrate. When printing larger structures with multiple split blocks, an insufficient interface or artifact can lead to misalignment between blocks. By removing bubbles and slowly cooling the Crystalbond 555, we are left with an ITO/Crystalbond interface that provides a robust and consistent interface signal across the entire substrate allowing for larger arrays to be printed. It should also be noted that the ITO/Crystalbond interface is on the bottom of the substrate, and structures are printed on the top. As a result, the z-offset must be adjusted to account for the PET thickness [9]. This offset is found by printing test structures and increasing the z-offset until the structures are visible on the top of the PET. A z-offset of 52 µm was added in this work to print structures on the non-ITO side.

Once the substrate was prepared, the Nanoscribe Dip-in Laser Lithography (DiLL) [15] process was used to print 3D structures. IP-S resist was drop cast onto the PET (Figure 3b), and the structures were printed with the 25X objective and a laser power of 50 mW. The laser power used for the base layer was dropped to 35 mW to alleviate bubbling at the IP-S/PET interface. Another challenge addressed in this fabrication process was printing long (e.g., > 1 mm) overhanging structures. Printing with IP-S resist traditionally requires support structures to prevent drift and misalignment during printing. To print large structures in general, the Nanoscribe needs to break printing steps into blocks – the 25x objective used in this work can print up to a 280 x 280 µm square area at one time before

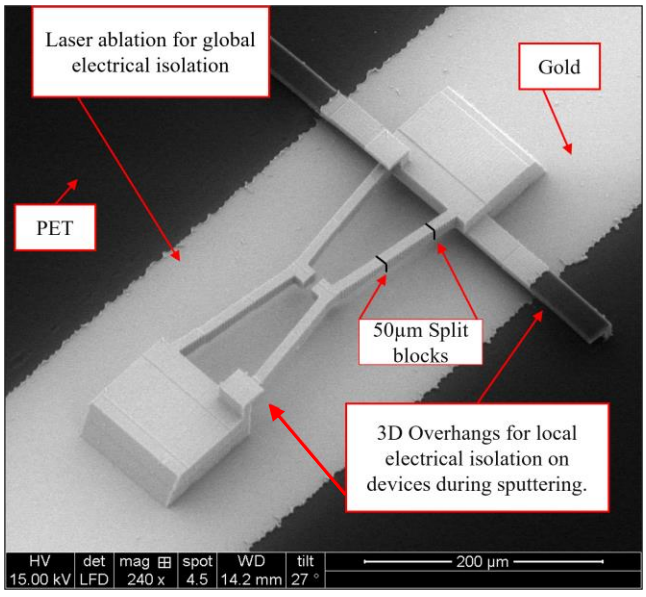

Figure 4: SEM of strain switch shows local and global electrical isolation as well as the long unsupported structures. Long overhanging structures are achieved by reducing split block size to 50µm.

the stage moves to print the next square. These areas are called 'split blocks'. We found that long overhanging structures could be achieved by reducing the split block size to 50 µm, which prevents drift in IP-S during printing (Figure 4). After printing, the structures were developed in PGMEA for 20 min and rinsed in IPA.

To provide electrical conductivity to the 3D polymer structures, gold was then sputtered to a thickness of 150 nm using a Perkin Elmer 6J Sputtering System. Two approaches were used to pattern the gold and provide electrical isolation. Previous work in used overhanging structures in 3D MEMS actuators to provide electrical isolation [10]. The overhanging structures can be added in the 3D design and provide self-shadowing to prevent metal from being deposited underneath during sputtering. In the second approach, we used an LPKF ProtoLaser U4 to selectively remove the deposited gold from both the substrate and printed structures. The sample was aligned using the established fiducials, and gold was removed using a laser power of 0.6 W, resulting in electrical isolation across the substrate. Both isolation approaches were used successfully in this process (Figure 4).

After laser ablation, the sample was placed on a hotplate at 70°C to release the PET substrate from the glass slide. The sample was rinsed in a bath of DI water to remove excess Crystalbond and then isopropyl alcohol was used as a final cleaning step. An example of a 42-sensor array printed using this process is shown in Figure 1, while a SEM of one of these structures is shown in Figure 4. The entire process from sensor CAD design to testing can be accomplished in a single day.

BIO-INSPIRED STRAIN SWITCH

This novel fabrication process was created to aid in developing a novel bio-inspired strain sensor designed to sense strain across a flexible wing. The sensor's design uses chevron-shaped beams [16] to mechanically amplify displacements due to strain (Figure 4). The amplified displacements close a contact switch when a specific strain threshold is reached. Unlike a traditional analog strain sensor that can provide continuous strain measurements, this new sensor design results in a digital indication of strain passing a given threshold and was inspired by the spike timing of biological campaniform sensilla [17].

The sensors' beams can be configured to detect tensile strain (Figure 1) or compressive strain (Figure 5). During printing, the pads of the sensors are isolated from one another using overhanging structures that act as self-shadowing during metal deposition. These

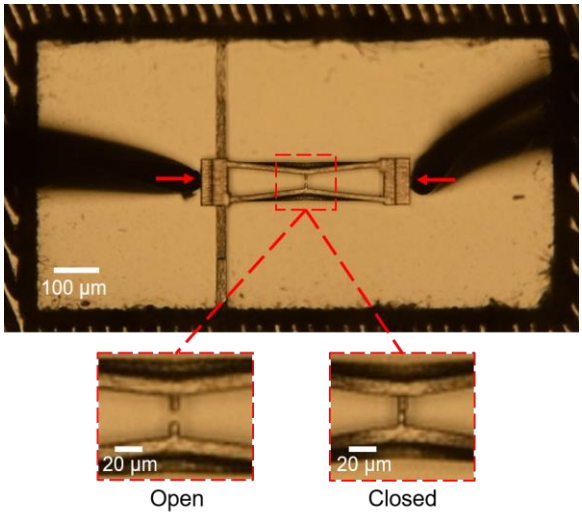

Figure 5: Activating the strain switch with probes. Arrows indicate probe direction causing strain due to compression closing the switch. Call outs zoom in on the contact area.

overhangs provide local electrical isolation on the sensors. Laser ablation was then used to globally isolate the structures from one another. Global and local electrical isolation in the resulting sensors were tested using a source measure unit (SMU) instrument (2410, Keithley) and probe station (Figure 5). A contact resistance of 37 Ω was also measured by inducing a compressive strain using probes, causing the switch to close.

The sensor was tested to detect bending strain in the substrate by connecting probes directly to an Arduino Uno microcontroller. The sample was placed in a cantilever configuration with the sensors at the base of the PET cantilever (Figure 6a). A probe was used to deflect the end of the cantilever, causing a compressive strain on the top of the substrate. One side of the sensor was connected to a ground pin and the other to a digital pin on the microcontroller. An internal pull-up resistor (20 kΩ) completes the voltage divider circuit (Figure 6b). The switch is normally open when the PET is flat, registering 5V on the digital pin. The end of the PET was deflected up, resulting in a compressive bending strain that closes the switch dropping the voltage to 0V. The digital signal generated

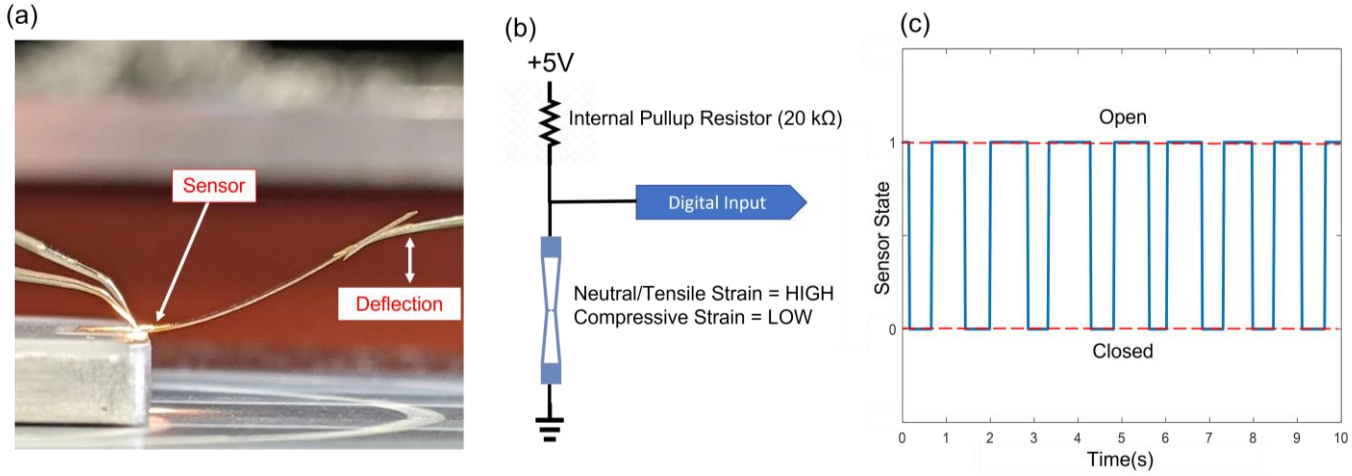

Figure 6. (a) Bending strain is tested on a probe station by deflecting the end of the PET. (b) The strain sensor replaces a switch in a voltage divider. The sensors signal can be captured by a digital pin on a microcontroller (c) Output of the digital signal from the microcontroller obtained by opening and closing the strain switch with bending strain.

from the sensor and measured on the Arduino Uno is shown in Figure 6c. Sampling the signal directly with the digital pin on the microcontroller demonstrates the ability to gain important data such as strain thresholds with precise timing and extremely low latency as compared to more traditional methods of measuring strain on wings [18]. In addition, no additional amplifiers or other circuitry is required. Similar to the biological campaniform sensilla sensors, the sensor's mechanical structure is designed to operate as a filter without requiring additional hardware.

CONCLUSION

This work presented a novel fabrication technique for 3D printing MEMS devices on highly flexible substrates. Using 3D printing, metal deposition, and laser ablation, MEMS arrays can be rapidly prototyped and tested in a single day. This fabrication process enabled the design and fabrication of a novel strain switch that activates at a specific threshold. The strain sensor uses ohmic contact as a transduction mechanism with a contact resistance of 37 Ω. The result is a sensor that requires no signal conditioning or amplification and can be observed with a digital pin on a simple microcontroller. This novel fabrication process opens the door for new and exciting MEMS devices in flexible applications.

ACKNOWLEDGEMENTS

This work is supported by NSF GRFP DGE1745016/ DGE2140739 and the Air Force Office of Scientific Research MURI award number FA9550-19-1-0386. The authors would like to thank the staff of the Claire & John Bertucci Nanotechnology Laboratory and Soft Lithography Lab at Carnegie Mellon University. Special thanks are given to Christina Kubicek for her help with photography.

REFERENCES

[1] J.-c. Tsai et al., "The evolution of mems displays," IEEE Transactions on Industrial Electronics, vol. 56, no. 4, pp. 1057–1065, 2008.

[2] M. Ahmed, I. E. Gonenli, G. S. Nadvi, R. Kilaru, D. P. Butler, and Z. Celik-Butler, "Mems sensors on flexible substrates towards a smart skin," SENSORS, 2012 IEEE, pp. 1–4, 2012.

[3] A. Tomar and Y. Tadesse, "Multi-layer robot skin with embedded sensors and muscles," in Electroactive Polymer Actuators and Devices (EAPAD) 2016, vol. 9798. SPIE, 2016, p. 979809.

[4] H.-S. Shin, Z. Ott, L. G. Beuken, B. N. Ranganathan, J. S. Humbert, and S. Bergbreiter, "Bio-inspired large-area soft sensing skins to measure uav wing deformation in flight," Advanced Functional Materials,vol. 31, no. 23, p. 2100679, 2021.

[5] E. Koch and A. Dietzel, "Skin attachable flexible sensor array for respiratory monitoring," Sensors and Actuators A: Physical, vol. 250, pp. 138–144, 2016.

[6] L. Zhang, Y. Jiang, B. Liu, M. Zhang, and W. Pang, "Highly flexible piezoelectric mems resonators encapsulated in polymer thin films," in 2018 IEEE Micro Electro Mechanical Systems (MEMS). IEEE, 2018, pp. 170–173.

[7] X. Yang and M. Zhang, "Review of flexible microelectromechanical system sensors and devices," Nanotechnology and Precision Engineering, vol. 4, no. 2, p. 025001, 2021

[8] Y. Lin, R. Zhou, and J. Xu, "Superhydrophobic surfaces based on fractal and hierarchical microstructures using two-photon polymerization: toward flexible superhydrophobic films," Advanced Materials Interfaces, vol. 5, no. 21, p. 1801126, 2018.

[9] I. Fiorello, O. Tricinci, G. A. Naselli, A. Mondini, C. Filippeschi, F. Tramacere, A. K. Mishra, and B. Mazzolai, "Climbing plant-inspired micropatterned devices for reversible attachment," AdvancedFunctional Materials, vol. 30, no. 38, p. 2003380, 2020.

[10] S. Kim, C. Velez, R. S. Pierre, G. L. Smith, and S. Bergbreiter, "A two-step fabrication method for 3d printed microactuators: characterization and actuated mechanisms," Journal of Microelectromechanical Systems, vol. 29, no. 4, pp. 544–552, 2020.

[11] B. R. Aiello, K. E. Stanchak, A. I. Weber, T. Deora, S. Sponberg, and B. W. Brunton, "Spatial distribution of campaniform sensilla mechanosensors on wings: form, function, and phylogeny," Current opinion in insect science, vol. 48, pp. 8–17, 2021.

[12] B. T. Hinson and K. A. Morgansen, "Gyroscopic sensing in the wingsof the hawkmoth manduca sexta: the role of sensor location and directional sensitivity," Bioinspiration & biomimetics, vol. 10, no. 5,p. 056013, 2015.

[13] T. L. Mohren, T. L. Daniel, S. L. Brunton, and B. W. Brunton, "Neural-inspired sensors enable sparse, efficient classification of spatiotemporal data," Proceedings of the National Academy of Sciences, vol. 115, no. 42, pp. 10 564–10 569, 2018.

[14] R. Kubicek, M. Babaei, and S. Bergbreiter, "Keeping it simple: Bio-inspired threshold-based strain sensing for micro-aerial vehicles," in 2021 IEEE/RSJ International Conference on Intelligent Robots and Systems (IROS). IEEE, pp. 7505–7511.

[15] J. S. Oakdale, J. Ye, W. L. Smith, and J. Biener, "Post-print uv curing method for improving the mechanical properties of prototypes derived from two-photon lithography," Optics express, vol. 24, no. 24, pp. 27 077–27 086, 2016.

[16] J. Guo, M. Suster, D. J. Young, and W. H. Ko, "High-gain mechanically amplified capacitive strain sensor," in SENSORS, 2005 IEEE. IEEE, 2005, pp. 4–pp.

[17] B. H. Dickerson, Z. N. Aldworth, and T. L. Daniel, "Control of moth flight posture is mediated by wing mechanosensory feedback," Journal of Experimental Biology, vol. 217, no. 13, pp. 2301–2308, 2014.

[18] Shin, Hee-Sup, et al. "Sensing skin for detecting wing deformation with embedded soft strain sensors." 2016 IEEE sensors. IEEE, 2016.

CONTACT

*R. Kubicek, rkubicek@andrew.cmu.edu

A HYBRID 3D MICRO-NANOPRINTING APPROACH FOR BIOMEDICAL MICROINJECTION NEEDLE ARRAYS

Sunandita Sarker[1,], Adira Colton[1], Ziteng Wen[1], Xin Xu[1], Piotr Walczak[2], Miroslaw Janowski[2], Yajie Liang[2] and Ryan D. Sochol[1]*
[1]University of Maryland, College Park, MD, USA
[2]University of Maryland School of Medicine, Baltimore, MD, USA

ABSTRACT

Microinjection protocols are critical to biomedical research and clinical applications, including for the delivery of emerging stem cell therapies that hold distinctive promise for treating neurodegenerative diseases. One pervasive challenge inherent to using traditional microneedles for such stem cell therapies, however, is that, because there is typically only a single opening at the tip, either: (*i*) too many cells are injected as a spheroid, which limits nutrients from reaching the interior stem cells, leading to undesired cell death; or (*ii*) not enough cells are injected to educe a therapeutic response. To provide a pathway that could ultimately bridge this gap, here we investigate a hybrid additive manufacturing (or "three-dimensional (3D) printing") approach to realize microneedle arrays at scales that are relevant and advantageous for microinjection into the brain. Specifically, we leverage "*ex situ* Direct Laser Writing (*es*DLW)" to 3D nanoprint arrays of 50 μm-in-diameter microneedles directly onto Digital Light Processing (DLP) 3D-microprinted capillaries. Microfluidic cyclic burst-pressure testing for input pressures up to 275 kPa (n = 100) revealed uncompromised fluidic integrity at the array-capillary interface. *Ex vivo* experiments performed on an excised mouse brain revealed that the microneedle arrays could not only withstand penetration into the tissue, but also yield effective microinjection of a surrogate fluid into the brain. In combination, these results suggest that the presented microneedle array strategy offers unique potential for biomedical microinjection applications.

KEYWORDS

Additive Manufacturing, 3D Printing, Direct Laser Writing, Two-Photon Polymerization, Digital Light Processing

INTRODUCTION

Microinjection technologies are widely employed in both research settings (*e.g.*, for developmental biology and transgenics) and clinical applications ranging from *in vitro* fertilization to intraocular injection [1–3]. For example, researchers have found that targeted microinjection of therapeutic drugs can improve the efficacy of treatments for cancer as well as for autoimmune and infectious diseases [4–5]. Among emerging medical treatments, one particular microinjection application that has garnered increasing attention is stem cell-based therapy—a class of medical procedures that involve the targeted microinjection of stem cells to repair damaged tissue (*e.g.*, in the spinal cord, brain, and joints) or improve a weakened immune system [6, 7]. Previously, we demonstrated the potential of stem cell therapies for treating neurological disorders [8, 9]. Yet, the efficacy of such treatments remains highly dependent on the underlying microinjection process, which significantly affects the survival of transplanted cells as well as the overall therapeutic efficacy [10, 11]. For example, if the number of stem cells injected is too large, then nutrient transport to cells located in interior regions can be obstructed, resulting in cell death [12, 13]. Conversely, if too few cells are injected, then—despite the likelihood of cell survival—the therapeutic effect will be limited [14]. Thus, new microinjection strategies are in critical demand.

CONCEPT

A shift from traditional microinjection needles that comprise a singular output port to microneedle arrays (with many output ports) offers a promising means to overcome the aforementioned microinjection-associated deficits for stem cell-based therapies. Although researchers have demonstrated the utility of mesoscale needle arrays for distributing drugs or target cells uniformly to a large area with minimal tissue damage [15,16], neurological stem cell therapies necessitate markedly higher injection densities (*e.g.*, 100–200 μm center-to-center needle spacing) and high-aspect-ratio needle tips (*e.g.*, >600 μm heights, 50 μm diameters). In addition, such arrays must be fabricated at the end of fluidic capillaries, which presents a considerable challenge for conventional microfabrication methods. Recently, we reported an "*ex situ* Direct Laser Writing (*es*DLW)" strategy for printing 3D microfluidic structures directly onto—and notably, fully sealed to—fluidic tubing that can be manipulated by hand [17], and then demonstrated this approach for microinjection needles with a singular tip [18]. In this work, we advance this *es*DLW concept, while remediating its alignment-associated drawbacks, to introduce a novel hybrid additive manufacturing strategy

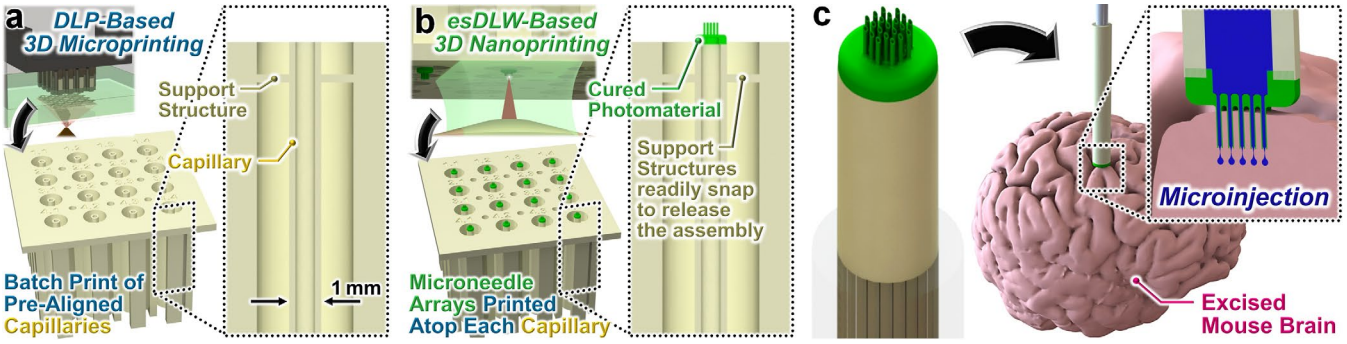

Figure 1: *Conceptual overview of the hybrid 3D micro-nanoprinting strategy for additively manufacturing microinjection needle arrays.* ***(a)*** *Digital Light Processing (DLP)-based 3D microprinting of 16 pre-aligned capillaries.* ***(b)*** *"Ex situ Direct Laser Writing (esDLW)"-based 3D nanoprinting of microneedle arrays directly atop—and fluidically sealed to—each capillary.* ***(c)*** *Individual microneedle array (after selective release by manually pushing the opposing side of a target capillary to break the thin supporting structures) integrated with an injector system to support the delivery of biomedical payloads (e.g., therapeutic drugs and/or stem cell suspensions) into the brain.*

978-1-940470-04-7/HH2022/$25©2022TRF
DOI 10.31438/trf.hh2022.6

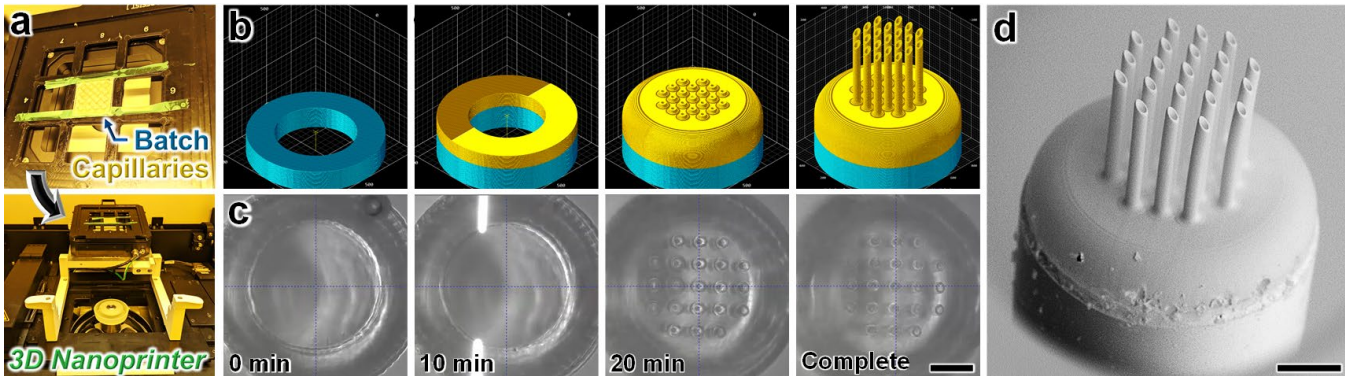

Figure 2: *Fabrication results.* ***(a)*** *DLP-printed batch capillaries loaded into the DLW 3D nanoprinter.* ***(b, c)*** *Computer-aided manufacturing (CAM) simulations* ***(b)*** *and corresponding micrographs* ***(c)*** *of the esDLW process for 3D nanoprinting a complete microneedle array directly onto a capillary in a single print run.* ***(d)*** *SEM micrograph of a fabricated microneedle array-capillary assembly. Scale bars = 200 μm*

for 3D nanoprinting microinjection needle arrays atop 3D-micro-printed capillaries to ultimately support stem cell therapies (**Fig. 1**).

The hybrid 3D micro-nanoprinting strategy consists of three fundamental steps. First, DLP-based 3D microprinting—a vat photopolymerization approach in which a photocurable material is selectively crosslinked layer by layer to produce 3D objects—is used to fabricate a batch of capillaries in designated array positions (**Fig. 1a**). In contrast to our prior works that required custom-built capillary holders that relied on undesired manual (*i.e.*, by hand/eye) alignment protocols [17, 18], batch printing of the capillaries allows for facile loading into the 3D nanoprinter with all capillaries in pre-defined positions and orientations. The second step entails *es*DLW printing of the microneedle arrays directly onto the tops of the DLP-printed capillaries. To do so, photomaterial is dispensed atop a capillary, and then a femtosecond pulsed IR laser is scanned in a point-by-point, layer-by-layer manner to selectively crosslink the photomaterial in target locations *via* two-photon (or multi-photon) polymerization phenomena (**Fig. 1b**). In the final step, individual microneedle array-capillary assemblies can be selectively released from the batch—*i.e.*, by manually pushing the opposing side of the capillary to break the thin support structures (**Fig. 1b – *inset***). Thereafter, the opposing end of the capillary can be interfaced with fluidic tubing or injector systems to facilitate the delivery of biomedical fluidic payloads (*e.g.*, therapeutic drugs and/or stem cell suspensions) into target sites, such as the brain (**Fig. 1c**).

MATERIALS AND METHODS

Digital Light Processing (DLP)-Based 3D Microprinting of the Pre-Aligned Capillaries in Batch

The computer-aided design (CAD) software, SolidWorks (Dassault Systèmes, France), was used to generate models of batch arrays of 16 capillaries. Each capillary was designed with an inner diameter (ID) of 500 μm and an outer diameter (OD) of 1 mm. Models were exported as STL files and imported into the slicer tool for the Miicraft M50 DLP 3D printer (CADworks3D, Canada). Capillary batches were printed using Clear Microfluidic Resin v7.0a (CADworks) with the layer height set to 50 μm. Following the DLP process, the prints were developed in methanol for approximately 10 s, and then methanol was perfused through each capillary to eliminate any residual resin from the interiors. Lastly, the prints were dried with pressurized air and cured under UV light for 10 s.

Ex Situ Direct Laser Writing (*es*DLW)-Based 3D Nanoprinting of Microneedle Arrays onto the Capillaries

The microneedle arrays—modeled with SolidWorks (Dassault Systèmes)—each comprised 21 identical needle tips (ID = 30 μm; OD = 50 μm; height = 700 μm). The models were exported as STL files and imported into the computer-aided manufacturing (CAM) software, DeScribe (Nanoscribe GmbH, Karlsruhe, Germany). The print settings included a hatching distance of 700 nm and a layer height of 2.5 μm. Initially, IP-Q photoresist (Nanoscribe) was dispensed atop the capillaries, and the batch assembly was loaded into the Nanoscribe Photonic Professional GT2 3D printer (**Fig. 2a**). For *es*DLW printing, the Dip-in Laser Lithography (DiLL) mode was used with a 10× objective lens, a laser power of 27.5 mW, and a laser scanning speed of 120,000 μm/s. The printing process was initiated with 50 μm of overlap with the top capillary surfaces. Following the *es*DLW process, the batch assembly was removed from the printer and developed using propylene glycol methyl ether acetate (PGMEA) for 60 min and isopropyl alcohol (IPA) for 5 min, and then allowed to dry under ambient conditions. Lastly, target microneedle array-capillary assemblies were manually released from the batch by pushing the opposing end of the capillary to yield complete detachment from the support structure connections.

Optical Characterization

All scanning electron microscope (SEM) images were captured using a TM4000 Tabletop SEM (Hitachi, Tokyo, Japan). Brightfield microscopy during microfluidic testing was performed using an inverted microscope (Motic AE31, Motic, Canada) connected to a charge-coupled device (CCD) camera (Moticam Pro 285B, Motic). For *ex vivo* microinjection experiments, optical characterizations were performed using the Monocular Max 300x microscope objective and a 41MP USB C-Mount Industry Microscope Camera Set (Hayear Electronics Co. Ltd., Shenzhen, China).

Microfluidic Experimentation

Fluidic testing was performed using the Fluigent Microfluidic Control System MFCS and OxyGEN software (Fluigent, France). DI water was inputted *via* fluidic tubing connected to the opposing end of the capillaries. Three separate sets of cyclic burst-pressure experiments were performed corresponding to applied pressures of approximately 75 kPa, 175 kPa, and 275 kPa for 5 s, but then set to 0 kPa for 5 s after each pressure increase for all cases. Each set of experiments were performed for n = 100 cycles while the microneedle array-capillary interface was monitored for potential signs of undesired leakage phenomena (*e.g.*, fluid exiting at points along the interface rather than out the tops of the microneedle tips).

Ex Vivo Mouse Brain Microinjection Experimentation

Brain tissue excised from a six-month-old male mouse (Wild-type C57BL/6 J, Jackson Laboratory) was used for *ex vivo* microinjection experiments. The brain with an intact dura mater was excised within 10 min of euthanasia and stored in phosphate-

buffered saline (PBS) (Sigma-Aldrich, Saint Louis, MO) on ice prior to testing. The tissue sample was handled gently before and during the experiment to maintain tissue integrity. The microneedle array-capillary assembly was interfaced with a custom-built nanoinjector (Narashige, MO10) to control the displacement and to perform microinjections with a surrogate fluid (blue-dyed DI water).

RESULTS AND DISCUSSION

Hybrid 3D Micro-Nanoprinting-Based Fabrication

The total DLP printing process was completed in 45 minutes, with the resulting batch capillaries resolved with overall dimensions that allowed for facile loading into the DLW 3D printer (**Fig. 2a**). CAM simulations and corresponding micrographs of the *es*DLW process for 3D printing a microneedle array directly onto a DLP-printed capillary are presented in **Figure 2b** and **2c**, respectively. The total *es*DLW printing process was completed within 25 minutes. SEM micrographs of fabrication results revealed effective alignment and integration of the microneedle arrays with the capillaries, without any signs of defects along the interface (*e.g.*, **Fig. 2d**).

Microfluidic Burst-Pressure Characterization

To investigate the mechanofluidic integrity of the microneedle array-capillary interface, we connected the opposing end of the capillaries to fluidic adapters (**Fig. 3a**) and performed cyclic burst-pressure tests while optically monitoring the microneedle array. Experimental results did not reveal any signs of undesired leakage phenomena (*e.g.*, fluid exiting *via* the interface rather than out of the needle tips) (**Fig. 3b**). In addition, quantified results for cyclic burst-pressure testing up to 275 kPa—notably higher that prior targets of 70 kPa [16]—similarly revealed uncompromised fluidic integrity, as evidenced by the flow rate returning to a consistent magnitude after each ramp up in applied pressure for all cases (*e.g.*, **Fig. 3c–e**).

Ex Vivo Mouse Brain Microinjection

Two sets of *ex vivo* experiments were performed with a brain excised from a euthanized mouse (**Fig. 4a**). As a fundamental measure of microneedle array efficacy, we initially investigated the ability to successfully penetrate the brain tissue without mechanical failure (*e.g.*, needle tip fracture). The microneedle array-capillary assembly was interfaced with a nanoinjector to facilitate controlled insertion while monitoring the displacement (*e.g.*, **Fig. 4b**). After a total displacement of 1 mm, the microneedle array was retracted, and the process was repeated twice more. SEM micrographs of the microneedle arrays following these repeated tissue puncture experiments did not reveal any signs of mechanical failure (*e.g.*, **Fig. 4c**).

To investigate the biomedical microinjection capability of the printed microneedle array, we loaded the microneedle array-capillary assembly with a surrogate fluid and then interfaced the assembly with the nanoinjector (**Fig. 4a**). Akin to the tissue penetration experiments, we used the nanoinjector to insert the microneedle array into the brain tissue, but in this case, we then used the pneumatically controlled nanoinjector to deliver the surrogate fluid into the tissue (**Fig. 4d**). After retracting the microneedle array, we washed the surface of the injection site with PBS to eliminate any residual fluid from the surface. Subsequent optical characterizations revealed successful penetration and microinjection of the surrogate fluid into the brain tissue (*e.g.*, **Fig. 4e**).

CONCLUSION

Microinjection protocols underlie a diversity of applications in biomedical fields, yet traditional microneedle architectures with singular tips suffer from limited utility, such as for stem cell therapy. In this work, we presented a novel hybrid additive manufacturing strategy for printing microinjection needle arrays at scales that are

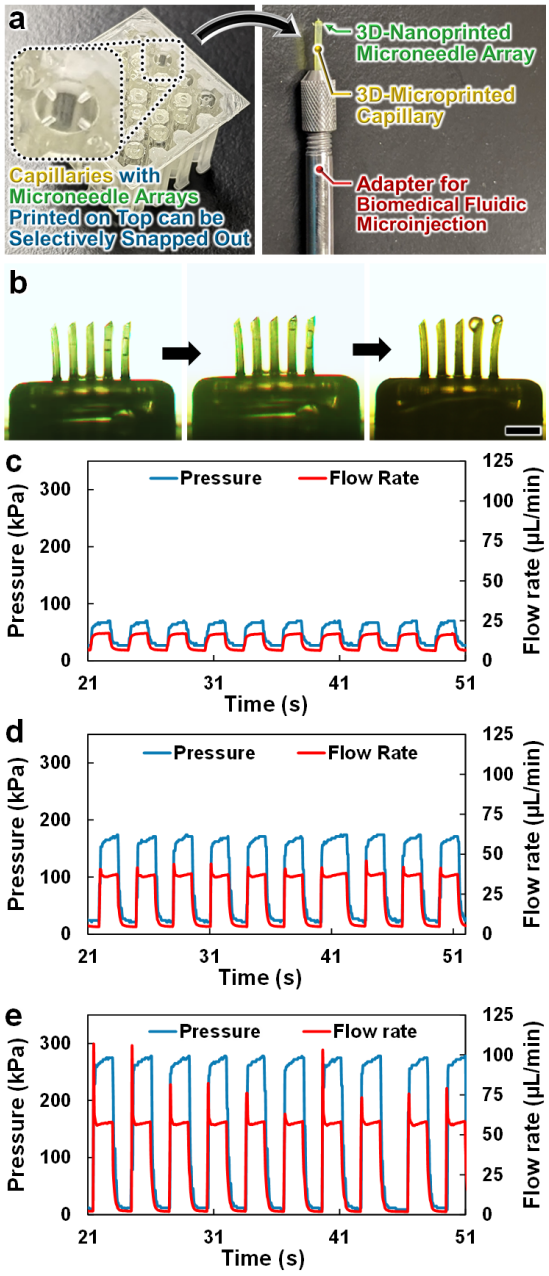

Figure 3: *Experimental results for microfluidic characterizations.* ***(a)*** *Example of a microneedle array-capillary assembly individually released from the batch and then interfaced with an adapter for fluidic loading.* ***(b)*** *Sequential micrographs during fluidic infusion. Scale bar = 200 µm.* ***(c–e)*** *Results for cyclic burst-pressure testing with DI water during representative intervals for input pressure cycles targeting:* ***(c)*** *75 kPa;* ***(d)*** *175 kPa; and* ***(e)*** *275 kPa.*

relevant and beneficial for emerging stem cell therapies for treating neurological disorders. Specifically, we combined DLP-based 3D printing with our *es*DLW approach to print microneedle arrays capable of withstanding 275 kPa pressure cycling and repeated insertion into an excised mouse brain. Notably, the demonstrated *ex vivo* microinjection of a surrogate fluid into a mouse brain represents a critical proof of principle for the presented strategy to offer utility for stem cell therapy. While future efforts should focus on interrogating the efficacy of the microneedle arrays for the delivery of stem cell suspensions, the current results for the presented

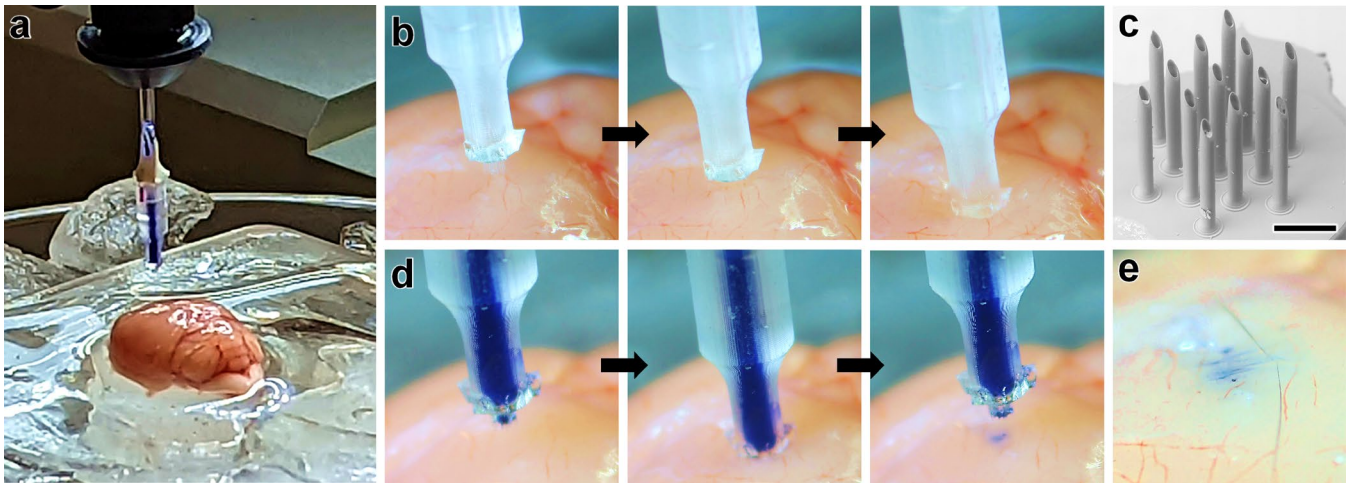

Figure 4: *Experimental results for ex vivo microinjection into an excised mouse brain.* ***(a)*** *Experimental setup for microneedle array-capillary assembly interfaced with a custom-built nanoinjector.* ***(b,c)*** *Tissue puncture results.* ***(b)*** *Sequential images during microneedle array insertion into brain tissue.* ***(c)*** *SEM micrograph of microneedle array after retraction from the brain tissue. Scale bar = 200 µm.* ***(d,e)*** *Microneedle array-based microinjection results for a surrogate fluid (blue-dyed DI water).* ***(d)*** *Sequential images before (left), during (middle), and after (right) microinjection into brain tissue.* ***(e)*** *Expanded view of the post-injection site.*

strategy serve as a critical foundation as an enabling technology for new microinjection applications that promote human health.

ACKNOWLEDGEMENTS

We greatly appreciate the contributions of members of the Bioinspired Advanced Manufacturing (BAM) Laboratory and the technical staff of Terrapin Works as well as the Robert E. Fischell Institute for Biomedical Devices at the University of Maryland, College Park.

REFERENCES

[1] J. Puschhof, *et al.*, "Intestinal organoid cocultures with microbes", *Nature Protocol,* 16, (2021).

[2] S. Rafiq, C.S. Hackett, R.J. Brentjens, "Engineering strategies to overcome the current roadblocks in CAR T cell therapy", *Nature Reviews Clinical Oncology,* 17 (2020).

[3] C. Askew et al., "Tmc gene therapy restores auditory function in deaf mice", *Science Translational Medicine,* 7 (2015).

[4] M. Halasz, *et al.*, "Integrating network reconstruction with mechanistic modeling to predict cancer therapies", *Science Signaling,* 9 (2016).

[5] Y. Oda *et al.*, "Discovery of anti-inflammatory physiological peptides that promote tissue repair by reinforcing epithelial barrier formation", *Science Advances,* 7 (2021).

[6] F.K. Wong, *et al.*, "Microinjection of membrane-impermeable molecules into single neural stem cells in brain tissue", *Nature Protocol*, 9 (2014).

[7] M.H. Amer *et al.*, "Translational considerations in injectable cell-based therapeutics for neurological applications: concepts, progress and challenges, *NPJ Regenerative Medicine,* 2 (2017).

[8] Y. Liang, L. Ågren, A. Lyczek, P. Walczak, J.W.M. Bulte, "Neural progenitor cell survival in mouse brain can be improved by co-transplantation of helper cells expressing bFGF under doxycycline control", *Experimental Neurology,* 247 (2013).

[9] Y. Liang, P. Walczak, J.W.M. Bulte, "The survival of engrafted neural stem cells within hyaluronic acid hydrogels", *Biomaterials,* 34 (2013).

[10] B. Wahlberg *et al.*, "*Ex vivo* biomechanical characterization of syringe-needle ejections for intracerebral cell delivery", *Scientific Reports,* 8 (2018).

[11] A.S. Lee *et al.*, "Prolonged survival of transplanted stem cells after ischaemic injury *via* the slow release of pro-survival peptides from a collagen matrix", *Nature Biomedical Engineering,* 2 (2018).

[12] J. Tchou *et al.*, "Safety and Efficacy of Intratumoral Injections of Chimeric Antigen Receptor (CAR) T Cells in Metastatic Breast Cancer", *Cancer Immunology Research,* 5 (2017).

[13] D.E. Discher, D.J. Mooney, P.W. Zandstra, "Growth Factors, Matrices, and Forces Combine and Control Stem Cells", *Science,* 324 (2009).

[14] L.M. Marquardt *et al.*, "Designer, injectable gels to prevent transplanted Schwann cell loss during spinal cord injury therapy", *Science Advances,* 6 (2021).

[15] S. Chu, N. Uplekar, S. Liu, R. Ghodssi, "Complementary Capillary System Integrated Microneedles for Autonomously Localized Therapeutics Loading", *Journal of Microelectromechanical Systems,* 29 (2020).

[16] S. Liu *et al.*, "Biomimetic Barbed Microneedles for Highly Robust Tissue Anchoring", *IEEE 33rd International Conference on Micro ElectroMechanical Systems (MEMS),* (2020), pp. 885-888.

[17] R. Acevedo *et al.*, "3D Nanoprinted External Microfluidic Structures *Via Ex Situ* Direct Laser Writing", *IEEE 34th International Conference on Micro ElectroMechanical Systems (MEMS)*, (2021), pp. 10–13.

[18] Z. Wen, R. Acevedo, K. Rand-Yain, R.D. Sochol, "3D Nanoprinted Microinjection Needles *Via Ex Situ* Direct Laser Writing", The 25th International Conference on Miniaturized Systems for Chemistry and Life Sciences (MicroTAS), (2021).

CONTACT

*S.Sarker, tel: +1-301-405-6928; ssarker1@umd.edu

TOWARDS A CMOS INTEGRATED PIEZOELECTRIC MEMS PROCESS DESIGN KIT

Benyamin Davaji[1,2], Justin Kuo[1,3], Matteo Rinaldi[2], and Amit Lal[1,3]*
[1]Cornell University, Ithaca, New York, USA
[2]Northeastern University, Boston, Massachusetts, USA
[3]Geegah LLC, Ithaca, New York, USA

ABSTRACT

Piezoelectric AlScN/AlN thin films have enabled the integration of CMOS and MEMS with a wide variety of MEMS devices. Compared with the CMOS fabless design/foundry manufacturing model, where a PDK with multiple different devices is available for designers, there are very few shared MPW piezo-MEMS processes, and there are none that can support multiple different types of devices. A Piezo-MEMS PDK would enable CMOS designers to make systems from piezo-MEMS devices, not just MEMS experts. A Piezo-MEMS PDK that utilizes libraries of MEMS transducers and circuits is needed to fuel the development of piezoelectric MEMS systems to broader CMOS and sensors/actuators communities. In this work, we demonstrate the development of a process flow that supports both released resonators and bulk coupled GHz bulk ultrasonic transducers. We demonstrate functioning devices that consist of GHz BAW, FBAR, and CMR devices.

KEYWORDS

AlN, AlScN, Piezoelectric, MEMS, PDK

INTRODUCTION

CMOS-based integrated circuits are based on the existence of Process Design Kits (PDK) which guarantees device performance for a multitude of devices. A typical CMOS process supports a variety of devices such as transistors, diodes, resistors, capacitors, and inductors and these devices are available as parametric cells (P-Cells) in a process development kit (PDK) that allow layouts and simulation models to be automatically generated for different device sizes – designers do not need to know how to perform TCAD or FEM modeling to use these devices. Furthermore, due to the limited number of thin film stack options that designers have access to, multi-project wafer (MPW) runs can be easily done, lowering the barrier to entry and allowing designers to prototype designs for a relatively low cost.

In the past, MEMS design kits have focused on electrostatic MEMS. These include the MUMPS and SANDIA SUMMIT processes. These processes had a significant impact on the MEMS community allowing vast penetration into research and commercial sectors. Similarly, CMOS integrated electrostatic MEMS has been a research focus and has yielded commercial successes [19, 21]. Generally, the packaging required for electrostatic MEMS, and the higher voltages prevents the technology from scaling to deep sub-micron transistors where supply voltages are limited to ~1V. Similarly, recently AlN/CMOS integration approaches have been implemented onto CMOS nodes up to 130nm. This technology node is still an older technology, which is not an active node for the CMOS community. This disparity prevents the accessibility of MEMS to the much larger circuit design community. Furthermore, MEMS processes, including MEMS on CMOS processes, are typically optimized for a single device type. Innovation is often on the device itself, and substantial FEM simulations of devices are conducted, as a typical design requires an extensive understanding of process parameters and device operation. There is no current equivalent MEMS on CMOS process/PDK that offers the same flexibility to support multiple types of devices, support for MPW runs, and the same ease of use for designers as a CMOS, at a CMOS node that is compatible with the vast majority of CMOS designs. Such a MEMS PDK, were it available, would enable any CMOS designer to make systems using MEMS devices – by making well-characterized P-Cells of MEMS devices available, incorporating MEMS devices into integrated circuits would be as simple as instantiating an on-chip inductor or MIM capacitor into a CMOS design today.

The target platform of choice for this work is aluminum nitride (AlN) based Piezo-MEMS process, as shown in Fig. 1. Integration of MEMS on CMOS offers several key advantages including reduced electrical parasitics allowing for higher SNR and lower power consumption, high interconnect density allowing for large sensor arrays, and reduced device form factor. While other MEMS technologies such as electrostatic MEMS are capable of being integrated into CMOS, Piezo-MEMS stands out in the sheer variety of devices enabled by thin film AlN/AlScN. The CMOS compatibility of AlN has enabled numerous MEMS devices to be integrated onto CMOS, including FBAR resonators [1], piezoelectric micromachined ultrasonic transducers (PMUT) [2], piezoelectric transformers [3], contour-mode resonators (CMR) [4], microphones [5], and GHz ultrasonic transducers [6-7]. Other devices enabled by thin film AlN or AlScN include piezoelectric gyroscopes [8], optical waveguides and modulators [9], RF switches [10], and ferroelectric memories [11], among many others.

For a MEMS thin film stack to be suitable for a common PDK platform with the possibility of MPW runs, the allowable layer thicknesses must be restricted to a limited number of variations, much as how CMOS processes allow designers only a limited choice over metal layer thicknesses. Therefore, the target devices supported by the PDK must primarily have their functionality determined through layout/lithography, and not through changing layer thicknesses.

As a result of these considerations, the target devices chosen for the PDK are CMRs, PMUTs, and GHz transducers. These devices all feature significant amount of functionality that is lithographically "programmable." For CMRs, their resonance frequency is determined by their electrode spacing [12]. PMUT center frequency is determined by the transducer radius [13]. The center frequency for GHz transducers is set by the AlN and top dielectric thin film layer thicknesses, but several key functions are lithographically definable such as adjusting acoustic beam width through transducer sizing, adjusting echo amplitudes through transducer spacing, and adjusting diffraction characteristics through layout [14]. This flexibility allows GHz transducers to be used in a variety of configurations such as for GHz ultrasonic imaging [15], ultrasonic communication channels [16], temperature sensing [17], and clock oscillators [18]. By allowing users some choices in AlN and top dielectric layer thicknesses, more control over device operating frequencies can be realized. In addition, due to their commercial relevance and because a release step is supported as part

978-1-940470-04-7/HH2022/$25©2022TRF
DOI 10.31438/trf.hh2022.7

of the process, released membrane resonators such as FBARs can be realized on the process.

THIN FILM LAYER STACK

The process was developed at the Cornell NanoScale Science and Technology Facility (CNF) and the thin film layer stack chosen for the process is shown below. The choice of layers starting from bottom to top are 1) SiO2 release layer (1000 nm), 2) AlN buffer layer for electrical insulation purposes (50 nm), 3) bottom Ti/Pt electrode (100/20 nm), 4) AlN piezoelectric layer (0.5, 1 and 1.5 µm), 5) top Ti/Al electrode (200/20 nm), and 6) top Si_xN_y buffer layer (300-900 nm). The process was fabricated on both 4-inch wafers and 8-inch wafers. 4-inch wafers are more convenient for fabrication in CNF due to more tool compatibility. The same process

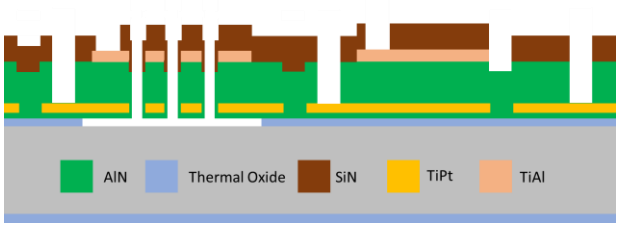

Figure 1. Cross-section of the Piezo-MEMS process flow

was also run with 8-inch wafers, due to the need to develop a process that can work with 8-inch CMOS wafers. This choice of layer stack up allows for both released devices and bulk coupled GHz transducers. GHz transducers and resonators can also be realized by a top dielectric etch above the devices to remove the nitride above the top electrode of the devices.

MASK LAYOUT

The reticle layout is shown in Fig. 2, where a 10 x 10 mm reticle size has been chosen to allow for 1x4 multilayer masks to be used. Devices included on the reticle include several variations of GHz transducer devices, PMUTs, CMR resonators, FBARs, piezoelectric in plane bimorphs, and process calibration structures.

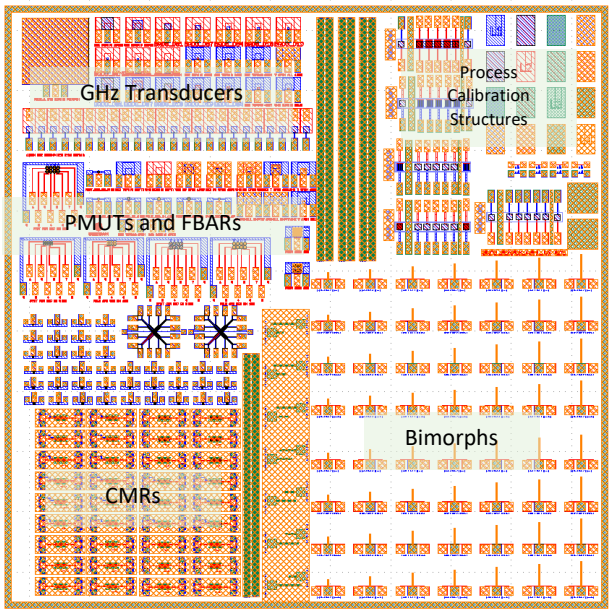

Figure 2: Mask Layout

DEVICE FABRICATION AND PROCESS FLOW

An ASML 248nm DUV process was used to achieve the required resolution (~400 nm) where the tool is compatible with both substrate sizes (100 and 200 mm). The UV210 DUV positive resist (500 nm) with UV42P antireflection coating (62 nm) is applied by an automatic Suss MicroTec Gamma cluster for all layers. Standard (ASML Combi reticle) PM and SPM_X, and SPM_Y ASML marks are used for alignment between layers. New alignment marks are added to each new layer and used for aligning process in the next layer.

The process starts with thermal oxides (1000 nm) grown on DSP Si substrates. As this process is intended as a feasibility study, release layer patterning and planarization steps were not performed, thus resulting in the need to do timed etch release (different for each set of devices) which results in nonuniformities in the release cavities. Next, a thin (50 nm) isolating bottom AlN layer was deposited with an OEM Endeavor M1 40kHz ac reactive sputtering system. A Pt/Ti (100/20 nm) film was deposited with the DC sputtering process for bottom electrode metallization. The Pt film deposition process was optimized to achieve XRD-RC of ~3-3.5 deg (FWDM). The bottom electrode was patterned with 1st mask and was patterned using the multi-step Ion Beam Etching (IBE) process (AJA International). A multiangle process was utilized to remove the fencing artifact in the IBE process. Then the AlN piezo layer was deposited while the film stress for each thickness was precisely tuned to be as close as neutral using the Stress Adjustment Unit (SAU, resistor box) in the Endeavor M1 system. The stress measurement was performed using two angles (FleXus) and carried out to keep the total wafer bow under 40 µm to avoid handling issues with robot transfer systems.

The top electrode metallization (Ti/Al) was deposited using DC magnetron sputtering and was patterned by 2nd mask layer. The top electrode patterns are etched by the ICP-RIE process (Plasma-Therm 770) using Cl2 and Ar chemistry with added CH4 for

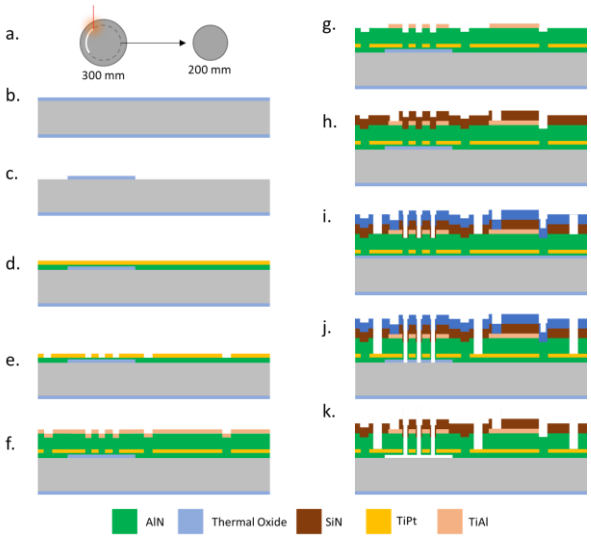

Figure 3. The process flow with released and solidly mounted AlN transducers and SixNy buffer layer for bimorphs. Thickness of ALN is 1.5µm, thickness of SixNy is 0.9µm.

sidewall profile control, followed by a short SF6 exchange reaction step to avoid corrosion of Al patterns (due to instability of AlCl3). Then the elastic layer (SiN) was deposited using the PECVD process and a tight film stress control to achieve minimized (<+/- 50 MPa) residual film stress. The SiN layer was patterned by the 3rd mask layer and was etched using the ICP process (Oxford 100) in Ch2F2

plasma chemistry to achieve vertical sidewalls. Then, a hard mask deposition and a Cl2-based ICP process were used for etching AlN film (4th mask) for access to the bottom electrode and access to oxide (release holes). The AlN etch process was developed to achieve highly vertical sidewalls and minimize sidewall erosion effects [20].

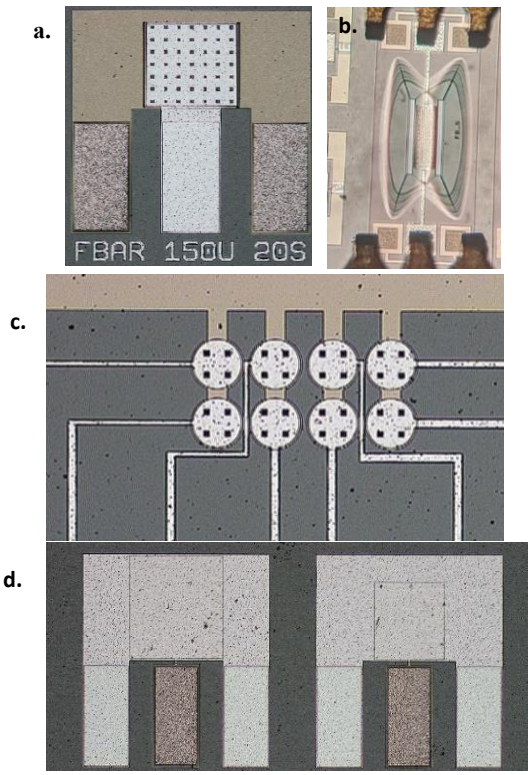

Figure 4. Fabricated devices (a) FBAR (150x150µm), (b) CMR (150x100µm), (c) PMUTS (2x4 array, R=50µm, (d) GHz transducers (200µmx200µm).

MEASUREMENT RESULTS

After fabrication, several devices - GHz transducers, FBAR and CMR resonators – were tested to confirm that they work (Fig. 4). Due to poor selectivity of the buffer layer to the oxide sacrificial layer, PMUT device yield was poor and therefore not tested at this point. Using a GSG probe, a 100 µm square GHz transducer was tested in pulse-echo mode by applying a 50 ns, 2.55 GHz, 3.5V amplitude RF pulse to drive the transducer and measuring the received echoes from the same transducer with a high-frequency oscilloscope. The amplitude of the first acoustic echo was measured to be >80mVpp amplitude through a 3dB attenuator (Fig 5a), and is comparable to previously reported echo amplitudes (albeit with different thin film stacks). Resonators were tested by using a network analyzer (ENA 5061) to measure impedance and S-parameters of device resonances (Fig 5b). Due to how signal and ground pads are on different metal layers (top electrode and bottom electrode, respectively) with no vias connecting the layers, de-embedding shorts were difficult to realize and therefore the resonator structures were not de-embedded – hence measured resonances will have relatively low quality factors due to parasitic loading from pads (100 µm by 200 µm). The FBAR resonator was a simple square shape of 150 µm x 150 µm dimension. Release holes were placed within the structure due to the timed etch. The tested CMR device was designed with 5.54 µm pitch and 170 µm long fingers, with 4 finger pairs. The FBAR and CMR resonance frequencies matched the design frequencies of 2.5 GHz and 800 MHz, as shown in Fig. 5(b) and 5(c).

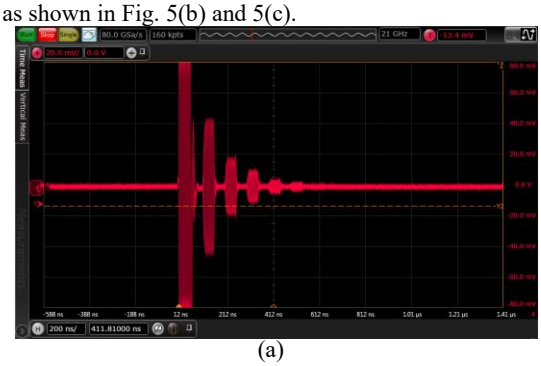

(a)

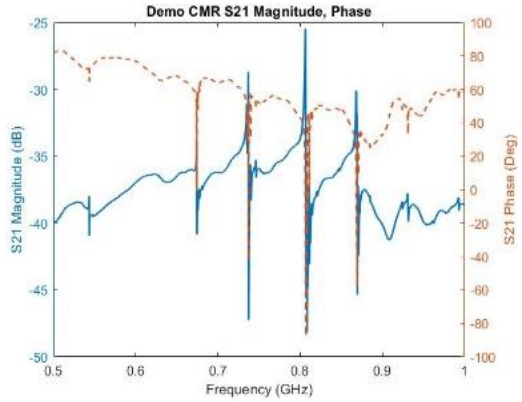

(b)

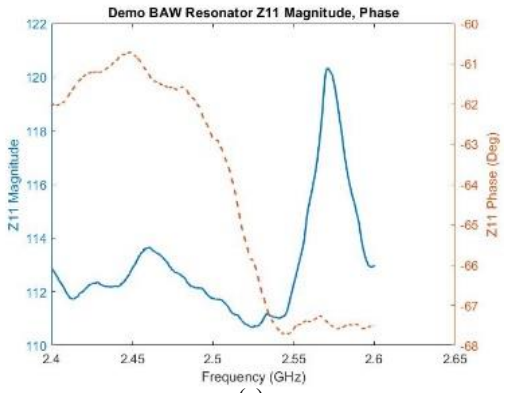

(c)

Figure 5. Device measurements: (a) Receive signal for 100 µm GHz BAW transducer, (b) CMR S11 measurement, (c) 100 µm FBAR Z11 measurement.

CONCLUSIONS AND DISCUSSION

This work has successfully demonstrated the feasibility of integrating both bulk-coupled GHz ultrasonic transducer devices and resonator CMR and FBAR type devices on the same process flow. Several fabrication issues remain to be addressed such as the top SiN layer getting etched in the vapor HF release process, and unoptimized stress in the released AlN films. The process flow has the potential to enable a wide variety of MEMS devices by changing the thickness of two layers, namely the buffer and the piezoelectric layer.

In addition, in this iteration, the process flow was kept simple as a proof of concept to show that different Piezo-MEMS devices

can be fabricated using the same process flow. Several important features need to be added to the process flow to make it suitable for both post-CMOS integration and commercial use. These include 1) a patterned release layer – this allows released devices of different geometries to be more easily fabricated by simplifying the release etch step, 2) vias between top and bottom electrode and between bottom electrode and CMOS metallization – these vias allow the Piezo-MEMS electrodes to connect to the CMOS metal stack, and 3) a trimming step for adjusting resonator resonance frequencies.

Furthermore, to transform this work into a full PDK, several key components, in addition to the final optimized process flow, need to be developed. We envision two versions of the PDK – an initial MEMS only layout PDK and a final MEMS on CMOS PDK. The layout PDK will be implemented for KLayout, due to the free and open-source nature of the software, which enables easy access, and also due to the support for Python scripting and DRC checking. In addition to the necessary files for setting up the software layout environment, it is necessary to also provide reference designs with example FEM models and measured S-parameter data, which is usually not provided with current MEMS PDKs but would give designers increased confidence in their designs. A CMOS-MEMS PDK will need to be implemented in Cadence Virtuoso, as that is the primary software supported by most CMOS foundry PDKs. In addition to the numerous layout environment setup files required for Virtuoso, other components that need to be provided include 1) DRC and LVS rule decks in either Cadence PVS or Siemens Calibre, 2) schematic simulation models and measured S-parameters for reference devices, and 3) layout P-Cells to automatically generate MEMS device layouts. In current PDKs, schematic models are generally not provided due to the amount of work required to develop, however, they are extremely important for CMOS designers to verify that their circuits interact correctly with the MEMS devices.

ACKNOWLEDGEMENTS

The authors would like to acknowledge funding from DARPA SBIR Phase I and Phase II under the MEMS PDK program. Help in process development was instrumental from CNF staff, especially Tom Pennell. This work was performed in part at the Cornell NanoScale Facility, a member of the National Nanotechnology Coordinated Infrastructure (NNCI), which is supported by the National Science Foundation (Grant NNCI-2025233).

REFERENCES

[1] G. Pillai, A. A. Zope, J. M. -L. Tsai and S. -S. Li, "3-GHz BAW composite resonators integrated with CMOS in a single-chip configuration," 2016 IEEE International Frequency Control Symposium (IFCS), 2016.

[2] Jiang, X., Lu, Y., Tang, HY. et al. “Monolithic ultrasound fingerprint sensor”, Microsystems and Nanoengineering, 3, 17059 (2017).

[3] J. Segovia-Fernandez et al., "Monolithic AlN MEMS-CMOS resonant transformer for wake-up receivers," 2017 IEEE International Ultrasonics Symposium (IUS), 2017.

[4] E. Calayir et al., "Self-healing narrowband filters via 3D heterogeneous integration of AlN MEMS and CMOS chips," 2017 IEEE International Ultrasonics Symposium (IUS), 2017.

[5] J. Segovia-Fernandez et al., "Monolithic piezoelectric Aluminum Nitride MEMS-CMOS microphone," 2017 19th International Conference on Solid-State Sensors, Actuators and Microsystems (TRANSDUCERS), 2017, pp. 414-417.

[6] M. Abdelmejeed et al., "Monolithic 180nm CMOS Controlled GHz Ultrasonic Impedance Sensing and Imaging," 2019 IEEE International Electron Devices Meeting (IEDM), 2019.

[7] J. Kuo, A. Baskota, S. Zimmerman, F. Hay, S. Pethybridge and A. Lal, "Gigahertz Ultrasonic Imaging of Nematodes in Liquids, Soil, and Air," 2021 IEEE International Ultrasonics Symposium (IUS), 2021.

[8] F. T. Goericke, G. Vigevani, I. I. Izyumin, B. E. Boser and A. P. Pisano, "Novel thin-film piezoelectric aluminum nitride rate gyroscope," 2012 IEEE International Ultrasonics Symposium, 2012, pp. 1067-1070.

[9] S. Zhu et al., "Aluminum Nitride Ultralow Loss Waveguides and Push-Pull Electro-Optic Modulators for Near Infrared and Visible Integrated Photonics," 2019 Optical Fiber Communications Conference and Exhibition (OFC), 2019.

[10] T. Wu et al., "Design and fabrication of AlN RF MEMS switch for near-zero power RF wake-up receivers," 2017 IEEE SENSORS, 2017.

[11] X. Liu et al., “Post-CMOS Compatible Aluminum Scandium Nitride/2D Channel Ferroelectric Field-Effect-Transistor Memory,” Nano Letters, 2021, 21, pp. 3753-3761.

[12] M. Rinaldi, C. Zuniga, C. Zuo and G. Piazza, "Super-high-frequency two-port AlN contour-mode resonators for RF applications," in IEEE Transactions on Ultrasonics, Ferroelectrics, and Frequency Control, vol. 57, no. 1, pp. 38-45, Jan. 2010.

[13] Daisuke Akai, Takeo Katori, Daisuke Takashima, and Makoto Ishida, "Sensitivity and resonance frequency with changing the diaphragm diameter of piezoelectric micromachined ultrasonic transducers", AIP Conference Proceedings 1709, 020010 (2016).

[14] A. Ravi, “CMOS Compatible Planar GHz Fresnel-Type Ultrasonic Actuator: Design and Applications in Microfluidics and Acousto-Optics,” Ph.D. dissertation, Cornell University, Ithaca, NY, Dec. 2021.

[15] J. C. Kuo, J. T. Hoople, M. Abdelmejeed, M. Abdel-moneum and A. Lal, "64-Pixel solid state CMOS compatible ultrasonic fingerprint reader," 2017 IEEE 30th International Conference on Micro Electro Mechanical Systems (MEMS), 2017.

[16] J. Hoople, J. Kuo, S. Ardanuç and A. Lal, "Chip-scale reconfigurable phased-array sonic communication," 2014 IEEE International Ultrasonics Symposium, 2014, pp. 479-482, doi: 10.1109/ULTSYM.2014.0119.

[17] M. Abdelmejeed, J. C. Kuo and A. Lal, "Thermal wavefront imaging using GHz ultrasonics," 2017 IEEE International Ultrasonics Symposium (IUS), 2017.

[18] M. Abdelmejeed, J. C. Kuo and A. Lal, "AlN GHz ultrasonic pulse diffraction based transmit-receive oscillator with 1 PPM stability," 2017 19th International Conference on Solid-State Sensors, Actuators and Microsystems (TRANSDUCERS), 2017, pp. 106-109.

[19] J. H. Smith, S. Montague, J. J. Sniegowski, J. R. Murray and P. J. McWhorter, "Embedded micromechanical devices for the monolithic integration of MEMS with CMOS," Proceedings of International Electron Devices Meeting, 1995, pp. 609-612.

[20] B. Davaji, M. Abdelmajeed, A. Lal, T. Pennell and V. Genova, "Sputtered AlN Lateral Bimorph: Process Integration Challenges and Opportunities," 2020 Joint Conference of the IEEE International Frequency Control Symposium and International Symposium on Applications of Ferroelectrics (IFCS-ISAF), 2020.

[21] Gary K. Fedder, Henry Baltes, Osamu Tabata, Jan G. Korvink, Christofer Hierold, and Oliver Brand. CMOS-MEMS. John Wiley & Sons, 2005.

CONTACT

*Geegah Inc., tel: +1-607-319-3399; info@geegah.com

SENSORS THAT MAKE COMMUNITY SENSE

Mina Sartipi
University of Tennessee, Chattanooga, USA

The twenty-first century is an urban living century. It is predicted that by 2050 about 64% of the developing world and 86% of the developed world will be urbanized. Urbanization creates significant pressure on vital city systems. Smart City research focuses on addressing these challenges by applying big data analytics to existing data sources and to data collected from sensors deployed in cities. Data enables local government and researchers to have a holistic view of their environment, define their goals, identify mitigation mechanisms, deploy the solutions, and measure the impacts over time. Interventions and refinements may be necessary as these impacts are being evaluated. Big data analytics can be utilized in any aspect of city life to improve the social, economic, and environmental well-being of urban residents.

An example of a smart city project is the goal of increasing accessibility for those at a socio-economic disadvantage, as well as seniors and individuals with physical disabilities. This is particularly important in smart transportation, health, and infrastructure. Longitudinal data on transportation accessibility is not readily available in many communities. Therefore, sensors that are low cost, scalable, and capable of being weatherproof must be deployed at large to acquire this data, which will allow the needs of the communities to be observed in real time.

In this talk, I will present the ongoing cross-disciplinary research and strategic visions for urbanism and smart cities advancement with a focus on people and quality of life. As an example, I will introduce the urban testbed in downtown Chattanooga, equipped with several sensors, computing resources, and communication capabilities. In addition to the ongoing efforts on the testbed, I will present mobility solutions that are sustainable, efficient, accessible, and go beyond the scope of what we once believed could be possible.

PERIOD TRIPLING STATES AND NON-MONOTONIC ENERGY DISSIPATION IN COUPLED MEMS RESONATORS

Mingkang Wang[1,2], Diego J. Perez-Morelo[1,2], Daniel Lopez[3,1], and Vladimir A. Aksyuk[1]
[1]Microsystems and Nanotechnology Division, National Institute of Standards and Technology, Gaithersburg, MD 20899 USA
[2]Institute for Research in Electronics and Applied Physics, University of Maryland, College Park, MD 20742, USA
[3]Materials Research Institute, Penn State University, University Park, PA 16802, USA

ABSTRACT

When two eigenmodes are at internal resonance, i.e. they have commensurate eigenfrequencies, their coupling strength can be significantly enhanced. Rich nonlinear dynamics have been shown at internal resonance. In this work, we present a novel non-monotonic energy dissipation rate of microelectromechanical systems (MEMs) at internal resonance. We demonstrate that the MEMS can selectively dissipate via two largely distinctive pathways, solely depending on the choice of their relative initial phase. Remarkably, these novel and complicated behaviors can be understood by an intuitive parametric-oscillator-like model. Our work illuminates a path to dissipation engineering, frequency stabilization, and sensitivity enhancement.

KEYWORDS

Dissipation, internal resonance, non-monotonic energy dissipation rate, period-tripling states

INTRODUCTION

Understanding energy dissipation is critical both for fundamental science and practical applications, such as for quantum information [1,2] and fundamental timing and sensing applications [3–5]. A fundamental picture of energy dissipation is that a non-equilibrium harmonic oscillator exponentially losses energy to a thermal bath. Based on this basic picture, many efforts are made to engineer the dissipation rate by either modifying the coupling strength with the thermal bath, such as via phononic bandgap structures [6], or introducing an extra coupling source, i.e. another bath - another oscillator [7–9]. Dissipation engineering has very different goals, for example, a switch demands a high energy dissipation rate for a short transition time [10,11], while more commonly, a low dissipation rate is desired for good isolation of oscillators from the environment which is a benefit for many scenarios, such as extending coherence time of quantum computer [12–14], reducing thermal noise for sensing and timing purposes, and reducing power consumption. In particular, a selective dissipation rate without disturbing other parameters of the system could be a good compromise for the different needs.

Internal resonance [15] is a competent candidate for dissipation engineering via mode coupling. Different from the commonly used parametric coupling of two modes with arbitrary eigenfrequency relationships [16,17], internal resonance happens only when their frequencies have a commensurate relationship (e.g. 1:3), and therefore, has stronger coupling [18]. Recently, internal resonance is intensively studied in the nano/micro-electro-mechanical systems (N/MEMs) and shows rich nonlinear dynamics, such as period-tripling states [19,20], and frequency stabilization in a nonlinear oscillator [21]. Regarding the dissipation at internal resonance, previous works observed anomalous decay rates during the free ringdown of the coupled system. Due to the rapid energy exchange between the modes at internal resonance, one mode in the free ringdown system could present either a faster [8] or slower [7] dissipation rate depending on the system parameter. However, due to the limitation of the setup, only one mode of the system was controllable and measurable, largely limiting the understanding of these novel behaviors. Moreover, recent theoretical research [22] points out that by choosing proper initial conditions of the two modes, even richer nonlinear dynamics could show up, such as the non-monotonic amplitude dependence of decay rate and phase-dependent dissipation paths.

Here we experimentally demonstrate a selective non-monotonic dissipation rate of a double-clamped beam at internal resonance. The two modes under investigation are two eigenmodes of the beam with nearly commensurate eigenfrequencies (1:3) and strong Duffing nonlinearity. By preparing two modes at specific initial conditions, then releasing them and recording their free ringdown simultaneously, we observe that they either lock at internal resonance or bypass it during ringdown. Such selection can be controlled by tuning their initial relative phase before ringdown. If they lock, the high-frequency mode (mode 2) performs as a period-3 parametric drive to the low-frequency mode (mode 1). It creates a period-tripling state, which resembles the period-doubling states for parametric resonators [23]. Under such states, mode 2 transfers energy to mode 1, making it experience an energy gain while the whole system still loses energy continuously. Finally, when mode 2's energy is lower than the parametric drive threshold, the two modes unlock and dissipate with their intrinsic energy loss. Remarkably, the locked state can last several times longer than the intrinsic dissipation time of mode 1 and of the system. During this process, mode 1 exhibits a non-monotonic dissipation rate as a function of the system energy. In contrast, if they bypass at internal resonance, we observe a reverse effect, i.e. mode 1 transfers energy to mode 2 and shows a transient faster dissipation rate. For the two cases, the coupled-mode system shows distinct system dissipation rates since the individual intrinsic dissipation rates of the two modes are different. This locking and bypass dissipation trajectories and the modes' behaviors during locking can be well described by an intuitive period-tripling model where mode 2 acts as a parametric drive to mode 1. This switchable and non-monotonic dissipation rate induced by strong modal coupling could shed light on extending the coherence time and improving frequency stabilization of general resonators used in sensing and timing applications.

SYSTEM AND MEASUREMENT

As shown in Fig. 1(a), the system under investigation is a clamped-clamped beam with two side gates for driving the system and performing an electrical measurement. A laser vibrometer performs optical measurement, simultaneously. The device is placed in a vacuum chamber with pressure $< 1 \times 10^{-3}$ Pa. The lowest order in-plane mode (mode 1) and torsional mode (mode 2) shown in Fig. 1(b) are of eigenfrequencies $\omega_1/2\pi \approx 64.6$ kHz and $\omega_2/2\pi \approx 199.9$ kHz, respectively, with nearly commensurate relationship ($\omega_1 \approx \omega_2/3$). Their intrinsic dissipation rates without coupling are significantly different with the measured value of $\Gamma_1/2\pi \approx 1.5$ Hz and

$\Gamma_2/2\pi \approx 3.3$ Hz, respectively.

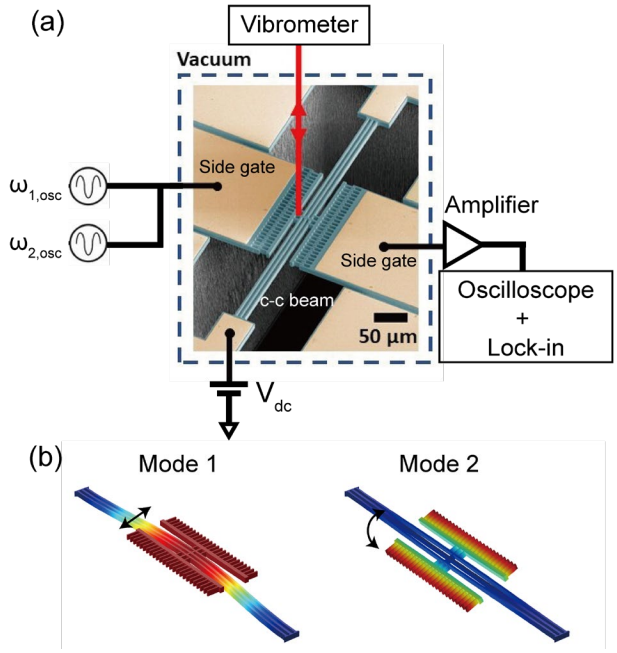

Figure 1: (a) Measurement schematics and false-colored SEM micrograph of the clamp-clamp (c-c) beam MEMS. Optical and electrical measurements are performed, simultaneously. (b) Simulated mode shape of the two coupled modes.

For characterization, the two modes are driven separately, responding with oscillating frequencies $\omega_{1,osc}$ and $\omega_{2,osc}$. When the driving force is strong, mode 1 shows the spring hardening effect while mode 2 presents the softening effects, shown as the orange and green dots in Figure 2, respectively. The *x*-axis of mode 2 (green) is scaled by a factor of three ($\omega_{2,osc}/3$) to compare with mode 1. Here the two modes are driven separately, i.e. when one mode is driven, the other one remains mostly at thermal equilibrium with the bath. The dip on mode 1's spectrum (orange) corresponds to the internal resonance frequency of $\omega_{1,osc} = \omega_2/3$ where the model coupling is the strongest, resulting in some energy transfer to mode 2 from mode 1 [24].

In the ringdown experiment, we drive the two modes separately to their initial amplitude $A_{1,0}$ and $A_{2,0}$, labeled as red dots. At time $t = 0$, we turn off their drive simultaneously to let them freely decay. Following their Duffing backbone (black arrows in Figure 2), their frequencies shift due to the exponentially decaying amplitude (Fig. 3) and reach the internal resonance when their oscillating frequency $\omega_{1,osc} = \omega_{2,osc}/3$ (black dots in Figure 2). Since mode 2's softening effect, the internal resonance frequency during ringdown (black dot) is somewhere between the initial frequency of mode 2 (red dot) and the eigenfrequency of mode 2 (black dashed line).

NON-MONOTONIC ENERGY DISSIPATION RATE

At internal resonance, the two modes either lock or bypass each other depending on the initial relative phase. Figures 3(a) and 3(b) present the frequency and energy of the two modes for the locking case. Before entering internal resonance, the two modes exponentially decay (Fig. 3b) with their intrinsic dissipation rates. Following their Duffing backbone, $\omega_{1,osc}$ decreases while $\omega_{2,osc}$ increases (Fig. 3a) shown as the black arrows in Fig. 2. After entering the locked states, $\omega_{1,osc}$ locks to $\omega_{2,osc}$ and oscillates around it, while $\omega_{2,osc}$ is not largely affected by mode 1. It can be explained considering the situation where mode 2's energy is much larger than mode 1. Only when the two modes are nearly unlocked, mode 1's and mode 2's energies are comparable, and the two modes both present oscillations.

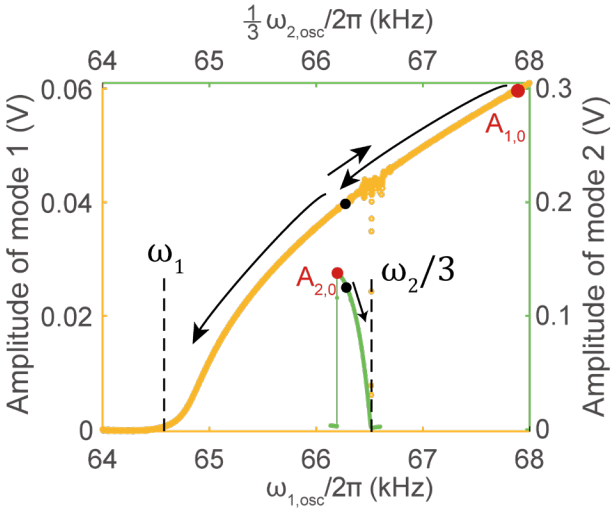

Figure 2. Spectrums of mode1 and mode2 are labeled by yellow and green dots. The oscillating frequency of mode2 is divided by 3. The two modes have opposite Duffing coefficients. In ringdown experiments, we set the initial conditions at $A_{1,0}$ and $A_{2,0}$ (red dots), respectively, and turn off the drive simultaneously. They evolve to equilibrium following the black arrows. After being locked at the internal resonance, the black dots, Mode1 experiences frequency and amplitude increase shown as the short black arrow.

The complete equation of motion for this coupled-mode system is written as:

$$\ddot{q}_1 + \Gamma_1\dot{q}_1 + \omega_1^2 q_1 + \alpha_1 q_1^3 + 3g_{12}q_1^2 q_2 = 0 \quad (1)$$

$$\ddot{q}_2 + \Gamma_2\dot{q}_2 + \omega_2^2 q_2 + \alpha_2 q_2^3 + g_{21}q_1^3 = 0 \quad (2)$$

where q_1 and q_2 are the modal displacement, α_1 and α_2 are the Duffing coefficients with opposite signs, and g_{12} and g_{21} are the coupling rate. As $q_2 \gg q_1$, Eq. (2) can be simplified to a Duffing oscillator while Eq. (1) can be rewritten as:

$$\ddot{q}_1 + \Gamma_1\dot{q}_1 + \omega_1^2 q_1 + \alpha_1 q_1^3 = q_1^2 F_2(t)\cos[\Phi_2(t)] \quad (3)$$

where the interaction term in Eq. (1) is regarded as a parametric drive with time-varying frequency $\omega_2(t) = \dot{\Phi}_2(t)$ and amplitude $F_2(t)$. Eq. (3) depicts a parametric oscillator under a period-three drive, i.e. $\omega_2(t)/3 = \omega_1(t)$. Similar to parametric oscillators under the period-two drive, the period-three drive creates period-tripling states [25,26] that are degenerate with $2\pi/3$ relative phase difference.

During locking, mode 2's eigenfrequency continuously shifts to a higher frequency, pulling Mode 1 to a higher frequency and higher amplitude on its Duffing backbone (short arrow in Fig. 2). As a result, mode 1 shows an anomalous negative dissipation rate (energy gain), as shown in the inset of Fig. 3(b), while the system continuously loses energy. At the end of the locking state, mode 2 is not able to provide enough parametric drive to mode 1, therefore, the two modes unlock from each other, and dissipate again following their own intrinsic dissipate rates. The locking state length, or coherent time, depends on the initial energy of the system. Remarkably, the locking state can last up to ≈ 0.26 s (≈ 0.14 s in Fig. 3) which is around 3 times the intrinsic dissipation time of mode 1 ($1/\Gamma_1 \approx 0.10$ s) and 5 times the system dissipation time ($1/\Gamma_2 \approx 0.05$ s).

The dynamics of the system can be fully modeled by Eq. (1-2). However, here we only focus on its long-term evolution (~1/Γ) and ignore the time-averaged interaction energy. Under such assumptions, intuitively, the energy loss by mode 2 equals the energy gain by mode 1 after excluding their intrinsic losses:

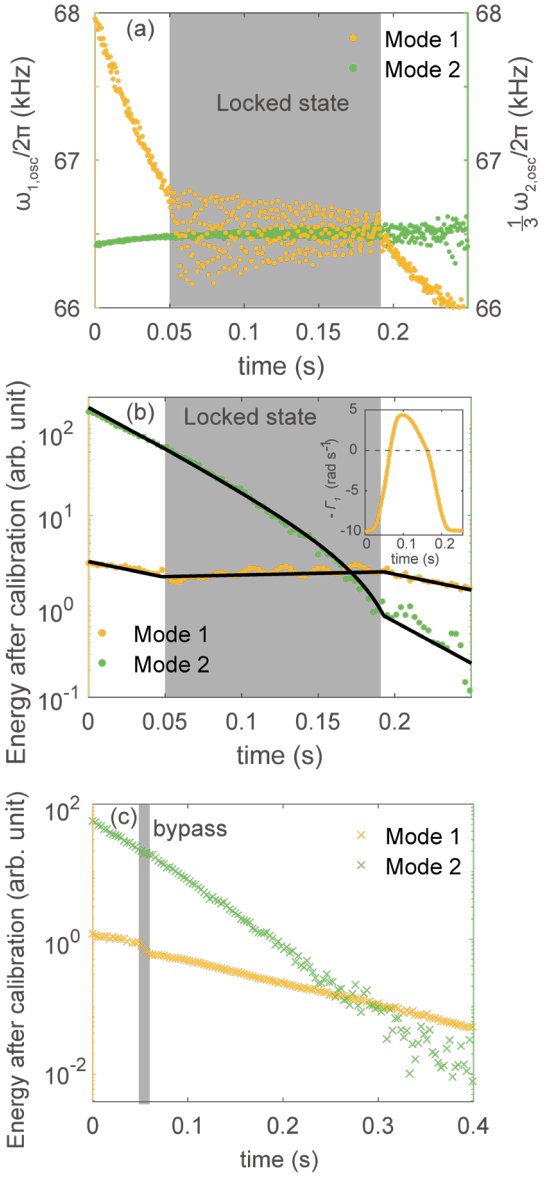

Figure 3. Oscillating frequencies and energy of the two locked modes are presented in (a) and (b), respectively. The yellow and green dots correspond to mode1 and mode2, respectively. The inset of (b) shows the measured relative energy change rate (effective -Γ_1), illustrating a non-monotonic and negative dissipation rate (energy gain) during locking. The bypass case is shown in (c). A rapid energy loss is observed for mode 1 at internal resonance, colored gray.

$$\frac{dE_1}{dt} = -\Gamma_1 E_1 + P \quad (4)$$

$$\frac{dE_2}{dt} = -\Gamma_2 E_2 - P \quad (5)$$

where $E_1 \propto q_1^2$ and $E_2 \propto q_2^2$ are the energy of mode 1 and mode 2, P is the energy exchange rate. As mode 1 amplitude is nearly a constant, $P \approx \Gamma_1 E_1$ can be considered a constant. The black lines in Fig. 3(b) show the fitted E_1 and E_2 with only one fitting parameter P.

For the bypass case, except for a short rapid energy decay of mode 1 at the internal resonance (gray area in Fig. 3(c)), the two modes continuously exponentially decay with their intrinsic loss rates. The lock or bypass depends on the relative phase between the two modes at the initial state. We can select the dissipation path of the system by setting their initial phase.

Intuitively, the lock or bypass is decided by the energy transfer direction at internal resonance. The direction is governed by their relative phase. For example, if mode 2's phase $\varphi_2/3$ is ahead compared to φ_1, the energy flows from mode 2 to mode 1 and pumps mode 1. Their oscillating frequencies can be maintained at internal resonance although both slowly increase. On the contrary, if mode 1's phase leads, it transfers energy to mode 2 at internal resonance which makes their frequencies bypass internal resonance quickly.

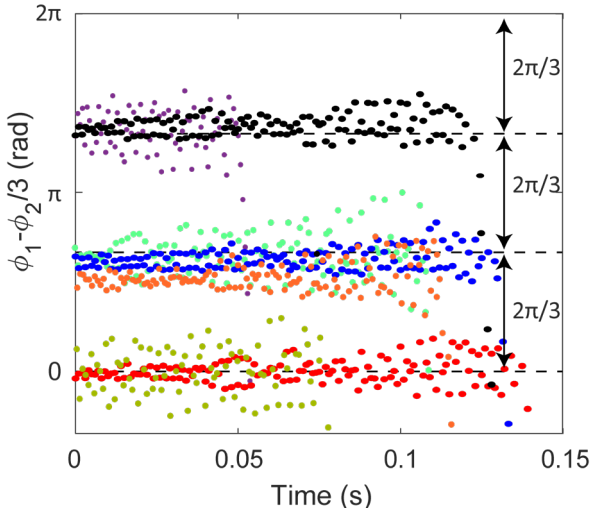

Figure 4. Relative phase of mode1 (φ_1) and mode2 (φ_2) in 7 repeating experiments. φ_1- $\varphi_2/3$ exhibits discrete values of (0, 4π/3, 2π) at period tripling states.

To demonstrate the period-tripling model, we repeat the same ringdown experiment, and we find the system exhibits phase-locking with discrete relative phase φ_1- $\varphi_2/3$ = n×2π/3 shown in Figure 4 where n is an integer. It is consistent with the period-tripling interpretation. The discrete relative phase resembles the n×2π/2 period-doubling states for parametric oscillators.

SUMMARY

In conclusion, we have demonstrated the ability to select the energy dissipation pathways of a coupled system at the internal resonance (i.e. two modes with 1:3 eigenfrequencies). By setting the relative initial phase between the two coupled modes, the two modes can either enter the designated phase-locking state or bypass it during their free ringdown. In the phase-locking path, the coupling from the high-frequency mode (mode 2) acts as a period-three parametric drive to the low-frequency mode (mode 1), locking the phase and making φ_1- $\varphi_2/3$ nearly constant. During the phase-locking, the frequency of the two modes varies with their decaying amplitude along with their Duffing amplitude-frequency relationship while maintaining the 1:3 internal resonance relationship. Since the two modes have opposite Duffing coefficients and mode 2's energy is much larger than mode 1,

"follower" mode 1 exhibits a frequency increase together with "leader" mode 2, resulting in an energy gain during the locking. It makes mode 1 presents an anomalous non-monotonic energy dissipation rate during the ringdown. Remarkably, the locking time can be nearly 6 times longer than the system dissipation time scale $1/\Gamma_2$ and 3 times longer than the intrinsic dissipation time scale $1/\Gamma_1$ of mode 1 itself. The findings of phase-locking states and selectable dissipation rates are useful for energy dissipation engineerings, such as for fast switches or low-dissipation timing/sensing devices. The proposed intuitive period-tripling model provides a picture to understand the complicated dynamics in coupled nonlinear resonators.

ACKNOWLEDGEMENTS

We thank Dr. Steven Shaw, Dr. Ori Shoshani and Dr. David A. Czaplewski for useful discussions. We thank Dr. Jason J. Gorman, Dr. Damián H. Zanette, Dr. J. Alexander Liddle, and Dr. Marcelo Davanco for reviewing this paper and giving meaningful suggestions. M.W. and D.J.P. are supported by the Cooperative Research Agreement between the University of Maryland and the National Institute of Standards and Technology Center for Nanoscale Science and Technology, Award 70NANB14H209, through the University of Maryland.

REFERENCES

[1] F. Verstraete, M. M. Wolf, and J. Ignacio Cirac, *Quantum Computation and Quantum-State Engineering Driven by Dissipation*, Nature Physics **5**, 9 (2009).

[2] M. Steffen, S. Kumar, D. P. DiVincenzo, J. R. Rozen, G. A. Keefe, M. B. Rothwell, and M. B. Ketchen, *High-Coherence Hybrid Superconducting Qubit*, Phys. Rev. Lett. **105**, 100502 (2010).

[3] X. Liu, J. F. Vignola, H. J. Simpson, B. R. Lemon, B. H. Houston, and D. M. Photiadis, *A Loss Mechanism Study of a Very High Q Silicon Micromechanical Oscillator*, Journal of Applied Physics **97**, 023524 (2004).

[4] M. Li, H. X. Tang, and M. L. Roukes, *Ultra-Sensitive NEMS-Based Cantilevers for Sensing, Scanned Probe and Very High-Frequency Applications*, Nature Nanotechnology **2**, 2 (2007).

[5] M. Weinberg, R. Candler, S. Chandorkar, J. Varsanik, T. Kenny, and A. Duwel1, *Energy Loss in MEMS Resonators and the Impact on Inertial and RF Devices*, in *TRANSDUCERS 2009 - 2009 International Solid-State Sensors, Actuators and Microsystems Conference* (2009), pp. 688–695.

[6] Y. Tsaturyan, A. Barg, E. S. Polzik, and A. Schliesser, *Ultracoherent Nanomechanical Resonators via Soft Clamping and Dissipation Dilution*, Nature Nanotechnology **12**, 776 (2017).

[7] C. Chen, D. H. Zanette, D. A. Czaplewski, S. Shaw, and D. López, *Direct Observation of Coherent Energy Transfer in Nonlinear Micromechanical Oscillators*, Nat Commun **8**, 15523 (2017).

[8] J. Güttinger, A. Noury, P. Weber, A. M. Eriksson, C. Lagoin, J. Moser, C. Eichler, A. Wallraff, A. Isacsson, and A. Bachtold, *Energy-Dependent Path of Dissipation in Nanomechanical Resonators*, Nature Nanotech **12**, 631 (2017).

[9] X. Dong, M. I. Dykman, and H. B. Chan, *Strong Negative Nonlinear Friction from Induced Two-Phonon Processes in Vibrational Systems*, Nature Communications **9**, 1 (2018).

[10] A. F. Vakakis, O. V. Gendelman, L. A. Bergman, D. M. McFarland, G. Kerschen, and Y. S. Lee, *Nonlinear Targeted Energy Transfer in Mechanical and Structural Systems* (Springer Science & Business Media, 2008).

[11] H. Okamoto, I. Mahboob, K. Onomitsu, and H. Yamaguchi, *Rapid Switching in High-Q Mechanical Resonators*, Appl. Phys. Lett. **105**, 083114 (2014).

[12] C. Langer, R. Ozeri, J. D. Jost, J. Chiaverini, B. DeMarco, A. Ben-Kish, R. B. Blakestad, J. Britton, D. B. Hume, W. M. Itano, D. Leibfried, R. Reichle, T. Rosenband, T. Schaetz, P. O. Schmidt, and D. J. Wineland, *Long-Lived Qubit Memory Using Atomic Ions*, Phys. Rev. Lett. **95**, 060502 (2005).

[13] M. Stern, G. Catelani, Y. Kubo, C. Grezes, A. Bienfait, D. Vion, D. Esteve, and P. Bertet, *Flux Qubits with Long Coherence Times for Hybrid Quantum Circuits*, Phys. Rev. Lett. **113**, 123601 (2014).

[14] Y. Wang, M. Um, J. Zhang, S. An, M. Lyu, J.-N. Zhang, L.-M. Duan, D. Yum, and K. Kim, *Single-Qubit Quantum Memory Exceeding Ten-Minute Coherence Time*, Nature Photonics **11**, 10 (2017).

[15] L. Manevitch and A. I. Manevich, *The Mechanics Of Nonlinear Systems With Internal Resonances* (World Scientific, 2005).

[16] J. D. Teufel, T. Donner, D. Li, J. W. Harlow, M. S. Allman, K. Cicak, A. J. Sirois, J. D. Whittaker, K. W. Lehnert, and R. W. Simmonds, *Sideband Cooling of Micromechanical Motion to the Quantum Ground State*, Nature **475**, 359 (2011).

[17] I. Mahboob, K. Nishiguchi, H. Okamoto, and H. Yamaguchi, *Phonon-Cavity Electromechanics*, Nature Physics **8**, 5 (2012).

[18] A. H. Nayfeh and D. T. Mook, *Nonlinear Oscillations* (John Wiley & Sons, 2008).

[19] N. Lörch, Y. Zhang, C. Bruder, and M. I. Dykman, *Quantum State Preparation for Coupled Period Tripling Oscillators*, Phys. Rev. Research **1**, 023023 (2019).

[20] J. Gosner, B. Kubala, and J. Ankerhold, *Relaxation Dynamics and Dissipative Phase Transition in Quantum Oscillators with Period Tripling*, Phys. Rev. B **101**, 054501 (2020).

[21] D. Antonio, D. H. Zanette, and D. López, *Frequency Stabilization in Nonlinear Micromechanical Oscillators*, Nat Commun **3**, 1 (2012).

[22] O. Shoshani, S. W. Shaw, and M. I. Dykman, *Anomalous Decay of Nanomechanical Modes Going Through Nonlinear Resonance*, Sci Rep **7**, 18091 (2017).

[23] H. B. Chan and C. Stambaugh, *Activation Barrier Scaling and Crossover for Noise-Induced Switching in Micromechanical Parametric Oscillators*, Physical Review Letters **99**, (2007).

[24] S. Houri, D. Hatanaka, M. Asano, R. Ohta, and H. Yamaguchi, *Limit Cycles and Bifurcations in a Nonlinear MEMS Resonator with a 1:3 Internal Resonance*, Appl. Phys. Lett. **114**, 103103 (2019).

[25] J. Gosner, B. Kubala, and J. Ankerhold, *Relaxation Dynamics and Dissipative Phase Transition in Quantum Oscillators with Period Tripling*, Phys. Rev. B **101**, 054501 (2020).

[26] Y. Zhang and M. I. Dykman, *Nonlocal Random Walk over Floquet States of a Dissipative Nonlinear Oscillator*, Phys. Rev. E **100**, 052148 (2019).

CONTACT

*V. Aksyuk, tel: +1-301-975-2867; vladimir.aksyuk@nist.gov

HETEROGENEOUS INTEGRATION FOR HYBRID ACOUSTIC DEVICES: GAN/CU/YIG MAGNETOELASTIC HBARS

Vikrant J. Gokhale[1], Brian P. Downey[1], Pallavi Dhagat[2], Albrecht Jander[2], Shawn Mack[1], D. Scott Katzer[1], Jason A. Roussos[1], and David J. Meyer[1]

[1]US Naval Research Laboratory, Washington DC, USA

[2]Oregon State University, Corvallis, OR, USA

ABSTRACT

This work presents the heterogeneous integration of thin film acoustic devices using micro-transfer printing (MTP). Our approach enables the transfer of a high quality acoustic transducer grown epitaxially on a source substrate (6H-SiC), onto a target substrate that is not compatible with epitaxy [here, yttrium iron garnet (YIG)], with no degradation in measured RF/acoustic performance. The resulting integrated device is a magnetoelastic high overtone bulk acoustic resonator (ME-HBAR), which can hybridize acoustic and spin waves (phonons and magnons). We describe the MTP process, along with RF/acoustic and magnetoelastic characterization of the ME-HBAR.

INTRODUCTION

It is well known that the performance and capabilities of a microelectronic system can be enhanced by the heterogeneous integration of various optimized sub-components in the form of 'chiplets' onto a common target substrate. Depending on the application, the target substrate could simply be a cost-effective platform (CMOS wafer with readout routing), a flexible platform (rapid roll-to-roll assembly), or an efficient thermal spreader for power electronics (diamond). Alternately, one can choose a functional target substrate with physical characteristics that are crucial to the MTP device operation. In prior work, we have shown that epitaxial AlGaN/GaN high electron mobility transistors (HEMTs) can be individually transferred to an arbitrary target substrate using micro-transfer printing (MTP) [1], without significant change in performance. We add to this capability by demonstrating the MTP integration of epitaxially grown GaN-based piezoelectric RF-MEMS devices.

As a demonstration of this principle and capability, we take GaN-based epitaxial high overtone bulk acoustic resonators (epi-HBARs) grown on 6H-SiC, and transfer the piezoelectric transducers to a ferrimagnetic yttrium iron garnet ($Y_3Fe_5O_{12}$ or YIG) substrate, forming magnetoelastic HBARs (ME-HBARs). The transfer is mediated by an epitaxial NbN sacrificial layer, and a commercially available pick-and-place MTP tool and process that can be scaled to industrial manufacturing. The MTP process decouples the highly optimized Group III – Nitride epitaxy process from the functional YIG target substrate. To the best of our knowledge, this is the first demonstration of MTP integration of individual MEMS acoustic transducers.

The resulting YIG ME-HBARs can support low-loss propagation and confinement of both acoustic and spin waves simultaneously. Such hybrid phonon-magnon coupled devices can be used as sensors, magnetically tunable oscillators, filters, or parametric amplifiers, with applications for both classical and quantum signal processing systems [2-6]. While ME-HBARs have been fabricated by evaporating/sputtering metals and piezoelectric layers on to YIG and other ferroic substrates, the fabrication of such devices is constrained by nucleation dynamics, sputtered grain size/quality, axis optimization, and thermal budgets of the deposition process, all of which restrict the type and quality of potential material combinations [7, 8].

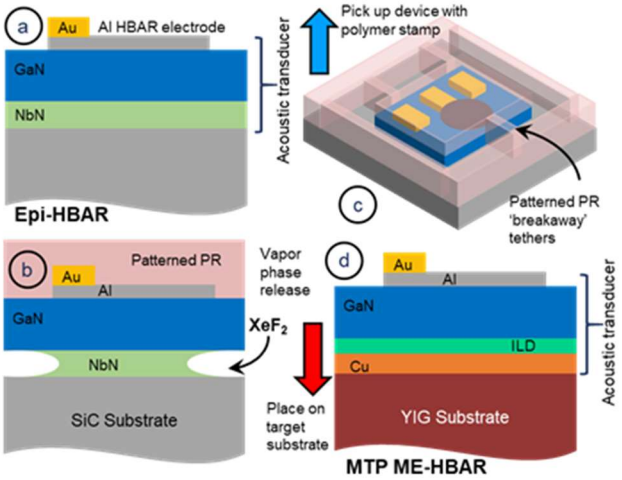

Figure 1: Micro-transfer printing (MTP) process flow to transfer a GaN-based piezoelectric acoustic transducer grown epitaxially on 6H-SiC, to a ferrimagnetic YIG substrate, forming a magnetoelastic GaN/Cu/YIG HBAR. Not to scale.

While HBARs made from YIG thin films have been demonstrated (with gadolinium gallium garnet as the substrate), the phonon-magnon interaction volume in such devices is restricted only to the YIG film [9, 10]. Unlike electronic or surface acoustic wave devices, the main physical phenomena in ME-HBARs (phonons and magnons) traverse the bonded interface, and thus can interact in the entire substrate.

FABRICATION PROCESS

Epitaxial transducer heterostructure

The design, development, and RF/acoustic characterization of epi-HBARs grown on SiC substrates using molecular beam epitaxy (MBE) has been described in previous work [11, 12]. The subsequent MTP process flow for the ME-HBAR is summarized in Fig. 1. First, an AlGaN/GaN/AlN/NbN heterostructure (thicknesses of 25 nm/1.2 µm/45 nm/50 nm respectively) is grown on a 370 µm thick 6H-SiC substrate). The *c*-axis oriented AlGaN/GaN/AlN piezoelectric layers are grown at temperatures up to 725 ˚C. The combination of heterostructure and epitaxial source substrate is carefully chosen to provide a) close lattice matching required for electronic-grade AlGaN/GaN, and b) the acoustic impedance matching required for efficient power transfer [13]. For the purposes of this experiment, the AlGaN barrier was etched using a Cl_2/BCl_3 plasma, removing the 2D electron gas at the AlGaN/GaN interface. The circular top electrode (Cr/Al, 10 nm/50 nm) is fabricated by electron beam evaporation, and liftoff. Thick Au contact pads (200 nm) are deposited and patterned next to the transducer to provide a coplanar waveguide (CPW) for RF input signals. 'As-grown' epi-HBARs are characterized to gauge their baseline RF/acoustic performance and properties. Next, a trench is etched around individual devices (Cl_2/BCl_3 plasma), isolating individual devices, and providing access to the underlying NbN sacrificial release layer.

978-1-940470-04-7/HH2022/$25©2022TRF
DOI 10.31438/trf.hh2022.9

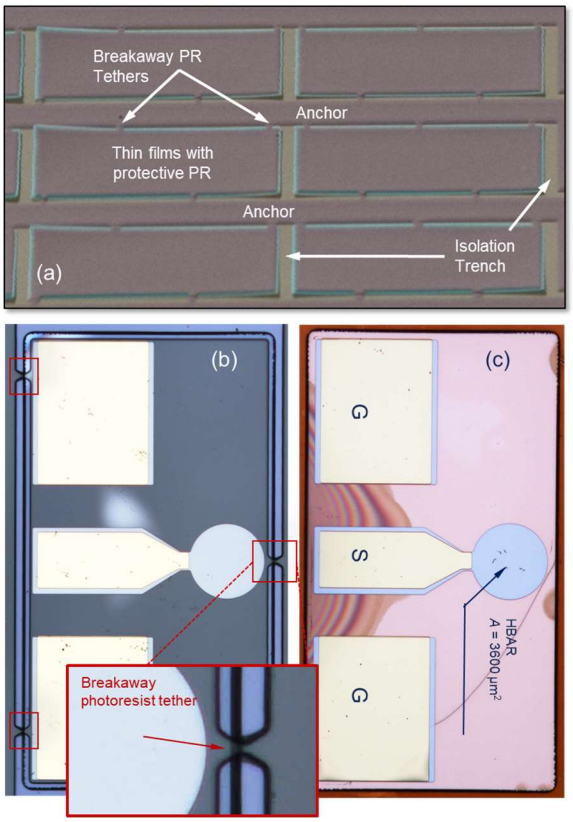

Figure 2. (a) False color electron microscope image of an array of released GaN chiplets before the MTP process. Optical microscope images of (b) released devices held in place with breakaway PR tethers (inset), and (c) transfer printed onto a Cu/YIG surface.

A photoresist (PR) layer is subsequently patterned to provide mechanical anchors on the SiC substrate and 'breakaway' tethers to hold the HBARs in place during the release etch, and to provide a protective layer on top of the HBARs during transfer (Fig. 2). The NbN layer is then selectively removed using XeF_2 vapor phase etching, releasing the GaN acoustic transducers [14], but leaving them suspended by the PR tethers (Fig. 2).

Micro Transfer Printing of individual transducers

Separately, a 100 nm thick Cu film is evaporated on to a 350 μm thick <111> YIG target substrate (MTI Corporation). YIG is a magnetostrictive and ferrimagnetic material well known for its low acoustic and spin wave damping. The Cu film has low acoustic mismatch with YIG, and replaces NbN as the bottom electrode in the transducer. A diluted Intervia 8023-10 interlayer dielectric (ILD) is spun onto the Cu/YIG target substrate forming an adhesion layer (measured to be 10 nm thick). An X-Celeprint MTP tool [15, 16] is used to transfer individual GaN acoustic transducers from the source substrate to specific locations on the Cu/YIG target substrate, forming an Al/GaN/AlN/Cu/YIG ME-HBAR. A UV flood exposure and bake cures the ILD, and O_2 plasma removes ILD from the open areas of the target substrate. Critically, unlike the 725 °C MBE step used to grow the heterostructure, a post-transfer hotplate bake at 185 °C is the highest process temperature step for the YIG target substrate. Optical microscope images of the post-transfer ME-HBAR (Fig. 2) show that while there is some curling due to stress, the transducer electrode is transferred into contact with the target substrate. Stress compensating films or patterns in the open areas of the chiplet can be explored in the future.

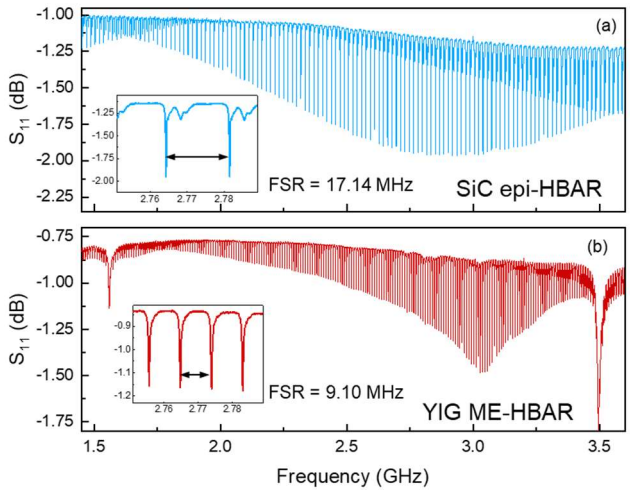

Figure 3. A comparison of the RF reflection spectra of the epi-HBAR and the ME-HBAR after successful transfer printing. Note the expected decrease in FSR associated with the slower acoustic velocity in the YIG substrate.

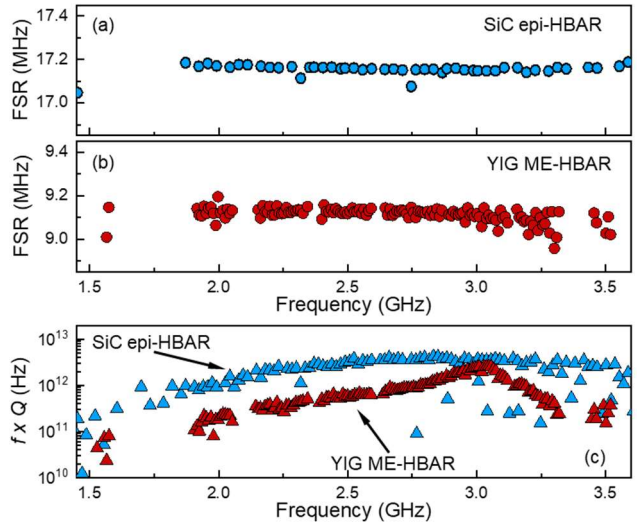

Figure 4. A comparison of the RF reflection spectra of (a) the epi-HBAR, and (b) the ME-HBAR after successful transfer printing. Note the expected decrease in FSR associated with the slower acoustic velocity in the YIG substrate. (c) Measured ($f \times Q$) products for both the epi-HBAR and the ME-HBAR show that there is no degradation in performance due to the MTP process.

DEVICE CHARACTERIZATION

Radio frequency / acoustic characterization

For any HBAR, important RF/acoustic parameters include the multi-mode RF spectral envelope, the spacing between overtones (the free spectral range or FSR), and the frequency-quality factor figure of merit ($f \times Q$) product for all m modes. We compare the epi-HBARs as grown on 6H-SiC with the corresponding ME-HBARs by characterizing their RF/acoustic performance.

All devices shown here are measured at room temperature using a vector network analyzer (VNA) and coplanar ground-signal-ground (GSG) probes. High resolution, sequential sweeps are acquired and the composite spectra are shown in Fig. 3. While there are changes in the shape of the RF reflection envelope, the RF reflection response (S_{11}) of the ME-HBAR is not significantly degraded when compared to that of the original epi-HBAR,

indicating good transfer. The two strong but low-Q modes at 1.55 GHz and 3.50 GHz in the ME-HBAR spectrum (Fig. 3(b)) are believed to be unwanted surface cavity overtones trapped by the parallel edges of the chiplet. These modes can be easily eliminated by apodizing the chiplet or by the use of damping layers.

To a first order, the FSR for any HBAR can be approximated as $FSR = v/2t$, where v is the substrate acoustic velocity and t is the substrate thickness. A detailed study of the FSR, its dependence on the heterostructure, and its use as a diagnostic for impedance matching can be found in prior work [13]. Here, FSR values of 17.14 MHz (Fig. 3(a)) and 9.10 MHz (Fig. 3(b)) are experimentally observed for the epi-HBAR and ME-HBAR respectively. Based on the substrate thicknesses, we can extract acoustic velocities of 12,684 m/s for the epi-HBAR and 6370 for the ME-HBAR. Extracted values are close to values from the literature: 13,300 m/s for SiC and 6220 m/s for <111> YIG [2, 17]. The extracted $f \times Q$ products for both the epi-HBAR and the ME-HBAR show that there is no obvious degradation in performance for the MTP ME-HBAR relative to the original epi-HBAR (Fig. 4(c)). Further experiments are needed to investigate the performance of the best performing SiC based epi-HBARs ($f \times Q > 10^{15}$ Hz at room temperature) when transferred to YIG and other target substrates. Specifically, it would be useful to separate losses due to the transfer interface and the adhesion ILD film from the losses in the target substrate.

Magnetoelastic characterization

In order to characterize their magnetoelastic performance the MTP ME-HBARs are wire-bonded and mounted on a rotating stage within the gap of a laboratory electromagnet. The frequency response of the ME-HBARs is measured as a function of magnetic field, **B**. Two representative measured responses are shown in Fig. 4, for zero applied magnetic field, and for an applied magnetic field of B_x = 56 mT (in-plane component), and B_z = 180 mT (normal component). In a spectral region near 2.75 GHz (the 305th mechanical overtone mode of the ME-HBAR), coupling and hybridizing of the acoustic waves with corresponding spin wave modes at this magnetic bias is observed [18], leading to a shift in the resonant frequency of the acoustic modes. In a narrow part of this region near $m = 305$, the phonon-magnon coupling completely attenuates the mechanical mode. The dispersion of the phonon-magnon coupling can be verified by plotting the frequency of each mode 'm' against the corresponding wavenumber $1/\lambda = m/2t$. The effect of hybridizing into magnetoelastic waves is clearly visible as a deviation from the normally linear dispersion of acoustic waves around 2.75 GHz (Fig. 5). While the HBAR provides multiple phonon modes over a wide RF spectrum by design, an appropriate magnon mode can be selected by tuning the magnetic bias. Comprehensive experiments along with a detailed model of the multi-mode magnon-phonon hybridization shall be discussed in future work. The frequency shift of mode $m = 305$ is shown in Fig. 6 as a function of the in-plane and normal components of the magnetic field. The bright arc in the top right corner of Fig 6(a) corresponds to conditions where the spin wave and acoustic wave dispersion curves cross and form hybrid magneto-elastic waves with high damping. Sufficiently far from this crossover, the magnetization dynamics and associated damping can be neglected and the frequency shift attributed to the ΔE effect, a dependence of the elastic modulus on the magnetization state in magnetostrictive materials [19]. The ΔE effect is highlighted in Fig. 6(b), with an expanded color scale. A frequency tuning of up to 100 kHz (~1% of the FSR) can be achieved in this regime with no discernable effect on the damping.

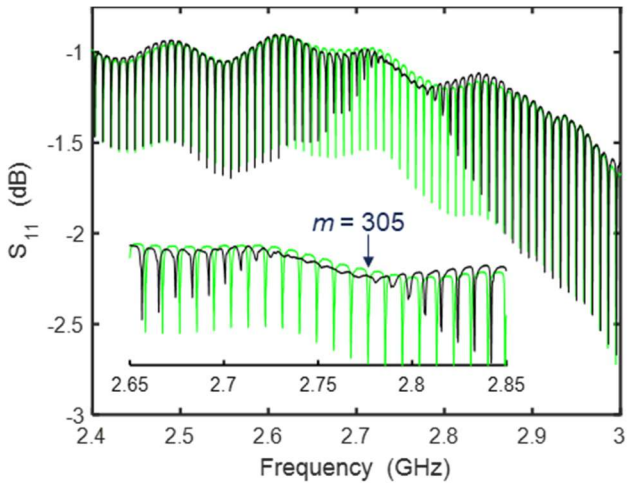

Figure 4. RF reflection spectra (S_{11}) of the wire-bonded and mounted GaN/Cu/YIG ME-HBAR comparing the resonances at zero field (green), and at B_x = 56 mT, B_z = 180 mT (black). Over a range of frequencies, the phonon-magnon coupling causes a frequency shift in the acoustic modes. The inset magnifies the spectral region near m = 305 where phonon-magnon coupling completely attenuates the mechanical mode, effectively switching it off.

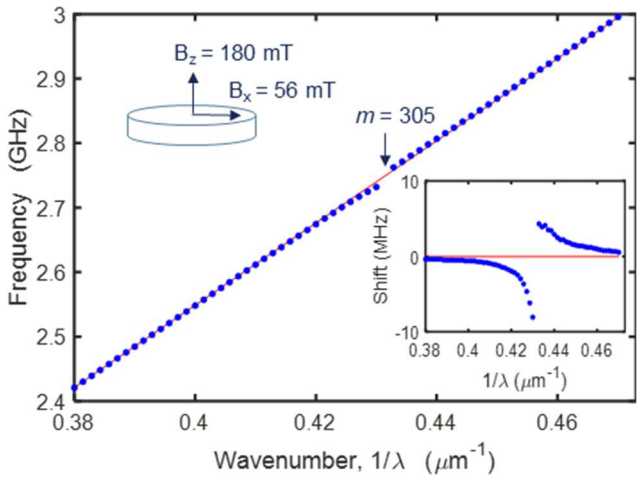

Figure 5. Magnetoelastic dispersion relation of the GaN/Cu/YIG ME-HBAR under the biasing conditions B_x = 56 mT and B_z = 180 mT. The inset shows the magnetoelastic frequency shift from the best-fit linear dispersion.

For a YIG-based ME-HBAR to be used as a tunable magnetoelastic oscillator or a filter, a ~1% tuning range would allow, for example, the active fine-tuning of the center frequency of a narrow-band filter (or an ensemble of periodic narrow-band filter modes that are within the hybridization range), but is insufficient for band switching. The acoustic velocity change due to the ΔE effect is, to first order, proportional to the magnetostriction coefficient λ_s of the magnetic material. YIG has a moderate magnetostriction of λ_s =2.4 ppm. Other ferrites such as Ni-Co-ferrite and Ni-Mn-Co-ferrite have λ_s in excess of 100 ppm [20] and would appear to be promising candidates for MTP resonators with much larger tuning ranges, and could be investigated along similar lines.

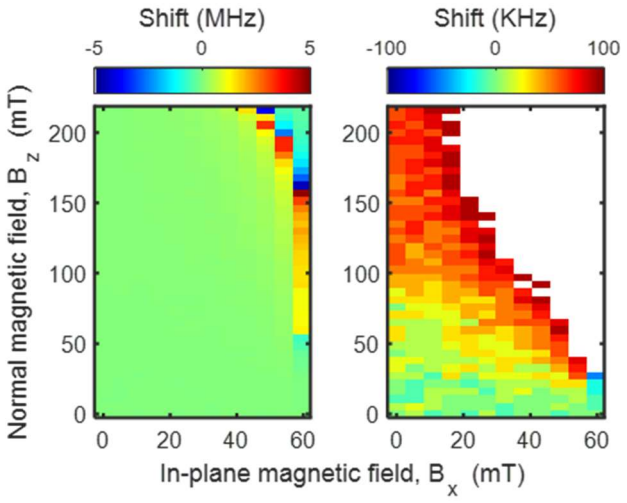

Figure 6. Shift in the frequency of acoustic resonant mode $m = 305$ (~ 2.75 GHz) as a function of in-plane and normal magnetic field. The shift is relative to zero magnetic field. (a) Large frequency shifts are accompanied by significant damping of the acoustic mode, while (b) frequency tuning with negligible dissipation can be achieved over a smaller range.

CONCLUSION

We have presented a demonstration of the MTP process that simplifies the often-conflicting demands of integrating incompatible epitaxial thin films and substrates. Unlike wafer-scale piezoelectric film transfer techniques, MTP can integrate various best-in-class RF/acoustic devices, along with electronic or optical components, to an arbitrary target substrate. As an example, we have transferred high quality acoustic transducers made from electronic-grade GaN on to a ferrimagnetic YIG substrate. The resulting ME-HBAR clearly demonstrates phonon-magnon mode coupling. Among other applications, this ME-HBAR can be used as a magnetically tunable RF/acoustic MEMS oscillator or filter. Integrated subsystems consisting of HEMTs, HBARs or other acoustic devices, could be transferred to YIG or other ferroic substrates. Beyond the widely hailed benefits to electronics manufacturing offered by the heterogeneous integration of chiplets, MTP processes can be used to integrate high quality electronic, optical, or acoustic functions on any target substrates appropriate to a particular application.

REFERENCES

[1] B. P. Downey, A. Xie, *et al.*, "Micro-transfer Printing of GaN HEMTs for Heterogeneous Integration and Flexible RF Circuit Design," in *Device Research Conference (DRC)*, 2020, pp. 1-2.

[2] J. Xu, C. Zhong, *et al.*, "Coherent Pulse Echo in Hybrid Magnonics with Multimode Phonons," *Physical Review Applied,* vol. 16, p. 024009, 2021.

[3] N. I. Polzikova, S. G. Alekseev, *et al.*, "Acoustic excitation and electrical detection of spin waves and spin currents in hypersonic bulk waves resonator with YIG/Pt system," *Journal of Magnetism and Magnetic Materials,* vol. 479, pp. 38-42, 2019.

[4] I. Lisenkov, A. Jander, and P. Dhagat, "Magnetoelastic parametric instabilities of localized spin waves induced by traveling elastic waves," *Physical Review B,* vol. 99, p. 184433, 2019.

[5] P. Chowdhury, A. Jander, and P. Dhagat, "Nondegenerate Parametric Pumping of Spin Waves by Acoustic Waves," *IEEE Magnetics Letters,* vol. 8, pp. 1-4, 2017.

[6] P. Chowdhury, P. Dhagat, and A. Jander, "Parametric Amplification of Spin Waves Using Acoustic Waves," *IEEE Transactions on Magnetics,* vol. 51, pp. 1-4, 2015.

[7] J. D. Adam, B. R. McAvoy, and H. L. Salvo, "Magnetically Tunable High Overtone Microwave Resonators," in *40th Annual Symposium on Frequency Control*, 1986, pp. 392-393.

[8] H. L. Salvo, R. A. Moore, *et al.*, "Properties of Tunable Yig Hbars," in *IEEE 1987 Ultrasonics Symposium*, 1987, pp. 337-340.

[9] N. Polzikova, S. Alekseev, *et al.*, "Acoustically driven magnetic excitations in BAW resonators with magnetic layers," in *2013 IEEE International Ultrasonics Symposium (IUS)*, 2013, pp. 216-219.

[10] A. Litvinenko, R. Khymyn, *et al.*, "Tunable Magnetoacoustic Oscillator with Low Phase Noise," *Physical Review Applied,* vol. 15, p. 034057, 2021.

[11] V. J. Gokhale, B. P. Downey, *et al.*, "Epitaxial bulk acoustic wave resonators as highly coherent multi-phonon sources for quantum acoustodynamics," *Nature Communications,* vol. 11, p. 2314, 2020.

[12] V. J. Gokhale, B. P. Downey, *et al.*, "Temperature evolution of frequency and anharmonic phonon loss for multi-mode epitaxial HBARs," *Applied Physics Letters,* vol. 117, p. 124003, 2020.

[13] V. J. Gokhale, B. P. Downey, *et al.*, "Engineering Efficient Acoustic Power Transfer in HBARs and Other Composite Resonators," *Journal of Microelectromechanical Systems,* vol. 29, pp. 1014-1019, 2020.

[14] B. P. Downey, D. S. Katzer, *et al.*, "XeF2 etching of epitaxial Nb2N for lift-off or micromachining of III-N materials and devices," *Journal of Vacuum Science & Technology A: Vacuum, Surfaces, and Films,* vol. 35, p. 05C312, 2017.

[15] *X-Celeprint Ltd*. Available: https://x-celeprint.com/technology

[16] C. Bower, M. Meitl, and R. S. Cok, "Micro-transfer-printed acoustic wave filter device," US Patent 11,139,797, 2021.

[17] H. M. Chou and E. D. Case, "Characterization of some mechanical properties of polycrystalline yttrium iron garnet (YIG) by non-destructive methods," *Journal of Materials Science Letters,* vol. 7, pp. 1217-1220, 1988.

[18] C. Kittel, "Interaction of Spin Waves and Ultrasonic Waves in Ferromagnetic Crystals," *Physical Review,* vol. 110, pp. 836-841, 1958.

[19] F. J. R. Schülein, E. Zallo, *et al.*, "Fourier synthesis of radiofrequency nanomechanical pulses with different shapes," *Nature Nanotechnology,* vol. 10, pp. 512-516, 2015.

[20] A. P. Greifer, "Piezomagnetism of biased ferrites," *Journal of Applied Physics,* vol. 35, pp. 1065-1066, 1964.

UNDERWATER ACOUSTIC TWEEZERS CAPABLE OF TRAPPING LARGE AND HEAVY PARTICLES

Kianoush Sadeghian Esfahani, Yongkui Tang, Jaehoon Lee, Matin Barekatain, and Eun S. Kim
Department of Electrical and Computer Engineering
University of Southern California, Los Angeles, CA 90089, USA

ABSTRACT

This paper describes acoustic tweezers capable of trapping large and heavy objects with 523.8 kHz sound waves. The tweezers are fabricated on a 4-mm-thick Lead Zirconate Titanate (PZT) substrate with a Fresnel air-cavity lens placed on its top surface. The fabricated tweezers are operated with continuous or pulsed 523.8 kHz sinusoidal waves, and offer multiple simultaneous trapping zones (up to 40), long range trapping (3-164 mm away from the tweezers), and trapping of large (up to 5mm in diameter) and heavy (up to 5.75 g/cm^3 in density) particles or microspheres. In addition to trapping, electrical control of the vertical position of the trapped particle has been achieved with the tweezers placed horizontally.

KEYWORDS

Acoustic tweezers, acoustic transducer, focused ultrasound, Fresnel lens, air cavity lens, particle trapping, multiple focal points.

INTRODUCTION

Contactless and heatless trapping of microparticles is highly desirable in manipulating particles that are prone to damage by physical contact or heat. Contactless trapping and manipulation of a particle has been achieved with optical tweezers [1], magnetic tweezers [2], etc. However, optical tweezers are not capable of trapping large and heavy objects without generating large amount of heat, and also do not work well where the medium is optically opaque, while magnetic tweezers require a magnetic label, unless the particle is magnetic. Acoustic tweezers, on the other hand, are able to trap large and heavy objects since acoustic waves are mechanical waves that are inherently capable of delivering deep trapping well. Moreover, acoustic tweezers can trap all kinds of particles in all kinds of medium, without generating substantial heat.

In this paper, we demonstrate an acoustic tweezers capable of trapping heavier and larger objects at a record level compared to previous reports over a large volume with multiple simultaneous trappings.

DESIGN

The acoustic tweezers are built on a 4-mm-thick PZT substrate (that has the fundamental thickness resonance at 523.8 kHz, much lower than our previous acoustic tweezers for trapping large and heavy particles) with electrodes on its top and bottom faces patterned into circles so that a voltage applied to the top and bottom electrodes may produce acoustic waves, most effectively at the fundamental resonance frequency. Polydimethylsiloxane (PDMS) film patterned with four Fresnel annular rings (to form Fresnel air cavity rings or lens) is bonded on to the top electrode. The radii of the annular rings R_n are designed into Fresnel half-wavelength bands (FHWB) [3], with annular rings sectored into 18 pie sectors (each occupying a 20° pie shaped when viewed from the top, as shown at the upper row of Fig. 1, for three different focal lengths with each set of 6 sectors targeting a focal length), according to

$$R_n = \sqrt{n\lambda \times (F_n + \frac{n\lambda}{4})} \quad (1)$$

where λ is the wavelength of acoustic wave in water at 523.8 kHz, while F_n is the focal length associated to the nth circle [4-5]. As illustrated in the lower row of Fig. 1, the air cavities in the PDMS membrane block the acoustic waves that will destructively interfere at the desired focal lengths, due to acoustic impedance mismatch between air (0.4 kRayl) and liquid/solid (more than 1 MRayl). The eighteen symmetric sectors consist of three sets of six sectored Fresnel rings designed for three focal lengths of 9, 10.75, 12.5 mm within which trapping zone is developed due to the interference of the three focused acoustic beams (Fig. 1).

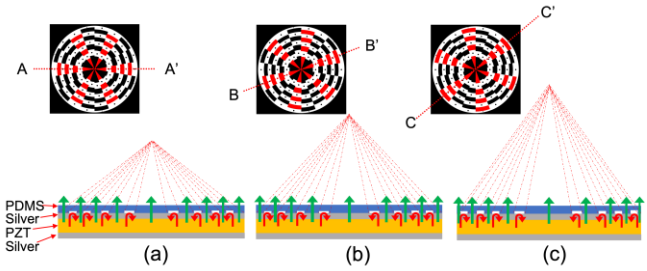

Fig. 1: (a)-(c) top views and cross-sectional views (across A-A', B-B' and C-C') of the acoustic tweezers with three sets of 6 sectors on the top view with the associated focal points in the cross-sectional views. By actuating all the three sets at the same time, a trapping zone is formed within the three focal points.

FABRICATION

The acoustic tweezers are fabricated through the steps illustrated in Fig. 2. To fabricate the air-cavity lens on PDMS membrane, 40 µm thick SU-8 is coated on a 4" x 4" glass substrate and patterned into annular rings (Fig. 2a), which will be air cavity rings in the PDMS membrane. In order to avoid collapse of the PDMS membrane in the air cavity rings, 300-µm-diameter circular holes are added in the SU-8 annular rings, so that those may later be filled with PDMS to function as mechanical support pillars. After treating the SU-8 mold with silane to make it hydrophobic for easy peel-off of PDMS membrane from the SU-8 mold later, PDMS solution is poured onto the glass substrate with SU-8 mold, which then is placed in a mechanical jig with a clamping mechanism (which sandwiches the poured PDMS on the glass substrate containing the SU-8 mold with another glass substrate that is fixed in the mechanical jig, as the distance between the two glasses is controlled by a micromanipulator) for thickness control of the PDMS layer (Fig. 2b). After reaching the desired PDMS thickness (200 µm), the PDMS is heat cured in oven for four hours, followed by peeling off from the mold and trimming to the desired size.

On a 4-mm-thick PZT substrate with pre-deposited 10-µm-thick silver layer on its top and bottom sides, the electrodes are patterned into circles (Fig. 2c). A 10-µm-thick SU-8 layer is then spin-coated on the top surface of the PZT (the surface on top of which PDMS membrane as Fresnel lens will be placed), followed by soft-bake, blank exposure with UV-light, and post exposure-bake (Fig. 2d). The fully cured SU-8 layer provides enough stiction and adhesion for the PDMS membrane (detached from the glass substrate after Fig. 2b) and allows a stable placing of the membrane onto the PZT. The PDMS membrane is then aligned and placed on

978-1-940470-04-7/HH2022/$25©2022TRF
DOI 10.31438/trf.hh2022.10

Solid-State Sensors, Actuators, and Microsystems Workshop
Hilton Head Island, South Carolina, June 5-9, 2022

the PZT surface where there is SU-8 adhesion layer (Fig. 2e). After soldering wires on the top and bottom electrodes, we conformally deposit 20-μm-thick Parylene layer for electrical insulation (Fig. 2f). Top-view photo of the fabricated tweezers along with the mask pattern for SU-8 mold and the cross-sectional view of the fabricated tweezers are shown in Fig. 3.

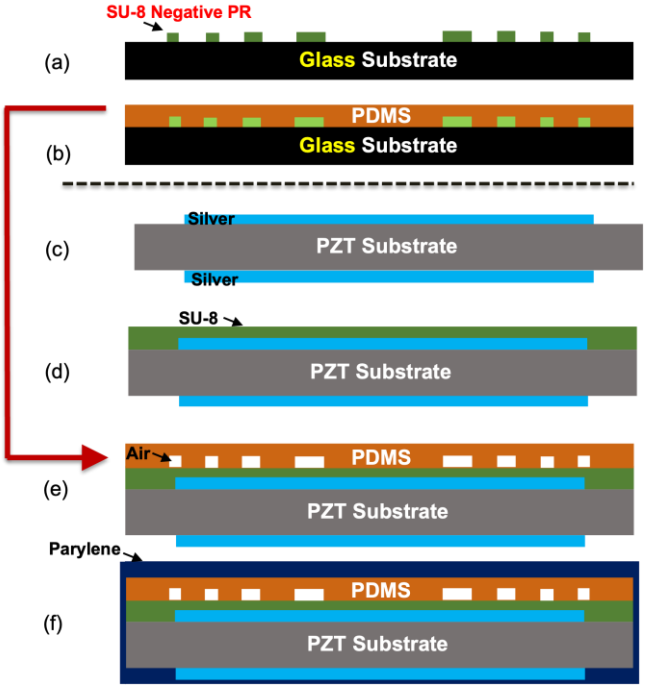

Fig. 2: Brief fabrication steps: (a) pattern SU-8 mold of annular rings on a glass substrate, (b) cast PDMS mix on the SU-8 mold, followed by heat curing and trimming, (c) pattern top and bottom electrodes on a 4 mm thick PZT, (d) spin-coat SU-8 adhesion layer over the PZT, (e) detach the PDMS membrane from the glass substrate, align and place the PDMS membrane on the PZT, and (f) deposit Parylene for electrical insulation.

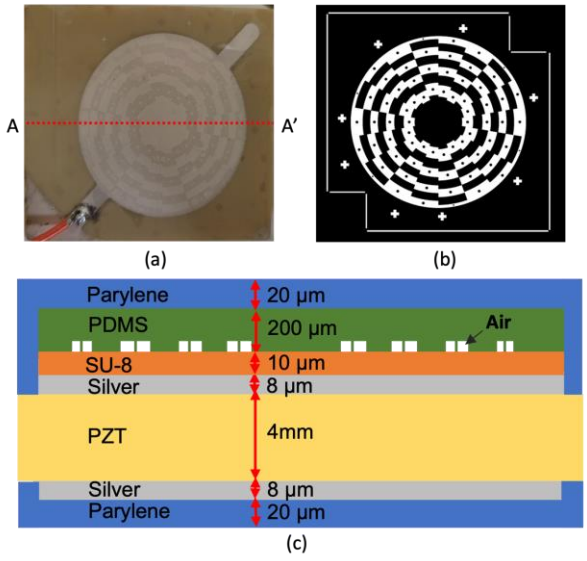

Fig. 3: (a) Top-view photo of the fabricated tweezers, (b) the mask pattern for air-cavity lens, and (c) the cross-sectional view (across A-A') with 300-μm-wide vertical lines in air cavity regions being the support pillars to prevent collapse of the PDMS membrane.

EXPERIMENTAL RESULTS

All the experiments with the fabricated tweezers are done in water with various particles and microspheres in a beaker with the acoustic tweezers placed horizontally or vertically. The tweezers are driven by a continuous sinusoidal wave of 523.8 kHz (equal to fundamental resonance frequency of the PZT substrate in thickness-mode) via a power amplifier capable of delivering the voltage and power, as illustrated in Fig. 7.

Horizontal Placement

With the tweezers placed horizontally, we have obtained trapping of a 4.2 mg Tin particle with density of 5.75 g/cm^3 and diameter of 1.12 mm, a polystyrene polymer sphere with diameter of 2.96 mm and density of 1.05 g/cm^3 (14.2 mg), and a 5 mm in diameter polystyrene polymer sphere (Fig. 4). A list of the trapped particles along with their densities and diameters as well as the minimum peak-to-peak applied voltage for trapping is shown in Table 1.

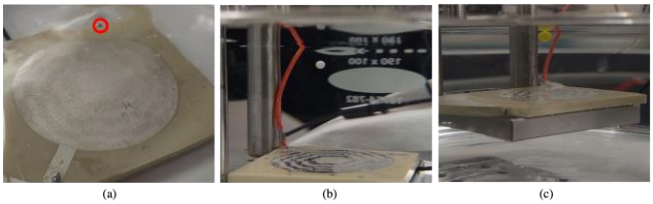

Fig. 4: Photos of trapping (a) a 4.2 mg Tin particle (1.5 mm in its longest direction) with the weight corresponding to a 1.12 mm in diameter, if it was spherical, (b) a white microsphere with diameter of 2.96 mm and density of 1.05 g/cm^3, and (c) a yellow microsphere with diameter of 5 mm and density of 1.03 g/cm^3 when the tweezers is placed horizontally.

Table 1: Various microspheres trapped with the tweezers being driven with a continuous 523.8 kHz sinusoidal wave.

Diameter (mm)	Density (g/cm^3)	Applied Peak-to-Peak Voltage for Trapping (Volts)
0.35	1.13	9.00
0.60	5.75	33.3
0.65	1.10	10.0
0.92	5.75	33.3
1.00	1.03	10.8
1.12	5.75	34.2
2.96	1.05	12.6
5.00	1.03	24.3

In addition to trapping large and heavy particles, simultaneous trapping of multiple microspheres is present (Fig. 5), mainly due to relatively low acoustic-wave loss in water at such a relatively low frequency of 523.8 kHz, leading to more pronounced impacts of wave reflections from water-air and water-beaker interfaces (resulting in more trapping points) than a similarly constructed tweezers operating beyond 1 – 2 MHz [6]. The number of the trapped microspheres is larger for smaller and lighter microspheres. In case of the microspheres with 1 mm in diameter and 1.03 g/cm^3 density, simultaneous trapping of up to 40 microspheres is observed, while only about three 2.97-mm-diameter microspheres of 1.05 g/cm^3 density are trapped simultaneously.

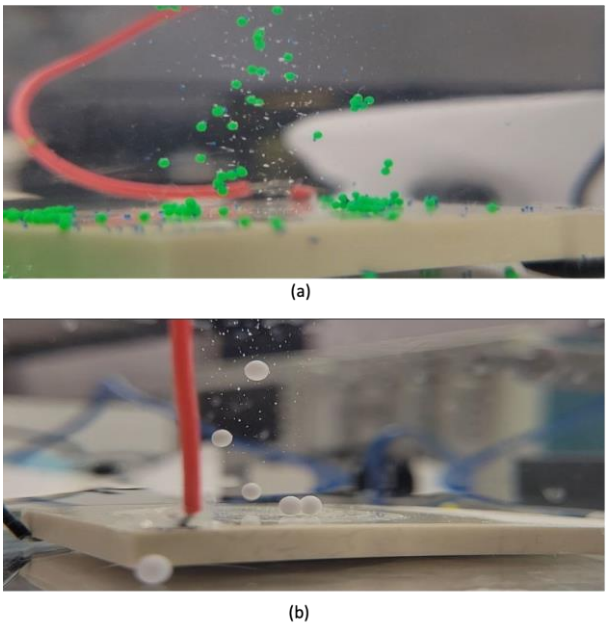

Fig. 5: Photos of trapping (a) multiple microspheres with 1.03 g/cm^3 density and 1 mm in diameter and (b) three 2.97-mm-diameter microspheres of 1.05 g/cm^3 density at three different vertical locations.

Vertical Placement

Vertical placement of the tweezers also produces particle trapping, albeit less number of simultaneous trappings and smaller trapped-particle diameter and density (Fig. 6). In one instance, four 1-mm-diameter microspheres of 1.03 g/cm^3 density are simultaneously trapped over 42 – 164 mm from the tweezers placed vertically (Fig. 6b).

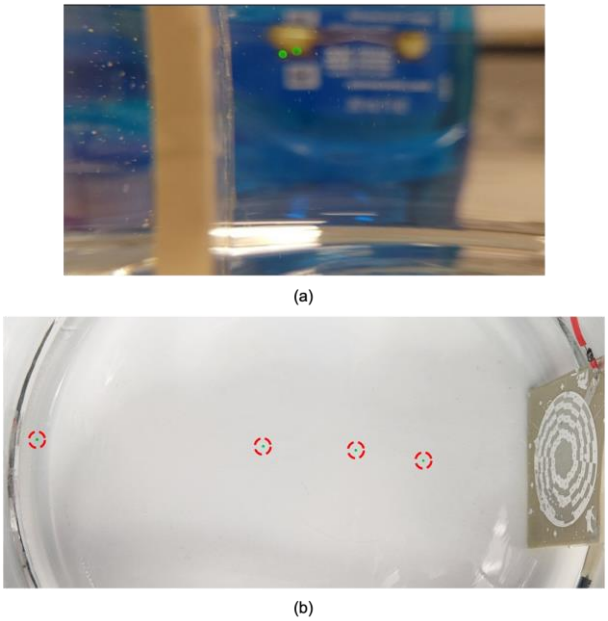

Fig. 6: Photos of (a) trapping two 1-mm-diameter microspheres of 1.03 g/cm^3 density with the tweezers placed vertically at a distance of about 7mm from the tweezers, and (b) trapping of same microspheres at different horizontal distances (42 – 164 mm) from the tweezers.

Manipulation of Trapped Particle

With a particle (or particles) trapped by a tweezers, the tweezers is moved in a set up shown in Fig. 7, in order to investigate whether and how well the trapped particle(s) follows the tweezers movement. In all our previous acoustic tweezers, the trapped particles followed the movement of the tweezers very reliably and repeatably [7].

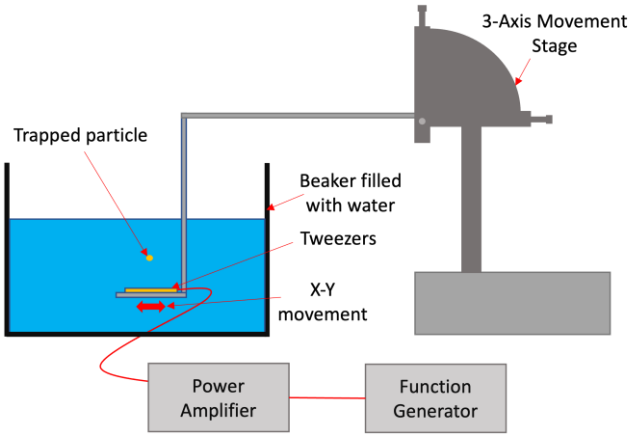

Fig. 7: Experimental setup to move the tweezers in 3-dimentional space, while particles are trapped by the tweezers, with the water-containing beaker remaining stationary.

However, with the tweezers operating at 523.8 kHz, we observe that the trapped particle remains stationary with respect to the beaker and does not follow the tweezers movement. Such behavior can be explained by noting that wave attenuation is relatively small at 523.8 kHz, compared to several MHz, and therefore the effects of the reflected waves from liquid-solid and liquid-air interfaces are quite pronounced, resulting in multiple trapping zones closely placed to each other with each zone having a relatively small energy well. In one experiment, the trapped particle remains stationary with respect to the beaker, even when the tweezers is moved 23 mm in one direction. (Fig. 8)

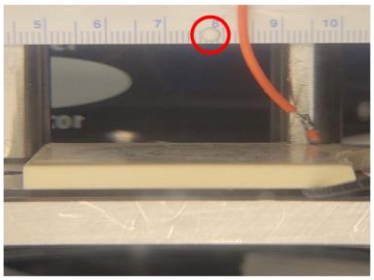

Fig. 8: Photo of a trapped particle remaining stationary, as the stage that holds the tweezers is moved slowly over tens of mm via a 3-axis movement stage.

Electrical Control of Vertical Position of Trapped Particle

We have explored electrical control on the vertical position of the trapped particle with respect to the tweezers placed horizontally, using applied voltage vs time as illustrated in Fig. 9. The idea is to trap a particle with a high voltage (V_H), release the trapped particle by reducing the applied voltage to a low value (V_L) for a brief period (P_w), so that the released particle may fall down due to gravity during P_w, and then increase the voltage back to V_H to trap the particle again, this time at a lower vertical location after the particle

having fallen a distance mainly determined by P_w. By trapping a particle and then letting the particle fall followed by trapping it again, a particle can be trapped at various vertical positions, the spacing of which is mainly determined by the duration of low applied voltage (P_w), as shown in Fig. 10. The trajectory of the particle during the falling period P_w is almost vertical, as gravity plays the main role to pull it down, when the particle is initially trapped within a radius of 1 cm from the center of the tweezers and the maximum vertical distance of the trapped particle from the tweezers is 7 cm. For electrical control over the vertical distance beyond 7 cm from the tweezers, the high and low voltage levels need to be modified, since the radius of the trapping region is narrower. In case of trapping a 1-mm-diameter microsphere with 1.03 g/cm^3 density over a vertical distance of 21.5 – 15 cm, the needed V_H and V_L are 22.5 and 13.5 $V_{p\text{-}p}$, respectively, while for vertical distances below 15 cm, the V_H and V_L are 13.5 and 4.5 $V_{p\text{-}p}$, respectively.

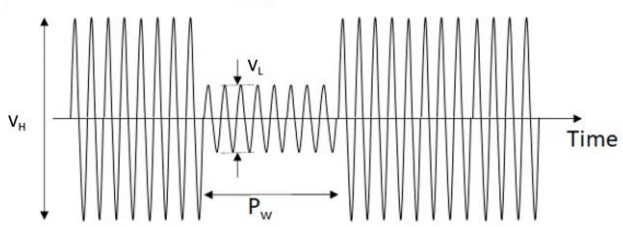

Fig. 9: Applied voltage vs time for electrical control of the vertical position of the trapped particle with the tweezers; particle trapped with a high applied voltage (V_H), particle released with a low applied voltage (V_L) for a brief period P_w during which the particle falls due to gravity, and then particle trapped again with a high voltage at a lower location after falling a short distance.

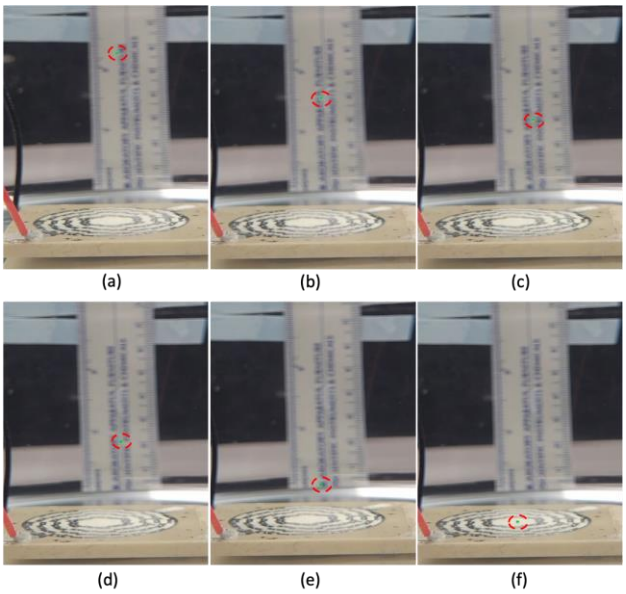

Fig. 10: Photos showing electrical control of the position of a trapped particle along the vertical direction: (a) a trapped particle with 14.4 $V_{p\text{-}p}$ (523.8 kHz) applied to the tweezers, (b) the particle trapped at a lower position by decreasing the applied voltage to 5.4 $V_{p\text{-}p}$ for ≈ 0.3 sec and increasing it back to 14.4 $V_{p\text{-}p}$, and (c) – (e) the particle trapped at lower positions by repeating the pulsed operation with the duration of the lower applied voltage determining the amount of the distance between two adjacent trapped positions.

DISCUSSION

The acoustic tweezers operating at 523.8 kHz can trap large and heavy particles, many of them simultaneously due to low acoustic loss in the medium (owing to the relatively low frequency) making reflections from liquid-air and liquid-solid interfaces not easily dying out. However, the trapped particle remains stationary, as we move the tweezers, apparently being trapped in different trapping zones. This phenomenon will likely be alleviated or modified with reduced trapping zones, which, though, comes at the cost of reduced effectiveness in trapping large and heavy particles, unless acoustic absorbers are incorporated on the liquid-air and liquid-solid interfaces.

CONCLUSION

The acoustic tweezers presented in this paper offer capability in trapping large and heavy solid particles in liquid medium without damaging the particles due to physical contact or heat. Though the movement of the trapped particle by moving the tweezers does not happen in the current operating mode, electrical control over the vertical position of the trapped particle has been shown to be easily achievable. Other electrical controllability of the trapped particle whether it is rotation or linear translation is likely to be possible, through modification on the tweezers design and applied voltage level and timing.

ACKNOWLEDGEMENT

This work is supported by National Institutes of Health under grant R01GM134352.

REFERENCES

[1] D. G. Grier, “A revolution in optical manipulation,” Nature, vol. 424, no. 6950, pp. 810–816, Aug. 2003.

[2] Z.M. Wang, R.G. Wu, Z.P. Wang, and R.V. Ramanujan, “Magnetic Trapping of Bacteria at Low Magnetic Fields,” Scientific Reports, vol. 6, no. 1, Jun. 2016

[3] Y.-L. Tu, S.-J. Chen, and Y.-R. Hwang, “Design of Fresnel Lens-Type Multi-Trapping Acoustic Tweezers,” Sensors, vol. 16, no. 11, p. 1973, Nov. 2016.

[4] D. Huang and E.S. Kim, "Micromachined Acoustic-Wave Liquid Ejector," IEEE/ASME Journal of Microelectromechanical Systems, vol. 10, pp. 442-449, September 2001.

[5] L. Zhao and E.S. Kim, “Acoustic Tweezers for Trapping Late-Stage Zebrafish Embryos,” The 32nd IEEE International Conference on Micro Electro Mechanical Systems (MEMS 2019), Seoul, Korea, January 27 - 31, 2019, pp. 57 – 60.

[6] Y. Tang and E.S. Kim, “Ring-Focusing Fresnel Acoustic Lens for Long Depth-of-Focus Focused Ultrasound With Multiple Trapping Zones,” Journal of Microelectromechanical Systems, vol. 29, no. 5, pp. 692–698, Oct. 2020.

[7] Y. Choe, J.W. Kim, K.K. Shung, and E.S. Kim, “Microparticle Trapping in An Ultrasonic Bessel Beam,” Applied Physics Letter, vol. 99, 233704 (2011).

CONTACT

*K. Sadeghian Esfahani, tel: +1-323-337-2823; ksadeghi@usc.edu

ADDRESSING THE GRAND CHALLENGES OF CLIMATE CHANGE

Dr. Leslie Field
Bright Ice Initiative, Inc., SmallTech Consulting, LLC, and Stanford University, USA

ABSTRACT

Climate change may not have been our main objective when we chose to specialize in MEMS and Nanotechnology. We may have been drawn in by opportunities in defense, fitness, pollution monitoring, or automotive safety. What called to me were biomedical applications, and the fact that MEMS is interdisciplinary, fascinating, and has seemingly boundless potential to solve real problems.

Over the years I've directed more and more of my work towards climate change-related challenges, to preserve a habitable world for our children, and for the ecosystems and species on which we all depend. I've also taught at Stanford on Engineering, Entrepreneurship and Climate Change for over a decade, because the next generations will have to work hard to address problems arising from climate change.

The approach I've developed over the years to preserve polar ice is not MEMS-based, but it does use what I learned about thermodynamics and micro- and nano-scale materials, to create a highly-leveraged approach to locally increase surface reflectivity to preserve ice in key locations.

In this talk, I'll address the timing and urgency of evaluating, testing, and potentially implementing localized and safe interventional climate change solutions for some of the largest challenges humanity and our ecosystems have ever faced. I'll describe the challenges and accelerating positive feedback loops in the Arctic, and the challenges and importance of preserving glacial ice. I'll describe some promising solutions and work from around the globe that addresses a number of critically important climate challenges, and the large and inclusive framework we all must keep in mind in order to create viable solutions.

Increasingly, we need to look to indigenous knowledge, and the people living closest to nature and the land, to be sure we include this expertise and wisdom in anything that we might consider doing in terms of intervention. It turns out that in order to address the problems of climate, we must work with transparency and permissions, and we must remember our connection to this earth, these ecosystems, and all the people and species we share this planet with, in order to create useful, viable, acceptable, and effective solutions to the world's most dire problems.

I've heard that climate change is the one area in which the experts are far more worried than the general public. I hope this presentation will help you understand even more about some of the most important climate effects, feedbacks, and impacts we need to worry about and address, to preserve our future, and that you will share your knowledge about the climate realities with your colleagues, families and friends. We need larger awareness to create and implement the solutions needed, in time to avert the worst scenarios. If you're not already working on climate challenges, I hope you'll consider how you might in your "spare time" bring your engineering, scientific and inventive skills, and your humanity, to address the grandest challenges we have ever faced.

HIGHEST FIGURE OF MERIT MICROACOUSTIC RESONATOR FOR MID-BAND 6G APPLICATIONS

Gabriel Giribaldi, Michele Pirro, Meruyert Assylbekova, Luca Colombo, and Matteo Rinaldi
Northeastern SMART Center, Northeastern University, Boston, USA

ABSTRACT

This paper reports on outstanding microacoustic resonators in the 7-11 GHz range of operation, opening the mid-band 6G filtering challenge. By leveraging the superior piezoelectric performance of highly-doped Scandium Aluminum Nitride ($Sc_{0.3}Al_{0.7}N$), Lateral Field Excited (LFE) Cross-sectional Lamé Mode Resonators (CLMRs) were fabricated with a simple (ideally 2-masks) and optimized micro-machining process, attaining record-breaking performance in terms of 3dB quality factor (Q_{3dB}) and single-mode electromechanical coupling (k_{tSM}^2) in that frequency range. Moreover, exploiting CLMRs' lithographic tunability of the resonance frequency, a span of more than 4 GHz in the frequency operation of such devices was achieved on the same chip without complication of the micro-machining process. The fabrication was carried-out on 200 mm wafers, being therefore compatible with industrial grade MEMS foundries. Finally, considerations are drawn in terms of required resonator performance to enable the synthesis of microacoustic filters for the future sixth-generation mobile network.

KEYWORDS

MEMS, CLMR, Sc-doped AlN, RF front-end, 6G, RF filters

INTRODUCTION

The rapid evolution of mobile networks in the last decade has radically changed the way we perceive and interact with the world. Such a technological revolution recently culminated in a first commercial deployment of the fifth-generation cellular wireless (5G), showcasing record-high data-rates [1] and opening windows for the development of the cutting-edge applications of tomorrow. The newly introduced 5G comes with two main frequency bands, the sub-6GHz and the mm-wave one (24-100 GHz). While the first is already highly exploited, the latter has been implemented with limited use cases. Nevertheless, the insatiable demand for technology to furtherly pervade our lives is already pushing research toward the 6G era. In that framework, new frequency bands will be allocated, going from the sub-GHz devoted to extreme wide area Internet of Things and rural areas coverage to the sub-THz for ultra-short-range communication with maximized data-rate [2]. According to [2], the frequency spectrum allocated to urban areas will be the 7-20 GHz band, providing an excellent trade-off between network capacity and coverage.

Although the bright premises, the practical implementation of such a 6G capacity revolution requires radically new technologies. In particular, heavy innovation in the radio frequency front-ends (RFFE) will be indispensable to allow for the 6G to become a reality.

The focus of the present work is on the filtering elements, RFFE blocks with the fundamental task of removing any undesired frequency component which may corrupt the carrier signal. In particular, the expected transition from the 100 MHz component carrier bandwidth of 5G to the 400 MHz of 6G [2] will require tremendous improvements in the performance of the microacustic filters. This directly translates into more and more stringent requirements for the Microelectromechanical (MEM) resonators used as their building blocks. Specifically, the devices will need higher operating frequencies (f_s>7 GHz) in order to work in the new bands, high electromechanical coupling (k_t^2>4%) in order to allow for a bandwidth of >400 MHz and relatively high quality factors (Q>250) to ensure low loss and proper filter selectivity. Those specifications result in the unprecedented requirement of a technological Figure of Merit (FoM) $f_s \cdot Q \cdot k_t^2$>100GHz.

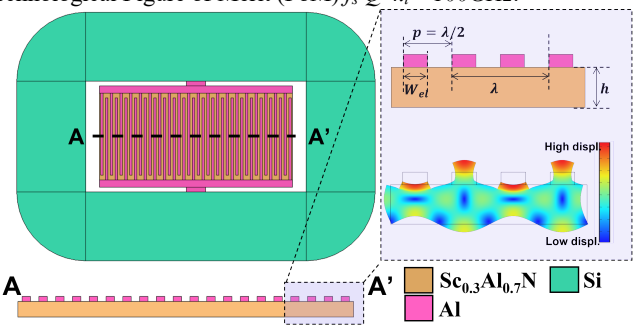

Figure 1: 3D and 2D view of a CLMR from this work, with highlighted relevant dimensions. In particular, the horizontal acoustic wavelength (λ), the pitch (p), the electrode width (W_{el}), and the piezoelectric thickness (h). Moreover, the CLMR mode-shape, obtained via COMSOL Multiphysics Finite Element Modeling simulation is given.

The current state-of-the art in terms of microacoustic resonators is constituted by thin-Film Bulk Acoustic Resonators (FBARs), developed in the '90s [3]. Since their commercialization, an incredible amount of research has been conducted to solve FBARs' limitations related to lithographic frequency tunability and scaling >5 GHz [4][5][6]. Nevertheless, the lower performance or higher fabrication complexity of alternative solutions have relegated them to the research realm, leaving FBARs as the only market player. Only recently the Cross-sectional Lamé Mode Resonator (CLMR) technology has been proposed [7] (Fig.1), attaining performance comparable to FBARs, but also achieving lithographic frequency tunability and offering unprecedented scaling capabilities with demonstrated f_s of 11 GHz [8] and 23 GHz [9] (overtone) with Q>600 and 250, respectively, employing a single interdigital electrode configuration. Nevertheless, due to the relatively low piezoelectric coupling achievable with such electrodes on AlN (k_t^2<2%), those devices did not meet the bandwidth requirements of the emerging mid-band 6G spectrum. Doping of AlN with large concentrations of Sc (>20%) has been recently demonstrated as an effective solution to achieve a 3-to-5-fold k_t^2 improvement in CLMRs [10][11]. Nevertheless, such a k_t^2 increase has been so far attained at the cost of a reduced $f_s \cdot Q$ product FoM, particularly for Sc concentrations ≥20\% due to limitations in material quality, resonator design, and/or micro-machining process [12][13].
This paper presents therefore the first technological solution for the mid-band 6G filtering challenge. In particular, we experimentally demonstrate microacoustic resonators operating in the 7-11 GHz range with record-breaking FoM, and we show devices with $f_s \cdot Q \cdot k_t^2$>140 GHz. Differently from the state-of-the-art in the same frequency range [12][13][14], we not only achieve a ~4X k_t^2-boost through high Sc-doping but we also demonstrate that high $f_s \cdot Q$ products, comparable to the one of the more mature AlN, can be achieved in highly-doped ScAlN resonators, which provides an

978-1-940470-04-7/HH2022/$25©2022TRF
DOI 10.31438/trf.hh2022.11

answer to the most important outstanding question in this research field. Finally, we draw considerations about the possible commercialization and mass production of such devices, also thanks to the very easy fabrication process carried out on MEMS-foundry standard 200 mm wafers, ScAlN post-CMOS compatibility, and the very good agreement of experimental results and finite element modeling (FEM) simulations.

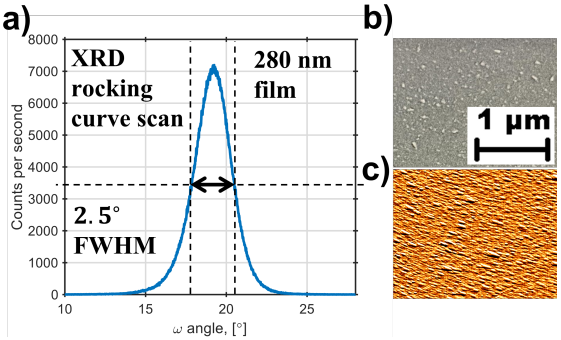

Figure 2: a) X-Ray Diffractometry (XRD) Rocking Curve scan of the 280 nm ScAlN film employed in this work. (b) and (c) show Scanning Electron Microscope (SEM) and Atomic Force Microscope (AFM) top views of the film's surface, respectively.

FABRICATION

Highly c-axis oriented ScAlN films

A 280 nm $Sc_{0.3}Al_{0.7}N$ thin-film was deposited on a high-resistivity 200 mm Si<100> wafer via reactive sputtering utilizing an industrial grade EVATEC Clusterline II tool. A 12" compound $Al_{0.7}Sc_{0.3}$ casted target was employed as source. A thorough optimization process was followed in order to obtain the high film quality. In particular, the metrics of interest were: the Full Width Half Maximum (FWHM, Fig.2a, with a measured value of 2.5°), the in-plane stress and stress gradient, the surface roughness, and the Abnormally Oriented Grains (AOGs) count (Fig.2b-c). Moreover, the sputtering process could count on a high throughput (47 nm/min). The recipe utilized a Nitrogen flow of 90 sccm, a power of 6 kW applied to the AlSc target, a chuck-height of 20 mm, and a temperature to 300°C.

Microacoustic resonators

After the film was deposited, the etch of the piezoelectric layer took place in order to define the resonant plates. The process took advantage of an optimized dry etching recipe performed in an Oxford Inductively Coupled Plasma (ICP) Reactive Ion Etching (RIE) tool, in conjunction with an oxide mask deposited via Plasma Enhanced Chemical Vapor Deposition (PECVD) and etched in fluorine chemistry. The ScAlN etching recipe utilized chlorine chemistry and high argon flow, with 10 sccm of Cl_2, 6 sccm of BCl_3, and 28 sccm of Ar. High power levels were utilized, with 300 W RF and 600 W ICP power. The etching pressure was 10 mTorr. After the etch of the piezo-layer, the oxide mask was stripped in 49% hydrofluoric acid (HF). The combination of an optimized etching recipe and a hard mask resulted in straight sidewalls (>70°).
Subsequently, the nanometric finger electrodes (W_{el}=*140-300 nm*) were defined via electron beam lithography and Aluminum thermal evaporation. In terms of photoresist, the e-beam step employed a bi-layer of PMGI SF3 (lift-off resist) and PMMA A7. The lift-off itself was performed in Microposit Remover 1165 heated at 85°C. In order to ease the very low throughput e-beam step, only the finger electrodes were defined, while the routing was fabricated in a second moment utilizing a direct writer and Aluminum sputtering and lift-off. In the scenario of a possible mass production of such devices, the e-beam and direct writer litho steps could be combined with the aid of a deep-UV stepper. Finally, the devices were released via XeF_2 isotropic etching (Fig.3 for a view of the fabrication steps and SEMs of fabricated devices).

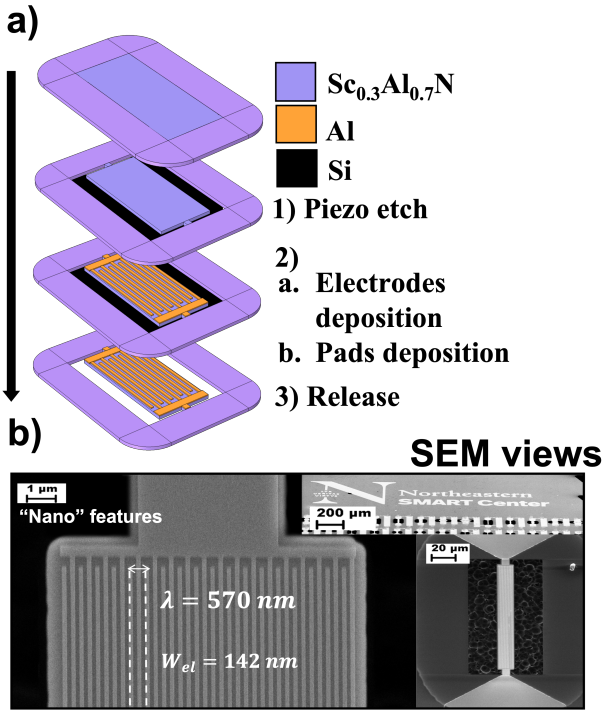

Figure 3: a) Employed micro-machining process and b) SEM pictures of devices presented in this work.

EXPERIMENTAL RESULTS

The device testing was carried out through direct probing with two Cascade GSG150 RF probes. The devices scattering parameters were recorded utilizing a Keysight N5221A network analyzer.
The fabricated resonators exhibited resonances in the 7-11 GHz range, therefore demonstrating a wide on-chip tunability of the operating frequency without major k_t^2 degradation. The admittance responses (Y_{12} vs. frequency) of outstanding devices are reported in Fig.4a, along with relevant metrics and FoM. Moreover, Fig.4b shows a comparison of the admittance response of a resonator of this work with the AlN-based one of [8], working at the same frequency. By employing COMSOL® Multiphysics, the same devices were *a-posteriori* FEM-simulated. In this way, the simulations could count on the actual measured geometrical dimensions. A mechanical quality factor equal to the 3dB one of the measured resonators was superimposed. In order to simulate ScAlN, not present in the COMSOL library, a custom material utilizing the ab-initio equations derived in [10] for the piezoelectric and mechanical properties was employed. As dielectric constant, instead, an experimentally extracted value of 17 was used. It was measured with an aixACCT TF2000 thin-film characterization tool with a procedure similar to the one of [15]. The simulation admittance results are shown in Fig.4a. Moreover, Fig.4c-d reports a comparison of the measured resonance frequency and electromechanical coupling between the experimental measurements and the simulations, as function of the geometrical ratio of the piezoelectric thickness and the horizontal acoustic wavelength (h/λ). Each single datapoint is the result of a set of 3 measurements on similar devices. As it can be observed, the f_s value can be predicted with a high degree of accuracy, with a maximum relative error of about 2%. In terms of k_t^2, it can be

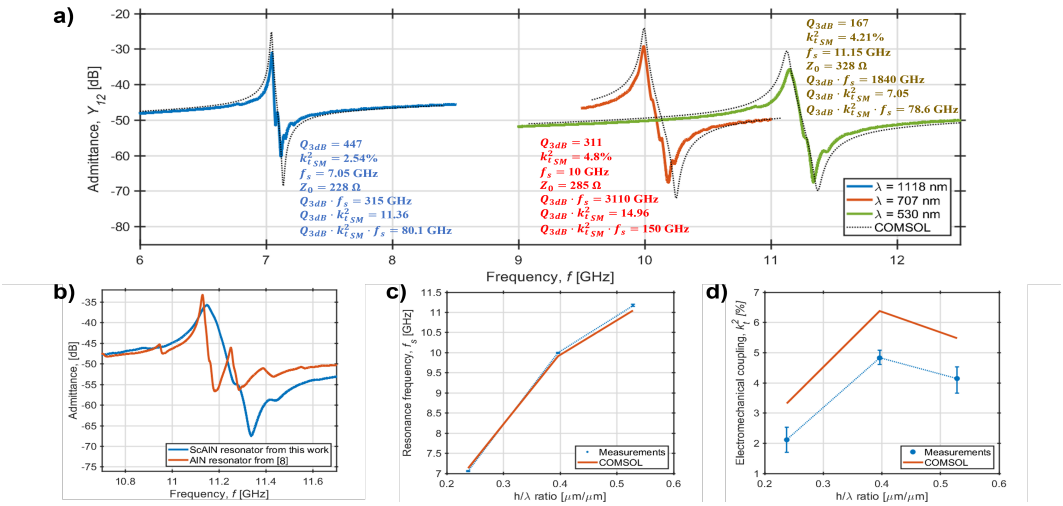

Figure 4: a) Admittance Y_{12} plots vs. frequency of three showcase resonators of this work, with highlighted main metrics and FoM. In b), a ScAlN resonator of this work is compared to a similar design in AlN from [8], showing the 3.3-fold k_t^2 improvement. In c) and d), the experimental results are compared to a-posteriori COMSOL simulations in terms of resonance frequency and k_t^2, respectively. Each datapoint is the result of the average on 3 similar devices, and the extreme cases are shown in the error bars.

observed that the trend of the measurements matches the one of the simulations, with maximum coupling for $h/\lambda = 0.4$ as in [11]. Nevertheless, there is an offset between the two curves. This is because (i) all the material properties in COMSOL besides the dielectric constant come from *ab-initio* calculations and do not necessarily reflect the real values and (ii) the simulations do not take into account material non-idealities, such as a FWHM of 2.5° and some (even if few) AOGs on the top surface. Further optimization in the thin-film deposition parameters has to be performed in order to reduce the gap between measurements and simulations.

IMPACT

The unprecedented performance of the aforementioned devices opens wide possibilities in the world of RF-MEMS. In fact, it firstly sparkles new interest in the CLMR technology, now seen as a possible solid alternative to FBARs in the framework of commercial filtering devices above 5 GHz. Moreover, the obtained resonator quality factors, especially in such a frequency range, prove that recurring to high Sc-doping of AlN, though boosting the electromechanical coupling through an enhancement of the piezoelectric coefficients, does not necessarily translate in a Q degradation as stated in [16]. Furthermore, the demonstrated wide on chip tunability of the resonance frequency obtained simply by lithographically adjusting the horizontal acoustic wavelength allows, in that frequency range, to sweep the device operation of several GHz without major deterioration of the k_t^2. This provides a substantial improvement in design flexibility compared to FBARs and allows to cover multiple bands with filters fabricated on the same substrate without overcomplications of the micro-machining process, thus providing cost-effectiveness. Finally, the present devices represent the first attempt to solve the mid-band 6G filtering challenge. The scatter plots of Fig.5 show a comparison of the devices of this work with similar designs (AlN and ScAlN CLMRs) present in the literature, showcasing the undisputed performance superiority in terms of relevant FoM, as a result of all-around design and fabrication optimizations. Moreover, in the same plots the optimal region of operation of MEMS resonators allowing the synthesis of microacoustic filters for the 6G mid-band is highlighted.

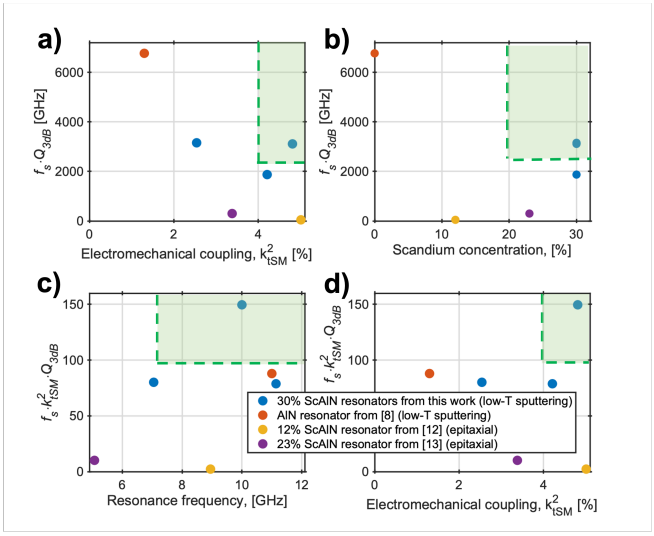

Figure 5: Scatter plots comparing the performance of the resonators in Fig.4a to the ones of [8] (with a sputtered piezoelectric layer) and [12][13] (with an epitaxial piezoelectric layer, therefore not CMOS-compatible). The metrics are the 3dB quality factor (Q_{3dB}) and the single-mode electromechanical coupling (k_{tSM}^2). The optimal performance region for the synthesis of high-performance filters for the mid-band 6G spectrum is highlighted.

CONCLUSIONS

The present work introduced and opened the 6G mid-band filtering challenge, with the final aim of enabling the filtering hardware required for the next-generation mobile network in urban areas. In particular, the focus was on highly-doped ScAlN and CLMR technology for the piezo-material and the design counterparts, respectively. Their combination is foreseen by the authors to allow for the synthesis of high-performance, compact and cost-effective microacoustic filters and duplexers for the RF front-

ends of future commercial mobile devices.

Outstanding microacoustic resonators in the 7-11 GHz range of operation have been presented, with the most performing one featuring $Q_{3dB} \cdot k_{tSM}^2 \cdot f_s > 140\ GHz$, along with accurate post-fabrication Finite Element Modeling simulation results. Such an accomplishment is the result of an all-around optimization process targeting high-quality and highly-doped ScAlN thin films on 200 mm substrates, most-performing designs, and minimization of fabrication-related design non-idealities, e.g. resonator plate sidewalls, layer to layer misalignment, and finger coverage.

Finally, devices from this work have been compared with similar designs with resonance frequency above 5 GHz, showing a significant degree of improvement in the most relevant figures of merit.

ACKNOWLEDGEMENTS

This work was supported by Raytheon Missiles and Defense under contract No. 4202341711. The author also wants to thank the staff of the Kostas Nano and Microfabrication Research Center at Northeastern University and the one of the Center for Nanoscale Systems at Harvard University.

REFERENCES

[1] "IEEE 5G and beyond technology roadmap white paper," 2017.

[2] H. Holma, H. Viswanathan, and P. Mogenses, "Extreme massive MIMO for macro cell capacity boost in 5G-advanced and 6G," in Nokia Bell Labs, White paper, 2021.

[3] R. C. Ruby and P. P. Merchant, "Tunable thin film acoustic resonators and method for making the same," in US Patent US5587620A, 1996.

[4] M. Rinaldi, C. Zuniga, and G. Piazza, "5-10 GHz AlN contour-mode nanoelectromechanical resonators," in 2009 IEEE 22nd International Conference on Micro Electro Mechanical Systems, pp. 916–919, 2009.

[5] M. Rinaldi, C. Zuniga, C. Zuo, and G. Piazza, "Super-high-frequency two-port AlN contour-mode resonators for RF applications," IEEE Transactions on Ultrasonics, Ferroelectrics, and Frequency Control, vol. 57, no. 1, pp. 38–45, 2010.

[6] S. Gong and G. Piazza, "Design and analysis of lithium–niobate-based high electromechanical coupling RF-MEMS resonators for wideband filtering," IEEE Transactions on Microwave Theory and Techniques, vol. 61, no. 1, pp. 403–414, 2013.

[7] C. Cassella, Y. Hui, Z. Qian, G. Hummel and M. Rinaldi, "Aluminum Nitride Cross-Sectional Lamé Mode Resonators," in Journal of Microelectromechanical Systems, vol. 25, pp. 275–285, April 2016.

[8] M. Assylbekova, G. Chen, G. Michetti, M. Pirro, L. Colombo, and M. Rinaldi, "11 GHz lateral-field-excited aluminum nitride cross-sectional Lamé mode resonator," in 2020 Joint Conference of the IEEE International Frequency Control Symposium and International Symposium on Applications of Ferroelectrics (IFCS-ISAF), pp. 1–4, 2020.

[9] M. Assylbekova, G. Chen, M. Pirro, G. Michetti, and M. Rinaldi, "Aluminum nitride combined overtone resonator for millimeter wave 5G applications," in 2021 IEEE 34th International Conference on Micro Electro Mechanical Systems (MEMS), pp. 202–205, 2021.

[10] M. A. Caro, S. Zhang, T. Riekkinen, M. Ylilammi, M. A. Moram, O. Lopez-Acevedo, J. Molarius, and T. Laurila, "Piezoelectric coefficients and spontaneous polarization of ScAlN," in Journal of Physics: Condensed Matter, vol. 27, May 2015.

[11] G. Giribaldi, L. Colombo, B. Fabio, C. Cassella, and M. Rinaldi, "Investigation on the impact of scandium-doping on the k_t^2 of $Sc_xAl_{1-x}N$ cross-sectional Lame' mode resonators," IEEE International Ultrasonics Symposium 2020, 2020.

[12] M. Park, Z. Hao, R. Dargis, A. Clark, and A. Ansari, "Epitaxial aluminum scandium nitride super high frequency acoustic resonators," Journal of Microelectromechanical Systems, vol. 29, no. 4, pp. 490–498, 2020.

[13] M. Park and A. Ansari, "Epitaxial $Al_{0.77}Sc_{0.23}N$ SAW and lamb wave resonators," in 2020 Joint Conference of the IEEE International Frequency Control Symposium and International Symposium on Applications of Ferroelectrics (IFCS-ISAF), pp. 1–3, 2020.

[14] M. Park, Z. Hao, D. G. Kim, A. Clark, R. Dargis, and A. Ansari, "A 10 GHz single-crystalline scandium-doped aluminum nitride Lamb-wave resonator," in 2019 20th International Conference on Solid-State Sensors, Actuators and Microsystems Eurosensors XXXIII (TRANSDUCERS EUROSENSORS XXXIII), pp. 450–453, 2019.

[15] M. Pirro, B. Herrera, M. Assylbekova, G. Giribaldi, L. Colombo, and M. Rinaldi, "Characterization of dielectric and piezoelectric properties of ferroelectric AlScN thin films," in 2021 IEEE 34th International Conference on Micro Electro Mechanical Systems (MEMS), pp. 646–649, 2021.

[16] R. H. Olsson, Z. Tang, and M. D'Agati, "Doping of aluminum nitride and the impact on thin film piezoelectric and ferroelectric device performance," in 2020 IEEE Custom Integrated Circuits Conference (CICC), pp. 1–6, 2020.

CONTACT

Gabriel Giribaldi, giribaldi.g@northeastern.edu

X-BAND FERROELECTRIC-ON-SI FIN BULK ACOUSTIC RESONATORS (FOS-FINBAR) WITH *f.Q* OF 0.8×10^{13}

Faysal Hakim and Roozbeh Tabrizian
Department of Electrical and Computer Engineering, University of Florida, USA

ABSTRACT

This abstract reports on ferroelectric-on-Si fin bulk acoustic resonators (FoS-FinBAR) operating at ~X-band with large quality factors (Q) as high as 1032, and a record-high frequency-Q product ($f\times Q$) nearing 10^{13}. This high performance is achieved through a novel fabrication process that enables perfect control over the three-dimensional geometry of the device and its transducer electrodes, as well as crystalline quality of the constituent materials. The process is based on (a) crystallographic-orientation-dependent etching of Si micro-fins with perfectly straight sidewall and aspect ratio exceeding 20:1, (b) conformal atomic-layer-deposition of sidewall ferroelectric transducers, and (c) three-dimensional patterning of transducer electrodes. FoS-FinBARs with a fin width of 1.2µm and hafnia-zirconia transducer of 50nm thickness are presented. The devices are operating in 3rd width-extensional bulk acoustic mode at 7.75 and 7.78 GHz, with Qs of 961 and 1032, and electromechanical coupling (k_t^2) of 1.29% and 0.89%, respectively. The large $f\times Q$ of 0.8×10^{13} at ~8 GHz, solidly-mounted structure, lithographical frequency scalability, and the CMOS-compatible fabrication process of the X-band FoS-FinBARs highlight their potential to realize multi-frequency and monolithically integrated oscillators and channel-select filters.

KEYWORDS

Ferroelectric, Hafnia-Zirconia, Fin Bulk Acoustic Resonator (FinBAR), X-band, Three-dimensional Patterning, Sidewall Transducer, High Q, CMOS Compatible.

INTRODUCTION

Current wireless spectrum resource, extending from 0.3 to 6 GHz, is on the verge of congestion due to exponential increase in the number of users introduced by internet of things, and the emergence of broadband applications such as metaverse. To address the grand challenge of spectrum limitation, new wireless technologies aim to use spread-spectrum techniques based on reconfiguration over numerous bands, and also extension to operate in untapped spectrum in cm- and mm-wave regimes [1]. These goals, however, are currently intangible, due to the fundamental limitations of available frequency control technologies.

The frequency control in existing wireless systems is indispensably dependent on piezoelectric bulk acoustic wave (BAW) resonator technologies to realize RF filters and oscillators for front-end modules. Current piezoelectric BAW resonators, created in aluminum nitride (AlN) films and operating in thickness mode, are fundamentally incapable to realize spread-spectrum frequency generation and control for modern wireless systems operating in super- and extremely-high-frequency regimes. This is primarily due to their limited lithographic frequency scaling and large area that prevents single-chip multi-band integration and impose large footprint consumption. Further, the k_t^2 and Q of these resonators significantly drop at higher frequencies, due to significant degradation of sputtered AlN quality at lower thicknesses required for frequency scaling [2-4]. To overcome these limitations, new technologies are developed based on alternative materials (*e.g.*, lithium niobate, scandium-aluminum nitride) and high-order modes [5-9]. However, these approaches do not provide transforming solution, since they still rely on planar architectures and inherit similar limitations of AlN BAW, although incrementally relieve frequency and integration limits.

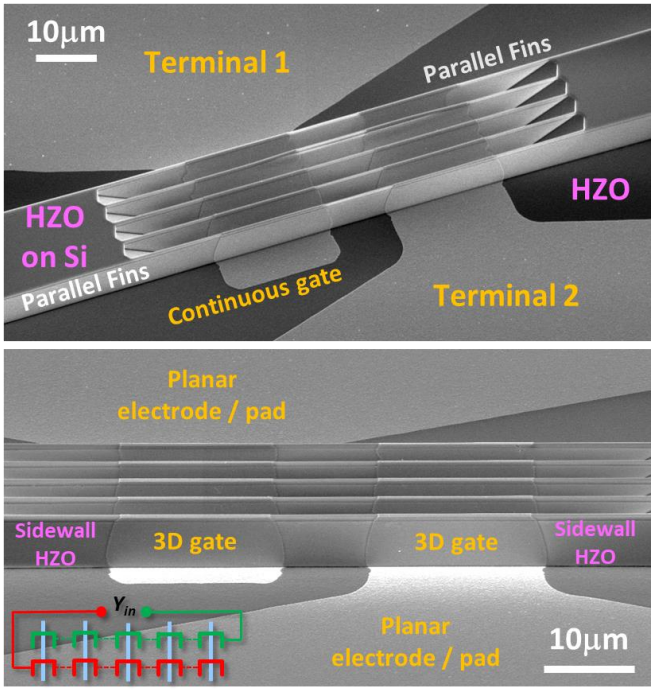

Figure 1: SEM images of multi-gate HZO-on-Si FinBAR, highlighting the fins, 3D-patterend gates and planar pads. The inset shows the connection of gates to form two terminals.

An alternative three-dimensional fin bulk acoustic resonator (FinBAR) technology has been developed in this regard that operates on excitation of bulk acoustic modes in high aspect-ratio semiconductor fins [10-12]. Benefiting from the width variation and single-crystallinity of fins, this technology offers multitude advantages over planar counterparts such as extreme lithographical frequency scalability, high Q, improved power handling and linearity, and an order of magnitude smaller footprint [13]. Realizing FinBARs however requires addressing major manufacturing challenges including growth of textured piezoelectric films and low-loss metal electrodes on the sidewall, and definition of high-aspect ratio fins with minimum width variation across the height. These features are essential to achieve high k_t^2 and Q width-extensional resonance modes in FinBARs.

In this work, we present a new generation of ferroelectric-on-silicon (FoS) FinBARs based on a novel fabrication process that creates mirror smooth and perfectly straight fin profile, high quality sidewall piezoelectric films, and three-dimensional patterning of low-loss electrodes / gates on the sidewall of the fins. Proof of concept devices are presented at 8 GHz, based on 1.2µm-wide Si fin, 50nm-thick hafnia-zirconia (HZO) sidewall piezoelectric transducer, and atomic-layer-deposited tungsten (W) gates, showing a record-high $f\times Q$ of ~0.8×10^{13}. Figure 1 shows the scanning electron microscopy (SEM) images of fabricated FoS-FinBAR from different angles, highlighting the ideal geometry of fins, 3D-patterened gates, and arraying scheme used to increase transduction area and reduce admittance.

978-1-940470-04-7/HH2022/$25©2022TRF
DOI 10.31438/trf.hh2022.12

FOS-FINBAR DESIGN AND MODELING

FoS-FinBAR is modeled using Mason's waveguide-based approach [14], to identify the resonance frequency, Q and k_t^2 based on the transducer and electrode thicknesses, fin width, and fundamental material properties. Figure 2 (a) shows the model created from cascading acoustic waveguides that represent metal electrode, HZO piezoelectric film, and Si fin. The model represents two W-HZO-W sidewall transducers that are placed on the two ends of the Si fin. Each waveguide, created from a lossy elastic medium with a wavenumber k, is modeled with series (Z_s) and shunt (Z_p) impedances in T-shaped network where:

$$Z_s = jZ\tan\left(\frac{kd}{2}\right), \quad Z_p = -jZ/\sin(kd) \qquad (1).$$

Here, $k = \frac{2\pi f d}{v}\left(1 - \frac{j}{2Q_m}\right)$, and d, Z, v, and Q_m are layer thickness, acoustic impedance, longitudinal acoustic velocity, and material quality factor, respectively. Besides, the equivalent waveguide model of the piezoelectric layer includes a lossy static capacitor (C_0) and a transformer with efficiency (η) defined by longitudinal piezoelectric coefficient (e_{33}), defined as:

$$C_0 = \frac{\varepsilon A}{d}, \quad \eta = e_{33}\frac{C_0}{\varepsilon} \qquad (2),$$

where, A is the sidewall transduction area and ε is the dielectric constant of the piezoelectric film. Figure 2 (b) shows the admittance of the FoS-FinBARs operating in 3rd width-extensional modes. The resonators are modeled with 50nm HZO sidewall transducer sandwiched between 30nm W electrodes, and based on using different Si fin widths, to highlight the lithographical frequency scalability of FoS-FinBARs.

When targeting for a particular resonance frequency value, the transducer stack thickness and fin width can be tailored to achieve

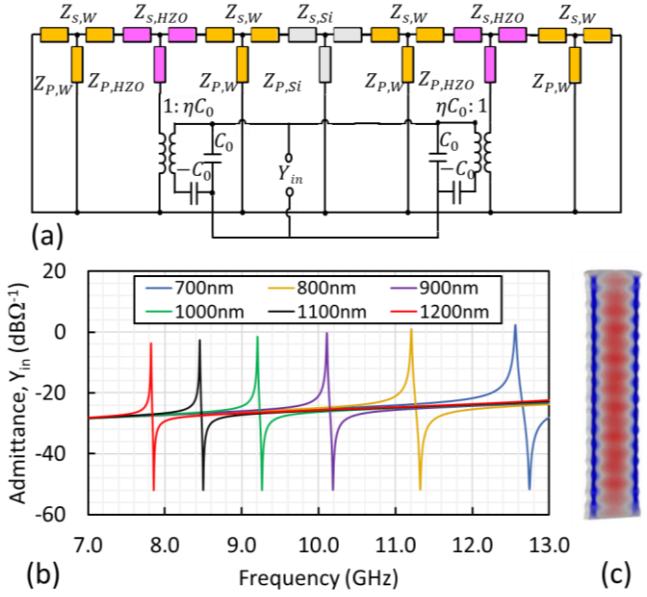

Figure 2: (a) Electrical equivalent circuit model from Mason's waveguide approach for FoS-FinBAR; (b) Simulated admittance of FoS-FinBARs with different fin widths, operating in 3rd width-extensional bulk acoustic mode (WE_3), highlighting lithographical frequency scalability; (c) COMSOL simulated cross-sectional mode-shape of FoS-FinBAR operating in WE_3 mode.

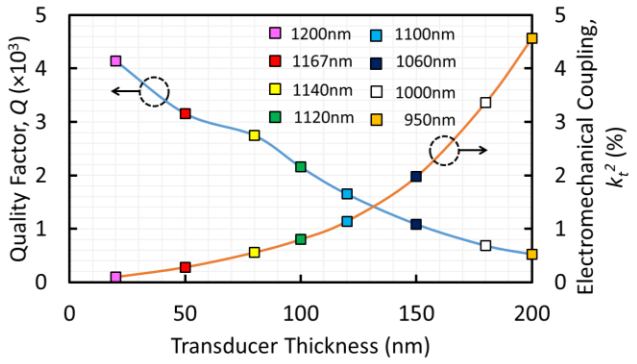

Figure 3: Simulated performance metrics (quality factor, Q on left Y-axis and electromechanical coupling, k_t^2 on right Y-axis) for 8 GHz FoS-FinBARs created from different combinations of HZO transducer thickness and fin width.

the desirable k_t^2 and Q. Figure 3 shows the simulated (using Mason's model) Q and k_t^2 of 8 GHz FoS-FinBAR created from proper combination of transducer thickness and fin width to achieve 8 GHz resonance frequency for the 3rd width-extensional mode. Opting for narrower Si fins and thicker HZO transducer thickness results in lower Q and higher k_t^2 values. This is due to the higher fraction of electromechanically active volume of the resonator and also the higher energy dissipation in HZO film compared to single-crystal Si fin. On the other hand, opting for wider fins and thinner sidewall HZO thickness results in a Q increase and k_t^2 drop. This results in a nearly constant $k_t^2.Q$ product at any frequency, regardless of the relative thickness of HZO transducer and width of Si fin.

FABRICATION PROCESS

Figure 4 shows the fabrication process flow of the presented FoS-FinBAR. To achieve mirror-smooth fin sidewall with negligible width variation across height, crystallographic-orientation dependent Si etch is performed. In this process, (110)

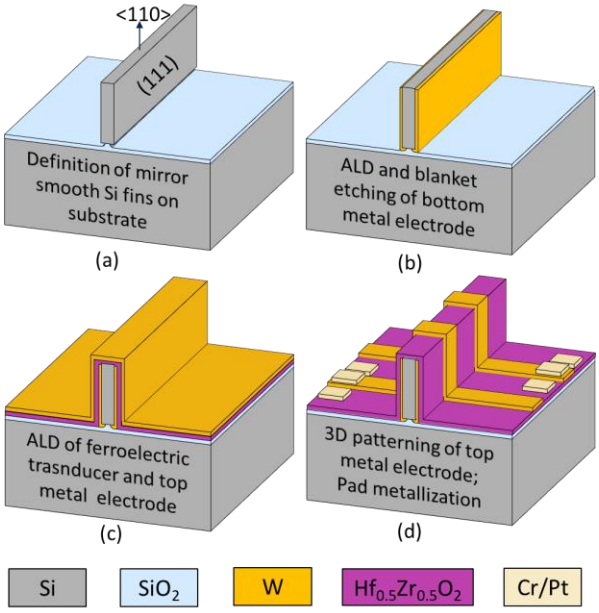

Figure 4: Three mask fabrication process flow of FoS- FinBARs: (a) wet-etching Si fins with (111)-plane etch-stop; (b) ALD and selective patterning of the first W electrode; (c) ALD of ferroelectric HZO transducer and top metal followed by crystallization annealing; (d) 3D patterning of top gates by isotropic dry etch.

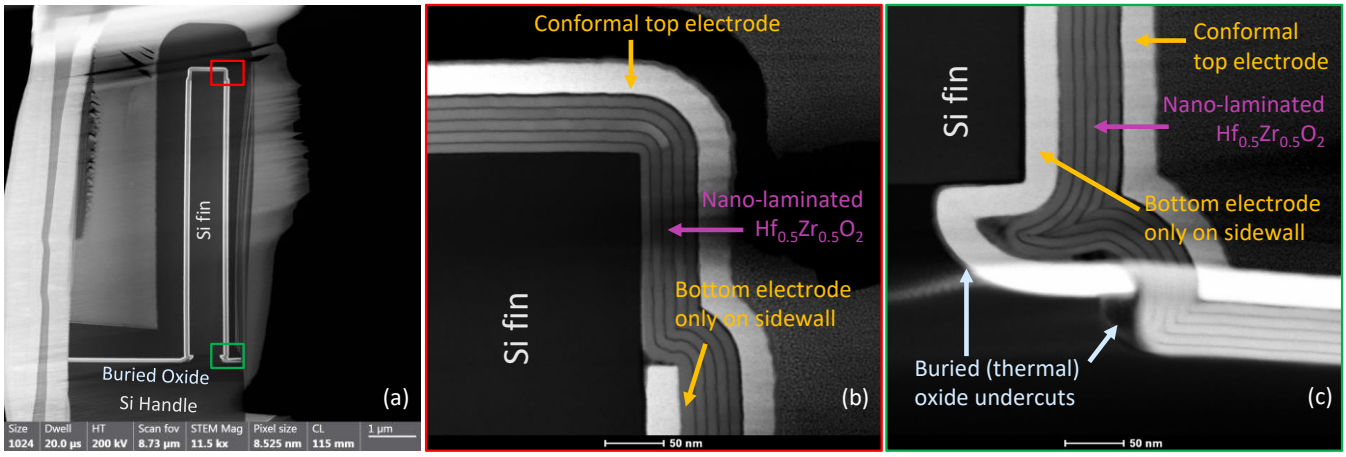

Figure 5: (a) HR-TEM image of ferroelectric-on-Si FinBAR cross-section, highlighting the high aspect ratio and perfectly straight fin sidewalls; Zoomed in HR-TEM images of (b) top and (c) bottom corners of FoS-FinBAR (red and green boxes in (a), respectively) highlighting mirror smooth sidewall, sidewall-only bottom electrode, and conformally deposited metal-ferroelectric-metal transducer stack.

oriented 6μm-thick SOI substrate is etched in 2.3% TMAH solution at 65°C, using SiO_2 hard mask. The heated wet-etching enables creation of high aspect-ratio (> 20:1) Si fins with perfectly vertical sidewalls defined by (111) plane, which acts as a etch stop (Fig. 4 (a)). Once the fins are patterned, a 30nm W layer is deposited using plasma-enhanced ALD. This is followed by blanket dry-etching to remove W everywhere except the sidewall of fins (Fig. 4 (b)). Next, the nano-laminated hafnia-zirconia film, constituting of five ~10nm $Hf_{0.5}Zr_{0.5}O_2$ layers interrupted with 1nm alumina (Al_2O_3) interlayers, is deposited using ALD, and followed by crystallization in polar orthorhombic phase by rapid thermal annealing (Fig. 4 (c)). The nano-lamination is essential to scale the thickness of sidewall transducer beyond the ~20nm limit at which the morphology is transformed to non-polar, and nonpiezoelectric, tetragonal phase [15]. Next, a 30nm W layer is deposited by ALD and three-dimensionally patterned by isotropic dry-etch in SF_6 to create the top electrodes / gates (Fig. 4 (d)). Finally, 250nm thick Pt/Cr layer is deposited using lift-off to create low-loss routing and pads.

Figure 5 shows cross-sectional high-resolution transmission electron microscopy (HR-TEM) images of FoS-FinBAR. Figure 5(a) shows the high-aspect ratio FoS-FinBAR cross-section with 6μm tall and 500nm wide fins with sidewall ferroelectric transducer. Figure 5(b) and 5(c) show successful patterning of bottom electrode, as shown at top and bottom corners of the fin, highlighting the presence of bottom electrode only on sidewalls. This is essential for reduction of static feedthrough that degrade FoS-FinBAR admittance. The conformal nature of HZO film and top W gate is also evident. This conformality is essential to create arrayed fin schemes for scaling transduction area and facilitate electrical measurement of the devices using planar pads.

CHARACTERIZATION OF FOS-FINBAR

The fabricated FoS-FinBARs are measured to evaluate the ferroelectric, and hence, piezoelectric, behavior of the sidewall HZO transducer and the RF admittance. The ferroelectric behavior is measured using Radiant PiezoMEMS tester. Figure 6 (a) shows the measured polarization hysteresis loop for the FoS-FinBAR, highlighting a large remanent polarization of 23.6 μC/cm^2 with coercive field of 2.52 MV/cm, indicating properly poled transducer. The admittance of FoS-FinBARs is extracted by measuring reflection response (S_{11}) of the one-port resonator using a Keysight N5222A Vector Network Analyzer. Figure 6 (b) shows measured admittance of two identical FoS-FinBARs randomly selected across the 100mm wafer, highlighting frequencies of 7.75 GHz and 7.78 GHz, with a sub-1% offset, Qs of 961 and 1032, and k_t^2 of 1.29% and 0.89%, respectively.

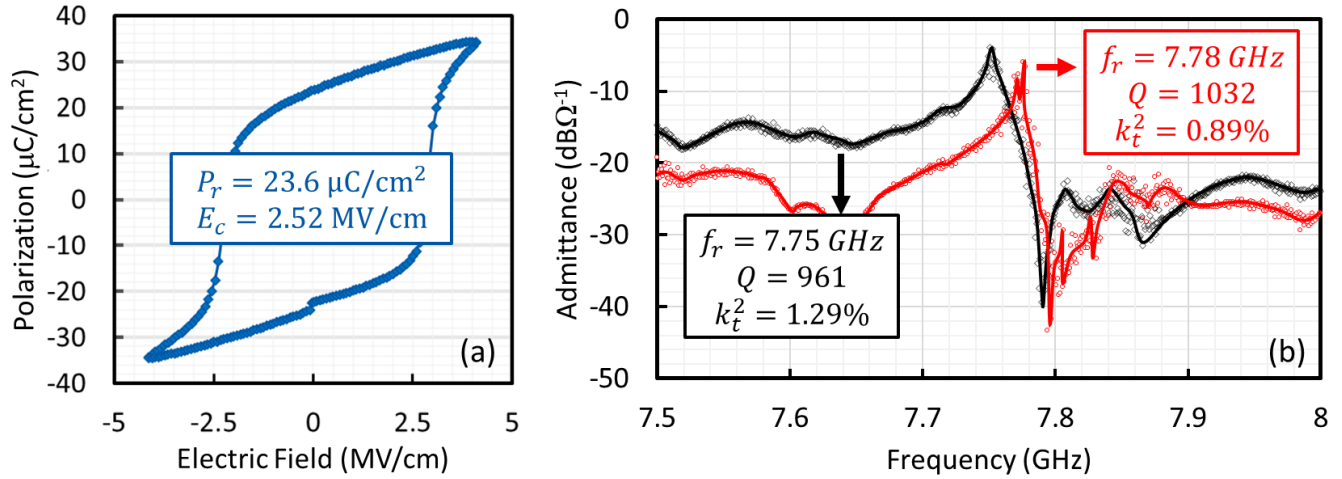

Figure 6: (a) Measured polarization-electric field hysteresis loop of FoS-FinBAR, highlighting the ferroelectricity and piezoelectricity of sidewall HZO transducer; (b) measured RF admittance of fabricated FoS-FinBARs operating at 7.75GHz and 7.78 GHz, with f.Q of 0.8×10^{13}.

CONCLUSION

This paper presents novel Ferroelectric-on-Si Fin Bulk Acoustic Resonators (FoS-FinBAR), based on the use of a novel fabrication process. The process enables creation of perfectly straight high aspect-ratio fins with mirror-smooth sidewalls, highly piezoelectric sidewall transducers based on atomic layer deposited ferroelectric hafnia-zirconia and tungsten electrodes, and three-dimensional patterning of electrodes and gates. FoS-FinBAR prototypes are presented at ~ 8 GHz with Qs as high as 1032 and k_t^2 as high as 1.3%, resulting in highest $f.Q$ product of 0.8×10^{13}. The extreme lithographical frequency scalability, CMOS-compatible materials and fabrication process, and high k_t^2 and Q, tailorable with fin width and transducer thickness, highlights the promise of FoS-FinBAR technology for realization of cm- and mm-wave integrated oscillators and filters for spread-spectrum wireless systems.

ACKNOWLEDGEMENTS

This project is supported by DARPA Young Faculty Award program. The authors would like to thank DARPA program manager Dr. Timothy Hancock for his support of this work. The authors would also like to thank the staffs at Nanoscale research facility at the University of Florida.

REFERENCES

[1] M. Matthaiou, O. Yurduseven, H. Q. Ngo, D. Morales-Jimenez, S. L. Cotton and V. F. Fusco, "The Road to 6G: Ten Physical Layer Challenges for Communications Engineers," in *IEEE Communications Magazine*, vol. 59, no. 1, pp. 64-69, January 2021, doi: 10.1109/MCOM.001.2000208.

[2] R. Aigner, G. Fattinger, M. Schaefer, K. Karnati, R. Rothemund and F. Dumont, "BAW Filters for 5G Bands," *2018 IEEE International Electron Devices Meeting (IEDM)*, San Francisco, CA, USA, 2018, pp. 14.5.1-14.5.4, doi: 10.1109/IEDM.2018.8614564.

[3] E. Iborra, M. Clement, J. Capilla, and V. Felmetsger, "Low-thickness high-quality aluminum nitride films for super high frequency solidly mounted resonators," *Thin Solid Films*, 520(7), 3060-3063, 2012.

[4] U. Zaghloul and G. Piazza, "Synthesis and characterization of 10 nm thick piezoelectric AlN films with high c-axis orientation for miniaturized nanoelectromechanical devices." *Applied Physics Letters* 104.25 (2014): 253101.

[5] Y. Yang, R. Lu, L. Gao, & S. Gong, "10–60-GHz Electromechanical Resonators Using Thin-Film Lithium Niobate". *IEEE Transactions on Microwave Theory and Techniques*, vol. 68, p. 5211-5220, 2020.

[6] M. Assylbekova, G. Chen, G. Michetti, M. Pirro, L. Colombo & M. Rinaldi, "11 GHz Lateral-Field-Excited Aluminum Nitride Cross-Sectional Lamé Mode Resonator," *In 2020 Joint Conference of the IEEE International Frequency Control Symposium and International Symposium on Applications of Ferroelectrics (IFCS-ISAF),* p. 1-4, IEEE,2020.

[7] M. Park, Z. Hao, D. G. Kim, A. Clark, R. Dargis and A. Ansari, "A 10 GHz Single-Crystalline Scandium-Doped Aluminum Nitride Lamb-Wave Resonator," *2019 20th International Conference on Solid-State Sensors, Actuators and Microsystems & Eurosensors XXXIII (TRANSDUCERS & EUROSENSORS XXXIII),* Berlin, Germany, 2019, pp. 450-453, doi: 10.1109/TRANSDUCERS.2019.8808374.

[8] M. Ghatge, V. Felmetsger and R. Tabrizian, "High $k_t^2.Q$ Waveguide-Based ScAlN-on-Si UHF and SHF Resonators," *2018 IEEE International Frequency Control Symposium (IFCS)*, 2018, pp. 1-4, doi: 10.1109/FCS.2018.8597447.

[9] S. Rassay, D. Mo, C. Li, N. Choudhary, C. Forgey and R. Tabrizian, "Intrinsically Switchable Ferroelectric Scandium Aluminum Nitride Lamb-Mode Resonators," in *IEEE Electron Device Letters*, vol. 42, no. 7, pp. 1065-1068, July 2021, doi: 10.1109/LED.2021.3078444.

[10] M. Ramezani, M. Ghatge and R. Tabrizian, "High-Q silicon fin bulk acoustic resonators for signal processing beyond the UHF," *2017 IEEE International Electron Devices Meeting (IEDM)*, 2017, pp. 40.1.1-40.1.4, doi: 10.1109/IEDM.2017.8268524.

[11] M. Ramezani, M. Ghatge and R. Tabrizian, "High $k_t^2.Q$ silicon Fin Bulk Acoustic Resonators (FinBAR) FOR chip-scale multi-band spectrum analysis," *2018 IEEE Micro Electro Mechanical Systems (MEMS)*, Belfast, UK, 2018, pp. 158-161, doi: 10.1109/MEMSYS.2018.8346508.

[12] M. Ramezani, M. Ghatge, V. Felmetsger and R. Tabrizian, "A Super-High-Frequency Non-Released Silicon Fin Bulk Acoustic Resonator," *2019 IEEE MTT-S International Microwave Symposium (IMS)*, Boston, MA, USA, 2019, pp. 516-519, doi: 10.1109/MWSYM.2019.8700907.

[13] F. Hakim, T. Tharpe and R. Tabrizian, "Ferroelectric-on-Si Super-High-Frequency Fin Bulk Acoustic Resonators With $Hf_{0.5}Zr_{0.5}O_2$ Nanolaminated Transducers," in *IEEE Microwave and Wireless Components Letters*, vol. 31, no. 6, pp. 701-704, June 2021, doi: 10.1109/LMWC.2021.3067509.

[14] W. P. Mason, *Physical Acoustics Principles and Methods, vol. 1A*. New York: Academic Press, 1964.

[15] S. Riedel, P. Polakowski, and J. Müller, "A thermally robust and thickness independent ferroelectric phase in laminated hafnium zirconium oxide," *AIP Advances*, vol. 6, pp. 095123, 2016.

CONTACT

*Faysal Hakim, tel: +1-352-745-9511; hakimfaysal@ufl.edu.

POWER HANDLING CHALLENGES OF HIGH K_T^2 ALSCN LAMB WAVE RESONATORS

Mingyo Park[1], Yue Zheng[1], and Azadeh Ansari[1]*
[1]Georgia Institute of Technology, Atlanta, Georgia, USA

ABSTRACT

This work reports on the first demonstration of a first-order symmetric (S_1) mode Lamb-wave resonator (LWR) based on sputtered $Al_{1-x}Sc_xN$ (x~%30), with a large electromechanical coupling coefficient (k_t^2) up to 13.7%, and frequencies in the range of 340 MHz up to 9.9 GHz. To fulfill the high-power requirements for today's radio frequency applications, we introduced a comprehensive study on the characterization of the resonator nonlinearity depending on device *Q*, and the power-handling capability based on different Sc/(Sc+Al) ratios and thermal conductivities. Additionally, we report the highest k_t^2 AlN-based LWRs of 13.7% and bode *Q* of 334 at 2.7GHz. This work shows the first study of 1-dB gain compression point vs. Sc/(Al+Sc).

KEYWORDS

Acoustic resonators/filters, Lamb-wave resonators, First-order symmetric (S_1) mode, Aluminum scandium nitride, Electromechanical coupling coefficient, Power handling capability, 1-dB gain compression point, Duffing nonlinearity, Thermal conductivity.

INTRODUCTION

Multiple passbands radio frequency (RF) filters meet the needs of miniaturization and integration for fifth-generation new radio (5G NR) communications. Lamb-wave resonators (LWRs) are widely studied for implementation in RF front-end modules. Compared to film bulk acoustic resonators (FBARs), LWRs offer single-chip, multi-frequency, multi-band solutions with flexibility over the interdigitated transducer pitch/geometry defined by lithography [1], [2]. Compared to Rayleigh surface acoustic wave (SAW) resonators, LWRs enable higher frequencies and larger quality factor (*Q*) and electromechanical couplings (k_t^2) by taking advantage of high overtone modes (i.e., A_1 and S_1), and higher phase velocities with better acoustic wave confinement in the piezoelectric-layer [3]–[6]. Aluminum Scandium Nitride ($Al_{1-x}Sc_xN$) has been popular in the acoustic community in recent years [7]–[9], showing enhanced piezoelectricity to compensate for pure AlN's moderate k_t^2, an essential metric for acoustic devices to determine the filter's fractional bandwidth. In addition to *Q*, the insertion loss, and bandwidth, wireless communication devices call for high-performance filters that offer enhanced power-handling capability and less intermodulation distortion for filter band/channel selection [8]-[9].

Emerging RF power requirements have increased the overall system heating. In order to maintain device reliability and performance, filters must be able to handle high power levels and efficiently dissipate the additional heat. Several factors limit the power-handling ability of RF filters, including self-heating, which leads to thermal breakdown, and device nonlinearities that affect the filter transfer response. Given the high-power operation requirements in 5G, the high-temperature study of acoustic resonators is critical due to the self-heating of the device under high power operation [12]. Our group has previously studied the thermal conductivity (TC) of AlN and AlScN films [13] and reported that AlScN shows significantly lower TC than pure AlN, which can lead to severe self-heating [12], [13]. The lower TC challenges the power handling of the device, showing a tradeoff of k_t^2. Therefore, characterizing the power-handling of AlScN-based resonators needs to be studied for high-power RF applications.

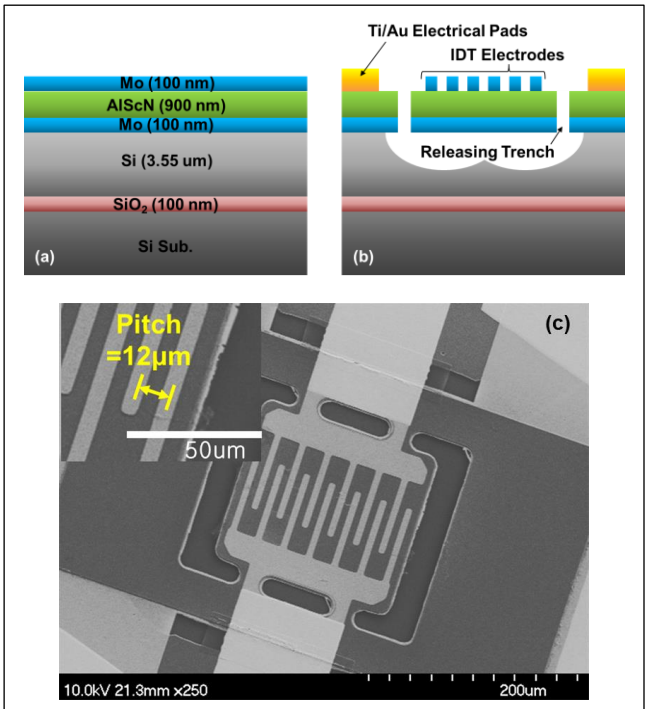

Figure 1: Cross-sectional schematic of (a) initial sample with the sputtered deposited Mo(100 nm)/AlScN(900 nm)/Mo(100 nm) on SOI substrate and (b) fabricated LWR released from the front side with isotropic etching of the 3.55 um-thick Si device layer. (c) SEM image of AlScN LWR with 12 um IDT pitches.

In this work, we report on the first demonstration of first-order symmetric (S1) LWR based on $Al_{0.7}Sc_{0.3}N$, with high phase velocities and large k_t^2 [3], presenting frequencies as high as 9.9GHz and k_t^2 values up to 13.7%. We take advantage of the enhanced k_t^2 by using 30% Sc/(Al+Sc) ratio in AlScN films, as well as utilizing a bottom electrode (BE) as the ground electrode. Here, we report the highest k_t^2 AlN-based LWRs of 13.7% and bode *Q* [5] of 334 at 2.7GHz. The resonator nonlinearity is evaluated based on the *Q* of the device under driving power levels in terms of peak frequency shift. The power-handling capability is analyzed based on different Sc/(Sc+Al) ratios and TC values, showing a reduction of P1dB at higher Sc/(Al+Sc) ratios. This work is the first study of P1dB vs. Sc/(Al+Sc).

FABRICATION PROCESS

LWRs with the resonant stack of molybdenum (Mo)/$Al_{0.7}Sc_{0.3}N$/Mo and thicknesses of 100 nm/900 nm/100 nm, respectively, are sputter-deposited on a silicon-on-insulator (SOI) substrate at VTT Technical Research Centre of Finland. Figure 1 shows a cross-sectional schematic of (a) the initial sample wafer stack and (b) fabricated LWR. The fabrication process is started by

978-1-940470-04-7/HH2022/$25©2022TRF
DOI 10.31438/trf.hh2022.13

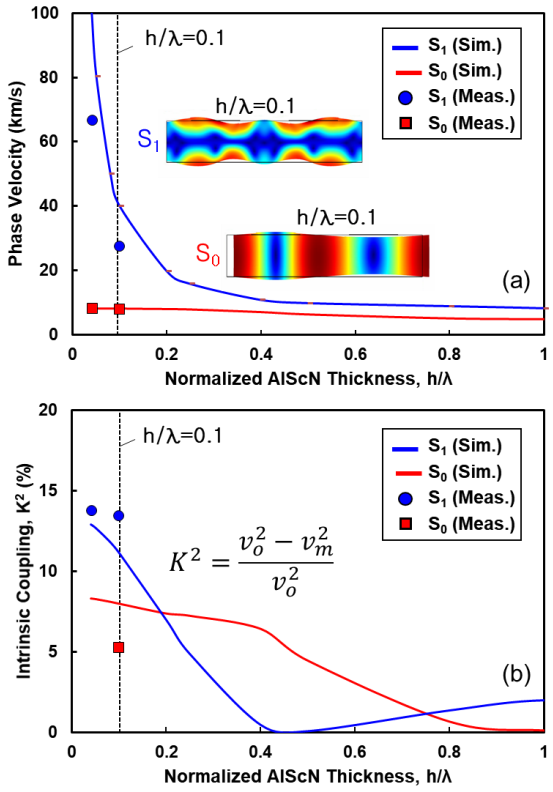

Figure 2: (a) Phase velocity and (b) Intrinsic coupling (K^2) of FEA simulation and measured data points of LWR S0, and S1 modes based on normalized $Al_{0.7}Sc_{0.3}N$ thickness (h/λ), along with mode shapes at h/λ=0.1 without electrode.

etching down the top Mo layer with reactive ion etching (RIE) under SF_6-based chemistry to pattern interdigital transducer (IDT) electrodes. The $Al_{0.7}Sc_{0.3}N$ piezoelectric layer is etched via an inductively coupled plasma (ICP) ion-etching tool with chlorine-based chemistry. The device is released from the Si device layer by being exposed to xenon difluoride (XeF2) Si etcher through releasing trenches. Figure 1 (c) illustrates the scanning electron microscope (SEM) image of the fabricated 12µm-pitched LWR released from the front side.

$AL_{0.7}SC_{0.3}N$ LAMB WAVE RESONATORS DESIGN

Resonator Electromechanical Characterization

Figure 2 is simulated with finite element analysis (FEA) using the evaluated piezoelectric coefficient and elastic constants, including Sc/(Al+Sc) ratio of 30% [7] to characterize dispersion curves of two different symmetric modes (S_0 and S_1). Figure 2 illustrates the simulated phase velocity and intrinsic coupling (K^2) of S_0 and S_1 LWR with BE based on normalized $Al_{0.7}Sc_{0.3}N$ thickness (h/λ), plotted with measured data points. Figure 2(a) describes the excited two resonance modes along with the displacement mode shape at h/λ=1, showing the symmetric deformation shape in the piezoelectric layer.

The K^2 is calculated based on the phase velocity of the electrically free piezo-layer surface (v_o) and the shorted surface (v_m). As shown in Figure 2, the higher-order LW mode shows better K^2 and much higher phase velocities, particularly when the film thickness is thin relative to wavelength (h/λ<0.4).

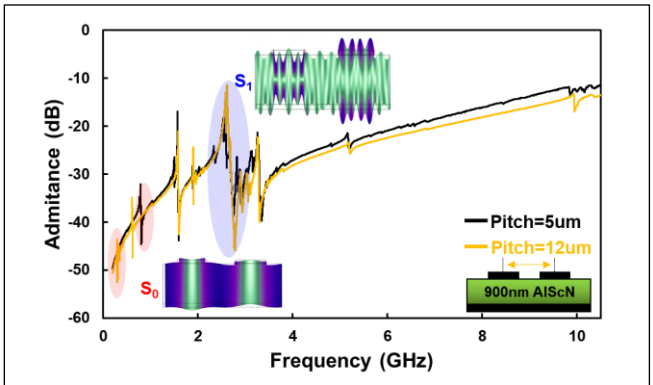

Figure 3: Measured admittance frequency response with the frequency range from 0.2 to 10.5 GHz of 5 um and 12 um-pitched $Al_{0.7}Sc_{0.3}N$ LWR showing multi-resonance modes along with the mode shapes including 100 nm-thick top and bottom Mo electrodes.

Table 1: Device performance of S_0 and S_1 modes at h/λ=0.1 and 0.04.

h/λ	Mode	f_r (GHz)	k_t^2 (%)	Q_{bode}	Phase (km/s)
0.1	S0	0.79	5.2	104	7.9
0.1	S1	2.59	13.4	274	27.4
0.04	S0	0.34	2.12	189	8.3
0.04	S1	2.62	13.7	334	66.8

Experimental Frequency Response and Resonant Mode Characteristic of Lamb Wave Resonators

The proposed LWRs are measured in an RF probe station, and resonance characteristic curves are tested by an Agilent N5224B Network Analyzer after performing a short-open-load-through (SOLT) calibration. Figure 3 demonstrates the measured wideband admittance frequency response of 5 µm and 12 µm-pitched devices with a frequency ranging from 0.2 to 10.5 GHz.

In the wideband frequency response, LWR shows a multi-resonant frequency response with various modes, including undesired spurious modes. The difference in resonance frequency is observed from the S_0 mode between 5 µm and 12 µm-pitched devices due to different wavelengths (λ) followed by the definition of resonance frequency (f=v/λ) [14]. On the other hand, similar resonance frequencies are observed from S_1 mode between 5 µm and 12 µm-pitched devices. Since the phase velocity of the S_1 LW mode is more dispersive than the S_0 mode, a larger phase velocity below h/λ<0.4 compensates decrease in frequency caused by a larger wavelength. The highest measured phase velocity of S_1 mode is 66800m/s, more than 8 times larger than the phase velocity of S_0 mode at h/λ=0.04.

The electromechanical coupling coefficient (k_t^2) is defined by the following equation [14], [15]:

$$k_t^2 = \frac{\pi^2}{4} \times \frac{f_s(f_p - f_s)}{f_p^2} \quad (1)$$

Where f_s is the series and f_p is the parallel resonant frequency determined from the measured admittance (Y_{11})-parameter of the device. The Q of LWR is analyzed by bode Q based on the measured phase group delay of the S-parameter [7]. Table I summarizes the evaluated device performance of S_0 and S_1 LWR in $Al_{0.7}Sc_{0.3}N$ films. The highest k_t^2 of 13.7% and bode Q of 334 can be achieved at the resonant frequency of 2.7 GHz, yielding a $Q \times k_t^2$ figure of merit

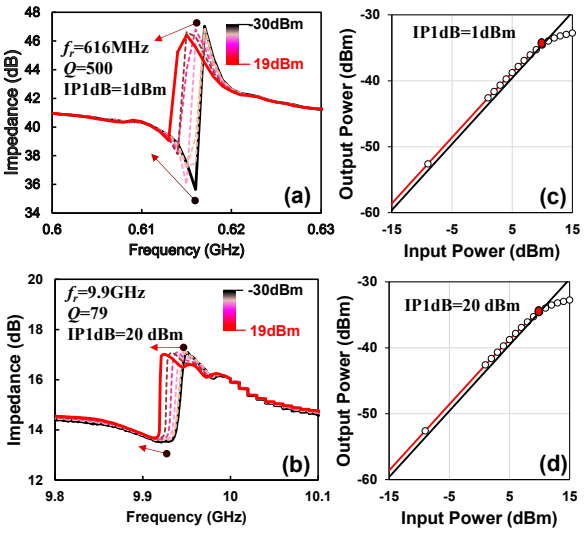

Figure 4: Measured impedance with the power sweep range from -30 to 19dBm on resonance mode with (a) Q of 500 including (c) measured P1dB=1dBm and (b) Q of 79 including (d) measured input P1dB=20dBm, showing duffing nonlinearity at high power.

(FoM) of 45.7. Such a result is 9 times larger than FoM of 5.4 in S_0 LWR at the resonant frequency of 790 MHz. Thus, elaborating higher-order LW modes can lead to a higher frequency filter solution without compromising other key performance parameters.

DEVICE POWER CHARACTERISTICS AND EXPERIMENTAL RESULTS

Device Nonlinearity based on the Quality Factor

Figure 4 demonstrates the power measurement of the $Al_{0.3}Sc_{0.7}N$ LW device. Figure 4 (a)-(b) show the measured impedance (Z-parameter) of two resonance modes at the resonance frequency of 616 MHz and 9.9 GHz by a sweeping power range of -30 dBm to 19 dBm. Duffing nonlinearity is commonly observed when the input signal of sufficiently high power gives rise to access to the nonlinear regime. The devices and materials exhibit various stiffness phases to exploit their chaotic motion in nonlinear systems showing the softening or hardening effect in the mode [16]. As increase the input power, Duffing effect induces a resonant frequency shift due to softening effect in mode, as presented in Figure 4 (a)-(b).

Furthermore, in order to characterize device power handling capability, gain compression point (P1dB) is measured as shown in Figure 4 (c)-(d). The standard setup for P1dB testing involves 2-port terminals, and each port is connected to a signal generator as the input and a spectrum analyzer as the output. The signal generator frequency is adjusted to the targetted resonance frequency, and the output power is swept to explore the 1-dB compression point.

Figure 4 shows the characterization of the resonator nonlinearity depending on device Q. Compared to the low Q (=79) resonance mode with input P1dB of 20 dBm, a relatively poor power-handling of 1 dBm is observed in the high Q (=500) resonance mode showing more intense Duffing nonlinearity as power increases. Such results prove that power handling capability is challenged in high Q devices because of device nonlinearity.

Impact of Thermal conductivity on Power Handling Capability

Recent study [17] report on the correlation between $Al_{1-x}Sc_xN$ thermal conductivity and (1) x% in $Al_{1-x}Sc_xN$, and (2) $Al_{1-x}Sc_xN$ thickness to analyze overheating of piezoelectric film which limits power handling capability of the device. Figure 5 (a) [13] describes measured thermal conductivity with a fitted curve based on Sc concentration, presenting a decreasing trend in thermal conductivity with increasing Sc. For example, the 400 nm-thick pure AlN provides a 30 times decreased thermal conductivity than 400 nm-thick $Al_{0.74}Sc_{0.26}N$ [13]. In terms of thermal conductivity values depending on film thickness, a higher thermal conductivity value is observed in thicker $Al_{1-x}Sc_xN$ films [17].

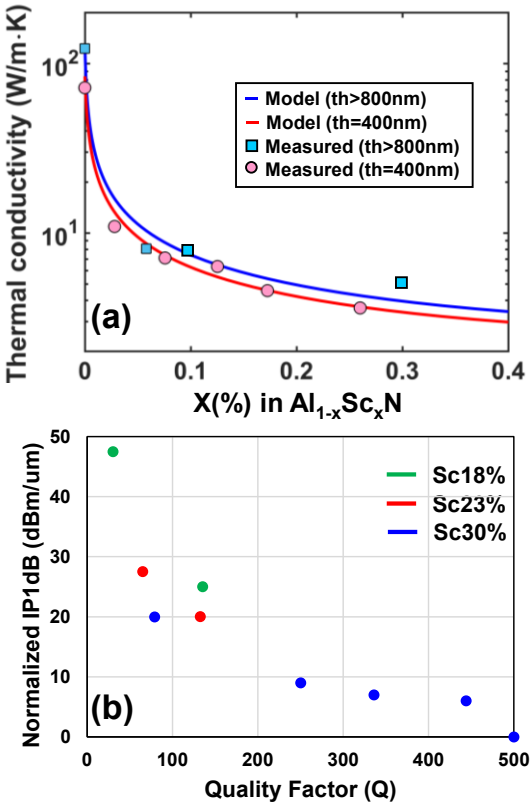

Figure 5: (a) Measured and fitted thermal conductivity curve based on x= Sc/(Al+Sc) for $Al_{1-x}Sc_xN$ thickness (th) of th=400nm and th>800 nm films. (b) Measured normalized input power 1dB compression point (IP1dB) based on Q of $Al_{1-x}Sc_xN$ device with x=18, 23, 30%.

Based on this behavior, this work analyzes the power handling capability is analyzed based on different Sc/(Sc+Al) ratios and their corresponding thermal conductivity values. Figure 5 (b) shows the measured input power P1dB based on Q and Sc/(Al+Sc) ratio. Input P1dB is normalized by AlScN thickness considering the effects of power handling on film thickness [18], [19]. LW devices based on $Al_{1-x}Sc_xN$ film with various x=18, 23, 30% are measured and evaluated in compliance with the effects of the Q of each device. Normalized input P1dB shows a decreasing trend as Q increases caused by device nonlinearity due to high Q.

Moreover, input P1dB presents a decreasing trend as Sc/(Al+Sc) increases due to low thermal conductivity in accordance with high x in $Al_{1-x}Sc_xN$ film. Table 2 summarizes the previous LWRs and this work. To the best of the authors' knowledge, this work shows the highest k_t^2 (=13.7 %) of any AlN-based S_1 mode LWR reported up to date.

Table 2: Comparison table of LWR device metrics of previous work and our work.

	$\frac{Sc}{Sc+Al}$ (%)	M*	f_r (GHz)	k_t^2 (%)	Q	IP1dB (dBm)
[10]	0	S_0	1.5	NA	1500	25
[10]	0	S_1	0.2	1.4	1225	20
[4]	0	S_0	3.5	3.59	550	NA
[3]	0	S_1	1.38	0.71	2181	NA
[9]	32	S_0	0.04	10.2	700	NA
This Work	30	S_1	2.6	13.7	334	5.5

M : Mode*

CONCLUSION

High power handling is a crucial requirement for today's RF filter and duplexer applications. Lamb-wave resonator with higher-order modes is one of the alternative technologies to offer solutions to a growing high power market, providing single-chip, high resonant frequency, and multi-frequency RF modules without degrading the filter's FoM.

In this work, we presented a comprehensive study on the characterization of the power-handling of AlScN-based resonators for high-power RF applications. The resonator nonlinearity is evaluated based on Q, and the power-handling capability is analyzed based on different Sc/(Sc+Al) ratios and TC values, showing a decrease of P1dB at higher Sc/(Al+Sc) ratios. We report on the first demonstration of first-order symmetric (S1) LWR based on $Al_{0.7}Sc_{0.3}N$, with high phase velocities of 66800m/s and large k_t^2 up to 13.7%, presenting frequencies as high as 9.9GHz. To the best of the authors' knowledge, we report the highest k_t^2 AlN-based LWRs of 13.7% and bode Q of 334 at 2.7GHz. Furthermore, this work is the first study of P1dB vs. Sc/(Al+Sc).

ACKNOWLEDGEMENTS

The authors would like to acknowledge the VTT Technical Research Centre of Finland for providing the wafer.

REFERENCES

[1] H. Campanella, Y. Qian, C. O. Romero, J. S. Wong, J. Giner, and R. Kumar, "Monolithic Multiband MEMS RF Front-End Module for 5G Mobile," J. Microelectromechanical Syst., vol. 30, no. 1, pp. 72–80, 2021, doi: 10.1109/JMEMS.2020.3036379.

[2] M. Park, J. Wang, R. Dargis, A. Clark, and A. Ansari, "Super High-Frequency Scandium Aluminum Nitride Crystalline Film Bulk Acoustic Resonators," in 2019 IEEE International Ultrasonics Symposium (IUS), Oct. 2019, pp. 1689–1692, doi: 10.1109/ULTSYM.2019.8925598.

[3] J. Zou et al., "Spectrum-clean S1 AlN Lamb wave resonator with damped edge reflectors Spectrum-clean S1 AlN Lamb wave resonator with damped edge reflectors," Appl. Phys. Lett., vol. 116, no. 2, Dec. 2019, doi: 10.1063/1.5128961.

[4] A. Gao, J. Zou, and S. Gong, "A 3.5 GHz AlN S1 lamb mode resonator," 2017 IEEE International Ultrasonics Symposium (IUS), Sep. 2017, doi: 10.1109/ULTSYM.2017.8092161.

[5] A. Kourani, Y. Yang, and S. Gong, "A Ku-Band Oscillator Utilizing Overtone Lithium Niobate RF-MEMS Resonator for 5G," IEEE Microw. Wirel. Components Lett., vol. 30, no. 7, pp. 681–684, Jul. 2020, doi: 10.1109/LMWC.2020.2996961.

[6] J. Zou, C. M. Lin, Y. Y. Chen, and A. P. Pisano, "High-frequency and low-resonance-impedance lamb wave resonators utilizing the S1 mode," 2015 Transducers - 2015 18th Int. Conf. Solid-State Sensors, Actuators Microsystems, TRANSDUCERS, pp. 2025–2028, Jun. 2015, doi: 10.1109/TRANSDUCERS.2015.7181353.

[7] M. Park, Z. Hao, R. Dargis, A. Clark, and A. Ansari, "Epitaxial Aluminum Scandium Nitride Super High Frequency Acoustic Resonators," J. Microelectromechanical Syst., vol. 29, no. 4, pp. 490–498, Aug. 2020, doi: 10.1109/JMEMS.2020.3001233.

[8] M. Park, J. Wang, and A. Ansari, "High-Overtone Thin Film Ferroelectric AlScN-on-Silicon Composite Resonators," IEEE Electron Device Lett., vol. 42, no. 6, pp. 911–914, 2021, doi: 10.1109/LED.2021.3070274.

[9] G. Esteves et al., "Al0.68Sc0.32N Lamb wave resonators with electromechanical coupling coefficients near 10.28%," Appl. Phys. Lett., vol. 118, no. 17, pp. 0–5, 2021, doi: 10.1063/5.0047647.

[10] H. Campanella, M. Narducci, N. Wang, J. Bo, and W. Soon, "RF-Designed High-Power Lamb-Wave Aluminum – Nitride Resonators," IEEE Transaction on Microwave Theor and Techniques, vol. 63, no. 2, pp. 331–339, Feb. 2015.

[11] H. Campanella, L. Khine, and J. M. Tsai, "Aluminum nitride lamb-wave resonators for high-power high-frequency applications," IEEE Electron Device Lett., vol. 34, no. 2, pp. 316–318, 2013, doi: 10.1109/LED.2012.2230609.

[12] C. Yuan at al., "Phonon heat conduction in Al 1-x Sc x N thin films," in Materials Today Physics, vol. 21, 200498, pp. 1–19, 2021.

[13] Y. Zheng, M. Park, A. Ansari, C. Yuan, and S. Graham, "Self-Heating and Quality Factor: Thermal Challenges in Aluminum Scandium Nitride Bulk Acoustic Wave Resonators," 21st Int. Conf. Solid-State Sensors, Actuators Microsystems, TRANSDUCERS 2021, pp. 321–324, Jun. 2021, doi: 10.1109/Transducers50396.2021.9495613.

[14] M. Park, Z. Hao, D. G. Kim, A. Clark, R. Dargis, and A. Ansari, "A 10 GHz Single Crystalline Sc-AlN Lamb-wave Resonator," 2019 20th International Conference on Solid-State Sensors, Actuators and Microsystems & Eurosensors XXXIII, Jun. 2019, doi: 10.1109/TRANSDUCERS.2019.8808374.

[15] M. Park and A. Ansari, "Epitaxial Al0.77Sc0.23N SAW and Lamb Wave Resonators," in IFCS-ISAF 2020 - Joint Conference of the IEEE International Frequency Control Symposium and IEEE International Symposium on Applications of Ferroelectrics, Jul. 2020, doi: 10.1109/IFCS-ISAF41089.2020.9234850.

[16] R. Lu and S. Gong, "Study of thermal nonlinearity in lithium niobate-based MEMS resonators," 2015 Transducers - 2015 18th Int. Conf. Solid-State Sensors, Actuators Microsystems, TRANSDUCERS 2015, pp. 1993–1996, 2015, doi: 10.1109/TRANSDUCERS.2015.7181345.

[17] Y. Song et al., "Thermal Conductivity of Aluminum Scandium Nitride for 5G Mobile Applications and beyond," ACS Appl. Mater. Interfaces, vol. 13, no. 16, pp. 19031–19041, 2021, doi: 10.1021/acsami.1c02912.

[18] N. Klein et al., "Microwave properties of MgB2 thin films," IEEE Trans. Appl. Supercond., vol. 13, no. 2, pp. 3253–3256, 2003, doi: 10.1109/TASC.2003.812214.

[19] A. Leon et al., "RF power-handling performance for direct actuation of germanium telluride switches," IEEE Trans. Microw. Theory Tech., vol. 68, no. 1, pp. 60–73, 2020, doi: 10.1109/TMTT.2019.2946145.

CONTACT

*M. Park; m.park@gatech.edu

MANUFACTURING NEXT-GENERATION MICROELECTRONICS

Carl E. McCants
Defense Advanced Research Projects Agency (DARPA), Arlington, Virginia, USA

ABSTRACT

At the 2021 DARPA Electronics Resurgence Initiative (ERI) Summit and MTO (Microsystems Technology Office) Symposium, plans for the next iteration, named ERI 2.0, were discussed. One of the areas DARPA is planning to pursue is manufacturing complex 3D microsystems. The R&D needed for advanced microelectronics manufacturing would include the design, assembly, testing, and digital emulation of 3DHI (3-Dimensional Heterogeneous Integration) microsystems, with an emphasis on: a) Multi-chip, multi-technology assembly and packaging; b) Tools for design, simulation, and test; c) Security; d) 3DHI interconnects; and e) Thermal management and power delivery. This paper will discuss challenges related to manufacturing complex 3D microsystems.

KEYWORDS

3DHI, advanced microelectronics, multi-chip packaging.

INTRODUCTION

ERI History

ERI had its genesis 5 years ago with the recognition that continued US leadership in microelectronics was threatened in both the defense sector and commercial industry. In January 2017, the President's Council of Advisors on Science and Technology, or PCAST, issued a report titled "Ensuring Long-Term U.S. Leadership in Semiconductors". The report stated the following: 1) U.S. semiconductor innovation, competitiveness, and integrity face major challenges; 2) A concerted push by China to reshape the market in its favor, using industrial policies backed by over one hundred billion dollars in government-directed funds threatens the competitiveness of U.S. industry and the national and global benefits it brings; and 3) The United States will only succeed in mitigating the dangers posed by Chinese industrial policy if it innovates faster.[1] Out of this came four major factors (Figure 1):

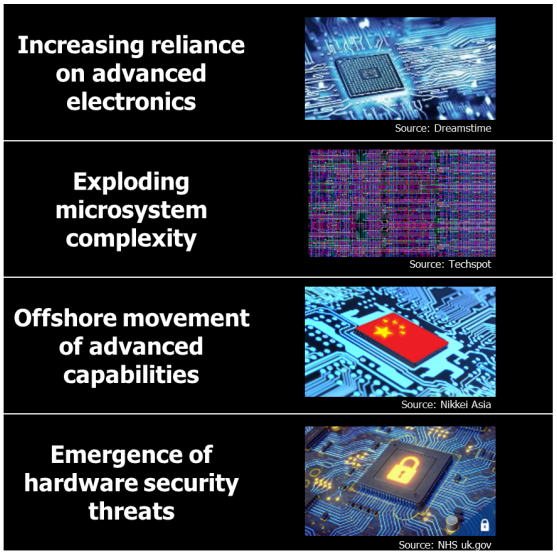

1. The increased reliance on and strategic importance of advanced electronics for national security and economic competitiveness. Microelectronic components are found in everything from toasters to televisions, mobile platforms to automobiles, but also aircraft to satellites.
2. The exploding complexity of microsystems that we see in state-of-the-art CPUs, GPUs, FPGAs, and other System-on-chip/System-in-package configurations.
3. The offshore movement of advanced manufacturing capabilities.
4. The recognition and emergence of hardware security threats that can impact the confidentiality, integrity, and reliability of microelectronics used in both consumer and defense applications.

From these four factors, six focus areas were proposed as seen in Figure 2:

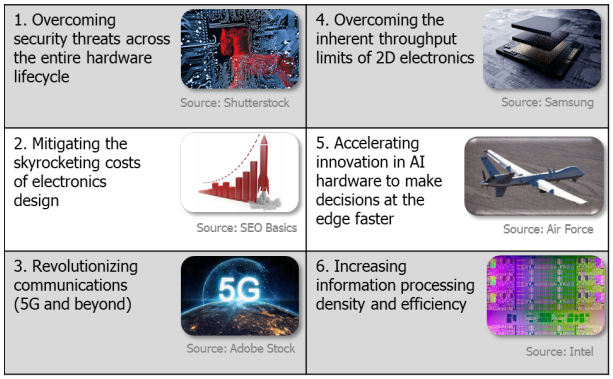

- Overcoming security threats across the entire hardware lifecycle
- Mitigating the skyrocketing costs of electronic design
- Revolutionizing communications (5G and beyond)
- Overcoming the inherent throughput limits of 2D electronics
- Accelerating innovation in AI hardware to make decisions at the edge faster
- Increasing information processing density and efficiency

ERI Present

In looking back at where we were in 2017 and where we are today, those factors appear even stronger than they did when ERI was initiated, with new trends emerging, and consensus need for action to address some of these trends, which include:

- Enormous off-shore investments in commercial electronics by near-peer allies and adversaries have only grown since the start of ERI, particularly as manifested by the consolidation of leading-edge silicon manufacturing and an increasing footprint into state-of-the-art packaging by pure-play foundries[2]

Copyright retained by Authors

- Microelectronics supply chain integrity concerns, spurred by the disruptions due to COVID-19 and the global nature of the supply network[3]
- The formation of multinational alliances for 3DHI R&D and manufacturing[4]

The result is that ERI will continue to strategically invest and seed new approaches and technologies to maintain the U.S. position in electronic systems. In addition, recognition of the importance of microelectronics technologies has been increasing dramatically within the DoD and other government agencies. Finally, substantial investment in microelectronics has been identified as a key priority within not only the DoD, but across the whole of government. [5]

ERI Highlights

Since its inception, ERI has increased participation of non-traditional partners from commercial industry in DARPA programs. ERI has fostered collaborative projects involving 6 of the top 10 semiconductor sales leaders. In addition, ERI has fostered collaborative projects involving all 5 top defense contractors and all of the top 10 research universities per US News & World Report rankings. More importantly, dialogue has increased with many of these entities, although we are still striving to increase the base of those participating in our funded research (Figure 3).

Research successes in ERI over the past year include processor architectures that are >100X faster than standard CPU/GPUs (HIVE); development of programmable hardware architectures to increase processing efficiency (SDH); integration of machine learning into tools for end-to-end electronics design (IDEA); data privacy research to process information while it remains encrypted such that data is protected (DPRIVE); FETT Bug Bounty, DARPA's first crowdsourced leveraging of "white hat" hackers (SSITH); Integration of an FPGA core with a photonic transceiver in a multi-chip module (PIPES); early demonstrations of 22nm FinFETs for specific Defense Industrial Base (DIB) applications (Domestic Foundries); and provided open licensing with commercial technology vendors to DARPA researchers (DARPA Toolbox). In addition, over the past year, we have created several new ERI programs in computing, algorithms, filters, and heterogeneous integration.

MANUFACTURING COMPLEX MICROSYSTEMS

ERI Future Plans

With the benefit of hindsight, ERI has demonstrated that it is possible to engage the academic, commercial, and US Government microelectronics communities in relevant, cutting-edge, dual-use research projects. It is also possible to provide leap-ahead capabilities in computational efficiency, heterogeneous integration, hardware security, electronics design, AI components, and secure communications through these collaborations that benefit both the USG and private sector. However, maintaining technical advantage will require continuous innovation, and maintaining US supremacy in semiconductor technologies over the long-term will demand national investment in disruptive technologies. A fundamental assumption that informed the direction of ERI 2.0 is that future microelectronics innovation will not be driven by transistor scaling but will instead be tied to the ability to design, fabricate, and test and model the performance of complex 3D assemblies composed of heterogeneous microelectronic technologies. [6-9] In that context, lab-to-fab capability also represents an opportunity and the potential to accelerate and re-shore future manufacturing.

Taking all this into account, in ERI 2.0, DARPA MTO will continue innovating the next generation of microelectronics through the initial six areas and add two new areas. The first area is R&D for advanced manufacturing. This includes the design, assembly, testing, and digital emulation of 3DHI microsystems, with an emphasis on the following:

- Multi-chip, multi-technology assembly and packaging
- Tools for design, simulation, and test
- Security
- 3DHI interconnects
- Thermal management and power delivery

The first area also includes developing electronics for harsh environments – radiation, high temperature, high voltage or current, and low temperature.

The second area is next-generation microelectronics prototyping. The primary objective is to create a national capability for 3DHI by establishing a public-private partnership, or PPP, for research services and low-volume production. An additional objective is to emphasize design innovations and enhance the use of manufacturing automation in the package, assembly, and testing process. The expectation is that this will:

- Reduce cycle-time for R&D and pilot manufacturing for 3D electronics assembly
- Ensure a more secure supply chain with a domestic facility and capabilities driven by future industry needs
- Provide technology for advanced packaging and assembly, with the potential for significant cost reduction in microsystems

Advanced 3DHI R&D Challenges

Knowing the right question to ask, creating a viable path to transition, and focusing on manufacture – these lessons form a virtuous loop, in which manufacturing challenges help inform the next set of questions to go answer. Knowing the right question to ask is central to DARPA's ability to do its job well. Some examples we are thinking about at DARPA MTO now include:

- Will advanced interfaces (die-to-die, wafer-to-wafer, die-to-wafer, and so forth) obviate conventional fabrication and packaging?
- Would assembly approaches allow complex systems to be disaggregated into more basic primitives?
- How will dense 3DHI assemblies be designed and tested?
- Will new manufacturing technologies, like fine-scale printing and additive manufacturing, enable precisely aligned lateral interconnects and through-substrate-vias?

- How can the electronics within advanced 3D assemblies and packages be powered… and how can they be cooled?
- Are there new materials and thermal strategies to extend temperature operation range for 3D assemblies?
- How will multi-domain, integrated EDA tools for 3DHI be achieved?
- How can complete digital models of 3DHI systems be developed and validated?

This initial set of questions has led to the development of the following focus areas for 3DHI manufacturing:

- Multi-chip, multi-technology assembly / packaging
  - Compatible die-to-die, wafer-to-wafer, die-to-wafer, and wafer-to-board processes
  - Desktop assembly
- 3DHI interconnects
  - Precisely aligned lateral interconnects through fine-scale printing and additive manufacture
  - Post-commercial-3DHI TSVs (through-substrate-via)
- Thermal and power
  - Embedded thermal management within assembly and package
  - Materials to extend temperature operation range
  - Low-loss passives for power distribution
  - Efficient power conversion in assembly / package
- Tools for design, simulation, and test
  - 3DHI metrology
  - Multi-domain, integrated EDA tools for 3DHI
  - Validation of complete digital models
- "MOSIS-like" 3DHI prototyping services
  - Baseline 3DHI fabrication processes
  - 3DHI multi-project and taxi run demos with ADK (assembly design kit)

Creating a viable transition path for these new technologies will be another central focus of ERI 2.0. In a world in which domestic production accounts for only 12% of chip manufacturing and just 3% of packaging, how do we create ways in which innovation can be developed and leveraged for commercial and defense applications? DARPA ERI 2.0 will address the question "How do we build a sustainable path for innovation to move from the laboratory to industry?"

As part of the manufacturing thrust, we will continue towards the goal of getting advanced technologies prototyped and into the hands of transition partners and users. This includes continuing to develop the microelectronics technologies in ERI and all of the MTO thrusts areas. We will also be working with our government partners, industry, and academia to determine if a public private partnership in advanced microelectronics manufacturing and heterogeneous integration is something we can make a reality over the next year.

ACKNOWLEDGEMENTS

The author would like to thank Justin Hodiak, Arnett Brown, Sharon Woodruff, and Rebecca Dietz for their input and review of this manuscript.

REFERENCES

[1] President's Council of Advisors on Science and Technology, "Ensuring Long-Term Leadership in Semiconductors", 2017, pp. 4 - 11.

[2] https://www.semiconductors.org/taking-stock-of-chinas-semiconductor-industry/

[3] https://www.whitehouse.gov/briefing-room/statements-releases/2021/04/12/readout-of-white-house-ceo-summit-on-semiconductor-and-supply-chain-resilience/.

[4] https://asia.nikkei.com/Business/Tech/Semiconductors/TSMC-s-Japan-project-attracts-over-20-participant-companies

[5] https://www.commerce.gov/news/press-releases/2022/04/analysis-chips-act-and-bia-briefing

[6] https://www.raytheon.com/sites/default/files/technology-today/2019/issue2/wp-content/uploads/2019/05/Raytheon_TechnologyToday_Issue2_2019.pdf, p12.

[7] Chuanqian Shi, Zhanan Zou, Zepeng Lei, Pengcheng Zhu, Wei Zhang, and Jianliang Xiao, "Heterogeneous integration of rigid, soft, and liquid materials for self-healable, recyclable, and reconfigurable wearable electronics", *Science Advances*, 6, 94 (2020).

[8] Julian Ho and Jessie Shen, "Intel, TSMC gearing up for heterogeneous 3D IC integration", *Digitimes*, 18 June 2020.

[9] Ravi Mahajan, "The Case for Heterogeneous Integration", *EE Times*, 24 August 2018.

CONTACT

*Carl E. McCants, tel: +1-703-526-2808; carl.mccants@darpa.mil

A MEMS MICROVALVE FOR THE SPACECRAFT ATMOSPHERE MONITOR (SAM) INSTRUMENT

Cecile Jung-Kubiak, Risaku Toda, Abhijit Shevade, M. Bulut Coskun, Sofia Rahiminejad, Matthew Dickie, Clifford Frez, John Gill, and Mina Rais-Zadeh***
Jet Propulsion Laboratory, California Institute of Technology, Pasadena, CA 91109 USA

ABSTRACT

This paper reports on the design, simulation, and characterization of a MEMS gas microvalve (MV) intended to be used as part of the Spacecraft Atmosphere Monitor (SAM) instrument, a highly miniaturized gas chromatograph mass spectrometer (GC-MS) for the International Space Station (ISS). All performance requirements at the system level were considered for flow and pull-in voltage simulations, and multiple tradeoffs were considered to ensure successful operation of SAM. Results of a selection of three MV generations are presented and discussed, including our latest generation, Rev ψ, that meets all the key performance requirements with significant margin with a measured sampling flow above 0.34 sccm and pull-in voltage below 255 V for a current lower than 1 μA.

KEYWORDS

Atmosphere monitor, International Space Station, ISS, gas chromatograph, gas valve, GC-MS, mass spectrometer, MEMS, microvalve

INTRODUCTION

The Spacecraft Atmosphere Monitor (SAM) instrument is a highly miniaturized gas chromatograph mass spectrometer (GC-MS), which can separate, identify, and quantify mixtures of chemicals completely autonomously. Over the years, SAM has undergone technological advancements for its potential application as an air quality monitoring instrument aboard the International Space Station (ISS). The first generation of SAM was deployed on ISS in July 2019 and had been monitoring the major components found in air: oxygen, carbon dioxide, nitrogen and methane, as well as checking humidity levels in real time [1]. The next generation of SAM, expected to launch by 2024, will also measure trace gases, using multiple MEMS components: a Pre-concentrator (PC), a Microvalve (MV), and a miniature Gas Chromatograph (GC) [2]. The MEMS PC and GC have already been tested as a sub-system, and results were presented in [3].

In this paper, we concentrated on the most challenging MEMS component of SAM, the MV, and the key SAM system requirements associated with it, which are:

1. electrostatically actuated with voltage and current limits of 300 V and 0.5 mA during operation,
2. being robust against 28 psi of pressure differential for all 5 moveable membranes,
3. minimum of 0.3 sccm of air flow across the system when PC is being loaded,
4. leak rate lower than 5e-5 Torr.l/s.

To meet these requirements, the MV has been through multiple design, fabrication, and test cycles, feeding achievable process and structural parameters back to optimize the overall MV design.

MICROVALVE DESIGN AND TOPOLOGY

The MV comprises of 4 layers (T-CAP, VC, MEM, and B-CAP) bonded using Au-Au compression bonding. T-CAP and B-CAP are 500 μm thick CZ silicon wafers, T-CAP is housing multiple microfluidic channels and gas inlets for Sample (S), Vent (V), Carrier (C), and the 2 gas ports to connect to PC. B-CAP is sealing the back of the 5 membranes and housing the Injection (I) port. The 5 membranes are independent electrostatic parallel plate actuators created across the VC to MEM interface. Both VC and MEM wafers are SOI (Silicon-On-Insulator) wafers, with a highly doped device layer and a FZ handle layer. Figure 1 shows a schematic of the MV chip, with an exploded view highlighting the geometry of the microfluidic channels, placement of the ports and location of the 5 membranes. Figure 2 shows the picture of a fabricated wafer along with an image of a MV chip and a scanning electron microscope (SEM) of a membrane on the MEM layer.

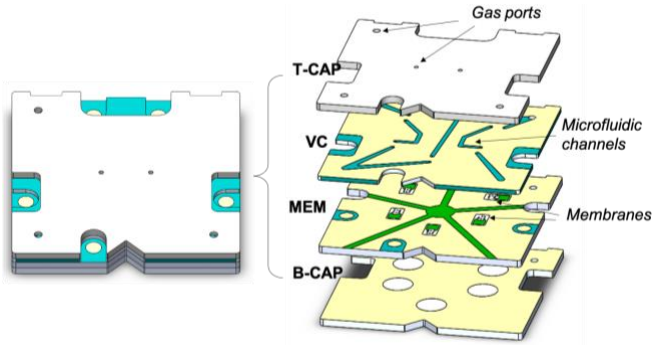

Figure 1. The MV chip and its exploded view, showing the 4-layers (T-CAP, VC, MEM and B-CAP) as well as the gas ports, microfluidic channels and the 5 membranes.

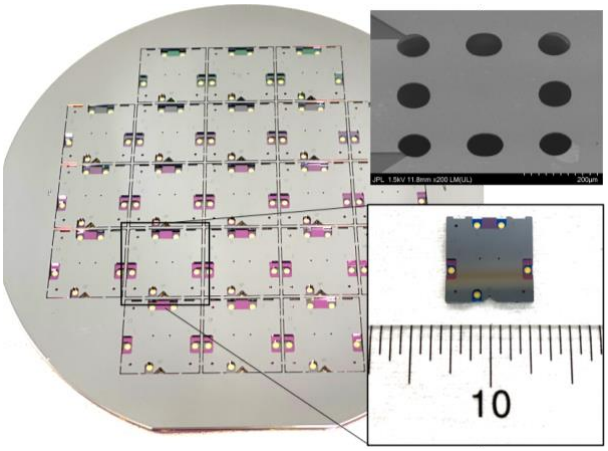

Figure 2. Fully fabricated wafer with multiple MVs. Insets show an SEM image of a membrane on the MEM layer and an individual MV.

Membrane design considerations were reported in detail in [4], including strategy to meet SAM requirements #1 and #2. Two membrane designs were simulated and fabricated, a 300 μm wide MEM design (300MEM) and a 400 μm wide MEM design (400MEM); images of both membrane designs are presented in Figure 3. The other requirements are explained in more detail in the following sections.

978-1-940470-04-7/HH2022/$25©2022TRF
DOI 10.31438/trf.hh2022.14

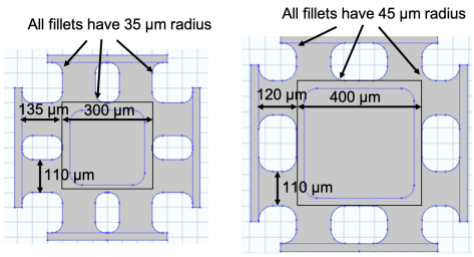

Figure 3. Design geometry for the 300MEM (left) and the 400MEM (right). Both were fabricated and tested against the SAM requirements for the MV.

SAMPLING FLOW REQUIREMENT

During sampling, the cabin air is being pulled from the sampling port, across the S-MEM, through PC, across the V-MEM, and through the vent port with a sampling pump (from TCS). Figure 4 shows the schematic of the system for that step, with the flow path highlighted in green.

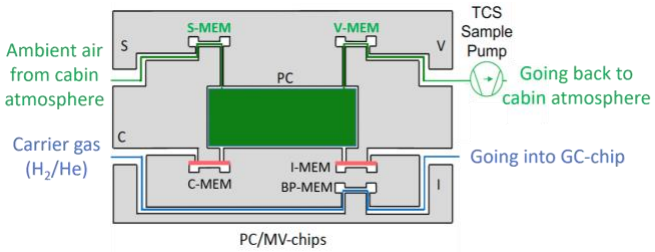

Figure 4. Simplified representation of the sampling step during SAM operation. The PC is being loaded with the ambient air using a TCS sample pump (green path). S-MEM and V-MEM are in the open position, while C-MEM and I-MEM are closed. Carrier gas is being pushed into the GC-chip via the BP-MEM (blue path).

The laminar airflow in the MV channels was modeled using COMSOL Multiphysics software (version 5.6). Simulations were performed for different pressure drop scenarios across the whole system. CAD designs were imported, domains for flow were defined, and flow equations with fine meshing were used to obtain the various flow rates. Figure 5 shows a 3-D representation of the PC-MV system, with microfluidic channels and the pressure difference plotted for the S-MEM and the V-MEM.

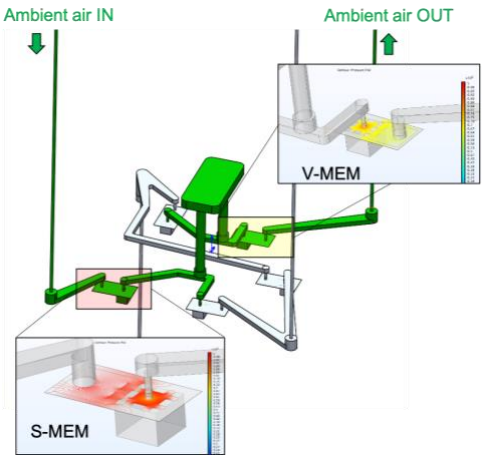

Figure 5. 3-D representation of the PC-MV microfluidic channels during sampling step (green path). Pressure difference across the system is simulated with close-up views on S-MEM and V-MEM.

The gap between VC to MEM and the diameter of the gas ports play a significant role on the sampling flow. Gas ports diameters ranging from 50 µm to 300 µm were considered, to accommodate higher flow while keeping the fabrication protocol feasible.

Another important parameter is the overall pressure difference created by the sampling pump, and how the pressure is distributed across the system. Early testing showed that the two membranes on the sampling flow path (S-MEM and V-MEM) could become deformed, and thus their design/sizing would impact the overall sampling flow if they were too flexible. Testing of MV Rev α showed that the sampling pump, while running at 5V, was creating a roughly 5 psi pressure difference across the whole system. This value was used to calculate the pressure difference for each membrane, for each VC-MEM gap, and ports sizing combination.

Additional COMSOL simulations were performed for both MEM designs, and pressure differences for a valve ranging from 1 psi to 3 psi, to simulate the membrane deformation for each case. We used a pressure profile across the valve similar to a truncated pyramid, divided each design in 50 µm squares (10×10 matrix for 300MEM, 14×14 matrix for 400MEM), and run the simulations assuming 100 µm diameter gas ports.

Figure 6 shows how the membranes were segmented, with each segmented boundary seeing some percentage of the total pressure load, and the resulting membrane deformation for 1 psi and 3 psi pressure difference for a valve.

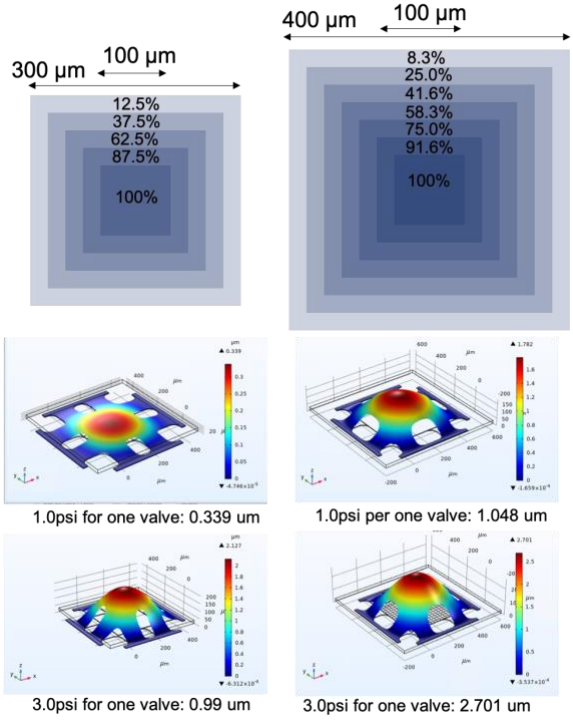

Figure 6. Membrane deformation for each valve were simulated using a segmented matrix and a gradual phasing of the pressure difference across the valve. Values for 1 psi and 3 psi are plotted for both 300MEM and 400MEM.

Figure 7 and Table 1 show a summary of simulated sampling flow for various gaps, various membrane geometries, and port sizing, with the expected membrane deformation for each case based on the pressure difference for each valve.

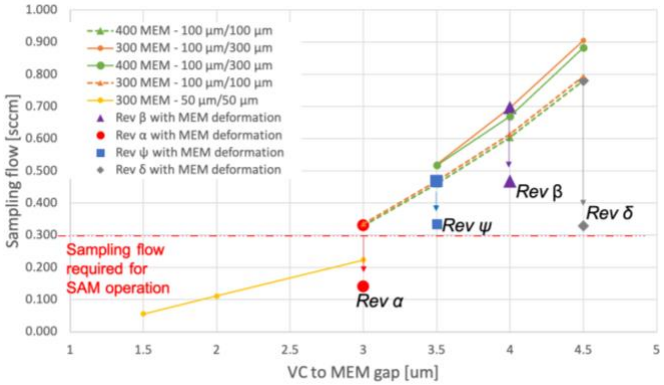

Figure 7. Simulated sampling flow at 5 psi pressure difference across the system, for various MEM sizing, holes sizing and VC to MEM gaps. The expected sampling flows, taking into account the deformation of the movable membrane, are also plotted for a selection of 4 MV generations.

Table 1. Simulated pressure difference across S- and V-MEM and resulting MEM deformation for various designs, assuming 5 psi pressure difference across the system.

Rev ID	MEM design	Hole sizing	VC to MEM gap	Pressure difference across S-MEM and V-MEM (each)	Expected MEM deformation
Rev α	400MEM	100 µm / 100 µm	3 µm	2.1 psi	~ 2 µm
Rev β	300MEM	100 µm / 300 µm	4 µm	1.6 psi	~ 0.56 µm
Rev ψ	300MEM	100 µm / 100 µm	3.5 µm	1.7 psi	~ 0. 57 µm
Rev δ	400MEM	100 µm / 100 µm	4.5 µm	1.8 psi	~ 1.7 µm

VOLTAGE AND CURRENT REQUIREMENTS

Electrical system requirements for the MV chip are listed as voltage and current limits of 300 V and 0.5 mA during operation. The proposed MVs are parallel-plate electrostatic actuators that would close when a voltage above the pull-in level but below the maximum allowable supply voltage (300 V) is applied.

A single MV can then be modelled as a parallel-plate actuator and pull-in voltage (V_{pi}) can be estimated using the following equation,

$$V_{pi} = \sqrt{\frac{8k_{eff}d^3}{27\varepsilon A_{eff}}}, \quad (1)$$

where k_{eff}, d, ε, and A_{eff} are the effective stiffness, equivalent air gap, permittivity of air, and effective electrode area. Expected pull-in voltage for different revisions of MVs are shown in Table 2.

Table 2. Comparison of measured sampling flows and pull-in voltages with simulations, for a selection of 3 MV generations.

Rev ID	Simulated flow for VC to MEM gap	Simulated flow taking into account MEM deformation	Measured sampling flow	Simulated pull-in voltage with no pressure difference	Measured pull-in voltages
	ΔP = 5 psi	ΔP = 5 psi	ΔP = 5 psi		
Rev α	0.329	~ 0.140	0.035 – 0.178 (20 microvalves measured)	100 V	70V – 130 V (20 microvalves measured)
Rev β	0.699	~ 0.468	0.429 – 0.462 (10 microvalves measured)	280 V	240 V – 350 V (10 microvalves measured)
Rev ψ	0.468	~ 0.335	0.331 – 0.371 (10 microvalves measured)	224 V	220 V – 255 V (10 microvalves measured)

While electrostatic actuators do not draw much current in ideal conditions, unintended low resistance paths between the membranes or within the layers of MV chip can lead to leakage currents exceeding 0.5 mA. Therefore, electrical mapping of all connections VC-MEM and MEM-MEM is performed through I(V) traces, showing currents lower than 1 µA and all resistances above 500 MΩ.

LEAK-RATE REQUIREMENT

To ensure proper operation of the full SAM system, the overall leak-rate of the MEMS PC+MV+GC chain needs to be lower than 5e-5 Torr.l/s. The leak rate of the MV is measured by pumping the MV through the I port (while S/V/C and PC ports are physically plugged,), with a leak detector for 30 min and then inserting the whole block into a Helium filled bag. Helium will penetrate through the block and the MV and once the rate is stable for more than 30min, the leak test is completed.

With our none-ideal wafer bonder tool, we see a large difference in measured leak rates, between the dies at the periphery of the wafer and the dies at the center of the wafer. Thermal analysis of the temperature gradient across the full stack during bonding informed us that there is a loss of about 15 ^{0}C from the side of the wafer to the center of the wafer, which would impact the Au-Au compression bond quality and in turn negatively impact the leak-rate. One way to improve the leak rate is to epoxy seal the periphery of the MV, which has shown to reduce the leak rate by a factor of 10 to 50 times.

REVα AND REV β DISCUSSION

As explained in the leak-rate section, the wafer-level bonding quality is a key factor to have operational MVs, with sampling flow and pull-in voltages being highly dependent on the VC to MEM distance. If the bonding is poor, the VC and MEM plates can be further apart, which will give more flow but will also drive the pull-in voltage higher. This was our main issue for MV generation Rev α and Rev β, and why most of the MVs in Rev β were not meeting the pull-in voltage requirement.

The other very important aspect is the removal of the buried-oxide (BOX) under the membrane, on the MEM SOI wafer. If the BOX is not completely removed, and some oxide is left on the corners/legs of the movable membranes, they will buckle up. This will play against the VC to MEM distance, thus lowering the sampling flow and the pull-in voltage. This was the second issue affecting MV generation Rev α, and it explains why both sampling flow and pull-in voltages for that generation were so wide spread. Experimental results for those two generations are summarized in Table 2.

REV ψ FABRICATION PROCESS AND RESULTS

Learning from our experience and from all our various simulations, we fabricated the final round of MV Rev ψ. For this fabrication run, the 300MEM was selected, with a 3.5 µm physical gap before membrane deformation. When taking into account the ~0.56 µm membrane deformation, the physical gap during sampling would be a little less than 3 µm, for an expected sampling flow of 0.335 sccm.

All 4 layers of the MV are fabricated on 4-inch (100 mm) wafers, using conventional photolithography processes, combined with Fluorine-based ICP for any oxide etching and Deep Reactive Ion Etching (DRIE) for any silicon etching:

- Both T-CAP and B-CAP wafers have an initial step of Cr/Pt/Au lift-off process followed by silicon DRIE on the top side and bottom side of the wafers.

- On the VC SOI wafer, silicon DRIE is performed first on both sides, to define the pillars, the electrical plate and the through holes, followed by the growth of 1 μm of thermal oxide to ensure electrical isolation of all the structures. Subsequent steps include removal of the BOX and TOX (Thermal Oxide) layers with Fluorine ICP and Cr/Pt/Au lift-off process on both sides of the wafer, followed by a final silicon DRIE step on the top side.
- On the MEM SOI wafer, each membrane island is defined first, followed by growth of 2 μm of thermal oxide for electrical isolation. Subsequent steps include removal of the TOX layer with Fluorine-ICP and Cr/Pt/Au lift-off process on both sides of the wafer, followed by silicon DRIE on the top side to define the membranes, and silicon DRIE/Fluorine ICP on the bottom side to remove the silicon and BOX underneath the membranes.

Flatness of the membranes are confirmed using a Veeco Wyko optical profilometer and I(V) traces are performed to confirm MEM-MEM electrical isolation before bonding. All four wafers were bonded at once; we performed a wafer-to-wafer manual alignment under an infrared (IR) microscope, and we bonded at 320 ^{0}C, using 20 kN force for 16 hours.

For Rev ψ, the pull-in voltage was simulated at about 224 V. 15 MVs were measured and results are included in Table 2. Most of the MVs on the periphery of the wafer showed excellent leak-rates of 1e-6 Torr.l/s or lower, sampling flow of 0.34 sccm and pull-in voltages of 230 V. The MVs located towards the center of the wafer, that showed higher leak rates, were epoxy sealed to meet the leak rate requirement. More than 90% of those MVs exhibited a leak rate better than 2e-5 Torr.l/s post-epoxy. They also have a slightly higher sampling flow and pull-in voltages, as expected, but still meeting the SAM system requirements.

Figure 8 presents a typical flow measurement performed as part of our acceptance tests, with cycling of a V-MEM on one of the tested dies from Rev ψ, using 230 V as the pull-in voltage, and showing gas flow being stopped when the membrane is actuated.

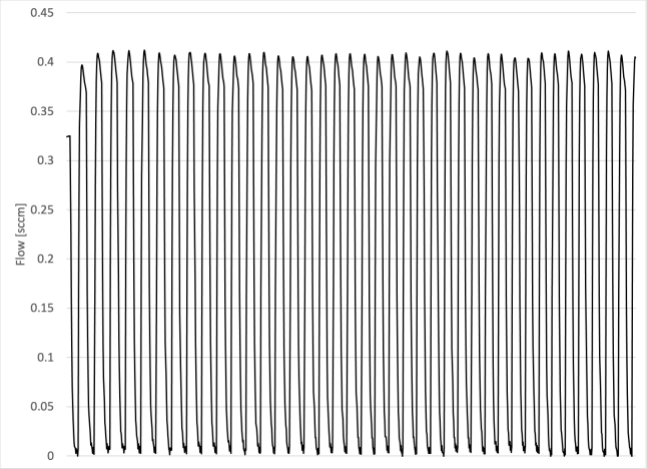

Figure 8. Cycling of a V-MEM from Rev ψ, at 230 V. The membrane is commanded "close" for 20 sec (230 V applied), then commanded "open" for 20 sec (0 V), and both commands are looped for 40 cycles.

CONCLUSION

In this paper, we reported on the development of a MEMS gas microvalve (MV) for the Spacecraft Atmosphere Monitor (SAM) instrument. Focusing on the key system parameters associated with the MV, we carefully simulated, designed, and fabricated a MV that could provide a sampling flow above 0.3 sccm, with a voltage and current below 300 V and 0.5 mA respectively and a leak rate of less than 5e-5 torr.l/s. Our latest MV generation, Rev ψ, provides a sampling flow above 0.34 sccm, a pull-in voltage below 255 V, a current below 1 μA, and a leak rate better than 2e-5 Torr.l/s. This MV generation is now being assembled with the rest of the SAM MEMS components, the PC and the miniature GC, with the full SAM instrument expected to be launched to the ISS by 2024.

ACKNOWLEDGEMENTS

We would like to acknowledge the fruitful discussions with Drs. B. Bae, M. Homer, R. Kidd, F. Zhong, C. Malone, H. Kraus, J. Urrutia, S. Madzunkov, and M. Darrach. The research was carried out at the Jet Propulsion Laboratory, California Institute of Technology, under a contract with the National Aeronautics and Space Administration (80NM0018D0004). © 2022. California Institute of Technology. Government sponsorship acknowledged.

REFERENCES

[1] S. Madzunkov *et al*., "Progress report on the Spacecraft Atmosphere Monitor," International Conference on Environmental Systems, 2016.

[2] M. Darrach *et al*., "Status and results of the Spacecraft Atmosphere Monitor technology demonstration instrument", International Conference on Environmental Systems, 2022.

[3] B. Bae *et al*., "MEMS Preconcentrator and Gas Chromatograph Chips for the Spacecraft Atmosphere Monitor", *21st International Conference on Solid-State Sensors, Actuators and Microsystems (Transducers)*, 2021.

[4] M. B. Coskun *et al.*, "A MEMS microvalve array for gas flow control", *IEEE MEMS conference*, 2022.

CONTACT

*C. Jung-Kubiak; tel:+1-818-354-1658; cecile.d.jung@jpl.nasa.gov
**M. Rais-Zadeh; mina.rais-zadeh@jpl.nasa.gov

EXPLOITING NONLINEAR PROPERTIES OF VO_2 IN A MMWAVE ANTENNA-COUPLED SENSOR

Shangyi Chen[1], Mark Lust[2], and Nima Ghalichechian[3]*
[1]University of Pennsylvania, Philadelphia, Pennsylvania, USA
[2]The Ohio State University, Columbus, Ohio, USA
[3] Georgia Institute of Technology, Atlanta, Georgia, USA

ABSTRACT

We present the design, fabrication, and measurement of the antenna-coupled microbolometer using the phase change material vanadium dioxide (VO_2) for millimeter wave (mmWave) imaging applications. The nonlinear properties of VO_2 are exploited to achieve a large responsivity of 6.55×10^4 V/W by biasing the sensor through the metal-insulator transition (MIT) region. The overall performance of the sensor is also enhanced by suspending the device on the alumina (Al_2O_3) buffer layer membrane. The operating frequency band of the coplanar waveguide (CPW) fed dipole antenna is 31 – 55 GHz with on-wafer probe measurements. The radiation pattern of the 4×4 sensor array is demonstrated by the radar cross-section (RCS) technique using a highly precise robotic antenna measurement system.

KEYWORDS

Microbolometer, VO_2, antenna, millimeter wave, phase change material

INTRODUCTION

The bolometer is a sensor to quantify the radiation power through a material with a temperature dependent resistance. Since it was first introduced in 1880 [1], the bolometer has been widely used as a detector in a thermal camera for security screening, biomedical, and military applications. The functionality of the bolometer relies on the characteristic of the sensitive material's thermal coefficient of resistance (TCR). Electrical responsivity which is a chief figure of merit of the bolometer is directly proportional to TCR. Hence, one critical strategy to improve the responsivity of the bolometer is to utilize a material with a large TCR. Unfortunately, traditional microbolometers utilize linear materials that have small TCR (0.1%/K-0.3%/K), such as platinum [2], titanium [3], and bismuth [4].

Vanadium dioxide (VO_2) is an electrical phase change material that adopts insulating monoclinic (M1) phase (space group $P2_1/c$) below the transition temperature (~68 °C) and metallic tetragonal rutile (R) phase (space group $P4_2/mnm$) above the transition temperature [5-8]. Thus, VO_2 thin film whose electricity exhibiting a sharp change in the metal-insulator-transition (MIT) is appealing for a microbolometer to improve the responsivity. Especially, the TCR of VO_2 in the MIT region in our previous study can reach up to 171%/K [8, 9]. However, there are few studies demonstrating improved properties of microbolometer utilizing nonlinear properties of VO_2. For instance, VO_2 thin films have been utilized in the linear TCR region for infrared (IR) microbolometers as reported in [10]. Specifically, an eight-element uncooled VO_2 microbolometer linear array which exhibited a responsivity over 10 kV/W was described. While their proposed architecture was an on-substrate design, the reported large responsivity was mainly due to the large electrical resistivity of VO_2 thin films in the dielectric phase, which is unsuitable for the antenna coupling. The VO_2 microbolometer employing the phase-transition region and targeting for IR operation was described in [11]. The VO_2 microbolometer was biased on the semiconducting-metal phase transition with negative electrothermal feedback. Due to the on-substrate design and low quality of the deposited film with large hysteresis, only a small responsivity of 108 V/W with the ac bias technique was obtained.

Here, we employ VO_2 as the sensitive material to take the advantage of its large TCR in the MIT region to achieve high responsivity [12]. Our previous studies analytically demonstrated the approaches to enhance the responsivity of the microbolometer by the utilization of VO_2's nonlinearity in the MIT region and air suspension [9, 13, 14]. Also, the architecture of VO_2 thin film on alumina (Al_2O_3) buffer layer by the atomic layer (ALD) technique is adopted in this report to design and fabricate the sensor [8]. The VO_2 microbolometer is coupled with a dipole antenna and coplanar waveguide (CPW) designed to operate at 30 – 60 GHz. The CPW is used for excitation and biasing. The antenna transfers the electromagnetic power to VO_2 for sensor. The targeted millimeter wave (mmWave) band has obvious advantages over IR band, as mmWave is able to pass through opaque objects such as fog and clouds and can be used for imaging in harsh environments. To improve the thermal isolation as well as the antenna radiation efficiency, the VO_2 sensor is suspended on the Al_2O_3 buffer layer from the silicon (Si) substrate by the deep reactive ion etching (DRIE) process. Additionally, we utilize the 4×4 VO_2 microbolometer array to analyze the antenna radiation pattern as a proof of concept for future mmWave imaging camera.

MICROBOLOMETER DESIGN AND FABRICATION

To quantify the performance of the microbolometer, one figure of merit is the electrical responsivity, which is defined as

$$\Re = \frac{\Delta V}{\Delta P}. \quad (1)$$

ΔV is the change of the voltage output due the input power variance ΔP. The antenna is necessary to be employed in the microbolometer especially at the mmWave band to absorb the radiated power. The architecture of the proposed VO_2 microbolometer is demonstrated in Figure 1. The VO_2 microbolometer is coupled to a CPW-fed dipole antenna with a frequency range of 30 – 60 GHz. The dipole antenna (with a length of 4.4 mm and width of 1.5 mm) is designed to receive the radiated power at the mmWave band, resulting in a resistance change of the VO_2 sensitive material. The CPW feed structure is integrated for excitation and biasing. The dimension of the VO_2 sensor is 10 μm × 60 μm × 0.1 μm. The buffer layer Al_2O_3 is employed to provide a good basis for VO_2 property and mechanically support the sensor. The electrical resistivity contrast and maximum TCR in the MIT region of our fabricated VO_2 thin film on annealed Al_2O_3 buffer layer are 1.46×10^4 and 171%/K [8, 9]. In addition, the thermal isolation and antenna radiation are improved by releasing the senor from the Si substrate with a main cutout diameter of 5 mm and strategically placed ring structures.

The three-layer photolithography process is employed to fabricate the sensor as described in Figure 2. First, a 48-nm-thick Al_2O_3 is deposited on the 4-inch 300-μm-thick double-side polished Si substrate using the ALD process. The as-deposited Al_2O_3 buffer is annealed by the rapid thermal annealing (RTA) process to achieve

978-1-940470-04-7/HH2022/$25©2022TRF
DOI 10.31438/trf.hh2022.15

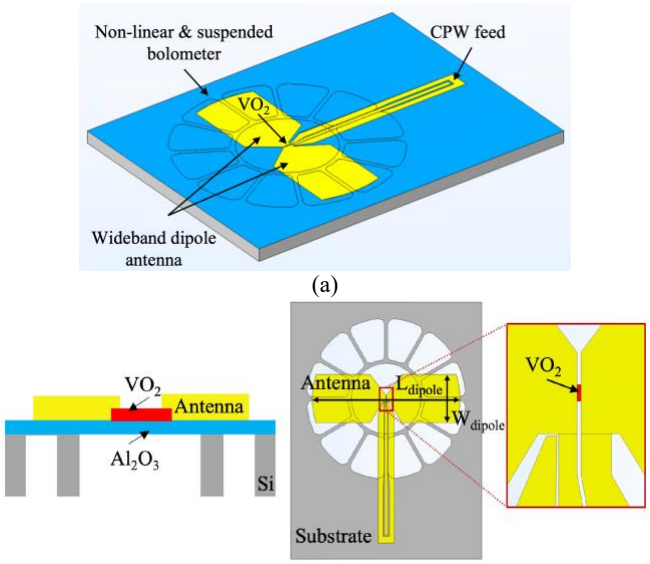

Figure 1: Antenna-coupled VO_2 microbolometer: (a)3D view, (b) cross-section view, and (c) top view.

the crystalline structure. The 100-nm-thick VO_2 thin film is then grown by reactive DC sputtering as detailed in [8], followed by a photolithography step. The VO_2 thin film is etched by the reactive ion etching (RIE) process for the sensor. The CPW-fed antenna is fabricated with a 250-nm-thick layer of gold using the e-beam evaporation and lift-off process. Finally, the device is released by etching the Si backside using the DRIE process.

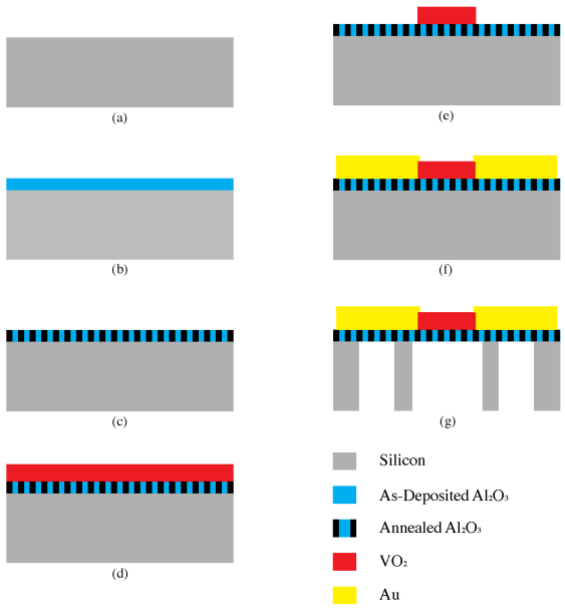

Figure 2: Fabrication process of antenna-coupled VO_2 microbolometer: (a) double-side polished Si, (b) ALD of Al_2O_3 buffer, (c) RTA of Al_2O_3 buffer, (d) sputtering of VO_2, (e) VO_2 RIE, (f) E-beam evaporation and lift off process for Au, and (g) Si backside DRIE.

MEASUREMENTS AND DISCUSSIONS

The antenna characterization, DC performance, and detection properties are carried out for the fabricated sensors.

Antenna Tests

The antenna tests include the impedance match analysis with the CPW-fed sensor and radiation measurements with the 4×4 sensor array. The CPW-fed sensor is measured on the probe station (Cascade M150) with a ground-signal-ground (GSG) 65 GHz probe (Infinity from FormFactor). A calibration standards substrate is used before mmWave measurements. The mmWave power is applied to the VO_2 microbolometer through the CPW by one port from the 67 GHz vector network analyzer (VNA). To excite the sensor, the DC electrical signal is applied with the same probe. A source meter (Keysight B2901A) is used to record the applied bias signals and the corresponding measured output signals. Figure 3 shows the on-wafer test setup and the arrangement of the probe with a detailed view of the probe on the sample. An external polyimide insulated heater (Omega Engineeing, Inc) is used under the sample to activate the sensor near the MIT region. A DC voltage of ~16.7 V is applied to the external heater using a power source (Keysight B2962A) and the surface temperature is measured to be ~59.4 °C by a thermocouple temperature probe. Figure 4 demonstrates the return loss (S_{11}) in frequencies ranging from 25 – 65 GHz measured by the VNA. VO_2 is at the dielectric phase without the DC voltage bias, and the antenna is not fully matched. With a DC voltage bias of 7 V that tunes the microbolometer through the MIT region, the frequency band ($S_{11} \leq$ -10 dB) increases, and the single element is matched from 31 – 55 GHz.

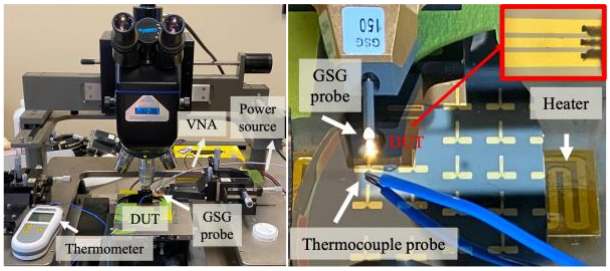

Figure 3: (a) The test setup for on-wafer measurement and (b) the detailed view of the probe on the sample.

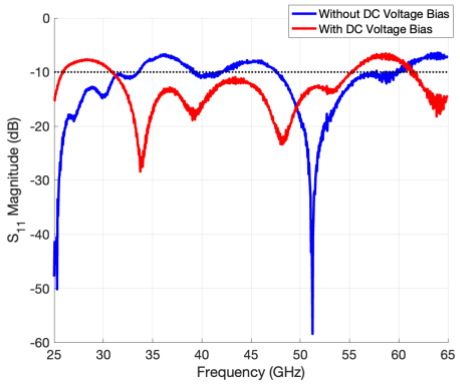

Figure 4: The S-parameter of the VO_2 microbolometer's antenna.

The gain pattern of the 4×4 VO_2 antenna-coupled microbolometer array operating at broadside is measured, as the antenna will only receive incoming radiation at narrow incidence angles in the full imaging system. We use the radar cross-section (RCS) technique which is a non-contact backscattering approach and featured to replace the cables and probs for the antenna gain measurement at the mmWave band [15]. As there is presently no

read-out-circuit to control DC bias of the VO_2, the VO_2 resistors are in insulating state with a resistance of ~100 kΩ, giving high RF reflection ($S_{11} \approx 0$ dB). The VO_2 geometry in the array is adjusted from that in the CPW-fed sensor to be 10 µm × 200 µm. Therefore, in a full ROIC-controlled device, initial impedance of VO_2 can be set to ~75 Ω using temperature and DC voltage; this impedance will then fluctuate according to power level of incoming RF signal. As shown in Figure 5, we utilize a 6-axis robot system (Fanuc LR Mate200iD) developed in our previous study [16] with a dual-horn monostatic radar setup to measure radiation pattern. The standard gain horn antennas (QSH-SL-50-75-V-20) are used to establish signal floor by scanning the test setup without the microbolometer array in place. The 4×4 VO_2 microbolometer array is aligned with the horn antenna attached to the robot visually with a laser pointer, and a half-circle trajectory is carried out with a 0.33° angular resolution at a radius R=350mm from the end of the robot arm. The transmission coefficient (S_{21}) from the transmitting to the receiving horn antennas is obtained at 60 GHz during the trajectory. With constant distance, horn antenna gain, and wavelength, target gain factor varies only with excitation angle, so normalized antenna gain is proportional to S_{21}. Figure 6 shows normalized antenna array gain pattern with main lobe at 0° and side-lobes at ±20°, ±30°, and ±60° in E-plane and side lobes in H-plane, ranging from ±30° to ±60°. To account for the RCS contributions at the central angles from silicon, the measured curves in Figure 6 are adjusted by $n(2\text{-}\cos 2\theta)$, with n=2.5 in E plane and n=1.5 in H plane. In a fully realized imaging system, this antenna array design would successfully function at broadside. Although it has no need for receiving at the wider angles, they are beneficial for verifying simulated pattern.

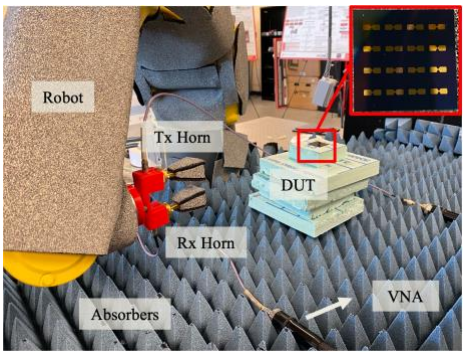

Figure 5: The test setup for RCS measurement.

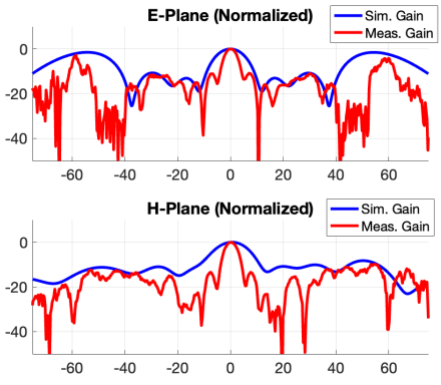

Figure 6: The normalized gain pattern of the 4×4 array.

DC/RF Characterization and Detection Properties

To excite the CPW-fed sensor through the MIT region, the DC bias and RF power are applied. The static I-V test of the CPW-fed VO_2 microbolometer is obtained as shown in Figure 7 when applying RF signal between 35 – 65 GHz controlled by the VNA. The RF power level ranges from -25 dBm – 0 dBm (3.1 µW – 1 mW). At each power level, the double-sweep voltage bias is applied, and the current is measured by the source meter. When the voltage bias increases, VO_2 starts from the linear dielectric phase, moves through the MIT region with a resistance of ~248 Ω where there is a sharp increase in the current, and enters the linear metallic region (~89 Ω resistance). As the voltage decreases, the hysteresis phenomenon is obvious and finally VO_2 moves back to the dielectric state. The required voltage triggering MIT decreases as the RF power increases as can be seen in Figure 7. The threshold voltage shift confirms that the microbolometer can sense the electromagnetic power change as low as -25 dBm (3.16 µW). The threshold voltage versus the input power is shown in Figure 8.

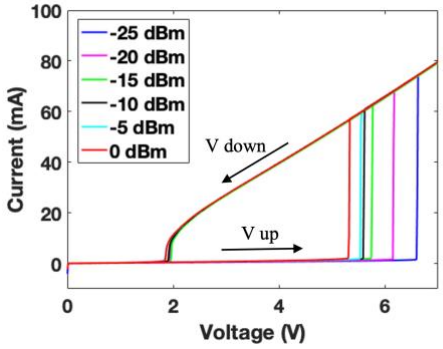

Figure 7: I-V curve of the VO_2 microbolometer.

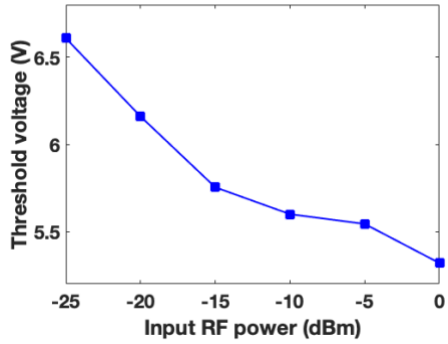

Figure 8: Threshold voltage versus input RF power.

The DC responsivity can be estimated from the ratio of the threshold voltage shift over the input power change to the VO_2 microbolometer, as defined in Eq. (1). The extracted DC responsivity versus corresponding RF power change is shown in Figure 9. Due to the nonlinear properties of VO_2 in the MIT region, the responsivity is highly nonlinear and has a larger value with a smaller RF power change. By the utilization of VO_2's large TCR in the MIT region and air suspension, our sensor can achieve a maximum DC responsivity of 6.55×10^4 V/W, which is $>10^2$ times larger than the state-of-the-art antenna-coupled microbolometers [17, 18] shown in Table 1.

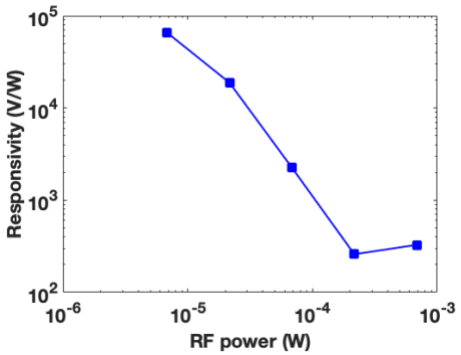

Figure 9: Responsivity versus RF power.

Table 1: Antenna-coupled microbolometer comparison.

	Specifications and performance		
	Material	Dimension (μm^3)	Responsivity (V/W)
This work	VO_2	10×60×0.1	6.55×10^4
[17]	Nb	10×1×0.35	85
[18]	$PrBa_2Cu_3O_{7-x}$	2×5×0.07	33

CONCLUSION

In this paper, the nonlinear properties of VO_2 thin films are exploited in the antenna-coupled microbolometer. The CPW-fed antenna operates in the frequency band of 31 – 55 GHz. For the proof of concept of an imager, the radiation pattern of the 4×4 sensor array is measured with the RCS technique. By biasing the sensor in the MIT region with the large TCR of VO_2 and using air suspension, our sensor demonstrates a high responsivity of 6.55×10^4 V/W. This work demonstrates the potential of employing VO_2 in a microbolometer to achieve a high responsivity for future mmWave imaging arrays.

ACKNOWLEDGEMENTS

This material is based upon work supported by the US National Science Foundation (NSF) CAREER Award under Grant No. 1845370 and 2149886, the Air Force Research Lab (AFRL)/Defense Associated Graduate Student Innovators (DAGSI) Award No. RY6-OSU-19-2-AFRL2, and AFOSR Lab Task 21RYCOR019 supported by Dr. Ilya Vitebskiy.

REFERENCES

[1] S. P. Langley, "The bolometer and radiant energy," *Proceedings of the American Academy of Arts and Sciences,* vol. 16, pp. 342-358, 1880.

[2] S. Yoneoka *et al.*, "ALD-metal uncooled bolometer," in *2011 IEEE 24th International Conference on Micro Electro Mechanical Systems*, 2011, pp. 676-679.

[3] A. Tiwari, H. Satoh, M. Aoki, M. Takeda, N. Hiromoto, and H. Inokawa, "Fabrication and analytical modeling of integrated heater and thermistor for antenna-coupled bolometers," *Sensors and Actuators A: Physical,* vol. 222, pp. 160-166, 2015.

[4] D. Neikirk, W. W. Lam, and D. Rutledge, "Far-infrared microbolometer detectors," *International journal of infrared and millimeter waves,* vol. 5, no. 3, pp. 245-278, 1984.

[5] J. B. Goodenough, "The two components of the crystallographic transition in VO2," *Journal of Solid State Chemistry,* vol. 3, no. 4, pp. 490-500, 1971.

[6] K. Liu, S. Lee, S. Yang, O. Delaire, and J. Wu, "Recent progresses on physics and applications of vanadium dioxide," *Materials Today,* vol. 21, no. 8, pp. 875-896, 2018.

[7] R. Shi *et al.*, "Recent advances in fabrication strategies, phase transition modulation, and advanced applications of vanadium dioxide," *Applied Physics Reviews,* vol. 6, no. 1, p. 011312, 2019.

[8] M. Lust, S. Chen, C. E. Wilson, J. Argo, V. Doan-Nguyen, and N. Ghalichechian, "High-contrast, highly textured VO2 thin films integrated on silicon substrates using annealed Al2O3 buffer layers," *Journal of Applied Physics,* vol. 127, no. 20, p. 205303, 2020.

[9] S. Chen, M. Lust, and N. Ghalichechian, "Multiphysics simulation of hypersensitive microbolometer sensor using vanadium dioxide and air suspension for millimeter wave imaging," *Microsystem Technologies,* vol. 27, no. 7, pp. 2815-2822, 2021.

[10] C. Chen, X. Yi, X. Zhao, and B. Xiong, "Characterizations of VO2-based uncooled microbolometer linear array," *Sensors and Actuators A: Physical,* vol. 90, no. 3, pp. 212-214, 2001.

[11] C. D. Reintsema, E. N. Grossman, and J. A. Koch, "Improved VO2 microbolometers for infrared imaging: operation on the semiconducting-metallic phase transition with negative electrothermal feedback," in *Infrared Technology and Applications XXV*, 1999, vol. 3698, pp. 190-201: International Society for Optics and Photonics.

[12] S. Chen, M. Lust, and N. Ghalichechian, "Antenna-coupled VO2 microbolometer for mmWave sensing," *IEEE Sensors Journal,* (under review).

[13] S. Chen, B. Ghassemiparvin, and N. Ghalichechian, "The design of high-responsivity millimeter wave imager using vanadium dioxide microbolometers," in *12th European Conference on Antennas and Propagation*, 2018, pp. 1-4.

[14] S. Chen, M. Lust, and N. Ghalichechian, "A vanadium dioxide microbolometer in the transition region for millimeter wave imaging," in *2019 IEEE International Symposium on Antennas and Propagation and USNC-URSI Radio Science Meeting*, 2019, pp. 1641-1642.

[15] J. Li, C. Matos, S. Chen, and N. Ghalichechian, "Fundamental improvement to the efficiency of on-chip mmWave phased arrays using MEMS suspension," *IEEE Antennas and Wireless Propagation Letters,* vol. 20, no. 4, pp. 473-477, 2021.

[16] C. Matos, J. Humanchuk, and N. Ghalichechian, "Robotically-controlled antenna measurement system for millimeter-wave applications," *Microwave and Optical Technology Letters,* vol. 63, no. 5, pp. 1520-1525, 2021.

[17] A. J. Miller, A. Luukanen, and E. N. Grossman, "Micromachined antenna-coupled uncooled microbolometers for terahertz imaging arrays," in *Terahertz for Military and Security Applications II*, Orlando, FL, 2004, vol. 5411, pp. 18-24.

[18] A. Scheuring *et al.*, "Thin Pr–Ba–Cu–O film antenna-coupled THz bolometers for room temperature operation," *IEEE Transactions on Terahertz Science and Technology,* vol. 3, no. 1, pp. 103-109, 2013.

CONTACT

*N. Ghalichechian, tel: +1-404-894-5867; nima.1@gatech.edu

KILOVOLT PYROELECTRIC VOLTAGE GENERATION AND ELECTROSTATIC ACTUATION WITH FLUIDIC HEATING

*Di Ni[1], Ved Gund[1], Landon Ivy[1], and Amit Lal[1]**

[1]SonicMEMS Laboratory, School of Electrical and Computer Engineering, Cornell University, Ithaca, NY, USA

ABSTRACT

Integrated micro power generators are crucial components for micro robotic platforms to demonstrate untethered operation and to achieve autonomy. Current micro robotic electrostatic actuators typically require hundreds to thousands of voltages to output sufficient work. Pyroelectricity is one such source of high voltages that can be scaled to small form factors. This paper demonstrates a distributed pyroelectric high voltage generation mechanism to power kV actuators using alternating exposure of crystals to hot and cold water (30^0C to 90^0C water temperature). Using this fluidic temperature control, a pyroelectrically generated voltage of 2470 V was delivered to a 2 pF storage capacitor yielding a 6.10 µJ stored energy. A maximum energy of 17.46 µJ was delivered to a 47 pF capacitor at 861 V. The recirculating water can be used to heat a distributed array of converters to generate electricity in distant robotic actuator sections. The development of this distributed system would enable untethered micro-robot to be operated with a flexible body and free of battery recharging, which advances its applications in the real world.

KEYWORDS

Pyroelectricity, lithium niobate, distributed high voltage generation, microrobotic actuator, electrostatic actuator, micro power source.

INTRODUCTION

Micro-robotic actuators, such as electrostatic, piezoelectric, and dielectric elastomer actuators (DEAs), require high voltages to operate. Recent developments in DEAs and electrostatic actuators have resulted in microrobots of 1 cm^3 scale operating at kVs [1], [2]. Because of these demands in high voltage amplitude, the majority of existing micro robot platforms are tethered to external power supplies [3], [4], which limits their applications in the real world for autonomous operation. Moreover, electrostatic actuators greatly benefit from operating with larger voltages due to the improved electromechanical coupling that enables them to have better efficiencies and higher force densities [1]. Yet, building compact power sources that can generate sufficient actuation voltage for micro actuators [3], [5], [6] while fulfilling the small size, weight, and power (SWaP) constraint remains to be a great challenge [3], [5], [6].

To deliver sufficient voltages to actuators mentioned above, integrated power electronic circuits are commonly used to boost voltages from a few volts to thousands of volts. Table 1 compares the existing techniques used for low-to-high voltage conversion. For insect-scale robots (0.1-1 cm^3), the µ-HV supply should be compact and light in order to add the least amount of extra payload, while generating 0.2-10 kV for decent operations of the actuators. Power electrical converters, such as boost and flyback converters, use solenoid inductors as energy storage units. The RoboBee robot used a custom-wound inductor with a very light weight of 5 mg, and achieved a maximum voltage of 190V and a moderate efficiency of 55% [7]. Such small inductors are also extremely hard to make and have a yield of less than 50%. Unlike these electromagnetic coupling converters where inductors are necessary, piezoelectric transformers convert AC primary voltage to a secondary voltage using electromechanical coupling with strain amplification [8], [9]. Though they have benefited from small sizes and high energy density, piezoelectric transformers generally have low voltage gain, fixed operation frequency, and suffer from large leakage at high voltages [7], [10]. Recently, switched capacitor converters have achieved HV while maintaining relatively small sizes. These converters replace inductors with capacitors for energy storage and realize voltage gain through the control of switching transistors [11]. However, these converters need specialized high-voltage CMOS circuitries for precise switching, and generally have a limited gain of ~10x due to the complexity in exact timing.

Table 1: Comparison of existing µ-HV supplies

Converters	***Size***	***Mass***	***Output Voltage***	***Efficiency***
Flyback Converter [7], [12]	*178* cm^3	*100 g*	*5000 V*	*~ 75%*
	0.1 cm^3	20 mg	260 V	~ 70%
Switched capacitor [11]	0.12 mm^3	300 mg	1500 V	~ 80%
Piezoelectric Transformer [9], [12], [13]	< 1 mm^2 PCB surface	2 g	500 V	50% (theoretical)
Pyroelectric generator (this work)	0.2 cm^3 (without fluidic channel)	570 mg	2500 V	< 0.1%

Pyroelectricity provides another promising approach to generating high voltages in small and lightweight form factors. Pyroelectric materials have spontaneous polarization, whose amplitude is modulated reversibly with oscillating temperatures. As a result, a pyroelectrically-generated voltage is built across the crystal surfaces. One of the most widely used pyroelectric materials, lithium niobate ($LiNbO_3$, or LN), has been demonstrated for kilovolts voltage generation within a small volume of 0.2 cm^3 with a simple architecture consisting of only three parts: a heater, a pyroelectric crystal, and a regulating switch [14]–[16]. Resistive heating in these systems utilizes electrical energy and can ideally be replaced by using ambient thermal energy.

In this work, we demonstrate distributed pyroelectric voltage generation and actuation with fluid-mediated heating and cooling, which serves as an alternative to the resistive heating approach reported previously [14], [15]. This system provides capabilities for scavenging the broadly existing thermal energy in the environment and converting it to electricity, and enabling untethered microrobot to operate without the need for battery recharging. An array of pyroelectric crystals is physically connected in series by being glued to the fluidic channel. The fluid delivers heat to each of the crystals, while slowly losing the heat content in the fluid. The voltage generated on each crystal can power an actuator locally, minimizing the parasitic capacitance and wiring complexity usually encountered from high-voltage compatible wiring.

This paper is arranged as follows: an introduction to the distributed pyroelectric high voltage system is first provided,

978-1-940470-04-7/HH2022/$25©2022TRF
DOI 10.31438/trf.hh2022.16

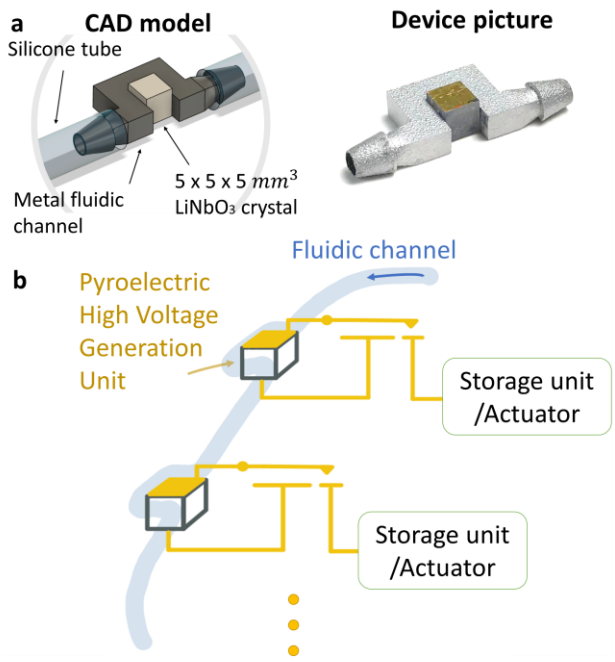

Figure 1: Schematic of the pyroelectric high voltage generation system. ***a.*** *Each pyroelectric crystal (5x5x5 mm^3 $LiNbO_3$, coated with gold on the top and bottom surfaces) is surrounded with a 3D printed metal holder.* ***b.*** *The fluidic channel is used to heat and cool an array of crystals with running liquid. Charges generated on the crystals enable the local powering of actuators, or voltage delivery to a single storage capacitor.*

followed by the equivalent thermal circuit of a unit. The experimental results on voltage stored on capacitors and actuation of an electrostatic actuator is then addressed.

DISTRIBUTED PYROELECTRIC HIGH VOLTAGE GENERATION

The pyroelectric effect is caused by the change of spontaneous polarization under the temperature variation. The amount of heat delivered to the crystal determines the quantity of charge and voltage generated on the crystal. With a temperature change of ΔT, the amount of pyroelectric charge can be estimated from:

$$Q_{pyroelectric} = pA\Delta T$$

where p is the pyroelectric coefficient and A is the surface area of the crystal.

Due to the inevitable charge leakage within the crystal and charge-neutralization with the free-floating electrons and ions in the air, the generation rate of pyroelectric charges must exceed the leakage of charges for the voltage to steadily accrue. Thus, the rate of temperature change is also an important parameter to be considered in modeling the final voltage reachable on a pyroelectric crystal. The pyroelectric crystal operates as a current source, whose amplitude is determined by:

$$i_{pyro} = pA\frac{\mathrm{d}T_{pyro}}{dt}$$

A KCL analysis for the circuit shown in Fig. 3a, can be used to determine the pyroelectric voltage V_{pyro}:

$$i_{pyro} = (C_{pyro} + C_{store} + C_{Parasitic})\frac{dV_{pyro}}{dt} + \frac{V_{pyro}}{R_{leak}}$$

and R_{leak} represents equivalent resistance for charge leakage paths.

Figure 1 shows an overview of the system, consisting of the Pyroelectric High Voltage Generation (PHVG) units, and a fluidic channel used to connect 3D-printed alloy crystal holders. Each of the lithium niobate crystals serves as s pyroelectric voltage generator. Due to its low permittivity, low dielectric loss, moderate pyroelectric coefficient, and easy commercial availability of high-quality wafers, lithium niobate is an ideal material for this system. The preparation of $LiNbO_3$ crystals consisted of two steps: (i) a z-cut, 5 mm thick, 1-inch diameter wafer was first sputtered with Au on both surfaces; (ii) the wafer was diced into 5 x 5 mm^2 pieces using DISCO dicing saw. The crystal is surrounded on 3 sides by a 3D-printed metal channel made of aluminum alloy (Alsi10Mg), which was designed to have good thermal conductivity to transfer the fluid heat to the crystal. A thin layer of thermal adhesive (MG Chemicals 8329TCS) was used to fix the crystal into the 3D printed corner.

Figure 1b shows a schematic of the distributed system. Multiple PHVG units are connected in series with a fluidic channel. A peristaltic liquid pump was used to pump hot/cold liquid from the storage tank to circulate in the tube, enabling the thermal energy converted to electricity at multiple crystal sites. We used water as a preliminary test liquid, whose temperature was varied between 30^0C and 90^0C, with a hot plate used to heat a beaker of water which served as the recirculation reservoir. While being heated/cooled, pyroelectrically-generated voltages are produced across the surfaces of a $LiNbO_3$ crystal. The built-up charges are shared between the pyroelectric crystal and the capacitance of an electro-mechanical electrostatic switch connected in series with one of the crystal electrodes. The switches act as a gap-varying capacitor and experiences pull-in instability at the threshold voltage determined by the gap to the drain and actuation area. Since the heat-driven events happen with a frequency of less than 10 Hz, the current loss on the mechanical switch is very small. Once the pyroelectric voltage reaches the pull-in instability point, the mechanical switch closes and delivers the pyroelectric voltage to the load, which can be either a storage capacitor or a capacitive actuator. In the current setup, the loaded actuators are limited to capacitive actuators due to the limited charge $LiNbO_3$ can generate owing to a smaller surface area. For current-driven actuators, other pyroelectric crystals, such as PMN-PT and PZT, may serve as better alternatives.

The system enables high voltages to be generated at the distributed PHVG sites, limited only by the dielectric breakdown of air. Such an architecture will aid in powering a robot with many actuators, such as the soft robot introduced in [17], where DEAs are employed at each bending joint of a snake robot. The key advantage of this design is the localized actuation and storage of kilovolts of voltages, which avoids the charge dissipation and arcing in charge delivery.

EQUIVALENT THERMAL CIRCUIT MODEL

Figure 2a shows the equivalent thermal model of a PHVG unit, which accounts for the thermal resistance and capacitance of the components. The liquid was modeled as a heat source, whose temperature was assumed to remain constant during the heat transfer process. This is a reasonable assumption because, as compared to the metal alloy and the crystal, the running water has a much higher heat capacity and consequently a higher equivalent thermal capacitance and mass. The thermodynamics of a running liquid were not included in this model for simplicity. $LiNbO_3$ crystals were bonded with thermal adhesive to the metal channels for optimal heat transfer from the circulating fluid. The heat from the liquid needs to propagate through the metal channel and the thermal adhesive layer to reach the crystal, therefore these three modules (metal channel, thermal adhesive, crystal) are connected in series. Each module was modeled as a combination of a thermal resistor with a temperature

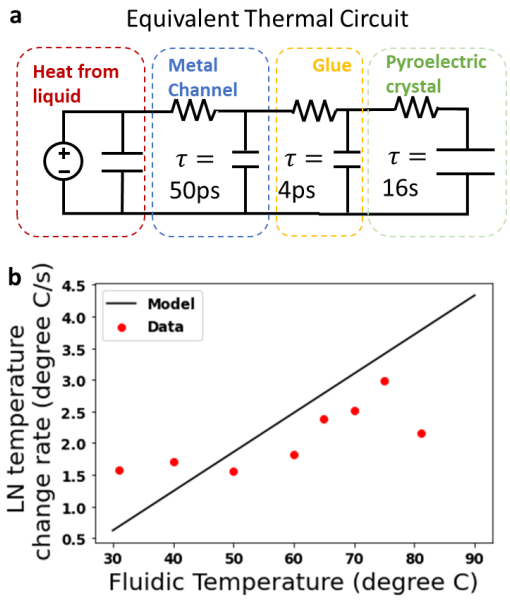

Figure 2. Characterization of the thermal properties. ***a.*** *An equivalent thermal circuit model consists of a metal channel, thermal glue, and a pyroelectric crystal. The heated liquid is considered as an energy source with pulse output.* ***b.*** *The rate of temperature change happened on a LN crystal temperature is linearly proportional to the temperature of the liquid.*

drop, and a heat storage capacitor. The time constant of the thermal conduction can be calculated with: $\tau = RC$ where R is the thermal resistance from the fluid to the crystal, and C is the thermal capacitance of the crystal and the crystal holder. Both the metal alloy and the thermal adhesive have high thermal conductivities and short propagation paths (metal channel wall thickness 500 μm, thermal adhesive thickness <100 μm), heat can be transferred from the liquid to the pyroelectric crystal in less than 100 picoseconds.

Figure 2b shows the experimental measurements of the temperature change rate dT/dt of a crystal heated by water at different temperatures, along with the simulation results from the equivalent circuit model. Since the series-connected thermal resistors are linear components, the model predicts a linear relationship between the heating source and the temperature change rate at the pyroelectric crystal. For each experimental point, the maximum temperature change rates at given fluidic temperatures were plotted as measured with an IR camera and a bonded resistance temperature device (RTD). The measured data shows an increase in the changing rate with increasing water temperature. A deviation from the linear model is potentially due to variation in the thermal resistance of the adhesive due to varying adhesive thickness, as well as fluctuations due to heat transfer to the RTD device and surface emissivity for IR measurements.

EXPERIMENTAL RESULTS

The PHVG system was then tested to deliver high voltages to storage capacitors. Figure 3a shows the electrical circuit used for these experiments. A PHVG unit was connected in parallel with a storage capacitor and a cantilever beam. The voltage measurement setup follows [16], where displacements of the cantilever beam connected to a $LiNbO_3$ crystal were measured with a laser and calibrated to convert the observed displacement to estimate generated voltages. This indirect measurement technique is useful because it has no charge consumption during measurement.

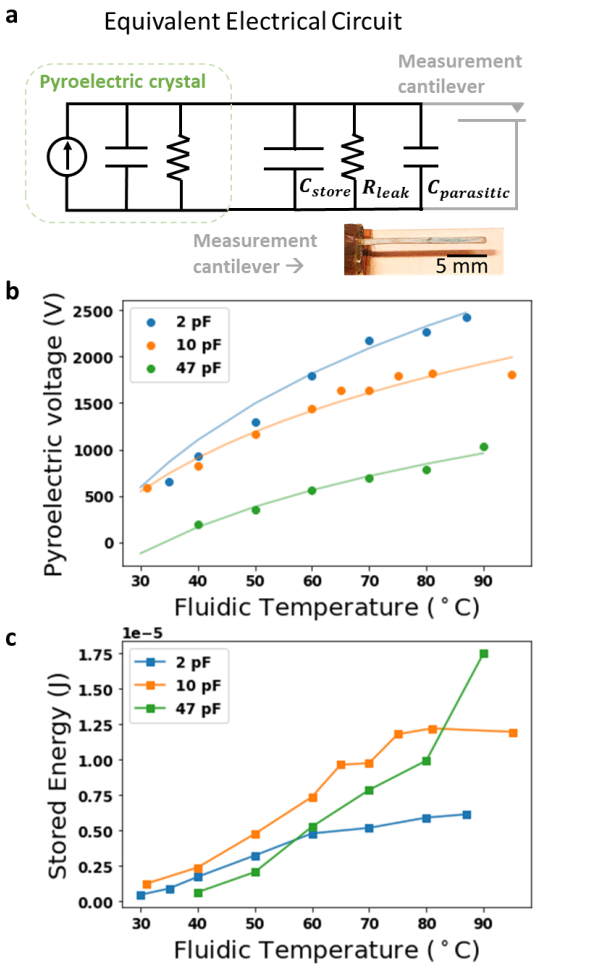

Figure 3. Electrical characterization of the pyroelectric system. ***a.*** *The electrical circuit of the system where a storage capacitor is connected to Lithium Niobate. A cantilever beam is used to measure voltage delivered to the capacitor.* ***b.*** *The maximum voltage delivered to three capacitors of 2, 10, and 47 pF. The solid lines represent exponential fitting of the data* ***c.*** *The maximum energy delivered to three capacitors.*

Three capacitors, with values of 2pF, 10pF, and 47 pF, were used as loads separately to store the voltage generated from pyroelectric crystals driven by the fluidic heat transfer. Figure 3b shows the voltage delivered to and the energy stored on three capacitors. The experiments were conducted at room temperature (25^0C). The larger a storage capacitor is, the more charges it needs to build the voltage up. A maximum voltage of 2.47 kV was achieved on a 2 pF storage capacitor at a fluidic temperature of 90^0C. Figure 3c shows the total energy $E = \frac{1}{2}CV^2$ stored on a capacitor. A maximum energy of 17.46 µJ was delivered to a 47 pF capacitor at 861 V.

Figure 4 shows an electrostatic actuator driven by the pyroelectric high voltage generator. The actuator consists of two pieces filled with arrays of pillars, such that it can have a high surface area-to-volume ratio that results in a high energy density [1]. A maximum displacement of 2.5 µm was achieved when actuated by the PHVG system, which corresponded to a voltage of 1033 V. This demonstration shows that PHVG system has successful fluidic control of robotic actuation.

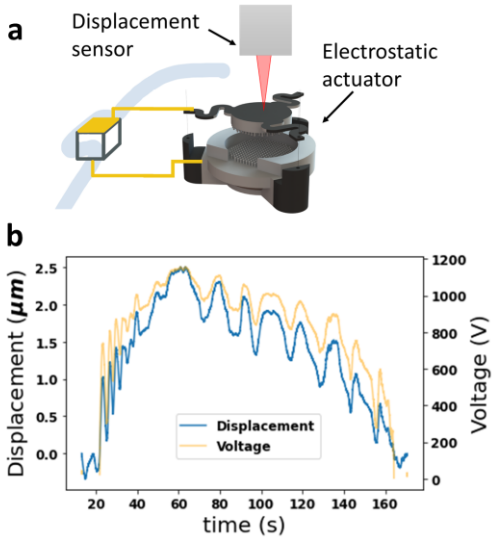

Figure 4. Actuation of a microrobot actuator. (a) A kilovolts electrostatic actuator was driven with the PHVG system. The displacement of the actuator was recorded with a laser sensor. (b) The displacement performance of the electrostatic actuator.

CONCLUSIONS

In this work, we demonstrated a distributed high voltage generation system utilizing the pyroelectric effect and mechanical switches. A fluidic channel was used to deliver thermal energy to several high voltage generators, which presents a pathway toward a microrobotic platform with multiple actuators and a single ambient heating/cooling source. This architecture not only allows kilovolts of voltage to be generated at multiple sites but is inherently designed to make use of extra thermal energy scavenged from the environment for sustainable operation.

Further efforts are needed to simplify the setup and shrink the SWaP of the system. For example, [18] provides an inspiration for utilizing the liquid-vapor phase transitions to induce temperature change and eliminating the use of an external pump. To drive actuators with large capacitance or high voltage requirements, multiple crystals can deliver the voltage to a single storage capacitor.

ACKNOWLEDGEMENTS

This work is supported by the NSF EFRI program (award number 1830924), and made use of the Cornell NanoScale Facility (NSF Grant NNCI-2025233) for device fabrication.

REFERENCES

[1] D. Ni, R. Heisser, B. Davaji, L. Ivy, R. Shepherd, and A. Lal, "Polymer interdigitated pillar electrostatic (PIPE) actuators," *Microsystems and Nanoengineering*, vol. 8, no. 1, 2022, doi: 10.1038/s41378-021-00328-0.

[2] X. Ji *et al.*, "An autonomous untethered fast soft robotic insect driven by low-voltage dielectric elastomer actuators," *Science Robotics*, vol. 4, no. 37, Dec. 2019, doi: 10.1126/SCIROBOTICS.AAZ6451/SUPPL_FILE/AAZ6451_SM.PDF.

[3] C. Chen, Y. Tang, H. Wang, and Y. Wang, "A review of fabrication options and power electronics for flapping-wing robotic insects," *International Journal of Advanced Robotic Systems*, vol. 10, pp. 779–786, 2013, doi: 10.5772/51186.

[4] M. Sitti, "Micro- and Nano-Scale Robotics".

[5] A.M. Flynn, "Gnat Robots", Accessed: Mar. 13, 2022.

[6] N. T. Jafferis, E. F. Helbling, M. Karpelson, and R. J. Wood, "Untethered flight of an insect-sized flapping-wing microscale aerial vehicle," *Nature 2019 570:7762*, vol. 570, no. 7762, pp. 491–495, Jun. 2019, doi: 10.1038/s41586-019-1322-0.

[7] M. Karpelson, "Power Electronics Design for a Flapping-Win Robotic Insect A dissertation presented," 2011.

[8] A. V. Carazo, "Piezoelectric Transformers: An Historical Review," *Actuators 2016, Vol. 5, Page 12*, vol. 5, no. 2, p. 12, Apr. 2016, doi: 10.3390/ACT5020012.

[9] J. Yang, "Piezoelectric transformer structural modeling - A review," *IEEE Transactions on Ultrasonics, Ferroelectrics, and Frequency Control*, vol. 54, no. 6, pp. 1154–1170, Jun. 2007, doi: 10.1109/TUFFC.2007.369.

[10] J. D. Boles, E. Ng, J. H. Lang, and D. J. Perreault, "DC-DC Converter Implementations Based on Piezoelectric Transformers," *IEEE Journal of Emerging and Selected Topics in Power Electronics*, pp. 1–1, Nov. 2021, doi: 10.1109/JESTPE.2021.3128595.

[11] B. Mabetha, Y. Li, B. L. Dobbins, and J. T. Stauth, "Analysis and implementation of a cm-scale switched capacitor converter for low power, kilovolt-range applications," *Conference Proceedings - APEC*, pp. 208–213, Jun. 2021, doi: 10.1109/APEC42165.2021.9487330.

[12] D. Kuang-Chen Liu, J. Friend Ã, and L. Yeo, "A brief review of actuation at the micro-scale using electrostatics, electromagnetics and piezoelectric ultrasonics", doi: 10.1250/ast.31.115.

[13] E. L. Horsley, M. P. Foster, and D. A. Stone, "State-of-the-art piezoelectric transformer technology," *EPE*, 2007, doi: 10.1109/EPE.2007.4417637.

[14] D. Ni, K. B. Vinayakumar, V. Pinrod, and A. Lal, "Multi Kilovolt Lithium Niobate Pyroelectric Cantilever Switched Power Supply," *Proceedings of the IEEE International Conference on Micro Electro Mechanical Systems (MEMS)*, vol. 2019-Janua, no. January, pp. 970–973, 2019, doi: 10.1109/MEMSYS.2019.8870799.

[15] D. Ni, B. Davaji, R. Shepherd, and A. Lal, "3D Printed Pyroelectric Lithium-Niobate High Voltages Source with Pull-in Regulated Output," *Proceedings of the IEEE International Conference on Micro Electro Mechanical Systems (MEMS)*, vol. 2020-Janua, pp. 586–589, 2020, doi: 10.1109/MEMS46641.2020.9056438.

[16] D. Ni, V. Gund, and A. Lal, "PCB Integrated Linbo3 Pyroelectric High Voltage Supply with Electrostatic Switch Regulator," *21st International Conference on Solid-State Sensors, Actuators and Microsystems, TRANSDUCERS 2021*, pp. 968–971, Jun. 2021, doi: 10.1109/TRANSDUCERS50396.2021.9495642.

[17] Z. Xing, J. Zhang, D. McCoul, Y. Cui, L. Sun, and J. Zhao, "A Super-Lightweight and Soft Manipulator Driven by Dielectric Elastomers," *Soft Robotics*, vol. 7, no. 4, pp. 512–520, Aug. 2020, doi: 10.1089/SORO.2018.0134/ASSET/IMAGES/LARGE/SORO.2018.0134_FIGURE10.JPEG.

[18] D. Zabek, J. Taylor, V. Ayel, Y. Bertin, C. Romestant, and C. R. Bowen, "A novel pyroelectric generator utilising naturally driven temperature fluctuations from oscillating heat pipes for waste heat recovery and thermal energy harvesting," *Journal of Applied Physics*, vol. 120, no. 2, p. 024505, Jul. 2016, doi: 10.1063/1.4958338.

CONTACT

*Di Ni; dn273@cornell.edu

A HIGH-Q SOLID DISK BAW GYROSCOPE IN MONOCRYSTALLINE 4H SILICON-CARBIDE WITH SUB-PPM AS-BORN FREQUENCY SPLIT

Zhenming Liu, Ardalan Lotfi, Michael P. Hardin, and Farrokh Ayazi
Georgia Institute of Technology, Atlanta, GA, USA

ABSTRACT

This paper demonstrates, for the first time, a solid disk capacitive bulk-acoustic wave (BAW) gyroscope in monocrystalline 4H-SiC, with a promising angle random walk of 0.03°/√h, fabricated at wafer level using DRIE of a bonded SiC-on-Insulator (SiCOI) substrate. The 3MHz gyroscope operates in m=3 elliptical mode with a very small as-born frequency split of sub-ppm owing to the excellent in-plane isotropic lattice of 4H-SiC. Statistical data of resonator characterization across the 4-inch SiCOI wafer is reported, showing consistently small frequency splits and high *Q* factors, uncommon in Si substrates. The cross-coupling between two gyroscopic modes is compensated via electrostatic spring softening, while the 3mm disk resonator is driven to >300nm amplitude, paving the way towards the development of high-performance SiC BAW gyroscopes.

KEYWORDS

Silicon carbide resonator, *Q* factor, MEMS gyroscope, novel substrate for MEMS resonator

INTRODUCTION

Over the past decades, high-performance gyroscopes for inertial navigation have drawn much attention owing to the growing market in autonomous vehicles, indoor navigation, and dead reckoning [1]. Navigation grade gyroscopes require vibration immunity, large dynamic range, high signal-to-noise-ratio (SNR), and small bias instability, making traditional low-frequency large-mass tuning fork gyroscopes unsuitable. Instead, bulk acoustic wave (BAW) resonant gyroscopes with high mechanical stiffness operating in the megahertz range have been proven to be a promising design to meet the above requirements [2~5]. Due to their resonant (i.e. mode-matched) operation, where the frequencies of two gyroscopic modes overlap, the scale factor and SNR of a BAW gyroscope are amplified by the mechanical *Q* factor. To date, the BAW resonators in single crystalline silicon substrates have already achieved *Q* factors near its physical limit set by the Akhiezer damping [6,7]. Earlier this year, Qualtre Panasonic reported on a capacitive BAW gyroscope in (100) silicon with a bias instability of 0.25°/hr operating in closed-loop configuration that extended the device bandwidth to greater than 200Hz [8].

Looking beyond silicon, monocrystalline 4H silicon carbide-on-insulator (4H-SiCOI) substrate is a promising platform for the implementation of inertial-grade MEMS gyroscopes owing to SiC's exceptionally high Akhiezer limit which dwarfs that of Si by ~30× [6,7,9]. Moreover, the hexagonal crystal symmetry of 4H-SiC is amenable to excellent mode degeneracy between the m=3 BAW gyroscopic elliptical modes in disk resonators. Some recent works have shown that m=3 modes of capacitive disk resonators in 4H-SiC exhibit ultra-low dissipation levels ($Q > 3\times10^6$), and as-born frequency splits near 13 ppm [10,11]. In fact, mechanical *Q*'s up to 20×10^6 have been reported in 4H-SiC disk and lamé mode resonators [11]. However, SiC is a hard to etch material, and its precision DRIE with high aspect ratio had not been demonstrated until very recently [12~15], at odds with electrostatic tuning, which usually require small capacitive gap for effective mode matching and alignment of resonant gyroscopes. This paper will show the great potential of the 4H-SiC substrate for gyroscope application. In particular, with statistical data of small as-born mode split in disk resonators fabricated at wafer-level, mode-matching, including quadrature cancelation, was demonstrated despite the relatively large capacitive gaps. For the first time, gyroscope performance of 4H-SiC BAW disk resonator with DRIE capacitive transducers is reported, paving the way towards navigation-grade performance and beyond using SiC BAW gyroscopes.

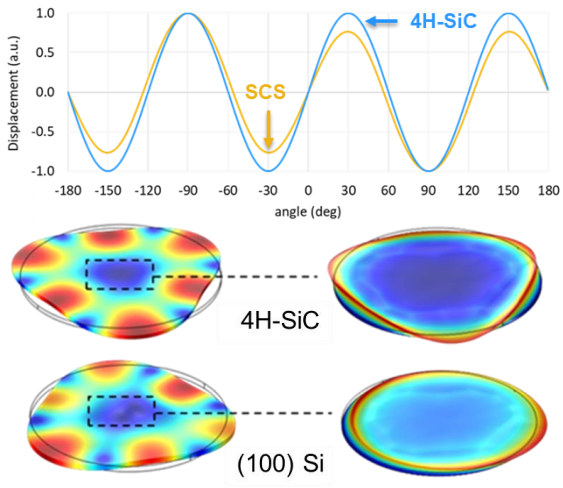

Figure 1: (Top) All antinodes of m=3 mode in 4H-SiC have equal displacement as opposed to the non-uniform mode shape in (100) Si. (Bottom) The central anchor for m=3 mode is symmetrically balanced in 4H-SiC disk while having a net in-plane displacement in (100) Si disk.

DESIGN AND METHOD

BAW disk gyroscope design in 4H-SiC

The elliptical modes in disk resonators are commonly used for capacitive BAW gyroscopes due to their mode degeneracy and high gyroscopic coupling factors [2~7]. In (100) single-crystalline silicon (SCS), the young's modulus is 90° symmetric, resulting in the same angular separation as between the two m=3 modes. However, due to the asymmetry in other directions of SCS lattice, the modal displacements at each of the anti-nodes are different, resulting in a net displacement at the center node, where the resonator will be anchored at. Such displacement will cause a strain energy coupling between the resonator and substrate, leading to the acoustic energy dissipating into the handle layer and significantly reducing Q_{anchor}. More importantly, the substrate coupling makes the resonator sensitive to the mounting conditions and compromises the mode degeneracy. Process variations like anchoring misalignment can introduce excessive stiffness and damping cross-coupling between the two elliptical modes. Hence, anchoring decoupling is necessary for a reliable SCS BAW gyroscope and is typically done by adding a decoupling network near the center node to eliminate stress at the anchor, but at the cost of introducing excessive thermal elastic damping (TED) [3,4]. Though for silicon, the achievable *Q* is limited by the relatively low intrinsic Akhiezer loss before the TED becomes dominant.

978-1-940470-04-7/HH2022/$25©2022TRF
DOI 10.31438/trf.hh2022.17

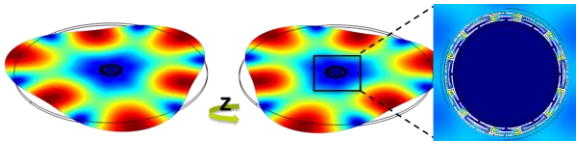

Figure 2: m=3 elliptical mode in 4H-SiC resonator, showing the central decoupling network design.

On the contrary to Si, 4H-SiC possesses hexagonal crystal symmetry. The two m=3 modes have uniform modal displace at all the anti-node with a strain equilibrium at the center anchoring and ideally zero substrate coupling (Figure 1). While a decoupling network is no longer required, a 4H-SiC BAW gyroscope can potentially be designed with a solid disk resonator with minimum TED and eventually reach the Akhiezer limit of $f \cdot Q = 6\times10^{14}$ Hz.

The ultra-high Q factor significantly reduces the motional impedance, and thus, even with a relatively large gap size, a 4H-SiC BAW resonator can be effectively actuated electrostatically. In addition, large DC voltages can be applied for polarization, which further guarantees the low motional impedance and high electrical scale factor. While the gap size limits the linear displacement range in capacitive parallel plate, it is favorable for a 4H-SiC BAW gyroscope to have a moderate gap to reach a higher mechanical scale factor with a maximum driven amplitude near a few hundred nanometers. Because of the high young's modulus of SiC, the mechanical linearity range can support such a large driving amplitude.

However, the challenge for high stiffness BAW gyroscopes in using a wider capacitive gap is the effective tunning range. The advantage of ultra-high Q in 4H-SiC is only preserved when the two gyroscopic modes are mode matched. To make sure the two m=3 modes can overlap with a limited tunning range, one must design the gyroscope taking into account the process variations that may compromise the mode degeneracy. Therefore, in this work, despite a center decoupling network not being necessary for high Q_{acnhor}, we still put a folded beam network at the center of a 3mm diameter disk resonator to minimize the as-born mode split from the potential process imperfection. The gyroscope mode shape and displacement at the decoupling beam is shown in Figure 2. While a similar design has proven effective in silicon substrate [4], the design is more robust when implemented in 4H-SiC, owing to the symmetric mode shapes. Table 1 highlights the simulated frequency split in 4H-SiC compared to (100) SCS due to common process variations. 24 electrodes with an effective gap size near 2.7μm are uniformly placed around the disk resonator for capacitive transduction and electrostatic tunning. The loaded Q_{TED} is expected to be 9×10^6 with moderate sidewall roughness, and overall Q should remain higher than the Akheizer limit of Si resonators.

Fabrication

The resonators are fabricated on a 4-inch SiCOI substrate with a device layer thickness of 40μm following a 3-mask process similar to that described in [14]. The SiC device layer is etched through at the wafer level using a Synapse™ module by SPTS, a high-density plasma etch tool designed to etch strongly bonded materials. The

Table 1. Frequency split simulation of m=3 BAW disk gyro in (100) Si and 4H-SiC with common process variations

	Frequency split	
Process variation	**(100) Si**	**4H-SiC**
Disk ovalness: 1%	251.91	0.23
Non-vertical trench: 1°	0.65	0.13
Crystal misalignment: 1°	35.77	0.25

Table 2. As born frequency splits and Q factors measured from 10 SiC disk resonators randomly picked across wafer

Device	Δf [ppm]	Q_1 [Million]	Q_2 [Million]
1	0.66	1.803	1.719
2	0.33	1.447	1.531
3	8.3	1.863	1.660
4	3.1	1.492	1.278
5	13.6	2.173	2.008
6	5.2	1.786	1.744
7	2.3	1.356	1.132
8	7.3	1.875	1.368
9	7.3	1.510	1.228
10	6.9	1.633	1.537
Average	***5***	***1.694***	***1.520***

SiC DRIE recipe was developed and carried out at SPTS technologies, with the detailed recipe published in [13,15].

RESULTS AND DISCUSSIONS

Resonator characterization

Over 10 disk resonators across the wafer were characterized and summarized in Table 2, and the as-born frequency response of the resonator showing $Q > 2$M is shown in figure 3. The average as-born frequency split and Q factors are 5ppm and 1.6 million, with good consistency across the wafer. The resonator Q factor is limited by the thermoelastic damping in the decoupling network and surface roughness from the process imperfection, including damage at the top of the SiC DRIE trench due to insufficient mask thickness and some residual surface roughness from grinding (Figure 4).

The mechanical noise equivalent rate (MNEΩ) of a MEMS gyro is inversely proportional to its driving amplitude. The large gaps provided a linear transduction range for studying the 4H-SiC

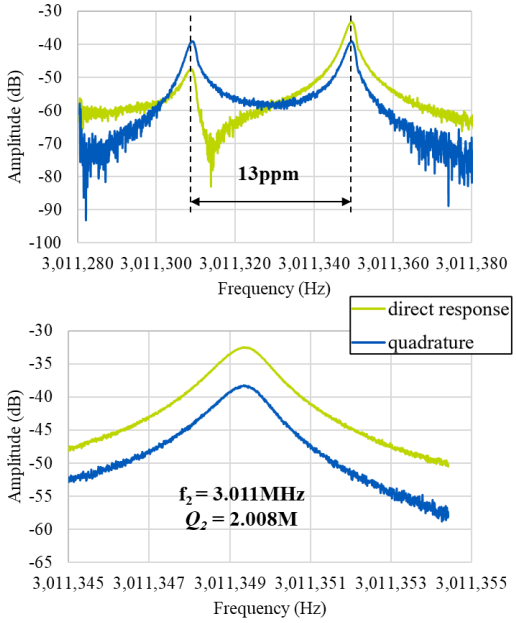

Figure 3: (Top) Large span frequency response of the disk resonator (device 5 from table 2) with highest Q and (Bottom) zoom-in measurement showing Q>2 million. It also shows the worst as-born frequency split in 4H-SiC (13ppm) which is still better than SCS disk resonator with similar design.

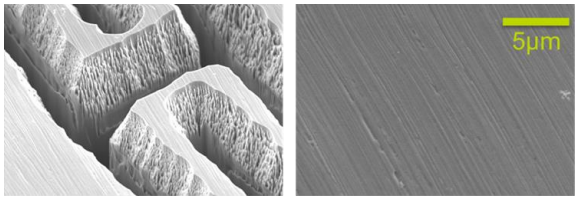

Figure 4: (Left) Roughness at the top of SiC DRIE trench. (Right) Grinding striations on the surface of SiCOI wafer.

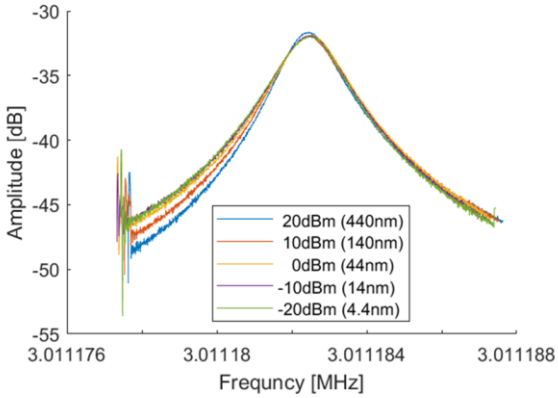

Figure 5: The resonant peak of m=3 mode remains mostly linear with actuation powers up to 20dBm.

resonator linearity under large drive amplitudes. Figure 5 shows the m=3 mode frequency response of a device versus input power. The 4H-SiC resonator is linearly driven up to 440nm, limited by the output supply. The corresponding displacement amplitudes are obtained from FEA simulation.

Gyroscope performance

Two disk resonators with sub-ppm frequency splits were further operated as gyroscopes with similar results. Figure 6 shows one of the gyroscopes wire-bonded on a test circuit board. The two m=3 mode peaks overlap each other within the -3dB bandwidth (Figure 7). Owing to the small as-born mismatch, complete mode matching, including quadrature nulling, can be achieved via

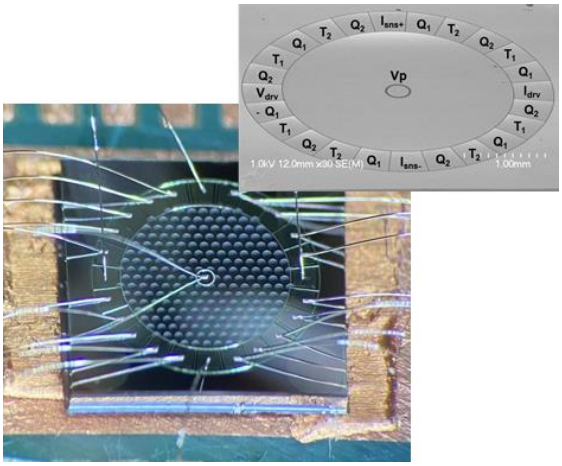

Figure 6: A diced 4H-SiC BAW gyroscope mounted on PCB with all 24 electrodes and center post wire-bonded. The perforated handle layer release pattern can be seen through the transparent SiC device layer. The resonator SEM is shown at inset with electrode configuration labeled.

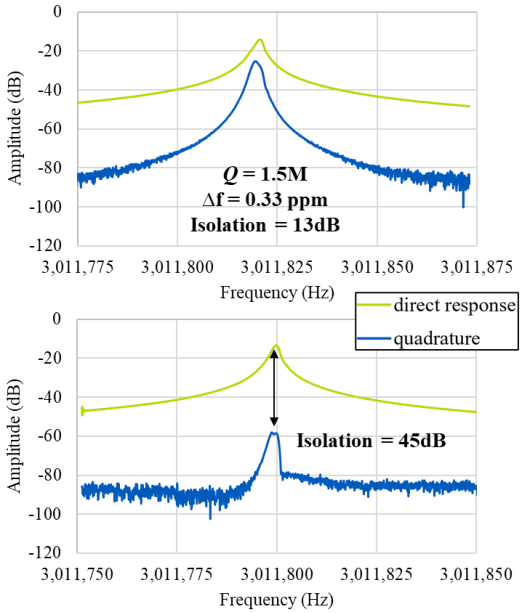

Figure 7: (Top) As-born frequency response of a resonator with 0.33ppm frequency split and 13dB cross-mode isolation (quadrature). (Bottom) The isolation is improved to 45dB with 46V DC tuning voltage applied for quadrature nulling.

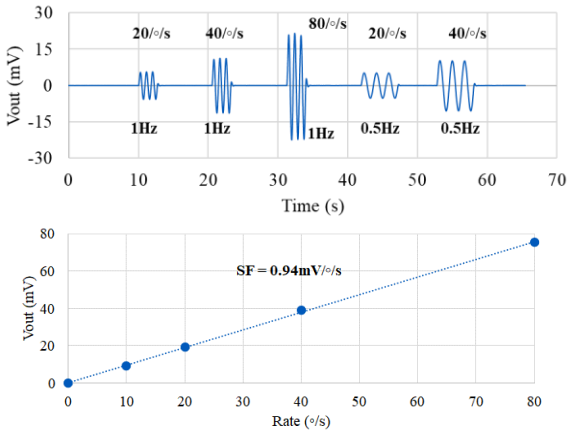

Figure 8: (Top) Output response to different rotation rates at two frequencies in 1 minute. (Bottom) A linear sensitivity of 0.94mV/°/s is measured with 350nm driving amplitude.

electrostatic tuning with 2.7µm gaps. The mode-matched 4H-SiC BAW gyro response was recorded over 1 minute without any noticeable drift, and a linear scale factor of 0.97mV/°/s is measured (Figure 8). The Allan deviation of the device was measured under different driving amplitudes (Figure 9). The lowest angle random walk of 0.03°/√h and BI of 11°/h reported here are from resonator driven with a large amplitude of 350nm.

Towards navigation grade 4H-SiC BAW gyro

Due to the high tuning voltages required, mode matching and alignment is currently achieved in an open-loop configuration, while the best BI from state of the art silicon BAW gyros are recorded in closed-loop dynamic quadrature tunning [6]. As such, BI of the 4H-SiC gyroscope can be greatly improved with a similar closed-loop quadrature configuration (future work).

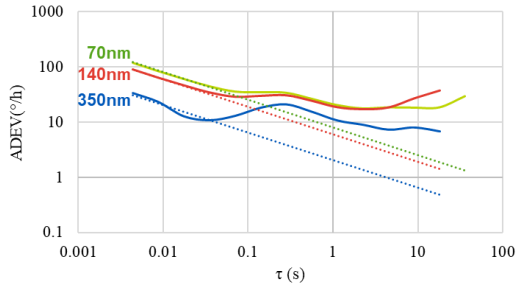

Figure 9: Measured Allan deviation of a SiC BAW gyroscope, the angle random walk (ARW) with -0.5 slope linear fit is measured to be 0.13°/√h, 0.09°/√h, and 0.03°/√h with 70/140/350nm excitation amplitude for the 3mm disk.

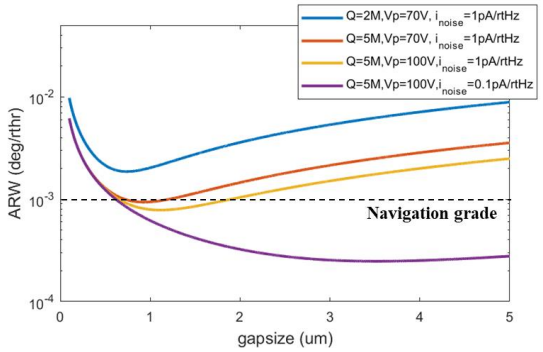

Figure 10: The projected ARW of a 3MHz 4H-SiC BAW disk resonant gyroscope with improved Q, DC bias voltage, and circuit noise, exceeding the navigation grade when maximally driven to a tenth of its capacitive gap size.

It is also worth noting that as the driving power increases, flicker noise becomes more dominant in the overall BI, as the input-referred noise scales with the AC actuation voltage. While the gyroscope is maximumly driven to minimize the mechanical noise equivalent rate, a high-performance gyroscope requires the electrical noise equivalent rate (ENEΩ) to be in a comparable range. This can be done by improving the input-referred noise of the interfacing circuit, increasing the polarization DC voltage, and further improving the *Q* factor. The demonstrated *Q* is compromised by the trench damage at the decoupling network, which induced excessive TED; there is still a lot of room for *Q* improvement before reaching the Akhiezer limit. While the total noise is a function of gap size (and driving amplitude), Figure 10 predicts the expected noise performance under different conditions.

CONCLUSION

We reported the gyroscope performance of capacitive BAW disk resonators fabricated at wafer level on 4H-SiC on insulator substrate for the first time. The 4H-SiC disk resonators consistently show small frequency splits between the two gyroscopic m=3 elliptical modes, which relaxes the electrostatic tunning requirement and allows for complete mode matching even with a relatively large 2.7μm transduction gap. The average *Q* of 1.5 million demonstrated in this work is challenging to achieve in a similar design in (100) Si and can be further improved by improving the fabrication process. The large transduction gap size defined by DRIE allows a large linear actuation range for higher scale factor and SNR, demonstrating an ARW of 0.03°/√h. The measured bias instability is relatively large, which is attributed to lack of closed-loop quadrature nulling and un-optimized electronics, expected to improve substantially.

ACKNOWLEDGEMENTS

This material is based on research sponsored by Army Research Laboratory under agreement number W911NF-19-2-0345. The US Government is authorized to reproduce and distribute reprints for Government purposes notwithstanding any copyright notation thereon. The views and conclusions contained herein are those of the authors and should not be interpreted as necessarily representing the official policies or endorsements, either expressed or implied, of Army Research Laboratory (ARL) or the US Government. The authors wish to thank staff at SPTS technologies for DRIE of SiCOI substrate.

REFERENCES

[1] F. Ayazi, "Multi-DOF inertial MEMS: From gaming to dead reckoning," in 2011 16th International Solid-State Sensors, Actuators and Microsystems Conference, Jun. 2011, pp. 2805–2808.

[2] H. Johari et al., "Capacitive Bulk Acoustic Wave Silicon Disk Gyroscopes," IEDM, 2006.

[3] D. E. Serrano et al., "Substrate-decoupled, bulk-acoustic wave gyroscopes: Design and evaluation of next-generation environmentally robust devices," Micro. & Nano., vol. 2, no. 1, p. 16015, Dec. 2016.

[4] H. Wen et al., "A Hermetically-Sealed 2.9MHz N=3 Disk BAW Gyroscope with Sub-Degree-Per-Hour Bias Instability," IEEE MEMS, 2020, pp. 741–744.

[5] M. Parajuli et al., "Sub-Deg-per-Hour Edge-Anchored Bulk Acoustic Wave Micromachined Disk Gyroscope, JMEMS, vol. 30, no. 6, pp. 836-842, 2021

[6] J. Rodriguez et al., "Direct Detection of Akhiezer Damping in a Silicon MEMS Resonator," Scientific Reports, vol. 9, no. 1, p.2244, Dec. 2019

[7] Daruwalla et al., "Epitaxially-grown thick polysilicon for BAW disk resonator gyroscopes with very low dissipation," in 2018 IEEE MEMS, 2018, pp. 1008–1011.

[8] D. E. Serrano et al., "0.25 deg/h Closed-Loop Bulk Acoustic Wave Gyroscope" IEEE Inertial, 2022

[9] F. Ayazi et al., "Energy dissipation in micromechanical resonators," in Proc. SPIE 2011, vol. 8031, p. 803119.

[10] B. Hamelin et al., "Monocrystalline Silicon Carbide Disk Resonators on Phononic Crystals with Ultra-Low Dissipation Bulk Acoustic Wave Modes.," Sci Rep, vol. 9, no. 1, p. 18698, Dec. 2019

[11] J. Yang et al., "Capacitive Lamé Mode Resonators in 65 μm Thick Monocrystalline Silicon Carbide with Q-Factors Exceeding 20 Million," IEEE MEMS, 2020, pp. 226–229.

[12] F. Ayazi et al., "(Invited) Nano-Precision Deep Reactive Ion Etching of Monocrystalline 4H-SiCOI for Bulk Acoustic Wave Resonators with Ultra-Low Dissipation," ECS Transactions, vol. 97, no. 4, pp. 3–13, 2020

[13] A. Barker et al., "Advances in back-side via etching of SiC for GaN," Solid State Technology, vol. 56, pp. 20–23, Feb. 2013.

[14] Hamelin et al., "Monocrystalline 4H Silicon Carbide-on-Insulator Substrates for Nav-Grade Planar BAW Gyroscopes," 2021 IEEE Inertial 2021, pp. 1–4.

[15] A. Lotfi et al., "Wafer-Level High-Aspect-Ratio Deep Reactive Ion Etching of 4H-Silicon Carbide On Insulator Substrates," Solid-State, Actuators, and Microsystems Workshop, 2022

CONTACT

*Z. Liu, zhenming_liu@gatech.edu
*F. Ayazi , ayazi@gatech.edu

BIOLOGY-INSPIRED INTELLIGENCE IN THE DESIGN, CONTROL, AND POWER SYSTEMS OF INSECT-SIZED FLYING ROBOTS

Sawyer B. Fuller[1*]
[1]Department of Mechanical Engineering, University of Washington, Seattle, Washington, USA

ABSTRACT

A technology grand challenge for micro-systems that weigh far below a gram is giving them mobility and autonomy. We posit that creating intelligent, self-contained system so will require a confluence of biological inspiration, a formalized co-design process for all of their elements ranging from controllers to power sources to sensors, and a fabrication process that allows for rapid design iteration.

KEYWORDS

Microrobotics, flying insect robotics, biology-inspired robotics, autonomous systems

This paper is about a technology grand challenge for micro-sized systems that are well below a gram: making them mobile and autonomous. Yet the potential is enormous. Unlike their larger autonomous robotic brethren, micro-robots can operate in more confined spaces, in close proximity to humans without safety hazard, and potentially operate persistently using sources of energy readily available in the environment, such as light, heat, or radiofrequency sources, that are too minute for larger robots. Despite these advantages and countless emerging applications in agriculture, industrial inspection, and even low-launch cost space missions, such systems have not yet been realized. Sub-gram robots have not shown any significant degree of autonomy, that is, ability to sense and respond intelligently to the environment [1].

Lack of autonomy in small devices can largely be attributed to two key causes. The first is simply the challenge to miniaturize the mass and power consumption of the sensor suite. And the second is the need to re-consider many of the technologies that have been successful in larger robotic systems in light of the changed physics associated with small scale. As scale reduces, the dominant effect of many important physical processes changes, leading to so-called "phase transitions" in which a substantially different technological approach suddenly becomes viable as the size scale of the system reduces.

The solutions entail three key technical competencies.

The first is the ability to look closely at and analyze the solutions used by biology. Biology is, as a rule, not beholden to preconceptions of how the world ought to work; instead, it is able, through evolution, to perform a more exhaustive exploration of the solution space than a human might consider. That said, it is important to also observe biology with a keen eye, because many of its characteristics are driven by considerations that are distinct from those of the micro-roboticist. Almost all materials used in biology must be solution-processed in water, restricting the materials set. To date, at least, it is hard to imagine a need for sexual reproduction in robots. And communication by nerve cells is much slower than electrical conductors. Biology could never have realized a jet engine, a microprocessor, or even a wheel, for that matter. Nevertheless, it still far exceeds man-made systems in many important areas, most notably in self-assembly, evolution and learning, and dynamic and robust motor control. It is these latter elements that serve as the most important inspiration for current roboticists.

The second is an ability, to a larger extent than has been necessary on larger robots, for a process to co-design the robotic system to balance conflicting needs in all of its facets, from mechanical design, to choice of sensors, to control system, to energy storage and collection. These considerations of course are primarily driven by the task the robot is to pursue. Only by doing so can we hope to achieve the mechanical and sensor efficiency that will be needed for tiny autonomous systems to operate for a significant fraction of the time.

And the third is a manufacturing process to create the mechanical and electrical systems of the microrobot. It must be relatively fast, to allow for what inevitably turns out to be many physical iterations of mechanical and electrical systems. And the ability to incorporate a range of materials including high-performance composites, can be an advantage.

A discussion of some recent advances in the area of flying microrobots follows, including some by the Autonomous Insect Robotics Laboratory at the University of Washington that I direct.

The first comes in the area of manufacturing: early architects of robotic insects recognized that scaling physics did not favor electromagnetic motors. This led to a focus on creating a flexure-based manufacturing method known as Smart Composite Microstructures (SCM) [2] and the use of muscle-like reciprocating actuators powered by electrostatic forces that scale down more favorably in terms of efficiency and power density than magnetic coils [3]. In biology, a phase transition can be observed in the flight apparatus of small flying animals: the very smallest, including flies, bees, and hummingbirds, flap continuously rather than gliding. This can be attributed to the increasing relative effect of viscosity as scale reduces, which eventually results in a very low glide ratio and therefore inefficient gliding flight [4]. The confluence of flexure-based manufacturing, electrostatic actuation, and flapping-wing flight led to the first lift > weight on a sub-gram flying device [5] and subsequent controlled flight [6].

The sensor systems of micro-robotic aircraft are also beholden to scaling physics. One aspect we observe in small flying animals such as the fruit fly is a reliance on a multiplicity of sensors, each of which is by itself limited, but when used in conjunction can provide for high performance. In forward flight, fruit flies have a very low-latency sense of their airspeed, but it is corrupted by the ubiquitous presence of air currents, which confound any ability to measure ground speed. They additionally carry large compound eyes that, by observing how the visual scenery moves by, that is, using "optic flow," can provide a more or less absolute estimate of ground speed, but with significant added "noise" uncertainty. Flies' solution is simply to add together the effects of these two feedback terms; the result is a flight control system that is both high bandwidth and able to compensate for wind disturbances [7]. We have recently begun to realize a flight control architecture inspired this finding that is able to operate on the conceptual mass and power budget for a controller even as the robot scales down to on the order of 10 mg [8].

The last element is how to weigh different considerations in the co-design of complete systems. Recent theoretical work has begun to realize a framework that can place these considerations together into a finite set of "realizations" of different controller, actuator, and sensor types so that pareto fronts of equal competence can be identified [9]. These can be used to, for

Copyright retained by Authors

example, identify optimal choices from a commercial perspective.

The unifying theme is a notion of biology-inspired "intelligence" in the design of all of the interconnected elements of the microrobotic system. It is remarkable how biology, through evolution, is able to simultaneously and in concert adapt the entire system, from its mechanics, sensing, and control in a way that improves its functional fitness. We as microroboticists can only hope to some day begin to do the same.

ACKNOWLEDGEMENTS

This work is partially funded by the National Science Foundation (award# FRR-2054850).

REFERENCES

[1] R. St. Pierre and S.Bergbreiter, "Toward Autonomy in Sub-Gram Terrestrial Robots," *Annual Review of Control, Robotics, and Autonomous Systems*, Vol. 2, No. 1 (2019), p. 231-252.

[2] A. M. Hoover, E. Steltz, and R.S. Fearing, "RoACH: An autonomous 2.4 g crawling hexapod robot," *IEEE/RSJ International Conference on Intelligent Robots and Systems* (2008), pp. 26–33.

A.B. Author, C.D. Author, and E.F. Author, "Title of Article, Enclosed in Quotation Marks", *Thin Solid Films Journal*, 206, 94 (1992).

[3] W. S. N. Trimmer, "Microbots and Micromechanical Systems," *Sensors and Actuators*, Vol. 19 (1989), p. 267-287.

[4] S. F. Hoerner, "Fluid-dynamic drag: practical information on aerodynamic drag and hydrodynamic resistance," Hoerner Fluid Dynamics, Midland Park, NJ, 1965.

[5] R. J. Wood, "The First Takeoff of a Biologically Inspired At-Scale Robotic Insect," *IEEE Trans. Robot*, Vol. 24, No. 2 (2008), p. 341–347.

[6] K. Y. Ma, P. Chirarattananon, S. B. Fuller, and R. J. Wood, "Controlled flight of a biologically inspired, insect-scale robot," *Science*, Vol. 340, No. 6132 (2013), p. 603–607.

[7] S. B. Fuller, A. D. Straw, M. Peek, R. M. Murray, and M. H. Dickinson, "Flying Drosophila stabilize their vision-based velocity controller by sensing wind with their antennae," *Proc. Nat. Acad. Sci.* (2014) Vol. 111, No. 13, pp. E1182–1191.

[8] S. B. Fuller, Z. Yu, and Y. Talwekar, "Visual flight control for 10 mg gnat robots," (*in prep*.)

[9] A. Censi, "A Mathematical Theory of co-design," *arXiv preprint*, arXiv:1512.08055.

[10] G. Zardini, A. Censi, E. Frazzoli, "Co-design of autonomous systems: From hardware selection to control synthesis," *European Control Conference (ECC)* (2021), pp. 682–689.

CONTACT

*Sawyer B. Fuller: minster@uw.edu

MINIATURIZED CAPSULE SYSTEM FOR HYDROGEN SULFIDE DETECTION IN THE GASTROINTESTINAL TRACT

Justin M. Stine[1,2,4], Santiago Botasini[2,4], Luke A. Beardslee[2], Joshua A. Levy[2,3,4], and Reza Ghodssi[1,2,4]*
[1]Department of Electrical and Computer Engineering, [2]Institute for Systems Research,
[3]Department of Materials Science and Engineering, and [4]Robert E. Fischell Institute for Biomedical Devices,
University of Maryland, College Park, Maryland, USA

ABSTRACT

This work presents an ingestible capsule platform for real-time, wireless detection of hydrogen sulfide (H_2S) as a biomarker of inflammation in the gastrointestinal (GI) tract. The design integrates an analog front-end (AFE) potentiostat and Bluetooth Low Energy (BLE) microcontroller on a flex-rigid printed circuit board (PCB) with a miniaturized electrochemical H_2S sensor to perform amperometric measurements with the desired capsule form factor. Packaged within a 3D-printed shell, the capsule successfully monitors physiological H_2S concentrations within a linear range of 3.7–12 ppm with sensitivity of 0.17 µA/ppm, providing a framework for non-invasive, on-site monitoring of gaseous biomarkers in the GI tract.

KEYWORDS

Ingestible Capsule, Hydrogen Sulfide, Gastrointestinal Tract

INTRODUCTION

Digestive diseases, such as inflammatory bowel disease (IBD), have been intimately linked with alterations of the gut microbiome and are a chronic source of intestinal inflammation; however, the underlying etiology is unclear [1]. Understanding the interactions between intestinal microbiota and epithelial tissue dysregulation would inform disease diagnosis and treatment. Transient gaseous molecules, such as H_2S, nitric oxide (NO), and hydrogen peroxide (H_2O_2), are key mediators of inflammation within the GI tract, and have been implicated as potential biomarkers for disease screening [2]. These biomarkers are short-lived, making it difficult to accurately detect their concentration in the body [3]. Thus, non-invasive approaches to accurately determine the role of the gut microbiome in the development of GI disorders are needed.

Of the inflammatory markers mentioned, endogenous H_2S – produced by sulfate-reducing bacteria (SRB) in the intestinal microbiome – is involved in both pro- and anti-inflammatory processes, providing a non-specific marker to diagnose GI inflammation [4]. However, current methods for monitoring gut microbial H_2S production in real-time are lacking. Previous studies have measured H_2S concentrations in flatus, which can be highly invasive, and via stool analysis, which lack the temporal and spatial resolution to accurately represent the current state of the intestines [5]. Breath testing also is not sufficient, as little gut microbial-produced H_2S reaches the breath due to its short circulating half-life and measurements are susceptible to interference from H_2S produced by oral microbes, which are indistinguishable [6]. Therefore, miniaturized systems capable of real-time and localized monitoring of bacteria-derived inflammatory markers *in situ* are essential to detect transient markers.

Existing endoscopic surveillance methods rely on direct visualization of the mucosa and are unable to detect molecular biomarkers of microscopic disease [7]. Recently, endoscopic capsules, such as the PillCam SB [8] and Atmo Capsule [9], have been utilized to non-invasively access the small bowel, enabling visual inspection of the GI tract and local measurement of physiological analytes (e.g., Atmo Capsule: oxygen, temperature, hydrogen, and carbon dioxide). However, there are currently no reported ingestible capsules that detect H_2S. We previously reported both electrochemical H_2S sensing and bioimpedance sensing on the benchtop using existing commercial off-the-shelf (COTS) components at MicroTAS 2021 [10], highlighting their potential utility to monitor H_2S as a marker of inflammation.

In this work, we have significantly advanced the PCB electronics design and modified the COTS H_2S sensor from [10] to enable integration into a miniaturized, wireless capsule platform. Furthermore, a 3D-printed package was made using digital light processing (DLP) to achieve a capsule form factor of 15 x 34 mm, which is compatible for studies in porcine animal models. The current capsule system was deployed in a custom gas testing set-up for evaluation of H_2S concentration. Overall, this work progresses the current state-of-the-art for wireless, ingestible capsule technologies and has the potential to improve the precision of localized sensing approaches for GI diagnostics.

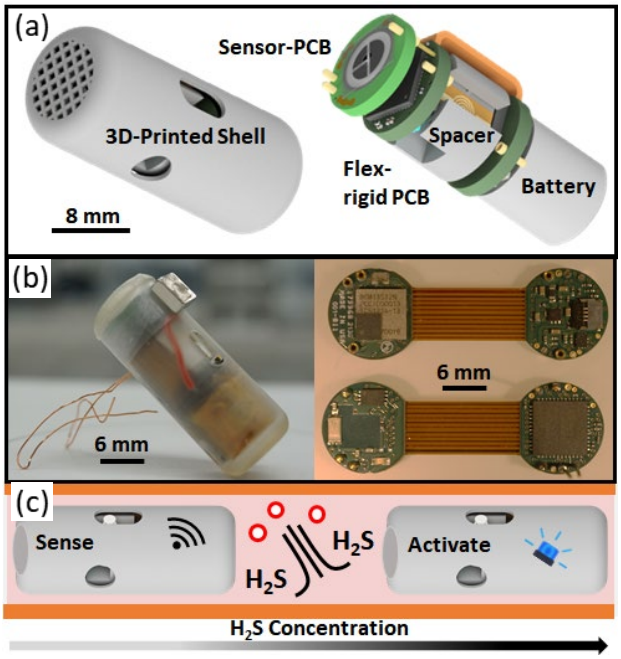

Figure 1: Overview of the ingestible capsule platform for real-time detection of H_2S. (a) Rendered image and (b) photographs showing the flex-rigid PCB encapsulated inside a DLP 3D-printed shell (dimensions: 15 x 34 mm). (c) Operational scheme of the capsule, where increasing H_2S concentration will activate a prompt (blue LED) if threshold H_2S level is reached.

DESIGN OF CAPSULE SYSTEM

Figure 1a shows a schematic of the capsule system comprised of a flex-rigid PCB, a modified electrochemical H_2S sensor-PCB, and a 3D-printed spacer encapsulated in a DLP 3D-printed shell. Similarly to [11], a combination of rigid and flexible substrates

978-1-940470-04-7/HH2022/$25©2022TRF
DOI 10.31438/trf.hh2022.18

Solid-State Sensors, Actuators, and Microsystems Workshop
Hilton Head Island, South Carolina, June 5-9, 2022

allows the electronics to bend with the battery (Figure 1b). The system is designed to continuously perform electrochemical measurements to monitor for elevated H_2S concentrations based on a predetermined threshold (Figure 1c).

Capsule Electronics

The PCB layout was designed using EAGLE (Autodesk, San Rafael, CA) to create two separate electronics boards: a circular 12 mm Sensor-PCB with an 8 mm cutout for inserting the H_2S and pin headers for interfacing with the AFE, and a flex-rigid PCB, containing the AFE circuitry and BLE microcontroller (MCU-BLE). An overview of the flex-rigid PCB utilized for the capsule electronics is shown in Figure 2a. Specifically, the flex-rigid PCB incorporates several key COTS components: (1) an AFE potentiostat IC (AD5941, Analog Devices) for generating sensor excitation signals, as well as to amplify the output current of the sensor and digitize the signal using an onboard analog-to-digital converter, (2) an MCU-BLE (BGM13S, Silicon Labs) paired with an external 2.45 GHz antenna (WLA.01, Taoglas) for wireless data acquisition (signal power: 0 – +18 dBm) and energy management, and (3) a 3.3 V voltage regulator, (TPS610981, Texas Instruments), paired with a 3.0 V lithium manganese coin cell battery (2L76, Energizer) and a magnetic reed switch (HSR-502RT, Hermetic Switch) to power the electronics.

The flex-rigid PCB was commercially fabricated on a double-sided 6-layer FR-4 ceramic substrate with embedded polyimide flex regions (15 mm in length) connecting the traces between two rigid boards (Sierra Circuits, Sunnyvale, CA), thus allowing the PCB to bend. When bending the flex regions (bend radius: 1.2 mm) no significant changes to signal noise was observed. As shown in Figure 2b, all traces between the MCU and AFE (across the flex region) connected digital inputs and outputs, as well as VDD and GND. Analog signals were processed directly between the Sensor-PCB and AFE, implying the dominant source of system noise was from the absence of filtering at the AFE sensor inputs/outputs. The Sensor-PCB and AFE on the flex-rigid PCB were attached using three gold header pins (22-gauge), connecting the working (WE), counter (CE), and reference (RE) electrodes. The coin cell battery (170 mAh) was connected to the flex-rigid PCB using 30-gauge threaded wire fixed with copper and Kapton tapes, while the magnetic reed switch was soldered between the (+) battery terminal and the voltage regulator. The assembled stacked electronics were inserted into the DLP 3D-printed shell (microfluidic resin, CadWorks3D).

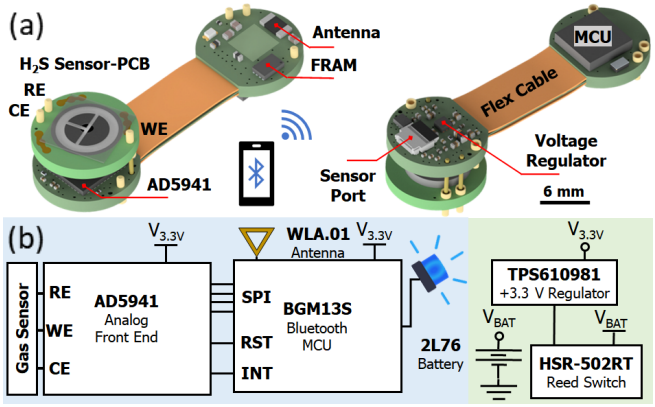

Figure 2: (a) CAD Rendering of the PCB electronics: sensor encapsulated inside a DLP 3D-printed shell and the flex-rigid PCB. (b) Circuit diagram of the PCB. Power consumption: 5 mA (idle, BLE) and 10 mA (active, BLE).

Integration of the modified H_2S sensor

The H_2S sensor is comprised of three bare carbon electrodes screen-printed on a permeable membrane, which were extracted from an existing COTS H_2S sensor (3SP-H2S-50, SPEC Sensors). Each sensor dye is submerged into a liquid electrolyte reservoir and attached to a plastic laminate backing (2 mm cutout) with WE, CE, and RE electrodes connected to separate conductive carbon tape pads (15 x 15 mm). This construction allows H_2S to readily access the sensor surface while electrolyte can diffuse through the permeable membrane to the bottom-side of the sensor, isolating the conductive pads.

The modified electrochemical H_2S sensor is depicted in Figure 3. An electrolyte reservoir (6 mm inner diameter) was 3D-printed, using fused filament fabrication (FFF) (MK3S+, Prusa), with biocompatible polylactic acid (PLA, Hatchbox). The sensor-pad dye was trimmed to roughly 10 mm in diameter and placed on top of the reservoir, encapsulating 10 µL of 0.5 M acetic acid as the electrolyte. The sensor was sealed with epoxy about the sensor-well interface (carbon pads exposed). The assembled sensor was inserted into the Sensor-PCB cutout and electrode connections between the copper pads were made using 36-gauge wires and silver epoxy (MG Chemicals). Gas permeable Teflon tape was cut to size (10 x 10 mm) and fixed on top of the H_2S sensor. This assembly method was employed to rapidly integrate a H_2S sensor within a capsule form factor and highlight the modular integration of the Sensor-PCB with the flex-rigid PCB.

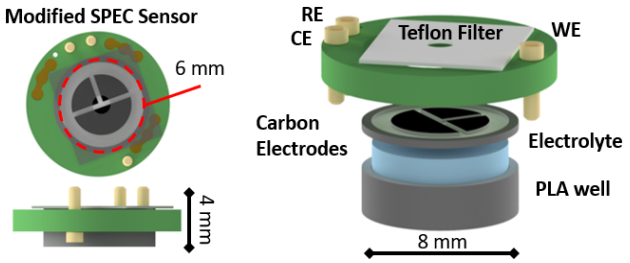

Figure 3: Modified electrochemical H_2S sensor assembly: shown as the top-down, cross-sectional, and exploded view of the H_2S sensor and Sensor-PCB attachment.

OPERATION OF CAPSULE PLATFORM

The capsule prototype was controlled wirelessly using a custom phone app. This allowed remote initiation of amperometric measurements and the ability to change the energy modes of the onboard electronics to minimize power consumption. Known challenges associated with wireless ingestible capsules include a lack of sufficient power to transmit signals through the body and limited operational lifetime due to restrictions on battery size, resulting from excess current consumption from idle components and wireless communication [12]. By default, the system operates in idle mode consuming 5 mA of current. When an amperometric measurement is initiated, the AFE is placed in active mode (10 mA with BLE), while sequentially exciting the electrochemical sensor and recording the readout signal. The MCU then periodically interrogates the AFE (100 ms sampling rate) and transfers data to be wirelessly transmitted to the phone until a predetermined number of measurements is obtained, returning the capsule to idle mode. As shown in Figure 4a, a magnetic reed switch allows the electronics to be turned on and off depending on proximity to an external magnetic field. Here, a small permanent magnet (1 cm^2) when placed within ~2 cm of the reed switch is sufficient to disconnect the system and turn of the blue indicator light emitting diode (LED). This allows the capsule to consume no current between packaging and being used.

The capsule has been designed to operate based on H_2S-driven feedback control of other downstream capsule functions. As a proof of concept, this was demonstrated by lighting an LED when the H_2S sensor detected gas at or above a set threshold (~8 ppm) (Figure 4b). This system design would enable biofeedback-driven control and provide alerts to users of patterns of inflammation throughout the GI tract based on the inflammatory marker of interest. Furthermore, in a realistic environment it is expected that sensor drift would need to be accounted for when setting a threshold concentration, therefore considerations for progressively updating the threshold value would be required.

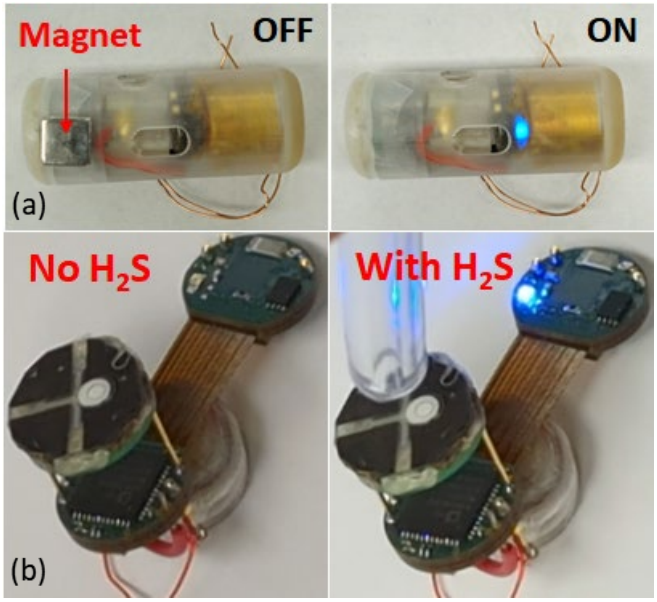

Figure 4: Photograph of assembled capsule demonstrating (a) the on/off state of the capsule prototype in the proximity of a small magnet (~2 cm) and (b) initializing an LED sequence once a threshold concentration of H_2S (8 ppm) is reached.

EXPERIMENTAL SETUP

The sensor-equipped capsules were evaluated in a custom-made gas set-up, providing a controllable environment for sensor assessment. A schematic detailing the design of the gas venting set-up is shown in Figure 5. To generate various gas concentrations, pulses of H_2S were applied by controllably venting 50 ppm of non-flammable nitrogen-diluted H_2S gas (Gasco, Huntington Beach, CA) into a plastic chamber (364 mL) until a desired ppm was reached. A flow regulator (Gasco) with a shut-off valve was attached to each gas tank, providing a constant flow rate of 0.2 SLPM (standard liter per minute) into the chamber. The open-close state of the flow regulator was toggled remotely using a bi-polar stepper motor (Nema-17, Stepper Online) and driver (A4988, Pololu). The duration of the gas pulse (H_2S ppm in chamber) was controlled by a two-way solenoid air valve (gas valve) connected to each gas tank, creating an interlock to resist leaking. The chamber was returned to a 0-ppm state by opening a motorized ball valve (US Solid) and forcibly purging air via a 12-V vacuum pump (Karlsson Robotics) into the chamber over a 10 s interval. The state of all valves, motors, and pumps was controlled via an Arduino development kit (Mega2560, Adafruit). Though the setup can replicate the proper ratios of gases found in the GI tract, due to the size of the setup and safety considerations (flammability), high ppm H_2S gas composition was not tested.

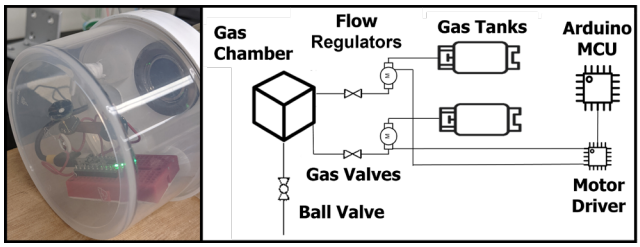

Figure 5: Photograph and schematic of the gas testing set-up.

CHARACTERIZATION OF MINIATURIZED CAPSULE SENSING SYSTEM

Physiological concentrations of H_2S in healthy adults within the GI tract ranges between 10.2–100 ppm and can deviate depending on the state of the gut, particularly in patients with ulcerative colitis [13]. Utilizing the gas testing setup, concentrations of H_2S, ranging from 3.7–15.6 ppm, were generated by gradually increasing the gas infill time into the chamber. An infill time of 2 s resulted in an H_2S concentration of 3.7 ppm, where increasing infill time at 2-s intervals resulted in the desired peak of 15.6 ppm H_2S. After each infill period the chamber was kept closed for 30 s, holding the ppm of H_2S constant for evaluation with the miniaturized capsule system, followed by air venting. Gas concentrations were independently validated using unmodified 3SP-H2S-50 SPEC sensors connected to a benchtop potentiostat (CHI Instruments) and AD5941 development kit (Analog Devices) [9].

Figure 6a shows the wireless amperometric gas measurements performed by the sensor-integrated capsule with an excitation voltage of 0 V (vs. C) over 2.5 hours at a 100 ms sampling rate. Increasing H_2S concentrations were measured over several time-controlled H_2S pulses, separated by a 6-minute interval, which were recorded continuously with the capsule platform then wirelessly transmitted to the phone app. Three consecutive pulses were applied for each H_2S concentration. A current range of 0.25 – 2.2 µA was observed corresponding to 3.7–15.6 ppm H_2S, which were well within the sensing range of the capsule electronics. The resulting calibration plot, as shown in Figure 6b, was found by correlating the calculated ppm of H_2S in the chamber to the averaged peak current response (N = 3 pulses), displaying a linear current response between 3.7–12 ppm (correlation coefficient R2 = 0.998) with a sensitivity of 0.17 µA/ppm.

This result exhibits an excellent sensitivity, although the linear range found here is lower than desired to target physiological GI concentrations. It was found that at higher gas concentrations, beyond 12 ppm, a slight drift in the sensor response was observed, which deviated from its expected linear behavior. This drift may be caused by the eventual drying of the liquid electrolyte over time due to repeated air purging cycles during prolonged monitoring experiments (over 2 hours). The addition of humidity control in the chamber would be a suitable resolution to increase the sensor's linear range and operational lifetime. Furthermore, the GI tract is composed of a mixture of gases: nitrogen, oxygen, methane, hydrogen, and carbon dioxide [13]. Most notably hydrogen is readily abundant (50%) and a known interferent of electrochemical measurements of H_2S, therefore thorough assessment of the selectivity of any H_2S sensor against known interferents is needed. The authors also recognize further characterization of the wireless signal propagation is necessary to ensure a robust Bluetooth link in the GI environment under non-ideal conditions. Overall, the results indicate reliable and rapid response to dynamically changing H_2S concentrations and demonstrate a proof-of-concept capsule with sensor-driven control.

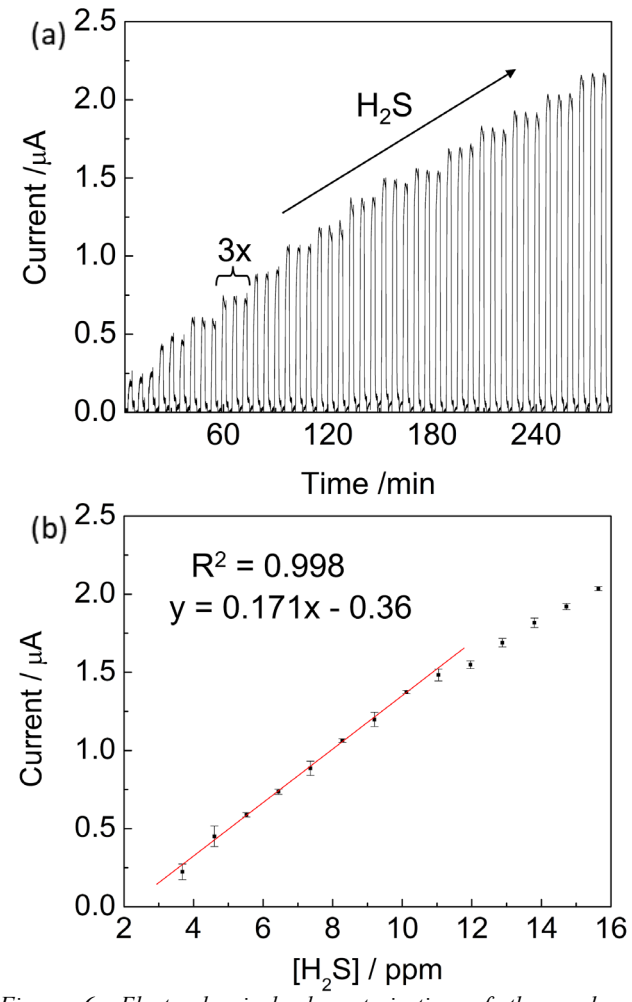

Figure 6: Electrochemical characterization of the packaged capsule: (a) amperometric measurements are recorded wirelessly in the gas-testing chamber (100 ms sampling rate). H_2S gas is pulsed at a ~6 min interval for increasing infill times to obtain gas concentrations between 3.7-15.6 ppm. (b) A resulting calibration curve was observed (N = 3) and displayed a linear response and sensitivity of 0.171 μA/ppm.

CONCLUSIONS

This work demonstrates one of the first capsule-based approaches for wireless detection of H_2S towards an ingestible diagnostic tool for locally identifying GI inflammation. The developed system integrates a modified COTS H_2S sensor-PCB with PCB electronics into a clear resin shell, providing a platform for studying the dynamics of transient gaseous inflammatory markers in the GI tract. When assembled, the capsule achieves a miniaturized form factor (15 × 34 mm) and successful continuous monitoring of H_2S at sub-physiological concentrations, realizing the goals of our previously reported work.

Future work will aim to thoroughly assess the selectivity of the H_2S sensor for known interferents, such as methane, hydrogen, and carbon dioxide at expected ratios in the GI tract, as well as perform bioimpedance measurements to confirm the intestinal tissue state. Overall, this platform demonstrates reliable sensor performance, and provides insight on the challenges and systems integration steps required to develop miniaturized capsules for understanding the relation between the gut microbiome and inflammatory diseases within the GI tract.

ACKNOWLEDGEMENTS

This work was supported by the National Science Foundation ECCS Program under Award #1939236. The authors acknowledge support from the Clark Doctoral Fellows Program.

REFERENCES

[1] M.J. Bull and N.T. Plummer, "Part1: The Human Gut Microbiome in Health and Disease," *Journal of Integrative Medicine*, 13, 17–22 (2014).

[2] M. Bhatia and R.R. Gaddam, "Hydrogen Sulfide in Inflammation: A Novel Mediator and Therapeutic Target," *Antioxidants & Redox Signaling,* 34, 1368-1377, (2021).

[2] M.E. Inda, M. Jimenez, Q. Liu, N.V. Phan, J. Ahn, C. Steiger, A. Wentworth, et. al., "Ingestible Capsule for Detecting Labile Inflammatory Biomarkers in situ," *bioRxiv*, (2022).

[3] D.R. Linden, "Hydrogen Sulfide Signaling in the Gastrointestinal Tract," *Antioxid. Redox Signal*, 20, 818-830 (2014).

[4] D.R. Linden, M.D. Levill, G. Frrugia, and J.H. Szurszewski, "Endogenous Production of H_2S in the Gastrointestinal Tract: Still in Search of a Physiologic Function," *Antioxid Redox Signal*, 12, 1135-1140, (2010).

[5] A. Birg, A. Hu, and H.C. Lin, "Reevaluating our Understanding of Lactulose Breath Tests by Incorporating Hydrogen Sulfide Measurements," *JGH Open*, 3, 228-233, (2019).

[6] L.A. Beardslee, G.E. Banis, S. Chu, S. Liu, A. A. Chapin, J.M. Stine, P.J. Pasricha, and R. Ghodssi, "Ingestible Sensors and Sensing Systems for Minimally Invasive Diagnosis and Monitoring: The Next Frontier in Minimally Invasive Screening," *ACS Sensors*, 5, 891-910 (2020).

[7] D. Friedel, R. Modayil, and S. Stavropoulos, "Colon Capsule Endoscopy: Review and Perspectives," *Gastroenterol. Res. Pract.*, 2016, 9643162, (2016).

[8] K. Kalantar-zadeh, K.J. Berean, N. Ha, A.F. Chrimes, K.X, D. Grando, J.Z, Ou, N. Pillai, J.L. Campbell, R. Brkljaca, K.M. Taylor, R.E. Burgell, C.K. Yao, S.A. Ward, C.S. McSweeney, J.G. Muir, and P.R. Gibson, "A Human Pilot Trial of Ingestible Electronic Capsules Capable of Sensing Different Gases in the Gut," *Nature Electronics*, 1, 79-87 (2018).

[9] J.M. Stine, S. Botasini, L.A. Beardslee, and R. Ghodssi, "Design of a Wireless, Multimodal Sensing Platform for Detecting Inflammatory Markers in the GI Tract," *25th International Conference on Miniaturized Systems for Chemistry and Life Sciences (MicroTAS)*, Palm Springs, CA, 10/10-14/21, (2021), pp. 1827-1828.

[10] C. Cheng, Y. Ue, X. Li, Z. An, F. Zhang, B. Su, and Q. Liu, "A Wireless, Ingestible pH Sensing Capsule System Based on Iridium Oxide for Monitoring Gastrointestinal Health," *Sensors and Actuators B: Chemical*, 349, 130781, (2021).

[11] S. Yang, V.Sencadas, S.S. You, N.Z. Jia, S.S. Srinivasan, H.Huang, A.E. Ahmed, J.Y. Liang, and G. Traverso, "Powering Implantable and Ingestible Electronics," *Advanced Functional Materials*, 31, 2009289, (2021).

[12] D. Dordevic, A. Jancikova, M. Vitezova, and I. Kushkeych, "Hydrogen Sulfide Toxicity in the Gut Environment: Meta-analysis of Sulfate-reducing and Lactic Acid Bacteria in Inflammatory Processes," *Journal of Advanced Research*, 27, 55-69 (2021).

[13] K. Rodgers, *The Digestive System*, Britannica Educational Publishing, New York, 2010.

CONTACT

*Reza Ghodssi, tel: +1-301-405-8158; ghodssi@umd.edu

BIOPOWER-IN-GUT: AN INGESTIBLE BACTERIA-POWERED BATTERY CAPSULE

Maryam Rezaie[1], Zahra Rafiee[1], and Seokheun Choi[1,2]*
[1]Bioelectronics & Microsystems Laboratory, Department of Electrical & Computer Engineering, State University of New York at Binghamton (SUNY Binghamton), Binghamton, New York, USA
[2]Center for Research in Advanced Sensing Technologies & Environmental Sustainability, SUNY Binghamton, Binghamton, New York, USA

ABSTRACT

We report an ingestible, millimeter-sized microbial fuel cell (MFC) capsule that can provide a realistic and practical power solution for ingestible electronics. The capsule integrates a pH-sensitive enteric membrane, a germinant-containing layer, and a microfluidic hydrogel-based anodic channel pre-inoculated with *Bacillus subtilis* spores as dormant biocatalysts, which are directly connected to an integrated MFC. When the pH-sensitive membrane dissolves in a designated gut location with a specific pH, the hydrophilic hydrogel in the anodic channel absorb the gut fluids washing the germinant to trigger the spore germination and generate microbial metabolic electricity in our world's smallest MFC. When the capsule is designed to work in the human intestine, it generates electricity only in the neutral pH solution achieving maximum power and current densities of 64μW/cm^2 and 435 μA/cm^2, respectively, which are substantially higher than the other energy harvesting techniques.

KEYWORDS

Ingestible biobatteries, microbial fuel cells, bacteria-powered batteries, *Bacillus subtilis*, spore germination

INTRODUCTION

Ingestible electronic devices are on the verge of being useful for many healthcare procedures, as evidenced by the commercial success of the capsule endoscope [1]. During the passage of the swallowable devices through the gastrointestinal (GI) tract, the capsules can enable direct visualization of the GI tract and monitor its environment for *in vivo* diagnostics and accurate therapy [2]. However, current technology relies on primary batteries to operate, which causes challenges in realizing compact and long-lived advanced functionality because of their bulky size, and finite energy budgets [3]. Furthermore, toxic battery materials or potential mucosal injury hinders the practical and sustained use of ingestible electronics. Power autonomy is a critical requirement for prolonged monitoring systems, so they can work continuously, independently, and self-sustainably. Alternatively, many energy harvesting methods have been proposed to take advantage of body-produced thermal, mechanical, and acidic energies [4]. However, these body energies are not always available or sometimes not enough for practical applications because of the lack of temperature gradients and slow mechanical movements in the GI tract. Acidic energy harvesting is also limited to the stomach with its low pH.

In this work, we create an ingestible bacteria-powered battery capsule functionalized with spore-forming *Bacillus subtilis* which can generate electricity in the human body intestine. The system has a standard size "0" with 0.68 mL volume and 21.7 mm length integrating a conductive anodic chamber with a commercially available neutral pH-sensitive enteric membrane. The neutral pH-sensitive membrane resists the acidic stomach environment but dissolves in the neutral pH environment of the intestines. The smart capsule generates power after dissolving enteric-coating and dispersing germinant powder through adsorption of gut fluid in the bacteria-containing hydrogel (Figure 1). This work demonstrates the promising potential of the spore-forming MFC as an innovative power source for next-generation ingestible applications.

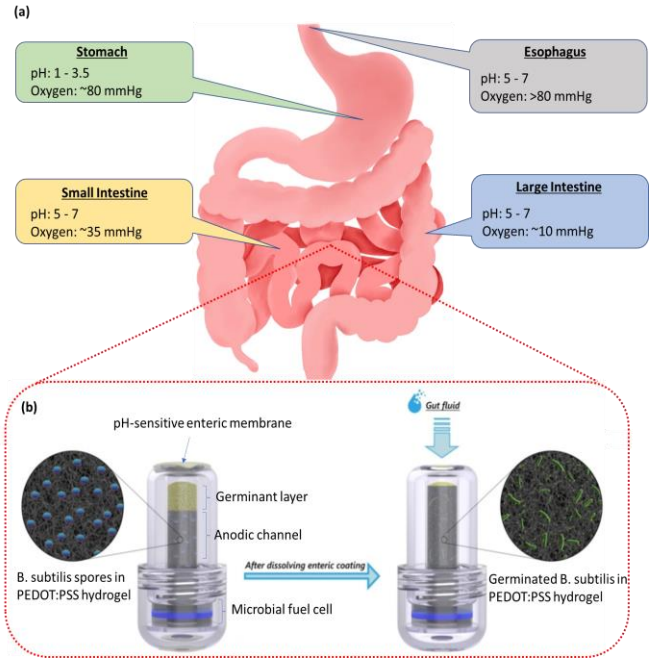

Figure 1: (a) Physicochemical characteristics of the GI tract, and (b) the ingestible MFC system and its working principle.

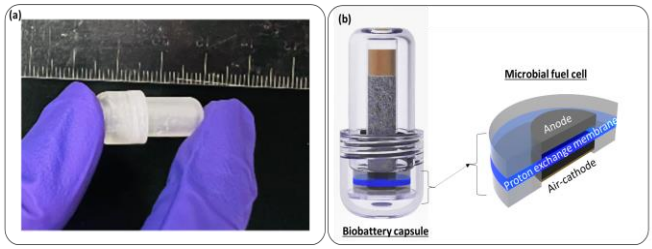

Figure 2: (a) Images of the assembled capsules and (b) the MFC configuration integrated in the capsule.

EXPERIMENTAL PROCEDURE

Capsule design and fabrication

The capsule was fabricated by stereo-lithography-based 3-D printing (Formlabs Form 3B) with high-temperature resin (Figures 1 & 2) [5]. The printed capsule was rinsed in 99% pure isopropyl alcohol (IPA) for 15 minutes to remove remnants and then post-cured with an UV cure station for 60 minutes to complete the

978-1-940470-04-7/HH2022/$25©2022TRF
DOI 10.31438/trf.hh2022.19

polymerization. The top capsule part including the anodic channel and the germinant layer was screwed into the bottom part having the MFC system.

MFC fabrication

For the MFC structure, an anode and a cathode sandwiched a proton exchange membrane (Nafion 17 membrane), which were all thermally bonded between two poly (methyl methacrylate) (PMMA) layers (Figure 2) [6]. The PMMA layers were designed by AutoCAD and patterned by a laser micromachine (Universal Laser Systems VLS 3.5). The anode was prepared by introducing a mixture of poly (3,4-ethylene dioxythiophene): poly (styrene sulfonate) (PEDOT: PSS) and dimethyl sulfoxide (DMSO) into an untreated carbon cloth. The cathode was constructed on wet-proofed carbon cloth with four layers of polytetrafluoroethylene (PTFE) coating. The cathode was loaded with 10% Pt catalysts for the oxygen reduction reaction. This air-cathode is optimal for the reduction process in the oxygen-dissolved gut environment (Figure 1). The anode and the cathode were pierced with a thin conductive wire as a current collector.

Cultivation and sporulation of *Bacillus subtilis*

Bacillus subtilis strain 168 was acquired from the American Type Culture Collection (ATCC) and was cultivated in Luria Broth (LB) medium at 37°C. The bacterial sporulation was induced by nutrient exhaustion on LB agar plates [7, 8]. The formed endospores were collected from the plate and pelleted by centrifugation at 4000 rpm for 4 minutes. The harvested spores were resuspended in distilled water and stored at 4°C

Anodic channel preparation

The anodic channel was filled with a conductive PEDOT:PSS hydrogel including the bacterial spores. The PEDOT: PSS solution was vigorously stirred for 4 hours, and then the DMSO was added to improve the conductivity of the PEDOT:PSS. The suspension was stirred for 3 hours at room temperature and then the solution was placed in a Teflon autoclave at 180°C for 24 hours. After cooling down to normal temperature, the synthetic material became a porous scaffold structure. *B. subtilis* spores were introduced into the structure and the lyophilization process was conducted in a freeze-drying system (FreeZone Plus 2.5 Liter Cascade Benchtop Freeze Dry System, Labconco, USA).

Germinant layer preparation

The germinant solution was composed of L-Valine (10 mM) and AGFK (10 mM L-Asparagine, 33.6 mM D-Glucose, 33.6 mM D-Fructose, 60 mM KCl) in the LB medium. The solution was freeze-dried in the lyophilization system, which was introduced as the germinant layer on top of the anodic channel. GerA, GerB, and GerK are well-known germinant receptors of B. *subtilis*, that can trigger their spore gemination [7, 8]. GerA interacts with L-Valine while GerB and GerK recognize AGFK.

pH-sensitive polymer membrane

Eudragit® L100 (neutral pH-dependent enteric membrane) was generously donated by Evonik (NJ, USA). 4 g of Eudragit® L100 powder was dissolved in a mixture of 8.8 g of Isopropyl alcohol (IPA) and 6.62 g of acetone. The suspension was vortexed for 15 minutes and sonicated for 60 minutes. Then, it was used in film coating of the capsule to prevent any release of germinant powders/spores and any introduction of the gut fluids in the upper GI tract. A pH 7.0 solution was prepared with a mixture of 100 mL of 0.1 M potassium phosphate and 60 mL of 0.1 M sodium hydroxide in deionized (DI) water. By mixing 46.2 mL of 0.1 M hydrochloric acid, 100 mL of 0.1 M potassium hydrogen phthalate, and 51 mL of DI water, the lowest pH solution was prepared. A pH 6.8 solution was prepared with 6.8 g potassium phosphate and 0.88 g sodium hydroxide in 1000 mL DI water. Its pH was adjusted with 1M NaOH.

Electrical measurement setup

We measured the voltage drops across external resistors by using a data acquisition system (DATAQ Instruments). The current and power outputs were calculated with the connected resistors (470 kΩ, 240 kΩ, 160 kΩ, 100 kΩ, 75 kΩ, 47 kΩ, 33 kΩ, 22 kΩ, 15 kΩ, 10 kΩ, 2 kΩ, 1.5 kΩ, 470 Ω, and 360 Ω). Output densities were normalized to the anode area of the MFC.

RESULTS AND DISCUSSION

Innovation and operating principle

This work is part of a global effort to enable a new generation of smart, stand-alone, and long-lived ingestible electronics designed to serve as practical clinical tools for diagnostics and therapy in the GI tract [9, 10]. While there are many ambient energy resources available in the human body to provide various implantable electronics with sustainable power, the GI tract contains extremely harsh conditions, lacking potential energy sources [11, 12]. Even the latest wireless power transfer and mechanical or thermal energy harvesting techniques are not well suited to ingestible systems [3]. The performance of the wireless power transfer significantly depends on the uncontrollable position and orientation of the devices while it is challenging to securing reliable and practical energy resources from thermal gradients and mechanical movement in the GI tract. On the other hand, the microbial energy harvesting methods in the GI tract are significantly more feasible and can provide superior self-sustaining features with long-term stability because they contain complete enzyme pathways and continuously regenerate biocatalytic enzymes as part of their natural metabolism [13]. Moreover, researchers reported some human gut bacteria can transfer electrons to the exterior of their cells in the nutrient-rich and anaerobic gut environment [13-19]. This intriguing discovery and our additional preliminary data on the electrogenicity of five gut bacterial species inspired us to examine opportunities for a novel microbial power supply in the GI tract [20]. However, it is very challenging to use the human gut-inhabiting microorganisms directly extracted from the host because those incorporated in the capsule cannot maintain their viability and balance their populations throughout the GI tract having different environmental conditions.

In this work, we developed a long-lasting ingestible MFC by using a spore-forming gut bacterium, *Bacillus subtilis*, which can use its survival strategy in harsh gut environmental conditions. *B. subtilis* belongs to a group generally recognized as safe (GRAS) and are usually found in the human gut while their endospores can survive even in the extremely acidic environment of the stomach and tolerates a variety of harsh fabrication conditions with hot/cold temperature, desiccation, high pressure, and other chemical processes, offering flexibility in manufacturing, and long-term operation and stable storage of the capsules [6, 7]. The hydrophilic hydrogel pulls the gut fluid into the anodic channel to trigger the spore germination and provides a promising electrical interface with the germinated bacterial cells to active the MFC.

pH-dependent voltage outputs

The capsules were exposed into several pH solutions which mimicked the different GI environments. Three measurements were conducted along the GI tract, esophagus (pH 7.0 for 1 minutes), stomach (pH 2.6 for 3 hours), and small intestine (pH 6.8 for 3

hours). The neutral pH-sensitive membrane resisted the acidic stomach environment but dissolved in the neutral pH environment of the intestines (Figure 3). Because the ingestible system will have the lowest residence time of tens of seconds in the esophagus with the neutral pH environment, it will not work in the esophagus. The type and thickness of the pH-sensitive membrane can control the operation selectively in different gut areas.

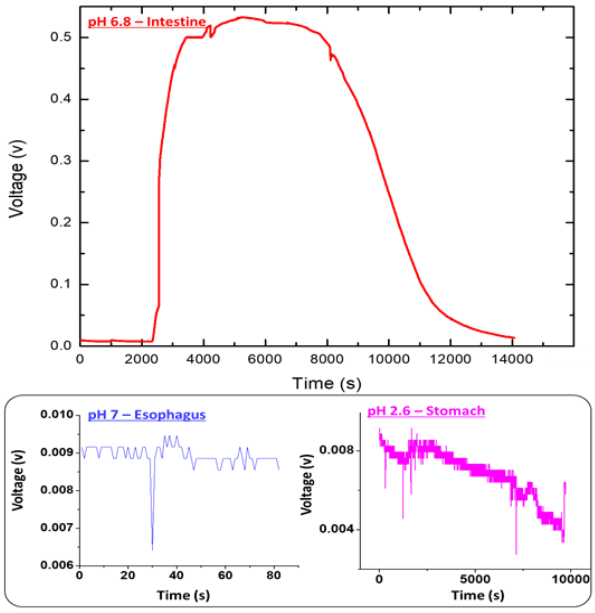

Figure 3: Continuous measurements of the voltages generated from the capsule in different pH solutions.

Power and current generation

A consistent rise was observed in electrical performance as the germination time was increased from 15 minutes to 60 minutes while the control without the spores generated negligible outputs (Figure 4). This demonstrates that the power generation originates from the metabolism of the germinated *B. subtilis* cells. As the spores continued their gemination process with the time, the open circuit voltage (OCV), the current density and the power density improved considerably and reached the maximum in 60 minutes, producing 0.54 V of OCV, 64μW/cm^2 of power density, and 435 μA/cm^2 of current density. This can be attributed to the progressive metabolic improvement in germinated *B. subtilis* cells over time. When the potential gut fluids with germinants triggered the germination of the spores and returned to their vegetative state, the cellular respiration began, generating bioelectricity [6, 7, 22]. Our great performance can be attributed to the revolutionized anodic compartment. Usually, the anode and the anodic chamber play a critical role in affecting the performance of the MFC because its performance depends mainly on the metabolic activity of bacterial cells in the anodic part [16]. The anode component requires a microporous structure large enough to support bacterial growth and a conductive scaffold for stable, consistent bacterial electron transfer. Constructing anodes that are simultaneously biocompatible, conductive, porous, and microfluidic remains challenging especially for miniaturized biological fuel cells. In this work, a highly porous and conductive hydrogel scaffold was innovatively developed by a simple one-step hydrothermal synthetic method and successfully integrated into an extremely small capsule. This work creates a standardized design for the microfabrication of a compact MFC for ingestible applications.

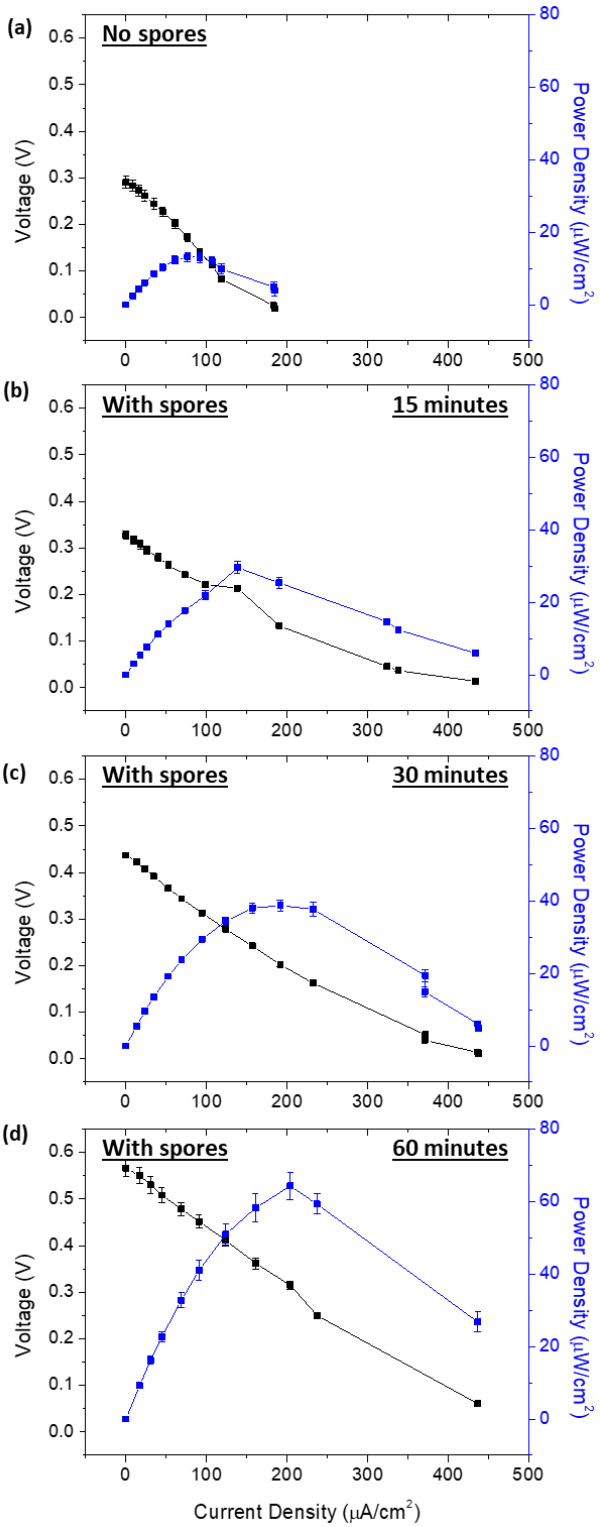

Figure 4: Polarization curves and power outputs of the MFC capsules (a) without and with B. subtilis spores measured at (b) 15 minutes, (c) 30 minutes, and (d) 60 minutes after the enteric membrane dissolves. A consistent rise is observed in open circuit voltage (OCV), power density, and current density as the germination time is increased from 15 minutes to 60 minutes. This can be contributed to the progressive increase in successfully germinated cells over time.

CONCLUSION

The work developed, *for the first time*, a self-contained, self-sustained ingestible MFC battery for devices that can diagnose diseases or deliver drugs where they are needed. The MFC generated reliable and long-lasting power from microbial metabolism in the potential gut environment, delivering on-board energy to the next generation of ingestible devices. This work provided a novel approach to produce electrical power in the gut and improve MFC performance for practical ingestible applications. Reported work on microbial energy harvesting for ingestible electronic applications was unavailable or quite limited because microbial cytotoxicity may pose health concerns. However, if we consider that humans possess more bacterial cells than human cells in their bodies, the direct use of bacterial cells as a power resource interdependently with the human body is conceivable for ingestible electronics. Furthermore, the human gut is home to millions of microorganisms and an ideal place for their cultivation. Because we used the bacterial strain belonging to a group generally recognized as safe, we expect a minimal foreign-body response. Moreover, the GI tract that takes care of various foreign materials for digestion represents one of the human organ systems that cause the least foreign body immune response and consequent malfunction of the ingestible devices. In this work, our MFCs were limited to *in vitro* testing in simulated gut fluids with appropriate pH but we will validate whether the MFC can generate power with *in vivo* animal testing.

ACKNOWLEDGEMENTS

This work was supported mainly by the National Science Foundation (CBET #2100757, ECCS #2020486, and ECCS #1920979), and partially by the Office of Naval Research (#N00014-21-1-2412).

REFERENCES

[1] L.A. Beardslee, G.E. Banis, S. Chu, S. Liu, A.A. Chapin, J.M. Stine, P.J. Pasricha, R. Ghodssi, "Ingestible Sensors and Sensing Systems for Minimally Invasive Diagnosis and Monitoring: The Next Frontier in Minimally Invasive Screening," *ACS Sensors*, 5, 891-910 (2020).

[2] C. Steiger, A. Abramson, P. Nadeau, A.P. Chandrakasan, R. Langer, G. Traverso, "Ingestible electronics for diagnostics and therapy," *Nature Reviews Materials*. 4, 83-98 (2019).

[3] P. Nadeau, D. El-Damak, D. Gletting, Y.L. Kong, S. Mo, C. Cleveland, L. Booth, N. Roxhed, R. Langer, A.P. Chandrakasan, G. Traverso, "Prolonged energy harvesting for ingestible devices," *Nature Biomedical Engineering*, 1, 0022 (2017).

[4] S. Yang, V. Sencadas, S.S. You, N.Z. Jia, S.S. Srinivasan, H. Huang, A.E. Ahmed, J.Y. Liang, G. Traverso, "Powering Implantable and Ingestible Electronics," *Advanced Functional Materials*, 31, 2009289 (2021).

[5] H.R. Nejad, B.C.M. Oliveira, A. Sadeqi, A. Dehkharghani, I. Kondova, J.A.M. Langermans, J.S. Guasto, S. Tzipori, G. Widmer, S.R. Sonkusale, "Ingestible osmotic pill for in vivo sampling of gut microbiomes," *Advanced Intelligent Systems*, 1, 1900053 (2019).

[6] L. Liu, S. Choi, "Self-sustainable, High-power-density Bio-solar Cells for Lab-on-a-chip Applications," *Lab Chip*, 17, 3817-3825 (2017).

[7] J. Ryu, M. Landers, S. Choi, "A Sweat-Activated, Wearable Microbial Fuel Cell for Long-term, On-demand Power Generation," *Biosensors and Bioelectronics*, 205, 114128 (2022)

[8] J. Ryu, S. Choi, "Bioelectricity Production from Sweat-Activated Germination of Bacterial Endospores," *Biosensors and Bioelectronics*, 186, 113293 (2021).

[9] N.V. Helleputte, A.J.G. Even, F. Leonardi, S. Stanzione, M. Song, C. Garripoli, W. Sijbers, Y. Liu, C.V. Hoof, "Miniaturized electronic circuit design challenges for ingestible devices," *Journal of Microelectromechanical Systems*, 29, 645-652 (2020).

[10] G.E. Banis, L.A. Beardslee, J.M. Stine, R.M. Sathyam, R. Ghodssi, "Capacitive sensing of triglyceride film reactions: a proof-of-concept demonstration for sensing in simulated duodenal contents with gastrointestinal targeting capsule system," *Lab on a Chip*, 20, 2020-2032 (2020).

[11] X. Huang, L. Wang, H. Wang, B. Zhang, X. Wang, R.Y.Z. Stening, X. Sheng, L. Yin, "Materials strategies and device architectures of emerging power supply devices for implantable bioelectronics," *Small*, 16, 1902827 (2020).

[12] D. Jiang, B. Shi, H. Ouyang, Y. Fan, Z.L. Wang, Z. Li, "Emerging implantable energy harvesters and self-powered implantable medical electronics," *ACS Nano*, 14, 6436-6448 (2020).

[13] M. Mohammadifar, M. Tahernia, J.H. Yang, A. Koh, and S. Choi, "Biopower-on-Skin: Electricity generation from sweat-eating bacteria for self-powered e-skins," *Nano Energy*, 75, 104994 (2020)

[14] L.A. Cahoon, N.E. Freitag, "The electrifying energy of gut microbes," *Nature*, 562, 43-44 (2018).

[15] S.H. Light, L. Su, R. Rivera-Lugo, J.A. Cornejo, A. Louie, A.T. Iavarone, C.M. Ajo-Franklin, D.A. Portnoy, "A flavin-based extracellular electron transfer mechanism in diverse Gram-positive bacteria," *Nature*, 562, 140-144 (2018).

[16] M. Tahernia, E. Plotkin-Kaye, M. Mohammadifar, Y. Gao, M. Oefelein, L. Cook, S. Choi, "Characterization of Electrogenic Gut Bacteria," *ACS Omega*, 5, 29439-29446 (2020).

[17] G. Pankratova, D. Leech, L. Gorton, L. Hederstedt, "Extracellular electron transfer by the Gram-positive Bacterium Enterococcus faecalis," *Biochemistry*, 57, 4597-4603 (2018).

[18] D. Keogh, L.N. Lam, L.E. Doyle, A. Matysik, S. Pavagadhi, S. Umashankar, P.M. Low, J.L. Dale, Y. Song, S.P. Ng, C.B. Boothroyd, G.M. Dunny, S. Swarup, R.B.H. Williams, E. Marsili, K.A. Kline, "Extracellular electron transfer powers Enterococcus faecalis biofilm metabolism," *mBio*, 9, e00626-17 (2018).

[19] Y. Gao, M. Mohammadifar, and S. Choi, "From microbial fuel cells to Biobatteries: Moving toward on-demand micro-power generation for Small-scale Single-Use Applications," *Advanced Materials Technologies*, 4, 1970039 (2019).

[20] S. Choi, "Electrogenic Bacteria Promise New Opportunities for Powering, Sensing, and Synthesizing," *Small*, 2107902 (2022).

[21] A. Fraiwan, S.P. Adusumilli, D. Han, A.J. Steckl, D.F. Call, C.R. Westgate, S. Choi, "Microbial Power-generation Capabilities on Micro-/Nano-structured Anodes in Micro-sized Microbial Fuel Cells," *Fuel Cells*, 14, 801-809 (2014).

[22] M. Landers, and S. Choi, "Small-scale, Storable Paper Biobatteries Activated Via Human Bodily Fluids," *Nano Energy*, 97, 107227 (2022)

CONTACT

*Prof. S. Choi, tel: +1-607-777-5913; sechoi@binghamton.edu

MONITORING OF PHYSIOLOGICAL FLOW WITH A MICROFABRICATED ELECTROCHEMICAL PARYLENE FLOW SENSOR

Xuechun Wang[1], Trevor Hudson[1], Kee Scholten[1], Elliot Myong[1], J. Gordon McComb[2] and Ellis Meng[1]
[1]University of Southern California, Los Angeles, California, USA
[2]Children's Hospital Los Angeles, Los Angeles, California, USA

ABSTRACT

A microfabricated electrochemical impedance-based flow sensor for inline monitoring of physiological fluid flow was demonstrated to track cerebrospinal fluid (CSF) flow changes in a week-long, live porcine study. This impedimetric sensor was benchmarked against a Sensirion LD20 thermal liquid flow sensor at the benchtop, followed by a CSF drainage study using an external ventricular drain (EVD) in the pig. Sensor resolution was improved ~2× to 26.2 µL/min at low flow versus previous work, and operation expanded to 0-1000 µL/min. Using separate calibrations for low and high flow ranges, accuracy at low flow rates (0-200 µL/min) was improved more than six-fold compared to prior work. High sensitivity, resolution, accuracy, and stable RMS error were demonstrated in the porcine study. The performance of the impedimetric sensor was comparable to the LD20 benchmark showing the sensor's capability of monitoring flow dynamics in implanted hydrocephalus shunts.

KEYWORDS

Parylene C, flow sensor, impedimetric sensor, hydrocephalus

INTRODUCTION

Elevated intracranial pressure (ICP) in hydrocephalus patients resulting from the imbalance between production, absorption, and circulation of cerebrospinal fluid can be treated using an implanted drainage shunt to remove excess CSF. However, shunts fail often due to clogging, which is challenging to detect from symptoms including headache, nausea, and vomiting; these are general, nonspecific, and may be indicative of other maladies [1]. A suspected shunt malfunction can involve a hospital visit for diagnostic imaging, including magnetic resonance imaging, computed tomography, and plain X-rays. The additional imaging is costly and can expose patients to radiation.

Sensors have been developed to monitor CSF flow dynamics for detecting such shunt malfunction. The only FDA-approved device in the market is ShuntCheck from NeuroDx Development which measures CSF flow rate. This device is positioned on the skin and aligned to the implanted shunt catheter. An ice pack is set upstream, cooling the flowing CSF, which is detected via the induced temperature gradient downstream using a thermistor. This approach can cause discomfort but, more importantly, has limited resolution and accuracy. Other sensors being developed include ultrasonic sensors, which measure volumetric flow in shunts transdermally [2] but have low resolution and are impractical to wear.

The ideal sensor would be implanted in line with the shunt, be able to measure both CSF flow and ICP, and have a life span of decades. An external handheld device would be used to record flow and pressure as well as being able to recalibrate for drift, as both CSF flow and ICP can vary from second to second depending on body position, fluctuations in blood pressure, and respiration. Thermal flow sensors can be implanted [3], but most have a silicon construction which is subject to corrosion, fracture, and exposure to the body environment while operating *in vivo* [4]. Sensors having biocompatible construction, such as Parylene, could perform better for *in vivo* applications over time [4].

We developed a sensor made from biocompatible and non-corroding Parylene C, capable of measuring flow and temperature in real-time through electrochemical impedance transduction of biological saline solutions. Here, sensor calibration and resolution were improved for CSF flow monitoring, and the first demonstration of the sensor in the pig is reported.

MATERIALS AND METHODS

The impedimetric sensor consists of an upstream, resistive, serpentine platinum (Pt) heater (~400 Ω) and downstream sensing electrode pairs (exposed Pt) on a Parylene substrate (Fig. 1) [5]. Multilayer micromachining on a silicon support wafer was used to fabricate the sensor [6]. A 10 µm thick Parylene insulation layer was deposited through chemical vapor deposition (CVD). To define the metal features, a 2 µm thick AZ 5214-IR photoresist layer was spin-coated, and Pt (2000 Å) was deposited through e-beam deposition followed by lift off in heated acetone and rinses in isopropanol alcohol (IPA) and deionized (DI) water. Another 10 µm thick Parylene layer was then deposited. 15 µm thick AZ 4620 photoresist was spin-coated to serve as the sacrificial layer. The metal pad, electrode sites, and device shape were etched out through deep reactive ion etching. Photoresist was removed by sequential acetone, IPA, and DI water baths, and the individual sensor was released using a razor blade to cut along the etched shape. The device was thermoformed in a vacuum oven at 200 °C for 48 hours to enhance the adhesion between Parylene and metal layers.

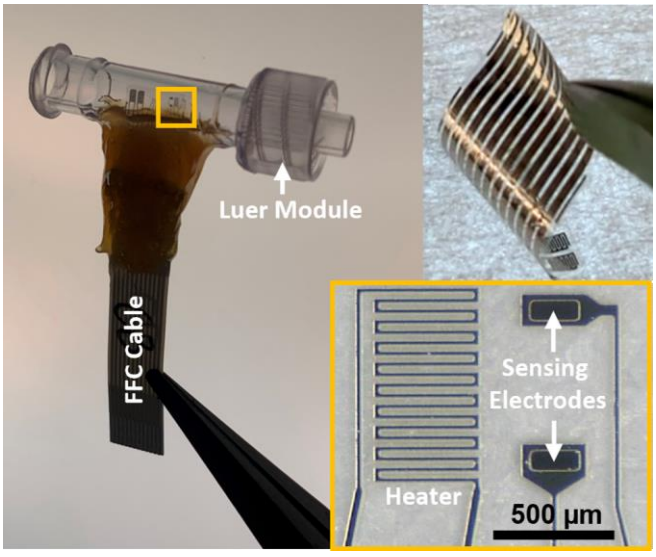

Figure 1. Low profile, flexible sensor die packaged in a Luer module. Fabricated Parylene impedimetric sensor after release from the silicon substrate. Inset shows a close-up of the flow sensor elements (yellow box).

The flow was detected using a time-of-flight approach: the upstream heater was activated by a voltage pulse, then heat transfer downstream was detected via the electrolyte's impedance response,

978-1-940470-04-7/HH2022/$25©2022TRF
DOI 10.31438/trf.hh2022.20

which is sensitive to thermal changes. Specifically, the maximum rate of impedance change – defined here as the heating slope (HS, %/s) – during the 10-second heater activation was used to transduce the flow rate (Fig. 2) [6][7]. Measurements were acquired every 80 s (including 60 s for cooling between measurements) to minimize the overheat temperature (~2 °C). Impedance was acquired at 50 kHz to maximize the contribution from solution resistance.

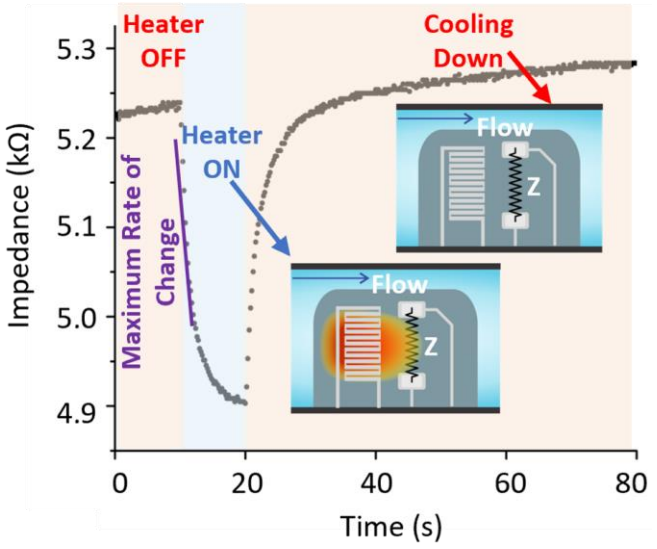

Figure 2. Impedance response of sensor over a heating cycle. Flow rate is transduced from the normalized maximum rate of impedance (Z) change during the "Heater ON" phase (10-20 s).

The contact pad region was attached to a PEEK adhesive backing and mated to an FFC cable through a zero-insertion force (ZIF) connector. This assembly was packaged with the sensor positioned in the lumen of a luer module and affixed with epoxy (EpoTek 353 ND-T) for integration into the EVD system (Fig. 1). The sensor was connected to a printed circuit board (PCB) with a commercial flow sensor LD20 (Sensirion) via the FFC (Fig. 3). A cable interfaced the PCB to the power source and recording system, allowing both the impedimetric and LD20 sensors to be activated to acquire simultaneous flow measurements.

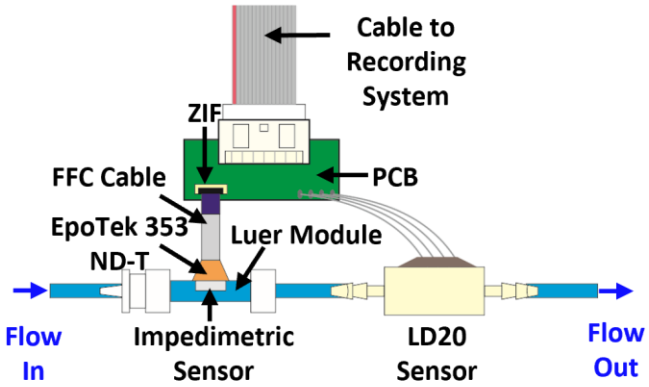

Figure 3. Schematic of fully packaged impedimetric and LD20 sensors. Blue arrows indicate the direction of CSF flow.

The sensor was calibrated at the benchtop using phosphate-buffered saline and compared against the LD20 sensor over the flow range of 0 to 1000 µL/min. For the low flow range of 0 to 200 uL/min, one calibration measurement was taken every 20 µL/min. The measurement was taken every 250 µL/min for the higher flow rate. To simulate *in vivo* conditions, the testing setup was placed in a temperature-controlled chamber (Fig. 4). A temperature probe was used to actively monitor the temperature of the reference PBS to ensure the liquid flowing through the sensor reached the expected temperature. The fluid temperature was varied around body temperature (37 °C), 20, 30, and 40 °C specifically to investigate the impact of temperature on sensitivity.

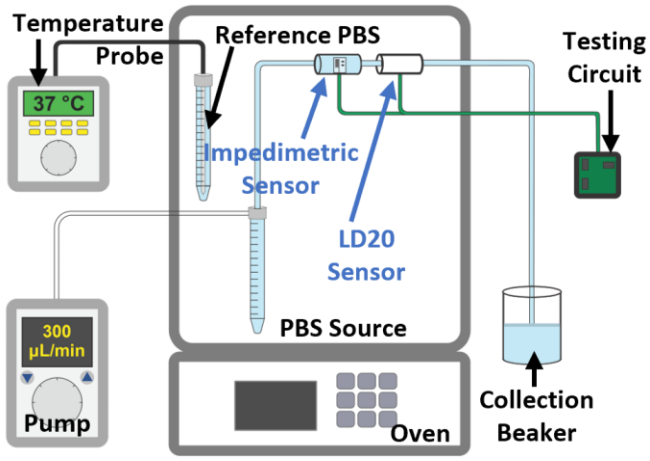

Figure 4. Benchtop testing setup for calibrating the sensor. Phosphate-buffered saline (PBS) flow and an oven were used to mimic the body's warm saline environment.

RESULTS AND DISCUSSION

Flow sensor calibration curves at various heater power settings (10, 20, and 40 mW) were evaluated (Fig. 5). At 10 mW, the sensitivity (slope of the plotted curve in Fig. 5) was low for flow

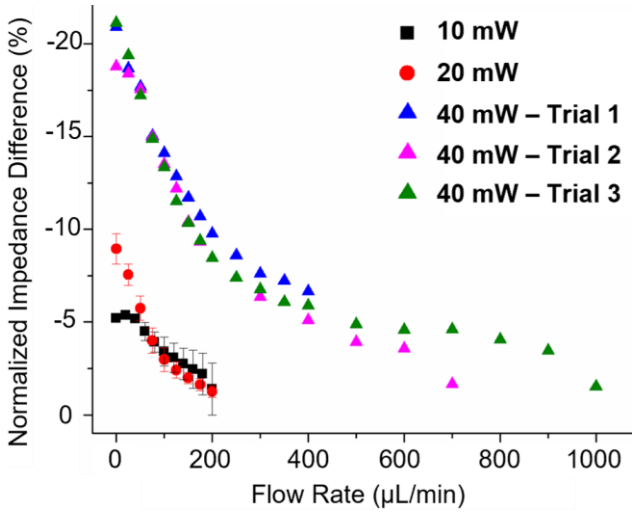

Figure 5. Impedimetric sensor calibration at different heater input powers. The sensitivity (Δ%/µL/min) increased significantly, especially in the low flow range when input power doubled from 10 to 20 mW but did not improve beyond 20 mW.

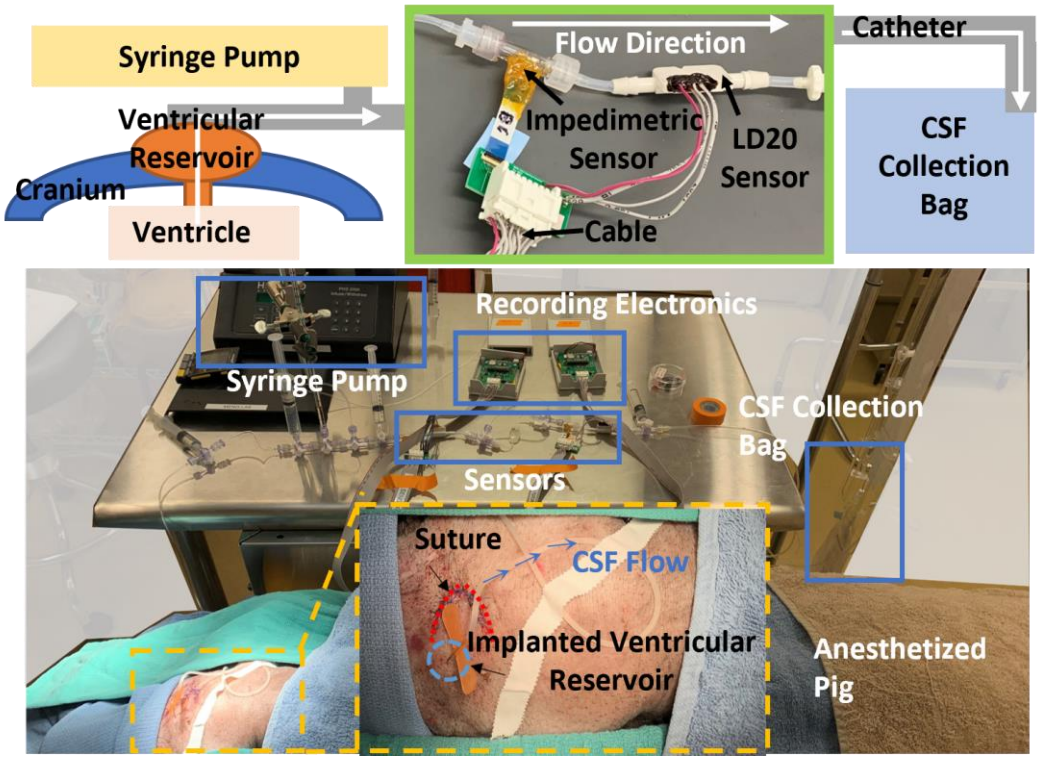

Figure 6. Testing setup for the porcine study. The ventricular catheter was implanted into the ventricle with the reservoir under the scalp then the wound was sutured. A needle with a catheter was connected to the reservoir (yellow dashed box) to access CSF via the shunt either for draining or infusing. Flow sensors were connected to the output for measuring the flow rate and temperature of CSF.

rates under 100 µL/min. Curves at 20 and 40 mW had similar slopes. Sensitivity did not improve above 20 mW; this heater setting was selected to conserve power.

A non-linear response with flow rate was recorded, requiring two separate calibrations. For flow > 200 µL/min, HS was linearly correlated with flow rate (R^2=0.94) but quadratic for lower flow rates (R^2=0.95). By considering different regression curves by flow range, the sensor accuracy (% error) improved over sixfold compared to previous work [6] for the low flow rate domain, which corresponds to the typical CSF flow range observed in patients with an EVD [2]. Longer response times are expected at low flow, further supporting two separate calibrations [8].

An impedimetric sensor and LD20 were connected to an EVD, installed in a 36 kg 10-month-old Yucatan female pig, and used to take periodic CSF flow measurements for one week (Fig. 6). An incision was made on the pig's scalp, and a burr hole (diameter of ~1.5 - 3 cm) was drilled for inserting the ventricular catheter to target the pig's left lateral ventricle. The burr hole was placed on the coronal suture ~1 - 1.5 cm from the midline. Proper ventricular catheter placement was confirmed by the outflow of CSF from the sidearm of the silicone reservoir. The ventricular catheter reservoir was sutured to the pericranium with the sidearm plugged. The skin was closed with two layers of sutures and marked over the reservoir for future access.

CSF was drained from the ventricle through the reservoir, directing flow through the sensors to a collection bag. Access to the CSF was achieved using a 25-gauge butterfly needle to puncture through the reservoir. The same line was connected to a syringe pump to infuse artificial CSF (aCSF) into the pig's ventricle to modulate ICP for mimicking the hydrocephalus condition. Impedimetric sensors successfully tracked temperature and flow

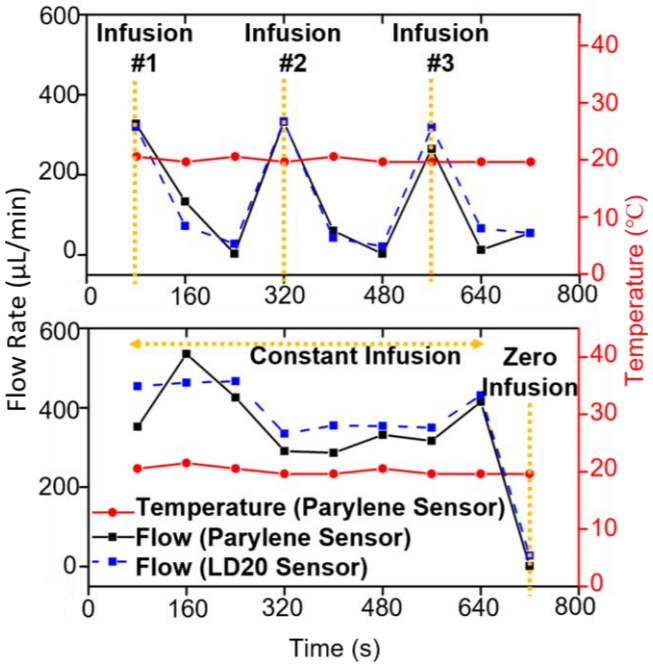

Figure 7. Flow and temperature of pig CSF acquired by impedimetric Parylene and LD20 sensors. (Top) Results for sequential aCSF bolus infusions at 80, 320, and 560 s, respectively. Measurements were obtained after infusion. (Bottom) Results for constant aCSF infusion. The infusion was stopped after 640 s, and measurements were taken during infusion.

rate (Fig.7) under bolus and constant aCSF infusion. Comparison to LD20 flow measurements showed good agreement (Fig. 8). The impedimetric sensor reliably tracked flow at different time points over one week: day 1 (surgery day), 6, and 7 (Fig. 9). A stable RMS error of 21.39, 36.62, and 32.25 µL/min was recorded.

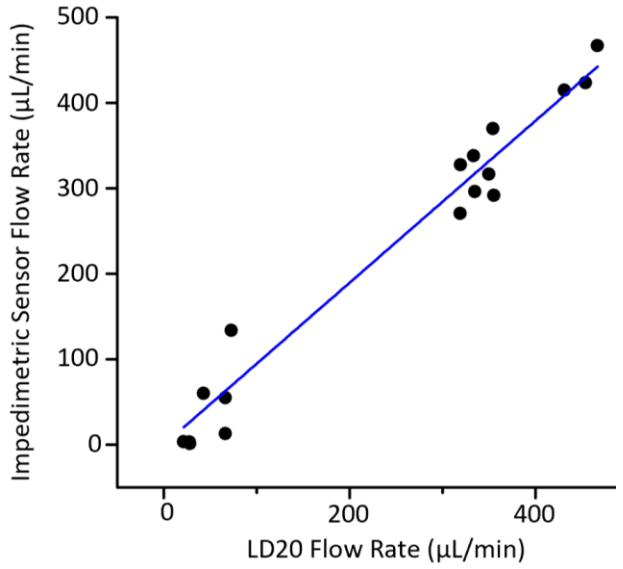

Figure 8. The measured flow rate of the impedimetric sensor (y) was linearly correlated to the LD20 sensor (y=0.95 x, R^2=0.99).

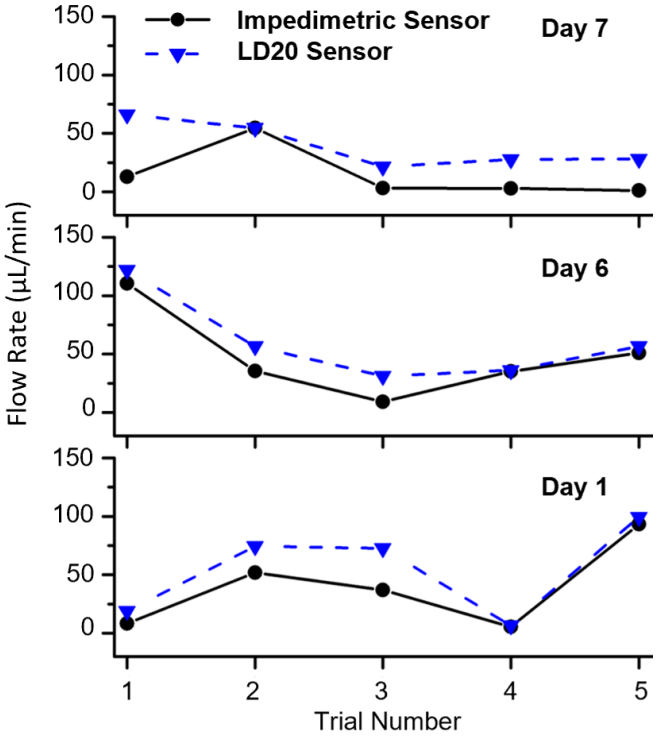

Figure 9. Comparison of flow measurements over one week for the impedimetric and LD20 sensors (implantation on Day 1).

The sensor system used for the porcine study was wired to a recording PCB with an SD card slot for storing the data. A lithium polymer battery was used to power up the PCB and sensors. Future work involves developing a fully implantable sensor system, including miniaturization of the recording electronics.

CONCLUSION

This work demonstrated a Parylene flow sensor based on electrochemical impedance transduction and successful flow and temperature measurements in a live shunted pig for one week. The sensor tracked CSF flow in real-time from the pig brain ventricle with good agreement with a commercial sensor (LD20). This paves the way for the application of the sensor for *in vivo* long-term monitoring of physiological flow in hydrocephalus patients.

ACKNOWLEDGEMENTS

The authors would like to thank Dr. Bradley Ahrens, Dr. Lynlee Stevey, and Vivian La for their assistance in the animal study. The authors also express special thanks to Dr. Donghai Zhu for his input on fabrication and the USC Biomedical Microsystems Laboratory members for their assistance. This work was supported in part by the National Science Foundation under award numbers EFRI-1332394 and IIP-182773, USC Coulter Translational Research Partnership Program, and the USC Ming Hsieh Institute Award.

REFERENCES

[1] J.M. Spirig, M. N. Frank, L. Regli, and L. H. Stieglitz, "Shunt Age-related Complications in Adult Patients with Suspected Shunt Dysfunction. A Recommended Diagnostic Workup", *Acta Neurochirurgica*, 159, 8 (2017).

[2] T. Pennell, J.L. Yi, B. A. Kaufman, and S. Krishnamurthy, "Noninvasive Measurement of Cerebrospinal Fluid Flow Using An Ultrasonic Transit Time Flow Sensor: A Preliminary Study", *Journal of Neurosurgery: Pediatrics PED*, 17, 3 (2016).

[3] T. Bork, A. Hogg, M. Lempen, D. Müller, D. Joss, T. Bardyn, P. Büchler, H. Keppner, S. Braun, Y. Tardy, and J. Burger, "Development and *In-Vitro* Characterization of An Implantable Flow Sensing Transducer for Hydrocephalus", *Biomedical Microdevices*, 12, 4 (2010).

[4] K. Scholten and E. Meng, "Materials for Microfabricated Implantable Devices: A Review", *Lab on a Chip*, 15, 22 (2015).

[5] A. Baldwin, L. Yu, and E. Meng, "An Electrochemical Impedance-Based Thermal Flow Sensor for Physiological Fluids", *Journal of Microelectromechanical Systems*, 25, 6 (2016).

[6] T. Hudson, A. Baldwin, A. Samiei, P. Lee, J.G. McComb, and E. Meng, "A Portable Multi-Sensor Module for Monitoring External Ventricular Drains", *Biomedical Microdevices*, 23, 45 (2021).

[7] T. Hudson, A. Baldwin, E. Christian, J.G. McComb, and E. Meng, "Testing A Multi-Sensor System for Hydrocephalus Monitoring in External Ventricular Drains", 2019 20th International Conference on Solid-State Sensors, Actuators and Microsystems & Eurosensors XXXIII, Berlin, Germany (2019).

[8] C. Sosna, T. Walter, and W. Lang, "Response Time of Thermal Flow Sensors", 2010 Eurosensors XXIV, Linz, Austria (2010).

CONTACT

*X. Wang, tel: +1-213-8213897; xuechunw@usc.edu
*E. Meng, tel: +1-213-8213949; ellismen@usc.edu

PROBING THE LIFE IN BUBBLES – NANOPLASMONIC QUANTIFICATION OF PATHOGEN-DERIVED EXTRACELLULAR VESICLES IN BLOOD

Tony Y. Hu[1,2,3]

[1]The Center for Intelligent Molecular Diagnosis, Tulane University, New Orleans, LA, USA
[2]Department of Biochemistry and Molecular Biology, Tulane University, New Orleans, LA, USA
[3]Department of Biomedical Engineering, Tulane University, New Orleans, LA, USA

ABSTRACT

Extracellular vesicles (EVs) are small membrane-bound vesicles secreted by all cells, circulate at high levels, and convey nucleic acids, peptide/proteins, lipids. EVs secreted by microbial pathogens or infected or malignant cells represent an excellent source of biomarkers, but technical challenges have prevented development of EV-based assays. With the advanced technologies, we have identified and validated new biomarkers for rapid pathogen differentiation (e.g. SARS-CoV-2 and mycobacterial), early disease diagnosis (including cancer), and/or real-time evaluation of disease response. Our multidisciplinary expertise enables us to employ the characteristic properties of engineered nanodevices to improve the capture and detection of circulating biomarkers.

KEYWORDS

Extracellular vesicles, Blood-based biomarker, Early detection, Personalized diagnosis

INTRODUCTION

Diagnostics for infectious and malignant diseases often exhibit poor specificity/sensitivity, hindering early detection and treatment evaluation, but development of improved assays is limited by several challenges, including absence of disease-specific factors, low biomarker concentrations, and interfering factors. We have been developing novel strategies to overcome these obstacles, exploiting proteomic information and nanomaterial properties to generate integrated assay platforms for personalized medicine.

Extracellular vesicles (EVs) are small membrane-bound vesicles secreted by all cells that circulate at high levels and carry nucleic acid, peptide/protein, and lipid cargoes, and membrane-associated receptors and ligands from a parent cell to local or distant cells, where EV uptake can modify recipient cell behavior. EVs have thus been considered to be potential markers that carry specific biological information underlying both physiological mechanisms (e.g., intercellular communication [1] and regulation of the immune response and morphogenesis [2, 3]) and pathological processes (e.g., cancer[4], viral and bacterial infection [5], and neurodegenerative diseases [6]) by transferring cargoes with effector functions [7], but technical challenges have thus far prevented development of EV-based assays. Lack of unique, exosome-specific markers has hindered research into EVs biogenesis and function, thus, an isolation steps are often required for analyzing exosomes in both basic research and clinical application. Most EV assays require purified EVs, but EV isolation methods are slow, labor-intensive and highly variable, rendering them impractical for most clinical applications.

To address this need, we have developed a novel, streamlined procedure in which EVs are captured directly from serum or plasma by an antibody recognizing a common EV membrane protein and then hybridized with antibody-conjugated gold nanorods (AuR) and nanospheres (AuS) that respectively bind a common and a disease-specific EV membrane protein. Only EVs secreted by diseased cells bind both probes, and the resulting AuR-EV-AuS complexes produce a plasmon that markedly shifts the spectrum and the intensity of scattered light to distinguish target EVs from AuR-EV complexes that emit weak signal at a different wavelength [8].

This assay requires ≤1μL and thus permits longitudinal analysis of EV biomarker targets in mouse models of human disease, which was not feasible with existing EV assay methods. We applied this ability to analyze a mouse model of pancreatic cancer, finding that plasma concentrations of tumor-derived EVs correlated with time after tumor initiation and tumor volume. This ability should provide valuable insight into cancer progression, metastasis, and drug resistance in mouse models of cancer and infectious disease. We have also reported that tumor-derived EV expression in human plasma could distinguish PDAC cases, including early stage (T1 + T2) cases, from non-malignant controls with similar symptoms, and that diagnostic performance of this assay (89% sensitivity and 85% specificity) exceeded that reported for serum/plasma CA 19-9 (80% and 75%) and CEA (50% and 78%) assays.

This EV assay requires the analysis of high-magnification dark field images, whose acquisition can be time-intensive. We have therefore devised a low-magnification version of this assay that does not require user focusing during image capture and have adapted it for readout on a cell phone attachment, enhancing its application in resource-limited settings [9, 10].

We have also adapted this basic design to produce the first EV assay to distinguish between: 1) altered abundance of target EVs with stable biomarker expression, 2) altered biomarker expression in a stable target EV population, and 3) changes in both target EV abundance and biomarker expression. This addresses an existing deficit in EV biomarker data, since current assays analyze an EV biomarker level in a sample without considering which of the above mechanisms is responsible for a biomarker difference, but this information can have important implications since distinct pathways can regulate EV secretion and EV biomarker expression. Further, our proof-of-principle results in a population of subjects with and without pancreatic cancer have indicated that normalizing target EV biomarker signal to total EV abundance in this manner dramatically improved the ability to resolve these populations when compared to discrimination using biomarker signal alone.

Copyright retained by Authors

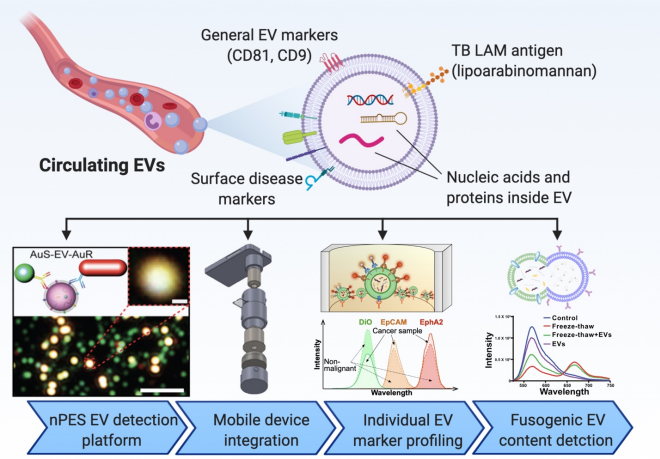

Figure 1: EV biomarker detection platforms. *Circulating EV can carry multiple surface and luminal factors that can serve as markers of specific diseases, their stage, prognosis, and response to treatment. We have developed (**Left**) a nanoplasmonic enhanced scattering (nPES) assay to directly detect disease-associated protein or lipid markers on the surface of EVs present in patient serum or plasma samples and (**Middle Left**) have developed an inexpensive and portable mobile phone-based device to read these assays in resource limited settings. We subsequently modified this assay platform (**Middle Right**) to permit multiplex quantitation of two disease biomarkers, employing quantum dot probes and EV lipid labeling to normalize EV biomarker signal and thereby distinguish functionally distinct mechanisms responsible for EV biomarker changes. To analyze biomarkers present in the lumen of disease-associated EVs directly from serum or plasma samples, we next developed a liposome-based assay (**Right**) in which antibody-labeled liposomes carrying molecular beacons recognize and fuse with target EV populations to produce fluorescent signal(s) in proportion to biomarker abundance in the EV lumen.*

The above assays are designed to rapidly read biomarkers on the surface of EVs, since the analysis of potential biomarkers carried as EV cargoes normally requires the isolation of the biomarker material from lysates of a total or target EV population, which can reduce assay sensitivity and specificity due to the variable purity and background of the EV fractions generated for these assays. To address this issue, my group is developing a purification-free assay for such analyses in which customized liposomes containing molecular beacons are directed to bind to target EV populations through specific recognition of an EV surface marker, ensuring that the biomarker signal of these can be read directly from serum or plasma samples.

EVs are unique, encapsulated biomolecules that are abundantly secreted by all cells and carry crucial biological information from their cell of origin. These nanometric particles can be detected in different biofluids (e.g., blood, cerebrospinal fluid, urine, saliva) via procedures with close-to-no invasiveness. However, EV analysis is not yet clinically translatable due to the requirement for a purification step and the lack of a standard technique for reproducible, high yield, pure exosomes. The explosive rise in studying exosomes as promising biomarkers for disease diagnosis, prognosis, and treatment monitoring (in maladies such as cancer, infectious diseases, and neurodegenerative diseases), now more than ever, underscores the necessity of developing highly sensitive, reproducible, and scalable techniques that can examine and implement clinically relevant applications of EVs. Since all the currently known size-based and affinity-based assays have inherent drawbacks for clinical applicability, researchers have turned to nanoplasmonic structures and explored them as novel compact devices with great potential to make to the clinics. Therefore, many distinct types of plasmonic metamaterials are readily functionalized with molecules that exhibit affinity to target biomarkers and thus be employed as biosensors in multiple different applications. The specificity of such biosensors can be facilely modified by altering the specificity of their conjugated affinity molecules, such that specific antibodies can be employed to recognize EV biomarkers associated with particular diseases or disease stages to permit disease diagnosis, staging, and treatment monitoring. However, for such plasmonic biosensors to have clinical utility, they must satisfy several essential requirements. These include the ability to (1) rapidly analyze unprocessed clinical specimens, such as serum or plasma, in a high-throughput manner; (2) allow more sensitive and specific detection of existing biomarkers, or novel biomarkers not evaluable by other methods, and (3) utilize simple, efficient, high-yield, and cost-effective fabrication and characterization procedures. Although most current nanoplasmonic assays do not yet meet one or more of these requirements, and therefore future studies are necessary to address these issues and ultimately demonstrate the utility of a refined assay platform in a clinical validation study, (1) the versatility of plasmonic materials that can be designed, fabricated, and tailored to work at a range of biological wavelengths, (2) the promise of reaching the ultra-low limit of detection, (3) the potential for making compact, portable silicon-based devices with a low footprint, and (4) the possibility of making purification-free, automated assays with no or close-to-zero operator bias, make nanoplasmonic sensing and detection a rising approach in EV research.

REFERENCES

1. Colombo, M., G. Raposo, and C. Théry, *Biogenesis, secretion, and intercellular interactions of exosomes and other extracellular vesicles.* Annual review of cell and developmental biology, 2014. **30**: p. 255-289.
2. Fuccillo, M., A.L. Joyner, and G. Fishell, *Morphogen to mitogen: the multiple roles of hedgehog signalling in vertebrate neural development.* Nature Reviews Neuroscience, 2006. **7**(10): p. 772-783.
3. van den Brink, G.R., *Hedgehog signaling in development and homeostasis of the gastrointestinal tract.* Physiological reviews, 2007. **87**(4): p. 1343-1375.
4. Minciacchi, V.R., M.R. Freeman, and D. Di Vizio. *Extracellular vesicles in cancer: exosomes, microvesicles and the emerging role of large oncosomes*. in *Seminars in cell & developmental biology*. 2015. Elsevier.
5. Rodrigues, M., et al., *Role of extracellular vesicles in viral and bacterial infections: pathogenesis, diagnostics, and therapeutics.* Theranostics, 2018. **8**(10): p. 2709.
6. Thompson, A.G., et al., *Extracellular vesicles in neurodegenerative disease—pathogenesis to biomarkers.* Nature Reviews Neurology, 2016. **12**(6): p. 346.
7. Théry, C., et al., *Minimal information for studies of extracellular vesicles 2018 (MISEV2018): a position statement of the International Society for Extracellular Vesicles and update of the MISEV2014 guidelines*, in *J Extracell Vesicles*. 2018, Taylor & Francis: HOBOKEN. p. 1535750-n/a.
8. Liang, K., et al., *Nanoplasmonic quantification of tumour-derived extracellular vesicles in plasma*

microsamples for diagnosis and treatment monitoring. Nature biomedical engineering, 2017. **1**(4): p. 1-11.
9. Amrollahi, P., et al., *Ultra-sensitive automated profiling of EpCAM expression on tumor-derived extracellular vesicles.* Frontiers in genetics, 2019. **10**: p. 1273.
10. Wan, M., et al., *Using nanoplasmon-enhanced scattering and low-magnification microscope imaging to quantify tumor-derived exosomes.* JoVE (Journal of Visualized Experiments), 2019(147): p. e59177.

PASSIVE 3D-PRINTED FULLY ELASTIC PILL FOR SAMPLING OF GUT MICROBIOME

Ruben Del-Rio-Ruiz[1,2], Cihan Asci[1,2], Rachel Owyeung[1], Giovanni Widmer[3] and Sameer Sonkusale[1,2]*
[1]Nano Lab, Advanced Technology Laboratory, Tufts University, USA
[2]Department of Electrical and Computer Engineering, Tufts University, USA
[3]Cummings School of Veterinary Medicine, Tufts University, USA

ABSTRACT
Sampling of gut microbiome upstream of the colon is challenging and expensive. Research has shown that ingestible devices are effective in sampling microbiome, however existing designs are complex and suffer from high levels of contamination from untargeted regions. This paper aims to present a simple sampling design concept with a self-closing mechanism relying on swellable polyacrylate beads that close the inlet to prevent contamination. The pill is fully elastic, lightweight, biocompatible, battery-less realized using stereo-lithography based 3D-printer. Herein, it is believed that such an ingestible device will increase the understanding of spatial diversity of gut microbiome and its response to medical conditions and treatments, using a non-invasive and simple technique.

KEYWORDS
Biomedical microdevices, Gastrointestinal tract, Gut microbiome, Ingestible, Capsules, Pills, Microbiome.

INTRODUCTION
Technologies capable of noninvasively sampling the luminal content of the GI tract have the potential to improve our understanding of the role of microbiome in health and various medical conditions. Microbial conditions in the gut are typically inferred from the analysis of fecal DNA and fecal metabolites [1]. This approach is inadequate for characterizing the microbiome upstream of the distal colon [2, 3]. To gain new insights into the many beneficial functions of the gut microbiota, it is essential to sample in different locations in the gut, particularly organs located upstream of the colon. Orally ingestible medical devices for gut engineering have been reported for sensing and diagnosis [4-8]. Most devices are rigid, and some require complex fabrication and assembly techniques.

Additive manufacturing has the potential to transform the design and fabrication of ingestible devices by its ability to realize true 3D structures monolithically using biocompatible materials with wide range of properties (e.g., elastic). Such manufacturing technique involves a layer-by-layer construction of the designed pill using a 3D printer. Among the various 3D printing technologies, stereo-lithography (SLA) based 3D printing provides a balance between the print resolution, print time, build volume and cost.

Our prior work on ingestible pills for sampling the gut microbiome [3] relied on a 3D printed pill containing a battery-less osmotic pump and was validated in animal models. However, the design suffered from leakage and post-sampling contamination due to the lack of a closing valve. In this paper, we report the first elastic battery-less ingestible pill for sampling intestinal microbiome from the small intestine with a self-closing mechanism to prevent contamination and leakage. Pills elasticity allows for ease of sample intake as a result of peristaltic motion of the GI tract. The pill's sampling and locking mechanisms have been tested using different viscosity and granulation fluids. Enteric coating dissolutions and contamination tests using dyes have been performed to demonstrate the functionality of the pill and its ability to avoid leakage and contamination, respectively.

WORKING PRINCIPLE
The 3D printed elastic pill is placed inside a pH-sensitive enteric coated capsule to delay sampling until it enters the small intestine, where the coating dissolves in the higher pH environment (Figure 1). Natural peristaltic motion ensures mobility to the pill through the GI tract without any active motion. Upon exposure to the fluid from small intestine, the enteric coating dissolves, allowing lumen to freely flow through the two-side inlets. The pills elasticity ensures a natural pumping action as a result of peristaltic pressure, greatly assisting the overall sample intake. The pill contains highly hydrophilic sodium polyacrylate beads, both as an absorbent for passive suction, and for locking the intake when the beads are swollen. After the pill's reservoir reaches sufficient volume and the beads have expanded enough to close the inlet, we deem the sampling is completed. The pill then travels through the rest of the GI tract and is finally collected from the feces to study the gut microbiome.

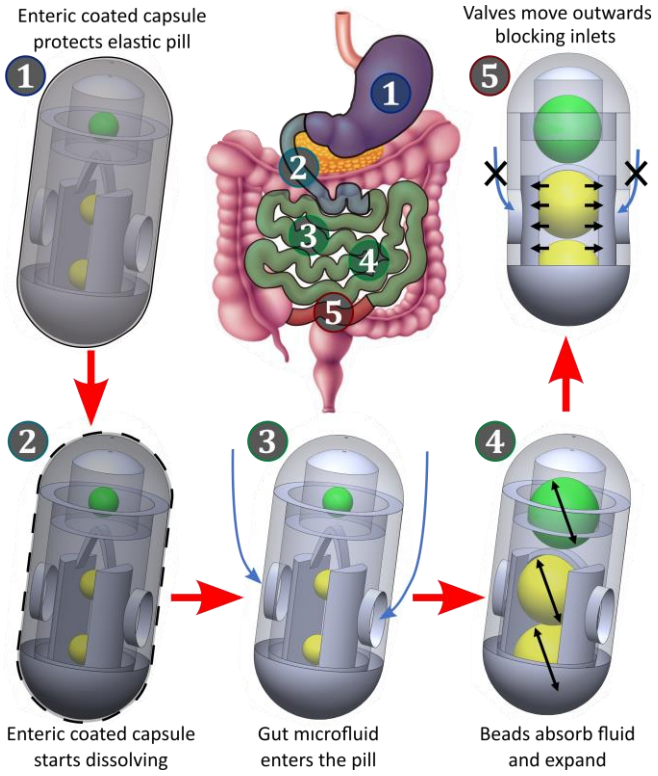

Figure 1: Sampling principle of the elastic ingestible pill. (Exact locations of the pill's status within the small intestine, will vary depending on the pill's enteric coating and pH levels through the GI tract.) 3D designed images were created using SolidWorks CAD tool.

978-1-940470-04-7/HH2022/$25©2022TRF
DOI 10.31438/trf.hh2022.21

PILL DESIGN AND FABRICATION

The overall design of the pill is shown in Figure 2. The elastic pill consists of three main parts—an elastic case, two internal valves, and three sodium polyacrylate beads. SLA-based 3D printing was used to fabricate the ingestible device's casing using a bio-compatible/photo- curable elastic resin (Formlabs Elastic 50A V1) using a Form 2 printer (Formlabs Inc., Somerville, MA, USA).

The elastic pill comprises an external wall thickness of 1mm, an overall pill height and width of 20 and 9mm, respectively; two internal valves height and width of 9.1 and 4mm, respectively, and a gap between valves of 2.61mm (Figures 2.a and 2.b). The gap between valves is specifically designed for 3mm-diameter beads, to ensure that their position stays fixed within the pill. A 1mm gap between each valve and inlet is designed (Figure 2.c) to allow inward flow while the pill is sampling. Two elliptical holes with a height and width of 4 and 2mm, respectively, are located on two opposite sides of the pill (Figure 2.d). The two vertical valves are attached to the bottom of the pill and to each other, forming a bridge, to guarantee that the valves do not lock the inlets until beads are fully expanded.

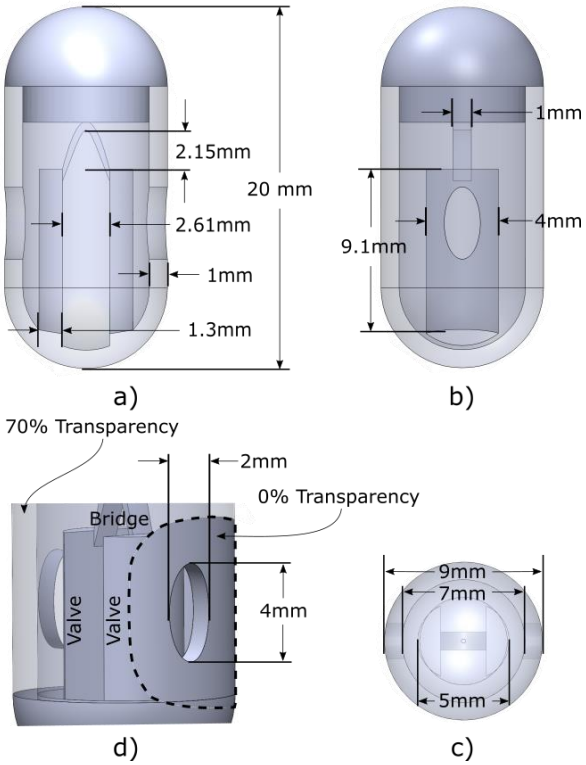

Figure 2: 3D schematic of the overall design of the elastic pill, a) side, b) front, and c) top views. d) Perspective view illustrating the side-inlets' dimensions of the elastic pill. (Partial transparencies have been added to better understand the internal parts of the pill.) 3D designed images were created using SolidWorks CAD tool.

The case of the pill was designed using a CAD tool such as SolidWorks (Dassault Systems SolidWorks Corporation, Waltham, MA). It is composed of two main sections: The bottom case has two-sided elliptical inlets and two internal microvalves for closing of the inlets autonomously. The top case is utilized as a shield for the pill once the beads are inserted.

The assembly process of the pill is as follows (Figure 3): Two sodium polyacrylate beads are inserted in the bottom section of the pill, in between the two valves. Afterwards, one sodium polyacrylate bead is placed inside the top section of the pill. The two sections are then attached using the same elastic resin (Formlabs Elastic 50A V1) and cured in the FormCure photocuring device (Formlabs Inc.) for 20 min. at 60°C. The pill is finally inserted in a pH-sensitive enteric coated capsule, to prevent it from sampling in the stomach's acidic environment.

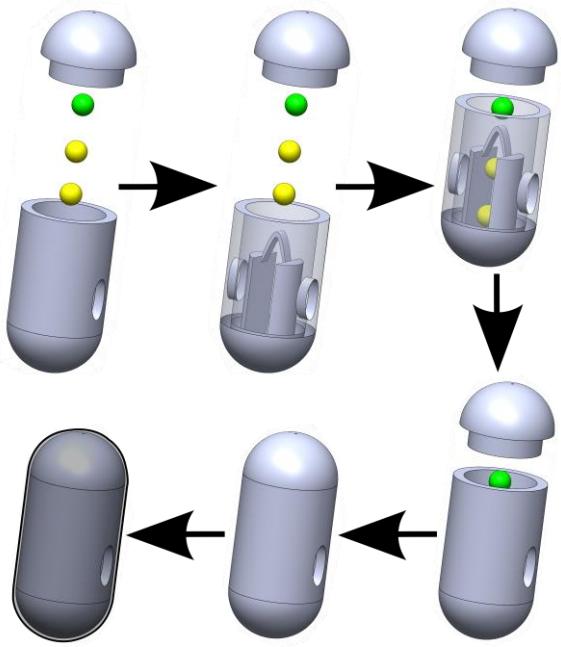

Figure 3: Assembly scheme of an elastic ingestible pill. (Some transparencies have been added to better illustrate the internal cavities of the proposed pill design.) 3D designed images were created using SolidWorks CAD tool.

RESULTS AND DISCUSSIONS

The sampling and locking mechanisms were first tested in-vitro, by inserting two red beads in the bottom section of the pill, in between the two valves. The pills were then placed vertically in a container filled with DI water, as shown in Figure 4.a (approximated viscosity of water was 8.90×10^{-4}Pa·s). DI water started flowing into the pill through the two side inlets, making the red beads expand. The internal gap between valves started increasing, until the valves fully locked the inlets, as shown in Figures 4.a and 4.b. A second experiment was performed with a higher viscosity sample (0.8Pa·s) and granulation, such as banana puree, to test sampling and locking performance. The pills' sampling performance was tested by measuring the time required to acquire the sample from the DI water and banana puree, until the valves fully locked the inlets. Results showed that within 20- and 90-minutes minutes, the beads were fully swollen, and inlets locked, preventing additional acquisition of DI water and banana puree, respectively (Figures 4.b and 4.c). The viscosity increment and granulation of the banana, in comparison to DI water, are the two main factors for the sample rate decrement. Yet, in both experiments, the beads fully expanded, pushing the valves outwards, and fully locking the elastic pills' inlets.

This work did not study the variation in size of the inlet-holes or valves. Yet, several deductions were obtained from preliminary design studies: sampling rate could be improved by increasing the cross-sectional area of the inlet, increasing the gap between inlets and valves, and by reducing the valve's overall width. Nevertheless, these variables are limited by the overall external

and internal sidewalls of the pill, overall height of the pill, and the required leakage and contamination performance level. Therefore, a trade-off between sampling rate, pill size and leakage/contamination performance needs to be met, to obtain the desired elastic ingestible device.

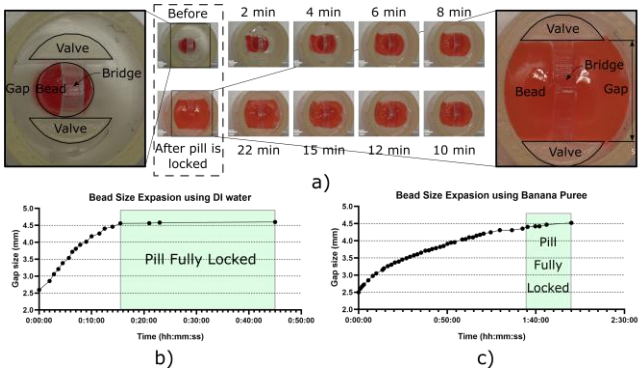

Figure 4: The locking mechanism performance of the elastic pill. a) Sequence of microscope images from pre-sampling stage of the bead inside of pill, until pill is fully locked with bead swollen. Images are captured with a Keyence VHX digital microscope, using -1° tilt angle, X30 magnification, and E20 lens. Top case of the pill is removed for sake of clarity during experiment. b) Graph illustrating the bead's (gap between valves) expansion progress over time using DI water. c) Graph illustrating the bead's (gap between valves) expansion progress over time using banana puree.

The elastic pill is covered with a pre-defined pH-sensitive enteric coating to delay sampling until it enters the small intestine, where the coating dissolves in the higher pH environment. To validate this initial sampling concept of the pill, the enteric coating performance was tested. The dissolution profile for the enteric coating can be controlled by an appropriate choice of polymer(s). The fabrication and testing of lab-made enteric coatings was not the focus of this study. Nonetheless, the elastic pills were inserted in commercial enteric capsules that could withstand up to pH 5. The enteric coating dissolution was tested by immersing enteric coated pills in a pH 2 buffer and kept in motion with a magnetic stirrer. Pills with gelatin-based capsules were also immersed and stirred in a neutral buffer for comparison purposes. Results showed that the enteric coated pills remained intact even after 2 hours of immersion and motion, where the gelatin-based pills' capsules dissolved withing 10 minutes as expected. The enteric coated pills were then transferred to an undyed pH 6 buffer, and stirred, where the coating dissolved exposing the inlets for sampling.

The results showed that the enteric capsule protects the pill from the stomach's acidic environment until it reaches the small intestine where it dissolves, allowing gut microbiome to enter the elastic pill. Farther studies and redesigns of the enteric coating could provide the pill with a more accurate initial sampling point. This, combined with a user-defined pill design, could more precisely define the start and finish sampling location within the small intestine, to better treat and diagnose gut conditions.

Finally, rigorous contamination tests were performed (Figure 5) by inserting post water sampling in a solution containing Rhodamine B dye and measuring any color change with a UV-Vis spectroscopy (Figure 5.a). We expect the content of the pill not to change color to prove no contamination.

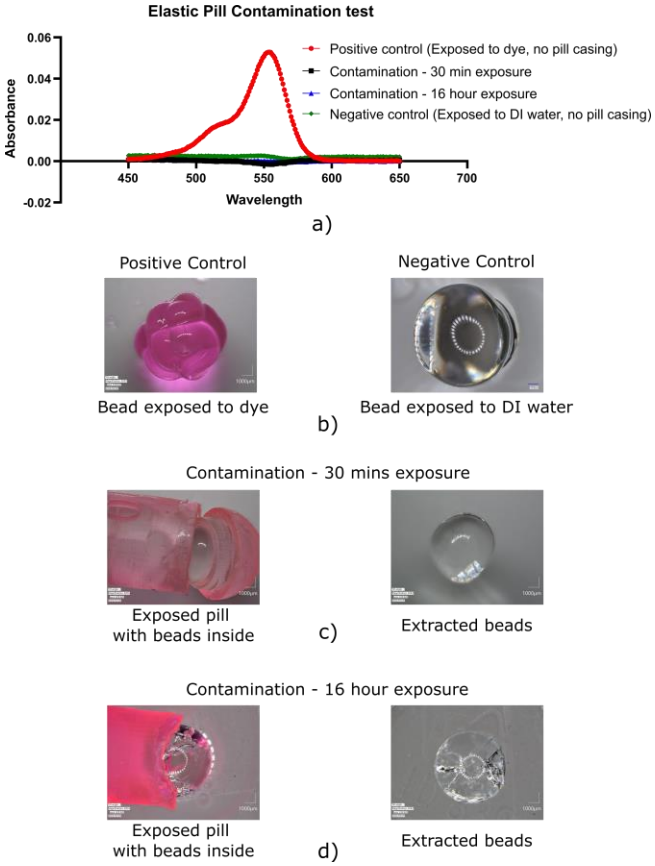

Figure 5: Contamination test performance of the elastic pill. a) Graph illustrating UV-Vis absorption spectrum results from the pills contamination experiments. Images are captured with a Keyence VHX digital microscope, using -1° tilt angle, X20 magnification, and E20 lens. Microscope images are taken to illustrate the difference in color between b) the positive and negative controls, where beads where directly exposed to dye and DI water, respectively; and contamination tests, where fully locked elastic pill were exposed to dye for c) 30 minutes and d) 16 hours.

A negative and positive control were first tested, by submerging beads in DI water and 20nmol Rhodamine/mL aqueous solution, respectively. Once beads were fully expanded (Figure 5.b), they were individually soaked in 3mL of DI water for 30 min. and their absorbance measured using UV-Vis spectroscopy.

Two contamination tests were then performed by submerging post-sampled and fully locked pills in 20nmol Rhodamine/1mL DI water for 30 minutes and 16 hours, as shown in Figures 5.c and 5.d, respectively.

The UV-Vis Spectroscopy showed a positive control with an absorbance peak of 554nm (Figure 5.a). Yet, the negative control and the contamination tests did not show any absorbance peaks at the same wavelength. Therefore, no measurable contamination was detected, indicating that the automatic closing valve worked as expected.

CONCLUSIONS AND FUTURE WORK

The proposed elastic ingestible pill can be realized using a SLA based 3D printer using an elastic resin. The fabrication process is simple and does not require any labor-intensive fabrication steps as would be required using a cleanroom or machine shop. Moreover, the design is scalable in size, which it can be used for sampling in small to large animals. Results from in-vitro experiments show that

the proposed elastic pill design is capable of sampling reliably with negligible leakage and contamination using different viscosity and granulation fluids.

Future research will focus on adjusting the composition of the enteric coating to control the initial sampling location in the GI tract. Further experiments will also be performed on the pill's side-inlets and valves by adjusting its size and design to alter the sampling rate and farther decrease potential leakages. Finally, validation of the elastic pills will be performed in ex-vivo sections of the GI track and in-vivo, in pig animal models.

ACKNOWLEDGEMENTS

Authors would like acknowledge support of NIH grant R21AI144521 for this work.

REFERENCES

[1] J. Qin, R. Li, Jeroen Raes, et al., "A human gut microbial gene catalogue established by metagenomic sequencing" *Nature*, 464, 03 (2010).

[2] D. Kumral, and A. Zfass, "Gut movements: A review of the physiology of gastrointestinal transit", *Digestive Diseases and Sciences*, 63, 10 (2018).

[3] H. R. Nejad, B. Oliveira, et al., "Ingestible osmotic pill for in vivo sampling of gut microbiomes", *Advanced Intelligent Systems*, 1, 07 (2019).

[4] N. Mandsberg, J. Christfort, et al., "Orally ingestible medical devices for gut engineering", *Advanced Drug Delivery Reviews*, 165-166, 05 (2020).

[5] W. Weitschies, L. Muller, et al., "Ingestible devices for studying the gastrointestinal physiology and their application in oral biopharmaceutics", *Advanced Drug Delivery Reviews*, 176 (2021).

[6] C. Steiger, A. Abramson, et al., "Ingestible electronics for diagnostics and therapy", *Nature Review Materials*, 83-98, 4 (2019).

[7] M. Koziolek, M. Grimm, et al., "Investigation of pH and temperature profiles in the GI tract of fasted human subjects using the Intellicap® System", *J. Pharm. Sci.,* 2855-2863, 104 (2015).

[8] C. Cheng, Y. Wu, et. al., "A wireless, ingestible pH sensing capsule system based on iridium oxide for monitoring gastrointestinal health", *Sensors and Actuators B: Chemical*, 130781 (2021).

CONTACT

*S. Sonkusale, tel.: +1-617-627-5113; sameer.sonkusale@tufts.edu

BIOMIMETIC ANCHORING SYSTEM FOR SUSTAINED AND LOCALIZED GASTROINTESTINAL DRUG DELIVERY

Joshua A. Levy[2,3,5], Michael A. Straker[2,4,5], Luke A. Beardslee[2], and Reza Ghodssi[1,2,5]*
[1]Department of Electrical and Computer Engineering, [2]Institute for Systems Research,
[3]Department of Materials Science and Engineering, [4]Fischell Department of Bioengineering,
[5]Robert E. Fischell Institute for Biomedical Devices,
University of Maryland, College Park, Maryland, USA

ABSTRACT

We present a novel application of biomimetic spiny microneedles for an anchoring drug deposit (SMAD) enabling long-term localized treatment of lesions within the GI tract. Mechanical characterizations in *ex-vivo* intestinal tissue demonstrate a 22-fold higher anchoring force than traditional conical molded microneedle (MMN) arrays. Additionally, payload diffusion experiments demonstrate that the SMAD can predictably deliver drugs, locally, to a site of interest with comparable performance to MMNs, indicated by strong logarithmic correlation (R^2=0.9773) across SMAD and MMN data. We anticipate this work will permit exploration of localized GI tract drug delivery, facilitating targeted treatment to reduce adverse drug side effects.

KEYWORDS

Drug Delivery, Gastrointestinal Tract, Tissue Anchoring, Direct Laser Writing

INTRODUCTION

Gastrointestinal (GI) disorders are currently managed by systemic oral and intravenous administration of drugs, resulting in broad dispersal of the therapeutic agents throughout the body [1]. Many therapeutics for gastrointestinal disorders, like immune modulating agents and corticosteroids, are accompanied by adverse side effects that are a consequence of high levels of systemic drug absorption [1], [2]. When delivering these therapeutics systemically, excess agent is required to achieve adequate treatment at sites of interest. Targeted treatment, achieved by delivery to specific locations in the GI tract, could offer comparable remediation of inflammatory sites without the use of excess therapeutic agent. This targeted delivery method serves to reduce side effects related to common GI drugs and lessen excess drug usage and, consequently, drug costs.

A variety of technologies currently exist to increase the regional specificity of drug delivery in the GI tract. Notably, pH-sensitive tablet coatings enable region-specific (stomach, small intestine, etc.) release of the encapsulated therapeutic agents. Additionally, mucoadhesive coatings can be leveraged to slow the transit of a tablet by attaching to mucus-lined tissue; thus, promoting focused release in a target region of the GI tract [2]. However, these technologies only enable broad regional targeting of drug delivery, making it impossible to direct treatment to specific locations in the GI tract. Though helpful, these technologies fail to address the need for location-specific delivery of therapeutic agents.

Enhanced regional targeting has also been achieved using ingestible devices. Although intended for different applications, great focus has been placed recently on ingestible devices for delivery of biological macromolecules such as insulin. Traverso et al. have previously demonstrated a microneedle device for delivery of insulin in the small intestine, controlled by dissolution of a pH-responsive polymer [3]. Abramson et al. demonstrated a self-orienting mm-scale applicator (SOMA) for insulin delivery in the stomach [4], as well as a luminal unfolding microneedle injector (LUMI), for biologic delivery in the small intestine [5]. These microsystems advancements empower site-specific delivery; however, the devices still operate using a broad region-targeting approach.

Targeted and moderately localized delivery has been achieved using fluid release capsule mechanisms. Multiple systems have been developed that use MEMS actuators for site-specific fluid drug delivery [6]–[9]. Additionally, magnetic locomotion and localization systems have been used to facilitate delivery of therapeutics at specific locations in the GI tract. Dietzel et al. utilized a magnetic localization and fluid drug release device to control the location of drug release [10]. However, the precision of drug localization is limited in these systems due to the fluid spread that occurs after drug release. Lee et al. utilized a similar magnetic actuation concept to apply dissolving drug-loaded microneedle patches to the small intestine mucosa to achieve location specific treatment [11]. Although the demonstrated ingestible capsule device showed successful delivery in *ex-vivo* tissue, the authors noted challenges with adhesion of the dissolving molded microneedles (MMNs) to the tissue, inhibiting the potential for prolonged delivery of therapeutics *in-vivo*.

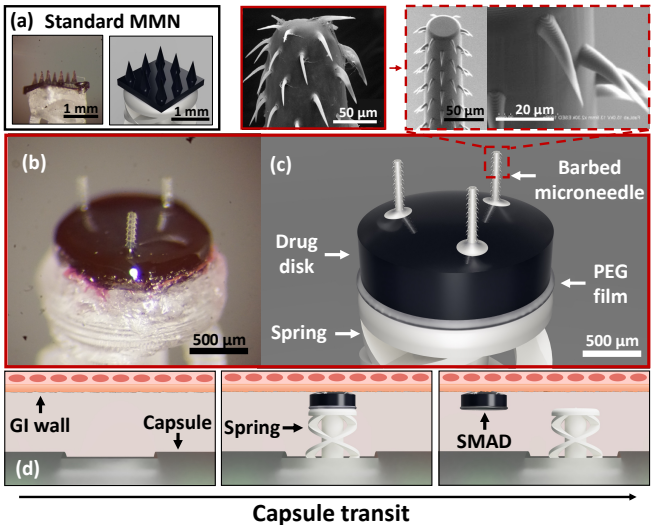

Figure 1: (a) Image and rendering of a standard 3x3 conical molded microneedle (MMN) array attached to the thermomechanical spring actuator and (b) image of SMAD attached to spring actuator. (c) Schematic overview of novel hybrid fabricated SMAD attached to actuator using water-soluble polyethylene glycol (PEG). Three barbed microneedles are attached to the drug disk using epoxy adhesive. (inset, left) Spiny headed worm proboscis from [12] and (inset, right) SEM image of biomimetic anchoring microneedle from [13]. (d) Spring actuator fires on command during capsule transit through the small intestine. The SMAD is anchored in the mucosal tissue by the barbed microneedles, leaving the deposit in the tissue to release the loaded drug by diffusion.

978-1-940470-04-7/HH2022/$25©2022TRF
DOI 10.31438/trf.hh2022.22

To address the need for a reliable mechanism capable of highly localized and sustained therapeutic delivery, we demonstrate the application of biomimetic spiny microneedles, previously developed in our group [13], as an anchor for a dissolving drug deposit (Fig. 1). The spiny microneedles in this system are attached to a solvent-cast water-soluble drug disk that distributes therapeutic agent through a diffusion process. The system is designed to complement a previously demonstrated thermomechanical spring actuator [14] and is mechanically removed from this actuator after anchoring to the GI mucosa. Characterization of the system showed greatly increased anchoring capabilities of the SMAD when compared to traditional molded microneedles — signifying both improved tissue adherence and system reliability. The SMAD also demonstrates the ability to deliver model drug as efficiently as penetrating MMNs in an agarose medium.

EXPERIMENTAL METHODS

SMADs were fabricated by a hybrid process merging direct laser writing (DLW) of the barbed microneedles presented in [13] and solvent casting of model drug disks (∅=2 mm, t=500 µm) from 20 %w/v polyvinyl alcohol (PVA) containing FD&C Blue #1.

DLW of Barbed Microneedles

Barbed microneedles were fabricated by DLW using a similar protocol to that previously demonstrated in our group by Liu et al. [13]. The microneedles are 650 µm in height with a 74 µm tip diameter and a 300 µm flared base for enhanced adhesion to the drug disk. Each needle contains a total of 72 backward-facing barbs with high sharpness (~1 µm) that promote robust tissue anchoring. DLW was performed using the Dip-in Laser Lithography (DiLL) mode on a fused silica substrate with the Nanoscribe Photonic Professional GT (Nanoscribe GmbH, Karlsruhe, Germany). Biocompatible (ISO-10993-5) IP-S photoresist was used with a 25x objective and a slicing distance of 1 µm to fabricate a 3-needle array. Needles were printed upside down in a triangular pattern, supporting reliable attachment to the drug disk and control over the spatial arrangement of the needles on the fabricated structure. Post print, needle arrays were cleaned in propylene glycol monomethyl ether acetate (PGMEA) for 15 min, followed by 5 min in isopropyl alcohol.

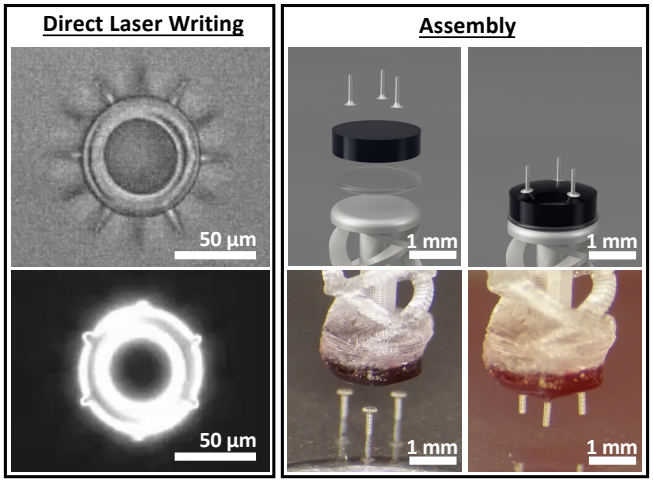

Figure 2: (left) DiLL mode DLW of barbed microneedle using Nanoscribe (NA=0.8). (right) Assembly of drug deposit structure by PEG attachment of the drug disk to the spring actuator then adhesion of the spiny microneedles using Loctite M-21HP biocompatible (ISO-10993) medical device epoxy adhesive.

Solvent Casting of Model Drug Disk

Model drug disks are fabricated by solvent casting a film containing 20 %w/v PVA (MW 31-50 kDa) (Sigma Aldrich, St. Louis, MO, USA) with FD&C blue #1 dye to visualize drug diffusion. The solvent is allowed to evaporate for 24 h, then drug disks (∅=2 mm) are punched from the resultant film.

Assembly of SMAD

Drug disks are first attached to the previously demonstrated spring actuator [14] with ~1.5 µg of melted polyethylene glycol (PEG). As can be seen in Fig. 2, the disk is then lowered onto the flared bases of the 3-microneedle array and adhered using Loctite M-21HP biocompatible (ISO-10993) epoxy adhesive (Henkel Corporation, Stamford, CT, USA). After 4 h is allowed for the epoxy resin to cure, the SMAD assembly is retracted, detaching the barbed microneedles from the fused silica substrate.

Solvent Casting of Conical Molded Microneedles

MMNs were fabricated by solvent casting PVA containing FD&C blue #1 dye, an identical composition to the solution used for solvent casting of model drug disks. Polydimethylsiloxane (PDMS) microneedle molds were acquired from Blueacre Technology Ltd. (Dundalk, Co Louth, Ireland). The microneedle mold has a 11x11 array of 600 µm needles with a base diameter of 300 µm, and an interspacing of 600 µm on center. 500 µL of the PVA solution was deposited on the needle array mold, then placed under vacuum for 15 min to remove air from the needle mold voids. The solvent was allowed to evaporate for 24 h, then a 3x3 needle array was cut from the molded part. The 3x3 array was then attached to the spring actuator using 1.5 µg of melted PEG.

Mechanical Anchoring and Removal Testing

Mechanical tests were performed to compare SMAD and MMN tissue anchoring and removal forces. This was done using an Instron 5942 universal test apparatus (Instron Corporation, Norwood, MA, USA) equipped with a 50 N load cell. All tests were performed using a crosshead speed of 1 mm/min. Spring actuators fitted with MMN or SMAD tip structures were lowered onto tissue samples until reaching the previously reported actuator force of 75 mN [14]. Tissue samples were pre-coated with a ~2 mm layer of 1X PBS (Sigma Aldrich, St. Louis, MO, USA) to simulate the presence of mucus and aqueous intestinal media on the tissue surface. Upon reaching the 75 mN force, the tissue was moved 2 mm laterally to imitate the longitudinal motion experienced in the GI tract. The sample is then retracted, resulting in the detachment or sustained attachment of the respective tip structures. Detachment or removal force was measured for each sample to determine the strength of the tip structure attachment when compared to the anchoring force for each type of tip structure. Tip detachment force was determined as the removal force of the SMAD from the actuator.

Model Drug Delivery

Dye-loaded SMAD (n=5) and MMN (n=5) samples were applied to a thin agarose surface and dye diffusion was tracked at predetermined time intervals from 0 to 168 h. Images of each sample were captured at each time point in a light-controlled environment, enabling a quantitative image analysis approach for data interpretation using MATLAB R2021b (MathWorks Corporation, Natick, MA, USA). From each image, the red color channel was isolated, and the resultant grayscale was binarized with a threshold intensity of 40 %. The resulting binary matrix was used to determine the areal dye spread and diffusion radius as a function of time. After 168 hr, the agarose samples were submerged in DI water to allow the dye to be diluted to within the linear regime of optical density.

Optical density of diluted samples was then obtained using a Molecular Devices SpectraMax Plus spectrophotometer (San Jose, CA, USA). Optical density measurements were compared to a calibration curve to determine the initial dye mass for each sample. These values are used to account for concentration-related differences in diffusion behavior, enabling a more pertinent comparison of model drug delivery.

RESULTS AND DISCUSSION

The SMAD was evaluated qualitatively by lateral removal experiments to imitate the longitudinal motion of a capsule in the GI tract. Performance of the SMAD was then quantitatively compared to that of a 3x3 MMN array, looking at mechanical removal and anchoring properties as well as the dynamics of drug delivery from each structure.

Removal by Lateral Translation

A capsule in the GI tract will experience periodic peristaltic movements; thus, a significant component of force will be applied perpendicular to the actuation direction. To model this, the SMAD was attached to an actuator and translated laterally (Fig. 3) until the SMAD structure was removed. Removal occurs at approximately 3 mm deflection, corresponding to 3 mm of capsule transit within the intestine.

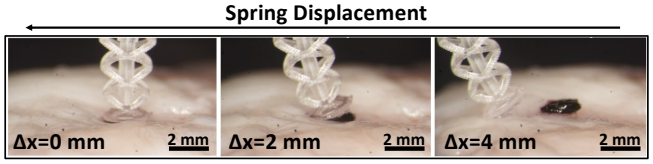

Figure 3: Tissue anchoring and deposit removal upon ca. 3 mm lateral deflection of the spring actuator. Lateral motion is intended to simulate capsule transit through the GIT.

Mechanical Characterization of Tissue Anchoring

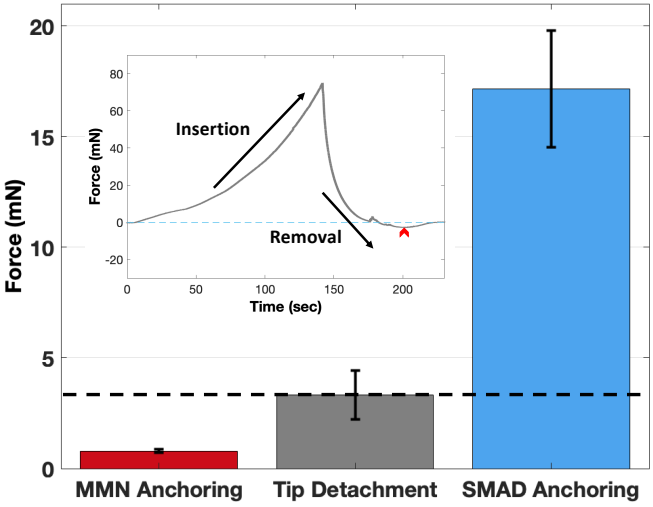

Figure 4: SMAD anchoring force (17.2 mN) exceeds required detachment force (3.3 mN) while MMN anchoring force (0.8 mN) is insufficient. Dashed line indicates detachment force threshold. Error bars represent standard error (n=4). Inset: Force loading throughout insertion and removal. Red arrow indicates tip detachment force.

Firm tissue anchoring is critical for removal of the SMAD from the actuator, but it also enables robust adherence to the target region and, consequently, reliable prolonged therapeutic delivery. Fig. 4 shows mechanical removal and tip detachment data of the SMAD compared to MMNs. 'Tip detachment force' refers to removal force of the SMAD or MMN structure from atop the actuator, while 'anchoring force' refers to the force required to remove the SMAD or MMN structure from the tissue sample. The conical MMNs showed a low anchoring force of 0.8±0.1 mN compared to the 3.3±1.1 mN force required to detach the tip structure from the actuator. Conversely, the SMAD demonstrated an anchoring force of 17.2±2.6 mN, a 22-fold improvement over the conical MMNs and significantly higher than the detachment force. The exceptional anchoring ability of the structure compared to the MMNs affects more reliable tissue anchoring and system operation. The inset in Fig. 4 illustrates the force loading and unloading during experimentation, including a red arrow indicating the point of detachment or removal.

Model Drug Delivery

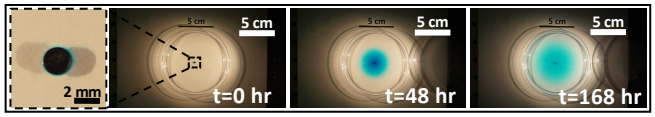

Figure 5: Diffusion of dye from drug disk at selected time points over 168 hr. Illumination is controlled across all samples to mitigate error in the image processing used to determine radius of diffusion.

Fig. 5 shows the release and subsequent diffusion of dye from a SMAD sample at 0 hr, 48 hr, and 168 hr. At 48 hr, the visually discernable perimeter of dye diffusion is at a radial distance of ~1.8 cm, while this expands to ~2.5 cm after 168 hr. 5 samples of each SMAD and MMN were characterized using this diffusion approach, as represented quantitatively in Fig. 6.

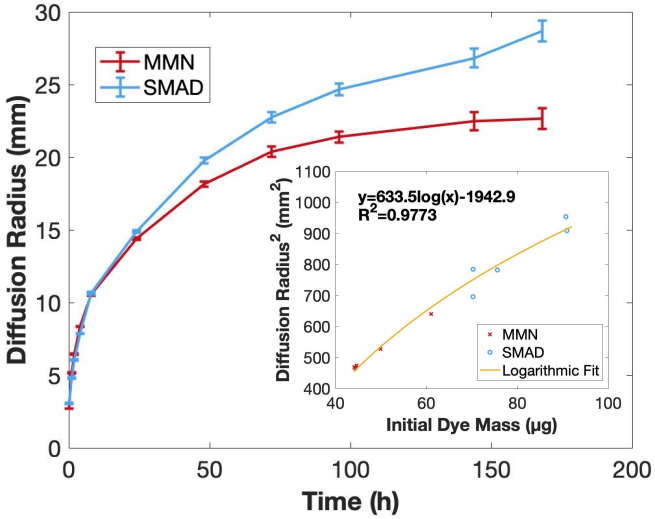

Figure 6: Diffusion profile of SMAD and MMN up to 168 hr. Error bars indicate standard error (n=5). Inset: Final squared diffusion radius (t=168 hr) shows a logarithmic correlation to initial dye mass (R^2=0.9773) predicted by the solution to Fick's second law for radial diffusion distance. The logarithmic fit coefficient predicts a diffusion constant of $D=2.6 \times 10^{-10}$ m^2/s that agrees strongly with previously reported value ($D= (2.5 \pm 0.2) \times 10^{-10}$ m^2/s) for dye diffusion in agar gel [15] confirming the relevance of the calculated logarithmic correlation coefficient.

Fig. 6 shows the mean diffusion radius at each measured time point for the SMAD and MMN. By initial observation, there exists a discrepancy between the extent of diffusion from the MMN and

SMAD. However, a difference in outcomes can be expected due to variations in initial dye mass between MMN and SMAD structures.

The thin agarose diffusion medium constrains diffusion to two dimensions; thus, this case most closely resembles 2D Fickian diffusion. The time-dependent concentration profile pertaining to this diffusion case is described by equation 1, where C is concentration, C_0 is initial concentration, D is the diffusion constant in the given medium, t is time, and r is radial distance.

$$C=C_0 \frac{1}{\sqrt{4\pi Dt}} e^{-\frac{r^2}{4Dt}} \quad (1)$$

The extent of diffusion from each sample can be measured by the radial diffusion distance at which the dye concentration exceeds a threshold value. With consistent lighting, the threshold concentration value corresponds to a constant light intensity value in the dye spreading image. Thus, the red channel light intensity with blue dye can be used as a direct indicator of the local dye concentration — enabling a quantitative treatment of the diffusion to account for differences in initial dye content across samples. For a given intensity threshold (T) solving for the thresholded squared radial diffusion distance (r^2) yields equation 2.

$$r^2=4Dt\left(ln(C_0) - ln\left(2T(\pi Dt)^{\frac{1}{2}}\right)\right) \quad (2)$$

At a specific measurement time, D, t, and T are constant and r^2 carries a logarithmic dependence on the initial concentration; therefore, one time point can be used to compare the relationship between r^2 and C_0 for the SMAD and MMN cases. The inset in Fig. 6 uses t=168 hr to compare the radial diffusion distance with initial dye mass in the context of equation 2. The data, across both groups, obeys the equation with R^2=0.9773. To validate the logarithmic character, a diffusion coefficient of $D=2.6\times10^{-10}$ m^2/s was calculated from the logarithmic coefficient using equation 2. This value is in strong agreement with previously reported values for the diffusion of dye in agar gel ($D= (2.5 \pm 0.2) \times 10^{-10}$ m^2/s) [15], corroborating the logarithmic data trend.

CONCLUSION

In this paper we introduce the first application of biomimetic barbed microneedles toward drug delivery in the GI tract. This is accomplished by a spiny microneedle anchoring deposit (SMAD) structure, composed of the spiny microneedles attached to a dissolving drug loaded PVA deposit. The high resolution (~1 μm) of the DLW process enables high sharpness and firm tissue anchoring. SMADs with the barbed microneedles anchored with a 22-fold higher tissue retention force than conical molded microneedles — reliably overcoming the force required for removal of the SMAD from the spring actuator. SMADs also demonstrated comparable drug delivery characteristics to the standard MMNs through model drug delivery in an agarose medium. After correction for the initial dye mass in each sample, the SMAD and MMN data showed high correlation (R^2=0.9773) indicating predictable and comparable performance. Overall, the robust anchoring provided by this system will enable location-specific and long-term anchoring of a drug deposit to facilitate prolonged treatment of target locations in the GI tract, opening new possibilities for therapeutic treatment of GI diseases.

ACKNOWLEDGEMENTS

This work was supported by the National Science Foundation ECCS Program under Award #1939236. The authors acknowledge support from the Clark Doctoral Fellows Program, TerrapinWorks, the University of Maryland NanoCenter and its FabLab.

REFERENCES

[1] K. E. Trinkley and M. C. Nahata, "Treatment of irritable bowel syndrome," *Journal of Clinical Pharmacy and Therapeutics*, 36, 3 (2011).

[2] S. Hua, "Advances in Oral Drug Delivery for Regional Targeting in the Gastrointestinal Tract - Influence of Physiological, Pathophysiological and Pharmaceutical Factors," *Frontiers in Pharmacology*, 11 (2020).

[3] G. Traverso, C.M Schoellhammer, A Schroeder, R. Maa, G.Y Lauwers, B.E. Polat, D.G. Anderson, D. Blankschtein, R. Langer, "Microneedles for Drug Delivery via the Gastrointestinal Tract," *J Pharm Sci*, 104, 2 (2015).

[4] A. Abramson, E. Caffarel-Slavador, M. Khang, A. Vegge, F. Hubalek, *et al.*, "An ingestible self-orienting system for oral delivery of macromolecules," *Science*, 363, 6427 (2019).

[5] A. Abramson *et al.*, "A luminal unfolding microneedle injector for oral delivery of macromolecules," *Nature Medicine*, 25, 10 (2019).

[6] P. Xitian, L. Hongying, W. Kang, L. Yulin, Z. Xiaolin, and W. Zhiyu, "A novel remote controlled capsule for site-specific drug delivery in human GI tract," *International Journal of Pharmaceutics*, 382, 1–2 (2009).

[7] X. Pi *et al.*, "A novel micro-fabricated thruster for drug release in remote controlled capsule," *Sensors and Actuators A: Physical*, 159, 2 (2010).

[8] J. Cui, X. Zheng, W. Hou, Y. P. Zhuang, X. Pi, and J. Yang, "The study of a remote-controlled gastrointestinal drug delivery and sampling system," *Telemedicine and e-Health*, 14, 7 (2008).

[9] L. Hongying, X. Pi, C. Zhou, X. Zheng, W. Hou, and Z. Wen, "Design of site specific delivery capsule based on MEMS," *3rd IEEE International Conference on Nano/Micro Engineered and Molecular Systems, NEMS* (2008)

[10] C. T. Dietzel, H. Richert, S. Abert, U. Merkel, M. Hippius, and A. Stallmach, "Magnetic Active Agent Release System (MAARS): Evaluation of a new way for a reproducible, externally controlled drug release into the small intestine," *Journal of Controlled Release*, 161, 3 (2012).

[11] J. Lee, H. Lee, S. hyun Kwon, and S. Park, "Active delivery of multi-layer drug-loaded microneedle patches using magnetically driven capsule," *Medical Engineering & Physics*, 85 (2020).

[12] O. M. Amin, R. A. Heckmann, and N. van Ha, "Acanthocephalans from fishes and amphibians in Vietnam, with descriptions of five new species," *Parasite*, 21 (2014).

[13] S. Liu, S. Chu, G. E. Banis, L. A. Beardslee, and R. Ghodssi, "Biomimetic Barbed Microneedles for Highly Robust Tissue Anchoring," *Proceedings of the IEEE International Conference on Micro Electro Mechanical Systems (MEMS)* (2020).

[14] J.A. Levy, J.M. Stine, L.A. Beardslee, and R. Ghodssi, "Thermally Released Spring-Loaded Platform for Capsule Based Drug Delivery and Sensing.," *67th AVS Symposium & Exhibit*. Virtual (2021).

[15] A. Simonsen, A. Røyset, L. O. Svaasand, O. J. Løkberg, T. Lindmo, and T. Støren, "Measurement of dye diffusion in agar gel by use of low-coherence interferometry," *Optics Letters, 28, 14* (2003).

CONTACT

*R. Ghodssi, tel: +1-301-405-8158; ghodssi@umd.edu

DIAMOND QUANTUM SENSORS

Victor Acosta
University of New Mexico, USA

ABSTRACT
Color centers in wide-bandgap semiconductors have emerged as a leading platform in the field of quantum sensing, broadly defined as the use of qubits to measure environmental parameters. In my lab at the University of New Mexico, we are using Nitrogen-Vacancy (NV) spin qubits in diamond to image magnetic phenomena in condensed-matter and biological systems over a broad range of length scales.

At the nanometer scale, we build diamond magnetic microscopes to image, for example, the paramagnetic crystals produced by malaria parasites. At the micrometer scale, we embed diamond quantum sensors inside microfluidic chips to perform nuclear magnetic resonance spectroscopy at the scale of single cells. At the millimeter scale, we use magnetic flux concentrators to detect femtotesla-level magnetic fields, with potential applications in medical imaging and navigation.

Recently, there has been interest in using sensitive diamond quantum sensors to search for new particles such as 'axions'--hypothetical particles which could explain the mysterious dark matter which comprises the majority of mass in the universe. This involves probing for several hypothetical interactions between NV electron spins and moving masses. To maximize sensitivity, we are developing lateral MEMS oscillators that provide continuously-driven sinusoidal motion with high peak displacement (~1 micrometer) at a relatively high frequency (~1 MHz).

I will provide an overview of the field, discuss recent results and ongoing challenges, and outline future directions.

GIANT NON-RECIPROCITY THROUGH FREQUENCY MODULATION OF A TWO DEGREE-OF-FREEDOM MICROMECHANICAL RESONATOR

James M.L. Miller[1], Jianing Zhao[1*], Chae Hyuck Ahn[2], Eldwin J. Ng[2], Vu Hong[2], Yushi Yang[2], Nicholas E. Bousse[2], Thomas W. Kenny[2], and Gaurav Bahl[1]*
[1]University of Illinois at Urbana-Champaign, Urbana, IL, USA
[2]Stanford University, Stanford, CA, USA

INTRODUCTION

The measured response of a passive resonator is fundamentally reciprocal: switching the drive and sense ports results in the same measured admittance. Previously, it has been shown that a non-reciprocal admittance (for producing isolator and circulator behavior) can be generated by applying spatiotemporal modulations on spatially extended systems composed of multiple resonators and waveguides [1-6]. In this work we show that, in fact, these spatial complexities are unnecessary, and that giant non-reciprocal admittances can be produced within a single microelectromechanical system (MEMS) device (Fig. 1a) by simply temporally modulating its degenerate degrees-of-freedom (DoF), i.e. by considering the DoF axis as an extra dimension. We demonstrate this principle by repurposing a wafer-scale encapsulated MEMS gyroscope (Fig. 1b) which features two degenerate modes. By modulating these modes, we are able to induce a synthetic Hall effect [1, 2] resulting in a non-reciprocity ratio greater than 40 dB. This result is among the largest demonstrations of non-reciprocal MEMS including hybrid electronics-MEMS [7-10], acoustoelectric effect [11-13], parity-time symmetry [14], and piezoelectric nonlinear stiffening [15]. Moreover, we show that this giant non-reciprocal impedance is highly reconfigurable and can be easily implemented without the use of complicated electronic circuits or elaborate networks of coupled resonators.

METHODS

Our test system is an electrostatic ring resonator (originally a gyroscope) having two degenerate third-order wineglass modes, and multiple available interface electrodes as depicted in Fig. 1c. Two electrodes that individually have strong overlap with the wineglass modes are selected as input/output ports. Notably, the wineglass modes have some intrinsic mechanical coupling, which is necessary to have a non-zero admittance between the input/output ports, and to induce the synthetic Hall effect mechanism. This intrinsic coupling can be observed through the avoided crossing behavior when a tuning voltage V_t is used to adjust the relative modal frequencies (Fig. 2). Starting from a fixed operating point, frequency modulations are applied using voltages $V_{mod,1}$ and $V_{mod,2}$ with a relative phase offset of 90° to induce the non-reciprocal admittance, with the modulation frequency selected to satisfy the phase-matching condition [1]. The device is fabricated in an epitaxial encapsulation process, which produces stable crystalline micromechanical resonators in a hermetic vacuum-sealed environment [16]. The combination of the vacuum environment and the radially symmetric mode shape confers high quality factor for the

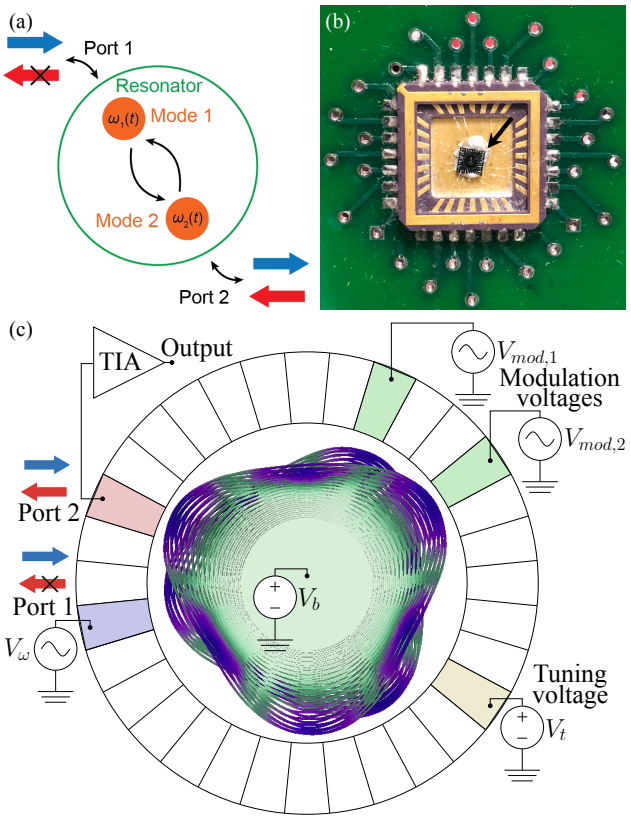

Figure 1: (a) A schematic illustrating the non-reciprocal mechanism. Appropriately modulating the resonance frequencies of two coupled modes within a resonator can induce a differing response when the ports are reversed. (b) A photograph of the encapsulated MEMS gyroscope that is employed for the non-reciprocity demonstration. (c) The wineglass mode configuration to achieve non-reciprocity by modulating the modal frequency. The tuning voltage V_t induces modal coupling between two degenerate order-3 wineglass modes to form two hybridized modes.

wineglass modes, enabling a relatively weak modulation to induce large non-reciprocity ratios.

RESULTS AND DISCUSSION

We tune the wineglass modes to the point of closest approach (Fig. 2) where the two modal peaks have approximately the same admittance response, by adjusting the tuning voltage V_t. Using coupled mode theory, we can simulate the admittance response for this system when modulations are applied. This theory predicts that the strongest non-reciprocal effect

978-1-940470-04-7/HH2022/$25©2022TRF
DOI 10.31438/trf.hh2022.23

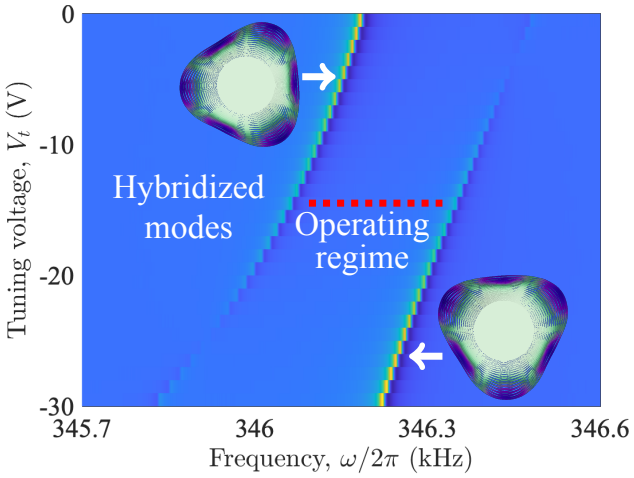

Figure 2. The surface plot of the admittance amplitude Y versus tuning voltage V_t and drive frequency in the vicinity of the modal coupling hybridization regime.

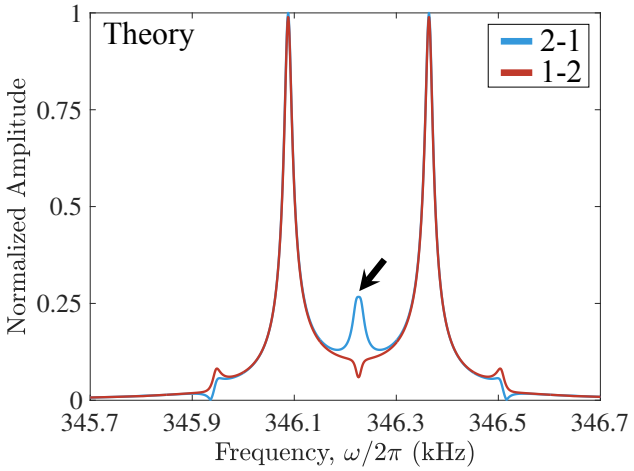

Figure 3. A simulation by coupled mode theory for the model depicted in Fig. 1a to predict the non-reciprocal effect in the central sideband, following reference [1].

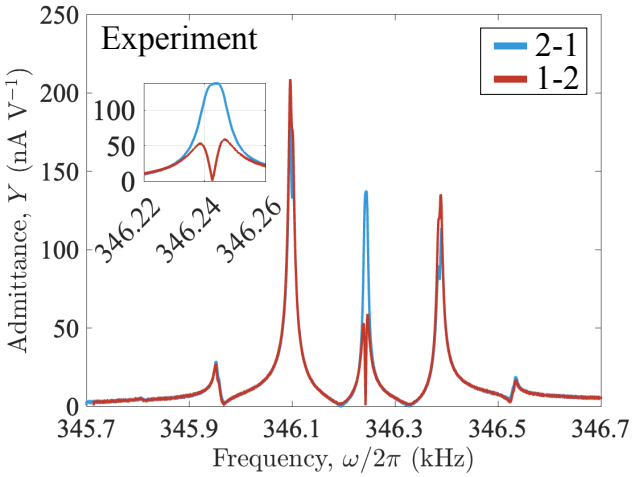

Figure 4. The admittance amplitude of the modulated hybridized resonator system in the forward (blue) and reverse (red) directions, with central peak inset. The capacitive feedthrough is de-embedded prior to plotting.

appears at the midpoint between the modes when the modulation frequency is set to half of the frequency separation between the two mode peaks (Fig. 3). The experimental measurements are presented in Fig. 4 showing a giant non-reciprocal admittance contrast of >40 dB for the central peak. To measure the 1-2 admittance response, the input/output ports are swapped relative to the configuration for measuring the 2-1 admittance response. The admittance curves are obtained from the frequency sweeps by first de-embedding the parasitic feedthrough using measurements under zero biasing and employing the transimpedance gain of the amplifier. Since the phase-matching condition is affected by the relative modal separation, which can be tuned via V_t, the modulation frequency is selected based on the modal separation.

CONCLUSION

We demonstrate a non-reciprocal isolator through frequency modulation of two coupled mechanical modes of a MEMS gyroscope. Our isolator achieves a non-reciprocity ratio greater than 40 dB, which is among the largest non-reciprocity ratios for MEMS-based non-reciprocal devices. Such a strategy may be useful for chip-scale isolation within a complementary metal-oxide-semiconductor (CMOS) compatible fabrication process. Since this electrostatic modulation approach is highly effective, future work will leverage this platform to enter the gyration regime for the demonstration of non-reciprocal phase shifters.

REFERENCES

[1] C.W. Peterson *et al.*, Phys. Rev. Lett. **123**, 063901 (2019).
[2] S. Kim *et al.*, APL Photon. **6**, 011301 (2021).
[3] G. Trainiti and M. Ruzzene. New J. Phys. **18**, 083047 (2016).
[4] Y. Wang *et al.*, Phys. Rev. Lett. **121**, 194301 (2018).
[5] H. Nassar *et al.,* Nat. Rev. Mater. **5**, 667 (2020).
[6] A. Nagulu, N. Reiskarimian, and H. Krishnaswamy, Nat. Electronics **3**, 241 (2020).
[7] M.M. Torunbalci *et al.*, IEEE Microw. Wirel. Co. Lett. **28**, 395 (2018).
[8] Y. Yu *et al.*, J. Microelectromech. Syst. **28**, 933 (2019).
[9] C. Xu and G. Piazza, J. Microelectromech. Syst. **28**, 409 (2019).
[10] R. Lu *et al.*, IEEE Trans. Microw. Theory Techn. **67**, 1516 (2019).
[11] H. Zhu and M. Rais-Zadeh, IEEE Electron Device Lett. **38**, 802 (2017).
[12] S. Ghosh *et al.*, Proc. IEEE Transducers 2017, pp. 1939-1942.
[13] H. Mansoorzare and R. Abdolvand, IEEE Electron Device Lett. **41**, 1444 (2020).
[14] L. Shao *et al.*, Nat. Electronics **3**, 267 (2020).
[15] L. Shao *et al.*, arXiv preprint arXiv:2101.01626 (2021).
[16] Y. Yang *et al.*, J. Microelectromech. Syst. **25**, 489 (2016).

PCB-BOT: THE FIRST STEPS OF A 4 MG LEGGED MICROROBOT

*Sukjun Kim, Regan Kubicek, and Sarah Bergbreiter**
Department of Mechanical Engineering, Carnegie Mellon University, Pittsburgh, Pennsylvania, USA

ABSTRACT

The design, fabrication, and system integration of insect-scale robots are still significant challenges in the field of small-scale robotics. In this work, we present the 4 mg PCB-bot, the lightest legged microrobot actuated without an external field (e.g., magnetic field). The PCB-bot has 3D printed leg mechanisms directly integrated onto a flexible printed circuit board (FPCB). The 4.4 mm long PCB-bot has four legs which can be controlled to drive an inchworm-like crawling gait. The PCB-bot took its first steps and achieved a maximum velocity of 1.2 mm/s (0.27 body lengths per second) when powered by 250 V, 50 Hz square waves applied via wire tethers.

KEYWORDS

Microrobotics, 3D Printing, Two-Photon Polymerization

INTRODUCTION

Microrobots at the scale of small insects have great potential for search and rescue, surveillance, and inspection missions as they can easily access spaces where humans and larger-scale robots cannot go [1, 2]. However, creating small scale robots that can navigate and interact with complex 3D environments like their insect counterparts (e.g., ants, termites) is a significant challenge due to limited 3D fabrication and integration methods at the sub-millimeter scale. Although the recent advent of 3D printing at the microscale with two-photon polymerization (TPP) has enabled rapid prototyping of 3D actuated mechanisms [3] and microrobots [4], they still lack a capability to be integrated with essential electronic components for autonomous robots such as wires, batteries, and microcontrollers.

In this work, we demonstrate PCB-bot, a 4 mg legged microrobot fabricated by 3D printing with TPP on a flexible printed circuit board (FPCB). The robot has four legs that are driven by 3D torsional comb-drive actuators [5]. The actuators with legs are directly 3D printed on the FPCB followed by a subsequent metal sputtering process to achieve electrical conductivity. Since the robot body is the FPCB, electronic components can be easily integrated onto the robot. As a demonstration, the PCB-bot was directly soldered to copper wires to test tethered locomotion on its feet and took its first steps.

ROBOT DESIGN AND FABRICATION

A robot was designed with a flexible printed circuit board (FPCB) as the main body and four 3D printed electrostatic torsional actuators with legs. The isometric view of the robot is shown from the ventral side in Fig. 1(a). The design of the actuator which drives the legs is based on the 3D torsional comb-drive actuator in [5]. A false-colored SEM image of the actuator is shown in Fig. 1(b). The actuator consists of 3D round comb-drives with torsional springs at both ends of the moving comb. When voltage is applied to the actuator, the moving comb rotates around the torsional spring axis due to electrostatic force generated between the moving and static combs (Fig. 1(c)).

The robot moves forward by taking advantage of anisotropic friction of the angled feet; the feet are designed to slide forward on the ground while remaining fixed when moving in the opposite direction. The two sets of actuators at the front and the back of the robot are designed to rotate in opposite directions but the legs are angled in the same direction (Fig. 2). When the robot is actuated, an electrostatic torque swings the legs. The hind legs swing backward but the rear feet hold their position on the ground due to high friction. The fore legs swing forward and can slide on the surface (Fig. 2(b)). When the actuators are powered off, the torsional actuators return to their original position due to a spring torque at the hip. During this phase, the fore legs hold their position on the surface while the hind legs slide forward (Fig. 2(c)).

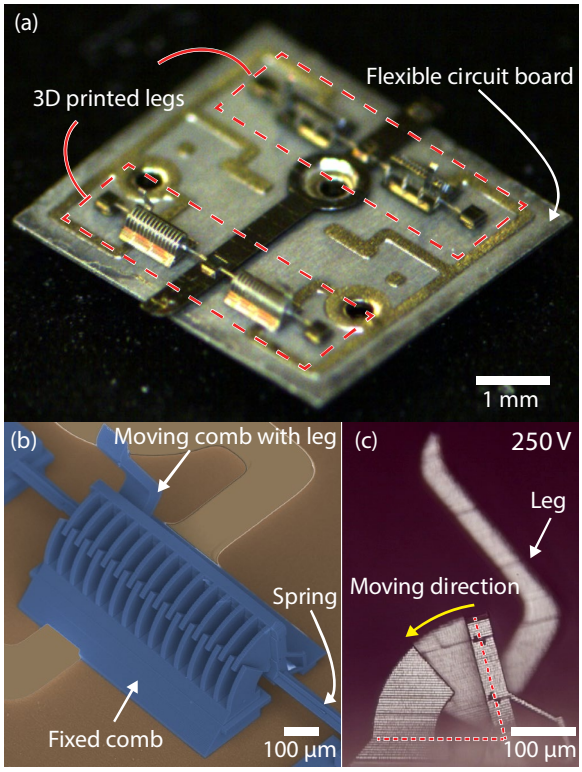

Figure 1: (a) The fabricated robot shown from the ventral side. (b) An SEM image of the actuator with a leg. The leg is directly 3D printed on the flexible printed circuit board. (c) The side view of the leg mechanism when actuated.

The robot was fabricated by directly 3D printing legs with actuators on a 100 µm thick double-sided FPCB (4.4 X 4.8 mm^2). The FPCB was cleaned and heat-pressed prior to printing to flatten the board. The FPCB was attached to a glass substrate using gel-like photoresist (IP-G, Nanoscribe GmbH) which successfully held the FPCB flat during printing. Desired 3D structures including the microactuators and legs were directly printed on the FPCB by TPP (Nanoscribe Photonic Professional GT +, Nanoscribe GmbH) with IP-S photoresist (Nanoscribe GmbH). The printed structures were developed in propylene glycol methyl ether acetate (PGMEA, Sigma-Aldrich) for 2.5 h and immersed in isopropyl alcohol (IPA, VWR) for 5 min. During this process, both IP-S and IP-G were developed, and the robot was released from the glass substrate. 60 nm of aluminum was sputter deposited over the robot (Perkin Elmer, 2400-8L) to add a conductive surface to the 3D printed actuators. Finally, 50 AWG copper wires (SP155, MWS Wire Industries) were hand-soldered to copper pads on the opposite side of the FPCB with solder paste (SMDLTLFP10T5, CHIPQUIK) to power the robot.

978-1-940470-04-7/HH2022/$25©2022TRF
DOI 10.31438/trf.hh2022.24

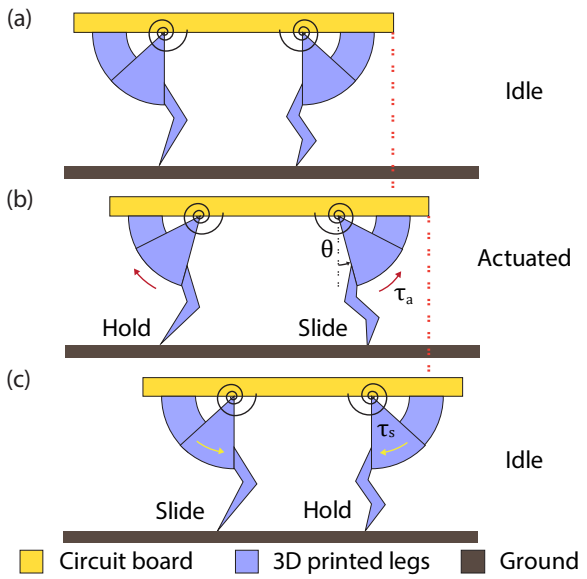

Figure 2: The working principle of the robot locomotion. The schematic of the robot is shown from the side view. (a) The robot in its idle state. (b) The robot in its actuated state. The actuation torque (τ_a) swings the legs and generates an angular displacement (θ). (c) The robot at its idle state. The spring torque (τ_s) at the hips swings the legs back to the original position.

RESULTS AND DISCUSSIONS

Both quasi-static and dynamic behavior of the legs are characterized as shown in Fig. 3. The error bars show the standard deviation between data points. We observe that the 3D comb drive's angular displacement is linearly proportional to V^2 as expected from the model in [5]. A maximum angular displacement of 9° was achieved at 250 V. In Fig. 3(b), the angular displacement of the actuator with varying frequency is plotted. The voltage was kept to 250 V. The frequency was swept from 1 Hz to 100 Hz. Although the angular displacement decreases as the frequency goes higher, the

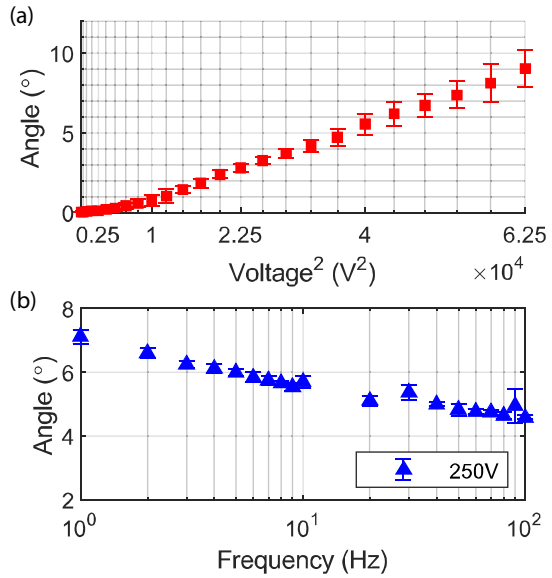

Figure 3: Actuator characterization results. (a) A quasi-static angular displacement of the actuator with varying voltage. (N = 9) (b) A dynamic characterization result with varying frequency. The applied voltage is fixed to 250 V. (N = 3)

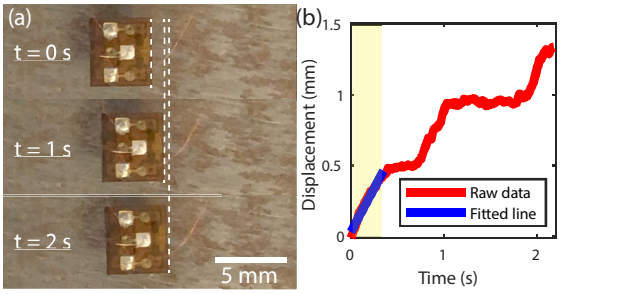

Figure 4: Walking robot characterization results. (a) Three sequential images with 1 s interval from the top view. The robot is shown from the dorsal side. The inset shows the waveform shape that is applied to the robot. (b) The displacement of the robot with respect to time. A linear function was fitted to calculate the velocity of the robot (1.2 mm/s).

actuator could stably generate displacement up to 100 Hz.

The 4.4 X 4.8 X 0.7 mm^3 tethered robot was placed on a flat acrylic plate and was connected to a power supply (2400, Keithley) which generated a 250 V square wave at 50 Hz. Three captured images taken at 1 s intervals clearly show that the tethered robot can take steps and move forward (Fig. 4(a)). From the video, the position of the robot was tracked and plotted in Fig. 4(b). Due to external forces applied to the robot from soldered copper wires and friction from the acrylic plate, the displacement of the robot was not linear. From the plot, the maximum velocity of the robot was fitted which was 1.2 mm/s, or 0.27 body lengths per second.

3D printing on FPCBs opens up significant design space for insect-scale robots. By taking advantage of extremely fast design and fabrication cycles with the capability to create complex 3D structures, the mobility of the robot can be improved. For example, the locomotion can be optimized for non-smooth terrain by adjusting foot geometries and leg movements. In addition, improved actuation torque can increase robot's payload capacity which then enables an integration of small, low-power controllers and power electronics with the FPCB framework to further increase robot autonomy.

REFERENCES

[1] A. M. Flynn, "Gnat robots (and how they will change robotics)," Working Paper 295, 1987.

[2] R. St. Pierre and S. Bergbreiter, "Toward autonomy in sub-gram terrestrial robots," Annual Review of Control, Robotics, and Autonomous Systems, vol. 2, pp. 231–252, 2019.

[3] S. Kim, C. Velez, R. St. Pierre, G. L. Smith, and S. Bergbreiter, "A two-step fabrication method for 3d printed microactuators: characterization and actuated mechanisms," Journal of Microelectromechanical Systems, vol. 29, no. 4, pp. 544–552, 2020.

[4] R. St. Pierre, W. Gosrich, and S. Bergbreiter, "A 3d printed 1 mg legged microrobot running at 15 body lengths per second," in Solid State Sensors, Actuators, and Microsystems Workshop, Hilton Head, SC, vol. 3, 2018.

[5] S. Kim and S. Bergbreiter, "Fabrication and characterization of 3d printed out-of-plane torsional comb-drive actuators for microrobotics," in 2021 21st International Conference on Solid-State Sensors, Actuators and Microsystems (Transducers), pp. 6–9, IEEE, 2021.

CONTACT

*Sarah Bergbreiter, sbergbre@andrew.cmu.edu

SCALABLE FABRICATION OF ACTIVE NANOGAPS WITH SUB-NANOMETER TUNABILITY FOR NANOSCALE SENSORS AND ACTUATORS

Weikun Zhu[1], Peter F. Satterthwaite[1] and Farnaz Niroui[1]
[1]Massachusetts Institute of Technology, USA

ABSTRACT

We present a platform for scalable fabrication of mechanically-active nanogaps with sub-nanometer tunability for extreme miniaturization of microelectromechanical systems with applications in sensors and actuators. In our approach, molecular layers serve as nanoscale springs to overcome stiction due to surface adhesive forces and enable dynamic and reversible reconfiguration at the few-nanometer regime. Our additive manufacturing approach is based on dry and high-yield contact printing of bottom-up assembled nanoparticles. Using this technique, we fabricated arrays of active plasmonic resonators with a nanoparticle-on-mirror design and a molecular spacer. Under temperature cycling, this platform allows for the optical detection of sub-nanometer thermal expansion of the resonator nanogap, demonstrating the extreme sensitivity of these nano-actuators.

KEYWORDS

Additive manufacturing, Bottom-up fabrication, Plasmonic resonators, Contact printing, Molecular springs

INTRODUCTION

Miniaturized microelectromechanical devices with critical dimensions few-nanometers in size have long been desired for their improved sensitivity, energy-efficiency and speed, enabling new applications. However, building devices reliably at this scale has been a long-standing challenge as the dominating surface adhesive forces at the nanoscale can lead to stiction, inducing structural instability and collapse during fabrication or operation. Here, we present a platform for scalable fabrication of mechanically-active nanogaps with sub-nanometer tunability using molecular springs. Our approach presents two unique features to balance the surface forces. First, the molecular layer provides structural support for miniaturization to sub-5 nm dimensions. Second, its tailorable mechanical properties yield controlled and reversible tuning. Scalable and deterministic fabrication of such mechanically-active hybrid organic-inorganic constructs is beyond the capabilities of conventional techniques. To this end, we present an additive manufacturing strategy based on dry and high-yield contact printing of bottom-up assembled nanoparticles.

We demonstrate our platform in form of an active gold nanoparticle-on-mirror plasmonic resonator composed of a metallic nanostructure separated from an underlying metallic thin-film by a nanometer-thin dielectric molecular spacer, as shown in Figure 1. In this structure, the optical response is sensitive towards minute changes in the gap size [1, 2]. This provides a powerful probe of the mechanical tunability at the sub-nm regime, while also serving as building blocks for engineering of emerging nanoscale sensors, actuators, reconfigurable optical devices and tunable metasurfaces.

FABRICATION APPROACH

Our fabrication technique relies on a two-step additive manufacturing process, shown in Figure 2a. First, synthesized gold (Au) nanoparticles with a molecular coating are deterministically positioned through capillary assembly onto a lithographically-defined topographical template made out of polydimethylsiloxane (PDMS). Then, the assembled particles are transfer-printed onto a template-stripped gold receiving substrate with sub-nm surface uniformity. Unlike existing techniques which require solvents, surface modifications or sacrificial release layers to promote the transfer [3, 4], we achieve > 95% transfer yield and < 50 nm positional accuracy in a single dry contact-and-release step without any mediations. This is achieved by engineering the van der Waals forces during transfer through template design. As a result, surfaces remain pristine and well-defined molecular gaps can be realized. An example 50 × 50 array of nanoparticle-on-mirror resonators based on ~ 54 nm gold nanocubes with ~ 1.5 nm molecular spacer is shown in Figure 2b.

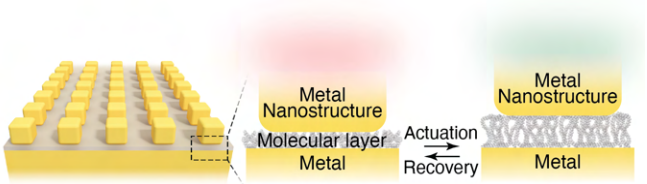

Figure 1: Mechanically-tunable nanogaps with molecular springs in the form of particle-on-mirror plasmonic resonators with a reversibly tunable optical response.

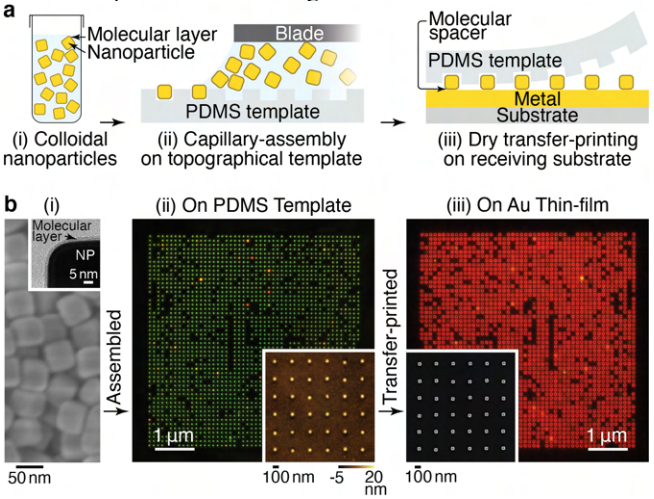

Figure 2: Scalable fabrication of tunable molecular nanogaps with nanoparticle contact printing. (a) Fabrication process: (i) Au nanocubes are synthesized with a molecular surface coating. (ii) Individual nanocubes are assembled using capillary assembly onto a lithographically-defined PDMS template. (iii) Assembled nanocubes are dry-transferred onto a template-stripped Au substrate. (b) Example particle-on-mirror resonators formed using the process in (a). (i) Scanning electron microscope (SEM) image of colloidal Au nanocubes with the inset showing a transmission electron microscope (TEM) image of the molecular layer formed on a nanocube surface. (ii) Dark-field image of assembled 50 × 50 array of ~ 54 nm Au nanocubes, with the inset atomic force microscope (AFM) image showing the surface topography. (iii) Dark-field image of the 50 × 50 array dry-transferred onto a template-stripped Au film forming plasmonic resonators with ~ 1.5 nm active molecular nanogaps. The inset shows a representative SEM image of the transferred nanocubes.

978-1-940470-04-7/HH2022/$25©2022TRF
DOI 10.31438/trf.hh2022.25

ACTIVE NANOGAPS WITH SUB-NM TUNABILITY

Figure 3 highlights the dependence of the plasmonic response of the resonators to the gap between the nanoparticle and the underlying metal thin-film. We fabricated arrays of resonators with different Al_2O_3 thicknesses deposited through atomic layer deposition. The dark-field scattering spectra show a blue shift in the plasmonic resonance wavelength as the gap size increases, which matches closely with the expected resonance modeled using a finite-difference time-domain simulation.

To demonstrate the dynamic and reversible tunability afforded by a molecular spacer, we tested the resonators in Figure 2b under thermal cycling. In this design, the molecular layer is composed of ~ 1.5 nm-thick mixture of Triton X-45 and sodium dodecyl sulfate. Shown in Figure 4, as the sample is heated to 50°C, the molecular layer undergoes thermal expansion, resulting in an increase in the gap size and accordingly, a blue shift in the resonance wavelength. Once cooled, the molecular layer relaxes and reduces the gap, leading to a red shift in resonance. Due to the extreme sensitivity of the optical resonance to gap dimensions [1, 2], highlighted in Figure 3c, the observed ~ 1.2 nm resonance shift upon heating corresponds to a mere ~ 26 pm-displacement in the gap region. This highlights the potential of molecular springs as a platform to realize controlled and reversible mechanical tuning at the sub-nm scale.

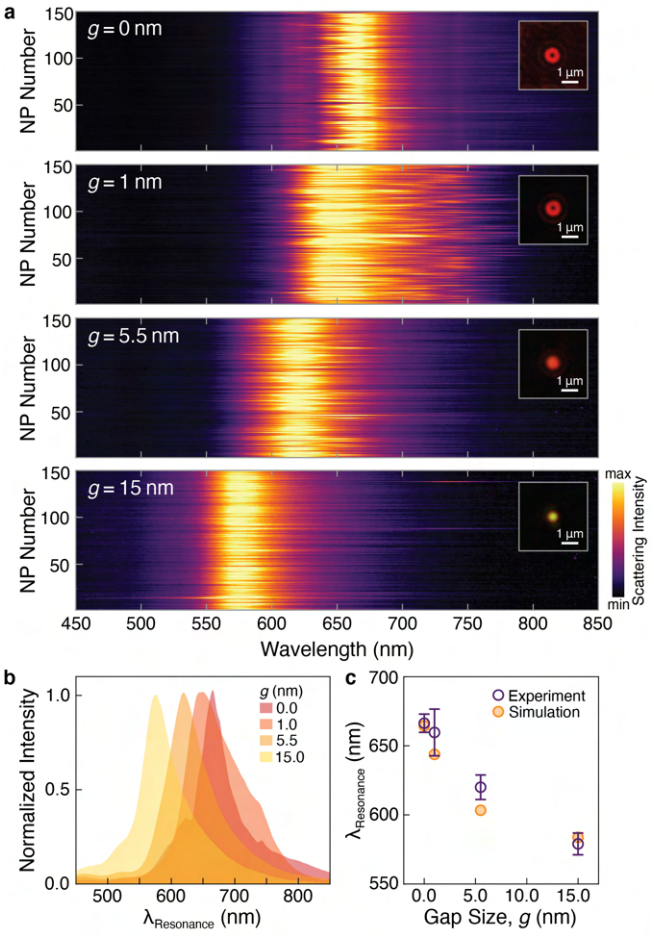

Figure 3: Strong dependence of plasmonic response to the nanogap size, g. (a) Scattering spectra of nanoparticle (NP)-on-mirror resonators with different thickness Al_2O_3 spacers showing a blue shift in the plasmonic resonance wavelength ($\lambda_{Resonance}$). The inset to each plot shows a dark-field image of a resonator. The change in the plasmonic response with the gap size is further displayed in (b) the scattering spectra ensemble average of resonators at different nanogap size, and (c) experimental and simulated resonance wavelength at each nanogap size.

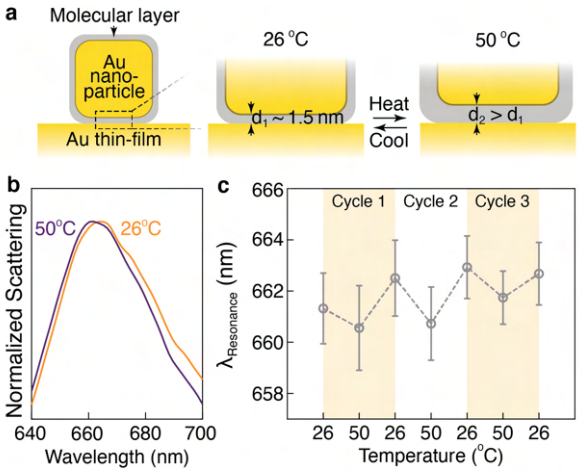

Figure 4: Molecular gap with controlled and reversible sub-nanometer tunability. (a) Schematic of the plasmonic resonators undergoing temperature cycles which induce changes in the gap due to thermal expansion of the molecular spacer. (b) A blue shift in the resonance wavelength is observed as the sample is heated and molecular gap expands. (c) Changes in the resonance wavelength shown through several heating and cooling cycles display a reversible tunability.

CONCLUSION

In summary, we have demonstrated an approach for scalable fabrication of precisely-defined mechanically-active nanogaps with sub-nanometer tunability using molecular springs. This platform provides a unique opportunity for dramatic miniaturization of mechanically-active devices to the extreme nanoscale, a process that is not feasible through conventional approaches. This opens up diverse opportunities for new applications in sensors, actuators and reconfigurable optical devices and systems.

ACKNOWLEDGEMENTS

This work is supported by the National Science Foundation (NSF) Award CMMI-2135846.

REFERENCES

[1] J.J. Baumberg, J. Aizpurua, M.H. Mikkelsen, and D.R. Smith, "Extreme nanophotonics from ultrathin metallic gaps", *Nature Materials*, 18, 668 (2019).

[2] R.T. Hill, J.J. Mock, A. Hucknall, S.D. Wolter, N.M. Jokerst, D.R. Smith, and A. Chilkoti, "Plasmon ruler with angstrom length resolution", *ACS Nano*, 6, 9237 (2012).

[3] T. Kraus, L. Malaquin, H. Schmid, W. Riess, N.D. Spencer, and H. Wolf, "Nanoparticle printing with single-particle resolution", *Nature Nanotechnology*, 2, 570 (2007).

[4] J.B. Lee, H. Walker, Y. Li, T.W. Nam, A. Rakovich, R. Sapienza, Y.S. Jung, Y.S. Nam, S.A. Maier, and E. Cortés, "Template dissolution interfacial patterning of single colloids for nanoelectrochemistry and nanosensing", *ACS Nano*, 14, 17693 (2020).

CONTACT

*fniroui, tel: +1-617-324-7415; fniroui@mit.edu

A STRETCHABLE NEURAL INTERFACE FOR VAGUS NERVE STIMULATION: FABRICATION AND ELECTROCHEMICAL CHARACTERIZATION

Jongcheon Lim[1,2,3], Matthew P Ward[1,2,3,4], John B Furness[5], Luis C Populin[6], and Hyowon Lee[1,2,3]*
[1]Weldon School of Biomedical Engineering, Purdue University, West Lafayette, IN, USA
[2]Birck Nanotechnology Center, Purdue University, West Lafayette, IN, USA
[3]Center for Implantable Devices, Purdue University, West Lafayette, IN, USA
[4]Indiana University School of Medicine, Indianapolis, IN, USA
[5]Department of Physiology and Anatomy, University of Melbourne, Parkville, Vic, Australia
[6]Department of Neuroscience, University of Wisconsin-Madison, Madison, WI, USA

ABSTRACT
Soft, stretchable design can improve long-term stability of neural interface devices. Here we present our latest efforts to design, fabricate and evaluate stretchable thin-film cuff electrode devices for vagus nerve stimulation, which have Y-shaped kirigami microstructures. We fabricated stretchable Y- microstructured thin-film cuff electrodes by using conventional photolithography and reactive ion etching. The monolithic device design enables easier transfer to a different substrate without having to use the traditional PDMS-stamp-based transfer printing technique. We then characterized the electrochemical properties of the electrode/electrolyte interface and evaluated the charge injection limits as stimulating neural electrodes. Although the microstructured electrodes show up to 3.68 times higher impedance than the Euclidean geometry electrode due to the reduced surface area, they show up to 2.13 times higher charge storage capacities and 12.1 % higher charge injection limits, which may be useful for a chronic neural interface.

KEYWORDS
Vagus Nerve Stimulation, Stretchable, Kirigami, Neural Interface.

INTRODUCTION
Vagus nerve stimulation (VNS) is an effective method to treat neurological disorders such as drug-resistant epilepsy and depression. It is also known to be therapeutic for other inflammatory diseases such as inflammatory bowel disease (IBD) [1]. Slowly conducting (<1 m/s) unmyelinated C-fibers in the vagus nerve are thought to drive the anti-inflammatory effects of those diseases [2]. Previously, a study reported applying VNS in a sheep model to treat IBD by using a silicone-based flat interface nerve electrode (FINE) [2]. FINE ensures good contact between the electrode and nerve by applying moderate pressure to maximize stimulation efficiency for C-fibers, which are known to have a higher activation threshold than other types of myelinated fibers [3], by maintaining intimate electrode-to-nerve distance. However, this interface can potentially damage the nerve if it applies pressure higher than 30 mm Hg to flatten the fascicle [4]. Moreover, the silicone wall of the FINE cuff is thick (thickness = 0.5-0.8 mm), which can apply restrictive mechanical forces to the nerve or surrounding tissue due to its volume. The volumetric footprint around the nerve can be reduced by making the cuff with a flexible thin-film substrate such as polyimide (PI). Even though PI thin-film substrates are flexible, they have a GPa range of Young's modulus and the cylindrical geometry from the cuffing can add even more structural rigidity, which can potentially damage the nerve by the mismatching mechanical behavior under ambient motion. The issue can be mitigated by making the PI substrate stretchable. Vachicouras *et al.* (2019) suggested a strategy to make the PI stretchable by making a Y-shaped kirigami pattern to the substrate [5]. However, they used relatively expensive methods, such as ion-milling, to fabricate complex geometry.

Herein we present a relatively conventional microfabrication process to make the Y-shaped kirigami patterned structure for a more compliant and reliable interface for vagus nerve stimulation. Furthermore, we investigated whether there are any improvements in electrochemical characteristics of the electrode/electrolyte interface for the Y-shaped kirigami patterned electrodes, which have a higher perimeter to surface area (PSA) ratio than the rectangular electrode geometry. A previous study on microelectrodes with high PSA electrode geometry, such as Vicsek fractal geometry, suggests that the charge injection limit can be enhanced by improving the diffusion-limited Faradaic charge interactions [6]. We conducted experiments to determine whether similar performance improvement may apply to macroelectrodes with microstructures.

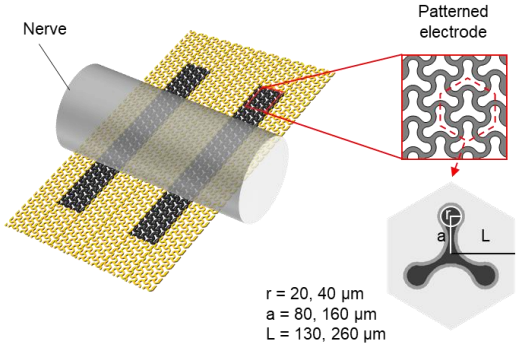

Figure 1: Schematic illustration of the concept of a stretchable thin-film cuff electrode device based on a Y-shaped kirigami structure

MATERIALS AND METHODS
Design of the Device
We chose the Y-shaped kirigami pattern based on literature in which the mechanical properties resulting from design parameters (r, a, L) were experimentally optimized to increase overall compliance against tensile strain (Figure 1) [5]. In this work, we made two versions of the peripheral nerve interface which we named "r20" and "r40". The first, r20, used shape parameters: r = 20 µm; a = 80 µm; L = 130 µm. The second version, r40, has design parameters increased by a factor of two. Figure 2 shows the layout of the device with important dimensions annotated. The entire device except for the contact pad part is perforated with a Y-shaped kirigami hole pattern. The electrode contact dimensions were determined based on the diameter of the rhesus macaque's cervical vagus nerve, which is known to be around 2 mm [7]. We adopted the multi bipolar cuff array design from a previous study that used FINE [2]. The device has three cuffs: one stimulation electrode, which is the first cuff from the left in Figure 2, and two recording electrodes with different conduction distances (10 mm and 20 mm).

978-1-940470-04-7/HH2022/$25©2022TRF
DOI 10.31438/trf.hh2022.26

The purpose of having an array of recording electrodes is to better identify electrically evoked compound action potential volleys with different conduction velocities. The extra space in the flaps of the cuff can be used for handling the device and for the closure mechanism by suturing them together or applying self-adhesive glue or gel. The contact pads are designed to be compatible with ZIF-clip headstage connectors (Tucker-Davis Technologies, Alachua, FL, USA).

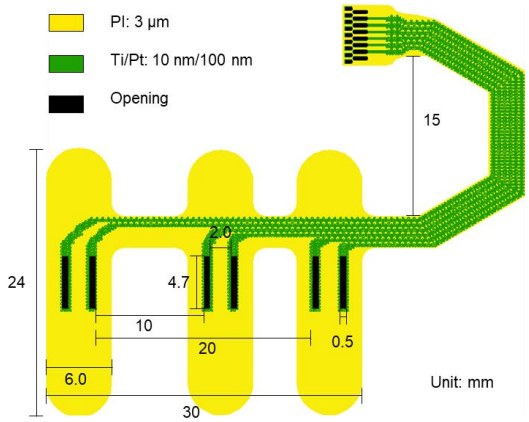

Figure 2: Layout of the device with important dimensions annotated.

Device Fabrication

Figure 3 shows the fabrication process. The PI resin (PI 2545, HD Microsystems, Parlin, NJ) was spin-coated (thickness = 1.5 µm) and cured on a 100-mm silicon wafer at 300 °C. A positive photoresist (PR, AZ9260, MicroChem, Newton, MA, USA) was used to make the metal trace pattern. We used a maskless aligner (MLA150, Heidelberg Instruments, Germany) for the exposure and alignment processes. After the 1st photolithography, the wafer was sputtered with 10 nm of titanium (Ti) and 100 nm of platinum (Pt) followed by a lift-off process. Another PI layer (thickness = 1.5 µm) was cured on the wafer as a passivation layer. The wafer was coated with a thicker layer (~20 µm) of PR by spinning and baking twice for the 2nd photolithography. The pattern was aligned by using an automatic alignment feature of MLA150. After the exposure and development, we used the reactive ion etch (RIE) process with oxygen plasma (50 sccm at 100 W in 50 mTorr for 60 min) to define the outline of the device. The same process was repeated in the 3rd photolithography and RIE for the opening of the electrodes. After visual observation under the microscope, the device was released from the wafer by partially etching the silicon with a buffered oxide etch within 15 min and rinsed 5 times with de-ionized water, then transferred to another substrate using water for further handling.

Electrochemical Characterizations

We conducted cyclic voltammetry (CV) and electrochemical impedance spectroscopy (EIS) in phosphate-buffered saline (PBS, ThermoFisher Scientific, MA, USA) solution using a potentiostat (SP-200, Bio-Logic Inc, Seyssinet-Pariset, France) with three-electrode configuration: Electrode contact of the device as a working electrode, graphite counter electrode and Ag/AgCl with 3 M KCl reference electrode (RE-1CP, ALS Co. Ltd., Tokyo, Japan). CV was scanned between -0.6 V and 0.8 V versus the reference electrode with a scan rate of 50 mV/s. GSAs of the No microstructure, r40 and r20 are 2.35 mm^{-1}, 0.899 mm^{-1}, and 0.969 mm^{-1} respectively, and were used to calculate the current density.

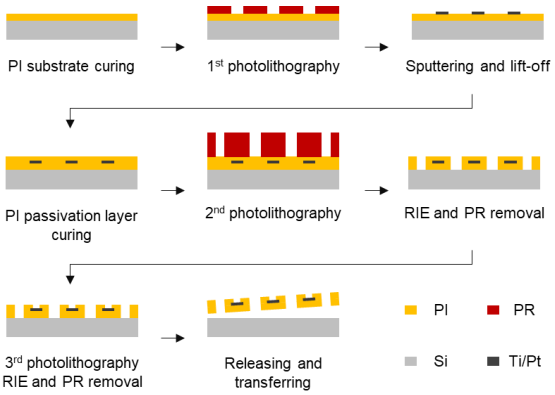

Figure 3: Schematic illustrations of the fabrication process of the device

Voltage Transient Measurements

We conducted voltage transient measurements using a stimulus isolator (BSI-1A, BAK Electronics, Inc, Umatlla, FL. USA) in the same experiment setup used for the electrochemical characterizations. We used a cathodic-first alternating monophasic current-controlled stimulus waveform. The pulse repetition frequency, train duration, and pulse duration were set at 50 Hz, 1 sec, and 1 ms, respectively. The current pulse was monitored by measuring voltage between 100-Ω-resistor, which is connected in series to the stimulator. Data was acquired via an I/O device (USB-6361, National Instruments, Austin, TX, USA).

RESULTS AND DISCUSSION

Figure 4a shows the device as fabricated on the wafer substrate. The entire body of the device is monolithically constructed and can be transferred to another substrate without having to use the PDMS-stamp-based transfer printing technique, which is traditionally used to transfer stretchable thin-film interconnect patterns but requires proficiency for successful results. Our device maintains its shape when it's floating on the surface of the water.

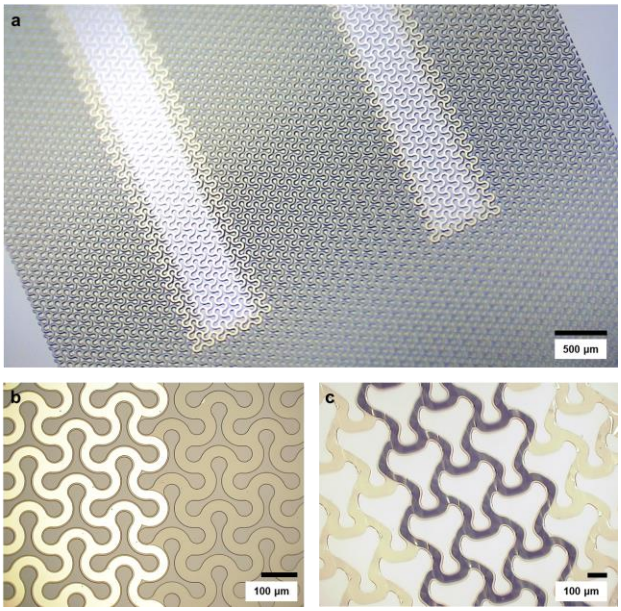

Figure 4: Representative images of the fabricated device. (a) The fabricated device on a silicon wafer. Optical microscope images of the device after transferring to a glass substrate (b) and mechanically stretched (c).

After gently being placed on a wet glass substrate, the substrate can be inclined at a certain angle to make the drying front formed at the top and to recede directionally below, so that the device can be transferred flat on the glass substrate. Figure 4b shows an optical microscopy image of the device after it is transferred to a glass substrate. We did not observe any notable damage on the device after the transfer. The device is stretchable due to the Y-shaped kirigami structure as it is shown in Figure 4c.

Results of CV and EIS Measurements

Figure 5a shows representative CV plots of the electrodes. All three electrodes show representative characteristic electrochemical reactions at the Pt/PBS interface: Current densities increase toward 0.8 V from the oxidation of Pt, and negative peaks appear between -0.2-0 V from the reduction of Pt. From the CV measurements, we can compare cathodic charge storage capacity (CSC_c), which is a measure of total injectable charge density at a near-equilibrium condition. We calculated CSC_c from the charge storage capacity (CSC) of voltammograms using the following equation [8]:

$$CSC = \frac{1}{\nu A}\int_{E_c}^{E_a} |i| dE \; (C/cm^2) \quad (1)$$

Where E is potential versus Ag/AgCl reference electrode; i is measured current; E_a and E_c are positive and negative potential limits; A is GSA, and ν is the scan rate. Figure 5c shows the mean and standard deviation of CSC_c for the electrodes (N=6, each electrode). r20 shows the highest CSC_c (3.65 ± 0.377 mC cm^{-2}) compared to r40 (2.39 ± 0.188 mC cm^{-2}) and the electrode without microstructure (1.71 ± 0.128 mC cm^{-2}). That is, r20 can inject the most charge density at a near-equilibrium condition where the charge is injected sufficiently slow to let faradaic charge interaction and double-layer charging occur throughout the entire electrode region. The higher overall current density from the CV of r40 and r20 could be attributed to the increased perimeter of the microstructured electrodes, where we expect a higher current density than the central region. A more detailed investigation of the spatial current density profile should be made in the future to further analyze the effect of the increased perimeter of the electrodes. Figure 5b shows representative Bode plots from the EIS. Impedance values (mean and standard deviation, N=6, each electrode) at 1 kHz were plotted in Figure 5d for a comparison. r40 and r20 have higher impedance at 1 kHz, which are 2.58 ± 0.562 kΩ and 2.42 ± 0.332 kΩ respectively compared to that of the electrode without microstructure, which is 0.701 ± 0.120 kΩ. It is important to note that r40 and r20 have 0.383- and 0.412-times smaller GSAs respectively compared to the electrode without microstructure.

Results of Voltage Transient Measurements

We conducted voltage transient measurements to estimate charge injection limits for the electrodes. Figure 6a shows representative voltage transients (solid lines) of a cathodic phase and the following charge balancing anodic phase along with the monitored current pulse (blue dashed line) at 1 mA of pulse current amplitude and 1 ms of pulse duration. Maximum cathodic potential excursion (E_{mc}) was estimated by taking the potential value at the point where the actual current pulse ends as shown in the inset of Figure 6a. We investigated E_{mc} for all the electrodes at pulse current amplitudes between 0 mA to 2 mA (Figure 6b). Mean and standard deviation was obtained from 50 stimuli at each pulse current amplitude. Charge injection limits were interpolated from the intercepts of lines drawn by mean E_{mc} and the cathodic electrolysis limit of water at the surface of Pt (brown dashed horizontal line) [8].

The estimates are organized in Table 1. Although the maximum current amplitudes at the cathodic limit for r40 (0.494 mA) and r20 (0.459 mA) were almost two-fold smaller than that of the electrode without microstructure (1.06 mA), estimated charge injection limits were higher for r40 (0.0550 mC cm^{-2}) and r20 (0.0474 mC cm^{-2}) compared to the electrode without microstructures (0.0453 mC cm^{-2}) due to the smaller GSAs. It is important to note that the GSA of the electrodes is around 1 mm^2 range; therefore, regarded as macroelectrodes rather than microelectrodes, which have a GSA of around 5,000 μm^2 [8]. Macroelectrodes have an order of magnitude lower charge injection limit than microelectrodes because they have a larger underutilized central region, where transport of ions is more limited than the perimeter [8].

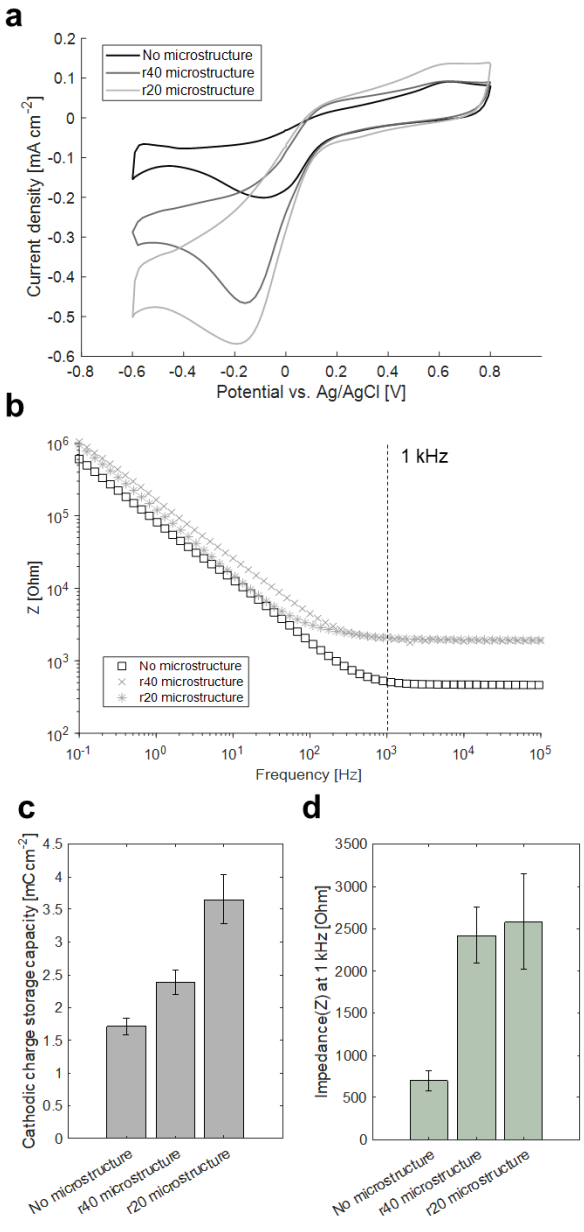

Figure 5: Electrochemical characterization of the electrodes in PBS solution: (a) CV plots. (b) EIS Bode plots. (c-d) CSC_c (c), and impedance at 1 kHz (d) for different designs of electrodes (N=6, each).

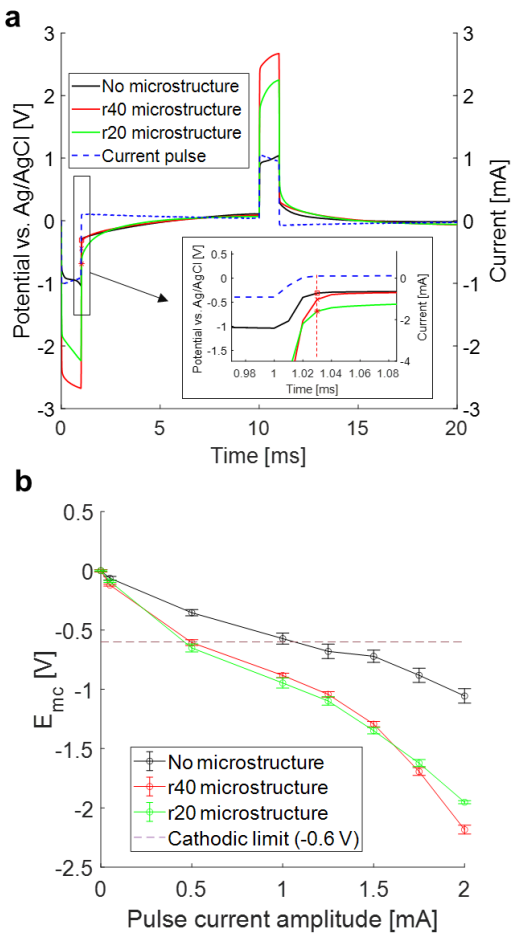

Figure 6: Voltage transient analysis: (a) Representative voltage transient plot for each type of electrode. (b) Estimated E_{mc}s for the different designs of electrodes.

Table 1: GSA and charge injection limit of each electrode design.

	No μstructure	r40 μstructure	r20 μstructure
GSA (mm^{-2})	2.35	0.899	0.969
Charge injection limit ($mC\ cm^{-2}$)	0.0453	0.0550	0.0474

Summary and Future Plan

We found that the kirigami structure reduces the GSA of the electrode thereby increasing the impedance, yet results in the enhancement of CSC_c, which is a measure of the total charge available for a stimulating electrode [8]. The results from voltage transient measurements suggest that the kirigami structured electrodes perform slightly better than non-structured Pt electrodes in terms of charge injection limit. This result agrees with a previous study in our group, which suggests that electrodes with high PSA geometry, such as Vicseck fractal geometry, show enhancement of charge injection limit [6]. However, it is not clear whether the diffusion-limited Faradaic charge transfer is significantly improved in this stretchable electrode design, which features macroelectrodes with microstructures. We expect the performance may be further enhanced by coating the surface of the electrode with platinum-iridium (Pt-Ir) alloy or iridium oxide (IrO_2). We also expect these microscale patterns will accelerate the corrosion of the Pt electrodes. This may be mitigated potentially by using Pt-Ir or IrO_2 coating or a layer of graphene [9]. We plan to conduct tensile testing while measuring the electrical conductivity to characterize the electromechanical responsiveness of the stretchable conductive traces of the device along with the electrical and/or mechanical failure limits. Local stress applied by the global stretch of the kirigami pattern can be analyzed by conducting finite element analyses. Furthermore, we plan to quantify any functional benefit of these stretchable peripheral interfaces *in vivo* and identify potential failure modes of the device. Ultimately, we expect to use the device we developed for advanced studies of VNS for the treatment of IBD as well as for neuromodulations of various other parts of the autonomic nervous system.

ACKNOWLEDGEMENTS

This work was supported by the NIH SPARC OT2 OD023847 project.

REFERENCES

[1] J. Meregnani, D. Clarençon, M. Vivier, A. Peinnequin, C. Mouret, V. Sinniger, C. Picq, A. Job, F. Canini, M. Jacquier-Sarlin, and B. Bonaz, "Anti-inflammatory effect of vagus nerve stimulation in a rat model of inflammatory bowel disease." *Autonomic Neuroscience* 160.1-2 (2011): 82-89.

[2] S.C. Payne, O. Burns, M. Stebbing, R. Thomas, A.D. Silva, A. Sedo, F. Weissenborn, T. Hyakumura, M. Huynh, C.N. May, and R.A. Williams, "Vagus nerve stimulation to treat inflammatory bowel disease: a chronic, preclinical safety study in sheep." *Bioelectronics in Medicine* 1.4 (2018): 235-250.

[3] R.M. McAllen, A.D. Shafton, B.O. Bratton, D. Trevaks, and J.B. Furness, "Calibration of thresholds for functional engagement of vagal A, B and C fiber groups in vivo." *Bioelectronics in medicine* 1, no. 1 (2018): 21-27.

[4] D.J. Tyler, and D.M. Durand, "Chronic response of the rat sciatic nerve to the flat interface nerve electrode. *Annals of biomedical engineering*, *31*(6), pp.633-642 (2003).

[5] N. Vachicouras, O. Tarabichi, V.V. Kanumuri, C.M. Tringides, J. Macron, F. Fallegger, Y. Thenaisie, L. Epprecht, S. McInturff, A.A. Qureshi, and V. Paggi, "Microstructured thin-film electrode technology enables proof of concept of scalable, soft auditory brainstem implants." *Science translational medicine* 11.514 (2019).

[6] H. Park, P. Takmakov, and H. Lee. "Electrochemical evaluations of fractal microelectrodes for energy efficient neurostimulation." *Scientific reports* 8, no. 1 (2018): 1-11.

[7] M.L. Settell, N.A. Pelot, B.E. Knudsen, A.M. Dingle, A.L. McConico, E.N. Nicolai, J.K. Trevathan, J.A. Ezzell, E.K. Ross, K.J. Gustafson, and A.J. Shoffstall, "Functional vagotopy in the cervical vagus nerve of the domestic pig: implications for the study of vagus nerve stimulation." *Journal of neural engineering* 17, no. 2 (2020): 026022.

[8] S.F. Cogan, "Neural stimulation and recording electrodes." *Annu. Rev. Biomed. Eng.* 10 (2008): 275-309.

[9] H. Park, S. Zhang, A. Steinman, Z. Chen, and H. Lee. "Graphene prevents neurostimulation-induced platinum dissolution in fractal microelectrodes." *2D Materials* 6, no. 3 (2019): 035037.

CONTACT

*H. Lee, hwlee@purdue.edu

AN EQUIPMENT-FREE PAPERTRONIC SENSING SYSTEM FOR POINT-OF-CARE MONITORING OF ANTIMICROBIAL SUSCEPTIBILITY

Zahra Rafiee[1], Maryam Rezaie[1], Olya Noruz Shamsian[1], and Seokheun Choi[1,2]*

[1]Bioelectronics & Microsystems Laboratory, Department of Electrical & Computer Engineering, State University of New York at Binghamton (SUNY Binghamton), Binghamton, New York, USA

[2]Center for Research in Advanced Sensing Technologies & Environmental Sustainability, SUNY Binghamton, Binghamton, New York, USA

ABSTRACT

We create a simple, rapid, equipment-free papertronic sensor array that is connected to a visual readout, allowing the naked eye to access antibiotic effectiveness against pathogenic bacteria, *Pseudomonas aeruginosa* PA01. The sensing approach quickly monitors microbial bioelectricity which is based on their metabolic activities and is inversely proportional to the concentration of antibiotics. Each sensing system consists of a two-electrode microbial sensing unit, an interface circuit for sensor signal amplification, and an electronic visual display with a light-emitting diode (LED), which are all mounted onto a paper-based printed circuit board. The bioelectricity in the sensing unit is amplified by the transistor and is transduced into LED illumination when a pre-defined electric current corresponding to a bacterial sample with a certain antibiotic concentration is obtained. Only within an hour, the system generates reliable, discrete visual responses to monitor antibiotic efficacy and provides the right doses for treatment against bacterial infections.

KEYWORDS

Antimicrobial susceptibility testing, papertronics, extracellular electron transfer, microbial fuel cells, high-throughput sensing

INTRODUCTION

Bacterial infections are extremely difficult to be correctly diagnosed and effectively cured because disease can rapidly occur at any places in human body and can be easily spread to other humans and animals [1]. Moreover, a recent study shows that COVID-19 patients have a much greater chance of acquiring secondary bacterial infections, significantly increasing the mortality rate [2]. Effective treatment of the infections relies on the capability to rapidly assess antibiotic effectiveness against the bacterial samples and promote appropriate antibiotic use [3]. The careless and excessive use of antibiotics can lead to a strong natural selection for antimicrobial resistance, posing a more serious threat to public health and the economy [4-7]. Therefore, a rapid and simple antimicrobial susceptibility testing (AST) for anyone, anywhere, and anytime is urgently required to guide effective antibiotic usages and to surveil the antimicrobial resistance rate [8-10]. Although emerging genotypic ASTs are highly sensitive and rapid, the technique must go through complicated central laboratory tests with bulky, expensive, and sophisticated sequencing-based molecular analyzers and prior knowledge of the resistance genes is required. This renders the genotypic ASTs unfit as surveillance or early detection methods for unknown bacterial infections [9, 10]. Typical "gold standard" phenotypic ASTs are based on trained personnel and relatively time-consuming process for culturing and monitoring, practically preventing rapid and early diagnostic analysis of antibiotic resistance [7, 8]. Even our latest advance in paper-based phenotypic ASTs required external readout systems, hampering on-site point-of-care (POC) diagnostic testing [11].

In this work, we allowed rapid POC antibiotic susceptibility testing with an equipment-free all-electrical sensing approach integrated into a low-cost, disposable, and portable papertronic device (Figure 1). Our AST approach monitored extracellular electron transfer (EET) by bacterial cells, parallely and controllably formed on this papertronic sensing array (Figure 2). The transferred electrons are based on microbial metabolic activities and are inversely proportional to the concentration of potential antibiotics, leading to the rapid antimicrobial susceptibility testing (Figure 2).

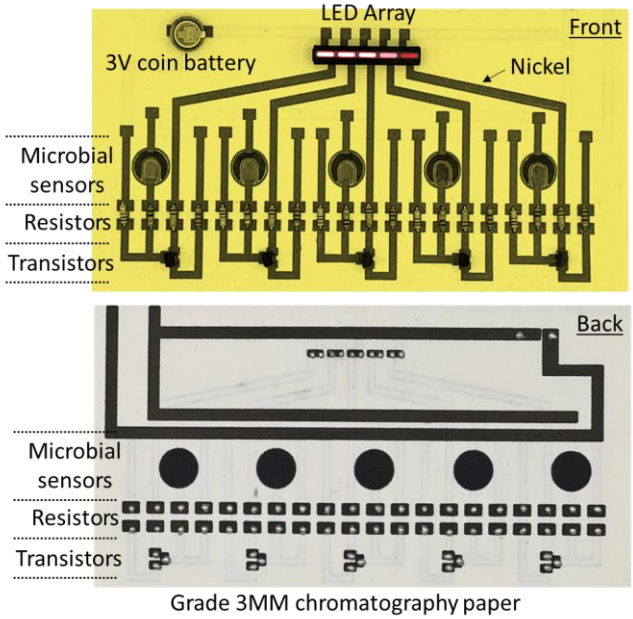

Figure 1: Photo images of the papertronic sensing system for point-of-care monitoring of antimicrobial susceptibility (Front and back views).

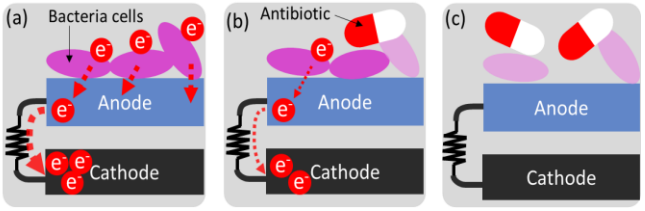

Figure 2: Schematic illustration of our AST technique. The sensing approach quickly monitors microbial bioelectricity which is based on their metabolic activities and is inversely proportional to the concentration of antibiotics.

EXPERIMENTAL PROCEDURE

Device fabrication

To define hydrophilic and hydrophobic regions, the paper substrate (Whatman 3MM Chr paper) was wax-printed by a solid-wax printer (Figure 3) [12, 13]. This is followed by a

978-1-940470-04-7/HH2022/$25©2022TRF
DOI 10.31438/trf.hh2022.27

heat-treatment at 160°C for 50 seconds. On the patterned hydrophilic regions, the microbial sensing units and the electrical interfaces (i.e. metallic wires) were constructed. The sensing unit has an anode and a cathode separated by a wax-based ion exchange membrane in a horizontal configuration. The anode was engineered to be conductive and hydrophilic so that the aquatic bacterial samples can be readily introduced and their electrogenic activities can be accessed.

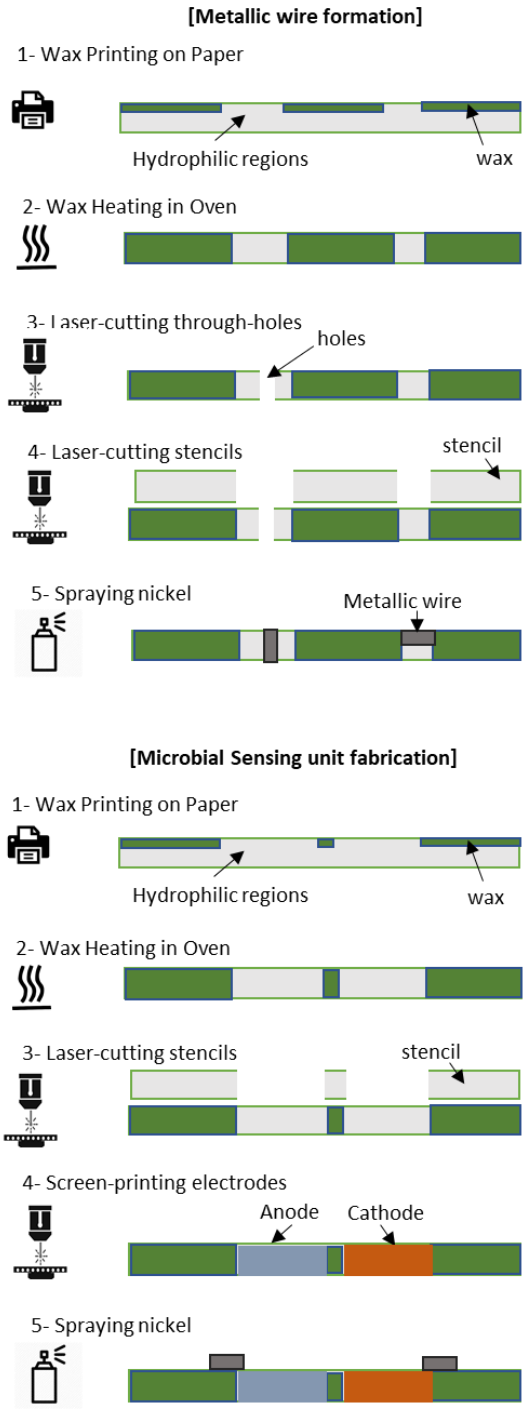

Figure 3: Fabrication process

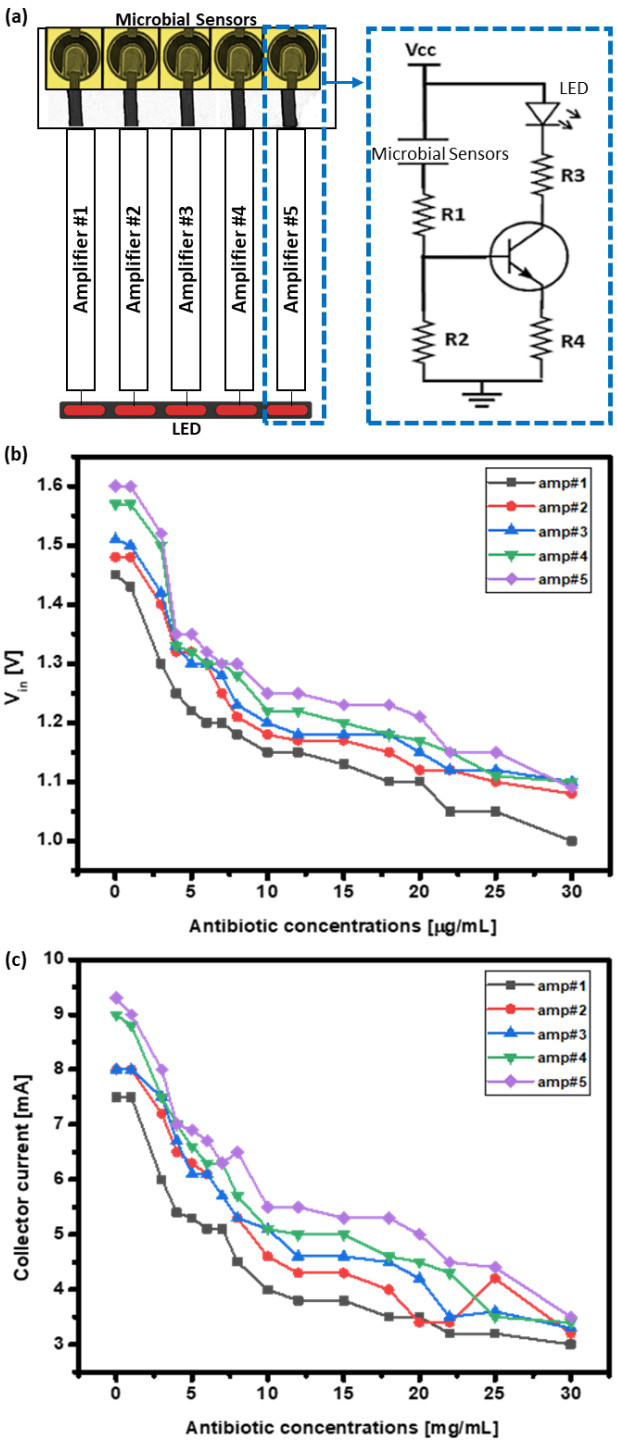

Figure 4: (a) Schematic illustration of the electric circuit for five antibiotic concentrations in the bacterial sample, (b) transistor voltage inputs, and (c) their collector currents in response to varying antibiotic levels.

A mixture of poly (3,4-ethylene dioxythiophene): poly (styrene sulfonate) (PEDOT: PSS) and dimethyl sulfoxide (DMSO) was introduced into the anodic region, followed by addition of 3-glycidoxypropy-trimethoxysilane. The cathode was prepared with Ag_2O catalysts. When the bacterial cells perform the metabolic activities, electrons and protons are produced where the electrons

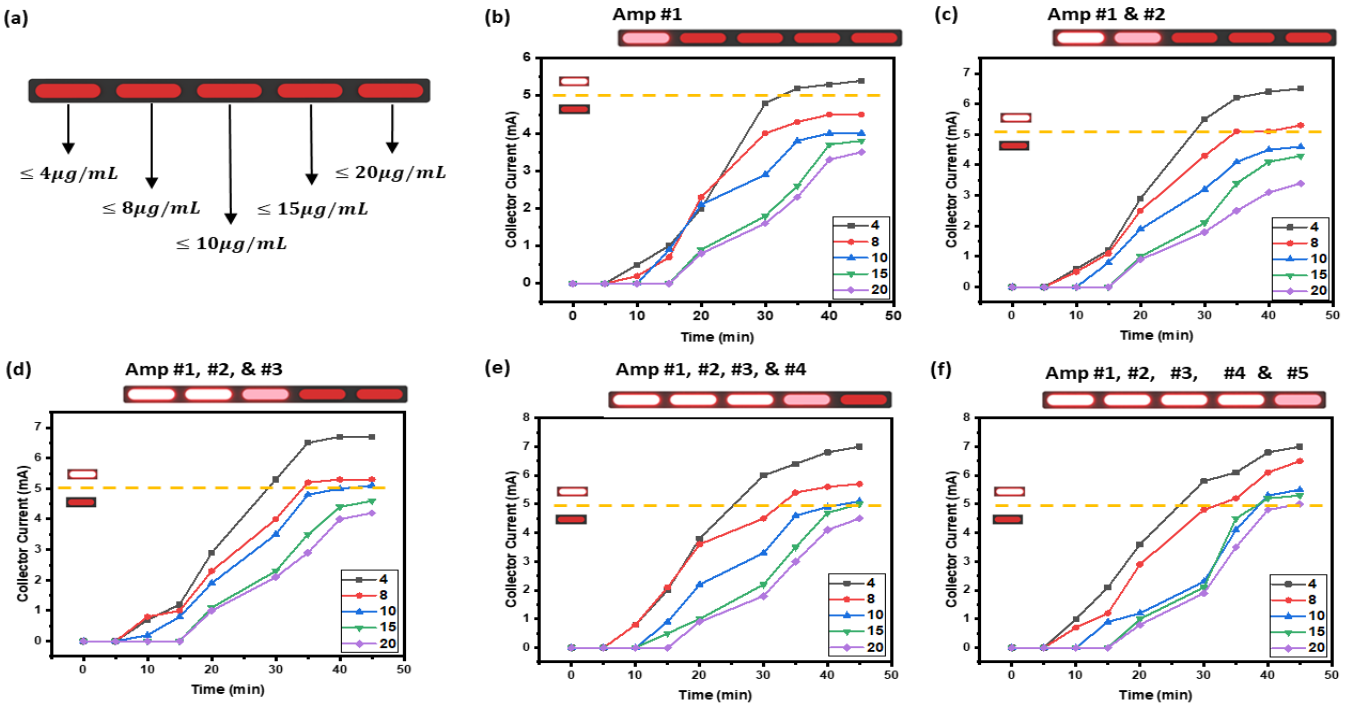

Figure 5: (a) Optical outputs of the AST sensing system (each LED indicator in the array corresponds to a certain antibiotic level in the bacteria sample). (b-f) LED responses and the current outputs of the sample with a different antibiotic level.

move to the cathode through an external load and the protons travel to the cathode through the ion exchange membrane. All electrical components were inserted into plated through holes on the patterned paper and connected to the metallic nickel wires with the conductive silver paste (Figure 3).

Bacterial sample preparation

Pseudomonas aeruginosa PA01 strain was selected as the test species because it is a well-known pathogen that can cause infections in humans and considered as electricity-producing bacteria. The bacterial sample was prepared in Luria Broth (LB) medium with an optical density at 600 nm (OD_{600}) of 1.0.

Antibiotic solution preparation

Gentamicin (GEN) was selected as antibiotics because it is highly effective against *P. aeruginosa* by inhibiting protein synthesis and affecting the integrity of the cell wall [14]. 4 μg/mL, 8 μg/mL, 10 μg/mL, 15 μg/mL and 20μg/mL GEN in sterile LB were prepared. Then, 5uL of the prepared antibiotic samples were dropped on the anodic reservoirs and pre-dried at room temperature for 5h.

Circuit configuration

The microbial sensing units were directly connected to the interface circuit for sensor signal amplification, and the electronic visual display with the LEDs (Figure 4) [15, 16]. The bacterial electricity generation was amplified by the transistor interface circuit and assessed by turning the LED array on and off. The interface circuit included five Darlington transistors with different values of R1 and R2 resistors. R1 and R2 resistors were carefully selected to generate a signal specific to an antibiotic concentration in the bacterial sample. R3 and R4 were chosen to generate a transistor input voltage and to turn the LED on and off.

RESULTS AND DISCUSSION

This work is part of a global effort to enable an innovative, rapid, easy-to-use, and high-throughput AST platform for pathogenic bacteria and thus provide effective antibiotic treatment guidelines while minimizing the unnecessary use of antibiotics [7, 8]. Genotypic and phenotypic AST methods have been dramatically advanced to determine the antibiotic susceptibility of bacterial cells [9, 10]. However, antibiotic susceptibility depends on laborious and time-consuming procedures [17-19]. The bacterial cells are exposed to antibiotics for a relatively long time, and then they are dislodged for microscopic examination of viability. This available standard protocol and susceptibility testing is limited to a few bacterial strains, which is only accessible to the ASTM standard subscribers (www.astm.org). The proposed work of this project is unique. No other group has proposed an AST platform that can provide real-time and high-throughput all-electrical monitoring capability with rapid and easy-to-control incubation time of bacteria with pre-defined antibiotics. This technique will be advanced as the proposed EET-based AST approach enables an entirely new technique in guiding antibiotic treatment for bacterial infections. This will also spur the development of additional theory and understanding of bacterial EET-based sensing, antibiotics distribution through bacterial cells, and antibiotic resistance development.

Our papertronic AST sensor array enabled simple visual monitoring of bacterial metabolic activities against different antibiotic concentrations. Our system integrated five 2-electrode sensing units into signal amplifier circuits connected to LED reporting units (Figure 1). The bioelectricity metabolically produced from the bacterial sample with a different antibiotic level

was amplified by the transistor, which triggered a LED when a pre-defined current level was obtained (Figure 4). The resistors (R1 & R2) were adjusted so that each LED indicator in the array corresponded to a certain antibiotic level in the bacteria concentration with OD_{600} of 1.0 within the 5μL of the sensing reservoir (LED#1: ≤ 4μg/mL, LED#2: ≤ 8μg/mL, LED#3: ≤ 10 μg/mL, LED#4: ≤ 15 μg/mL, and LED#5: ≤ 20 μg/mL) (Figure 5). For example, if all the LEDs light up, the sample has the lowest antibiotic concertation (≤ 4μg/mL). The LED #1 corresponded to 4μg/mL concentration which is the typical minimum inhibitory concentration of antibiotic gentamicin toward *P. aeruginosa* PA01. If the bacteria become resistant to the pre-defined antibiotic level, the current will be decreased to stop the illumination of the designated LEDs.

CONCLUSION

Antibiotic resistance (AMR) has increased worldwide in the 21st century, developing more infections that can be untreatable. Rapid antimicrobial sustainability testing (AST) has become increasingly important as drug-resistant infections become harder to treat. In this work, we reported a rapid AST sensor array by using the direct conversion of the amplified bacterial electrogenic signal to discrete visual perception. The proposed sensor array allowed the simple, easy-to-use, low-cost, high-throughput, sensitive AST by using a paper-based electronics and a amplification circuit with a LED indicator array. Our device can be a practical POC tool that provides immediately actionable healthcare information at a reduced cost, revolutionizing public healthcare in developed and developing countries. It is also expected that research into pathogens for emulating and elucidating multiple, correlated key parameters in forming multiple bacterial strains, thereby enabling a versatile platform for fundamental studies of antibiotic resistance development.

ACKNOWLEDGEMENTS

This work was supported mainly by the National Science Foundation (CBET #2100757, ECCS #2020486, and ECCS #1920979), and partially by the Office of Naval Research (#N00014-21-1-2412).

REFERENCES

[1] S. Doron, S.L. Gorbach, "Bacterial Infections: Overview," *International Encyclopedia of Public Health*, 273-282 (2008).

[2] A.A. Karbelkar, A.L. Furst, "Electrochemical diagnostics for bacterial infectious diseases," *ACS Infectious Diseases*, 6, 1567-1571 (2020).

[3] R. Mohan, A. Mukherjee, S.E. Sevgen, C. Sanpitakseree, J. Lee, C.M. Schroeder, P.J.A. Kenis, "A multiplexed microfluidic platform for rapid antibiotic susceptibility testing," *Biosensors and Bioelectronics*, 49, 118-125 (2013).

[4] M. Frieri, K. Kumar, A. Boutin, "Antibiotic resistance," *Journal of Infection and Public Health*, 10, 369-378 (2017).

[5] R.K. Shanmugakani, B. Srinivasan, M.J. Glesby, L.F. Westblade, W.B. Cardenas, T. Raj, D. Erickson, S. Mehta, "Current state of the art in rapid diagnostics for antimicrobial resistance," *Lab on a Chip*, 20, 2607-2625 (2020).

[6] A. Vasala, V.P. Hytonen, O.H. Laitinen, "Modern tools for rapid diagnostics of antimicrobial resistance," *Frontiers in Cellular and Infection Microbiology*, 10, 308 (2020).

[7] H. Leonard, R. Colodner, S. Halachmi, E. Segal, "Recent advances in the race to design a rapid diagnostic test for antimicrobial resistance," *ACS Sensors*, 3, 2202-2217 (2018).

[8] B. Behera, A. Vishnu, S. Chatterjee, V.S.N. Sitaramgupta, N. Sreekumar, A. Nagabhushan, N. Rajendran, B.H. Prathik, H.J. Panday, "Emerging technologies for antibiotic susceptibility testing," *Biosensors and Bioelectronics*, 142, 111552 (2019).

[9] A. van Belkum, C.D. Burnham, J.W.A. Rossen, F. Mallard, O. Rochas, W.M. Dunne Jr., "Innovative and rapid antimicrobial susceptibility testing systems," *Nature Reviews Microbiology*, 18, 299-311 (2020).

[10] D.J. Shin, N. Andini, K. Hsieh, S. Yang, T. Wang, "Emerging analytical techniques for rapid pathogen identification and susceptibility testing," *Annual Reviews of Analytical Chemistry*, 12, 41-67 (2019).

[11] Y. Gao, J. Ryu, L. Liu, S. Choi, "A simple, inexpensive, and rapid method to assess antibiotic effectiveness against exoelectrogenic bacteria," *Biosensors and Bioelectronics*, 168, 112518 (2020).

[12] Y. Gao, S. Choi, "Merging Electric Bacteria with Paper," *Advanced Materials Technologies*, 3, 1800118 (2018).

[13] L. Liu, S. Choi, "A Paper-based Biological Solar Cell," *SLAS Technology*, 25, 75-81 (2020).

[14] N.L. Martin, T.J. Beveridge, "Gentamicin interaction with Pseudomonas aeruginosa cell envelope," *Antimicrob. Agents. Chemother*. 29, 1079-1087 (1986).

[15] M. Tahernia, M. Mohammadifar, D.J. Hassett, S. Choi, "A portable papertronic sensing system for rapid, high-throughput, and visual screening of bacterial electrogenicity," *Biosensors and Bioelectronics*, 165, 112348 (2020).

[16] M. Mohammadifar, M. Tahernia, S. Choi, "An Equipment-free, Paper-based Electrochemical Sensor for Visual Monitoring of Glucose Levels in Urine" *SLAS Technology*, 24, 499-505 (2019).

[17] G. Maugeri, I. Lychko, R. Sobral, A.C.A. Roque, "Identification and antibiotic-susceptability profiling of infectious bacterial agents: a review of current and future trends," *Biotechnology Journal*, 14, 1700750 (2019).

[18] E.A. Idelevich, K. Becker, "How to accelerate antimicrobial susceptibility testing," *Clinical Microbiology and Infection*, 25, 1347-1355 (2019).

[19] J. Dietvorst, L. Vilaplana, N. Uria, M. Marco, X. Munoz-Berbel, "Current and near-future technologies for antibiotic susceptibility testing and resistant bacteria detection," *Trends in Analytic Chemistry*, 127, 115891 (2020).

CONTACT

*Prof. S. Choi, tel: +1-607-777-5913; sechoi@binghamton.edu

CMOS-NANOWELL BASED HYBRID SMART BANDAGE FOR LONG TERM MONITORING OF WOUND HEALING VIA CYTOKINE QUANTIFICATION IN-SITU

Chengjie Zhu[1], Pengfei Xie[2], Ryan Thorpe[1], Jesus Maldonado[1], Suneel Kumar[2], Aaron Mazzeo[2], Mehdi Javanmard[2], Francois Berthiaume[2] and Kaushik Sengupta[1]
[1]Princeton University, NJ, USA
[2]Rutgers University, NJ, USA

ABSTRACT

Long-term monitoring of the chronic wound can allow autonomous wound healing. Prior attempts that sense wound closure dynamics in bandage forms are based on pressure, temperature and pH, lacking specific bio-molecular information that is critical for accurate acquisition of growth factors in various wound healing stages. This work presents a hybrid CMOS/nanowell co-design approach to target cytokine level to predict wound closure dynamics. The complete impedance spectroscopy chip is designed and fabricated in TSMC 65 nm LP process and is integrated on a flexible PCB compatible to "Smart Bandage" forms along with nanowell sensors located at the back and peripheral circuits. The proposed system demonstrates the sensitivity of IL-6 cytokine on the order of 100 pg/mL, and shows strong correlations to the standardized ELISA tests. This proposed CMOS/nano hybrid approach shows a path towards highly multiplexed and low-cost "Smart Bandages" for autonomous closed-loop wound monitoring and healing applications.

KEYWORDS

Smart bandages, cytokine, wound healing, impedance spectroscopy, nano-fabrication, ELISA.

INTRODUCTION

Over 6 million of people in US is currently living under complications resulting from unhealed chronic wounds. Long-term monitoring of chronic wounds, coupled with on-demand medication, could enable autonomous wound healing systems, thus paving the way towards patient-specific and wound-specific treatments that optimize the local immune and angiogenic responses, and eventual healing. Currently, the treatment of chronic wounds requires frequent visits to physicians and consecutive openings of the bandages for visual check. Unnecessarily disturbing the wound environment, and limiting wound evaluation to few observable features may contribute to slow healing and the risk of bacterial infection and sepsis [1]. The key technology to minimize the risks is to enable point-of-care diagnostic devices in compact packages, based on integrated circuit technology, such as CMOS (complementary-metal-oxide-semiconductor) [8-10]. For chronic wound healing monitoring, such devices are typically packages in the form of "smart bandages". Prior works on smart bandages have shown capabilities of detecting healing stages from largely biophysical and non-specific markers such as pressure, temperature, and pH [1-3]. However, these methods lack specific bio-molecular information, yet there is extensive knowledge of the roles of chemokines, cytokines, and growth factors in various stages of wound healing.

In this work, we present a CMOS-chip/nanowell based hybrid smart bandage interface that allows in-situ real-time and long-term label-free quantification of cytokine release from skin directly on complex wound fluids. We monitor specific cytokine binding kinetics on nanowell surface through impedance spectroscopy controlled by the custom CMOS chip. A co-design of the nanowell sensor and the CMOS chip achieves ELISA-level sensitivity demonstrating quantitative analysis of IL-6 released, and monitoring of wound healing stages over a period of two weeks from mouse wound fluids. Collectively, this allowed for the first smart bandage capable of detecting sub-pM levels of cytokine target concentrations in complex wound fluids in-situ, with high correlation to the standardized ELISA tests.

MATERIALS AND METHODS

Nanowell Sensor Fabrication

The general fabrication procedure of the nanowell sensor follows prior works [4-5]. Here, fused silica is chosen as the sensor substrate. As illustrated in Fig. 2, multiple layers of metal and insulation oxide are located in each nanowell. In general, the fabrication procedure can be summarized as follows: 1) a 5 nm thickness of chromium is sputtered as the adhesive layer followed by 150 nm of gold deposition on the fused silica substrate. 2) Standard liftoff procedures are followed by a 40 nm aluminum oxide through atomic layer deposition (ALD). 4) The second layer of electrode (again 5 nm chromium and 150 nm gold) is patterned on top of aluminum oxide by following step 1) and 2). 5) A final aluminum oxide layer is deposited through ALD on top of all electrodes to confine the electric field excitation within the nanowells. This can reduce the area for non-specific binding and selectively control the immobilized antibodies in the nanowells.

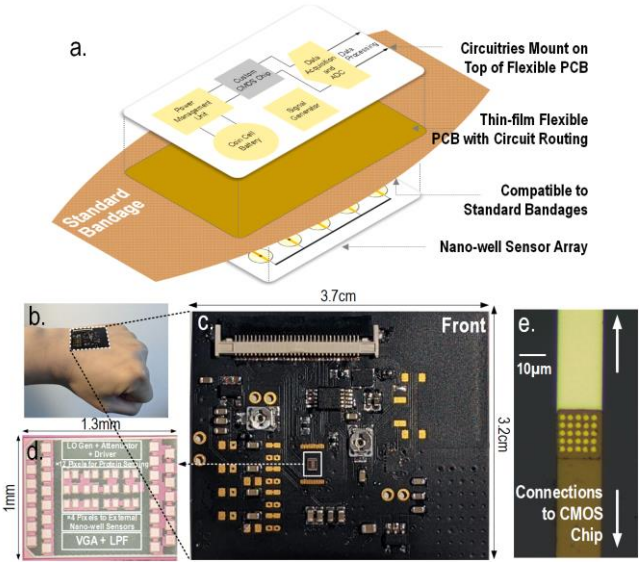

Figure 1. a) and b) CMOS/nanowell hybrid smart bandage. c) Flexible PCB with the custom silicon chip d) Micrograph of the custom-designed CMOS IC in a 65nm CMOS process. e) Microscopic photograph of nanowell sensor.

As shown in Fig. 2, an overlapping area of 20 × 20 µm^2 is separated by aluminum oxide to generate a current path to analyze the solution inside the nanowell. The two layers of the metals are

978-1-940470-04-7/HH2022/$25©2022TRF
DOI 10.31438/trf.hh2022.28

routed externally and can be eventually wire-bonded to the back of the flexible board.

Finally, a thin layer of PDMS (~ 500 um) with an opening area of 5 mm is attached to the surface of the substrate through covalent bonding after treatments in oxygen plasma chamber [4-5]. The purpose of the PDMS well is to confine the wound fluid liquid for more consistent incubation. The final assembled sensor is shown in Fig. 1, along with a microscopic photograph of the nanowell.

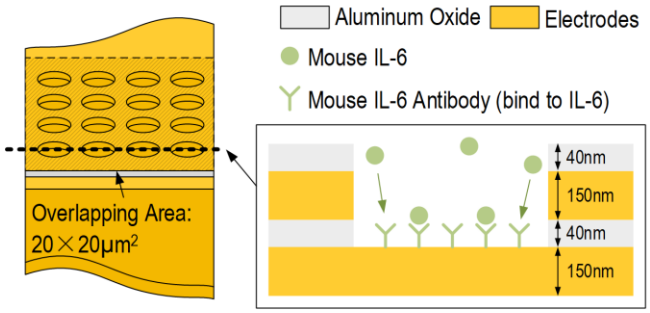

Figure 2. Cross-sectional view of the nano-well sensor, showing mouse IL-6 protein binding to IL-6 antibody resulting in impedance change between electrodes.

Mouse Wound Fluid Collection Procedure

Wound samples from mice were collected according to a protocol approved by the Institutional Animal Care and Use Committee (IACUC) at Rutgers University. The samples were collected post-surgery from the dorsal skin on a 10-week old mouse (Fig. 4). In summary, the mice were anesthetized by isoflurane one day prior to surgery. On the day of surgery, the mice were scrubbed with betadine and 70% ethanol three times followed by a biopsy punch (Integra LifeSciences; Princeton, New Jersey) to create a wound size of roughly 10 mm in diameter on mice dorsal skin. The wound is then covered with Tegaderm dressing to protect from infection.

During the wound fluid collection on day 3, 7, and 10, Tegaderm dressing is removed and dropped in a tube containing 1 mL of 1x PBS buffer solution. The tube is then centrifuged to collect the supernatant that is used for wound fluid sample for later measurements. Fig. 4 illustrates the wound closure dynamics of the mouse dorsal skin on days 3, 7, and 10 respectively.

SYSTEM ARCHITECTURE

Impedance Sensing Architecture

The impedance sensing circuit on-chip is designed and fabricated in TSMC 65 nm LP process and is based on direct-conversion sensing architecture as presented in prior works [6-7]. To sense this complex impedance change in nanowells, the CMOS chip excites the nanowell sensor at 700 kHz with 50 mVpp amplitude. The sensed current is processed on-chip with integrated trans-impedance amplifier. The amplified signal is then down-converted through in-phase (I) and quadrature (Q) clock to DC analog voltages that is low-pass filtered (10 kHz) to remove higher orders of harmonics to acquire the impedance information.

Nanowell Impedance Sensing

To better understand the EIS sensing mechanism in nanowell, an equivalent circuit model of the nanowell has been shown in Fig. 3, where R_s is the bulk fluid resistance, C_{DL} is the double-layer capacitance and R_p is the polarization resistance. The operating frequency of the impedance analysis of the nanowell sensor has been experimentally proven to be the best between 500 kHz to 1 MHz to prevent the non-ideal inductive effect of metal traces (existing at higher frequencies beyond 1 MHz), while capable of penetrating the double-layer capacitance (C_{DL}) for the sensor to tap into the protein binding events [4]. As shown in Fig. 2 and 3, when the cytokine binds to the nanowell sensor surface with immobilized probe antibody of mouse IL-6, it blocks the ion transfer in the double-layer inside the nanowells that lead to an impedance increase from the binding event [4-5]. An increase in impedance translates to a decrease in current after the nanowell channel is excited with voltage. Finally, the change in current can be captured by the on-chip TIA (Fig. 5), resulting in a positive signal.

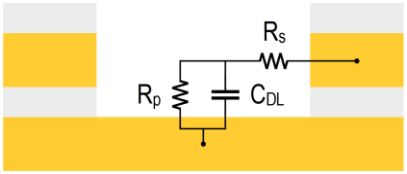

Figure 3. An equivalent circuit model inside the nanowell, showing the polarization resistance (R_p), double-layer capacitance (C_{DL}), and bulk fluid resistance (R_s).

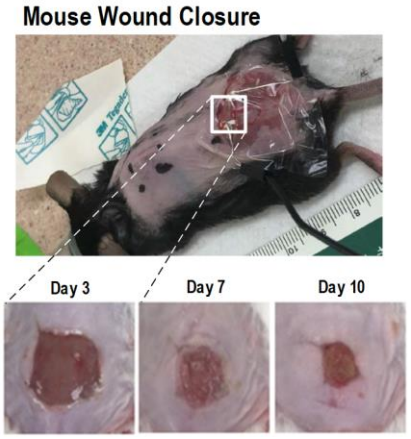

Figure 4. Mouse wound fluid collection with wound closure dynamics on day 3, 7 and 10.

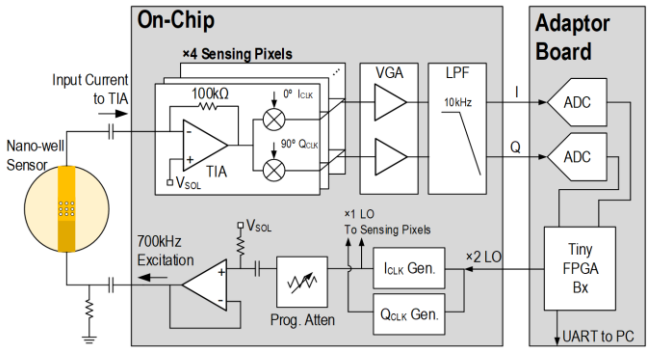

Figure 5. CMOS direct conversion transmitter/receiver architecture for impedance spectroscopy for label free detection of cytokines in complex wound fluids.

Smart Bandage Packaging

Fig. 1 illustrates the envisioned smart bandage with electronic circuits mounted on top. The nanowell sensor is located at the back to avoid obtrusion to skin. Fig. 1 shows the CMOS/nanowell cytokine sensing system on a flexible PCB with a dimension of 3.7 × 3.2 cm^2 compatible with the bandage form factor. The front side is mounted with a multi-channeled CMOS impedance spectroscopy receiver along with peripheral modules that offer power management, signal generation, and data acquisition. On the back of the sensor, we offer connections to the two electrodes of the nanowell sensors.

In addition, we choose to design an adaptor board in the prototyped system to control and monitor signal processing. The adaptor and the flexible board are communicated through a ribbon cable. In the adaptor board, we implemented a sigma-delta ADC (MCP3564, Microchip) and an FPGA (tinyFPGA BX) for data acquisition and communication to PC through UART protocol. We also implemented an LCD display panel and push buttons for easier user interface.

Ideally, all functionalities shall be implemented on a battery-powered flexible smart bandage with built-in wireless data communication. Here, we demonstrate the core functionalities of cytokine protein detection for wound healing monitoring in a wired system setup.

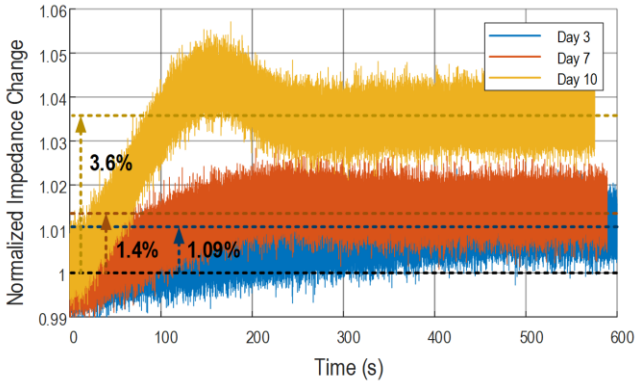

Figure 6. Real-time impedance impedance measurement of the CMOS/nanowell smart sensor showing varying normalized impedance of 3.5%, 1.4% and 1.09% at steady state in collected would sample fluid (containing cytokine IL-6) at day 3, 7, and 10 of the wound healing stages.

MEASUREMENT RESULTS

CMOS/nanowell Mouse IL-6 Cytokine Measurement Results

The measurements of the collected wound fluid sample start by diffusing 5 µL mouse IL-6 antibody to the nanowell sensor with 20 µL 1X PBS buffer solution pre-stabilized in the nanowell sensor to emulate the physical environment [4]. After the antibody diffusion to the nanowell, an additional 20 µL of 1× PBS buffer is added. This procedure is to eliminate any signal variations due to the addition of PBS buffer [4]. Finally, 5 µL of collected wound fluid is added and the complete impedance variation is recorded against time.

Fig. 6 shows the normalized impedance amplitude variation of the nanowell sensor measured at 700 kHz of excitation after the 5 µL wound fluid is added. We record the normalized impedance change of 3.6, 1.4, and 1.09% at steady state (of roughly ~10 min of signal recording) for wound fluid samples collected from days 3, 7, and 10 respectively. We then performed four trial measurements for each collected sample and the results are summarized in Fig. 7.

The steady-state impedance demonstrates the varying concentrations of cytokine release from the day of incision to final healing. As Fig. 7 shows, the cytokine release is the highest on day 3 and then slowly declines as the wound goes through the normal progression of inflammation, proliferation, and maturation.

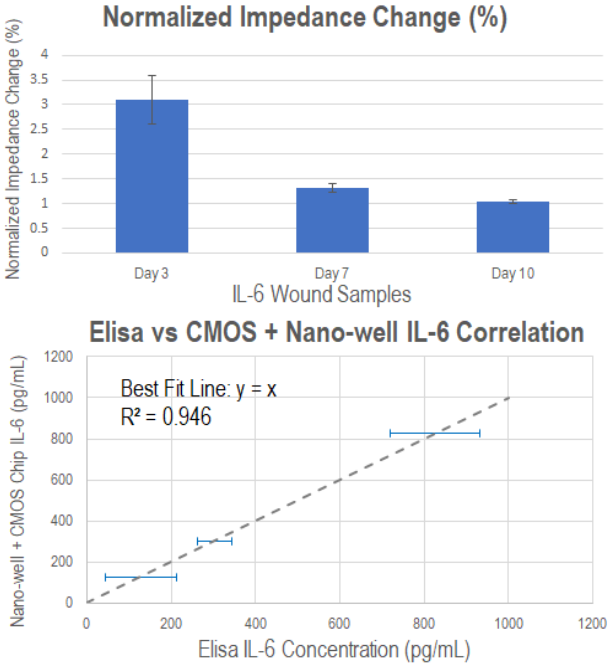

Figure 7. Measured IL-6 release profile in the mouse wound fluid (as measured with the smart bandage) showing decrease in cytokine release as the wound progress towards healing (top). A correlation plot of IL-6 measured in wound fluids with the CMOS/nano-well against a standard ELISA measurement, demonstration high correlation factor of $R^2 = 0.946$ (bottom).

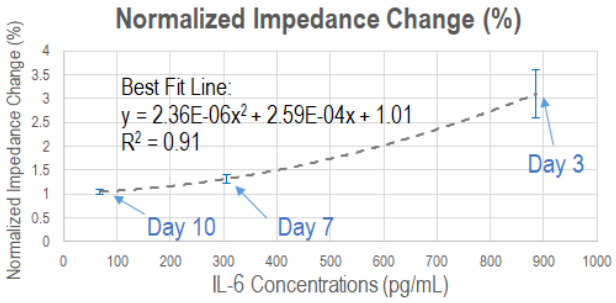

Figure 8. A best-fit line used to find the correlation between the normalized impedance and ELISA measurement results of the mouse wound fluid.

Comparisons and Correlations to ELISA Tests

In addition, we compared our results to standardized ELISA tests of IL-6 in the collected wound fluids. The IL-6 ELISA tests were performed in a commercial assay (INITROGEN, Thermo Fisher Scientific, USA) by following protocols from the manufacturer. The fluorescent absorbance is recorded using a plate reader at 450 nm wavelength to characterize the IL-6 cytokine concentration which is used for later studies on the correlation to the IL-6 measurements using the CMOS-nanowell sensor.

As shown in Fig. 8, $y = 2.36\times10^{6}\ x^2 + 2.59\times10^{-6}\ x + 1.01$ is used as the best-fit line for the CMOS-nanowell measurements.

Table 1: Comparisons with other state-of-the-art "Smart Bandages" for chronic wound healing monitoring

	This Work	A. Pal et al. [3]	M. Farooqui et al. [2]	P. Mostafalu et al. [1]
Dimensions	**3.7 × 3.2 cm²**	3.8 × 1 cm² (Estimated)	3.8 × 1 cm² (Estimated)	3 × 2 cm²
Sensing Modelities	**Impedance spectroscopy**	Chronoamperometry (Potentiostat), impedance spectroscopy (pH) and pressure.	Capacitive (CDC)	Temperature, potentiometry (pH) and heater-based drug release.
IC Chip	**Custom designed CMOS chip**	LMP9100 (potentiostat), AD5933 (impedance)	LC717A00AJ (CDC)	N.A.
Process/Manufacturer for IC Chip	**Custom Chip TSMC 65 nm LP**	TI, ADI	On Semi	N.A.
Electrode Implementations	**Nanowell sensor on glass substrate**	3 electrode configuration for pH. Omniphoic paper-based capatcitive sensor (OPSBs) for capacitive sensor (OPSBs).	Carbon ink electrodes on kapton tape	Heater electrodes on parylene substrate. Carbon/PANI, and silver electrodes on PET substrate.
Biomarker/Sensing Target	**Cytokine (IL-6)**	pH (Impedance); Uric acid (potentiostat)	Blood and pressure (CDC)	pH
Calibration /Correlation	**ELISA**	Impedance calibrated with standard pH measurement.	Pressure calibrated	Temperature and PH Calibrated.
Protein Sensing Capability	**Yes**	No	No	No
Minimum Measured Concentration /Sensitivity	**100 pg/mL**	0.2 mM (Uric acid/potassium ferricyanide)	10μL blood ~0.5pF	~50 mV/pH

Finally, the correlation between the CMOS-nanowell and ELISA is plotted in Fig. 7, showing a very high correlation to the ELISA assay, with $R^2 = 0.946$. This result demonstrates a highly reliable label-free cytokine protein sensing system for wound healing monitoring applications in a bandage form.

Finally, the performance of the CMOS-nanowell smart bandage system is summarized in Tab. 1 and compared against other state-of-the-art smart bandage systems from prior works. This work shows, for the first time, a miniaturized smart bandage system with bio-molecular sensing capability to detect cytokine concentration from the mouse wound fluids, reaching L.O.D. of ≈ 100 pg/mL of IL-6 cytokine concentration.

CONCLUSION

In summary, this work has shown, for the first time, a CMOS-nanowell sensor system that is co-designed for chronic wound healing monitoring applications. Specifically, we demonstrate IL-6 cytokine measurements from the collected mouse wound fluids. In addition, normalized impedance sensing results showed high correlation to standardized ELISA tests, demonstrating the reliability of the proposed smart bandage sensing system. The proposed system can also be easily implemented to adapt to other cytokines such as TNF-α to allow multiplexed measurements for better wound healing prediction. This hybrid approach shows a path towards highly multiplexed, low-power, compact, and low-cost smart bandages for autonomous closed-loop wound monitoring and healing devices.

ACKNOWLEDGEMENT

The authors would like to thank DARPA BETR Program for the funding support.

REFERENCES

[1] P. Mostafalu, et al., "Smart bandage for monitoring and treatment of chronic wounds," *Small*, vol. 14, no. 33, p. 1703509, 2018.

[2] M. F. Farooqui and A. Shamim, "Low cost inkjet printed smart bandage for wireless monitoring of chronic wounds," *Scientific Reports*, vol. 6, no. 1, 2016.

[3] A. Pal, D. Goswami, H. E. Cuellar, B. Castro, S. Kuang, and R. V. Martinez, "Early detection and monitoring of chronic wounds using low-cost, omniphobic paper-based smart bandages," *Biosensors and Bioelectronics*, vol. 117, pp. 696–705, 2018.

[4] P. Xie et al., "Real Time Cytokine Quantification in Wound Fluid Samples Using Nanowell Impedance Sensing," *2021 21st International Conference on Solid-State Sensors, Actuators and Microsystems (Transducers)*, 2021.

[5] S. R. Mahnoodi et al., "Single-step label-free nanowell immunoassay accurately quantifies serum stress hormones within minutes" *Science Advances*, vol. 7, no. 27, 2021.

[6] C. Zhu, et al., "CMOS-Based Electrokinetic Microfluidics With Multi-Modal Cellular and Bio-Molecular Sensing for End-to-End Point-of-Care System," *IEEE Transactions on Biomedical Circuits and Systems*, 2022, vol.15, no.6, 2021.

[7] C. Zhu et al., "18.2 CMOS-Driven Pneumatic-Free Scalable Microfluidics and Fluid Processing with Label-Free Cellular and Bio-Molecular Sensing Capability for an End-to-End Point-of-Care System," *2021 IEEE International Solid- State Circuits Conference (ISSCC)*, 2021.

[8] C. Zhu, et al., "A packaged ingestible bio-pill with 15-pixel multiplexed fluorescence nucleic-acid sensor and bi-directional wireless interface for in-vivo bio-molecular sensing," *2020 IEEE Symposium on VLSI Circuits*, 2020.

[9] L. Hong, et al., "Nano-Plasmonics and electronics co-integration in CMOS enabling a pill-sized multiplexed fluorescence microarray system," *Biomedical Optics Express*, vol. 9, no. 11, p. 5735, 2018.

[10] L. Hong, et al., "Fully integrated fluorescence biosensors on-chip employing multi-functional Nanoplasmonic optical structures in CMOS," *IEEE Journal of Solid-State Circuits*, vol. 52, no. 9, pp. 2388–2406, 2017.

DROPBLOT DESIGN INTEGRATES DROPLET MICROFLUIDICS WITH SINGLE-CELL ELECTROPHORESIS FOR TARGETED PROTEOMICS

Yang Liu[1*] *and Amy E. Herr*[1]
[1]University of California, Berkeley, California, USA

ABSTRACT

Single-cell analyses are revolutionizing biomedicine and biology, with genomics (DNA) and transcriptomics (RNA) tools leading the way. At the protein-level, single-cell analyses are limited to mass spectrometry and immunoassays. Neither assay provides comprehensive coverage of proteome for single cells, missing key protein forms (called isoforms). Here, we introduce a hybrid droplet-electrophoresis device, termed "DropBlot", to detect proteins from patient-derived tissue biospecimens relevant to clinical medicine and pathology. The DropBlot takes advantage of water-in-oil (W/O) droplets to encapsulate single cells derived from chemically fixed tissues, thus providing a picoliter-volume reaction chamber in which said cells are lysed and subjected to harsh lysis conditions (100ºC, 2 hours), as needed for fixed cells. We report an all-in-one microdevice to facilitate cell-laden droplet loading with >98% microwell occupancy. Droplets remain intact under the electric field and protein isoforms are shown to electromigrate out of the droplet and into a microfluidic separation channel where protein sizing takes place via the action of electrophoresis in a photoactive polyacrylamide (PA) gel.

KEYWORDS

Proteoform, Droplet, Microfluidics, Fixed Cells, Single-Cell Immunoblotting.

INTRODUCTION

Microanalytical tools underpin many of the single-cell genomic (DNA) and transcriptomic (RNA) advances of recent years.[1] Similarly, microfluidic tools are playing a significant role in understanding single-cell level protein expression and function;[2, 3] as is critical for disease diagnostics[4]. Proteoforms are different phenotypes (forms) of protein molecules translated by the same gene[5], and play a vital role in cell states and cellular heterogeneity.

While a suite of single-cell protein analysis tools have been developed, many rely on antibody probes that have low specificity and cannot differentiate the similar proteoform molecules.[6] A workhorse method to analyze the lysate of individual cells is capillary electrophoresis (CE), which conducts protein electrophoresis in fused silica capillaries. However, the low-throughput and analyte loss due to absorption bottleneck its application in the measurement of single-cell heterogeneity.[7, 8] Mass spectrometry is another powerful tool to analyze proteoforms without antibody probes. While promising in single-cell analysis, mass spectrometry can presently only detect high abundance species and small-to-intermediate sized proteins.[9, 10]

As a complement to existing tools that have difficulty detecting proteoforms, our group has pioneered single-cell immunoblotting microanalytical tools design and clinical translation[11, 12]. The immunoblotting tools utilize an 'open microfluidic' design concept, with no enclosed channels. An open microwell (no 'lid') is used to isolate and manipulate a single cell prior to lysis and protein electrophoresis. Nevertheless, the 'open' microwell structures suffer from diffusion-based protein target losses even before analysis. These target losses limit the duration of lysis (5-60 sec), which makes the device unable to analyze **F**ormalin-**F**ixed and **P**araffin-**E**mbedded (FFPE) specimens that are widely used in clinical pathology labs and diagnostics[13, 14] and require harsh conditions to reverse protein crosslinks and extract target proteins[15]. To address these cell preparation challenges, we present a hybrid droplet-electrophoresis device (DropBlot) designed to support harsh-cell lysis conditions and, thus, applicability to the ~1 billion patient-derived FFPE tissue samples preserved in clinical repositories.

RESULTS AND DISCUSSION

Overview of DropBlot

DropBlot (Figure 1a) incorporates a droplet generation device with a single-cell immunoblotting chamber, on which droplet trapping, cell lysis, on-chip protein separation, antigen probing, and nucleic acid recovery are performed. To our knowledge, this is the first such hybrid design. In this device (Figure 1b), cell suspensions and lysis buffer are encapsulated into water-in-oil (W/O) droplets. Droplets are then loaded onto PA-gel stippled with microwells. A suspension of cell-laden droplets is then loaded via gravity-based sedimentation onto the microwell setup. Cells are then chemically lysed while encapsulated in the droplets, with each droplet centered in a microwell. The droplet, enclosed by mineral oil, prevents protein lysate loss due to the diffusion and sustains stability under harsh lysis conditions (high temperature, long-time incubation). After the harsh lysis step completes, protein analysis is initiated by

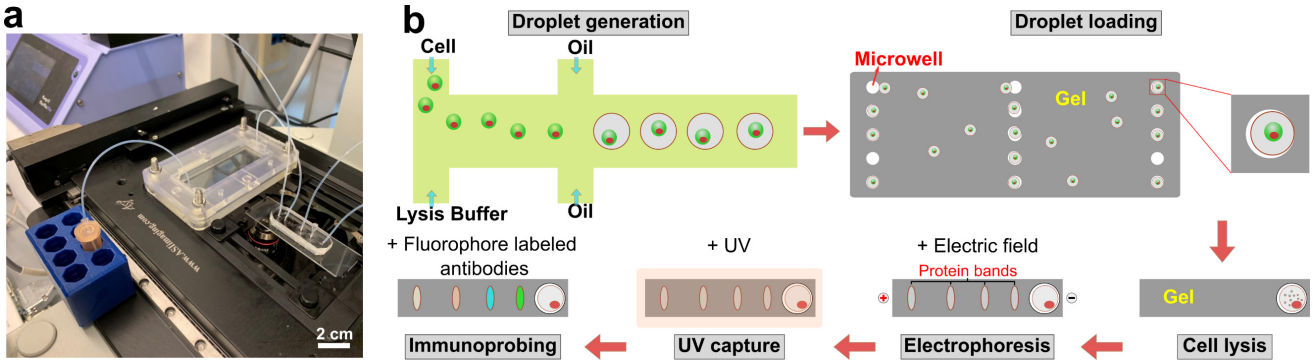

Figure 1: DropBlot: a hybrid droplet and single-cell protein electrophoresis bioMEMS device to understand the proteome of even rugged cell specimens. (a) A photo of the device assembles with droplet generation stage and all-in-one electrophoresis chamber. (b) Workflow for single-cell electrophoresis using the integrated system.

978-1-940470-04-7/HH2022/$25©2022TRF
DOI 10.31438/trf.hh2022.29

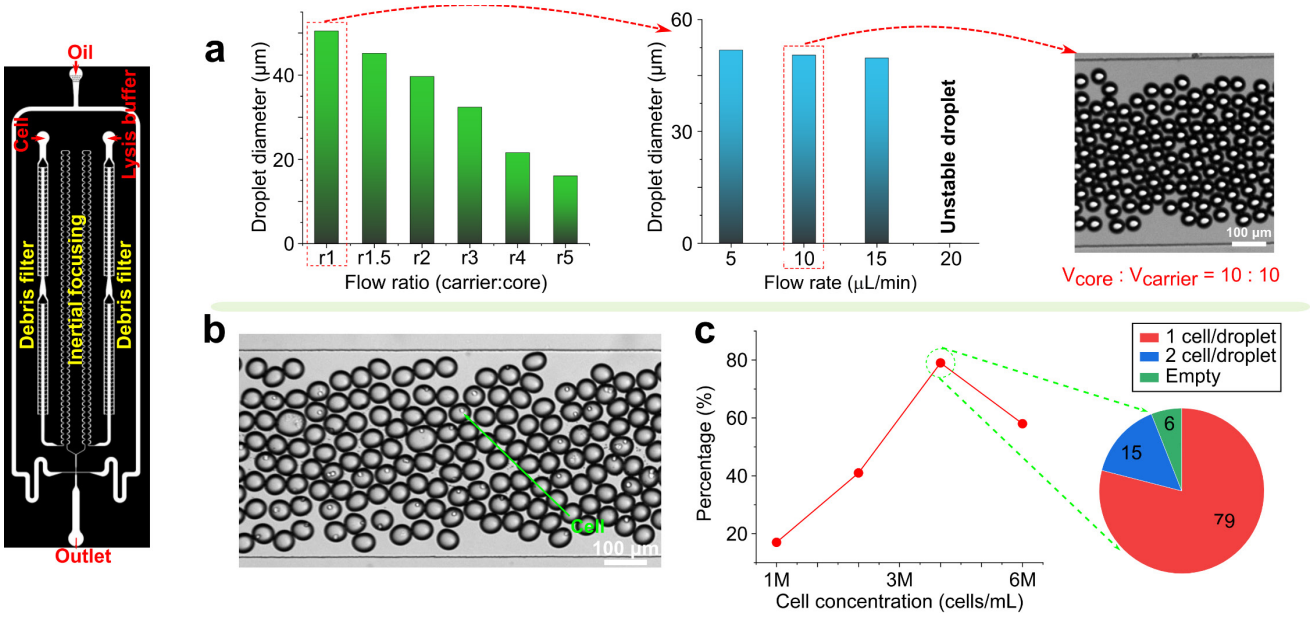

Figure 2: Optimization of droplet generation for cell encapsulation. (a) Study of droplet size with different parameters: flow ratio between carrier and core medium (left); flow rate of core medium when the flow ratio was 1 (middle). Stable droplets of 50 μm in diameter were generated (right). (b) Bright-field images of cell encapsulation when the initial concentration was 3M cells/mL. (c) The percentage of droplets containing one cell with a different initial cell concentration.

applying an electric field to the PA gel and droplet system, causing protein electromigration out of the W/O droplet and into the PA-gel molecular sieving matrix. Once protein electrophoresis initiates, protein targets separate based on differences in electrophoretic mobility (proportional to molecular mass or 'size'). Resolved proteins are covalently bonded to the gel by UV-initiated capture and then labeled with fluorescent antibodies. Using microscopy, we observe that the droplets remain intact after in-gel immunoblotting.

Droplet Generation and Cell Encapsulation

The first requirement for single-cell encapsulation is the sustained creation of homogeneous, high concentration cell suspensions and lysis buffer with or without barcode beads. For this purpose, we designed a droplet-generation device containing 3 major components: (1) filters to remove debris from lysis buffer and cell suspension; (2) sigmoidal microchannels with alternating curvatures to inertially focus particles into a narrow stream. (3) Droplet generation region to produce W/O droplets. The inertial-focusing region was designed based on our previous work[16] and has been reported to efficiently align cells at low flow rates (10 – 100 μL/min).

Using a syringe, we injected mineral oil containing 2% Span 80 surfactant into the OIL inlet, while cell suspension and lysis buffer were separately injected into corresponding inlets. The dependence of droplet size was investigated using flow ratios ($V_{carrier}$: V_{core} = 1-2), producing droplets with diameters ranging from 41 to 51 μm (Figure 2a). To increase the cell capture efficiency, different concentrations of cells were tested with the 5 million per mL cell concentration yielding the highest percentage (79%) of droplets loaded with just one cell (Figure 2 b-c). There were 6% of droplets loaded with zero cell and 15% of droplets loaded with two cells.

Droplet Stability Study and In-Droplet Cell Lysis

Cells were chemically lysed in droplets with RIPA-like buffer containing Sodium Dodecyl Sulfate (SDS), Sodium Deoxycholate, Triton X-100, and Tris-Glycine. This new system is robust to various lysis temperatures (23-100ºC) and durations (1–180 min) and is designed to retrieve antigens from fixed or FFPE samples. To investigate in-droplet cell lysis, we screened cells in a range of SDS lysis buffer concentrations, which have strong hydrophilic properties and the hydrophilic-lipophilic balance (HLB) value of SDS is 40. We observe an emulsion pattern that is dependent on SDS concentration. We further observe stable droplet generation with ≤0.5% SDS in the core medium (Figure 3a). Furthermore, the

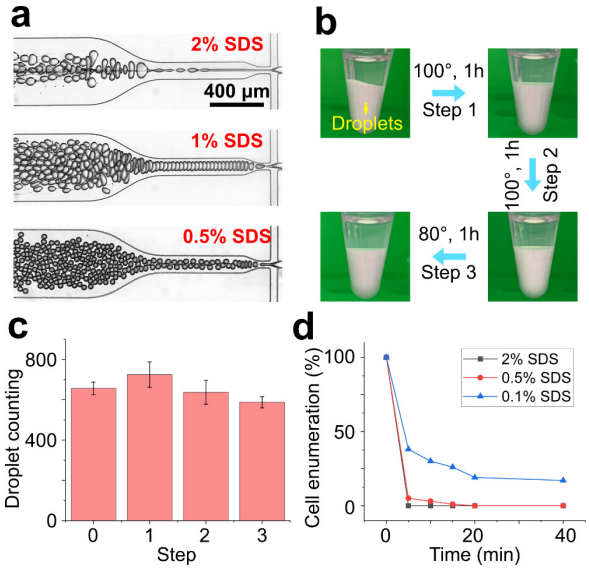

Figure 3: Study of droplet stability with different lysis buffer and incubation conditions. (a) Droplet generations with 0.5 – 2% SDS in the core medium (Vcore : Vcarrier = 10:15). (b) Stability of droplets containing 0.5% SDS under a series of incubations. (c) Droplet enumeration after incubations (step1: 100ºC for 1h; step 2: 100ºC for 1h; step 3: 80ºC for 1h). Droplets were incubated and imaged on a glass slide with a hydrophobic surface. (d) Cell (MCF7) lysis with different concentrations of SDS at 95 ºC.

50 µm W/O droplets loaded with 0.5% SDS maintained stability under harsh conditions: 100ºC for 2 hours and 80ºC for 1 hour, used for the lysis of the FFPE sample (Figure 3b-c). The lysis efficiency of cells was determined by the concentration of SDS presented in the lysis buffer. MCF7 (human breast cancer cell line) cells isolated in droplets were observed completely lysed within 15 min using 0.5% SDS at room temperature (Figure 3d). Lysis buffer with 2% SDS can lyse cells within 5 minutes while the buffer with 0.1% SDS cannot completely lyse cells and about 25% of cells remain intact after 40 minutes of incubation.

Validation of Droplet Sealing with Protein Ladder

The W/O droplets act as a closed reaction chamber in which we perform cell lysis. To measure the protein-permeability of these droplets, we loaded a cocktail of known protein standards mixed with lysis buffer (SDS: 0.5%) into droplets and measured the mean

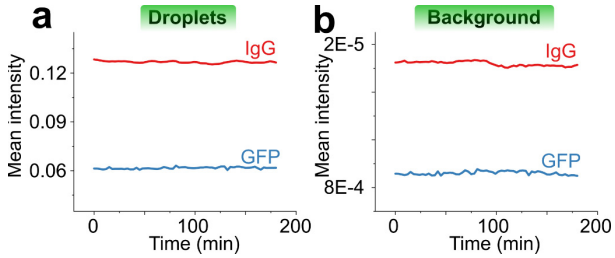

Figure 4: Droplet diffusion assay in W/O droplet. (a) Mean fluorescence intensity of ~300 droplets over time (0–180min). (b) Mean fluorescence intensity of background over time (0-180min).

fluorescence intensities of individual proteins (Immunoglobin (IgG*, 150 kDa) labeled with AF647 and Green Fluorescent Protein (GFP, 26kDa)). As is shown in Figure 4a, there was no obvious fluorescence intensity change during the 180-min assay (room temperature). Meanwhile, the intensity of the background did not increase over time (Figure 4b). We can conclude that W/O droplets with lysis buffer are stable and prevent protein loss from the cell-laden droplet during a 180-min experiment.

Protein Electrophoresis with DropBlot

Using a customized loading chamber, more than 98% of microwells on the gel were occupied with one lysate-laden droplet (Figure 5a), thus providing a convenient, well-controlled approach to sample loading into each microwell for subsequent electrophoretic analysis of each protein lysate. Here, we generated droplets with 50 µm in diameter and loaded the droplets onto the gel platform (with an array of 60-µm diameter microwells in the gel). An applied electric field strength of 40 V/cm was applied to the system for the electrophoresis step. Using fluorescence microscopy, protein (BSA, Bovine Serum Albumin) electromigrated out of the droplet and then out of the microwell and into the molecular sieving gel for electrophoresis (Figure 5b, t = 20s). The droplet remains intact after electrophoresis. The fluorescence intensity of each lane (Figure 5c) was analyzed with MATLAB to calculate the migration distance. While we demonstrate an electric field of 40 V/cm to resolve BSA, future experiments of different strengths would help to balance the electrolysis and Joule heating. We will develop a model to simulate the protein migration in the DropBlot and optimize parameters including droplet position, electric field strength, and electrophoresis time. Furthermore, we will investigate the conditions that are required to achieve maximum separation resolution for proteins isoforms, such as Her2.

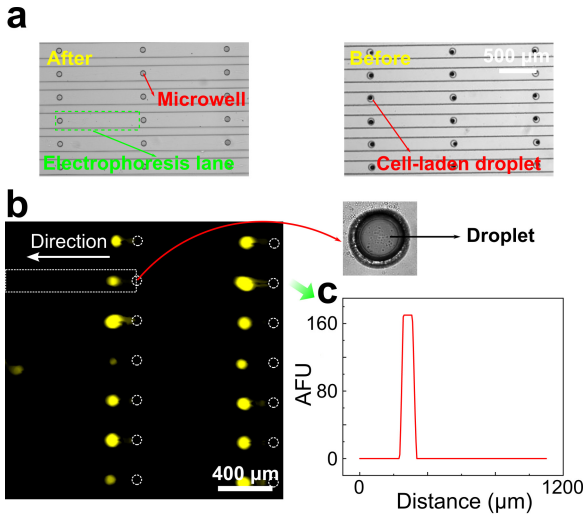

Figure 5: Protein electrophoresis with the DropBlot device. (a) Droplets loading onto polyacrylamide gel with microwells. Top: before loading. Bottom: after loading. (b) Fluorescence imaging of BSA (left) and bright-field image of the droplet at the 20s lapsed separation time. Electric field: 40V/cm. (c) Background subtracted fluorescence intensities (AFU) of one separation lane

CONCLUSION

Here we report a novel hybrid droplet-electrophoresis device (DropBlot) to deconvolve protein isoforms of fixed/FFPE samples at a single-cell level. The preliminary data confirmed the feasibility of this setup, wherein cells loaded in the droplet can be completely lysed under harsh conditions and extracted proteins can migrate out of the droplet and be resolved on the PA gel. Nucleic acids will be extracted from droplets after electrophoresis and are then processed to analyze DNA or mRNA. DropBlot will be tested with various fresh cancer cell lines and cells dissected from FFPE tissue. We anticipate that DropBlot will broaden the applications of single-cell immunoblotting in pathological diagnosis using FFPE cancer specimens.

METHODS

Fabrication of Droplet Generation Chips. Single emulsion generation chips were fabricated using standard soft lithographic techniques. SU-8 3050 (Kayaku Advanced Materials) was used to fabricate masters with a height of 60µm. PDMS was prepared with Sylgard 184 Silicone Elastomer Kit (Ellsworth Adhesives) and mixed with a ratio of 10:1. After curing (70ºC, 3 hours), the PDMS device was further baked for 48 hours at 80ºC to recover the hydrophobicity.

Polyacrylamide Gel fabrication. Wafer microfabrication and silanization are described in our previous work.[12] To prepare an 8%T polyacrylamide gel, the gel precursor solution was mixed with 30% (wt/wt) Acrylamide/bis-acrylamide (Sigma-Aldrich), N-(3-((3-benzoylphenyl) formamido)propyl) methacrylamide (BPMA, Pharm Agra Labs), 10X tris-glycine buffer (Sigma-Aldrich), and ddH_2O. Gels were chemically polymerized for 20 min with 0.08% (w/v) ammonium persulfate (APS, Sigma-Aldrich) and 0.08% (v/v) TEMED (Sigma-Aldrich). After polymerization, gels were collected with a razor blade and released from the wafer and stored in the RIPA-like buffer.

Cell Culture. Human breast cancer cell line (MCF7-GFP, ATCC) was used in this study. Cells were cultured in DMEM

medium (Thermofisher) supplemented with 10% (v/v) fetal bovine serum (Benchmark), 1% (v/v) penicillin/streptomycin solution (Thermofisher), and 0.1 mM non-essential amino acid solution (Thermofisher). The cells were cultured in the incubator (37ºC, 5% CO_2) and were released through incubation with 0.05% trypsin-EDTA solution (Thermofisher). The concentration of harvested cells was measured with a hemocytometer (Hausser Scientific) and resuspended with PBS to a specific concentration.

Fluidics Assembly and Generation of W/O droplet. Harvested cells or purified proteins were resuspended in PBS and injected into the cell inlet. Cell suspension and lysis buffer were mixed prior to the emulsion region. 2% (v/v) Span 80 surfactant (Sigma Aldrich) was spiked into mineral oil (Sigma Aldrich) and used as the carrier solution. Flow rates of the substrate and carrier solution were actively controlled by a syringe pump (Chemyx). The flow rates of each solution were adjusted to generate droplets of different sizes. Droplets could be collected in a 1.5mL Eppendorf tube or be directly loaded onto PA-gel with customized PDMS channels.

Protein Diffusion Assay. Proteins of different molecular weights were diluted to 5 μM with PBS. In this assay, we used Alexa-Fluor 647 labeled donkey anti-rabbit secondary antibody (IgG, Thermofisher) and rTurboGFP (Evogen). Proteins were encapsulated into 50 μm droplets and observed under an inverted microscope (Olympus) for 180 min.

Protein Electrophoresis using DropBlot. BSA(Bovine Serum Albumin)-loaded droplets were settled down on the PA-gel, which was placed in a customized electrophoresis chamber. 7.5 mL running buffer, containing 1X Tris-Glycine and 1% (v/v) SDS, was poured onto the chamber. We supplied a constant voltage of 240 V (the target voltage for an electric field of 40V/cm). Immediately After electrophoresis, the power was shut off and migrated proteins were photocaptured by 45 s UV exposure. The slides were then rinsed with deionized water and imaged with a microscope.

ACKNOWLEDGEMENTS

This work was funded by the National Institutes of Health (NIH) R01CA20301. We sincerely thank Herr Lab members Gabriela Lomeli and Ana Martinez for initial training on the operation of the single-cell western blot. We acknowledge all members of the Herr Lab at UC Berkeley. We are also grateful to R&D Machine Shop at UC Berkeley for the fabrication of the chamber.

CONTACT

*****Yang Liu, tel: + 1-706-254-6443; yl2021@berkeley.edu

REFERENCES

[1] E. Papalexi and R. Satija, *Nat Rev Immunol*, 2018, **18**, 35-45.
[2] A. J. Dickinson, P. M. Armistead and N. L. Allbritton, *Anal Chem*, 2013, **85**, 4797-4804.
[3] A. D. Hargis, J. P. Alarie and J. M. Ramsey, *Electrophoresis*, 2011, **32**, 3172-3179.
[4] S. Doll, F. Gnad and M. Mann, *PROTEOMICS–Clinical Applications*, 2019, **13**, 1800113.
[5] L. M. Smith and N. L. Kelleher, *Nature methods*, 2013, **10**, 186-187.
[6] Y. Liu, X. Chen, Y. Zhang and J. Liu, *Analyst*, 2019, **144**, 846-858.
[7] R. T. Kennedy, M. D. Oates, B. R. Cooper, B. Nickerson and J. W. Jorgenson, *Science*, 1989, **246**, 57-63.
[8] T. M. Olefirowicz and A. G. Ewing, *J Neurosci Methods*, 1990, **34**, 11-15.
[9] B. Budnik, E. Levy, G. Harmange and N. Slavov, *Genome Biol*, 2018, **19**, 161.
[10] Y. Zhu, G. Clair, W. B. Chrisler, Y. Shen, R. Zhao, A. K. Shukla, R. J. Moore, R. S. Misra, G. S. Pryhuber, R. D. Smith, C. Ansong and R. T. Kelly, *Angew Chem Int Ed Engl*, 2018, **57**, 12370-12374.
[11] S. M. Grist, A. P. Mourdoukoutas and A. E. Herr, *Nat Commun*, 2020, **11**, 6237.
[12] E. Rosas-Canyelles, A. J. Modzelewski, A. Geldert, L. He and A. E. Herr, *Nat Protoc*, 2021, **16**, 1062-1088.
[13] A. Smith, M. Galli, I. Piga, V. Denti, M. Stella, C. Chinello, N. Fusco, D. Leni, M. Manzoni, G. Roversi, M. Garancini, A. I. Pincelli, V. Cimino, G. Capitoli, F. Magni and F. Pagni, *J Proteomics*, 2019, **191**, 114-123.
[14] B. Heijs, S. Holst, I. H. Briaire-de Bruijn, G. W. van Pelt, A. H. de Ru, P. A. van Veelen, R. R. Drake, A. S. Mehta, W. E. Mesker, R. A. Tollenaar, J. V. Bovee, M. Wuhrer and L. A. McDonnell, *Anal Chem*, 2016, **88**, 7745-7753.
[15] A. Ly, A. Buck, B. Balluff, N. Sun, K. Gorzolka, A. Feuchtinger, K. P. Janssen, P. J. Kuppen, C. J. van de Velde, G. Weirich, F. Erlmeier, R. Langer, M. Aubele, H. Zitzelsberger, L. McDonnell, M. Aichler and A. Walch, *Nat Protoc*, 2016, **11**, 1428-1443.
[16] Y. Liu, W. Zhao, R. Cheng, A. Puig, J. Hodgson, M. Egan, C. N. Cooper Pope, P. G. Nikolinakos and L. Mao, *Lab Chip*, 2021, **21**, 2738-2750.

FIELD-DEPLOYABLE MICROFLUIDIC IMMUNOASSAY DEVICE FOR PROTEIN DETECTION

Gihoon Choi[1], Betty Mangadu[1], Yooli K. Light[1], and Robert J. Meagher[1]*
[1]Biotechnology and Bioengineering Department, Sandia National Laboratories, Livermore, California, USA

ABSTRACT

We present a field-deployable microfluidic immunoassay device in response to the need for sensitive, quantitative, and high-throughput protein detection at point-of-need. The portable microfluidic system facilitates eight magnetic bead-based sandwich immunoassays from raw samples in 45 minutes. An innovative bead actuation strategy was incorporated into the system to automate multiple sample process steps with minimal user intervention. The device is capable of quantitative and sensitive protein analysis with a 10 pg/ml detection limit from interleukin 6-spiked human serum samples. We envision the reported device offering ultrasensitive point-of-care immunoassay tests for timely and accurate clinical diagnosis.

KEYWORDS

Microfluidics, field-deployable, immunoassay, protein detection, automated sample preparation

INTRODUCTION

Identifying specific protein biomarkers is a critical clinical procedure for timely and cost-effective diagnosis. Therefore, the development of mobile and low-cost technology for sensitive protein detection is of interest in the clinical setting [1]. Qualitative lateral flow strips are commonly used for rapid, portable immunoassay tests. However, their sensitivity highly depends on the types of the sample matrix. The qualitative readout of lateral flow strips is inadequate for some conditions that require quantitative analysis for a correct decision. On the contrary, the enzyme-linked immunosorbent assay (ELISA) is a gold standard technique for sensitive and quantitative detection of proteins, allowing detection limit in some cases down to femtomolar concentration [2]. However, complicated sample handling steps, long turnaround time, and bulky benchtop scanners limit its use at the point-of-need [3]. Alternatively, the microfluidic approach is well suited for on-site clinical diagnosis because of its inherent attributes of portability, low sample/reagent volumes, and automated processing [4]. To this end, extensive research efforts have been made to translate laboratory-quality immunoassays into a microfluidic format over the past decade [5-7].

Microfluidic immunoassays frequently involve using solid-phase particles, so-called bead-based ELISA, because a high surface-to-volume ratio promotes antigen-antibody binding. Use of beads significantly reduces the assay time while improving the sensitivity, making bead-based assays ideal for sequential immunoassay procedures (i.e., streamlined incubation, purification, and reaction). However, the primary consideration to implementing bead-based immunoassays in microfluidics relies on the strategic actuation of beads and liquid droplets in a controllable manner.

The most intuitive approach is a flow-based microfluidic immunoassay platform [5]. The sequence was performed by sequentially merging reagent inflows to bead-containing droplets via T-junction, then extracting beads using a magnet. Despite its automated capability, tubing and infusion pumps are not preferred for portability. As an alternative, a centrifugal microfluidic platform can drive the beads for the streamlined immunoassay process without peripheral devices [6]. However, centrifugal force can only direct the beads in one direction. Therefore, a complicated sample sequence that requires multi-directional bead operation (e.g., agitation) is limited. Electrowetting-based digital microfluidics (DMF) enables flexible discrete droplet actuation (move, split, and merge) on the hydrophobic surface [7], this method holds great promise for adapting magnetic bead-based immunoassay. However, active magnetic bead actuation for resuspension and agitation is challenging to implement in a droplet, especially with a stationary magnetic trap. In addition, the adsorption of proteins and detergents causes biofouling or cross-contamination, affecting surface wettability and creating challenges for reproducibility with complex sample matrices. As opposed to controlling droplets against stationary beads, active magnetic actuation on beads can alleviate such problems. For example, Chiou et al. developed a system that electromagnetically actuates magnetic beads in stationary droplets [8]. However, the system is only compatible with certain types of beads (e.g., large size, high susceptibility) because small electromagnets cannot provide sufficient magnetic fields to induce strong magnetic forces on small beads. The necessity to use large beads is at odds with benefit of high surface-to-volume ratio to maximize sensitivity. Although numerous works have been reported, integrating reliable, robust, and automated front-end immunoassay is still a common hurdle for most existing point-of-care microfluidic devices.

Herein, we present a field-deployable microfluidic immunoassay device for sensitive protein detection with autonomous sample preparation capability. The system consists of a mobile analyzer and a compact microfluidic chip. The platform integrates electromechanical and optical subsystems, and the microfluidic chip contains eight spatially isolated testing units spaced for 8-channel pipette compatibility. An embedded programmable planar electromagnetic microactuator array actuates the permanent magnet. Thus, magnetic beads can be reliably manipulated against the stationary droplets by strong magnetic interaction, enabling an autonomous sample process. The system facilitates the whole immunoassay process (i.e., incubation, purification, and chemiluminescent reaction) from raw samples in 45 minutes total processing time for 8 samples. The device achieved a detection limit of 10 pg/ml with Interleukin-6 (IL-6) in human serum. The sensitive, quantitative, and high-throughput immunoassay device will enable timely and accurate diagnosis at the clinical site.

MATERIALS AND METHODS

Instrumentation

Fig. 1A shows a system overview of the microfluidic immunoassay system. The platform was designed in SolidWorks, 3D printed and assembled in the lab. The fully integrated system has a footprint of 11×12×8 cm and contains optical and electromechanical subsystems. ***Optical subsystem:*** A low-noise CMOS imager (ULS24, Anitoa Systems) was integrated into the system to measure the chemiluminescent signal. The image sensor surface is directly in contact with the microfluidic channel to maximize the collection of blue emission light (peak wavelength: 425 nm). In this optical configuration, the sensing area (3.6×3.6 mm) sufficiently covers the detection zone of the individual testing unit without an optical lens or filter. We attached mylar reflective

978-1-940470-04-7/HH2022/$25©2022TRF
DOI 10.31438/trf.hh2022.30

film on top of the permanent magnet located at the bottom of the detection zone during the chemiluminescent measurement to further increase the light collection. ***Electromechanical subsystems:*** Integrated electromechanical subsystems include linear, rotary, and electromagnetic actuators. For a linear actuator, a rack-and-pinion mechanism converts the rotary motion of the stepper motor into a linear motion using in-house fabricated rack/pinion gears. A unipolar stepper motor enables the precision positioning of the microfluidic chip. On the right edge of the rack, a high-torque servomotor was installed as a rotary joint to rotate the microfluidic chip (Fig. 2 - step 2). A custom-printed planar electromagnetic microactuator array is used to actuate a neodymium magnet (grade: N52) that further manipulates the magnetic beads in a microfluidic channel in a programmed manner. Each rectangular-shaped planar coil has a copper trace with a width of 170 µm, a thickness of 36 µm, and a pitch of 170 µm. Adjacent planar coils are partially overlapped in different printed circuit board (PCB) layers with a 4.5 mm gap. It is noteworthy that magnetic force follows an inverse square relationship with distance [9]. Therefore, a neodymium magnet close to the coil center can be actuated by a small electromagnetic field with low power consumption (<2.5W). To transport a neodymium magnet from one location to another, the localized electromagnetic field is generated from the coil one at a time by sequentially switching the transistor. A customized PCB with an embedded microcontroller unit (MCU) operates all integrated electronic components. The entire system is powered by either a USB connection or a DC power adapter (5V, 500 mA)

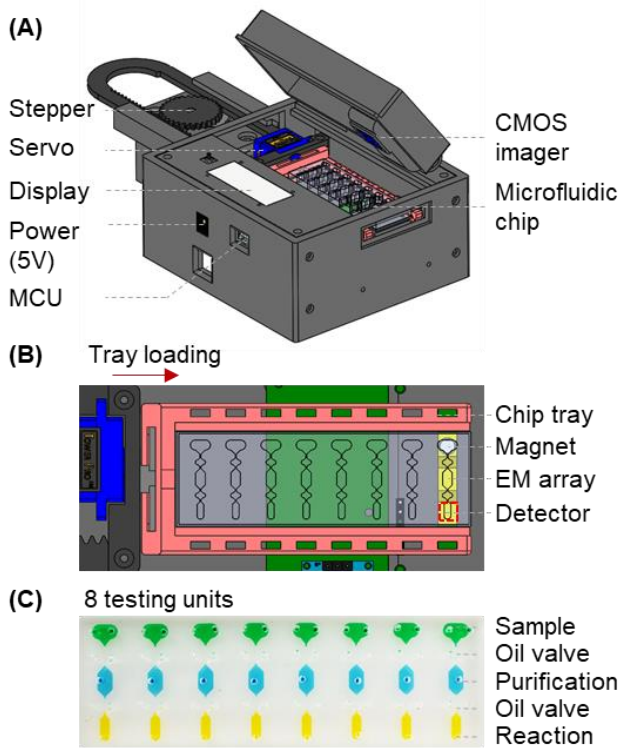

Figure 1: System overview. (A) Platform design. (B) Top-down view. Rack/pinion linear actuator moves microfluidic chip in the x-direction to align with planar electromagnetic microactuator array. The detector vertically aligns with the reaction chamber (red square) (C) Photo of a microfluidic chip showing eight independent testing units. Before the test, all reagents were preloaded in a ready-to-use fashion (food dyes were loaded for illustration purposes).

Microfluidic chip

A microfluidic chip was constructed by casting polydimethylsiloxane (PDMS) into a 3D-printed reusable master mold. A negative mold was printed with a commercial resin-based stereolithography 3D printer (Form 3, Formlabs). After printing, the mold was sonicated with isopropyl alcohol, then post-cured in a UV box at 60 °C for 30 minutes. The mold surface was silane-modified following oxygen plasma treatment to avoid PDMS sticking to the mold surface and prevent uncured resin residues from interfering with PDMS curing. To fabricate the PDMS device, curing and elastomer agents were thoroughly mixed in 1:10 (m/m), degassed in a vacuum desiccator, then cured at 65 °C for 2 hours. Reagent-loading holes were punched on a PDMS stamp and irreversibly bonded to a glass slide following oxygen plasma treatment.

The compact reagent microfluidic chip (25×70 mm) has eight spatially isolated testing units spaced for standard 8-channel pipette compatibility (Fig. 1C). Each testing unit has a sample, purification, and reaction chambers. These three chambers contain 15 µl of sample diluent with 25 µg of functionalized magnetic beads, 15 µl of washing buffer (PBS with 0.5% TWEEN-20), and 8 µl of chemiluminescent substrate, respectively. In addition, two oil valves hold 10 µl of mineral oil with 1% ABIL to separate the chambers. All reagents required for magnetic bead-based sandwich immunoassay were pre-loaded into the chip before the test.

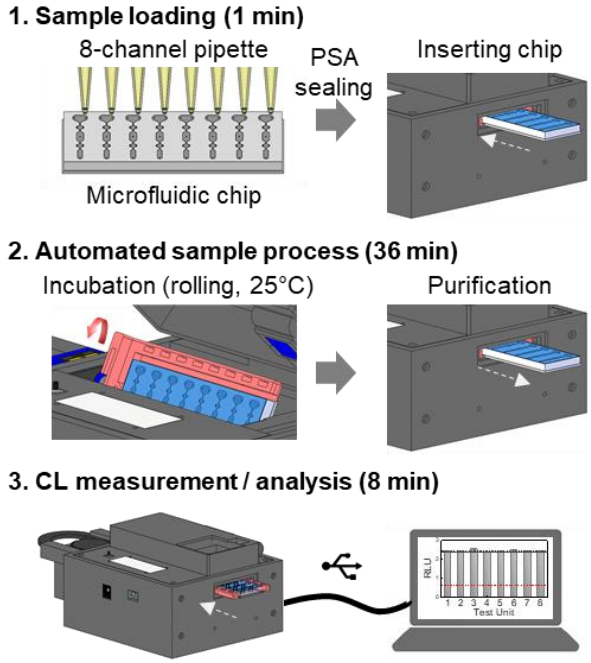

Figure 2. Overall operation workflow. Within 45 minutes, the automated immunoassay platform can process eight tests from a sample matrix (e.g., human serum) with minimal user intervention.

Workflow

The workflow of the device comprises sample loading, automated sample process, and chemiluminescent (CL) measurement/analysis (Fig. 2). Briefly, 15 µl of human serum is loaded into each sample chamber using an 8-channel pipette, then sealed with clear pressure-sensitive adhesive (PSA). Once a prepared microfluidic chip is inserted, the platform facilitates the automated sample process (i.e., incubation and purification). During the incubation, the microfluidic chip tumbles to prevent the

bead settlement and promote the formation of capture antibody-coupled magnetic beads, antigen, and HRP-linked antibody complex for CL detection. After the sample preparation, the CL signal from each testing unit is measured one at a time; then analyzed using a custom-developed program.

Bead-based immunoassay for protein detection

The integrated magnetic bead-based sandwich immunoassay has three components: capture bead, detector antibody, and target protein samples. ***Capture bead preparation:*** 30 µg of target-specific polyclonal antibody was covalently coupled to 1 mg of epoxy-activated superparamagnetic bead surface using a commercially available antibody-coupling kit (14311D, Invitrogen). After overnight incubation at room temperature, antibody-coupled beads were thoroughly washed three times with purification buffer to remove the unbound antibody excess and then blocked with SuperBlock agent (37518, Thermo Scientific) to prevent non-specific binding. The final stock concentration of the capture bead was set to 10 mg/ml. ***HRP-labeled detector preparation:*** monoclonal antibody was labeled with HRP conjugation kit (ab102890, Abcam). The final concentration of the HRP-labeled detector was adjusted to 1 µg/ml with phosphate buffer saline (PBS) with 0.05% tween-20. ***Target protein sample preparation:*** protein was spiked into PBS and human serum to validate the assay and sample matrix effect.

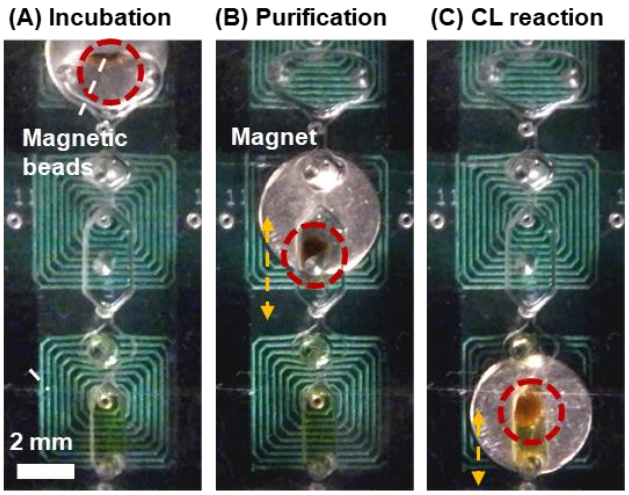

Figure 3. Automated sample preparation. The planar electromagnetic array actuates the permanent magnet to drag magnetic bead into desired working chamber through channel.

Automated sample preparation

For automated microfluidic sample preparation, magnetic beads were actuated against the stationary reagent droplets in the fluidic channel/chamber by controlled neodymium magnet motion on electromagnet micro-actuators. The integrated sample preparation consists of incubation, purification, and CL reaction steps (Fig. 3). During the incubation step, functionalized bead specifically captures the complex of the target protein and HRP-conjugated detection antibody into the sample chamber (Fig. 3A). After the incubation, the neodymium magnet drags the target-captured magnetic beads to the purification chamber. For purification (Fig. 3B), magnetic beads were agitated back and forth to remove the reagent carryovers (i.e., unbound analyte and detector antibodies) from the sample chambers. Thoroughly washed beads were then transferred to the reaction chamber for CL measurement (Fig. 3C).

A funnel-shaped microfluidic channel between chambers and valve assists in forming the magnetic bead cluster and maximizes the magnetic force acting on the beads for efficient bead capture. Note that the mass of the magnetic bead cluster is proportional to the magnetic force [10]. The addition of 1% ABIL EM-90 surfactant in mineral oil lowers the interfacial tension at the aqueous-to-oil interface; thus, magnetic beads can easily transport from chamber to chamber without significant loss.

RESULTS AND DISCUSSION

Uniformity of eight testing units

Since the microfluidic immunoassay device facilitates eight tests, unit-to-unit consistency is a prerequisite for quantitative comparison. We used an IL-6 detection assay as a model to assess uniformity between channels. An identical concentration of purified IL-6 aliquot was loaded into each testing unit, and then processed using the automated protocol. The quantitative results among eight testing units showed excellent uniformity with slight variation (Fig. 4, black-dotted lines), implying good optical alignment (i.e., CMOS sensor, final position of beads in reaction chamber). The unit-to-unit consistency indicates robust reagent mixing and washing during the sample preparation, and consistent transfer of magnetic beads throughout the process. While manual sandwich immunoassays on microplates (e.g., ELISA) is prone to human errors due to iterative liquid exchanging steps, the integrated autonomous sample process mitigates such errors and allows eight tests on the mobile immunoassay platform.

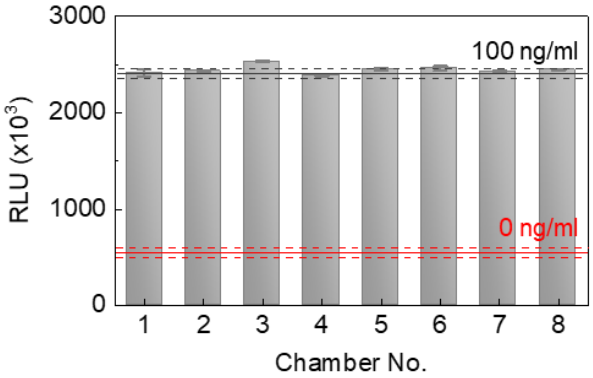

Figure 4. Chamber-to-chamber consistency among eight testing units (100 ng/ml: 2410 ± 50, 0 ng/ml: 548 ± 20. Clear CL signal differences were observed between 0 and 100 ng/ml IL-6 samples.

Sensitivity test

We next validated and optimized the analytical sensitivity of the device using an IL-6 detection assay. 10-fold serial dilution of IL-6 (10^{-3} – 10^{3} ng/ml) was spiked in human serum to mimic complex protein samples. The device automatically carried out the sandwich immunoassay on the microfluidic chip. The detection limit was determined as the lowest analyte concentration with a 3×standard deviation higher than the signal background. As shown in Fig 5, the linear standard curve showed the device's quantitative ability. The detection limit of 10 pg/ml was achieved with the presence of sample matrix. This level of sensitivity is comparable to a benchtop plate reader [2].

We further investigated how the integrated sample purification process enhances the device performance against the sample matrix effect. Without the on-chip sample purification, an order of magnitude higher detection limit (i.e., ~480 pg/ml) and decreased signal-to-background ratios were observed for pure PBS and complex serum spiked samples, indicating the clear presence

of the sample matrix effect. More specifically, the small amount of unbound HRP-labeled antibodies was carried over to the reaction chamber with beads due to viscous human serum. The incorporated washing step mitigates such sample matrix hindrance and enables sensitive protein detection.

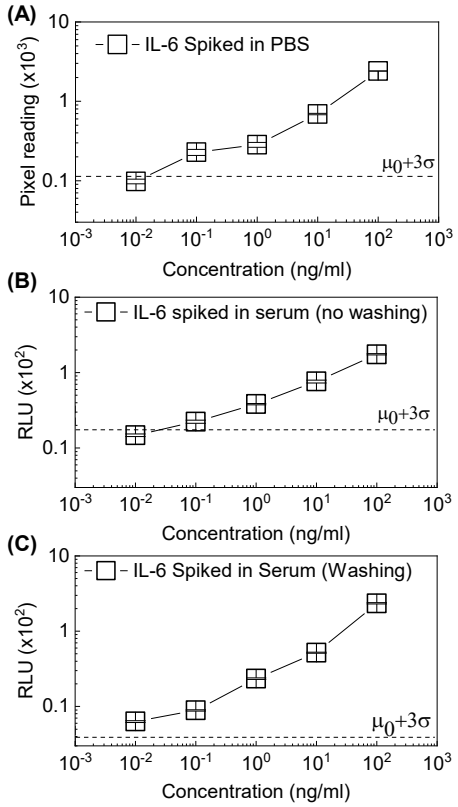

	in PBS (no wash)	in serum (no wash)	in serum (wash)
S:B	4.2	2.8	5.2
LOD (pg/ml)	480	480	10

Figure 5. Sensitivity test results with/without built-in washing process. Signal-to-background (S:B). Error bars were obtained from triplicates.

CONCLUSION

In summary, we developed a microfluidic immunoassay device for sensitive and high-throughput detection of proteins in the field. The system consists of a mobile analyzer and a reagent-compact microfluidic chip. The embedded electromagnetic microactuator actuates the permanent magnet in a programmed manner to facilitate the sequential incubation and purification during the immunoassay process. Within 45 minutes, the system automatically prepares eight samples for CL measurement from human serum. The excellent unit-to-unit consistency indicated eight testing units' robust sample process with minimal bead loss and optical uniformity. Besides, the linear standard curve showed the quantitative ability of the platform. The device achieved a detection limit of 10 pg/ml with IL-6 spiked in human serum. Finally, we confirmed that integrated sample purification reduced the non-specific signal originating from the sample matrix effect, thus, improving the detection sensitivity. Although we only tested the IL-6 detection assay for device validation, it can be adaptable to identify various proteins by conjugating capture antibodies specific for the target of interest on magnetic beads. The reported device will enable highly sensitive immunoassays for accurate and timely diagnosis at point-of-need.

ACKNOWLEDGEMENTS

The reported work is funded by Sandia National Laboratories Laboratory Directed Research and Development (LDRD) Program project 218341. This paper describes objective technical results and analysis. Any subjective views or opinions that might be expressed in the paper do not necessarily represent the views of the U.S. Department of Energy or the United States Government. Sandia National Laboratories is a multimission laboratory managed and operated by National Technology & Engineering Solutions of Sandia, LLC, a wholly owned subsidiary of Honeywell International Inc., for the U.S. Department of Energy's National Nuclear Security Administration under contract DE-NA0003525.

REFERENCES

[1] J.F. Rusling, C.V. Kumar, J.S. Gutkind, V. Patele, "Measurement of biomarker proteins for point-of-care early detection and monitoring of cancer," Analyst 135, 2496–2511 (2010).

[2] S. Zhang, A. Garcia-D'Angeli, J.P. Brennan, and Q. Huo, "Predicting detection limits of enzyme-linked immunosorbent assay (ELISA) and bioanalytical techniques in general," Analyst 139, 439–445 (2014).

[3] A.I. Barbosa and N.M. Reis, "A critical insight into the development pipeline of microfluidic immunoassay devices for the sensitive quantitation of protein biomarkers at the point of care,"Analyst 142(6), 858-882 (2017).

[4] Y. Shi, P. Ye, K. Yang, J. Meng, K. Guo, z. Pan, Q. Bayin, and W. Zhao, "Application of Microfluidics in Immunoassay: Recent Advancements," Journal of Healthcare Engineering 2021, Article ID 2959843, 1-24 (2021).

[5] L. Metzler, U. Rehbein, J. Schönberg, T. Brandstetter, K. Thedieck, and J. Rühe, "Breaking the Interface: Efficient Extraction of Magnetic Beads from Nanoliter Droplets for Automated Sequential Immunoassays," Analytical Chemistry 92, 10283-10290 (2020).

[6] C. Koh, U.Y. Schaff, M.E. Piccini, L.H. Stanker, L.W. Cheng, E. Ravichandran, B. Singh, G.J. Sommer, and A.K. Singh, "Centrifugal Microfluidic Platform for Ultrasensitive Detection of Botulinum Toxin," Analytical Chemistry 87, 922-928 (2015).

[7] L. Coudron, M.B. McConnell, I. Munro, D.K. McCluskey, I.D. Johnston, C.K.L. Tan, M.C. Tracey, "Fully integrated digital microfluidics platform for automated immunoassay; A versatile tool for rapid, specific detection of a wide range of pathogens," Biosensor and Bioelectronics 128, 52-60 (2019).

[8] C. Chiou, D.J. Chin, Y. Zhang, and T. Wang, "Topography-assisted electromagnetic platform for blood-to-PCR in a droplet," Biosensors and Bioelectronics 50, 91-99 (2013).

[9] A. Beyzavi and N. Nguyen, "Modeling and optimization of planar microcoils," Journal of Micromechanics and Microengineering 18, 095018 (2008).

[10] Z. Long, A.M. Shetty, M.J. Solomon, and R.G. Larson, "Fundamentals of magnet-actuated droplet manipulation on an open hydrophobic surface," Lab on a Chip 9, 1567-1575 (2009).

CONTACT

*R.J. Meagher, tel: +1-925-294-6847; rmeaghe@sandia.gov

HYDROGEL ACTUATED MICRONEEDLE (HAM) WOUND PATCH

Rebecca Campbell [1], Jun Ying Tan [2], Alanis Santiago[1], Jungkwun Kim[2], and Albert Kim[1]*

[1] Department of Electrical and Computer Engineering, Temple University, Philadelphia PA 19122 USA

[2] Department of Electrical and Computer Engineering, Kansas State University, Manhattan KS 66506 USA

ABSTRACT

Chronic wounds present an expensive and time-consuming issue that affects patients each year. The challenges presented by chronic wounds stem from the drastic variations between cases, resulting in unsolvable for the long term. To address the chronic wounds and their variations, we present a Hydrogel Actuated Microneedle (HAM) wound patch. The HAM patch creates a feedback system based on the pH level of the wound state. The wound exhibits various pH levels depending on the state. It is much more effective if therapeutic agents (e.g., antimicrobial ointment, cellular growth factors) can be deployed at the most relevant dermis layer. To this end, a pH-sensitive hydrogel that responds to the present conditions of the wound can be used to pose a microneedle in a deeper or shallow region of the wound and delivers therapeutic agents. Such an approach can overcome variations from wound to wound. By having this self-positioning device with a 2.1 mm actuation range, we reduce the amount of clinical intervention within the treatment process and improve device versatility. Force and expansion studies confirm the capability of the HAM patch to push through tissue and descend into the wound. The HAM patch exceeds the average treatment depth and force of needle-based treatments.

KEYWORDS

Hydrogel, Actuator, Wound healing, Chronic wounds, Microneedle.

INTRODUCTION

Chronic wounds impact over 6.5 million individuals in the United States annually, with treatment expenditures exceeding $25 million [1], [2]. A highly efficient intrinsic host defense mechanism monitors and repairs wounds in a timely and organized manner. However, certain conditions, such as poor circulation, neuropathy, diabetes, difficulty in moving, and repeated mechanical force/stress, might interrupt the wound healing phase leaving it unresolvable for several months [2], [3]. For example, diabetic patients are more vulnerable to chronic wounds in the form of foot ulcers, leading to 75-85% of amputations [4]. As such, innovation is needed to accelerate the healing of chronic wounds stemming from an in-depth analysis of the added complexities in the healing process.

Current methods of treatment for chronic wounds follow four steps. Initially, the wound is assumed to be in the least severe state, and strategies for infection reduction and pressure alleviation, such as antibiotics and offloading, are utilized [5]. Offloading a chronic wound consists of removing mechanical stress/strain from the injured area via the application of bandages and braces. If this is unsuccessful, the wound is considered more severe and challenging to heal, and treatment advances to the next level. In this stage, medicine targets matrix metalloproteinases (MMPs) that degrade healthy tissues and physical debridement to remove unhealthy tissue [5]. Debridement is a surgical technique where the necrotic tissue is removed manually by a physician. If these techniques fail, biological methods are utilized, such as introducing collagen into the wound [6]. Finally, amputation is required if none of these methods are successful [5].

To avoid amputation, many innovations have been made to several of these techniques [7]. Qiao et al., for example, used copper-sulfide nanodots to kill drug-resistant bacteria and accelerate wound healing [8]. This process uses a bio-safe medium in order to suspend CuS nanoparticles within the wound; when activated with a laser, the nanodots will release copper ions [8]. However, like most innovative methods for chronic wound treatment, this requires an external stimulant, laser-activation, to be repeatably applied in a clinical setting. Regrettably, these present wound healing treatments frequently overlook the state of the wound.

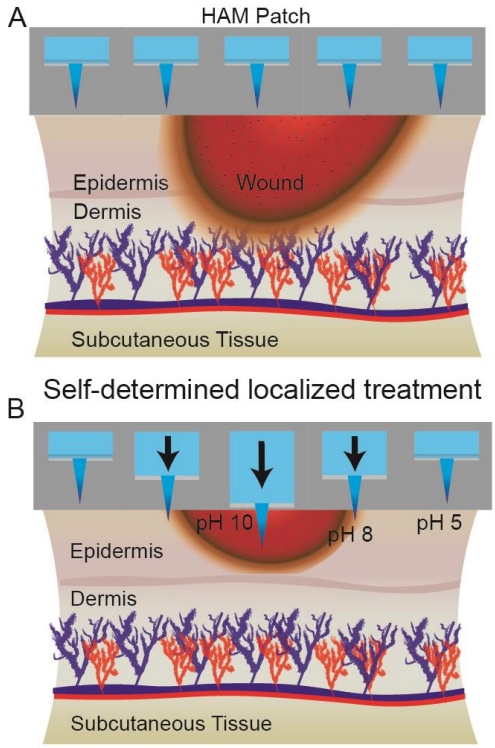

Figure 1: HAM device self-adjusting within the tissue (A) Initial application to wound (B) Microneedles responding to higher and lower pH values

To enable appropriate adjustments to the wound, we present a novel wound state-responsible patch using pH-sensitive hydrogel as a base actuator that lifts a microneedle array for a self-adjusted wound stimulator called Hydrogel Actuated Microneedle (HAM) wound patch. The HAM patch seeks to resolve the need for external clinical stimulation but utilizes the information, i.e., pH level, inside the wound. The pH of the skin is generally between 4 and 6, which is slightly acidic, providing better resistance against pathogenic bacteria. In contrast, chronic wounds raise pH up to 10 (basic), promoting bacteria growth more efficiently. The healing process moves this back to a slightly acid state, pH 5, where the wound is healed [9], [10]. As illustrated in Figure 1, the proposed HAM patch consists of a hydrogel as a base block and a microneedle array as a movable plate, constrained

978-1-940470-04-7/HH2022/$25©2022TRF
DOI 10.31438/trf.hh2022.31

in a 3D printed flexible patch. The pH changes due to the wound state activate the hydrogel layer and swell in acidic pH or shrink in basic pH. Since the hydrogel is constrained, such chemo-mechanical actuation exerts to the opening side where the microneedle array plate is placed. This actuation poses the microneedle deeper into the chronic wound (higher pH), inhibiting bacterial activity and stimulating epithelial cells. Upon the wound recovering from the chronic condition, microneedles are retracted as is dictated by the pH level.

WORKING MECHANISMS

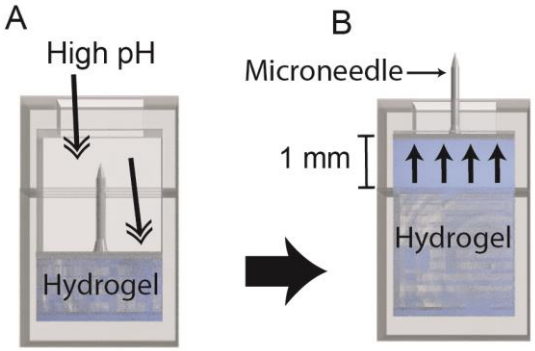

Figure 2: (A) Single cell of the HAM patch introduced to pH 10 solution, (B) resulting swelling of the hydrgoel

Figure 2 illustrates the working mechanism. The HAM patch uses two main mechanisms for operation. The first is the chemo-mechanical properties of the pH-sensitive hydrogel, and the second is the properties of constrained swelling of hydrogel. Chemically, this physical change is due to the ionic nature of the hydrogel. The hydrogel contains acidic ionic chains, which build up a charge when the external conditions contain a higher ionization [11]. This results in the lower pH values causing the increase in charge and pushing the acidic chains away from one another, hence swelling.

Once the dyed gel is formed, it becomes sensitive to environmental pH changes. In a free condition, hydrogel isosmotically swells in a basic environment or shrinks in an acidic environment. Since the swelling/shrinking is directed isotopically, all forces from this actuation are directed radially outward. To maximize the chemo-mechanical actuation and to achieve a single direction force, the hydrogel is constrained. In an ideal non-constrained isotopically swelling hydrogel, no additional stress or strain forces need to be considered. However, once an immovable blocking force is presented to one side, the stress and strain forces between the surfaces need to be considered.

Marcombe et al. reported such constrained hydrogel can be modeled as a hyper-elastic solid [12]. Several key assumptions and simplifications are made in this theory. Firstly, a hydrogel is ideal and takes the free energy to be a summation of the polymers, ionic effects, acidic groups, and entropy added in its formation [12]. In addition, the model is assumed to be electroneutral, which neglects charge interactions between the hydrogel surface and the external solution. This can be done since most hydrogel applications are on a scale larger than Debye length, which is the measure of electrostatic effects in relation to an electrolyte [12]. The concertation of the ionic species within the hydrogel, $C_{\alpha,gel}$, is the product of the ionic species in the solution, $c_{\alpha,sol,}$ and the determinate of the swelling volume F, $det\boldsymbol{F}$, Equation 1 [12].

$$C_{\alpha,gel} = c_{\alpha,sol}\, det\boldsymbol{F} \tag{1}$$

This combined with the continuum mechanics relation for stress between nominal and true, and the assumption of work summations, yields the Equation 2 [12].

$$\sigma_{ij} = \frac{NkT}{det\boldsymbol{F}}\left(F_{iK}F_{jK} - \delta_{ij}\right) - (\Pi_{sol} + \Pi_{ion})\delta_{ij} \tag{2}$$

In which σ_{ij} is the stress on the system, N represents the number of polymer chains within the network, kT is the temperature of the system, δ_{ij} is the total deformation due to the applied expansion, and Π is the difference of osmotic pressures due to the solution and the imbalance of ions. Based on Equation (1) and (2), the true stress of the hydrogel in relation to the nominal stress can describe the stress under constraints in different solutions as Equation 3 [12]. Equation 3 works as a model for the hydrogel expansion based on the ionic difference between the hydrogel and the external solution.

$$N_A K_a = c_{H^+}^{ref} \exp\left(-\frac{\gamma}{kT}\right) \tag{3}$$

Here, we used Avogadro's number, N_a, the pK_a of the solution in addition to the specific concentration of H^+ ion in the acidic chains within the hydrogel. Lastly, we used the enthalpy of the acidic dissociation from expansion, γ [12].

FABRICATION

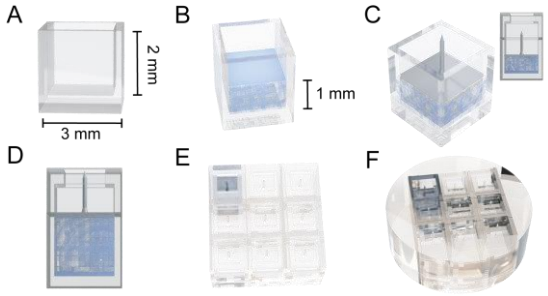

Figure 3: Fabrication of one cell of the HAM patch, (A) soft 3d printed HAM cell, (B) case is filled with 1mm thick hydrogel solution, (C) microneedle is placed on the curing hydrogel, (D) stopper application to casing, (E) Final HAM device with 9 cells, (F) HAM cells inside of circular patch.

The fabrication process is illustrated in Figure 3. First, the hydrogel was prepared by mixing acrylamide (AAm, Sigma) with methacrylic acid (mAA, Sigma) along with tetramethyl ethylenediamine (accelerator, Sigma) and N,N'-methylenebisacrylamide (crosslinker, Sigma). To better visualize the pH changes of the hydrogel, a phenol red indicator dye was added, allowing for a visible color change for ease of measurement. For a wound patch, a 3D-printed flexible patch was created consisting of an array of one or more rectangular cells (2 x 2 x 3 mm^3) (Flexible resin, Formlab 2) (Figure 3A, B). Each cell was filled with a 1mm thick hydrogel. This initial structure directed the actuation force to a moveable microneedle platform. The microneedle array was prepared using UV- light diffraction based off previous work [13]. Then, the microneedle platform was treated with γ-Methacryloxypropyltrimethoxysilane 99.04% (MPS) solution. The MPS treatment promoted the adhesion between the hydrogel and the

microneedle platform. The MPS treatment was initiated by soaking the microneedles in a solution of 10% of MPS in acetone for one hour, followed by evaporating acetone on a hot plate at 60 C for two hours. Note that such temperature was determined not to damage the microneedle. The MPS treated microneedle platform was then placed on top of the hydrogel block (Figure 3C). To retain the microneedle platform within the patch, a stopper was added (Figure 3D). This stopper included a chamber with a height of 1 mm, thus providing room for actuation. A height of 1 mm was chosen to allow the microneedle to be slightly below the stopper in its neutral state and fully extended in its swollen state. The same procedure was repeated for each cell in an array (Figure 3E). Lastly, the assembled microneedle array with hydrogel block was mounted in an easy-to-use, flexible, circular base (Figure 3F). By assembling the patch as a collection of smaller hydrogel cells on a flexible substrate, the HAM patch can adjust to the necessary depth individually as dictated by the pH level. Since each cell is acting as its own system, if one section of the wound begins to heal faster than another, the patch can react accordingly. The HAM patch prototype then underwent a pre-soak process where it was submerged in deionized water overnight. The pre-soak process allowed for the hydrogel to reach an equilibrium state at a neutral pH, ensuring the resulting actuation is caused by the appropriate pH level and not water absorption.

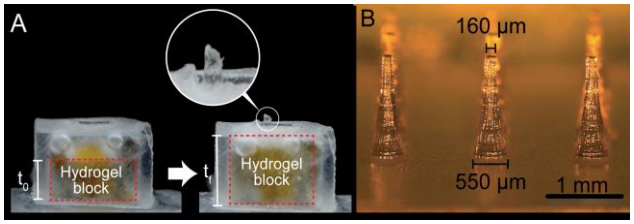

Figure 4: (A) Single HAM cell before and after presoak procedures. (B) Macro-picture of the microneedle

RESULTS

When initial equilibrium was reached the final height of the hydrogel layer is 2 mm, as seen in Figure 4. After the pre-soak, the validation of the pH-sensitive actuation of the HAM patch began by exposing it to different pH level solutions. For these tests, a pH buffer solution with pH 10 (BioPharm) was chosen to mimic the chronic wound environment. For experimental ease, the patch was inverted for all tests. Our validation procedure focuses on two aspects: force from the hydrogel actuation and height of microneedle extrusion. In order to get the maximum effects from the hydrogel, three different cell footprints were tested. Our smallest size featured a 2 mm-by-2 mm footprint, the medium size utilizes a 3mm-by-3 mm footprint, and the largest utilizes a 4 mm-by-4 mm footprint. For all three footprints, the height of the hydrogel was fixed at 2 mm tall. By testing these sizes, we optimized the dimensions of a single cell.

In order to test actuation force, a single hydrogel-microneedle cell of the HAM patch was placed in a small chamber filled with the pH 10 solution. The force from the resulting expansion was measured using a force meter (Torbal), which was placed above the HAM cell contacting the tip of the microneedle. While the HAM cell was left to expand for 90 minutes, the force was recorded simultaneously (Figure 5). The 2 mm-by-2 mm footprint of hydrogel bases exerted the highest force (262 mN), while the 4 mm-by-4 mm dimension showed almost no force even though some swelling was observed. The measured force exceeds the reported required force for skin penetration (250 mN) [14]. This skin penetration threshold is shown in a dashed line in Figure 5. However, in most cases, the HAM patch would be used on an open skin, which requires a minimal force to rip and penetrate the skin tissue.

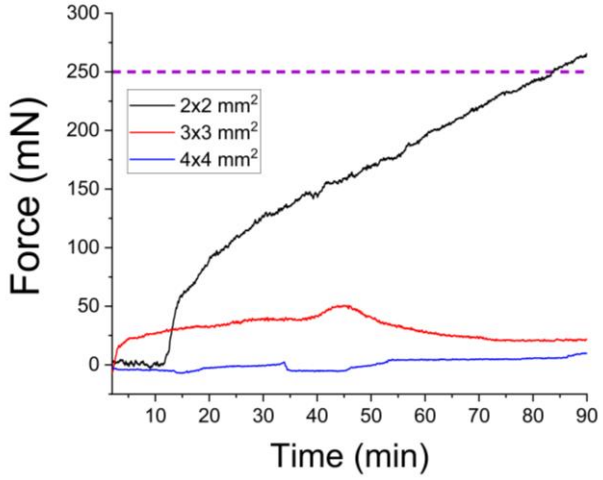

Figure 5: Force measurements for three hydrogel dimensions

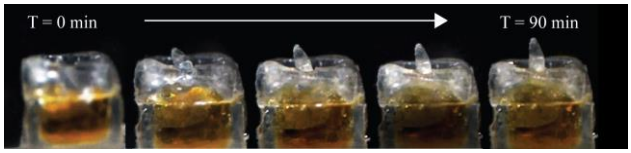

Figure 6: Example images of microneedle actuation when exposed to pH 10 environment for 90 min

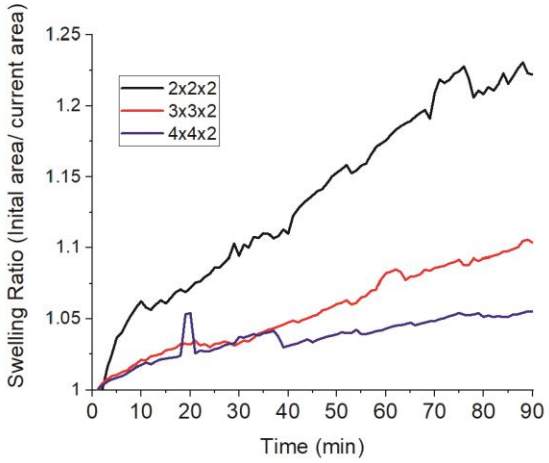

Figure 7: Swelling ratios comparison for the swelling of three hydrogels.

In addition to being able to move through tissues, the HAM patch must reach deep enough to be effective. For quantification of the HAM actuation height, an imaging trace was used. The HAM cell was photographed every 60 seconds over a 90 min span from the side of the chamber. An example of these images is shown in Figure 6. As the hydrogel expanded, the microneedle platform was lifted. The increased area from the dyed hydrogel was measured using ImageJ software.

This value was reported in terms of the swelling ratio, i.e., the ratio of the initial area over the current area. Figure 7 shows the swelling ratio results. We observed that the smallest footprint (2mm by 2mm) showed the most actuation. The overall growth translated to 2.1 mm in height, which allowed the full extrusion of the needle into the wound. Considering some of the clinical trials of needle-based wound treatment depths of 0.2 mm to 0.5 mm [15], the HAM patch with 2 mm by 2 mm cell was able to exceed the maximum depth 4-fold. Note that this maximum depth could also be controlled with a mechanical stopper, which can be customized for various applications.

Overall, we could confirm that out of three footprint dimensions (2mm-by-2mm, 3mm-by-3mm, and 4mm-by-4mm) the smallest dimension displayed sufficient force and actuation to adequately address a chronic wound. The compact size of a singular cell also allowed for more microneedles on a patch which will increase the precision of treatment.

CONCLUSION

The hydrogel actuated microneedle exhibited promising results, making it a feasible candidate in future wound healing applications. From our results, we found that the hydrogel actuation had a sufficient actuation range to allow for full penetration of the microneedle. We have also confirmed that the HAM patch is able to generate enough force to penetrate unbroken skin if needed. For future studies, we will further scale down the design, and incorporate mechanisms for drug delivery and advanced healing techniques. Using these advances the HAM patch provides a promising application, for chronic wound treatments without the need for repeated clinical intervention.

ACKNOWLEDGEMENT

The project was partially supported by the National Science Foundation (ECCS-2054492)

REFERENCES

[1] S. Guo and L. A. DiPietro, “Critical review in oral biology & medicine: Factors affecting wound healing,” *Journal of Dental Research*, vol. 89, no. 3, pp. 219–229, 2010, doi: 10.1177/0022034509359125.

[2] L. Alexander, S. Andreas, S. Grabbe, and J. Dissemond, “In X uence of pH on wound-healing : a new perspective for wound-therapy ?,” pp. 413–420, 2007, doi: 10.1007/s00403-006-0713-x.

[3] G. Gethin, “The significance of surface pH in chronic wounds,” vol. 3, no. 3, pp. 52–55, 2007.

[4] A. J. Boulton, L. Vileikyte, G. Ragnarson-Tennvall, and J. Apelqvist, “The global burden of diabetic foot disease,” *Lancet*, vol. 366, no. 9498. 2005. doi: 10.1016/S0140-6736(05)67698-2.

[5] R. Nunan, K. G. Harding, and P. Martin, “Clinical challenges of chronic wounds: Searching for an optimal animal model to recapitulate their complexity,” *DMM Disease Models and Mechanisms*, vol. 7, no. 11, 2014, doi: 10.1242/dmm.016782.

[6] S. S. Mathew-Steiner, S. Roy, and C. K. Sen, “Collagen in wound healing,” *Bioengineering*, vol. 8, no. 5, 2021, doi: 10.3390/bioengineering8050063.

[7] X. Zhang, W. Shu, Q. Yu, W. Qu, Y. Wang, and R. Li, “Functional Biomaterials for Treatment of Chronic Wound,” *Frontiers in Bioengineering and Biotechnology*, vol. 8. 2020. doi: 10.3389/fbioe.2020.00516.

[8] Y. Qiao *et al.*, “Laser-Activatable CuS Nanodots to Treat Multidrug-Resistant Bacteria and Release Copper Ion to Accelerate Healing of Infected Chronic Nonhealing Wounds,” *ACS Applied Materials and Interfaces*, vol. 11, no. 4, 2019, doi: 10.1021/acsami.8b21766.

[9] L. A. Schneider, A. Korber, S. Grabbe, and J. Dissemond, “Influence of pH on wound-healing: A new perspective for wound-therapy?,” *Archives of Dermatological Research*, vol. 298, no. 9. pp. 413–420, Feb. 2007. doi: 10.1007/s00403-006-0713-x.

[10] G. Gethin, “The significance of surface pH in chronic wounds,” *Wounds*, vol. 03, no. 03, pp. 54–56, 2007.

[11] S. Nesrinne and A. Djamel, “Synthesis, characterization and rheological behavior of pH sensitive poly(acrylamide-co-acrylic acid) hydrogels,” *Arabian Journal of Chemistry*, vol. 10, no. 4, 2017, doi: 10.1016/j.arabjc.2013.11.027.

[12] R. Marcombe, S. Cai, W. Hong, X. Zhao, Y. Lapusta, and Z. Suo, “A theory of constrained swelling of a pH-sensitive hydrogel,” *Soft Matter*, vol. 6, no. 4, pp. 784–793, 2010, doi: 10.1039/b917211d.

[13] J. Y. Tan, A. Kim, and J. ‘JK’ Kim, “Modeling, characterization, and fabrication of bell-tip microneedle array by diffraction and self-aligned lens effects,” *Applied Physics Letters*, vol. 119, no. 2, 2021, doi: 10.1063/5.0055073.

[14] S. P. Davis, B. J. Landis, Z. H. Adams, M. G. Allen, and M. R. Prausnitz, “Insertion of microneedles into skin: Measurement and prediction of insertion force and needle fracture force,” *Journal of Biomechanics*, vol. 37, no. 8, pp. 1155–1163, Aug. 2004, doi: 10.1016/j.jbiomech.2003.12.010.

[15] H. Wang *et al.*, “Effectiveness of fire needle combining with moist healing dressing to promote the growth of granulation tissue in chronic wounds: A case report,” *International Journal of Nursing Sciences*, vol. 7, no. 3, 2020, doi: 10.1016/j.ijnss.2020.05.008.

CONTACT

*A.Kim, tel: +1-678-316-7733; albertkim@temple.edu

UV-BASED, IN-SITU, LOW POWER, WIRELESS SOIL CARBON MEASUREMENT SYSTEM

Steven Tran, Rabiul Hasan, Ashrafuzzaman Bulbul, Seungbeom Noh, Carlos Mastrangelo, and Hanseup Kim*
Electrical and Computer Engineering, University of Utah, Salt Lake City, UT, USA

ABSTRACT

This paper reports the development and initial testing of a UV based soil organic carbon prediction system that takes advantage of the interaction of micro-LED UV emissions with the soil to estimate the total amount of soil organic carbons (SOC) for the first time. This unique system comprises of an optical CO_2 sensor, 415-nm UV LEDs, a micro-controller programed with a sleep mode algorithm and a LoRa based wireless communication electronics, all of which were integrated into a 25-cm-long soil-penetrating shank structure. The prototype utilized a photo-oxidation effect that near-instantly yielded CO_2 when a long-wavelength UV interacts with the soil. Energy from the UV emissions act as a catalyst in the formulation of singlet oxygen molecules, which then goes through a dismutation and Fenton reaction to produce hydroxyl radicals. These radicals will eventually interact with the dissolved organic carbon (DOC) component of the soil to actively form CO_2 molecules. Thus, this method was able to eliminate the conventional tedious soil sample extraction process and high-powered machinery commonly used in today's soil carbon analysis. This constructed prototype successfully produced photo-oxidated CO_2 of up to 128 ppm from soil at a depth of 15 cm within 30 minutes of UV exposure, while consuming an average power of 167.71 mW per 150 min sampling period. Preliminary deployment of the device at four locations around the United States successfully showed the feasibility of accurate, in-situ predictions of SOC, relatively closely matching the national soil database from the United States Department of Agriculture (USDA) relatively well with an average error of 2.64%.

KEYWORDS

Soil Organic Carbon (SOC) measurement, Ultra-Violet, In-Situ, Carbon Prediction, Photo-Oxidation

INTRODUCTION

With rapidly growing concerns over climate changes in recent years, carbon monitoring and sequestration in large agricultural land become vital means in diagnosing and resolving the problem [1]. Today there are 4.62 billion hectares of farmland in the world, which produces roughly 10% of the world's greenhouse gases according to the Food and Agriculture Organization (FAO) [2]. Of these 4.62 billion hectares, only a small percentage of the land utilize agricultural practices for carbon sequestration, limiting the potential in reducing global climate change [3]. Studies have also shown that for every 5–10° C increase in the average temperature, the CO_2 production from soil respiration within agricultural soil doubles, resulting in a cycle of ever-increasing concern [4]. Thus, the efforts in soil carbon monitoring and sequestration in large agricultural lands carries significant impacts toward global efforts in suppressing climate changes.

Current state-of-the-art soil carbon measurement methods can be primarily categorized into two categories, active and passive carbon measurements, depending on whether data is acquired from underground soils or not, all of which are unsuitable in one way or another in producing precise SOC estimation over a large area. Passive measurement techniques include infrared spectroscopy, satellite imaging, and eddy covariance. These techniques quantify parameters, such as light reflection or color variances, which can be correlated to the total soil carbon resulting in rapid soil analysis only at the surface of soils, thus suffering from high uncertainty and being limited in the estimation accuracy in comparison to the gold standard, the dry soil combustion technique. On the other hand, the active carbon measurement techniques, including the wet-oxidation and soil burning techniques, rely on (1) sampling and relocation procedures of soil from a field to a laboratory setting involving extensive excavation and a serial process unsuited for near real time, in-situ measurements and (2) power-hungry analysis methods, such as combustion, heating, or laboratory ultra-violate lasers, limiting the feasibility of in-situ measurement due to significant power consumption.

These limitations seen in existing soil carbon measurements can potentially be resolved by combining the functionality of both a MEMS micro-bolometer and a micro-UV LED, for a direct, sampling-free, and low-power system capable of actively producing CO_2 directly from the soil. Previous research has shown that UV exposure can be utilized to extract carbon from a soil component called dissolved organic carbon (DOC) through a photo-chemical reaction [5]. Using the process of photo-oxidation, previous research demonstrated the feasibility of quantifying a subset of soil carbons in correlation to the total SOC amounts [6]. However, these previous oxidation methods involved sampling and transferring of soils to a laboratory, producing a time-delayed analysis and is impractical-for-large-area analysis, as well as the usage of a high-powered and bulky UV lasers [5]. Unlike the bulky UV lasers, a micro-UV LED can provide a compact form factor and thus enable multiple depth analysis.

This paper reports the development and the initial testing of the first, within our knowledge, near-real-time, on-spot, and in-soil carbon measurement system. Specifically, this paper reports the operation principle, device prototyping, test methods, and the field testing results of the in-soil SOC predictions based on the developed UV based soil carbon prediction system.

OPERATION PRINCIPLE

The key operation principles are centered around (1) the production of CO_2 through the UV extraction of photo-oxidative carbons from the soil and (2) the in-situ measurement of the produced CO_2 by commercial or MEMS sensors. First, the shank of the sensor system is implanted into the ground. Once implanted, the UV LED is turned on, inducing a photo-oxidative reaction and CO_2 sampling. By exposing UV light to the soil, singlet oxygens are created, acting as catalysts for the full photo-oxidation reaction. Through the process of dismutation and a Fenton reaction, the energy from the singlet oxygen helps release hydroxyl radicals. These radicals then react with the aromatic carbons that are part of the dissolvable organic matter (DOM) component of soil resulting in the complete photo-oxidation reaction that converts the aromatic carbons into CO_2 [7]. The CO_2 extracted from the soil then diffuses across the through holes on the shank, which is then quantified by an integrated non-dispersive infrared (NDIR) sensor, which will be later replaced with a MEMS micro-bolometer. Once the UV LED is turned off, the CO_2 level in the shank then reduces back to the leveled state that represents the microbial-respirated CO_2 output. The measured sensor values are subsequently transmitted to a cellular gateway where the data is transferred to a database and utilized in estimating the total soil organic carbon quantity. As

978-1-940470-04-7/HH2022/$25©2022TRF
DOI 10.31438/trf.hh2022.32

compared to the "gold standard" dry combustion technique, described in Fig. 1, the manufactured UV-based photo-oxidation system allows for in-situ SOC measurement, resulting in accurate, rapid, and low-power measurements. These measurements are free of biases caused by time-delayed, soil transportation which may cause a reduction in nutrients or beneficial microbes in soil samples [8]. This method also reduces the average test time from 1-5 days down to 2.5 hours by removing the tedious and power consuming process of sampling and burning soil.

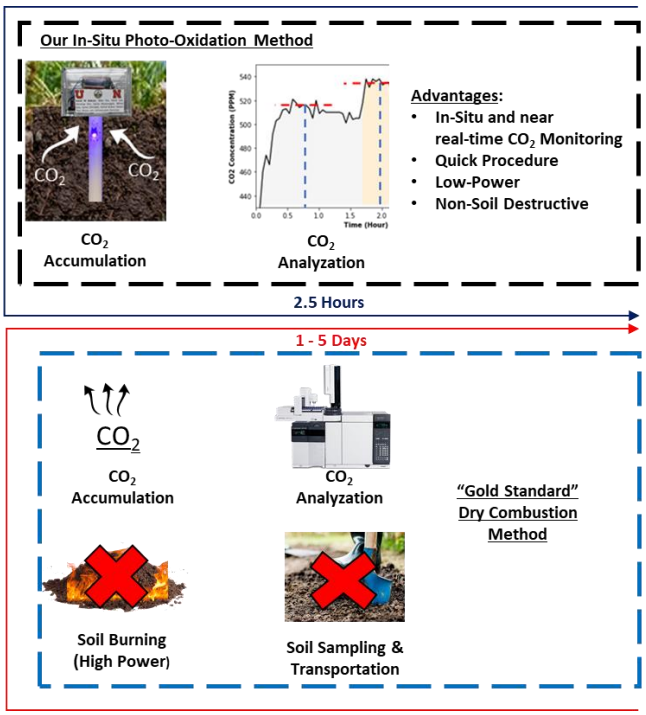

Fig 1. In-situ photo-oxidation based methods allows for near real time-monitoring, lower power, and is non-soil destructive in comparison to the current "Gold Standard" dry combustion methods.

Device Prototyping

System Components and integration

Figure 2 summarizes the components makeup of the prototype, which consists of an optical CO_2 sensor, 415 nm UV LED, a micro-controller programed with a sleep mode algorithm, a LoRa based wireless communication electronics, and a 25 cm support shank structure. The entire sensing system was powered by a 3.7 V, 18650 battery which sits atop a 3D printed base encased in a 4.0 x 8.0 x 7.8 cm^3 acrylic rectangular prism to shield the circuitry from environmental hazards (e.g., wind, rain) during in-situ testing in soil. The prototyped system averaged a power consumption of 167.71 mW, in addition to a UV with a 30-min on period during a single sampling period (Power consumed by UV LED: 420.47 mW). With each component of the device supported by a 3.7 V battery, the estimated energy consumption per sampling period (150 min) for the sensor system was 617.9 mJ/sec, resulting in a prototype lifetime of ~44 days.

The optical CO_2 sensor (Sensair S8) utilized in the current prototype was an off-the-shelf nondispersive infrared (NDIR) sensor that identified the CO_2 levels through ratioing the input and output intensities of the infrared at 4.26 µm. Note that the selected 4.26 µm was the wavelength that CO_2 molecules strongly absorbed. This optical sensor held a volume of 8.5×32.7×19.7 mm^3 and was integrated within a circuitry that allowed for a time-controlled sleep mode. This sleep mode operation was controlled by a clock-based algorithm that cyclically powered an Arduino pro-mini microcontroller on and off, which would subsequently power on and off all other electrical components within the sensing system to reduce the overall power consumption. Future prototypes will utilize a fabricated micro-bolometer array that is capable of precisely quantifying the captured CO_2 within the device at low concentration through the absorption of reflected infrared off of gas molecules.

The prototypical system utilized a high-density UV LED from LuminLED that irradiated a UV intensity of 35 W/cm^2 from a tiny footprint of 1.3×1.3 mm^2 at a wavelength of 415 nm. Each LED was embedded along the side of the shank at the soil depth of interest for UV emissions to act as a catalyst for the photo-oxidation process in yielding CO_2. Current prototype measured the CO_2 at a depth of 15 cm within the soil. The UV LED, powered by an additional 3.7-V 18650 battery, was surrounded by 11 through-holes with a 0.25-mm radius. These through holes permitted the diffusion of the extracted carbon molecules from the soil into the shank as a result of the relative pressure difference between the inner and outer shank interface.

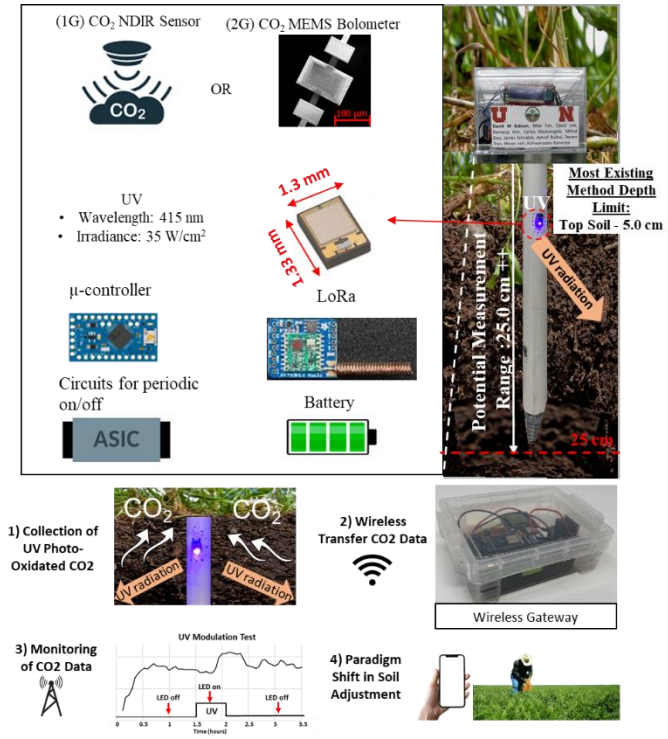

Fig 2. UV based soil carbon measuring system prototype full body image, circuit components, and overarching working principle.

Diffusion Hole Design

Through empirical testing, it was observed that the design of diffusion through holes could be adjusted or minimized the response time for the detection of microbial respirated and photo-oxidated CO_2. The response time, required to detect a saturated CO_2 concentration within the shank, was modeled by an analogy to that of a simple RC circuit electrical system. First, the speed at which CO_2 diffused into the shank was estimated by calculating a time constant (τ) that could be described by the quotient of the total volume (V) of present CO_2 by the CO_2 flow rate (Q) (Eq. 1). Here Q was obtained by Fick's law of diffusion of gas as a function of a pressure gradient at a discrete time, which was described in Eq. (2).

In Eq. (2), ΔP was the pressure difference at the through hole shank interface at a particular time, N was the number of holes, r was the radii of the holes, D was the diffusivity constant of CO_2, and h was the distance of diffusion, all of which is visually depicted in Fig. 3. The combination of Eq. 1 and Eq. 2 produced the time constant (Eq. 3) that indicated the charging and discharging rate of the prototype. The charging and discharging periods formula were then used to minimize the UV-exposure periods by optimizing the CO_2 production and power consumption. Based on empirically determined results, 11 through holes with a radius of 0.25 mm was selected to keep the time constant beneath 30 min as well as complying to any dimensional constraints. The 30 min period was selected such that the detection of the steady-state photo-oxidative and microbial-respirated CO_2 levels would be achieved within 60 min over various soils, while limiting power consumption below 200 mW.

$$\tau = \frac{V}{Q} \quad (1)$$

$$Q = \frac{\frac{\int_0^t \Delta P}{t} * N * r^2 * \pi * D}{h} \quad (2)$$

$$\tau = \frac{V * h * t}{\int_0^t \Delta P * N * r^2 * \pi * D} \quad (3)$$

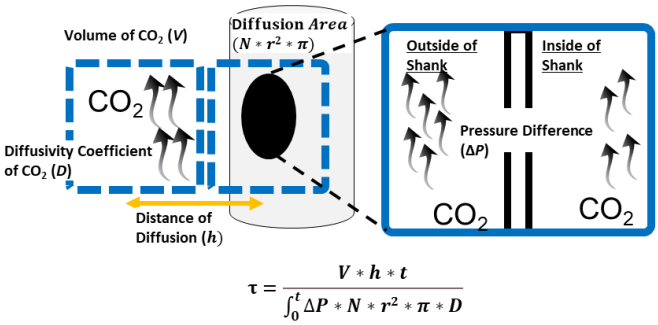

$$\tau = \frac{V * h * t}{\int_0^t \Delta P * N * r^2 * \pi * D}$$

Fig 3. Visualization of the CO_2 permeation model due to a pressure interface of the diffusion through holes of the CO_2 prediction system.

TEST METHODOLOGY

Photo-Oxidation Based Real Time In-Soil CO_2 Measurements

To quantify the amounts of the produced photo-oxidative CO_2, the system utilized a time dependent modulation of the UV-LED located 15-cm below the soil. This UV-LED was activated and deactivated for 30- and 60-minutes intervals, respectively, while monitoring the formulation of photo-oxidated CO_2 captured within the shank structure utilizing a calibrated optical NDIR sensor over both on/off periods. Note that the measured CO_2 amounts, during the on period, was the combined summation of photo-oxidative, microbial respirated, and atmospheric CO_2. Thus, from the measured CO_2 quantity, the off-period baseline, which included microbial respirated and atmospheric CO_2, was subtracted to calculate only the quantity of photo-oxidative CO_2. Since the atmospheric CO_2 amounts could be measured above ground, all three CO_2 amounts could be computed. During the UV modulation periods, the sensor system was periodically turned on for 10 seconds to collect the baseline CO_2 data and off for 3 min before repeating the next sampling cycle to reduce the overall power consumption of the system. During the 30 min UV-on period, a UV LED consuming an average power of 420.47 mW, was used to produce photo-oxidative CO_2, while the CO_2 sensor system continuously measured in an identical manner as during the UV-off period. The described photo-oxidated, real-time CO_2 measurements were then performed at 4 locations in the US (Salt Lake City, Utah; Boise, Idaho; Savoy, Illinois; Lincoln, Nebraska) in order to verify the effectiveness of the in-situ, photo-oxidative method in obtaining accurate SOC values over various soil types. All field testing was performed between June and August in 2021. Tests were done during a timeframe when both the temperature and humidity were both relatively consistent throughout the duration of each test without on-going precipitation to limit any biases.

SOC Estimation

To enable prediction of the total SOC amounts in soil, an initial version of a CO_2-to-SOC conversion algorithm was developed. The initial version of the algorithm was produced by utilizing a least square linear regression model that minimizes the error between the collected data set at a depth of 15 cm and was compared to the SOC data from the USDA soil survey data set at the corresponding depth. Note that the USDA data set was collected and updated by the National Cooperative Soil Survey over the past century, providing a gold standard for comparison.

RESULTS

Real Time In-Soil CO_2 Measurements

Initial real-time, in-soil measurements in Salt Lake City (Fig.4) showed (1) that UV LED instantly produced photo-oxidative CO_2 levels up to 22 ppm, which were sufficiently detectable by an optical sensor within 30 min of testing at a soil depth of 15 cm; and (2) that it was feasible to distinguish photo-oxidative CO_2 levels from microbial-respirated levels in near real-time within the soils. Figure 4 shows the measured CO_2 levels over a 3.5-hour period starting with the implantation of the prototype into the soil at the 0-hour point. In the first 0.5-hour period, the measured CO_2 levels saturated at 516 ppm, settling to the baseline of CO_2 levels in the soil. The baseline CO_2 levels were composed of the microbial-respirated and atmospheric CO_2 levels. Once saturated at 0.5-hour point, the measured CO_2 levels of 516 ppm remained stable. This saturated concentration was higher by 83 ppm than the initial atmospheric CO_2 level of 433 ppm with the difference indicating the microbial-respirated CO_2 level. When the UV LED was activated, the CO_2 level subsequently increased by 22 ppm within a 14.4 minute time frame and was saturated at roughly 538 ppm with 30 minutes of UV exposure, confirming the feasibility of utilizing micro-LEDs to produce UV-oxidated CO_2 for near real-time and on-spot measurement. Upon saturation of the CO_2 concentration, the LEDs were deactivated. Within an 18.6 minutes time frame, the CO_2 level remained saturated before decreasing back to the baseline, in which another 47.7 minutes was needed before the baseline data was stabilized.

Four different field testing sites were used to verify the potential usage of the UV-based, soil carbon prediction system. These results showed (1) that the photo-oxidation based CO_2 generation and measurement were applicable to different soil types and (2) that there was a clear correlation of the CO_2 amount to the types of soils, as shown in Fig. 5. Soils tested at the Salt Lake City and Boise locations were grouped as non-agricultural soils with natural vegetation, while those in Lincoln and Savoy were grouped as agricultural farmland soils that were actively utilized to produce crops. When normalized to an atmospheric CO_2 level of 433 ppm, each collected data set from Salt Lake City, Boise, Savoy, and Lincoln showed different microbial-respirated CO_2 levels of 79 ppm, 47 ppm, 289 ppm and 199 ppm respectively. Once the

microbial-UV LED was activated, the CO_2 level increased producing a photo-oxidation of 26 ppm, 46 ppm, 128 ppm and 101 ppm for each test site.

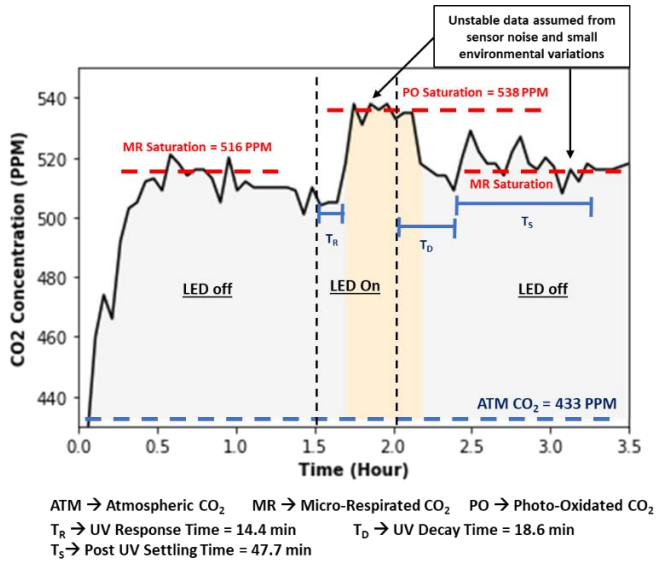

Fig 4. Measurement of CO_2 concentration by the developed prototype at a soil depth of 15 cm over time with the modulation of UV exposure. It was a 3.5 hr. test sampled in Salt Lake City, Utah for CO_2 collection. The measurement clearly showed three major CO_2 components (atmospheric, microbial-respirated, and photo-oxidated).

SOC Estimation

Based on the four site measurement data, a linear line of best fit algorithm was produced and utilized to produce an initial prediction of the total SOC values that showed high correlation to the USDA National Survey data. The established linear algorithm is shown in Eq. 4, where x was the measured photo-oxidation CO_2 level by the prototype.

$$(\text{Eq. 4})\ SOC\% = 0.008 * X + 0.8584$$

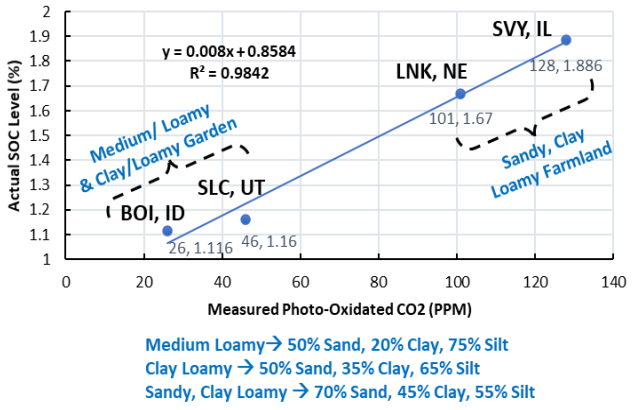

Fig 5. Captured Photo-Oxidated CO_2 in relation to the actual SOC values as reported by the soil survey database done by the USDA. A high correlation between the CO_2 and SOC is observed.

The linear SOC predictor equation (Eq. 4) predicted SOC% for the four different sites of Salt Lake City, Boise, Savoy, and Lincoln sites, which were plotted in Fig.5. Each site produced a prediction error 4.44%, 5.72%, 0.19%, and 0.22% respectively, resulting in an average percent error of 2.64% when matched with the USDA SOC soil survey data. The data also showed that there was a clear correlation between the soil types, the produced CO_2, and the actual SOC% amounts with a coefficient of determination of 0.984 (Fig. 5). This result indicated a potentially successful system that could accurately determine soil SOC% within various soils, implying a new paradigm in underground SOC measurement.

CONCLUSION

A UV-based, soil carbon prediction system was successfully developed to predict the soil organic carbon levels in-situ with the soil with an average error of 2.64%, improving upon the disadvantages seen in traditional techniques by being accurate, quick, and in-situ. Additionally, the prototype showed that a UV-based system was capable of consistent, near instantaneous CO_2 production with a time constant of 18.36 min, allowing the transient photo-oxidated and microbial-respirated CO_2 to be determined within 30 minutes. These results offer a preliminary demonstration for the possible usage of an in-situ, low power, wireless soil organic carbon prediction system that can predict the SOC% with relative accuracy within various types of soil.

ACKNOWLEDGEMENTS

This research work was generously supported by the cooperative agreement of the ARPAE program (Program Manager: Dr. David Babson, Dr. David Lee, and Dr. Calden Stimpson). The microfabrication was performed in the Utah Nanofabrication Facility in the University of Utah.

REFERENCES

[1]Morgan, J. A., Follett, R. F., Allen, L. H., Del Grosso, S., Derner, J. D., Dijkstra, F., … Schoeneberger, M. M. (2010). Carbon sequestration in agricultural lands of the United States. Journal of Soil and Water Conservation, 65(1), 6A–13A. doi:10.2489/jswc.65.1.6a

[2]"*Land use in agriculture by the numbers*," May. 7, 2020. Accessed on: Dec. 15,2021. [Online].Available:https://www.fao.org/sustainability/news/detail/en/c/1274219/

[3]J. Newton "Reviewing U.S. Carbon Sequestration", Feb. 2021. Accessed on: Dec.15,2021. [Online].Available: https://www.fb.org/marketintel/reviewing-u.s.-carbon-sequestration

[4]Bardgett, R., Freeman, C. & Ostle, N. Microbial contributions to climate change through carbon cycle feedbacks. ISME J 2, 805–814 (2008). https://doi.org/10.1038/ismej.2008.58

[5]Varadachari, Chandrika & Mitra, Somnath & Ghosh, Kunal. (2017). Photochemical Oxidation of Soil Organic Matter by Sunlight. Proceedings of the Indian National Science Academy. 83. 223. 10.16943/ptinsa/2016/48858.

[6]Brandt, L. A., Bohnet, C., and King, J. Y. (2009), Photochemically induced carbon dioxide production as a mechanism for carbon loss

[7]Georgiou, C. D., Sun, H. J., McKay, C. P., Grintzalis, K., Papapostolou, I., Zisimopoulos, D., … Margiolaki, I. (2015). *Evidence for photochemical production of reactive oxygen species in desert soils. Nature Communications, 6(1).* doi:10.1038/ncomms8100

[8]Falkengren-Grerup, U. (1995). Effects of Long-Term Storage on Some Chemical Properties of Forest Soil Samples. *Ecological Bulletins*, *44*, 129–132. http://www.jstor.org/stable/20113156

LEAF-MOUNTED MICRONEEDLE-BASED MULTISENSORY PLATFORM FOR MULTIPLEXED MONITORING OF PHYTOHORMONES IN LIVE PLANTS

*Nafize I. Hossain and Shawana Tabassum**
The University of Texas at Tyler, Tyler, TX, USA

ABSTRACT

This paper presents a first-of-its-kind leaf-mounted microneedle-based multisensory platform for *in situ* monitoring of salicylic acid and indole-3-acetic acid in the leaves of a live plant. The multiplexed system has a built-in temperature sensor for temperature correction. The sensor could accurately detect salicylic acid and indole-3-acetic acid levels with detection limits of 1μM and 0.10μM, respectively. The measured hormone levels were corrected based on the variations in leaf temperature in an actual field condition. Since phytohormone signaling is a plant's first response to environmental stresses, early identification of these stress hormones will help growers to implement site-specific interventions and mitigate productivity losses. Moreover, our continuous and *in situ* sensor will advance future research on improving plant growth in space missions (NASA Space Biology's research priority).

KEYWORDS

Microneedle sensor, multisensory platform, leaf-wearable sensor, multiplexed monitoring, salicylic acid, indole-3-acetic acid.

INTRODUCTION

Plants have sophisticated systems to detect and respond to environmental stimuli. Real-time measurement of plant parameters is crucial to gauge the adverse ecological impacts and intervene early. Studies report that drought stress alone yielded 21% and 40% of global reductions in wheat and maize productions, respectively, between 1980 and 2015 [1]. The impacts of these stressors on crop yield are often not detected early enough to mitigate crop damage. Environmental stresses induce a progressive change in the levels of phytohormones, which are circulated throughout the plant via xylem and phloem. Thus, the levels of phytohormones can serve as early signals of plant stress [2-5]. Salicylic acid (SA), jasmonic acid (JA), abscisic acid (ABA), and indole-3-acetic acid (IAA) are among the most important regulators of induced defense mechanisms [6-10]. Progressive variations in their levels have been reported in many drought, salt, and cold/heat-stressed plants. Moreover, exogenous application of these hormones mitigates oxidative stress in plants [11-16]. The interconnected signaling pathways of these hormones are central to the plant's ability to fine-tune the induction of defenses in response to stresses. *However, the dynamic interaction mechanism of these hormones under environmental stress conditions is not fully elucidated due to the lack of knowledge and technology needed to facilitate the use of in situ sensors.*

The traditional approaches to conducting molecular analyses of plants include liquid chromatography (LC), nuclear magnetic resonance (NMR) imaging, and infrared (IR) spectroscopy. Although LC and NMR methods are highly sensitive and selective, they are limited to laboratory settings [17]. In addition, they are non-continuous, disruptive, time-consuming, laborious, and expensive (>$100k): the tissue samples need to be collected in the field and brought to the laboratory periodically and throughout the growing season. Moreover, the collected samples lose their functionality due to the need to transport long distances to the lab. The time lag between sample collection and analysis prevents follow-up and dynamical studies [17]. Due to the complexities and time delays associated with these techniques, only a few plants are sampled, and extrapolations are made about the whole population, thereby neglecting the significant variations between plants across a field. The infrared and thermal imaging techniques provide a non-disruptive view of the action of the stressors in plants. Still, they lack accuracy, do not provide quantitative analysis of metabolites, and are effective only at late crop responses. Unmanned aerial systems have emerged as an attractive tool for aerial scouting. They can fly to waypoints, hover, and collect high-resolution data (millimeters per pixel) from large acres of the field quickly. However, they do not conduct chemical profiling of the plant and are very power-hungry, requiring human intervention for battery recharge/replacement. It can take an entire 8-hours workday to exhaustively collect high-definition images from every zone in an 80-acre crop field [18, 19]. The commercial in-situ crop sensors (e.g., FloraPulse and Dynamax) do not provide real-time and continuous monitoring of stress responses in plants. They only monitor sap water content and do not provide chemical measurements (e.g., metabolite or nutrient), hence stress profiling. To summarize, *none of the traditional/commercial plant monitoring technologies can provide real-time and continuous assessment of stress responses in plants.*

In contrast, our proposed leaf-mounted multisensory platform has competitive advantages over the existing methods through providing continuous and *in situ* monitoring capabilities, multiplexed detection of stress-related hormones, wireless data transfer capability, and energy efficient and low-cost solution, while incurring minimal damage to the plant. The emerging *in situ* leaf sensors are limited to monitoring leaf temperature, humidity, and volatiles [20]. Although some microneedle structures are reported for plants, they are limited to drug delivery or impedance monitoring [20]. Real-time tracking with our proposed sensor will reduce the losses of valuable cash crops, including cannabis, the fifth most valuable crop in the United States behind corn, soybeans, hay, and wheat.

This work addresses the limitations of traditional plant monitoring techniques through:

a. developing a novel leaf-mounted, bioagent-free microneedle-based multisensory platform for multiplexed monitoring of salicylic acid (SA) and indole-3-acetic acid (IAA) in the leaves of a live plant
b. embedding a temperature sensor on the same chip for *in situ* temperature correction of the phytohormone measurements
c. elucidating phytohormone dynamics under water stress.

DEVICE MANUFACTURING

The entire system is comprised of a leaf-wearable multisensory module and a data logger.

Formation of the Microneedle Electrodes

The 2cm x 1cm device was comprised of three-electrode-based electrochemical sensors. Each electrode was made of an array of square-based pyramid-shaped microneedles with a height of 800μm, a base width of 800μm, and each side making a 30^0 angle with the tip (Fig. 1a). The entire platform was designed with a stereolithography 3D printer using a biocompatible resin. The working electrodes: WE_{SA}, WE_{IAA}, $WE_{T,}$ and the counter electrode

978-1-940470-04-7/HH2022/$25©2022TRF
DOI 10.31438/trf.hh2022.33

(CE) were coated with graphene ink, while the reference electrode (RE) was covered with Ag/AgCl paste and subsequently cured at 100°C for 60 minutes. Figure 1b illustrates the microscopic images of the fabricated multisensory platform carrying the microneedle electrodes.

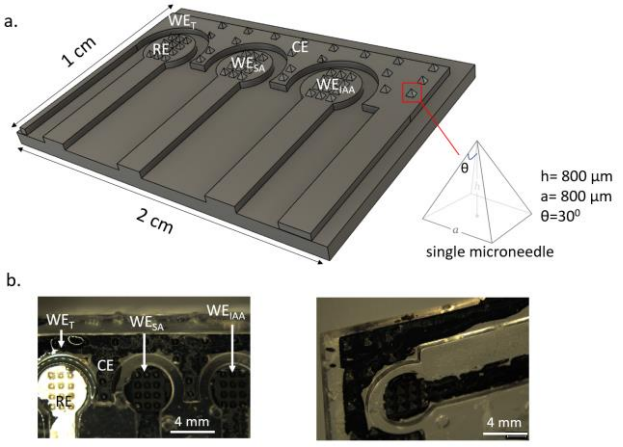

Figure 1: (a) The microneedle sensor (left) and a single needle (right). (b) Microscopic images (top and side views) of the microneedle sensor.

Formation of the Target-Specific Coatings

The WE_{SA} was coated with a copper-based metal-organic framework (CuMOF) for SA detection [21], WE_{IAA} with gold nanoparticle decorated graphene hydrogel nanocomposite (AuNP-GH) for IAA detection [22], and WE_T with PEDOT:PSS crosslinked by (3-glycidyloxypropyl)trimethoxysilane (GOPS) for temperature detection [23].

Synthesis of the CuMOF coating started by dissolving 0.4 g of polyvinyl pyrrolidone (PVP) in 8 mL of dimethylformamide (DMF) and 8 mL of ethanol. Next, a homogeneous mixture of 46.6 mg of copper nitrate hydride and 10.8 mL of 2-amino terephthalic acid was prepared in 4 mL of DMF, which was added to the previously prepared PVP solution and heated at 100°C for 5 hours. The resulting green residue was dissolved in 40 mL of DMF and heated in an oven at 100°C for 8 hours. The solution was cooled down to room temperature and subsequently centrifuged at 1000 rpm for 30 minutes. The resulting CuMOF precipitates were collected and dried at 100°C. The CuMOF powders were added to carbon black (CB) at a weight ratio of 2:1 and dissolved in deionized water at a 2 mg/mL concentration. After adding 0.01% w/v of Nafion, the solution was sonicated for 30 minutes. Finally, 1 µL of the resulting nanocomposite solution was drop coated on the WE_{SA} electrode surface.

The AuNP-GH was synthesized according to the method described in [22]. Briefly, 1 mg mL^{-1} of graphene oxide suspension was prepared. 20 mL of this suspension was added to 2 mL of 0.8511 mg mL^{-1} chloroauric acid solution and 1 mL of triethylenetetramine. The resulting mixture was sonicated for 10 minutes and then heated at 140^0C for 12h. The obtained AuNP-GHs were cooled down to room temperature and then freeze-dried for 24 h to form powders that were stored in a desiccator.

To print the temperature sensing layer, 100 mg of PEDOT:PSS solution and 50 mg of non-ionic surfactant Triton X-100 solution (1.3wt% in DI water) were mixed with GOPS (at a GOPS to PEDOT:PSS weight ratio of 9:1). The resulting mixture was centrifuged for 15 min and degassed for 5 min. The solution was drop cast on the working electrode, WE_T (Fig. 1) followed by annealing at 140 °C in air for 30 min to remove the solvent and enable the cross-linking process. Finally, a 25 µm-thick Kapton tape was used as the encapsulation layer to cover the PEDOT:PSS coating.

Data Logger

The commercially available handheld EmStat 3 potentiostat (BASi, Inc.) was used to perform the electrochemical measurements of SA and IAA. The onboard temperature sensor was resistive, generating resistance variations in response to varying leaf temperatures. A separate ESP32 feather development board was used to acquire and process the temperature measurements. The temperature sensor was connected in series with a known resistor, and a built-in analog to digital converter on the ESP32 board measured the analog voltages across the sensor. The measured resistance values across the temperature sensor were further verified with a benchtop LCR meter (Applent, AT 3817).

RESULTS AND DISCUSSION

Characterization of the Composite Coatings

The CuMOF coating was characterized by Fourier Transform Infrared (FTIR) spectroscopy, as is demonstrated in Fig. 2a. The FTIR spectrum confirmed the presence of amino groups and -OH and C=O functional groups, also reported in [24]. The AuNP-GH coating was characterized by ultraviolet-visible (UV-Vis) spectroscopy, which indicated the presence of Au molecules and C=O bonds (Fig. 2b).

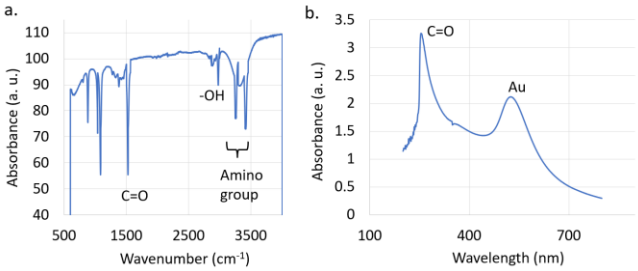

Figure 2: (a) Characterization of CuMOF coating with FTIR. (b) Characterization of AuNP-GH with UV-Vis.

Electrochemical Detection of SA and IAA Hormones

Differential pulse voltammetry (DPV) was employed for electrochemical measurements of varying SA and IAA levels. The sap was collected from live cabbage plants and spiked with hormones to prepare the SA and IAA concentrations depicted in Fig. 3. In the potential range from -1V to 1.5V, the reduction peak current for CuMOF occurred at around -0.06 V, while the oxidation peak current of SA appeared at 0.82 V (Fig. 3a). Owing to the reasonable separation between the redox potentials, the ratio of the two peak currents was plotted against the SA levels to generate the calibration plot in Fig. 3b. Next, the IAA redox peak current at ~0.85 V (Fig. 3c) was plotted against the IAA concentrations to generate the calibration plot in Fig. 3d. With increasing SA/IAA levels in sap, the redox peak currents for SA/IAA increased due to the oxidation of the hormones by the selective coating. The sensitivity of the SA sensor was calculated as 0.005 μM^{-1} with a detection limit of 1 µM. The sensitivity of the IAA sensor was calculated as 0.76149 µA μM^{-1} with a detection limit of 0.1 µM.

Selectivity, Reproducibility, and Repeatability Studies

The hormone sensors exhibited good selectivity against common interfering species found in sap, as depicted in Fig. 4. The sensors were tested against different interfering species (e.g., Jasmonic acid, L-Cysteine, glucose, citric acid, and ascorbic acid)

and their mixture, commonly found in the plant sap. It was observed that the sensors demonstrated a higher relative signal in response to the target hormones as compared to the interfering species. The relative signal is defined by the following equation [21]:

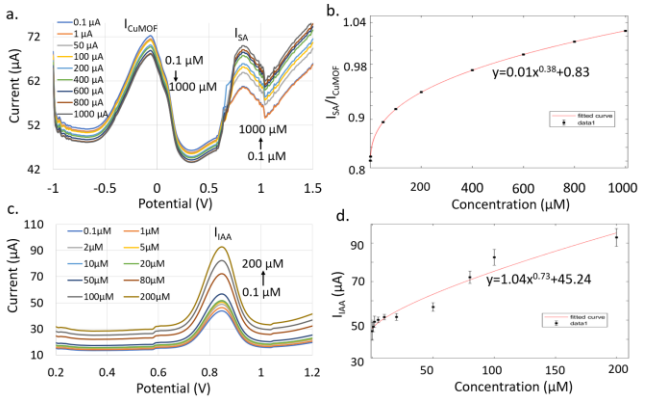

Figure 3: (a) DPV responses and (b) calibration plot of the SA sensor for varying SA concentrations (sensitivity= 0.005 μM^{-1}). (c) DPV responses and (d) calibration plot of the IAA sensor for varying IAA concentrations (sensitivity=0.76149 μA μM^{-1}).

$$Relative\ Signal = (R_a - R_b) / R_b \quad (1)$$

where R_a represents the ratio of the redox peak currents of the analyte and the CuMOF coating. R_b represents the ratio of the base current to the CuMOF peak current of a blank solution.

The hormone sensors also demonstrated excellent reproducibility for 4 repeated measurements with less than 1% deviation (Fig. 5a-b). In addition, with increased temperature, the sensor calibration curves shifted upwards with less than 10% deviation (Fig. 5c-d). Hence, temperature correction was done with an in-built temperature sensor (the results are reported in the next section).

The sensors demonstrated repeatable characteristics under cyclic variations in hormone levels (the same concentrations used for calibration), indicating the feasibility of field deployment (Fig. 5e-f).

Real-time Hormone Measurements with Temperature Correction

The microneedle sensor was mounted on the leaf of an unstressed (control) and a water-stressed cabbage plant (Fig. 6a), and SA levels were measured. The stressed plant was not irrigated for three days. The unstressed plant was irrigated 10 hours before the test. Figure 6b shows the calibration plot of the onboard temperature sensor. Figure 6c shows the temperature-corrected real-time SA levels of water-stressed and control plants measured over 7 days with the microneedle sensor. A progressive increase in the SA level was observed in the stressed plant. Next, two sensors were mounted at different heights (0.5 and 6.5 cm) of the same plant. The sensors could accurately measure the SA dynamics across the plant, as was evident from the difference in the SA rise time (3 hours) captured by the leaf sensors (Fig, 6d). The measurements were repeated with three plants and confirmed by the liquid chromatography (LC) tests. As shown in Fig. 6c, the hormone levels measured with the gold standard LC were very close to the levels measured with our sensor, thereby validating the accuracy of the microneedle sensor. Real-time and continuous measurements of hormone levels will advance the research in elucidating the dynamic interaction mechanism of the hormones under environmental stress conditions.

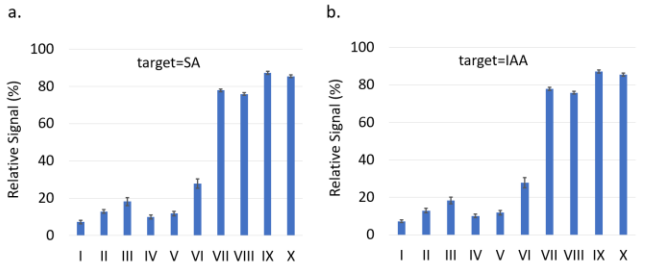

Figure 4: Selectivity tests of (a) SA and (b) IAA sensors. Here, I -X denote: (I) Jasmonic acid (JA)=50 μM, (II) L-Cysteine (L-Cys)=50 μM, (III) glucose=50 μM, (IV) citric acid=50 μM, (V) ascorbic acid=50 μM, (VI) a mixture of JA, L-Cys, glucose, citric acid, and ascorbic acid (50 μM each), (VII) target hormone=100 μM, (VIII) a mixture of ascorbic acid, JA, L-Cys, glucose, citric acid, ascorbic acid (50 μM each), and target=100 μM, (IX) target (SA=900 μM or IAA=200 μM), (X) a mixture of ascorbic acid, JA, L-Cys, glucose, citric acid, ascorbic acid (50 μM each), and target (SA=900 μM or IAA=200 μM).

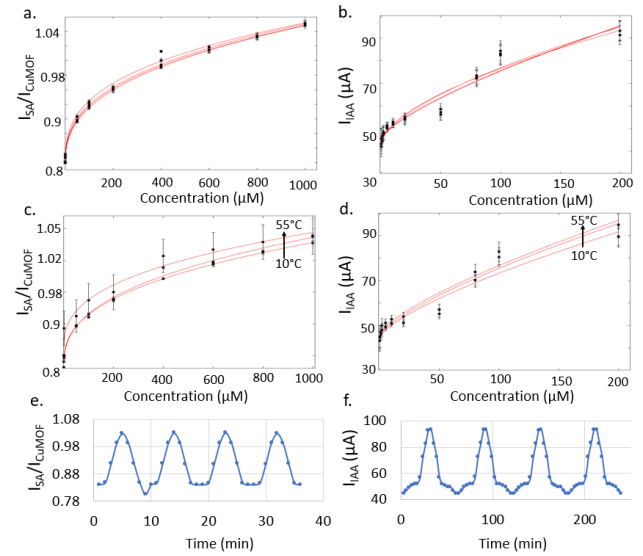

Figure 5: Reproducibility tests with 4 identical (a) SA and (b) IAA sensors. Shifts in (c) SA and (d) IAA calibration plots for temperature variations (10°C→55°C). Cyclic tests of (e) SA and (f) IAA sensors for different hormone levels.

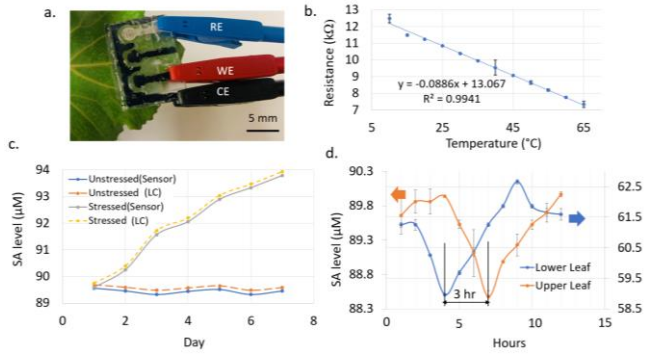

Figure 6: (a) Optical image of the microneedle sensor mounted on the leaf. (b) Calibration plot of the temperature sensor showed a sensitivity of 0.0886 kΩ/°C. (c) Real-time SA variations in water-stressed vs. control plants for 7 days. Here, LC represents liquid chromatography. (d) SA dynamics over 12 hr, repeated with 3 plants.

CONCLUSION

This work reports a leaf-mounted microneedle sensor with temperature correction capability to enable *in situ* and real-time profiling of two potent stress-related phytohormones, which will yield a foundational understanding of dynamic hormonal interactions under environmental conditions and early identification of crop stresses. Real-time crop profiling will help growers implement timely and site-specific applications of agrochemicals to mitigate potential impacts in production. In addition, the results will help guide researchers in the development of plant cultivars with greater stress tolerance. Future work will include the multiplexed detection of other defense-related phytohormones, including methyl jasmonate and abscisic acid.

ACKNOWLEDGEMENTS

This work was supported by the University of Texas System Board of Regent's Rising STARs award and the University of Texas at Tyler's Internal grant award.

REFERENCES

[1] S. Fahad, A. A. Bajwa, U. Nazir, S. A. Anjum, A. Farooq, A. Zohaib, S. Sadia, W. Nasim, S. Adkins, S. Saud, M. Z. Ihsan, H. Alharby, C. Wu, D. Wang, and J. Huang, "Crop production under drought and heat stress: plant responses and management options", *Frontiers in Plant Science*, 8, 1147 (2017).

[2] A. R. Seilaniantz, M. Grant, and J. D. G. Jones, "Hormone crosstalk in plant disease and defense: More than just jasmonate-salicylate antagonism", *Annu. Rev. Phytopathol.*, 49, 317–343 (2011).

[3] S. H. Spoel and X. Dong, "How do plants achieve immunity?: Defense without specialized immune cells", *Nature Reviews Immunology*, 12, 89–100 (2012).

[4] J. Yang, G. Duan, C. Li, L.Liu, G. Han, Y. Zhang, and C. Wang, "The crosstalks between Jasmonic acid and other plant hormone signaling highlight the involvement of Jasmonic acid as a core component in plant response to biotic and abiotic stresses", *Frontiers in Plant Sci.*, 10, 1349 (2019).

[5] Z. Q. Fu and X. Dong, "Systemic acquired resistance: Turning local infection into global defense", *Annual Review of Plant Biology*, 64(1), 839–863 (2013).

[6] I. A. Vos, C. M. J. Pieterse, and S. C. M. van Wees, "Costs and benefits of hormone-regulated plant defences", *Plant Pathology*, 62(S1), 43–55 (2013).

[7] L. Philippot, J. M. Raaijmakers, P. Lemanceau, and W. H. van der Putten, "Going back to the roots: the microbial ecology of the rhizosphere", *Nature Reviews Microbiology*, 11, 789–799 (2013).

[8] M. A. Mir, R. John, M. N. Alyemeni, P. Alam, and P. Ahmad, "Jasmonic acid ameliorates alkaline stress by improving growth performance, ascorbate glutathione cycle and glyoxylase system in maize seedlings", *Scientific Reports*, 8, 2831 (2018).

[9] R. Bari and J. D. G. Jones, "Role of plant hormones in plant defense responses", *Plant Mol. Biol.*, 69, 473–488 (2009).

[10] B. N. Kunkel and C. P. Harper, "The roles of auxin during interactions between bacterial plant pathogens and their hosts", *J. Experimental Botany*, 69, 245–254 (2018).

[11] N. Saruhan, A. Saglam, A. Kadioglu, "Salicylic acid pretreatment induces drought tolerance and delays leaf rolling by inducing antioxidant systems in maize genotypes", *Acta Physiol. Plant*, 34, 97–106 (2012).

[12] A. H. Elhakem, "Salicylic acid ameliorates salinity tolerance in maize by regulation of phytohormones and osmolytes", *Plant, Soil and Environment,* 66, 533–541 (2020).

[13] A. A. H. A. Latef, A. Akter, and Md. T. Ul-Arif, "Foliar application of auxin or cytokinin can confer salinity stress tolerance in Vicia faba L", *Agronomy*, 11, 790 (2021).

[14] M. Sharma and A. Laxmi, "Jasmonates: emerging players in controlling temperature stress tolerance", *Frontiers in Plant Sci.*, 6, 1129 (2015).

[15] G. Li, C. Zhang, G. Zhang, W. Fu, B. Feng, T. Chen, S. Peng, L. Tao, and G. Fu, "Abscisic acid negatively modulates heat tolerance in rolled leaf rice by increasing leaf temperature and regulating energy homeostasis", *Rice*, 13, 18 (2020).

[16] Agnieszka Bielach, Monika Hrtyan, and Vanesa B. Tognetti, "Plants under stress: involvement of auxin and cytokinin", *Int. J. Mol. Sci.*, 18(7), 1427 (2017).

[17] A. Galieni, N. D'Ascenzo, F. Stagnari, G. Pagnani, Q. Xie, and M. Pisante, "Past and future of plant stress detection: an overview from remote sensing to positron emission tomography", *Frontiers in Plant Sci.*, 11, 609155 (2021).

[18] Z. Zhang, J. Boubin, C. Stewart, and S. Khanal, "Whole-field reinforcement learning: a fully autonomous aerial scouting method for precision agriculture", *Sensors*, 20, 6585 (2020).

[19] J. Cerro, C. C. Ulloa, A. Barrientos, and J. de L. Rivas, "Unmanned aerial vehicles in agriculture: a survey", *Agronomy*, 11, 203 (2021).

[20] H. Yin, Y. Cao, B. Marelli, X. Zeng, A. J. Mason, C. Cao, "Soil sensors and plant wearables for smart and precision agriculture," *Adv. Mat.*, 33 (2021).

[21] N. I. Hossain, T. Noushin and S. Tabassum, "Leaf-FIT: A Wearable Leaf Sensor for In-Situ and Real-Time Monitoring of Plant Phytohormones", Proceedings of the *2021 IEEE Sensors*, pp. 1-4, doi: 10.1109/SENSORS47087.2021.9639842.

[22] X. Cao, X. Zhu, S. He, X. Xu, Y. Ye, and S. Gunasekaran, "Gold nanoparticle-doped three-dimensional reduced graphene hydrogel modified electrodes for amperometric determination of indole-3-acetic acid and salicylic acid", *Nanoscale*, 11, 10247-10256 (2019).

[23] Y. -F. Wang, T. Sekine, Y. Takeda, K. Yokosawa, H. Matsui, D. Kumaki, T. Shiba, T. Nishikawa, and S. Tokito, "Fully printed PEDOT:PSS-based temperature sensor with high humidity stability for wireless healthcare monitoring", *Sci. Rep.*, 10, 2467 (2020).

[24] S. Wang, W. Deng, L. Yang, Y. Tan, Q. Xie, and S. Yao, "Copper-based metal-organic framework nanoparticles with peroxidase-like activity for sensitive colorimetric detection of staphylococcus aureus", *ACS Appl. Mater. Interfaces*, 29, 24440–24445 (2017).

CONTACT

*S. Tabassum; stabassum@uttyler.edu

POLYMER AND STAINLESS STEEL-BASED 3D MICROELECTRODE ARRAYS (3D MEAS), WITH PENTA-MODAL SENSING CAPABILITIES FOR THE INVESTIGATION OF ELECTROGNIC CELLS

Charles M. Didier[1,†], *Julia Freitas Orrico*[1,†], *Omar S. Cepeda-Torres*[1,2,†], *Aliyah Baksh*[1], *Jorge Manrique Castro*[1] *and Swaminathan Rajaraman*[1]

[1] University of Central Florida, Orlando, FL, USA, [2] Polytechnic University of Puerto Rico, San Juan, PR

[†] Equally Contributing Authors

ABSTRACT

Benchtop tissue cultures have historically provided major breakthroughs in biological research. Modern "on-a-chip" and Microphysiological Systems (MPS) demand integrated sensing/stimulation modalities, to produce complex, multiplexed datasets. To this end, novel fabrication strategies incorporating readily available materials, including polymers and steel alloys, are exciting avenues for the development of such multifunctional biosensors. Here, we showcase a Penta-Modal biosensor platform, which incorporates a transparent polymer substrate (for cellular image analysis), stainless steel (SS) 3D microelectrode array (3D MEA) structures, with an included 3D microfluidic adaptation, and both temperature and analyte sensing capabilities all on a single chip. Together, this device demonstrates the potential for a highly versatile data collection regimen, in a compact one-chip platform.

KEYWORDS

Multi-Modal Biosensor, Optical Clarity, 3D Microelectrode Array (3D MEA), Interdigitated Electrodes, Analyte Sensor, Temperature Sensor, Transmitted Light Microscopy

INTRODUCTION

In vitro organ-on-a-chip models have become one of the most exciting emerging technologies. Built at the intersection of micro/nanoengineering and cellular biology, specialized arrangements of living cells are better able to simulate physiology at the cellular, tissue and organ level **[1,2].** Recent complexities of these models demand a balance of sensing and stimulation modalities, and strategies for procuring multifaceted, long-term datasets **[1]**. This is especially relevant with respect to MPS, which integrate complex biology, various materials with advanced sensors, and require unprecedented combinatorial biological detail to evaluate *in vitro* systems (ex. brain, heart, or muscle) seamlessly in the same platform, producing more physiologically relevant datasets. 3D MEA sensors have become highly desired as advanced sensors in MPSs for obtaining electrophysiological signals from electrically active cells, networks, and complex assemblies **[3,4]**. For many MPS, 3D MEAs can form the base of the sensing/stimulation platforms on to which other sensing modalities can be integrated **[4]**.

These other modalities include potentially 2D/3D microfluidics, which may be utilized to chemically stimulate cells whose response is further monitored through transparent/optical means (transparency to enable high content assays can be thought of as another sensing modality). Additionally, temperature control and maintaining homeostasis are vital in efforts to address MPS interfacing outside of an incubator environment **[5]**. For precise control of cellular growth and health, key analyte detection would also allow for maintenance of cellular homeostasis **[6]** and could additionally be utilized in combination with 2D/3D microfluidics to detect culture health during chemical stimulation. Thus electrochemical, electrophysiological, and temperature sensing/stimulation, along with transparency and microfluidic-mediated assays allow for a ***total of five sensing/stimulation modalities*** which are achieved on a single chip **[2-9]**. Our prior work demonstrated a tri-modal, polymer 3D MEAs (*electrical, optical, and microfluidics*) **[3]**.

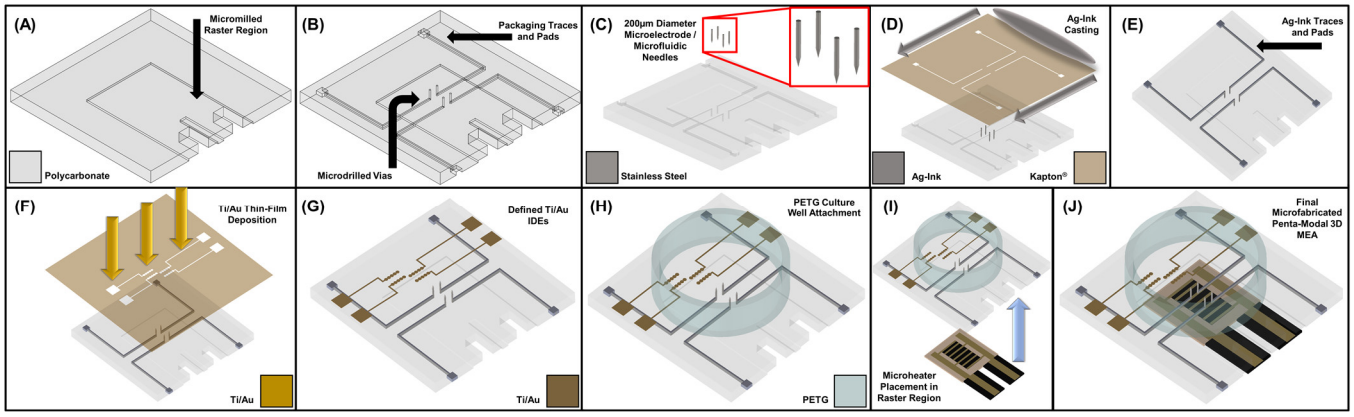

Figure 1: *Process flow schematic for the fabrication of the Penta-Modal biosensor. (A) Micromilled bulk polycarbonate (PC) with a raster-region with a thin cut-out where the microheater is to be placed. (B) Micromilling and microdrilling of packaging traces, pads, and through-vias respectively. (C) Magnetic-assisted insertion of microneedles to define the bulk 3D MEA structure. (D) Precision Silver (Ag)-ink casting of the traces, pads and vias from (C), utilizing a laser micromachined Kapton® mask. (E) Final cured Ag-ink, defining the functional packaging for the 3D MEA sensing modality. (F) Thin-film, electron beam deposition of Titanium (Ti) / Gold (Au) IDEs and contact pads, for the temperature and analyte-sensing modalities. (G) Final defined IDEs on the top surface of the polycarbonate substrate. (H) PET-G culture well attachment with 10:1 polydimethylsiloxane (PDMS). (I) Microheater placement into the raster-region on the underside of the substrate. (J) Final fabricated Penta-Modal 3D MEA biosensor platform.*

978-1-940470-04-7/HH2022/$25©2022TRF
DOI 10.31438/trf.hh2022.34

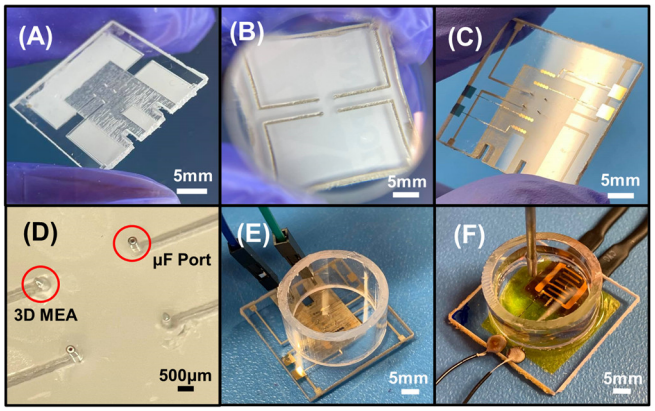

Figure 2: *Optical images detailing selected fabrication stages of the Penta-Modal biosensor from Figure 1. (A) Optical image corresponding to Figure 1B. In this image, the protective film is left partially in place to better contrast each micromilled, microdrilled, or microrastered element. (B) Optical image corresponding to Figure 1E. The cured Ag-ink is precision aligned to reside within the desired packaging traces and pads. (C) Optical image corresponding to Figure 1G. Both Ti/Au IDEs for the thermal and analyte sensor have been deposited, and ink-cast tracing leading to the inserted 3D MEAs can be observed, along with the microrastered microheater region. (D) Close-up optical image of the central device region from (C). Microfluidic (μF) ports are a facile substitution or addition to the 3D microelectrode insertion vias, and additional microfluidic ports may be added elsewhere in the culturing area. (E) Optical image of the culture well attachment fabrication step from Figure 1H. (F) Optical image of a fabricated biosensor from Figure 1J. In this image, the microheater is attached in the micro-raster-region for testing the devices' temperature sensing capabilities.*

Herein we expand this platform, by demonstrating a biosensor which additionally encompasses temperature and analyte-sensing, to provide a ***Penta-Modal Sensing Platform for Electrogenic Cellular Constructs***, towards procuring comprehensive MPS data analytics.

MATERIALS AND METHODS

A 24mm (length) by 24mm (width) by 1.75mm (thick) substrate was micromilled from bulk polycarbonate (T-Tech, USA; **Figure 1**). Within this substrate, a 300μm (length) by 300μm (width) by 300μm (depth) volume was microrastered on the back of the chip for microheater placement (**Figure 1A**). Subsequently, packaging areas were defined utilizing 1mm^2 contact pads and 200μm (width) traces (**Figure 1B**). Additionally, 220μm (diameter) by 500μm (depth) vias were microdrilled. All the micromilling/microdrilling was performed in a single step. Stainless steel (SS) needles (DBC^{TM}, South Korea; 200μm diameter) were trimmed to 1.85mm (height) and inserted utilizing magnetic insertion **[3]** to define 3D microelectrodes/microfluidic ports with a functional height of ~100μm (**Figure 1C**). Traces were defined with conductive Ag-ink (MasterBond, USA) casting before curing at 60°C for 24-hours (**Figure 1D**). A 750μm pitch circle-in-line geometry Kapton® (DuPoint, USA; 25μm thick) shadow mask was UV-laser micromachined (QuikLaze, USA) and Titanium (Ti; 100nm) / Gold (Au; 400nm) Interdigitated Electrodes (IDE) were defined through these masks with electron-beam deposition (Thermionics, USA). Next, a 16mm (inner diameter) by 5mm (height) PET-G culture well was attached with PDMS (Dow Corning, USA). A resistive micro-heater (Pelonis Technologies, USA: 1.05μA compliance/0.5-7V voltage) was subsequently affixed to the microrastered volume on the backside of the chip. IR imaging (Perfect Prime, USA) validated expected temperatures (results not shown). Full spectrum (100Hz-40MHz) impedance/phase were obtained utilizing Bode 100 (Omicron Labs, USA), for all impedance-based measurements. Root Mean Square (RMS) noise measurements were obtained using the Axion BioSystems MUSE® electrophysiological system (Axion Biosystems Inc., USA). Approximately, 1:100 dilutions of anti-L-Glutamine antibodies (Abcam, UK) were created in Dulbeccos phosphate buffered saline (Sigma, USA; DPBS). Mixed air plasma treatment (Plasma Etch, USA; 20s) was applied on analyte IDEs, prior to the deposition of 40μl of the diluted antibody, which was subsequently incubated at 22°C for 1-hour, and then removed before gentle cleaning with DPBS. A volume of 0.2-20mM L-Glutamine was utilized to assess the conjugated sensor's capabilities. Imaging of various aspects of the device was performed with Atomic Force Microscopy (AFM, Veeco, USA; tapping mode), Scanning Electron Microscopy (SEM, Zeiss, Germany), and optical imaging (iPhone XS; Apple, USA). Cell culture assays were performed utilizing C2C12 myocyte cells (ATCC, USA), with imaging occurring at 5 days *in vitro* (DIV). Cellular imaging was performed on the Keyence BZ-X810 confocal microscope (Keyence, Japan), and fluorescent live/dead confirmation staining was performed utilizing a standard Calcein AM / Propidium Iodide kit (Thermo Fisher Inc., USA).

RESULTS AND DISCUSSIONS

To achieve the "Penta-Modality" of the device, previously studied optical clarity, 3D microfluidics, and 3D microelectrode performance **[3]**, along with temperature and analyte sensing are demonstrated (**Figure 2**). 3D MEA impedance and phase sweeps (**Figure 3 A&B** respectively) were obtained across the full 10Hz-40MHz frequency spectrum utilizing electrochemical impedance spectroscopy (EIS). The biologically relevant 1kHz value, indicated an impedance of **2.76 kΩ**, and a phase signature of **-55°,** which are well within literature defined values **[9,10]**. This phase signature implies a more capacitive dominance of the circuit at the critical electrophysiologically relevant frequency of 1 kHz, however examination of the Nyquist plot for this data is necessary to precisely determine other properties of the 3D microelectrode. The averaged RMS noise before and after addition of DPBS are indicated as an inset in **Figure 3A**. The values were reduced from an average of **18.26 μV** to **7.8μV** upon addition of saline, which indicates suitability for electrophysiology due to a **<10μV** average **[9]**.

EIS was additionally utilized to assess the performance of the temperature-sensing IDE (**Figure 3 C&D**). After calibration through IR imaging confirmation (data not shown), temperature variations were assessed utilizing the attached microheater to vary DPBS temperatures. For the characterization of the thermal IDE sensor, previous impedance studies indicated that the solution resistances (R_s) and charge transfer resistances (R_{ct}) are more prevalent at higher frequencies, along with some impact at the at lower frequencies **[9,10]**. Lower frequencies however are often impacted by environmental noises, leading to necessarily complex post-processing to interpret data. Thus, higher frequencies would produce reliable physiologically relevant temperature change metrics across the room temperature to physiological range (22°C-42°C) tested. Decreases in impedance were expected due to increased ionic species motility in the saline solution when subject to higher temperatures. This would also be expected in salt-containing cell culture-media. If temperatures of interest were much higher, then an rapid increase in impedance would be expected due to increased concentrations of ionic species, resulting from evaporative effects. Performing ΔR/R analysis of the high frequency

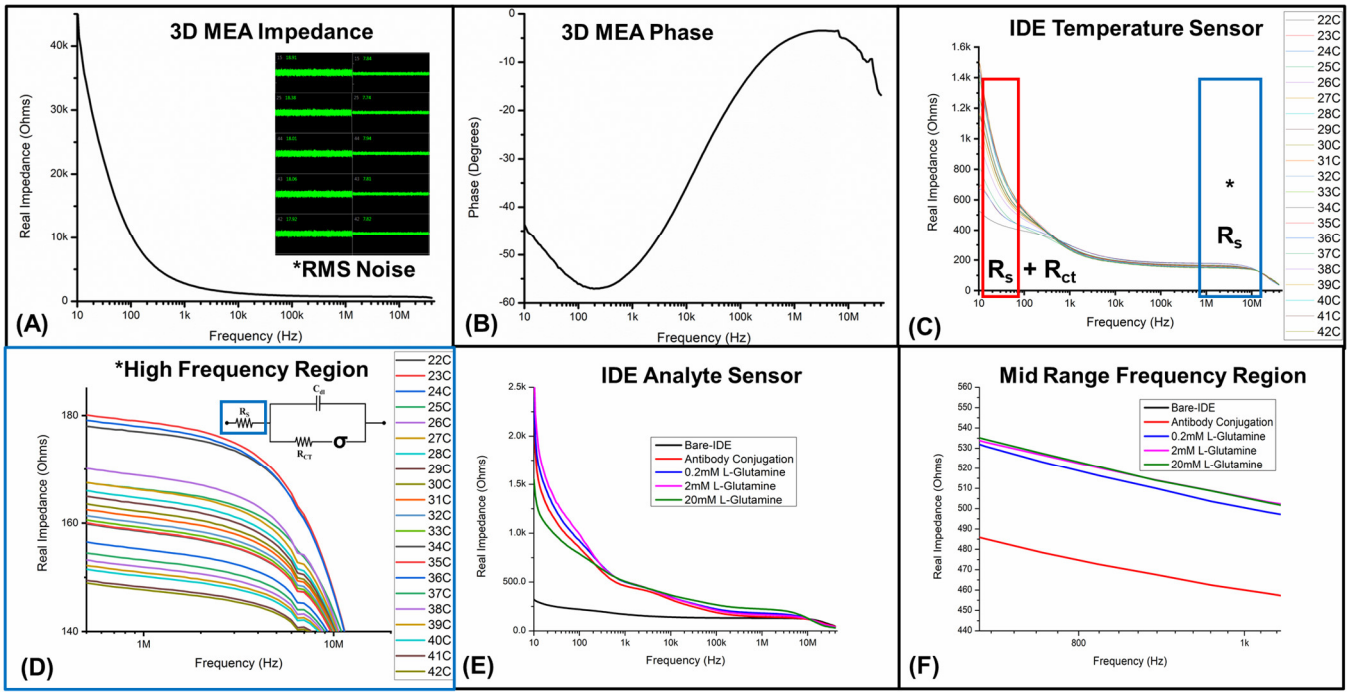

Figure 3: *Electrical impedance-based characterization of the 3D MEA, temperature, and analyte IDE sensors. (A&B) Full spectrum impedance and phase measurements of the 3D MEA structures. The 1kHz impedance of* ***2.76 kΩ****, and a phase signature of* ***-55°*** *are well within literature defined values* ***[9,10]****. (C&D) Impedance-based characterization of the temperature sensing IDE, utilizing the attached microheater to vary DPBS temperatures. (E&F) Impedance-based characterization of the analyte-sensing IDE. 1kHz impedance readings illustrate an increase as expected due to the added components atop the IDE.*

regions allowed for a better examination of impedance trends, to address if this hypothesis would hold true. A reliable trend was observed from the regression value of R^2***=0.975*** across all temperatures and illustrated a linear decrease of these impedance values at higher frequencies (1-10MHz) **[9,10]** across the physiologically relevant (**22°C-42°C**) temperatures. ΔR/R analysis for the aforementioned low frequency region were also assessed in a similar manner, however, the observed regression value (R^2***=0.660***) confirmed the unsuitability of the lower frequencies (10Hz-500Hz) for temperature sensing. These results serve to validate the utilization of the IDE sensor at higher frequencies, as a method for temperature sensing in the penta-modal 3D MEA platform. The relative success of the sensors performance for temperature applications near room temperature, it should be noted, did deviate slightly from expected results. Contextually however, the irregular temperature readings did occur near "room temperature" (22°C-25°C), which are less relevant for maintaining cellular homeostasis, and may be addressed through adjustments to sensitivity in future iterations. Additionally, creation of a calibration curve for this sensor would enable for software corrections in practical applications, as a strictly impedimetric reading serves as proof of its utility for potential signal differentiation.

Similarly, for analyte-sensing IDEs, impedance spectroscopy could be utilized to detect differential readings as the conjugation state of the sensor was adjusted (**Figure 3 E&F**). For sensing biologically relevant analytes, we determined that mid-range frequencies (600Hz-1.1kHz) exhibited the potential for reliable recordings. While the frequency of interest may vary in analyte detection **[11]**, our impedance readings around the 1kHz frequency for the chosen application, exhibited an increase in impedance. This was expected due to biological conjugation atop the IDE, which led to a modified capacitance value **[12]**. The double layer capacitance (C_{DL}) of the electrode system is expected to heavily impact the overall impedance values expressed around 1kHz **[9]**, and this should in fact be mirrored by a decrease in the phase values. Both of these trends were observed. Regression values from the ΔR/R plot, and the calculated R^2***=0.822*** provides an affirmative indication of its effectiveness. Of note, the 2mM and 20mM L-Glutamine concentrations appeared to potentially have reached the saturation point of this sensor ability to detect the antibody assay, which could be improved through conjugation chemistries, and/or adjustments in antibody solution concentration.

Figure 4 contains the SEM, AFM imaging of the IDE conjugation state and cells imaged on the Penta-Modal MEA. SEM image of the Ti/Au IDE along with a 3D microelectrode of the assembled device from **Figure 1J,** can be observed in **Figure 4A**. The enhanced SEM image in **Figure 4B** details the presence of conjugated antibodies on the Au IDE surface. **Figure 4C** is an AFM image of the unconjugated surface, which has a minimal surface roughness (**<12nm**) due to solely the evaporated metal. This is contrasted with **Figure 4D** which contains the conjugated antibodies. Larger roughness (**<66nm**) can be observed in this image, illustrating the functionalization of the IDE surface. However, this image additionally shows how a simple plasma treatment regimen can be used to avoid complex conjugation chemistries. **Figure 4 E-G** contains the optical and fluorescent imaging of C2C12 myocyte cells on the device at 5 days *in vitro* (DIV), demonstrating the optical clarity of the device. Calcein AM, and Propidium Iodide were utilized for live/dead cell viability, and to validate the transparency of the device for fluorescent imaging.

CONCLUSIONS

In this work, we demonstrated a combinatorial approach to the realization of a penta-modal biosensor for the investigation of electrogenic cells. We incorporated the capabilities for electrophysiology (through 3D MEA integration), optical

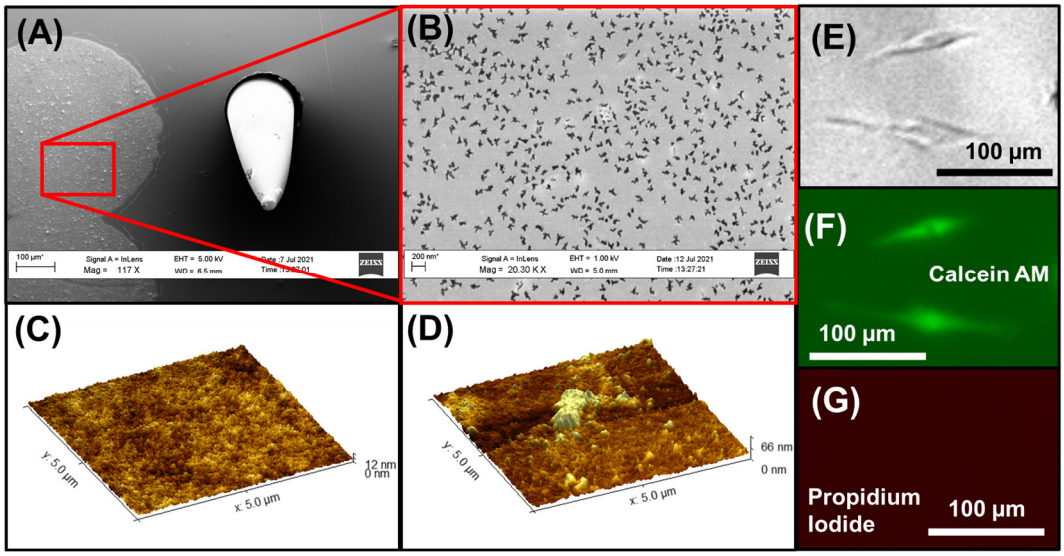

Figure 4: *Atomic Force Microscopy (AFM), Scanning Electron Microscopy (SEM), and fluorescent imaging of various parts of the device and cell assay. (A) SEM image of the Ti/Au IDE along with a 3D microelectrode of the assembled device from Figure 1J. (B) Enhanced SEM image of the conjugated antibodies on the Au IDE surface. (C&D) AFM images of the IDE showing the unconjugated surface of the IDE (C), which has a minimal surface roughness (**<12nm**) due to the evaporated metal. This is contrasted with (D) which contains the conjugated antibodies. Larger roughness (**<66nm**) can be observed in this image, illustrating the functionalization of the IDE surface. (E-G) Optical and fluorescent imaging of C2C12 myocyte cells on the device at 5 DIV, demonstrating the optical clarity of the device. (E) Optical imaging of the cells. (F) Calcein AM, live staining of the cells. (G) Propidium Iodide stain, for live/dead cell confirmation.*

interrogation (transparency), and microfluidic perfusion as established previously, and additionally enabled temperature and analyte sensing capabilities through impedimetric analysis of integrated IDEs on chip. Here, the 3D MEAs demonstrated comparable 1kHz performance and RMS noise to other devices reported in literature, and an alternate fabrication scheme to integrate microfluidic ports into the device were shown. The temperature sensor IDE successfully demonstrated the ability to sense different temperatures across the 22°C-42°C range, by utilizing higher frequency impedimetric analysis. An analyte sensing IDE was additionally demonstrated by utilizing a simple plasma-enhanced antibody conjugation protocol. Different concentrations of L-Glutamine were then sensed using the mid-frequency range from an impedance sweep. Finally, C2C12 myocytes were grown and imaged through the device, utilizing both optical and fluorescent means.

ACKNOWLEDGEMENTS

The authors would like to acknowledge funding provided through NIH UG3TR003150 grant, NSF EEC 2050266 (NSF REU O. S. Cepeda-Torres) and UCF ORC Doctoral Fellowship (C. M. Didier).

REFERENCES

[1] W. Anderson et al., *"Advances in 3D neuronal microphysiological systems: towards a functional nervous system on a chip,"* In Vitro Cellular & Developmental Biology-Animal, 2021.

[2] Q. Wu, et al. *"Organ-on-a-chip: Recent breakthroughs and future prospects,"* Biomedical engineering online, 2020.

[3] J. Freitas Orrico, et al. *"Fabrication and Characterization of 3D Microelectrode Arrays (3D MEAS) with Tri-Modal (Electrical, Optical, and Microfluidic) Interrogation of Electrogenic Cell Constructs,"* 21st International Conference on Solid-State Sensors, Actuators and Microsystems (Transducers), 2021.

[4] C. Didier, et al. *"Development of in vitro 2D and 3D microelectrode arrays and their role in advancing biomedical research,"* Journal of Micromechanics and Microengineering, 2020.

[5] D. Nieto, et al. *"Laser microfabrication of a microheater chip for cell culture outside a cell incubator,"* Colloids and Surfaces B: Biointerfaces, 2017.

[6] M. Kondzior, et al. *"Antibody-electroactive probe conjugates based electrochemical immunosensors,"* Sensors, 2014.

[7] N. Rusli, et al. *"Miniaturized Electrochemical Device for In-Situ Monitoring of Glucose, Lactate, Dissolved Oxygen, PH, and Temperature in Yeast Culture,"* 21st International Conference on Solid-State Sensors, Actuators and Microsystems (Transducers). IEEE, 2021.

[8] A. Baldwin, et al. *"An electrochemical impedance-based thermal flow sensor for physiological fluids,"* Journal of Microelectromechanical Systems, 2016.

[9] D. Borkholder. *"Cell-based biosensors using microelectrodes,"* Stanford University Thesis, 1999.

[10] S. Rajaraman. *"Micromachined three-dimensional electrode arrays for in-vitro and in-vivo electrogenic cellular networks,"* Georgia Institute of Technology Thesis, 2009.

[11] M. Strong, et al. *"Faradaic electrochemical impedance spectroscopy for enhanced analyte detection in diagnostics,"* Biosensors and Bioelectronics, 2021.

[12] S. MacKay, et al. *"Using impedance measurements to characterize surface modified with gold nanoparticles,"* Sensors, 2017.

CONTACT

*Swaminathan Rajaraman, tel: +1-407-823-4339; Swaminathan.Rajaraman@ucf.edu

PROGRAMMABLE MAGNETIC ROBOT (PROMAGBOT) FOR AUTOMATED NUCLEIC ACID EXTRACTION AT THE POINT OF NEED

Anthony J. Politza, Tianyi Liu, and Weihua Guan[*]
The Pennsylvania State University, University Park, Pennsylvania, USA

ABSTRACT

For numerous diseases across the globe, nucleic acid testing remains the clinical standard. However, there is a need for these methods to be field deployable. Recent improvements in optical detection and isothermal amplification have pushed POCT devices closer to laboratory standards. However, sample preparation remains a bottleneck that has not seen improvements. Here we present an automated device using paramagnetic beads for nucleic acid extraction in under 10 minutes. Linking our device with microfluidics creates a system that is fully automated, user-friendly, ultra-portable, notably accessible, and sample adaptable.

KEYWORDS

POCT; Electromagnet; Magneto-fluidic; Nucleic Acid Extraction; Sample Preparation

INTRODUCTION

Nucleic acid testing (NAT) remains the clinical standard for identifying and quantifying infectious diseases[1]. However, the laboratory procedures for these methods require long waiting periods, trained staff, and expensive hardware to analyze the testing results [2]. Point-of-care (POC) devices introduce NAT in low-resource regions by simplifying the steps into compact and portable form-factors [2, 3]. However, recent developments have improved amplification and detection methods to be better suited in low-resource areas[4-6]. While necessary, complete NAT contains a bottleneck for point-of-need testing: sample preparation. Standard methods require extensive manual processes, laboratory devices, toxic chemicals, and trained professionals. These issues severely limit the scope of POC devices when providing quality NAT. Numerous sample preparation systems for laboratories, lab-on-chip systems, and some POC devices depend on silica columns, membranes, or organic solvents. An alternative, silica coated paramagnetic beads (PMBs), offer a solution by eliminating the need for noxious chemicals and simplifying device complexity.

Devices that take advantage of PMBs for POCT applications include bead control through permanent magnets, electromagnet (EM) controls, EM actuated magnets, centrifuge style rotation, automated pipetting, and fluid flow methods [7, 8]. While effectively integrating PMBs into their system, these devices still lack practical applications to field deployment and are only capable of single style extraction. This gap creates the need for a fully automated, user-friendly, ultra-portable, notably accessible, and sample adaptable device system.

This work demonstrates a programmable magnetic robot (ProMagBot) capable of automated nucleic acid extraction. The entire ProMagBot system can be utilized in areas of low resources for nucleic acid extraction of multiple sample mediums in under 10 minutes.

RESULTS & DISCUSSION

ProMagBot Overall Device Design

As seen in **Figure 1a,** the ProMagBot system is composed of multiple parts: (from top to bottom) the top casing, camera, light guide, user interfacing features, the Raspberry Pi 4, a spacer and viewing window, the electromagnetic PCB, the bottom casing, microfluidic cartridge, and the compact battery. Overall, the project can be divided into three subcategories: A computer vision system (**Figure 1b**), microfluidic cartridge (**Figure 1c**), and an electromagnetic PCB paired with a permanent magnet (**Figure 1d**). Locating a permanent magnet above electromagnetic coils allows this device to employ a novel magnet-on-top (Mag-On-Top) approach to magneto-microfluidic separation of nucleic acids. Computer-aided tracking of the permanent magnet within the electromagnetic coil array provides rigidity to the magnet pathway. It allows for redundancies in motion that are lacking in other forms of magnet actuation in POCT devices.

User interaction with the device follows the steps highlighted in **Figure 2**. First, the user collects the sample off chip and transfers it to a collection tube. Using a one hundred µL pipette, the user transfers the lysate mixture into the microfluidic cartridge. Then, the user can power on the device. Once on, the device will initiate a bootup sequence, and when ready, indication LEDs will flash. The device will run for 8-10 minutes. The device will signal when the extraction is complete using the indicator lights. Then, the user removes the cartridge from the device. Lastly, the eluted nucleic acids can be removed from the cartridge.

Microfluidic Cartridge Design

For the ProMagBot system, a three-layered microfluidic cartridge is utilized to separate, contain, and encompass the extraction solutions. This cartridge is designed to bind the PMBs assay to nucleic acids in the lysis chamber. In part one of this step, the lysis buffer adds detergents and surfactants to the sample to break down cells, bacteria, and viral particles (**Figure 3i**). In part two, the binding buffer adds chaotropic salts and decreases the pH of the solution to an ideal condition for nucleic acids to bind with the silica PMBs. The permanent magnet located vertically above the cartridge will help in this mixing process before dragging the nucleic acid-bead complexes (NABC) through the first of the oil valves into the washing chamber. In this chamber, the solution gradually increases pH. It includes other non-toxic chemicals to help remove unwanted proteins and salts (**Figure 3ii**). The magbot will encourage mixing and then move the NABC to the elution chamber. Here the pH level of the solution is significantly higher than the starting solution to reverse the binding process. In a basic environment, the nucleic acids dissociate from the PMBs, which can then be removed via a magnet (**Figure 3iii**). The remaining solution in the elution chamber is a concentrated batch of nucleic acids ready for extraction by the user.

Electromagnetic PCB Design

One advantage of the ProMagBot system is running off a compact battery. The ProMagBot device contains Groups and Blocks of electromagnetic coils that are actuated in series to accomplish this. First, this creates stepwise coils that can be used sequentially to move a magnet in one direction or another. Second, this significantly reduces the complexity of the device's electrical components by removing the need for a multiplexer. Using six MOSFET switches, the device contains 4 directions of motion (±x,±y). In **Figure 4a**, the coil layout is visualized for both the X and Y directions.

In either direction, a Block containing three separate coils also belongs to a unique Group. Blocks repeat seven times in both X and Y directions, while Groups remain linked together through the PCB. When one Group activates, all coils within that Group and Block

978-1-940470-04-7/HH2022/$25©2022TRF
DOI 10.31438/trf.hh2022.35

activate as well. In this manner, the permanent magnet position is defined as: ($X_{i,j}$, $Y_{m,n}$), where X signifies the X-direction Blocks and Groups, *i* ranges from 1 to 7 (# of repeated Blocks), and *j* represents the Group number from 1 to 3. Similarly, Y signifies the Y-direction Blocks and Groups, where *m* represents the Block number from 1 to 7, and *n* demonstrates the Group number from 1 to 3. For any given moment, along any given pathway, the magbot is defined in both the X and Y direction by the Block and Group that last attracted it.

Figure 4b demonstrates how the permanent magnet moves by stepwise motion. In these images, the magbot starts aligned with coils X-Group-2 and Y-Group-2. The previous Y-Direction coil switches off, and the next coil powers on to move the magnet one step down. Ergo, in Step-1, X-Group-2 remains on, the Y-Group changes, and Group-3 is now powered. Likewise, for Steps 2 & 3, the X-Group coils are manipulated identically to move the magnet along the X-Direction. In Step-3, it is critical to note that the magnet moves upward to realign with Y-Group-2. By these methods, the power efficiency of the ProMagBot is kept to a minimum. It allows the device to remain equipment-free and deliverable to low-resource areas because of its internal battery.

Computer Vision-based Control

One drawback to our Block and Group setup of electromagnetic coils is that there are no internal referencing mechanisms to ensure that the magbot is located where the control program assumes. To solve this problem, we have implemented a computer vision algorithm to control the magbot. The algorithm analyzes the magbot position after each motion step and compares that against the preplanned pathway points. Three unique pathways were defined, demonstrating that the algorithm can integrate with the EM coils. The magbot sequentially moves to each defined point by the computer vision program. These pathways in **Figures 5a, b, and c**, exaggerate movement in the four cardinal directions. From these demonstrations, it is clear to visualize that the magbot is capable of movement in any direction and has the potential to follow any programmable pathway.

CONCLUSION

To summarize, our ProMagBot system can extract nucleic acids in under 10 minutes while also remaining well suited for low-resource areas. Silica-coated paramagnetic beads (PMBs) are used within the lab-on-chip cartridge to bind nucleic acids after sample lysis. The cartridge contains the chemical chambers and volumes needed, encloses all liquids, and separates the solutions using oil valves. These features create a stable and robust cartridge that is portable, easy to handle, and user-friendly. The ProMagBot device completes the nucleic acid extraction by pulling the PMBs through oil valves into washing and elution chambers that purify the nucleic acids. When the magbot moves away from the central microfluidic channel, the PMBs are relieved from the magnetic field and then passively precipitate. Thus, increasing the mixing inside the chamber compared to other devices. The device utilizes a 2D array of EM coils for magbot movement in X and Y directions. Using the 2D EM coils coupled to a computer vision control algorithm, the pathway for movement is adaptable and programmable for the magbot (ProMagBot). While the EM coils provide movement in X and Y directions, the computer vision algorithm adds tracking redundancy to movement. Also, power consumption is minimized, and multiple extraction runs operate off one compact battery. Overall, the ProMagBot device is a highly streamlined setup capable of nucleic acid extraction. ProMagBot minimizes user interference, increases usability, broadens accessibility, expands convenience, and embraces accommodation.

MATERIALS & METHODS

Microfluidic Cartridge

Inside the microfluidic cartridge, there are four separate components. The three main chambers house the lysate mixed and loaded from the user, 80 (µL) of washing buffer, and 30 (µL) of elution buffer (Invitrogen ChargeSwitch Kit). The last remaining component is mineral oil (80 µL x2) that separates the chambers, sourced from Sigma Aldrich. The cartridge itself is composed of three stacked layers: base, channel spacer, and cover. These layers are 1/32”, 1/16”, and 1/32” thick polymethyl methacrylate (PMMA) purchased from E-Plastics.com and bonded together using a chemical solvent. These layers were designed using PTC Creo and then laser-cut using a VLS3.60DT machine from Universal Laser Systems.

ProMagBot device and EM control board

All components of the ProMagBot device mount within a 3D printed case made of ABS plastic sourced from MakerBot.com. The case, spacers, and viewing windows were modeled using PTC Creo. The magnetic robot is a permanent magnet, 0.25” in diameter, with a magnet density of N50. All electronic components such as the indication LEDs, pushbuttons, switches, or connectors were purchased from Digikey.com. The Zippy Compact battery and connectors to match were purchased from HobbyKing.com. The Raspberry Pi 4 and Pi Camera module v2 were purchased from Canakit.com. The EM PCB was custom designed using Autodesk Eagle and then fabricated by OshPark.com.

Computer Vision module

Computer vision and magnetic robot tracking were created using a Raspberry Pi camera module v2 paired with a Raspberry Pi 4. The module mounts 3.5 in. away from the magnetic robot and stage. The stage illuminates from light created by two 120-degree wide-angle LEDs inside a light guide (Digikey.com). The image capturing and magnetic robot detection automatically operates by a custom Python script on the Pi 4 using built-in and OpenCV libraries.

Data analysis method and statistics

All statistical analysis was computed using MATLAB R2020. Data processing was managed within MATLAB, with plots generated as well.

ACKNOWLEDGEMENTS

Funding for this work comes from the National Institutes of Health (R61AI147419), the National Science Foundation (1902503; 1912410; 2045169), and the Pennsylvania State University (CoB Seed). Any opinions, findings, conclusions, or recommendations expressed in this work are those of the authors and do not necessarily reflect the views of the National Institutes of Health and National Science Foundation.

CONTACT

*Weihua Guan, tell: +1-814-867-5748; wzg111@psu.edu

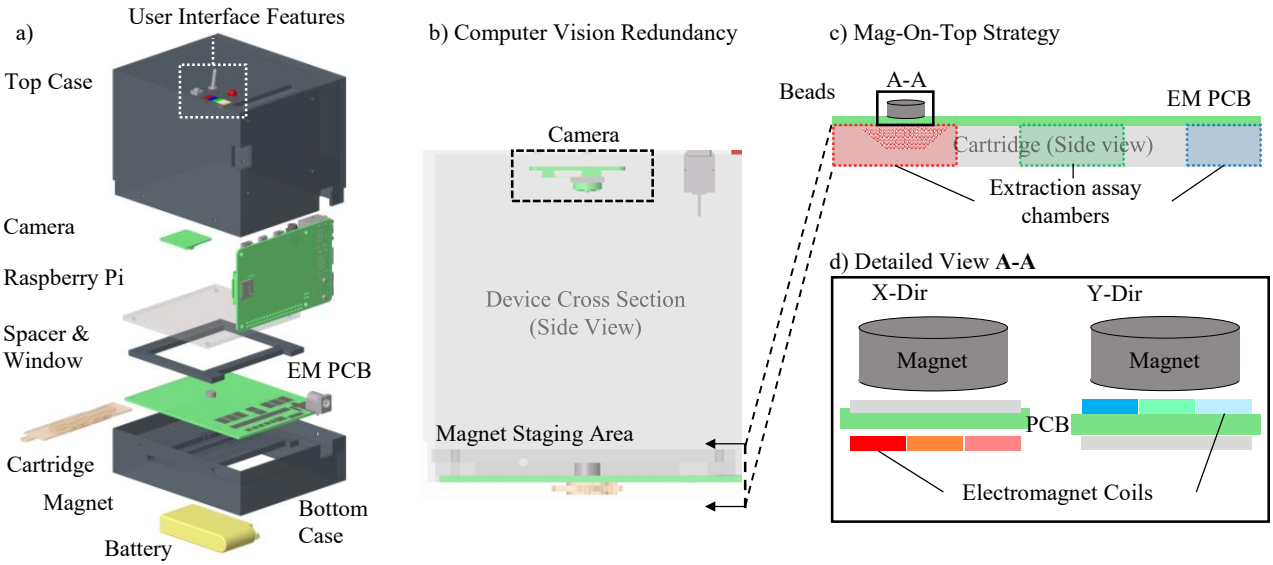

Figure 1. Modeling images of the overall device schematic and the associated internal subsections. a) 3D modeled view of the device highlight all internal components. b) device cross section that demonstrates the geometry setup for the computer vision module and staging area. c) Side view of the microfluidic cartridge to establish the physical relationship between the magnetic robot, PCB, and PMBs. d) Detailed view of the specific geometry of the EM PCB where coils are located on top and bottom of the board.

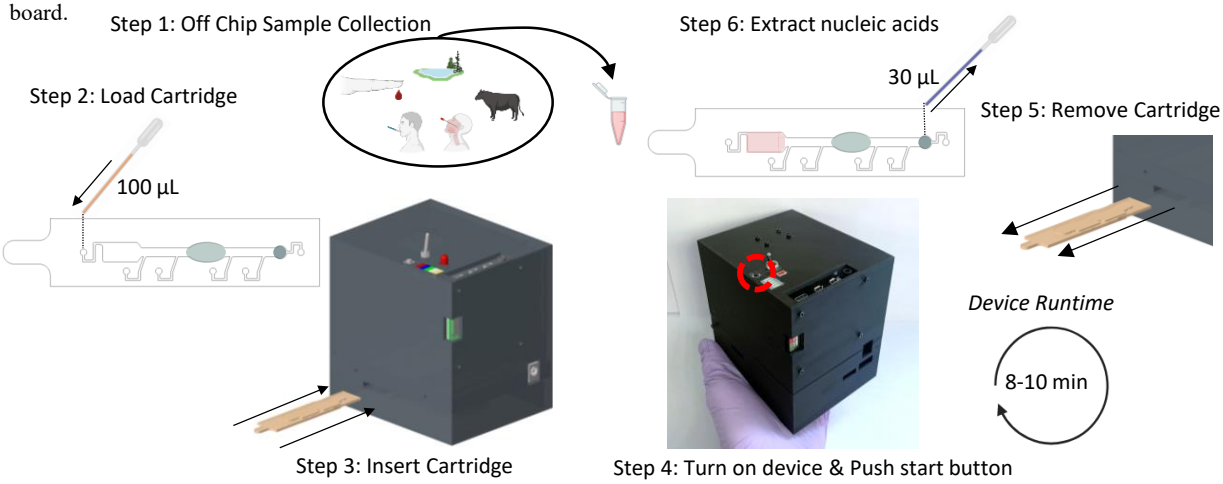

Figure 2. Device workflow from start to finish highlighting users input of sample collection to an output of eluted nucleic acids. Any manually required steps are straight forward and keep the device user-friendly.

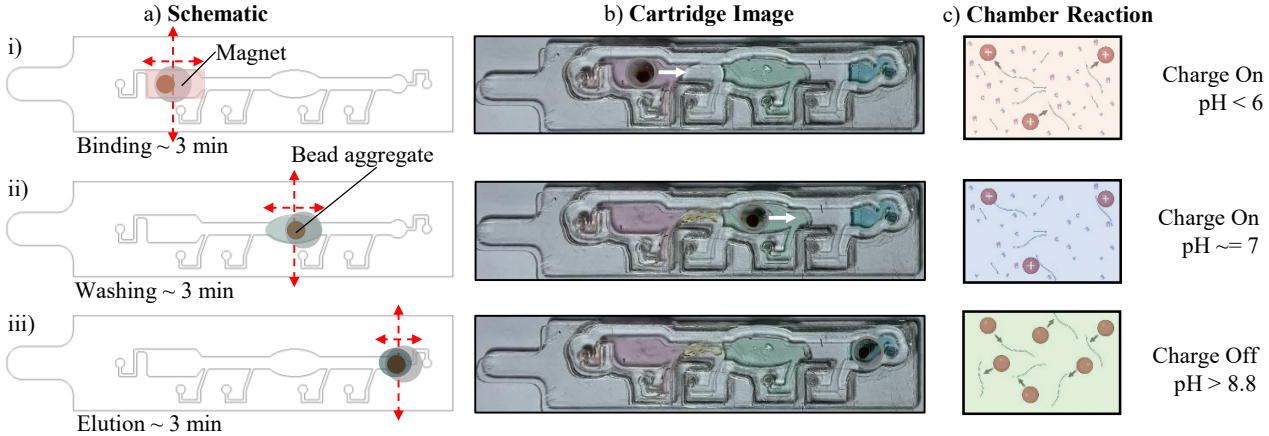

Figure 3. Schematic overview of the magnet pathway during microfluidic cartridge extraction. a) Illustrated pathway that the magnetic robot will follow during each mixing chamber. b) Captured images of the microfluidic cartridge with beads inside that are moved along by manual magnetic robot movement. c) Chemical reaction diagrams of the charge switchable beads. i, ii, and iii) correspond to the PMBs and magnetic robot aligned with the three solution chambers for lysing, washing, and elution.

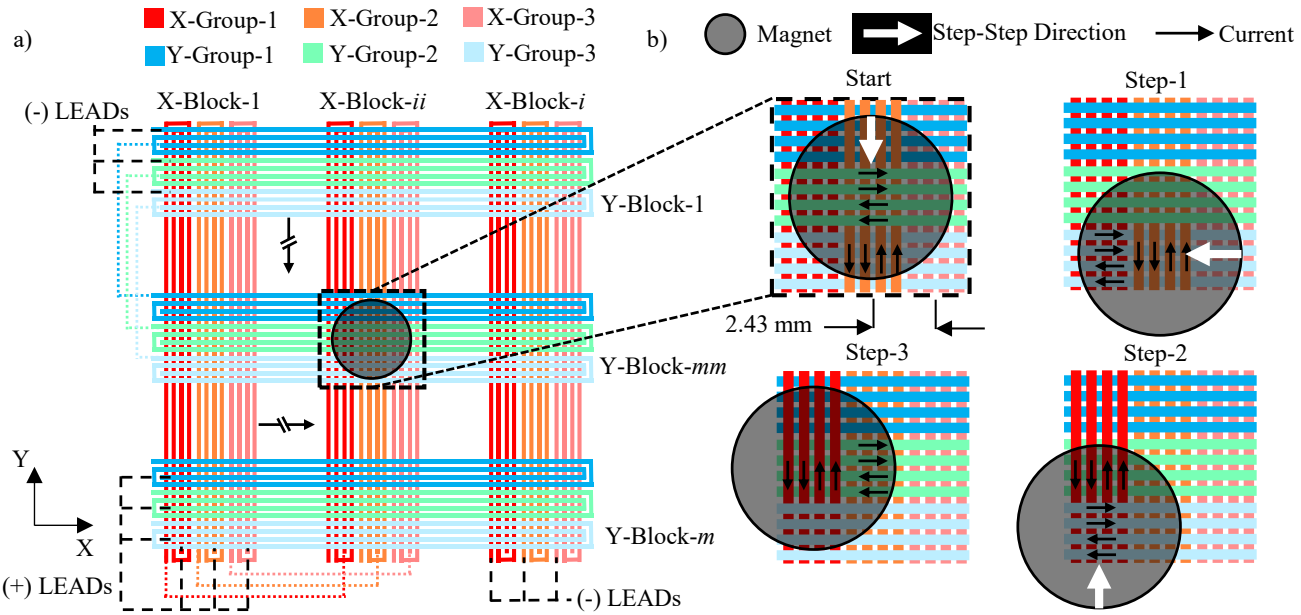

Figure 3. Overall schematic of the electromagnetic coils that appear on the ProMagBot PCB. a) Electromagnetic coil diagram highlighting the coil geometry on the PCB board. b) Enhanced view of the magnetic robot interaction with current induced coils. Shown from Start to Step-3, the magnetic robot can be moved up, down, left, right or vice versa.

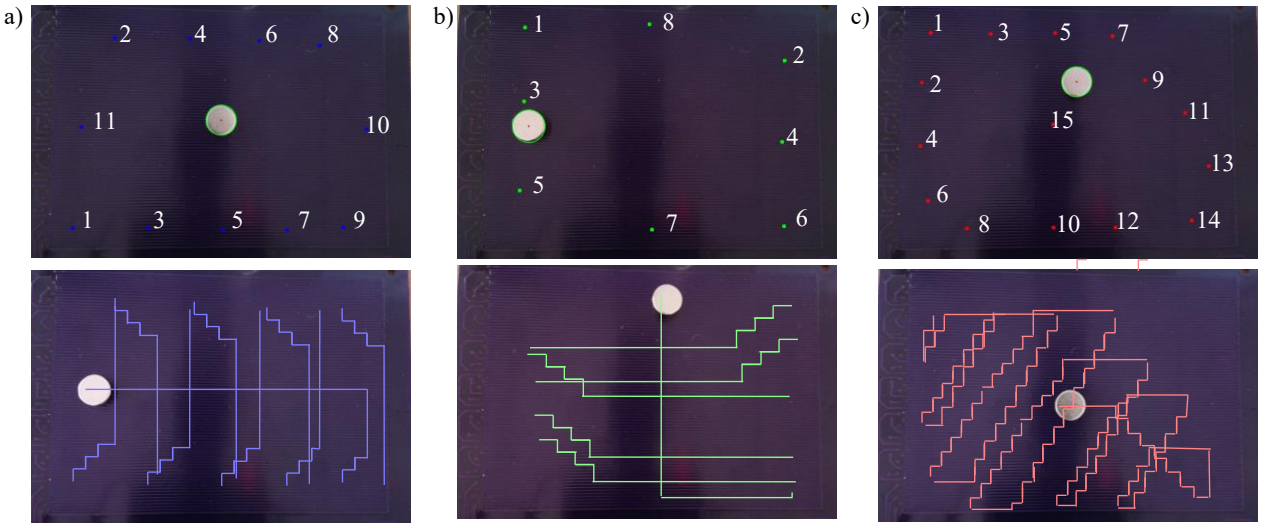

Figure 4. Pictures from device camera representing potential pathways for the magnetic robot to travel. a) ,b) and c) all show images of the magnetic robot traveling along various sinusoidal pathways.

REFERENCES

[1] A. Niemz, T. M. Ferguson, and D. S. Boyle, "Point-of-care nucleic acid testing for infectious diseases," *Trends in biotechnology,* vol. 29, no. 5, pp. 240-250, 2011.

[2] L. Zhang, B. Ding, Q. Chen, Q. Feng, L. Lin, and J. Sun, "Point-of-care-testing of nucleic acids by microfluidics," *TrAC Trends in Analytical Chemistry,* vol. 94, pp. 106-116, 2017.

[3] Y. Zhang, and N.-T. Nguyen, "Magnetic digital microfluidics–a review," *Lab on a Chip,* vol. 17, no. 6, pp. 994-1008, 2017.

[4] J. Park, D. H. Han, and J.-K. Park, "Towards practical sample preparation in point-of-care testing: user-friendly microfluidic devices," *Lab on a Chip,* vol. 20, no. 7, pp. 1191-1203, 2020.

[5] W. Jung, J. Han, J.-W. Choi, and C. H. Ahn, "Point-of-care testing (POCT) diagnostic systems using microfluidic lab-on-a-chip technologies," *Microelectronic Engineering,* vol. 132, pp. 46-57, 2015.

[6] P. Craw, and W. Balachandran, "Isothermal nucleic acid amplification technologies for point-of-care diagnostics: a critical review," *Lab on a Chip,* vol. 12, no. 14, pp. 2469-2486, 2012.

[7] S. M. Azimi, G. Nixon, J. Ahern, and W. Balachandran, "A magnetic bead-based DNA extraction and purification microfluidic device," *Microfluidics and nanofluidics,* vol. 11, no. 2, pp. 157-165, 2011.

[8] S. M. Berry, A. J. LaVanway, H. M. Pezzi, D. J. Guckenberger, M. A. Anderson, J. M. Loeb, and D. J. Beebe, "HIV viral RNA extraction in wax immiscible filtration assisted by surface tension (IFAST) devices," *The Journal of Molecular Diagnostics,* vol. 16, no. 3, pp. 297-304, 2014.

SOFT INJECTABLES USING SMART THREADS FOR DOSE-CONTROLLED DRUG DELIVERY

Mossab K. Alsaedi[1,2], Riddha Das[1,3], Hojatollah Rezaei Nejad[1,3], Atul Sharma[1,3], and Sameer Sonkusale[1,2,3,4]*
[1]Nano Lab, Advanced Technology Laboratory, Tufts University, Medford, Massachusetts, USA
[2]Department of Chemical and Biological Engineering, Tufts University, Medford, Massachusetts, USA
[3]Department of Electrical and Computer Engineering, Tufts University, Medford, Massachusetts, USA
and [4]Department of Biomedical Engineering, Tufts University, Medford, Massachusetts, USA

ABSTRACT

Transdermal drug delivery is a promising alternative to conventional drug delivery approaches, such as oral ingestion and hypodermic injection. Hypodermic injections are often painful, and oral ingestion of drugs requires the administration of doses higher than the needed to compensate for enzymatic degradation and poor absorption of drugs. Current transdermal drug-delivery platforms include microneedles, which resolve the pain aspect of conventional drug delivery approaches. However, microneedle patches are impractical as they are easily peeled off with motion and sweat. In this study, we propose soft injectables comprised of sutures that are loaded with drugs for painless and localized sustained drug delivery in the dermis layer of the skin. They stay in place during the course of delivery and are suitable for any skin type.

KEYWORDS

Transdermal drug delivery, smart threads, sutures, injectables, chemotherapy, implants, drug delivery.

INTRODUCTION

Oral administration of drugs often results in poor absorption and suffers from enzymatic degradation in the liver or the GI tract that reduces their efficacy [1,2]. The alternative is a painful injection using hypodermic needles. Transdermal delivery using microneedles offers a relatively painless route of drug delivery through interstitial fluid, where the release of drugs can be sustained over long periods of time and tuned through size, number, and matrix composition of microneedles [2,3] (Figure 1). However, microneedles can still cause skin inflammation, may not penetrate reliably in all skin types, are prone to breakage, and can peel off due to sweating or motion, which makes them highly unreliable for drug delivery. We propose *soft injectables,* which are drug-loaded sutures for drug delivery through the interstitial fluid. Like microneedles, they are painless, as they are injected in the dermis layer of skin using fine needles. Unlike microneedles however, they are not prone to being peeled off with motion or by sweating and do not cause inflammation as they are realized using medical-grade sutures as substrates. Use of threads for drug delivery in the context of wound healing [1] and as sutures [4,5] was investigated by our group, and by others [6], however they were not used as injectables. Soft injectables using threads provide precise control over drug quantity by simply controlling their lengths. While transdermal applications have been proposed, threads can also be implanted in deeper organs/tissues as implants.

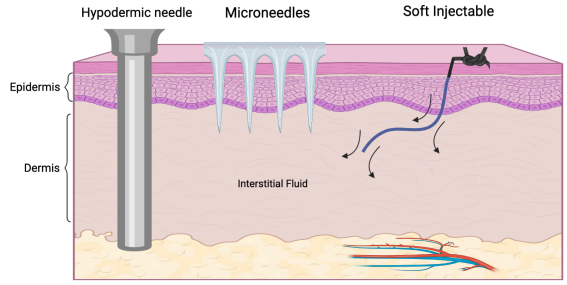

Figure 1. Illustration and comparison of transdermal (microneedles and injectable) and dermal drug delivery platforms.

In this study, we introduce a new class of thread-based injectables for dose-controlled drug delivery demonstrated by using rhodamine B (model dye) and *in-vitro* experiments with 5-Fluorouracil (5-FU), which is a cancer drug, and studying its release on cancer cells.

APPROACH

The approach uses natural wetting of threads to load the drugs onto them. Threads are made of multiple fibers that are combined and woven together. These fibers can be natural fibers, such as silk and cotton, or synthetic ones, such as polyester and nylon [7]. Hydrophilicity and wettability are two important properties of threads when it comes to drug loading. Different surface chemistries and structural morphologies of threads result in their varying wettability degrees [7]. Therefore, surface plasma treatment (surface oxidation) is used to increase threads' wettability and hydrophilicity [7]. Furthermore, the uniformity of a thread's surface allows for more precise wetting [8]. In addition to selecting the thread with the appropriate surface uniformity and wettability, the length of the thread can also be controlled to control amount of drug loaded and released.

A drug-loaded, thread soft injectable can be administered in different ways. It can be inserted through a catheter tube after the tube reaches the desired depth. It can also be sutured in through the skin using a fine surgical needle, keeping part of it on the surface of the skin to hold the injectable in place. Because these injectables are soft and flexible, they would be less painful and more stable when kept in place during the course of drug delivery compared to rigid microneedles. The microneedles, being rigid patches on the surface of the skin, do not conform to the soft and flexible nature of the skin and the underlying tissue.

We propose the use of the soft injectables for delivery of 5-FU, which is a common drug that is used to treat a wide range of cancers, including breast cancer and aerodigestive-tract cancers, and is administered intravenously [9]. It is converted to active metabolites upon entering a cell. Its cytotoxicity is attributed to the active metabolites' hindering RNA synthesis and inhibiting thymidylate synthase enzymes in cancer cells [9]. In our case, 5-FU can be delivered to cancer tumors, such as skin cancer, through drug-loaded injectable threads rather than the more invasive intravenous approach or painful microneedles.

EXPERIMENTAL METHODS

Drug loading onto medical-grade threads

First, we evaluated the drug-loading capacity of different

978-1-940470-04-7/HH2022/$25©2022TRF
DOI 10.31438/trf.hh2022.36

Solid-State Sensors, Actuators, and Microsystems Workshop
Hilton Head Island, South Carolina, June 5-9, 2022

available thread type: polyester threads, cotton threads, polyester sutures, and Polysorb™ sutures. Specifically, the wet and dry weights of threads were compared. All threads were first plasma treated for 10 minutes. Then, they were weighed before being submerged in deionized (DI) water overnight. The threads are then weighed again after being in water overnight. Difference in weight before and after submerging threads in water is then calculated to generate the bar chart in Fig. 2.

Visual monitoring of drug release from thread

To visualize drug-release mechanism into biological tissue, we visually monitored the diffusion of rhodamine B from a polyester suture into an agarose gel. A 2-cm polyester suture was plasma treated for 10 minutes then submerged in a 1 mg/mL rhodamine B-DI water solution overnight. The suture is then dried in ambient air for at least 6 hours. Once the suture is dry, it is inserted in an agarose gel (2% w/v agarose in 1X phosphate-buffered saline (PBS)). Images of the agarose gel are taken at 0, 5, and 10 minutes from inserting the suture (Fig. 3).

Dose-controlled release of 5-Fluorouracil from sutures

We evaluated the total drug release as a function of thread length to elucidate controlling drug dose by controlling thread length. 5-FU release profile was obtained by first submerging plasma treated sutures of lengths 0.6 cm, 6 cm, and 60 cm overnight in 4 mg/mL 5-FU solution (in 1X PBS). The sutures are then dried in ambient air for at least 6 hours. Then, the sutures are put in 1X PBS. Ultraviolet visible spectroscopy (UV-Vis) measurements of the solution containing the 5-FU-loaded sutures are obtained at 5, 15, 30, 60, 150, and 240 minutes from submerging the suture in 1X PBS. UV-Vis spectra were used to generate the release profile in Fig. 4.

Cancer-cell viability study with chemotherapeutic injectables

Lastly, we released a cancer drug from threads into cultured cancer cells to demonstrate biocompatibility and effective dose-controlled drug release by analyzing cell viability. Loading 5-FU on 2, 3, and 4 cm sutures for cell viability studies follows the same procedure previously mentioned for 5-FU release profile. However, the sutures are submerged in 12 mg/mL solution of 5-FU in DI water instead of 1X PBS. Once sutures are dry, they were sterilized under UV light for 2 hours then added to cultured HeLa cells for 48 hours of incubation. Fluorescence measurements produced the cell viability data in Fig. 5.

RESULTS AND DISCUSSION

Threads' uptake

We compare different threads for their drug loading capacities by assessing their water uptake. Fig. 2 shows results using non-resorbable polyester and cotton threads, polyester sutures, and resorbable Polysorb™ sutures. Loading capacities are attributed to the threads' surface properties. Cotton consists of less organized fibers with more open pockets that can take up more fluid, but random topography results in less control over amount (error bars in Figure 2e). Polysorb™ sutures also exhibit less uniform uptake (error bars in Figure 2e). For purpose of demonstration, we chose polyester sutures for their uniform drug loading capacity. Water uptake of polyester thread, polyester suture, cotton thread, and Polysorb™ suture: 28.1±4.66 µg/mm, 57.9±10.3 µg/mm, 229±18.4 µg/mm, and 506±288 µg/mm, respectively (n=7).

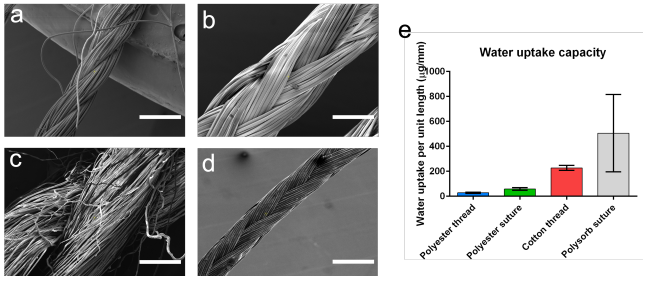

Figure 2. Water uptake is correlated to thread fiber organization. SEM images of (a) polyester thread (b) polyester suture and (c) cotton thread (d) Polysorb™ suture (scale bars = 300 µm). (e) Water uptake of polyester thread, polyester suture, cotton thread, and Polysorb™ suture (n=7).

Visual monitoring of dye diffusion from polyester suture

The diffusion of a model drug, rhodamine B dye, from soft injectable sutures was monitored to help visualize the drug-release mechanism into biological tissue. Fig. 3 shows a time lapse of the dye's release profile into an agarose gel, which is the artificial skin model in this study. All the dye that was loaded on the suture diffused from the thread into the surrounding agarose gel in only 10 minutes.

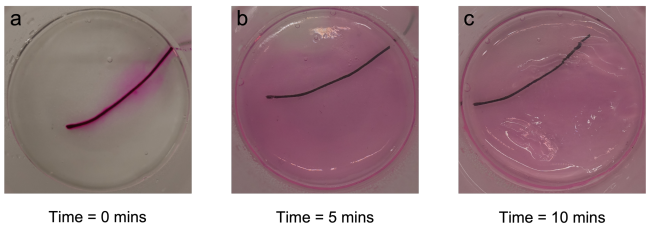

Figure 3. Visual monitoring of model drug - rhodamine B dye: shows drug diffusion off injectable (namely drug loaded polyester suture) in skin model made from agarose gel matrix (a) when suture is initially inserted (at 0 minutes), (b) after 5 minutes, (c) after 10 minutes.

Dose-controlled release of 5-Fluorouracil from sutures

To show control over quantity of drug released by controlling suture length, 5-FU was released in 1X PBS from suture of different lengths. Sutures of lengths 0.6 cm, 6 cm, and 60 cm each released different quantities of 5-FU. These lengths were chosen for characterization and to correlate thread's length with amount of drug released. The longer the suture is, the more 5-FU it released, which is attributed to the increase in drug loading with increasing suture length. Fig. 4 shows the release profile of 5-FU in from drug-loaded sutures of different lengths in the first 240 minutes after the suture was submerged in 1X PBS. Total amount of drug released after 240 minutes from 0.6 cm, 6 cm, and 60 cm long sutures is 0.0193±0.000438 mg, 0.0470±0.0148 mg, and 0.431±0.0543 mg, respectively (n=3). It is inferred from Fig. 4 that the majority, if not all, of the loaded drug is released within the first 15 minutes. Whereas releasing 5-FU from microneedles achieves less than 5% cumulative permeability in the first 10 hours [10].

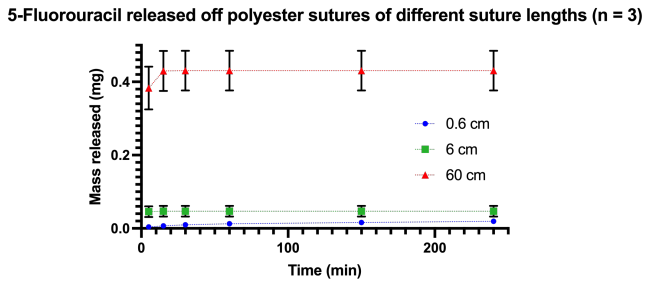

Figure 4. Longer threads release more drugs. The release profile of 5-Fluorouracil from injectables made from drug-loaded polyester sutures (0.6 cm, 6 cm, and 60 cm length) in 1X PBS over the period of 240 minutes.

Drug delivery with chemotherapeutic injectables

HeLa cells were chosen as cancer cell model to study *in-vitro* drug release. 5-FU-loaded injectable sutures showed considerable reduction in cell viability compared to bare threads, demonstrating successful drug delivery from polyester threads (Fig. 5a). Furthermore, polyester-suture injectables demonstrated excellent biocompatibility. Cell viability after 48 hours of being in contact with bare sutures was 99.1±2.83%, 93.9±1.87%, and 93.1±12.8% for bare 20 mm, 30 mm, and 40 mm long sutures, respectively. The 5-FU-loaded soft injectables demonstrated lower cell viability with higher suture length, which is attributed to the increase in amount of drug released with increasing suture length. The cell viability after 48 hours of being in contact with drug-loaded injectables was 67.9±2.46%, 64.7±5.09%, and 50.6±2.90% for 20 mm, 30 mm, and 40 mm long sutures, respectively. The number of dead HeLa cells after 48 hours of being in contact with a bare suture and a drug-loaded suture can also be visually compared under the microscope (Fig. 5b and 5c). These results demonstrate the potential of utilizing the threads for drug delivery.

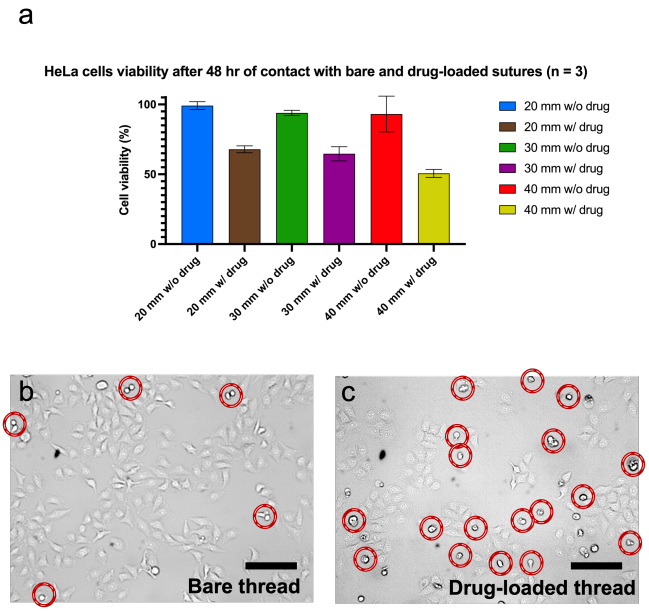

Figure 5. Soft injectables are biocompatible, and when loaded with chemotherapeutic drugs, decrease viability of cancer cells when in physical contact. (a) Cell viability of HeLa cells with the presence of bare polyester sutures as injectables and drug-loaded injectables (5-Fluorouracil loaded onto 20 mm-, 30 mm-, and 40 mm-long sutures) after 48 hours of incubation. The cell viability in presence of drug-loaded sutures was reduced considerably due to the release of the drug. Microscope images of cultured HeLa 48 hours after being in contact with (b) bare polyester suture and (c) drug-loaded polyester suture. Dead cells are circled in red. All scale bars are 80 μm.

CONCLUSION

Soft injectables can substitute conventional and painful drug delivery methods, such as using hypodermic needles, or unreliable methods, such as using microneedles or oral ingestion. In this study we explore medical-grade polyester sutures as soft injectables for transdermal drug delivery. Sutures are coated with drugs through wetting. Polyester sutures show appropriate and uniform loading capacity. Controlling the injectables' length allows for the control of the drug dose released. The release of a model drug (rhodamine B dye) was qualitatively analyzed, and the release of a cancer drug (5-fluorouracil) was quantitatively analyzed. Furthermore, chemotherapeutic soft injectables were explored. They demonstrated biocompatible properties and successful release of 5-fluorouracil within cultured cancer cells environment, resulting in lower cancer cell viability, as expected with increasing injectables' lengths. This study showcases a new class of thread-based injectables for dose-controlled drug delivery.

REFERENCES

[1] P. Mostafalu et al., "A Textile Dressing for Tempotal and Dosage Controlled Drug Delivery", *Adv. Funct. Mater.*, 17023399, 27 (2017).

[2] M.R. Prausnitz and R. Langer, "Transdermal drug delivery", *Nature biotechnology*, 1261-8, 26, 11 (2008).

[3] H. Nejad, A. Sadeqi, G. Kiaee et al., "Low-cost and cleanroom-free fabrication of microneedles", *Microsyst Nanoeng*, 17073, 4 (2018).

[4] G. Kiaee et al., "A pH-Mediated Electronic Wound Dressing for Controlled Drug Delivery", *Adv. Healthcare Mater.*, 1800396, 7 (2018).

[5] S. Sonkusale and P. Mostafalu, "Thread-based integrated functional devices", U.S. Patent Application No. 15/749,207

[6] M. L. Hakim et al., "Local drug delivery from surgical thread for area-specific anesthesia", *Biomed. Phys. Eng. Express*, 015028, 6 (2020).

[7] W. Tan et al., "Go with the capillary flow. Simple thread-based microfluidics", *Sensors and Actuators B: Chemical*, 129670, 334 (2021).

[8] H. Rezaei Nejad, A. Sadeqi, and S. Sonkusale, "Thread as a precise sampling and delivery platform", *The 24th International Conference on Miniaturized Systems for Chemistry and Life Sciences (μTAS 2020)*, (2020).

[9] D. Longley, D. Harkin, and P. Johnston, "5-Fluorouracil: mechanisms of action and clinical strategies", *Nat Rev Cancer*, 330-338, 3 (2003).

[10] B. Yang et al., "Bilayer dissolving microneedle array containing 5-fluorouracil and triamcinolone with biphasic release profile for hypertrophic scar therapy." *Bioactive Materials*, 2400-2411, 6.8 (2021).

CONTACT

*S. Sonkusale, tel: +1-617-627-5113; sameer.sonkusale@tufts.edu

TOWARDS DETERMINISTIC LATERAL DISPLACEMENT-BASED CONTINUOUS-FLOW MICROFLUIDIC PARTICLE REACTORS *VIA* DIRECT LASER WRITING

Adira Colton[1], Olivia M. Young[1], Talha Razaulla[2], Roseanne Warren[2], and Ryan D. Sochol[1]*
[1]University of Maryland, College Park, Maryland, USA
[2]University of Utah, Salt Lake City, Utah, USA

ABSTRACT

Multi-stage fluidic reaction schemes for suspended particles (*e.g.*, micro/nanospheres, cells, bacterial species, and extracellular vesicles) underly a diversity of chemical and biological applications. Conventional methods for executing such protocols can be exceedingly time, labor, and/or cost intensive. Microfluidic strategies can address these drawbacks; however, such technologies typically rely on clean room-based microfabrication that suffer from similar deficits for manufacturing the chips. To simultaneously overcome these challenges, here we explore the use of the submicron-scale additive manufacturing approach, "Two-Photon Direct Laser Writing (DLW)", as a means for fabricating micro-fluidic "Deterministic Lateral Displacement (DLD)" arrays capable of passively guiding suspended particles across discrete, adjacent flow streams—the fundamental capability of continuous-flow multi-stage particle microreactors. Experimental results from microfluidic experimentation with 5 μm-in-diameter fluorescent particles revealed effective particle transport across flow streams, with 87.5% of fluorescent peaks detected in the designated, opposing outlet following the DLD array. These results suggest utility of the presented approach for micro- and nanoparticle-based microfluidic reactors targeting wide-ranging chemical and biological applications.

KEYWORDS

Additive Manufacturing, Direct Laser Writing, Deterministic Lateral Displacement, Microfluidics, 3D Printing

INTRODUCTION

Continuous-flow particle-based microreactors are uniquely suited for biological and chemical applications that are predicated on multi-stage fluidic reaction schemes (*e.g.*, layer-by-layer depositions, sandwich assays), including for micro/nanoparticle coatings and preparation of advanced functional materials [1-6]. To take advantage of these scaling-induced benefits, such as low sample and reagent volumes as well as high control of micro-environmental conditions, numerous researchers have explored strategies for passively transporting micro/nanoparticles across parallel flow streams [7]. Previously, our group reported a continuous-flow micropost array railing approach [8] and demonstrated its use for a six-stage cytokine-detection sandwich assay on microparticle substrates [9]. Unfortunately, this approach requires the arrayed posts to match the size of the target particles, thereby restricting the size of the particles that can be processed to the minimum feature size of the manufacturing technology [8,9]. In contrast, "Deterministic Lateral Displacement (DLD)" technologies—continuous-flow fluidic systems comprising micro/nanoposts arrayed at an angle with respect to the primary flow direction—circumvent the aforementioned issue by enabling the handling of suspended particles that are much smaller than the size of the arrayed posts [10-15]. Unfortunately, conventional methods for manufacturing such microfluidic systems are generally time, cost, and labor intensive [16,17]. Thus, alternative approaches that address these issues are in critical demand.

CONCEPT

Previously, we demonstrated the use of the submicron-scale additive manufacturing (or "three-dimensional (3D) printing) technology, "Two-Photon Direct Laser Writing (DLW)", for printing vertically stacked DLD arrays inside of microfluidic channels to enable size-based particle sorting within a single flow stream [18]. In this work, however, we investigate the potential for DLW-based DLD arrays to instead serve as a means for passively guiding suspended microparticles into adjacent, discrete flow streams—a key proof of concept for continuous-flow particle-based microreactors. To elucidate this capability, we use DLW to print a negative master mold (**Fig. 1a**), which we then replicated to produce an enclosed polydimethylsiloxane (PDMS)-on-glass microfluidic device. The overall concept is presented in **Figure 1b**, which entails designing the geometric dimensions of the system—*i.e.*, the gap spacing between microposts (G) and the angle of the array (θ) with respect to the flow direction—to ensure that the diameter of the target particles is larger than the critical diameter (D_C) based on the DLD array. Researchers previously reported [12] an empirical formula for these relationships as:

$$D_C = 1.4G \times tan(\theta)^{0.48} \quad (1)$$

Importantly, the height of the posts is not present in *Equation 1*, as the height only affects the throughput, and not the railing capability.

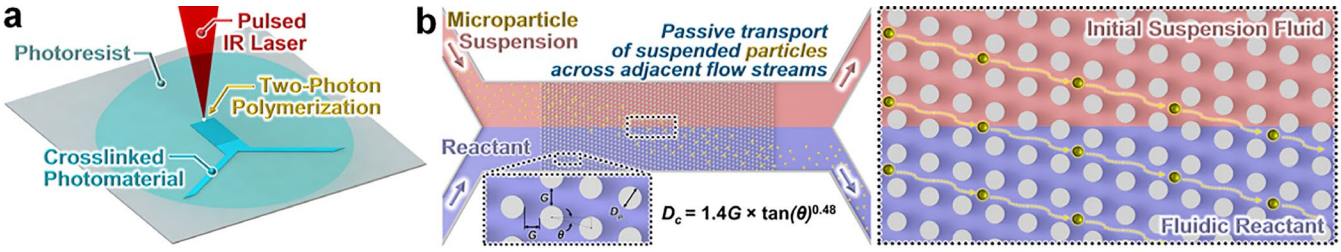

Figure 1: *Conceptual illustrations of a "Direct Laser Writing (DLW)"-based "Deterministic Lateral Displacement (DLD)" array continuous-flow microfluidic particle reactor.* ***(a)*** *DLW of the microfluidic system master mold onto a Si wafer.* ***(b)*** *Microfluidic system overview. Suspended microparticles are inputted via the top left channel, enter the DLD array to be passively guided into the distinct, adjacent "reactant" flow stream, and outputted via the bottom right channel. The critical (i.e., minimum) diameter (D_C) of suspended particles that can be transported is based on the gap spacing (G) and the angle of the array (θ) with respect to the primary flow direction.*

978-1-940470-04-7/HH2022/$25©2022TRF
DOI 10.31438/trf.hh2022.37

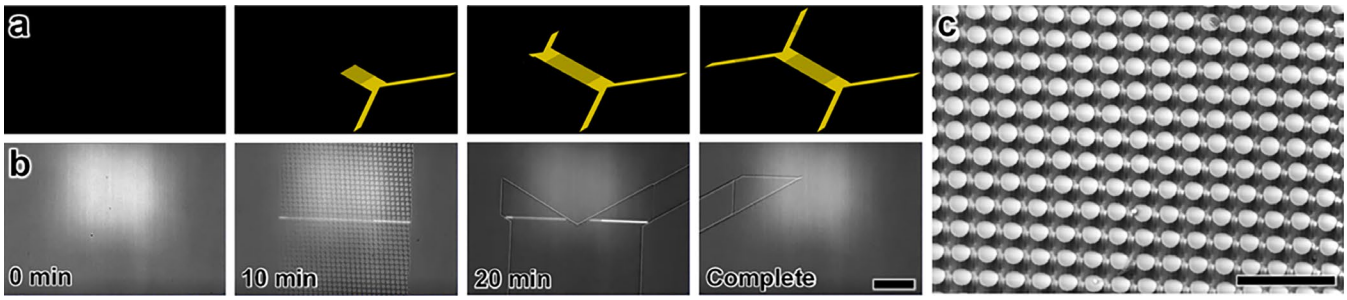

Figure 2: *Fabrication Results.* ***(a,b)*** *Sequential images of* ***(a)*** *computer-aided manufacturing (CAM) simulations, and* ***(b)*** *the corresponding DLW-based printing process of the mold onto a Si wafer. Scale bar = 250 μm.* ***(c)*** *SEM micrograph of print results. Scale bar = 200 μm.*

To avoid stiction-based print failures, the height of the posts, and therefore the channel, was limited to 20 μm. As a result of the unique DLD geometry and its relation to the flow direction, suspended microparticles will be guided by the DLD array away from their initial suspension fluid into a distinct, adjacent reactant fluid (**Fig. 1b – *expanded view***).

MATERIAL AND METHODS

Direct Laser Writing (DLW) of the Deterministic Lateral Displacement (DLD) Array Negative Mold

The overall DLW-based strategy for manufacturing the fully enclosed PDMS-on-glass microfluidic devices is based on a methodology reported previously by our group [19]. Briefly, the negative master mold of the microchannels and DLD array were modeled using the computer-aided design (CAD) software, SolidWorks (Dassault Systems, France), and then exported as an STL file. This file was then imported into the computer-aided manufacturing (CAM) software, DeScribe (Nanoscribe, Karlsruhe, Germany), for slicing and generation of point-by-point, layer-by-layer laser writing path. The cross section of the microchannel was designed with a trapezoidal shape for easier removal of PDMS off the mold [18,19].

A Si substrate (25 mm × 25 mm) was rinsed with acetone and isopropyl alcohol (IPA) and then dried with N_2 gas before being loaded into a Plasma Cleaner (Pie Scientific, Union City, CA) for 30 min at 75 Watts. A drop of IP-Q photoresist (Nanoscribe) was manually dispensed onto the Si substrate, and then both the substrate and resist were heated on a 65 °C hot plate for 10 min. This substrate was then loaded into the Nanoscribe Photonic Professional GT printer in the Dip-in Laser Lithography (DiLL) configuration with the 10× objective lens. Following the DLW printing process, the fabricated mold was developed *via* successive immersion in propylene monomethyl ether acetate (PGMEA) and IPA, and lastly, dried with N_2 gas.

PDMS-on-Glass Microfluidic Device Fabrication

A 10:1 mixture of PDMS (Slygard 184, Dow Corning, Corning, NY) was poured over the master molds and placed on a hot plate at 65 °C for approximately one hour. The nearly cured PDMS was then carefully peeled from the molds and punched with 0.75 mm-in-diameter ports at inlet and outlet locations. The PDMS was rinsed with IPA and DI water, and then O_2 bonded to 30 mm circular borosilicate glass substrates (#1.5, Bioptechs Inc. Butler, PA). The sealed device was then placed on a hot plate at 65 °C overnight to promote the integrity of the PDMS-to-glass bond adhesion and to ensure full curing of the PDMS.

Experimental Characterization

Scanning electron microscope (SEM) images were captured using a TM4000 Tabletop SEM (Hitachi, Tokyo, Japan). Microfluidic experiments were performed using the Fluigent Microfluidic Control System (MFCS). Two solutions/suspensions were prepared for testing: (*i*) a buffer solution of 2% Tween 20 in DI water for input into the bottom port, and (*ii*) a microparticle suspension comprised of 2% Tween 20 in DI water and 1% v/v 5 μm-in-diameter microparticles with fluorescence at 500 nm. Fluorescence results were obtained *via* an inverted fluorescence microscope (Axio Observer.Z1, Zeiss, Germany) connected to a camera (Axiocam 503 Mono, Zeiss). To quantify the locations of the suspended microparticles within the images, the fluorescence micrographs were processed using ImageJ (NIH, Bethesda, MD) to measure the intensities of fluorescence at the locations of the microparticles upon entry, within the DLD array, and upon exit [20].

RESULTS AND DISCUSSION

DLW-Based Fabrication

CAM simulations and corresponding micrographs of the DLW printing process for the molds are presented in **Figure 2a** and **2b**, respectively. Fabrication results of the DLD array in PDMS revealed effective replication of the G = 7.5 μm, θ = 0.1 rad geometries (**Fig. 2c**), which corresponds to D_C = 3.5 μm (*Eq. 1*). Due to shrinkage phenomena associated with both the print and PDMS, the initial model was designed to ensure such size changes would still result in a final device suitable for handling target 5 μm-in-diameter particles. To achieve the intended G = 7.5 μm, we originally designed the posts with a diameter of 22 μm and with G = 5.5 μm, which resulted in the final device exhibiting 20 μm-in-diameter posts, thereby enlarging G to the intended 7.5 μm (**Fig. 2c**).

Microparticle-Based Microfluidic Experimentation

To investigate the functionality of the DLD device for the passive transport of suspended particles across adjacent flow streams, we performed continuous-flow microfluidic experiments with suspended 5 μm-in-diameter particles while monitoring the positions of the particles with respect to the two flow streams using fluorescence imaging. The fluorescence imaging of the particles as they traveled through the DLD and across flow streams revealed several key trends. First, similar to that reported in prior works [16,18] we observed a degree of particle clogging at the beginning of the DLD array, as evidenced by the brighter regions at the entrance of the DLD arrays (**Fig. 3a**). The surfactant, Tween 20, which was mixed into the particle suspension solution, mitigated some of the clogging and allowed for the majority of inputted particles to enter the array and exit the array (**Fig. 3b,c**). In the middle regions of the array, we observed that, while the overall path of the suspended microparticles appeared to trend toward the adjacent flow stream, the particles did appear to backtrack in part at various points (**Fig. 3b**). Although such behavior suggests that the D_C was too close to the diameter of the inputted particles, it was not detrimental to the overall particle guidance efficacy as the majority

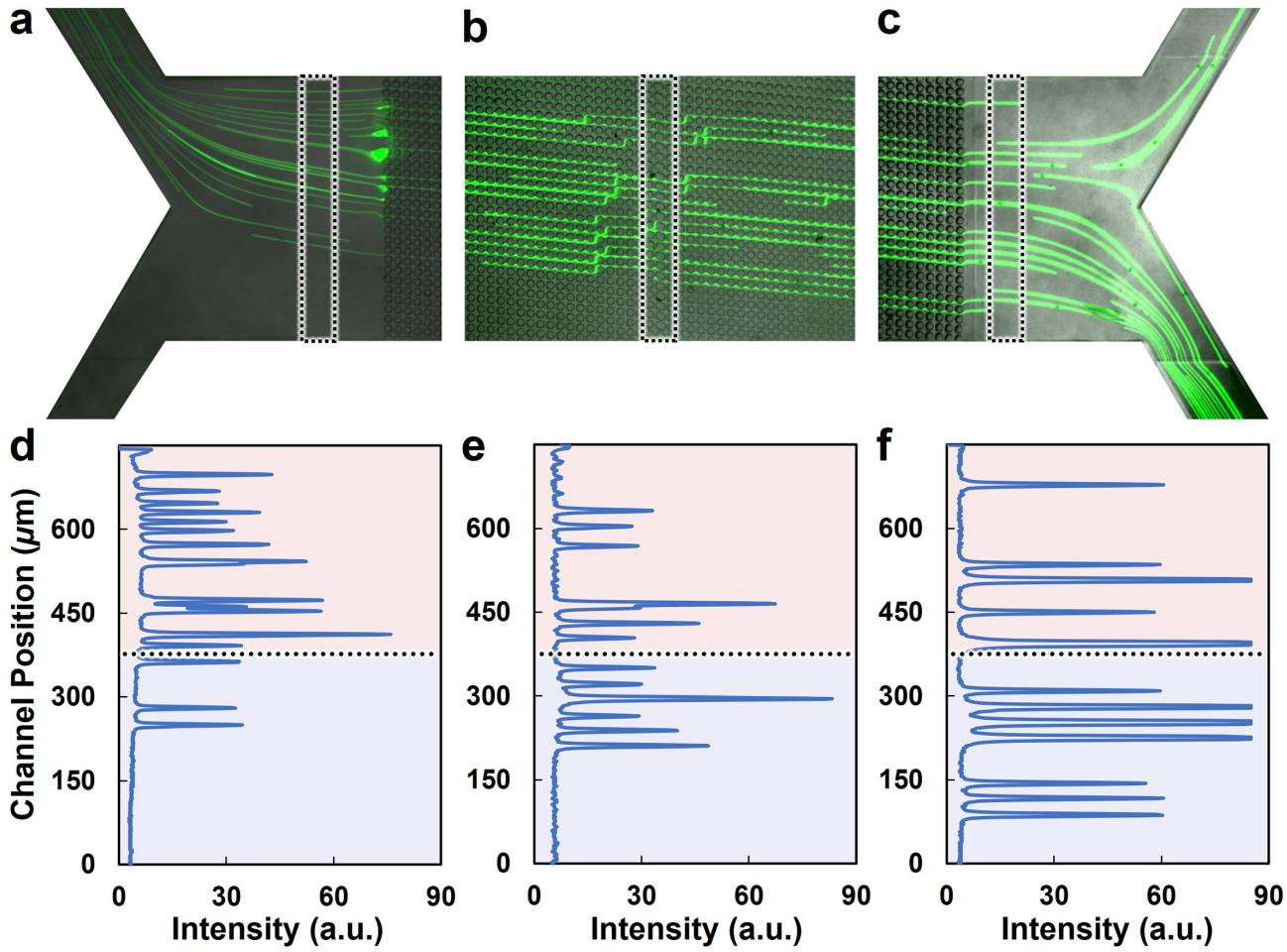

Figure 3: *Microfluidic experimental results for DLD-based microparticle transport of suspended 5 μm-in-diameter fluorescent particles across discrete, adjacent flow streams. Fluorescence micrographs* ***(a–c)*** *and corresponding quantified fluorescence intensity results along the width of the channel* ***(d–f)*** *for regions of interest (dotted boxes):* ***(a,d)*** *preceding the entrance of the DLD array,* ***(b,e)*** *in the middle of the DLD array, and* ***(c,f)*** *after exiting the DLD array.* ***(d–f)*** *Dotted line denotes the middle of the microchannel, separating the microparticle suspension fluid (light red) from the 'reactant' fluid (light purple).*

of inputted particles successfully traversed into the adjacent flow stream (**Fig. 3c**).

To evaluate the change in location of the particles within the device, we captured fluorescence images at entrance, middle, and exit regions of the DLD array as particles flowed through and quantified the fluorescence intensity along the channel at each region (**Fig. 3d–f**). These results revealed a marked shift from the majority of peaks in the top region when initially entering the DLD array (**Fig. 3d**) to the bottom region after exiting the array (**Fig. 3f**). To further interrogate the efficacy of the DLW-based DLD array for microparticle transport across flow streams, we also captured and quantified fluorescence images at both of the inlets and outlets. These results revealed a significant shift from before (**Fig. 4a,b**) and after (**Fig. 4c,d**) the DLD array. In particular, while we observed 100% of fluorescent peaks associated with the initial suspension fluid inlet (as expected) (**Fig. 4a**), we found less than 15% of the fluorescent peaks remained after the array at the top suspension fluid-associated outlet (**Fig. 4c**) as the majority of the peaks were instead at the surrogate 'reactant'-associated outlet (**Fig. 4d**). These results suggest utility for the DLW-based DLD array for passive guidance of suspended microparticles into an adjacent flow stream.

CONCLUSION

Here we investigated the potential of leveraging DLW to enable DLD arrays capable of passively transporting suspended microparticles across distinct, adjacent flow streams. The fabrication and experimental results suggest efficacy for this approach, which could offer a novel pathway to new classes of continuous-flow, multi-stage particle reactors for target applications [21,22]. In future works, this strategy could be extended to design systems with multiple DLD arrays in series and additional fluidic inputs to passively execute multi-stage fluidic reaction schemes. Because the DLW-based manufacturing strategy bypasses the need for clean room-based photolithography protocols, the presented approach can also reduce the time, cost, and labor requirements associated with past works [8,9].

Although DLD arrays are highly effective at particle sorting by size, in their current form, they present multiple issues in that they have limited throughput and can be prone to clogging [12,13]—challenges that would be amplified with multi-stage microreactor comprising numerous, successive DLD arrays within a single device. Previously, our group has demonstrated a multi-layer (or vertically stacked" DLD array manufactured *via* DLW-based 3D

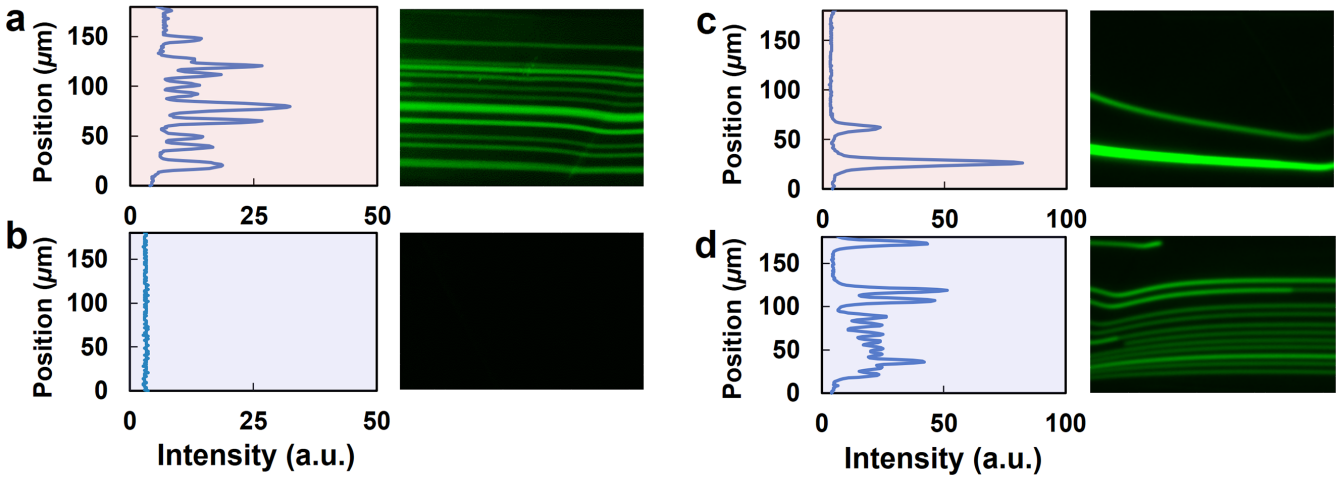

Figure 4: *Quantified fluorescence intensity results (left) and corresponding fluorescence micrographs (right) associated with the* ***(a,b)*** *inlets and* ***(c,d)*** *outlets for the* ***(a,c)*** *microparticle suspension fluid and the* ***(b,d)*** *surrogate 'reactant' fluid.*

printing that effectively sorted microparticles and nanoparticles based on size [18]. Future efforts should focus on investigating the potential of extending the vertically stacked DLD array strategy to incorporate the parallel flow transport concepts presented here, which could, in turn, provide novel means to enable multi-stage particle reactors that yield high throughput (while bypassing clogging failures) for wide-ranging applications in chemical and biological fields.

ACKNOWLEDGEMENTS

We greatly appreciate the contributions of the members of the Bioinspired Advanced Manufacturing (BAM) Laboratory as well as Terrapin Works Staff at the University of Maryland, College Park. This work was supported in part by U.S. National Science Foundation Awards CMMI-1761395 and CMMI-1761273. A.C. and O.Y. were supported by the Clark Foundation Doctoral Fellowship Program.

REFERENCES

[1] M. Zhang, *et al.*, "Pickering emulsion droplet-based biomimetic microreactors for continuous flow cascade reactions", *Nature Communications*, 13, 1 (2022).

[2] Y. Gu *et al.*, "Acoustofluidic centrifuge for nanoparticle enrichment and separation", *Science Advances*, 7, 1 (2021).

[3] J.S. Santana and S.E. Skrabalak, "Continuous Flow Routes toward Designer Metal Nanocatalysts", *Advanced Energy Materials*, 10, 11 (2020).

[4] J. Sui *et al.*, "Continuous Synthesis of Nanocrystals via Flow Chemistry Technology", *Small*, 16, 15 (2020).

[5] L. Wågberg and J. Erlandsson, "The Use of Layer-by-Layer Self-Assembly and Nanocellulose to Prepare Advanced Functional Materials", *Advanced Materials*, 33, 28 (2021).

[6] J.J. Richardson *et al.*, "Technology-driven layer-by-layer assembly of nanofilms", *Science*, 348, 6233 (2015).

[7] J.H. Swisher, *et al.,* "Nanoreactors for particle synthesis", *Nature Reviews Materials*, (2022).

[8] R.D. Sochol *et al.*, "Continuous flow multi-stage microfluidic reactors via hydrodynamic microparticle railing", *Lab on a Chip*, 12, 20 (2012).

[9] R.D. Sochol, *et al.* "Dual-mode hydrodynamic railing and arraying of microparticles for multi-stage signal detection in continuous flow biochemical microprocessors", *Lab on a Chip*, 14, 8 (2014).

[10] L.R. Huang *et al.,* "Continuous Particle Separation Through Deterministic Lateral Displacement", *Science*, 304, 5673 (2004).

[11] J.P. Beech *et al.*, "Active Posts in Deterministic Lateral Displacement Devices", *Advanced Materials Technologies*, 4, 9 (2019).

[12] N. Tottori and T. Nisisako, "Degas-Driven Deterministic Lateral Displacement in Poly(dimethylsiloxane) Microfluidic Devices", *Analytical Chemistry*, 91, 4 (2019).

[13] R. Nasiri *et al.*, "Microfluidic-Based Approaches in Targeted Cell/Particle Separation Based on Physical Properties: Fundamentals and Applications", *Small*, 16, 29 (2020).

[14] A. Hochstetter *et al.*, "Deterministic Lateral Displacement: Challenges and Perspectives", *ACS Nano*, 14, 9 (2020).

[15] T. Salafi *et al.*, "A Review on Deterministic Lateral Displacement for Particle Separation and Detection", *Nano-Micro Letters*, 11, 1 (2019)

[16] B.H. Wunsch, *et al.*, "Nanoscale lateral displacement arrays for the separation of exosomes and colloids down to 20 nm", *Nature Nanotechnology*, 11, 11 (2016).

[18] A.T. Alsharhan *et al.*, "Direct Laser Writing for Deterministic Lateral Displacement of Submicron Particles", *Journal of Microelectromechanical Systems*, 29, 5 (2020).

[17] B.H. Wunsch *et al.*, "Gel-on-a-chip: continuous, velocity-dependent DNA separation using nanoscale lateral displacement", *Lab on a Chip*, 19, 9 (2019).

[19] A.C. Lamont *et al.*, "Geometric Determinants of In-Situ Direct Laser Writing", *Scientific Reports*, 9, 1 (2019).

[20] C.A. Schneider, W.S. Rasband, and K.W. Eliceiri, "NIH Image to ImageJ: 25 years of image analysis", *Nature Methods*, 9, 7 (2012).

[21] H. Ren *et al.*, "Multiplexed serpentine microchannels for high-throughput sorting of disseminated tumor cells from malignant pleural effusion", *Sensors and Actuators B: Chemical*, 337 (2021).

[22] A.S. Clark and A. San-Miguel, "A bioinspired, passive microfluidic lobe filtration system", *Lab on a Chip*, 21, 19 (2021).

CONTACT

*Adira Colton, acolton1@umd.edu

UTILIZATION OF VARYING TRANSIENT RESPONSE TIMES IN GRAVIMETRIC AND IMPEDIMETRIC MULTIVARIATE GAS SENSOR WITH SINGLE POLYMERIC SENSING FILM FOR ENHANCED SELECTIVITY

Steven A. Schwartz[1,2], Luke A. Beardslee[2,3,4*], and Oliver Brand[1,2]*
[1]School of Electrical and Computer Engineering, Georgia Institute of Technology, Atlanta, Georgia, USA
[2]Institute for Electronics and Nanotechnology, Georgia Institute of Technology, Atlanta, Georgia, USA
[3]Naval Submarine Medical Research Laboratory, Groton, Connecticut, USA
[4]Emory University School of Medicine, Atlanta, Georgia, USA
*Current Affiliation

ABSTRACT

We report on the ability to discriminate between multiple volatile organic compounds (VOCs) utilizing variations in the transient response times of the gravimetric and impedimetric responses of a single micromachined multivariate gas sensor. The novel resonant gravimetric microsensor with a collocated capacitive transducer based on an interdigitated electrode (IDE) enables the simultaneous observation of both mass loading and dielectric changes in the same polymeric sensing film upon sorption of analyte. A 2D dispersion of the multivariate responses demonstrates separation between aromatics and alcohols due to variations in the transient response times along with varying concentration-dependences of these responses.

KEYWORDS

Resonant gas sensor, multivariate sensor, multivariate gas sensor, selectivity enhancement, multivariate dispersion.

INTRODUCTION

Chemical sensing has applications ranging from home safety and health monitoring to industrial process monitoring, environmental hazardous monitoring, and homeland security. Many of these applications have relied (and often still rely) on laboratory or benchtop-sized analytical tools, such as gas chromatography - mass spectrometry (GC-MS) systems, which limits portability and in-field usability. To both increase the utility and ubiquity of chemical sensors, microelectromechanical systems (MEMS)-based chemical microsensors have been developed. MEMS-based gas sensors are often classified based on the sensor's transduction principle or the sensing material used to interact with the target chemical. Across all classes of chemical microsensors, high sensitivity, low limit of detection, long-term stability, and high selectivity are desired. Of these properties, selectivity remains the most difficult to improve due to the tradeoff with the reversibility of the analyte interaction with the sensing layer [1]. Therefore, methods of selectivity enhancement without tailoring the sensing layer chemistry are extremely desirable.

Among the many types of sensing materials, polymeric sensing films are a well-studied class for gas microsensors due to the tailorability of the material chemistry, ease of deposition, and partial selectivity to a wide variety of compounds. Moreover, polymeric-film based chemical sensors leverage absorption-based volumetric diffusion-limited processes, compared to adsorption-based surface interactions, enabling high sensitivities in microsensors for the detection of volatile organic compounds (VOCs). Of these polymer-based gas microsensors, two prominent subclasses are gravimetric and impedimetric sensors. Gravimetric microsensors, such as resonant gas sensors, detect mass changes upon sorption of an analyte into the sensing material. On the other hand, impedimetric sensors, including chemocapacitive and chemoresistive sensors, detect changes in the electrical properties of a sensing film due to analyte penetration.

The steady-state and transient responses have been characterized for polymer-coated gravimetric resonant devices [2] and for polymer-coated chemocapacitive sensors [3]; both sensor types demonstrate remarkable sensitivity to a wide variety of VOCs. However, in both cases, the selectivity of these sensors is limited for a single sensing film-transducer pair, because of the partial selectivity of the polymer coating itself. In univariate sensors, selectivity is often derived from the variation in sensitivities for each analyte which is a function of concentration [1,4]. Thus, quantification can only be performed in the case where the gases present are known a-priori. This is undesirable for many applications as there is often a need to quantify not only how much of something is in the air (quantification), but also what is in the air (speciation). To overcome the sensing-film based selectivity limitation, multivariate sensing in which a single sensor produces multiple outputs can be leveraged. A comprehensive review of multivariate gas sensors and the many combinations of transducers and signal types utilized can be found in [4].

For a multivariate sensor with multiple outputs, with the sensor responses depending on the partition coefficient to varying degrees or a product of multiple material property relationships, additional selectivity can be derived by comparing variations in these relations. This is often visualized using a multi-dimensional dispersion in which data is plotted as a function of the sensor outputs rather than gas concentration [4] and has been demonstrated for the multivariate sensor used here [5]. However, this previous study only considered a comparison of the steady state data. In this paper, it is investigated if such variations hold true for transient characteristics of the sensor responses as well and if these variations are distinct from steady-state selectivity.

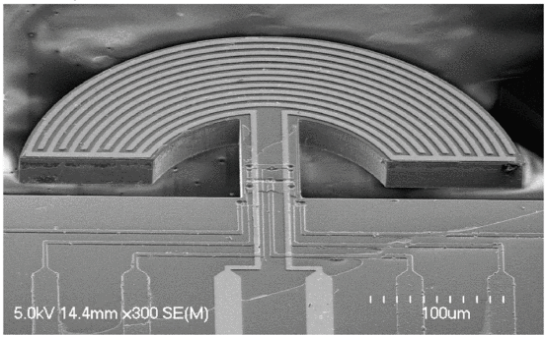

Figure 1: SEM image of gravimetric/impedimetric multi-sensor with hammerhead-shaped resonator and IDE on top of the semicircular annulus. Reprinted with permission [5].

SENSOR DESIGN & TESTING

Sensor Design & Characterization

The multivariate sensor builds on an established hammerhead-shaped resonator platform reported in [5,6], consisting of a semicircular annulus of 100/200μm inner/outer radius supported by a 100μm long and 45μm wide cantilever beam. An interdigitated

978-1-940470-04-7/HH2022/$25©2022TRF
DOI 10.31438/trf.hh2022.38

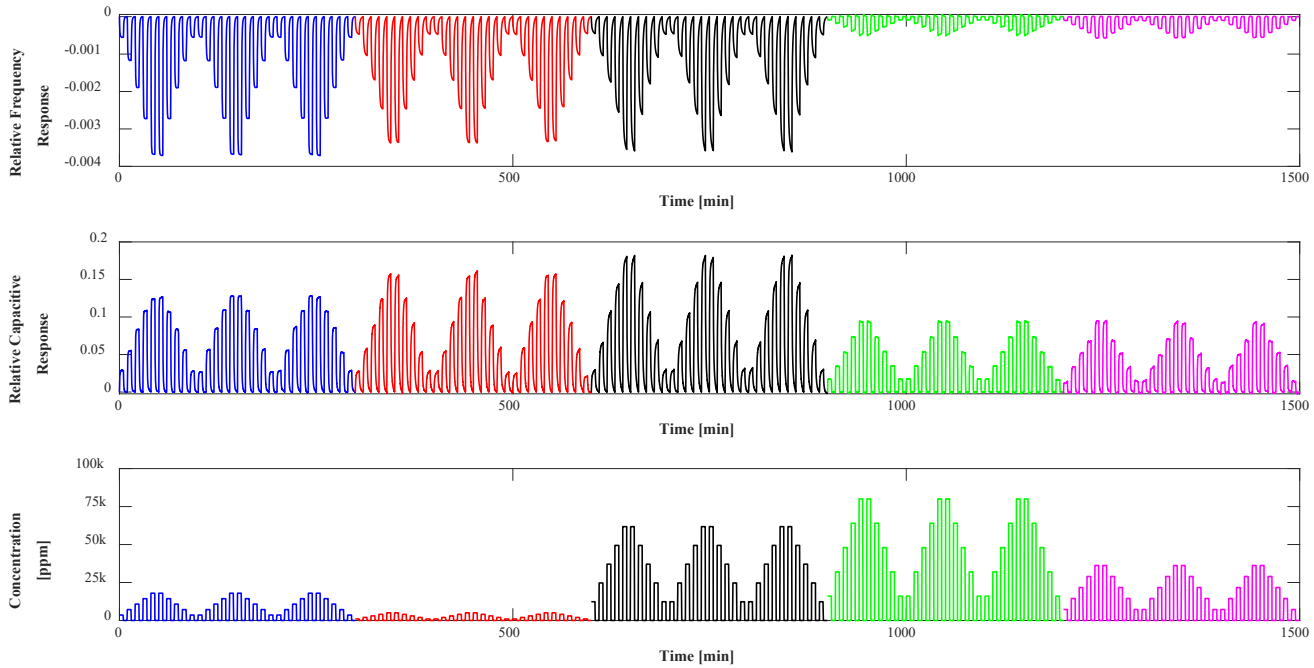

Figure 2: Timeseries of baseline corrected multisensor responses, i.e., measured relative frequency change and relative capacitance change, as well as respective exposure concentrations when exposing the PECH-coated sensor to different concentrations of the 5 tested gases: toluene (blue), m-xylene (red), ethylbenzene (black), methanol (green), ethanol (pink).

electrode (IDE) structure is overlayed on the surface of the device, enabling multivariate sensing using a single polymeric film (Figure 1). In this IDE structure both the electrode width and edge-to-edge spacing are 2µm. The resonator-based gravimetric sensor utilizes thermal excitation and piezoresistive sensing and is operated at its in-plane resonance mode using a closed-loop circuit, with the frequency being read out by a frequency counter. The capacitance of the IDE is simultaneously monitored using a high-precision LCR meter. For this work, an approximately 2µm sensing film of polyepichlorohydrin (PECH) was deposited on the annulus region of the device via spray coating with a shadow mask.

Gas Testing Procedure

The device was tested utilizing a custom-built gas measurement setup described in [5,6]. This measurement setup enables in-flow gas testing of chemical sensor devices with automated concentration ramping and exposure/purge cycling capabilities. Analyte concentration generation is performed using a temperature-controlled bubbler-vaporizer setup in which the saturated partial pressure of the target VOC is generated and then diluted through the control of flow rates in the system's gas lines via multiple mass flow controllers. Exposure/purge cycling is performed through the use of a 4-way solenoid valve enabling rapid transition between the analyte-filled exposure line and a purging line of pure carrier gas. The use of the solenoid valve and minimal headspace of the flow cell enables near ideal concentration stepping, minimizing systemic error in the transient response characteristic.

GAS SENSING MEASUREMENTS

Gas Testing Timeseries Data

Figure 2 shows the representative timeseries data collected from the multivariate sensor when exposed to different concentrations of five gases consisting of two VOC subclasses, aromatics and alcohols. Toluene, m-xylene, and ethylbenzene were the aromatic hydrocarbons selected as they are part of the BEXT class of industrial gases involved in the petroleum and plastics industry, while the alcohols, methanol and ethanol, were selected due to their heavy use as industrial solvents in chemical plants and consumer-use items such as windshield wiper fluid and industrial cleaners. Each gas was tested at five concentrations utilizing the bubbler-based gas measurement setup. For each analyte gas, the sensor is subsequently exposed to multiple cycles of increasing and decreasing analyte concentrations, with each 5-minutes analyte exposure followed by a corresponding purge of similar length using UHP nitrogen. The data highlights the repeatability of the sensor response, as well as the characteristic diffusion-limited response patterns for the different analytes. It should be noted that while the transient responses here are created using the test setup, similar transients can be generated by rapidly heating/cooling the sensor [7].

The sensor responses are displayed in relative quantities, enabling an improved comparison of the results for each gas test which were performed separately and consecutively over the course of a week with minimal changes in the baseline signal. The data shown here has been concatenated into a single timeseries to improve visualization of the variation in responses to each gas. Additionally, the data has been baseline corrected to remove signal drift.

Transient Response Analysis

In this work, the T_{90} response time, defined by the time it takes to reach 90% of the steady-state response, has been explored as it had been identified before as a useful metric to improve gas discrimination in polymer-based impedimetric sensors [3]. Figure 3 shows the extracted T_{90} for each sensor response as a function of analyte concentrations for the five gases. For this data set the last available datapoint at the end of the five-minute period was used in place of saturation limit as some gases do no reach full saturation of their gravimetric response within the five-minute period (see Figure 2). The response time for a particular analyte depends on the analyte concentration, as noted previously [2,3,8] for gas sensors utilizing polymeric films. The data was fit with a second-order polynomial demonstrating the quadratic dependence of the T_{90} response time on

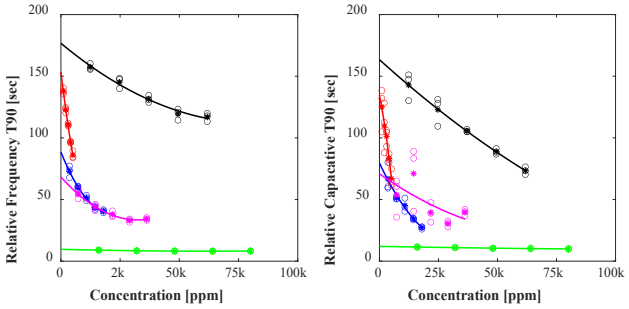

Figure 3: T_{90} response times extracted from gravimetric (frequency) and impedimetric (capacitance) responses as a function of analyte concentration for five tested gases: toluene (blue), m-xylene (red), ethylbenzene (black), methanol (green), ethanol (pink).

analyte concentration. There is both noticeable separation of analytes based on their transient response time and noticeable variation in their concentration dependence. This separation provides a means of selectivity and gas identification if the concentration is known.

To provide a means for gas identification without the need for a-priori knowledge of the gas or concentration information, a 2D dispersion of the frequency response times versus the capacitive response times is shown in Figure 4(B), along with the 2D dispersion of the steady-state responses for comparison in Figure 4(A). For the steady-state dispersion, the aromatics and alcohols are well separated at high concentrations, but the discriminatory power of this dispersion fades as the analyte concentration approaches zero. This limitation was not observed for the 2D dispersion of the transient response times as all five gases are spatially separated and their intercepts do not converge to zero. Notably, these curves do not lay on the x=y line as would be expected if the transient behavior was the same for both sensor responses. In particular, it was observed that, for the aromatics, the capacitive response is faster than the gravimetric/frequency response, while this behavior is reversed for the alcohols. Thus, both 2D dispersions provide discrimination of the five gases with separation/clustering of the aromatic and alcohols.

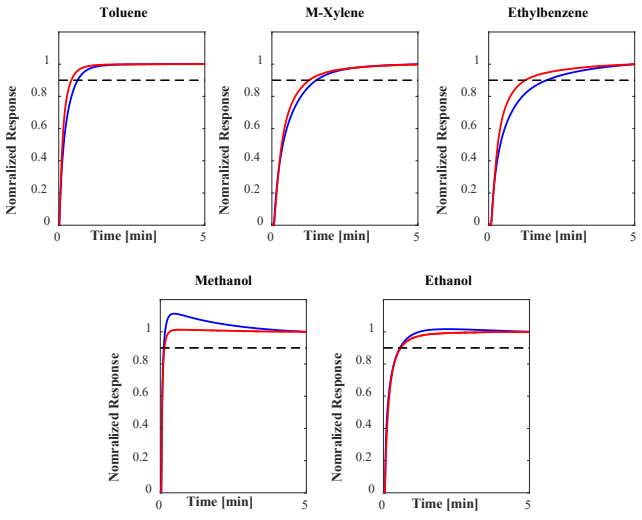

Figure 5: Comparison of normalized gravimetric (blue) and impedimetric (red) transient responses at maximum concentrations for all 5 tested gases with T_{90} reference line (black, dashed).

In Figure 5, the transient response for each analyte was further

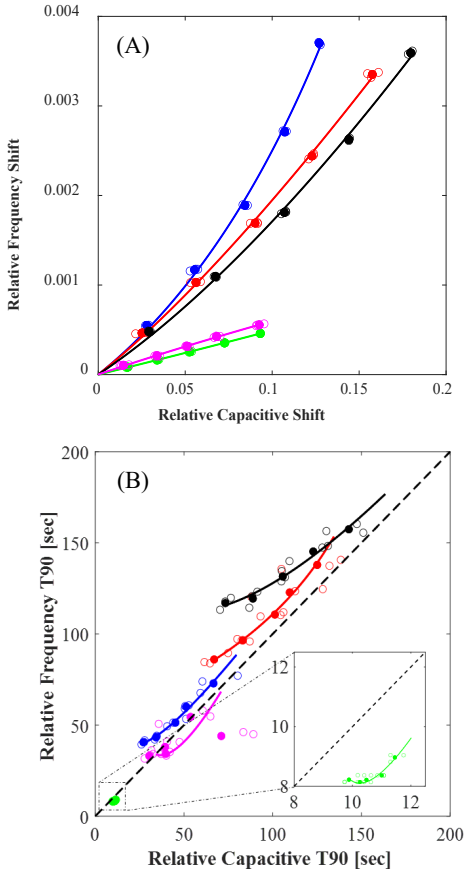

Figure 4: 2D dispersions of the (A) multisensor steady-state response and (B) T_{90} response data extracted from the gravimetric (frequency) and impedimetric (capacitance) responses. In (B) identical T_{90} response times for both signals would fall onto the dashed x=y line. Open circles represent extracted T_{90}, while closed circles represent averages for multiple measurements. Color coding as in Figure 2 & 3.

investigated by comparing the normalized responses of the two sensor outputs at all time points within a single 5-minute exposure at the maximum concentration of each gas. It can be clearly seen that for aromatics the capacitive transient response is quicker whereas for the alcohols the opposite is true. Moreover, in the gravimetric response of the alcohols, the normalized response exceeds a value of 1 which is an indication that the gravimetric response had a maximum within the exposure cycle rather than at the end. This is confirmed in Figure 2 if one zooms in on an individual relative frequency response of an alcohol. Further experimental investigation into this behavior is warranted.

DISCUSSION

The following discussion of the observed phenomena considers the literature for transient responses in polymer-coated sensors [2,3,8,9]. The transient responses of both transduction mechanisms are based on diffusion. Thereby, the gravimetric response can be directly related to the fractional mass uptake due to analyte diffusion into the sensing film, while the capacitive response is composed of contributions from both dielectric property changes of the sensing film due to incorporation of polarizable analyte into the polymer matrix and the swelling of the polymer [3,9]. Moreover, local dielectric property changes due to analyte diffusion into the sensing film create a spatially varying contribution to the sensor's capacitive

response due to the fact that the fringing of the electric field in the IDE creates non-uniform field density which is largest close to the electrode edges. Swelling-based contributions to the capacitive response are mainly due to the increase in the sensing film height which causes the volumetric replacement of air with its lower dielectric constant with sensing film with higher dielectric constant. It has been shown that 95% of all electric field lines of an IDE-based capacitor are contained within ½ the periodicity of the electrodes [10]; for the IDE in this paper, this critical thickness would be 4μm. Importantly, swelling is only important for thin sensing films, i.e., sensing film thicknesses smaller than this critical thickness, as is the case in this work.

The gravimetric sensor detects a mass change as soon as the analyte molecule enters the sensing film. In contrast, the capacitive response contribution due to the dielectric constant change of an analyte molecule increases as the analyte diffuses deeper into the sensing film due to the non-uniform electric field distribution. As a result, the capacitive response due dielectric property changes should always slower than the gravimetric response. How can we then explain the observed faster capacitive response in case of the aromatics? It is believed that the swelling-based contributions to the capacitive response provide a means for the transient response to be "front-loaded": the initial sensing film surface is closer to the electrodes and is pushed further away into lower electric field regions due to swelling. Thus, the swelling-based component to the capacitive signal is strongest at the beginning of the analyte diffusion. If this swelling-based contribution to the capacitive sensitivity dominates the capacitive response, like in the case of the aromatics, then it is possible for the capacitive response to respond faster than its gravimetric counterpart.

The implications of this are three-fold. First, for capacitive sensors with thin polymer coatings three components can contribute to the capacitive sensitivity of the device, yielding three sources for selectivity: (1) the partition coefficient, (2) the relationship of the dielectric constants of the sensing film-analyte pair, (3) the effects of the analyte-dependent swelling behavior. The second implication is that the enhanced selectivity due to the multivariate sensor does not come at the expense of additional sensor response time. In fact, the enhanced selectivity should be more pronounced for thinner sensing films where all above components contribute to the sensor response. The third implication is that the thickness of the polymer film can be used as an additional mechanism to tune the variation in multivariate responses and, thus, the discriminatory performance.

CONCLUSION

Through the use of a novel micromachined multivariate sensor with a single polymeric sensing film, the transient behavior of gravimetric and capacitive sensor responses was investigated. Comparison of the transient sensor responses in 2D dispersion showed enhanced discriminatory ability compared to steady-state response alone, as the discriminatory power of the steady-state dispersion is concentration dependent while the transient response time dispersion is not. Observations of a counter-intuitive "front-loaded" transient behavior in which the capacitive response time was faster than the gravimetric response times for aromatics were noted and investigated within the framework of existing literature. The mechanism for this response time enhancement is hypothesized to be the result of swelling-induced changes in the capacitive response due to the use of a thin sensing film. Furthermore, this work highlights the ability of the multisensor to enhance selectivity not only through use of the steady-state dispersions but also transient response time dispersions at no additional cost to the sensor designer. Finally, this work may pave the way for future work targeting enhanced selectivity mechanisms with drastically improving sensor response times, which is a critical for monitoring VOCs in industrial environments and closed operational settings.

ACKNOWLEDGEMENTS

This work was funded in part by the U.S. Defense Health Agency, US Navy J9 Sustainment (Naval Submarine Medical Research Laboratory work unit F1811). The work was performed in part at the Georgia Tech Institute for Electronics and Nanotechnology, a member of the National Nanotechnology Coordinated Infrastructure (NNCI), which is supported by the National Science Foundation (ECCS-2025462).

The views expressed in this conference proceeding reflect the results of research conducted by the author(s) and do not necessarily reflect the official policy or position of the Department of the Navy, Department of Defense, nor the U.S. Government. LAB has been an employee of the U.S. Government. This work was prepared as part of his official duties. Title 17 U.S.C §105 provides that 'Copyright protection under this title is not available for any work of the United States Government'. Title 17 U.S.C §101 defines a U.S. Government work as a work prepared by an employee of the U.S. Government as part of that person's official duties.

REFERENCES

[1] J. Janata, Principles of Chemical Sensors, Springer, New York, 2009.

[2] J-J. Su, C. Carron, S. Truax, K. S. Demirci, L. A. Beardslee, and O. Brand, "Assessing polymer sorption kinetics using micromachined resonators," Int. Solid-State Sensors, Actuators and Microsystems Conf. (Transducers 2011), IEEE (2011) pp. 1420-1423.

[3] A. Kummer, T. Burg, and A. Hierlemann, "Transient signal analysis using complementary metal oxide semiconductor capacitive chemical microsensors," *Analytical Chemistry*, 78, 279-290 (2006).

[4] R. A. Potyrailo, "Multivariable sensors for ubiquitous monitoring of gases in the era of internet of things and industrial internet," *Chemical Rev.*, 116, 11877-11923 (2016).

[5] S. A. Schwartz., O. Brand, and L. A. Beardslee, "Micromachined mass-sensitive and capacitive chemical multisensor using single polymeric sensing film," IEEE Int. Conf. on Micro Electro Mechanical Systems (MEMS), IEEE (2020) pp. 721-724.

[6] L.A. Beardslee, C. Carron, K. S. Demirci, J. Lehman, S. Schwartz, I. Dufour, S. M. Heinrich, F. Josse, and O. Brand, "In-plane vibration of hammerhead resonators for chemical sensing applications," *ACS Sensors*, 5, 73-82 (2019).

[7] C. Carron, P. Getz, S. M. Heinrich, F. Josse, and O. Brand, "Cantilever-based resonant microsensors with integrated temperature modulation for transient chemical analysis." Int. Solid-State Sensors, Actuators and Microsystems Conf. (Transducers 2015), IEEE (2015), pp. 1511-1514.

[8] J. Comyn, ed, *Polymer Permeability*, Springer, 2012.

[9] A. M Kummer, "Tuning sensitivity and discrimination performance of CMOS capacitive chemical microsensor systems," PhD Thesis, ETH Zurich, 2004.

[10] P. Van Gerwen, W. Laureyn, W. Laureys, G. Huyberechts, M. Op De Beeck, K. Baert, J. Suls, W. Sansen, P. Jacobs, L. Hermans, and R. Mertens, "Nanoscaled interdigitated electrode arrays for biochemical sensors," *Sensors and Actuators B: Chemical*, 49, 73-80 (1998).

CONTACT

*Oliver Brand, tel: +1-404-894-9425, oliver.brand@ece.gatech.edu

A 7 GHZ ACOUSTICALLY COUPLED FILTER WITH INTRINSIC SWITCHABILITY USING FERROELECTRIC SCANDIUM-ALUMINUM NITRIDE

Sushant Rassay, Dicheng Mo, and Roozbeh Tabrizian*
Department of Electrical and Computer Engineering, University of Florida, USA

ABSTRACT

This paper reports, for the first time, on an intrinsically switchable acoustically coupled filter at ~7 GHz, created using 200nm-thick ferroelectric scandium-aluminum nitride ($Sc_{0.28}Al_{0.72}N$) film. The filter operates based on coupling local thickness-extensional bulk acoustic wave (BAW) modes through zeroth-order symmetric (S_0) Lamb wave, in a monolithic structure with properly defined interdigitated transducers (IDTs). For the first time, intrinsic switchability of the acoustically coupled filter is achieved by depolarizing the transducer through application of low-frequency pulses and exploiting the ferroelectric behavior in $Sc_{0.28}Al_{0.72}N$. A filter prototype is presented with a center frequency of 6.9 GHz, -3dB bandwidth (BW) of 196 MHz (3% fractional BW), and a passband insertion-loss of ~6dB. The filter is switched between on and off states through application of 108V pulses at 25kHz between one of the IDT ports and the bottom electrode, resulting in on/off isolation exceeding 20dB. The high performance and intrinsic switchability along with the ultraminiaturized footprint of the presented super-high-frequency monolithic filter, highlights its potential for applications in configurable front-end module of the modern 5/6G wireless systems.

KEYWORDS

Ferroelectric, intrinsic switchability, scandium-aluminum nitride, acoustically coupled filter.

INTRODUCTION

With the exponential growth in wireless data traffic, due to the emergence of novel applications such as metaverse, IoT, and connected transportation, spectrum management becomes increasingly crucial. To accommodate the ever-increasing data rates, modern wireless technologies aim to use numerous new bands extended over ultra- and super-high-frequency regimes. Additionally, modern wireless systems increasingly rely on reconfigurable RF front-ends (RFFE) to enable low-latency communication and efficient use of spectrum resources.

Currently, spectral processing at the RFFE is performed by single-frequency / band electrically coupled bulk acoustic wave (BAW) filters that are arrayed through external switches. With the radical increase in communication bands, this architecture is not scalable considering the excessive increase in the number of filters and switches, and the resulting overhead on footprint and power consumption.

On the other hand, acoustically coupled filters provide several advantages over their electrically coupled counterparts that can alleviate the RFFE scaling to adopt new communication bands. These include reduction in the overall footprint of the filter, and lessening fabrication, routing and packaging complexities [1-3]. Acoustically coupled filters were introduced by Lakin, *et. al.*, in 2002 [4], and ever since have been widely explored as an alternative to electrically coupled filters.

This acoustic filter architecture operates based on effective coupling of two local thickness-extensional BAW resonance modes, excited under input and output IDTs, through guided Lamb waves. Benefiting from a single structure, While acoustically coupled filters provide significant reduction in footprint, and fabrication and integration complexity, they suffer from a higher insertion loss and

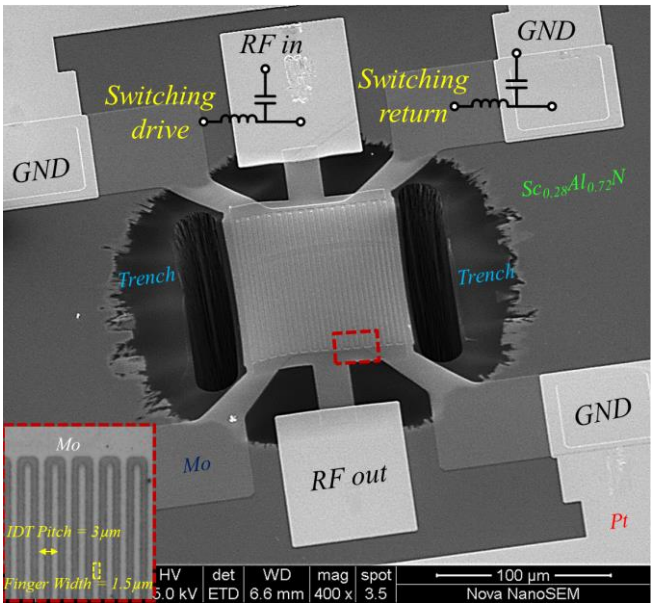

Fig. 1. The SEM image of the two-port intrinsically switchable acoustically coupled $Sc_{0.28}Al_{0.72}N$ filter. The RF and switching ports are identified. The inset shows the IDT dimensions.

lower bandwidth due to the partial electrode coverage inherent to the IDT design. However, these shortcomings can be relieved by using scandium-aluminum nitride films that provide substantially higher electromechanical coupling coefficient (k_t^2), compared to AlN. Additionally, the recent discovery of ferroelectricity in scandium-aluminum nitride [5] enables the use of polarization tuning for reconfiguration of acoustic resonators and filters [6-9].

In this work, we demonstrate the first intrinsically switchable acoustically coupled filter at 7 GHz, implemented in 200nm-thick $Sc_{0.28}Al_{0.72}N$ film. The intrinsic switchability is achieved through polarization tuning due to the ferroelectric behavior of $Sc_{0.28}Al_{0.72}N$. Figure 1 Shows the scanning electron microscope (SEM) image of the acoustically coupled filter, along with the RF and switching ports configuration.

OPERATION PRINCPLE

In this work, the acoustically coupled filter is realized by coupling the local thickness-extensional BAW under input and output IDTs through the S_0 Lamb wave. The BAW modes, which play a similar role to the shunt elements in ladder-type electrically coupled filters, are localized under IDT fingers due to the acoustic impedance mismatch with non-electroded regions. These local BAW modes are coupled together through the S_0 Lamb wave propagating across the non-electroded regions. With proper design of IDT pitch and electrode width, the Lamb wave propagation results in a second resonance mode with a frequency slightly higher than the anti-resonance of the local BAW modes. This Lamb mode plays a similar role to the series element in ladder-type electrically coupled filters. This operation concept is schematically shown in fig. 2, where the BAW and Lamb modes are represented by RLC

978-1-940470-04-7/HH2022/$25©2022TRF
DOI 10.31438/trf.hh2022.39

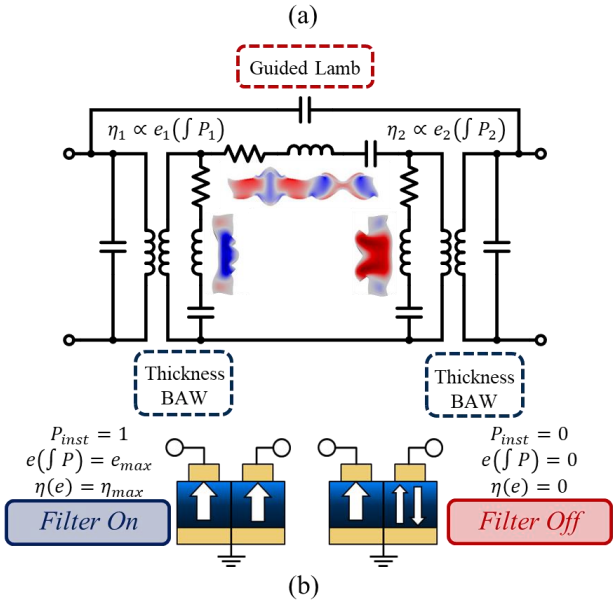

Fig. 2. (a) Electromechanical equivalent model of the acoustically coupled filter and the constituent resonance modes. (b) Conceptual intrinsic switching principle showing the filter in On and off states. These states are defined by the net polarization under the IDT ports.

branches placed in shunt and series, respectively. The COMSOL simulated deformation mode-shape for each element is also shown.

The electromechanical transduction of the filter is represented by two transformers at the input and output ports, along with the corresponding static capacitors. The transformer ratios are identified by the IDT finger width and are proportional to the piezoelectric coefficients (e_{ij}) of the film. Considering the ferroelectricity in $Sc_{0.28}Al_{0.72}N$, e_{ij} can be tuned by polarization switching through application of low-frequency pulses with amplitude close to the coercive field [9]. Depending on the magnitude and number of applied switching pulses, a finite number of ferroelectric domains (*i.e.*, single-crystal grains within the polycrystalline $Sc_{0.28}Al_{0.72}N$ film) reverse their polarity. This results in cancelation of electromechanical transduction and reduces effective e_{ij} in pulsed region of the film. In an ideal case, when the polarization in half of ferroelectric domains is reversed, the effective e_{ij} is nulled and electromechanical transduction is switched off.

The intrinsic switching principle is represented in equivalent model of the filter (fig. 2) by polarization-dependent transduction efficiency of transformers. Upon application of sufficient pulses between one or both of IDTs and the bottom electrode through a bias-tee, the net polarization (*i.e.*, $\int P$) under one or both IDT ports is nulled, and the filter is switched off. Continuing application of switching pulses, to fully reverse the polarization of the entire domains, switches the filter back to the on state.

FABRICATION PROCESS

The fabrication process flow for realization of the $Sc_{0.28}Al_{0.72}N$ acoustically coupled filters is shown in fig. 3. The process consists of DC sputtering deposition of 100nm Mo layer, atop a 30nm AlN film that serves as the seed for (110)-textured growth of Mo. Bottom Mo layer is then patterned using a boron trichloride (BCl_3) based recipe in a reactive-ion-etching inductively coupled plasma (RIE-ICP) system. To ensure crack-free growth of the subsequent films, the Mo film is patterned using tapered photoresist masks created

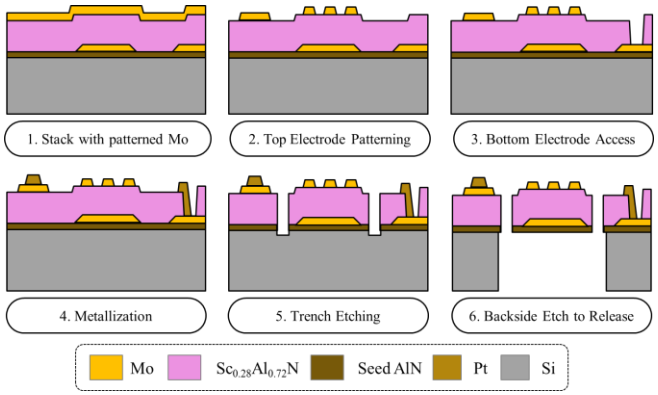

Fig. 3. Fabrication process flow for implementation of acoustically coupled filter in a 200nm-thick $Sc_{0.28}Al_{0.72}N$ films, based on using a six-mask process for patterning electrodes and releasing structure.

by proximity exposure method. The resulting tapered sidewalls of the bottom Mo patterns enables crack-free growth of the $Sc_{0.28}Al_{0.72}N$ layer.

Following bottom electrode patterning, a c-axis textured 200nm-thick $Sc_{0.28}Al_{0.72}N$ layer is deposited using reactive magnetron sputtering from segmented scandium-aluminum targets [10, 11]. Next, a 150nm thick Mo layer is DC sputtered and patterned using SF_6 in RIE-ICP, to create top IDT ports of the filter.

This is followed by etching $Sc_{0.28}Al_{0.72}N$, using a Cl_2-based recipe in RIE-ICP, to access bottom Mo. Next, a 500nm-thick platinum (Pt) is lifted-off to create the pads. Lateral geometry of the resonator is then formed by etching trenches using a high power Cl_2/BCl_3 based recipe in the RIE-ICP system and PECVD SiO_2 as the hard-mask. Finally, the device is released from the backside of the Si substrate by deep reactive ion etching (DRIE).

CHARACTERIZATION

The RF performance of the fabricated filters are characterized using Keysight 5222A Vector Network Analyzer (VNA), along with a short-open-load-through (SOLT) calibration procedure enabled by CS-5 calibration kit. Ferroelectric hysteresis characterization and filter switching is performed using a Radiant PiezoMEMS ferroelectric tester.

The measured filter transmission and reflection responses (*i.e.*, $|S_{21}|$ and $|S_{11}|$) are shown in fig. 4. A center frequency of 6.9 GHz, a

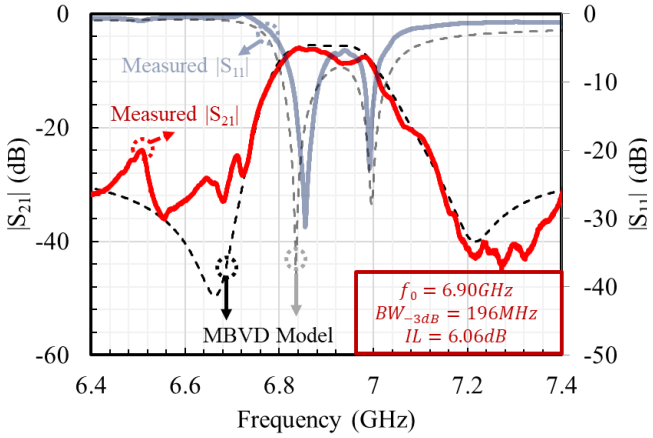

Fig. 4. The measured $|S_{21}|$ and $|S_{11}|$ responses of the filter with a BW_{-3dB} of ~196MHz at 6.9GHz. The measured response is compared to the response obtained from the MBVD model shown in fig. 5.

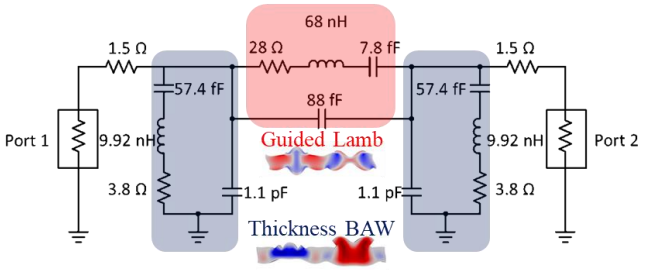

Fig. 5. The electrical equivalent circuit of the acoutically coupled filter. The deformation shape of consitutent BAW and Lamb modes are also shown by the corresponding resonator element.

BW_{-3dB} of 196 MHz (~3% fractional bandwidth), and an insertion loss (IL) of 6.06dB is extracted.

Figure 4 also shows the fitted response from the MBVD model of the filter, with electrical equivalent circuit detailed in fig. 5. An accurate match of the measured and modeled responses is evident, confirming the discussed operation principle of the acoustically coupled filter.

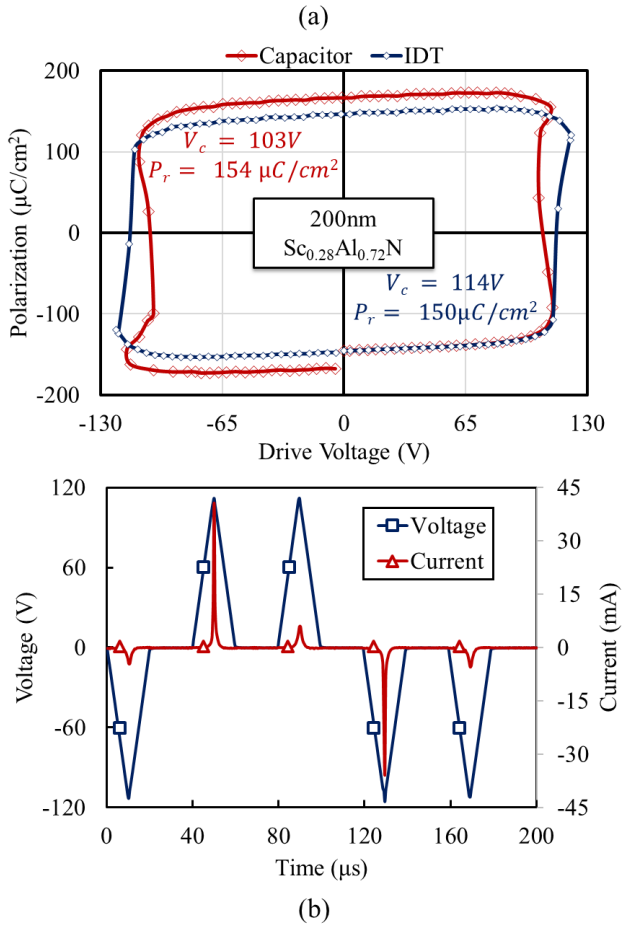

Fig. 6. (a) Comparison of the measured polarization-voltage hysteresis loops at one of the IDT ports (prior to resonator release) and a 100μm×100μm capacitor. (b) Measured instantaneous current for the PUND test to determine accurate voltage needed for switching filter between on and off states.

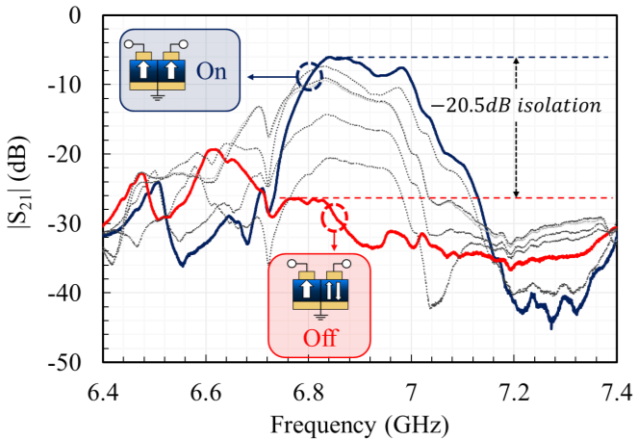

Fig. 7. Measured transmission response of the acoustically coupled filter and its evolution upon application of single triangular pulses at -108V leading to depolarized (i.e., off) state after the fifth pulse.

To identify the required switching voltage, the polarization hysteresis of ferroelectric $Sc_{0.28}Al_{0.72}N$ film is measured. Figure 6 (a) shows the polarization hysteresis loop under the IDTs in comparison with a 100μm×100μm capacitor. The polarization loops are measured by applying bipolar triangular pulses at 100kHz frequency and with 125V amplitude. A 114V coercive voltage is extracted from the loop for IDT capacitor, which identifies the switching voltage of the filter. Figure 6 (b) shows the instantaneous current measured upon driving the IDT capacitor with a 45kHz negative positive-up-negative-down (PUND) pulse sequence. The significant change in instantaneous current when the sign of driving voltage pulse is changed corresponds to the $Sc_{0.28}Al_{0.72}N$ film polarization transitioning between metal- and nitrogen-polar states.

A pulse amplitude of 108V, which is slightly smaller than the coercive voltage, is used for filter switching. This enables access to depolarization state with nulled electromechanical transduction (*i.e.*, the filter Off state) with application of 5 pulses. Pulsed switching is performed using 25kHz triangular monopolar train with a voltage of 108V, to depolarize / polarize resonator for Off/On operation.

Figure 7 shows the filter transmission response evolution from the On-state to Off-state (*i.e.*, depolarized transducer) by application of monopolar triangular pulses to one of the resonator ports. The resonator turns completely off after application of 5 pulses, resulting in a ~20.5dB isolation. While application of negative monopolar pulses on one of IDT ports results in the gradual increase of the IL in filter passband, it may induce undesirable excitation of spurious modes, as evident in fig. 7. These modes can be further suppressed by application of the switching depolarization pulses to the second IDT port. This will be further explored in future publications.

CONCLUSION

This paper, for the first time, demonstrates an intrinsically switchable acoustically coupled filter created in $Sc_{0.28}Al_{0.72}N$, with a center frequency of ~6.9 GHz and a BW_{-3dB} of 196 MHz. Intrinsic switchability is achieved through application of consecutive triangular monopolar pulses of 108V to one of IDT ports of the filter, resulting in polarization and depolarization of the piezoelectric transduction to switch the filter between On and Off states, respectively. The filter operation principle, based on coupling thickness-extensional BAW modes with S_0 Lamb waves, concept is presented, and the switching principle based on ferroelectric polarization tuning in $Sc_{0.28}Al_{0.72}N$ is discussed. The filter prototype is switched between On and Off states through application of 25kHz

pulses at 108V to one of the filter ports. An on/off isolation of ~20.5dB is achieved. The high performance and intrinsic switchability of the presented $Sc_{0.28}Al_{0.72}N$ acoustically coupled filter highlight its potential for application in configurable super-high-frequency RF front-end of emerging 5G/6G systems.

ACKNOWLEDGEMENT

The authors would like to thank the staff at Nanoscale Research Facility at the University of Florida with device fabrication support. This work was supported in parts by the Defense Advanced Research Projects Agency (DARPA), Tunable Ferroelectric Nitrides (TUFEN) Program under Grant HR00112090049, and the National Science Foundation (NSF) through the CAREER award (Grant ECCS-1752206).

REFERENCES

[1] R. Abdolvand and F. Ayazi, "Monolithic Thin-Film Piezoelectric-on-Substrate Filters," 2007 IEEE/MTT-S International Microwave Symposium, 2007, pp. 509-512, doi: 10.1109/MWSYM.2007.380519.

[2] T. Pensala, T. Makkonen, J. Dekker and M. Ylilammi, "Laterally Acoustically Coupled BAW Filters at 3.6 GHz," 2018 IEEE International Ultrasonics Symposium (IUS), 2018, pp. 1-4, doi: 10.1109/ULTSYM.2018.8579900.

[3] W. Pan, V. A. Thakar, M. Rais-Zadeh and F. Ayazi, "Acoustically coupled thickness-mode AIN-on-Si band-pass filters-part I: principle and devices," in IEEE Transactions on Ultrasonics, Ferroelectrics, and Frequency Control, vol. 59, no. 10, pp. 2262-2269, October 2012, doi: 10.1109/TUFFC.2012.2451.

[4] K. M. Lakin, "Coupled resonator filters," 2002 IEEE Ultrasonics Symposium, 2002. Proceedings., 2002, pp. 901-908 vol.1, doi: 10.1109/ULTSYM.2002.1193543.

[5] S. Fichtner, N. Wolff, F. Lofink, L. Kienle, & B. Wagner, "AlScN: A III-V semiconductor based ferroelectric," *Journal of Applied Physics*, 125(11), 114103 (2019).

[6] S. Rassay, F. Hakim, M. Ramezani and R. Tabrizian, "Acoustically Coupled Wideband RF Filters with Bandwidth Reconfigurablity Using Ferroelectric Aluminum Scandium Nitride Film," 2020 IEEE 33rd International Conference on Micro Electro Mechanical Systems (MEMS), 2020, pp. 1254-1257, doi: 10.1109/MEMS46641.2020.9056353.

[7] S. Rassay, D. Mo, C. Li, N. Choudhary, C. Forgey and R. Tabrizian, "Intrinsically Switchable Ferroelectric Scandium Aluminum Nitride Lamb-Mode Resonators," in *IEEE Electron Device Letters*, vol. 42, no. 7, pp. 1065-1068, July 2021, doi: 10.1109/LED.2021.3078444.

[8] S. Dabas, D. Mo, S. Rassay and R. Tabrizian, "Intrinsically Tunable Laminated Ferroelectric Scandium Aluminum Nitride Extensional Resonator Based on Local Polarization Switching," 2022 IEEE 35th International Conference on Micro Electro Mechanical Systems Conference (MEMS), 2022, pp. 1050-1053, doi: 10.1109/MEMS51670.2022.9699790.

[9] D. Mo, S. Rassay and R. Tabrizian, "Intrinsically Switchable Ferroelectric Scandium Aluminum Nitride Bulk Acoustic Wave Resonators," 2021 21st International Conference on Solid-State Sensors, Actuators and Microsystems (Transducers), 2021, pp. 317-320, doi: 10.1109/Transducers50396.2021.9495634.

[10] V. Felmetsger, M. Mikhov, M. Ramezani and R. Tabrizian, "Sputter Process Optimization for Al0.7Sc0.3N Piezoelectric Films," 2019 IEEE International Ultrasonics Symposium (IUS), 2019, pp. 2600-2603, doi: 10.1109/ULTSYM.2019.8925576.

[11] S. Rassay, F. Hakim, C. Li, C. Forgey, N. Choudhary, & R. Tabrizian, "A Segmented-Target Sputtering Process for Growth of Sub-50 nm Ferroelectric Scandium–Aluminum–Nitride Films with Composition and Stress Tuning", *physica status solidi (RRL)–Rapid Research Letters*, 15(5), 2100087, (2021).

CONTACT

*Sushant Rassay, tel: +1-321-616-1298; sushantrassay@ufl.edu.

A FLEXIBLE ORIGAMI OPTO-ELECTRO ARRAY FOR IN VIVO OPTOGENETIC STIMULATION AND ELECTROPHYSIOLOGY RECORDINGS FROM DORSAL ROOT GANGLION

Yan Gong[1], Xiang Liu[1], and Wen Li[1]
[1]Michigan State University, USA

ABSTRACT
In this study, a thin-film, three-dimensional (3D) opto-electro array with 4 addressable microscale light-emitting diodes for surface illumination of dorsal root ganglions (DRGs) and 9 penetrating electrodes for simultaneous recordings of light-evoked DRG activities is described for Developing a tool to better understand the relationship between spindle length-sensitive afferents from hip muscles and both interlimb coordination and gait selection. Importantly, using the origami design concept, the array can be fabricated directly on a silicon wafer in a two-dimensional (2D) configuration, which can transform into a 3D structure by folding.

KEYWORDS
Thin-Film, Opto-Electro Array, Origami, Optogenetic.

INTRODUCATION
Developing a tool to better understand the relationship between spindle length-sensitive afferents from hip muscles and both interlimb coordination and gait selection is an active area of biomedical microelectrochemical systems research. Future tools must be flexible and configurable, given the evolving understanding of both neuroscience mechanisms and clinical outcomes. We describe a thin-film, three-dimensional (3D) opto-electro array (Fig.1) with 4 addressable microscale light-emitting diodes for surface illumination of dorsal root ganglions (DRGs) and 9 penetrating electrodes for simultaneous recordings of light-evoked DRG activities. Inspired by origami concept [1], a trench structure combined with magnetic material to form a hinge structure on a flexible polymer substrate, The opto-electro array can rely on this hinge structure to automatic raising up to achieve the function of 2D to 3D conversion. Compared with the traditional 3D array fabrication, this origami folding technique can reduce the probe fabricating difficulty and cost, especially in the production of relatively long probes (>1mm). Moreover, fabricating a 2-dimensional opto-electro array by photolithography enables independently control the shape, and the length of individual microneedles, thereby forming an array of different lengths to meet the requirements of optogenetic stimulation and electrophysiology recording.

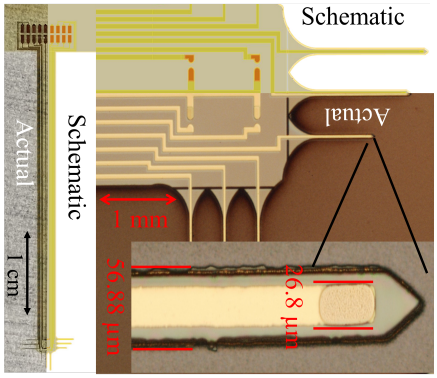

Fig. 1. Schematic diagram of the flexible origami opto-electro array vs. images of the fabricated array.

METHOD
In this study, polyimide was chosen as the substrate and packaging material. Particularly, PI-2600 low stress polyimide (PI, HD MicroSystem™, Parlin, NJ, US) is used, because its high-temperature stability (up to 400 °C) [2], and high bendability [3]. While using flexible materials as probe array, compared to solid materials, low stress polyimide material provides a certain degree of mechanical buffering that avoids damaging the soft tissue [4]. Fig.2 depicts the core fabrication process flow of the opto-electro array. Specifically, (Fig.2-1) A 1μm thick layer of silicon dioxide as a sacrificial layer was deposited on the wafer by PECVD. Etching the sacrificial layer at the last step ensured that the probe can be released from the wafer smoothly. PI was spun on the adhesion promoter (VM652), and the thickness of PI was about 5μm. After PI was cured, 200nm copper layer was thermal evaporated on PI layer as hard mask, followed by a reactive ion etching processing. (Fig.2-2) Gold was selected as the electrode material, and the designed circuit was patterned by photolithography. (Fig.2-3) Another PI layer was fabricated by same way to encapsulate the probe and define the detection windows and mounting pads. (Fig.2-4) Next, a 500nm copper layer was thermal evaporated on the designated location that can reinforce the gold layer to prevent the metal peel off due to soldering. (Fig.2-5) flexible arrays were released from wafer. (Fig.2-6) LEDs were soldered on the device. Meanwhile, the simulation results (Fig.3) show that after bending, the stress points are concentrated in the preset trench structure. The design purpose is to reduce the force applied to the wire as much as possible, and to safely increase the force applied to the substrate to ensure its deformation. Ideally, a part of the thickness of the cantilever structure will "sit" on the bottom structure to keep the bent state stable.

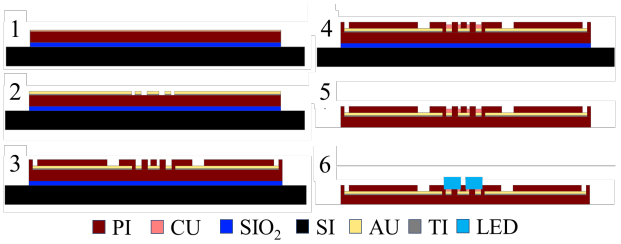

Fig. 2. Fabrication process flow of the opto-electro array.

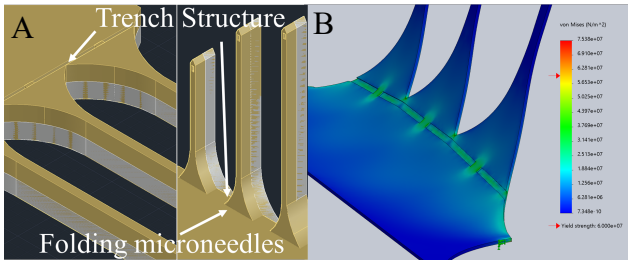

Fig. 3. (A) Schematic diagram of the trench structure. (B) FEM Simulation of the force distribution on the trench area.

978-1-940470-04-7/HH2022/$25©2022TRF
DOI 10.31438/trf.hh2022.40

DISCUSSION

Although the results from the current stage are relatively preliminary, they still demonstrate the feasibility of the flexible origami opto-electro array. The optical and thermal properties of the probe after implantation were also investigated by in vitro experiments (Fig.4 and 5). Fig. 4 shows that the LEDs installed on the probe are sufficient to affect the target area with a light intensity of 1mw/mm^2 at 1mm away from the LEDs, suitable for activating channelrhodopsin [5,6]. Fig. 5 shows that the temperature rise caused by continuously powered LEDs in 30 minutes is less than 1.5ºC, which would not cause severe damage to the nerves in a short term. The average impedance of the electrophysiological recording probe by EIS measurement is 239 KΩ (n=3) at 1000Hz (Fig.6). Furthermore, the maximum brain tissue force is known to be 1000 μN and based on buckling force calculation formula [7], the theoretical yield strength of a single probe in our array is 993 μN. This means that the probe cannot penetrate brain tissue smoothly, and this calculation result is consistent with the actual insertion experiment results. It means that Polyethylene glycol (PEG) coating technique will be further introduced to enhance the strength of the microneedle to penetrate the tissue [8,9]. In the future, the device will be assembled with an external electronic head stage [10] and tested in cat models to validate its capability for optogenetic stimulation and electrophysiology recordings from DRGs.

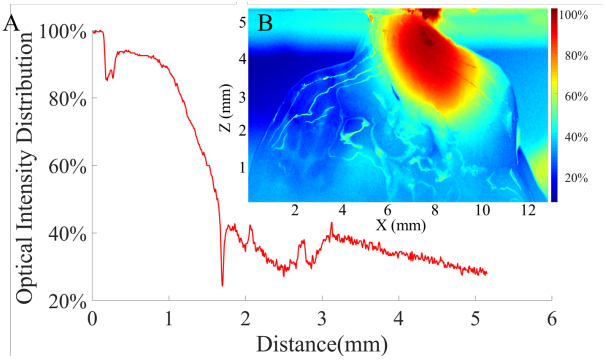

Fig. 4. (A) Optical intensity distribution measured from the μ-LED to the surrounding mouse brain. (B) Photo image of the optical intensity distribution around the μ-LED in the mouse brain (input power = 15mW/optical power =3.85mW)

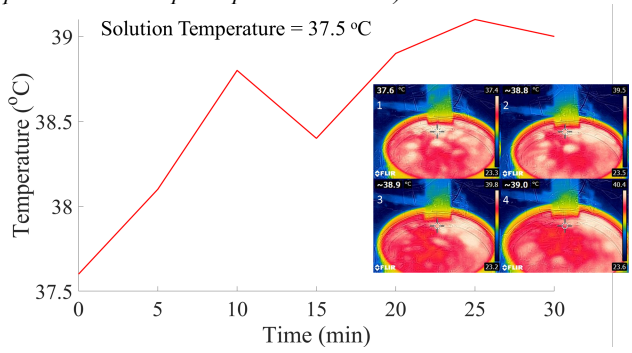

Fig. 5. Time-dependent temperature fluctuation of the LED (input power = 10mW), measured in PBS solution with a FLIR infrared thermal imaging camera at 10 cm distance. Inset shows the infrared images taken (1) at 0 min, (2) at 10 min, (3) at 20 min and (4) at 30 min.

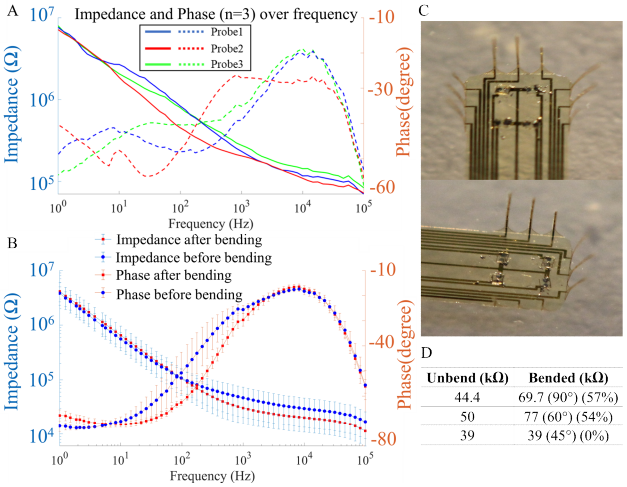

Unbend (kΩ)	Bended (kΩ)
44.4	69.7 (90°) (57%)
50	77 (60°) (54%)
39	39 (45°) (0%)

Fig. 6. (A) Electrochemical impedance of the electrodes measured over a broad frequency range from 1-100 kHz. (B) Comparison of the broad-band impedance of the electrodes (n=4) before and after bending. (C) Photo images of the bent probes. (D) Impedance of the bent probes measured at different bending angles.

ACKNOWLEDGEMENTS

This project is supported by National Science Foundation under award numbers ECCS-2024270

REFERENCES:

1. Park, Yoonseok, et al. "Three-dimensional, multifunctional neural interfaces for cortical spheroids and engineered assembloids." Science Advances 7.12 (2021): eabf9153.
2. Kim, B. J., and Meng, E. (2015). Review of polymer MEMS micromachining. J. Micromechanics Microengineering 26, 13001.
3. Hassler, C., Boretius, T., and Stieglitz, T. (2011). Polymers for neural implants. J. Polym. Sci. Part B Polym. Phys. 49, 18–33.
4. Wasikiewicz, J. M., Roohpour, N., and Vadgama, P. (2013). “Packaging and coating materials for implantable devices,” in Implantable Sensor Systems for Medical Applications (Elsevier), 68–107.
5. Kwon, Ki Yong, et al. "Opto-μECoG array: A hybrid neural interface with transparent μECoG electrode array and integrated LEDs for optogenetics." IEEE transactions on biomedical circuits and systems 7.5 (2013): 593-600.
6. Khan, Wasif, et al. "Inductively coupled, mm-sized, single channel optical neuro-stimulator with intensity enhancer." Microsystems & nanoengineering 5.1 (2019): 1-12.
7. Maxfield, Brent. "Essential MATHCAD for Engineering, Science and Math." Moscow. Academic.
8. Yang, Weiyang, Yan Gong, and Wen Li. "A review: electrode and packaging materials for neurophysiology recording implants." Frontiers in Bioengineering and Biotechnology (2021): 1515.
9. Zhang, Wenguang, et al. "Implanting mechanics of PEG/DEX coated flexible neural probe: impacts of fabricating methods." Biomedical Microdevices 23.1 (2021): 1-16.
10. Zhao, Linran, et al. "Wireless Multimodal Neural Interface Device for Neural Control Studies." 2021 IEEE Biomedical Circuits and Systems Conference (BioCAS). IEEE, 2021.

A $SC_{0.28}AL_{0.72}N$ LAMINATED BULK ACOUSTIC WAVE RESONATOR WITH SELF-OVEN-CONTROLLED SWITCHABILITY

Shaurya Dabas, Dicheng Mo, Sushant Rassay, and Roozbeh Tabrizian*
Department of Electrical and Computer Engineering, University of Florida, USA

ABSTRACT

This abstract reports an intrinsically switchable 7.01 GHz thickness-extensional bulk acoustic wave (BAW) scandium-aluminum nitride ($Sc_{0.28}Al_{0.72}N$) resonator with a reduced switching voltage using self-ovenization. The resonator is created from alternative stacking of two $Sc_{0.28}Al_{0.72}N$ layers with three electrode layers, enabling tailorability of transducer polarization across the thickness and based on ferroelectricity. Upon aligning the polarization of the two $Sc_{0.28}Al_{0.72}N$ layers in the same or opposite directions, the electromechanical coupling of the thickness-extensional mode is maximized or nulled, resulting in operation of the resonator in On and Off states, respectively. Besides, the switching voltage is significantly reduced by self-ovenization of the resonator through a DC-biased serpentine-shaped top electrode and due to the temperature-dependent reduction in $Sc_{0.28}Al_{0.72}N$ coercive field. A prototype is demonstrated at 7.01 GHz with a k_t^2 of 6.95% and a loaded Q of 72.2. The intrinsic switchability is successfully demonstrated with and without self-ovenization, using 25kHz triangular pulses with 80.6V and 63.6V amplitude, respectively. The presented results highlight the potential of self-ovenization to reduce the large switching voltage of $Sc_{0.28}Al_{0.72}N$ resonators and filters for configurable RF front-end applications.

KEYWORDS

Intrinsic switchability; ferroelectric; scandium aluminum nitride; Joule heating; ovenization; bulk acoustic wave resonator.

INTRODUCTION

Scandium-aluminum nitride ($Sc_xAl_{1-x}N$) is growingly considered to replace aluminum nitride films that are currently used for creation of radio-frequency acoustic resonators and filters for wireless systems. The significantly larger electromechanical coupling (k_t^2) that only increases with Sc content enables realization of filters with higher bandwidth and lower loss. Further, the newly discovered ferroelectricity in $Sc_xAl_{1-x}N$ provides unprecedented opportunities for realization of intrinsic switchability and tunability without the need for external switches and varactors. This is highly desirable considering the adoption of multi-band RF front-end to accommodate efficient communication in crowded and congested ecosystem of the modern connected world [1,2].

Using polarization tuning for intrinsic switching has been widely explored in acoustic resonators created in perovskite ferroelectric or paraelectric films, such as PZT and BST [3-5]. These materials generally provide a soft ferroelectric behavior, where the polarization, dielectric constant, and piezoelectric coupling can be continuously tuned by application of a DC voltage. This is not the case in $Sc_xAl_{1-x}N$ resonator with hard ferroelectric behavior, where the box-shaped hysteresis loop only allows binary polarization states with similar electromechanical coupling [6]. Targeting the intermediate polarization states through application of DC voltage is also not trivial in $Sc_xAl_{1-x}N$, considering the undesirably close breakdown and coercive fields. Besides, the large coercive field of $Sc_xAl_{1-x}N$, which is nearly two orders of magnitude higher compared to conventional perovskites, results in very large switching and tuning voltages that is hard to provide on chip.

Despite these challenges, a new wave of intrinsically switchable $Sc_xAl_{1-x}N$ BAW and Lamb wave resonators are recently

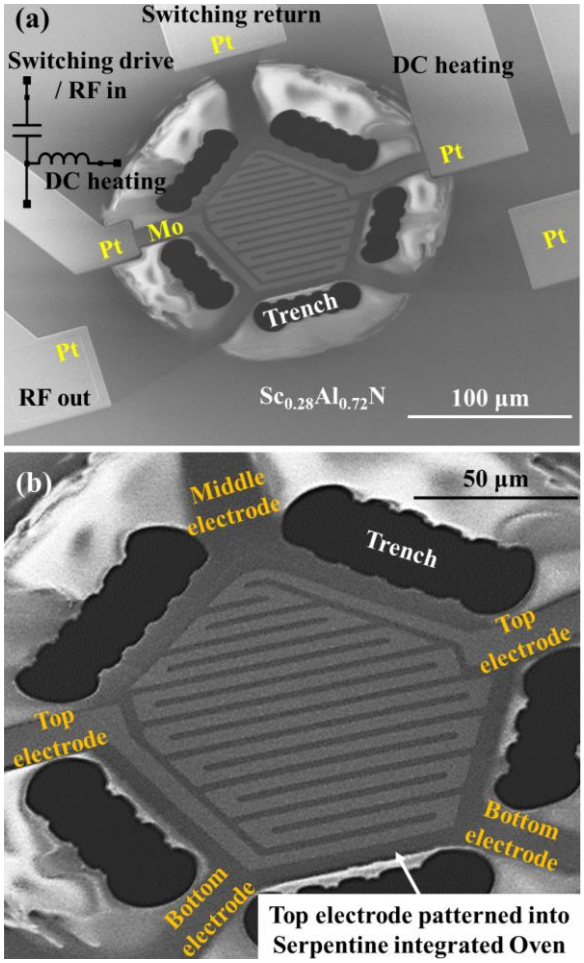

Fig. 1. (a) Top-view SEM image of the intrinsically switchable BAW resonator created in laminated $Sc_{0.28}Al_{0.72}N$ *transducer. (b) Zoomed-in SEM of the top electrode which is patterned to form integrated oven for Joule heating the resonator.*

demonstrated, based on tuning polarization through application of low-frequency pulses [7-12]. In these approaches, switching pulses with slightly lower voltage than coercive is applied, to enable "transducer depolarization" through reversing c-axis in a fraction of ferroelectric domains and reducing the net electromechanical coupling by charge cancellation. This approach, however, is not reliable due to the uncertain nature of partial domain switching.

In this work, for the first time, we demonstrate certain and repeatable switchability in BAW resonator by laminating two $Sc_{0.28}Al_{0.72}N$ layers and controlling their individual polarization. This laminate resonator shown in Fig. 1(a) enables switching of the resonator between On and Off states, upon pulsed poling of the two $Sc_{0.28}Al_{0.72}N$ layers in the same or opposite direction, respectively. Besides, we demonstrate a novel approach for reduction of switching voltage based on self-ovenizing the resonator through Joule heating. Self-ovenization by Joule heating by applying a DC current through the serpentine top electrode (Fig. 1(b)) enables a significant reduction in coercive field and switching voltage.

978-1-940470-04-7/HH2022/$25©2022TRF
DOI 10.31438/trf.hh2022.41

Solid-State Sensors, Actuators, and Microsystems Workshop
Hilton Head Island, South Carolina, June 5-9, 2022

OPERATION PRINCIPLE

The intrinsically switchable resonator is created from alternative stacking of two $Sc_{0.28}Al_{0.72}N$ layers within three molybdenum (Mo) electrodes. Exciting the fundamental thickness extensional (TE_1) mode in ferroelectric requires alignment of mechanical mode shape, ferroelectric polarization, and applied electric field. Accordingly, upon switching the polarization of the two $Sc_{0.28}Al_{0.72}N$ layers in opposite directions, the net polarization (P) across laminate thickness is reduced to zero, which results in a nulled electromechanical coupling of the TE_1 mode, and the resonator is turned off. Such switching is not achievable in a single-layer BAW resonator, considering the hard ferroelectric behavior of $Sc_xAl_{1-x}N$. This characteristic limits the practical polarization of each ferroelectric domain to either up or down; thus, depolarization approaches used in soft ferroelectric and piezoelectric materials (*e.g.* PZT and BST) is not applicable. Depolarization of $Sc_xAl_{1-x}N$ can be achieved through partial switching of domains using low-frequency pulses with slightly lower value compared to coercive. However, this approach is highly uncertain and achieving repeatable depolarized state is not practical. The comparison of intrinsic switching in single-layer and laminated $Sc_xAl_{1-x}N$ transducer is conceptually shown in Fig. 2. It is evident how the laminated transducer enables deterministic switching based on complete polarization reversal in the bottom $Sc_xAl_{1-x}N$ layer, to oppose the top and null the electromechanical coupling for TE_1 mode.

In this work, the laminated transducer is further equipped with a serpentine-shaped top electrode to enable integrated ovenization of the resonator through application of a DC current and via Joule heating. The integrated heater enables temporary ovenization of the resonator during polarization switching, to benefit from large reduction in coercive field of $Sc_xAl_{1-x}N$ [6]. This facilitates reduction of the resonator switching voltage.

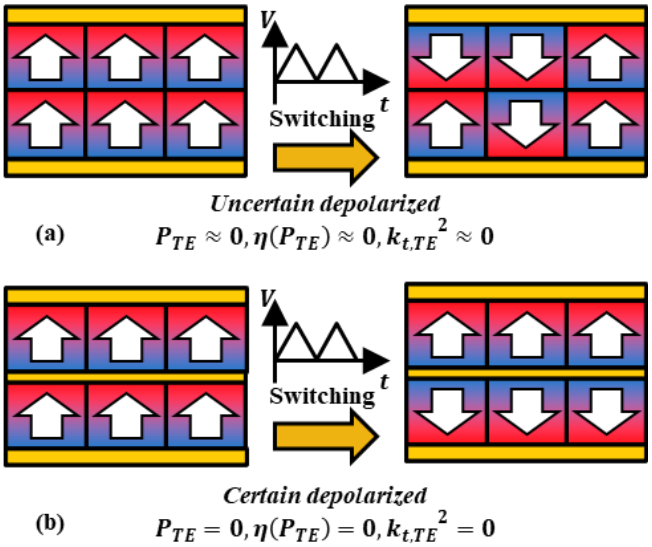

Figure 2. (a) Single-layer resonator switching by depolarizing the ferroelectric film. This is difficult as it requires extremely precise pulse control to pole exactly 50% of crystal domains into the opposite direction. (b) The deterministic switching concept of the presented laminated double-layer resonator, based on complete polarization reversal in one of the layers.

FABRICATION PROCESS

Figure 4 shows a detailed process flow. The laminated resonator is created by sputtering a 50nm bottom Mo electrode atop

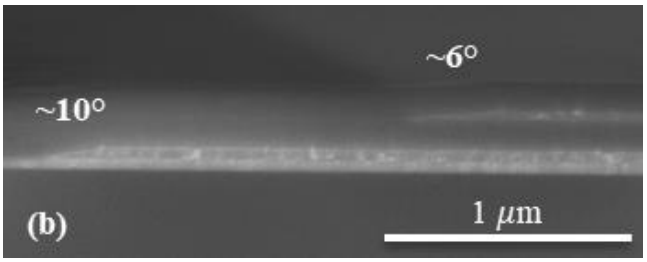

Figure 3. Tapered sidewall of bottom and middle Mo electrodes enables crack-free growth of $Sc_{0.28}Al_{0.72}N$ layers.

of a 50nm AlN seed layer. The AlN seed layer helps textured growth of (110) Mo and facilitate crystalline growth of subsequent $Sc_{0.28}Al_{0.72}N$ films in c-axis orientation. Further, the seed layer ensures the suppression of abnormal grains with undesired crystal morphology [13, 14]. After patterning the bottom Mo electrode, 140nm bottom $Sc_{0.28}Al_{0.72}N$ film is sputtered followed by deposition and patterning of 50nm middle Mo electrode. Finally, 140nm of top $Sc_{0.28}Al_{0.72}N$ film is sputtered followed by deposition and patterning of the top 50nm Mo electrode into serpentine heaters. The bottom and middle Mo electrodes are patterned using proximity-exposed photoresist etch-mask and BCl_3 dry-etch recipe to form a highly tapered sidewall profile. This profile is shown in Fig. 3 and is required to ensure crack-free growth of $Sc_{0.28}Al_{0.72}N$ layers.

After completion of the transducer stack, bottom and middle electrodes are accessed by dry etching of $Sc_{0.28}Al_{0.72}N$ layers using a high-power Cl_2 recipe. A thick platinum (Pt) layer is deposited using liftoff, to serve for low-loss routings and pad. Trenches are then etched to define the geometry of the resonator. Finally, the device is released by etching Si handle-layer from backside via the Bosch process in a DRIE tool. In this step, the AlN seed layer serves as an etch stop to prevent over-etch into the device and its bottom Mo electrode.

CHARACTERIZATION

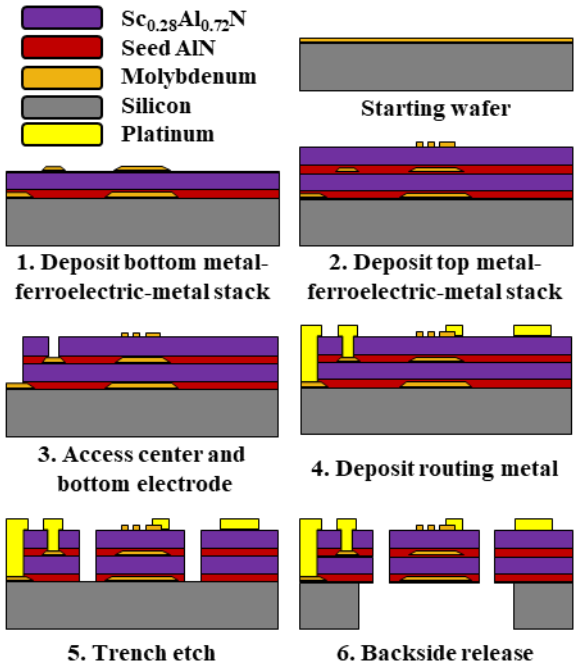

Figure 4. a six-step process flow for laminated bulk acoustic wave resonator with self-oven-controlled switchability.

The laminated $Sc_{0.28}Al_{0.72}N$ BAW resonators are characterized using ferroelectric and RF measurement. The ferroelectric polarization hysteresis and switching behavior of the constituent $Sc_{0.28}Al_{0.72}N$ layers are measured using a Radiant PiezoMEMS ferroelectric tester with DC probes, and the DC heating voltage across the serpentine electrode are applied using Keysight E36105A DC power supply. Besides, the resonator admittance is extracted from the reflectance (S_{11}) measured using Keysight N5222A PNA vector network analyzer (VNA) with GSG probes calibrated using short-open-load-though procedure with CS-5 calibration substrate. All the measurement are conducted on the Semi-Probe PSL4 RF probe station.

Ferroelectric characterization

The polarization hysteresis loop of the 140nm bottom $Sc_{0.28}Al_{0.72}N$ layer is extracted by exciting the film with 84V, 25kHz bipolar triangular pulses. The polarization hysteresis loop is measured under ovenization through application of different DC voltages across the serpentine electrode. Figure 5 shows the measurement setup, highlighting the ovenization voltage application through a bias-tee. Figure 6 shows the measured hysteresis loops for different DC ovenization voltages, highlighting the reduction of coercive field at higher DC voltages, corresponding to increased temperature of the film. This indicates the reduction in the voltage required for switching resonator upon application of the ovenization. It should be noted that the apparent scaling of the loop

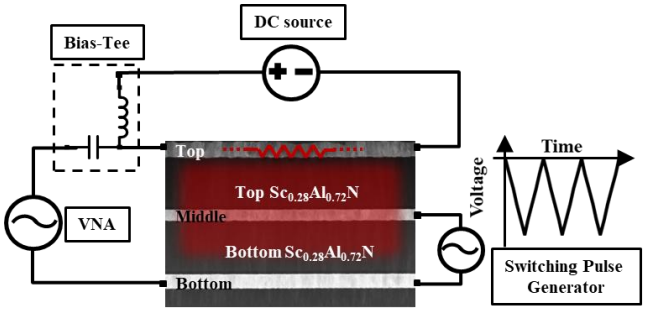

Figure 5. Schematic demonstration of the measurement setup for switching the laminated thickness-extensional resonator. The cross-section of the resonator is shown along with the DC source and pulse generator used for ovenization and polarization switching, respectively.

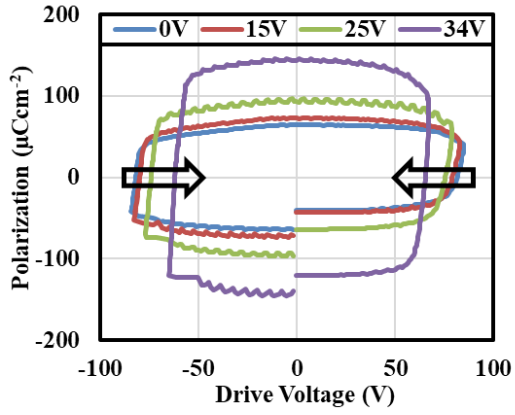

Figure 6: Evolution of the PV loop for bottom $Sc_{0.28}Al_{0.72}N$ layer, for different ovenization voltage (applied across top electrode). The large drop in coercive voltage with increasing ovenization voltage is evident. The apparent increase in polarization is due to increase in leakage current at higher temperatures.

in y-axis direction upon increased ovenization voltage direction is due to an increased feedthrough current at higher temperatures, rather than any change in remanent polarization of the film.

RF characterization

The resonator admittance is extracted from the measured S_{11}, and the k_t^2 and Q are calculated using [15,16]:

$$k_t^2 = \frac{\pi^2}{8}\left(\frac{f_p^2 - f_s^2}{f_s^2}\right), Q = \frac{f}{2}\left|\frac{\partial \varphi_Y}{\partial f}\right| \quad (1).$$

Here, f_s and f_p are the series and parallel resonant frequency, and φ_Y is admittance phase. Figure 7 here shows the measured admittance of the resonator, as evolving from on-state to off-state upon pulsed switching. A k_t^2 of 6.95% and a Q of 72.2 is measured for the resonator operating in TE_1 BAW mode at 7.01 GHz. The resonator switching is performed by application of two 25kHz 80V monopolar triangular pulses across the bottom $Sc_{0.28}Al_{0.72}N$ layer to induce polarization reversal. The intermediate state, *i.e.*, the admittance after the first pulse, is also shown in Fig. 7. Figure 8 shows the change in switching voltage upon application of DC ovenization voltages, highlighting a ~21% reduction (from 80.5V to 63.6V) once applying 34V DC across the serpentine-shaped top electrode.

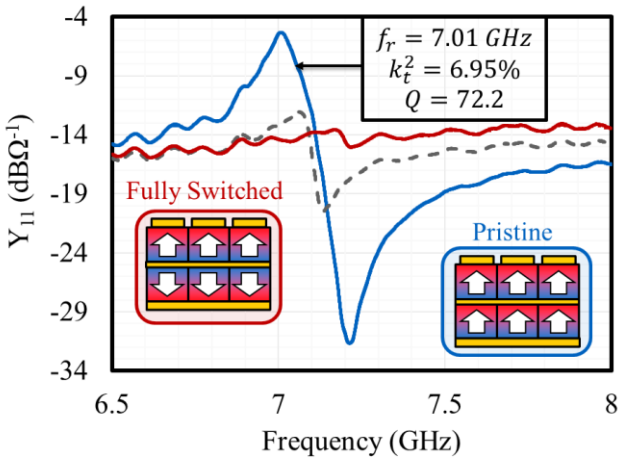

Figure 7: Measured admittance of the laminated ScAlN BAW resonator. The pristine (blue) curve corresponds to the on state; the fully switched (red) admittance response corresponds to the off state by poling the bottom ScAlN layers in opposite direction. The on/off switching resulted in ~10dB isolation. The inset schematics show the polarization direction of ScAlN layers in on and off states.

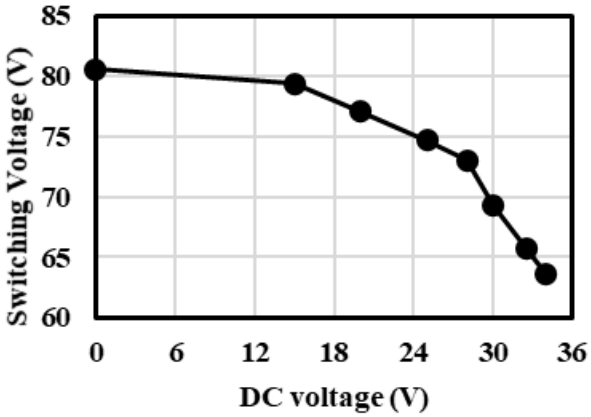

Figure 8: The measured switching voltage for different ovenization voltages. Application of larger ovenization voltage results in significant drop in coercive filed and resonator switching voltage.

CONCLUSION

This paper demonstrates self-oven-controlled intrinsically switchable thickness-extensional BAW $Sc_{0.28}Al_{0.72}N$ resonator operating at 7.01 GHz, with a k_t^2 of 6.95% and Q of 72.2. The intrinsic switchability is realized by using a laminated transducer architecture from alternative stacking of two $Sc_{0.28}Al_{0.72}N$ with three metal electrodes. This configuration enables tailoring transducer polarization across the stack. Once the polarization of the two $Sc_{0.28}Al_{0.72}N$ layers are switched in opposite direction, the resonator is switched off due to the charge cancellation upon excitation of fundamental thickness-extensional mode. The resonator switching voltage is reduced from 80.6V to 63.6V through self-ovenization using a serpentine-shaped top electrode. This concludes the effectiveness of self-ovenization concept for reduction of the large switching voltages in configurable $Sc_{0.28}Al_{0.72}N$ resonators and filters.

ACKNOWLEDGEMENT

The authors would like to thank the University of Florida Nanoscale Research Facility cleanroom staff for fabrication support. This work was supported by Defense Advanced Research Projects Agency (DARPA), Tunable Ferroelectric Nitrides (TUFEN) Program under Grant HR00112090049 and National Science Foundation (NSF) grant ECCS 1752206.

REFERENCE

[1] M. Matthaiou, O. Yurduseven, H. Q. Ngo, D. Morales-Jimenez, S. L. Cotton and V. F. Fusco, "The Road to 6G: Ten Physical Layer Challenges for Communications Engineers", *IEEE Communications Magazine*, 59, 1 (2021).

[2] R. Ruby, "A Snapshot in Time: The Future in Filters for Cell Phones", *IEEE Microwave Magazine*, 16, 7 (2015).

[3] H. Chandrahalim, S. A. Bhave, R. G. Polcawich, J. S. Pulskamp and R. Kaul, "PZT transduced high-overtone width-extensional resonators above 1 GHz", IEEE International Ultrasonics Symposium, Rome, Italy (2009), pp. 2145-2148.

[4] Y. He, B. Bahr, M. Si, P. Ye and D. Weinstein, "A tunable ferroelectric based unreleased RF resonator", *Microsystems & nanoengineering*, 6, 8 (2020).

[5] M. Z. Koohi and A. Mortazawi, "Negative piezoelectric-based electric-field-actuated mode-switchable multilayer ferroelectric FBARs for selective control of harmonic resonances without degrading K_{eff}^2", *IEEE Transactions on Ultrasonics, Ferroelectrics, and Frequency Control*, 67, 9 (2020).

[6] S. Fichtner, N. Wolff, F. Lofink, L. Kienle, and B. Wagner, "AlScN: A III-V semiconductor based ferroelectric", *Journal of Applied Physics*, 125, 11 (2019).

[7] S. Rassay, D. Mo, C. Li, N. Choudhary, C. Forgey and R. Tabrizian, "Intrinsically Switchable Ferroelectric Scandium Aluminum Nitride Lamb-Mode Resonators", *IEEE Electron Device Letters*, 42, 7 (2021).

[8] J. Wang, M. Park, S. Mertin, T. Pensala, F. Ayazi and A. Ansari, "A Film Bulk Acoustic Resonator Based on Ferroelectric Aluminum Scandium Nitride Films", *Journal of Microelectromechanical Systems*, 29, 5 (2020).

[9] S. Dabas, D. Mo, S. Rassay and R. Tabrizian, "Intrinsically Tunable Laminated Ferroelectric Scandium Aluminum Nitride Extensional Resonator Based on Local Polarization Switching", *2022 IEEE 35th International Conference on Micro Electro Mechanical Systems Conference (MEMS)*, Tokyo, Japan (2022), pp. 1050-1053.

[10] S. Rassay, F. Hakim, M. Ramezani and R. Tabrizian, "Acoustically Coupled Wideband RF Filters with Bandwidth Reconfigurability Using Ferroelectric Aluminum Scandium Nitride Film", *2020 IEEE 33rd International Conference on Micro Electro Mechanical Systems (MEMS),* Vancouver, BC, Canada (2020), pp. 1254-1257.

[11] D. Mo, S. Rassay and R. Tabrizian, "Intrinsically Switchable Ferroelectric Scandium Aluminum Nitride Bulk Acoustic Wave Resonators", *2021 21st International Conference on Solid-State Sensors, Actuators and Microsystems (Transducers)*, Orlando, FL, USA (2021), pp. 317-320.

[12] J. Wang, Y. Zheng and A. Ansari, "Ferroelectric Aluminum Scandium Nitride Thin Film Bulk Acoustic Resonators with Polarization-Dependent Operating States", *Physica Status Solidi (RRL)–Rapid Research Letters*, 15, 5(2021).

[13] V. Felmetsger, M. Mikhov, M. Ramezani and R. Tabrizian, "Sputter Process Optimization for Al0.7Sc0.3N Piezoelectric Films", *2019 IEEE International Ultrasonics Symposium (IUS)*, Glasgow, UK (2019), pp. 2600-2603.

[14] S. Rassay, F. Hakim, C. Li, C. Forgey, N. Choudhary, and R. Tabrizian, "A Segmented-Target Sputtering Process for Growth of Sub-50 nm Ferroelectric Scandium–Aluminum–Nitride Films with Composition and Stress Tuning", *Physica Status Solidi (RRL)–Rapid Research Letters*, 15, 5 (2021).

[15] R. Lu, M. -H. Li, Y. Yang, T. Manzaneque and S. Gong, "Accurate Extraction of Large Electromechanical Coupling in Piezoelectric MEMS Resonators", *Journal of Microelectromechanical Systems*, 28, 2 (2019).

[16] D. A. Feld, R. Parker, R. Ruby, P. Bradley and S. Dong, "After 60 years: A new formula for computing quality factor is warranted", *2008 IEEE Ultrasonics Symposium*, Beijing, China (2008), pp. 431-436.

Contact information

* Shaurya Dabas, tel: +1-407-533-1385; shauryadabas@ufl.edu.

AN ACCURATE TEMPERATURE REGULATING SCHEME BASED ON A RESISTOR WITH TAILORED NONLINEARITY FOR EVAPORATIVE DRUG DELIVERY

Frank Goldschmidtboeing[1], Mohammadreza Saberi[1], Timo Gerach[1], Luca Conrad[1], Eiko Hager[1], Uttunga Shinde[1], Muhannad Ghanam[1], Uwe Pelz[1], Niklas Romming[2], Lasse Cornils[2], Jan Jaklin[2], Marc Kessler[2] and Peter Woias[1]*

[1]University of Freiburg, Freiburg, Germany

[2]Hauni Maschinenbau GmbH, Hamburg, Germany

ABSTRACT

We present the temperature regulation scheme of a resistive silicon heater for evaporative drug delivery to the lungs. The nonlinear specific resistance to temperature behavior of boron doped silicon is used to enable an absolute temperature measurement of the heater without the need of a calibration procedure. Experiments demonstrate that the evaporated mass can be controlled by the heater temperature. The evaporated mass versus heater temperature is linear in the region of useful heater temperatures.

KEYWORDS

evaporative drug delivery to the lungs, silicon resistive heater, nonlinear specific resistance to temperature curve

INTRODUCTION

Evaporation of medical substances has been identified as a promising route for future drug delivery to the lungs [1,2,3,4]. This application demands a reliable temperature control to avoid overheating and thereby destroying the medical substance. A high dosing accuracy is needed to guarantee proper dosing of the drug. A MEMS-based silicon device to fulfill these requirements has been demonstrated in [5], where the basic function of our device was shown. Here, we show a temperature regulations scheme, that guarantees an accurate temperature control of the silicon heating component even with varying initial resistance of the heating element and simultaneously varying ambient temperature.

SYSTEM DESIGN AND FABRICATION

A schematic of the evaporation device is shown in Fig. 1. It consists of an electronic steering device, that powers the heater and regulates its temperature and the disposable drug reservoir with the resistive heater and mouth piece as a vapor outlet.

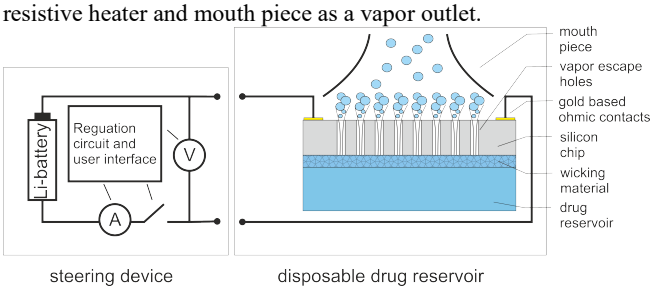

Figure 1: Schematic of the evaporation device

The resistor is directly driven by a rechargeable lithium ion battery with a nominal voltage of 3.7 V. A low resistance MOSFET is used to switch the power delivered to the heater on and off according to the measured resistance of the heater. The resistance of the heater is about 1.2 Ω when heated to the evaporation temperature, therefore, with a nominal voltage of 3.7V a maximum instantaneous power of 11.4 W can be delivered to the heater.

The heater current and voltage are measured every 2 ms allowing to determine the instantaneous power and the actual resistance of the heater. Two regulation algorithms can be chosen. The first algorithm regulates the temperature to a pre-set value by a two-point regulation scheme. The heater is switched off, as soon as the resistance (temperature) reaches a threshold and switches on again if it falls below a second, slightly smaller threshold..In this case the average input power can be evaluated as parameter describing the status of the heating device. In the following this algorithm will be called temperature regulation algorithm.

The second algorithm regulates the input power by determining the average input power of the last few timesteps and by choosing the on or off-state accordingly. Here, the temperature curve can be evaluated as a second parameter describing the evaporation event. This algorithm will be called power regulation in the following.

Both algorithms need a precise temperature measurement by evaluating the instantaneous resistance of the heating element to ensure that no overtemperature on the heater leads to a degradation of the drug or the solvent.

The fabrication of the silicon heater was described in detail in [5]. Fig. 2 shows the silicon heater connected to a flexible PCB by silver sintering. This technology enables stable operation up to temperatures of 300°C.

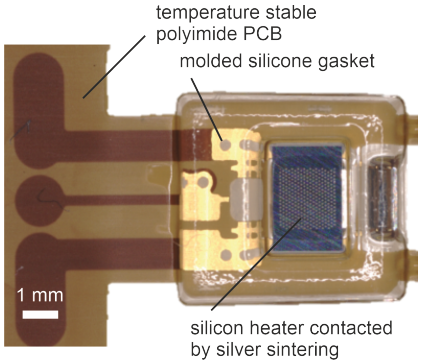

Figure 2: Packaging of the MEMS heater chip

The doping element and level of the MEMS heater were chosen to achieve a total room temperature resistance of 1 Ω with a reasonable aspect ratio of the chip, i.e. a square shaped perforated evaporation area and contacts areas on two sides leading to chip with 3 mm length and 2 mm width. Furthermore, an adapted specific resistance versus temperature curve is required to enable a resistive temperature measurement without prior calibration. The measurement method described in this paper requires a temperature independent resistance at room temperature and a preferably linear temperature dependence in the evaporation range of 200°C to 300°C.

The specific resistance of semiconductors typically decreases with temperature because more carriers are lifted into the conduction band at higher temperatures. A soon as virtually all doping levels are ionized another effect comes into play, further

978-1-940470-04-7/HH2022/$25©2022TRF
DOI 10.31438/trf.hh2022.42

increase in temperature leads to more carrier scattering and therefore lower carrier mobility, so the resistance increases again. Therefore, a small region of temperature independent resistance, where both effects compete, exists. The above-mentioned criteria are met, if this region can be shifted to room temperature and if a specific resistance value of about 20 mΩcm can be achieved.
We have chosen a boron doping concentration of 4 10^{18} cm^{-3} with a specific resistance obtained from theory [6] shown in Fig. 3.

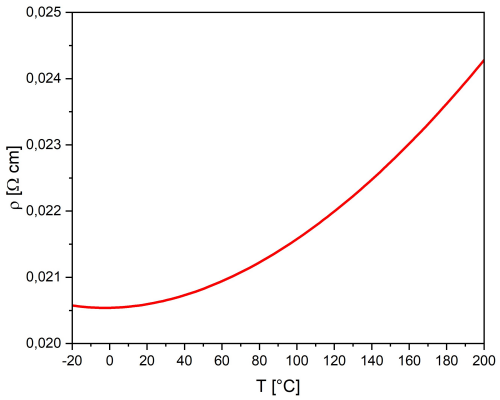

Figure 3: Theoretical specific resistance of boron doped silicon with a concentration of 4·10^{18} cm^{-3}

MEASUREMENT SETUP

First, measurements were conducted to evaluate the resistance to temperature curve of the fabricated chips. Precise measurements were taken in the temperature range of -20°C to 150°C in a climate chamber with a four-wire measurement setup (Keithley Source Meter 2450). The temperature was raised in steps of 5 K and resistance values were taken after 5 minutes of waiting time to secure thermal equilibration.

Higher temperatures of 160°C to 300°C could only be reached by resistive heating of the chips. For this, the resistance was regulated by the temperature regulation algorithm and the temperature of the chip was measured by the infrared-camera Optris PI 450, Optris GmbH, Berlin Germany. The mean temperature of a center region of the chip was taken as the chip temperature, although the effect of the small holes in the chip might influence its value.

A second set of measurements was done to find the relation of chip temperature, heating power and generated aerosol mass. Fig. 4 shows a schematic of the full measurement set-up while Fig. 5 shows a photograph of the heating device, with the heater cartridge and the filter holder.

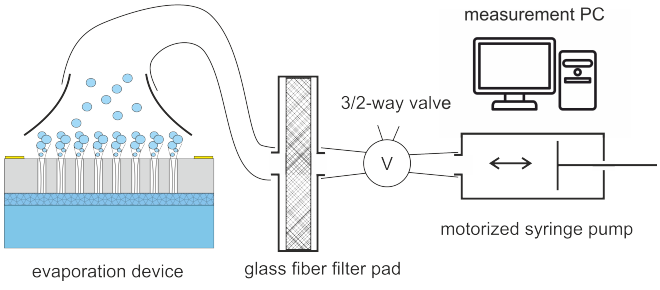

Figure 4: Schematic of the aerosol mass measuring system

In the experiments, the heater is powered for a period of 3s with one of the two regulation algorithms. A drug-free solvent mixture of water, propylene glycol and glycerol is used. The resistance versus time curves for each evaporation event is recorded with a sampling rate of 2 ms. The vapor is generated directly below the heater and escapes through the holes. After that the vapor condenses to an aerosol with a mass median droplet diameter of approximately 1 µm. An air flow of 1.2 l/min is generated by a motor-driven syringe pump and draws the aerosol through a glass fiber filter. A small part of the aerosol droplets hit the tubing and remains there, while the major part condenses inside the filter. The filter is weighted every ten evaporation events to determine the average aerosol mass per event.

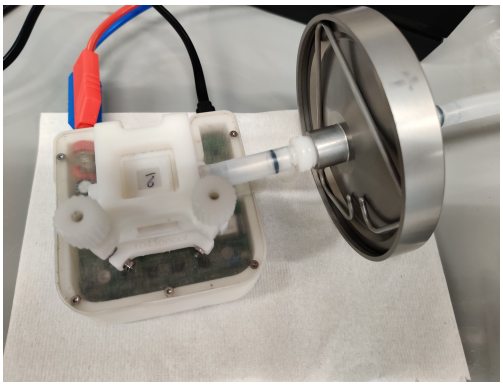

Figure 5: Photograph of the steering electronics (bottom) with a liquid cartridge mounted on top and the filter pad holder connected

RESULTS AND DISCUSSION

The characterization of resistance versus temperature behavior is summarized in Fig. 6. The resistance is scaled by the measured resistance at room temperature and the scaled resistance is denoted by *F*. This scaling compensates for tolerances of the chip dimensions, especially the chip thickness. The measurements in the climate chamber (blue dots and the measurements with the IR-camera align quit well, with a small offset of the IR-camera values to higher temperatures. These IR-camera values also show a higher noise. This noise is due to the different resistance measurement system. The resistance was measured with the miniaturized microcontroller based steering electronics and not with a highly accurate multimeter as in the climate chamber measurements. Also, the temperature measurement is less accurate due to the influence of the tiny holes inside the MEMS heater.

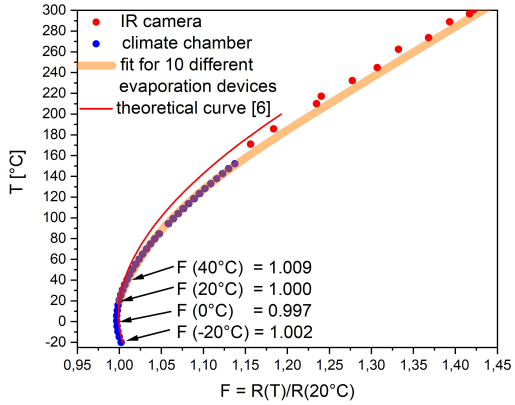

Figure 6: Summary of the measured temperature dependence of the MEMS heaters

The thin red line shows the theoretical specific resistance versus temperature curve from Fig. 3. It fits well to the measured data. The small deviation is probably due to the tolerance of the doping level of the wafers.

The thick orange curve shows a curve fitted to the results of IR-measurements of ten different MEMS heaters and the climate chamber measurement of a single MEMS heater. The IR-measurement points lie all within a margin of ±15 K around this curve, but we assume that the main part of this tolerance is due to the temperature measurement inaccuracy. This orange curve is used for all heaters to determine the heater temperature from the resistance value.

As mentioned above, all measurements are normalized by the room temperature resistance. As this resistance is virtually constant from -20°C to +40°C the exact temperature of this measurement is of no importance. That is why it can be measured at any time by the electronic steering device without any information about the temperature of the liquid cartridge. The different values of F shown in figure 6 demonstrate, that a maximum error of 0.9% occurs at a temperature of 40°C.

The evaporation experiments were conducted with the power regulation algorithm. Fig. 7 shows the aerosol mass versus heating power measured at laboratory temperature of 20°C. Each dot consists of the average data of ten successive evaporation events. An error of ±0.2 mg is assumed for the mass measurement, which is a typical standard deviation when the same MEMS heater is characterized multiple times under the same conditions. The power regulation algorithm regulates the power within a better than 1% accuracy, which makes the error bars smaller than the dots.

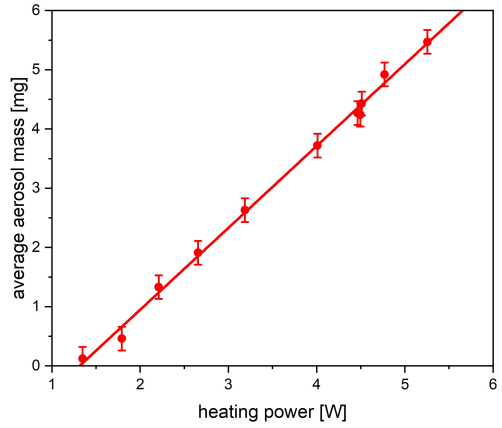

Figure 7: Average aerosol mass versus heating power for ten evaporation events with a duration of 3 s each

The fitted line clearly shows the linear behavior of the aerosol mass versus temperature curve with a small offset. This is to be expected as most of the power is used for heating up the liquid and overcoming the latent heat of evaporation. Nevertheless, there is still an accuracy problem because this linear curve will be shifted left or right and also slightly change its slope depending on the temperature of the heater cartridge. If the cartridge is very cold, more energy is needed to heat up the liquid, i.e. the slope of the curve gets lower. Also, more heat is dissipated to the surrounding, i.e. the offset increases. Therefore, the heater temperature is also monitored.

The heater temperature saturates to a constant value after about 0.3 s. The evaporation has then reached a quasi-static regime where the heat flow into the liquid equals the evaporative heat loss. This temperature is monitored by averaging the temperature value for the period from 2 s to the end of the evaporation after 3 s. The resulting graph of average aerosol mass versus saturation temperature is shown in Fig 8.

A linear relation between saturation temperature and aerosol mass is clearly visible for temperatures higher than 210°C. This temperature measurement is independent on the ambient temperature as described earlier. The relation of saturation temperature to aerosol mass is also independent of the ambient temperature, as it only depends on the heat transfer between the MEMS heater and the evaporating liquid. The saturation temperature unfortunately varies for evaporations with the same heating power as indicated by the error bars. We believe that this variation is caused by the random formation of gas bubbles at the interface that alter the heat transfer.

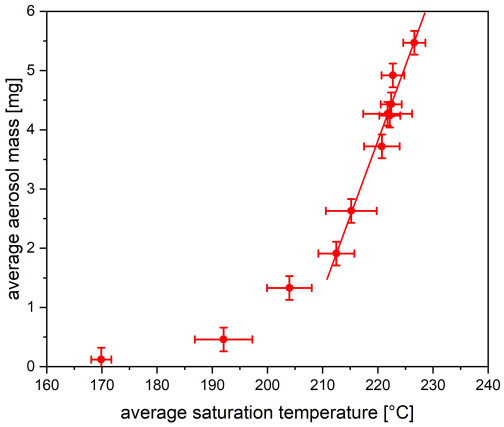

Figure 8: Average aerosol mass versus average saturation temperature for ten evaporation events with a duration of 3 s each.

This interpretation is supported by the slow variation of the heater temperature that is typically observed when driving the heater with the power regulation algorithm (Fig. 9). The curves for a constant power of 3.2 W differ by maximum of about 20 K and also the averaged saturation temperature varies between 203 °C and 216°C.

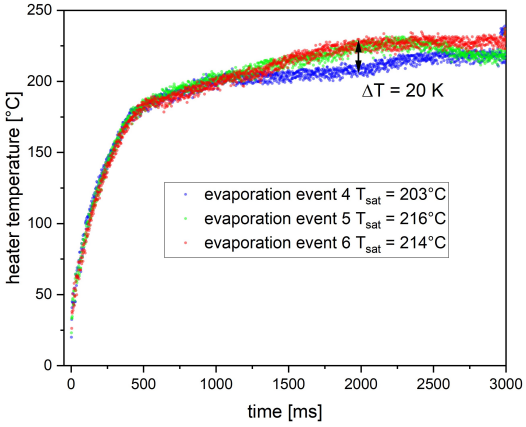

Figure 9: Typical heater temperature versus time characteristics of three successive evaporation events with power regulation

Fig. 10 shows a dosing event with four pre-set temperature values as an example of a temperature regulated dosing event. The temperature plateaus are much flatter compared to the characteristics of the power regulated characteristics from Fig 9. In turn, the instantaneous power varies to compensate for the varying heat transfer characteristic due to the bubbles at the heater interface.

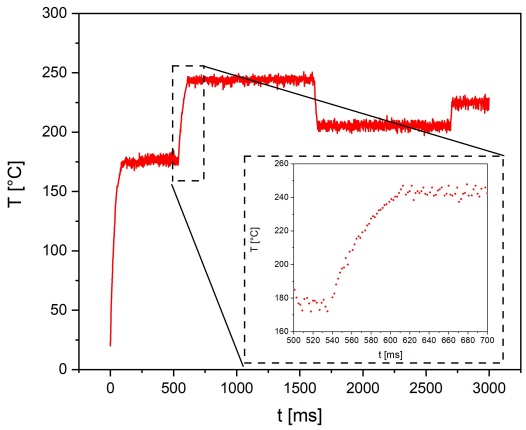

Figure 10: Heater temperature versus time characteristics of an evaporation event with four pre-set temperature values

The figure also demonstrates the fast heat-up and cool down phases of the MEMS heater. The fast heat-up is due to the power margin of the system. While the highest average power for a proper function is in the range of about 5 W, the maximum power for a hot heater (R = 1.2 Ω) with a battery voltage of 3.7 V is 11.4 W, which means that there is an extra power 6.4 W available for a fast heat up even in the boiling regime. The fast cooling down in the boiling regime is explained by the high power-loss due to evaporation. As no power is fed into the system while cooling down a power of several watts is dissipated by the evaporation.

CONCLUSION & OUTLOOK

We have shown two regulation schemes for the driving of a MEMS heater for evaporative drug delivery. First a power regulated scheme and second a temperature regulated scheme were demonstrated. With both driving schemes two parameters can be extracted to characterized the dosing event, the average power and the saturation temperature. Both parameters have their advantages and disadvantages for predicting the aerosol mass and therefore the delivered drug dose.

The average power is a precise measure of the delivered aerosol mass but only as long as the temperature of the cartridge and the surrounding is known. The saturation temperature on the other hand is a measure of the aerosol mass that is independent on the cartridge temperature and ambient temperature but suffers from a lower accuracy. We believe that a combination of both methods will lead to better prediction of the aerosol mass than each method alone.

Future work will concentrate on characterizing multiple cartridges with different ambient and cartridge temperatures and to find a reliable model that predict the administered drug dose on the basis of the average heating power, the saturation temperature and probably the ambient temperature.

ACKNOWLEDGEMENTS

We gratefully thank the Laboratory for Electrical Instrumentation and Embedded Systems for the opportunity to use their climate chamber.

REFERENCES

[1] Vazda, et.al, “Evaporation of fentanyl from ceramics for pulmonary drug delivery: a pilot study”, Conference on Materials Science and Engineering (2021)

[2] A. Vazda, Wei Xia, Håkan Engqvist, “The use of heat to deliver fentanyl via pulmonary drug delivery", International Journal of Pharmaceutics: X, Volume 3 (2021)

[3] K. Dinh et al., “In vitro aerosol characterization of Staccato® Loxapine”, Int. J. Pharm., 403 (2011)

[4] Pourchez, et al., "Assessment of new-generation high-power electronic nicotine delivery system as thermal aerosol generation device for inhaled bronchodilators", Int. J. Pharmaceutics, vol. 518, no. 1 (2017)

[5] F. Goldschmidtboeing et al., "Heater for Controlled Evaporation of Liquids for Personalized Drug Delivery to the Lungs," Journal of Microelectromechanical Systems, vol. 29, no. 5 (2020)

[6] https://www.pvlighthouse.com.au/resistivity, accessed January 13th, 2022

CONTACT

*Frank Goldschmidtboeing, tel: +49-761-203-7496; fgoldsch@imtek.de

LASER-INDUCED GRAPHENE PRESSURE SENSORS MANUFACTURED VIA INKJET PCB PRINTER

Landon Ivy[1†], Ved Gund[1], Benyamin Davaji[1,2], Carlos Ospina[3], Di Ni[1], Peter Doerschuk[4], and Amit Lal[1]
[1]The *Sonic*MEMS Laboratory, School of Electrical and Computer Engineering
Cornell University, Ithaca, NY, USA
[2]AIMS Laboratory, Department of Electrical and Computer Engineering
Northeastern University, Boston, MA, USA
[3]BotFactory Inc.
Long Island City, NY, USA
[4]Doerschuk Research Group, Meinig School of Biomedical Engineering
Cornell University, Ithaca, NY, USA
[†]Email: lsi8@cornell.edu

ABSTRACT

This paper demonstrates two firsts for the fields of laser-induced graphene (LIG) sensors and printed electronics (PE): (1) a LIG Kapton circular diaphragm gauge pressure sensor with a multi-resistor network; (2) the wiring and encapsulation of said sensor, printed with conductive and dielectric inks (CI and DI) utilized by the BotFactory SV2 thermal Inkjet PCB printer. In addition, the PE tool allows for automated solder paste dispensing and the pick-and-place of electronic components to form complete functioning microsystems, consisting of microcontrollers, thin-film batteries, passive components, antennas, etc. These capabilities further enhance the prospect of LIG sensors by providing to them off-grid power, read-out circuitry, amplification, and simple wireless data transmission.

KEYWORDS

Printed Electronics; Laser Induced Graphene (LIG); Pressure Sensors; Flexible Electronics.

INTRODUCTION

Low-cost, flexible microsystems are an ideal solution for health and environmental monitoring. A significant challenge in flexible electronics is to realize sensing and computation capability diversity while maintaining rapid prototyping. PE can enable rapid prototyping of electronic components; however, PE have lacked a proven sensor mechanism for mechanical forces – it is challenging to make microelectromechanical systems (MEMS) sensors and transducers in flexible electronics, comparable with the performance of silicon-based MEMS. LIG provides a quick and easy way to fabricate complex graphene-like piezoresistive microstructures for applications such as strain and chemical sensing [1–4]. This work describes the design and fabrication of a novel LIG pressure sensor utilizing a membrane-based device, insulating and conducting features formed by inkjet deposition, and graphene-like sensing elements formed by the laser pyrolization of a flexible Polyimide (Kapton) substrate.

Current Diaphragm Pressure Sensors on the Market and in the Literature

A key component for mechanical sensing is a strain gauge. Several LIG strain gauges have been reported with exceptional sensitivity [1,2,4]—some even approaching an order of magnitude greater than those of metal foil sensors (MFSs) [3]. Although some have been simulated [5], no PE fabricated LIG diaphragm gauge pressure sensors have been experimentally demonstrated or characterized. Our group has previously demonstrated chemical vapor deposition (CVD) graphene-based sensors and actuators, with high piezoresistive gauge-factor response and large mechanical actuation, leading us to use graphene-based sensors in our current device [6, 7].

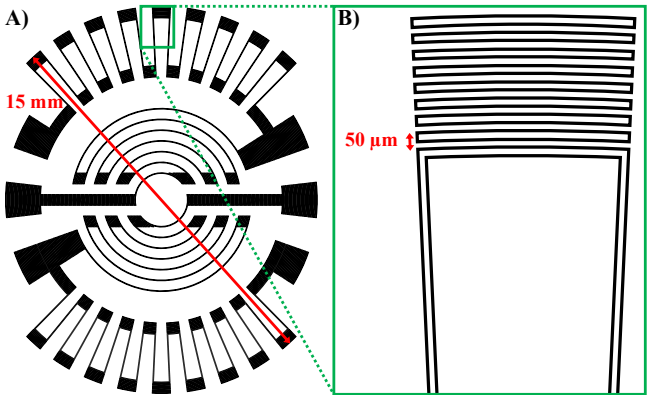

Fig. 1. A) Parametric CAD model of pattern to be laser hatched into Kapton film by the VLS3.60's laser beam which has a spot size of 25.4 µm. B) Magnification showing that hatch lines in this sketch are separated by 25 µm.

LIG-SENSORS WITH PE

Given its inherent pressure measurement versatility, a diaphragm type pressure sensor was determined to be the most desirable for this application. With a diaphragm-based sensor, the instrumented membrane side can be exposed, vacuum-sealed, or pneumatically connected by ports for measuring gauge, absolute, or differential pressures, respectively [9]. This work demonstrates an exposed-sensor for gauge measurements. Due to its radially symmetric stress distributions, a circular—rather than the more common rectangular—type diaphragm was chosen [8].

978-1-940470-04-7/HH2022/$25©2022TRF
DOI 10.31438/trf.hh2022.43

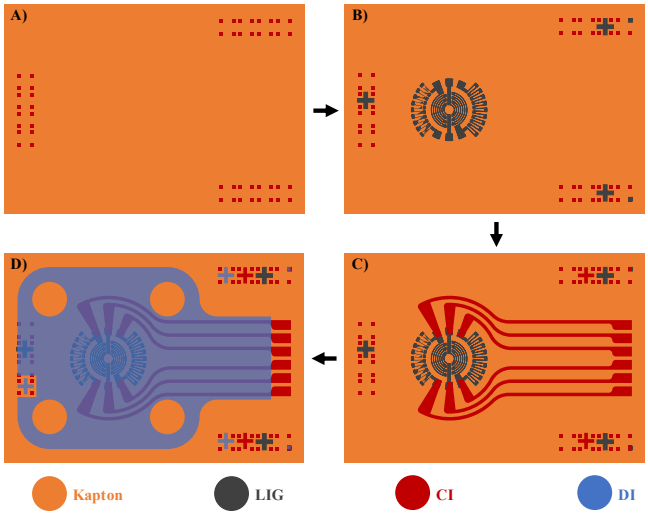

Fig. 2. Inkjet/Laser Process Flow: (A) BotFactory SV2 inkjet-printed conductive ink (CI) alignment marks on the Kapton sheet. B) Define the piezoresistors using laser pyrolization, using the conductive ink alignment marks as reference. C) SV2 prints CI electrical traces to form interconnects and contacts to the LIG sensor. D) SV2 printed dielectric ink (DI) protection layer film for passivation and damage from external sources.

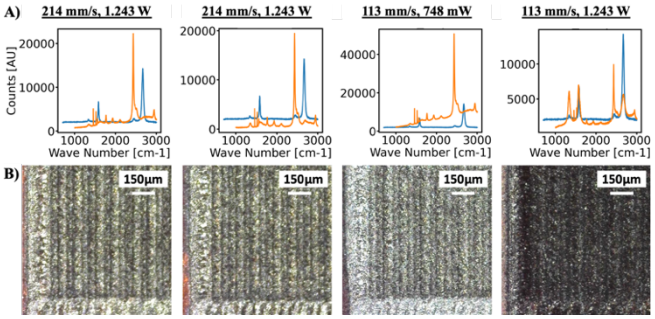

Fig. 3. A) Raman spectrums of the laser-induced graphene (orange) characterization patterns (LIGCPs) and high-quality monolayer graphene on HZO reference (blue), designed to identify the proper combination of laser power and travel rate; the winning combination of 1.243 W and 113 mm/s shows the three characteristic peaks of LIG: The D, G, and 2D peaks at 1360 1580, and 2720 cm-1, respectively. There is a Kapton LIGCP shown in Fig. 4A. B) Optical images of the respective LIGCPs.

For our initial attempt at device making, we prioritized fabrication, assembly, and measurement refinery over rigorously optimizing the design, and experimentally verifying the functionality of, said devices; this task of mathematically/empirically characterizing and optimizing sensor performance is important but was left as a future investigation. Given the explained motive, it should make sense why deciding on a graphene hatching pattern was not a difficult task, so long as the pattern was radial and designed to maximize trace resistance change in response to strain. Much inspiration was taken from the metal patterns of several commercially available circular diaphragm MFSs. To maximize sensor sensitivity, we decided to implement a design which could be read out in a Wheatstone full bridge configuration that allows differential measurements and common mode-supression from power supply variations and other interfering signals. To enable this option, the pattern features a network of four resistors consisting of two outer and two inner resistors expected to operate under compressive and tensile stress, respectively. For the purpose of convenience and verification, the four LIG piezoresistors were interconnected in such a way as to allow independent measurements of respective resistances; there were six CI traces printed overall (Fig. 2D).

A Cheap Substitute Pressure Sensor which can be Locally and Independently Produced in Under a Day

Whether one is looking for an alternative to traditional MFSs due to their typically long lead and ship times, high cost, untailored offerings, or relatively stagnant improvement, LIG based flexible sensors with simplified PE packaging demonstrate the potential to provide a locally produced, immediate, affordable, custom, and potentially superior alternative with higher sensitivity. Even if one still prefers the precision and reliability of a MFS, the LIG process' ability to quickly substitute (even if only temporarily) the MFS in the event of it being damaged or otherwise rendered defective, remains an irrefutable benefit.

CONCEPT AND DEVICE DESIGN

The fundamental figures of merit of a pressure sensor are: (i) the maximum pressure that the membrane can detect and is primarily determined by the yield strength of the membrane material which is roughly 69 MPa for Kapton [10], (ii) pressure measurement repeatability, i.e., after calibrating the piezoresistive sensor—where a function was identified which maps the resistance network state to the correct actual pressure—the mapping should not drift with time or actuations (repeatability is undermined if maximum tolerable pressure is exceeded), (iii) the sensitivity of the device which depends on the sensor material characteristics and device geometry, and (iv) the minimum detectable pressure which sets the sensor resolution and depends on the mechanical and electrical noise from the membrane vibrations and resistive sensors respectively.

Design of Pressure Sensor Circular Diaphragm

Before starting the design or fabrication of any pressure sensors, sufficient laser pyrolysis parameters of laser power and writing speed were determined from resulting LIG characterization patterns (LIGCPs) (Fig. 4) by comparing the LIG cells' raman spectrum to that of monolayer graphene (Fig. 3). The resistor network hatch pattern was designed completely parametrically in Fusion 360 and is shown in Fig. 1.

Fabrication Process

The first fabrication step (Fig. 2) was to print four sets of three alignment windows per device on a 125 µm thick sheet of Kapton. After loading and aligning the 25.4 µm optics and marked Kapton, the laser carbonized traces were ablated using a VersaLaser VLS3.60 CO_2 laser. A thin rubber gasket with a central (16 mm diameter) diaphragm hole and four outer fastening holes, was also cut using the VersaLaser. Finally, silver leads (partially overlapping the graphene pattern at six points) and blanket insulation layers were deposited using the SV2 printer. An ObJet30 Pro 3D printer made the remaining two components which would form the airtight test chamber (Fig. 5A–B): The top part, having the same profile as the gasket but much thicker, and the bottom part with its four outer fastening holes, underside nut retention slots, female Luer lock input, and 1/8" NPT output. This configuration proves a ready-to-use in-line pressure sensor that allows us to easily swap out various iterations of the membrane device for rapid testing.

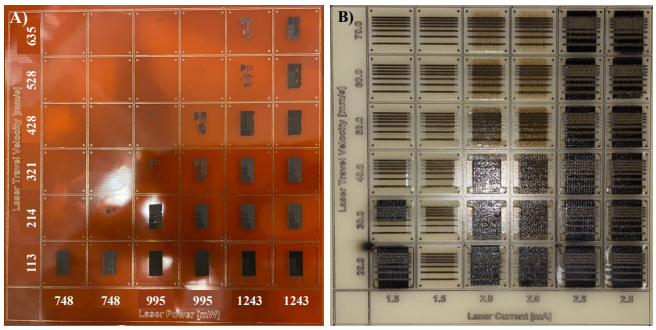

*Fig. 4. LIG was defined on **Kapton (A)**, and **FR4 (B)** with SV2 printed CI traces and DI encapsulation shown on FR4 but not on Kapton.*

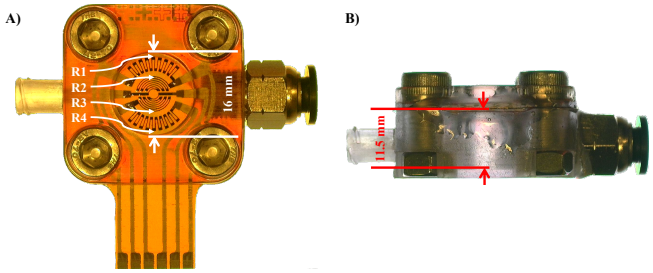

Fig. 5. A) Close-up top view of a fully assembled circular diaphragm pressure sensor with resistor locations. B) Side view of the assembled sensor showing the stack order: Test chamber bottom, gasket, sensor, then test chamber top.

STRESS TESTING AND SENSOR CHARACTERIZATION

The experimental setup is shown in Fig. 6. The reduced volume and increased pressure within the closed pneumatic circuit were induced via syringe pump and measured via pressure sensor, respectively. The DTS-025-02 was used to measure membrane displacement. This data, as well as the resistance data, were recorded for four trials (two in the morning and two at night). Fig. 7 shows the average linear sensitivity was approximately $5*10^{-5}$ kPa^{-1} which is comparable to previously achieved sensitivities [1].

CONCLUSION AND FURTHER STUDIES

Future work will include FEA optimization of Kapton thickness, piezoresistor lengths, and their locations, for maximum sensitivity with high linearity. The second-generation devices will study the variances in resistances, sensitivities, gauge-factors, and pressure ranges. In summary, this work demonstrated that a high-sensitivity, flexible membrane of strain-gauges can be fabricated, all using PE. This process enables a pathway to allow pressure and piezoresistive accelerometers, force sensors, and gas sensors using graphene multi-sense capabilities with laser-annealing and rapid prototyping cleanroom-less approach.

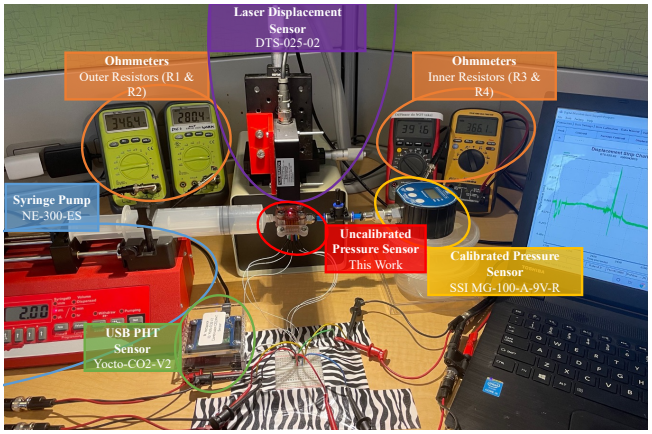

Fig. 6. Experimental setup which produced the data for Fig. 7.

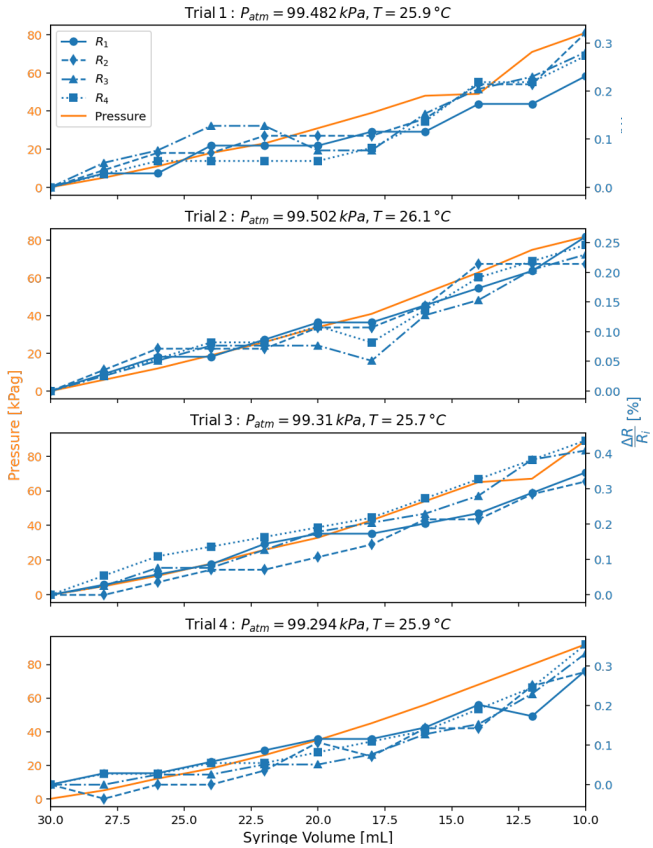

Fig. 7. The percent change in resistance of the four resistors (physical locations specified in Fig. 5A) and the membrane pressure in orange were measured with respect to the reduction of internal volume caused by the syringe pump. From trial 1, at 30 mL, R_1,R_2,R_3, and R_4 were 346.3, 280.3, 391.6, and 366.0 kΩ, resp., while, for the other 3 trials, they varied by approx. 0.1 Ω.

ACKNOWLEDGEMENTS

This work was performed in part at the Cornell NanoScale Facility (CNF), a member of the National Nanotechnology Coordinated Infrastructure (NNCI), supported by the National Science Foundation (Grant ECCS-1542081). Material characterization was performed at the Cornell Center for Materials Research (CCMR) Shared Facilities which are supported through the NSF MRSEC program (DMR-1719875). This material is based on research sponsored by Army Research Laboratory under agreement

number W911NF-19-2-0345. The U.S. Government is authorized to reproduce and distribute reprints for Government purposes notwithstanding any copyright notation thereon. The views and conclusions contained herein are those of the authors and should not be interpreted as necessarily representing the official policies or endorsements, either expressed or implied, of Army Research Laboratory (ARL) or the U.S. Government.

REFERENCES

[1] A. Kaidarova, N. Alsharif, B. Oliveira, M. Marengo, N. Geraldi, C. Duarte, and J. Kosel, "Laser-Printed, Flexible Graphene Pressure Sensors," *Global Challenges*, **4**, 2000001, 2020.

[2] T. Han, A. Nag, R. Simorangkir, N. Afsarimanesh, H. Liu, S. Mukhopadhyay, Y. Xu, M. Zhadobov, and R. Sauleau, "Multifunctional flexible sensor based on laser-induced graphene," *Sensors*, **19**, 3477, 2019.

[3] S. Luo, P. Hoang, and T. Liu, "Direct laser writing for creating porous graphitic structures and their use for flexible and highly sensitive sensor and sensor arrays," *Carbon*, **96**, 522, 2016.

[4] R. Rahimi, M. Ochoa, and B. Ziaie, "Direct laser writing of porous-carbon/silver nanocomposite for flexible electronics," *ACS Appl. Mater. Interfaces*, **8**, 1617, 2016.

[5] M. Nag, A. Kumar, and B. Pratap, "A novel graphene pressure sensor with zig–zag shaped piezoresistors for maximum strain coverage for enhancing the sensitivity of the pressure sensor," *Int. J. Simul. Multidisci. Des. Optim.*, **12**, 14, 2021.

[6] H. Hosseinzadegan, C. Todd, A. Lal, M. Pandey, M. Levendorf, and J. Park, "Graphene has ultra high piezoresistive gauge factor." *2012 IEEE 25th international conference on micro electro mechanical systems (MEMS)*. IEEE, 2012.

[7] V. Gund, A. Ruyack, S. Ardanuc, and A. Lal, "Graphene one-shot micro-valve: Towards vaporizable electronics." *2015 28th IEEE International Conference on Micro Electro Mechanical Systems (MEMS)*. IEEE, 2015.

[8] A. DeHennis and J. Chae, "Pressure Sensors," *Comprehensive Microsystems*, **2**, pp 101–133, 2008.

[9] W. Bolton, "Control Systems," *Elsevier*, 12, 2002.

[10] L. Baxter, K. Herrman, R. Panthi, K. Mishra, R. Singh, S. Thibeault, E. Benton, and R. Vaidyanathan, "Thermoplastic micro- and nanocomposites for neutron shielding," *Micro and Nanostructured Composite Materials for Neutron Shielding Applications*, **3**, pp 53–82, 2020.

ETCH-HOLE FREE, LARGE GAP WAFER SCALE ENCAPSULATION PROCESS FOR MICROELECTROMECHANICAL RESONATORS

Gabrielle D. Vukasin[1], Nicholas E. Bousse[2], Anne L. Alter[3], and Thomas W. Kenny[2]
[1]Bosch LLC, USA
[2]Stanford University, USA
[3]Apple, USA

ABSTRACT

We present a fabrication process for wafer-level encapsulated MEMS devices that allows for large masses without etch-holes with small and large transduction gaps. This combination of features allows for large masses with combdrive transduction with reduced thermoelastic dissipation. The omission of wafer bonding in this process reduces the footprint of an encapsulated device and creates a hermetically sealed cavity free of particles and organics. We present the performance of a bulk mode resonator (Q = 1.7M) and a flexural mode resonator (Q = 11k, 68k) that utilizes the small and large transduction gap capability. These devices exemplify the ability of this fabrication process to create single die containing high-Q silicon-based timing references and inertial sensors.

KEYWORDS

Resonant MEMS; Wafer-Level Encapsulation; Thin Film Encapsulation; High Quality Factor Resonator; MEM Timing Reference.

INTRODUCTION

Many products in the electronics industry contain a timing reference and inertial sensors, including smart devices, wearables, Internet-of-Things (IOT), small electronics, etc. Many of these applications could benefit from a single chip containing a timing reference and inertial sensors to reduce manufacturing cost and to decrease the footprint of the sensors. However, the different design requirements for timing references and inertial sensors result in the need for different fabrication processes, which results in different encapsulation methods.

In the past, timing references in smart devices and other small electronics used quartz oscillators. However, quartz-based timing references are very large and are not CMOS compatible and thus are expensive to batch fabricate [1]. Microelectromechanical (MEM) timing references have a smaller footprint and are compatible with CMOS fabrication processes. MEM timing references need to contain high-Q resonators with extremely low frequency drift. This requires an ultra-clean and low-pressure cavity. This leads to the need of these resonators to be hermetically packaged at the wafer level, which is demonstrated by the fact that the only commercially successful MEM timing products are manufactured using wafer-scale pre-release encapsulation [2].

MEM inertial sensors need to be encapsulated and have large and small transduction gaps. Most modern MEM inertial sensors are encapsulated using a wafer-bonded post-release package that allows for capping structures with large transduction gaps [3][4]. However, this method has significant drawbacks for resonant MEM inertial sensors. Generally, it is impossible to eliminate adsorbed water and other organic molecules from the surfaces of a released MEM resonator prior to wafer bonding or sealing, which can reduce device yield and cause drift and aging [5]. Even for sensors that can tolerate this drift and contamination, such as gyroscopes, these wafer bonding processes require that significant area is allocated to sealing rings, which increases minimum device size [6].

In-process thin film encapsulation solves many of the issues that plague wafer bonding [7-10]. Epitaxial silicon thin-film encapsulation builds an in-process capping layer in an ultra-clean epitaxial reactor at a high temperature, which allows sealing of MEM resonators inside an ultra-clean cavity without any residual molecular contamination [11]. This creates a low pressure, particle-free, and oxide-free environment that enables the resonators to be extremely stable over time [12]. This process also creates silicon-based resonators with smooth sidewalls, which ensures repeatable mechanical properties and prevents crack formation, or fatigue [13]. Additionally, no sealing rings are required, so device footprint is minimized.

While hermetic epitaxial wafer-scale encapsulation results in clean, stable resonators, the added complexity of the processing makes it harder to include other desired features. Inertial sensors for high dynamic range applications require large transduction gaps and high-frequency timing resonators rely on large, etch hole free masses, both of which are hard to achieve with epitaxial wafer-scale encapsulation.

We propose a hybrid process, described in Figure 1, that combines previous work of an etch-hole free variant of epitaxial encapsulation [14] with a large gap variant of epitaxial encapsulation by using sacrificial oxide posts [15]. Removing etch-holes in bulk-mode resonators with large masses reduces thermoelastic dissipation (TED), thereby increasing the Q of the resonator [16]. This new combination of processes supports a much broader range of resonator designs by allowing for large and small transduction gaps, etch-hole free large resonant masses, top electrodes, and low-pressure encapsulation without wafer bonding.

FABRICATION PROCESS

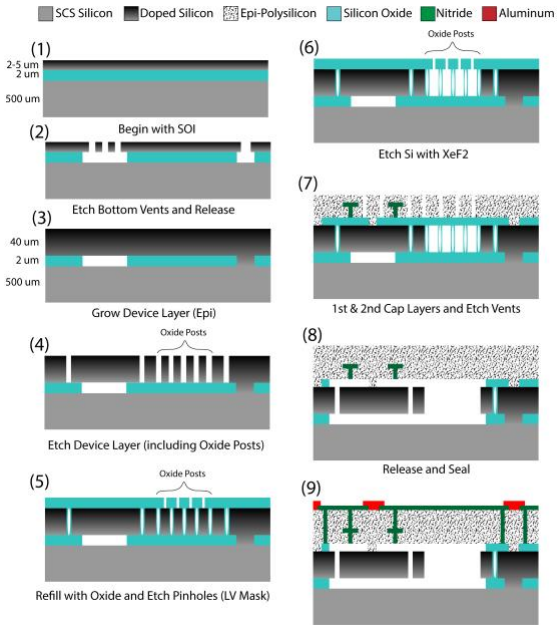

978-1-940470-04-7/HH2022/$25©2022TRF
DOI 10.31438/trf.hh2022.44

Figure 1: The process flow of this fabrication process a) starts with an SOI wafer. b) Vents are etched with DRIE and then areas beneath large masses are released with vapor phase HF. c) Immediately following, the device layer is grown with doped epitaxial silicon growth, d) and then devices and oxide posts (in large gap areas) are patterned with DRIE. e) LPCVD oxide (using TEOS) refills device trenches and trenches defining oxide posts. Vents are etched through the top oxide layer in large gap areas between the oxide posts. f) XeF_2 removes silicon from the large gap areas through the vents. g) More LPCVD oxide refills the vents and builds up the top oxide layer. Vias to the device layer are etched, then the first and second cap layers are deposited using epitaxial silicon. Vents for device release are etched with DRIE. h) The devices are released with vapor phase HF and sealed in a low pressure, high temperature epitaxial reactor. i) Finally, contacts to the device layer are patterned and isolated from the rest of the cap with nitride. Aluminum contact are patterned with aluminum etchant.

This process starts with an SOI wafer with a 2-5 µm device layer and 3 µm box oxide, illustrated in Figure 1a. Vents are etched with deep-reactive ion etching (DRIE) in areas where large masses are desired. Through these vent holes, vapor phase HF etches the oxide beneath large masses to release them, Figure 1b. Immediately following, the device layer is grown with doped epitaxial silicon growth, sealing the vent holes as well. The devices are patterned using DRIE with 20:1, 40:1, and 60:1 trench depth to width ratios. Trenches where oxide posts are desired, in large gap areas, are also patterned during this step, as seen in Figure 1d. Next, oxide is deposited in a low-pressure chemical vapor deposition (LPCVD) process using Tetraethylorthosilicate (TEOS) to conformally refill device trenches and the trenches defining the oxide posts. The oxide refill results in keyholes in the trenches because the trenches are sealed at the top before enough oxide deposits on the side walls of the high aspect ratio trenches. Vents are etched through the top oxide layer in large gap areas between the oxide posts using a fluorine-based magnetically-enhanced reactive ion etch (MERIE), as seen in Figure 1e. Vapor phase XeF_2 isotropically etches silicon from the large gap areas through the vents (Figure 1f). Figure 2 illustrates a cross-section of a cavity created by a XeF_2 etch of silicon in the device layer where a large transduction gap is desired, leaving oxide posts to support the top layer of oxide. The keyholes in the oxide posts formed by the conformal LPCVD oxide are visible.

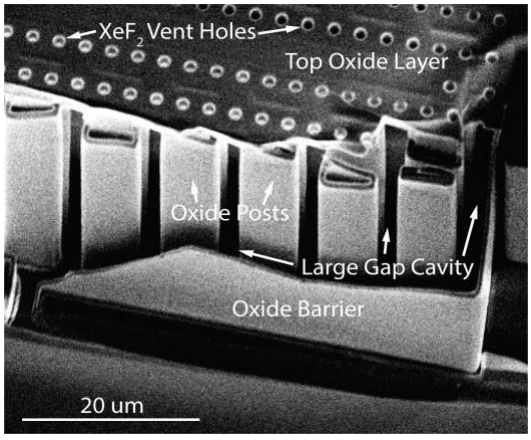

Figure 2: SEM of large gap cavity after XeF_2 etch.

More LPCVD oxide refills the vents and increases the thickness of the top oxide layer to 3 µm. Vias to the device layer are etched with fluorine-based MERIE, then the first and second cap layers are deposited using epitaxial silicon. Top electrodes are defined with DRIE and are isolated with nitride above devices intended to be released. Vents for device release are etched in the cap layers with DRIE, as illustrated in Figure 1g. The devices are released with vapor phase HF and sealed in a low pressure, high temperature epitaxial reactor with a third and final capping layer (Figure 1h). Finally, contacts to the device layer are patterned and isolated from the rest of the cap with a LPCVD low-stress nitride. Aluminum contact are patterned with aluminum etchant. Figure 1i depicts the cross-section of the final device.

Through this process, large gaps of up to 50 µm wide and 40 µm deep were created. Figure 3a illustrates the top view of a 50 µm by 450 µm trench. Additionally, resonators with large masses were successfully encapsulated without etch holes, as depicted in the SEM in Figure 3b.

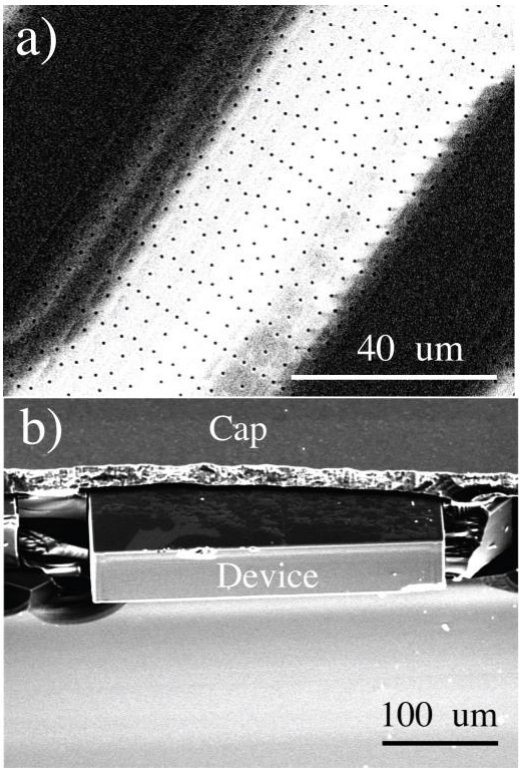

Figure 3: SEM images of a) the top view of a large gap cavity 50 µm wide and 450 µm long after the XeF_2 etch, and b) a cross-section of an encapsulated etch-hole free square bulk-mode resonator from this process.

DEVICE RESULTS

Figure 4 shows the frequency responses and mode shapes of a bulk-mode resonator consisting of a 400µm wide etch-hole free square plate and a large displacement beam resonator with 11.5 µm transduction gaps, both of which were recently fabricated in the first complete run of this process. Figure 3b depicts a cross-section of the square bulk-mode resonator with no etch-holes. The absence of etch-holes allows this square bulk-mode resonator to have a quality factor of 1.7M because the TED induced in the bulk mass in the isochoric Lamé mode shape, depicted in Figure 4a, is negligible without the strain gradients caused by the etch-holes.

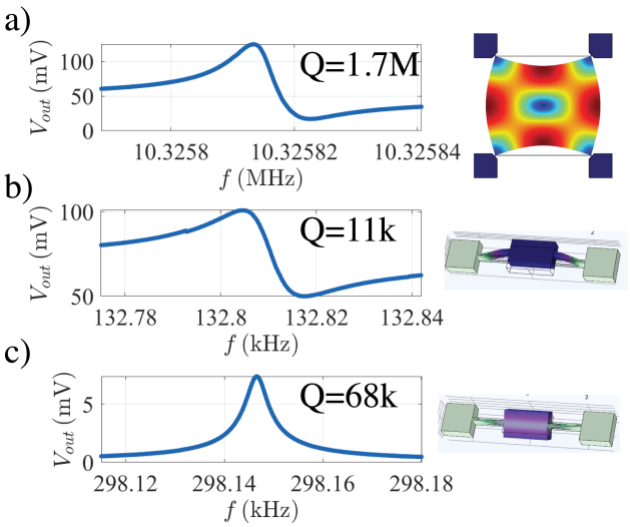

Figure 4: Mode shapes and frequency responses of a) the Lamé mode of a square bulk-mode resonator fabricated without etch-holes with a Q of 1.7M, which is achievable due to low TED contribution without etch-holes, b) an in-plane flexural mode of a large displacement resonator made possible with the large gap process, and c) a torsional mode of the same large displacement resonator.

The simple flexural mode resonator represents a device that can be used as a displacement-based or resonant accelerometer. The in-plane mode represents the ability to design a displacement-based accelerometer with a large mass, no etch-holes, and large transduction gaps to support high dynamic range. The Q for such a device could be designed or tuned to a lower Q to serve as a displacement-based accelerometer [17-19]. Disc resonant gyroscopes were also created in this process.

This work demonstrates co-fabrication of high-Q resonators for application in timing references as well as large displacement resonators for applications in accelerometers and gyroscopes to be fabricated on the same chip for the first time.

CONCLUSION

We presented a fabrication process to create hermetically sealed resonant MEMS where high-Q timing references and inertial sensors can be fabricated on the same die without wafer bonding. This high temperature epitaxial encapsulation process allows for small and large transduction gaps (tested up to 50 µm wide) and etch-hole free large masses. This process increases the design space for future resonant and non-resonant MEMS.

ACKNOWLEDGEMENTS

This work was supported in part by the National Science Foundation Collaborative Research Program under Grant CMMI-1662464 and CMMI-1662619 and in part by Defense Advanced Research Projects Agency's Precise Robust Inertial Guidance for Munitions (PRIGM) Program, managed by Ron Polcawich and Robert Lutwak. The fabrication work was performed at the nano@Stanford labs, which are supported by the National Science Foundation as part of the National Nanotechnology Coordinated Infrastructure under award ECCS-2026822.

REFERENCES

[1] A. Partridge, H.C. Lee, P. Hagelin, and V. Menon, "We Know that MEMS is Replacing Quartz. But Why? And Why Now?", 2013 Joint European Frequency and Time Forum and International Frequency Control Symposium, EFTF/IFC (2013), pp. 411–416.

[2] "SiTime", SiTime Corp. SiTime, 2021. https://www.sitime.com/.

[3] J. Seeger, M. Lim, and S. Nasiri, "Development of High-Performance, High-Volume Consumer MEMS Gyroscopes", Technical Digest of the 2010 Solid-State Sensor and Actuator Workshop, Hilton Head Isl., SC, 6/06-10/10, Transducer Research Foundation, Cleveland (2010), pp. 61-64.

[4] M. Esashi, "Wafer Level Packaging of MEMS", *Journal of Micromechanics and Microengineering*, 18, 073001 (2008).

[5] V. Kaajakari, J. Kiihamaki, A. Oja, H. Seppa, S. Pietkainen, V. Kokkala, and H. Kuisma, "Stability of Wafer Level Vacuum Encapsulated Single-Crystal Silicon Resonators", Technical Digest of the 13th International Conference on Solid-State Sensors, Actuators and Microsystems, TRANSDUCERS '05 (2005), pp. 916-919.

[6] K. Najafi, "Micropackaging Technologies for Integrated Microsystems: Applications to MEMS and MOEMS", Proc. of Micromachining and Microfabrication Process Technology VIII, (2003).

[7] L. Lin, R.T. Howe, and A.P. Pisano, "Microelectromechanical Filters for Signal Processing", *Journal of Microelectromechanical Systems*, 7, 286 (1998).

[8] B.H. Stark and K. Najafi, "A Low-Temperature Thin-Film Electroplated Metal Vacuum Package", *Journal of Microelectromechanical Systems*, 13, 147 (2004).

[9] C. Gillot, E. Lagoutte, P.L. Charvet, F. Souchon, and N. Sillon, "Wafer Level Thin Film Encapsulation for MEMS", Technical Digest of the 2005 Conference on High Density Microsystem Design and Packaging and Component Failure Analysis, (2005), pp. 1-4.

[10] C. O'Mahony, M. Hill, Z. Olszewski, and A. Blake, "Wafer-Level Thin-Film Encapsulation for MEMS", *Microelectronic Engineering*, 86, 1311 (2009).

[11] R.N. Candler, W.-T. Park, H. Li, G. Yama, A. Partridge, M. Lutz, and T.W. Kenny, "Single Wafer Encapsulation of MEMS Devices", *IEEE Transactions on Advanced Packaging*, 26, 227 (2003).

[12] B. Kim, R. N. Candler, M. A. Hopcroft, M. Agarwal, W.-T. Park, and T. W. Kenny, "Frequency Stability of Wafer-Scale Film Encapsulated Silicon-Based MEMS Resonators", *Sensors and Actuators A: Physical*, 136, 125 (2007).

[13] A. L. Alter, I. B. Flader, Y. Chen, L. C. Ortiz, D. D. Shin, and T.W. Kenny, "Characterization of Accelerated Fatigue in Thick Epi-Polysilicon Vacuum Encapsulated MEMS Resonators", *Journal of Microelectromechanical Systems*, 29, 1483 (2020).

[14] Y. Yang, E. J. Ng, Y. Chen, I. B. Flader, and T. W. Kenny, "A Unified Epi-Seal Process for Fabrication of High-Stability Microelectromechanical Devices", *Journal of Microelectromechanical Systems*, 25, 489 (2016).

[15] Y. Chen, I. B. Flader, D. D. Shin, C. H. Ahn, J. Rodriguez, and T. W. Kenny, "Robust Method of Fabricating Epitaxially Encapsulated MEMS Devices with Large Gaps", *Journal of Microelectromechanical Systems*, 26, 1235 (2017).

[16] L. Shao and M. Palaniapan, "Effect of Etch Holes on Quality Factor of Bulk-Mode Micromechanical Resonators", *Electronics Letters*, 44, 938 (2008).

[17] W.J. Venstra, H.J.R. Westra, and H.S.J. van der Zant, "Q-factor Control of a Microcantilever by Mechanical Sideband Excitation", *Applied Physics Letters*, 99, 151904 (2011).

[18] J.M.L. Miller, A. Ansari, D.B. Heinz, Y. Chen, I.B. Flader, D.D. Shin, L.G. Villanueva, and T.W. Kenny, "Effective Quality Factor Tuning Mechanisms in Micromechanical Resonators", *Applied Physics Reviews*, 5, 041307 (2018).
[19] N.E. Bousse, J.M.L. Miller, H.-K. Kwon, G.D. Vukasin, and T.W. Kenny, "Quality Factor Tuning of Micromechanical Resonators via Electrical Dissipation", *Applied Physics Letters*, 116, 023506 (2020).

CONTACT

*G.D. Vukasin, tel: +1-609-240-1174; gvukasin@stanford.edu

IMPACT OF ASPECT RATIO ON VOLTAGE GAIN OF QUARTZ TRAPPED-ENERGY RESONATORS

Mary E. Galanko Klemash[1], Dylan Bruno[2], Tobias M. Kiebala[2], Ryan Rudy[1], Victor Farm-Guoo Tseng[1] and Sarah S. Bedair[1]*

[1] U. S. Army Combat Capabilities Development Command – Army Research Laboratory, USA

[2] Rochester Institute of Technology, USA

ABSTRACT

This work examines the impact of electrode aspect ratio on the performance of quartz trapped-energy mode resonators in front-end wake-up receivers. In a series of resonators designed around 93 MHz with aspect ratio (AR) ranging from 1 to 2, voltage gain was directly measured at various load impedances relevant to the WUR application. Gain and quality factor (Q) are consistently maximized in devices with small resonator electrode AR, *i.e.*, approaching a width-to-length ratio of 1. This finding is in contrast with past design practices for quartz filters, where aspect ratios were chosen to minimize spurious modes in oscillators and timing applications rather than maximizing voltage gain as detailed in this work. The improved performance of devices with AR = 1 applies across a range of load impedances expected in the application as a front-end for a near-zero-power wake-up receiver.

KEYWORDS

piezoelectric devices, resonator filters, VHF resonators, wake-up receivers, Internet of Things (IoT)

INTRODUCTION

Ultra-low-power receivers are critical components of present and future Internet of Things (IoT) sensor networks. These networks are widely used to monitor distributed and inaccessible locations, such as large-scale infrastructure and agriculture. These use cases often require ultra-sensitive receivers that are available to respond to infrequent, long-range signals for months or years without battery replacement. Traditional receiver architectures cannot meet these demands for sensitivity and energy efficiency at the same time. Ultra-low-power, long-lived wake-up receivers (WURs) are one promising solution. WURs enable "near-zero" standby power consumption while remaining sensitive to a known signal. A particular modulation frequency and bit sequence triggers the WUR to briefly energize additional sensing and communication hardware. Recent work has demonstrated highly sensitive WURs over a wide frequency range, with standby power consumption as low as 10 nW [1], [2]. Key challenges include maintaining small size and high interference rejection.

Quartz piezoelectric resonators are well suited for use as a front-end in ultra-low-power WURs. The low material loss and high intrinsic quality factor (Q_m) of quartz resonators provide state-of-the-art passive voltage gain over a very narrow bandwidth [3], enabling high interference rejection in environments with crowded radio frequency (RF) spectrum usage. Quartz thickness-shear mode resonators are already a prominent commercial technology for oscillators and timing devices. These "trapped-energy" resonators typically excite a quartz membrane between opposing metal electrodes [4]. This resonator topology allows just a few critical design choices: the center frequency $\omega_r = 2\pi f_r$, which is defined to first order by the membrane thickness t; the parallel-plate shunt capacitance C_0 between the electrodes; and the electrode shape. In the common case of rectangular electrodes, the shape is defined by aspect ratio (AR) = length (L) / width (w).

Although t and C_0 are key design parameters, prior investigations have not considered the impact of electrode aspect ratio (AR = length L / width w) on the performance of quartz wake-up receiver front-ends. In prior literature on quartz trapped-energy resonators for timing applications, the typical approach to electrode geometry optimization is to suppress spurious modes [4], [5]. In general, this practice does not maximize quality factor, which in turn maximizes voltage gain and receiver sensitivity.

Based on the dominance of losses around the edge of the resonator [6], this work proposes that for a given device capacitance C_0, perimeter area should be minimized, giving AR = 1. A series of 1-port quartz resonators was fabricated with fixed f_r, fixed C_0, and AR varying between 1 and 2. Despite inter-device variation, devices with AR = 1 have the highest average voltage gain and observed quality factor Q_{gain}. This finding is broadly relevant for quartz resonators, a mature technology conducive to widespread commercial use, and for other material systems under development (e.g., [7]).

DESIGN

Resonator Design

Fig. 1 illustrates a typical quartz "trapped-energy" thickness-shear mode resonator topology. Each monolithic quartz substrate has diameter 5 mm and contains a central stepped area, or

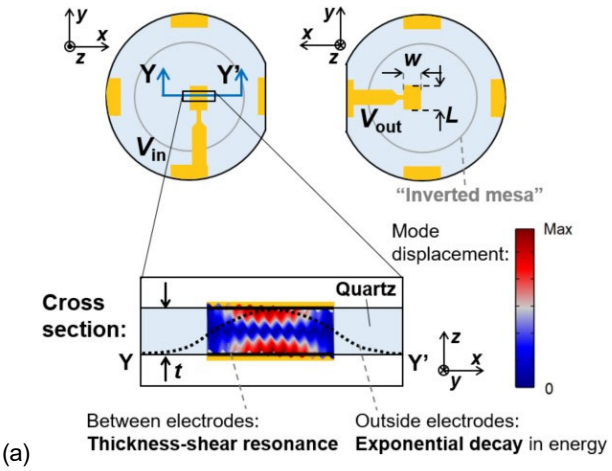

Figure 1: (a) Diagram of 1-port quartz resonator topology and thickness-shear mode shape. (b) Equivalent circuit model of quartz resonator and integrated system.

978-1-940470-04-7/HH2022/$25©2022TRF
DOI 10.31438/trf.hh2022.45

"inverted mesa," where the substrate is thinned to achieve a specific membrane thickness that defines f_r. Electrodes, traces, and pads are patterned in gold with nominal thickness around 120 nm on each side of the substrate. Rectangular electrodes with width w and length L are aligned on the top and bottom of the membrane to enclose a quartz area with thickness t and area $w \times L$. This rectangular prism-shaped section of the membrane is mass-loaded by the electrodes so that the thickness-shear mode resonance f_r of the electrode area is below the resonant frequency f_s of the surrounding membrane. Therefore, an AC voltage across the electrodes around frequency $f_r < f_s$ excites thickness-shear mode standing waves that do not propagate outside the electrode area, creating "trapped" energy in vibration modes [4]. Fig. 1(a) shows the result of a finite-element eigenfrequency simulation for the thickness-shear mode. Displacement is maximized at the membrane surface near the center of each electrode.

Fig. 1(b) shows the equivalent circuit of each thickness-shear mode resonator. C_0 arises from the parallel-plate capacitance between opposing electrodes. Other equivalent circuit values R_m, L_m, C_m are defined by f_r, C_0, and intrinsic material values for quality factor Q and electromechanical coupling factor k^2 [8]. Each trace between an electrode and a pad introduces series resistance $R_{trace} \approx 2.5\ \Omega$. In this work, the input voltage is sourced by a signal generator modeled by V_S and $Z_0 = 50\ \Omega$, in place of a WUR antenna with this equivalent circuit. The load impedance is modeled by a resistance R_L and capacitance C_L in parallel, representing the input impedance of the circuit block that loads the quartz resonator in the WUR front-end application. To measure V_{out} and ensure that it is as close as possible to the practical WUR front-end output voltage, this work uses active probes that are also modeled by input impedance $R_L \parallel C_L$ with similar values.

Minimizing Trapped Energy Loss

In prior literature on quartz trapped-energy resonators for timing applications, the most common approach to electrode geometry optimization is to maximize the separation between the fundamental frequency f_r and higher-frequency spurious modes. Shockley et al. [4] suggest doing so by ensuring that the electrode width is small enough to suppress all inharmonic overtone standing waves. Sheahan [5] refines this equation and substitutes quartz material parameters to predict a fixed optimal AR = 1.26.

This analysis does not consider energy loss from the resonator into the surrounding substrate. Shockley et al. [4] estimate that energy E decays exponentially with distance d from the electrode:

$$E = E_0 e^{-2\gamma d} \qquad (1)$$

where E_0 is proportional to the square of displacement and γ is an attenuation constant. Mindlin [6] calculates total strain energy around the resonator boundary using a surface integral over the perimeter. Assuming Equation (1) is uniform around the edge of the resonator, using this surface integral, the energy loss is approximately proportional to Equation (1) and to the resonator perimeter surface area $(2w + 2L) \times t$. Also, Q_m, a metric of energy storage relative to loss, will be higher for resonators with higher ratios of volume to surface area. Although general sources of loss in piezoelectric resonators are more complicated and are still under study [9], this work approximates that without excitation of spurious modes, the quality factor and therefore the voltage gain are maximized when $w + L$ is minimized, giving AR = 1.

Experimental Design

To specifically examine the impact of AR on performance, a series of 1-port AT-cut quartz trapped-energy resonators were fabricated within a custom commercial process (Microsemi High Performance Timing, Microchip Inc., Mount Holly Springs, PA) using the topology illustrated in Fig. 1. Each resonator had $f_r \approx 93.2$–94.2 MHz, varying AR = 1–2, and $C_0 \approx 165$ fF or $C_0 \approx 230$ fF. These two C_0 values were chosen to match the range of load capacitances expected in WUR integration while probing the impact of specific C_0 value on AR vs. gain trends. Because prior work has shown significant post-fabrication performance variation between individual resonators of a given design, this study included duplicate resonators of each design: 3 duplicates of each AR with $C_0 \approx 165$ fF, and 6 of each AR with $C_0 \approx 230$ fF.

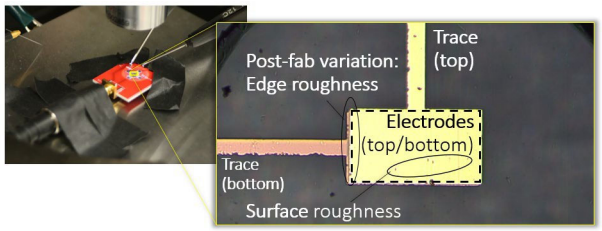

Figure 2: A typical fabricated quartz trapped-energy resonator and testbed. Traces, electrodes, and post-fabrication electrode variations are labeled.

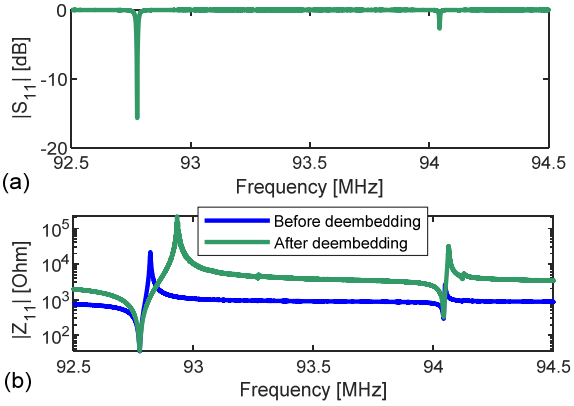

Figure 3: (a) S_{11} (de-embedded) and (b) input impedance (raw and de-embedded) versus frequency in a representative 1-port quartz resonator, measured with load $R_L \approx 0$. The closest spurious mode f_{spur} appears >10,000 ppm above the primary resonance f_r = 92.78 MHz.

RESULTS

Fig. 2 shows a typical voltage gain testbed and fabricated resonator, including electrodes with post-fabrication variation. To measure RF parameters and voltage gain, the input pad of each quartz substrate was mounted to a custom printed circuit board (PCB) on Rogers 4003 material (Rogers Corp., Chandler, AZ) using Loctite Ablestik 84-1LMI conductive silver epoxy (Henkel Electronic Materials, Irvine, CA). Input signals are routed through an SMA connector on this trace. Fig. 3 shows representative S_{11} and impedance measurements. The nearest spurious mode occurs >10,000 ppm above the primary resonance. This separation, >100× the bandwidth of either peak, is sufficient to prevent energy leakage between modes and to fit the application.

Voltage gain V_{out} / V_S is directly observed by applying $V_S = 40$ mV and landing Picoprobe high-impedance active probes (GGB Industries, Naples, FL) on the quartz output pad (V_{out}). At each load, observed quality factor $Q_{gain} = f_r / \Delta f$ is calculated by measuring the −3 dB bandwidth of V_{out}. A range of load impedances are applied by using 3 Picoprobe models that present

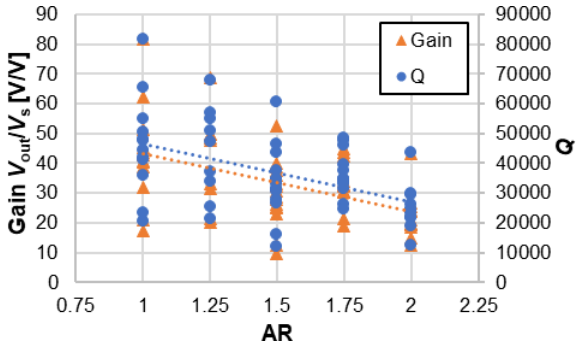

Figure 4: Voltage gain (V_{out} / V_s) and quality factor (Q), measured at load impedance R_L = 10 MΩ || C_L = 180 fF, versus aspect ratio for a series of 1-port quartz resonators with C_0 ≈ 165−230 fF.

different R_L, C_L, and by landing combinations of two probe models simultaneously such that their R_L, C_L add in parallel. The voltage gain of each device is measured several times to ensure that the result is not subject to test variations, such as probe contact quality. Typical variation between consecutive measurements is < 5%. These gain measurements were performed for each device with any C_0 and are analyzed both together and for fixed C_0 ≈ 230 fF.

All Devices

At a representative load impedance R_L = 10 MΩ || C_L = 180 fF, comparable to the input impedance of a high-performance WUR design [1], Fig. 4 illustrates trends in gain and Q_{gain} versus AR across both C_0 values. Average gain and Q_{gain} decrease proportionally with increasing aspect ratio. Although large variations in gain occur at each AR, a decrease in average gain is evident with increasing AR. Variations in gain and Q_{gain} are attributed to post-fabrication variation between resonators and are consistent with prior observations [3]. For each C_0 separately and for the complete dataset in Fig. 4, Table 1 compares the average and standard deviation in Q_{gain} for AR = 1 and AR = 2. Overall, the average Q_{gain} is about 46% higher at AR = 1 versus AR = 2. At both ARs, Q_{gain} is higher at higher C_0. This observation further suggests that lower ratios of perimeter area to electrode area enable more efficient energy trapping and less leakage.

Most notably, gain measurements in Fig. 4 show that 1-port quartz resonators can exhibit voltage gain over 80 V/V or 38 dB when loaded by a realistic WUR input impedance. This performance exceeds that of lumped-element electromagnetic component front-ends used in WURs in this frequency range [1].

Table 1: Q Measurements at Maximum and Minimum Aspect Ratio at Load R_L = 10 MΩ || C_L = 180 fF.

C_0	AR = 1		AR = 2	
	Average Q	*Standard Deviation*	*Average Q*	*Standard Deviation*
165 fF	35,100	12,300	23,300	2,500
230 fF	54,300	15,200	26,900	10,400
Any C_0	46,300	16,700	25,100	7,500

Fixed C_0

Fig. 5 examines voltage gain vs. AR exclusively for C_0 ≈ 230 fF at five high-impedance loads presented by active probes. The maximum load impedance is presented by the Picoprobe Model 19C, which has C_L ≈ 60 fF and very high R_L (>> 1 GΩ). Fig. 5(a) shows that the highest and most variable gain

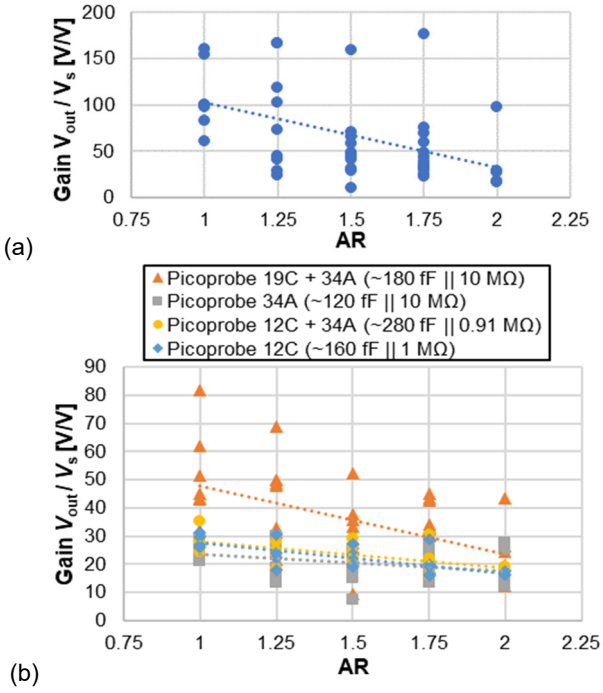

Figure 5: Voltage gain V_{out} / V_s (referenced to 50 Ω source) versus aspect ratio (AR) for a series of 1-port quartz resonators with C_0 ≈ 230 fF. (a) Gain vs. AR at maximum load impedance (~60 fF); gain is maximal and widely variable but increases at low AR. (b) Gain vs. AR at an array of realistic load impedances.

measurements occur at this load, consistent with prior observations [3]. The ultra-high-impedance probe appears to be more sensitive to contact quality and other variations between devices and between tests. Although high-impedance measurements are informative as an upper limit on voltage gain, remaining tests focus on lower load impedances, where gain measurements are less variable and are more realistic for the WUR application. For 4 load impedances with total R_L ≈ 0.9-10 MΩ and C_L ≈ 120-280 fF, Fig. 5(b) illustrates a uniform decrease in both average and maximum voltage gain with increasing aspect ratio. The average and standard deviation of voltage gain measurements are higher for certain combinations of R_L, C_L, generally higher gain for higher R_L and a particular C_L. This behavior is attributed to a known dependence of measured gain upon the electrical quality factor of the load impedance ($Q_{elec,load}$). Prior work has shown that voltage gain is limited to $Q_{elec,load}$ for the high-impedance loads of interest for wake-up receiver front-ends [10]. Loaded gain is modeled as an inverse sum of the observed open-circuit voltage gain $A_{v,OC}$ and electrical quality factor of the testbed/device materials and load:

$$A_{v,meas} \approx 1 / [\, \tan\delta_{quartz} + \tan\delta_{PCB} + 1/Q_{elec,load} + 1/A_{v,OC} \,] \qquad (2)$$

where tanδ denotes the electrical loss tangent of the quartz or PCB material. Unlike many piezoelectric resonator materials, the quartz material loss $\tan\delta_{quartz}$ < 0.0001 is so low that it may be omitted from Equation (2). The Rogers 4003 PCB material used in this work has $\tan\delta_{PCB}$ ≈ 0.002. Finally, for any load modeled by parallel resistance R_L and capacitance C_L, $Q_{elec,load}$ may be approximated as

$$Q_{elec,load} \approx \omega_r R_L C_L . \qquad (3)$$

To explore this scaling, Fig. 6 shows gain versus $1/Q_{elec,load}$. Voltage gain is measured at the same four realistic load

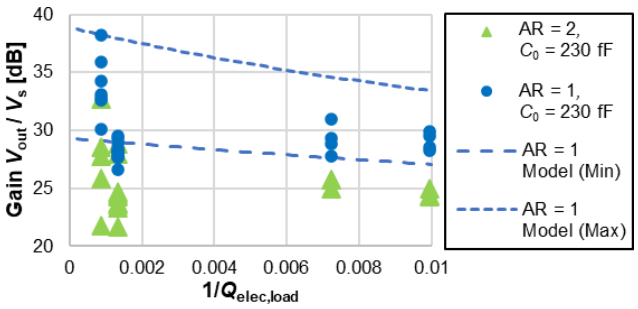

Figure 6: Voltage gain versus inverse of load electrical Q ($Q_{elec,load}$) for duplicate 1-port quartz resonators with $C_0 \approx 230$ fF and either AR = 1 or AR = 2. Dashed lines indicate model of voltage gain vs. $1/Q_{elec,load}$ are extrapolated from the highest and lowest gain measured at $1/Q_{elec,load} \approx 0.001$.

impedances examined in Fig. 5(b). Especially at the maximum $Q_{elec,load}$ applied (R_L = 10 MΩ || C_L = 180 fF), voltage gain varies significantly for a given design and load impedance but is maximized for AR = 1. Notably, at the minimum $Q_{elec,load}$ ($1/Q_{elec,load} \approx 0.01$), the average voltage gain offered by AR = 1 is higher than that of devices with AR = 2 by nearly 70%, much higher than the standard deviation of the data. These results suggest that especially in receiver circuits with lower $Q_{elec,load}$, such as those with input resistance $R_L \leq 1$ MΩ, minimizing AR is critical to maximum performance.

Gain vs. $Q_{elec,load}$ data may be compared with the Equation (2) model. Dashed lines in Fig. 6 indicate modeled $A_{v,meas}$ as modeled by extrapolating Equation (2) from the maximum and minimum voltage gain measured at the highest $Q_{elec,load}$ shown (lowest $1/Q_{elec,load} \approx 0.001$). Although most gain measurements fall between the estimates of these two functions, this envelope tends to overestimate voltage gain at lower load impedances. This discrepancy shows that improved models of gain versus $Q_{elec,load}$ and other sources of testbed loss are necessary as future work.

Future work will also examine relationships between aspect ratio, post-fabrication variation, and spurious mode placement. Additionally, similar studies of gain versus $Q_{elec,load}$ are needed in other quartz resonator designs. It is important to validate this trend at other resonant frequencies across the design range for these resonators, about 50-200 MHz. Resonators at higher frequencies may have different limitations governing resonator size versus relative spurious mode frequency. Finally, a similar study is required on gain vs. AR in 2-port quartz resonant transformers. 2-port devices are comprised of two monolithic coupled resonators, each based on the 1-port device geometry in this work. The 2-port configuration offers more design flexibility, especially in impedance matching with an antenna. In addition to varying AR, a study on 2-port resonators should vary the separation between the two coupled resonators. Although minimizing AR is still expected to minimize losses to the surrounding substrate, additional trade-offs may exist between AR, electrode separation, and yield.

CONCLUSIONS

This work shows that choosing aspect ratio (AR) = 1 maximizes voltage gain in a class of custom commercially fabricated 1-port thickness-shear mode quartz resonators. These findings broadly inform design the trapped-energy resonators to improve performance in RF sensing. Over a range of load impedances found in ultra-low-power wake-up receiver applications, resonators with AR = 1 enable voltage gain up to 80 V/V. This performance is competitive with electromagnetic transformers, but with much higher out-of-band rejection and a smaller form factor. Compared with an electromagnetic matching network around 100 MHz, which uses bulky lumped-element inductors [2], the quartz resonator has >70× smaller footprint and very low profile (<< 1 mm). While the design principles in this work apply to other resonator topologies and material systems under development, the manufacturability and low cost of quartz thickness-shear resonators provide easy, accessible prototyping and a low barrier to integration in commercial IoT.

ACKNOWLEDGEMENTS

This work was supported in part by the Army Research Laboratory under Grant W911NF-21-2-0052 and in part by the Defense Advanced Research Projects Agency (DARPA) Microsystems Technology Office (MTO). The views and conclusions contained in this document are those of the authors and should not be interpreted as representing the official policies, either expressed or implied, of the Army Research Laboratory, DARPA, or the U.S. Government. The U.S. Government is authorized to reproduce and distribute reprints for Government purposes notwithstanding any copyright notation here.

The authors wish to thank T. Daniels and D. Swarner at Microchip, Inc. for assistance with custom resonator fabrication.

REFERENCES

[1] P.-H. P. Wang, H. Jiang, L. Gao, P. Sen, Y.-H. Kim, G. M. Rebeiz, P. P. Mercier and D. A. Hall, "A 6.1-nW wake-up receiver achieving −80.5-dBm sensitivity via a passive pseudo-balun envelope detector," *IEEE Solid-state Circuits Lett.,* vol. 1, no. 5 (2018).

[2] H. Jiang, P.-H. P. Wang, L. Gao, C. Pochet, G. M. Rebeiz, D. A. Hall and P. P. Mercier, "A 22.3-nW, 4.55 cm2 temperature-robust wake-up receiver achieving a sensitivity of −69.5 dBm at 9 GHz," *IEEE J. Solid-State Circuits,* vol. 55, no. 6 (2020).

[3] M. E. Galanko Klemash, S. S. Bedair, D. A. Diamond, R. Q. Rudy, V. F.-G. Tseng, J. S. Pulskamp, and I. Kierzewski, "1-port piezoelectric resonators with >100 V/V gain," *J. MEMS*, vol. 29, no. 5 (2020).

[4] W. Shockley, D. R. Curran, D. J. Koneval, "Trapped-energy modes in quartz filter crystals," *J. Acoustical Soc. America*, vol. 41, no. 4 (1967).

[5] D. F. Sheahan, "An improved resonance equation for AT-cut quartz crystals," *Proc. IEEE*, vol. 58, no. 2 (1970).

[6] R. D. Mindlin, "High frequency vibrations of crystal plates," *Quarterly of Appl. Math*., vol. 19, no. 1 (1961).

[7] Z. Zhao, Z. Qian, and B. Wang, "Energy trapping of thickness-extensional modes in thin film bulk acoustic wave filters," *AIP Advances*, vol. 6, no. 015002 (2016).

[8] V. Kaajakari, *Practical MEMS*, Las Vegas, NV: Small Gear Publishing (2009).

[9] M. Wild, M. Bring, E. Halvorsen, L, Hoff, and K. Hjelmervik, "The challenge of distinguishing mechanical, electrical and piezoelectric losses," *J. Acoustical Soc. America*, vol. 144, no. 2128 (2018).

[10] S. S. Bedair, J. S. Pulskamp, R. Rudy, R. Polcawich, R. Cable and L. Griffin, "Boosting MEMS piezoelectric transformer figures of merit via architecture optimization," *Electron Device Letters,* vol. 39, no. 3 (2018).

CONTACT

* M. E. Galanko Klemash, tel: +1-301-394-1103; mary.e.galanko.civ@army.mil

LARGE TILT-ANGLE PHOTOTHERMAL OPTICAL BEAM STEERING USING MICROPATTERNED CNT-BASED INFRARED ABSORBER ON MULTILAYER THIN FILM STRUCTURES

Harris J. Hall[1], Sean A.McDaniel[1], Fahima Ouchen[1,2], Jose L. Figueroa[1,2], David Torres[1], Piyush J. Shah[1,3], Emily M. Heckman[1], and LaVern Starman[1]

[1]Air Force Research Laboratory, Wright-Patterson AFB, Ohio, USA

[2]KBR Inc., Dayton, Ohio, USA

[3]Apex Microdevices, West Chester, Ohio, USA

ABSTRACT

This work demonstrates photothermal actuation of asymmetrically patterned multi-layer thin film structures across a large range of mechanical tilt motion (up to 28° maximum). The device design constrains motion to 1D and is fabricated via post processing on a polysilicon foundry process. A key aspect is the micropatterning of an aerosol jet printed CNT coating as a stress free infrared absorber that enhances the response. Experimental results of the photothermal (λ=1532 nm) unit step response for both CNT coated and uncoated structures show linear tilt behavior up to ~ 50 W/cm^2 with CNT coated structures improving photosensitivity four fold. Beyond this irradiance level, the tilt magnitude responses suggests a mechanical bifurcation being triggered in the CNT coated structures. These results show significant potential for photo-actuated smart structures suitable for tunable optical beam steering applications.

KEYWORDS

Photothermal actuation, CNT, multi-layer, micro-optics; optical beam control, infrared absorber

INTRODUCTION

Light induced mechanical actuation has long been of interest for autonomous microsystems that require electrical isolation, often due to cost, complexity, or energy limitations. Some compelling examples manipulate the incident radiation itself by modulating the transmitted power ([1], [2]) or by altering the optical phase characteristics ([3], [4]). Our team has been interested in developing devices that when illuminated with a strong optical source can preferentially steer a portion of the incident radiation off-axis in a tunable fashion to large angles. This idea of "steering light with light" affords an unconventional self-powered smart structures approach to enable wireless optical beam scanning and steering.

We previously reported up to 9° of photothermally induced steady-state mechanical tilt at ~54 W/cm^2 irradiance with large deformation multilayer film structures that resemble the shape of a tetragonal pyramid [3]. These structures were constructed from selectively patterned regions of gold and silicon nitride films on polysilicon and exploit the residual stress inherent within these films to elevate the structure out of plane upon removal of the underlying sacrificial layer. This prior work added a 200 nm thick chromium film to one "side" of the pyramid to create asymmetric infrared (IR) absorption and subsequent tilting behavior upon illumination with an IR laser. However, these devices suffered from significant film delamination of the Cr layer, cross-coupled motion, and burn-in effects .

In this work, we address these deficiencies by modifying the structural design to better constrain the motion to one dimension (1D) tilt and by incorporating a patterned CNT-based film in place of the Cr as the infrared absorber. We show through experimental examination of the photothermal unit step behavior considerable improvement in dynamic range, photosensitivity, and directionality of the steady-state tilt response in comparison to prior work and offer some insight to the device dynamics.

Device Background

The devices characterized in this work are shown in Figure 1a-b and include a variant with and without the CNT infrared absorber in order to enable direct experimental comparison of photothermal actuation performance. The layout and geometry is identical to the structures previously examined in [3], expect these structures only have a single "arm" highly deformed out of plane upon removal of the sacrificial layer causing the central plate to be initially tilted 21° (see Figure 1c). As in prior work, the deformation of this arm is a result of the alternating tensile stress gold and compressively stressed silicon nitride films on the surface of the polysilicon structure which effectively creates a series of S-shaped deformation profiles that elevate that portion of the structure. Figures 2a-b. illustrate the film stack used in this arm for a single S-shaped cantilever with the addition of the CNT IR absorber on the surface. Device operation is almost entirely dependent on the photothermal response of this single raised arm whose internal thermal film stresses relax when heated, reducing deformation and subsequently the tilt angle of the central plate as illustrated in Figure 2c. The effect of the CNT coating is only considered on this single raised arm as the other three arms in the structure are not patterned with the compressive nitride layer.

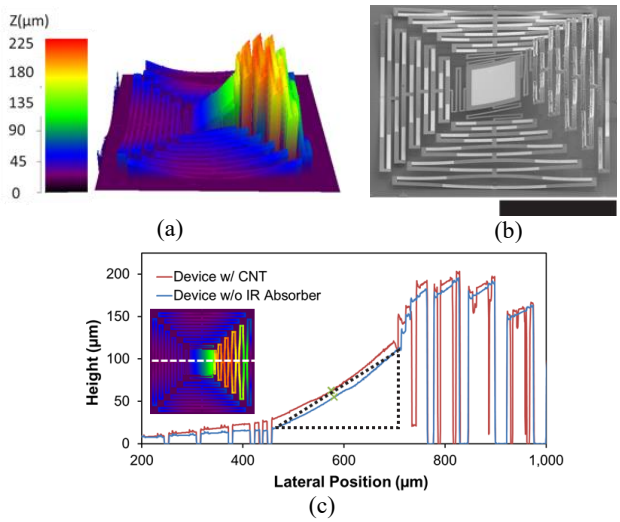

Figure 1: Post HF release characterization (a) 3D confocal microscope surface height image of Si_3N_4 on right arm only without IR absorber (b) SEM image of device with CNT absorber coating on the right arm. Scale bar is 500 μm in length. (c) 1D center cross-section of each device. Both structures have near equivalent tilt on 21° and cross axis tip of <1°, with a difference in piston height of ~8 μm.

978-1-940470-04-7/HH2022/$25©2022TRF
DOI 10.31438/trf.hh2022.46

These three other arms have little self-induced deformation and thus remain relatively fixed during operation effectively serving as support springs for the central reflective plate. This "single-arm" design reduces the structure's degrees of freedom essentially eliminating piston and cross axis tip motion upon actuation, making it advantageous for controlled 1D tilt motion.

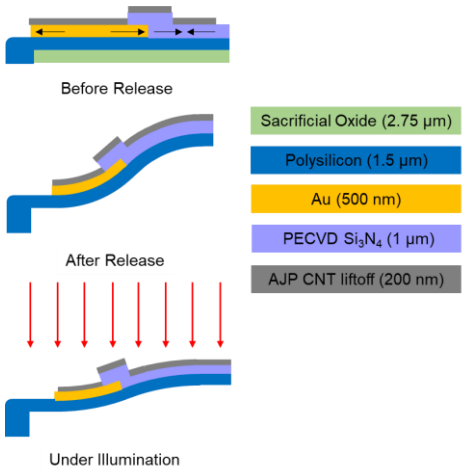

Figure 2: Simplified cross-section of a single multi-layer film cantilever with CNT coating. Note there is no effective stress in the CNT coating.

FABRICATION

The device fabrication process used the same core methods outlined in Refs [3,4] with the PECVD nitride layer (1µm thick) directly post-processed onto PolyMUMPS™ foundry produced die. Film thicknesses are summarized in Figure 2. The CNT coating was patterned through a combined use of aerosol jet printing (AJP) and liftoff processing (see Figures 1b, 3a-c). The AJP utilized a commercial ink (NINK-1100, NanoLab Inc.) and printed at room temperature using a 150 µm diameter nozzle. The CNT liftoff process used a standard AZ5214 photoresist (1.5 µm thick) and acetone spray gun, followed by rinses in isopropyl alcohol and deionized water. While the yield uniformity of the film was imperfect and discontinuous, the coverage was clearly sufficient for use as an IR absorber. The resulting contrast in CNT patterning was clearly superior when compared against our groups CNT film subtractive patterning attempts inspired by [5] (see Figure 3d).

Similar processing of AJP metals [6], oxides [7], and graphene oxide films [8], has been reported but to our knowledge this is the first demonstration liftoff with AJP CNTs. An important advantage of the CNT coating is that it has no significant film stress and thus minimal impact on the initial deformation (see Figure 1c). This decoupling of the infrared absorption from the structure greatly simplifies design.

EXPERIMENTAL SETUP

Both the steady-state and dynamic rise and fall photothermal step responses were examined experimentally using the setup illustrated in Figure 4a-b. A step excitation was applied using an infrared fiber laser (IPG photonics, λ = 1532 nm) focused across the width of the structure (spot size = 970 µm diameter) at increasing irradiance levels each for a 2 sec exposure time controlled using an automated beam block. The mechanical tilt (i.e. beam steering response) was measured by observing the reflection of a second low power visible laser (λ = 632 nm, spot size = 200

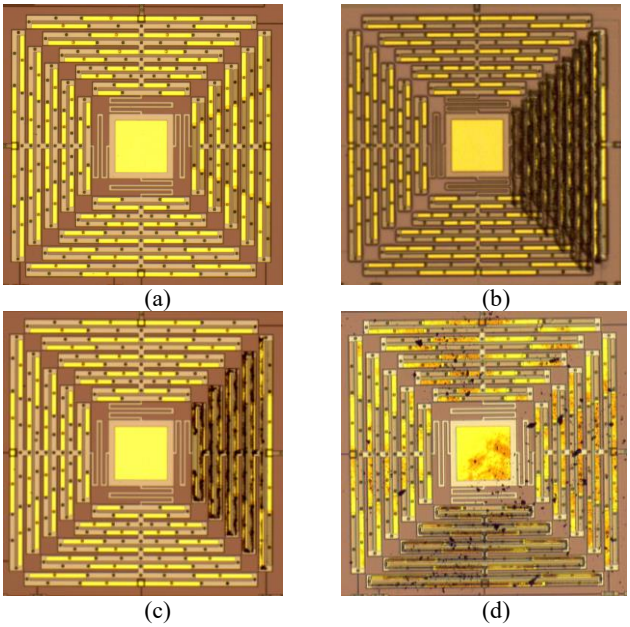

Figure 3: Patterning of CNTs as IR absorber (a) Si_3N_4 on right arm only w/o IR absorber pre-HF release (b) device after aerosol jet printing on patterned liftoff resist (c) same device after liftoff before HF release (d) attempted subtractive patterning 4-arm Si_3N_4 structure (as in [3]) with a CNT/nanodiamond/PMMA blend (inspired by [5]) on bottom arm

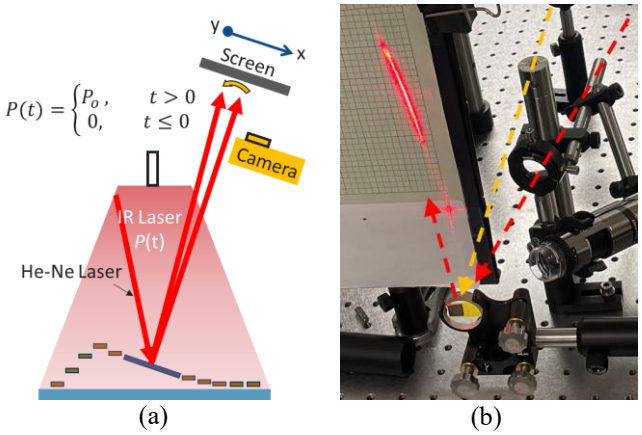

Figure 4: Experimental Setup (a) Graphical Illustration (b) Actual image of device under test and spot on screen. Red and orange dashed lines illustrate the visible and infrared beam paths respectively. The high speed camera imaging the screen is not shown.

µm diameter) off of the Au coated central plate onto a screen (distance = 11.1 cm) with a high speed camera (KronTech Chronos 1.4 - 6456 fps). Two separate test series were performed on each of the two devices, one with a CNT coating and one without. Each series increased the laser power and applied each condition twice to capture any burn-in effects and check for repeatability in the measurement. The "low power" series (see Figure 5) ramped the incident irradiance from 4.7 W/cm^2 to 68.8 W/cm^2 in increments of ~8-12 W/cm^2 while the "high power" series ramped from 48.4 W/cm^2 to 142.2 W/cm^2 in increments of ~11-30W/cm^2. The power increments had some variation due to inherent nonlinearities in the laser source power voltage control. All power levels were

calibrated using a power meter in the plane of the device prior to the start of the experiment.

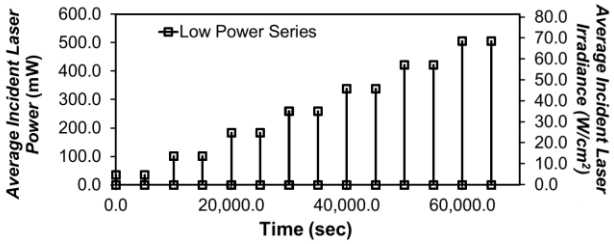

Figure 5. Low Power Unit Step Experimental Test Series. Camera is triggered for 3.25 sec capture with a 2 sec laser on time. High Power Series (not shown) is structured similar.

The raw video data sets collected were each post-processed using ImageJ and MATLAB to perform background removal and appropriately determine the center of mass (CoM) of the laser spot for each frame. The spot motion, from which optical tilt magnitude is measured, was converted from the CoM pixel position to angle based upon the geometry of the setup. The steady-state position for each point was determined by averaging the CoM of the central 100 frames (~ 1 sec after the step) during laser illumination . The rise and fall times were extracted from the 10% and 90% tilt magnitudes relative to initial and steady-state positions using 15th order polynomial fits to the rise and fall regions of each data set.

RESULTS AND DISCUSSION

As an example, the results for a single photothermal step response for the structure without the infrared absorber coating at an irradiance of ~ 45 W/cm^2 are shown in Figure 6a-e. In this instance the tilt motion of the structure is highly unidirectional and continuous in nature as desired.

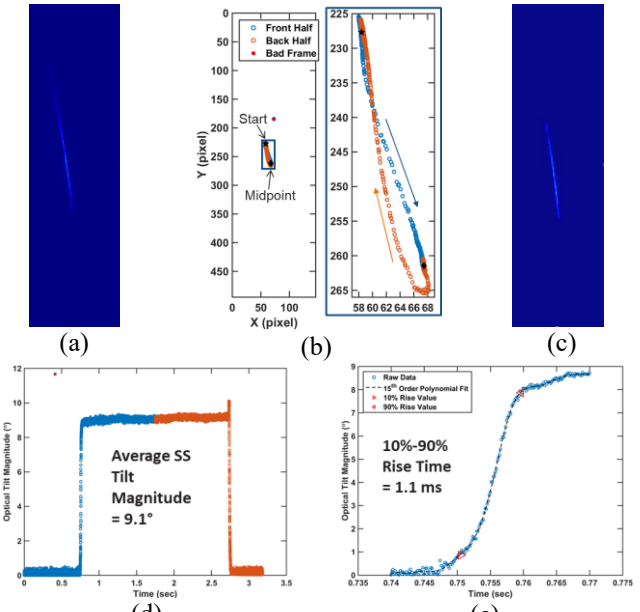

Figure 6: Portion of example unit step data set (w/o CNT 338 mW) at 6456 fps (a) Post-processed He-Ne laser spot screen image (artificially colored) at "Start" (unilluminated) (b) Laser spot CoM on screen, motion shown by colored arrows (c) Post-processed He-Ne laser spot screen image near "Midpoint" (illuminated) (d) Optical Tilt Magnitude time series relative to initial position (e) same series examining rise response. The fall response (not shown) is similar with a 1.1 ms fall time.

The compiled steady-state results from both low power and high power series for both the CNT coated and uncoated devices are shown in Figure 7a-b. The steady-state results are positive in multiple respects. First, the results show no evidence of device deterioration and negligible burn-in effects for both devices across the full range of optical power levels examined. Second, at moderate irradiance levels (~5-50 W/cm^2) the response trends are highly linear for both devices which is preferable for targeted design. Third, the CNT devices coated structures are 4x more photosensitive and have 3x larger tilt range than the uncoated structures within this linear operating region. And lastly the CNT coated device exhibits a larger than expected angular range (28° max mechanical tilt) that saturates > 60 W/cm^2. The maximum tilt magnitude is unexpected because it exceeds the initial mechanical tilt (21°) shown in Figure 1, which suggests the possibility of a structural nonlinearity being triggered at higher incident optical power that causes the central plate to have some tilt in the opposite direction as opposed to lying flat on the substrate.

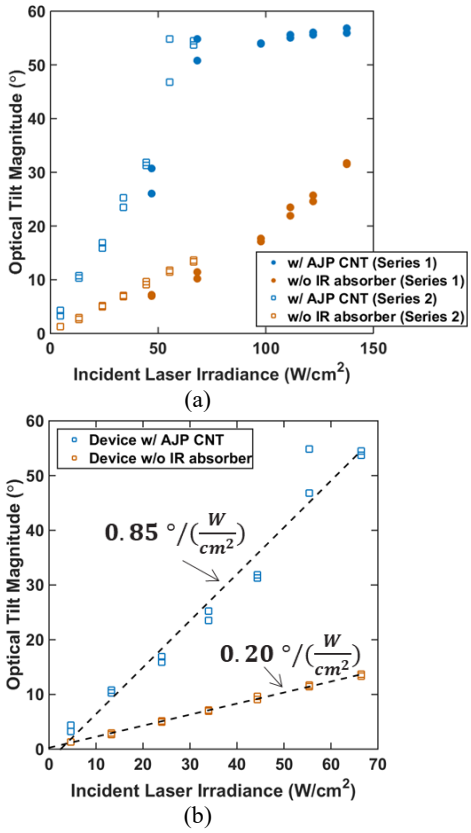

Figure 7: Steady-State Experimental Results (a) Compiled Optical Tilt Magnitudes for both High Power (Series 1) and Low Power (Series 2) Series (b) Low Power results with resulting photo sensitivities from linear least squares fitting.

A compilation of the dynamic 10%-90% rise time results for the low power series of both devices are shown in Figure 8a. The results clearly show a linear trend in these times with laser irradiance which is coincident with linear motion. Least squares fits to these plots show 4x the rise time sensitivity with respect to irradiance for the CNT coated devices vs. the uncoated devices which is coincident with the 4x increase in tilt photosensitivity. The data shows that the rise time is almost entirely dependent on the resultant tilt angle and independent of the CNT coating. For

example, based upon the linear fits in Figures 7b and 8a, the irradiance required for 10° tilt is 14.2 W/cm^2 for the CNT coated device and 48.3 W/cm^2 for the uncoated, but the rise times are near equivalent at 1.16 ms and 1.20 ms respectively. The trends in 90%-10% fall times (not shown) are near equivalent. All rise and fall response times were measured to be less than 8 ms.

At higher irradiance levels (> 50 W/cm^2) the CNT coated structure exhibits a rapid jump in angular motion (Figure 8b) as evidenced by the gaps between sample points before reaching SS. The purple colored trace at 68.2 W/cm^2 shows the existence of an intermediate unstable mechanical state. This intermediate state is not always overserved when the test points are repeated. These results strongly suggest some form of a thermomechanical bifurcation is being triggered.

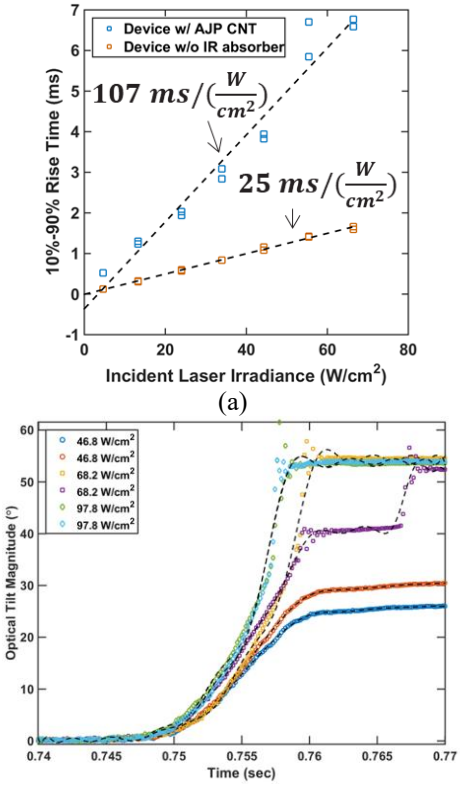

Figure 8: Dynamic Experimental Results (a) Compiled Optical Tilt Magnitude Rise Times for Low Power Series (b) Optical Tilt Magnitude Rise Behavior of CNT coated device near and above bifurcation threshold

CONCLUSIONS AND FUTURE WORK

The results of this work clearly demonstrate photothermal tilt control using the thermal stress relaxation mechanism of an asymmetrically constructed large deformation thin film structure for mechanical angles up to 28° in magnitude. The work also clearly demonstrates the utility of using AJP CNTs in conjunction with liftoff as a means for clean selective patterning of a stress-free infrared absorber on MEMS devices.

Future work is being directed towards incorporating geometric nonlinearity into our finite element simulations of the structures to enable predictive design (not shown) and towards expanding investigation into the structural bifurcation behavior observed. Lastly, improved blends of CNT feedstock for the AJP that can provide more uniformity across a broad range of surfaces are offered as a further area for improvement.

ACKNOWLEDGEMENTS

A portion of this work was supported under contract award FA807518D0015 by the Air Force Research Laboratory for on-site support by KBR Inc. The authors would like to thank Mr. Andrew Browning (AFRL) for plasma etching, Mr. Daniel Brooks (AFRL) for SEM imaging, and Mr. Juan Pastrana (Michigan State University) for helpful discussion.

REFERENCES

[1] X. Zhang, Z. Yu, C. Wang, D. Zarrouk, J.-W.T. Seo, J.C. Cheng, A.D. Buchan, K. Takei, Y. Zhao, J.W. Ager, et al. "Photoactuators and motors based on carbon nanotubes with selective chirality distributions." *Nature Communications,* 5, 2983 (2014),

[2] H. Zeng, O.M. Wani, P. Wasylczyk, R. Kaczmarek, A. Priimagi, "A. Self-Regulating Iris Based on Light-Actuated Liquid Crystal Elastomer." *Advanced Materials* 29, 1701814 (2017)

[3] H.J. Hall, S. McDaniel, P. Shah, D. Torres, J. Figueroa, L. Starman, "Photothermal Optical Beam Steering Using Large Deformation Multi-Layer Thin Film Structures. Micromachines", 12, 428 (2021). doi:10.3390/mi12040428

[4] H.J. Hall, S. McDaniel, D. Torres, P. Shah, L. Starman, "Photothermal Frequency Response Characterization of Large Deformation Multi-layer Thin Film Structures." In Proceedings of the 2020 IEEE Joint International Frequency Control Symposium— International Symposium on Applications of Ferroelectrics (IFCS-ISAF), Keystone, CO, USA, (2020)

[5] V.J. Gokhale, O. A. Shenderova, G. E. McGuire, M. Rais-Zadeh, "Infrared Absorption Properties of Carbon Nanotube/Nanodiamond Based Thin Film Coatings" *Journal of Microelectromechnical Systems*, 23, 1, (2014) doi: 10.1109/JMEMS.2013.2266411

[6] Y. Fu, Y. R. Liang, Y. Cheng and P. Wu, "A Combined Process of Liftoff and Printing for the Fabrication of Scalable Inkjet Printed Microstructures on a Flexible Substrate," in *IEEE Transactions on Electron Devices*, vol. 62, no. 4, pp. 1248-1254, (2015), doi: 10.1109/TED.2015.2401599.

[7] Y. Fu, J. Pan, K. Tsou and Y. Cheng, "A Flexible WO3-Based pH Sensor Array for 2-D pH Monitoring Using CPLoP Technique," in *IEEE Electron Device Letters*, vol. 39, no. 6, pp. 881-884, (2018), doi: 10.1109/LED.2018.2826013

[8] Y.-M. Fu, M.-C. Chou, C.-H. Kang, Y.-T. Cheng, P.-W. Wu, G.-Y. Chen, E. B. Secor, M. C. Hersam, "An Inkjet Printing Technique for Scalable Microfabrication of Graphene-Based Sensor Components", *Access IEEE*, vol. 8, pp. 79338-79346, (2020) doi: 10.1109/ACCESS.2020.2990501.

CONTACT

*H.J. Hall, tel: +1-937-713-8980; harris.hall.3@us.af.mil

LOW POWER 38.4 MHZ MEMS BASED REFRENCE CLOCK FOR QUARTZ REPLACEMENT WITH LESS THAN 30 PPM FREQUENCY STABILITY

Sarah Shahraini[1], Timo Huusari[1], Somnath Kundu[1], Hao Luo[1], Parvin Akhkandi[2], Yasaman Majd[2], Eduardo Alban[1], Brent Carlton[1], Ruth Vidana Morales[1], Jason Mix[1], Reza Abdolvand[2], Mohamed Abdelmoneom[1] and Nasser Kurd[3]

[1]Intel Labs, Hillsboro, OR, USA

[2]University of Central Florida, Orlando, FL, USA

[3]Design Engineering Group, Intel, Hillsboro, OR, USA

ABSTRACT

A 2.4 mW, 1ps RMS jitter temperature stable 38.4 MHz Thin Film Piezoelectric on Silicon (TPoS) MEMS based reference clocking chiplet implemented in Intel FinFET 22nm is presented as a viable traditional quartz crystal replacement. The TPoS full clock receiver comprises the TPoS resonator chiplet, pierce oscillator driver circuitry and the outer buffer converting the sinusoidal oscillation to a square digital clock. A 30ppm total frequency change across a temperature range from -40°C to 120°C is accomplished via a combination of passive compensation in the TPoS resonator structure and active temperature compensation using a fractional N Phase Locked Loop (PLL). Such competitive performance is achieved through a combination of the High-quality factor, low motional resistance, and the compensated composite structure of TPoS resonators along with design optimization of the 22FFL clock receiver circuitry.

KEYWORDS

Reference clock, MEMS contour mode resonator, Active temperature compensation.

TPOS RESONATOR DESIGN

Frequency scalable contour mode Scandium doped AlN on silicon TPoS resonator is designed as the frequency selective component of the oscillator demonstrated in this work due to their high-quality factor, low motional resistance, frequency scalability to few GHz and Quartz comparable ageing [1]. A third-order contour mode TPoS resonator is designed at 38.4 MHz as the reference clock to compare against performance of a 38.4 MHz industry standard off the shelf quartz crystal.

The resonators are fabricated on a relatively thick (20 µm) Ntype-doped <100> crystalline cut SOI topped with 1 µm sputtered 20% Scandium doped AlN film. The measured frequency response for this resonator is shown in Figure 1. Unloaded quality factor of 5.2k and motional resistance of 195 Ohms are measured at 38.38 MHz for this resonator.

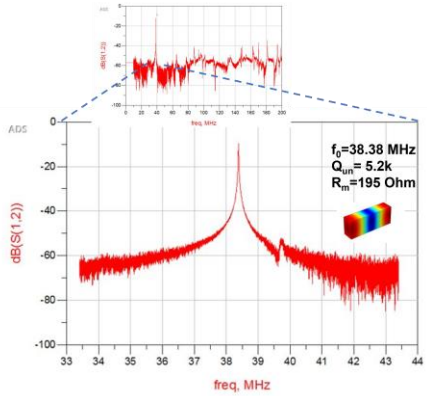

Figure 1: The measured frequency response for TPoS resonator (frequency selective component in the system).

A low level of passive temperature compensation is achieved with a lightly doped silicon layer yielding a temperature stability of about 1900 ppm for the extended temperature range (-40 °C to 120 °C).

OSCILLATOR DESIGN

The oscillator architecture is shown in Figure 2. It consists of a Pierce oscillator core, an amplitude/bias control block, a voltage shaper, and a fractional-N PLL for active temperature compensation.

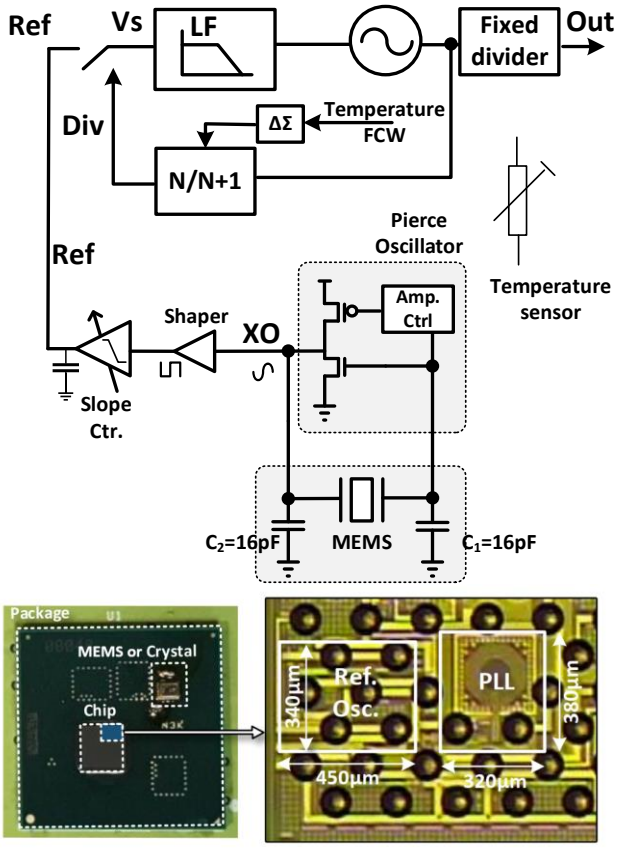

Figure 2: Architecture for the reference clock chiplet including, pierce oscillator core, shaper, fractional-N PLL, XTAL/MEMS and temperature senor.

The pierce core provides the negative resistance required to sustain the oscillation and the voltage shaper at the output of the Pierce oscillator converts the sinusoidal waveform to square wave to provide the clock reference for the PLL. A type-I sampling frac-N PLL is then used to compensate for the temperature dependent instabilities using a temperature sensor. The frac-N PLL has an output range from 2 to 2.48GHZ which is wide enough to cover

978-1-940470-04-7/HH2022/$25©2022TRF
DOI 10.31438/trf.hh2022.47

the MEMS temperature drifting range. The PLL's output clock is further Integer divided down to generate the target 38.4MHz output. MEMS resonator temperature drift error is corrected by changing the ΔΣ fractional word and hence the PLL's clock frequency. The PLL's 24 bit long fractional word is fine enough to correct the divided output clock within a 30ppm temperature stability.

MEASURED RESULTS

Measurement setup is shown in Figure 3. The same CMOS Pierce oscillator and driver are tested both with MEMS resonator and quartz crystal at 38.4 MHz for fair comparison.

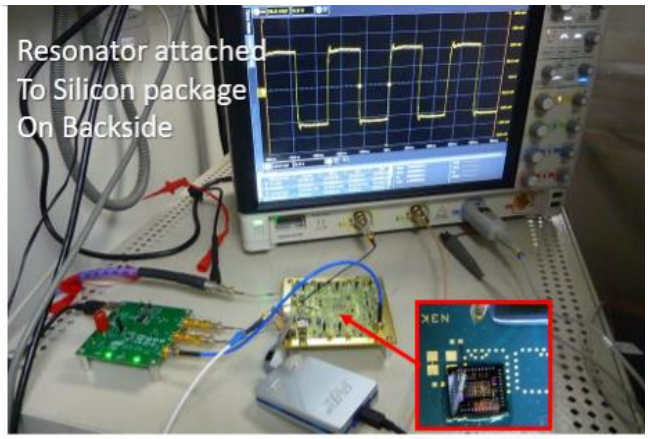

Figure 3:The measurement setup.

The measured RMS jitter (integration bandwidth 12kHz to 5 MHz) and clock signal power are plotted over temperature range of -40 ℃ to 120 ℃ and shown in Figure 4. The clock signal power reduces with increase in temperature while the integrated RMS jitter increases from a minimum of about 110 fs at -30 ℃ to a maximum of 220 fs at 120 ℃.

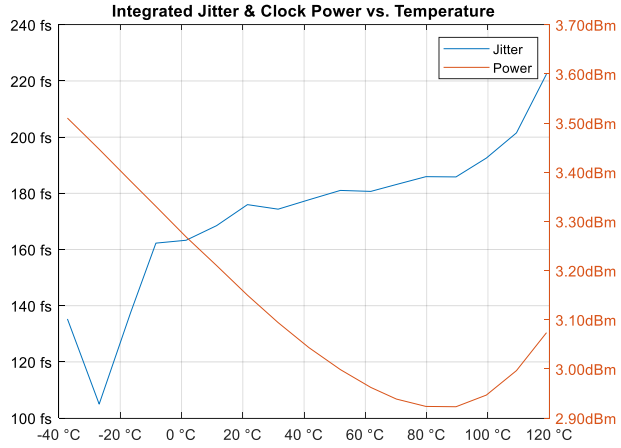

Figure 3: The measured RMS jitter (integration bandwidth 12kHz to 5 MHz with 4.1mW power) over a temperature range of -40 ℃ to 120 ℃. Clock signal power is also plotted over the same temperature range.

The frequency stability is also plotted in Figure 5 for the same extended temperature range with and without active temperature compensation. The frequency stability of the oscillator would be improved from 1900 ppm to less than 30 ppm by using active temperature compensation. The additional power consumption for the fractional N-PLL section is about 1.4 mW.

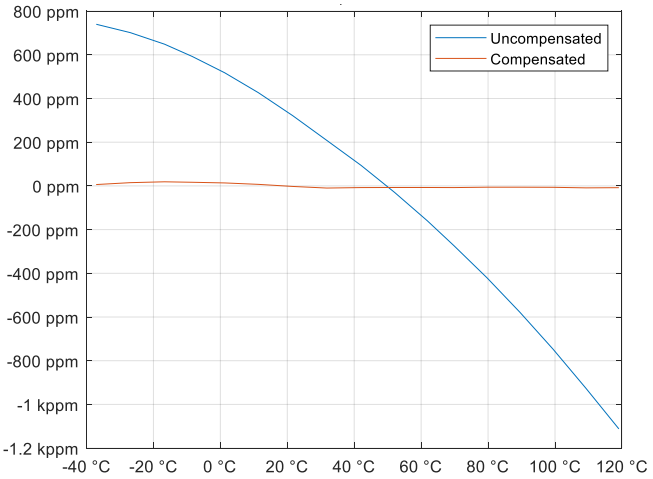

Figure 4: Frequency stability with and without active temperature compensation.

The performance for 38.4 MHz MEMS based and Quartz based reference clocks are compared at room temperature in TABLE 1. The presented demonstration clearly shows the viability of TPoS MEMS reference oscillators with similar performance as standard crystal oscillators with the key advantage of frequency scalability of the center frequency up to couple of GHz. This scalability could enable high frequency MEMS based reference clocks directly for high-speed IO systems and potentially eliminate the need for additional PLLs to save power and silicon area.

Table 1: TPOS MEMS based clock performance comparison to Xtal based Reference Clock

	38.4 MHz TPoS MEMS based Clock	38.4 MHz Xtal based Clock
Power	4.1 mW/1mW	3.9mw/1mw
Jitter (12KHz-25 MHz)	356 fs/1090fs	306 fs/841 fs
Startup Time	~ 75 µs	~ 292 µs/~ 60 µs (LCVCO start up [2])
Temperature stability (-40 ℃ - 120℃)	30 ppm (active compensation, additional 1.4 mW for ATC)	70 ppm

REFERENCES

[1] S. Shahraini et al., "Resilient Ultra Stable CMOS-MEMS Oscillator with Receiver in Intel 22FFL Technology," 2021 IEEE 34th International Conference on Micro Electro Mechanical Systems (MEMS), 2021, pp. 949-952, doi: 10.1109/MEMS51782.2021.9375330.

[2] H. Luo et al., "A Fast Startup Crystal Oscillator Using

Impedance Guided Chirp Injection in 22 nm FinFET CMOS," in IEEE Journal of Solid-State Circuits, vol. 57, no. 3, pp. 688-697, March 2022, doi: 10.1109/JSSC.2021.3136237.

[3] H. Luo et al., "A 12MHz/38.4MHz Fast Start-Up Crystal Oscillator using Impedance Guided Chirp Injection in 22nm FinFET CMOS," 2021 IEEE Custom Integrated Circuits Conference (CICC), 2021, pp. 1-2, doi: 10.1109/CICC51472.2021.9431500.

[4] S. Kundu et al., "A 2-to-2.48GHz Voltage-Interpolator-Based Fractional-N Type-I Sampling PLL in 22nm FinFET Assisting Fast Crystal Startup," 2022 IEEE International Solid- State Circuits Conference (ISSCC), 2022, pp. 144-146, doi: 10.1109/ISSCC42614.2022.9731560.

CONTACT

*S.Shahraini , sarah.shahraini@intel.com

MAGNETOHYDRODYNAMIC PROPULSION FOR MICROROBOTS

Ethan Leong and Camilo Velez
University of California, Irvine, Irvine, California, USA

ABSTRACT

This work demonstrates the feasibility of a magnetohydrodynamic (MHD) thruster for autonomous microscale propulsion in seawater and the benefit of using a novel Halbach cylinder configuration to increase exit speeds, thrust, and thruster velocity. MHD propulsion can provide reversible mobility in conductive fluids such as seawater without moving parts by utilizing a magnetic field and current density orthogonal to each other to propel fluid via the Lorentz force (thrust). An MHD thruster at small scales has been demonstrated to be reasonable and functional within microfabricated ranges.

KEYWORDS

Magnetohydrodynamic, magnetics, microrobots, motors.

INTRODUCTION

Microrobotic propulsion through a liquid medium has mostly been categorized as magnetic, chemical, or biologically assisted. Magnetic propulsion has been widely used because of favorable scalability at microscale and the ability to penetrate a large variety of materials [1,2]. Among the magnetic swimming locomotion strategies, oscillating and rotational motion are the most common. Although, they rely on an external control of magnetic fields [3], which limit the autonomy of the microrobot. A promising alternative for untethered autonomous magnetic locomotion of microrobots is magnetohydrodynamics (MHD). The concept of MHD utilizes a constant magnetic field and current density orthogonal to each other to create the Lorentz force, where conductive fluid can be propelled backwards to impart forward motion and thrust on an attached vehicle. An MHD thruster for microrobotic motion is a unique locomotive method that has not been published before. Previous efforts in using MHD for thrust have been conducted at the macroscale with a common setup of two magnets and two electrodes each at a set distance apart [4,5], requiring higher magnetic fields for thrusts comparable to similar macroscale propulsive mechanisms. Such higher magnetic fields would yield higher fluid speeds, as examined for MHD pumping applications [6,7]. Recent developments in microscale fabrication of magnets have showcased magnetic fields comparable to that at the macroscale [8,9], which warrants an examination of MHD propulsion for viable motion at the microscale.

This work proposes two configurations for an MHD thruster. The first is a **"magnet pair"** configuration**,** where two cube magnets aligned in series with magnetic poles pointing in the same direction are separated apart by a set distance to include a nozzle and two electrodes. The second is a proposed **"Halbach cylinder"** configuration that strengthens and homogenizes the magnetic field within the nozzle to impart higher exit speeds and thrust. Analytical equations were defined for MHD, and finite element simulation models were constructed such that the configurations were compared. The magnet pair configuration was then validated using mesoscale experimental assembly and characterization. The goal of this work is to determine the feasibility of MHD propulsion for microrobots and its enhancement due to a Halbach cylinder.

EXPERIMENTAL METHODS

The general principle of MHD is the propulsion of an electrically conductive Newtonian fluid using the Lorentz force.

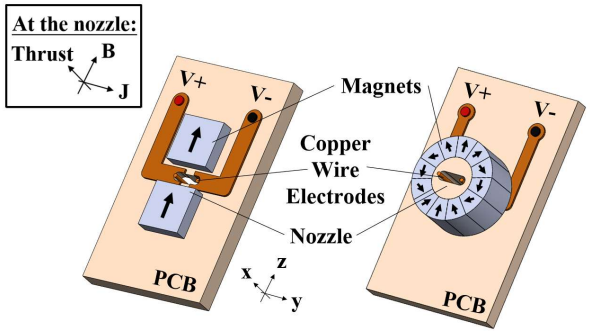

(a) (b)

Figure 1: MHD propulsion concept (inset). (a) Proof-of-concept magnet pair MHD thruster using a PCB with electrodes and 64 mm³ embedded cube magnets. (b) Halbach cylinder MHD thruster.

This is represented in Fig. 1 with a conceptual diagram for the two thrusters proposed in this work. Modeling this principle involves coupling electric and magnetic fields through the Maxwell equations as well as the Navier-Stokes equation. The set of equations that fully describe the MHD concept is [4,6]:

$$\boldsymbol{J} = \sigma(-\nabla V + \boldsymbol{u} \times \boldsymbol{B}), \quad (1)$$

$$\boldsymbol{F} = \boldsymbol{J} \times \boldsymbol{B}, \quad (2)$$

$$\boldsymbol{\rho}\left[\frac{\partial \boldsymbol{u}}{\partial t} + (\boldsymbol{u}\cdot\nabla)\boldsymbol{u}\right] = -\nabla \boldsymbol{p} + \boldsymbol{\mu}\nabla^2\boldsymbol{u} + \boldsymbol{F}. \quad (3)$$

The current density between electrodes ($\boldsymbol{J}$) is described by Eq. (1) using Ohm's Law, where σ is the fluid's electrical conductivity, V is the electric potential, $\boldsymbol{u}$ is the fluid velocity vector, and $\boldsymbol{B}$ is the magnetic flux density field (sometimes called magnetic field). The force over the conductive media produced by coupling current density and magnetic field is described in Eq. (2) and named the Lorentz force ($\boldsymbol{F}$). The fluid velocity vector ($\boldsymbol{u}$) can be calculated by incorporating the force $\boldsymbol{F}$ into the Navier-Stokes equation described in Eq. (3), where ρ, t, μ, and p denote the density, time, dynamic viscosity, and pressure of the conductive fluid. Additional conditions for magnetic flux conservation (where magnetic monopoles cannot exit: $\nabla \cdot \boldsymbol{B} = 0$) as well as fluid continuity (for incompressible flow cases: $\nabla \cdot \boldsymbol{u} = 0$) should be conserved.

Analytical model development for a Halbach cylinder

Due to the novel approach, special attention was given to the model of the magnetic field produced within the bore of a Halbach cylinder. Analytical calculations and simulations were done for model validation. B_{cyl} is the cylinder's magnetic field that varies with the size of the inner (r_i) and outer (r_o) radii (assuming infinite long cylinders) in the equation:

$$B_{cyl} = B_r \ln(r_o/r_i), \quad (4)$$

where B_r is the saturation magnetic field [10]. This model assumes a continuous variation of magnetization direction around the cylinder, but authors represented the cylinder with a 12-magnet segmentation that yielded ~95% accuracy with respect to the model [11]. Each magnet segment has a specific angle of magnetization

978-1-940470-04-7/HH2022/$25©2022TRF
DOI 10.31438/trf.hh2022.48

calculated by $\eta = 2\theta$ where η is the magnet's angle of magnetization – measured from the vertical axis – and θ is the angle from the vertical axis to the permanent magnet (where both angles are clockwise positive) [10].

For scaling analysis, r_i is selected as the smallest feature size and denoted as λ. The non-dimensional outer radius coefficient (β) is defined as the outer radius-to-inner radius ratio $\beta = r_o/r_i = r_o/\lambda$. Similarly, the non-dimensional length coefficient (γ) is defined as the cylinder length (L)-to-inner radius ratio: $\gamma = L/r_i = L/\lambda$.

Finite element analysis

Simulation of the magnetic field and fluid velocities for the magnet pair and Halbach cylinder thrusters were conducted in COMSOL Multiphysics based on [12], which contains the *Magnetic Fields-No Currents*, *Electric Currents*, and *Laminar Flow* domains. Magnetic flux directions and material magnetic properties were defined under *Remanent Flux Density* conditions. For the magnet pair configuration, two N50 cube magnets, copper wire electrodes, and a PCB substrate with the nozzle were fully recreated in a saltwater solution. The Halbach configuration replaced the cube magnets with 12 segments of N50 magnets (as described in the last section) while keeping the rest of the setup identical. The cylinder was kept at the same magnetic volume as the pair with β = 2 and γ = 1.

Scalability analysis

Characterization of the magnet pair and Halbach cylinder thruster require evaluating if a forward motion can be generated at different thruster dimensions. Both thrusters with identical magnetic volume (β = 2 and γ = 1), constant applied voltage of 3 V, constant electrode gap, current, and nozzle cross-sectional area were scaled between 10 µm ≤ λ ≤ 1000 µm for comparison.

A dynamic analysis for the thrusters was calculated in MATLAB with extracted mass flow rates and mean nozzle exit velocities simulated with COMSOL. The thrust force and the resulting opposing drag force were calculated as a culmination of pressure forces and shear stresses on the thruster. We propose to utilize the steady-state thrust equation of a jet engine on a MHD propulsor due to its jet-like nature:

$$T = \dot{m}_e u_e - \dot{m}_\infty u_\infty, \qquad (5)$$

where thrust (T) is dependent on the mass flow rate ($\dot{m}$) and velocity (u) at the exit (e) and freestream (∞) [5]. Furthermore, the flow is assumed to be incompressible because the velocities in the system are much lower than the speed of sound, meaning that $\dot{m}$ can be assumed to be constant throughout the system due to fluid continuity, where $\dot{m}$ is the product of ρ, nozzle cross-sectional area, and u_e. The static thrust (T_0) is defined as the thrust at rest (u_∞= 0), leading to the definition of the non-dimensional number T_0/W (static thrust-to-weight ratio) as the maximum acceleration (a) of the thruster with respect to the weight of the thruster (in other words the a/g ratio, with g as the gravitational acceleration).

For drag forces on microrobots, the Kahn-Richardson formulation can be used:

$$D = \pi r^2 \rho u_\infty^2 (1.84Re^{-0.31} + 0.293Re^{0.06})^{3.45}, \qquad (6)$$

where drag (D) is a function of the thruster radius (r) and Reynolds number (Re), which is the product of ρ, u_∞, and characteristic length (l) all divided by μ [13]. Because the magnetic volumes of both configurations are identical and a function of λ, both r and l are equal to λ.

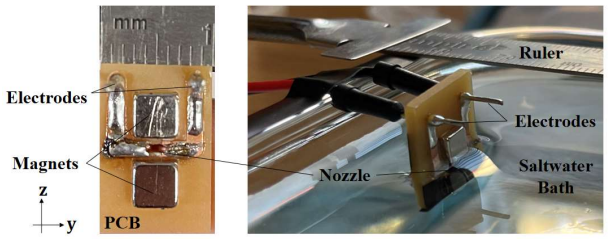

(a) *(b)*

Figure 2: Fabricated proof-of-concept magnet pair MHD thruster. (a) Top view of the thruster. (b) Experimental setup.

Fabrication and characterization of a magnet pair thruster

A proof-of-concept magnet pair MHD thruster was milled from a 1600 µm thick FR1 printed circuit board (PCB) substrate (Nomad 3 CNC). A drilled cutout through the center defined the fluid nozzle as an oval-shaped hole 1600 µm × 1794 µm × 794 µm (x-y-z) in size. Two ~320 µm wide copper wire electrodes were soldered on opposing sides of the nozzle for power connection. Two 4 mm cube N50 magnets were embedded above and below the nozzle to complete the active section of the MHD thruster. Fig. 2a showcases the assembled proof-of-concept pair thruster.

Static characterization of the thruster to evaluate its nozzle exit velocity was conducted by fixing the device in place and immersing it in a 50 mS/cm conductive saltwater solution just above the nozzle (Fig. 2b). The device was powered with constant voltage by a tabletop power supply (BK Precision 9140). Electrically conductive red dye was dipped into the solution to record fluid motion with a camera. High-speed video was recorded above the solution to track the dye's motion, measure its distance travelled, and determine the mean nozzle exit velocity (MATLAB).

Microbubbles during the experiment evidenced a chemically reactive process (electrolysis) due to electric current flow in the conductive fluid. These bubbles deter MHD flow by decreasing the conductive fluid volume and increasing the electrical resistance through the fluid [14]. In other words, the production of more ions within the solution comes at the expense of more nonconductive bubbles formed while power is applied. This evidence suggested the need to electrically characterize the MHD process. A cyclic voltammetry test upon the proof-of-concept thruster setup (without the embedded magnets) in identical saltwater solution was performed to evaluate the relationship between applied voltage and resulting current. A positive 3 Vp-p 200 mHz triangle wave voltage signal was applied as input and the resulting current signal was measured using oscilloscope current probes (Tektronix MSO44).

RESULTS

Magnet pair model

Simulations of the magnetic flux density (B) were conducted for the magnet pair to match fields produced by commercially purchased 4mm cube N50 magnets. The maximum B field between both magnets separated by a given gap was measured. Fig. 3 validates the concept that increasing the magnet gap leads to a decreasing B field. To accommodate for the chosen nozzle y-dimension value of 1794 µm, a separation distance of 2000 µm was chosen to allow for ample separation of the electrical circuit from the magnets. This gap yields a maximum B field value of 0.67 T. Further analysis of the B field at this distance (not included in this document) indicated that a relatively uniform B field is set across the nozzle area.

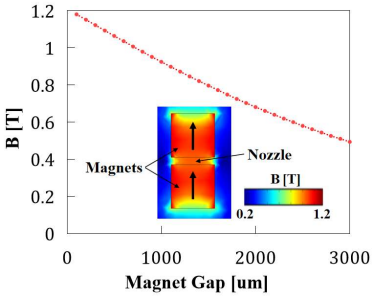

Figure 3: Magnetic flux density (B) simulation for the magnet pair at different gap distances.

Halbach cylinder model

Fig. 4 displays a parametric analysis of the B field for the different design variables of λ, γ, and β. Fig. 4a simulated the B field at 10 μm ≤ λ ≤ 10 m in increasing increments of $10^{0.1}$ for parametric values of β with γ = 1000 (to approximate an infinitely long cylinder) to observe how the B field changes with inner radius. Analysis of the graph showcased that B was constant within the microscale range (10 μm to 1000 μm). The B field was then simulated for $1 \leq \gamma \leq 30$ in increasing increments of 1 for parametric values of β as λ was kept at 10 μm to observe the change in B field with length (Fig. 4b). The simulated data revealed that the B field increased initially when γ increased but then approached a steady-state value. Because the B field is constant at microscale and approaches a steady-state value with increasing length, β was varied to evaluate B and its results were compared to the analytical B field values obtained via Eq. (6) (Fig. 4c). The results indicate that the simulated B field values are consistent with Eq. (6) and correspond to the steady-state B field values in Fig. 4b.

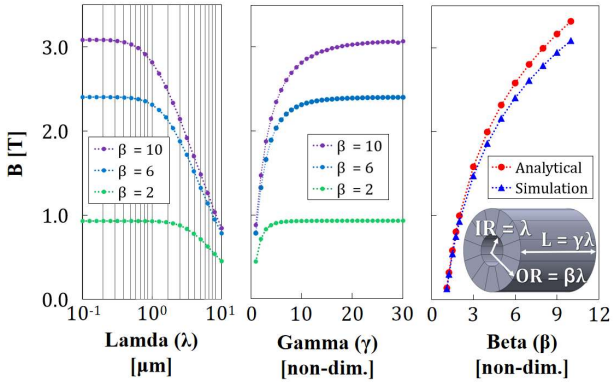

(a) (b) (c)

Figure 4: Magnetic flux density (B) simulations with respect to λ, γ, and β for a Halbach cylinder. (a) Simulation for 10 μm ≤ λ ≤ 10 m parametric with β (2, 6, and 10). (b) Simulation for 1 ≤ γ ≤ 30 with λ = 10 μm parametric with β (2, 6, and 10). (c) Analytical and simulated values for 1.1 ≤ β ≤ 10. Halbach cylinder concept and dimensions (inset).

Magnet pair and Halbach cylinder thruster comparison

A magnetic field and fluid velocity comparison between the magnet pair and Halbach cylinder thrusters is presented in Fig. 5. Fig. 5a demonstrates that an increased B field is achieved when replacing the proof-of-concept magnet pair configuration from Fig. 1a with a potential microfabricated Halbach cylinder considering an equivalent magnetic volume from Fig. 1b. A 600 mT increase in the B field produced by the Halbach cylinder

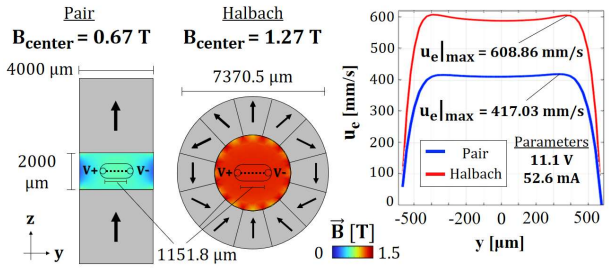

(a) (b)

Figure 5: Multiphysics simulation of the magnet pair and Halbach cylinder (β = 2, γ = 1). (a) MHD thruster configurations with B color plots in the nozzle area. (b) Projection of the fluid exit velocity profiles across the nozzle y-axis (dotted line between electrodes).

configuration translates into a ~191 mm/s maximum exit velocity increase for the Halbach cylinder configuration (Fig. 5b). Therefore, using a Halbach cylinder in replacement of a magnet pair for MHD propulsion is beneficial in achieving higher mean exit velocities.

The magnet pair configuration and Halbach cylinder configuration simulation models for the scaling analysis showcase that each thruster can provide forward motion if microfabricated, but the Halbach cylinder configuration provides a notable increase in propulsion than the magnet pair (Fig. 6). Eq. (5) and (6) were used to evaluate the thrust and drag of each size and configuration by varying u_∞. Because thrust decreases and drag increases with increasing u_∞, a steady-state condition (or cruise condition) is reached when thrust is equal to drag. Solving for u_∞ at this condition yielded the maximum thruster velocity ($u_\infty|_{max}$), or maximum velocity that a thruster can move at.

For all graphs, the Halbach cylinder provides a consistent increase of T_0/W and $u_\infty|_{max}$ with respect to the magnet pair configuration, indicating that this configuration will always provide superior MHD propulsive characteristics. Analysis of the data indicates that T_0/W increases up to a maximum of 0.12 and 0.056 for the Halbach and magnet pair configurations respectively but begins to decrease beyond that (Fig. 6a). This indicates that an optimum size for building the most powerful Halbach cylinder or magnet pair MHD thruster exists and is around $\lambda = 10^{-3.9}$ μm. An examination of Fig. 6b displays that $u_\infty|_{max}$ for thruster movement at this size and mass is ~21.5 mm/s and ~12 mm/s for the Halbach cylinder and magnet pair configurations respectively.

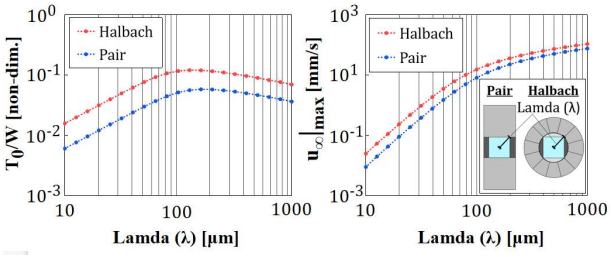

(a) (b)

Figure 6: Scalability analysis for the MHD thruster. (a) Static thrust-to-weight ratio (T_0/W) of the magnet pair and Halbach cylinder (β = 2, γ = 1) MHD thruster configurations. Simulations valid for 3 V. (b) Maximum velocity ($u_\infty|_{max}$) of each thruster configuration at 3 V. Definition of λ (inset).

Magnet pair MHD thruster characterization

Here we demonstrate that a MHD thruster at small scales is

reasonable and present its functionality within microfabricated ranges (Fig. 7). The proof-of-concept magnet pair MHD thruster drove water at a mean nozzle exit velocity of 51.4 mm/s with a current value of 174.27 mA and an applied voltage of 11.1 V (Fig. 7a). The nonzero mean exit velocity value demonstrates that the MHD concept applies at microfabricated ranges.

For the experimental analysis using a triangular input signal, current values begin below or near zero, as seen with the orange data points, and start to steadily increase in a linear fashion between 1 V and 1.5 V as seen with the blue data points (Fig. 7b). The standard-state potential of the oxygen oxidation reaction at the anode is 1.229 V, which correlates to the voltage at which the current values begin to become fully positive. Therefore, MHD flow can only be consistently activated above 1.229 V, which results in a linear relationship between current and voltage for the proof-of-concept device setup.

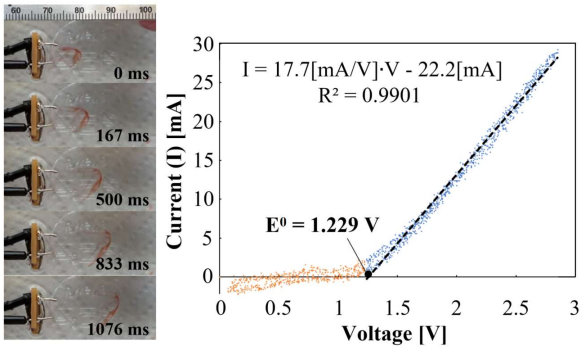

(a) *(b)*

Figure 7: MHD experimental results. (a) Frame-by-frame analysis of the MHD flow stream dye at 11.1 V. (b) Electrical characterization of the copper wire electrodes in 50 mS/cm saltwater.

CONCLUSIONS

Comparison of the fabricated magnet pair thruster with a potential microfabricated Halbach cylinder configuration demonstrated a ~90% increase in B field and a ~54% increase in nozzle exit velocity. A maximum T_0/W of 0.056 and 0.12 for the scaled magnet pair and Halbach cylinder configurations respectively indicate that $\lambda = 10^{-3.9}$ μm is the most optimal size, which results in a maximum thruster velocity of ~12 mm/s and ~21.5 mm/s respectively. Experimental analysis of the fabricated model showcase that the MHD concept is feasible at small scales and that the electrical relationship between current and voltage is linear above the standard-state potential of the oxygen oxidation reaction. Results presented in this paper demonstrate that MHD propulsion for microrobots is feasible and that using a Halbach cylinder in replacement of a magnet pair will greatly increase nozzle exit speed, thrust, and thruster velocity. Microscale MHD propulsion is possible, reasonable, and promising for increased autonomous underwater mobility of microrobots. Future developments in thin film magnetic materials and selective patterning of those films (such as the ones proposed by [15]) will enable this promising technology to increase microrobot autonomy.

ACKNOWLEDGEMENTS

The authors gratefully acknowledge funding support from the Henry Samueli School of Engineering, Department of Mechanical and Aerospace Engineering. We thank the students from the Magnetic, Microsystems, & Microrobotics lab for their contribution.

REFERENCES

[1] A. Kurt and R. T. Özbek, "Locomotion methods of microrobots and targeted drug delivery", *Demiroglu Science University Florence Nightingale Journal of Transplantation*, 5 (1-2), 39-46 (2020). DOI: 10.5606/dsufnjt.2020.015

[2] Y. Tu, F. Peng, and D. A. Wilson, "Motion Manipulation of Micro- and Nanomotors", *Advanced Materials*, 29 (39), 1701970, 2017. DOI: 10.1002/adma.201701970

[3] A. de Oliveira Barros and J. Yang, "A Review of Magnetically Actuated Milli/Micro-Scale Robots Locomotion and Features", *Critical Reviews in Biomedical Engineering*, 47(5), 379-394, 2019. DOI: 10.1615/CritRevBiomedEng.2019030299

[4] C. Chan, J. Cheng, C. Zeng, J. Huang, Y. Chen, Y. Chen, T. T. Pham, W. Chao, J. Jeng, T. Liu, K. Pan, Y. Li, and C. Chen, "Design of Marine Vehicle Powered by Magnetohydrodynamic Thruster", *Magnetohydrodynamics*, vol. 56, no. 1, pp. 51-65, 2020. DOI: 10.22364/mhd.56.1.5

[5] D. Cébron, S. Viroulet, J. Vidal, J. Masson, and P. Viroulet, "Experimental and theoretical study of magnetohydrodynamic ship models", *PLoS ONE*, 12(6), e0178599, 2017. DOI: https://doi.org/10.1371/journal.pone.0178599

[6] L. P. Aoki, M. G. Maunsell, and H. E. Schulz, "A Magnetohydrodynamic Study of Behavior in an Electrolyte Fluid Using Numerical and Experimental Solutions", *Engenharia Térmica (Thermal Engineering)*, vol. 11, no. 1-2, pp. 53-60, 2012. DOI: 10.5380/reterm.v11i1-2.62001

[7] A. V. Lemoff and A. P. Lee, "An AC magnetohydrodynamic micropump", *Sensors and Actuators B*, 63 (3), pp. 178-185, 2000. DOI: 10.1016/S0925-4005(00)00355-5

[8] N. G. Akdogan and O. Akdogan, "Synthesis of Nd-Fe-B/Fe hybrid micro-magnets", *AIP Advances*, 9, 125139, 2019. DOI: https://doi.org/10.1063/1.5130412

[9] J. Ewing, Y. Wang, and D. P. Arnold, "High-current-density electrodeposition using pulsed and constant currents to produce thick CoPt magnetic films on silicon substrates", *AIP Advances*, 8, 056711, 2018. DOI: https://doi.org/10.1063/1.5007272

[10] R. Bjørk, C. R. H. Bahl, A. Smith and N. Pryds, "Optimization and improvement of Halbach cylinder design", *Journal of Applied Physics*, 104, 013910, 2008. DOI: 10.1063/1.2952537

[11] K. Halbach, "Specialty magnets", *AIP Conference Proceedings*, 153, 1277, 1987. DOI: https://doi.org/10.1063/1.36378

[12] COMSOL Inc., "Magnetohydrodynamics", 2019. https://www.comsol.com/model/magnetohydrodynamics-74511

[13] M. Sitti, *Mobile Microrobotics*, MIT Press, 2017. ISBN: 9780262036436

[14] T.F. Lin, J. B. Gilbert, and R. Kossowsky, "Sea-water magnetohydrodynamic propulsion for next-generation undersea vehicles", Annual Report, Pennsylvania State University, 1990.

[15] C. Velez, "Engineering microscale magnetic devices for next-generation Microrobotics". University of Florida. 2017. http://ufdc.ufl.edu/UFE0051516/00001

CONTACT

*E. Leong, +1-650-200-9185; emleong1@uci.edu
*C. Velez, +1-352-575-7581; cvelezcu@uci.edu

MICRO ENERGY HARVESTER USING ACOUSTICALLY RESONATING BUBBLE FOR BIOMEDICAL IMPLANTATION

Wenbo Li, Anthony Mercader, and Sung Kwon Cho[*]
University of Pittsburgh, USA

ABSTRACT

We present a micro acoustic energy harvester utilizing a micro bubble resonator, which is much smaller than existing acoustic resonators. PVDF-TrFE is used as piezo material on a PDMS diaphragm that encapsulates a micro bubble amplifying the structural resonance and thus energy harvesting efficiency. Geometries of the diaphragm and bubble are carefully designed to match and maximize the structural resonance of piezo layer, diaphragm, and bubble. The maximum harvested power is measured at 1.8-μW, which is 7 times higher than the case without the bubble. The current harvester can be applied to implantable biomedical devices since acoustic waves of low frequency (< 9-kHz) can reach deeper spots in the human body than other types of waves (ultrasound, electromagnetic wave, etc.).

KEYWORDS

Oscillating Bubble; Resonator; Piezoelectric.

INTRODUCTION

Energy harvesting has seen much interest in the past two decades as the power consumption of MEMS devices is steadily reduced. Harnessing energy from ambient or wirelessly applied sources is attractive as a way to negate the need for batteries in applications where replacement of a battery would be inconvenient, expensive, or impossible, such as in the case of medical implantable devices [1-3]. There are typically two methods to harvest energy biomedically, passive energy harvesting involves utilizing human movement such as heart movement or lung movement as energy source, while active energy harvesting involves using external energy source to transfer energy into human body [4]. Since human body movement usually has a fixed, relatively low frequency range, power generated can be low, and the energy level and frequency is uncontrollable, it is natural to seek active methods. Typically, acoustic energy harvesting has less attenuation compared to other active harvesting methods, and it can reach a further distance within human body. In the case of human tissue, there is a clear trend of reduced attenuation at lower frequency in all ranges studied, from ultrasound down to the audible range [5]. Thus, it should be clearly beneficial for acoustic energy harvesting applications to target lower frequencies.

Piezo material selection

To harvest acoustic wave energy, piezoelectric films are usually used. The equation describing the direct piezoelectric effect, the ability of the material to convert mechanical strain into electrical charge is

$$D_i = d_{ij}\, T_j + \varepsilon^T_{ik}\, E_k, \qquad (1)$$

where i, j, and k represent 3 spatial dimensions, D is the electrical displacement, d is the piezoelectric stress coefficients tensor, T is the mechanical stress vector, ε^T is the permittivity tensor, and E is the electric field vector [6]. It is clear from this equation that increasing the stress in the material will increase the power output. There are typically 2 modes under which piezoelectric materials operate, d_{31} and d_{33} mode. Basically, the film is under d_{31} mode when applied stress and harvested electric field is perpendicular to each other, and is under d_{33} mode when they are parallel. Another performance metric of interest is the electromechanical coupling coefficient, k which in essence takes into account that a more elastically compliant material will strain more under a given load, increasing conversion efficiency when compared to a material with equivalent piezoelectric coefficient, d [3].

Several thin film piezoelectric materials have been used for energy harvesting in the past. One of the most popular options is ceramics such as lead zirconate titanate (PZT). The typical advantage of the ceramic materials tends to be much higher piezoelectric d_{33} and d_{31} coefficient [6]. Current research progresses on biomedical acoustic energy harvesting are done mostly with PZT as material [7]. However, the power output of these devices is quite small to this day, and despite consistent improvement over the years, it is still necessary to improve the efficiency of these devices in order to increase viability for use in commercial devices. A common strategy to improve the efficiency is exploring different structural designs beyond the common and easy to implement cantilever [5] or membrane [8]. Different designs may seek to improve the efficiency by inducing greater strain for a given input as in the case of a cymbal design [9] and bi-stable beam [10], or lower the resonant frequency to target ambient vibrations in the case of the arc-based cantilever [11] to list some examples. In addition, PZT contains lead, which is not favorable to implantation devices.

Another typical material usually used for energy harvesting is polymer such as polyvinylidene fluoride (PVDF) and its copolymers [11]. Advantages of the polymer materials tend to be easier processing, biocompatibility, and flexibility. Though the polymers have much lower d_{33} and d_{31} coefficients, their greater flexibility leads to a still lower, but more comparable k_{33} and d_{31} electromechanical coupling coefficients when compared with the ceramics [12].

However, PVDF as a material used for biomedical acoustic energy harvesting has not been developed before, majorly because its energy level is low compared to that harvested from PZT so for the already low acoustic energy level using this material can be challenging. It is noticed by the authors that there have been no or few attempts as to include a resonator in the energy harvesting devices. It is not surprising as in every case found by the authors, the size of the resonator is significantly larger than the energy harvesting device itself, often one or two orders of magnitude when comparing the largest dimension and several orders of magnitude when comparing the smallest dimension (thickness). Typical acoustic resonators often take the shape of a tube resonator [13] or a Helmholtz resonator [14]. More recently, the sonic crystal has seen some interest for this purpose [15]. It is then critical to have a small sized resonator to improve power generation for biomedical use. Therefore, this study targets on using polyvinylidene fluoride trifluoroethylene (PVDF-TrFE) and developing a small-scale resonator to improve power efficiency while keeping its biocompatibility, flexibility and ease of fabrication which are deemed important for the intended application in medical implantable devices [16,17].

Acoustic bubble

Acoustic bubble is a common tool used in various microfluidics applications. Under different frequencies, bubbles go through volumetric or translational motion while generating an acoustic streaming field around its vicinity.[18] Acoustic bubbles were used to pick up objects [19], rotate them [20], induce strong mixing in flow [21], pump liquid [22], deliver drug [23] and

978-1-940470-04-7/HH2022/$25©2022TRF
DOI 10.31438/trf.hh2022.49

generate propulsion [24]. It was observed in these previous experiments that polymer bodies of bubble undergo oscillation upon application of acoustic field just as the liquid-air interface. It is then natural to wonder whether or not this vibration on bubble surfaces can be used as vibration source needed for acoustic energy harvesting applications. Previous study has demonstrated on a commercial cantilever beam that bubble oscillations can be used as energy harvesting vibration source [25]. But no comparison was done on whether including a bubble in acoustic harvesting system would enhance power harvesting performance. In this article, an attempt is made toward developing a small-scale bubble-based resonator that operates under low frequency range (~5kHz) with PVDF-TrFE as harvesting material. A comparison is made between harvesters with or without bubble resonator.

DESIGN AND FABRICATION

Design idea of the device is to oscillate the piezoelectric film by an oscillating bubble so as to enhance the strain experienced by film and thus the power output. The system consists of several mechanical system: the acoustic bubble, the polymer diaphragm and the ceramic transducer. In order to maximize the harvested power, it is necessary to predict each resonant frequency according to geometry and make them match. For the bubble, resonance is predicted with Minnaert equation [26]:

$$f_0 = \frac{1}{2\pi}\sqrt{\frac{3\kappa P_0}{\rho}}\frac{1}{R_0} \quad (2)$$

where f_0 is the resonant frequency of bubble, κ the heat capacity ratio, P_0 the pressure the bubble is under, ρ the density of fluid, and R_0 the radius of bubble. Bubbles are built into cylindrical shape with the similar diameter and height to spherical bubble radius so that resonant frequencies of these bubbles are assumed to be similar to that of spherical bubbles with the same volume. The resonant frequency of diaphragm is predicted with Ansys modal analysis while the transducer resonance characteristics is given by the manufacturer product datasheet. The designed resonant frequency is then aimed at 4.6 kHz, the round diaphragm dimension is calculated to be 1 mm in diameter and the bubble dimensions are designed to be 1 mm in diameter and 1.5 diameter in depth as shown in Fig. 1. In order to distinguish the difference of having a bubble on backside of diaphragm or not, a comparison is done between different cases of bubble arrangement. As is shown in Fig 1. (a) three bubble setups are tested and compared.

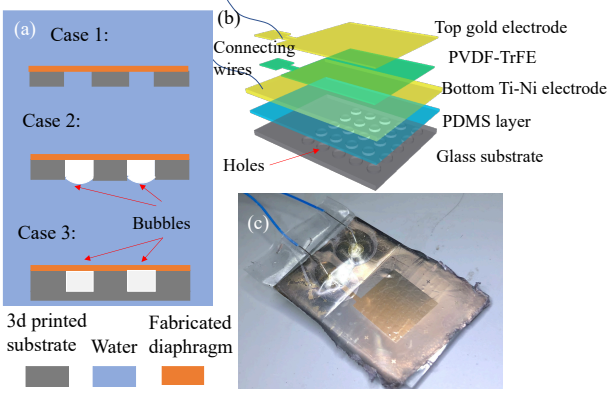

Figure 1 Device designs. (a) 3 different bubble configurations for comparison. (b) 3-D layer-by-layer device structure. (c) fabricated device.

Fabrication of the device consists of two parts, the substrate with cavities and a flexible PDMS film with PVDF-TrFE harvesting layer on top. Substrates was fabricated by laser cutting a glass substrate for case 1 and SLA 3d printing for cases 2 and 3. Process steps for flexible membrane are shown in Fig. 2, a silicon wafer was first coated with silane for easy PDMS detachment. Sylgard 184 PDMS and curing agent were mixed at ratio of 10:1 and spin coated on wafer at 4000 rpm, which gives 20 μm of PDMS layer. PDMS layer was then treated with oxygen plasma for 60s for better electrode adhesion. Then a layer of titanium and a layer of gold was e-beam evaporated onto PDMS. PVDF-TrFE (Solvene 300/P300 Sigma Aldrich) was dissolved in MEK solution (78-93-3 Sigma Aldrich) at 1:10 mass ratio and spin coated at 1500 rpm, thickness of this film is 3 μm. Another layer of gold is then e-beam evaporated and patterned with lithography. Excess PVDF-TrFE and photoresist were etched away with oxygen plasma using RIE. Electrodes were connected to lead wires with silver paste. The whole device is then coated with 2 μm parylene as insulation layer. Flexible membrane layer is then peeled off from wafer and placed on top of plastic substrate.

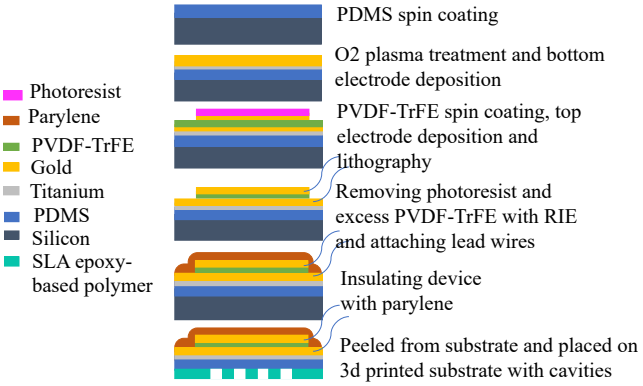

Figure 2 Fabrication process of the device.

RESULTS

Experimental setup is shown in Fig. 3. Comparison experiments are done in an acrylic tank, and the function generator outputs a 100 mV_{p-p} sinusoidal signal with varying frequencies. The amplifier amplifies the signal 200 times, which becomes 20 V_{p-p} and is fed to a ceramic piezoelectric actuator suspended in the tank. The fabricated energy harvesting device is put into the tank 5 cm away from the input actuator. The output from the harvester is read with a customized circuit with a load resistor and an oscilloscope.

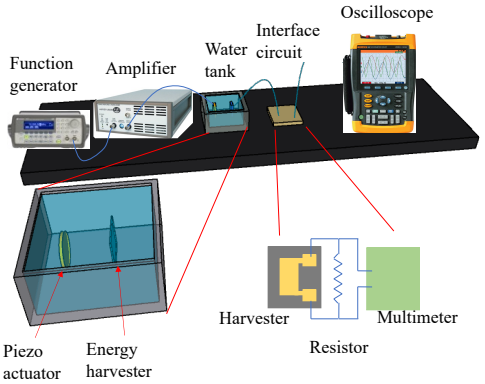

Figure 3 Experimental test set up.

A comparison study is carried out with 3 different cases shown in Fig. 1 (a), with all other parameters fixed. The power output is shown in the Fig. 4. Adding a bubble at the backside of the

diaphragm significantly increases the power output, and whether the bubble is open to liquid or closed does not affect the power output level.

In order to verify that the increase in harvested power originates from amplified diaphragm oscillation, an LDV (laser doppler vibrometer) system is then used to measure the vibration amplitude of the diaphragm.

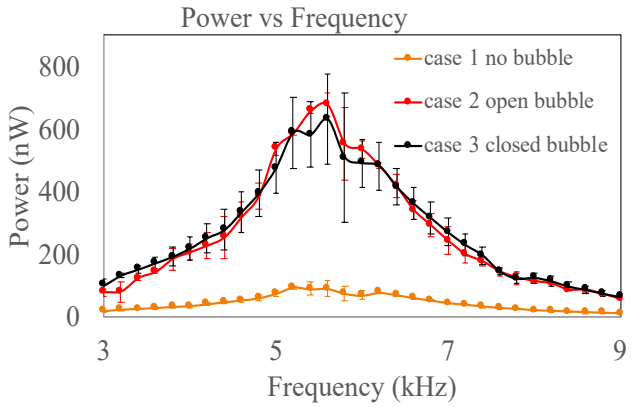

Figure 4 Power output comparison result.

The deflection of the diaphragm is measured to be increasing from 110 nm to 350 nm (Fig. 5 (a)) when a bubble is added (from case 1 to case 2 or 3). It is clear that the increase in oscillation amplitude is responsible for the increase in voltage output and thus the electrical power being harvested. A numerical calculation is carried out to verify that the deflection can indeed generate the voltages measured in our experiments. Ansys package is used to find the stress on the film when the diaphragm deflection is 111 nm and 350 nm. Deflections and the corresponding stress distributions are shown in Figs. 5 (b) and (c). Since the deflection amplitudes are similar for cases 2 and 3, they are considered as the same scenario in further simulation where the deflection of the diaphragm is large. The stress is simulated to be 0.5 MPa and 1.5 MPa, respectively when the deflections are 110 and 350 nm. Then, the obtained stress is taken into equation: $V = g_{31}\ \sigma_3\ t$ to calculate for the generated voltage. In the equation, V, g_{31}, σ_3, t represents the voltage output, the piezoelectric voltage constant, the applied mechanical stress, the thickness of film, respectively. The piezo voltage constant is 216 mV·m/N. The voltage output from the film is calculated to be 49 mV and 166 mV, respectively for small and large deflection. These matches our experimental results, which further confirms that the increase in voltage is due to the increase in the amplification of oscillation amplitude.

In order to find out the maximum output power of the device, impedance matching process is carried out by sweeping load resistor value from 1.5 to 172 kΩ. The voltage and power output is shown in Fig. 6 (a). It is found that 120 kΩ is the impedance of the device, and maximum power can reach up to 1.8 μW.

Furthermore, the effect of distance between the input actuator and harvester is also studied, power output as a function of distance is shown in Fig. 6 (b). The harvested power rises slightly as harvester moves further away from the transducer. In this case, it is found that the distance between the input actuator and harvester is not a critical parameter since the power output remains at same order of magnitude. When the wavelength is much smaller than the present experiment, the wave interference significantly affects the power output, and thus the distance is a critical parameter. However, In the present experiment, the acoustic wavelength is in the range of 10 centimeters, meaning that the acoustic oscillation pressure is a bulk oscillation in the tank. The variation in power output may possibly result from the different acoustic level at different tank locations.

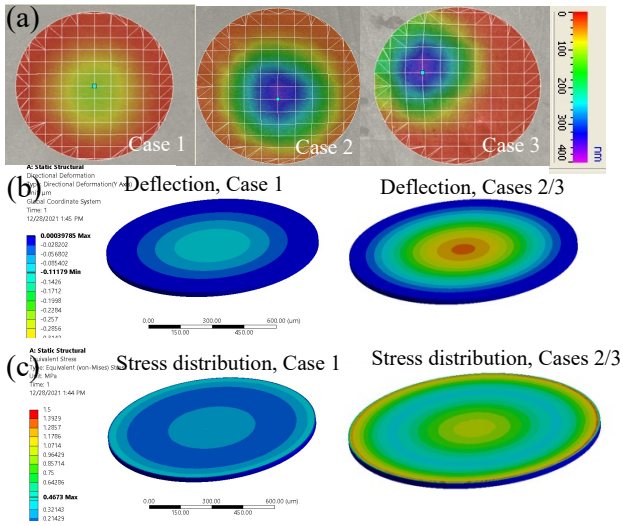

Figure 5 Validation of power output. (a) LDV results of the diaphragm oscillation amplitude of i) no bubble ii) open bubble and iii) closed bubble cases maximum deflection is measured to be 111 nm, 359 nm and 350 nm respectively. (b) Ansys simulation results, i) and ii) is deflection of small/large deflection diaphragm iii) and iv) is stress distribution on the small/ large deflection diaphragm.

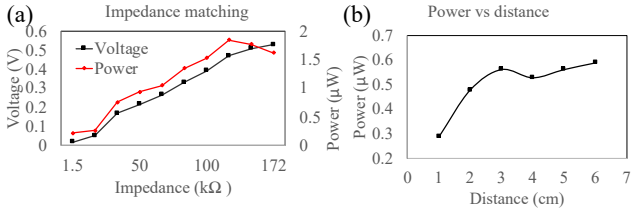

Figure 6 Power output level with (a) impedance (b) and distance between the input actuator and harvester.

The present microscale resonator for acoustic energy harvesting improves the harvested power by 7 times. In order to characterize the space utilization efficiency compared to the existing results, the area power density of the device is calculated by dividing the power density by the pressure level experienced and volume of the whole device. The present harvesting device has the space efficiency of 7.742×10^{-5} μW/cm^2·Pa·mm^3 while other existing work has the space efficiency of 3.1×10^{-7} μW/cm^2·Pa·mm^3, 9.6×10^{-10} μW/cm^2·Pa·mm^3, and 3.6×10^{-11} μW/cm^2·Pa·mm^3. [13-15] This clearly distinguishes our work in space utilization as bubble size is much smaller than other types of acoustic resonators. We hope that this method will not only improve acoustic energy harvesting process, but also improve the acoustic energy transduction and receiver field.

CONCLUSION

In this paper, we have demonstrated the possibility of an

acoustic bubble resonator with much smaller size than typical acoustic resonators. PDMS is used as substrate while PVDF-TrFE as piezo material. With this resonator, the power output level of this diaphragm-based polymer energy harvester was improved by 7 times than the case without the bubble resonator. This bubble resonator design can be further utilized in biomedical acoustic harvesting devices.

ACKNOWLEDGEMENTS

This work is in part supported by the National Science Foundation Project (ECCS-1951051).

REFERENCES

[1] S.R. Anton and H.A. Sodano, "A Review of Power Harvesting Using Piezoelectric Materials (2003–2006)", *Smart Materials and Structures*, 16, R1 (2007).

[2] K.A. Cook-Chennault, N. Thambi, and A.M. Sastry, "Powering MEMS Portable Devices—a Review of Non-Regenerative and Regenerative Power Supply Systems with Special Emphasis on Piezoelectric Energy Harvesting Systems", *Smart Materials and Structures*, 17, 043001 (2008).

[3] H.A. Sodano, D.J. Inman, and G. Park, "A Review of Power Harvesting from Vibration Using Piezoelectric Materials", *The Shock and Vibration Digest*, 36, 197 (2004).

[4] C. Dagdeviren, B.D. Yang, Y. Su, et al., "Conformal Piezoelectric Energy Harvesting and Storage from Motions of the Heart, Lung, and Diaphragm", *Proceedings of the National Academy of Sciences*, 111, 1927 (2014).

[5] W.-H.L. Wenli Zhou, Wen J. Li, "Analysis and Design of a Self-Powered Piezoelectric Microaccelerometer", *Smart Structures and Materials 2005: Smart Electronics, MEMS, BioMEMS, and Nanotechnology*, 5763, 233 (2005).

[6] J.W. Sohn, S.B. Choi, and D.Y. Lee, "An Investigation on Piezoelectric Energy Harvesting for Mems Power Sources", *Proceedings of the Institution of Mechanical Engineers, Part C: Journal of Mechanical Engineering Science*, 219, 429 (2005).

[7] B.L. Turner, S. Senevirathne, K. Kilgour, et al., "Ultrasound-Powered Implants: A Critical Review of Piezoelectric Material Selection and Applications", *Adv Healthc Mater*, 10, e2100986 (2021).

[8] M. Ericka, D. Vasic, F. Costa, et al., "Energy Harvesting from Vibration Using a Piezoelectric Membrane", *Journal de Physique IV (Proceedings)*, 128, 187 (2005).

[9] H.W. Kim, A. Batra, S. Priya, et al., "Energy Harvesting Using a Piezoelectric "Cymbal" Transducer in Dynamic Environment", *Japanese Journal of Applied Physics*, 43, 6178 (2004).

[10] A.F. Arrieta, P. Hagedorn, A. Erturk, et al., "A Piezoelectric Bistable Plate for Nonlinear Broadband Energy Harvesting", *Applied Physics Letters*, 97, 104102 (2010).

[11] D.J. Apo, M. Sanghadasa, and S. Priya, "Vibration Modeling of Arc-Based Cantilevers for Energy Harvesting Applications", *Energy Harvesting and Systems*, 1, 57 (2014).

[12] K.S. Ramadan, D. Sameoto, and S. Evoy, "A Review of Piezoelectric Polymers as Functional Materials for Electromechanical Transducers", *Smart Materials and Structures*, 23, 033001 (2014).

[13] S.B. Horowitz, M. Sheplak, L.N. Cattafesta, et al., "A MEMS Acoustic Energy Harvester", *Journal of Micromechanics and Microengineering*, 16, S174 (2006).

[14] S. Noh, H. Lee, and B. Choi, "A Study on the Acoustic Energy Harvesting with Helmholtz Resonator and Piezoelectric Cantilevers", *International Journal of Precision Engineering and Manufacturing*, 14, 1629 (2013).

[15] W.-C. Wang, L.-Y. Wu, L.-W. Chen, et al., "Acoustic Energy Harvesting by Piezoelectric Curved Beams in the Cavity of a Sonic Crystal", *Smart Materials and Structures*, 19, 045016 (2010).

[16] T. Sharma, S.-S. Je, B. Gill, et al., "Patterning Piezoelectric Thin Film PVDF–TrFE Based Pressure Sensor for Catheter Application", *Sensors and Actuators A: Physical*, 177, 87 (2012).

[17] T. Sharma, K. Aroom, S. Naik, et al., "Flexible Thin-Film PVDF-TrFE Based Pressure Sensor for Smart Catheter Applications", *Ann Biomed Eng*, 41, 744 (2013).

[18] P. Tho, R. Manasseh, and A. Ooi, "Cavitation Microstreaming Patterns in Single and Multiple Bubble Systems", *Journal of Fluid Mechanics*, 576, 191 (2007).

[19] S.K. Chung, Y. Zhao, U.-C. Yi, et al. "Micro Bubble Fluidics by EWOD and Ultrasonic Excitation for Micro Bubble Tweezers", 2007 IEEE 20th International Conference on Micro Electro Mechanical Systems (MEMS), Hyogo, Japan, 1/21-25/07, IEEE, New York (Year), pp. 31-34.

[20] D. Ahmed, A. Ozcelik, N. Bojanala, et al., "Rotational Manipulation of Single Cells and Organisms Using Acoustic Waves", *Nat Commun*, 7, 11085 (2016).

[21] R. Thameem, B. Rallabandi, and S. Hilgenfeldt, "Particle Migration and Sorting in Microbubble Streaming Flows", *Biomicrofluidics*, 10, 014124 (2016).

[22] A.R. Tovar and A.P. Lee, "Lateral Cavity Acoustic Transducer", *Lab Chip*, 9, 41 (2009).

[23] J. Jeong, D. Jang, D. Kim, et al., "Acoustic Bubble-Based Drug Manipulation: Carrying, Releasing and Penetrating for Targeted Drug Delivery Using an Electromagnetically Actuated Microrobot", *Sensors and Actuators A: Physical*, 306, 111973 (2020).

[24] F.W. Liu and S.K. Cho, "3-D Swimming Microdrone Powered by Acoustic Bubbles", *Lab Chip*, 21, 355 (2021).

[25] J. Jeon, J. Hong, S.J. Lee, et al., "Acoustically Excited Oscillating Bubble on a Flexible Structure and Its Energy-Harvesting Capability", *International Journal of Precision Engineering and Manufacturing-Green Technology*, 6, 531 (2019).

[26] M. Minnaert, "Xvi. On Musical Air-Bubbles and the Sounds of Running Water", *The London, Edinburgh, and Dublin Philosophical Magazine and Journal of Science*, 16, 235 (1933).

CONTACT

*S.K. Cho, tel: +1-412-624-9798; skcho@pitt.edu

ON THE GEOMETRY DESIGN OF ALN LAMB WAVE RESONATORS WITH PREDEFINED SHALLOW RELEASE CAVITIES

Tzu-Hsuan Hsu[1], Guan-Lin Wu[1], Yan-Ming Huang[1], Yens Ho[2], Yung-Hsiang Chen[2], Yelehanka Pradeep[3], Rakesh Chand[3], and Ming-Huang Li[1]*
[1]National Tsing Hua University, Hsinchu, Taiwan
[2]Vanguard International Semiconductor Corporation, Hsinchu, Taiwan
[3]Vanguard International Semiconductor Corporation Singapore PTE. Ltd., Singapore

ABSTRACT

In this work, we demonstrate a 700 MHz one-port aluminum nitride (AlN) S_0-mode *residual stress-resilient* Lamb wave resonator (LWR) with lithographically defined acoustic boundaries based on a CMOS-compatible 8-inch MEMS process, exhibiting a high-quality factor (Q) of 2,422 and an electromechanical coupling factor (k_{eff}^2) of 1.05%. Although a well-defined shallow "etch sandbox" provides a higher quality factor and better mechanical robustness to the LWR over conventional isotropic silicon etching processes, the performance of the LWR becomes sensitive to the deformation caused by residual stress in the thin films. In this work, with the assistance of laser scanning confocal microscopy, the physical contact between deformed LWR and the bottom of the cavity is identified as a new failure mode. We investigate three LWRs with different aspect ratios and anchors, revealing that the width of the anchors is the key to suppressing out-of-plane deformations. The residual stress-resilient wide-anchor LWR shows a promising f-Q product of 1.69×10^{12} and $k_{\text{eff}}^2 > 1.05\%$, which is comparable with that of state-of-the-art AlN LWRs.

KEYWORDS

High-Q, S_0-mode, Lamb Wave Resonator, Residual Stress.

INTRODUCTION

Radio frequency front-end (RFFE) has become a key building block within modern day wireless communication systems, serving as a crucial component in signal processing application. Device based on AlN technology has dominated the market in the past decades as it offers high phase velocity, CMOS compatibility, great manufacturability, and reliability [1]. Among various technologies used to realize acoustic devices in AlN, LWR has attracted much research attention as it inherited the multi-frequency flexibility of surface acoustic wave (SAW) devices while significantly shrank the overall footprint of the device. Although Bulk acoustic wave (BAW) resonators also provide such benefit, it is very challenging to achieve multi-frequency operation in a single chip. Hence, LWR devices can be seen as a promising candidate eyeing for a highly compact and integrated RFFE. Which is getting ever important in modern RFFE design since more and more functions and frequency bands are allocated in one single module. For instance, high frequency reference signal can simply be implemented on the same chip using LWR-based oscillators.

Comparing with other Lamb wave mode realized in AlN, fundamental symmetric (S_0) LWR has become popular research topic [2] as it offers high quality factor (Q) and moderate k_{eff}^2. The operation frequency of S_0 LWR can also be determined by the phase velocity and wavelength based on the excited S_0 wave. Moreover, since the acoustic energy is confined within the suspended plate, there are less energy loss in S_0 LWR. The suspended structure can simply be created by substrate removal. More specifically, to release and undercut the device, frontside isotropic substrate release is typically preferred. However, this approach releases both the device and unwanted undercuts below anchors or supporting tethers (As shown in Fig. 1(a) [3]). Although precise time control may help reducing this matter, it is impossible to achieve a precisely defined acoustic boundary. Prior studies have shown that energy loss caused by undercut in LWR is a key factor limiting their Q factor performance [4]. Therefore, several methods were proposed to define a precise acoustic boundary. By generating a predefined "release sandbox" enclosed by a etch-stop layer (as shown in Fig. 1(b)), it is possible to form a precisely defined acoustic boundary for Q enhancement [5][6]. Other technique such as introducing an etching barrier (as shown in Fig. 1(c)) has also been proposed [7] to partially predefine the release boundary. These techniques have all been proven to have positive effect towards achieving high Q in S_0 LWR.

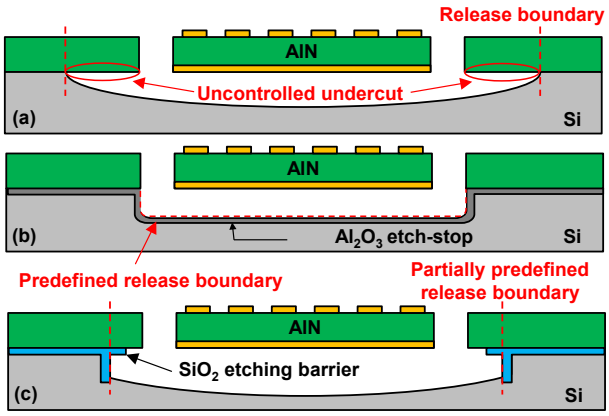

Figure 1. Comparison of three different release process to achieve suspended LWR without double side alignment and backside etching. (a) substrate isotropic etch [3]; (b) "release sandbox" [5][6]; (c) Etching barrier [7].

Therefore, in this work, we proposed such a S_0 LWR based on a shallow release trench approach. By specifically designed to operate at higher frequency as compared with previously published results [3,5-7], the correlation between release boundary and Q is again verified with shorter wavelength S_0 wave. Through different geometry designs, LWR with residual stress resilient design was successfully demonstrated. By identifying the unique failure mode for devices based on shallow release cavity, there are great potentials in mass fabrication of high Q LWR if the resonator avoids physical contact with the release cavity. By further incorporating techniques such as scandium (Sc)-doping [9], k_{eff}^2 comparable or higher than current BAW devices can also be achieved, making LWR a strong alternative for the next-generation highly integrated RFFE.

DEVICE DESIGN AND FABRICATION

The proposed S_0 LWR was fabricated in an 8-inch CMOS compatible MEMS foundry. To obtain the "release sandbox" feature,

978-1-940470-04-7/HH2022/$25©2022TRF
DOI 10.31438/trf.hh2022.50

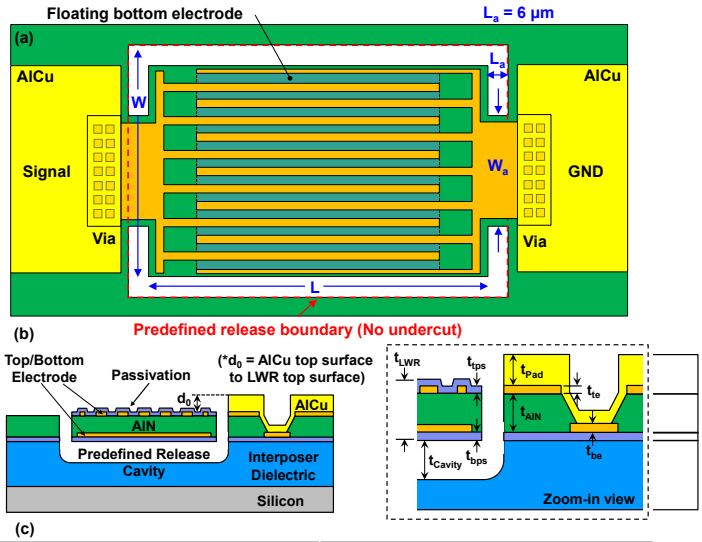

#	Symbol	Layer	Thickness	#	Symbol	Layer	Thickness
1	$t_{Pad} = d_0$	Pad (AlCu)	1000 nm	5	t_{be}	Bottom elec. (Mo)	250 nm
2	t_{tps}	Top passivation	200 nm	6	t_{bps}	Bottom passivation	100 nm
3	t_{te}	Top elec. (Mo)	250 nm	7	t_{Cavity}	Predefined cavity	8~900 nm
4	t_{AlN}	Device layer (AlN)	1000 nm	8	t_{LWR}	Total LWR thickness	1800 nm

Figure 2. Mock-up view of the proposed S_0 LWR (a) top-view (b) cross-sectional view and (c) the dimensions for the acoustic resonator's design parameters.

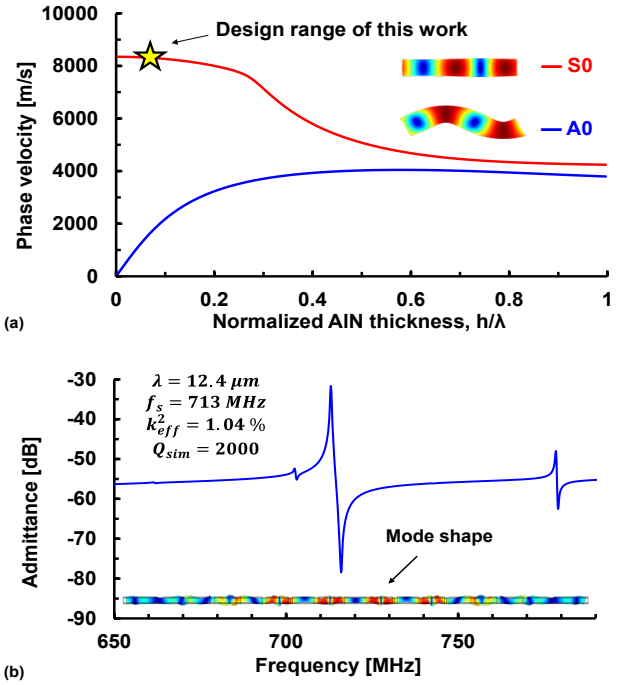

Figure 3. FEA simulation of the proposed resonator: (a) phase velocity dispersion of a 1 µm-thick AlN slab with thick (250 nm) Mo electrodes; (b) admittance magnitude of the proposed S_0 LWR.

an interposer dielectric layer was first deposited atop the handling Si wafer followed by etching of interposer to create cavity and refilling of sacrificial amorphous Si. Fig. 2 (a) illustrates the mock-up top-view of the proposed LWR in this work. Both top and bottom electrodes are based on molybdenum (Mo) with a thickness of 250 nm, a 1 µm thick layer of AlN is sandwiched between two electrodes. An addition 1 µm thick layer of AlCu serves as both routings and contact pads to reduce series resistance of the device. Fig. 2 (b) depicts the cross-sectional view of the LWR where the release cavity was defined within the interposer dielectric with a thickness of around 800 nm. Through this approach, the release region is well-defined and thus offers better acoustic energy confinement for attaining high Q resonator performance.

Lateral field excitation (LFE) is used to excite the proposed S_0 LWR. In this configuration. The top electrode of the LWR was made of interdigital transducers (IDT) while the bottom electrode is a metal plate at floating potential. Alternating voltage and ground potentials are being applied throughout the IDT structure, forming a mostly vertical electric field owing to the thin piezoelectric layer. Lateral stress was then induced through the piezoelectric constant e_{31}, forming a mode shape shown in Fig.3. Therefore, resonance can be excited simply by applying AC voltage signal to the MEMS device.

The phase velocity is first analyzed through investigating the dispersion behavior of S_0 wave propagating in the Mo-AlN-Mo stacking. The FEM simulation based on COMSOL Multiphysics [9] is depicted in Fig. 3(a). All the LWRs implemented in this work were designed at h_{AlN}/λ ratio < 0.1 to harvest the high phase velocity region of the S_0 mode. Furthermore, in this region the phase velocity of S_0-mode Lamb wave tends to stay rather constant, therefore making wavelength (or IDT pitch) the controlling factor determining the LWR frequency (as depicted in the phase velocity dispersion curve (Fig. 3 (a)), assuming a thickness-to-wavelength (h/λ) lower than 0.1). Therefore, by approximating the phase velocity into a constant value, the resonance frequency of the S_0 LWR designed at this h_{AlN}/λ range can be estimated through the follow equation:

$$f_r = \frac{v_p}{\lambda} = \frac{v_p}{2p} \quad (1)$$

v_p denotes the phase velocity of S_0 wave, λ is the wavelength, and p is the electrode pitch. Hence, through Eq. 1 it is noticed that λ is the key controlling factor for the LWR frequency. The frequency of the LWR can be scaled simply by defining a finer electrode pitch. To evaluate the electromechanical coupling of the S_0 LWR, the definition for k^2_{eff} is based on the definition mentioned in [10][11]:

Which can then be expressed as:

$$k^2_{\text{eff}} = \frac{\pi^2}{8} \times \left(\frac{f_p^2 - f_s^2}{f_s^2}\right) \quad (2)$$

The 2D full model finite-element analysis (FEA) based on one resonator design (λ=12.4 µm with 9 electrode pairs and aperture of 12λ) was carried out [Fig. 2(b)], which depicts a series resonant frequency (f_s) of 713 MHz and a k^2_{eff} of 1.04% with a given simulative Q-factor (Q_{sim}) of 2000.

MEASUREMENT SETUP AND RESULTS

Resonator performance characterization

The fabricated one-port S_0 LWR was measured in a RF probe station using GSG probes. Admittance response (Y-parameters) were obtained by conversion of scattering parameters (S-parameters) characterized in a Keysight E5071C vector network analyzer (VNA). All data was measured in a dry ambient condition with a typical driving RF power set to -10 dBm. In Fig. 4, the measured admittance response based on a S_0 LWR with wavelength of 12.4 µm is reported, exhibiting a high Q factor (Q_{fitted}) of 2,100 and k^2_{eff} of 1.05%, which agreed well with our prediction based on properly predefined acoustic boundaries. The Q_{fitted} and k^2_{eff} reported were based on a fitted multi-branch modified Butterworth van-Dyke (mBVD) model

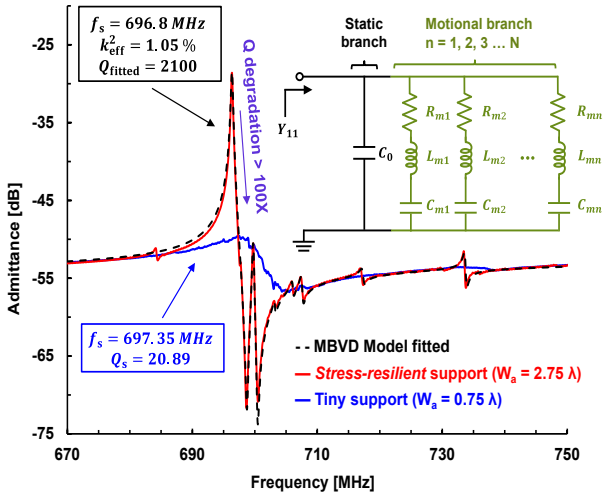

Figure 4. Measured admittance of fabricated S_0 LWRs with different resonator geomertie. A subplot is included to indicate the multi-branch MBVD model used to fit the admittance response.

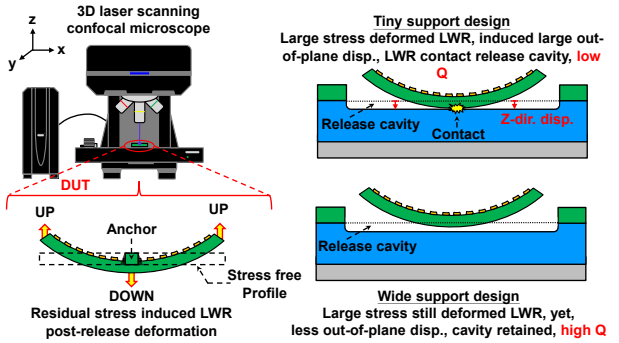

Figure 5. Measurement setup for the optical LWR deformation profile using the laser confocal microscopy and the inference of the contact-based failure mode.

as shown in the subplot of Fig. 4. The resonator is modeled based on the same multi-branch architecture introduced in [10] and contains n motional branches to include all spurious over the spectrum. However, comparing two similar S_0 LWRs with same wavelength (12.4 µm) and equal transducer capacitance (C_0) of 480 fF (as shown in Fig. 4) in terms of their admittance response. There existed a 100X quality factor degradation across LWR with wider anchor ($W_a = 2.75\lambda$, $Q = 2100$) and LWR with narrow anchor design ($W_a = 0.75\lambda$, $Q = 21$). The results present an unexpected low Q and exhibit an unusual trend as compared to previous research [12].

Optical surface profile measurement

To understand such a dramatic performance deviation, a 3-dimensional (3D) laser scanning confocal microscopy (Keyence VK-X series) is introduced for characterizing the surface profile of the LWRs, as shown in Fig. 5. Since it is speculated that such a large performance deviation between similarly sized devices is caused by the residual stress-induced physical contact between the resonator plate and the bottom of the cavity. The surface profile of multiple devices was captured and analyzed. As wider anchors offer higher mechanical stiffness, the out-of-plane deformation can be effectively suppressed to avoid contact while attain high-Q operation.

Fig. 6 depicts a comparison between three selected resonator types on the same wafer. LWR-A and LWR-C features similar geometry aspect ratio (W/L) of around 0.5 while LWR-B possess larger W/L of 1.33. It is noted that in our design, one of the plate dimensions in each resonator is fixed around 115µm, and the anchor width of LWR-C is 3.6X larger than LWR-A and LWR-B. By comparing the measured surface profile and the admittance response in Fig. 6, we can confirm that the decisive factor of Q in this platform being the amount of out-of-plane deformation (Δd) instead of aspect ratio or anchor size. As shown in Fig. 5(a), LWR-A devices exhibits a very low $Q < 100$ phenomenon as the Δd approaches the depth of the release cavity ($t_{\text{cavity}} \approx 800$ nm), which indicates a physical contact between the bottom of the LWR and the bottom of the cavity. Furthermore, by observing LWR-B devices, it showed that even if Δd is smaller than t_{cavity}, excessive proximity between the LWR and the interposer dielectric can still lead to significant performance degradation [Fig. 6(b), $Q = 263.23$, $\Delta d \approx$ 670 nm]. As a result, a wide support design that can provide sufficient mechanical stiffness to sustain the post-release deformation [in Fig. 6(c)] becomes an effective and simple stress resilience solution to attain high of over $Q >$ 2,400 for devices adapting sandbox-type shallow release cavities.

In addition to the out-of-plane deformation caused by residual stress, the stress curving of the LWR may also affect the performance. However, further investigation into the statistics in our measurement results depicted that the radius of curvature (R.O.C) of the deformed LWR along the wave propagation direction seems to have less effect on the overall Q factor. For instance, among the three types of LWR presented, the LWR-C devices feature highest Q factor despite having largest stress curving. Conversely, the Q factor of LWR-B devices are still 10X smaller than LWR-C devices even though stress curvature exhibit the least effect. Showing the less related correlation between device curvature and Q factor. Statistically, out of the 90 LWR-A type low Q (< 100) devices measured, 19 of which had their surface profile further captured using laser confocal microscopy and the results indicates a 100% correlation between low Q and out-of-plane deformation around 800 nm. Which further consolidates our speculation about the new failure mode for LWR based this type of shallow release cavities. Which is mostly caused by the boundary condition change due to the physical contact between LWR and release cavity.

CONCLUSIONS

In conclusion, a UHF S_0 LWR with both high Q factor of over 2400 and k^2_{eff} more than 1% was reported in this work. The precisely defined acoustic boundary can both provide good acoustic energy confinement and maintain good structural robustness. By utilizing the "release sandbox" concept, the unwanted undercut during substate isotropic release was completely removed. Therefore, an overall f-Q product of over 1.6×10^{12} can be achieved. However, devices exhibiting abnormally low Q were also discovered during our performance characterization. By analyzing the measured device performance and its corresponding surface profile, a new mode of failure for LWR based on shallow release cavity is identified. Concluding that although tiny support has long been proven to provide less anchor loss and higher Q, maintaining sufficient mechanical stiffness to withstand the residual stress deformation can be an alternative if increasing cavity depth is not feasible. By avoiding contact between LWR and cavity. the ideal boundary condition for a high Q LWR device can still be maintained even in a shallow release cavity.

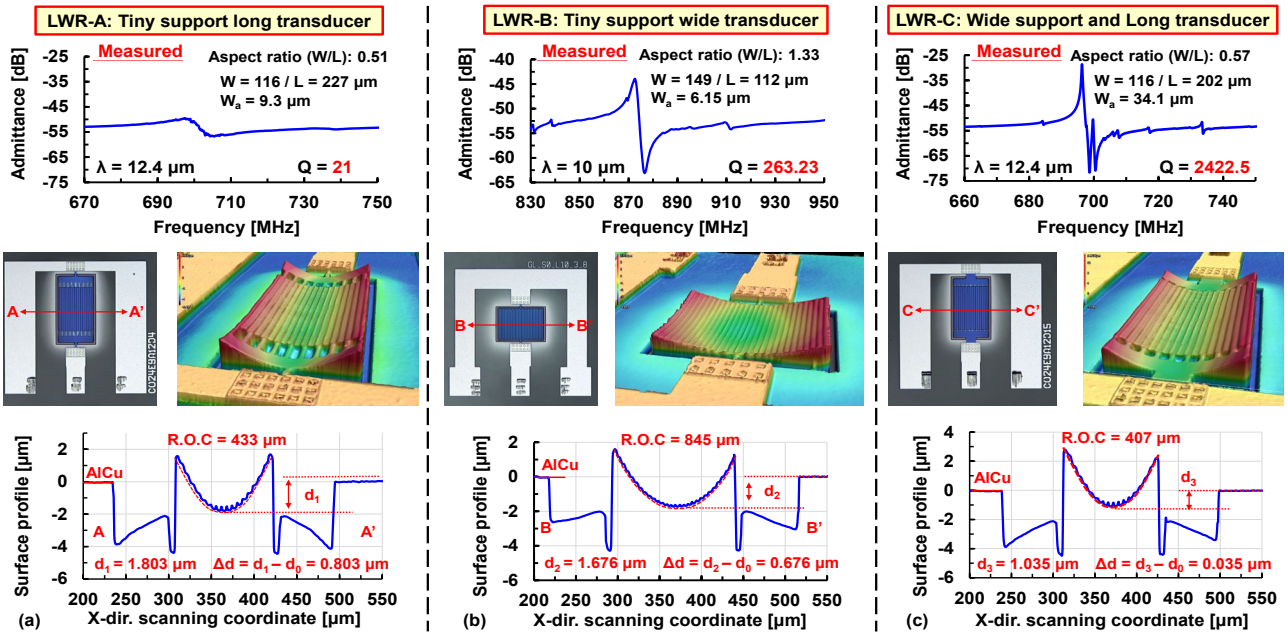

Figure 6. Measurement data across three transducer designs: (a) tiny support with small transducer aspect ratio (LWR-A); (b) tiny support with large transducer aspect ratio (LWR-B); (c) wide support with small transducer aspect ratio (LWR-C). All profile measurements were referenced to the top surface of the AlCu layer and the 3D profile images were rendered with a 400X magnification.

ACKNOWLEDGEMENTS

The author would like to acknowledge Vanguard International Semiconductor Corporation for the device fabrication, and the Taiwan Semiconductor Research Institute (TSRI) for the assistance and measurement facility during device performance acquisition. This work was partially supported by the Ministry of Science and Technology (MOST) of Taiwan under Grant MOST 110-2636-E-007-012 (Young Scholar Fellowship Program).

REFERENCES

[1] S. Mahon and R. Aigner, "Bulk Acoustic Wave Devices – Why, How, and Where They are Going," in *Proc.* CS MANTECH Conference, pp. 15-18, Austin, Texas, USA, May 2007

[2] V. Yantchev and I. Katardjiev, "Thin film Lamb wave resonators in frequency control and sensing applications: a review," *J. Micromech. Microeng.*, vol. 23, pp. 043001, Mar. 2013.

[3] C.-M. Lin, V. Yantchev, J. Zou, Y.-Y. Chen, and A. P. Pisano, "Micromachined One-Port Aluminum Nitride Lamb Wave Resonators Utilizing the Lowest-Order Symmetric Mode," *J. Microelectromech. Syst.*, vol. 23, pp. 78-91, Feb. 2014.

[4] B. Gibson, K. Qalandar, C. Cassella, G. Piazza and K. L. Foster, "A Study on the Effects of Release Area on the Quality Factor of Contour-Mode Resonators by Laser Doppler Vibrometry," *IEEE Trans. Ultrason., Ferroelectr., Freq. Control*, vol. 64, no. 5, pp. 898-904, May 2017.

[5] A. Gao, M. Winterkorn, Y. Yang, R. Lu, J. Provine and S. Gong, "Boosting Qs of AlN Resonators by Redefining Acoustic Boundaries," in *Proc.* IEEE 32nd Int. Conf. Micro Electro Mech. Syst. (MEMS), pp. 883-886, Seoul, Korea (South), Jan. 2019.

[6] H. Campanella, Y. Qian, C. O. Romero, J. S. Wong, J. Giner and R. Kumar, "Monolithic Multiband MEMS RF Front-End Module for 5G Mobile," *J. Microelectromech. Syst.*, vol. 30, no. 1, pp. 72-80, Feb. 2021.

[7] A. Lozzi, A. De Pastina, L. G. Villanueva and E. T. Yen, "Release area confinement in contour mode resonators," in *Proc.* IEEE International Ultrasonics Symposium (IUS), pp. 1-4, Washington, DC, USA, Sep. 2017.

[8] https://www.comsol.ch/

[9] T. Yokoyama, Y. Iwazaki, T. Nishihara and J. Tsutsumi, "Dopant concentration dependence of electromechanical coupling coefficients of co-doped AlN thin films for BAW devices," in *Proc.* IEEE International Ultrasonics Symposium (IUS), pp. 1-4, Tours, France, Sep. 2016.

[10] R. Lu, M.-H. Li, Y. Yang, T. Manzaneque and S. Gong, "Accurate Extraction of Large Electromechanical Coupling in Piezoelectric MEMS Resonators," *J. Microelectromech. Syst.*, vol. 28, no. 2, pp. 209-218, April 2019.

[11] C. Cassella, N. Oliva, J. Soon, M. Srinivas, N. Singh and G. Piazza, "Super High Frequency Aluminum Nitride Two-Dimensional-Mode Resonators With k_t^2 Exceeding 4.9%," *IEEE Microwave and Wireless Components Letters*, vol. 27, no. 2, pp. 105-107, Feb. 2017.

[12] J. Segovia-Fernandez, M. Cremonesi, C. Cassella, and G. Piazza, "Anchor Losses in AlN Contour Mode Resonators," *J. Microelectromech. Syst.* vol. 24. no. 2. pp.265-275, Apr. 2015.

CONTACT

*Ming-Huang Li; mhli@pme.nthu.edu.tw

REALIZING THE WORLD'S SMALLEST GRAVIMETRIC SELF-RESETTING PARTICULATE MATTER SENSOR USING MEMS

Navpreet Singh[1], Mohannad Y. Elsayed[2], and Mourad N. El-Gamal[1]*
[1]McGill University, Montreal, Quebec, Canada
[2]MEMS Vision International Inc., Montreal, Quebec, Canada

ABSTRACT

We introduce a highly compact and low-cost gravimetric-based particulate matter (PM2.5) sensor, with the ability to self-reset, for continuous monitoring of air quality. The complete sensor solution consists of i) a mechanism to segregate the particles based on their aerodynamic size, ii) a mechanism to measure the mass of these separated particles, and iii) a mechanism to reset the sensor after each measurement. To address the barriers of affordability and ease-of-use usually encountered by other existing technologies, we propose here a compact gravimetric particulate matter sensing solution housed in a 20mm × 20mm × 15mm package, including all of the supporting electronics. The experimental results suggest that the solution proposed here is disruptive and has potential to revolutionize the field of gravimetric particulate matter sensing.

KEYWORDS

Particulate Matter (PM), MEMS, Sensors, Thermophoresis, Resonators, Piezoelectric, PiezoMUMPs

INTRODUCTION

Since the rise of the manufacturing industry and the increase in number of automobiles across the globe, the ambient air quality is on a steady decline [1]. The increase in the amount of the airborne particulate pollutants is a rising concern in developed as well as developing countries. These airborne particles consist of natural and man-made sources and their aerodynamic properties determine how far they can get into the human respiratory system [2]. Based on the size of these particles, particulate matter can be divided into two main categories:

• PM10: inhalable particles, with aerodynamic diameters of 10 micrometers and smaller; and

• PM2.5: fine inhalable particles, with aerodynamic diameters that are generally 2.5 micrometers and smaller

The World Health Organization (WHO) has set guideline limits to achieve the lowest concentration of particulate matter to minimize the risk of respiratory and cardiovascular diseases, and these guideline limits are as follows [3]:

Table 1: WHO limits for the annual and 24-hour mean of different particle sizes.

Particle Size	Annual Mean	24-hour mean
PM 2.5	10 µg/m^3	25 µg/m^3
PM 10	20 µg/m^3	50 µg/m^3

The health guidelines from WHO necessitate the need for developing new solutions to accurately measure the amount of particulate matter present in the air. The existing solutions to measure the PM concentration can be classified into two categories: gravimetric based and light scattering based [4, 5]. Gravimetric methods, the gold standard, directly measure the mass of the particles suspended in the air. The particles are collected on a filter over a certain period and are then weighed in a laboratory at the end of this fixed period. These methods are bulky in size, expensive and not suitable for real time sensing [6]. Whereas the sensors based on light scattering principle measure the amount of light scattered by the suspended particles in the air. This outputs the number of particles, which is later converted to mass by assuming the distribution and density of the particles. These assumptions often introduce inaccuracies in the measurements [7].

This work is aimed at designing a highly compact, accurate, low-cost, self-resettable, and easy to use gravimetric-based particulate matter sensor solution for portable applications [8]. Both PM10 and PM2.5 can penetrate deep into the lungs, but PM2.5 can even enter the bloodstream, hence posing severe health risks [2]. Hence, our solution aims at measuring the amount of PM2.5 suspended in the air. The overall system consists of i) a piezoelectric MEMS resonator which exhibits a shift in resonant frequency when mass is loaded on its membrane (reported in [9]), ii) a 3D printed virtual impactor, which is a mechanism that segregates particles based on their sizes (reported in [10]), and iii) a thermophoretic mechanism that helps resetting the sensor for continuous monitoring – a feature that no other MEMS based particulate sensing solution has achieved to date [11]-[13]. The full system design is presented here along with its experimental demonstration.

MATERIAL AND METHODS

This section briefly talks about the design of the different components of the system.

Resonator

A piezo-electric resonator is used to measure the mass of the particulate matter. The transduction principle of the resonator is the mass loading effect, i.e., an addition of a mass to the membrane results in a shift in its resonant frequency. The resonant frequency, f, of the plate can be determined as:

$$f = \frac{1}{2\pi}\sqrt{\frac{k_{eff}}{m_{eff}}} \quad (1)$$

where k_{eff} is the effective spring constant and m_{eff} is the effective mass of the resonator. On addition of Δm on the plate results in Δf shift in the resonant frequency as:

$$\Delta f = -\frac{f}{2m_{eff}} \quad (2)$$

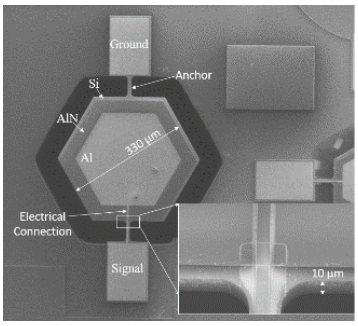

Figure 1: SEM of the resonator

978-1-940470-04-7/HH2022/$25©2022TRF
DOI 10.31438/trf.hh2022.51

Virtual impactor

The need to segregate the particulate matter based on their aerodynamic sizes arises from the WHO guidelines. The size of the particulate matter largely determines the extent of the damage caused to the environment and to the human health. Since we are targeting PM2.5, we need a mechanism to separate PM2.5 from the stream of particles flowing into the sensor.

A virtual impactor (figure 2) is a device that is used to separate the particles into two streams based on their aerodynamic diameter. Similar in operation to a conventional impactor, virtual impactor replaces the surface for impact with a virtual space of slow moving or almost stagnant air. Particles greater than 2.5 µm in size are collected in the minor flow channel, instead of colliding with the virtual impaction surface. Particles smaller than 2.5 µm (i.e., PM2.5) have smaller inertia because of their small size and are directed towards the major flow channel. By placing the resonator in the major flow channel, we can measure the amount of PM2.5 present in the air.

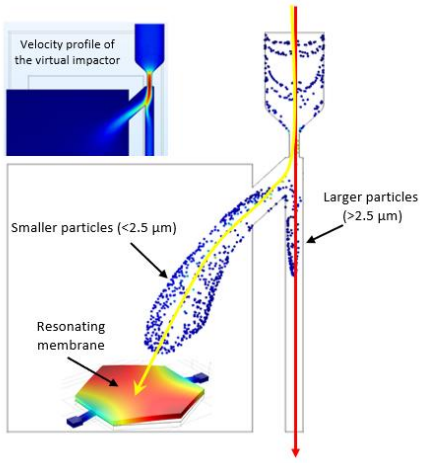

Figure 2: Virtual impactor with yellow streamline representing the trajectory of the particles < 2.5 µm, and the red streamline representing the trajectory of the particles > 2.5 µm.

Thermophoresis

Thermophoresis is the process of movement of colloidal particles or large molecules in a solution in response to thermal gradient. A colloidal particle or large molecule can be forced to move in a liquid or a gas with application of non-uniform thermal gradient. The mass flow rate J_m of these particles in a given fluid, resulting from thermal gradient ∇T, is given as [14]:

$$J_m = -\rho D \nabla c - \rho D_T c(1-c)\nabla T$$

where ρ is the density of the fluid, D is the coefficient of diffusion, D_T is the thermal coefficient of diffusion, and c is the concentration of particles as a mass fraction.

The coefficient of diffusion, D, is given by:

$$D = \frac{kT}{3\pi\eta d}$$

where k is the Boltzmann constant ($k = 1.38 \times 10^{-38}$ J/K), T is the temperature, η is the dynamic viscosity of the fluid and d is the diameter of the particles suspended in the fluid.

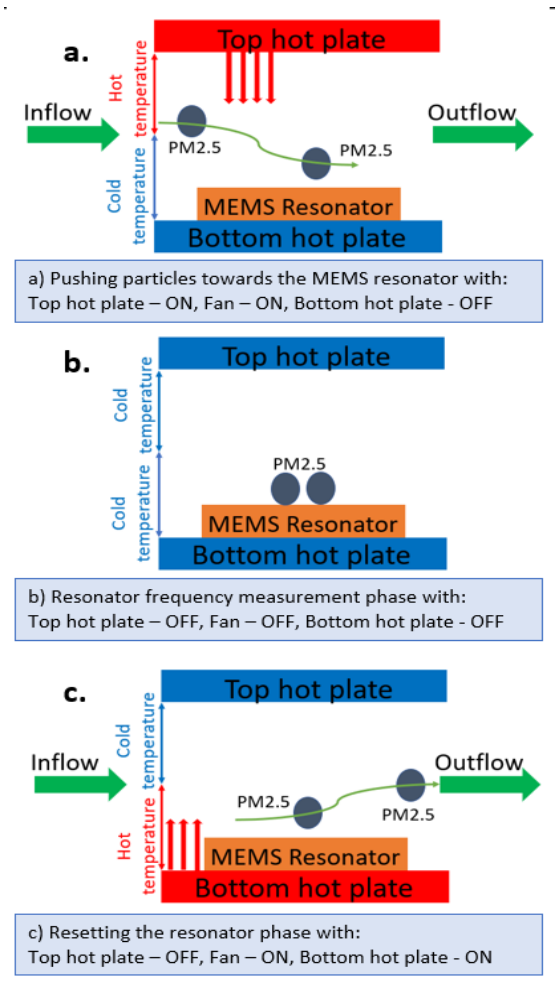

Figure 3: represents the conceptual diagram of our thermophoresis implementation. Both the hot plates, the top hot plate to push particles towards the resonator, and the bottom hot plate to push particles away from the resonator, have been implemented using resistors.

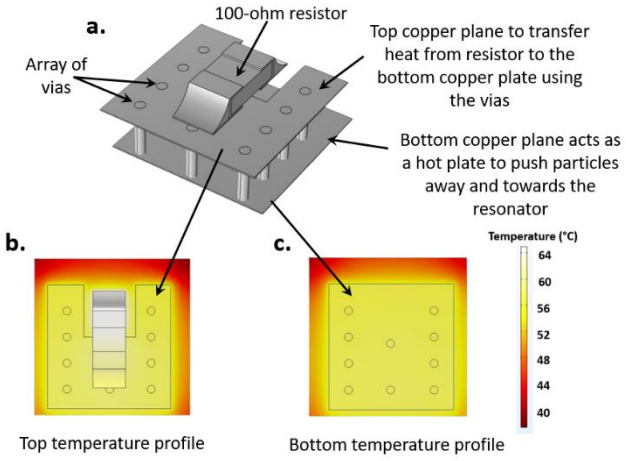

Figure 4: Thermal profile of the resistors and hot plates

Figure 3 represents the conceptual diagram of thermophoresis implementation in our sensor. Here, we use two hot plates, heated using surface mounted resistors, to push particles towards and away from the resonator. Heating the top hot plate pushes air molecules around the plate towards the MEMS resonator. Air molecules moving under the thermal gradient collide with the incoming particles and force them towards the resonator. After measuring the frequency response of the resonator, the resonator can be reset by turning on the bottom hot plate to push the air molecules (hence the particles) away from the resonator.

Figure 4 shows the simulation results from FEM studies carried out using COMSOL Multiphysics. Figure 5a shows the geometrical structure of a single hot plate implementation. Applying electrical power across the resistor heats up the resistor core, which heats up the copper plane which the resistor terminal is soldered to. This heat is transferred to the copper plane on the other side of the PCB using filled through-vias. Figure 5b and 5c present the temperature profile on both sides of the PCB. Such arrangement is used twice to implement the top and the bottom hot plates.

Electronic circuitry

The electronic circuit includes a closed loop oscillation circuit, coupled with a microcontroller circuit that drives the heaters and the fan. The fan is needed to maintain the flow of the particles inside the chamber. The MEMS resonator is combined in a feedback loop with an amplifier to create an oscillator whose frequency variation is then read using a microcontroller. An amplifier is needed to compensate for the motional resistance of the MEMS resonator and create an oscillator. An amplifier with a large gain-bandwidth is used due to the inherently large motional resistance of the MEMS resonator and the need to ensure that the phase shift around the loop is as close to zero as possible.

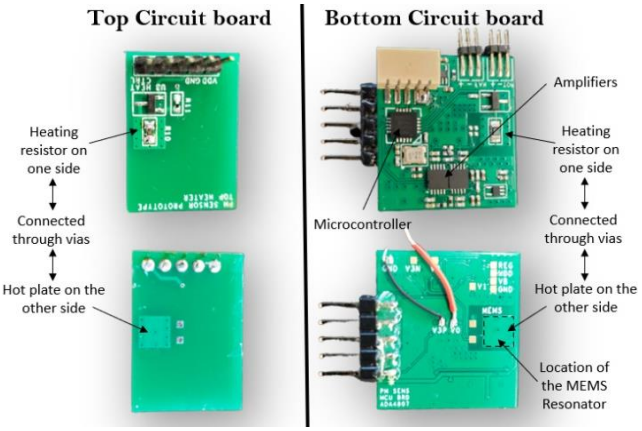

Figure 5: Top and Bottom circuit boards. The top circuit board includes a heating resistor and a transistor to control the operation on one side, and the top hot plate on the other. The bottom circuit board consists of the oscillator circuit and the microcontroller. The other side of the PCB has a designated location for the MEMS die, which is directly wire-bonded over the bottom hot plate area to reset the resonator.

Figure 6 presents a conceptual diagram of the whole solution, with MEMS resonator in a closed oscillation loop, forwarding signal to the microcontroller, which simultaneously controls the top and bottom hot plate and the fan.

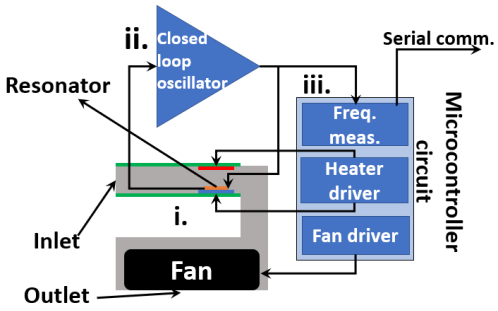

Figure 6: Conceptual diagram of the whole solution (i. 3D printed package that houses the MEMS resonator, ii. The closed loop oscillator and iii. the microcontroller that drives the top hot plate, bottom hot plate, and the fan.

Complete sensing solution

Figure 7 shows the assembled PM sensor solution, which measures 20mm × 20mm × 15mm. The complete solution consists of the 3D printed package with translucent resin, top PCB with the top hot plate and the bottom PCB with bottom hot plate, the oscillator circuit, and the microcontroller circuit. The fan and the top circuit are connected to the microcontroller circuit with wires soldered directly to the circuit (omitted here for clarity).

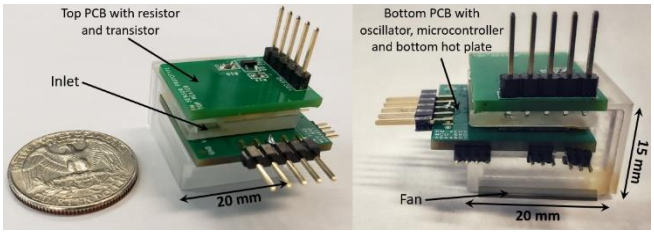

Figure 7: Complete sensor solution next to an American quarter.

TESTING

Incense stick is used as a source for particles to test the PM sensor. The particles in the incense smoke are mostly smaller than 2.5 µm in size (PM2.5) [15]. The incense smoke is introduced into a testing chamber to observe the response of the sensor. However, initial tests show that the incense smoke has a very high moisture content. To eliminate the problem of humidity, a drying column lined with silica gel packs is used to dehydrate the particles before and introduce them into the test chamber.

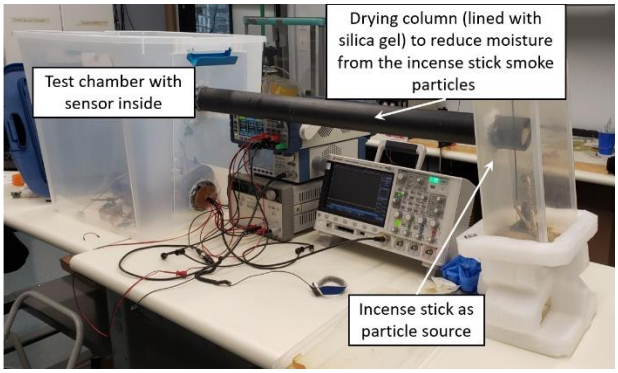

Figure 8: Test setup

The test setup (figure 8) consists of a small container which holds a burning incense stick generating particles, a transporting pipe (the drying column), and a large test chamber where we place our sensor to measure the introduction of particles. Particles travel through the drying column from the small container to the test chamber. And to release the particles, we can simply lift the lid of the test chamber and let the particles escape.

RESULTS

The piezoelectric resonator in the sensor has a resonant frequency of 1539.08 kHz. According to Sauerbrey equation, a mass deposition of incense particles should result in a shift in resonant frequency of the resonator. Introducing the particles into the test chamber results in a negative shift in the frequency, which drops to 1538.82 kHz. We then observe a rise (positive shift) in the resonance frequency on lifting the lid of the chamber slightly, letting some particles escape. This behavior is attributed to the setting and resetting of the resonator. The action is repeated, and we observe a fall in the frequency on closing the lid again as more particles continue to be introduced into the chamber. This resetting behavior is verified by completely removing the lid and letting all of the particle escape. We observe that the sensor resets 100% to its original resonance frequency.

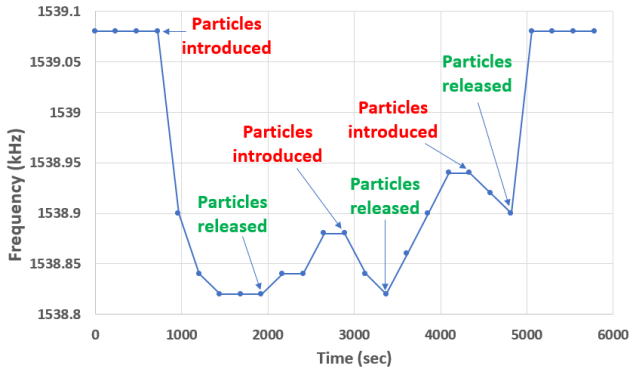

Figure 9: Response of the sensor to introduction and release of the particles from the testing chamber.

CONCLUSION AND FUTURE WORK

We have demonstrated here a fully functional gravimetric particulate matter sensor solution based on MEMS. The sensor is housed in a 20mm × 20mm × 15mm package, including all of the supporting electronics. It is the smallest reported to date, while operating in real-time. Compared to other works, the solution here also includes a novel and efficient mechanism for resetting the sensor automatically after every measurement.

One vital improvement for future developments will include humidity and temperature compensation. By incorporating a temperature and humidity sensor, we can minimize the ambient effects on the sensor measurements. Using an appropriate machine learning model, the sensor can be trained to compensate for these effects.

ACKNOWLEDGEMENTS

The authors gratefully acknowledge the support of CMC Microsystems for providing affordable access to the COMSOL Multiphysics software, and to the fabrication of the MEMS prototypes.

REFERENCES

[1] J. O. Anderson, J. G. Thundiyil, & A. Stolbach, "Clearing the air: a review of the effects of particulate matter air pollution on human health.", *Journal of medical toxicology: official journal of the American College of Medical Toxicology*, 8(2), 166–175.

[2] G. Shaddick, M. L. Thomas, P. Mudu, G. Ruggeri and S. Gumy "Half the world's population are exposed to increasing air pollution.", *npj Climate and Atmosphere Science* 3, 23, 2020

[3] "WHO Air quality guidelines for particulate matter, ozone, nitrogen dioxide and sulfur dioxide: global update 2005: summary of risk assessment". Available online: https://apps.who.int/iris/handle/10665/69477 (accessed on 03 March 2022)

[4] Z. Wang, L. Calderón, A. P. Patton, M. Sorensen Allacci, J. Senick, R. Wener, C. J. Andrews, and G. Mainelis, "Comparison of real-time instruments and gravimetric method when measuring particulate matter in a residential building", *Journal of the Air & Waste Management Association* (1995), 66(11), 1109–1120.

[5] F.M.J. Bulot, S. J. Johnston, P. J. Basford, N. H. C. Easton, M. Apetroaie-Cristea, G. L. Foster, A. K. R. Morris, S. J. Cox, and M. Loxham, "Long-term field comparison of multiple low-cost particulate matter sensors in an outdoor urban environment." *Scientific Reports*, 9, 7497 (2019).

[6] Ville de Montréal, Service de l'environnement, "Environmental Assessment Report 2019 Air quality in Montréal Service de l'environnement", ISSN 1925-6868; Montreal, Canada, 2019

[7] Tan B. K., Laboratory Evaluation of Low to Medium Cost Particle Sensors, Master of Applied Science, University of Waterloo, Waterloo, Ontario, Canada, 2017

[8] N. Singh, M. Y. Elsayed and M. N. El-Gamal, 2019 United States Patent Application US20210123849A1

[9] N. Singh, M. Y. Elsayed and M. N. El-Gamal, "Realizing a Highly Compact Particulate Matter Sensor With a MEMS-Based Resonant Membrane". *2019 IEEE Sensors*, 2019, 1-4

[10] N. Singh, M. Y. Elsayed, M. N. El-Gamal, "Towards the World's Smallest Gravimetric Particulate Matter Sensor: A Miniaturized Virtual Impactor with a Folded Design." *MDPI Sensors (Basel).* 2022 Feb 23;22(5):1727

[11] M. Maldonado-Garcia, V. Kumar, J. C. Wilson, and S. Pourkamali, "Chip-Scale Implementation and Cascade Assembly of Particulate Matter Collectors With Embedded Resonant Mass Balances", *IEEE Sensors Journal*, vol. 17, no. 6, pp. 1617-1625, 15 March, 2017

[12] J. P. Specht, and S. Esfahani, T. H. Tan, F. Sosada-Ludwikowska, R. Wimmer-Teubenbacher, A. Köck, M. Cole, and J. W. Gardner, "AlN FBAR Particle Sensor With a Thermophoretic Sampling Mechanism" *IEEE Sensors Journal*, vol. 21, no. 17, pp. 19427-19435, 1 Sept.1, 2021

[13] K. Hong-Lae, H. Jangseop, L. Sang-Myun, K. Hong-Beom, H. Jungho, and K. Yong-Jun, "MEMS-based particle detection system for measuring airborne ultrafine particles", *Sensors and Actuators A: Physical*, Volume 283, 2018, Pages 235-244

[14] P. Geelhoed, J. Westerweel, S. Kjelstrup, and D. Bedeaux, (2014) "Thermophoresis", *Li D. (eds) Encyclopedia of Microfluidics and Nanofluidics*. Springer, Boston, MA.

[15] Y. S. Cheng, W. E. Bechtold, C. C. Yu, and I. F. Hung, "Incense Smoke: Characterization and Dynamics in Indoor Environments", *Aerosol Science and Technology,* Pages 271-281, 13 June 2007

CONTACT

*N. Singh, tel: +1-514-924-0498; navpreet.singh@mail.mcgill.ca

RECONFIGURABLE ARCHITECTURE EXTENDING BANDWIDTH LIMITS OF MICRO-ACOUSTIC RF FILTERS

Giuseppe Michetti[1] *and Matteo Rinaldi*[1]
[1]SMART Center, Northeastern University, MA, USA

ABSTRACT

We propose a Radio Frequency (RF) filter architecture capable of instantaneous bandwidth (BW) reconfigurability introduced by periodic modulation of single-frequency piezoelectric RF resonators. This filter topology can attain passband BW that is directly proportional to the switching frequency used to modulate the resonators, therefore exceeding the limit imposed by the piezoelectric coupling coefficient k_t^2 in conventional micro-acoustic passive filters. Moreover, the filter is based on arrays of shunted single-frequency resonators, greatly simplifying filter banks' design, representing therefore a promising candidate to meet the market demands for real-time adaptive filters with a small footprint and large BWs as required by the increasing needs of large-data rates in 5G RF mobile systems. Preliminary results are shown by using 4 commercial Surface Acoustic Waves (SAW) resonators operating at 318 MHz wire-bonded with switching dies, obtaining a 4.5 dB Insertion Loss, and tunable BW between 300kHz and 1.05kHz (3:1), paired with a 23dB out-of-band rejection.

KEYWORDS

RF MEMS; Micro-acoustic RF Filter; Reconfigurable Filter; RF Front-End; Time-Variant Network

INTRODUCTION

Micro-acoustic resonators have drawn growing attention in both industrial and academic environments for their unique performance at RF, allowing for large-scale integration of miniaturized filters, with quality factors above 1000s, for their manufacturing processes prone to large volume scaling costs, their compatibility with CMOS processing equipment and thanks to the popularization of ladder networks for RF channel duplexing[1-3].

Progress in radio frequency (RF) mobile architectures is fostered by the need for larger and larger data rates required in high-quality video streaming, as well as a growing number of interactive services are offered in mobile applications, based on real-time processed calculations, remotely prompted through RF signals available on a cellular device - a paradigm known as *cloud computing*.[4,5]

Following these trends, a constantly growing number of micro-acoustic filters is required in compact radios, stressing the technological constraints underlying the fabrication control required to synthesize the various bands on piezoelectric thin films. At the same time, frequency scaling of RF bands toward now higher data rates system constitutes the bottleneck toward the deployment of micro acoustic technologies for future radio paradigms. [6-8].

Moreover, given the lack of real-time reconfigurable components in the RF front-end chains, radio networks rely more on more on digital controls and power-hungry real-time signal RF processing techniques, mining battery lifetime, and narrowing thermal margins. [9]

Achieving tunable filter bandwidths in a compact footprint would be highly desirable to implement a true real-time, hardware-in-the-loop dynamic optimization to allow for either larger BW when the large data rate is required or lower BW to mitigate channel noise, forming a closed-loop approach to robust RF adaptive communication relaxing the role of RF digital signal processing.[10-11]

In this scenario, we proposed a novel filter architecture capable of unprecedented reconfigurability leveraging spatio-temporal modulation of RF resonators. [12-13] In this work, we further optimized the network to demonstrate a 3:1 BW large tunability introduced by means clock phase sharing between identical micro-acoustic resonators. This network, when properly actuated, breaks the conventional limits set by micro-acoustic ladder topologies, showing the capability of realizing filter with wider BWs, as well as a true real-time control on said BW through modulation control.

METHODS

Switched Filter as a Dynamic Circuit

The circuit implementing the reconfigurable filter proposed in this work is drawn in Fig.1a, and it is generally composed of N branches connecting the two RF ports. Each branch is composed of a one-port resonator, shunted to the filter ground node, that is used to transfer energy from port 1 to port 2 and vice versa.

Note that in this circuit no through component exists between the RF ports; instead, a suitable network of two switches periodically actuated with 50% duty cycle in phase opposition provides the necessary path to ground so that each resonator gets charged /discharged for 50% of the modulation period T_m. In a

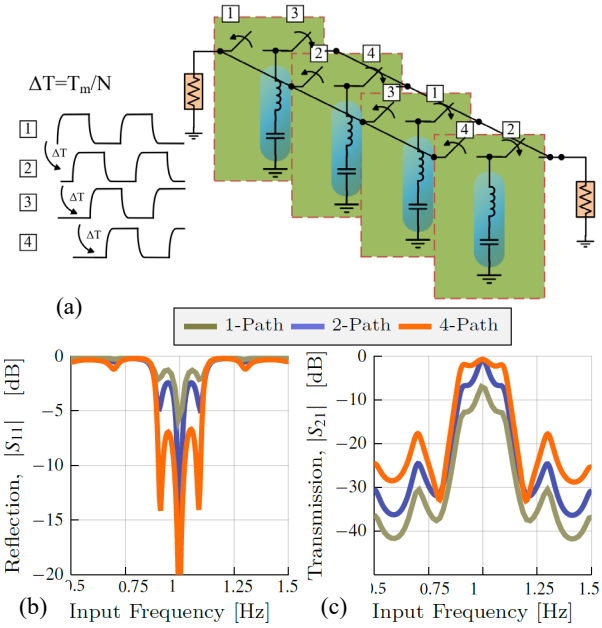

Figure 1:a) Schematic of a periodically modulated LTV filter, composed of N branches (in green shades) connecting the two RF ports through a staggered pattern of delayed ON/OFF phases. The staggering pattern is illustrated for N=4.
b) and c) represent respectively normalized reflection and transmission frequency response for 1,2 and 4 path filters composed of ideal resonators with Q_{load}=20 and actuated with F_m=10/ τ=5/(Q_{load} ω_0).

978-1-940470-04-7/HH2022/$25©2022TRF
DOI 10.31438/trf.hh2022.52

similar fashion to N-path filters, each branch is actuated with a delay $1/N/T_m$.

In this way, a dynamic regime of operation is induced in this circuit, implementing a specific class of circuits commonly referred to in the literature as linear-time-variant (LTV) networks.
The rise-time τ of such a network can be analyzed with conventional linear-time-invariant (LTI) techniques so that it can be expressed as $\tau=2Q_{load}/\omega_0$, where Q_{load} is the external quality factor of the resonator and ω_0 its resonant frequency.
A dynamic bandpass filter regime can be achieved as shown in Fig.2(b), when such resonators are excited with modulation frequencies F_m above 1/ τ. In this regime, energy is transferred through a mediated resonant storage mechanism as for LTI systems.

Note that for a simple one-port micro-acoustic resonator, like any other RF resonator technology, energy storage is maximized at its natural resonant frequency ω_0, so that a band-pass transfer function is achieved regardless of the technology used.

When using this LTV architecture, transmission poles required to synthesize filter passband are artificially generated at an infinite set of frequencies $Fres+kFm$. The first 2 intermodulation-induced transmission poles can be used to estimate the implemented filter bandwidth.

In other words, for this filter class:

$$BW\sim 2F_m \qquad (1)$$

Note that this BW might differ from the usual BW_{3dB} rating reported in passive filters, as the insertion loss (IL) at the band edges depends on the coupling of each resonator to the external ports, which is implemented through the switching network and therefore depends on the number of branches N used in the circuit.

To this point, it is interesting to visualize the impact of various N branches on its frequency response. Fig2(b) describes the reflection (S_{11}) and transmission (S_{21}) frequency response of a prototype filter scaled to 1Hz center frequency and with Q_{load}=20. For simplicity, S_{12} and S_{22} are not reported, given the symmetry of the circuit.

In Fig.2(b), one can see how with only 1 branch only 50% of the input energy can be passed, as the resonator is only connected to each port for 50% of T_m. Conversely, with 2 branches, all the input energy can be transferred through the resonators given the complementary actuation. At the same time, however, the passband shoulders at $F_{res}\pm F_m$ suffer from degraded IL.

Instead, when 4 branches actuated in quadrature are used the artificial poles at $F_{res}\pm F_m$ display an IL approaching the one at F_{res}, demonstrating a potential for practical use as a tunable BW passband filter. The BW achievable by this circuit is largely tunable through F_m. On the lower side, F_m is set by the inverse of the rise-time, as the resonator does not retain the input energy when $T_m>>1/\tau$. On the higher side, the in-band ripples between the pole at F_{res} and the ones at $F_{res}\pm F_m$ increase as F_m increases, eventually exceeding the usable 3dB margin.

Micro-acoustic Switched Filter

Using one-port piezoelectric micro-acoustic resonators in this filter architecture comes with several key advantages with respect to distributed or lumped RF resonators.

For a one-port micro-acoustic resonator:

$$Q_{load}\sim \pi^2/(2\, k_t^2\omega_0 C_0 Z_0) \qquad (2)$$

According to Eq.(2), a relatively small k_t^2 (1-10% depending on acoustic mode and piezoelectric film), ensures a relatively high Q_{load} and therefore a slower rise-time, which in turn results in fractional BW_{3dB} in the 1-10% range, requiring low-to-moderate modulation frequencies F_m (5-50MHz) for RF filters.

These attainable parameters make micro-acoustic technology an ideal candidate to deploy the LTV filter for software-defined protocols in mobile radios, where BW might be optimized in a hardware-in-the-loop type of architecture, within a compact footprint and reduced power consumption.

Resorting to a low F_m dynamic scheme leads to relaxed constraints in terms of power handling. In fact, most LTV networks implementing RF filters, such as the popular N-path filters[14-16], suffer from poor linearity under large-signal operation, as their F_m is typically comparable to the RF carrier, resulting in linearity constraints and therefore limited power handling.

Notably, when using the proposed architecture, the filter passband is not exclusively set by k_t^2, leaving room for larger achievable BWs with sufficiently high F_m. Fig.2(a) schematically demonstrates the inherent capability of this LTV filter to achieve 2-3fold larger instantaneous BW as a reference ladder filter, for the same micro-acoustic resonator k_t^2, F_{res}, Q, and C_0. On top of that, this LTV filter relies on identical resonators, whereas instead passive topologies commonly rely on close control of resonators' center frequency spacing to implement a usable passband.

This difference provides a significant advantage with respect to passive topologies, especially when frequency scaling is considered. Resonant frequency trimming of micro-acoustic devices has been pointed out in many sources as the main manufacturing bottleneck of scaling micro-acoustic filters in the mm-Wave spectrum, as well as the high bands of the 5G bands.

Lastly, as this LTV filter requires identical resonators, the usual constraints binding ladder filters' matching to 50Ω ports do not hold here, further simplifying micro-acoustic fabrication in this context.

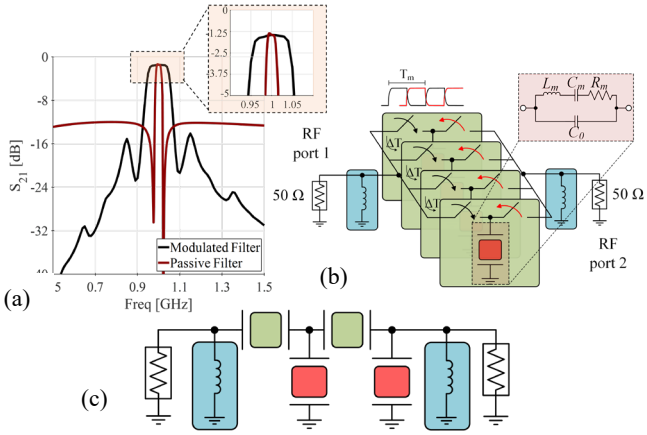

Figure 2 : a) Comparison of the transmission frequency response (S_{21}) of a 4-path micro-acoustic-based commutated LTV filter with 4 identical resonators centered at 1GHz and an equivalent conventional ladder filter composed of 4 resonators - schematics are respectively in b) and c). A typical model of a piezoelectric micro-acoustic resonator is sketched in the red inset of b). For both simulations, micro-acoustic technology using k_t^2=5% and Q=1k was employed. The LTV topology is modulated at a fractional $F_m=0.05F_{res}$. As noted in a), the LTV topology can implement much broader transmission BW for the same IL.

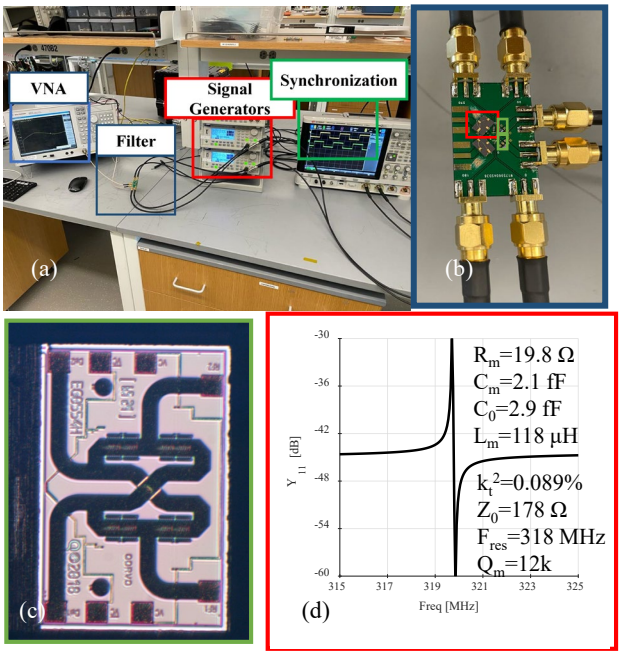

Figure 4: (a) Overview of the experimental setup used to characterize the LTV filter response, composed of two signal generators, synchronized in closed loop via MATLAB interface. The 4 modulation signals are fed to a custom PCB (in (b)) and the circuit is interfaced with two RF ports via coax cables. Scattering parameters are measured via a Keysight VNA as F_m is varied programmatically. In (c), a micrograph picture of the QORVO™ DPDT RF switch deployed in this experiment. In (d), a fitted response of the RFMI™ SAW resonators used in this demo and die attached to the PCB in (b).

RESULTS

An early-stage experimental demonstration is designed to address the filter performance with real micro-acoustic resonator components. A lab experimental setup is remotely programmed via MATLAB to acquire filter frequency response, across a sweep of modulation frequencies F_m. Accordingly to Eq.(2) an F_m range between 50 kHz and 300 kHz is selected.

RFMI™ packaged SAW resonators are selected as off-the-shelf components for this filter(Fig.4d), operating at F_{res}=318 MHz, with k_t^2=0.089%, C_0=2.9pF (corresponding to 172Ohm), and Q_m=12k and die attached to a custom PCB.

An off-the-shelf couple of QORVO™ Double-Pole-Double-Through (DPDT) die RF switch(Fig.4c) is die-attached to a custom PCB(Fig.4b), and the RF pins are wire-bonded to the SAW leads to implement a 4-path micro-acoustic switched filter.

Two couples of complementary modulation signals are generated in quadrature by using two TSG3152 TTI™ signal generators, and ultimately fed on the DPDT controls on the PCB. RF response is measured on a Keysight VNA and recorded programmatically as F_m is varied (Fig.1a).

Despite the high Q_m of the SAW, calculated motional resistance R_m approaches 20Ω due to extremely poor k_t^2, overall limiting the measured IL to circa 5dB (Fig.4a-b). and resulting in extremely narrowband operation between 300kHz and 1.05MHz.

Moreover, from Fig.4(a-b) the filter sidelobes follow the F_m scaling law discussed in the Methods, essentially confirming the predicted trends, and proving feasible real-time BW tunability without resorting to passive tunable components.

Linearity performance is measured using an RF power amplifier fed by a sinusoidal excitation at the filter center frequency (318MHz) resulting in a P_{1dB}=13.5dBm.

A comparison between the measured performance for the LTV switched filter and for an equivalent ladder filter can be drawn if it is assumed, for the ladder filter. that the same resonator performance in terms of Q_m, k_t^2 can be achieved when F_{res} and C_0 are properly scaled to satisfy the requirements to obtain a ladder-type filter response (for example, following the design guidelines explained in [17].)

When directly comparing the two responses, the measured LTV filter outperforms ladder filter BW by a factor of 3 (0.1% vs 0.033%) and displays a lower IL (8.4dB vs 4.5dB), despite nonidealities for ladder filter have not being accounted for.

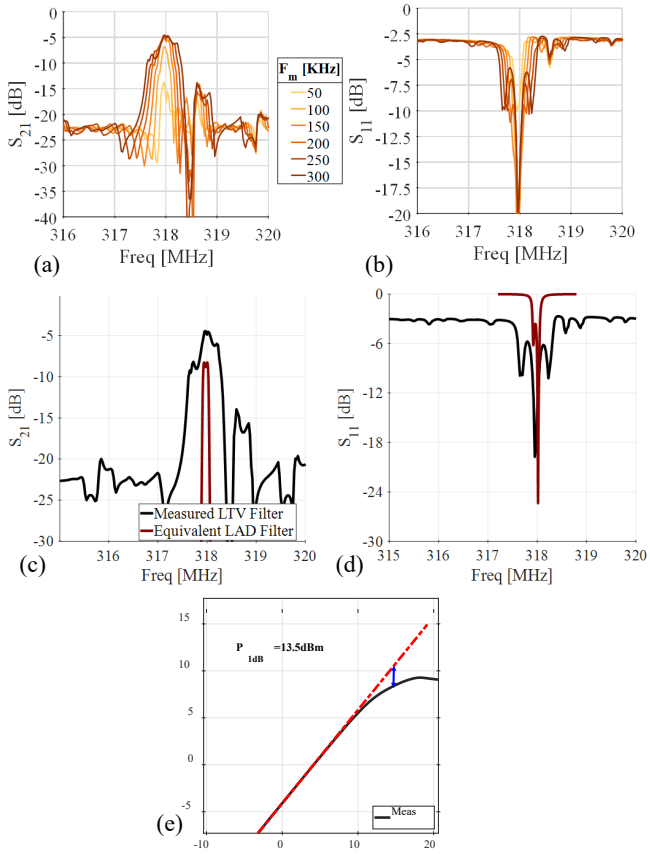

Figure 5: (a-b) Experimental results from the setup in Fig.3, in terms of transmission parameters (S_{21}) and reflection parameters (S_{11}) for various modulation frequencies F_m . Small fractional F_m correspond to achieved BW ranging from 0.03% to 0.1% for a peak IL of 4.5dB, mostly due to the poor $k_t^2$of the SAW resonators. Approximately 0.5dB IL is attributed to 5Ω R_{ON} of said DPDT Switches, while 4dB IL is attributed to 20Ω R_m of the SAWs. (Fig.3b). (c-d) Comparison of experimental LTV filter response with equivalent ladder filter implemented with resonator parameters from Fig.3b. The BW enhancement introduced by the LTV network is 3.3-fold with respect to the passive ladder network realized with the same technology. Moreover, the LTV filter exhibits lower IL given the same C_0,Q,k_t^2, for this narrowband filter design. (e) measured linearity of 13.5dBm, limited by the SAW power handling (as the DPDT power handling approaches 28dBm).

CONCLUSIONS

Despite the low absolute BW demonstrated in this experiment, due to the choice of off-the-shelf SAW resonator components, a filter architecture that can exceed the BW limits posed by the resonator k_t^2 has been proposed, modeled, and experimentally demonstrated in this work.

Details of micro-acoustic RF filter operation have been introduced to provide rule-of-thumb design guidelines for the interested filter designers, and clear comparisons have been provided to show that the filter indeed exceeds most performance of conventional ladder filters.

Moreover, a micro-acoustic RF filter with a native tunability has been presented and experimentally validated, with a unique BW tuning capability exceeding 5 to 1 without the need for tunable components but relying instead on a reconfigurable switching network.

REFERENCES

[1] T. Matsumura, M. Esashi, H. Harada and S. Tanaka, "Multi-band RF filter integrating different modes of AlN resonator by CMOS-compatible process," *2009 IEEE International Ultrasonics Symposium*, 2009, pp. 2141-2144, doi: 10.1109/ULTSYM.2009.5442012.

[2] R. Aigner, J. Ella, H. -. Timme, L. Elbrecht, W. Nessler and S. Marksteiner, "Advancement of MEMS into RF-filter applications," *Digest. International Electron Devices Meeting,*, 2002, pp. 897-900, doi: 10.1109/IEDM.2002.1175981.

[3] R. Ruby, "The 'how & why' a deceptively simple acoustic resonator became the basis of a multi-billion dollar industry," *2017 IEEE 30th International Conference on Micro Electro Mechanical Systems (MEMS)*, 2017, pp. 308-313, doi: 10.1109/MICRO-ACOUSTICYS.2017.7863403.

[4] F. Boccardi, R. W. Heath, A. Lozano, T. L. Marzetta and P. Popovski, "Five disruptive technology directions for 5G," in IEEE Communications Magazine, vol. 52, no. 2, pp. 74-80, February 2014, doi: 10.1109/MCOM.2014.6736746.

[5] L. Larson, "Rf and Microwave Hardware Challenges for Future Radio Spectrum Access," Proceedings of the IEEE, vol. 102, no. 3, pp. 321–333, 2014.

[6] S. Mahon, "The 5G Effect on RF Filter Technologies," in *IEEE Transactions on Semiconductor Manufacturing*, vol. 30, no. 4, pp. 494-499, Nov. 2017, doi: 10.1109/TSM.2017.2757879.

[7] W. J. Chappell, E. J. Naglich, C. Maxey and A. C. Guyette, "Putting the Radio in "Software-Defined Radio": Hardware Developments for Adaptable RF Systems," in Proceedings of the IEEE, vol. 102, no. 3, pp. 307-320, March 2014, doi: 10.1109/JPROC.2014.2298491.

[8] J. Mitola, "Cognitive Radio Architecture Evolution," in *Proceedings of the IEEE*, vol. 97, no. 4, pp. 626-641, April 2009, doi: 10.1109/JPROC.2009.2013012.

[9] J. Mueller *et al*., "Requirements for reconfigurable 4G front-ends," *2013 IEEE MTT-S International Microwave Symposium Digest (MTT)*, 2013, pp. 1-4, doi: 10.1109/MWSYM.2013.6697534.

[10] H. H. Sigmarsson, J. Lee, D. Peroulis and W. J. Chappell, "Reconfigurable-order bandpass filter for frequency agile systems," 2010 IEEE MTT-S International Microwave Symposium, 2010, pp. 1756-1759, doi: 10.1109/MWSYM.2010.5518024.

[11] E. Schmidhammer, T. Metzger and C. Hoffmann, "Multiplexers: A necessary extension for 4G/5G systems," 2016 IEEE MTT-S International Microwave Symposium (IMS), 2016, pp. 1-4, doi: 10.1109/MWSYM.2016.7540222.

[12] G. Michetti, M. Pirro, Y. Yu, G. Chen, C. Cassella and M. Rinaldi, "Reconfigurable N-Path MEMS Filter Based on the Periodic Commutation of Single Frequency Resonators," 2020 IEEE 33rd International Conference on Micro Electro Mechanical Systems (MEMS), 2020, pp. 1274-1277, doi: 10.1109/MEMS46641.2020.9056403.

[13] G. Michetti, A. Mekawy, L. Colombo, M. Pirro, A. Alù and M. Rinaldi, "Filter Architecture Operating Beyond the Q Limit and With Real-Time Bandwidth Tunability," *2021 IEEE MTT-S International Microwave Filter Workshop (IMFW)*, 2021, pp. 218-220, doi: 10.1109/IMFW49589.2021.9642298.

[14] A. Ghaffari, E. A. M. Klumperink, M. C. M. Soer and B. Nauta, "Tunable High-Q N-Path Band-Pass Filters: Modeling and Verification," in IEEE Journal of Solid-State Circuits, vol. 46, no. 5, pp. 998-1010, May 2011, doi: 10.1109/JSSC.2011.2117010.

[15] A. E. J. Ng and J. I. Sewell, "N-path and pseudo-N-path cells for switched-current signal processing," in *IEEE Transactions on Circuits and Systems II: Analog and Digital Signal Processing*, vol. 46, no. 9, pp. 1148-1160, Sept. 1999, doi: 10.1109/82.793705.

[16] K. Kibaroglu and G. M. Rebeiz, "An N-path bandpass filter with a tuning range of 0.1–12 GHz and stopband rejection > 20 dB in 32 nm SOI CMOS," 2016 IEEE MTT-S International Microwave Symposium (IMS), 2016, pp. 1-3, doi: 10.1109/MWSYM.2016.7539982.

[17] s. Menendez, P. de Paco, R. Villarino and J. Parron, "Closed-Form Expressions for the Design of Ladder-Type FBAR Filters," in *IEEE Microwave and Wireless Components Letters*, vol. 16, no. 12, pp. 657-659, Dec. 2006, doi: 10.1109/LMWC.2006.885610.

CONTACT

*G.Michetti, michetti.g@northeastern.edu

TEMPERATURE-STABLE THIN-FILM LITHIUM TANTALITE-ON-SILICON RESONATORS

Yasaman Majd, Hamideh Kermani, and Reza Abdolvand
University of Central Florida, Orlando, USA

ABSTRACT

In this paper, a novel passive temperature compensation method is introduced for the first time that could potentially result in canceling both the first and the second order temperature coefficients of frequency (TCF) in silicon-based resonators. The main idea of this work is to construct the resonator body from a thin film of X-cut Lithium Tantalite (LT) bonded to a degenerately n-type doped silicon film aligned to the [100] crystalline orientation. The two films individually exhibit quadratic TCF curves in opposing directions, hence the combined heterostructure is expected to result in a near-perfect compensation of the temperature variation of frequency. This idea is implemented with a 1.8 µm LT film bonded to an SOI wafer, and an overall frequency drift as low as 72 ppm has been observed over the temperature range of 0 ˚C to 90 ˚C at 96 MHz operation frequency for the fabricated contour-mode resonators which is a significant reduction compared to conventional silicon-based resonators and comparable to what is achievable in quartz resonators.

KEYWORDS

Frequency drift, stable resonators, X-Cut LT, highly doped silicon, TCF.

INTRODUCTION

Some of the main requirements for radio-frequency acoustic wave devices are to attain high temperature stability, and high -quality factor. It is due to such demands, that quartz crystal oscillators have been used in most electronic platforms. However, integration of quartz resonators with microelectronics and scaling their frequency is a challenge that has fueled research in seeking alternatives.

Recently, micro electro-mechanical (MEMs) resonators have gained popularity as a replacement for quartz resonators in some application due to their smaller size, lower power consumption, and the potential for CMOS compatibility. Nevertheless, the persistent deficiency of micro-electro-mechanical resonators compared to their Quartz counterparts is their relatively large frequency drift over temperature [1-3]. For example, in lightly-doped conventional silicon and lithium niobate (LN) MEMS resonators, the temperature coefficient of frequency (TCF) is approximately -30 ppm/°C and -80 ppm/°C, respectively, resulting in substantial frequency drifts (several thousand ppm) over the -40 °C-80 °C temperature range [3,4]. To address this deficiency, several active and passive compensation techniques have been developed to improve the temperature-frequency performance of silicon-based resonators [5].

The active compensation can be implemented through a myriad of techniques including electrostatic tuning, capacitive frequency pulling and oven-controlled frequency stabilization [5]. In all the aforementioned methods additional circuitry is involved which increases the power consumption and adds more system-level complexity.

On the other hand, the passive compensation techniques mainly focus on designing the intrinsic properties of the utilized materials to reduce the frequency drift due to the temperature change. Most of the successful passive temperature compensation approaches are based on degenerate doping of the silicon device layer [2] or using a composite structure that contains silicon dioxide (with positive TCE) to partly compensate for the negative frequency drift of silicon and piezoelectric materials, such as AlN and LN in MEMS resonators. However, the resulting overall temperature stability is usually not comparable to quartz due to the quadratic nature of the resulting TCF curve. In addition, silicon dioxide compensation layer unavoidably degrades quality factor and limits the achieved temperature range [3].

Unlike pure silicon and most typical piezoelectric material, the resonance frequency of thickness-shear mode devices built on X-cut lithium tantalite (LT) is approximately an upward quadratic function of the temperature, exhibiting a zero TCF, also known as a turnover temperature [6,7]. In this paper, we exploit a novel passive compensation method to achieve temperature-stability in LT-on-SOI resonators through precise alignment of the crystalline orientations in silicon and LT. The S0 lamb wave in these resonators is excited by a lateral electric field through a single interdigitated transducer (IDT), that enables integration of multi-frequency devices on a single chip.

THEORY AND DESIGN

In our recent report [8], we demonstrated that in contour mode resonators fabricated on an X-cut plate of LT and rotated with respect to the -Y-axis (Figure 1(a)) a turnover temperature is observed and the frequency vs. temperature plot is an upward quadratic function. Figure 1(b) depicts the simulated frequency drift versus temperature for rotated X-cut LT at θ =36, θ=40 and 44 deg as well as n-type doped (n ~ 6.6×10^{19} cm^{-3}) [100]-aligned silicon lateral-extensional resonators respectively [3,8].

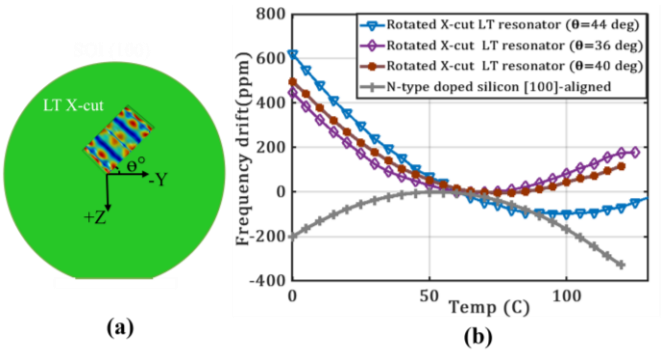

Figure 1:(a) The orientation of contour-mode resonators fabricated on LT substrate. (b) Simulated frequency drift versus temperature for rotated LT and degenerately n-type-doped silicon resonators [8].

As seen, LT resonators have the opposite TCF trend compared to highly n-type doped silicon. Observing this unique property has sparked the idea that by bonding thin-film LT on highly doped silicon, we could nullify both first and second-order terms of the TCF to achieve highly stable micro-machined resonators. To test this hypothesis, the proposed resonators were modeled and simulated in COMSOL Multiphysics by combining the slab of LT on n-type doped Si aligned to [100] using eigenfrequency analysis to examine and verify the hypothesis discussed above. The simulated stress profile of a one-port 7th order resonator as well as

978-1-940470-04-7/HH2022/$25©2022TRF
DOI 10.31438/trf.hh2022.53

Solid-State Sensors, Actuators, and Microsystems Workshop
Hilton Head Island, South Carolina, June 5-9, 2022

the cross-sectional view of the resonator's displacement are shown in Figure 2. with the design parameters of Table 1. The electrodes are placed on the top of the LT at mechanical antinodes to form the excitation lateral electric field.

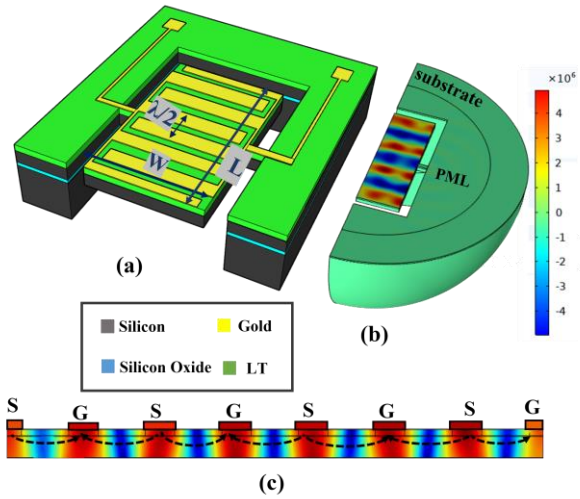

Figure 2:(a) The schematic view of a 7th-order harmonic contour-mode LT-on-Silicon resonator(b) simulated stress field of half of the resonator in y direction (c) displacement of resonator with electrodes placed at anti-nodes.

Table 1: The dimensions of the simulated resonator

Parameter	*Value*
Plate length *(L)*	238 µm
Plate Width *(W)*	154 µm
Silicon slab thickness	5 µm
LT slab thickness	1.5 µm
Wavelength (λ)	68 µm
Target resonant frequency	100 MHz

Two main factors that affect the temperature-induced frequency variations are change in effective Young's modulus, which depends on elastic constants, and thermal expansion. In our simulation, we neglect the thermal expansion since the change in elasticity is deemed to be the dominant effect. In the simulation the elasticity matrix of both LT and highly-doped silicon resonators is varied with temperature to find the frequency drift. The elasticity constants for LT and silicon were borrowed from [7] and [9], respectively.

Several series of simulations have been performed to study the effect of Si/LT thickness ratio as well as LT orientation with respect to the -Y-axis on the frequency vs temperature (Figures 3 and 4). As seen, for lower thickness ratios in a device (with rotation angle of 36-44 deg), the TCF behavior expectedly resembles that of the highly doped Si resonators and for higher ratios, it is similar to LT resonators. At a thickness ratio of ~0.3 a minimum frequency variation is achieved (Figure 3).

The simulation results of the composite structure with a thickness ratio of 0.3 are plotted in Figure 4 for different rotation angles of LT with respect to -Y-axis. A minimum frequency drift of 70 ppm between 0 C to 80 ˚C has been accomplished at θ=36 deg, confirming the initial hypothesis (Figure 4).

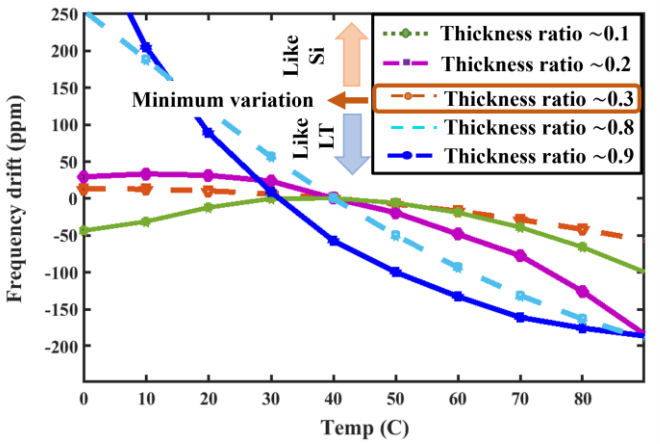

Figure 3: The simulated frequency drift versus temperature for different thickness ratios of LT/Si for the structure depicted in Figure 2.

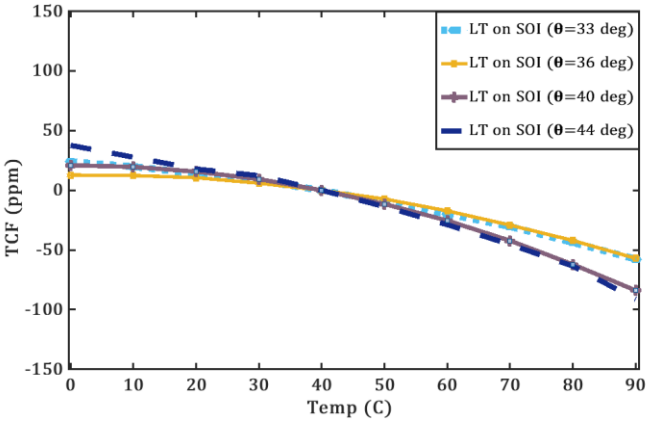

Figure 4: The simulated frequency drift versus temperature of the proposed resonator at different angles for the structure depicted in Figure 2.

DEVICE FABRICATION

The fabrication of the device summarized in Figure 5, starts with bonding a 4-inch lithium tantalate X-Cut substrate onto an SOI wafer and thinning it to the targeted thickness (e.g. 1.8µm). This step is outsourced and is accomplished by our industrial partner, "NGK Insulators". The SOI device and handle layer silicon thicknesses are 5 and 450 µm, respectively. To form the interdigitated electrodes on LT, Cr/gold (30nm/120nm) is deposited by an Ebeam evaporator and patterned through the lift-off process. In the next step, the boundary of the resonator is defined by plasma etching the full stack of the material (LT and silicon substrate) down to the SOI buried oxide (BOX) layer. LT is etched physically in an inductively-coupled argon plasma, while Si is etched in a deep reactive ion etching chamber (Bosch process). Finally, the backside of the substrate is etched to the BOX layer by Bosch process and the device is released by etching the BOX layer in the buffered oxide solution. The scanning electron micrographs (SEM) of one of the fabricated devices is shown in Figure 6.

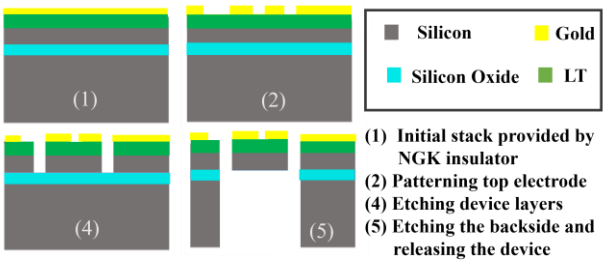

Figure. 5: The Process flow of fabrication resonators.

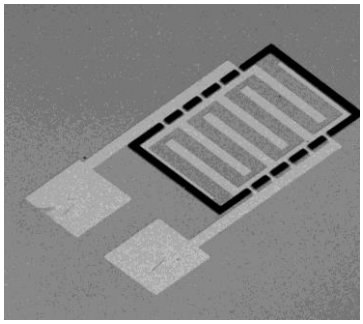

Figure. 6: The SEM of the resonator

EXPERIMENTAL RESULTS

The measured admittance response of a one-port resonator operating at 96 MHz is shown in Figure 7. The equivalent Butterworth-Van Dyke (BVD) model is used to extract the for Q, electromechanical coupling coefficient (K_t^2), motional components (C_m, L_m, R_m), and static capacitance (C_0). The K_t^2 and Q are calculated to be approximately 6.5 K and .04 % respectively.

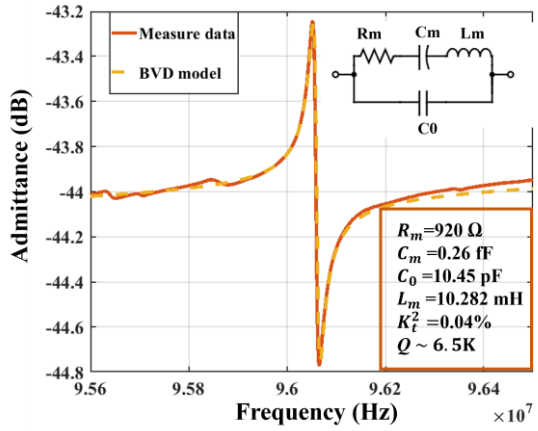

Figure 7: The simulated and measured frequency response of the resonator along with the extracted BVD model in the inset.

The frequency drift measurement is conducted in a cryogenic vacuum probe station (Figure 8). The sample holder is cooled by liquid nitrogen and heated with a resistive heater and the temperature is controlled by a PID controller within ±0.05°C. The frequency drift of the resonators at θ=36, θ=40 and θ=44 deg rotation angle between 0 ◦C to 90 ◦C have been measured and plotted in Figure 9.

A minimum frequency drift of around 72, 92 ppm have been obtained for the devices with rotation angles of θ=36 and θ=44 degrees. These values are significantly lower than conventional silicon-based MEMS resonators, AlN-based resonators [6] and Lithium Niobate (LN) resonators [4].

The observed increase in the temperature-induced frequency drift of the resonator roated at θ=40 deg (~500 ppm) confirms the simulations results indicating that the frequency variation strongly depends on the orientation.

The discrepancies between the trend of the measured and simulated frequency drift versus temperature could stem from the tolerance of the silicon doping, and rotation angle of LT which all cause change in frequency behavior of LT and Si. For example, in simulation, the doping of the slab of silicon is assumed to have a constant value of 6.6×10^{19} cm^{-3}, while the actual doping of Si is somewhere between 5×10^{19} to 6.6×10^{19} cm^{-3}. We predict that superior results could be achieved by improving the fabrication process and optimizing the thickness ratio of silicon and LT substrate as well as rotation angle of LT.

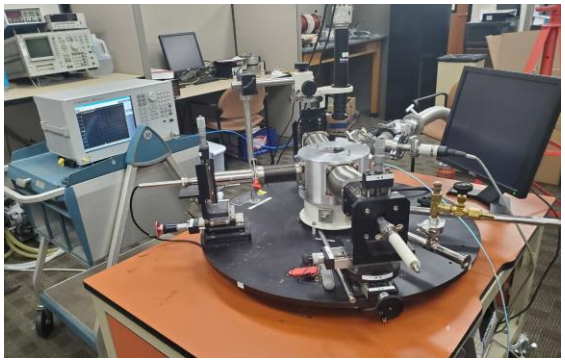

Figure 8: TCF measurement setup

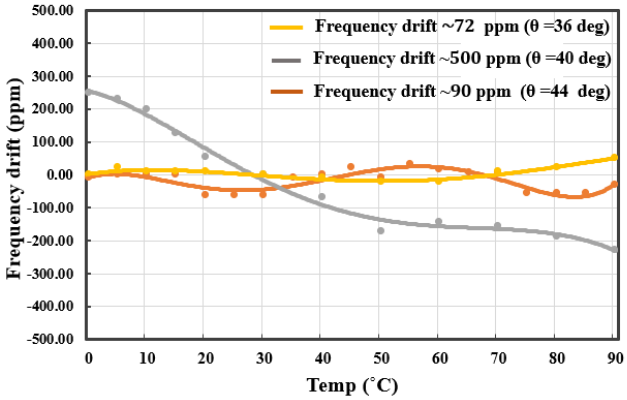

Figure 9: Measured frequency drift of the resonators versus temperature.

CONCLUSION

In this work a novel passive temperature-compensation technique based on an engineered substrate is presented in silicon micro-resonators, which addresses the important demands of most communication systems, including stability and high-quality factor. A thin layer of LT (1.8 µm thickness) has been overlayed on a 5 µm thickness n-type doped silicon to compensate for both the first and second order coefficients of frequency-temperature variation in silicon.

The proposed resonators operating at 96 MHz are shown to offer high quality factor (>6.5 K) and low frequency drift of 72 ppm

between 0 to 90 ˚C, which is a great improvement compared to conventional silicon resonators. These lateral-field excited contour mode resonators have the potential to be one of the best candidates for extremely stable time-keeping applications.

REFERENCES

[1] Wu. Guoqiang, Jinghui Xu, Eldwin Jiaqiang Ng, and Wen Chen, "MEMS resonators for frequency reference and timing applications.", Journal of Microelectromechanical Systems 29, no. 5 (2020): 1137-1166.

[2] Shahraini, Sarah, Hakhamanesh Mansoorzare, Amirreza Mahigir, and Reza Abdolvand, "Thickness-Lamé thin-film piezoelectric-on-silicon resonators.", Journal of Microelectromechanical Systems 29, no. 3 (2020): 296-305.

[3] Shahmohammadi, Mohsen, Brandon P. Harrington, and Reza Abdolvand, "Turnover temperature point in extensional-mode highly doped silicon microresonators.", IEEE transactions on electron devices 60, no. 3 (2013): 1213-1220.

[4] Burgess, J. W., and M. C. Hales. "Temperature coefficients of frequency in LiNbO3 and LiTaO3 plate resonators." Proceedings of the Institution of Electrical Engineers. Vol. 123. No. 6. IET, 1976.

[5] Bhugra, Harmeet, and Gianluca Piazza, eds. Piezoelectric MEMS resonators. New York, NY, USA:: Springer International Publishing, 2017.

[6] Onoe, Morio, T. Ashida, and K. Sawamoto. "Zero temperature coefficient of resonant frequency in an X-cut lithium tantalate at room temperature." Proceedings of the IEEE 57, no. 8 (1969): 1446-1448.

[7] R. T. Smith and F. S. Welsh, "Temperature Dependence of the Elastic, Piezoelectric, and Dielectric Constant of Lithium Tantalate and Lithium Niobate," Applied Physics, vol. 42, pp. 2219-2230, 1971.

[8] Yasaman Majd, Hamideh Kermani, Parvin Akhkandi, Garett Goodale. "Turnover Temperature in Lateral-Field-Excited Thin- Film Lithium Tantalate Contour Resonators." Accepted in 2022 Joint Conference of the European Frequency & Time Forum and the IEEE International Frequency Control Symposium.

[9] Jaakkola, Antti, Mika Prunnila, Tuomas Pensala, James Dekker, and Panu Pekko. "Determination of doping and temperature-dependent elastic constants of degenerately doped silicon from MEMS resonators." IEEE transactions on ultrasonics, ferroelectrics, and frequency control 61, no. 7 (2014): 1063-1074.

CONTACT

*Y.M. Public, tel: +1-304-413-6038; majd92@knights.ucf.edu

ULTRASONIC AIR-BORNE PROPULSION THROUGH SYNTHETIC JETS

Hai Liu, Akash Roy, Yongkui Tang, Matin Barekatain, and Eun Sok Kim*
Department of Electrical and Computer Engineering
University of Southern California, Los Angeles, California, USA

ABSTRACT

This paper presents acoustic propulsion in air by synthesis jets produced by ultrasounds. Various ultrasonic air-borne propellers have been fabricated on 0.37-mm-thick commercial card piezoelectric speakers (APS2513S-T-R, 25.2 × 16.6 × 0.37 mm^3 in size), and studied, with the propulsion force measured through a precision weight scale, as the orifice size, thickness, spacing between orifices, and number (in the orifice array) are varied. Also varied is the orifice depth profile, as the fabrication processes for the orifices produce varying profiles. Strongest acoustic propulsion of 5.4 mg is obtained at 66 kHz (far beyond audible range) with 14 × 14 orifice array made on a 0.1-mm-thick polyester plate (resulting in a propeller of 25.2 × 16.6 × 1.37 mm^3 in volume and 500 mg in weight). The acoustic propulsion force, though 93 times less than the propeller weight, is capable of making the propeller jump and move laterally.

INTRODUCTION

Synthetic air jet, a zero net mass flux with non-zero momentum, can be generated through a vibrating diaphragm in a cavity with orifice (Fig. 1a), and can be used for propulsion, thermal management, flow control, etc. [1-3]. Synthetic air jet produces more propulsion force at a lower frequency (with a higher wavelength) and has mostly been obtained with audible sounds (i.e., <10 kHz) [1-6], though a micro-machined synthetic jet actuator designed to work at ultrasonic frequencies has been reported without any measured propulsion force [7]. We earlier demonstrated air-borne acoustic propeller at audio frequency [8]. As the audible sound impacts nearby humans, we have explored synthetic jets in ultrasonic frequencies, and report our recent results on acoustic propulsion with ultrasounds, as we vary the orifice design and fabrication process. Also, reported is our experimental observation on the effects of temperature on propulsion force.

EXPERIMENT

Device

The propeller is built on a 0.37 mm thick commercial card piezoelectric speaker (APS2513S-T-R, 25.2 × 16.6 × 0.37 mm^3 in size) with an attached polyester sheet with orifices (Fig. 1b and Fig. 1c). The polyester cover sheet is attached to the speaker with a 0.9 mm thick tape, so that there is 0.9 mm air gap between the speaker and the cover sheet. Throughout the experiments, we have used sinusoidal signal of 20 $V_{peak\text{-}to\text{-}peak}$ to drive the speaker.

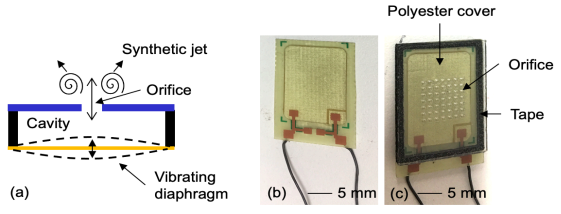

Figure 1: (a) Cross-sectional schematic of the synthetic jet generation, (b) photo of a piezoelectric card speaker, (c) photo of the acoustic propeller with the speaker and a laser-machined polyester cover with 7×7 orifices.

Propulsion force measurement

To quantify the propulsion force precisely, the propeller is placed over a precision scale (METTLER TOLEDO MS104S/03 with 0.1 mg resolution) through a hollow adaptor with the propeller's orifices facing up for downward propulsion force (Fig. 2).

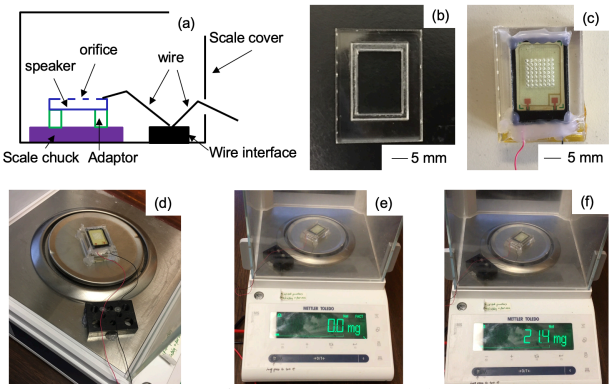

Figure 2: Propulsion force measurement through a precision weight scale: (a) schematic of the test set-up, (b) photo of the hollow adaptor, (c) photo of the acoustic propeller attached to the adaptor, (d) photo of the propeller (with the adaptor) on the scale along with the wire interface, (e) photo of the scale reading (0.0 mg) without power applied to the propeller, (f) scale reading (21.4 mg) with power applied to the propeller.

Orifice design and fabrication process

Four orifice design parameters (orifice thickness, orifice diameter, orifice array size, and spacing between the orifices) at three levels are evaluated for the propulsion force (Table 1).

Table 1: Parameters and levels of the orifice design

Parameters	Levels		
	1	2	3
Orifice thickness (μm)	500	100	50
Orifice size (μm)	420	100	50
Array size	3x3	7x7	14x14
Spacing (mm)	0.6	1.2	1.8

Two processes are studied for orifice fabrication on polyester sheet: laser drilling without photolithography and O_2 reactive ion etching (RIE) with photolithography. Laser drilling can produce each orifice fast (though one at a time) but produces slanted sidewall, while RIE takes hours to make the orifices on a relatively thick substrate, though it produces vertical sidewall.

Temperature measurement

The piezoelectric card speaker generates substantial amount of heat, at ultrasonic frequencies (though negligibly at audio frequencies for the same drive peak-to-peak voltage), and we have measured the temperature at the speaker with a point thermocouple (Fig. 3). The effect of the temperature rise on the propulsion force is

978-1-940470-04-7/HH2022/$25©2022TRF
DOI 10.31438/trf.hh2022.54

studied by operating the speaker with $20V_{pp}$ continuously at 66 kHz for 10 seconds to raise the temperature to 70 °C and then driving the speaker with various frequencies while the temperature at the speaker remains about 70 °C.

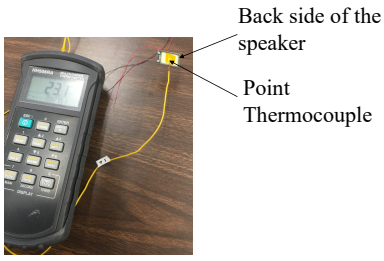

Figure 3: Temperature measurement at the card speaker, as the speaker is driven with various operating parameters.

RESULTS AND DISSCUSSION

Impact of orifice design

Twenty-six legs of orifice design parameters have been studied for propulsion force with laser drilling process (Table 2). We list the highest propulsion force between 17 – 50 kHz as the most desirable output, because humans cannot hear sound beyond 17 kHz and since the temperature at the speaker increases fast beyond 50 kHz (though we have obtained propulsion force around 66 kHz).

Table 2: Matrix of orifice design

Leg#	Levels				Highest propulsion force (17 – 50 kHz) (mg)
	Thickness	Diameter	Array	Spacing	
1	1	2	3	2	2.4
2*	2	3	3	3	1.4
3	3	3	1	2	0
4	1	1	2	1	1.4
5	2	1	2	2	2.7
6	3	3	3	1	0
7	1	1	1	3	2.1
8	2	2	1	1	0
9	3	2	2	3	0
10	1	3	2	1	1.4
11	2	2	1	2	3.1
12*	3	1	3	3	0
13	3	3	2	2	0
14	3	3	2	1	0.7
15	3	2	2	2	2.9
16	3	1	2	2	0
17	2	1	2	2	2.6
18	2	2	2	2	2.7
19	2	3	2	2	0
20	2	2	1	3	1.3
21	1	1	2	2	0.8
22	2	2	2	2	2.6
23	2	2	1	2	2
24	2	2	3	2	1.1
25	2	2	1	3	0.7
26	2	2	2	3	3.7

* *The array size is* 10×10 *with* $1.5mm$ *spacing between orifices in both orthogonal directions for Leg 2 and Leg 12 as there is not enough space on the polyester cover for Level 3 for both Array and Spacing.*

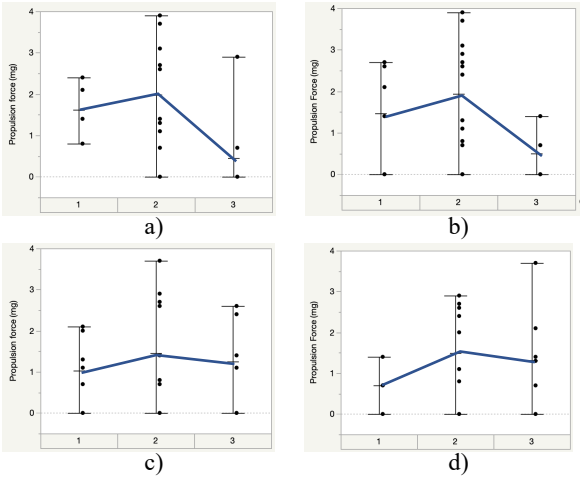

Figure 4: Measured propulsion forces vs orifice (a) thickness, (b) diameter, (c) array size, and (d) spacing.

According to the measured data shown in Fig. 4, the level 2 values for the orifice thickness, diameter, array size and space lead to higher propulsion force on the average. In general, a thicker orifice has higher acoustic resistance [4] and leads to a smaller propulsion force. However, when the orifice is too thin (e.g., 50 µm in this study), the polyester sheet is so flexible that the sheet itself vibrates in response to applied sound pressure, resulting in a decrease in propulsion force. A smaller orifice can lead to a stronger propulsion force due to higher acoustic streaming effect near a smaller orifice. However, acoustic resistance increases as the diameter is reduced. Also, note that Fig. 4 is based on the experiments listed Table 2, and does not mean that the orifice with the mid-level of each factor necessarily has the highest propulsion force. Leg 26 (Fig. 5) has the highest propulsion force (3.7 mg) with frequency higher than 17 kHz and widest frequency range with propulsion force in all these 26 legs.

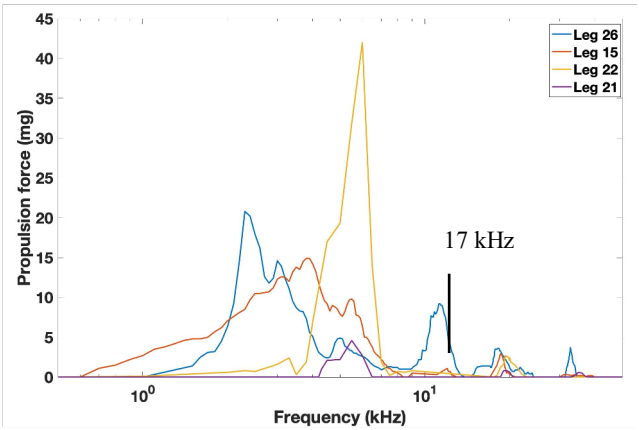

Figure 5: Measured propulsion force vs frequency for different orifice designs. Leg 26 (Table 2) produces acoustic propulsion around 20 kHz and 32 kHz with highest propulsion force 3.7 mg at 32.8 kHz.

Measured sound pressure levels of the speaker driven with $20V_{pp}$ for different legs in Table 2 are shown in Fig. 6, and we find that the frequencies where the propulsion force is strong (whether in audio or ultrasound range) (Fig. 5) are not necessarily the frequencies where the sound pressure levels (measured with and without the orifice-containing cover) are high (Fig. 6), due to the orifice size and thickness affecting the synthetic jet generation.

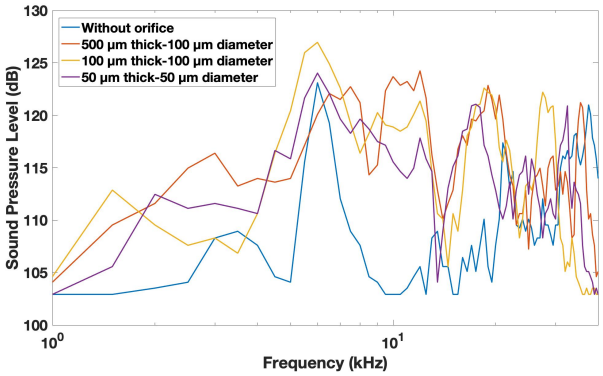

Figure 6: Open-field sound pressure level (in anechoic chamber) vs frequency without and with orifices.

Effect of orifice fabrication process

We have fabricated 100 μm thick orifices with 50 μm and 100 μm diameter on polyester sheet through oxygen RIE, following the steps illustrated in Fig. 7a. A 0.2μm thick sputter-deposited aluminum is used as an etch mask during RIE (Fig. 7a(i)). It takes about 9 hours to etch through the 100 μm thick polyester with the O_2 RIE at 250 Watt.

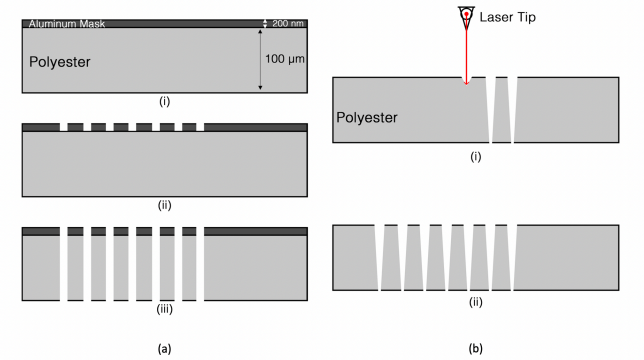

Figure 7: (a) Brief fabrication steps with O_2 RIE:(i) sputter-deposit 200nm thick Al on 100 μm thick polyester sheet, (ii) wet etch Al after photolithography, (iii) use RIE to etch polyester to form orifice; (b) fabrication with laser cutter:(i) use laser cutter to etch out orifices by controlling exposure power and radiation time, (ii) conical cross-sectional view of the orifices obtained with the laser cutter.

The etch rate of the polyester with oxygen plasma in RIE is found to be non-linear due to polyester etch-byproducts filling up the orifices. The orifices fabricated with RIE have vertical sidewalls (Fig. 7a(iii)), though the orifices made with a laser cutter have cone-shaped sidewalls (Fig. 7b(ii)). Orifice fabrication with a laser cutter is done over various thick polyester sheets by controlling the laser power and radiation time (Fig. 7b(i)). But the orifices by the laser cutter have conical cross-section due to thermal effects of the laser beam (Fig. 7b(ii)).

The cross sections of the orifices have been obtained by dicing the substrates with a Dicing Saw, and their images obtained with a microscope are shown Fig. 8. For the orifices with conical sidewalls, the side with larger diameter is aligned to face the speaker, the sound source.

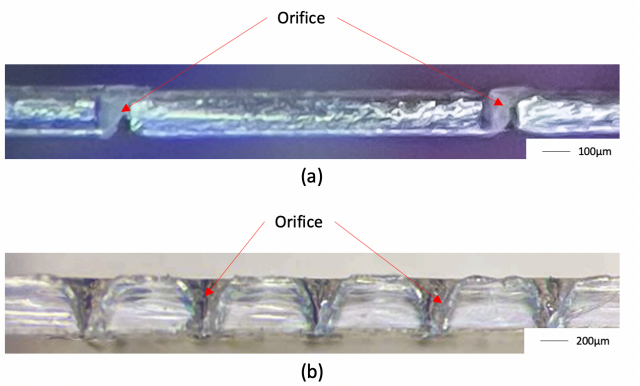

Figure 8: Cross sectional images of the orifices fabricated by (a) RIE showing vertical sidewalls, (b) a laser cutter showing conical sidewall

The laser-machined orifices have produced higher acoustic propulsion in both audible and ultrasound range. The device with 100-μm-diameter, 100-μm-thick orifices made by a laser cutter produces a peak of 5.4 mg propulsion over ultrasound range (at 66 kHz), about two times larger than the highest obtained over ultrasound range with the orifices made with RIE. Over the audible range, the orifices fabricated with a laser cutter performed far better than the ones made with RIE (Fig. 9). Based on our experiments, it is evident that for better acoustic propulsion, it is better to have orifice designs having conical structure to allow for acoustic focusing.

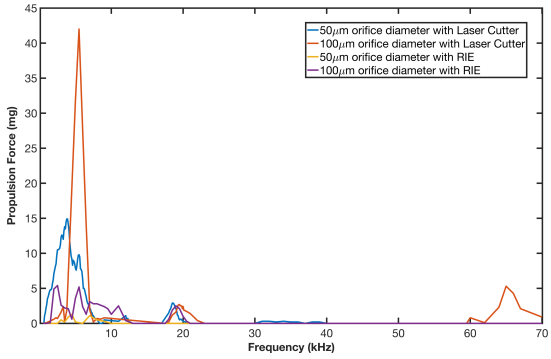

Figure 9: Measured propulsion force vs frequency with different orifices made with a laser cutter and RIE on 100 μm thick polyester sheets.

Temperature effect

As the speaker generates heat which strongly dependent on the applied frequency and voltage (with a higher frequency and higher voltage leading to faster temperature rise, according to Figs. 10 and 11), the acoustic propulsion force has been characterized. Although high temperature can damage the speaker; the temperature rise increases the propulsion force at some frequencies, though it decreases at some other frequencies, depending on the orifice design (Fig. 12), indicating that higher propulsion force can be achieved through proper temperature control.

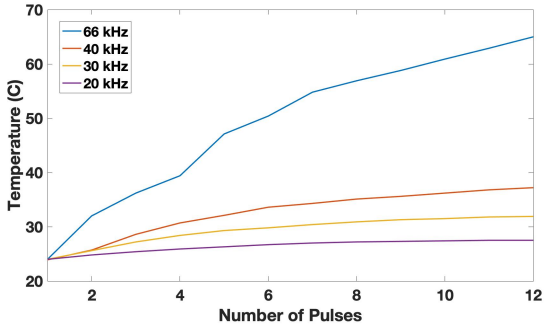

Figure 10: Speaker temperature vs the number of pulses as a function of sinusoidal frequencies (with 20V_{pp}, 40% duty cycle).

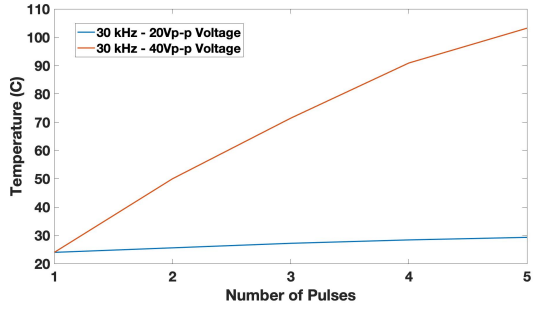

Figure 11: Speaker temperature vs the number of pulses as a function of voltage applied (with 30 kHz, 40% duty cycle).

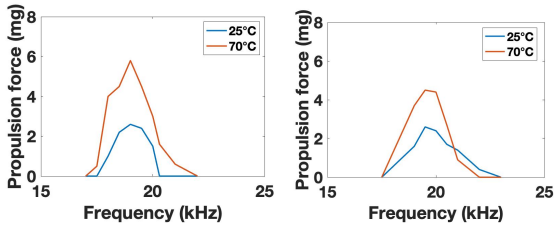

Figure 12: Propulsion forces vs frequency at 25 and 70 °C for the propeller (a) with 0.1 mm thick orifices of 100 µm in diameter and (b) with 0.1 mm thick orifices of 50 µm in diameter.

Propulsion phenomena

The propulsion forces generated by ultrasounds (without any audible sound) are shown to make the propellers jump and move laterally at about several mm/sec (Fig. 13).

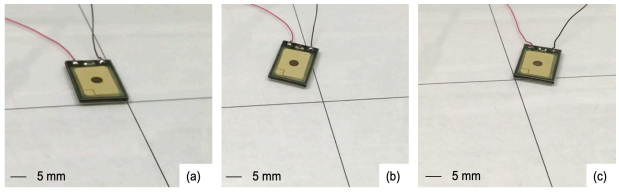

Figure 13: Photos showing movement of the propeller (with 100 µm thick orifices of 100 µm in diameter): (a) before power on, (b) 1 sec after 20 kHz, 20 V_{pp}, (c) 1 sec after 66 kHz, 20 V_{pp}.

SUMMARY

The propulsion forces generated through synthetic jets with air-borne ultrasound are measured quantitively through a precision scale, as the orifice parameters are varied. Among the parameters we have explored, the orifices with 100 µm thickness and 100 µm in diameter produce the highest propulsion force. Orifices with conical sidewall (obtained with laser drilling) are shown to produce higher acoustic propulsion force than orifices with vertical sidewall, when the side with a larger orifice opening faces the speaker. Also, temperature rise is found to have significant effect on propulsion force and may advantageously be used for enhancing propulsion force.

ACOKNOWLEDGEMENTS

This paper is based on the work supported by National Science Foundation under grant ECCS2017926.

REFERENCES

[1] A. P. Thomas, M. Milano, M. G. G'Sell, K. Fischer and J. Burdick, "Synthetic Jet Propulsion for Small Underwater Vehicles," Proceedings of the 2005 IEEE International Conference on Robotics and Automation, 2005, pp. 181-187

[2] S. J. Campbell, W. Z. Black, A. Glezer and J. G. Hartley, "Thermal management of a laptop computer with synthetic air microjets," ITherm'98. Sixth Intersociety Conference on Thermal and Thermomechanical Phenomena in Electronic Systems (Cat. No.98CH36208), 1998, pp. 43-50

[3] I. Wygnanski, and I. Wygnanski. "Boundary layer and flow control by periodic addition of momentum." In 4th Shear Flow Control Conference, p. 2117. 1997.

[4] U. Ingård, and S. Labate. "Acoustic circulation effects and the nonlinear impedance of orifices." The Journal of the Acoustical Society of America 22, no. 2 (1950): 211-218.

[5] M. Chiatto, "Design and Performance Evaluation of Piezo-Driven Synthetic Jet Devices." World Journal of Engineering and Technology 4, no. 03 (2016): 107.

[6] M. Mueller, L. Bernal, P. Miska, P. Washabaugh, T.-K. Chou, B. Parviz, C. Zhang, and K. Najafi. "Flow structure and performance of axisymmetric synthetic jets." In 39th Aerospace Sciences Meeting and Exhibit, p. 1008. 2001.

[7] M. Mueller, L. Bernal, R. Moran, P. Washabaugh, B. Parviz, T-K. Chou, C. Zhang, and K. Najafi. "Thrust performance of micromachined synthetic jets." In Fluids 2000 Conference and Exhibit, p. 2404. 2000.

[8] Y. Tang, and E.S. Kim. "Acoustic Propeller Based on Air Jets from Acoustic Streaming." In 2019 20th International Conference on Solid-State Sensors, Actuators and Microsystems & Eurosensors XXXIII (TRANSDUCERS & EUROSENSORS XXXIII), pp. 2068-2071. IEEE, 2019.

CONTACT

*Hai Liu, tel: +1-213-709-3516; hailiu@usc.edu

WIRELESS AND STAND-ALONE SUBMARINE PROPELLER BASED ON ACOUSTIC PROPULSION

Jaehoon Lee and Eun Sok Kim
Department of Electrical and Computer Engineering
University of Southern California, Los Angeles, CA 90089, USA

ABSTRACT

This paper presents a wireless and stand-alone subminiature propeller based on acoustic propulsion for the underwater robotic applications. The acoustic propulsion is generated by a MEMS-based self-focusing acoustic transducer (SFAT), fabricated on 1-mm-thick lead zirconate titanate (PZT) substrate, and operated at its thickness mode resonant frequency of 2.32 MHz. A 100F lithium-ion capacitor (LIC) is used as a power source due to its high energy and power densities. A drive electronic circuit is implemented on a flexible printed circuit board (PCB) and delivers $30V_{pp}$ sinusoidal signal to the acoustic propeller. The completed system is 18 x 18 x 38 mm^3 in volume and weighs 12.56 grams, resulting in a mass density of 1.020 g/cm^3. The acoustic propulsion generated by the acoustic propeller is measured to be 18.68μN with the electrical power of 358.7mW consumed by the propeller. Both vertical and horizontal propulsions are demonstrated successfully in sodium polytungstate (SPT) solution.

KEYWORDS

Acoustic propulsion, Wireless acoustic propeller, Underwater propeller, Self-focusing acoustic transducer, Lithium-ion capacitor.

INTRODUCTION

Underwater robotic systems can perform various tasks such as exploring, salvaging, and delivering in industrial and biomedical environments. Especially, miniaturized robots or microrobots with dimensions in micron scale will be extremely useful for healthcare, as those can deliver drugs and also carry imaging or surgical systems inside human body. Propulsion of underwater robots can be done with a mechanical propelling fan, which is easily worn and torn out, or can potentially damage the surrounding environment with its moving parts. Mimicking fish movement with structures like fish fins can be used for underwater propulsion, but still requires moving parts [1]. On the other hand, a self-focusing acoustic transducer (SFAT) can generate propulsion force in liquid without any moving parts, as it can produce focused ultrasound capable of acoustic propulsion. Thus, we have developed a SFAT-based underwater acoustic propeller by attaching an air-cavity reflector (made with an acrylic sheet) on the top side of the transducer to allow the waves (generated by SFAT) only on the bottom side of the SFAT, so that there is a net propulsion force directed upward, as illustrated in Fig. 1. Although, we reported an immersive underwater acoustic propeller previously [2], our previous work required electrical wires to deliver electrical power to the SFAT which, by the way, requires relatively high instantaneous power.

In this paper, we present the first acoustic propeller operating free of electrical wires through using a lithium-ion capacitor as the power source. This paper describes the design and fabrication process of the propeller along with the electronic circuits implemented on a flexible printed circuit board (PCB). Also presented are the experiment results in both vertical and horizontal propulsions.

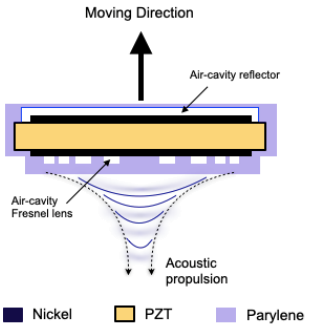

Figure 1: Conceptual illustration of generating acoustic propulsion with a Self-Focusing Acoustic Transducer (SFAT) with air cavity reflector and Fresnel air-cavity lens.

DESIGN AND FABRICATION PROCESS

System Design

The SFAT-based acoustic propeller integrates four parts on a single stand-alone platform (Fig.2): a self-focusing acoustic transducer for focused ultrasound (2.32MHz), a drive electronics on a flexible printed circuit board , a lithium-ion capacitor (LIC) for power, and a coil for wireless charging of the LIC. The flexible PCB wraps around the LIC located in the center, while the wireless power-charge receiving (WPRX) coil and the SFAT are placed at the top and bottom, respectively. The completed system (Fig.2b) is 18 x 18 x 38 mm^3 in volume and weighs 12.56 grams (which can be adjusted by filling the inside air volume with liquid or weight, if desired), resulting in a mass density of 1.020 g/cm^3.

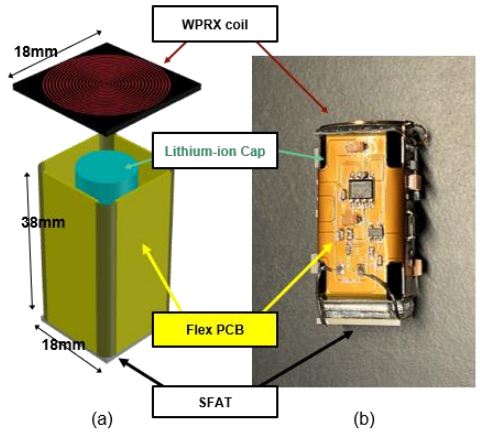

Figure 2: (a) Conceptual 3D schematic of the acoustic propeller and (b) photo of the completed acoustic propeller. Lithium-ion capacitor (LIC) cannot be seen in the photo as it is wrapped by the flexible printed circuit board (PCB).

978-1-940470-04-7/HH2022/$25©2022TRF
DOI 10.31438/trf.hh2022.55

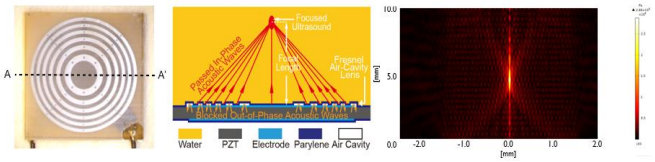

(a) (b) (c)

Figure 3: (a) Top-view photo of SFAT showing six air-cavity Fresnel rings on a 1-mm-thick PZT substrate, (b) schematic view of the cross-section across the dashed line (A-A') in (a), showing the focusing principle of SFAT, and (c) a finite element method (FEM) simulation, showing 5.0, 0.1 and 1.0 mm of focal length, diameter and depth, respectively.

Propeller Design and Fabrication

Self-focusing Acoustic Transducer (SFAT) is fabricated on 1-mm-thick lead zirconate titanate (PZT) substrate sandwiched by top and bottom nickel electrode layers. The nickel layers are patterned as circles, which are aligned concentrically, with the top circle having a larger diameter to compensate the top and bottom alignment error. The transducer focuses ultrasound through the air-cavity Fresnel half-wavelength band (FHWB) lens over the top electrode (Fig. 3), and the radii of the air-cavity rings are designed according to

$$R_n = \sqrt{n\lambda\left(F + \frac{n\lambda}{4}\right)} \qquad (1)$$

where λ and F are ultrasound wavelength in liquid and focal length (5 mm in this case), respectively [3]. Equation 1 ensures that the path length from each ring boundary to the focal point is longer than the focal length (F) by integer multiple (n) of half wavelength (i.e., nλ/2). The air cavity annular rings on the top electrode block the acoustic waves due to the acoustic impedance mismatch between air (0.4kRayl) and liquid (over 1MRayl), while the non-air-cavity rings allow the waves to pass through, so that the waves *constructively* interfere at the focal point, producing magnified intensity [4]. Finite element method (FEM) simulation (Fig. 3c) shows 5.0, 0.1, and 1.0 mm of focal length, focal diameter, and focal depth, respectively.

The air-cavity Fresnel lens is made of Parylene-D with AZ5214 photoresist acting as a sacrificial layer in the brief fabrication steps for SFAT shown in Fig. 4. The sacrificial layer defines the Fresnel lens and is removed with acetone to form the

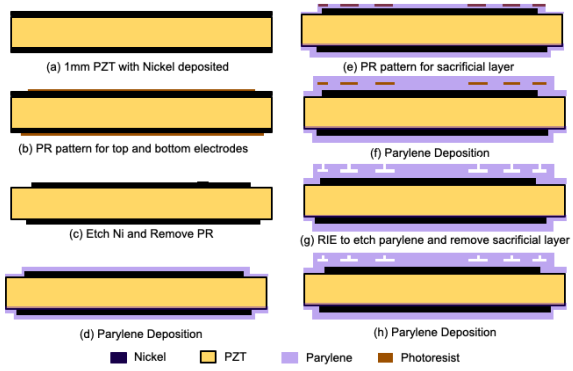

Figure 4: Brief fabrication steps of the SFAT used for the acoustic propeller.

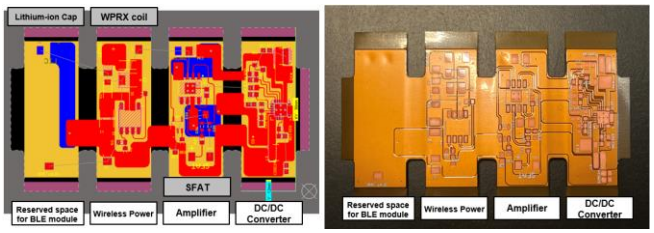

(a) (b)

Figure 5: (a) Schematic of the PCB layout showing the four main circuits sections and the places where SFAT and LIC will be connected and (b) photo of the fabricated flexible PCB before being folded into a 3D shape shown in Fig. 2b.

air-cavity rings through release holes made on Parylene-D with O_2 Reactive Ion Etching (RIE). The release holes are sealed with another Parylene layer deposition. On a fabricated SFAT, a laser-machined acrylic sheet (2 mm thick) is glued to the opposite side of the Fresnel lens in order to form the air-cavity reflector shown in Fig. 1, so that the propulsion may be only from one side.

When a sinusoidal voltage signal with its frequency matching the PZT's thickness-mode resonance (2.32MHz for 1-mm-thick PZT) is applied between the top and bottom electrodes, the PZT effectively generates acoustic waves, which are focused through the air-cavity FHWB rings. The waves from the side of the PZT where there is no lens are blocked by the air reflector made of the acrylic sheet to prevent any propulsion from that side which would have reduced the propulsion.

Electronic Circuit Design

The drive electronics made on a flexible PCB (Fig. 5) is composed of a DC/DC converter (Texas Instruments' TPS65131), an oscillator (Analog Devices' LTC1799) for generating a square wave (1kHz - 33MHz) and a power amplifier (Texas Instruments' THS3095), as illustrated in Fig. 6. The drive electronics delivers $30V_{pp}$ 2.32MHz sinusoidal signal to the propeller when powered by a 100F lithium-ion capacitor (Xeno Energy's XLC-1030). The output of a fully charged LIC is 3.8 V_{DC} and a DC/DC converter converts the input into +/-15V_{DC} dual outputs. The gain of the power amplifier is adjusted so that the output signal of a power amplifier may be $30V_{pp}$ 2.32MHz sinusoidal signal with sufficiently large power for the SFAT.

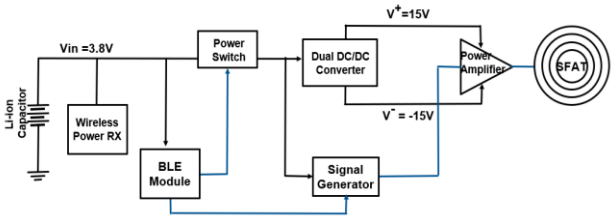

Figure 6: Functional block diagram of the circuit showing the power rails (black lines) and the signal rails (blue lines). Bluetooth low energy (BLE) module is to control the frequency and timing, and will be added in future.

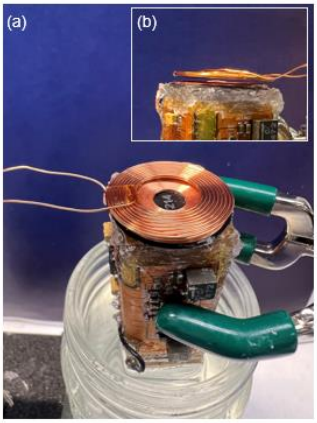

Figure 7: Photos showing (a) wireless charging of LIC, while the SFAT in the propeller is immersed in water to prevent thermal damage of the SFAT during the charging and (b) air gap between transmission (TX) and receiving (RX) coils maintained by a pair of rigid wires and a clamp holding TX and RX coils, respectively, with alignment between TX and RX coils achieved by a 3-axis micromanipulation stage.

Since the SFAT requires high instantaneous power to generate the acoustic propulsion, a power source with high output *power* density is required. Moreover, a power source with high *energy* density is needed to be able to operate the acoustic propeller for sufficient time. A lithium-ion battery (LIB), which is commonly used in a portable electronic device, has high energy density but low power density. On the other hand, a super capacitor, another power source, offers a relatively high instantaneous power density but low energy density. Furthermore, a super capacitor suffers from self-discharging, which gets worse at a higher temperature. Lithium-ion capacitor (LIC) is chosen over LIB and super capacitor due to its high energy and power densities. Moreover, LIC has an extremely low self-discharging characteristic even at a high temperature. Table 1 compares LIC with super capacitor and LIB.

Table1. Comparison of lithium-ion capacitor with super capacitor and lithium-ion battery

	Super Capacitor	Lithium-ion Capacitor	Lithium-ion Battery
Energy Density	Low (< 10Wh/kg)	Medium (~10Wh/kg)	High(10 -100Wh/kg)
Power Density	Medium(1kW/kg)	High(1k -10kW/kg)	Low(~0.1kW/kg)
Operating Voltage Range	0 - 3.0V	2.2 - 3.8 V	2.5 - 4.3V
Charge/Discharge Cycle	100k	100k	500 -1000
Self Discharge	Susceptible	Very low	Very low

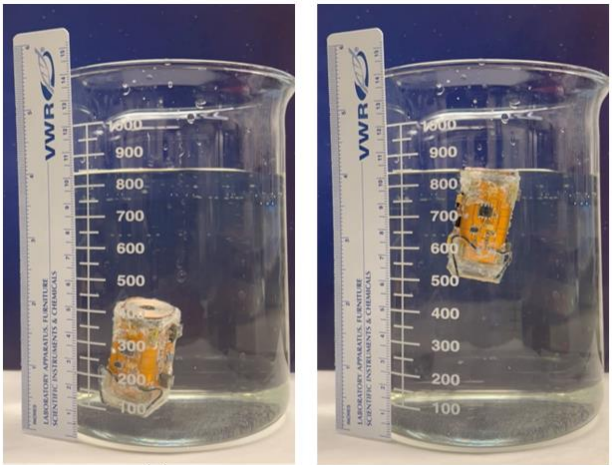

Figure 8: Photos of the acoustic propeller (a) floating close to the floor without acoustic propulsion and (b) soaring up to the surface of sodium polytungstate (SPT) solution (1.15g/cm^3) when the SFAT generates the acoustic propulsion.

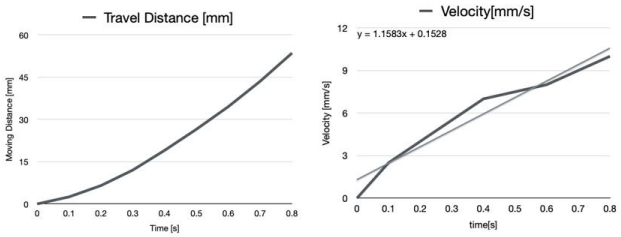

(a) (b)

Figure 9: (a) Measured traveling distance (in mm) and (b) velocity (in mm/s) of the acoustic propeller from the vertical propulsion shown in Fig. 8. The traveling distance is measured in every 100ms and the averaged acceleration is calculated to be 1.16 mm/s^2

The chosen 100F LIC is capable of delivering enough power and energy to the acoustic propeller to generate the acoustic propulsion in the water to make the propeller propagate stably for several minutes. The LIC is fully discharged before assembling the components for the propeller, in order to prevent potential damage to the SFAT (in air) due to the power from the LIC. After assembling all the components, 20µm thick Parylene is conformally deposited over all the surface of the assembled acoustic propeller to make the unit immersible in liquid. The LIC is wirelessly charged (with Taida Century Technology's T3168) through a wireless charging receiver (WPRX) coil (3- layers, 26µH, 1.1A, 520mΩ max) on the top of the assembled propeller unit, as shown in Fig. 7. The current flowing through the wireless charging coils is limited to 700mA to avoid potential damage to the Parylene layer due to excessive heat when the air-gap between the transmitting and receiving coils is less than 1mm.

EXPERIMENT RESULTS

Vertical Propulsion

For testing and quantifying the acoustic propulsion, the mass density of liquid solution is adjusted to be 1.15g/cm^3 by adding sodium polytungstate (SPT) powder into deionized water (DI water) at a weight ratio of 1:4.89 (SPT:water) such that the acoustic propeller sinks down close to the floor without generating any propulsion but still floats above the floor (Fig. 8a). The acoustic propeller floating in the liquid experiences the gravitational force downward as well as the upward buoyancy F_B

$$F_B = \rho g V \qquad (2)$$

where ρ, g and V are the mass density of liquid, gravitational constant, and object volume, respectively. As buoyancy is a function of the density of liquid, the position of the acoustic

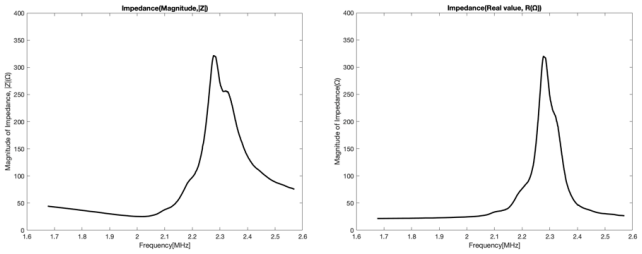

(a) (b)

Figure 10: Measured (a) impedance magnitude and (b) resistance portion of the impedance of the SFAT immersed in SPT solution, as a function of frequency.

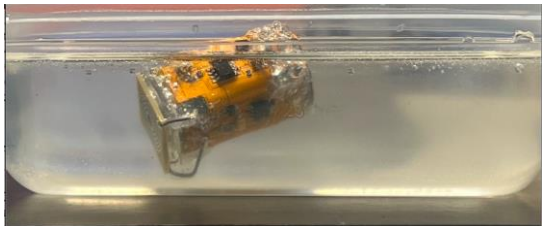

Figure 11: Photo of the acoustic propeller floating horizontally on sodium polytungstate (SPT) solution (1.20g/cm³).

propeller can be adjusted by changing the mass density of SPT solution.

When the SFAT generates acoustic propulsion upward, the propeller soars up to the surface of the liquid (Fig. 8b). With a continuous sinusoidal signal driving the propeller, the signal amplitude decreases gradually after being at 30 V_{pp} for 1.5 minutes, due to the LIC running out of energy, and when the amplitude becomes lower than 18 V_{pp}, the acoustic propulsion stops, after which the propeller still moves due to inertia for a while.

The acceleration of the vertical propulsion is obtained through measuring the traveling distance as a function of time (Fig. 9). From the acceleration, the acoustic propulsion force is calculated to be 18.68μN, when the LIC is fully charged, ignoring the friction and drag forces that resist the motion of the acoustic propeller.

The electrical power P_E consumed by the SFAT can be calculated with

$$P_E = \left(\frac{V_{rms}^2}{|Z|^2}\right) \times R \qquad (3)$$

where V_{rms}, $\underline{Z}$, and R are the root-mean-square (rms) voltage, SFAT's impedance, and the real part of the impedance, respectively. To measure the SFAT's impedance, we measure SFAT's one-port reflection coefficient S_{11} with a network analyzer (Hewlett-Packard's 8753D) while SFAT is immersed in the same SPT solution, and calculate the impedance, Z (=R+jX), using

$$Z = 50\,\Omega \times \frac{1+S_{11}}{1-S_{11}} \qquad (4)$$

The impedance magnitude |Z| and resistance R of the SFAT at its resonant frequency, which is measured as 2.27MHz, are 321.61 and 319.89 Ω, respectively (Fig. 10). However, at the 2.32MHz which the electronic circuit generates and delivers to the SFAT, |Z| and R are measured as 256.09 and 209.10Ω, respectively. Thus, the electrical power is to be 358.70mW, and the propulsion force per electrical power consumption by the SFAT is 52.07 μN/W.

Horizontal Propulsion

To move the acoustic propeller horizontally, SPT powder is added to DI water at a weight ratio of 1:3.54, resulting in the SPT solution's mass density being 1.20g/cm³ which leads to the acoustic propeller floating on the top surface of the solution while the SFAT part is still immersed in the solution as shown in Fig. 11. Since some portion of the acoustic propeller is exposed to the air, it experiences more drag force than the vertical movement. Also, as it is tilted with an angle of 27° on the surface, only 89% (cos27°) of acoustic propulsion contributes to the lateral motion.

Another way of estimating the acoustic propulsion is using a drag force. An object moving at a velocity, v, in a fluidic media experiences a drag force F_d

$$F_d = \frac{1}{2}\rho v^2 A C_d \qquad (5)$$

where ρ, A and C_d are the liquid density, cross-sectional area, and drag constant, respectively. When the acoustic propeller travels with the constant velocity, the acoustic propulsion force is equal to the drag force so that there is zero net force, leading to no acceleration. With the measured steady-state velocity of the acoustic propeller moving horizontally at 6 mm/s, the drag force F_d is calculated to be 11.51 μN. The calculated acoustic propulsion in the horizontal motion using the steady-state drag is smaller than that of the vertical propulsion because the propeller receives lower voltage and power from the LIC by the time when the acoustic propeller reaches the steady-state velocity.

SUMMARY

This paper presents a wireless acoustic propeller based on a self-focusing acoustic transducer (SFAT) powered by lithium-ion capacitor (LIC), particularly on the design and implementation of the propeller and its drive electronics along with the integrated system which includes the LIC power source. Also, experimental results in both vertical and horizontal propulsions have been demonstrated and characterized in sodium polytungstate solution with mass density of 1.15 - 1.20 g/cm³. The wireless acoustic propeller (18 x 18 x 38 mm³ in volume and 12.56 grams in weight) integrates all the SFAT-based propeller, dive electronics and power source. And a 2.32 MHz sinusoidal signal is obtained from the integrated signal generator, and amplified to 30 V_{pp} through the power amplifier powered by ±15 V_{DC} which is produced through the DC/DC converter from 3.8 V_{DC} of the LIC integrated in the acoustic propeller and wirelessly charged while the SFAT is immersed in liquid. When the 30 V_{pp} is applied to the propeller, it generates the maximum acoustic propulsion of 18.68μN, while the SFAT is measured to consume 358.70mW.

ACKNOWLEDGEMENTS

This paper is based on the work supported by National Science Foundation under grant ECCS2017926.

REFERENCES

[1] R. Du, Z. Li, K. Youcef-Toumi, and P. Valdivia y Alvarado, eds. "Robot fish: Bio-inspired fishlike underwater robots," Springer, 2015.

[2] L. Zhao and E.S. Kim, "Subminiature Underwater Propeller with Electrical Controllability of Steering," 2021 IEEE International Ultrasonics Symposium, 2021 pp. 1-4, doi: 10.1109/IUS52206.2021.9593504.

[3] K. Yamada, H. Shimizu, "Planar-Structure Focusing Lens for Acoustic Microscope", Journal of the Acoustical Society of Japan (E), vol.12, no.3, pp.123-129, 1991

[4] J. Lee and E.S. Kim, "Phase Array Ultrasonic Transducer Based on a Flip Chip Bonding with Indium Solder Bump," IEEE International Ultrasonics Symposium, Virtual Symposium, September 11 - 16, 2021

CONTACT

*J. Lee, tel: +1-206-902-8988; lee172@usc.edu

A FULLY STERILE, COST-EFFECTIVE, RAPIDLY ASSEMBLED, 3D PRINTER FOR BIOPRINTING OF ELECTROGENIC CELL CONSTRUCTS TO DEFINE FUNCTIONAL LAYERS AND ENHANCE SENSITIVITY OF CELL-BASED BIOSENSORS

Cacie Hart, Frank Sommerhage, and Swaminathan Rajaraman
University of Central Florida, Orlando, FL, USA

ABSTRACT

Here we present the conversion of an "off-the-shelf", cost-effective Fused Deposition Modelling (FDM) 3D printer to a fully functional and sterile bioprinter. Additionally, we have developed 3D printed micro-nozzles and compared the bioprinting capabilities of the micro-nozzles to that of standard hand plating, as well as bioprinting thorough a syringe needle. In order to characterize the bioprinting capabilities of the newly developed printer, cardiomyocyte HL-1 cells (a commonly used electrogenic cell line) were successfully printed and observed optically for 5 days *in vitro* (DIV). The micro-nozzle-based printing reports superior print quality and smaller confined geometries compared to the other methods suggesting efficient coupling of cells to potential functional biosensors and biomarkers further demonstrated on plasmonic Interdigitated Electrodes (pIDEs) **[1]**.

KEYWORDS

Bioprinting, 3D Printing, Electrogenic Cells, Micro-nozzles, HL-1 cells, Cell-based Biosensors

INTRODUCTION

In extrusion bioprinting, material (bioink and cells) is dispensed through a nozzle (or syringe) using either pneumatic or mechanical pressure (i.e. plunger, screw, etc.). The larger nozzle size of extrusion printers leads to less clogging when compared to inkjet printing **[2]**. This means that the potential to deposit higher densities of cells exists and that a wider range of bioinks with varying viscosities can be used. Extrusion bioprinting is typically a continuous flow process; however, in some cases, discrete spots may be deposited **[3]**.

Commercial extrusion bioprinters are exceedingly expensive (upwards of $200,000); thus, this technique is often overlooked in laboratory settings despite this technology being the most promising of the three major bioprinting technologies for clinical translation **[4]**. Most "hobby" 3D printers are extrusion printers, and these are extremely inexpensive and relatively open source since the original patents for this technology (FDM) expired some time ago. For this reason, there is potential for the cost to greatly decrease and to implement all the advantages of this technique by converting an "off-the-shelf" FDM printer to a bioprinter, similar to what was done for inkjet printing.

In addition to the cost, simplicity and the ability to "Do it Yourself (DIY)", extrusion bioprinting has many advantages over other techniques which can be exploited to define finicky electrogenic or electrically active cellular constructs. Extrusion printing allows for greater deposition and printer speed, which can facilitate scalability in a timely manner **[5]**. Extrusion bioprinting can accommodate a wide variety of bioinks inks including cell aggregates, cell-laden hydrogels, micro-carriers, and decellularized matrix components, while other techniques are only capable of printing cell-laden hydrogels **[6-9]**. Additionally, bioprinting at high cell densities is currently feasible only using extrusion bioprinting. Such a bioprinting process is biocompatible with reasonably small process-induced cell damage and injury compared to other techniques **[10, 11]**. Additionally, it is capable of producing anatomically correct porous constructs, which is challenging with other methods. Most importantly as mentioned earlier, from an implementation perspective, extrusion bioprinting techniques are easy to implement and can be used by those with limited exposure to the technology and laboratories in low-resource settings.

The major disadvantage of extrusion bioprinting is the limited resolution. The minimum feature size is generally well in excess of 100 µm **[10]**. This resolution is considerably lower than other techniques. Inkjet and laser-based bioprinting can achieve resolutions of 50 µm and 5 µm, respectively **[4]**.

Notable work on bioprinting using extrusion techniques has been performed by several groups. Khalil and Sun report on the extrusion bioprinting of 3D hydrogel scaffolds. In this study, rat heart endothelial cells were encapsulated in various hydrogel solutions, including alginate, fibrin, and chitosan, and printed. Their minimum feature sizes were shown to be approximately 250 µm **[12]**. Bertassoni et al. showed direct-write bioprinting of cell-laden methacrylated gelatin hydrogels. This work involved printing HepG2 and NIH3T3 cells suspended in a methacrylated gelatin hydrogel using a commercial extrusion bioprinter (NovoGen MMX Bioprinter). They showed minimum feature sizes of ~ 500 µm and their hydrogels needed ultraviolet exposure to set into defined patterns **[13]**. There has been other work reported in this area as well, however, extrusion bioprinting of "tricky to print and grow" electrically active cell constructs is largely missing from literature.

In this work, we fully convert a commercial "off-the-shelf" FDM printer into a cost-effective and customizable sterile bioprinter. Additionally, we demonstrate printing of electrogenic cells through both a hypodermic needle and a 3D printed micro-nozzle demonstrating reduced size constructs and superior coupling to underlying surfaces. The bioprinting process is compared to traditional hand plating as depicted schematically in **Fig. 1**. Lastly, we depict feasibility of cellular coupling by printing electrogenic cells atop plasmonic Interdigitated Electrodes **[1]**.

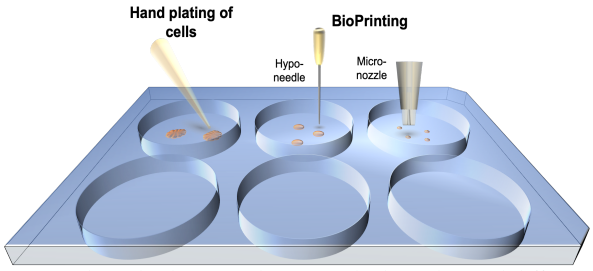

Fig.1*: A broad schematic depicting the hypothesized differences between hand plating (left), hypodermic hollow needle bioprinting (center) and micro-nozzle-based bioprinting in a 6-well plate. The size of the printed dots is expected to reduce as we move to the right.*

MATERIALS AND METHODS

A Tronxy X1 printer was fully assembled inside a biosafety cabinet to ensure sterility from the onset. All components of the

978-1-940470-04-7/HH2022/$25©2022TRF
DOI 10.31438/trf.hh2022.56

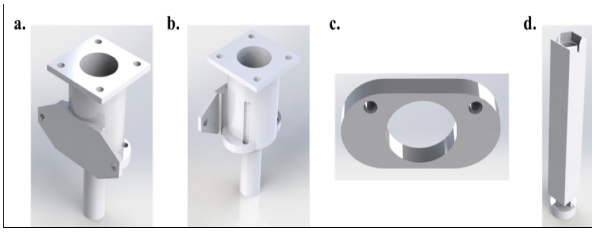

***Fig. 2**: Syringe pump schematics: a. and b. Final syringe pump body design. Designed to fit directly onto the extruder plate of the Tronxy X1; c. Syringe holder designed to keep the syringe fixed to the syringe pump during printing; d. Syringe insert. Designed to fit rubber syringe gasket for improved performance. The M5 hex nut is glued to the insert to ensure perfectly coupled movement.*

printer, as well as tools, were heavily sprayed with 70% isopropyl alcohol prior to introduction into the biosafety cabinet. The sterile environment of the biosafety cabinet needed to be maintained, as well. The purchased polymer extruder was not affixed to the printer, as a custom-built syringe pump was attached in its place.

The syringe pump was designed in SolidWorks and 3D printed on a separate RepRap FDM 3D printer (Tevo Tarantula) in 1.75mm polylactic acid (PLA) plastic in a rectilinear pattern with a 25% infill density at 35 mm/s with an extruder temperature of 200°C and a bed temperature of 60°C. The syringe pump was comprised of three parts: (1) the body (**Fig. 2A and B**), (2) the syringe holder designed to keep the syringe fixed to the syringe pump during printing (**Fig. 2C**), and (3) the syringe inserts (**Fig. 2D**).

In order to demonstrate smaller print sizes two different printing technologies were compared: a commercially purchased 30G hypodermic hollow needle (from BD) and 3D printed micro-nozzles. The latter devices were designed in SolidWorks. Outer nozzle dimensions were designed to a height of 16.4 mm and width of 6.25 mm at the top and 250 µm at the bottom (**Table I**). The inner nozzle dimensions were 4.25 mm top opening with a height of 6.4 mm, followed by a tapered cone area with a height of 5 mm, followed by a cylinder of 1 mm height and 100 µm width, and finally another cone leading to the opening that starts with a width of 100 µm and ends with 250 µm opening and is 500 µm in height. This design is subsequently printed on an Asiga Digital Light Processing (DLP) 3D Printer in High Temperature (FLAMHT01) resin from

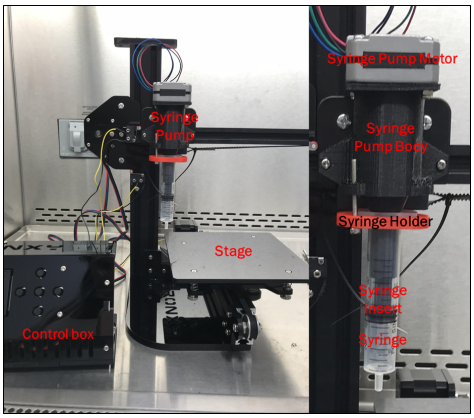

***Fig. 3**: Fully converted Tronxy X1 3D printer inside a biosafety cabinet. Left: wide view showing the entire set-up including the control box, stage, and syringe pump. Right: close-up of the syringe pump.*

FormLabs. After printing, the micro-nozzles were subjected to a

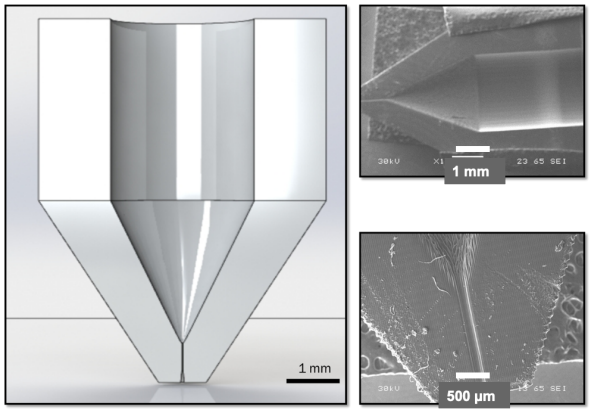

***Fig. 4**: 3D printed micro-nozzle: Left: SolidWorks schematic showing the intended design of the nozzle; Right Top: SEM of the full micro-nozzle; Right Bottom: SEM of the micro-nozzle outlet through which cells are printed/extruded.*

previously developed rigorous post-print treatment in order to ensure biocompatibility with cells **[14].**

Electrogenic cell constructs (HL-1 cells) were printed in a 3% w/v gelatin solution and maintained as previously described **[14, 15]**. Cells were printed using 30G dispensing needles, as well as 3D printed micro-nozzles on separate 6-well plates and pIDE substrates. Additionally, hand plating of cells on a third 6-well plate was used as a control. Cells were grown for 5 days *in vitro* (DIV) and then imaged using confocal microscopy (Keyence BZ-X800). Live/Dead assays was performed at 5DIV using previously reported techniques **[14]** after observation of cells throughout the time period.

RESULTS AND DISCUSSIONS

Extrusion printing of cells was modeled phenomenologically by Nair et al. **[16]**. This model predicts the viability of live cells in extrusion printing as function of nozzle diameter and shear pressure **[16]**. Plugging in the value of the measured 30G needle diameter (~312µm) and the micro-nozzle design diameter (250µm) in test shear pressures provides ***in excess of 90% cellular viability in both cases: 96.21% for hypodermic needle and 91.19% for micro-nozzle*** increasing the confidence of achieving successful results with our bioprinter design.

A Tronxy X1 printer was successfully assembled inside of a biosafety cabinet to ensure sterility from the onset. **Fig. 3** depicts an optical micrograph of the fully assembled printer. The micro-nozzle moves in the x and z directions, while a stage moves in the y direction. This gives the ***user complete special control*** of the cellular deposition process. In addition, ***micro-nozzles were successfully printed*** and post-treated for biocompatibility as depicted in the design and SEM images (**Fig. 4**).

Table I depicts the "gross" and "fine" features of the 3D printed micro-nozzles. The "gross" features printed close to the design value. However, the "fine" features did not have the same result. The cone structure at the bottom of the micro-nozzle could not be resolved. Possible design iterations, print angle variations and material changes are envisioned in future versions of the micro-nozzle to improve design to device of this component.

Initial testing of the converted 3D printer required many test prints. While the focus remained on dot printing due to the nature of the biosensor design (circular microelectrode arrays (MEAs) and pIDEs) and cell coupling to these sensors in our laboratory **[17]**, ***several other patterns were explored and printed***. These patterns can be observed as micrographs in **Fig. 5**. During this phase of the bioprinter characterization process, it was found that blanket coating

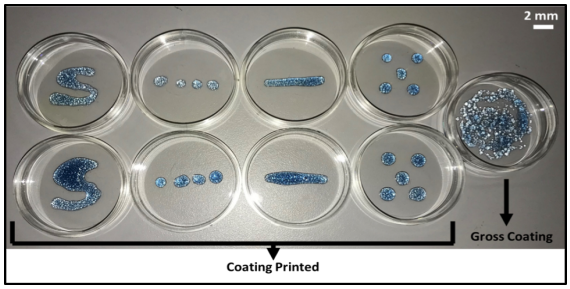

Fig. 5*: Cells were printed in a variety of patterns. Initially, the petri dishes were grossly coated with fibronectin. This resulted in full surface wetting due to the hydrophilic nature of both the petri dish and the fibronectin. To achieve the desired patterns, it was necessary to print the coating, as well. Printed patterns include dots, lines, and an S-shape depicting printing fibronectin followed by bioprinting of HL-1 cell-laden bioink. Scale bar on top is 2mm.*

of the cell plating surface with fibronectin to encourage cells to adhere to the surface caused full surface wetting upon droplet impact due to the hydrophilic nature of both the petri dish and the fibronectin **[18]**.

After these successful initial tests, HL-1 laden bioink was defined on 3 different 6-well plates: hand plating (control), hypodermic needle printing and printing through micro-nozzle. Additionally, test prints were performed on pIDE substrates. In order to compare the bioprinting through the 30G needles and the micro-nozzles with hand plating, the radius of the printed dots was measured throughout 5 DIV prior to the live/dead assay. The hypothesis going in was the 30G and micro-nozzle printing would dramatically reduce the dot sizes and provide the user with better control and coupling of cells to the underlying surface. The ***results followed the expected trends very well over the full assay of five days*** (**Fig. 6**). The hand plated spots were consistently the largest and uncontrolled. They had a radius of 2192 µm ± 111 µm (N=6) when initially plated and grew as expected over the course of the five days. The radius of the hand plated spots grew by 523 µm ± 81 µm over the course of five days. The spots printed with the 30G hollow, hypodermic needle were the "intermediate" sized spots, with their average radius being approximately 1351 µm ± 105 µm

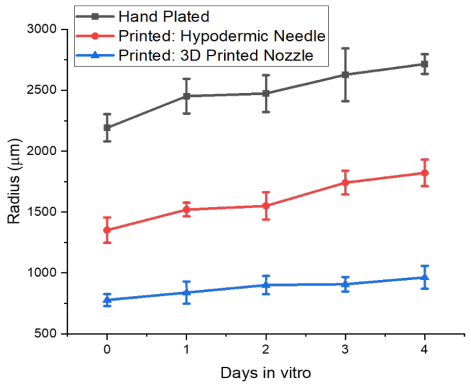

Fig. 6*: Comparison of sizes between spots that were hand plated, bioprinted using a hypodermic needle, and bioprinted using the 3D printed micro-nozzle. The 3D printed micronozzle provides the smallest spot sizes affording best control and cellular coupling to underlying surface.*

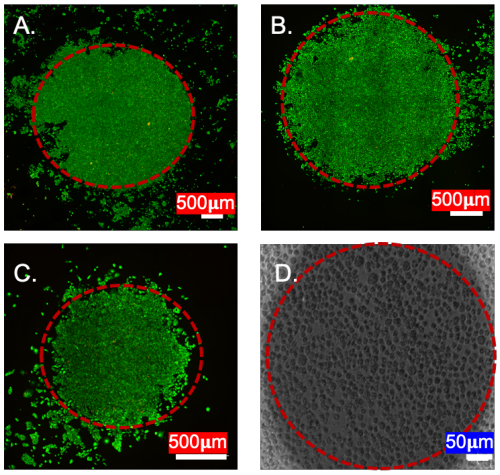

Fig. 7*: Live/Dead example confocal images of the three cell (HL1 cardiomyocytes) plating conditions at 5DIV and cells on pIDE biosensors [1]- A: hand plated; B: bioprinted using a hypodermic needle; C: bioprinted using the 3D printed micro-nozzle; and D: on plasmonic IDE sensors. All four conditions showed similar, excellent viability at 5DIV.*

(N=6) when printed and grew as expected over the course of the five days. The radius of the spots printed with the hypodermic needle grew by 470 µm ± 56 µm. Finally, the spots printed with the 3D printed micro-nozzle were the ***smallest of the three*** with their radius being approximately 775 µm ± 49 µm (N=6) when initially printed. They also grew as expected over the course of the five days. The radius of the spots printed with the 3D printed micro-nozzles grew by 188 µm ± 24 µm over the course of the five days. All three bioprinting conditions demonstrated ***excellent viability*** (**Fig. 7A-C**) in the live/dead assay at 5DIV. Additionally, the ***sensitivity of pIDEs can further be enhanced with superior coupling*** with printed electrogenic cells and the first steps towards this sensitivity enhancement were demonstrated (**Fig. 7D**).

CONCLUSIONS

The converted Tronxy X1 3D printer provides an excellent "do-it-yourself" solution for electrogenic cell bioprinting. Although the lowest achieved resolution is approximately 725 µm and can be improved in future experiments, it still provides better cell-electrode coupling when compared to hand plating on a biosensor device in addition to improving specificity and reducing costs of cell culture. This resolution can be improved with higher resolution micro-nozzles and improved 3D printed designs of these structures.

Table I: Design and Measured Dimensions of the Micro-Nozzle

Dimension	***Design Value***	***Measured Value***
Nozzle Height	*16.4mm*	*~16.4mm*
Top Nozzle Width	*6.25mm*	*~6.24mm*
Bottom Nozzle Width	*250µm*	*150 µm+/-11 µm*
Inner Nozzle Cone Opening	*4.25mm*	*~4.25mm*
Inner Nozzle Cone Height	*6.4mm*	*~6.4mm*
Cylinder Height	*1mm*	*1.5mm*
Cylinder Width	*100 µm*	*150 µm+/-11 µm*
Cone Height	*500 µm*	*Did not define*
Cone Width	*250 µm*	*Did not define*

Feasibility towards coupling these printed cells with biosensors such as plasmonic IDEs were further demonstrated. Moving forward such a technique will be invaluable to emerging areas such as personalized medicine, “clinical trials on a chip” and “patient-on-a-chip” technologies.

ACKNOWLEDGEMENTS

This work was supported by the University of Central Florida both from start-up funding of the PI (Prof. Rajaraman) and a doctoral support award for Ph.D. thesis completion (Ms. Hart).

REFERENCES

[1] C. Hart, K. Kumar, J. Li, J. Thomas, and S. Rajaraman, IEEE JMEMS, vol. 29, no. 5, pp. 1109 – 1111, 2020.

[2] J. He, X. Zhao, J. Chang, and D. Li, "Microscale Electro-Hydrodynamic Cell Printing with High Viability," Small, vol. 13, no. 47, p. 1702626, 2017, doi: 10.1002/smll.201702626.

[3] G. Gao, Y. Huang, A. F. Schilling, K. Hubbell, and X. Cui, "Organ Bioprinting: Are We There Yet?," Advanced Healthcare Materials, vol. 7, no. 1, p. 1701018, 2018, doi: 10.1002/adhm.201701018.

[4] J. Jang, J. Y. Park, G. Gao, and D.-W. Cho, "Biomaterials-based 3D cell printing for next-generation therapeutics and diagnostics," Biomaterials, vol. 156, pp. 88-106, 2018/02/01/ 2018, doi: https://doi.org/10.1016/j.biomaterials.2017.11.030.

[5] I. T. Ozbolat and M. Hospodiuk, "Current advances and future perspectives in extrusion-based bioprinting," Biomaterials, vol. 76, pp. 321-343, 2016/01/01/ 2016, doi: https://doi.org/10.1016/j.biomaterials.2015.10.076.

[6] T. Boland, V. Mironov, A. Gutowska, E. A. Roth, and R. R. Markwald, "Cell and organ printing 2: Fusion of cell aggregates in three-dimensional gels," The Anatomical Record Part A: Discoveries in Molecular, Cellular, and Evolutionary Biology, vol. 272A, no. 2, pp. 497-502, 2003, doi: 10.1002/ar.a.10059.

[7] V. Mironov, R. P. Visconti, V. Kasyanov, G. Forgacs, C. J. Drake, and R. R. Markwald, "Organ printing: Tissue spheroids as building blocks," Biomaterials, vol. 30, no. 12, pp. 2164-2174, 2009/04/01/ 2009, doi: https://doi.org/10.1016/j.biomaterials.2008.12.084.

[8] J. Malda et al., "25th Anniversary Article: Engineering Hydrogels for Biofabrication," Advanced Materials, vol. 25, no. 36, pp. 5011-5028, 2013, doi: 10.1002/adma.201302042.

[9] R. Levato, J. Visser, J. A. Planell, E. Engel, J. Malda, and M. A. Mateos-Timoneda, "Biofabrication of tissue constructs by 3D bioprinting of cell-laden microcarriers," Biofabrication, vol. 6, no. 3, p. 035020, 2014/07/22 2014, doi: 10.1088/1758-5082/6/3/035020.

[10] B. Duan, L. A. Hockaday, K. H. Kang, and J. T. Butcher, "3D Bioprinting of heterogeneous aortic valve conduits with alginate/gelatin hydrogels," Journal of Biomedical Materials Research Part A, vol. 101A, no. 5, pp. 1255-1264, 2013, doi: 10.1002/jbm.a.34420.

[11] S. Boularaoui, G. Al Hussein, K. A. Khan, N. Christoforou, and C. Stefanini, "An overview of extrusion-based bioprinting with a focus on induced shear stress and its effect on cell viability," Bioprinting, vol. 20, p. e00093, 2020/12/01/ 2020, doi: https://doi.org/10.1016/j.bprint.2020.e00093.

[12] S. Khalil and W. Sun, "Biopolymer deposition for freeform fabrication of hydrogel tissue constructs," Materials Science and Engineering: C, vol. 27, no. 3, pp. 469-478, 2007/04/01/ 2007, doi: https://doi.org/10.1016/j.msec.2006.05.023.

[13] L. E. Bertassoni et al., "Direct-write bioprinting of cell-laden methacrylated gelatin hydrogels," Biofabrication, vol. 6, no. 2, p. 024105, 2014/04/03 2014, doi: 10.1088/1758-5082/6/2/024105.

[14] C. Hart, C. M. Didier, F. Sommerhage, and S. Rajaraman, "Biocompatibility of Blank, Post-Processed and Coated 3D Printed Resin Structures with Electrogenic Cells," Biosensors, vol. 10, no. 11, p. 152, 2020. Available: https://www.mdpi.com/2079-6374/10/11/152.

[15] W. C. Claycomb et al., "HL-1 cells: A cardiac muscle cell line that contracts and retains phenotypic characteristics of the adult cardiomyocyte," Proceedings of the National Academy of Sciences, vol. 95, no. 6, pp. 2979-2984, 1998, doi: 10.1073/pnas.95.6.2979.

[16] K. Nair et al., "Characterization of cell viability during bioprinting processes," Biotechnology Journal, vol. 4, no. 8, pp. 1168-1177, 2009, doi: 10.1002/biot.200900004.

[17] N. Azim et al., “Precision Plating of Human Electrogenic Cells on Microelectrodes Enhanced with Precision Electrodeposited Nano-Porous Platinum for Cell-Based Biosensing Applications,” IEEE JMEMS, 28 (1), pp. 50-62, (2019).

[18] F. Grinnell and M. K. Feld, "Fibronectin adsorption on hydrophilic and hydrophobic surfaces detected by antibody binding and analyzed during cell adhesion in serum-containing medium," (in eng), J Biol Chem, vol. 257, no. 9, pp. 4888-93, May 10, 1982.

CONTACT

*Swaminathan Rajaraman, tel: +1-407-823-4339; Swaminathan.Rajaraman@ucf.edu

CONTROLLABLE STATIC BREATH-FIGURE PROCESSES TO FORM ORDERED 3-D MICROSTRUCTURES ON POLYDIMETHYLSILOXANE WITHOUT LITHOGRAPHY AND MOLDING

*Junce Cheng and Tingyi "Leo" Liu**
University of Massachusetts Amherst, MA, USA

ABSTRACT

We report a one-step lithography-free molding-free method to create highly-ordered hexagonally-packed 3-D micro-cavities on a soft polymeric material using a controllable static breath-figure formation process. To study the key control parameters that are missing in the existing literature for breath figure formation, we designed and built a system to monitor the real-time microscopic condensations at the under-curing polymeric interface with synchronous temperature measurement of water vapor and polymer interface altogether. Such a multimodal sensing system enabled us, for the first time, to visualize the entire breath figure formation process and correlate it to several key parameters to control the formation of breath figures.

KEYWORDS

Breath figure, 3-D microstructure, soft material, PDMS, molding-free, lithography-free, highly-ordered

INTRODUCTION

Breath figures are found in our daily lives whenever water vapor in the air condensates on a cold substrate, e.g., the fog on the cold window when a human breathes nearby, such as Figure 1(a). This simple phenomenon attracts great interest in research because the condensed water droplets may reorganize themselves via energy minimization and orientate into a highly ordered hexagonally-packed honeycomb configuration. If water droplets are condensed on a polymer fluid that is under curing, the polymer may be solidified with surface structures with the water condensates working as microscale molds, as depicted in Figure 1 (b).

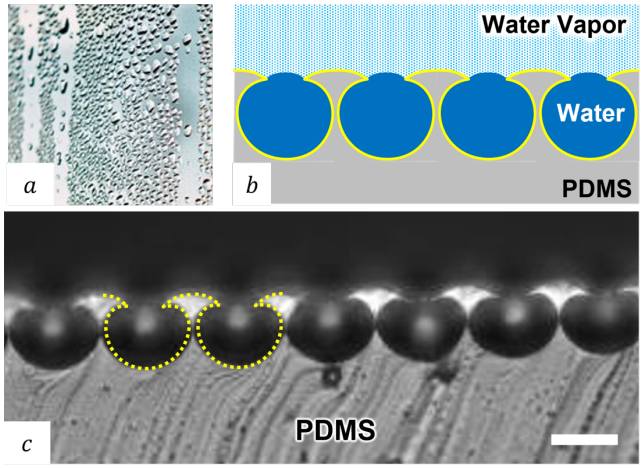

Figure 1: (a) Breath figure found in daily lives where tiny water droplets condensate on a cool aluminum substrate and self-orientate into an ordered dense pattern. (b) Schematic of breath figures formed at the interfaces of liquid PDMS in a humid environment. (c) An optical microscope image of the cross-section of the breath figure structures that were created on PDMS using the method described in this report. The scale bar is 10 μm.

Figure 1 (b) shows an example of this kind of process where the polymer under curing is an elastomer, polydimethylsiloxane (PDMS) [1]. Provided a humid environment, water drops can condense on the cool surface of an uncured PDMS, partially immersing in the PDMS and functioning as a molecularly smooth 3-D micro mold that can be easily removed by evaporating the water droplet once the PDMS is cured, as shown in Figure 1 (c). The well-ordered hexagonally packed breath figures also provide a unique opportunity to create hollow/porous structures and periodic patterns on various polymers that are mostly rigid [2-8]. Overall, the formation of breath figures shows great potential for surface patterning without going through the traditional MEMS processes [9]. Unlike usual micromanufacturing, breath-figures processes do not require a cleanroom setting to obtain micro- and nano-patterns through photolithography, resulting in a low-cost, time-efficient, and simple fabrication. Albeit all the potential advantages listed above, however, almost all of the reported breath figure formation processes were case-to-case successes capable of producing specific breath figures patterns from a particular polymer. This is because there exists a complicated coupled heat transfer relationship between water condensation and evaporation, resulting in the key parameters to obtain controllable breath-figure patterns are not well understood and thus success is largely obtained by trial and error. Therefore, in order to utilize breath figures for manufacturing, we need a better understanding of the underlying mechanisms with quantification of the key parameters contributing to the formation of various breath figures.

Current techniques to form breath figure patterns include dynamic processes [10] and static processes [1] that are highly specific to the processing polymers. In dynamic processes, a water vapor flow is dynamically controlled to maintain the vapor humidity in the process chamber. By tuning the humidity, the outcome breath figures were monitored and studied to help understand the underlying mechanisms [13]. However, due to the uncertainties caused by flow disturbance, the dynamic processes are difficult to repeat, resulting in inconsistent breath figures from process to process. Furthermore, the success of dynamic processes has been restricted to nonelastic polymers where the rigid plastics were dissolved in a volatile solvent that is more suspectable to evaporation than water. The breath figures are formed when both the solvent and water are evaporated. This method may not work for thermally cured elastomers because, rather than purely evaporating the solvent, most elastomers are formed via thermal curing with the development of covalent crosslinks where water droplets may be evaporated before elastomers are cured. The static processes, on the other hand, have been shown to realize breath figure patterns in a more consistent and repeatable manner, as well as on soft elastomers under curing. For example, static processes of uniform hexagonal breath figures formation on polydimethylsiloxane (PDMS) have been reported [1], showing great potential for soft materials patterning applications. However, the underlying mechanism of the breath figures formation in a closed heated container is unclear [1] due to the complicated multi-parameters heat transfer relationship between water condensation and evaporation and the lack of direct visualization in previous experiments [1]. In this paper, we will monitor the real-time temperature and images of breath figure

978-1-940470-04-7/HH2022/$25©2022TRF
DOI 10.31438/trf.hh2022.57

formation with a controllable static process to get a better understanding of the mechanisms behind this static breath figure formation process. Understanding the key controllable parameters like the cooling effect by changing the different supporting materials will help elucidate some of the underlying mechanisms. The existence of various adjustable parameters (e.g., PDMS base to curing agent ratio, PDMS volume, temperature etc.) gives us ample room to dictate the process and generate unique breath-figure patterns for various applications.

THEORY

While the mechanism to form controllable breath figures is somehow unclear, the requirements of water droplets to nucleate and grow on the under-curing polymer due to condensation is beyond question. When hot water vapor in the air encounters a cool liquid pool, water droplets will nucleate on the cool interface, as shown in Figure 2(a), becoming the water condensate required to form breath-figure patterns [3, 14]. Given the sufficiently small water droplets in this nucleation state, the force balance analysis is performed considering only the interfacial forces due to negligible gravitational effect compared to surface tensional effect at this scale. The force or stress balance is given in the two equations below:

$$\sigma_{12} \sin\theta_{12} = \sigma_{13} \sin\theta_{13} \quad (1)$$

$$\sigma_{23} \sin\theta_{13} = \sigma_{12} \sin(\theta_{12} + \theta_{13}) \quad (2)$$

where "1" is water, "2" is PDMS, and "3" is water vapor in our case. For the static breath figures formation process we studied in this report, water, PDMS, and air are put in an enclosed chamber, as shown in Figure 2 (b). In the beginning, the cooling water evaporates by heat, and then water vapor nucleates on the top of the cooling PDMS surface. Then water droplets increase the size because the speed of water condensation is faster than the speed of water evaporation at the interface of liquid water and vapor. Ratios of dimensions of water droplets maintain nearly the same although the surface tensions of water, PDMS, and vapor change slightly with temperature. During the growth of water droplets and crosslinking of PDMS, water droplets assemble themselves as islands in the hexagonal array that rarely merge or collapse [10]. However, the energy balance of assembly and merging is still under research. At the end of the process, PDMS cures completely and becomes warm. Water evaporates and leaves small openings (i.e., mouth) on the top of the PDMS film. Dictated by the interfacial tension between fluids 1, 2, and 3, these openings can be relatively small compared to the size of the cavities embedded in the bulk (e.g., PDMS).

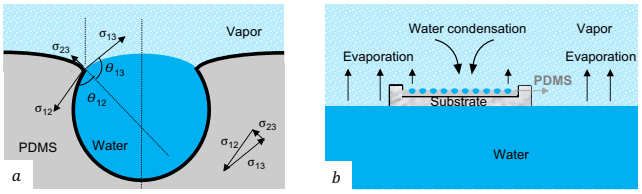

Figure 2: Mechanisms of breath figure: (a) Nucleation of water droplets on a cool PDMS liquid pool under curing. Water droplets are balanced by interfacial tensions at the three-phase interface. The stress at the three-phase interface can be represented by the Neumann triangle (shown in the bottom right corner). (b) In an enclosed heated container, water may serve as the vapor source for condensation while providing cooling to the substrate to induce condensation of water droplets on the liquid PDMS. The balance between the evaporation and condensation heat transfer is the key to forming breath figures in this static process, which is the focus of the current paper.

EXPERIMENTS

To get a better understanding of the mechanisms behind this static breath figure formation process, we designed a real-time multimodal sensing system for the characterization of the formation of breath figure patterns at the top surface of the polymer. Figure 3 shows the schematic of our experimental setup. The real-time visualization of water condensates on the top PDMS surface was monitored by a modular microscope imaging system (VIS vertical Mitutoyo widefield video microscope unit) with a long-working distance lens (20× Mitutoyo Plan Apo SL infinity corrected objective). The real-time temperature monitoring of water vapor and PDMS substrate was realized by the feedthrough connection of two thermocouples (RTD-805 air temperature RTD sensor from Omega Engineering and BB-IM-C08-M3 K-type surface thermocouple sensor from Biaobiao) across the oven (set as 50°C) to measure the temperature at multiple locations inside the enclosed container. Both thermocouples were connected to a data acquisition board (National Instruments NI CompactDAQ 9211) that recorded data at a rate of 4 samples/s. PDMS (Sylgard™ 184) was used as the experimental soft polymer to characterize the formation of breath figure patterns on elastomers. The mixing ratio of the PDMS part A:B (i.e., base vs. curing agent) was fixed at 5:1 in all of our experiments. We poured the degassed PDMS mixture into a holder made of a piece of silicon wafer (as the high thermal conductive substrate) and PDMS walls (to hold the liquid PDMS). The enclosed container has a transparent plastic cover for direct monitoring of condensation and thin metallic walls for conducting the heat from the oven to water to create water vapor.

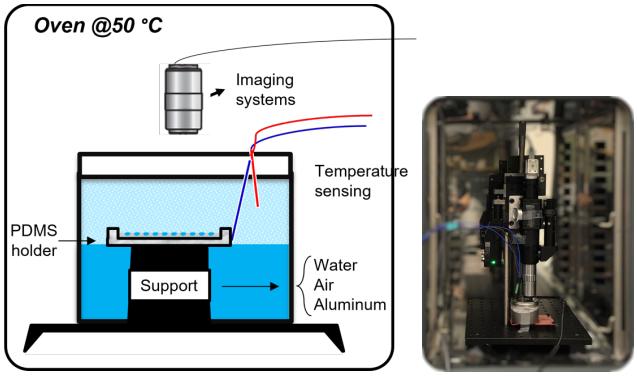

Figure 3: Experimental setup for real-time monitoring breath figure formation. The schematic on the left shows the setup and the picture on the right shows the actual setup built inside a convective oven with sensing and imaging signals feedthrough to NI DAQ and a computer outside the oven. The oven temperature was set to 50°C to slowly heat up the water inside the sealed container and cure the PDMS. The temperature of the water vapor and PDMS holder were measured by thermocouples fed through the container. An imaging system composed of the long-working-distance objective lens and a digital camera was set up to monitor the real-time condensation of water droplets on the under-curing PDMS surface.

To investigate the cooling effect on breath figure formation, the liquid PDMS was supported by three different materials, i.e., water, air, and aluminum, with very different thermal properties. The related heat transfer properties of these supporting materials are summarized in Table 1 together with the experimental breath figure patterns formed on PDMS. Synchronous condensation monitoring and temperature measurements were conducted for these three different supports to study their correlation to the breath figures.

Table 1. Summary of the thermal properties of the materials (water, air, and aluminum) that support the under-curing PDMS, the corresponding top view of the experimental breath figures, and their cross-sectional schematics.

	Water	Air	Aluminum
Thermal conductivity coefficients ($W \cdot m^{-1} \cdot K^{-1}$)	0.598	0.029	239
Isobaric mass heat capacity ($J \cdot g^{-1} \cdot K^{-1}$)	4.181	1.004	0.897
Thermal diffusivity (mm^2/s)	0.143	19	97
Resultant breath figures (top view)	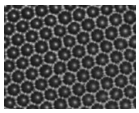		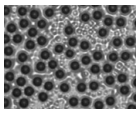
Cross section			

RESULTS AND DISCUSSION

Figure 4 shows the temperature curve of water vapor and the under-curing PDMS fluid. Initially, the temperature of water vapor increased more rapidly than the temperature of under-curing PDMS because air/vapor had a higher thermal diffusivity than water by which liquid PDMS was cooled. This generated a growing temperature difference between the water vapor and liquid PDMS, leading to faster water condensation over evaporation on the liquid PDMS, and thus resulting in water droplets formed on liquid PDMS and breath figures formation. Once the temperature of water vapor was close to the set temperature of the oven, it maintained at this highest temperature while the liquid PDMS temperature kept increasing from oven heating, causing the temperature difference between water vapor and liquid PDMS to become smaller so that water evaporation may be dominating over condensation during the curing of fluidic PDMS.

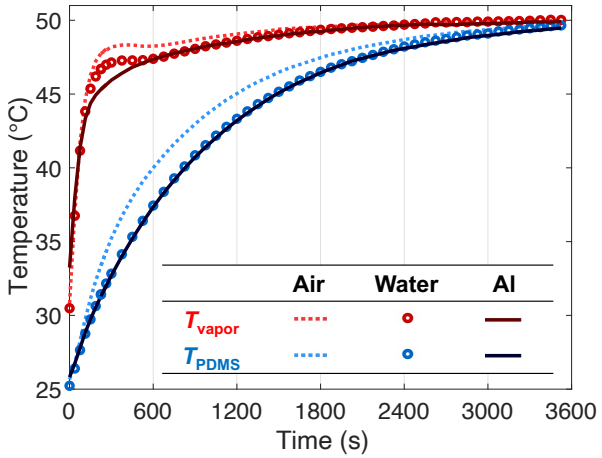

Figure 4: Temperature curves of water vapor (red) and the under-curing PDMS substrate (blue) monitored inside the enclosed container. Three different supports have been studied in this report: air (dots), water (circles), and aluminum (solid lines).

Figure 4 showed the images of breath figure formation on PDMS with different supporting materials in time sequences. In the first 60 seconds, water started to nucleate on the surface of liquid PDMS. The temperature difference was also nearly the same with different supporting materials according to Figure 4. Then, water droplets started to grow and self-orientate in different morphologies. If we sort the area between temperature curves of water vapor and PDMS (i.e., integration of temperature difference over time), the ascending order with an increasing area will be air supports, aluminum supports, and water supports, which is related to the phenomena shown in Figure 4. The breath figures were sparsely packed when the PDMS holder was supported by aluminum while breath figures were found to form shallow cavities (i.e., little water embedded in PDMS) when the PDMS holder was supported by air. Around 1400 seconds later, the morphologies of the top surface of PDMS were fixed, indicating that water condensation and migration are done with droplets reaching the maximum dimensions.

Combining information from Table 1, Figure 4, and Figure 5, we found that (1) while water and aluminum supports had almost overlapping temperature curves after 400 seconds, they showed a major difference around ~200-300 seconds. Such difference reduced the water condensation on the aluminum supported sample so that it did not have enough water droplets to self-orientate to form ordered patterns; (2) while water and air supports produced a similar top view of ordered water droplets, the low thermal conductivity of air prevents sufficient cooling from the water underneath the PDMS under-curing and thus causing a faster temperature increase of the under-curing liquid PDMS. This may result in early PDMS curing before water droplets were embedded in the liquid PDMS. While water droplets could continue to condensate and migrate on top of the increasingly viscous PDMS and evaporate completely in the end, they can no longer be embedded inside the PDMS and thus only produce very shallow cavities.

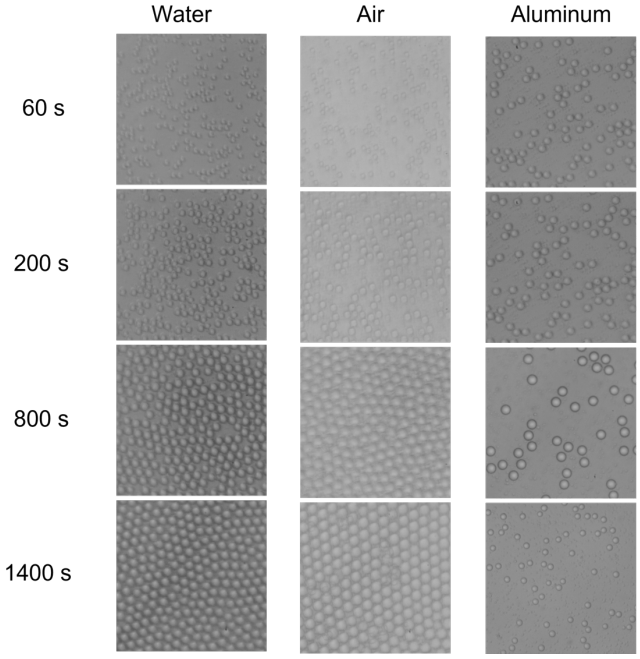

Figure 5: The time series images of breath figure formation on PDMS with different supporting materials. Water allows sufficient condensation and re-organization to form ordered breath figure patterns while the air support created ordered but very shallow patterns and the aluminum support created sparse water condensate. Each figure represents an area of 167 × 167 μm^2.

Using water as the support, highly-ordered breath figure patterns were successfully formed and cured on PDMS with confirmed SEM micrographs, as shown in Figure 6 with both the angled view and cross-section confirming the formation of breath figures. Our sample had a ~3-µm top open mouth and a ~14-µm diameter cavity. The yield of the highly-ordered pattern was ~90% in a 1 inch^2 area. The breath figure patterns assembled as cavity islands where neighboring cavities did not interconnect with each other, similar to other reports such as [10]. Despite of our control experimental study on thermal properties of various supporting materials, there remain many parameters that will affect the level of ordering and surface morphologies of the hexagonally-packed patterns. For example, the viscosity of PDMS fluid, the temperature difference between initial and final conditions, and the thermal properties of the coolant.

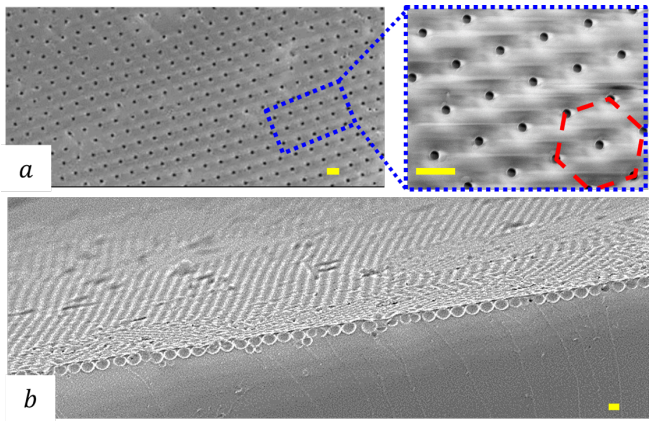

Figure 6: SEM images of breath figure pattern formed by PDMS with crosslinking ratio of 5:1. (a) top view; (b) cross-section view. Scale bars are all 10 µm.

CONCLUSIONS

In this work, we have presented a simple method to create 3-D microstructures on a soft elastomeric material (PDMS) controlled by a static breath figure process. To better understand the underlying mechanism, we have created a multimodal sensing system to simultaneously measure the vapor and liquid temperatures and record optical images of water condensation. Free of lithography and molding/demolding, this method provides an easy yet powerful way to obtain true 3-D microstructures on soft polymeric materials that are difficult to create with traditional MEMS processes. We foresee that the ability to form overhanging (i.e., re-entrant) microstructures without the difficulty of demolding will enable a wide range of applications in super-repellent surfaces, BioMEMS, and wearable devices, etc.

ACKNOWLEDGMENTS

This project is supported by Prof. T. Leo Liu's startup funds provided by the University of Massachusetts Amherst.

REFERENCES

1. S. Shojaei-Zadeh, S. R. Swanson, and S. L. Anna, Highly uniform micro-cavity arrays in flexible elastomer film, *Soft Matter,* 5. 4, (2009).
2. D. Beysens and C. M. Knobler, Growth of Breath Figures, *Physical Review Letters,* 57. 12, (1986).
3. C. M. Knobler and D. Beysens, Growth of Breath Figures on Fluid Surfaces, *Europhysics Letters (EPL),* 6. 8, (1988).
4. A. Steyer *et al.*, Two-dimensional ordering during droplet growth on a liquid surface, *Physical Review B,* 42. 1, (1990).
5. D. Beysens *et al.*, How does dew form?, *Phase Transitions,* 31. 1-4, (1991).
6. A. Steyer, P. Guenoun, and D. Beysens, Hexatic and fat-fractal structures for water droplets condensing on oil, *Physical Review E,* 48. 1, (1993).
7. D. Beysens, The formation of dew, *Atmospheric Research,* 39. 1, (1995).
8. D. Beysens, Dew nucleation and growth, *Comptes Rendus Physique,* 7. 9, (2006).
9. A. Zhang, H. Bai, and L. Li, Breath Figure: A Nature-Inspired Preparation Method for Ordered Porous Films, *Chemical Reviews,* 115. 18, (2015).
10. M. Srinivasarao *et al.*, Three-Dimensionally Ordered Array of Air Bubbles in a Polymer Film, *Science,* 292. 5514, (2001).
11. X. Li, X. Yu, and Y. Han, Polymer thin films for antireflection coatings, *Journal of Materials Chemistry C,* 1. 12, (2013).
12. H. T. Ham *et al.*, Macroporous Polymer Thin Film Prepared from Temporarily Stabilized Water-in-Oil Emulsion, *The Journal of Physical Chemistry B,* 110. 28, (2006).
13. L. Song, Study of Ordered Macroporous Polymer Films by Templating Breath Figures, (2005).
14. A. A. Nepomnyashchy *et al.*, Nucleation and growth of droplets at a liquid-gas interface, *Physical Review E,* 74. 2, (2006).

CONTACT

Prof. T. Leo Liu: Tel: +1 (413) 577-0927; leoliu@umass.edu

MRI COMPATIBLE MULTIFUNCTIONAL CARBON NANOFIBER NEURAL PROBE

*Ziqi Jia, Paritosh Rustogi, Jack W. Judy, and Yong-Kyu "YK" Yoon**
Electrical and Computer Engineering, University of Florida, Gainesville, FL, USA

ABSTRACT

In this work, a neural probe with carbon nanofiber (CNF) electrode and dual microfluidic channel that fabricated with partial exposure method has been demonstrated and tested. The probe has high resolution electrodes array that can achieve simultaneous electrophysiological modulation and drug delivery or fluid sampling. The probe is MRI compatible since it made from carbon and SU8 epoxy. Cyclic voltammetry (CV) and electrochemical impedance spectroscopy (EIS) scan have been applied to the probe to show the electrical properties. The structure and property of microfluidic channels are demonstrated by 3D reconstruction of nano computerized tomography (CT) scan and flow rate test with portable micropump.

KEYWORDS

Multifunctional Neural Flexible Probe, Carbon Nanofiber, MRI Compatible, Partial Exposure

INTRODUCTION

Ever since the first neural signal collected by tungsten wire in 1957 [1], neural probes capable of electrophysiological recording have helped neuron science researchers to develop deeper understanding to the dynamics of neuron cells, brain circuits and their relationship with animal behaviors [2]–[5]. After years of evolution, the neural probes nowadays can not only detect or deliver electrical signals, but also capable of drug delivery, fluid sampling and optical signal transmitting for optogenetic applications [6]–[8] These additional functions enable the bi-directional communications and lead to higher spatial or temporal resolutions.

Besides the commonly used electrical modulation, chemical modulation also plays an important role in neuropathology, such as the characterization of dysfunction in distinct brain circuits[9], [10]. Existing technologies like functionalized field-effect transistors, cell based biosensor and microdialysis tools enables the in vivo small and widely distributed neurotransmitter sensing[11], [12]. However, the neuropeptide, protein and other rare larger neurochemicals are left untouched[13]. Micro-invasive tools for brain interstitial fluid (ISF) sampling can assist the characterization of multiple biomarkers[14]. And the combination of the microfluidic channel and microelectrode array can further explore the electrical and chemical signals inside the brain.

Probes with microfluidic channel can also infuse drug cross brain blood barrier and avoid off-target effect of systemic injection. For example, such probes can infuse designer drug exclusively to designer receptors in the targeted brain region and monitor the electrical signals simultaneously [15], [16]. Instead of using steel canula, viral particles with specific gene can be delivered with the probe with fluidic channel to alter the gene expression of certain tissue to make it sensitive to optical stimulation[17]. Probe with microfluidic channel can infuse drugs like dexamethasone to reduce the inflammatory response right after insertion for signal to noise ratio (SNR) improvement [18].

Neural probes provide excellent spatiotemporal resolution at the implantation sites; however, the brain circuits contain multiple levels that highly corelated and work simultaneously. Though implant more probes into brain can increase spatial coverage, it's still difficult to record the entire brain. The magnetic resonance imaging (MRI) has lower temporal resolution but come with higher spatial coverage for entire brain. Also, the functional MRI (fMRI) can monitor the blood oxygen levels in the brain which inform researchers about the active level of brain regions. Thus, the combination of neural probe and MRI can effectively enhance the spatiotemporal resolution for neuron interrogation.

The major problem for combining conventional neural probes with MRI scanning is the artifacts around the implantation site that masks the images from tissue. The artifact is caused by the magnetic susceptibility mismatch between the electrode's materials and brain. Conventional materials for microelectrodes like tungsten, platinum, iridium have larger magnetic susceptibility mismatch with the brain than carbon. Therefore, electrode made from carbon can greatly reduce the MRI artifact size and offer higher spatial resolution. In addition, carbon electrode with higher resistivity has lower chances to cause injury due to eddy current induced heating during MRI compare with metals[19]. Thus, we would like to use carbon as electrode materials for electrophysiological modulation.

Carbon electrodes have different forms including graphene for transparent electrodes array, vertical aligned carbon nanotube electrodes for high surface area, glassy carbon for electrochemical stability, and carbon nanofiber pillar for better neuron cell adhesion [20]–[22]. Among those of carbon structures, carbon nanofiber derived from electrospun photoresist fiber pyrolysis has been chosen as electrodes for facile fabrication with lower cost.

Foreign body response is the primary cause of neural probe implants failure[23], [24]. This is caused by the trauma during surgical implantation and the post-surgery chronic micromotion between mechanically mismatched implant and brain tissue. Probes made from silicon or glass has young's modulus several magnitudes higher than brain, and cause scar tissue formation [6]. Such issue can be mitigated by using materials with lower young's modulus and design with smaller bending stiffness.

In this work, we present a neural probe with carbon nanofiber electrodes and two microfluidic channels for drug delivery and sampling. The carbon electrodes can lower the MRI artifacts around the tissue while CNF structure for cell adhesion promotion[19]. SU8 epoxy was used as mechanical structure for the probe to provide sufficient mechanical strength for surgical implantation while maintaining lower bending stiffness to reduce chronic tissue response.

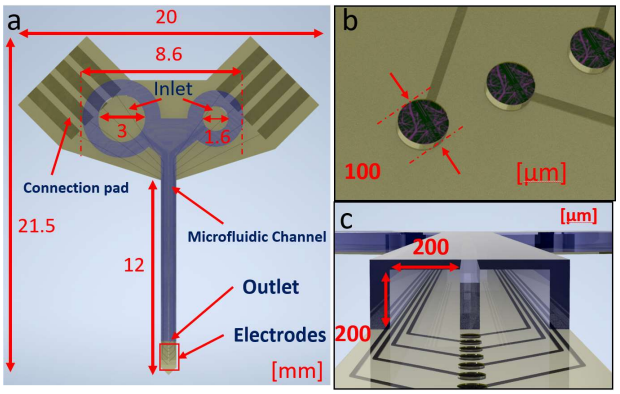

Figure 1. (a) Design details of CNF multifunctional neural probe (b) Carbon nanofiber electrodes (c) microfluidic channel outlet

978-1-940470-04-7/HH2022/$25©2022TRF
DOI 10.31438/trf.hh2022.58

NEURAL PROBE STRUCTURE AND DESIGN

The design goal of probe in this work is combining the carbon nanofiber electrodes for electrophysiological modulation and microfluidic channels for liquid sampling or drug delivery. SU8 photosensitive epoxy was chosen as the only materials for the probe design. SU8 as structural material for neural probes can be easily made into different form factors with microfabrication techniques [25], [26]. The microfluidic channel and substrate are made from SU8 for mechanical support and passivation while CNF electrodes and carbon traces are made from SU8 pyrolysis. Design details and dimension of the probe are shown if Fig 1 (a), the 100µm CNF electrodes that interact with neuron tissue are connected to zero insertion force (ZIF) connection pad with 20µm glassy carbon traces. The microfluidic channels have two outlets with different size that designed to accommodate tubes with different dimensions to connect with external pumps for actuation. In Fig 1(c), two microfluidic channels with 200x200 μm^2 cross-section area and opening adjacent to electrodes are placed on top of the substrate

Having sufficient mechanical strength to survive the surgical implantation and lowering bending stiffness to reduce scarring effect during post implantation micromotion are the two primary design concern of polymer neural probes. Previous paper has demonstrated that polymer shaft probe with sufficient buckling force is compatible with conventional implantation process[19] . And according to the literature, the probe need to have at lease 1mN[25] buckling force to survive the surgery. Equation (1) describe the buckling force of probe shank part for insertion in which E, b, h, L are young's modulus, width, thickness, length of the probe shank. Therefore, we design the minimum probe substrate thickness of 40 µm, width of 1mm and probe length of 120mm. The calculated buckling force is 2.98mN for the probe and it's already strong enough to survive the implantation surgery without considering the strengthen from microfluidic channel.

$$F = \frac{\pi^2 E b h^3}{5.88 L^2} \quad (1)$$

After implantation, the micromotion and mechanical mismatch between probe and brain tissue is the primary cause of inflammation and glial effect [7] and lowering the bending stiffness can effectively reduce the it.

$$K = \frac{E b h^3}{4 L^3} \quad (2)$$

According to equation (2), the bending stiffness value K of the same probe design will be 285 Nm^2 for silicon, 120 Nm^2 for glass and 6 Nm^2 for SU8 polymer probe. Comparing with silicon and glass for conventional neural probe, SU8 photosensitive epoxy has lower young's modulus, bending stiffness and thus better for neural probe construction.

FABRICATION METHODS OF NEURAL PROBE

The multifunctional neural probe is entirely made of SU-8 but with different fabrication techniques that including electrospinning, oil immersion exposure, partial exposure, and pyrolysis. The detailed fabrication process is shown in Fig 2. Fabrication starts from silicon wafers with 200nm thermally grown oxidation layers. The A1-A3 steps in Fig 2 show that the SU8 pattern of interconnections with 10um thickness are exposed by standard photolithography process while eight SU8 nanofiber pillars with 100 µm diameter are achieved by electrospinning and consecutive oil immersion lithography[22]. The patterned SU8 nanofiber and traces are turned into CNF and glassy carbon by 3 ºC/min slow ramping pyrolysis at 1000 ºC in 13 slm flowing nitrogen environment (A4 of Fig 2). In A5, SU8 layer with 40 µm thickness is patterned as a substrate of neural probes and in A6, a 250µm thick SU8 layer has been coated on top of it to define the microfluidic channels. The sidewall and top-wall of microfluidic channels whose cross-section area were defined with I-Line UV with 570 mJ/cm^2 fully exposure and 84 mJ/cm^2 partial exposure separately[26]. Then the exposed probe has been baked at 85°C for 15 minutes before 24 hours developing with stirring. The expected thickness with partial exposure techniques is 50µm. After developing, the carbon nanofiber neural probe with two microfluidic channels was released from the silicon substrate by submerging the wafer into buffered oxide etchant (BOE) for 48 hours.

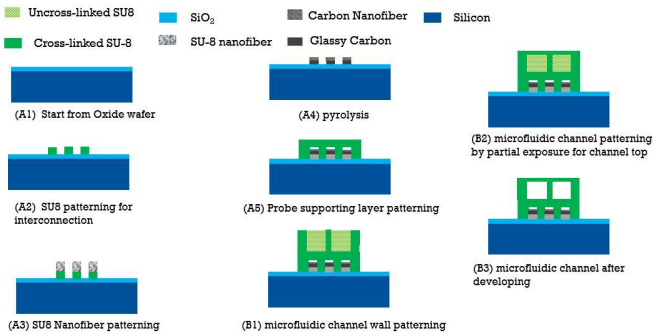

Figure 2. Fabrication process of the multifunctional neural probe, A1-A5 shows the fabrication of carbon nanofiber electrodes and B1-B3 shows microfluidic channel fabrication. (The white space on top of carbon nanofiber electrodes in A5-B3 indicate the opening on shank to expose electrode)

RESULTS AND DISCUSSION

The dimension of electrodes has been examined with scanning electron microscope (SEM) and tested with electrical impedance spectroscopy while the dimensions of microfluidic channels are measured by nano computerized topography (Nano-CT) and tested with micropump system.

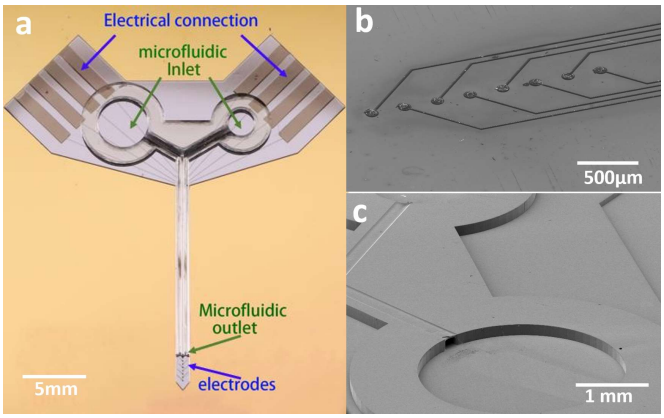

Figure 3. (a) Optical image of the multifunctional CNF neural probe (b) with an SEM image for electrodes and traces (c) microfluidic connection and inlet

Fig. 3 (a) shows the optical image of the fabricated neural probe structure including the inlet and outlet of microfluidic channels and electrical connection to interface with external circuits. The SEM image of carbon nanofiber electrodes and inlet of microfluidic

channel are included in of Fig 3 (b) and (c). Details of the 100 µm diameter carbon nanofibers electrode is demonstrated with SEM imaging in Fig 4. The CNF mesh with thickness around 15 µm sits on top of the glassy carbon trace and the diameter of single carbon nanofiber ranges from 100 nm to 600nm. The 3D mesh structure of the nanofiber provides higher neuron density compare with smooth silicon surface[19].

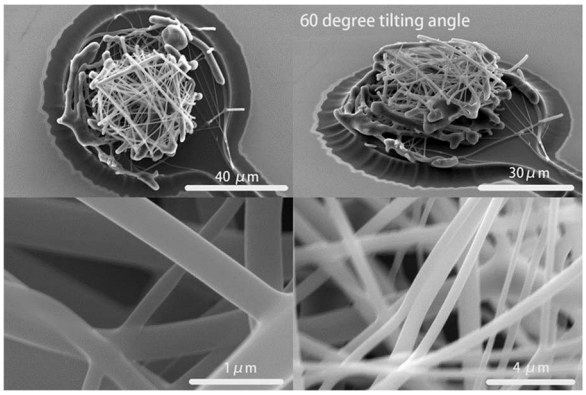

Figure 4. SEM images of carbon nanofiber electrodes

Electrochemical impedance spectroscopy (EIS) and cyclic voltammetry (CV) are carried out with three-electrode system which include a platinum counter electrode and an Ag/AgCl reference electrode in phosphate buffer saline (PBS) solution. EIS plot in Fig 5(a) shows that the impedance of carbon nanofiber electrodes is around 419±40 kΩ at 1 kHz. The CV curve in Fig 5(b) was measured within water window -0.6-0.8V in. The 10 scan cycles demonstrate the stability of the electrodes, and the approximate rectangular shape is expected for double-layer capacitance electrodes [6].

Nondestructive Nano-CT scanning has been performed to examine the microfluidic channel dimensions. During the scanning, tungsten target has been used to generate X-ray with 180kV 120µA electron beam and 1000 frames scanning have been collected and reconstructed into 3D file. The 3D structures of fabricated probe are cut into slices and shown in Fig 6 (a) and (b). Fig 6 (a) provides the side view and cross-section views of the channels and connection parts. The top wall is much thinner than substrate and sidewall of the probe. Also, top wall formed with partial exposure is continuous across the channel and free of defects that would cause the channel leakage.

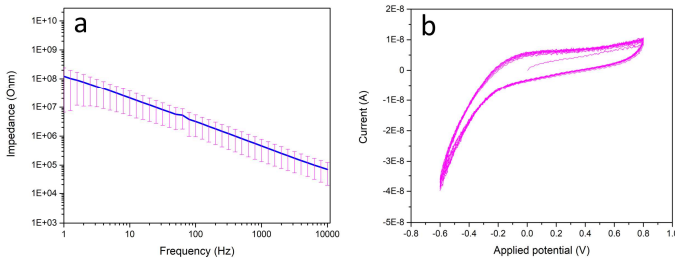

Figure 5. electrical measurement of the CNF electrodes (a) Electrochemical impedance spectroscopy measurement (b) cyclic voltammetry measurement

Fig 6 (b) shows the structure and cross-section view of probe shank whose area is approximately 200x200 µm^2 and top wall thickness is around 50 µm as designed. However, the shape of channel cross-sections is not perfect square but trapezoid and slight changes across slice 1-3. It's formed because of two factors, i) the nonhomogeneous exposure and ii) attenuation effect of SU8 photo resist during the photolithography process. For factor i), the top portion of the side wall absorbed more dosage than the lower part because of partial exposure only provides limited energy that cannot uniformly cover the entire sidewall. For reason ii), the UV light attenuated when passing through the 250 µm SU8 layers, so the lower portion of the sidewall has less crosslinking than top part.

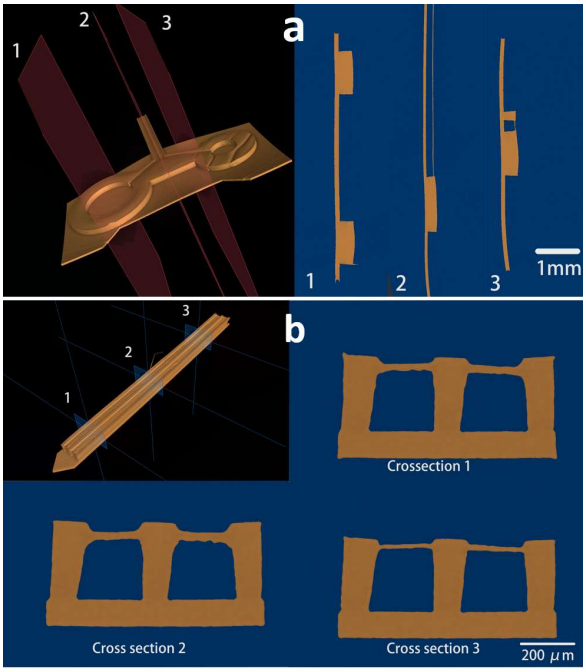

Figure 6. Nano-CT reconstruction view of microfluidic channel (a)connector region (b) shank regions

The microfluidic channel inlet was then connected to a micropump (mp6-liq, Bartels Mikrotechnik) driven by voltage upconverting transformer circuits. Water was used in the test and volume was converted from weight measurement. The pump generates pulsatile flow whose actuation frequency, amplitude can be tuned with external input. In this case we used function generator and source meter to adjust the frequency and amplitude. We chose 0.37V fixed input amplitude and alter pumping frequency for the microfluidic channel test. As shown in Fig. 7, the flow rate increases as frequency getting higher, and the lowest flow rate we achieved here is 10µl/min. Though the continuous flow rate is still higher than normal infusion rate[8], we can control the on/off time as time modulation to achieve lower flow rate.

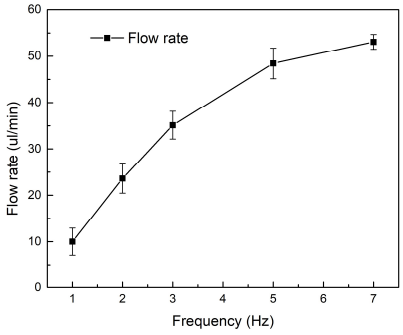

Figure 7. flowrate measurement of microfluidic channel with varying pump frequency

CONCLUSION

The polymer based CNF multifunctional neural probe capable of electrical recording and stimulation, drug delivery and liquid sampling has been designed and fabricated. The probe constructed with SU8 epoxy has suffient mechanical strength to withstand the surgical implantation while the tip has lower bending stiffness to reduce the tissue response over chronic micromotion. The fabrication flow doesn't involve mannual assembly so it has potential for batch manufacturing with lower cost. CV and EIS test has been carried out for the probe and resultant electrical impedance is 420 ±40 kΩ at 1kHz for the CNF electrodes. The CV curve indicates the stability and double layer capacitance mechanism of the elecrodes. The two microfluidic channel fabricated with partial exposure methods has been examined with nano CT scan and 3D reconstruction. They indicate the formation of the 200x200μm microfluidic channels and 50 μm channel top wall. The flowrate of the channels was tested with micropump actuated at different frequencies. The flow rate ranges from 10μl/min to 55μl/min in continous flow and can reach lower flowrate with time modulation. Though the results show validate the fabrication methods and functions of the probe, further in vivo studies can push the probe further as a platform for neural research.

ACKNOWLEDGEMENTS

The microfabrication and device characterization have been performed in Interdisciplinary Microsystems Group (IMG) and Nanoscale Research Facility (NRF) at the University of Florida.

REFERENCES

[1] D. H. Hubel, "Tungsten microelectrode for recording from single units," *Science*, vol. 125, 1957

[2] C. Dagdeviren *et al.*, "Miniaturized neural system for chronic, local intracerebral drug delivery," *Sci. Transl. Med.*, vol. 10, no. 425, p. eaan2742, Jan. 2018

[3] H. N. Schwerdt *et al.*, "Long-term dopamine neurochemical monitoring in primates," *Proc. Natl. Acad. Sci. U.S.A.*, vol. 114, no. 50, pp. 13260–13265, Dec. 2017

[4] C. A. Kuliasha *et al.*, "Sensing Nerve Activity with Scalable and Robust Nerve Interfaces," in *2019 IEEE SENSORS*, Montreal, QC, Canada, Oct. 2019, pp. 1–4.

[5] T. I. Kim, "Injectable, cellular-scale optoelectronics with applications for wireless optogenetics," *Science*, vol. 340, 2013

[6] A. Canales, "Multifunctional fibers for simultaneous optical, electrical and chemical interrogation of neural circuits in vivo," *Nat. Biotechnol.*, vol. 33, 2015

[7] S. Park *et al.*, "Adaptive and multifunctional hydrogel hybrid probes for long-term sensing and modulation of neural activity," *Nat Commun*, vol. 12, no. 1, Art. no. 1, Dec. 2021

[8] B. Wang *et al.*, "An implantable multifunctional neural microprobe for simultaneous multi-analyte sensing and chemical delivery," *Lab Chip*, vol. 20, no. 8, Art. no. 8, 2020

[9] A. M. Andrews, "Why Monitor Molecules in Neuroscience?," *ACS Chem. Neurosci.*, vol. 8, no. 2, pp. 211–212, Feb. 2017

[10] E. V. Romanova, J. T. Aerts, C. A. Croushore, and J. V. Sweedler, "Small-Volume Analysis of Cell–Cell Signaling Molecules in the Brain," *Neuropsychopharmacol*, vol. 39, no. 1, pp. 50–64, Jan. 2014

[11] V. I. Chefer, A. C. Thompson, A. Zapata, and T. S. Shippenberg, "Overview of Brain Microdialysis," *Current Protocols in Neuroscience*, vol. 47, no. 1, Apr. 2009

[12] N. Nakatsuka *et al.*, "Aptamer–field-effect transistors overcome Debye length limitations for small-molecule sensing," *Science*, vol. 362, no. 6412, pp. 319–324, Oct. 2018

[13] D. C. Castro and M. R. Bruchas, "A Motivational and Neuropeptidergic Hub: Anatomical and Functional Diversity within the Nucleus Accumbens Shell," *Neuron*, vol. 102, no. 3, pp. 529–552, May 2019

[14] R. Raman *et al.*, "Platform for micro-invasive membrane-free biochemical sampling of brain interstitial fluid," *Sci. Adv.*, vol. 6, no. 39, p. eabb0657, Sep. 2020

[15] G. M. Alexander *et al.*, "Remote Control of Neuronal Activity in Transgenic Mice Expressing Evolved G Protein-Coupled Receptors," *Neuron*, vol. 63, no. 1, pp. 27–39, Jul. 2009

[16] E. Vardy *et al.*, "A New DREADD Facilitates the Multiplexed Chemogenetic Interrogation of Behavior," *Neuron*, vol. 86, no. 4, pp. 936–946, May 2015

[17] O. Yizhar, "Optogenetics in neural systems," *Neuron*, vol. 71, 2011

[18] H. Shin, "Neural probes with multi-drug delivery capability," *Lab Chip*, vol. 15, 2015

[19] S.-P. Fang *et al.*, "High magnetic field fmri compliant carbon nanofiber neural probes," in *2017 19th International Conference on Solid-State Sensors, Actuators and Microsystems (TRANSDUCERS)*, Kaohsiung, Jun. 2017, pp. 1707–1710.

[20] D. Kuzum, "Transparent and flexible low noise graphene electrodes for simultaneous electrophysiology and neuroimaging," *Nat. Commun.*, vol. 5, 2014

[21] N. Goshi *et al.*, "Glassy carbon MEMS for novel origami-styled 3D integrated intracortical and epicortical neural probes," *J. Micromech. Microeng.*, vol. 28, no. 6, Art. no. 6, Jun. 2018

[22] P. F. Jao *et al.*, "Fabrication of carbon nanofibrous microelectrode array (CNF-MEA) using nanofiber immersion photolithography," in *2014 IEEE 27th International Conference on Micro Electro Mechanical Systems (MEMS)*, San Francisco, CA, Jan. 2014, pp. 498–501

[23] C. A. Kuliasha *et al.*, "ROBUST AND SCALABLE TISSUE-ENGINEERINED ELECTRONIC NERVE INTERFACES (TEENI)," in *2018 Solid-State, Actuators, and Microsystems Workshop Technical Digest*, Hilton Head, South Carolina, USA, May 2018, pp. 46–49

[24] J. A. Frank, M.-J. Antonini, and P. Anikeeva, "Next-generation interfaces for studying neural function," *Nat Biotechnol*, vol. 37, no. 9, pp. 1013–1023, Sep. 2019

[25] B. A. Wester, R. H. Lee, and M. C. LaPlaca, "Development and characterization of *in vivo* flexible electrodes compatible with large tissue displacements," *J. Neural Eng.*, vol. 6, no. 2, p. 024002, Apr. 2009

[26] Yong-Kyu Yoon, Jin-Woo Park, and M. G. Allen, "Polymer-core conductor approaches for RF MEMS," *J. Microelectromech. Syst.*, vol. 14, no. 5, pp. 886–894, Oct. 2005

CONTACT

* Y.K. Yoon, Tel: +1-352-392-5985; ykyoon@ece.ufl.edu

NON-HERMETIC PACKAGING FOR FLEXIBLE MEDICAL IMPLANTS BASED ON MULTI-STACK PARYLENE C/PDMS BILAYER THIN FILMS

Hao Chong[1], Steve J.A. Majerus[3], Kath M. Bogie[2,3] and Christian A. Zorman[1,3]*
[1]Department of Electrical, Computer and Systems Engineering, Case Western Reserve University, USA
[2]Department of Orthopaedics, Case Western Reserve University, USA
[3]Advanced Platform Technology Center, Louis Stokes Cleveland Veterans Affairs Medical Center, USA

ABSTRACT

Next generation flexible hybrid electronics (FHE) devices for implant applications require highly protective, mechanically compliant, wireless-compatible coatings for packaging. Such demanding requirements are not likely to be met by a single material. To address this issue, a multilayer, all-polymer packaging technology specifically for use in chronic implantation applications was designed. Based on parylene-C/PDMS bilayer films, the encapsulation approach was developed to package flexible implantable systems that incorporate the complex topographies associated with on-board electronics, interconnects and antennas. The multilayer packaging approach was initially evaluated using microfabricated planar interdigitated electrodes and then extended to 3D devices consisting of flexible polyimide printed circuit boards with on-board wireless transmission circuitry. Accelerated lifetime testing indicates that the estimated lifetime increases with increasing bilayer stacking number. We found that a triple bilayer stack with an overall thickness of ~225 μm has an estimated lifetime of over 3.5 years at physiological conditions.

KEYWORDS

Non-hermetic packaging, flexible medical implants, PDMS, parylene-C

INTRODUCTION

Advancements in MEMS for implanted biomedical systems has stimulated the development of high-impact medical technologies with some noteworthy examples being cardiac pacemakers [1] blood pressure monitors [2], retinal prostheses [3], and glucose monitors [4]. Recent developments in flexible hybrid electronics (FHE) is enabling a new generation of highly functional implantable devices for a diverse set of applications that leverage the mechanical flexibility and small form factor associated with FHE to produce highly functional electronic circuits that can conform to the irregular topographies associated with deployment. Next generation FHE devices for implant applications require highly protective, mechanically compliant and wireless-compatible coatings for packaging. Such demanding requirements are not likely to be met by a single material.

A variety of flexible polymeric materials have been identified for encapsulation of implantable systems based on their excellent barrier properties and biocompatibility. The list of candidate materials includes polyimide, parylene, liquid crystal polymer (LCP), and polydimethylsiloxane (PDMS). These materials are less protective than metals and ceramics and thus have not been widely adopted for long-term implant applications. However, recent studies have shown promising results regarding their potential for long-term encapsulation, in particular for devices fabricated on polymeric substrates. Parylene/metal/parylene multilayer coatings have been developed for use in flexible retinal implants, exhibiting longer lifetimes than a simple silicone-coated parylene layer [5]. Unfortunately, the metallic interlayer in these coatings challenges the incorporation of wireless components. For implantable microsystems with wireless powering or transmission functions, reliable packaging approaches based on insulating materials is desired, with polymers being particularly attractive for mechanically flexible devices.

In this paper, we describe the development of a multi-layer, non-hermetic packaging technology based on a bilayer structure consisting of PDMS and parylene-C. The stacked, bilayer structure capitalizes on the fact that failure-inducing defects in a single layer are likely to be terminated at a material interface [6]. Both PDMS and parylene-C are widely used in biomedical microdevices and can be processed into thin film bilayers on both planar substrates and those with complex 3D structures. The bilayer structure leverages the outstanding moisture barrier characteristics of parylene-C with the favorable mechanical and biocompatible properties offered by PDMS. The bilayer structure leverages the favorable attributes of these two materials while simultaneously compensating for their weaknesses. The bilayer structure accommodates for the poor moisture barrier characteristics of PDMS and the poor mechanical properties of thick parylene-C by capitalizing on the favorable properties of the other material. The multi-stack, bilayer architecture yields a non-hermetic encapsulant that is both highly protective of moisture intrusion and mechanically flexible.

PACKAGING PROCESS

The multilayer packaging approach involves cleaning and pretreatment of substrate surfaces followed by sequential deposition of PDMS and parylene-C films until the desired encapsulation thickness is achieved.

Surface Cleaning

The surface cleaning step involved sequential immersion of the substrate in beakers containing acetone, IPA, and DI water for multiple cycles (5 minutes per cycle). Each beaker was placed in an ultrasonic cleaner with the bath temperature set at ~70°C. To minimize the accumulation of particulates on substrate surfaces during and after substrate cleaning, the cleaning and packaging steps were performed in a Class 100 clean room.

Pretreatment of Substrate Surfaces

Although parylene-C has better barrier properties than PDMS, it generally exhibits poor adhesion to most substrate materials including metals and polymers. Adhesion of parylene can be improved by increasing the contact area to the substrate by roughening its surface. Parylene adheres well to PDMS because the enhanced surface roughness due to native defects on the PDMS surface can be filled by vapor-deposited parylene. Therefore, the excellent barrier properties of parylene can be fully utilized while addressing the issues associated with poor adhesion. In order to reduce the possibility of delamination between PDMS and parylene-C, MED-160 Silicone primer (NuSil Technology) was used as an adhesion promoter prior to PDMS deposition. MED-160 is known to improve the adhesion of silicones to various substrates including metals, ceramics, plastics and other silicone-based materials. It is also a medical grade material which makes it potentially well-suited for devices designed for use in clinical applications [7]. It has been shown that by using MED-160 as the adhesion promoter, the moisture undercut rate between PDMS and

978-1-940470-04-7/HH2022/$25©2022TRF
DOI 10.31438/trf.hh2022.59

parylene was reduced from 22.3 µm/day to 3.2 µm/day [8].

For the proposed packaging approach, MED-160 was applied to the substrate by dip-coating prior to the deposition of each PDMS layer. After substrate cleaning, MED-160 was applied by dip coating (L2006A1-US, Ossila) using a dip speed of 5mm/s, a withdrawal speed of 5mm/s and a dwell time of 10s. Excess primer was then removed by gentle wiping. Finally, the device was devolatilized for 2 hours at ambient temperature and humidity.

Multi-Stack Packaging

The PDMS coating process involved the following procedure. First, Parts A and B of MED-6600 were mixed at a weight ratio of 1:1 in a clean beaker. The mixture was then thoroughly stirred using a stainless steel rod to achieve a homogeneous blend. The mixture was then degassed for 3 minutes in a vacuum desiccator to remove air bubbles. The degassed PDMS was then deposited on the MED-160 coated substrate by dip coating using a dip speed of 5mm/s, a withdrawal speed of 5mm/s, and a dwell time of 60s. After the device was pulled from the PDMS mixture, it was suspended for 3 minutes to allow excess PDMS to drip off the substrate. The dip-coated device was then transferred to a fume hood for 30 minutes to evaporate the xylene solvent from the PDMS coating. This step is very important since xylene is both toxic and can inhibit the curing process. After solvent evaporation, the PDMS layer was cured at 65°C for 2 hours in an oven.

Parylene-C coatings were applied using a dedicated parylene deposition system (Model PDS 2010, Specialty Coating Systems, Inc.). The thickness of each parylene-C layer is controlled by the weight of parylene-C monomers used in each deposition process. To deposit a 5µm-thick layer, 9.54g of parylene-C monomer was used. After loading the system, the chamber was pumped down to a base pressure below 15 mTorr, after which the deposition process was initiated. The deposition process took about 2.5 hours. After deposition, the coated devices were removed from the chamber and prepared for PDMS deposition.

A multi-stack, bilayer encapsulant was produced on each substrate by repeating the deposition of MED-6600 and parylene-C films to achieve the desired number of bilayer units. Prior to each dip coating of MED-6600, MED-160 primer was dip-coated and devolatilized to enhance the adhesion between PDMS and parylene-C. Figure 1 shows a schematic of the cross-sectional view of the multi-stack, bilayer encapsulation.

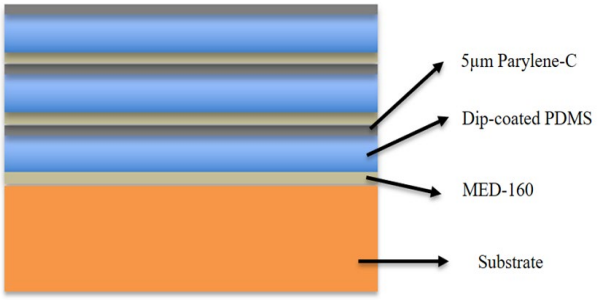

Figure 1: Schematic of the cross-sectional view of the multi-stack encapsulation.

EVALUATION USING INTERDIGITATED ELECTODES

Fabrication of Interdigitated Electrodes

For initial testing, interdigitated electrodes (IDEs) were fabricated on flexible, copper-clad polyimide substrates using a simple one mask process. The mask contained patterns for eight test coupons. Each IDE consisted of forty, 0.2 mm x 9.5 mm interdigitated electrodes and two, 2.5 x 2.5 mm^2 contact pads for hardwire connections to the data acquisition setup. The width of each electrode was 200 µm and the space between each electrode was 400 µm. The peripheral dimensions of each test coupon was 1.5 cm x 5 cm. Fabrication of IDEs test coupons utilized conventional microfabrication techniques including photolithography and wet etching. Single sided copper clad polyimide (LF8530R, DuPont) was selected as the substrate material.

Following IDE fabrication, the test coupons were packaged using the multi-stack, bilayer encapsulation described previously and illustrated schematically in Figure 2. The thicknesses of each PDMS and parylene-C layer was nominally 70 µm and 5 µm, respectively.

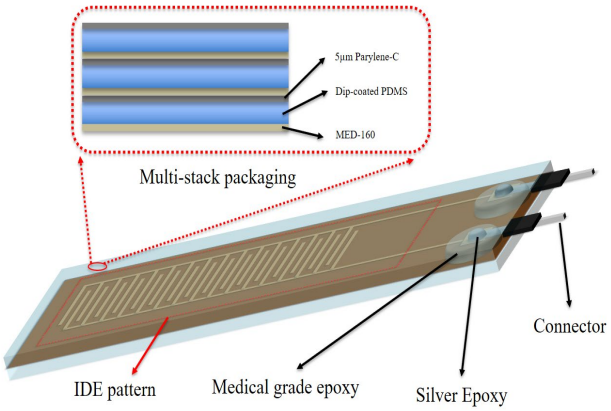

Figure 2: Schematic of a packaged IDE test specimen for accelerated lifetime testing.

Accelerated Lifetime Tests of Packaged IDEs

Standard accelerated lifetime testing was performed in order to estimate the lifetime of packaged devices under simulated physiological conditions in a practical testing period. For packaged implantable devices, accelerated lifetime tests are commonly performed by immersing test devices in heated saline (0.9%) or phosphate-buffered saline (PBS) to best simulate the body fluid environment.

The accelerated lifetime test for the packaged IDE test coupons was conducted by continuously measuring the surface insulation resistance of packaged IDEs under soak testing conditions. Three temperature baths (Isotemp 10L GP Bath, Fisher Scientific) were used to simultaneously test a total of 120 IDE test coupons at either 65°C, 75°C or 85°C. Each bath was filled with water, heated to the designated temperature and covered by an acrylic board to slow the evaporation of the bath water.

Each IDE test coupon was individually inserted in a glass vial filled with 0.9% saline and sealed by acrylic lids that had a small rectangular hole for electrical connections to the IDE. RTV sealant (Dow Corning) was applied on the lids to ensure tight sealing between the lid and glass vial as well as the electrical feedthroughs that penetrated the lid. IDE samples were then connected to a

multiplexer circuit. Multiplexers were controlled by digital signals sent from a programmed Arduino Uno board to enable automatic switching between the samples. One, 8-channel and eight, 16-channel multiplexers comprised the circuit, enabling up to 128 samples to be monitored for surface insulation resistance in sequential manner by rapidly switching between samples. Voltage signals from each sample were collected using an NI-MyDAQ™ data acquisition card and processed by a LabVIEW™ program to record the surface insulation resistance of the packaged samples. To evaluate the relationship between the effectiveness of protection and the packaging thickness, 24 samples with different bilayer stacking units were tested in each temperature bath for a total of 72 test coupons under test. For each temperature bath, test coupons were encapsulated with 1 to 3 bilayer units with 8 coupons comprising each bilayer group. Samples from each of the three bilayer groups was tested at 65°C, 75°C and 85°C. The water level in the baths was monitored to ensure that the vials remained immersed and thus the IDEs were held at a constant temperature. Plots of measured surface insulation resistance versus soak time for representative packaged IDE samples from the triple bilayer group evaluated at the three testing temperatures are shown in Figure 3.

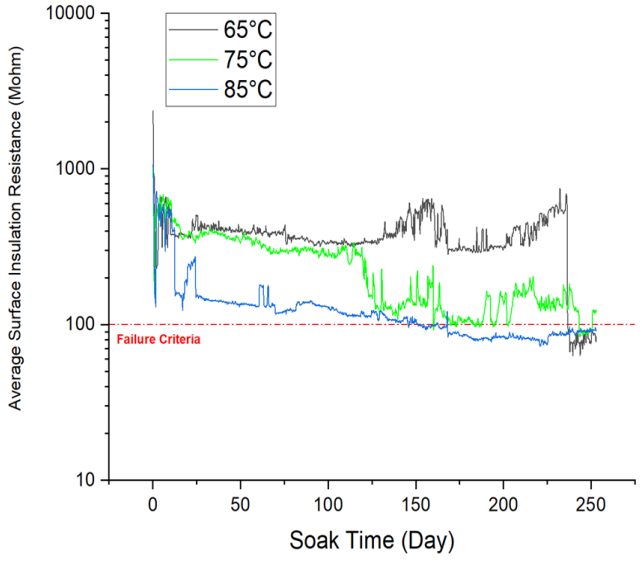

Figure 3: Representative plots of surface insulation resistance versus soak time for a set of three IDEs packaged with a triple bilayer encapsulant and tested in soak baths at 65°C, 75°C and 85°C

According to the Arrhenius equation, $\ln(t_i)$ is proportional to E_a/RT, where t_i is the time to failure at different temperatures, E_a is the activation energy, R is the gas constant and T is temperature [9]. Assuming that the degradation mechanism at 37°C is identical to the degradation mechanism at the three testing temperatures, a linear dependence enables prediction of package lifetime at physiological temperature based on the accelerated lifetime testing results. To this end, the average lifetimes were calculated for sample groups in which all 8 samples failed within the testing period and ln(t) was plotted as a function of 1/T (see Figure 4), where t is the average time to failure for a given bilayer group. For the single, double and triple bilayer groups, the package lifetime was estimated from a linear fit of the data. Based on these data, the estimated lifetimes of IDEs packaged using single, double and triple encapsulants at 37°C in saline are 2.73 years, 2.89 years, and 3.52 years, respectively. As expected, the estimated lifetime increases with increasing bilayer stacking number.

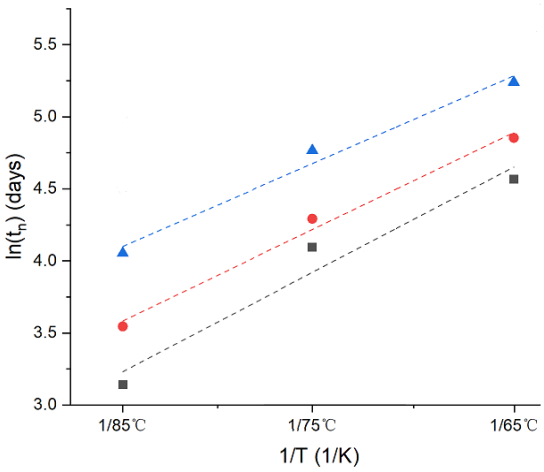

Figure 4: Plots of ln(t) vs 1/T for the single (■), double (●) and triple (▲) bilayer encapsulants.

EVALUATION USING FLEXIBLE WIRELESS DEVICES

Fabrication of Flexible Wireless Devices

Flexible wireless devices consisting of a passive amplifier circuit, programmable microcontroller, LCR circuit and associated peripherals were assembled on multilayer polyimide printed circuit boards manufactured by a commercial vendor (PCBWay). Assembly of the electronic components on these boards was performed manually. First, the flexible board was affixed to a glass slide using double-sided tape. Solder paste was then applied to contact pads on the board using a stainless steel stencil. The electronic components were then placed in their designated positions, followed by reflow soldering using a reflow oven. After soldering, the device was inspected under a microscope to ensure all electronics were soldered properly.

After an initial functionality test to verify device viability, medical grade epoxy was dispensed on the electronic components using a pressure-controlled micro dispensing system. The epoxy was then cured at 65°C in an oven for 1 hour. Medical grade epoxy offers additional reliability to the packaging in multiple ways. The epoxy serves to mechanically protect the solder joints which are likely to break when the device is bent during implantation and deployment. The epoxy does not add excessive rigidity to the device since it only covers the rigid electronics and their solder joints. Additionally, medical grade epoxy is an excellent barrier material which provides added protection from damage by moisture that may eventually penetrate through the polymer bilayers. The epoxy can also inhibit leaching of hazardous chemicals from the solder joints and electronics. These devices were packaged using a 7-bilayer encapsulant. Figure 5 shows photographs of a representative devices before and after the encapsulation process.

Accelerated Lifetime Tests of Packaged Flexible Wireless Devices

Three devices were assembled and packaged for accelerated lifetime tests. The packaging layers have an overall thickness of ~525 µm, which is much thinner than some of the discrete electronic components that comprise the device. These devices were placed in individual glass vessels and soak tested at either 65°C, 75°C or 85°C

in 0.9% PBS using the same test setup employed in the IDE study. On a daily basis, these devices were removed from the heated water baths for a short period to evaluate electrical functionality by connecting each device to a 2.5V power supply through a wired connection and collecting data using both the wired connection and the wireless circuitry. The microcontroller on the device was programmed to transmit wireless data for a period of 60 seconds after power up and successful transmission was indicated by a green indicator light on the wireless radio which continuously flashed during data successful transmission. Simultaneously, currents through the wired connection with the device in both working and sleeping modes were also measured.

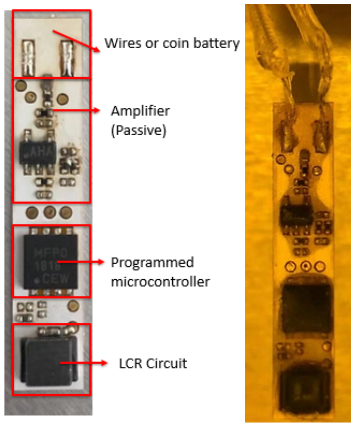

Figure 5: Photographs of an electronic device used to evaluate the multi-stack, bilayer package on 3D topographies: (left) before packaging and (right) after packaging.

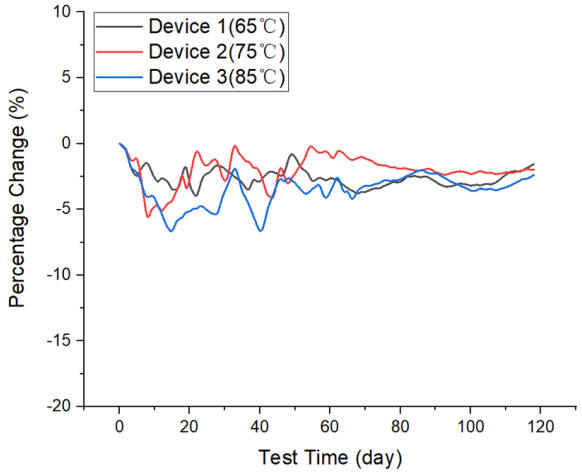

Figure 6: Percentage change in working mode supply current versus soak test time for the three externally powered devices tested at 65℃, 75℃ and 85℃.

The percentage change of average current in the working mode versus soak time for the three devices is presented in Figure 6. The maximum change of average working current was -4.21%, -6.04% and -6.83% for the devices tested at 65℃, 75℃ and 85℃, respectively. At Day 119, the percentage differences decreased to -1.55%, -1.94% and -2.83% for devices tested at 65℃, 75℃ and 85℃. These observed changes were not large enough to affect the normal operation of the microcontrollers and wireless functions. In fact, all three devices maintained wireless functionality over the entire testing period. Because these devices did not exhibit failure at the end of the testing period, a proper estimate of device lifetime could not be made. However, applying the 10°C rule to the data collected from sample tested at 85°C suggests that the equivalent lifetime could be as high as ~9 years at physiological temperature.

CONCLUSION

A non-hermetic packaging approach based on a parylene-C/PDMS bilayers for flexible implantable biomedical systems is described. Accelerated lifetime testing of IDE samples packaged using 3 units of the bilayer structure exhibited an estimated lifetime of over 3.5 years under physiological conditions using an all-polymer encapsulant that is only ~ 225 µm in overall thickness. Current and wireless functionality testing of packaged active devices suggest that the combination of medical-grade epoxy and the proposed multi-stack, bilayer package is able to provide sufficient protection for the electronic components of flexible implants designed for chronic use. For the flexible circuit packaging, accelerated lifetime tests on packaged devices reveal an acceptable level of small scale current fluctuations (less than 6%) during soak testing without any catastrophic failures of the programmed microcontroller.

ACKNOWLEDGEMENTS

We acknowledge the financial support of the Spinal Cord Injury Research Program, Department of the Army CDMRP (W81XWH-17-1-0149).

REFERENCES

[1] K.D Wise, "Wireless implantable microsystems: coming breakthroughs in health care," in Symposium on VLSI Circuits Digest of Technical Papers, 2002.

[2] D. Panescu, "MEMS in medicine and biology," IEEE Engineering in Medicine and Biology Magazine, vol. 25, 2006.

[3] E. Margalit et. al., "Retinal Prosthesis for the Blind," Survey of Ophthalmology, vol. 47, 2002.

[4] Y.J. Zhao et. al., " A MEMS viscometric glucose monitoring device," in The 13th International Conference on Solid State Sensors, Actuators, and Microsystems, vol. 2, 2005.

[5] F. Bottausci et al., "New sectorized implantable microelectrode fabrication, packaging and ageing for neural sensing and stimulation," in International IEEE/EMBS Conference on Neural Engineering, NER, 2015, vol. 2015-July, pp. 466–469.

[6] "Multi-layered poly-dimethylsiloxane as a non-hermetic packaging material for medical MEMS," S. Lachhman, C. A. Zorman, and W. H. Ko, Proc. Annu. Int. Conf. IEEE Eng. Med. Biol. Soc. EMBS, pp. 1655–1658, 2012.

[7] MED-160 Silicone premier data sheet, [Online]. Available: https://www.avantorsciences.com/assetsvc/asset/en_US/id/29018278/contents/en_us_tds_nusimed-160.pdf

[8] J. H. Chang, Y. Liu and Y. Tai, "Long term glass-encapsulated packaging for implant electronics," 2014 IEEE 27th International Conference on Micro Electro Mechanical Systems (MEMS), 2014, pp. 1127-1130.

[9] A. Plota and A. Masek, "Lifetime Prediction Methods for Degradable Polymeric Materials—A Short Review," Materials, vol. 13, no. 20, p. 4507, Oct. 2020.

CONTACT

* Christian A. Zorman, tel: +1-216-368-6117; caz@case.edu

PDMS MICROSTRUCTURES 3D-NANOPRINTED INSIDE UNCOATED, ENCLOSED PDMS-ON-GLASS MICROCHANNELS *VIA IN SITU* DIRECT LASER WRITING

Xin Xu, Olivia M. Young, Adira Colton, and Ryan D. Sochol
University of Maryland, College Park, MD, USA

ABSTRACT

Polydimethylsiloxane (PDMS) is one of the most commonly used materials for soft lithography protocols and microfluidics research. Yet, for emerging applications that rely on "*in situ* Direct Laser Writing (*is*DLW)"—approaches in which microstructures are additively manufactured directly inside of enclosed microfluidic channels—PDMS has presented a number of challenges as a microchannel material, primarily stemming from difficulties in facilitating sufficient adhesion between printed structures and the channel wall. To address such issues and enable the facile fabrication of PDMS-based *is*DLW-printed microfluidic technologies, here we introduce a novel strategy for printing PDMS microstructures directly onto and fluidically sealed to uncoated PDMS sidewalls of enclosed PDMS-on-glass microfluidic channels. We investigated microchannel geometry (*e.g.*, rectangular, trapezoidal, and semi-ovular cross sections) as a determinant in microfluidic print-to-wall sealing efficacy for 10 μm-thick fluidic barrier microstructures printed in channels with heights and widths of 50 μm. Microfluidic burst-pressure results revealed that semi-ovular channels yielded superior sealing integrity with pressure tolerances up to 350 kPa (*i.e.*, >5× that of our prior work), suggesting that the presented strategy offers unique promise to enable new classes of PDMS-based 3D microfluidic structures for biomedical and soft robotic applications.

KEYWORDS

Additive Manufacturing, 3D Printing, Direct Laser Writing, Two-Photon Polymerization, Polydimethylsiloxane, Microfluidics

INTRODUCTION

Among current additive manufacturing (or "3D printing") technologies, "Two-Photon Direct Laser Writing (DLW)" is offers unparalleled geometric control and print speeds for fabricating structures with feature resolutions on the order of 100 nm [1-3]. One limitation in the use of DLW for manufacturing microfluidic systems is that this submicron resolution can also represent a burden for fabricating the macro-to-micro interfaces (*e.g.*, inlet and outlet ports) required for fluidic loading, control, and retrieval [4,5]. One prominent approach to circumvent this issue is the concept of "*in situ* DLW (*is*DLW)", which entails 3D printing microstructures directly inside of enclosed microfluidic channels [6,7]. For manufacturing enclosed microfluidic channels, researchers have often turned to polydimethylsiloxane (PDMS)—a biocompatible silicone elastomer that, due in part to its advantages in soft lithography protocols, is widely employed across biomedical, microfluidics, and soft robotics fields [8-10]. Unfortunately, PDMS has proven to be a particularly challenging material for use in *is*DLW approaches for which the printed microstructures must fully adhere to the microchannel walls (to prevent fluidic leakage) [11-15].

Researchers have explored a number of strategies to mitigate these PDMS-based adhesion issues. For example, researchers have tried infusing silane-based glues after the *is*DLW printing process [16]. Previously, our group introduced the concept of using sol-gel surface coatings to enhance print-to-wall adhesion [5]—an approach other groups have recently adapted [17]. Such surface coatings, however, rely on time, labor, and/or cost-intensive protocols [5,17]. Thus, new manufacturing methodologies are needed to enable *is*DLW within uncoated, enclosed PDMS-based microfluidic devices.

CONCEPT

To address the aforementioned challenges associated with executing *is*DLW protocols with PDMS-based microfluidic devices, here we introduce a novel *is*DLW strategy that leverages a PDMS-based, DLW-compatible photomaterial to allow for PDMS microstructures to be printed directly onto untreated PDMS channels inside of enclosed PDMS-on-glass microfluidic devices (**Fig. 1**). Our approach involves three key steps. First, DLW is used to print a microchannel mold, which is then replicated with PDMS using established protocols [5]. After bonding the replicated PDMS to a glass slide, the second step involves the passive vacuum loading [18] of the liquid-phase, low-viscosity photomaterial, IP-PDMS (Nanoscribe GmbH, Karlsruhe, Germany), into the PDMS-of-glass microchannels (**Fig. 1a**). Lastly, the microdevice is loaded into the DLW 3D printer for *is*DLW printing of the microfluidic barrier directly inside of (and sealed to) the uncoated PDMS channels *via* a "ceiling-to-floor" photopolymerization process (**Fig. 1b**).

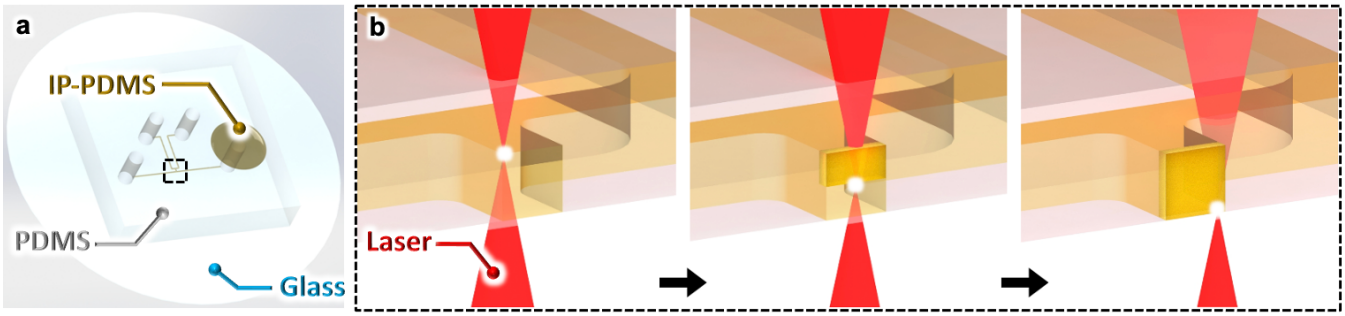

***Figure 1**: Concept of "in situ Direct Laser Writing (isDLW)" of polydimethylsiloxane (PDMS)-based microstructures directly inside of—and notably, fluidically sealed to—uncoated, enclosed PDMS-on-glass microfluidic channels. **(a)** Passive vacuum loading of the liquid-phase, low-viscosity photocurable material, IP-PDMS, into enclosed PDMS-on-glass microchannels. **(b)** The "ceiling-to-floor" isDLW process. A pulsed IR laser passes through an objective lens, immersion oil, glass substrate, and liquid-phase photomaterial to initiate spatially controlled photopolymerization (white) in a point-by-point, layer-by-layer methodology, ultimately producing a microstructure comprising cured PDMS-based photomaterial that is fully sealed to the entire luminal surface of the uncoated PDMS-on-glass channel.*

978-1-940470-04-7/HH2022/$25©2022TRF
DOI 10.31438/trf.hh2022.60

MATERIALS AND METHODS

"Direct Laser Writing (DLW)"-Based PDMS-on-Glass Microfluidic Device Fabrication

The PDMS-on-glass devices were fabricated as described previously [5]. Briefly, microchannel negative master molds were designed using the commercial computer-aided design (CAD) software, SolidWorks (Dassault Systèmes, France), and converted to the STL file format. All microchannels were designed with heights and widths of 50 μm; however, three distinct cross-sectional geometries were designed corresponding to rectangular, trapezoidal, and semi-ovular channel profiles. The STL files were then imported into the computer-aided manufacturing (CAM) software, Describe (Nanoscribe), to generate the laser writing path code for the DLW process. For the mold fabrication protocol, the slicing thickness and hatching parameters were set at 2.5 μm and 500 nm, respectively. Prior to the printing process, Si substrates (25 mm × 25 mm) were rinsed successively with acetone and isopropyl alcohol (IPA), and then dried with N_2 gas. The commercial photoresist, IP-Q (Nanoscribe), was deposited onto the Si substrates, which were then loaded into the Nanoscribe Photonic Professional GT2 DLW 3D printer using the 10× objective lens and Dip-in Laser Lithography (DiLL) configurations. After the DLW process, the substrates with printed patterns were developed in propylene glycol methyl ether acetate (PGMEA) for 25 min and IPA for 5 min to remove uncured residual photoresist. Developed molds were placed into a plastic petri dish, and a mixture of PDMS (Sylgard 184, Dow Corning, Corning, NY) prepared at a 10:1 (base to curing agent) ratio was then poured over the master molds, degassed, and placed on a hot plate set at 60 °C for 3 hours. Cured PDMS was then manually peeled off from the molds and punched with 0.75 mm inlet and outlet ports. The PDMS was rinsed with IPA and water, and then transferred to an O_2 plasma cleaner for bonding with 30 mm circular borosilicate glass substrates (#1.5, Bioptechs Inc., Butler, PA).

"*In Situ* DLW (*is*DLW)"-Based Fluidic Barrier Microstructure Fabrication

The fluidic barrier wall microstructures were modeled using SolidWorks (Dassault Systèmes) CAD software and designed with 10 μm overlap (with the PDMS microchannel and glass substrate) to promote fluidic sealing. The 3D CAD models of barrier designs corresponding to each channel profile were exported as STL files and then imported into Describe (Nanoscribe) CAM software for generation of the laser writing path code. The commercially available photoresist, IP-PDMS (Nanoscribe), was vacuum-loaded into the uncoated PDMS-on-glass microfluidic channels *via* the ports as described previously [18]. A droplet of immersion oil was placed on the underside of the glass substrate of the IP-PDMS-infused microdevice, which was then loaded into the Nanoscribe Photonic Professional GT2 DLW 3D printer with the 10× objective lens and oil-immersion mode configuration. For *is*DLW printing using IP-PDMS, the slicing thickness and hatching parameters were both set to 300 nm. The fluidic barrier microstructures were *is*DLW-printed by crosslinking the IP-PDMS in a point-by-point, layer-by-layer, "ceiling-to-floor" manner (*i.e.*, initially printing at the top of the PDMS microchannel and then ending the print at the glass substrate). Upon completion of the *is*DLW process, the microfluidic device was placed into an IPA solution for 20 min and then infused with fresh IPA through the microchannels to remove any residual photoresist. The device was then dried with N_2 gas.

Optical Characterization

Micrographs captured during the *is*DLW printing process of the barrier microstructures were carried out using the built-in Carl Zeiss Axio Observer inverted microscope (Zeiss, Germany) within the Nanoscribe Photonic Professional GT2 DLW 3D printer. Scanning electron microscopy (SEM) images were obtained using a TM4000 Tabletop SEM (Hitachi, Tokyo, Japan). To facilitate SEM imaging and characterizations of the *is*DLW-based prints, microchannels were first DLW-printed and molded to PDMS without bonding to glass substrates, and then the barrier microstructures (designed to have a slightly smaller height to prevent over-printing in which barrier walls exceed the height of microchannels) were printed in designated positions. Substrates and devices were rinsed with IPA and dried with N_2 gas prior to SEM imaging.

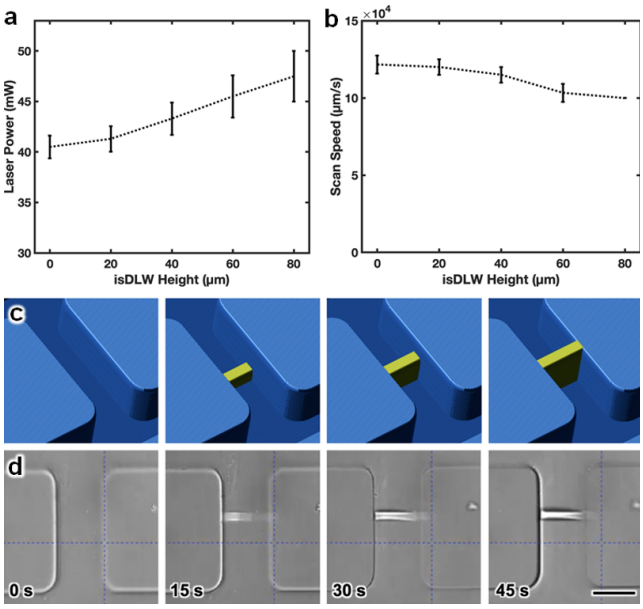

***Figure 2**: Fabrication results. **(a,b)** DLW print parameters associated with successful isDLW prints with respect to in-channel height. **(a)** Laser power. **(b)** Laser scan speed. Error bars = S.D.; n = 5. **(c, d)** Sequential computer-aided manufacturing (CAM) simulations **(c)** and corresponding micrographs **(d)** of the isDLW printing process for a barrier microstructure. Scale bar = 50 μm.*

Microfluidic Burst-Pressure Experimentation

Linear microfluidic burst-pressure experiments were performed using the Fluigent Microfluidic Control System (MFCS) and Flow Rate Platform and OxyGen software (Fluigent, France). This configuration allowed for simultaneous input pressure regulation and real-time monitoring and acquisition of both the pressure and flow rate data. To facilitate testing, microfluidic devices with *is*DLW-printed barrier microstructures were connected to fluorinate ethylene propylene fluidic tubing (Cole-Parmer, Vernon Hills, IL) *via* stainless-steel catheter couplers (20 ga., Instech, Plymouth Meeting, PA). Stainless steel catheter plugs (Instech) were inserted into superfluous ports. Burst pressure experiments were performed by applying an input pressure on one side of an *is*DLW-printed barrier microstructure, while fluid flow rates were recorded on the opposing side of the barrier structures. The input pressure was gradually increased at a rate of 2 kPa/s until the onset of leakage or burst events (*i.e.*, marked increases in the flow rate). Three experiments corresponding to each microchannel cross-sectional geometry (*i.e.*, rectangular, trapezoidal, and semi-ovular channel profiles) were performed. Data from all experiments were recorded in excel format and then processed using MATLAB (MathWorks, Natick, MA) to quantify the means and standard deviation (*S.D.*) of the pressure-flow rate relationships.

RESULTS AND DISCUSSIONS

PDMS-based *is*DLW Fabrication

To investigate the manufacturing efficacy of the *is*DLW strategy for printing microstructures inside of (and sealed to) enclosed, PDMS-on-glass microchannels that do not require pre-processing, such as surface coatings and chemical treatments [5,17], we explored the role of microchannel geometry in microfluidic sealing integrity. Using previously reported DLW-based micromolding protocols [5], we manufactured enclosed PDMS-on-glass microfluidic devices with a target region where the cross-sectional geometry of the 50 μm-tall microchannel was designed with either a rectangular, trapezoidal, or semi-ovular profile. We initially performed experiments to elucidate the DLW print settings that ensure appropriate exposure dosage at each height—*i.e.*, high enough to initiate photopolymerization, yet not too high to cause photomaterial burning issues. Fabrication results revealed that the effective laser power increased from 40.5±2.2 mW to 47.5±5.0 mW with height increasing from 0 to 80 μm, respectively (**Fig. 2a**), while the effective scan speed decreased from approximately 120 mm/s to 100 mm/s with height increasing from 0 to 80 μm, respectively (**Fig. 2b**). For consistency with prior reports for testing *is*DLW approaches [5,15,17], we examined manufacturing and microfluidic sealing efficacy using 10 μm-thick microfluidic barrier wall microstructures. CAM simulations and corresponding micrographs of the *is*DLW printing process are presented in **Figure 2c** and **2d**, respectively, with a total print time of approximately 45 s for each barrier structure.

SEM micrographs of the DLW-printed master molds, replicated PDMS microchannel cross sections, and *is*DLW-printed fluidic barrier microstructures within PDMS microchannels with the distinct channel geometries are presented in **Figure 3**. Fabrication results revealed that for 50 μm-tall channels, the printed barrier microstructures did not fully adhere to the sidewalls for the rectangular case (**Fig. 3a**); however, we did not observe such print-to-sidewall detachments for either the trapezoidal case (**Fig. 3b**) or the semi-ovular case (**Fig. 3c**). These fabrication results suggest that microchannels with effectively tapered sidewalls promote adhesion of *is*DLW-printed microstructures to the channel sidewalls, which is consistent with *is*DLW results from our prior studies [5,19].

Microfluidic Burst-Pressure Experimentation

To quantify the fluidic sealing integrity of the IP-PDMS barrier microstructures-to-PDMS microchannel interfaces, we performed linear microfluidic burst-pressure experiments for the distinct channel geometries (*i.e.*, rectangular, trapezoidal, and semi-ovular).

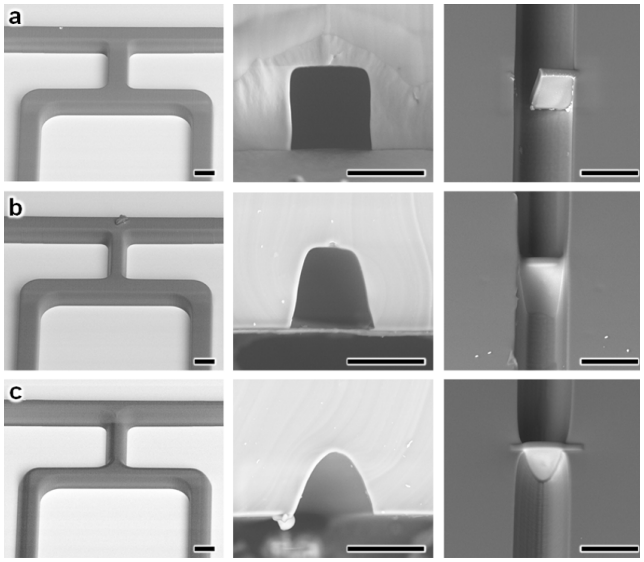

***Figure 3**: SEM micrographs of results for (left) DLW-printed master molds, (middle) replicated microchannel cross sections, and (right) barrier microstructures isDLW-printed in the micro-channels with **(a)** rectangular, **(b)** trapezoidal, and **(c)** semi-ovular cross-sectional geometries. Scale bars = 50 μm.*

The experimental results revealed that microchannel geometry can significantly affect the fluidic sealing efficacy of the *is*DLW-printed barrier structures (**Fig. 4**). Specifically, results for the rectangular channel profile revealed an onset of burst/leakage phenomena—indicated by abrupt increases in flow rate due to partial or full detachment of the barrier structure from the interior microchannel surfaces—at pressures below 200 kPa (**Fig. 4a**). The results for the trapezoidal channel profile revealed slightly higher burst pressures above 200 kPa (**Fig. 4b**). In contrast, the semi-ovular channel yielded the highest burst pressures of those examined in the current study, with fluidic sealing integrity maintained in excess of 350 kPa input pressures (**Fig. 4c**). These results for the semi-ovular channel geometry represent a >5× improvement *versus* our prior results for sol-gel-coated PDMS-on-glass microchannels [5]. Notably, even the results for the rectangular microchannel cross section—which exhibited the worst performance of the channel profiles investigated here—demonstrate significantly improved performance over the results reported in our prior work [5].

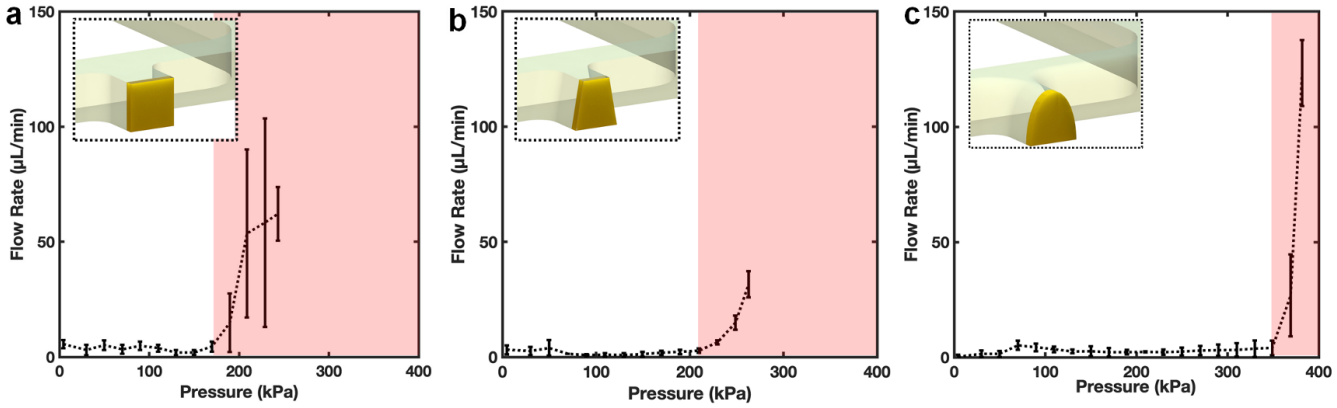

***Figure 4**: Quantified results for burst-pressure experiments with IP-PDMS barrier microstructures isDLW-printed inside of PDMS-on-glass microchannels corresponding to distinct cross-sectional profiles: **(a)** rectangular, **(b)** trapezoidal, and **(c)** semi-ovular. Red shaded regions denote undesired burst/leakage phenomena. Error bars = S.D.; n = 3 experiments per microchannel design.*

CONCLUSIONS

Recent advancements in the field of additive manufacturing provide significant promise for creating new classes of microfluidic systems that can, in turn, enable wide-ranging biomedical and soft robotic applications. In this work, we report the first demonstration of PDMS-based microstructures additively manufactured directly inside of—and notably, fluidically sealed to—uncoated, enclosed PDMS-on-glass microfluidic channels. The PDMS-based *is*DLW strategy and results presented in this work provide a preliminary foundation and guidelines for microstructure fabrication in PDMS without any pre-coating steps or post-printing infusions of glues. Akin to our prior studies [5,19], the fabrication and microfluidic burst-pressure testing results revealed that the microchannel cross-sectional geometry plays a critical role in the print-to-channel adhesion efficacy of the *is*DLW approach. In particular, we observed that 10 μm-thick barrier walls printed in 50 μm-tall microchannels with semi-ovular profiles nearly doubled the fluidic burst-pressure performance compared to that associated with the rectangular microchannel profiles. These results suggest that DLW-enabled microchannel geometries are preferable to standard rectangular profiles associated with conventional photolithography. Despite the relatively poor performance for the rectangular profile case, it should be noted that those results still represent a marked increase over our prior results that relied on time- and labor-intensive protocols for sol-gel coating of the PDMS channels [5]. One limitation of the current study is that, while the barrier microstructures were additively manufactured, their geometry is essentially 2.5D. Thus, future efforts should focus on interrogating the efficacy of the presented approach for fully 3D microstructures. Nonetheless, the notable fluidic sealing integrity results demonstrated here suggest that the presented *is*DLW strategy for printing PDMS-based microstructures within uncoated PDMS-on-glass devices offers a promising new pathway to diverse applications that benefit from geometrically sophisticated PDMS structures and systems at unprecedented size scales.

ACKNOWLEDGEMENTS

We greatly appreciate the contributions of members of the Bioinspired Advanced Manufacturing (BAM) Laboratory and the technical staff of Terrapin Works at the University of Maryland, College Park.

REFERENCES

[1] A. E. Goodling, S. Nagelberg, B. Kaehr, C. H. Meredith, S. I. Cheon, A. P. Saunders, M. Kolle, and L. D. Zarzar, "Colouration by total internal reflection and interference at microscale concave interfaces," *Nature*, vol. 566, no. 7745, pp. 523–527 (2019).

[2] M. Hippler, E. Blasco, J. Qu, M. Tanaka, C. Barner-Kowollik, M. Wegener, and M. Bastmeyer, "Controlling the shape of 3D microstructures by temperature and light," *Nature Communications*, vol. 10, no. 1 (2019).

[3] D. Nishiguchi, I. S. Aranson, A. Snezhko, and A. Sokolov, "Engineering bacterial vortex lattice via direct laser lithography," *Nature Communications*, vol. 9, no. 1 (2018).

[4] E. Montinaro, M. Grisi, M. C. Letizia, L. Pethö, M. A. Gijs, R. Guidetti, J. Michler, J. Brugger, and G. Boero, "3D printed microchannels for sub-nL NMR spectroscopy," *PLOS ONE*, vol. 13, no. 5 (2018).

[5] A. C. Lamont, A. T. Alsharhan, and R. D. Sochol, "Geometric determinants of in-situ direct laser writing," *Scientific Reports*, vol. 9, no. 1 (2019).

[6] M. H. Olsen, G. M. Hjortø, M. Hansen, Ö. Met, I. M. Svane, and N. B. Larsen, "In-chip fabrication of free-form 3D constructs for directed cell migration analysis," *Lab on a Chip*, vol. 13, no. 24, p. 4800 (2013).

[7] D. Wu, L.-G. Niu, S.-Z. Wu, J. Xu, K. Midorikawa, and K. Sugioka, "Ship-in-a-bottle femtosecond laser integration of optofluidic microlens arrays with center-pass units enabling coupling-free parallel cell counting with a 100% success rate," *Lab on a Chip*, vol. 15, no. 6, pp. 1515–1523 (2015).

[8] K. B. Justus, T. Hellebrekers, D. D. Lewis, A. Wood, C. Ingham, C. Majidi, P. R. LeDuc, and C. Tan, "A Biosensing Soft Robot: Autonomous parsing of chemical signals through integrated organic and inorganic interfaces," *Science Robotics*, vol. 4, no. 31 (2019).

[9] R. D. Sochol, A. T. Higa, R. R. Janairo, S. Li, and L. Lin, "Unidirectional mechanical cellular stimuli via micropost array gradients," *Soft Matter*, vol. 7, no. 10, p. 4606, (2011).

[10] R. Acevedo, M. A. Restaino, D. Yu, S. W. Hoag, S. Flank, and R. D. Sochol, "3D nanoprinted liquid-core-shell microparticles," *Journal of Microelectromechanical Systems*, vol. 29, no. 5, pp. 924–929 (2020).

[11] M. Restaino, N. Eckman, A. T. Alsharhan, A. C. Lamont, J. Anderson, D. Weinstein, A. Hall, and R. D. Sochol, "In situ direct laser writing of 3D graphene-laden microstructures," *Advanced Materials Technologies*, vol. 6, no. 8, p. 2100222 (2021).

[12] J. van 't Oever, N. Spannenburg, H. Offerhaus, D. van den Ende, J. L. Herek, and F. Mugele, "In-chip direct laser writing of a centimeter-scale acoustic micromixer," *Journal of Micro/Nanolithography, MEMS, and MOEMS*, vol. 14, no. 02, p. 1 (2015).

[13] L. Amato, Y. Gu, N. Bellini, S. M. Eaton, G. Cerullo, and R. Osellame, "Integrated three-dimensional filter separates nanoscale from microscale elements in a microfluidic chip," *Lab on a Chip*, vol. 12, no. 6, p. 1135 (2012).

[14] A.T. Alsharhan, O.M. Young, X. Xu, A.J. Stair, and R.D. Sochol, "Integrated 3D Printed Microfluidic Circuitry and Soft Microrobotic Actuators via *In Situ* Direct Laser Writing", *Journal of Micromechanics and Microengineering*, 31, 4 (2021).

[15] J. Y. Han, S. Warshawsky, and D. L. DeVoe, "In situ photografting during direct laser writing in thermoplastic microchannels," *Scientific Reports*, vol. 11, no. 1 (2021).

[16] J. Lölsberg, J. Linkhorst, A. Cinar, A. Jans, A. J. Kuehne, and M. Wessling, "3D nanofabrication inside rapid prototyped microfluidic channels showcased by wet-spinning of single micrometre fibres," *Lab on a Chip*, vol. 18, no. 9, pp. 1341–1348 (2018).

[17] A. Lüken, M. Geiger, L. Steinbeck, A. C. Joel, A. Lampert, J. Linkhorst, and M. Wessling, "Biocompatible micron-scale silk fibers fabricated by microfluidic wet spinning," *Advanced Healthcare Materials*, vol. 10, no. 20, p. 2100898 (2021).

[18] R. D. Sochol, S. Li, L. P. Lee, and L. Lin, "Continuous flow multi-stage microfluidic reactors via hydrodynamic microparticle railing," *Lab on a Chip*, vol. 12, no. 20, p. 4168 (2012).

[19] A. T. Alsharhan, R. Acevedo, R. Warren, and R. D. Sochol, "3D microfluidics *via* cyclic olefin polymer-based *in situ* direct laser writing," *Lab on a Chip*, vol. 19, no. 17, pp. 2799–2810 (2019).

CONTACT

Xin Xu, tel: +1-301-405-6928; xuxin97@umd.edu

ROOM TEMPERATURE SEAL-RING AU-TO-AU BONDING HERMETICITY AND RELIABILITY TESTING

Amrid Amnache[1,2], Paul Gond-Charton[3] and Luc G. Fréchette[1,2]*
[1]Institut Interdisciplinaire d'Innovation Technologique (3IT), Université de Sherbrooke, Sherbrooke, Canada
[2]Laboratoire Nanotechnologies et Nanosystèmes (LN2), CNRS UMI-3463, Université de Sherbrooke, Sherbrooke, Canada
[3]Teledyne Dalsa Semiconductor, Canada

ABSTRACT

Room temperature Au-to-Au bonding has shown a promising potential for microelectromechanical systems (MEMS) encapsulation. However, the long-term reliability remains one of the critical concerns for the integration of this bonding technology in MEMS wafer-level fabrication. We have demonstrated the hermeticity and reliability of room temperature Au-to-Au bonding of thin seal-rings as narrow as 40 µm. Hermiticity was demonstrated over more than one-year at ambient conditions, corresponding to a leak rate below 10^{-12} Pa.m^{3}s^{-1}. Also, accelerated hermeticity testing in an elevated temperature and humid environment has shown excellent reliability for the first time. This type of bonding appears to be a suitable method for MEMS wafer-level packaging that requires low temperatures and/or operation in harsh environments.

KEYWORDS

Wafer Bonding, Gold-to-Gold, Room Temperature, Hermeticity, Reliability.

INTRODUCTION

Microelectromechanical systems (MEMS) often require hermetic packaging to ensure their functionalities for long-term operation. The encapsulation serves to avoid damaging of the MEMS components during the fabrication steps e.g. dicing and chip handling, and to avoid contamination e.g. moisture and particles during the lifetime of the MEMS devices. For some MEMS such as inertial sensors [1], [2], the encapsulation serves also to maintain a certain ambient pressure inside the cavity to keep the operation stable during the MEMS lifetime. Those MEMS often require vacuum inside the cavity to keep their mechanical damping characteristics. Leakage overtime can result in lowering the sensitivity of the device and thus degradation of its functionalities. Today's robust and hermetic wafer-level bonding technologies, including thermocompression bonding [3], direct bonding [4], anodic bonding [5] and eutectic bonding [6], enable excellent encapsulation hermeticity even for prolonged lifetime of over 20 years [3]. Compared to components-level packaging, wafer-level bonding has a cost saving benefit since it enables batch processing [7], [8]. These wafer-level bonding technologies unfortunately need high thermal budget (>200°C) which limits the use of temperature-sensitive materials and the control of post-bonding thermomechanical stress.

Recently, a promising direct bonding method has been demonstrated at room temperature (RT) using thin gold films as intermediate bonding layers [9], [10]. Preliminary studies have shown excellent hermeticity with this bonding approach [9], but reliability test and the impact of seal-ring width have however not been reported before. It is important to predict how long the package formed using this bonding technology will remain hermetic overtime.

The objective in this work is to demonstrate the hermetic reliability of thin seal-rings formed by RT Au-to-Au bonding. This work also aims to obtain a quantitative study of the RT Au-to-Au bonding reliability in harsh environments.

HERMETICITY MEASUREMENT

The quality of RT Au-to-Au bonding is evaluated by studying the hermeticity. There are many test methods to evaluate hermeticity [11] including and not limited to helium leak test, Q-factor measurement, and Raman spectroscopy. In this work, the hermeticity is evaluated with two different methods: the membrane deflection and the Krypton-85 leak testing.

Membrane deflection method

We used the membrane deflection method to evaluate the hermeticity of the bond. It consists of a hermetically closed chamber formed by bonding a seal-ring between cap and cavity wafers under vacuum. The pressure difference between the cavity and the ambient induces deflection of a membrane formed in the cap wafer. The membrane needs to be flexible enough in order to obtain measurable deflection values. By measuring shift of the membrane deflection over time, the hermeticity can be estimated using the elasticity equations [4].

The membrane deflection, ω, can be calculated by the following equation [4]:

$$\omega = \alpha \frac{\Delta P\, a^4}{\delta^3} \frac{1-\gamma^2}{E} \quad (1)$$

where E is Young modulus, γ is Poisson's ratio, α is a constant (1/66 for square membranes), a is the membrane side length, δ is the membrane thickness, and ΔP is the pressure difference between the inside and outside of the cavity.

The maximum leak rate (MLR) can be estimated by the following equation [4]:

$$\mathrm{MLR} = \frac{\alpha\,(1-\gamma^2)}{E} \frac{a^2}{\delta^3 d} \frac{\Delta t}{\Delta \omega} \quad (2)$$

where d is the depth of the cavity, Δt is the elapsed time after bonding, and $\Delta\omega$ is the membrane deflection change over time.

This method has advantages to be non-destructive and simple for implementation. However, for accurate measurement, a long time would be necessary to measure any change of the membrane deflection.

Krypton-85 leak testing

The hermeticity of the bonded samples is also measured using the Kypton-85 leak testing method. This highly sensitive method has an advantage to be capable to measure lower leak rates with fast test time and relatively low cost. The method consists of using Kr-85 as a tracer gas to estimate the hermeticity

978-1-940470-04-7/HH2022/$25©2022TRF
DOI 10.31438/trf.hh2022.61

of the sealing. The sample is first put into a bombing chamber with a pressurized gas mixture of air and small quantities of Kr-85. If the sealing has a leak, the gas will enter the cavity. After the bombing cycle, the sample is analyzed using a scintillation counter, which is capable of detecting residual Kr-85 that have entered the cavity. The total leak rate can then be calculated. This method is also used to validate results from the membrane deflection method.

RELIABILITY VERIFICATION

The reliability of the Au-to-Au bonding is evaluated using autoclave standard testing. This known testing method [12]–[14] determines if the bonding can withstand temperature, humidity corrosion and pressure simultaneously. The samples to be tested are subjected to hot pressurized water vapor in an autoclave.

By assuming that the leak is caused by a capillary flow through the seal ring, the leak rate Q can be calculated by the Knudsen formula [15]:

$$Q = \frac{2\pi}{3}\frac{r^3}{l}\sqrt{\frac{8RT}{\pi M}}(P_2 - P_1) \quad (3)$$

where r is the capillary radius, l is the capillary length, R is the universal gas constant, T is the temperature, M is the molecular mass of gas, P_2 is the high pressure and P_1 is the low pressure.

The acceleration factor AF due to the pressure in the autoclave can be evaluated as the ratio between the leak rate at normal conditions of the product and the leak rate at the accelerated conditions. When using same gas at the accelerated test than at the normal conditions, the accelerated factor can be calculated by the following formula:

$$AF = \frac{(P_2 - P_1)_{normal}}{(P_2 - P_1)_{accelerated}} \quad (4)$$

BONDING PROCESS

Figure 1 illustrates the fabrication process flow of a wafer-level Au-to-Au bonding prior to hermeticity and reliability testing. A pair of two silicon wafers of 100 mm diameter are used to perform this bonding. One wafer of 350 µm thickness named cavity wafer and another wafer of 525 µm thickness named cap wafer. The cavity wafer serves to create the square cavity chamber and the deflecting membrane. First, the wafer is cleaned with RCA and then thermally oxidized to form 100 nm of SiO_2. This thin layer serves to protect the bonding surface from degradation through the microfabrication process, and will be removed before bonding. Lithography is performed followed by reactive ion etching (RIE) of the oxide layer. Using the same photoresist mask, 130 µm of silicon is etched by deep reactive ion etching (DRIE). The cavity, seal ring and the support walls are therefore patterned as illustrated in Fig.1a. Four different seal-ring widths are formed, 40, 80, 120 and 160 µm. In order to support the stress induced by the membrane deflection, thick walls are formed from each side of the seal ring. Intentional openings are created in the support walls to ensure access of environment gas to the seal ring. The photoresist is striped after etching using acetone and the cavity wafer is cleaned with Piranha solution (1:2 mixture of H_2O_2:H_2SO_4) for 10 min. Afterwards, the oxide layer is removed using hydrofluoric solution (HF 49%) for 15 s. The cap wafer as illustrated in Fig.1b serves to close and seal the cavity chamber once bonded to the cavity wafer. Prior to bonding,

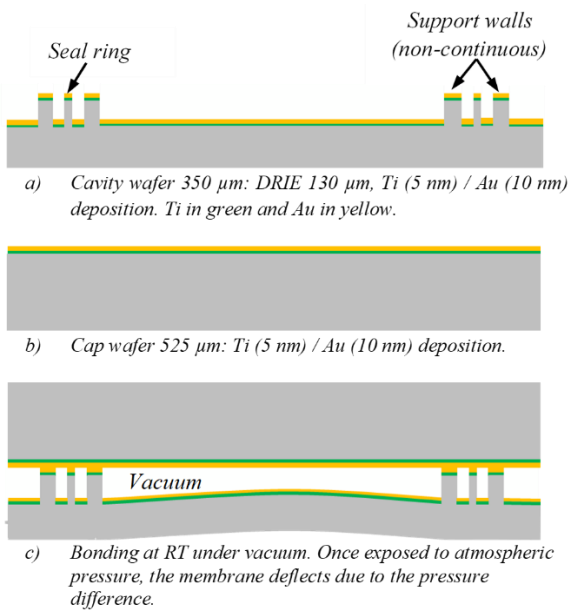

Figure 1: Process flow of RT Au-to-Au bonded devices prior to hermeticity and reliability testing.

the cap and cavity wafers are cleaned with RCA and then coated with 5/10 nm of Ti/Au by evaporation. Bonding is done under vacuum at ambient temperature creating hermetic vacuum chambers with membranes as illustrated in Fig.1c. The air pressure inside the bonding chamber is set to 1×10^{-5} mbar. Membranes are 3 or 10 mm width and 230 µm thick. Note that the variation of the membrane thickness is +/- 10 µm. The variation comes from the DRIE nonuniformity. A uniform contact load of 200 N is applied in order to initiate the bonding. It is important to note that the dwell time between the deposition of Ti/Au and the bonding was less than 15 min.

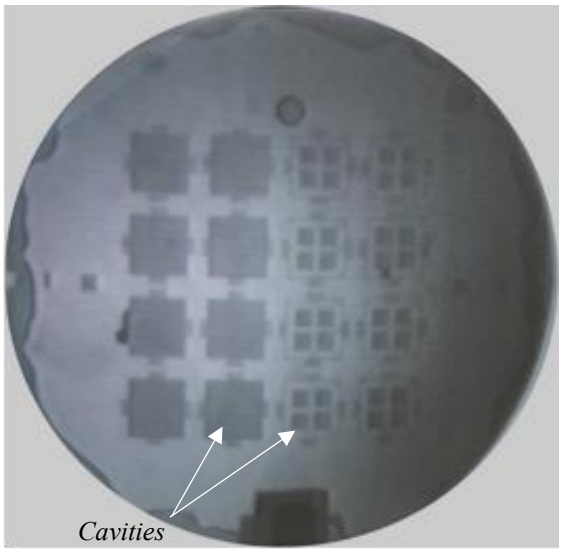

Figure 2: Infrared photograph showing the quality of Au-to-Au bonding at room temperature. Wafer diameter is 100 mm. It shows two set of cavities: 8 cavities with 10 mm membrane (left side) and 32 cavities with 3 mm membranes (right side).

Figure 2 shows an infrared characterization of the bonded wafers. It shows uniform bonding except defect on the wafer

edges and random voids that can be caused by dust particles. This process otherwise shows high quality wafer bonding at room temperature. The bonded wafers are diced into individual square chips to evaluate the hermeticity of the bond. Two set of cavities were fabricated: 8 cavities with 10 mm membrane and 32 cavities with 3 mm membranes as shown in Fig. 2. The curvature of the deflected membranes was seen just after dicing for the larger membranes.

EXPERIMENTS AND RESULTS

Storage life testing

A total of seven samples (10 mm square membranes) with different seal-ring widths were stored in air environment with controlled humidity and temperature (20°C, 1 atm, 40% RH). Results of the measured membrane deflection over time are shown in Fig.3. The maximum deflection (center of the membrane) was measured by a mechanical profilometer. In respect of the measurement errors, the experimental results match well with the analytical deflection calculated by eq. 1 to be 7.5 µm. It is observed that for all samples, the deflection remained unchanged over more than 400 days of storage. It can be concluded that there is no significant change in hermeticity of the seal. Furthermore, for the characterized elapsed time, the results show that there is no impact of the seal-ring width on the hermeticity. Additional time may be needed to observe such effect.

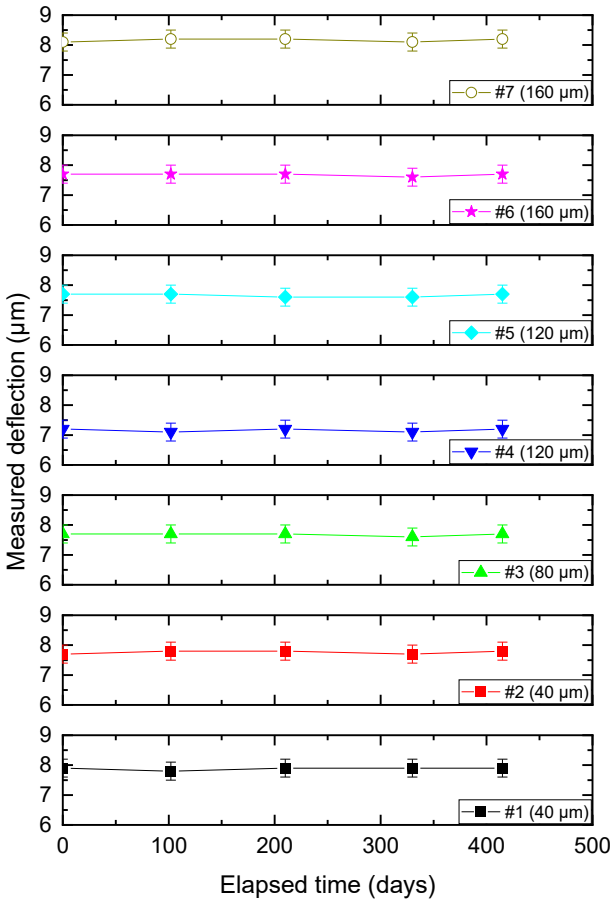

Figure 3: Measured membrane deflection with different seal-ring widths showing no leakage for over a year. The error bars of +/- 0.3 µm come from the profilometry measurement. Measurement began the same day after dicing the bonded wafers.

Figure 4 is the plot of the measured membrane deflection overtime of sample #1 (as plotted in Fig. 3) with the calculated deflection by eq. 2 assuming two different MLR (10^{-11} and 10^{-12} $Pa.m^3s^{-1}$). From the plot, it can be observed that there is a large difference between the deflection calculated for MLR of 10^{-11} $Pa.m^3s^{-1}$ and the real deflection change overtime of the sample #1. There is however no significant difference of the measured deflection and the calculated deflection for MLR of 10^{-12} $Pa.m^3s^{-1}$. The MLR is then estimated to be equal or less than 10^{-12} $Pa.m^3s^{-1}$ in this study. It is five orders of magnitude greater than the minimum leak rate required for various MEMS [11]. Additional testing time would be required to measure lower leak rate.

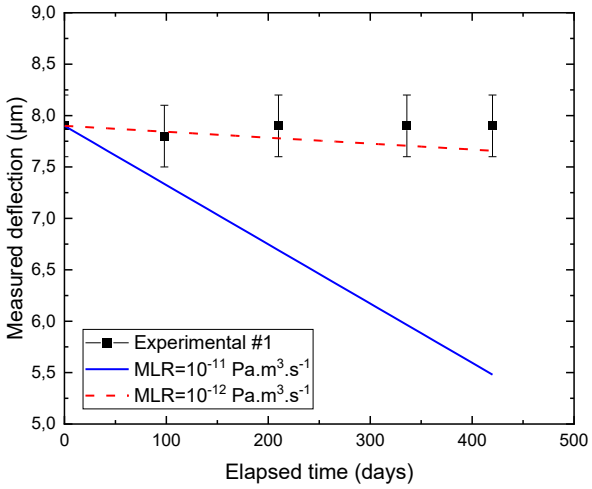

Figure 4 Evaluation of the maximum leak rate based on the membrane deflection change for sample #1.

Krypton-85 gross and fine leak testing

The hermeticity of the bonded samples was also analyzed using the Kypton-85 leak testing method (test done by Oneida Research Services) according to Mil-std-750F, method 1071.16. A total of 24 samples with membranes of 3 mm width are used to perform this test (cavities on the right side in Fig.2). Dry and wet gross leak tests, and fine leak test were conducted successively. Table 1 shows the leak test conditions and the failure criteria. A total of 18 samples passed the fine leak test with a detected leak rate $<5\times10^{-11}$ $Pa.m^3s^{-1}$. This result validated the measurement done using the membrane deflection method and shows one more time the high hermetic performance of the Au-to-Au bonding. Only 6 samples failed the wet gross leak. Bonding defects (random voids) as shown in Fig.2 are probably the reason. Same as for the membrane deflection results, there is no observed impact of the seal-ring width on the hermeticity.

Table 1 Kr-85 gross and fine leak test conditions.

Test method	Bombing time (hrs)	Bombing pressure (psia)	Failure criteria
Dry gross leak	0.05	30	Kr-85 counting >500 c/m
Wet gross leak	0.2	50	Red dye observed and/or Kr-85 detection
Fine leak	16.03	45	Leak rate $>5\times10^{-11}$ $Pa.m^3s^{-1}$

Accelerated reliability testing

In order to demonstrate the robustness of the RT Au-to-Au bonding, we pursue further with reliability testing. The same samples used to measure the membrane are put into a heated autoclave filled with steam at 120°C/2 bars/100% RH. Based on

visual observation, it was shown that all the seven samples survived testing. Quantitatively, the membrane deflection remained unchanged after testing for 216 hours., as shown in Fig. 5. As observed for the storage life testing, there is no impact of the seal-ring width on the membrane deflection change overtime. Probably, more testing time is needed to be able to detect any effect. By assuming the normal conditions for the product to be 50% RH and 20°C with the partial water vapor pressure of 12 mbar, the AF calculated by eq. 4 is 166. Thus, based on the testing results of 216 hours of autoclave, the bonding lifetime in the normal conditions can extend to more than 4 year.

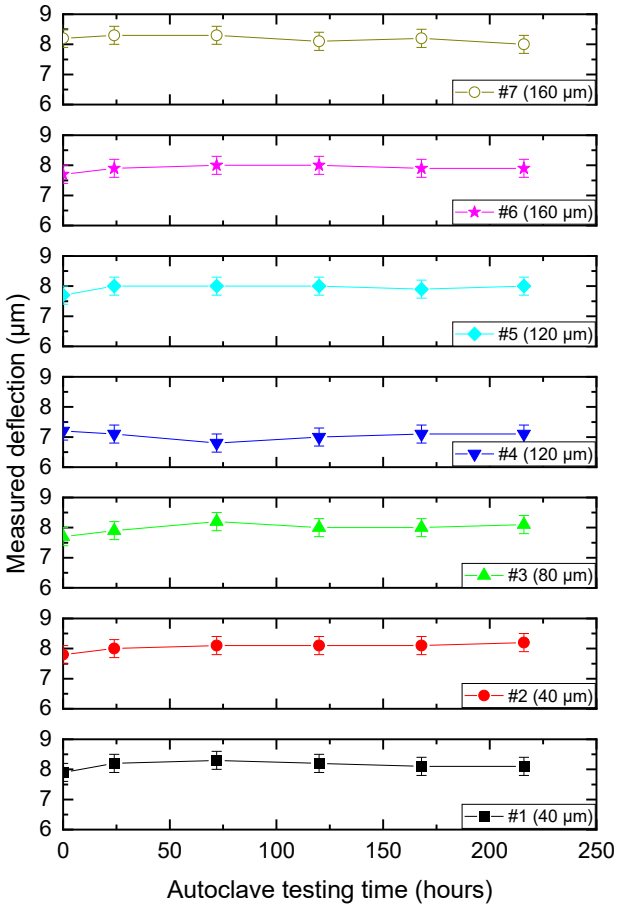

Figure 5: Measured membrane deflection with different seal ring widths showing no leakage for over 200 hr of autoclave testing.

CONCLUSION

The room temperature Au-to-Au bonding performed in this work showed potential for hermetic and reliable sealing with thin seal-rings, as narrow as 40 µm. The measured leak rate was found to be below 10^{-12} Pa.m^{3}s^{-1} using the membrane deflection method and below 5×10^{-11} Pa.m^{3}s^{-1} using the Kr-85 leak test method. Also, reliability testing has shown that this bonding method offers excellent reliability in harsh (hot and humid) environments. This allows MEMS researchers to consider this type of bonding in their applications needing hermetic and reliable operation, but with temperature sensitive materials that could not withstand traditional wafer bonding techniques.

ACKNOWLEDGEMENTS

The authors would like to thank Vincent Pares, Mohamed Walid Hassen and Doriane Hassaine Daoudji for their help towards the testing procedures. Support from the Canada Research Chair Program (NSERC), Canadian Foundation for Innovation (CFI) are gracefully appreciated.

REFERENCES

[1] I. B. Flader *et al.*, "Micro-tethering for fabrication of encapsulated inertial sensors with high sensitivity," *Journal of Microelectromechanical Systems*, vol. 28, no. 3, 2019.

[2] A. Efimovskaya *et al.*, "Compact roll-pitch-yaw gyroscope implemented in wafer-level Epitaxial Silicon Encapsulation process," 2017.

[3] J. Fan, L. Peng, K. H. Li, and C. S. Tan, "Wafer-level hermetic packaging of 3D microsystems with low-temperature Cu-to-Cu thermo-compression bonding and its reliability," *Journal of Micromechanics and Microengineering*, vol. 22, no. 10, 2012.

[4] R. Stricher *et al.*, "In Situ Doped Polysilicon (ISDP) Hydrophilic Direct Wafer Bonding for MEMS Applications," *ECS Journal of Solid State Science and Technology*, vol. 10, no. 6, 2021.

[5] A. Duan, K. Wang, K. Aasmundtveit, and N. Hoivik, "Characterization of wafer-level bonded hermetic packages using optical leak detection," in *International Symposium on Photoelectronic Detection and Imaging 2009: Material and Device Technology for Sensors*, 2009, vol. 7381.

[6] T. Akashi, H. Funabashi, H. Takagi, Y. Omura, and Y. Hata, "Wafer-level hermetic vacuum packaging by bonding with a copper-tin thin film sealing ring," *Journal of Micromechanics and Microengineering*, vol. 28, no. 4, 2018.

[7] C. S. Tan, J. Fan, D. F. Lim, G. Y. Chong, and K. H. Li, "Low temperature wafer-level bonding for hermetic packaging of 3D microsystems," *Journal of Micromechanics and Microengineering*, vol. 21, no. 7, 2011.

[8] J. Xu, Y. Du, Y. Tian, and C. Wang, "Progress in wafer bonding technology towards MEMS, high-power electronics, optoelectronics, and optofluidics," *International Journal of Optomechatronics*, vol. 14, no. 1. 2020.

[9] M. Yamamoto *et al.*, "Room-temperature pressureless wafer-scale hermetic sealing in air and vacuum using surface activated bonding with ultrathin Au films," *Japanese Journal of Applied Physics*, vol. 59, no. SB, 2020.

[10] T. Shimatsu and M. Uomoto, "(Invited) Room Temperature Bonding of Wafers with Thin Nanocrystalline Metal Films," *ECS Transactions*, vol. 33, no. 4, 2019.

[11] S. Millar and M. Desmulliez, "MEMS ultra low leak detection methods: A review," *Sensor Review*, vol. 29, no. 4, 2009.

[12] Y. T. Cheng, L. Lin, and K. Najafi, "A hermetic glass-silicon package formed using localized aluminum/silicon-glass bonding," *Journal of Microelectromechanical Systems*, vol. 10, no. 3, 2001.

[13] P. J. van der Wel *et al.*, "Hermeticity testing of capacitive RF MEMS switches," 2008.

[14] S. J. Ham *et al.*, "Characterization and reliability verification of wafer-level hermetic package with nano-liter cavity for RF-MEMS applications," 2007.

[15] Y. Tao and A. P. Malshe, "Theoretical investigation on hermeticity testing of MEMS packages based on MIL-STD-883E," *Microelectronics Reliability*, vol. 45, no. 3–4, 2005.

CONTACT

*Amrid Amnache, tel: +1-819-919-2628;
amrid.amnache@usherbrooke.ca

STABLE, ELECTRON-BEAM SUBLIMATED, NANOSTRUCTURED SILICON DIOXIDE ON POLYCARBONATE AND STAINLESS-STEEL AS A BIOADHERENT DIELECTRIC TOWARDS NEURAL MICROPHYSIOLOGICAL SYSTEMS

Charles M. Didier[1,†], David Fox[1,†], Aliyah Baksh[1,†], Kevin Pollard[2], Nisha Iyer[3], Alexander Bosak[2], Yuen Yee Li Sip[1], Julia Freitas Orrico[1], Randolph Ashton[3], Michael J. Moore[2], Lei Zhai[1] and Swaminathan Rajaraman[1]

[1] University of Central Florida, USA; [2] Tulane University, USA; [3] University of Wisconsin, USA

[†] Equally Contributing Authors

ABSTRACT

Towards the development of biosensors, novel material combinations often impart challenges in microfabrication and process integration, e.g., depositing traditional materials using established processing techniques on new substrate materials. Silicon dioxide, for example, has been widely used in MicroElectroMechanical Systems (MEMS) fabrication but is rarely used in devices in combination with polymers and steel alloys. Herein, we establish an avenue improving the adherence of such an oxide material to polycarbonate and 316L stainless steel via polydopamine mediated chemistry to construct a stable coating that is indicative of its dual purpose as both a dielectric material for microelectrodes and a cell adhesion promoter. This fabrication method is a significant step towards novel BioMEMS devices and integrated biological systems currently under development.

KEYWORDS

Silicon Dioxide (SiO_2), Nanostructuring, Polydopamine (PDA), Biological Interfaces, Microphysiological Systems.

INTRODUCTION

As the field of *in vitro* diagnostics advances **[1]**, ***innovations in constituent materials*** are required to enable necessary functional metrics. For realizing neural Microphysiological Systems (MPS) with integrated sensing/stimulation modalities **[2,3]**, ***insulating dielectric materials for enhanced cellular growth*** are of great importance **[4]**. However, material incompatibility often prevents many potential applications **[5]**. Silicon dioxide (SiO_2) as a dielectric material has been widely studied and utilized in traditional MEMS fabrication **[4,6]**, and its inherent inert/porous nature has continually motivated the utilization of SiO_2 as the functional surface for many BioMEMS devices. However, SiO_2 is no exception in that challenges exist to adapt its utilization towards non-traditional substrates and MPS integration, such as those incorporating polymers and metal alloys. Generally, SiO_2 has been deposited through thermal growth, plasma-enhanced deposition processes or precursor-mediated synthesis, and often occurs well outside temperatures/conditions polymers can withstand **[7]**. Additionally, mismatch in functional groups leads to superficial adhesion to polymers and metal alloys which is potentially disrupted by humidity/hydration-induced swelling **[8]**. Thus, strategies must be employed to enhance the adhesion of SiO_2 by utilizing established intermediary compounds. Ideally, said strategies should not interfere with desired optical properties of polymers, and be scalable for device integration in polymer-metal based microfabrication processes. ***Solution-based polydopamine (PDA) treatments*** **[9]** have been previously utilized to provide a linker molecule for such disparate materials. PDA, along with electron-beam sublimation of SiO_2 provides a ***novel, low-temperature avenue*** for stable, bio-adherent dielectric coatings which

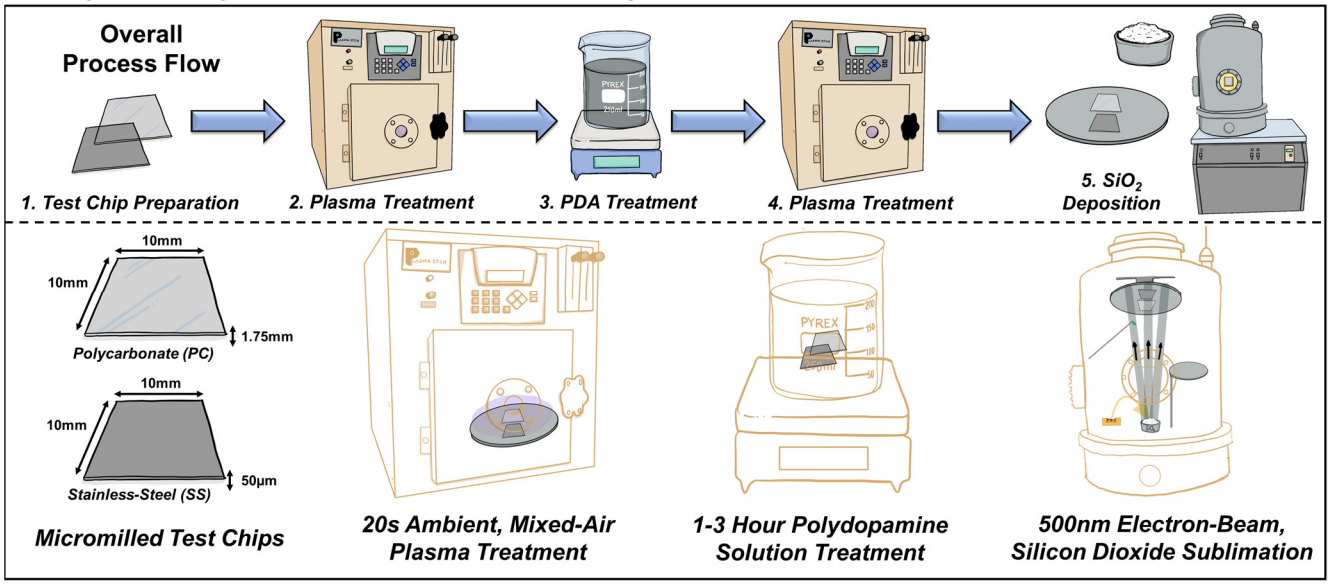

Figure 1: *Schematic representation of the overall treatment process flow for sample testing. First, test chips are micromilled from their respective substrates. The upper section describes the general treatment scheme, while the lower partition details each step. Samples were first treated in ambient, mixed-air plasma for 20s. Next, the samples were placed in a continuously stirring PDA-EDC solution for the designated 1-3 hours. The samples were washed three times in DI water and then dried with N_2 gas, before being treated again with ambient, mixed-air plasma for 20s. Prepared samples were stored in a vacuum chamber for transportation to the e-beam system. Once the samples were loaded, the chamber was pumped to an appropriate vacuum, and 500nm of SiO_2 was deposited via e-beam induced sublimation. Samples were subsequently stored under vacuum conditions until required for testing.*

978-1-940470-04-7/HH2022/$25©2022TRF
DOI 10.31438/trf.hh2022.62

additionally enable robust neural spheroid growth. Previously, MPS approaches utilizing accessible material/insulation strategies, which retain optical clarity (e.g., PDMS) have been explored **[3,10,11]**. Herein we ***explore an electron-beam sublimation of nanoporous silicon dioxide (SiO_2) technology*** onto polycarbonate (PC) substrate and 316L stainless-steel (**SS**) microelectrode materials **[11]** using PDA to stabilize adhesion. We subsequently characterize this method and validate its future potential for 3D Microelectrode Array (3D MEA)-based neural MPS.

MATERIALS AND METHODS

10mm^2 (length by width) test chips were micromilled from bulk sheets of 1.75mm thick PC and 50µm thick SS. These were subsequently cleaned in 70% isopropyl alcohol (IPA). A stirring solution of PDA (Sigma Aldrich, USA) was prepared as per Azim et al. **[9]**, utilizing a stock 1-ethyl-3-(3-dimethylaminopropyl)-carbodiimide (EDC) solution (Sigma Aldrich, USA) as a cross-linking enhancer. Test chips were plasma treated (Plasma Etch Inc., USA) in mixed air plasma for 20s, and then submerged in the solution for 1-3h for coating. Next, test chips were rinsed three times in DI water, dried with N_2 gas and stored under vacuum. PDA-coated chips were plasma treated again (20s) prior to electron-beam deposition of 500nm SiO_2 (Thermionics, USA; **Fig. 1**). Additional test chip treatments were prepared for analysis, control, and comparison. To simulate microelectrode dielectric stability in cell culture incubator conditions, coated SS chips were subjected to an incubator environment (>95% humidity) between 4-10 weeks, before scotch-tape peel test analysis of the adhesion was performed. ImageJ software (National Institutes of Health, USA) was utilized for image-based quantification of tape-peeled areas. Scanning electron microscopy (SEM) (Zeiss, Germany) and optical imaging (iPhone XS; Apple Inc., USA) were performed for surface feature comparison. Energy Dispersive X-ray Spectroscopy (EDS) (Zeiss, Germany) confirmation of SiO_2 composition was additionally performed during SEM imaging. X-ray Photoelectron Spectroscopy (XPS; Physical Electronics, USA) was utilized for compositional and chemical analysis of the plasma-treated PDA-PC. Water contact angle (WCA) measurements were obtained (DataPhysics Instruments, USA; OCA 15EC mode, SCA 20 module) to assess the relative surface energies at selected functionalization states. Ultraviolet-Visible spectroscopy (Agilent, USA) was performed to assess transparency of the PDA/SiO_2 coated PC substrates. Scotch-tap peel tests were performed by uniformly pressing the tape on to each sample, and then peeling with consistent force. Human iPSC-nociceptors (Anatomic Inc., USA) and Embryonic Stem Cell-derived – Spinal Cord Dorsal Horn (ESC-SCDH Ashton Lab, University of Wisconsin, USA) spheroids were plated within polyethylene glycol dimethacrylate (PEGDMA) channels on glass-control and SiO_2-coated polymer substrates with 3D SS electrodes. Calcein AM staining visualized organoid growth, 2-weeks after completion of terminal differentiation.

RESULTS AND DISCUSSIONS

Polycarbonate substrates and stainless-steel microelectrodes form the basis of novel 3D MEA-based neural MPS collaboratively under development between the University of Central Florida, Tulane University, and the University of Wisconsin **[11]**. In early trials of adhering SiO_2 to PC, layers of porous and flaking SiO_2 film were observed under SEM (**Fig. 2A-C,** without the addition of PDA). Additionally, serpentine "bubbles", partially released through surface incompatibility of 500nm thick SiO_2 with PC, were present which denoted delamination due to inherent stress within the thin film. However, these experiments confirmed the nanoporous nature of the oxide film, which indicated potential suitability for cellular applications. Previous published data **[10]** and internal studies confirmed 500nm SiO_2 films were sufficient as both a suitable dielectric and a stable insulation layer for 3D MEAs.

Fig. 2D-F illustrate the addition of PDA treatment before SiO_2 deposition on PC and SS substrates. As the PDA treatment time increases, a gradual darkening can be observed (**Fig. 2**, inset images), and the PDA clusters change in both size and uniformity. The 1-hour PDA treatment is shown in **Fig. 2D**, and the polydisperse topography observed may have contributed to film delamination during PDA-SiO_2 peel-tests through an inconsistent distribution of inherent forces within the combined thin film. In **Fig. 2E,** the 2-hour PDA treatment demonstrated a monodisperse topography, through

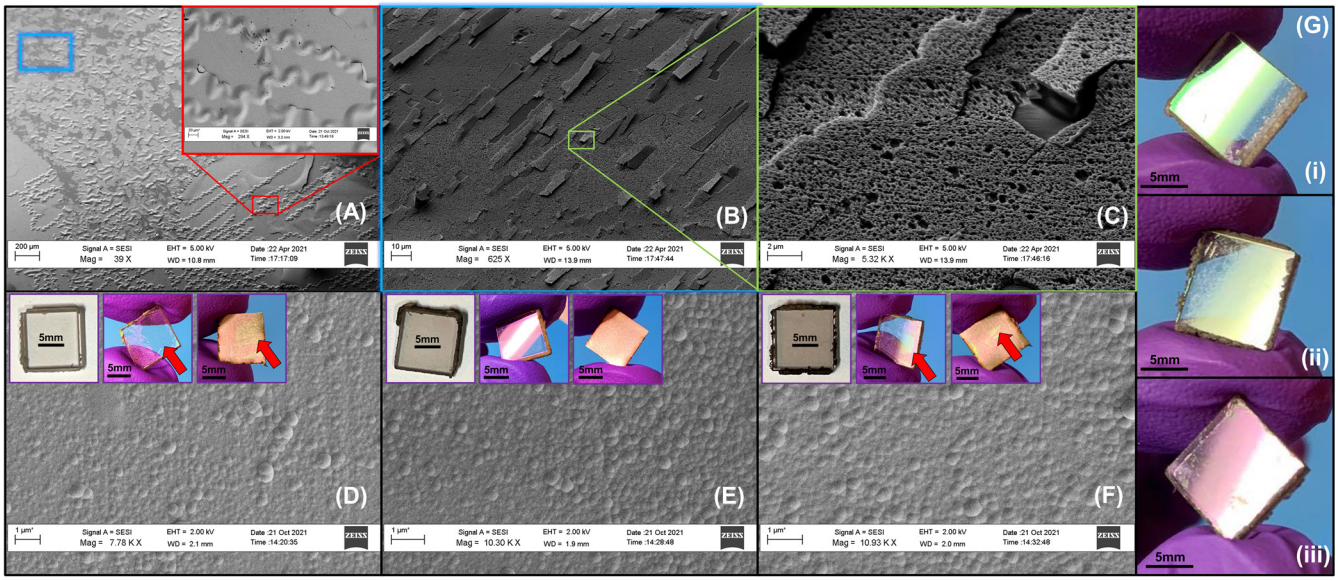

Figure 2: *SEM and optical images of SiO_2 adhesion testing. (A) SEM image of SiO_2 on PC without treatment. Inset details serpentine "bubbles," indicative of delamination. (B) Enhanced region of blue box from (A), illustrating flaking of SiO_2. (C) Enhanced region of (B), showing the nanoporous nature of the SiO_2. (D-F) Images detailing the addition of PDA treatment before SiO_2 deposition. Inset images show the minor darkening of the PC after PDA treatment, and tape-peel tests of both PC and SS (left to right). (D) 1-hour PDA treatment. (E) 2-hour PDA treatment. (F) 3-hour PDA treatment. (G) Lower concentration PDA treatment with SiO_2, illustrating color shifts from 1-hour (i), 2-hours (ii), and 3-hours (iii), that depict thin-film light interference phenomenon.*

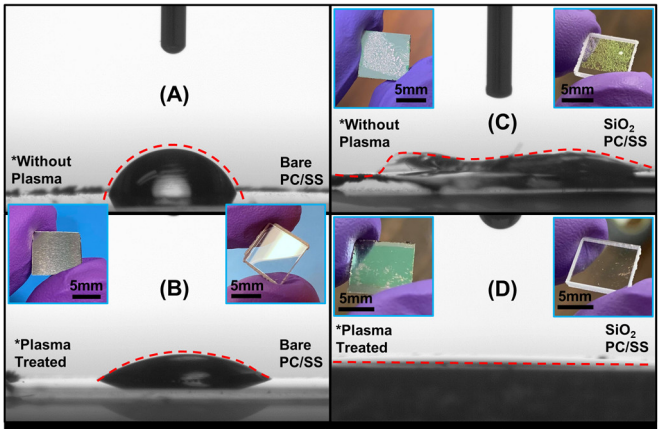

(E) Water Contact Angle (Young Laplace; θ)

Sample	Untreated	Plasma Treated	Untreated / SiO_2	Plasma / SiO_2	1Hr PDA	2Hr PDA	3Hr PDA
Polycarbonate	83.3 +/- 1.87	37.6 +/- 7.04	Delaminated	0	36.6 +/- 0.196	40.8 +/-2.94	*13.9 +/- 0.10
Stainless-Steel	86.4 +/- 12.2	36.1 +/- 2.48	Delaminated	0	45.5 +/- 1.93	40.6 +/- 4.02	40.6 +/- 0.05

Figure 3: *WCA measurements (N=3) for substrate treatment combinations. Inset images illustrate the samples utilized for measurement. (A-B) Confirmation of plasma treatments effects to increase surface energy, as (A) demonstrates a relatively hydrophobic surface, and (B) demonstrates a sharp shirt towards a more hydrophilic state. (C-D) WCA values for SiO_2 coated bare PC/SS, with and without plasma treatment. (C) Without plasma treatment, the samples optically have an uneven and cracked appearance, and upon contact with water are immediately* ***delaminated****. (D) With plasma treatment, the SiO_2 film is more consistent, and the WCA values are both* ***0*** *indicating a high surface energy. (E) Table containing WCA values and standard error margins. The PC value denoted with an (*), is due to its lower-than-expected WCA value; to be further investigated.*

which the most robust SiO_2 adhesion was observed. Tape residue can be observed (**Fig. 2**, insets) showing a highly adherent SiO_2 film, which again is likely due to an even dispersion of stresses within the thin film, coupled with plasma-enhanced binding of the oxide to the PDA across the surface. The 3-hour PDA treatment is showcased in **Fig. 2F**, which contains a polydisperse topography, containing larger PDA groupings. This once again contributed to poorer adhesion but was observed to be more robust than the 1-hour treatment. These results **overall indicate that the 2-hour PDA-SiO_2 treatment is ideal** and merits further characterization and usage. **Fig. 2G** additionally depicts how lower concentrations of the PDA treatment from 1-3h (**Fig. 2**i-iii, respectively), combined with SiO_2, demonstrate thin film light interference phenomenon with color shifts which might be further investigated in future works.

WCA measurements were first obtained to illustrate the necessity of plasma pre-treatments before PDA and SiO_2 adhesion. **Fig. 3** contains sample images from the WCA test which were utilized to calculate the Young-Laplace WCA, as well as representative images to illustrate the samples utilized in measurements. **Figs. 3A&B** serve as baseline confirmation of plasma treatments efficacy to increase surface energy on bare PC/SS as controls. The average WCA values of **83.3° +/- 1.87** (PC) and **86.4° +/- 12.2** (SS) in **Fig. 3A** show that the initial surfaces have lower surface energies (inversely related with higher WCA), denoting a hydrophobic state. This is contrasted with **Fig. 3B**, which shows that with plasma treated samples, the WCA values decrease to **37.6° +/- 7.04** (PC) and **36.1° +/- 2.48** (SS) which indicates higher surface energies, more suitable for the establishment of binding interfaces. In **Fig. 3C&D,** the next sample stage is depicted for SiO_2 coated PC and SS, varying only the usage of plasma treatment. Without plasma treatment, the films are immediately delaminated from both PC and SS, and optically have an irregular and cracked appearance (**Fig. 3C**). When plasma treatment is utilized prior to SiO_2 deposition, the SiO_2 film is stable longer, and presents a more uniform appearance (**Fig. 3D**). The WCA values of **0** indicate a very high surface energy, and excellent hydrophilicity. However, this film still degrades within hours of exposure to ambient humidity/water without PDA. The 1-hour PDA coating on PC and SS substrates demonstrated WCA values of **36.6° +/- 0.196** and **45.5° +/- 1.93**, respectively (**Fig. 3E**). The 2-hour PDA coated samples demonstrated values of **40.8° +/- 2.94** and **40.6° +/- 4.02**, respectively. The 3-hour coated samples demonstrated values of **13.9° +/- 0.10** and **40.6° +/- 0.05**, respectively. Further characterization of PC values is required to account for apparent inconsistencies with the moderate incremental decrease in WCA across PDA treatments.

To further motivate choice of the stable 2-hour PDA-SiO_2 coating, additional material characterizations were performed (**Fig. 4**). EDS analysis was performed on the e-beam deposited SiO_2, to confirm the retention of the deposited oxide composition (relative atomic percentages of **29.83% (Si)** and **69.60% (O), Fig. 4A**). Next, the ultraviolet-visible spectrum of different stages of coated PC substrates was tested, to ensure the usability of the selected coating time/method for transmitted light biological imaging applications (**Fig. 4B**). In the visual light range (400-700nm), while plain PC has ~90% optical clarity, the unstable, poorly adherent SiO_2 illustrates an irregular, anti-reflective type signature. Optical clarity was observed to decrease no more than ~5% transmittance with an hour increase in PDA treatment time, as expected from the increased observed darkening of the PC. Interestingly, corresponding PDA treatment times coupled with the 500nm of stable SiO_2 deposition demonstrated a moderate improvement of ~3% transmittance on average, in addition to an anti-reflective signature shift, which can be observed in the inset (**Fig. 4B**). With regards to coated SS

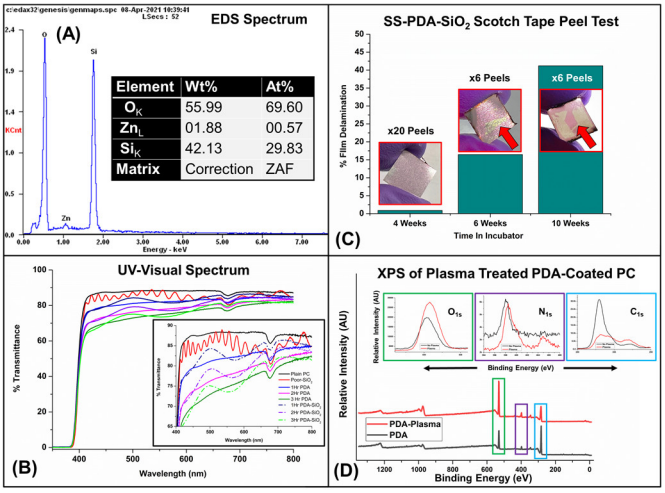

Figure 4: *Sample characterizations (N=3) of selected PDA and SiO_2 film samples. These results further motivate usage of the stable 2-hour PDA/SiO_2 coating. (A) EDS analysis of e-beam deposited SiO_2, confirming the retention of the deposited oxide composition. (B) Ultraviolet-Visible spectrum of different stages of coated PC substrates. (C) Scotch-tape peel tests, for 2-hour SS-PDA/SiO_2 films, after* ***4, 6, and 10 weeks*** *in a cell culture incubator. Inset images illustrate representative samples. (D) XPS spectra of crucial PDA interface, before and after plasma treatment.*

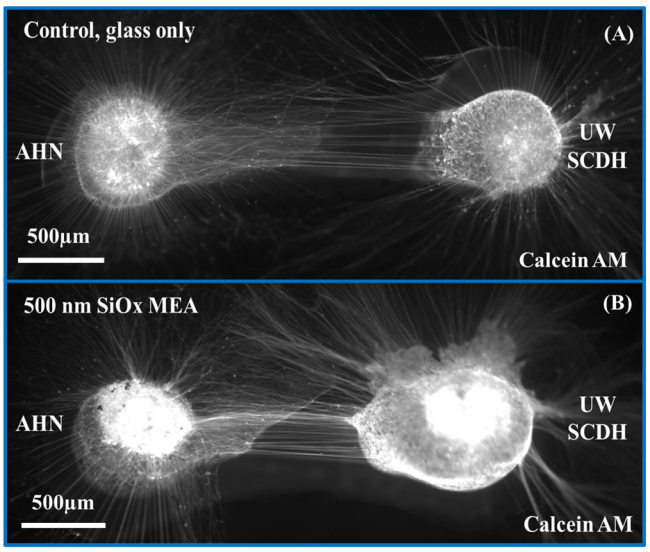

Figure 5: *Fluorescent Calcein AM staining of IPSC (Induced Pluripotent Stem Cell)-derived nociceptor and Embryonic Stem Cell (ESC)-derived spinal cord dorsal horn (SCDH) spheroid cultures within PEG channels, 2-weeks after terminal differentiation. (A) Growth on glass substrates for control, demonstrating robust growth of axonal projections, important for neuronal communication. (B) Growth on PC-SS substrates with functional SiO_2 surfaces, demonstrating differential but comparable growth and integration.*

samples, scotch-tape peel tests were performed on 2-hour SS-PDA-SiO_2 films, after **4, 6, and 10 weeks** in a cell culture incubator (**Fig. 4C**). The inset images included illustrate representative samples of the batches tested. After **>20 peel tests**, the 4-week samples proved highly stable, with the removal of **0.89% +/- 0.935** SiO_2 (i.e., **more than 99% SiO_2 was intact**). After 6-weeks, **6 peel tests** began to remove **16.5% +/- 7.49%** of the film. After 10-weeks, **6 peel tests** removed **41.2% +/- 37.3%** of the film and represents the highest variability among the measurements. Importantly, only adherence of the film and not its integrity was affected, indicating further that the chosen PDA-SiO_2 combination helped to alleviate the stress in the film, even when long-term hydration disrupted the binding to the substrate. Of note, only physically peeling the film prompted oxide removal at 10-weeks. In **Fig. 4D**, XPS spectra of crucial PDA interface was characterized, both before and after plasma treatments. Literature has established that PDA natively binds organic/inorganic surfaces through catechol groups **[12]**, which would indicate an ability for bond formation. However, treatment with mixed-air plasma was experimentally found necessary at all interfaces, resulting in significantly altered C_{1s} and N_{1s} binding energies, and suggesting higher Oxygen content binding sites. To demonstrate biocompatibility of manufactured substrates, nociceptor-SCDH spheroids were cultured atop PC/SS-PDA-SiO_2 substates in a 3D dual-hydrogel format for 2-weeks and stained with Calcein AM to show viability (**Fig. 5**). Excellent neurite outgrowth was observed, lending credence to the end-goal use within neural MPS.

CONCLUSIONS

In this work, we demonstrated a novel methodology for the realization of a stable SiO_2 dielectric and adhesion promoter functional layer on PC and SS. Due to the incompatibility of these materials with traditional SiO_2 deposition processes, a custom PDA process was utilized. We found that a 2-hour PDA treatment, coupled with mixed air plasma preparations, led to a stable 500nm SiO_2 definition on both materials. The SiO_2 coated SS additionally demonstrated excellent adhesion retention for 6-weeks in a cell culture incubator environment. We also characterized the compositional, optical, and chemical properties of the designed film and demonstrated excellent growth when incorporated within a novel, human neural 3D MPS.

ACKNOWLEDGEMENTS

The authors would like to acknowledge the funding provided through NIH UG3TR003150 and NIH UH3TR003150 grants, as well as through the UCF ORC Doctoral Fellowship (C. M. Didier). The authors acknowledge tool utilizations at NSTC, MCF-AMPAC, MSE and ECE at UCF.

REFERENCES

[1] W. Anderson et al., *"Advances in 3D neuronal microphysiological systems: towards a functional nervous system on a chip,"* In Vitro Cellular & Developmental Biology-Animal, 2021.

[2] L. Kramer et al., *"Modeling chemotherapy-induced peripheral neuropathy using a nerve-on-a-chip microphysiological system*," J. Pharm. & Tox. Methods, 2021.

[3] C. Didier et al., *"Fabrication and Characterization of 3D Microelectrode Arrays (3D MEAs) with" Edge-Wrapped" Metal Interconnects and 3D-Printed Assembly Rigs for Simultaneous Optical and Electrical Probing of Nerve-on-a-Chip® Constructs,"* IEEE 34th International Conference on Micro Electro Mechanical Systems (MEMS), 2021.

[4] G. H. Kim et al., *"Recent progress on microelectrodes in neural interfaces,"* Materials, 2018.

[5] X. Jin et al., *"Joining the un-joinable: adhesion between low surface energy polymers using tetrapodal ZnO linkers,"* Advanced Materials, 2012.

[6] H. Lee et al., *"Capacitive Measurements of SiO2 Films of Different Thicknesses Using a MOSFET-Based SPM Probe,"* Sensors, 2021.

[7] M. R. Amirzada et al., *"Surface roughness analysis of SiO2 for PECVD, PVD and IBD on different substrates,"* Applied Nanoscience, 2016.

[8] D. I. Kushner et al., *"Water sorption in electron-beam evaporated SiO2 on QCM crystals and its influence on polymer thin film hydration measurements,"* Langmuir, 2017.

[9] N. Azim et al., *"Polydopamine Surface Functionalization of 3D Printed Resin Material for Improved Polystyrene Film Adhesion,"* ACS Biomater. Sci. Eng., In Press, 2022.

[10] A. Kundu et al., *"Fabrication and characterization of 3D Printed, 3D microelectrode arrays for interfacing with a peripheral nerve-on-a-chip,"* ACS Biomaterials Science & Engineering, 2021.

[11] J. Freitas Orrico, et al. *"Fabrication and Characterization of 3D Microelectrode Arrays (3D MEAS) with Tri-Modal (Electrical, Optical, and Microfluidic) Interrogation of Electrogenic Cell Constructs,"* 21st International Conference on Solid-State Sensors, Actuators and Microsystems (Transducers), 2021.

[12] H. Lee et al., *"Mussel-inspired surface chemistry for multifunctional coatings,"* Science, 2007.

CONTACT

*Swaminathan Rajaraman, tel: +1-407-823-4339; Swaminathan.Rajaraman@ucf.edu

ULTRA-RAPID MICROFABRICATION OF HOLLOW-WELL MICRONEEDLES BY DIFFRACTION ULTRAVIOLET (UV) LITHOGRAPHY

Yuankai Li[1], Jun Ying Tan[1], Rebecca Campbell[2], Won Min Park[3], Albert Kim[2], and Jungkwun 'JK' Kim[1]
[1]Department of Electrical and Computer Engineering, Kansas State University, Manhattan KS 66506 USA
[2]Department of Electrical and Computer Engineering, Temple University, Philadelphia PA 19122 USA
[3]Department of Chemical Engineering, Kansas State University, Manhattan KS 66506 USA

ABSTRACT

This paper presents the fabrication of one-of-a-kind hollow-well microneedles using unique diffraction UV lithography. The microneedles incorporated a small pocket (well) at the tip for the drug reservoir, which enables unprecedentedly effective drug delivery than a traditional solid microneedle coated with a drug. The hollow-well microneedles were fabricated via diffraction UV lithography, which resulted in high aspect ratio microstructures. A batch microfabrication of the proposed diffraction lithography was successful by demonstrating over the 50 hollow-well microneedles on the single substrate. A mechanical test was performed on a hollow-well microneedle to determine its viability for skin penetration. The drug delivery of the hollow-well microneedle was investigated using pigskin. When compared to the typical drug-coated solid microneedle, the dispersed blue colored drug markings showed a substantial improvement.

KEYWORDS

Microneedle, diffraction UV lithography, hollow-well, reservoir, dip-coating, photosensitive resin

INTRODUCTION

Microneedle has expanded the practicality of transdermal patches by improving the drug delivery capability through the skin [1]. As a result, microneedle-related research topics have received increasing attention in the past two decades [2], especially in drug delivery system [3]. Coated microneedle, in particular, has shown some unique advantages over other types of microneedles. Unlike solid microneedle, which typically requires a two-step poke and applies process, pre-coated microneedle one-step administration feature maximizes the user compliance and the convenience, especially in the cosmetical application [4]. Biodegradable or dissolvable microneedle has been mainly used in cosmetics and pharmaceutical applications as it carries a relatively larger capacity in compared to coated microneedle, avoids waste of drugs unlike solid microneedle, and omits the need for an external pressure pump to enable drug delivery like hollow microneedle. However, dissolvable microneedle's mechanical properties vary as the capsulated drug type or fraction changes, which limits the availabilities of drugs [4]. Contrary to dissolvable microneedle, coated microneedle's mechanical properties remain unchanged regardless of the coated drug. In contrast to hollow microneedles, which are typically associated with a sophisticated fabrication process and high cost, dissolvable microneedle's relatively simple and straight forward fabrication process has shown greater feasibility for manufacturing over hollow microneedle [5]. In addition, various coating methods has been explored including dip-coating, drop-coating, immersion coating, gas jet drying, spray coating, electrohydrodynamic atomization (EHDA) process, and piezoelectric inkjet printing [4], [5], which enables a broad spectrum of materials and applications. Studies have reported successful delivery using a coated microneedle for gene therapy [6], vaccines [7], chitosan [8], hormones [9], cytokines [10], and insulin [11].

Its minimal invasive and convenient nature has proven to be a good replacement for a conventional hypodermic needle, which has been associated with painful and invasive administration [1]. However, several challenges still persist and prevent the popularization of drug delivery using coated microneedle in clinical practices. Low drug loading capacity, poor control of drug delivery, and low molecular weight drugs have been the major limitations of coated microneedle [12]. Inspired by these challenges, we have developed a novel hollow-well microneedle, which contains an innate well-type reservoir at the needle tip or body for larger drug loading capacity and wider drug availabilities, as shown in Fig. 1. The proposed hollow-well microneedle was fabricated based on the diffraction ultra-violet (UV) lithography process, which is a versatile fabrication method that has been used to fabricate solid and hollow microneedles with various aspects ratios [13]–[15]. Using a ring-shaped micropattern, the back-side UV exposure crosslinks a liquid-state photosensitive resin. The ring-shaped micropattern photomask is defined by translucent outer and opaque inner patterns. The outer shell first defines the overall microneedle shape. The resin residue that remains uncured inside the microneedle's hollow is then cured by second UV exposure from the topside, which forms a small pocket at the tip. The drug reservoir can be located while evading the tip by offsetting the inner pattern. It is also possible to realize multiple wells by increasing the number of inner patterns, which can be utilized for drug delivery with temporal control, a broader selection of drugs, or a higher dose. Due to its simple, rapid, and scalable fabrication capability, a hollow-well microneedle fabrication takes less than 30 min from start to finish. The proposed hollow-well microneedles indeed show the feasibility of improving the performance of coated microneedles due to enhanced drug delivery capability for transdermal application.

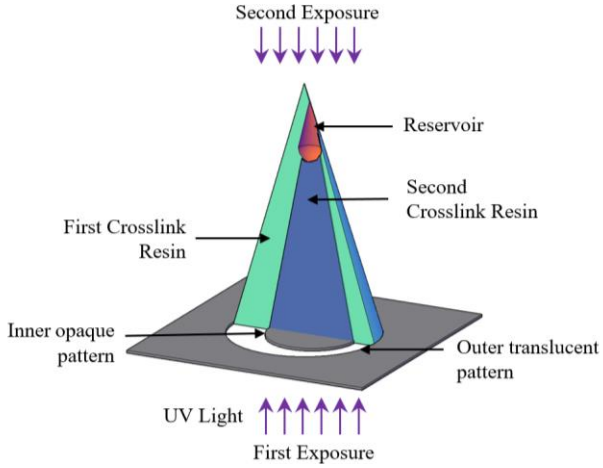

Figure 1. Conceptual drawing of the hollow-well microneedle.

978-1-940470-04-7/HH2022/$25©2022TRF
DOI 10.31438/trf.hh2022.63

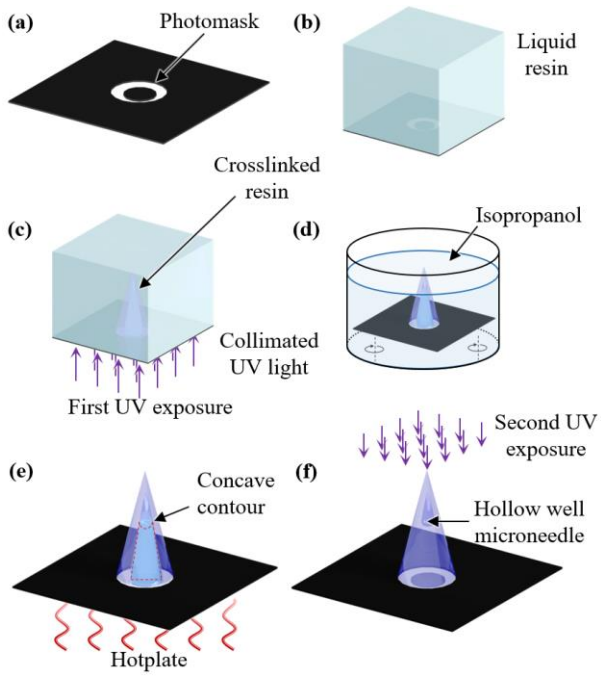

Figure 2. Fabrication process of the hollow-well microneedle. (a) Photomask. (b) Photosensitive resin coating. (c) First UV exposure. (d) Resin development. (e)Thermal treatment to form concave contour. (f) Second UV exposure and complete.

FABRICATION PROCESS

Fig. 2 illustrates the fabrication process of hollow-well microneedles, which includes a single resin coating, a partial development, and two steps of UV exposure processes. A photomask with a ring-shaped micropattern was prepared using a mask writer (SF-100 XPRESS, Scotech Co., Ltd.) on a chromium coated glass (soda-lime glass, Telic company) through lithography and wet etching processes. The photomask was used as the substrate and coated with photosensitive resin (Surgical guide resin, Formlabs Inc.). The first UV exposure was performed with a bottom-top direction through the micropattern to crosslink the resin and form the outer shell of the hollow-well microneedle while leaving the center uncrosslinked. A narrow band ultraviolet light emitting diode (UV-LED) exposure system [16] was used during the process to produce smooth microneedle surface [17]. The sample was developed in isopropanol for 2 minutes with moderate swirling. The sample was baked for 1 minute at 70°C to create the concave shape due to the capillary effect. Second top-bottom UV exposure was followed to crosslink the uncured resin for the well formation, completing the hollow-well microneedle.

RESULTS

Since the photomask pattern defines the geometry of the microneedle, various varieties of hollow microneedles were fabricated by varying the position and quantity of the interior pattern. Fig. 3 presents the hollow-well microneedle prototype using three different photomask designs, including the center-well microneedle, side-well microneedle, and dual-well microneedle. Fig. 3(a) shows a 700-µm tall and 300-µm wide center-well microneedle that was fabricated using a photomask with a center-aligned ring-shaped pattern as shown in the inset of Fig. 3(a). The micropattern has outer

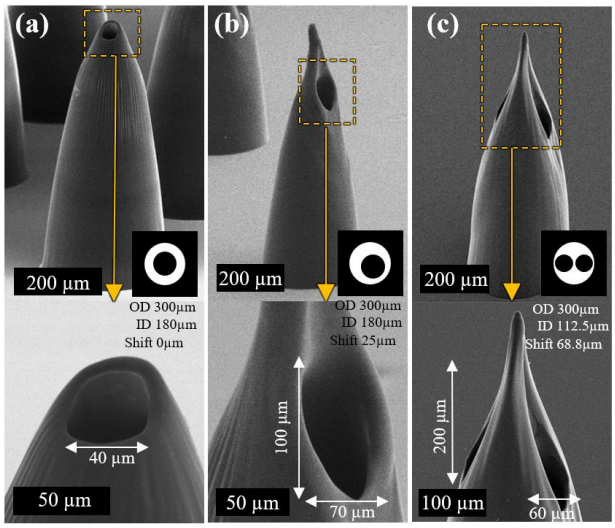

Figure 3. SEM images of the hollow-well microneedles fabricated with three photomask designs. (a) Center-well, (b) side-well, (c) dual-well (upper) and close-up (lower).

and inner diameters of 300 µm and 180 µm, respectively. As previously stated, the outer pattern dictates the overall shape of the microneedle, whilest the inner pattern specified the opening location and reservoir size. Since the micropattern was designed to be symmetrical around the center of the photomask, the UV exposure remains constant over the translucent region of the micropattern, which allows a uniform growth of the outer shell of the microneedle to form around the center axis with a hollow-well located at the center of the microneedle tip. The diameter of the aperture at the tip of the microneedle, on the other hand, was measured to be 40 µm, which is significantly less than the diameter of the inner pattern. This is due to the outer shell converging effect that was caused by the diffraction of the UV light, which as a result, reduced the size of the opening.

To demonstrate the versatility of the fabrication process, the side-well microneedle was fabricated as shown in Fig. 3(b). By shifting the inner pattern, the position of the reservoir can be relocated to enable the sharp tip. In this scheme, the size of the outer and inner patterns was kept the same as the center-aligned pattern, but the position of the inner pattern was shifted 25 µm from the center. This created an unbalanced UV exposure over the translucent region and uneven growth of the outer shell. The wider region formed the sharp tip due to the converging effect while the narrower region formed the opening of the reservoir, which completed the side-well microneedle with a height of 700 µm and an oval-shaped opening with a long side of 100 µm and a short side of 70 µm. Similarly, a dual-well microneedle was achieved by increasing the number of inner patterns as demonstrated in Fig. 3(c). The size of the inner pattern was reduced to 112.5 µm, and both were shifted 68.8 µm from the center to accommodate an additional inner pattern. This resulted in a slimmer oval-shaped opening with a long side of 200 µm and a short side of 60 µm. The height of the microneedle was 700 µm with a diameter of 300 µm. The dual-well microneedle was developed to improve drug loading capacity or allow two types of drug delivery at the same time. The proposed diffraction lithography technology enables the fabrication of a greater number of wells on the microneedle for the application of various drugs with

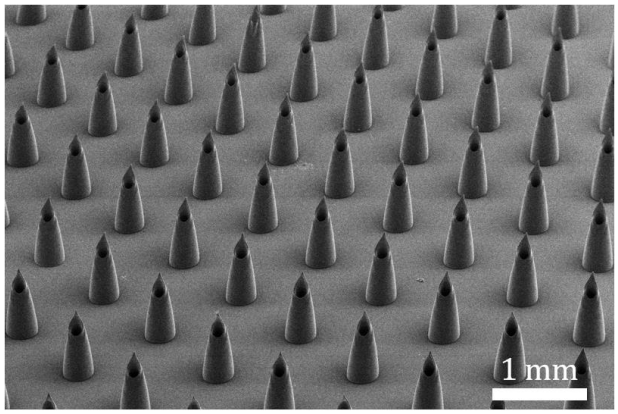

Figure 4. SEM of hollow-well microneedle array.

varying release times. However, because increasing the number of wells in the microneedle may result in mechanical instability, the design and fabrication process should be validated as well.

Fig. 4 shows a scanning electron microscope (SEM) image of a microneedle array with a 300-µm diameter and 700-µm height, indicating high uniformity and reliability of the batch fabrication. 400 hollow-well microneedles were successfully fabricated in this fabrication; however, due to the SEM's screen capture size, over 50 hollow-well microneedles were presented. Up to 3,600 microneedles on a 20×20 mm^2 substrate have been fabricated for higher drug loading capacity using the same fabrication process, without sacrificing the fabrication speed.

To verify the feasibility of the hollow-well microneedle, we conducted a mechanical test on a single hollow-well microneedle using a commercial force gauge (FC200, Torbal Inc.). The microneedle was mounted under the force gauge and the force gauge was programmed to compress the microneedle at a speed of 1.2 mm/min. Fig. 5 shows the mechanical test result of the hollow-well microneedle. Unlike a typical solid microneedle with a tip, which

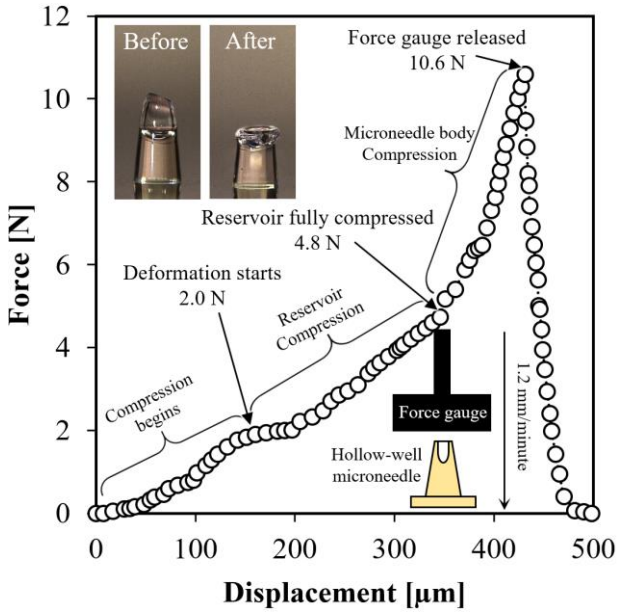

Figure 5. Mechanical test result of the hollow-well microneedle.

generates a sudden decline of force when the tip breaks [18], the tested microneedle projected a gradual increment of force with a slight change of slope at 2.0 N, indicating the deformation of the reservoir started. After that, the force gauge experienced a linear increment of force until 4.8 N before experiencing another change of slope, this indicates that the reservoir was fully compressed at 4.8 N. The force gauge was allowed to compress the microneedle until it passed the safety limit of the force gauge (10.6 N) and was commanded to release the pressure. The result shows that the hollow-well microneedle was exceptionally sturdy even with an empty reservoir equipped. Note that the presented force-displacement graph shows the tested result of a single microneedle, the tested microneedle remained intact on the substrate after experiencing up to 10.6 N of compression. The result has shown the feasibility and functionality of the hollow-well microneedle for safe transdermal applications.

A drug delivery analysis was conducted to compare the drug delivery efficiency of a conventional transdermal patch, coated microneedle, and hollow-well microneedle. All candidates were pre-coated with blue tissue dye prior to the applications. The candidates were allowed for passive diffusion after being applied onto a common pig cadaver skin, the result is shown in Fig. 6. A conventional transdermal patch was allowed a longer diffusion time of 30 minutes and was measured to have a maximum diffusion depth of 180 µm as shown in Fig. 6(a). The pre-coated microneedle and hollow-well microneedle were characterized to have the same height of 700 µm to eliminate the effect of insertion depth to the area of diffusion. Both microneedles were dip-coated into the tissue dye at the same time and allowed diffusion for 1 minute as shown in Fig. 6(b) and (c). As can be seen in the result, both microneedles were inserted equally deep into the skin at approximately 400 µm, but wider dispersion of dye was observed at the inserted site of the hollow-well microneedle, confirming a larger drug loading dosage for each administration.

CONCLUSIONS

This paper introduces rapid microfabrication of hollow-well needles based on diffraction UV lithography. The proposed microneedle equips a pocket structure (well) at the top of the

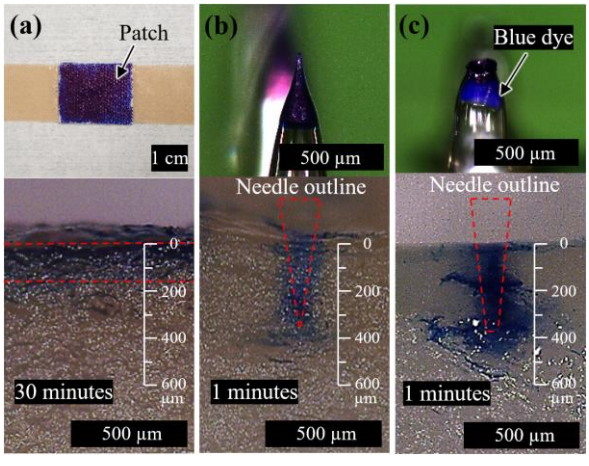

Figure 6. Drug delivery analysis on pig cadaver skin. Blue tissue dye coated (a) patch, (b) solid microneedle, (c) hollow-well microneedle (upper) and drug dispersion result (lower).

microneedle that serves as a drug reservoir. The reservoir offers a larger drug loading capacity, which allows a larger volume of drugs to be delivered by each microneedle. The reservoir also enables a broader spectrum of drugs that were not available for the surface coating to be delivered through the transdermal system. We demonstrated the fabrication process of the hollow-well microneedles was achieved through a relatively simple setup and processes including UV lithography and time-controlled development to form the well structure of the microneedle. In addition, various types of hollow-well microneedle can be easily fabricated using the same process with only slight changes on the photomask. Center-well microneedle was presented for maximizing the drug loading capacity, side-well microneedle was introduced to enable a sharp tip for smooth skin insertion, and dual-well microneedle was presented for delivery of two drugs through a single administration. A large-scale microneedle array was demonstrated within a single fabrication process, confirming the manufacturing feasibility. To verify the practicality of the hollow-well microneedle, a mechanical test was conducted and showed the microneedle could withstand up to 2.0 N before deformation and remained intact to substrate after 10.6 N of compression, denying the risk of fracturing and buckling during skin insertion. Lastly, a drug delivery analysis was performed to compare the drug delivery efficiency with the conventional transdermal patch, typically coated microneedle and the proposed hollow-well microneedle. The results have shown that hollow-well microneedle released the largest volume of the drug under the same circumstances. Diffraction UV lithography has shown great potential in fabricating various types of the microneedle, including the proposed hollow-well microneedles as well as the previously presented solid and hollow microneedles. Its versatility, reliability, and scalability in fabricating microneedle have shown great advantages over other microneedle fabrication methods. The proposed hollow-well microneedle has demonstrated outstanding performances, which shows great potential in the transdermal application.

ACKNOWLEDGMENT

The research was supported by National Science Foundation (NSF) CNS 2039014, ECCS 2054567, ECCS 2029086, and ECCS 2029077 as well as the Korea Institute for Advancement of Technology (KIAT) P163800009.

REFERENCES

[1] M. R. Prausnitz, “Microneedles for transdermal drug delivery,” *Adv. Drug Deliv. Rev.*, vol. 56, no. 5, pp. 581–587, Mar. 2004, doi: 10.1016/j.addr.2003.10.023.

[2] J. Halder, S. Gupta, R. Kumari, G. D. Gupta, and V. K. Rai, “Microneedle Array: Applications, Recent Advances, and Clinical Pertinence in Transdermal Drug Delivery,” *J. Pharm. Innov.*, vol. 16, no. 3, pp. 558–565, Sep. 2021, doi: 10.1007/s12247-020-09460-2.

[3] R. S. J. Ingrole, E. Azizoglu, M. Dul, J. C. Birchall, H. S. Gill, and M. R. Prausnitz, “Trends of microneedle technology in the scientific literature, patents, clinical trials and internet activity,” *Biomaterials*, vol. 267, p. 120491, Jan. 2021, doi: 10.1016/j.biomaterials.2020.120491.

[4] R. S. J. Ingrole and H. S. Gill, “Microneedle Coating Methods: A Review with a Perspective,” *J. Pharmacol. Exp. Ther.*, vol. 370, no. 3, pp. 555–569, Sep. 2019, doi: 10.1124/jpet.119.258707.

[5] R. Haj-Ahmad *et al.*, “Microneedle Coating Techniques for Transdermal Drug Delivery,” *Pharmaceutics*, vol. 7, no. 4, Art. no. 4, Dec. 2015, doi: 10.3390/pharmaceutics7040486.

[6] W. Chen, H. Li, D. Shi, Z. Liu, and W. Yuan, “Microneedles As a Delivery System for Gene Therapy,” *Front. Pharmacol.*, vol. 7, 2016, Accessed: Apr. 14, 2022. [Online]. Available: https://www.frontiersin.org/article/10.3389/fphar.2016.00137

[7] J. W. Lee and M. R. Prausnitz, “Drug delivery using microneedle patches: not just for skin,” *Expert Opin. Drug Deliv.*, vol. 15, no. 6, pp. 541–543, Jun. 2018, doi: 10.1080/17425247.2018.1471059.

[8] S. Gorantla, N. Dabholkar, S. Sharma, V. K. Rapalli, A. Alexander, and G. Singhvi, “Chitosan-based microneedles as a potential platform for drug delivery through the skin: Trends and regulatory aspects,” *Int. J. Biol. Macromol.*, vol. 184, pp. 438–453, Aug. 2021, doi: 10.1016/j.ijbiomac.2021.06.059.

[9] P. E. Daddona, James. A. Matriano, J. Mandema, and Y.-F. Maa, “Parathyroid Hormone (1-34)-Coated Microneedle Patch System: Clinical Pharmacokinetics and Pharmacodynamics for Treatment of Osteoporosis,” *Pharm. Res.*, vol. 28, no. 1, pp. 159–165, Jan. 2011, doi: 10.1007/s11095-010-0192-9.

[10] K. Kusamori *et al.*, “Development of a drug-coated microneedle array and its application for transdermal delivery of interferon alpha,” *Biofabrication*, vol. 8, no. 1, p. 015006, Jan. 2016, doi: 10.1088/1758-5090/8/1/015006.

[11] X. Jin, D. D. Zhu, B. Z. Chen, M. Ashfaq, and X. D. Guo, “Insulin delivery systems combined with microneedle technology,” *Adv. Drug Deliv. Rev.*, vol. 127, pp. 119–137, Mar. 2018, doi: 10.1016/j.addr.2018.03.011.

[12] K. Ita, “Transdermal Delivery of Drugs with Microneedles—Potential and Challenges,” *Pharmaceutics*, vol. 7, no. 3, pp. 90–105, Jun. 2015, doi: 10.3390/pharmaceutics7030090.

[13] J. Y. Tan, A. Kim, and J. ‘JK’ Kim, “Modeling, characterization, and fabrication of bell-tip microneedle array by diffraction and self-aligned lens effects,” *Appl. Phys. Lett.*, vol. 119, no. 2, p. 023501, Jul. 2021, doi: 10.1063/5.0055073.

[14] J. Y. Tan, A. Kim, and J. Kim, “Fabrication and Characterization of Hollow Microneedle Array using Diffraction UV Lithography,” presented at the 2021 Transducers - 2021 21st International Conference on Solid-State Sensors, Actuators and Microsystems (TRANSDUCERS), Jun. 2021.

[15] J. Kim, “Fabrication of SU-8 Microtowers for a 100-Turn Toroid Inductor,” in *2018 IEEE 13th Annual International Conference on Nano/Micro Engineered and Molecular Systems (NEMS)*, Apr. 2018, pp. 389–392. doi: 10.1109/NEMS.2018.8556894.

[16] S. F. Shiba, J. Y. Tan, and J. Kim, “Multidirectional UV-LED lithography using an array of high-intensity UV-LEDs and tilt-rotational sample holder for 3-D microfabrication,” *Micro Nano Syst. Lett.*, vol. 8, no. 1, p. 5, Apr. 2020, doi: 10.1186/s40486-020-00107-y.

[17] J. K. Kim, S. J. Paik, M. G. Allen, and F. Herrault, “UV-LED LITHOGRAPHY FOR 3-D HIGH ASPECT RATIO MICROSTRUCTURE PATTERNING,” in *2012 Solid-State, Actuators, and Microsystems Workshop Technical Digest*, Hilton Head, South Carolina, USA, May 2012, pp. 481–484. doi: 10.31438/trf.hh2012.127.

[18] S. P. Davis, B. J. Landis, Z. H. Adams, M. G. Allen, and M. R. Prausnitz, “Insertion of microneedles into skin: measurement and prediction of insertion force and needle fracture force,” *J. Biomech.*, vol. 37, no. 8, pp. 1155–1163, Aug. 2004, doi: 10.1016/j.jbiomech.2003.12.010.

A WEARABLE SYSTEM FOR ELECTROCHEMICAL SENSING OF SEROTONIN IN CRAYFISH

*Jinjing Han, Justin M. Stine, Ashley A. Chapin, Tawen Ho, Norma Pena-Flores, Jens Herberholz, and Reza Ghodssi**

University of Maryland, College Park, Maryland, USA

ABSTRACT

We present a wearable system for *in vivo* serotonin (5-hydroxytryptamine, 5-HT) detection in crayfish hemolymph (i.e., blood). Surface-modified electrodes, with 4.9x improved 5-HT sensitivity, were integrated with a 3D-printed package to perform cyclic voltammetry (CV) by connecting to potentiostat electronics, enabling real-time data readout. The system was mounted on the crayfish dorsal carapace allowing electrode implantation into the heart for continuous *in vivo* 5-HT measurements (over 75 min) with a benchtop potentiostat. This system successfully monitored 5-HT dynamics in the targeted region with a high temporal resolution, providing a reliable platform for real-time neurochemical sensing.

KEYWORDS

Biosensing, electrochemical devices, microelectrodes.

INTRODUCTION

5-HT is a key neurotransmitter in the brain, underlying mental illnesses such as anxiety and depression [1]. 5-HT modulates the behavior and physiology of vertebrate and invertebrate animals via neurohormonal routes. For example, stressed crayfish show increased levels of 5-HT in hemolymph, and injection of 5-HT into hemolymph induces anxiety-like behavior. HPLC is commonly used to determine 5-HT levels in hemolymph to study its physiological pathways [2]. However, such techniques are costly, time-consuming, and have a low temporal resolution.

Electrochemical methods have emerged as a simple and inexpensive alternative, capable of rapid detection of 5-HT in biological samples with high sensitivity and selectivity [3]. CFMEs are commonly used for detection of neurotransmitters, especially *in vivo* in rodents. However, these electrochemical systems require bulky benchtop equipment and wires to connect with the implanted microelectrodes, limiting animal movement [4]. Animal behavioral studies would benefit from real-time *in vivo* quantitative 5-HT measurements using a fully miniaturized, wireless, wearable system. This work presents a wearable system towards this goal, showing: (i) successful measurements of *in vivo* 5-HT in crayfish by wiring to a benchtop potentiostat, and (ii) a prototype of a fully miniaturized electrochemical sensing system integrated with a PCB potentiostat. This system has the potential to facilitate real-time 5-HT measurements in freely behaving animals.

SYSTEM DESIGN AND ASSEMBLY

Figure 1a shows a schematic of the wearable system comprised of a **3D-printed package** with **customized implantable electrodes**, which can perform electrochemical measurements driven by either a benchtop or miniaturized PCB potentiostat.

The three-electrode configuration includes a surface-modified CFME as a working electrode (WE), an Ag/AgCl wire as a reference electrode (RE), and a Pt wire as a counter electrode (CE) (Figure 1b). The CFME is modified by dip-coating in 0.5 mg/mL carbon nanotube dispersed 2.5% Nafion solution (Nafion-CNT), followed by electrochemical activation (Nafion-CNT/EC). Successful coating of the Nafion-CNT film and surface etching by electrochemical activation were observed using SEM. Ag is electrochemically converted to Ag/AgCl by oxidation in 1 M KCl.

The 3D-printed package consists of two components: (i) an alignment spacer printed with clear resin using digital light processing (DLP) (M50, CADWorks3D) to connect customized electrodes with potentiostat electronics, and (ii) a PLA enclosure printed with fused filament fabrication (FFF) (MK3S+, Prusa) to provide an interface with the crayfish. A small cutout (4 × 3 mm) on the bottom of the enclosure allows electrode access to the hemolymph in the crayfish heart.

A hole was drilled through the crayfish carapace using a 26G needle and small drill bits. The enclosure base was fixed onto the carapace using super glue. The alignment spacer was lowered onto the enclosure, through which the electrodes were implanted under the dorsal carapace directly into the heart. The device showed minimal impact on crayfish movement. A week after electrodes implantation and removal, the crayfish remained alive, indicating the potential for repeated measurements in the same animal.

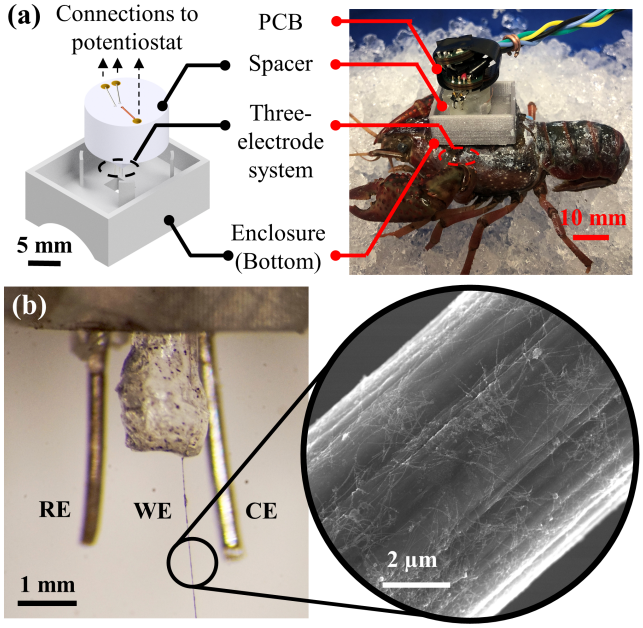

Figure 1: (a) Schematic of the wearable system and image of this system on an adult crayfish. Electrodes are implanted in the heart for in vivo hemolymph CV measurements. (b) Three-electrode electrochemical system with an SEM of the Nafion-CNT/EC WE.

RESULTS

The surface-modified WEs were characterized and compared with unmodified and partially modified CFMEs using CV. Figure 2 shows the anodic peak currents (Ipas) resulting from 5-HT detection at the WEs. While the bare CFMEs showed no response to 5-HT, the Nafion-CNT/EC CFMEs showed a 4.9x higher signal response than the Nafion-CNT CFMEs.

A PCB potentiostat, containing an analog-front-end (AFE) AD5941 and a microcontroller (MCU) BGM13S, was integrated with the customized electrode system and compared to a benchtop potentiostat for 5-HT detection using CV. The oxidation peak potentials (Epas) were observed to be 0.31 V for both instruments, while Ipas of 0.21 µA and 0.11 µA were recorded from the benchtop and PCB potentiostats, respectively (Figure 3). The cyclic

978-1-940470-04-7/HH2022/$25©2022TRF
DOI 10.31438/trf.hh2022.64

voltammogram recorded by the PCB was subject to system noise, which required data processing by a low pass filter to properly analyze the current peaks.

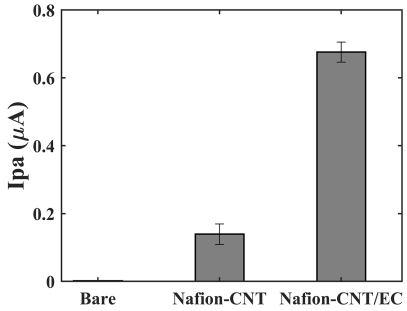

Figure 2: Ipas from CV signals of 10 μM 5-HT measured at bare, Nafion-CNT, and Nafion-CNT/EC surface-modified CFMEs (n=6). Average signals are 0 μA, 0.14 μA, and 0.68 μA, respectively, using a benchtop potentiostat (VSP-300, Biologic).

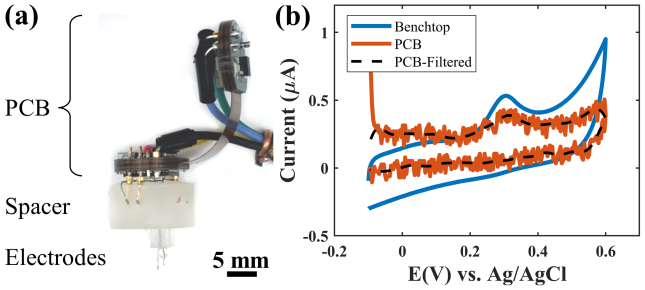

Figure 3: (a) Image of PCB-integrated electrode system used for 5-HT measurements. (b) Cyclic voltammograms of 10 μM 5-HT in PBS, comparing benchtop (CompactStat.h, Ivium) and PCB potentiostats using customized electrodes (Nafion-CNT/EC WE).

The PCB-integrated wearable system was then implanted into a crayfish heart to perform *in vivo* electrochemical measurements in hemolymph (Figure 4). The experimental setup is shown in Figure 1(a). The wearable system interfaced well with the crayfish carapace, facilitating minimally invasive measurements. The cyclic voltammograms for the *in vivo* hemolymph measurement had a similar shape compared to PBS, indicating successful *in vivo* electrochemical measurements (Figure 4b). 5-HT was undetectable in hemolymph, indicating low basal 5-HT concentrations. Two major challenges arose from this experiment. The Nafion-CNT/EC CFMEs have improved sensitivity but are fragile due to surface etching, which limits their lifetime in *in vivo* experiments. Future work will attempt to harden the electrodes with additional surface coatings. Furthermore, challenges in fabrication of the miniaturized electrode system resulted in low yield due to poor electrical connection between electrodes and PCB.

Given these challenges, *in vivo* measurements of 5-HT were performed using Nafion-CNT WEs and a benchtop potentiostat, which were more reliable. 5-HT was injected into the crayfish ventral sinus cavity, where it was expected to circulate through the animal to increase 5-HT concentration in the heart. CV was used to continuously monitor Ipas during this 5-HT circulation. The Ipa reached a maximum at 45 min after the 1st 5-HT injection (1 mL of 3 mM) and then started decreasing. The 2nd 5-HT injection (0.2 mL of 3 mM) was performed 65 min after the 1st injection, resulting in an increase in Ipa (Figure 5). These results indicate selectivity and successful continuous measurements of 5-HT *in vivo*, which follows the expected trend of changing 5-HT concentrations due to the repeated injections. For example, the 5-HT concentration may rise and fall as it circulates through the heart.

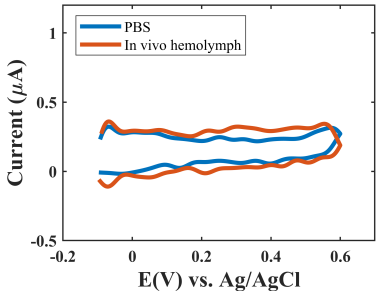

Figure 4: Filtered cyclic voltammograms of a PCB-integrated system using a Nafion-CNT/EC WE in crayfish hemolymph, showing a similar shape as PBS.

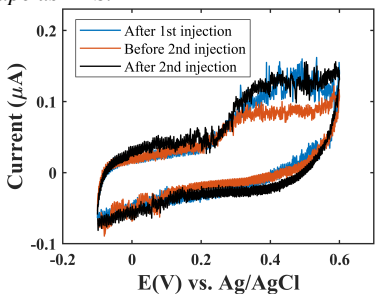

Figure 5: Cyclic voltammograms of in vivo 5-HT-spiked hemolymph using a benchtop potentiostat (CompactStat.h, Ivium) with a Nafion-CNT WE. The Ipas were 50.7 nA, 26.2 nA and 40.9 nA after the 1st injection (blue), before the 2nd injection (orange), and 10 min after the 2nd injection (black), respectively.

CONCLUSION

This work demonstrates a wearable system that integrates modified implantable electrodes with a 3D-printed package for electrochemical measurements in crayfish. The developed system has been integrated with a PCB potentiostat for miniaturization, as well as connected to a benchtop potentiostat for more sensitive electrochemical measurements. The PCB-integrated system achieved electrochemical measurements in hemolymph without 5-HT injection. When connected to a benchtop potentiostat, successful continuous monitoring of *in vivo* 5-HT was achieved in an anesthetized animal outside water. A fully realized PCB-integrated, miniaturized wearable system could potentially provide real-time measurements of 5-HT concentrations in freely moving animals, and identify the role of 5-HT in regulating various behaviors.

ACKNOWLEDGEMENTS

This work was supported by the National Science Foundation NCS #1926793. The authors acknowledge the support from the University of Maryland NanoCenter and its FabLab.

REFERENCES

[1] M. Berger, J.A. Gray, and B.L. Roth, The expanded biology of serotonin, *Annu. Rev. Med.* 60 (2009).

[2] P. Fossat, J. Bacque-Cazenave, P. De Deurwaerdere, J. Delbecque, and D. Cattaert, Anxiety-like behavior in crayfish is controlled by serotonin. *Science*, 344 (2014).

[3] M. Labib, E.H. Sargent, and S.O. Kelly, Electrochemical Methods for the Analysis of Clinically Relevant Biomolecules, *Chem. Rev.* 116, 16 (2016).

[4] E.C. Dankoski and R.M. Wightman, Monitoring serotonin signaling on a subsecond time scale, *Front. Integr. Neurosci.* 7:44 (2013).

CONTACT

*R. Ghodssi, tel: +1-301-405-8158; ghodssi@umd.edu

GAS-PERMEABLE POLYDIMETHYLSILOXANE-ON-SILICON MEMBRANES FOR EXTRACORPOREAL MEMBRANE OXYGENATION

Benjamin Chui, David Blauvelt, Francisco Baltazar, Tariq Haniff, Jarrett Moyer, Nicholas Higgins, Peter Oishi, and Shuvo Roy
University of California, San Francisco, California, USA

ABSTRACT

We have developed a simple, low-cost, and robust PDMS (polydimethylsiloxane)-on-silicon micromachined gas-exchange membrane that can form the basis of compact extracorporeal membrane oxygenation (ECMO) treatment for respiratory distress. We investigated two fabrication approaches, one of which involves a porous silicon support formed by traditional double-sided deep reactive ion etch (DRIE), while the other features a surface-micromachined "cavern" design with isotropically etched inter-connected buried cavities that serve as gas-flow channels. *In vitro* and *in vivo* testing has confirmed the functionality of both designs.

BACKGROUND

The COVID-19 pandemic highlighted the need for various respiratory-assistive devices such as mechanical ventilators and extracorporeal membrane oxygenation (ECMO) devices. Mechanical ventilators work by forcing air at high pressure into the patient's impaired lungs, but extended use can cause ventilator-induced lung injury (VILI). In contrast, ECMO bypasses the lungs altogether to transfer oxygen directly into the bloodstream, but its drawbacks include large size and operational complexity requiring high staff-to-patient ratios. Furthermore, the standard hollow-fiber membranes used in present-day ECMO devices require the use of anticoagulants (raising the risk of bleeding) and blood pumps (causing blood cell lysis) [1]. In recent years, various micro-machining approaches have been explored to address these issues [2, 3]. In particular, our group has demonstrated the use of a thin, gas-permeable PDMS layer on top of a porous silicon chip to facilitate efficient oxygen and CO_2 exchange between blood and air [4]. Such a microfluidics-based architecture (Fig. 1) aims to promote laminar blood flow and low pressure drop, potentially eliminating the need for anticoagulants and blood pumps.

DESIGN AND FABRICATION

In our earlier ECMO work, we bonded a 5µm-thick PDMS layer to a 1µm-thick polysilicon membrane that had 0.5µm pores and spacings [4]. Since this pore density was originally designed for liquid-to-*liquid* membrane filtration, we set out to develop an optimized membrane design for a liquid-*gas* interface. Using computational fluid dynamics (CFD) analysis, we determined that due to the high (lateral) diffusivity of gas molecules in PDMS, the silicon "membrane" could in fact have pores and spacings as large as 10µm and thicknesses of 50-100µm (10^5-10^6 times stiffer than before) without significantly affecting performance (Fig. 2).

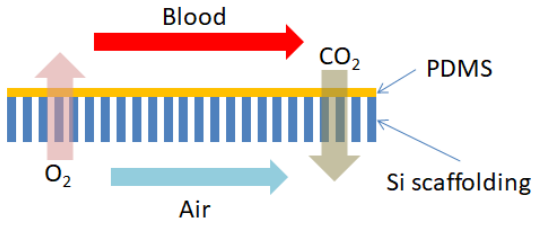

Figure 1: Basic concept of a micromachined ECMO chip with a PDMS membrane bonded to a silicon support chip. Oxygen diffuses from the air through the PDMS into the blood while CO_2 diffuses the other way, emulating the action of the lungs.

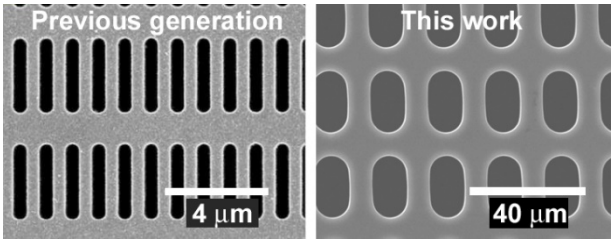

Figure 2: Two generations of our ECMO silicon scaffolding. Note order-of-magnitude difference in scale bars. The new design (right) can have greater pore spacing due to the high diffusivity of gas within the PDMS layer above the scaffolding. It also has a 50-100x thicker membrane for superior strength. These samples were imaged without PDMS to show the pores more clearly.

Consequently, we designed and fabricated a coarser silicon "scaffolding" with 10µm pores and spaces in a 50-100 µm-thick membrane on a 400-µm thick chip. We tried two different fabrication approaches for the silicon structure: Design A is a traditional double-sided process (Fig. 3a) in which we etched 10µm-wide pores in the top surface of the wafer and hollowed out the back side using DRIE, while Design B is a single-sided "cavern" design (Fig. 3b) where 50-100µm deep pores are etched into a monolithic wafer and lined with thermal oxide, the bottom of the pores are stripped of oxide, and an isotropic SF_6 etch is used to "carve out" an interconnected 2D array of gas-conducting cavities (Figs. 4a-e).

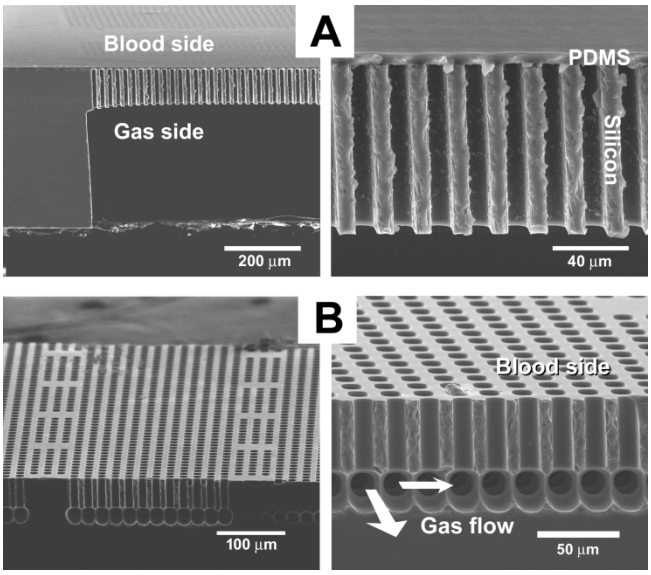

Figure 3: Scanning electron micrograph (SEM) cross-sections: (Design A) Double-side-DRIE chip with PDMS layer on top of silicon scaffolding. (Pores are faintly visible under the PDMS.) Right-hand figure shows close-up of PDMS layer; (Design B) Single-side-DRIE "cavern" chip (pre-PDMS) formed by isotropic SF_6 undercutting of oxide-lined holes. Right-hand figure shows close-up of connecting "caverns" that serve as 2D gas channels.

978-1-940470-04-7/HH2022/$25©2022TRF
DOI 10.31438/trf.hh2022.65

Solid-State Sensors, Actuators, and Microsystems Workshop
Hilton Head Island, South Carolina, June 5-9, 2022

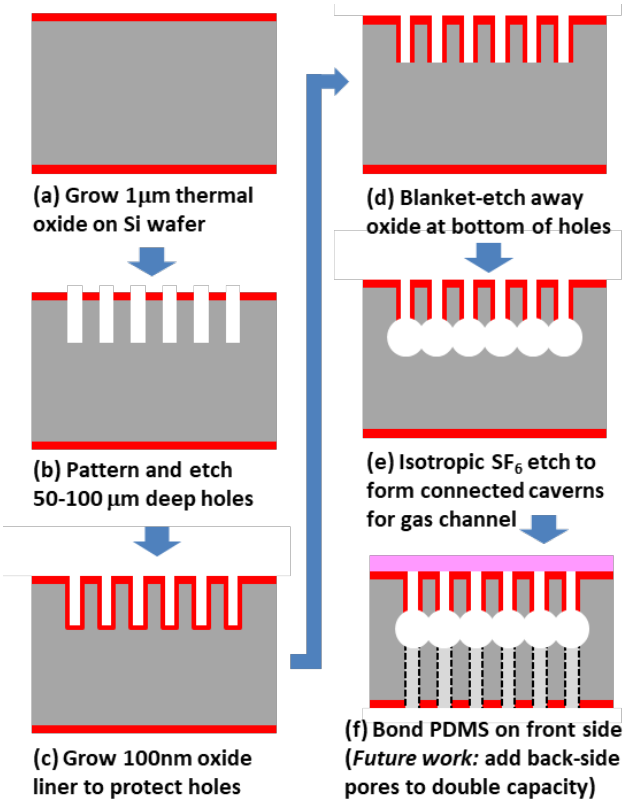

Figure 4: Process flow for the Design-B "cavern" ECMO chip.

An additional benefit of the "cavern" design, which was inspired by prior work on sub-surface isotropic reactive ion etching [5-7], is that access holes could be etched from *both* sides of the wafer into the central cavity, enabling double-sided functionality and a more efficient configuration for gas exchange (Fig. 4f).

DEVICE TESTING

ECMO chips from both designs were tested *in vitro* and *in vivo* for gas-exchange efficiency between air and liquid (Figs. 5-6). The Design-A "traditional" membranes had an *in vitro* gas-transfer flux of 0.013 mL/min and 0.024 mL/min at 2.5 and 10 psi respectively. The membranes were also tested in an extracorporeal pig model. They were able to be pressurized up to 25 psi of sweep gas without rupture or gas embolization, with a flux of 0.035 mL/min.

The Design-B "cavern" chip was tested *in vitro* and showed an oxygen flux of 0.010 mL/min at 2.5 psi of sweep gas pressure and 0.015 mL/min at 10 psi, somewhat lower than Design A due to the narrower internal gas channel. Overall, both designs performed robustly during assembly and testing in our laboratory setup, a promising step in the scale-up toward clinical-level devices [4, 8].

FUTURE APPLICATIONS

In addition to life-sustaining treatment for severe respiratory distress associated with COVID-19, our PDMS-on-silicon ECMO platform could potentially be used in portable lungs for chronic obstructive pulmonary disease (COPD) and patients awaiting lung transplant. It could also conceivably be used as an "artificial placenta" to treat extreme preterm babies (gestation age between 23-28 weeks), which is a category of patients that cannot get standard ECMO due to the risk of intracranial hemorrhage associated with anticoagulation [8].

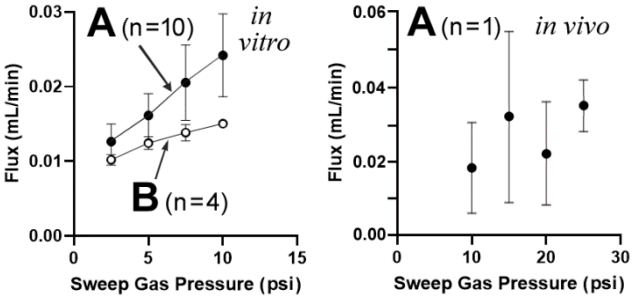

Figure 5: Measured gas flux through PDMS membrane from air to liquid for: Design-A chip in vitro *(left, solid dots) and* in vivo *(right); Design-B "cavern" chip* in vitro *(left, hollow circles). Chip size in both cases was 10×65mm (active membrane area 240mm^2).*

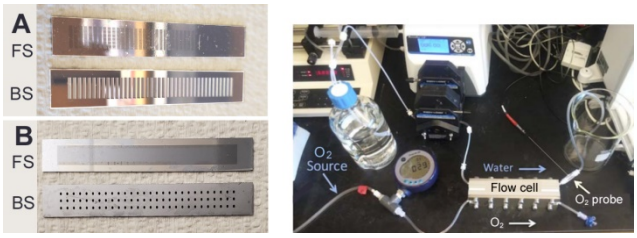

Figure 6: (Left) PDMS-coated ECMO chips from Designs A and B. FS=front side, BS=back side; (Right) Test bench showing a flow cell containing an ECMO chip, with water and oxygen flowing on either side, for measuring gas flux across the PDMS membrane.

This work was funded in part by NIH grant U01EB025136 and a Catalyzing Pediatric Innovation grant from the West Coast Consortium for Technology and Innovation in Pediatrics (CTIP). Wafer fabrication was performed at the Berkeley Marvell Nanolab, Stanford Nanofabrication Facility (SNF), Stanford Nano Shared Facilities (SNSF), and Rogue Valley Microdevices, Oregon, USA. The authors may be contacted through benjamin.chui@ucsf.edu.

REFERENCES

[1] T. Yeager, S. Roy, "Evolution of Gas Permeable Membranes for Extracorporeal Membrane Oxygenation", *Artif. Organs* 41(8), pp. 700-709 (2017).

[2] K.A. Burgess, H-H Hu, W.R. Wagner, and W.J. Federspiel, "Towards microfabricated biohybrid artificial lung modules for chronic respiratory support", *Biomed. Microdevices* 11, pp. 117–127 (2009).

[3] J. A. Potkay, "A high efficiency micromachined artificial lung", Proc. Transducers 2009, pp. 2234–7.

[4] A. Dharia, E. Abada, B. Feinberg, T. Yeager, W. Moses, J. Park, C. Blaha, N. Wright, B. Padilla, and S. Roy, "Silicon Micropore-Based Parallel Plate Membrane Oxygenator", *Artif. Organs* 42(2), pp. 166-173 (2018).

[5] K.A. Shaw, Z.L. Zhang, and N.C. MacDonald, "SCREAM I: A single-mask, single-crystal silicon, reactive ion etching process for microelectromechanical structures", *Sensors and Actuators* 40, pp. 63-70 (1994).

[6] M.J. de Boer, R.W. Tjerkstra, J.W. Berenschot, M. Elwenspoek, A. van den Berg *et al*, "Micromachining of buried microchannels in silicon", *J. MEMS* 9(1), pp. 94-103 (2000).

[7] C.M. Chang, O. Solgaard, "Si buried gratings for dielectric laser electron accelerators", *Appl. Phys. Letters* 104 (2014).

[8] D.G. Blauvelt, E.N. Abada, P. Oishi, S. Roy, "Advances in extracorporeal membrane oxygenator design for artificial placenta technology", *Artif. Organs* 45(3), pp. 205-221 (2021).

IN-SITU SAMPLE PROCESSING AND ELECTROENZYMATIC SENSING FOR RELIABLE DEHYDROGENASE-BASED WEARABLE BIOMARKER MONITORING

Xuanbing Cheng[1,2†], Jialun Zhu[1†], Shuyu Lin[1†], Sarah Forman[1,3], and Sam Emaminejad[1]*
[1]Interconnected and Integrated Bioelectronics Lab (I²BL), University of California, Los Angeles, CA, USA
[2]Department of Materials Science and Engineering, University of California, Los Angeles, CA, USA
[3]Department of Molecular, Cell, and Developmental Biology, University of California, Los Angeles, CA, USA
[†]Equal contribution

ABSTRACT

Dehydrogenase-based electroenzymatic sensors enable monitoring of a wide panel of clinically important biomarkers (*e.g.*, ketones) in a sample-to-answer manner. To adapt these sensors for non-invasive wearable biomarker monitoring, key challenges remain in terms of achieving low detection limit (due to the analyte dilution in non-invasively retrievable biofluids such as sweat) and mitigating the confounding effect of electroactive interferents. To overcome these challenges, we present an integrated bioanalytical microfluidic device, which features: 1) a sample processing module containing pre-deposited enzymes to efficiently consume electroactive interferents (here, ascorbic acid) within an introduced biofluid sample and 2) a carbon-nanotube-based electroanalysis module for highly sensitive dehydrogenase-based electroenzymatic sensing. We particularly adapted the *in-situ* bioanalytical capabilities of the device for reliable measurement of β-hydroxybutyrate (a major ketone body) at low concentrations. The experimental results support the suitability of our approach for wearable monitoring of β-hydroxybutyrate.

KEYWORDS

wearable biosensors, enzymatic, dehydrogenase-based sensing, in-situ sample processing, ketone

INTRODUCTION

Recent advances in wearable biosensors have presented new opportunities for personal health monitoring and transforming personalized medicine and healthcare. Through frequent harvesting of molecular level biomarker information from non-invasively retrievable biofluids (*e.g.*, sweat), wearable biosensors can track the individuals' dynamic physiological status, enabling timely, personalized, and actionable feedback for health management. In that regard, electroenzymatic sensors are especially useful as they can measure biomarker molecules in a sample-to-answer manner and with a high level of generalizability (*i.e.*, by swapping enzymes). In particular, nicotinamide adenine dinucleotide (NAD)-dependent dehydrogenase-based sensors can be exploited to target a wide panel of biomarkers. Owing to their quinone-based structure, these sensors can detect the reduced form of NAD (NADH)—as the end product of cascaded dehydrogenase-based reactions—and generate electrical signals that are proportional to the target biomarker concentrations.

However, deploying these sensors for non-invasive wearable monitoring of biomarkers is nontrivial. Firstly, they lack the required sensitivity to detect analytes that appear at diluted levels in non-invasively retrievable biofluids—for example, ketone molecules that get diluted by at least ~10× as they partition into sweat. Secondly, since these sensors rely on mediators for electrochemical analysis, their response is susceptible to the background interference stemming from endogenous electroactive species such as ascorbic acid (AA), rendering the measurements inaccurate.

Here, we overcome these challenges by devising an integrated bioanalytical microfluidic device, which features a sample processing module to eliminate the interferent species (specifically, AA) and a carbon-nanotube (CNT)-based electroanalysis module for highly sensitive dehydrogenase-based electroenzymatic sensing (Figure 1). To demonstrate the utility of the devised solution, the sensing interface was adapted to measure β-hydroxybutyrate (HB), which is an important biomarker of body's nutritional/metabolic status and its monitoring is critical for preventing fatal homeostatic disorders such as diabetic ketoacidosis [1].

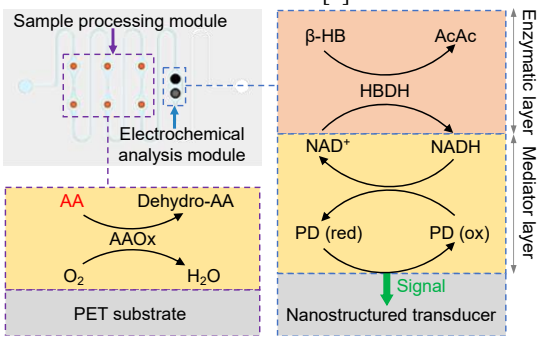

Figure 1: Schematic of the integrated bioanalytical microfluidic device and the corresponding sample processing and electrochemical sensing reactions taking place in the designated modules for reliable dehydrogenase-based sensing of HB. AAOx: ascorbate oxidase. AcAc: acetoacetic acid. HBDH: HB dehydrogenase. PD: 1,10-phenanthroline-5,6-dione.

RESULTS AND DISCUSSION

In our context, the sensitive and selective detection of NADH is the prerequisite for reliable dehydrogenase-based sensing, given that NADH is the measurable end product of the dehydrogenase-based reactions. We utilized 1,10-phenanthroline-5,6-dione (PD), as an electrocatalytic mediator for NADH oxidation, to lower the electrooxidation potential for NADH down to 0.1 V. Operation at this potential minimizes the background reactions stemming from the majority of endogenous electroactive interferents.

To enable fast electron transfer for PD-mediated NADH sensing, we utilized CNT for PD immobilization, since CNT renders high surface area and superior electrocatalytic performance. Accordingly, we fabricated the NADH sensing interface by drop-casting a CNT/PD solution (prepared with Nafion, as a binder) onto a gold electrode patterned flexible substrate (polyethylene terephthalate, PET). Figure 2a shows the response of the developed sensing interface to various NADH concentrations in a range from 10 to 50 μM with an estimated limit of detection of 0.22 μM.

We examined the selectivity of the developed NADH sensing interface, by testing its response toward 10 μM NADH spiked with a variety of common interferents present in biofluids (*e.g.*, ions, metabolites, endogenous electroactive species). As shown in Figure 2b, while most of the tested species had no influence on the NADH readout, the addition of a 10 μM AA generated a 2.5 times larger current response than the case with no interferents. The undesirable response of the NADH sensing interface to AA can be attributed to

978-1-940470-04-7/HH2022/$25©2022TRF
DOI 10.31438/trf.hh2022.66

the fact that the incorporated PD can also mediate the oxidation of AA [2], illustrating the importance of mitigating the AA interference.

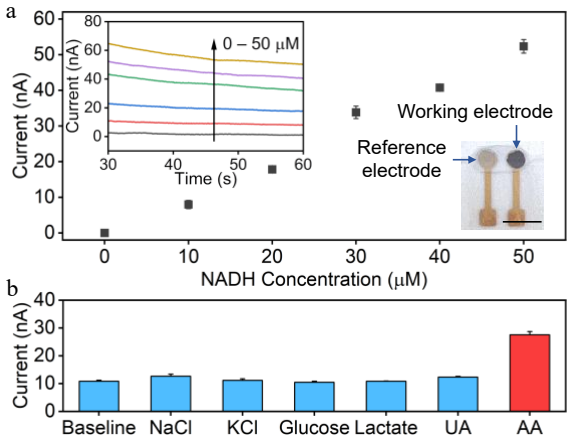

Figure 2: a) Calibration plot of the PD/CNT-based NADH sensing interface. Insets show representative chronoamperometric current responses to NADH for a NADH sensing interface, and an optical image of the NADH sensing interface. Scale bar indicates 5 mm. b) Selectivity study of the NADH sensing interface (all samples contain 10 μM NADH. NaCl: 10 mM; KCl: 2.4 mM; Glucose: 50 μM; Lactate: 5 mM; UA: uric acid, 59 μM). n = 3, error bars indicate standard error, testing buffer: 1× PBS.

We mitigated this interference by integrating a dedicated microfluidic sample processing module, which eliminates the AA in the introduced sample prior to dehydrogenase-based sensing. To this end, we utilized ascorbate oxidase (AAOx) and incorporated it within the microfluidic module (Figure 3a), since it can efficiently consume AA. To illustrate the module's AA consumption capability and its effectiveness for mitigating the AA influence on dehydrogenase-based sensing, we used the developed NADH sensing interface at the downstream of the module. Based on the sensor response and by referring to the sensor's pre-characterized NADH calibration plot, we estimated the NADH content of an introduced sample containing 10 μM NADH and 10 μM AA. We compared the results with that obtained from an unprocessed sample. As shown in Figure 3b, while the NADH sensing interface overestimated the NADH concentration by 119% for the unprocessed sample, it rendered an accurate NADH concentration estimation for the processed sample.

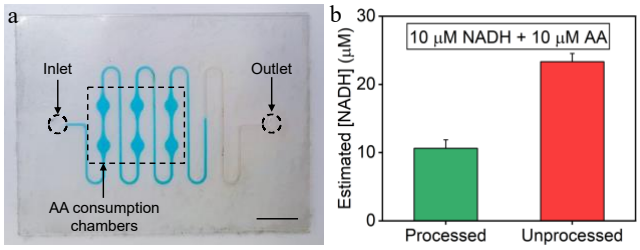

Figure 3: a) Optical image of the microfluidic module for in-situ sample processing. Scale bar indicates 1 cm. b) Estimation of the NADH concentration levels by the PD/CNT-based NADH sensing interface from the microfluidic structure processed and unprocessed samples containing 10 μM NADH and 10 μM AA. (n = 3, error bars indicate standard error, testing buffer: 1× PBS).

To demonstrate the utility of the devised solution for dehydrogenase-based sensing, we constructed a HB sensor based on the NADH sensing interface. Accordingly, we incorporated NAD^+ (cofactor) into the CNT/PD layer, then electrodeposited HB dehydrogenase (HBDH) onto the resultant sensing interface. In this way, the HBDH catalyzes the oxidation of HB and at the same time converts NAD^+ to electro-oxidizable NADH. Figure 4a shows the current response of the developed HB sensors within a concentration range of 50 to 400 μM (representing the clinically relevant concentration range of HB in sweat). To ensure the reliability of the HB sensor in complex biofluids, the sensor was challenged against a mixture of interfering species including KCl, NaCl, glucose, lactate, and UA. As shown in Figure 4b, the sensor had no response toward the interferents mixture. Negligible interference was also observed in the case of an *in-situ* processed sample containing AA (in contrast to the case of unprocessed AA sample). Collectively, the sensor- and device-level results indicate the suitability of the devised approach toward sensitive and reliable HB quantification for non-invasive wearable biomonitoring applications.

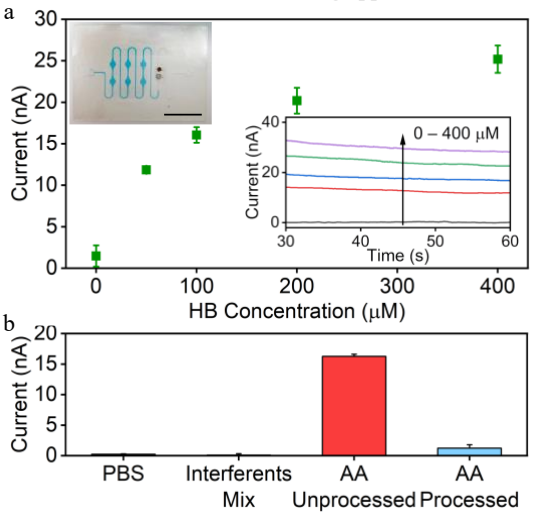

Figure 4: a) Calibration plot of the HB sensor. Insets show representative chronoamperometric current responses to HB for a HB sensor, and an optical image of the integrated bioanalytical microfluidic device. Scale bar indicates 2 cm. b) Selectivity study of the HB sensor. The interferents mix contains 10 mM NaCl, 2.4 mM KCl, 50 μM glucose, 5 mM lactate, and 59 μM UA. AA processed and unprocessed samples originally contain 10 μM AA. n = 3, error bars indicate standard error, testing buffer: 1× PBS.

ACKNOWLEDGEMENTS

This work is supported by National Institutes of Health (Grant: R21DK128711-01), Precise Advanced Technologies and Health Systems for Underserved Populations (PATHS-UP, National Science Foundation Engineering Research Center, Award: 1648451), and the startup package of S.E. provided by the UCLA Henry Samueli School of Engineering and Applied Sciences.

REFERENCES

[1] J.Y. Zhang, T. Shang, S.K. Koliwad, and D.C. Klonoff, "Continuous Ketone Monitoring: A New Paradigm for Physiologic Monitoring", *Journal of Diabetes Science and Technology*, 15, 4 (2021).

[2] M. Wu, X. Mao, X. Li, X. Yang, and L. Zhu, "1,10-phenanthroline-5,6-dione Adsorbed on Carbon Nanotubes: The Electrochemistry and Catalytic Oxidation of Ascorbic Acid", *Journal of Electroanalytical Chemistry*, 682 (2012).

CONTACT

*S. Emaminejad, emaminejad@ucla.edu

MONITORING BIOCHEMICAL REACTIONS USING MICROSPHERICAL GLASS SHELL WHISPERING GALLERY MODE RESONATORS

Vedant Sumaria[1], Rosemary Smith[2], and Srinivas Tadigadapa[1]*
[1]Northeastern University, Boston, USA
[2]University of Maine, Orono, ME

ABSTRACT

Chip-scale microspherical glass shell (MSG) whispering gallery mode (WGM) resonators offer a unique platform to configure a high sensitivity calorimetric biosensor. The MSG optical resonator is realized using the chip-scale glass blowing technique. The backside silicon is thinned to 50 µm and attached to a 3D printed reaction chamber. The bio-reaction occurs directly on the thinned silicon surface for highly effective coupling of heat from the reaction chamber to the MSG shell to result in a sensitive thermal sensor. We present the latest results to quantify the concentration-dependent oxidation of glucose-mediated by immobilized glucose oxidase on superparamagnetic nanoparticles. The volume of the samples tested was ~10 µl.

KEYWORDS

Calorimetric biosensor, whispering gallery, optical resonator, magnetic nanoparticles urea-urease, glucose-glucose oxidase.

INTRODUCTION

In this paper, we use chip-scale blown-glass microspherical shell structures as WGM resonators. The high-Q (10^6 – 10^7) resonators are highly sensitive to small changes in size or the refractive index of the microspherical shells and therefore exhibit a high-temperature sensitivity. The resonator can be configured as a highly sensitive calorimetric biosensor by inducing enzymatic reactions on the backside silicon surface of the resonators. The bioreactor is formed using a 3D printed reaction chamber which is epoxy glued onto the backside of the MSG resonator chip and glucose oxidase enzyme immobilized superparamagnetic nanoparticles are used to catalyze the exothermic reactions to glucose.

DESIGN & METHOD

The MSG shell resonators were fabricated using the chip-scale glass blowing process as described in [1]. Circular features of 250 µm diameter were etched to a depth of 250 µm on a 400 µm thick four-inch silicon using the DRIE process. 100 µm thick borosilicate glass was anodically bonded to the silicon at a pressure of 1026 Torr at 400 °C to form sealed cavities. The wafer was diced to individual devices and the glass was etched using 49% HF to 50 µm. Finally, the device is heated on a silicon nitride ceramic heater to a temperature of 775 °C in a vacuum chamber maintained at 100 Torr for 45 secs. This softens the borosilicate glass and expands the nitrogen within the cavity to create the spherical shell following which it is immediately cooled down to ambient temperature. Finally, the silicon substrate was thinned down to 300 µm using 25% TMAH at 90 °C leaving a 50 µm silicon below the etched cavity of the MSG resonator as shown in Fig. 1.

A tunable 1550 nm laser (Newport TLB-6728) was used as the excitation source for inducing optical resonance in the glass microspherical shells. The laser was tuned using a triangle wave at 10 Hz by 17 nm (or 2.12 THz) about the center wavelength of 1550 nm. The light was evanescently coupled to the resonator via a tapered optical fiber. The fiber tapering was performed using an in-lab-built ceramic heater. The bare fiber is heated to 1250 °C allowing the silica fiber to soften into a viscoelastic state. The heated cavity attains thermal equilibrium in about 120 s and thereafter the

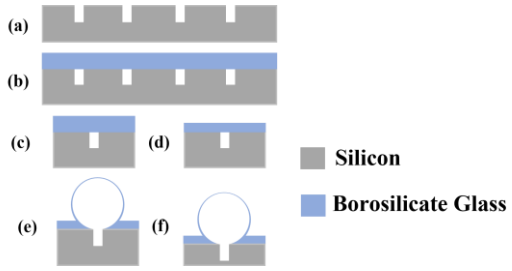

Figure 1: (a) Cylindrical Etch cavity of depth 250 µm in a 400 µm thick 4" silicon wafer. (b) 100 µm thick borosilicate wafer was anodically bonded to the wafer. (c) Devices are diced (d) 49% HF was used to thin the borosilicate glass to 50 µm. (e) The device was heated in a vacuum at 750 °C for 45 sec to create the MSG resonator. (f) Backside silicon was thinned using 25% TMAH to 50 µm in the region below the etched cavity.

translation stages were moved outwards at a constant pulling rate of 50 µm/s, while the transmission through the fiber was monitored on a photodetector. As the fiber is pulled, we observe multimode oscillations and finally with single mode at correct taper width. After about 18 mm of fiber elongation, the stages were stopped and the microheater was slowly allowed to cool down, to room temperature before removing the fiber from the heating source cavity.

A small change in size or refractive index can cause a significant shift in the resonance frequency. Both these quantities depend on temperature due to thermal expansion and thermo-optic effects respectively. This shift in resonance frequency of the resonator as a function of temperature was calibrated using a polyimide heater. Temperature sensitivity of 1.16 GHz/K was obtained. The system can resolve ΔT of up to 100 µK.

Fig. 2 shows the optical images of the biosensor. The spherical shell resonator with thinned backside silicon was attached to a 3D printed biochemical reaction chamber using thermal epoxy. The light was coupled to the resonator using a tapered fiber and resonance peaks are observed whenever the shell's equatorial circumference equals an integral number of the optical wavelengths. The excited resonance is seen as a dip in the transmission spectrum on the oscilloscope. The experimental setup to test the biochemical sensor is shown in Fig. 3. We use Pound-Drever-Hall (PDH) adaptive locking of the laser frequency at a fixed point on the slope

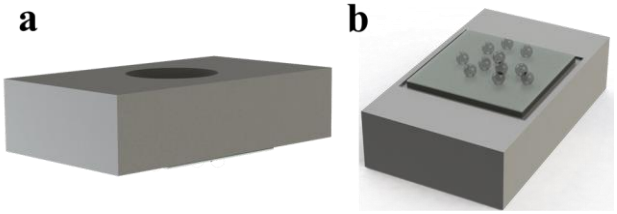

Figure 2: (a) Front side with circular cavity acting as the biochemical chamber. (b) Backside (inverted) with device stuck on the bioreactor using thermal epoxy. The backside etched silicon acts as the reaction surface for heat transfer from bioreaction to the MSG resonator.

978-1-940470-04-7/HH2022/$25©2022TRF
DOI 10.31438/trf.hh2022.67

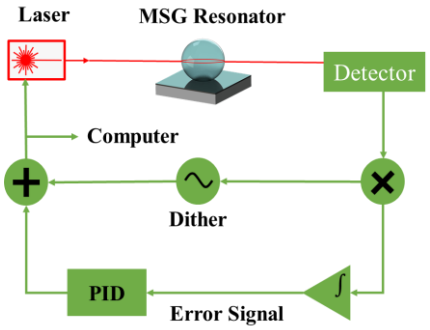

Figure 3: Schematic of adaptive locking sensing control system. A small high-frequency dither was used to modulate the driving laser frequency. When multiplied by the MSG resonator output and time-averaged, this dither signal generates an error signal whose amplitude is proportional to the difference between the current laser frequency and resonant frequency. This error signal is sent to a PID controller whose output is used to set the laser frequency, thus completing the feedback loop.

of the resonance curve [2] to track the shift in resonance frequency.

Chemical coprecipitation method was used to create superparamagnetic nanoparticles [3]. 2.36g of $FeCl_3.6H_2O$ and 0.86 $FeCl_2.4H_2O$ were dissolved in 40 ml of deionized water under a nitrogen atmosphere. This mixture was heated at 80 °C with nitrogen bubbling through it. 5 ml of ammonium hydroxide was added to this solution at a constant rate of 0.16 ml/min using a micropump.1 g of Fe_3O_4 nanoparticles are obtained after 30 mins and these superparamagnetic nanoparticles are separated using a neodymium magnet. These particles were further processed with a Sol-gel method to coat the superparamagnetic particles with Silica. 100 mg of the ferric oxide nanoparticles were dispersed in 50 ml of water with ultrasound for 10 min. A mixture of 1.0 ml of ethanol, 1.78 ml of TEOS (0.008 mol), and 1.0 ml of HCl (0.0024 M) was heated at 80 °C and stirred for 20 mins. Once the solution was clear and cooled, 0.5 ml of MPTMS was added. After 20 mins of stirring, a clear solution was obtained. This solution was added to the suspended nanoparticles in aliquots of 0.5 ml every 15 mins for two hours. The suspension was further stirred for another 30 mins to create silica over the ferric oxide nanoparticles with silane. These particles can be stored as dried nanoparticles or suspended in DI water. 50 mL of water containing Na_2HPO_4 (0.8 g) and 1 g of water-soluble carbodiimide (WSC) were used to dissolve 1 g of Ellman's reagent. 50 mg of the superparamagnetic nanoparticles were added to this mixture and stirred at 4 °C for 20 hours. The precipitate was separated magnetically and repeatedly washed with water. These nanoparticles are then mixed with a mixture of WSC (34.8 g), Glucose Oxidase (16.15 mg), and urea (2 M) dissolved in 10 mL (pH 5.5) of 0.1 M borate buffered solution. The mixture was stirred for 20 hours at 4 °C. The process ends with ultra-filtration to remove urea followed by magnetic separation of the nanoparticles. These nanoparticles with immobilized enzymes are stored at 4 °C.

RESULTS

Oxidation of glucose to gluconic acid in the presence of glucose oxidase has an associated enthalpy change of -80 kJ/mol. A precisely measured suspended nanoparticle solution with immobilized enzyme was first dropped over the silicon surface into the cylindrical reaction chamber. A neodymium magnet was placed below the device. This allows the particles to settle on the silicon surface and the phosphate buffer can be extracted using a micropipette. The laser is locked at the middle of the positive slope of the resonance frequency (1550 nm). As the glucose of various concentrations is dropped on the silicon surface with the immobilized enzyme on the nanoparticles, the resonance frequency shifts due to the exothermic nature of the reaction which results in a thermal expansion of the MSG shell. The change in responses is shown in Fig. 4 which represents the shift in resonance as the glucose molecules are catalyzed by the immobilized glucose oxidase and as the reaction completes, the signal drops to return to the base resonance frequency.

We studied the relative activity of the calibration sample at various pH values about the standard pH of 7.4. The pH of typical body fluids like plasma and serum is in the range of 7.35 – 7.45 [4]. We see the highest response for glucose at a pH of 7.4. The response drops to 20% as the pH is lowered to 4 and increased to 10. Following this, blood sample from a healthy patient is used to extract Serum. We observe a frequency shift of 110 MHz in the resonance frequency which from Fig.4 can be calculated as 4.72± 0.25 mM of Glucose.

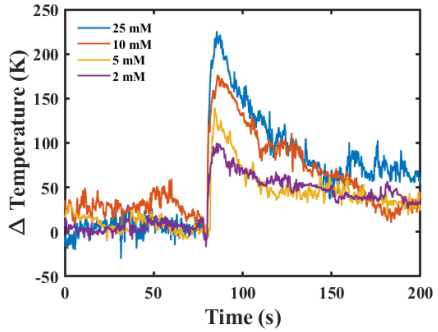

Figure 4: Time dependence of the output of the Microspherical Shell resonator for different concentrations of glucose solutions for liquid batch testing. Since a finite quantity of the analyte was dispensed in this experiment, the output increases initially, reaches a maximum, and finally decays with time.

CONCLUSION

In this paper, we configure chip-scale blown-glass microspherical shell WGM resonators as a highly sensitive glucose sensor. We present the shift in resonance as the glucose molecules are catalyzed by the immobilized glucose oxidase up to 2 mM concentrations. The volume of samples tested was ~10 µl. We also studied the relative activity for various pHs and observed the highest response at 7.4 pH. Finally, we see a response of 110 MHz shift in resonance frequency for serum processed from a healthy patient's blood sample. This matches 4.72± 0.25 mM of glucose which is in the normal range of 3.6 mM to 5.8 mM in healthy humans.

REFERENCES

[1] Zhang, Chenchen, et al. "On-chip glass microspherical shell whispering gallery mode resonators." *Scientific Reports* 7.1 (2017): 1-11.

[2] Drever, R. W. P., et al. "Laser phase and frequency stabilization using an optical resonator." *Applied Physics B* 31.2 (1983): 97-105.

[3] Ma, Zhiya, Yueping Guan, and Huizhou Liu. "Superparamagnetic silica nanoparticles with immobilized metal affinity ligands for protein adsorption." *Journal of Magnetism and Magnetic Materials* 301.2 (2006): 469-477.

[4] Boyanton Jr, Bobby L., and Kenneth E. Blick. "Stability studies of twenty-four analytes in human plasma and serum." *Clinical chemistry* 48.12 (2002): 2242-2247.

CONTACT
*V. Sumaria, tel: +1-814-880-0545; sumaria.v@northeastern.edu

DESIGN AND EXPERIMENTAL VALIDATION OF A PIEZOELECTRIC RESONANT MEMS PHASE COMPARATOR

Mathieu Gratuze and Frédéric Nabki*
École de Technologie Supérieure, LaCIME, Montréal, Québec, Canada

ABSTRACT

In this paper the design and experimental validation of the performances of a piezoelectric resonant microelectromechanical systems (MEMS) phase comparator is presented. Compared to the traditional integrated circuits, the potential benefits of a MEMS phase comparator include a low power consumption, higher sensitivity, higher selectivity and improved robustness. The design and experimental validation of a resonant MEMS phase comparator are presented. The operation of this resonant MEMS phase comparator is experimentally validated at a frequency of 108 kHz. This work is expected to lead towards the development of new applications for MEMS devices.

KEYWORDS

Piezo-eletricity, Phase Comparator, Phase Detector, MEMS, Resonator, Signal Processing, PiezoMUMPS.

INTRODUCTION

Signal processing can be achieved using micro-electro-mechanical systems (MEMS), as various instances have been proposed, including band pass, high pass and low pass filters, and resonators. Phase comparators are critical building blocks of various electronic systems, one of the most famous one being the phase-locked loop (PLL). They can also be encountered in diverse applications, such as motor control, radar and telecommunication systems, servo mechanisms, demodulators, clock and data recovery circuits (CDRs).

From a practical point of view, phase detectors can be divided into two main classes: linear phase detector and binary phase detector [1]. In the case of a linear phase detector, the transfer function is somewhat linear between the output and the input phase error, while binary phase detector produces an error signal that corresponds to the sign of the instantaneous phase error.

However, to the authors' best knowledge, literature on MEMS phase comparators is limited to the work of I. Dunk et al.[2], and that of J. Han et al. [3].[2] claims a device with the potential for higher sensitivity, higher selectivity, faster lock time, low power consumption and improved robustness. It makes use of Huygens Synchronization, the mechanical phenomenon behind the synchronization of two hanging pendulums. The work of J. Han et al. [3] consists in a power combiner with a thermoelectric power sensor to achieve a broadband MEMS phase comparator, at a much higher frequency (i.e. from 8 GHz to 12 GHz). However, this comes at the cost of a large power consumption (up to 1 W) [3].

This work targets a simpler structure to implement a piezoelectric resonant MEMS phase comparator: a simple clamped-clamped beam. Accordingly, the contributions of this work is the design and experimental validation of a piezoelectric resonant MEMS phase comparator.

THEORY AND OPERATION

The studied phase comparator MEMS resonator in this paper is a simple clamped-clamped beam with two electrodes each covering one half of the beam. The dimensions of the simulated MEMS are presented in detail in Table. The materials height and dimensions are consistent with the ones available in the commercial PiezoMUMPs process from MEMSCAP (Crolles, France), since this process is used for the fabrication of the prototypes in this work.

Table 1: Overview of the dimensions of the beam.

Parameter	Value
Length of the beam (um)	800
Width of the beam (um)	100
Separation between the electrodes (um)	5

It is well known electrode placement has an impact on the behavior of a MEMS resonator. Thus, two electrodes each covering one half of the beam have been used to either excite the mode shape of the first eigen mode (if the two excitation signals are in phase) or the mode shape of the second eigen mode (if the two excitation signal are in phase opposition). Thus, two excitation signals (F_{S1} and F_{S2}) have been defined:

$$F_{S1}(t) = A \sin(2\pi f_e t) \quad (1)$$
$$F_{S2}(t) = A \sin(2\pi f_e t + \Delta\varphi) \quad (2)$$

Where, A is the amplitude of the excitation signal in V, f_e is the frequency of the excitation signal in Hz, and $\Delta\varphi$ is the phase difference between the two signals.

FABRICATION AND EXPERIMENTAL RESULTS

The piezoelectric resonant MEMS phase comparator has been fabricated using the PiezoMUMPs process from MEMSCAP and a micrograph is shown in Fig.1a.

A laser vibrometer from Polytec, (Irvine, CA, USA) is used for experimental measurement. The test setup is presented in Fig.1b. Excitation of the resonant MEMS phase comparator is provided using a function generator type AFG3252 from Tektronix, (Beavertown, Or, USA) which can provide dual output signals with a controllable phase difference. Channels 1 and 2 are respectively connected to S1 and S2 pads which are shown in Fig.1a while the beam is grounded.

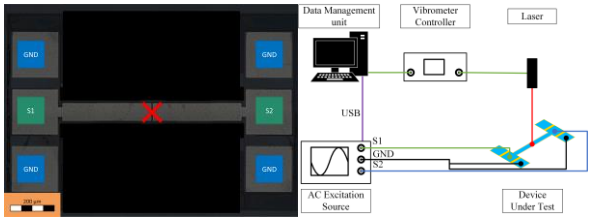

(a) (b)

Figure 1: (a) Micrograph of the fabricated resonant MEMS phase comparator, both electrodes are clearly identified along with the central (red) measurement point. (b) Schematic of the test bench.

Considering that that the resonant MEMS phase comparator will be excited by an excitation signal containing a single frequency, the recommendations made in [4] have been followed and the resonant MEMS phase comparator has been characterized using a pulsed sweep type excitation. The resulting frequency response is shown in Fig.2. It should be noted that when amplitude of the excitation is relatively large a non-linearity appears.

Table 2, show the good agreement between the measured

resonant frequency of the resonant MEMS phase comparator and the simulated behavior using COMSOL Multiphysics.

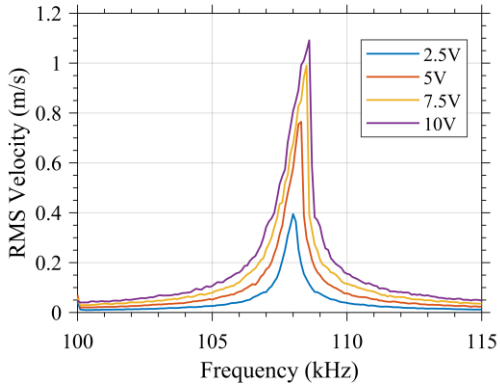

Figure 2: Measured RMS velocity of the central point of the resonant MEMS phase comparator (Δφ=0°)

Table 2: Summary of the characteristics of the resonances when the amplitude of the excitation signal is equal to 10 V_{pp}.

Parameter	Value
Simulated Resonant Frequency (kHz)	103.4
Measured Resonant Frequency (kHz)	108.6
Operating Bandwidth (kHz)	107.5-108.75

Afterwards, the phase difference, when keeping the amplitude and frequency of the excitation constant has been varied in the interval 0-360°. The influence of such variation is shown in Fig.3. It is clear to see that the RMS velocity of the central point can be used as a proxy to measure the phase difference between F_{S1} and F_{S2}

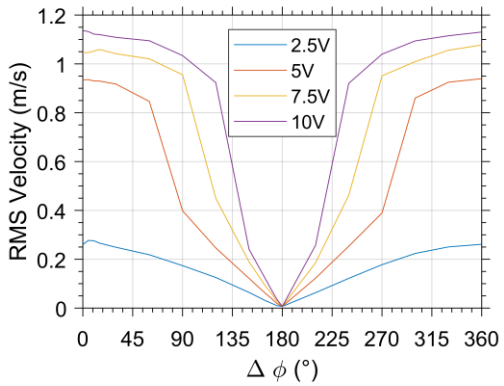

Figure 3: Influence of the variation of Δφ on the measured RMS velocity of the central point (f_e = 108 kHz)

To validate the operating principle of the resonant MEMS phase comparator, the heat map of the RMS velocity of the resonant MEMS phase comparator has been measured when , $\Delta\varphi$ is set to 0° (see Fig. 4a) and when $\Delta\varphi$ is set to 180° (see Fig. 4b).

It can be noted that the relationship between the RMS velocity $\Delta\varphi$ is not linear. Still, it is possible to estimate the amplitude of the RMS velocity of the central point as a function of $\Delta\varphi$:

$$Vpred(\Delta\varphi) = |V(\Delta\varphi=0|Ameas)\ sin(\Delta\varphi/2)| \quad (3)$$

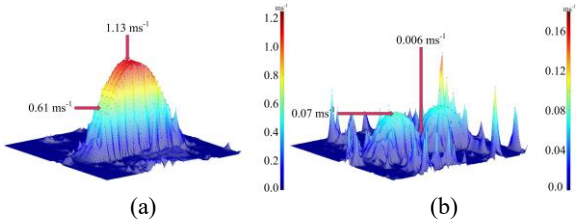

Figure 4: Visualization of the heat map of the RMS velocity of the resonant MEMS phase comparator, with A=10V, fe=108kHz and (a) Δφ equal to 0° (b) Δφ equal to 180°.

where $V(\Delta\varphi=0 \mid Ameas)$ is the measured RMS amplitude of the velocity of the measurement point as extracted from Fig. 2. This allows the determination of r^2, the squared Pearson product moment correlation between the estimation and the experimental results, this is shown in Table 3. The good agreement between estimation and measurement shows that the calibration of the resonant MEMS phase comparator will be simplified as it is not necessary to measure the value for all the values of $\Delta\varphi$. Nevertheless, it should be noted that the current operation of the phase comparator doesn't allow the determination of which signal comes first.

Table 3: Overview of performances the fitting function, f_e=108kHz.

Amplitude of the excitation (V)	Measured rms velocity when Δφ=0° (ms^{-1})	r^2
2.5	0.28	0.9951
5	0.94	0.9344
7.5	1.07	0.9685
10	1.13	0.92

CONCLUSION

In this paper the design and experimental validation of a piezoelectric resonant MEMS phase comparator was presented. The reported results show its potential for the development of integrated MEMS phase comparator.

ACKNOWLEDGEMENTS

The authors would like to thank CMC Microsystems for providing the layout design tools and enabling device fabrication.

REFERENCES

[1] B. Razavi, *Design of Integrated Circuits for Optical Communications, 2nd Edition*, 2nd ed. 2012.

[2] I. Dunk and H. Chandrahalim, "Microelectromechanical Phase Detectors for Phase-Locked Loop Applications," in *2020 IEEE SENSORS*, Oct. 2020, pp. 1–4.

[3] J. Han and X. Liao, "PLL application research of a broadband MEMS phase detector: Theory, measurement and modeling," *Solid-State Electron.*, vol. 132, pp. 6–11, Jun. 2017.

[4] M. Gratuze, A.-H. Alameh, S. Nabavi, and F. Nabki, "Control of Spring Softening and Hardening in the Squared Daisy," *Micromachines*, vol. 12, no. 4, p. 448, Apr. 2021.

CONTACT

*M. Gratuze; tel +1 438 728-8549 , mathieu.gratuze@etsmlt.ca

SIMULTANEOUS MOISTURE AND SALINITY MONITORING IN SOILS USING SPLIT RING RESONATOR(SRR) BASED SCANNING FREQUENCY TRANSMITTORY(SFT)

Sunghyun Hwang[1], William N. Carr[2] and Yong-Kyu Yoon[1]*
[1]Department of electrical and computer engineering, University of Florida, Gainesville, FL, USA
[2]NeptuneSensor, Gainesville, FL, USA

ABSTRACT

A new type of impedance spectrometry, the so called scanning frequency transmittory (SFT), is introduced for moisture and salinity monitoring in soils using a single split-ring resonator (SRR) sensor. The system concept has been experimentally verified using a passive SRR antenna-resonator with a vector network analyzer (VNA) and an ultra-high frequency (UHF) radio-frequency identification (RFID) tag readout. The demonstrated sensing system enables simultaneous monitoring of moisture and salinity in a simple configuration with remote readout, battery-free sensing, and cost-effectiveness advantageous for a practical implementation toward the Internet of Agriculture Things (IoAT).

KEYWORDS

Scanning frequency transmittory (SFT), split-ring resonator (SRR), radio-frequency identification (RFID), internet of agriculture things (IoAT), sub-soil monitoring, wireless sensing.

INTRODUCTION

As the world's population continues to grow, food production must be increased to meet the need for an estimated 9.8B world population by 2050. Moisture in soils is essential for plant growth. With global warming, the sea level increases, and the coastal areas are more vulnerable to the high salinity levels in soils affecting plant growth [1]. Simultaneous measurement of the moisture and salinity levels and controlling these levels would have a significant contribution to maximizing the crop harvests in agriculture. Previous studies have shown various ways to detect moisture levels such as Frequency Domain Reflectometry and Time Domain Reflectometry [2]-[3], which often are limited with moisture measurements only, and require complex electronic systems and high ownership costs.

In this work, we introduce a new type of impedance spectrometry that is named a scanning frequency transmittory (SFT) system using a split-ring resonator (SRR) antenna for simultaneous moisture and salinity monitoring in soils. The SFT system concept has been experimentally verified using a passive SRR antenna with a vector network analyzer (E5071C, Agilent Technologies Inc.) and wireless RFID reader-based test setup. A complementary split-ring resonator (CSRR) loaded transmission line and an SRR antenna are simulated and fabricated for experiments.

DESCRIPTION OF THE NEW SYSTEM

The SFT sensor comprises a metamaterial SRR antenna providing sensing at UHF frequencies. A schematic for the SRR SFT moisture and salinity sensing system is shown in Fig. 1. When the moisture concentration in soils changes, the air pores in the soils are replaced by water with a higher dielectric constant than that of air, resulting in an increased effective dielectric constant, thus downshifting the resonant frequency. Meantime, the salinity level in the water does not affect its dielectric constant but its conductivity and thus the loss factor and the Q-factor [4]. The effect of loss tangent and permittivity on the sub-soil is simulated with an SRR antenna operating at 920 MHz using a High-Frequency Structural Simulator (HFSS) as shown in Fig. 3. The loss tangent did not highly impact the change of the resonant frequency while impacting the Q-factor, i.e. the peak value. Meantime, the change in permittivity value causes the resonant frequency to shift [5].

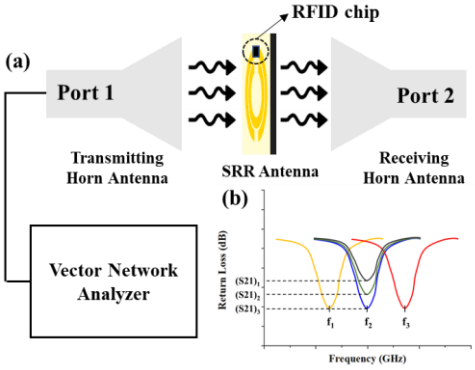

Figure 1. Scanning frequency transmittory (SFT) system: (a) A schematic for the concept, (b) f_1, f_2, and f_3 indicate different moisture levels. $(S21)_1$, $(S21)_2$, and $(S21)_3$ do different salinity levels.

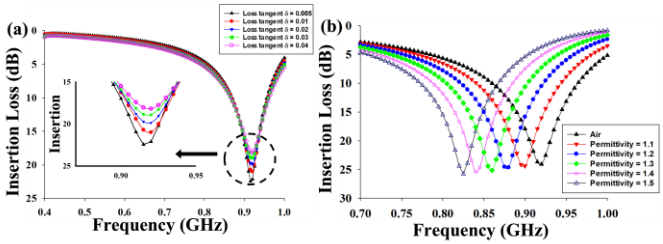

Figure 2. Simulated insertion loss (a) with different loss tangent δ and (b) with different permittivity.

SENSOR DESIGN AND FABRICATION

The SRR antenna is designed using HFSS for a sensor node as shown in Fig. 3. The antenna has a radius of 28 mm and an overall size of 60 × 60 mm^2. The antenna operates at 920 MHz in free space. The SRR structure shows several advantages as an RFID tag antenna such as low profile, compact size, long read range, and mitigation of blind spot.

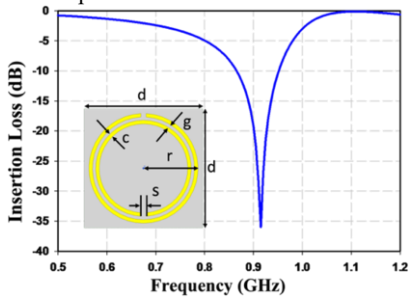

Figure 3. Simulation result of the SRR antenna and schematic configuration of the SRR (inset), where d = 60 mm, r = 28 mm, g = 2.2 mm, s =2.8 mm and c = 2 mm.

978-1-940470-04-7/HH2022/$25©2022TRF
DOI 10.31438/trf.hh2022.69

As a variation of resonator type SFT, a CSRR loaded transmission line is designed, simulated, and fabricated to verify the shift of resonant frequency surrounding the sensor. Fig. 4. shows fabricated sensors: (a) SRR sensing antenna integrated with an Alien Higgs3 RFID chip and (b) CSRR loaded transmission line. The SRR antenna is designed as 2.5 times bigger than the CSRR loaded transmission line, showing the improved efficiency and gain of the antenna at the same frequency (915 MHz), which enables longer and wider range detection as a sensor node. The antenna and transmission line are fabricated using milling machine on a printed circuit board (Rogers 4350B, Rogers Inc.) with a dielectric constant of 3.44 and a loss tangent of 0.004.

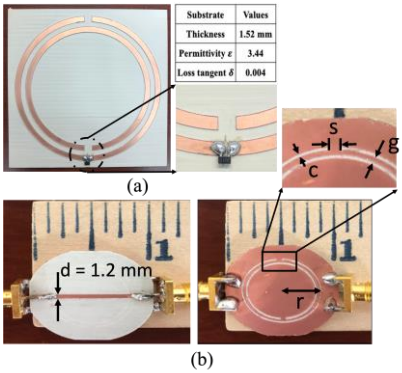

Figure 4. Images of fabricated sensors: (a) SRR sensing antenna and a close-up view of the Alien Higgs 3 RFID chip with a table showing the substrate properties, (b) Top view and bottom view of a 1-inch sized CSRR loaded transmission line, where r = 8.4 mm, g = 1.1 mm, s = 2.2 mm and c = 0.8 mm.

EXPERIMENT SETUP AND RESULTS

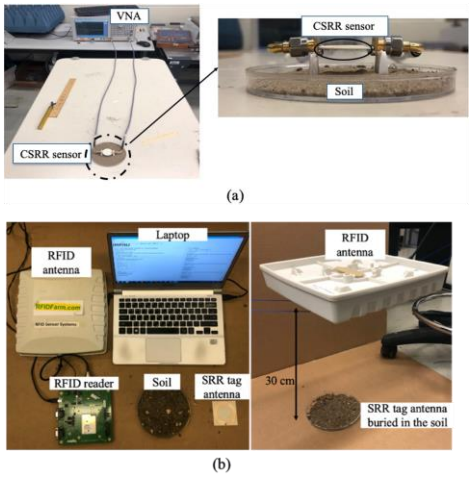

Figure 5. (a) Vector Network Analyzer based wired test setup, (b) Wireless RFID reader based test setup.

In this work, two types of sensing tests have been performed as shown in Fig. 5. First, the VNA has been utilized for s-parameter measurement in a planned frequency range for the proof of concept (Fig. 5a). Second, wireless remote readout experiments have been performed using a standard RFID reader and a passive RFID tag (Fig. 5b). The complete sensing system comprises a passive RFID tag loaded SRR and an Impinj RS2000 interrogator. For this test, the RFID readout antenna has been fixed at an altitude of 30 cm above the soil surface. The designed SRR antenna has been buried in the soils at 1.5 cm depth with various moisture and salinity levels.

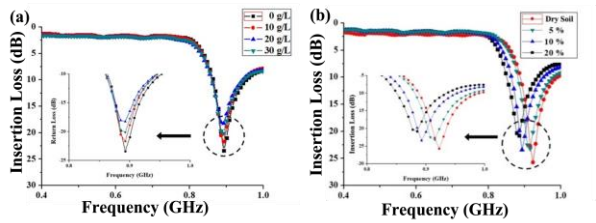

Figure 6. Measured insertion loss (a) at 10 wt% water with different salinity levels and (b) at different moisture levels.

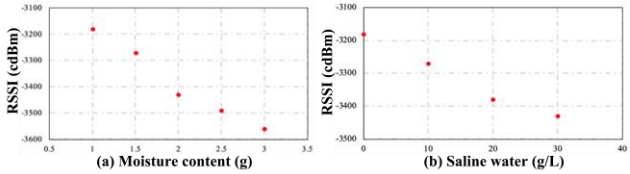

Figure 7. Measured RSSI (a) at different moisture levels and (b) at a different salinity level in 10 wt% moisturized soils.

Fig. 6a and 6b show the salinity and moisture-dependent s-parameters of the VNA-based setup, respectively. The salinity level shows little change in the center frequency of the antenna. However, the different moisture level has made an obvious change in the center frequency of the sensor as expected. Fig. 7 shows received signal strength indicator (RSSI) results (equivalent to S21), which are obtained from the wireless RFID reader. The decrease in RSSI value is due to the shift of resonant frequency at the different moisture content (Fig. 7a) and is due to the decrease in Q-factor at different saline content (Fig. 7b) as proved in the first experiment. Further studies should include the resonant frequency information when determining the effect of moisture and salinity content from a single RSSI value.

CONCLUSION

This work demonstrates a new type of impedance spectrometry that is called SFT using an SRR antenna for the simultaneous monitoring of moisture and salinity level in the soils. It is expected that the introduced SFT system will provide a wireless, battery-free sensor node, cost-effective monitoring system for simultaneous moisture and salinity sensing.

REFERENCES

[1] Qld.gov.au, (2016). *Impacts of salinity | Environment, land, and water* |Queensland Government. [online] Available at:https://www.qld.gov.au/environment/land/soil/salinity/impacts/ [Accessed 10 Jan. 2016].

[2] R. Muñoz-Carpena, C. M. Regalado, A. Ritter, J. Alvarez-Benedí, and A. R. Socorro, "*TDR estimation of electrical conductivity and saline solute concentration in a volcanic soil*," Geoderma, vol. 124, no. 3–4, pp. 399–413, 2005.

[3] A. Mortl, R. Muñoz-Carpena, D. Kaplan, and Y. Li, "*Calibration of a combined dielectric probe for soil moisture and porewater salinity measurement in organic and mineral coastal wetland soils*," Geoderma, vol. 161, no. 1–2, pp. 50–62, 2011.

[4] Y. Lasne et al., "*Effect of salinity on the dielectric properties of geological materials: Implication for soil moisture detection by means of remote sensing*," Int. Geosci. Remote Sens. Symp., 46, 6, (2007), pp. 3689–3693.

[5] Carr, William., U.S. Patent 10,690,609, June 23. 2020

CONTACT

*SH. Hwang, tel: +1-352-278-8325; sunghyun.hwang@ufl.edu

3-D PRINTED REDOX-ACTIVE ORGANIC ELECTRODES TO BRIDGE ACROSS BIOLOGY AND ELECTRONICS

Anwar Elhadad[1], and Seokheun Choi[1,2]*

[1]Bioelectronics & Microsystems Laboratory, Department of Electrical & Computer Engineering, State University of New York at Binghamton (SUNY Binghamton), Binghamton, New York, USA

[2]Center for Research in Advanced Sensing Technologies & Environmental Sustainability, SUNY Binghamton, Binghamton, New York, USA

ABSTRACT

An intimate and direct interface between inorganic electronics and living organisms will revolutionize the next generation of bioelectronics by bridging the signal and material gap between these two different fields. In this work, a redox-active microbial electrode is constructed as the novel interface by simultaneously 3-D printing and electropolymerizing 3,4-ethylenedioxythiophene (EDOT) in a liquid containing electrochemically active bacteria. A custom-made 3-D printer with a concurrent electrochemical control allows a scalable, template-free deposition of electrochemically active organic electrodes in a single printing. Electropolymerized poly(3,4-ethylenedioxythiophene) (PEDOT) acts as redox-active bridges by exploiting extracellularly transferred electrons generated from the bacterial respiration, constructing a seamless contact between the biological processes and the external abiotic systems.

KEYWORDS

3-D printing, redox-active, organic electrodes, bioelectronics, electrochemically active bacteria

INTRODUCTION

Recently, integrating living microbial cells with other building materials has attracted significant attention and has become a rapidly emerging field of study called "engineered living materials (ELMs) [1]." The Defense Advanced Research Projects Agency (DARPA) created the ELM program to significantly improve techniques for the manufacture and maintenance of military systems by exploiting the unique biological functional features. Specifically, electrochemically active bacteria have been considered an excellent biological component for the construction of redox-active electrodes to connect abiotic electronics and biotic living systems. The abiotic electronics exclusively use electrons for the signaling while the living systems rely on ionic molecules for communication, which makes it difficult to bridge the gap between these two fields. By responding to the metabolic ion gradients, the electrochemically active bacteria can generate electrons that can be used to connect the biological system and the inorganic electronics. Despite the vast potential and promise of this technique for the next generation of bioelectronics, there exists an unaddressed need to develop a simple, rapid, and controllable method to combine electrogenic bacteria with electrodes. In 2018, The Ajo-Franklin research group developed a novel technique to embed the bacteria in an electropolymerized polymer [2]. However, the combined material was not able to be patterned in a controllable manner. At Hilton Head 2020 workshop, we demonstrated an innovative proof-of-concept method to fabricate a bacteria-containing living electrode by combining a controllable 3-D printing method and a simple electrochemical polymerization technique [3]. The monomer precursor 3,4-ethylenedioxythiophene (EDOT) was printed into a 3-electrode electrochemical cell that contained microorganisms. The monomer was in-situ electrochemically polymerized to the conducting poly (3,4-ethylenedioxythiophene) (PEDOT) polymer, which entrapped and connected the electrochemically active bacteria to the electrode within 35 min. However, the electroactive materials were limited to the pre-defined microfluidic template with the 3-electrode system. The template could not allow any meaningful functions other than for studying purposes of the materials.

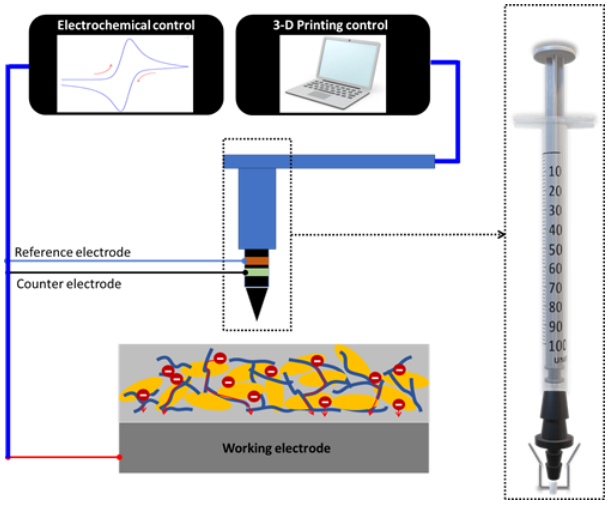

Figure 1: Electrochemical 3-D printing system. Simultaneous 3-D printing and electropolymerizing of a bacteria-containing polymer can construct a seamless biotic-abiotic interface.

TEST SETUPS AND RESULTS

In this work, we created a 3-D, template-free, microbial bioelectrode in a systematic and automated manner by using an electrochemical additive manufacturing technique (Figure 1). Electrochemical additive manufacturing has emerged as a new form of additive manufacturing, but its application has been limited to the deposition of metallic materials through the electrochemical reduction of metal ions. This technique finds the best-fit solution to construct our living bioelectrodes. The living electrode was fabricated by 3-D printing the polymer precursor EDOT in electrogenic bacteria-containing liquid and forming an electrochemically active biomaterial onto an abiotic graphite electrode through the in-situ electropolymerization of the monomer to the redox-active conducting PEDOT. The bioprinting syringe nozzle was modified by integrating an Ag/AgCl reference electrode and a platinum counter electrode which were connected to the external electrochemical control system. The electrodeposition was well-controlled with the potential application to the working electrode of a conductive substrate against the reference and counter electrodes (Figure 1 & Figure 2). When the bacteria containing EDOT liquid contacted the conductive substrate, a stable meniscus formed, and the desired structure was created. The cells were encapsulated within a copolymer matrix of PEDOT and alginate (Figure 2).

978-1-940470-04-7/HH2022/$25©2022TRF
DOI 10.31438/trf.hh2022.70

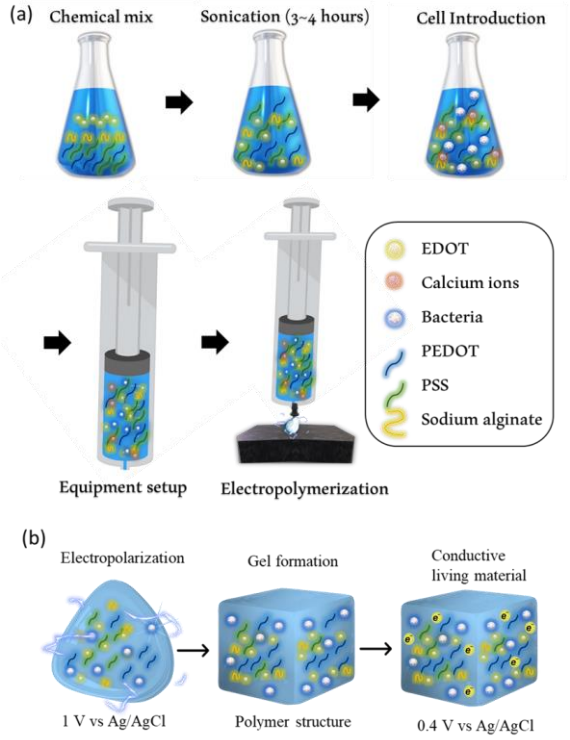

Figure 2: (a) The electropolymerization process to form a conductive microbial electrode. Electrochemical polymerization is followed by alginate crosslinking with $CaCl_2$. (b) Living electrode fabrication stages.

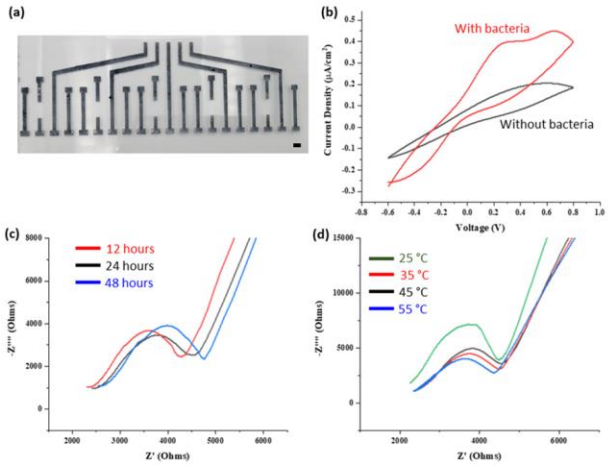

Figure 3: (a) 3-D printed conductive trace (the bar: 2mm), and (b) cyclic voltammetry curves of the electropolymerized PEDOT with and without bacteria. Electrochemical impedance spectroscopic profiles with storage time (c) and temperature (d).

The electropolymerized material was successfully printed as a living electrode in a controllable manner (Figure 3a). The bioelectrode demonstrated higher electrochemical activities and lower charge transfer resistance than that of the PEDOT-only sample (Figure 3b). The polymer maintained its gel structure when used or stored under different conditions. The polymer was storable up to 48 hours maintaining the viability of the cells

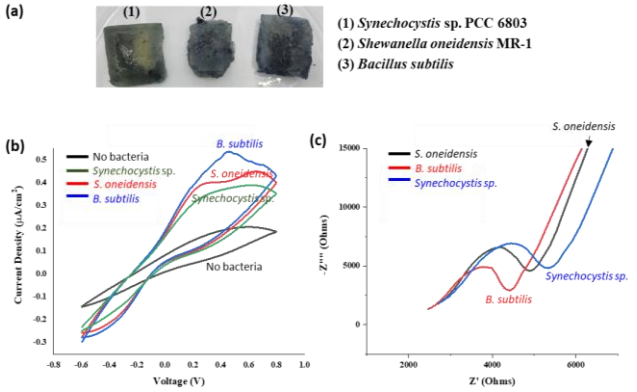

Figure 4: (a) Living electrodes with different types of bacteria ((1) Synechocystis sp. PCC6803, (2) Shewanella oneidensis MR-1, and (3) Bacillus subtilis), (b) their cyclic voltammetry curves and (c) electrochemical impedance spectroscopic profiles.

with the low charge transfer resistance (Figure 3c). Moreover, the gel was functional even when placed for 10 minutes in relatively hot temperatures up to 55°C before breaking (Figure 3d). The living electrodes with different types of electrochemically active bacteria were constructed and their electrochemical activities were characterized along with their electron transfer efficiencies (Figure 4). Our bioelectrodes showed more vigorous electrochemical activities with effective electron transfer capabilities, indicating that they could seamlessly bridge biological systems and abiotic electrodes.

CONCLUSION

This work created a great performing, very electrochemically active, and controllable microbial electrode. The living electrodes can dramatically reduce the physicochemical mismatch between the inorganic electrodes and the biological entities providing an effective coupling at the biotic-abiotic interface through biological electron conduits. Engineering such interfaces will be critical for advancing practical applications in bioelectronics such as *in vitro* biosensors, electronic medical implants, neuroprosthetics, and biofuel cells.

ACKNOWLEDGEMENTS

This work was supported mainly by the Office of Naval Research (#N00014-21-1-2412), and the NSF (CBET #2100757, ECCS #2020486, & ECCS #1920979).

REFERENCES

[1] A. Rodrigo-Navarro, et al., “Engineered living biomaterials,” *Nature Review Materials*, 2021, 6, 1175.

[2] T.J. Zajdel, et al., "PEDOT: PSS-based multilayer bacterial-composite films for bioelectronics," *Scientific reports*, 2018, 8, 15293.

[3] Y. Gao, J. Kim, J. Ryu, S. Choi, "Additive Manufacturing of Living Electrodes", Hilton Head Workshop 2020: A Solid-State Sensors, Actuators and Microsystems Workshop, May 31 - June 4, 2020, Hilton Head Island, SC. Published in the IEEE JMEMS Special Proceeding (Vol. 29, pp. 1069-1073, 2020)

CONTACT

*Prof. S. Choi, tel: +1-607-777-5913; sechoi@binghamton.edu

ADDITIVE BATCH MICROFABRICATION OF 3D METAL ELECTROSTATIC SWITCHES TOWARDS 3D PRINTED METAL MEMS

Bhushan Lohani[1], Sheikh D. Hossain[1], Thomas Starke[2], and Robert C. Roberts[1]
[1]The University of Texas at El Paso, USA
[2]3D MicroPrint GmbH, Germany

ABSTRACT

This paper presents the batch fabrication of an additively manufactured metal electrostatic microswitch to demonstrate device scaling and the lower dimensional limit of the process. Optimization in optical and printer parameters resulted in a decreased gap between two printed parts by a factor of six and an increase in resolution by a factor of 2.5 compared to our previous study, without fabrication failure. The electrostatic microswitches were batch fabricated via a Micro Laser Sintering (MLS) process, which is a precision form of metal powder-based additive manufacturing. The use of additive manufacturing to build metal microsystems opens up new avenues toward the low-cost fabrication of prototypes as well as low-volume systems eliminating the constraints of conventional cleanrooms.

KEYWORDS

Additive Manufacturing; Micro Laser Sintering; Electrostatic Switches; 3D Printing;

INTRODUCTION

Microelectromechanical Systems (MEMS) are vital components for a multitude of modern electronic devices [2]. The possibility of direct fabrication of such components from a design file [3] has great potential for the fabrication of electronics, transducers [4], and sensors [5, 6]. Additive manufacturing techniques such as MLS allows the fabrication of devices like electrostatic switches that benefit from higher plasticity and conductivity compared to their silicon counterparts using metal thin films, fabricated in conventional cleanrooms [6]. It also reduces fabrication steps like deposition, photolithography, etching, etc. which are expensive and use hazardous chemicals. MLS also uses a low-cost substrate compared to silicon. Recent advancements in MLS have enabled the fabrication of micro metal parts with features down to 15µm [7] from metal powder [8]. Superior dimensional consistency and improved surface roughness of MLS compared to other additive tools [9] make it a suitable process to fabricate microsystems. In this work, optimized machine settings and device design are employed to reduce the switch gap by a factor of 6 and increase the device resolution by a factor of 2.5 compared with our initial study [1].

An array of electrostatic switches with increased resolution has been batch fabricated utilizing the enhanced feature sizes and resolution of a new MLS system (DMP64, 3D MicroPrint GmbH) in order to investigate the minimum possible feature size. Figure 1 shows the CAD design of the optimized device with key parameters like beam thickness (a), beam gap (X), beam length (L), and length of the capacitive region (L1), all of which together determine the value of pull-in voltage. Switches with 1mm long beams were printed with varying gaps down to 15µm (~40µm previously) and a beam thickness of 40µm (~100µm previously). The process of fabrication involves layer-wise melting and fusing of metal powder in 5µm layers following the digital CAD design. 17-4PH stainless steel powder (D_{90} < 6µm) was used as the metal powder due to its optimized dimensional parameters on the system. The finer metal powder was extracted using vibratory

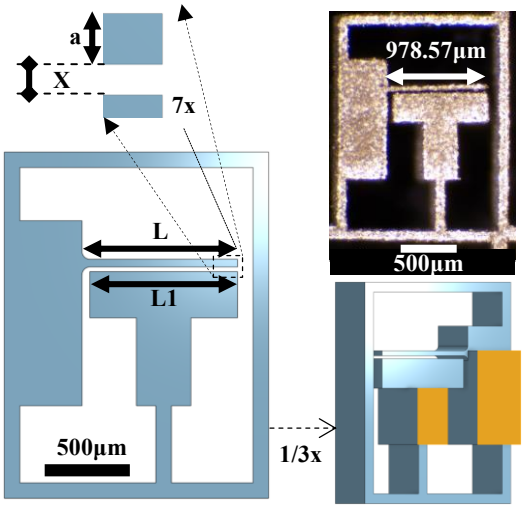

Figure 1: CAD Design of the switch: top view (left), isometric view of switch showing raised contact points in yellow (bottom right), and fabricated single device with dimension (top right).

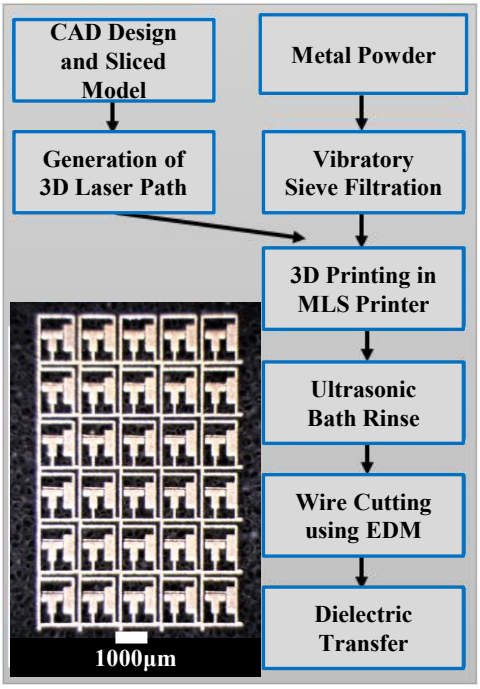

Figure 2: MLS Microfabrication process flow for the electrostatic switches with its dielectric transfer to a final arbitrary substrate. Batch fabricated devices (bottom left)

978-1-940470-04-7/HH2022/$25©2022TRF
DOI 10.31438/trf.hh2022.71

mesh sieves. The switches were batch fabricated, rinsed in an ultrasonic bath, separated from the build plate using EDM wire cutting, and separated individually (shown in Figure 1) to be transferred onto a dielectric substrate. The batch fabricated switches and full fabrication and dielectric transfer processes are shown in Figure 2.

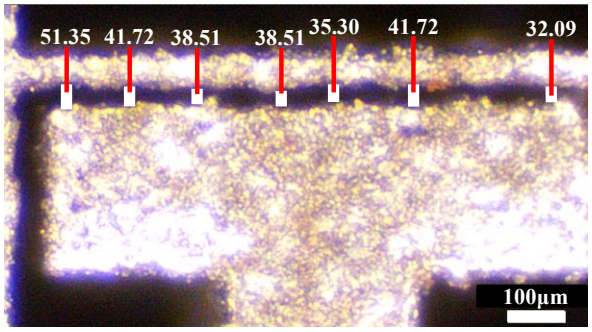

Figure 3: Close-up view of fabricated switch showing the beam and gaps (in µm) at different points along the length. (Average Gap=40.1±6.7µm).

RESULTS

The inset of Figure 2 shows the batch fabricated devices after release from the build plate. Figure 1 shows a single device with its as-printed dimensions. The close-up view of one of the devices is shown in Figure 3. The average deviation of the as-printed gap with respect to the designed gap for the switches was around 2.94%. Simulation of these redesigned switches estimates the device actuation will occur at voltages between 250V to 10kV depending on the gap (X). The simulation result for one of the switches (X=20µm) is shown in Figure 4, which actuates at around 1.3kVolts. Simulated actuation voltage for previous and present are compared for different gaps and to their breakdown voltage values in Figure 5. Although the pull-in voltage values are significantly reduced, they are still above the respective breakdown voltage values and hence require more work towards

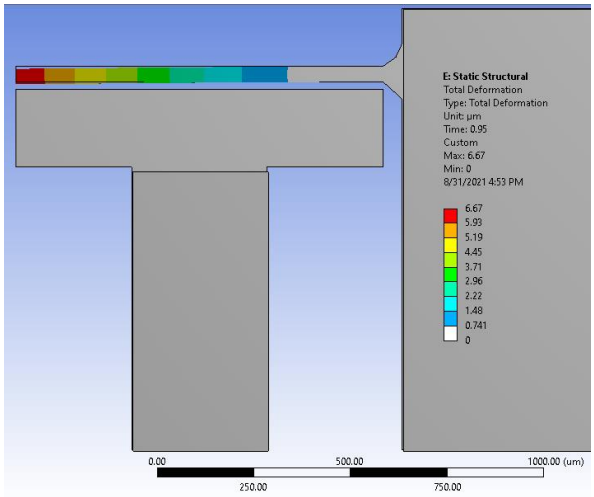

Figure 4: ANSYS electromechanical simulation results for a microswitch with a gap of 20µm demonstrating the tip of the cantilever beam deflecting by 6.67µm implying the gap reduces by 2/3rd when the pull-in voltage of 1.3kV is applied.

the development of the MLS system to increase resolution. However, this work demonstrates a large increase in the resolution of metal 3D printing for microfabrication with many microsystems applications.

CONCLUSION

This work demonstrates a new metal 3D microfabrication capability for the field, which may compete with subtractive manufacturing if the resolution is increased by improving the optics system and optimizing the slicing and print parameters. An improvement of the device gap by a factor of 6 and a decrease of minimum feature size by a factor of 2.5 were achieved in this work over previous investigations. The possibility of using metal additive manufacturing could reduce cost of fabrication, use of expensive substrate and hazardous chemicals for processing, and the procedure could be performed in a small controlled and contained environment as compared to conventional clean room. Focused research towards the development of this process, might lead to it not only complementing present conventional subtracting manufacturing but also competing with it.

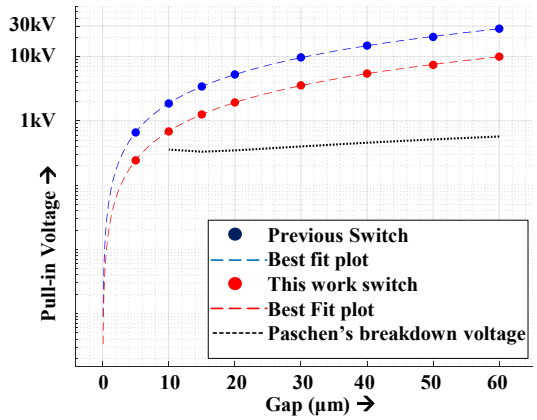

Figure 5: Pull-in Voltage versus electrostatic switch gap for the design of the work (red) and previous work [1] (blue). Paschen's breakdown voltage for 1atm in air is also shown

REFERENCES:

[1] B. Lohani *et al.*, *Journal of Microelectromechanical Systems*, vol. 29, no. 5, pp. 972–977, Oct. 2020.

[2] O. Ulkir, *Mater. Res. Express*, vol. 7, no. 7, p. 075015, Jul. 2020.

[3] T. Blachowicz and A. Ehrmann, *Micromachines*, vol. 11, no. 4, Art. no. 4, Apr. 2020.

[4] R. C. Roberts and N. C. Tien, in *2017 19th Intl. Conf. on Solid-State Sensors, Actuators and Microsystems (TRANSDUCERS)*, Jun. 2017, pp. 1233–1236.

[5] B. R. Liyarita, A. Ambrosi, and M. Pumera, vol. 30, no. 7, pp. 1319–1326, 2018.

[6] Y. Xu *et al.*, "The Boom in 3D-Printed Sensor Technology," *Sensors*, vol. 17, no. 5, Art. no. 5, May 2017.

[7] "Products - 3D MicroPrint GmbH." https://www.3dmicroprint.com/products/.

[8] P. Regenfuß, R. Ebert, and H. Exner, *Laser Technik Journal*, vol. 4, no. 1, pp. 26–31, 2007.

[9] V. Fiorese *et al.*, in *2020 IEEE/MTT-S International Microwave Symposium (IMS)*, Aug. 2020, pp. 1168–117

REGION-TARGETED BILAYER COATING TECHNOLOGY FOR INGESTIBLE DEVICES AND SYSTEMS

Michael A. Straker, Joshua A. Levy, Justin M. Stine, Vivian Borbash, Luke A. Beardslee, and Reza Ghodssi *
University of Maryland, College Park, Maryland, USA

ABSTRACT

We present a pH-responsive bilayer packaging strategy to protect capsule components intended for actuation in the small intestine from stomach acid. The bilayer is resistant to stomach acid but is removed in the small intestine (neutral pH). This structure consists of a water-soluble support layer, polyethylene glycol (PEG), and a pH-responsive polymer coating, Eudragit. We also demonstrate a realistic intestinal simulation apparatus to test physical bilayer removal against intestinal tissue with physiologically relevant forces. Using this simulator, bilayer removal was accomplished in approximately 15.6 min. This technology represents a low-complexity, versatile, and reliable approach to protect ingestible capsule components.

KEYWORDS

Packaging, Ingestible Device, Enteric Coatings, GI tract.

INTRODUCTION

Ingestible capsules offer a promising alternative to enable diagnostics and treatment in the small intestine when compared to traditional methods like endoscopy. Sensors and actuators in these devices for small intestinal targeting require simple and versatile packaging to protect from harsh acidic conditions in the stomach. Using a passive packaging strategy to shield internal components until their time of release without additional active mechanisms conserves valuable capsule space and energy. pH-responsive coatings are used extensively for tablet-based drug delivery [1] and as release triggers for ingestible devices [2]. Our lab has previously demonstrated this technique for the protection of small sensor openings (~250 µm) for biomarker detection in the small intestine [3]. However, fabricating a robust protective layer over a large open cavity (mm-scale) for actuator release using pH-responsive coatings is challenging using traditional coating methods alone.

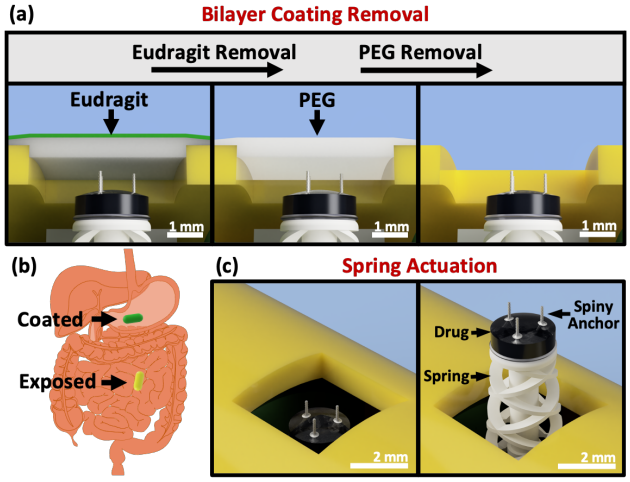

Figure 1: Overview of the packaging system in application. (a) The pH-sensitive polymer coating (green) remains intact and impermeable while in the stomach (pH 1.5-3). (b) In the small intestine, the pH rises (pH 6-7.4) causing polymer swelling and swift removal. The water-soluble PEG layer is then dissolved by the hydrated intestinal environment, thus revealing the capsule actuator cavity. (c) Spring actuator and drug delivery structure from [4].

In this work, we present a novel **f**reestanding **r**egion **r**esponsive **b**ilayer (FRRB) system (Fig. 1) capable of withstanding gastric acid toward the use of a mm-scale actuated drug delivery mechanism in the small intestine. This is accomplished utilizing a novel bilayer composed of a **rigid polyethylene glycol (PEG) support layer** and a flexible **pH-responsive Eudragit layer** that is removed in the small intestine. We also demonstrate the first evaluation of this type of protective system with *ex-vivo* gastrointestinal (GI) tissue, accounting for the blend of **chemical changes** and **mechanical abrasion** contributing to the degradation of the bilayer where beaker experiments fail to adequately approximate these GI conditions.

EX-VIVO INTESTINAL SIMULATOR

pH-responsive coatings swell and soften when the ambient pH exceeds the designed threshold value, however, complete dissolution does not proceed rapidly [1]. Hence, mechanical abrasion plays a critical role in removal of this protective outer coating once swelled. To approximate the abrasive characteristics of the GI tract most closely, a translational motion system was developed – allowing for the evaluation of bilayer removal against *ex-vivo* porcine small intestine tissue. The GI simulator (Fig. 2) is composed of four main components: (*i*) a rail and screw lead system that translates a (*ii*) capsule holder capable of mass loading to control force application on a test capsule, and (*iii*) a polydimethylsiloxane (PDMS) semi-cylindrical tissue holder channel (D=25 mm). This system enables control over the force and translation speed on real intestinal tissue to closely emulate the *in-vivo* interfacial conditions between a capsule and GI tissue.

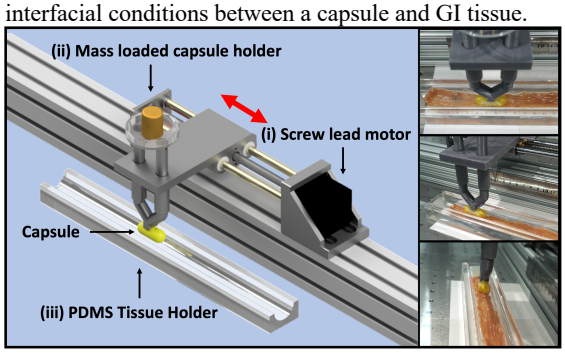

Figure 2: CAD rendering and images of the ex-vivo intestinal simulator system. Translation is facilitated by the screw lead motor which moves the rail-mounted platform attached to the capsule holder. A dish holding a 50g mass is attached to the top of two-pronged mass loaded capsule holder while a coated test capsule is fastened to the bottom. This applies a total of ~70g of mass from the top of the capsule to the tissue placed in the PDMS tissue holder to approximate circumferential peristaltic forces in the GI tract [5].

MATERIALS AND METHODS

Test capsules (∅=13 mm, L=32 mm) were 3D Printed with fused filament fabrication (FFF) of Polyethylene Terephthalate Glycol (PETG) using a Prusa i3 MK3S+ (Prusa). Test capsules contain openings of 4 x 4 x 5 mm (L,W,H). Approximately 0.17 g of PEG was melted on a 1 mil polyimide film, then transferred to the capsule surface to cover the capsule opening. The PEG was

978-1-940470-04-7/HH2022/$25©2022TRF
DOI 10.31438/trf.hh2022.72

allowed to solidify then the polyimide film was removed.

Eudragit® FL 30 D-55 (Evonik), a 30 %w/v dispersion of pH-sensitive polymer and plasticizer in water, was diluted to 1 and 10 %w/v formulations for dip coating. Samples were dip coated at a constant entrance and exit speed of 5.5 mm/sec with a submergence time of 1 sec via a custom fabricated dipping apparatus, then allowed to dry at room temperature for 30 min. Film thicknesses were measured in the constant thickness zone using a digital micrometer (Mitutoyo).

FRRB removal was first evaluated in simulated gastric fluid, submerging in a stirred 0.1 M acetate bath (pH=3) for a standard gastric emptying time of 3 h [1, 5]. FRRB permeation by simulated gastric fluid was observed using electrical probes inserted into the capsule cavity that become shorted after fluid enters the capsule.

FRRB mechanical removal was then assessed using the *ex-vivo* intestinal motion simulator. Porcine small intestine tissue (Animal Biotech Industries) was segmented into 20 cm portions and cut in half lengthwise. Tissue samples were laid into the PDMS tissue holder. Upon lowering the test capsule onto the tissue sample, the simulator moved it laterally at 1.4 cm/min, the mean longitudinal translation velocity in the small intestine [5]. FRRB removal was determined upon inspection.

RESULTS AND DISCUSSION

Dip-coated film thickness was found to be 0.3±0.2 µm, 2.0±0.3 µm, and 5.5±0.3 µm for 1, 10, and 30 %w/v Eudragit® FL 30 D-55 solutions, respectively, showing linear correlation (R^2=0.973) with a proportionality constant of 0.18 µm/(%w/v) (Fig. 3). Acid bath dissolution experiments showed that capsules coated with the PEG-Eudragit® FL 30 D-55 bilayer were not permeable after 3 hours, while capsules coated in PEG alone were permeated within 3 min.

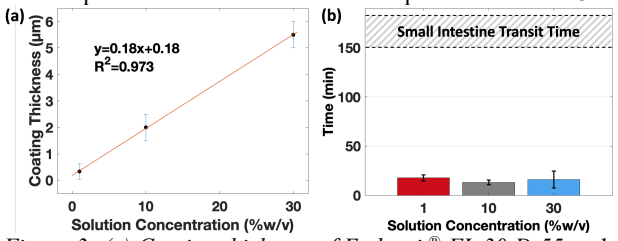

Figure 3: (a) Coating thickness of Eudragit® FL 30 D-55 at 1, 10, and 30% w/v. (b) FRRB removal time in the ex-vivo intestinal simulator fabricated with PEG and 1, 10, and 30% w/v Eudragit® formulations. Gray bar represents expected transit time.

Mechanical removal of FRRB coatings with 1%, 10%, and 30% Eudragit layers showed mean removal times of 17.7±1.8 min, 13.1±1.3 min, and 16.0±4.9 min, respectively (Fig. 3(b)), with an average of 15.6 min. This is approximately 1/10th of the range of small intestine transit times previously demonstrated for a capsule [4], labeled as a gray band. Thus, this system can protect capsule systems (actuators, sensors, openings) in transit through the low-pH stomach region and then rapidly reveal active subcomponents shortly after entering the small intestine target region.

Fig 3(b) showed that Eudragit coating thickness has negligible effect on the removal time of the bilayer, suggesting that the thicker PEG support layer is mostly responsible for removal time, and the Eudragit is only a protective coating to inhibit dissolution of the PEG layer. The Eudragit material showed rapid swelling and softening once placed on the neutral intestinal tissue, followed by rapid removal after the start of translational motion. The underlying PEG layer remained robust for ~15 min after Eudragit removal, followed by PEG disintegration, as can be seen in the image of a capsule sample after translation across *ex-vivo* tissue in Fig. 4.

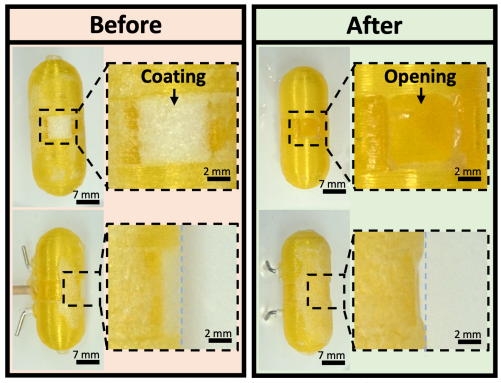

Figure 4: Capsule samples before and after ex-vivo intestinal simulator testing. Before testing, capsules have uniform surface coatings over actuation cavity. After testing, images show complete removal of the FRRB. Blue dashed line indicates capsule perimeter.

CONCLUSION

This work demonstrates an easily translatable strategy for supporting open cavities for actuators and sensors in ingestible devices, along with a novel *ex-vivo* intestinal simulation approach. Eudragit® FL 30 D-55 enteric coating at thicknesses of 0.3–6 µm resisted permeation in simulated gastric fluid, followed by rapid (~30 s) removal in a simulated small intestine environment. The PEG support layer remained intact throughout Eudragit removal, and dissolved within ~15 min, revealing the open cavity. The prompt removal of this support provides timely access of sensors and actuators to the small intestine for monitoring and intervention.

ACKNOWLEDGEMENTS

This work was supported by the National Science Foundation ECCS Program under Award #1939236. The authors acknowledge support from the Clark Doctoral Fellows Program, TerrapinWorks, the University of Maryland NanoCenter and its FabLab.

REFERENCES

[1] S. Hua, "Advances in Oral Drug Delivery for Regional Targeting in the Gastrointestinal Tract - Influence of Physiological, Pathophysiological and Pharmaceutical Factors", *Front. Pharmacol.*, 11 (2020).

[2] A. Abramson, E. Caffarel-Salvador, V. Soares, D. Minahan, R.Y. Tian, X. Lu, D. Dellal, Y. Gao, S. Kim, J. Wainer, J. Collins, S. Tamang, A. Hayward, T. Yoshitake, H.C. Lee, J. Fujimoto, J. Fels, M. R. Frederiksen, U. Rahbek, N. Roxhed, R. Langer, and G. Traverso, "A luminal unfolding microneedle injector for oral delivery of macromolecules", *Nat. Med.*, 25 (2019).

[3] G.E. Banis, L.A. Beardslee, J.M. Stine, R.M. Sathyam, and R. Ghodssi, "Gastrointestinal Targeted Sampling and Sensing via Embedded Packaging of Integrated Capsule System", *J. Microelectromech. Syst.*, 28, 2 (2019).

[4] J.A. Levy, M.A. Straker, L.A. Beardslee, R. Ghodssi, "Biomimetic Anchoring System for Sustained and Localized Gastrointestinal Drug Delivery", Hilton Head Workshop 2022: A Solid-State Sensors, Actuators, and Microsystems Workshop, Hilton Head, SC, June 5-9, (2022)

[5] L. Barducci, J.C. Norton, S. Sarker, S. Mohammed, R. Jones, P. Valdastri, B.S. Terry, "Fundamentals of the gut for capsule engineers", Prog. Biomed. Eng., 2 (2020).

CONTACT

*R. Ghodssi, (301) 405-8158; ghodssi@umd.edu

A SWEAT-BASED SELF-CHARGING POWER SYSTEM: INTEGRATION OF MICROBIAL ENERGY HARVESTING AND STORING DEVICES

Yang Gao[1], and Seokheun Choi[1,2]*

[1]Bioelectronics & Microsystems Laboratory, Department of Electrical & Computer Engineering, State University of New York at Binghamton (SUNY Binghamton), Binghamton, New York, USA

[2]Center for Research in Advanced Sensing Technologies & Environmental Sustainability, SUNY Binghamton, Binghamton, New York, USA

ABSTRACT

We demonstrate the first example of a wearable self-charging power system that offers (i) the high-energy harvesting function of a microbial fuel cell (MFC) and (ii) the high-power operation of a supercapacitor through charging and discharging. The MFC uses human skin bacteria as a biocatalyst to transform the chemical energy of human sweat into electrical power through bacterial metabolism, while the integrated supercapacitor stores the generated electricity for constant and high-pulse power generation even with the irregular perspiration of individuals. The all-printed paper-based power system integrates the horizontally structured MFC and the planar supercapacitor, representing the most favorable platform for wearable applications because of its lightweight and easy integrability into other wearable devices. The self-charging wearable system attains higher electrical power and longer-term operational capability, demonstrating considerable potential as a power source for wearable electronics.

KEYWORDS

Self-charging power systems, sweat-activation, microbial energy harvesting, wearables, supercapacitors

INTRODUCTION

Sweat-based energy harvesting techniques have attracted tremendous attention as a reliable and practical power solution for next-generation wearable electronics [1]. Sweat contains a large variety of chemical and biochemical substances that store sufficient energy to be harvested [2]. To date, the studies have been centered mainly around enzymatic fuel cells where redox enzymes convert the chemical energy of sweat into electrical energy [3-8]. However, due to their inherent short-term stability, the enzymatic catalysts have rendered the fuel cells unreliable and unstable for actual long-lasting wearable applications [3-8]. In 2020, our group, *for the first time,* used microorganisms as living enzymatic catalysts for sweat-based energy generation and successfully created a wearable microbial fuel cell (MFC) for longer and more stable power generation than the enzymatic fuel cells [9]. Because microorganisms contain many reproducible enzymatic catalysts and they can self-sustainably maintain their viability, microbial power generation can be more stable, reliable and robust for long-term wearable applications. We confirmed that many skin bacteria have electrogenic capability feeding off human sweat. Very recently, we enabled long-lasting microbial power generation using a spore-forming bacterium, *Bacillus subtilis*, which are usually found on plantar skin [10]. The spore-forming bacterium produced a sustainable power responding to the sweat availability through repeated sporulation and germination. However, this technology has suffered from its low performance.

In this work, a spore-forming MFC is integrated with a supercapacitor in paper, so that the harvested biological energy from the sweat can be charged and discharged for higher power generation (Figure 1). For simple fabrication and integration on a single paper, the MFC and the supercapacitor units are innovatively designed as a planar configuration. The MFC is horizontally structured where the anodic and the cathodic components are formed having a hydrophobic wax between them (Figure 1). The

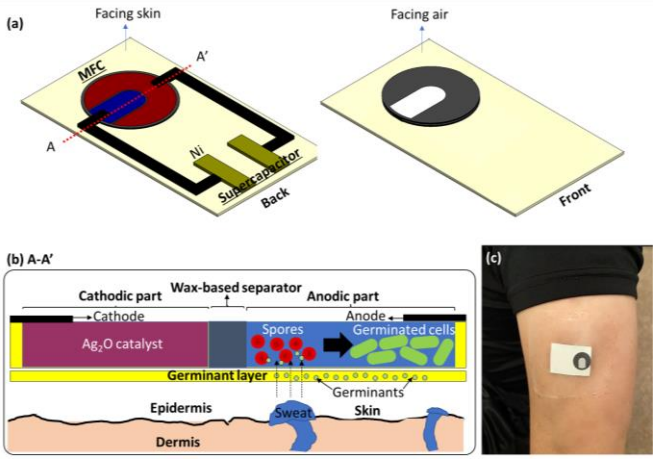

Figure 1: (a) Schematic illustrations of the self-charging power system integrating the MFC and the supercapacitor (back and front view), (b) the MFC inoculated with B. subtilis spores and its operating principle with sweat, and (c) the system applied to human.

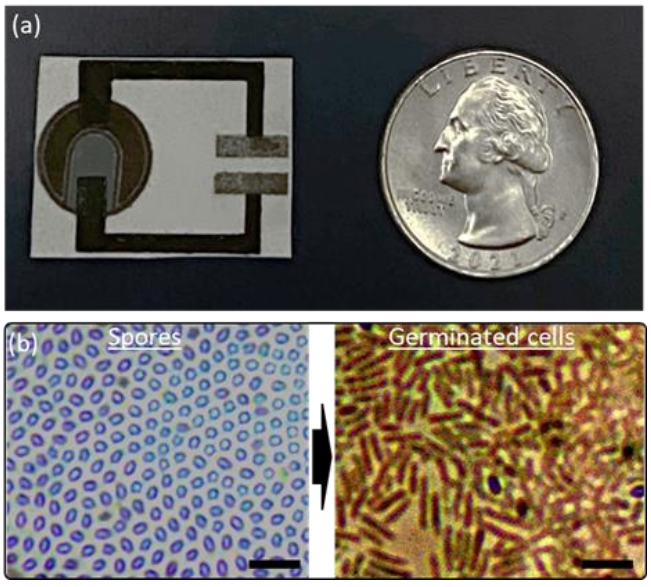

Figure 2: (a) Image of the assembled device and (b) microscopic images showing spore germination.

978-1-940470-04-7/HH2022/$25©2022TRF
DOI 10.31438/trf.hh2022.73

cathodic part is prepared with Ag_2O for the cathodic reaction. A germinant paper layer is placed on top of the spore-loaded anodic compartment, which allows for the MFC to be initiated by the sweat, as it washes the germinant into the anodic layer to begin germination and return to metabolic vegetative cells while generating power (Figure 2).

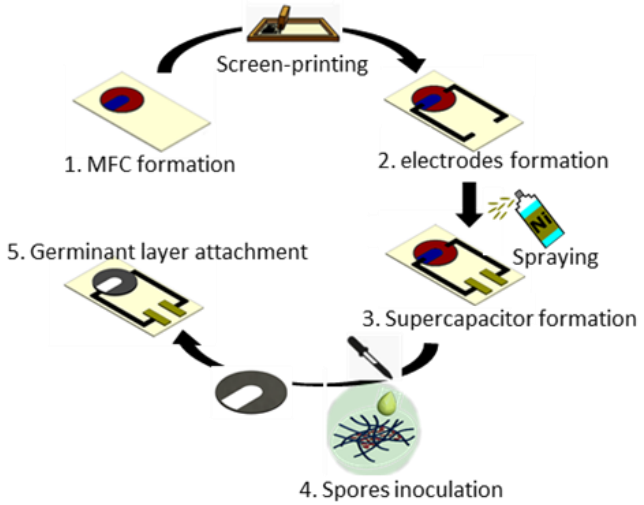

Figure 3: Device fabrication steps

EXPERIMENTAL PROCEDURE

Device fabrication

Previously, our group developed many paper-based MFCs, but all were limited to a vertical configuration where an anode, an ion exchange membrane, and a cathode were vertically aligned [11-13]. The vertical configuration needs multilayers and their precise alignment, requiring more complicated and high-cost manufacturing steps. Here, we, *for the first time*, created a horizontal MFC structure where all the device components were simply prepared in a single sheet of paper (Figure 1). Even the planar-type supercapacitor was readily constructed on the same paper with the MFC. Whatman Grade 1 filter paper was selected as the paper substrate for the self-charging system. The paper has the pore size of 11 µm which allowed inoculation of the bacterial spores (~ 1 µm in diameter) and conversion of the spores into the vegetative cells (~ 2~6 µm long and 1 µm in diameter) (Figure 2) [14, 15]. Detailed device fabrication steps are shown in Figure 3. All device boundaries and the ion exchange membrane for the MFC were prepared by printing the wax on both sides of the paper (Xerox Phaser, ColorQube 8570) and allowing the wax impregnation into the entire paper at 150 ºC for 45 seconds. The anodic part was first engineered with a conformal coating of conductive polymer, poly(3,4-ethylenedioxythiophene) polystyrene sulfonate (PEDOT:PSS). The cathodic part was prepared with Ag_2O for the cathodic reaction [11]. The solid-state supercapacitor was constructed with two Ni-spayed planar electrodes and poly(vinyl alchohol)/KCl electrolyte between them. The MFC and the supercapacitor were electrically connected by screen-printing a graphite ink. Then, the electricity-producing bacteria, *Bacillus subtilis*, were inoculated as spores. The dormancy of *B. subtilis* spores can preserve the bacteria for a long-term storage without denaturation or degradation. The germinant paper layer having L-Valine (10 mM) and AGFK (10 mM L-Asparagine, 33.6 mM D-Glucose, 33.6 mM D-Fructose, 60 mM KCl) was prepared in Whatman Grade 410 filter paper and attached to the MFC [14, 15]. *B. subtilis* spores are well-studied about their germination process where GerA, GerB, and GerK germinant receptors interact with L-Valine and AGFK and trigger the spore gemination. Because the 410 filter paper has much smaller pores than the MFC paper, we can minimize a potential risk of bacterial leakage from the MFC [15].

Cultivation and sporulation of *Bacillus subtilis*

We purchased *Bacillus subtilis* strain 168 from the American Type Culture Collection (ATCC) and cultivated them in Luria Broth (LB) medium at 37°C for 24 hours. Then, the cultured bacterial cells were induced to sporulate by nutrient exhaustion on agar plates [14, 15]. The formed spores were obtained from the plate and centrifuged for 4 minutes at 4000 rpm to pellet. The collected spores were washed, resuspended in distilled water, and stored at 4°C until use.

Electrical measurement setup

The voltage drops across 15 external resistors (No resistor, 470 kΩ, 240 kΩ, 160 kΩ, 100 kΩ, 75 kΩ, 47 kΩ, 33 kΩ, 22 kΩ, 15 kΩ, 10 kΩ, 2 kΩ, 1.5 kΩ, 470 Ω, and 360 Ω). were measured by using a data acquisition system (DATAQ Instruments), generating polarization curves and power outputs. The charging and discharging were carried out by using our customized electric relay circuit with Arduino software. The relay controlled the on and off states of the external circuit through the given resistor.

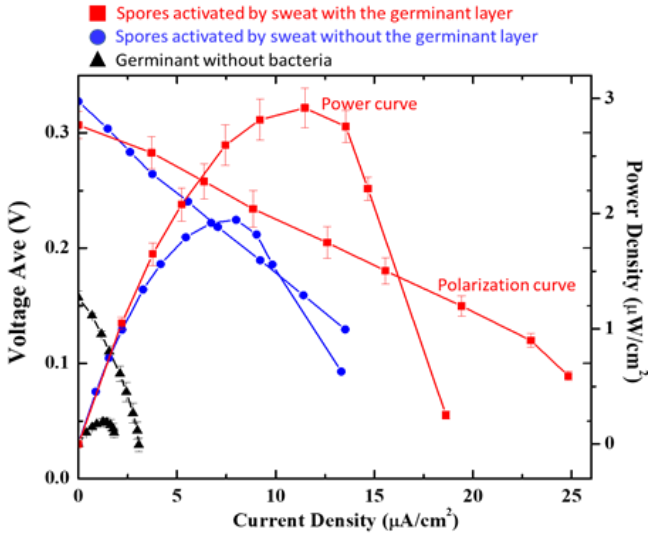

Figure 4: Polarization curves and power outputs of the MFCs (w/ and w/o a germinant layer) actuated by sweat. The control does not include bacterial cells.

RESULTS AND DISCUSSION

MFC performance

As shown in Figure 4, we characterized the MFC power generation by providing real human sweat samples taken from our group members with their consent. Our horizontally structured MFC generated significantly high power and current compared to the control without bacterial cells, indicating that the electricity production originates from the spore germination and their electron transfer activity. The MFC produced a maximum power density of 3 µW/cm^2 which is about 20 times larger than the control. It should be noted that the MFC even without the germinant layer produced a certain amount of power (1.9 µW/cm^2), which is in good agreement

with our previous study showing that human sweat contains potential chemicals to trigger the spore germination [10].

Supercapacitor performance

As shown in Figure 5, we characterized the supercapacitive function by intermittently connecting external resistors (1 kΩ, 10 kΩ, and 100 kΩ). After the device was fully charged, it was discharged through the given resistors, showing stable output performance under charging-discharging cycles. The external resistors controlled the discharging rate of the stored energy during the discharging operation. The 1 kΩ resistor allowed a more rapid discharge of the accumulated charges while the higher resistors provided a slower rate at discharge with a smaller current generation (Figure 5).

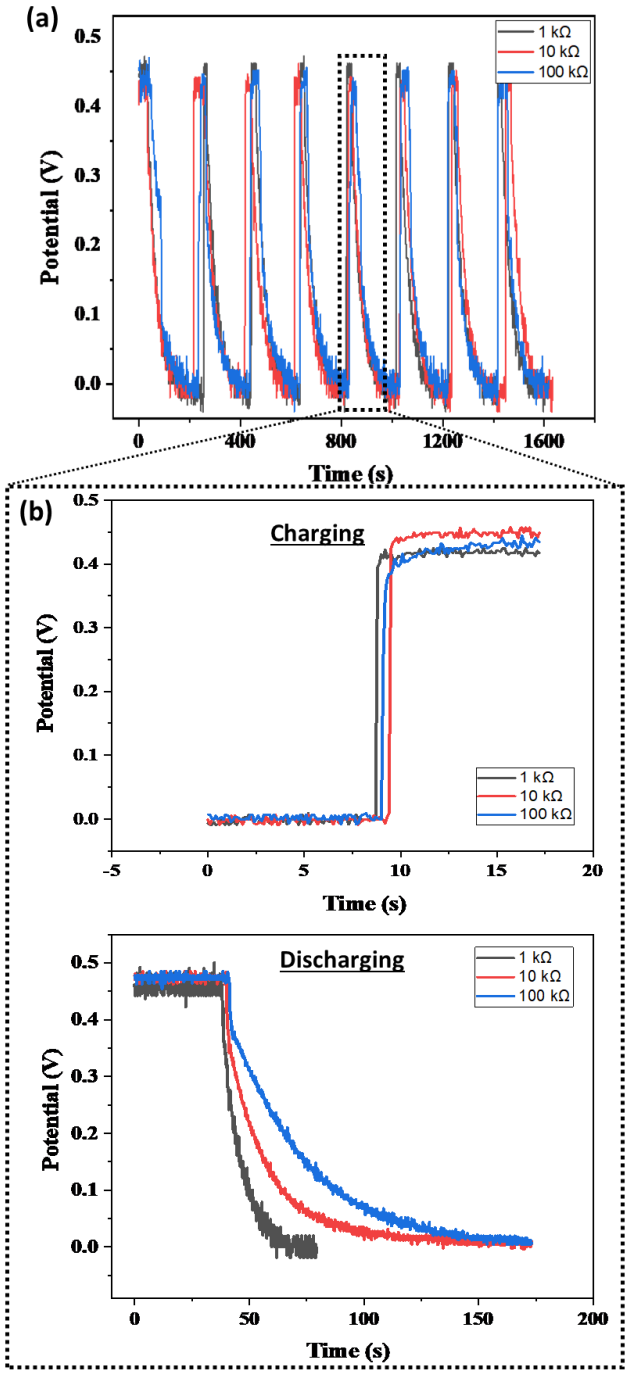

Figure 5: (a) Charging-discharging cycles of the supercapacitor with different external resistors. (b) A charge/discharge cycle

Performance of the self-charging power system

The low and short power generation of existing miniature MFCs have limited their capability to power useful applications in practice [16-19]. Increasing the size of the single device or stacking multiple devices in series/parallel can produce more power but it is not a suitable strategy for wearable applications where the device must be small enough to fit anywhere within the human body. Alternatively, energy storage devices like supercapacitors have been externally connected to the MFCs to boost their low power in a way that the supercapacitors are recharged by the MFCs and produce high electrical output during the discharge [21, 21]. However, the connection of the paper-based MFC to these external capacitors is more complicated, increasing the cost of the system with the performance degradation. As shown in Figure 1, the paper-based self-charging power system consisting of the horizontally structured MFC, and the supercapacitor was constructed on a single sheet of paper. Because this paper device is flexible, small, and thin, it can be applied directly to nonuniform small area of the human skin (Figure 1). This self-charging power system simultaneously generated electric energy from the bacterial metabolism with human sweat in the MFC and stored the energy in the supercapacitor. As shown in Figure 6, the self-charging hybrid power system generates much higher and longer voltage generation than the MFC only. This is because the energy electrostatically stored in the integrated supercapacitor can be delivered with higher and longer discharge output [22]. Moreover, microorganisms in MFCs can provide self-assembling, self-repairing, and self-maintaining operational capabilities with long-term stability [23-27]. The self-charging wearable system generated higher electrical power (~twice larger than the MFC only) and longer-term operational capability (stable current pulses for 25 minutes) (Figure 6).

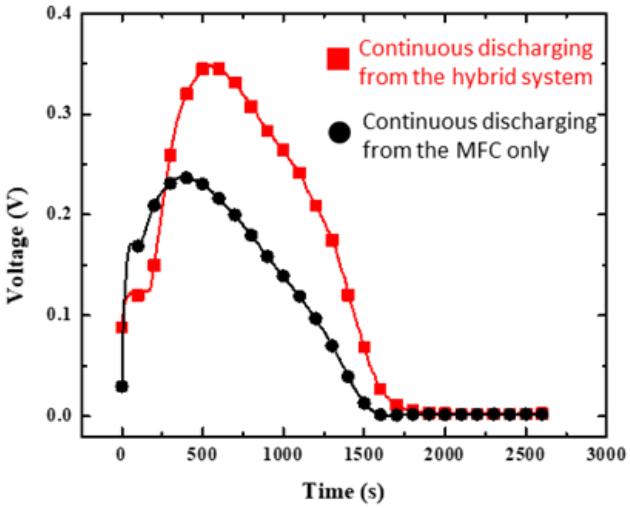

Figure 6: Continuous discharging profiles from the hybrid system and MFC only.

CONCLUSION

In this work, we, *for the first time*, report an integration of sweat-based MFC and a supercapacitor with an all-planar configuration on a single sheet of paper. The energy biochemically

harvested from the sweat can be charged and discharged for higher and longer power generation than the MFC only. The spore-forming bacterium, *Bacillus subtilis*, were used as the living biocatalysts. The MFC produced electricity when human sweat triggered the spore germination and reverted the spores to vegetative cells. Because the spores can withstand very unfavorable external conditions, the MFC shelf-life can be significantly extended without requiring special procedures. The germinant paper layer having small pore size innovatively enclosed the spore-loaded anodic compartment to promote the spore germination with sweat. In addition, the layer could minimize a potential risk of bacterial leakage from the MFC. The MFC produced 0.32 V of open circuit voltage, 3 $\mu W/cm^2$ of power density, and 18 $\mu A/cm^2$ of current density. The supercapacitor constructed with two planar electrodes and solid-state electrolyte on the same paper substrate exhibited reversible charge-discharge reactions, demonstrating stable output performance.

ACKNOWLEDGEMENTS

This work was supported mainly by the National Science Foundation (CBET #2100757, ECCS #2020486, and ECCS #1920979), and partially by the Office of Naval Research (#N00014-21-1-2412).

REFERENCES

[1] L. Manjakkal, L. Yin, A. Nathan, J. Wang, R. Dahiya, "Energy Autonomous Sweat-Based Wearable Systems," *Advanced Materials*, 33, 2100899 (2021).

[2] M. Barlya, H.Y.Y. Nyeln, A. Javey, "Wearable sweat sensors," *Nature Electronics*, 1, 160-171 (2018).

[3] H. Wu, Y. Zhang, A. Kjoniksen, X. Zhou, X. Zhou, "Wearable biofuel cells: advances from fabrication to application," *Advanced Functional Materials*, 31, 2103976 (2021).

[4] I. Jeerapan, J.R. Sempionatto, J. Wang, "On-body bioelectronics: wearable biofuel cells for bioenergy harvesting and self-powered biosensing," *Advanced Functional Materials*, 30, 1906243 (2020).

[5] X. Xiao, H. Xia, R. Wu, L. Bai, L. Yan, E. Magner, S. Cosnier, E. Lojou, Z. Zhu, A. Liu "Tackling the challenges of enzymatic (bio)fuel cells," *Chemical Reviews*, 119, 9509-9558 (2019).

[6] M. Rasmussen, S. Abdellaoui, S.D. Minteer, "Enzymatic biofuel cells: 30 years of critical advancements," *Biosensors and Bioelectronics*, 76, 91-102 (2016).

[7] M.H. Osman, A.A. Shah, F.C. Walsh, "Recent progress and continuing challenges in bio-fuel cells. Part I: Enzymatic cells," *Biosensors and Bioelectronics*, 26, 3087-3102 (2011).

[8] S. Choi, "Electrogenic Bacteria Promise New Opportunities for Powering, Sensing, and Synthesizing," *Small*, 2107902 (2022).

[9] M. Mohammadifar, M. Tahernia, J.H. Yang, A. Koh, S. Choi, "Biopower-on-Skin: Electricity generation from sweat-eating bacteria for self-powered e-skins," *Nano Energy*, 75, 104994 (2020).

[10] J. Ryu, M. Landers, S. Choi, "A Sweat-Activated, Wearable Microbial Fuel Cell for Long-term, On-demand Power Generation," *Biosensors and Bioelectronics*, 205, 114128 (2022).

[11] Y. Gao, S. Choi, "Merging Electric Bacteria with Paper," *Advanced Materials Technologies*, 3, 1800118 (2018).

[12] Y. Gao, M. Mohammadifar, S. Choi, "From microbial fuel cells to Biobatteries: Moving toward on-demand micro-power generation for Small-scale Single-Use Applications," *Advanced Materials Technologies*, 4, 1970039 (2019).

[13] L. Liu, S. Choi, "A Paper-based Biological Solar Cell," *SLAS Technology*, 25, 75-81 (2020).

[14] M. Landers, and S. Choi, "Small-scale, Storable Paper Biobatteries Activated Via Human Bodily Fluids," *Nano Energy*, 97, 107227 (2022).

[15] J. Ryu, S. Choi, "Bioelectricity Production from Sweat-Activated Germination of Bacterial Endospores," *Biosensors and Bioelectronics*, 186, 113293 (2021).

[16] S. Choi, "Microscale microbial fuel cells: advances and challenges," *Biosensors and Bioelectronics*, 69, 8-25 (2015).

[17] Y. Su, L. Lu, M. Zhou, "Wearable microbial fuel cells for sustainable self-powered electronic skins," *ACS Appl. Mater. Interface*, 14, 8664-8668 (2022).

[18] F. Qian, D.E. Morse, "Miniaturizing microbial fuel cells," *Trends in Biotechnology*, 29, 62-69 (2011).

[19] H. Wang, A. Bernarda, C. Huang, D. Lee, J. Chang, "Micro-sized microbial fuel cell: A mini-review," *Bioresource Technology*, 102, 235-243 (2011).

[20] M.C. Hatzell, Y. Kim, B.E. Logan, "Powering microbial electrolysis cells by capacitor circuits charged using microbial fuel cell," *Journal of Power Sources*, 229, 198-202 (2013).

[21] G. Papaharalabos, J. Greenman, A. Stinchcombe, I. Horsfield, C. Melhuish, I. Ieropoulos, "Dynamic electrical reconfiguration for improved capacitor charging in microbial fuel cell stacks," *Journal of Power Sources*, 272, 34-38 (2014).

[22] L. Liu, S. Choi, "A Self-Charging Cyanobacterial Supercapacitor" *Biosensors and Bioelectronics*, 140, 11354 (2019).

[23] M.H. Osman, A.A. Shah, F.C. Walsh, "Recent progress and continuing challenges in bio-fuel cells. Part II: Microbial cells," *Biosensors and Bioelectronics*, 26, 953-963 (2010).

[24] U. Schroder, F. Harnisch, "Life Electric—Nature as a Blueprint for the Development of Microbial Electrochemical Technologies," *Joule*, 1, 244 (2017).

[25] D.R. Lovley, "Electromicrobiology," *Annual Review of Microbiology*, 66, 391 (2012).

[26] B.E. Rittmann, "Opportunities for Renewable Bioenergy Using Microorganisms," *Biotechnology and Bioengineering*, 100, 203 (2008).

[27] N. Ulrich, K. Nagler, M. Laue, C. S. Cockell, P. Setlow and R. Moeller, "Experimental studies addressing the longevity of Bacillus subtilis spores - The first data from a 500-year experiment," *PLOS ONE*, 13, e0208425 (2018).

CONTACT

*Prof. S. Choi, tel: +1-607-777-5913; sechoi@binghamton.edu

CHARACTERIZATION OF APTAMER FUNCTIONALIZED GOLD ELECTRODES FOR HISTONE DETECTION

Hayley Richardson[1,2], Jeffrey Barahona[2], Gavin Carter[2], Francis J. Miller Jr.[3,4 5], Edgar Lobaton[2], and Spyridon Pavlidis[2]*

[1]Department of Materials & Science Engineering, NC State University, USA
[2]Department of Electrical & Computer Engineering, NC State University, USA
[3]Department of Medicine, Duke University, USA,
[4]School of Medicine, Wake Forest University, USA, [5]Salisbury Veterans Affairs Medical Center, USA

ABSTRACT

This paper presents findings on the development of an electrochemical histone sensor using gold electrodes functionalized with a histone-specific RNA aptamer sequence. This has applications for early detection of circulating histones which are associated with increased mortality of critically ill patients. Surface plasmon resonance was used to characterize the electrode functionalization process and examine the specific responses to calf thymus and human histones. Through SPR, we show statistically significant differentiation of the responses between different functionalization processes with $p < 0.05$ on the active and control flow cells. Electrochemical detection of calf thymus histone is subsequently demonstrated, whereby the importance of the spacer molecule was also studied. Initial sensing results showed a calf thymus histone concentration-dependent sensitivity of 7.8 mV/decade, which is an improvement to similar sensors in this field.

KEYWORDS

Histones, aptamers, electrochemical sensors, surface plasmon resonance, potentiometry.

INTRODUCTION

Extracellular histone proteins are toxic to cells and contribute to the development of acute respiratory dysfunction syndrome (ARDS) and multiple organ dysfunction syndrome (MODS). Serum levels of histones in patients are associated with mortality and can be as high as 3 ng/mL [1]. The early recognition of ARDS/MODS is critical for triaging and treating patients. A rapid, accessible method to detect and monitor elevated histone concentrations could be part of an effective strategy, but no point-of-care sensor for this purpose currently exists.

Affinity electrochemical biosensors rely on the formation of self-assembled monolayers (SAM) to serve as the interface with biological medium under analysis (Fig. 1). SAM creation is a key processing step for affinity sensing since the assembled molecules are crucial biorecognition elements (BREs) used to detect specific analytes or stimuli in an electrolyte. Aptamers are advantageous BREs in sensing because they can have high specificity to densely charge analytes and can be easily chemically modified for different applications [2]. Aptamers have also been employed as therapeutics.

Urak et al. published research on the design of several RNA aptamer sequences that selectively bind to both human and bovine histones [1]. Their work used immobilized histones on gold surface then measured aptamer binding to histones; however, this system was not developed with the intention of making an operable sensor, rather only as a functionalized chip for the purpose of verifying the binding activity in surface plasmon resonance (SPR) characterization. Ultimately, their study demonstrated the efficacy in aptamers as treatment of clinical conditions associated with MODS. The sensor in this paper is the reverse system of the one prepared in Urak's study. Here, the aptamers are the immobilized ligand and histones are the analyte in solution.

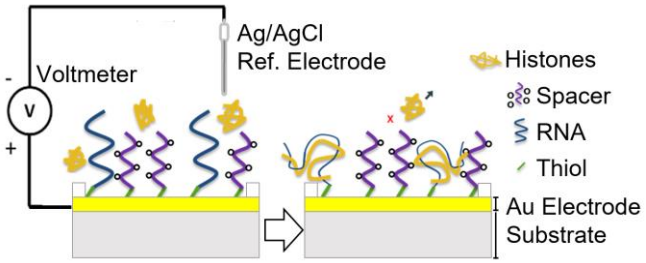

Figure 1: Cross-section of a functionalized gold electrode surface with a thiolated, histone-specific RNA aptamer and a spacer molecule (e.g., MCH or PEG-thiol). An off-electrode Ag/AgCl reference electrode was used.

The objectives of this study are to characterize the behavior of gold electrodes functionalized with histone-specific RNA aptamers, and subsequently assess their suitability for potentiometric detection. Initially, SPR was used to evaluate the ability of immobilized molecules to bind analytes from external solution. Since SPR is a mass-sensitive and optical technique, it is not affected by the ionic composition of the running buffer. Thus, this approach uncouples the measured binding interaction from any ionic non-specific binding that could arise when sensing in typical undiluted buffer solutions or serum [3]. Following observation of the binding kinetics via SPR, potentiometric sensing was evaluated. The important role of 6-mercaptohexanol (MCH) and poly(ethylene glycol) methyl ether thiol (PEG-thiol) molecules in determining non-specific adhesion was determined. These results represent the first report of an electrochemical histone sensor using RNA aptamer recognition elements, and therefore represent a significant step towards the realization of point of care injury monitoring

METHODS

Materials

Analytes calf thymus histone (CTH) and bovine serum albumin (BSA), spacer molecules 6-mercaptohexanol (MCH) and poly(ethylene glycol) methyl ether thiol (PEG-thiol), and regeneration chemicals NaOH and NaCl were all purchased from Sigma Aldrich [St. Louis, MO]. The other analytes of human histones H3.2 and H4 were purchased from New England Biolabs [Ipswich, MA].

The aptamer sequence 5'-Thiol-MC6-S-S-GGG AGG ACG AUG CGG ACU GGU GAA GGG AGG UAC UGC AGA CGA CUC GCC CGA-3' was synthesized by Integrated DNA Technologies (IDT) Inc. [Coralville, IA] and purchased together with TE resuspension buffer (10 mM tris(hydroxymethyl) aminomethane and 0.1 mM ethylenediaminetetraacetic acid). The aptamer was received dried and resuspended according to a previously reported method [4].

SPR consumables of HBS-EP+ running buffer (0.1 M HEPES, 1.5 M NaCl, 0.03 M EDTA and 0.5% v/v Surfactant P20) and sensor chips were purchased from Cytiva [Marlborough, MA].

978-1-940470-04-7/HH2022/$25©2022TRF
DOI 10.31438/trf.hh2022.74

Surface Plasmon Resonance

As noted above, a thiol modification was added to the 5' sequence end of the aptamer to tether it to gold surfaces. Alkanethiol compounds have been shown to organize on gold and form functional monolayers for a variety of applications [5]. The RNA aptamer was immobilization in-*situ* on a blank gold sensor chip in a Biacore T200 instrument. 1 µM aptamer solution was flowed on the active channel for 15 hours at 1 µL/min. 1 mM MCH was flowed on the active channel and control channel for five hours at 1 µL/min. Histone dilutions from 1.35 nM to 200 µM were solubilized in HBS-EP+. Dilutions of BSA were made with the same procedure. Binding was performed with a 180 second association injection and 600 second dissociation phase at 30 µL/min. Regeneration was done with a solution containing 50 mM NaOH and 1 M NaCl for 60 seconds at 30 µL/min with a 30 second baseline stabilization before injection the following concentration.

Potentiometric Sensor Electrode Functionalization

The SAM was formed overnight under ambient conditions following the previously reported method [4]. Separately, MCH or PEG-thiol spacer molecules were co-immobilized in the monolayer to aid in the dispersion and support of the aptamer molecules. Spacer molecules help reduce electrostatic charge repulsion and steric hindrance by physically distancing neighboring biorecognition elements [6]. Additionally, they limit potential non-specific adhesion (NSA) of analytes to bare gold surfaces and other biofouling from compounds in the solution.

Potentiometry

Potentiometric tests were done on thin-film gold electrodes from Micrux Technologies [Gijón, Spain] and tested in their bench-top multifluidic platform. The Ag/AgCl reference electrode was purchased from Microelectrodes, INC [Bedford, NH].

Potentiometric sensing tests were performed with a 1-channel Keysight B2901A Series Precision Source/Measure Unit with a custom designed LabVIEW GUI. The potential was measured between the working electrode and reference electrode. Fluid flow was controlled via a programmable syringe pump. HBS-EP+ buffer was flown through the system at 0.5 mL/min, then flow was terminated so that the buffer could sit stagnant on the electrodes for 10 minutes, after which the measured voltage was recorded for approximately 10 minutes. This process was repeated continuously from lowest to highest concentration.

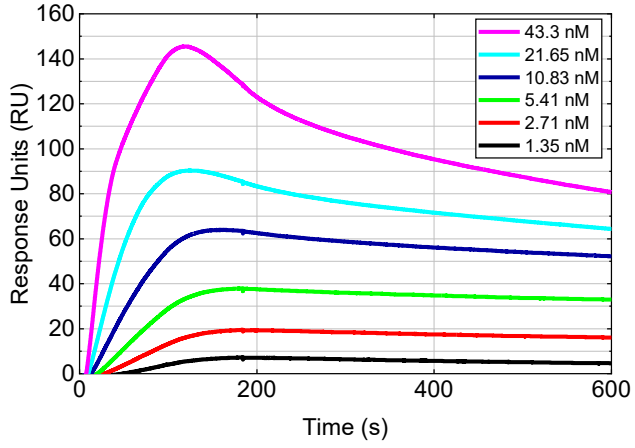

Figure 2: SPR sensogram for CTH from 1.35 to 43.3 nM. This is the aptamer only response, obtained by subtracting the signal produced by the control (MCH-only) surface from the signal produced by the active (aptamer + MCH) surface.

RESULTS & DISCUSSION

Surface Plasmon Resonance

To confirm the specificity of the aptamer surface and provide binding kinetics values, SPR experiments were performed using CTH and human histones, H3.2 and H4, as the target analytes, and BSA as an orthogonal control protein in 10 mM HBS-EP+ running buffer. The specific response of the aptamer-histone interaction was calculated by subtracting the response of the control surface (MCH only) from the active surface (RNA and MCH). Figure 2 displays the clear, concentration-dependent response that was observed.

Furthermore, a preliminary analysis of the morphological and response magnitude characteristics of the SPR data was completed to determine the separability of histone vs. non-histone inputs, which demonstrated distinct responses between the control and active sensor chips, thus illustrating the effectiveness of different ligand immobilization schemes. It was determined that there was baseline wander on the SPR results. As shown in Figure 3, the wander was uniform across the active and control cells, indicating incomplete regeneration of the flow cells. Future efforts will be made to optimize the regeneration conditions [7]. For this study, we removed the baseline wander from the data and zeroed the beginning of each cycle to view only the differences in response magnitude.

We performed two sets of tests to determine the separability of the histones. For both tests, we aggregated measurements from all the concentrations 3.13 nM to 400 nM sampled on the active and control channels. For the first set of tests, we used the maximum amplitude of the waveform at the end of the association phase of the SPR experiment. For the second set of tests, we used the value of the gradients of the SPR outputs at the beginning of the association phase. We hypothesized that the control surface would have different absorption characteristics, and the analytes would adhere at different rates even if they had similar response magnitudes.

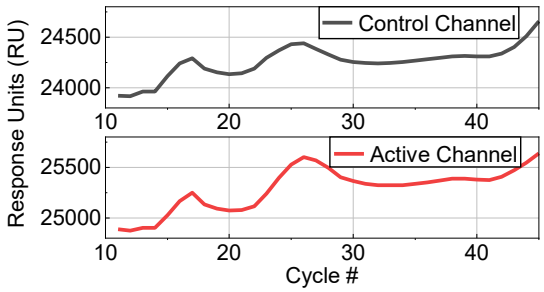

Figure 3: Graphs displaying baseline wander from cycle to cycle. The baseline was determined by the mean of the samples before the association phase begins on any given cycle.

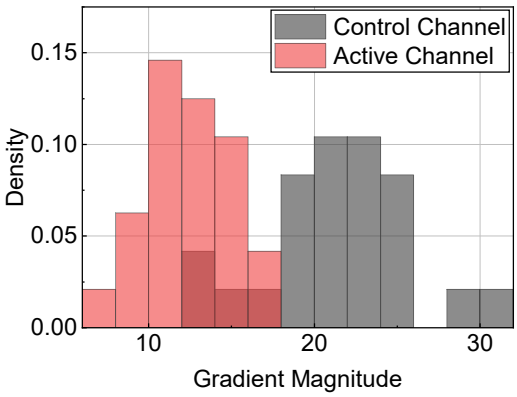

Figure 4: Histograms of the gradient magnitudes at the beginning of the association phase. These demonstrated the distributions of the maximum gradient magnitude of the different channels.

We found that, while the response's amplitude alone does not delineate the difference between control and test surface response to the analytes, the maximum magnitude of the gradients of the SPR outputs allow us to differentiate the active channels from the control channels with $p < 0.05$ (Fig. 4). However, there is insufficient data at the moment to use the same test to differentiate between analytes on the same cell to the same degree of certainty with the same test.

Using a 1:1 binding model, a dissociation constant (K_D) of 0.4 nM was extracted (χ^2 = 9.73 RU^2). For comparison, SPR experiments originally reported with the characterization of the histone-specific RNA aptamer estimated K_D = 4 nM [1]. This discrepancy is attributed to the different surface functionalization methods used in each case and the known heterogeneity of CTH. Figure 5 compares the SPR responses to the various analytes used at a fixed concentration of 200 nM. While H4 induced the highest absolute response in the active channel, the highest differential response was achieved for CTH. The presence of non-specific adhesion (NSA) motivated an investigation of spacer molecules.

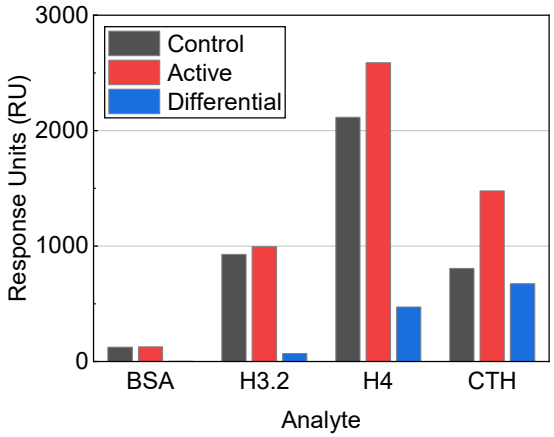

Figure 5: SPR response of the control and active surfaces to 200 nM of CTH, human histones (H3.2 and H4) and BSA. A differential response is also calculated. The active channel exhibits the largest response to H4, and selectivity is highest to CTH.

Potentiometric Sensing

The potentiometric sensor was designed with consideration from the SPR analysis, with output voltage shifts expected due to charge build-up of the bound analyte [8]. These measurements tested concentrations of CTH from 1.56 nM to 1000 nM. The voltage change was measured by subtracting the voltage of an initial buffer baseline from the voltage of the CTH solution after a five-minute stabilization period. Four different types of electrode surfaces were tested: bare gold, MCH, and PEG-thiol controls, and an active surface consisting of aptamer with PEG-thiol.

The appreciable NSA response in the SPR experiments prompted an initial study as to whether MCH could be replaced by PEG-thiol, a different spacer molecule, which may improve the aptamer's performance as a histone-specific BRE. MCH is a short alkanethiol with a six-length carbon chain with a polar hydroxyl head group [-OH]. It is commonly used in nucleotide monolayer formation to remove untethered physiosorbed aptamer from the surface and prevent uptake of unwanted analytes [9] [10]. Its small size ensures that it will backfill the existing space between aptamer to coat any exposed gold and that the aptamers will have sufficient space to fold when bound to histones.

The difference between PEG-thiol and MCH lie in their chain length and the location of their charge polarities in the molecule. The PEG-thiol used in this experiment had a number average molecular weight of 2 kDa. Instead of the hydroxyl termination like in MCH, PEG-thiol has repeating ether functional groups with electronegative oxygen atoms. This introduces additional charge to the monolayer, but not at the head group [$-CH_3$] which is most exposed to the histones in solution. Research done by Gutiérrez-Sanz et al. studied PEG blocking with different chain lengths and found that a mix monolayer of receptor antibodies and 10 kDa PEG had three times the signal response compared to a monolayer with antibodies and 0.5 kDa PEG [11].

Comprehensively, there is evidence that longer chain lengths have been found to reduce biofouling and non-specific adsorption, but at the risk of insulating the surface by preventing the charge transfer [12]. Inopportunely, longer chain molecules may prevent proper aptamer tertiary structure upon binding. If the aptamer:histone complex does not fold in close proximity to the electrode surface, the net electrostatic effect of the molecules' binding interaction may be outside of the Debye length (λ_D) [13]. With increasing distance away from the binding interaction, the electric fields generated from the charges are dampened through electrical screening by surrounding charges. The compromise of longer chain length for lower NSA is difficult to predict the results without experimentation since the electrical response will vary depending on the ionic density of the solution and the properties of the analyte [14].

For these reasons, measurements to compare the three different control surfaces were performed before testing the active surface (Fig. 6). While the MCH-coated surface mitigates NSA compared to a bare gold surface, it was found that NSA can be further reduced via the use of PEG-thiol. The differential voltage measurement for the bare gold surface when exposed to 1000 nM CTH was 171.3 mV. MCH and PEG-thiol were only 126.3 mV and 75.1 mV, respectively. If it is assumed that the surface sites between the aptamer are unoccupied if not co-immobilized with another molecule, then the difference between bare gold and PEG-thiol shows a 128% higher NSA voltage response when a spacer molecule is not used. Figure 6 shows the voltage change data for the three control surfaces fit with a logarithmic trendline ($R^2_{Bare\ Au}$ = 0.98, R^2_{MCH} = 0.98, and $R^2_{PEG\text{-}thiol}$ = 0.93). Given that it had the least change in voltage, and thus the least amount of NSA, PEG-thiol was selected as the spacer molecule for subsequent experiments.

An electrode was prepared with histone-specific aptamer and PEG-thiol to compare against the established PEG-thiol control electrode. Figure 7 shows how the change in voltage increased when aptamer was included on the electrode surface. The differential voltage change was calculated the same way as in the control surface comparison data. The co-SAM of aptamer and PEG-thiol data also follow a logarithmic response with $R^2_{Apt.+PEG}$ = 0.91.

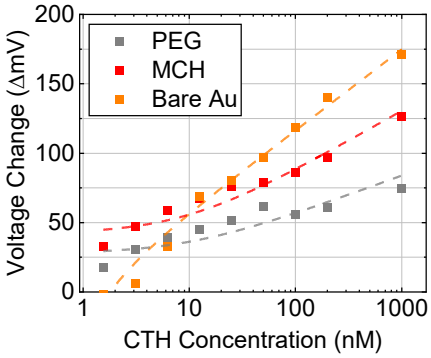

Figure 6: Potentiometric differential voltage response data for control surface of PEG, MCH, and bare gold. The dashed lines are trendlines fitted to the experimental data.

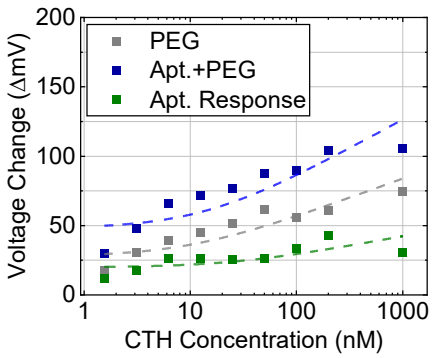

Figure 7: Potentiometric differential voltage response data for the active surface of RNA aptamer and PEG-thiol, the control response of PEG-thiol, and the subtracted voltage change (Apt Response). The dashed lines are trendlines fitted to the experimental data.

As an additional analysis, the voltage response of the PEG-thiol control electrode was subtracted from the aptamer and PEG-thiol active electrode to separate the NSA results from PEG-thiol. This data was plotted as the aptamer response (Fig. 7 "Apt. Response"). The largest calculated aptamer response was 43.2 mV for 200 nM CTH. This sensitivity found in this trendline is 7.8 mV/dec when tested in this type of electrolyte. The ability to test at this low nanomolar concentration was a magnitude improvement when comparing to the published histone sensing done by other groups [15].

CONCLUSIONS

Gold electrode surfaces functionalized with RNA aptamers specific towards CTH and Human Histone H4 have been characterized via SPR, subsequently leading to the first demonstration of potentiometric sensors capable of detecting physiologically relevant concentration of histones. PEG-thiol was the less electrostatically attractive blocking molecule investigated that allowed the aptamer to fold into the correct conformation for specific binding to CTH. This was determined based on the voltage response of different SAMs to different concentrations of CTH. Potentiometric biosensors are ideal low-power systems for the detection of protein molecules because of their sensitivity in physiologically relevant solutions. The isolated response of the CTH-specific aptamers in the monolayer had a sensitivity of 7.8 mV/dec in 10 mM HBS-EP+ when using PEG-thiol as a blocking agent. This sensor was able to detect a discernable signal for the lowest concentration of 1.56 nM CTH.

Further work will electrochemically sense human histones and continue developing classification methods to determine histone vs. non-histone input.

ACKNOWLEDGEMENTS

The authors are grateful for the SPR expertise of Dr. Brian Watts, BIA Core Facility Manager, at the Duke Human Vaccine Institute. This work was made possible by grants from the National Science Foundation (NSF) [Awards ECCS-1936793 (FJM) and ECCS-1936772 (SP and EL)].

REFERENCES

[1] K. T. Urak *et al.*, "RNA inhibitors of nuclear proteins responsible for multiple organ dysfunction syndrome," *Nat. Commun.*, vol. 10, no. 1, p. 116, Jan. 2019, doi: 10.1038/s41467-018-08030-y.

[2] A. Villalonga, A. M. Pérez-Calabuig, and R. Villalonga, "Electrochemical biosensors based on nucleic acid aptamers," *Anal. Bioanal. Chem.*, vol. 412, no. 1, pp. 55–72, Jan. 2020, doi: 10.1007/s00216-019-02226-x.

[3] R. L. Rich and D. G. Myszka, "Advances in surface plasmon resonance biosensor analysis," *Curr. Opin. Biotechnol.*, vol. 11, no. 1, pp. 54–61, Feb. 2000, doi: 10.1016/S0958-1669(99)00054-3.

[4] H. Richardson, G. Maddocks, K. Peterson, M. Daniele, and S. Pavlidis, "Toward Subcutaneous Electrochemical Aptasensors for Neuropeptide Y," in *2021 IEEE Sensors*, Oct. 2021, pp. 1–4. doi: 10.1109/SENSORS47087.2021.9639832.

[5] M. A. Pellitero and N. Arroyo-Currás, "Study of surface modification strategies to create glassy carbon-supported, aptamer-based sensors for continuous molecular monitoring," *Anal. Bioanal. Chem.*, Mar. 2022, doi: 10.1007/s00216-022-04015-5.

[6] M. Cerruti, S. Fissolo, C. Carraro, C. Ricciardi, A. Majumdar, and R. Maboudian, "Poly(ethylene glycol) Monolayer Formation and Stability on Gold and Silicon Nitride Substrates," *Langmuir*, vol. 24, no. 19, pp. 10646–10653, Oct. 2008, doi: 10.1021/la801357v.

[7] R. B. M. Schasfoort, "Chapter 1 Introduction to Surface Plasmon Resonance," pp. 1–26, 2017, doi: 10.1039/9781788010283-00001.

[8] A. Tarasov *et al.*, "A potentiometric biosensor for rapid on-site disease diagnostics," *Biosens. Bioelectron.*, vol. 79, pp. 669–678, May 2016, doi: 10.1016/j.bios.2015.12.086.

[9] R. Levicky, T. M. Herne, M. J. Tarlov, and S. K. Satija, "Using Self-Assembly To Control the Structure of DNA Monolayers on Gold: A Neutron Reflectivity Study," *J. Am. Chem. Soc.*, vol. 120, no. 38, pp. 9787–9792, Sep. 1998, doi: 10.1021/ja981897r.

[10] L. G. Carrascosa, L. Martínez, Y. Huttel, E. Román, and L. M. Lechuga, "Understanding the role of thiol and disulfide self-assembled DNA receptor monolayers for biosensing applications," *Eur. Biophys. J.*, vol. 39, no. 10, pp. 1433–1444, Sep. 2010, doi: 10.1007/s00249-010-0599-6.

[11] Ó. Gutiérrez-Sanz, N. M. Andoy, M. S. Filipiak, N. Haustein, and A. Tarasov, "Direct, Label-Free, and Rapid Transistor-Based Immunodetection in Whole Serum," *ACS Sens.*, 2017, doi: 10.1021/acssensors.7b00187.

[12] F. V. Oberhaus, D. Frense, and D. Beckmann, "Immobilization Techniques for Aptamers on Gold Electrodes for the Electrochemical Detection of Proteins: A Review," *Biosensors*, vol. 10, no. 5, May 2020, doi: 10.3390/bios10050045.

[13] I. M. Bhattacharyya and G. Shalev, "Electrostatically Governed Debye Screening Length at the Solution-Solid Interface for Biosensing Applications," *ACS Sens.*, vol. 5, no. 1, pp. 154–161, Jan. 2020, doi: 10.1021/acssensors.9b01939.

[14] N. Haustein, Ó. Gutiérrez-Sanz, and A. Tarasov, "Analytical Model To Describe the Effect of Polyethylene Glycol on Ionic Screening of Analyte Charges in Transistor-Based Immunosensing," *ACS Sens.*, vol. 4, no. 4, pp. 874–882, Apr. 2019, doi: 10.1021/acssensors.8b01515.

[15] T. Goda and Y. Miyahara, "Label-Free Monitoring of Histone Acetylation Using Aptamer-Functionalized Field-Effect Transistor and Quartz Crystal Microbalance Sensors," *Micromachines*, vol. 11, no. 9, Art. no. 9, Sep. 2020, doi: 10.3390/mi11090820.

CONTACT

*S. Pavlidis, tel: +1-919-513-3018; spavlidis@ncsu.edu

DIRECT LASER WRITING OF TRIANGULAR-WALLED MICROARRAYS ONTO GLASS DIFFUSERS TO ENABLE CONTROLLED REFLECTIVITY UNDER ADAPTIVE OPTICS OPHTHALMIC IMAGING SYSTEMS

Ian Rosenthal[1,2], Lucas Garcia-O'Donnell[1], Brian Ngoh[1], Zhuolin Liu[2], Daniel X. Hammer[2], Anant Agrawal[2], and Ryan D. Sochol[1]
[1]University of Maryland, College Park, MD, USA
[2]U.S. Food and Drug Administration, Silver Spring, MD, USA

ABSTRACT

Adaptive optics scanning laser ophthalmoscopy (AOSLO) is an emerging imaging modality capable of resolving photoreceptors and microscopic structures in the living human retina, allowing clinicians to non-invasively detect retinal pathologies unseen by other methods. Widespread clinical use of complex imaging systems like AOSLO often requires standardized system performance assessments with "phantoms"—accurate physical models of anatomical structures. To date, however, challenges in manufacturing retinal phantoms at relevant scales has hindered such standardization for AOSLO. To overcome these barriers, here we introduce novel microwell array phantoms that comprise triangular sidewalls—enabled by the submicron-scale geometric versatility of "Direct Laser Writing (DLW)"-based additive manufacturing—and are 3D printed directly onto glass diffusers. The array geometries mimic retinal photoreceptor mosaic attributes (cell diameter and spacing) and are combined with a glass diffuser surface texture, which allows for high control over reflectivity, critical for informative AOSLO image capture. Experimental AOSLO imaging results revealed peak-to-valley grayscale differentiation of 160±25.4 and 190±29.6 (a.u.) for the 5 μm and 9 μm center-to-center arrays, respectively, suggesting attainment of phantom performance pertinent to the evaluation of AOSLO spatial resolution. Thus, the concepts presented here establish a pathway for new classes of AOSLO phantoms to support greater clinical use.

KEYWORDS

Adaptive Optics, Additive Manufacturing, 3D Printing, Direct Laser Writing, Two-Photon Polymerization, Phantoms

INTRODUCTION

Adaptive optics scanning laser ophthalmoscopy (AOSLO) is uniquely suited for detecting and monitoring retinal diseases by visualization of key retinal cells and structures [1] *via* correction of aberrations present in the human eye [2]. First demonstrated by Liang *et al*., adaptive optics operates with a wavefront sensor to measure the magnitude of ocular aberrations and a deformable mirror to correct the wave aberrations [3]. AOSLO systems can resolve single photoreceptors within their mosaic [4]. Other relevant microscopic structures, including ganglion cells [5], vasculature [6], Henle fibers [7], and retinal pigment epithelial cells, can also be investigated in detail with AOSLO [8]. Despite such promise, concerns regarding the repeatability of optical measurements remain a significant barrier to mainstream clinical adoption of AOSLO systems [9].

Retinal "phantoms"—physical models that recapitulate the structural and optical characteristics of *in vivo* anatomy—offer the potential to address these issues by standardizing AOSLO system performance assessment to minimize undesired clinical variability [10]. Unfortunately, manufacturing photoreceptor mosaic phantoms at biologically relevant scales without compromising reflectivity performance has remained a critical challenge. For example, micropost array-based phantoms produce irregular patterns and require protocols that increase the potential for undesired variations [11, 12]. Notably, the micropost structure contributes to anti-reflectivity properties that reduce the phantom capabilities as the arrays at spacings expected to be resolved appear as dark regions [13]. Recent advances in the two-photon (or multi-photon) additive manufacturing strategy, "Direct Laser Writing (DLW)", provides distinctive benefits for fabricating retinal phantoms at accurate length scales and with unparalleled freedom in geometric design [14-16]. By harnessing this technology, here we shift away from established micropost array-based approaches to instead investigate novel DLW-enabled microwell array phantoms with triangular sidewalls that are 3D printed directly onto glass diffuser substrates.

CONCEPT

The overall concept for DLW-based 3D printing of triangular-walled microwell arrays onto a glass diffuser (which comprises a random surface texture) for the optics community are presented in **Figure 1**. The diffuser is mounted in a DLW 3D printer where the roughened surface—immersed in a photocurable material—is aligned with the objective lens (**Fig. 1a**). Importantly, in contrast to prior work in which phantoms were manufactured onto smooth substrates [17], the decision to print the phantom atop the relatively rough texture of the glass diffuser is motivated by the capacity for such surfaces to yield uniform light distribution in the wavefront sensor image for stable adaptive optics correction. Next, a 3D

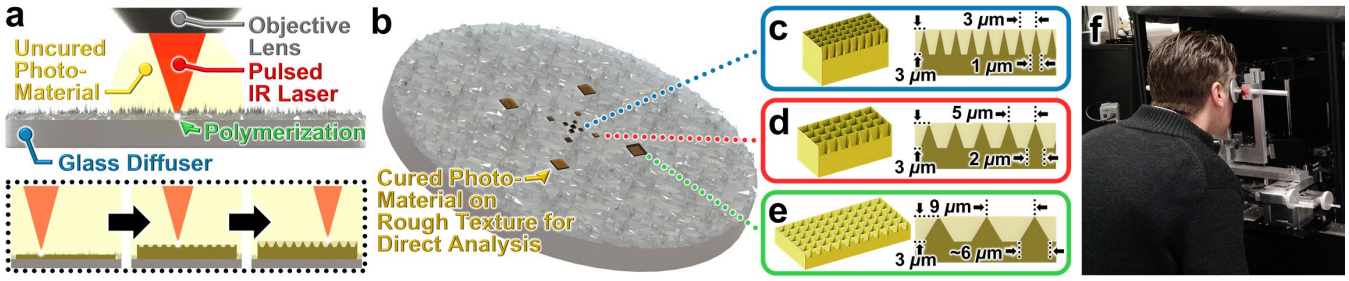

***Figure 1**: Concept of "Direct Laser Writing (DLW)"-based triangular-walled retinal phantoms for Adaptive Optics Scanning Light Ophthalmoscopy (AOSLO). **(a, b)** Concept of DLW-print microwell arrays onto a glass diffuser. **(c–e)** Cross sections of **(c)** 3 μm, **(d)** 5 μm, and **(e)** 9 μm center-to-center designs. **(f)** Example of AOSLO imaging a human subject.*

978-1-940470-04-7/HH2022/$25©2022TRF
DOI 10.31438/trf.hh2022.75

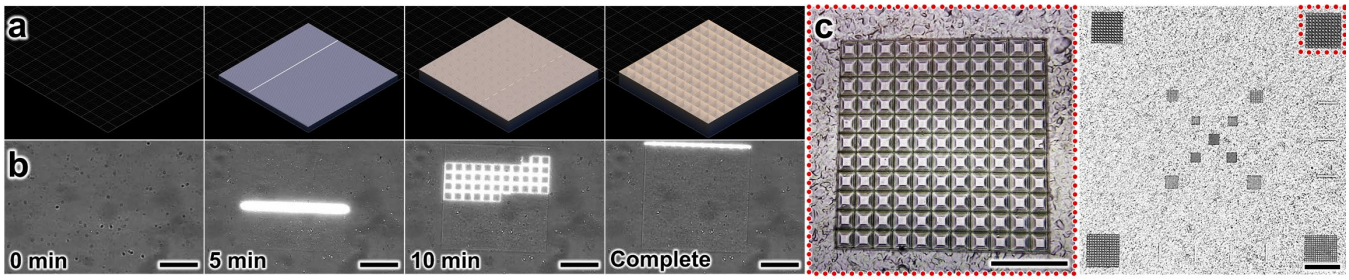

***Figure 2**: Sequential images of **(a)** simulations, and **(b)** the corresponding DLW printing process for a representative array. Scale bars = 20 µm. **(c)** Brightfield of the retinal phantom comprising multiple, distinct arrays (highlighting the 9 µm array). Scale bar = 20 µm; Expanded view scale bar = 100 µm.*

microwell array is printed directly onto the diffuse surface by scanning a femtosecond pulsed infrared (IR) laser point-by-point, layer-by-layer, to induce polymerization of the photomaterial in target locations (**Fig. 1a – *inset***). The glass diffuser-structure assembly is removed from the DLW printer and placed in a developer solution to remove any uncured photomaterial, leaving the microwell array adhered to the surface of the glass diffuser (**Fig. 1b**). Due to the geometric control and submicron feature resolution afforded by the DLW technology, each triangular-walled microwell array can be designed with distinct dimensions (*e.g.*, **Fig. 1c–e**) that are relevant to AOSLO imaging of the human retina (**Fig. 1f**).

MATERIALS AND METHODS

DLW-Printing of 3D Microwell Structures

All DLW protocols in this work are based on the use of a Nanoscribe Photonic Professional GT2 DLW 3D printer (Nanoscribe GmbH, Karlsruhe, Germany). Prior to printing, borosilicate ground glass diffusers (DG10-1500, Thorlabs, Inc., Newton, NJ), with a thickness of 2 mm and a diameter of 25.4 mm, were washed and rinsed with acetone and isopropyl alcohol (IPA). Once dried, the surface designated for print adhesion was placed face-up in a tabletop Plasma Cleaner (PIE Scientific, Union City, CA) and exposed to Oxygen plasma for 30 minutes. Once the cycle was complete, the substrate was placed in a bath of ethanol/3-(trimethoxysilyl)propyl methacrylate solution for 1 hour. The substrate was removed from the solution, rinsed with acetone and DI water, and dried. Then, the glass diffuser was mounted into the Nanoscribe DLW printer with a single droplet of IP-Dip2 photoresist (Nanoscribe). The substrate is mounted in the "Dip-in Laser Lithography (DiLL)" configuration, with the lens immersed in the photoresist.

The computer-aided design (CAD) software, SolidWorks (Dassault Systèmes, France), was used to generate 3D models of the triangular-walled microwell arrays with varying center-to-center distances. These distances were selected to mimic photoreceptor mosaics of the human eye across the macula at different retinal eccentricities to evaluate the resolution capabilities of AOSLO systems for clinical use. Each model was exported as an STL file and then imported into the computer-aided manufacturing (CAM) software, Describe (Nanoscribe), for laser writing path generation. All designs included 100 nm hatching and 100 nm layer heights with 2 contours spaced 100 nm apart.

All designs were printed with the 63× objective lens in DiLL mode with a laser power of 35 mW and a laser scanning speed of 25 mm/s. Due to the abnormal surface texture and to account for any unintended deviations, the surface interface of the glass diffuser was found manually. The DLW printing process was initiated with approximately 3 µm of overlap into the glass (with respect to the surface interface). Following the DLW process, the diffuser-print

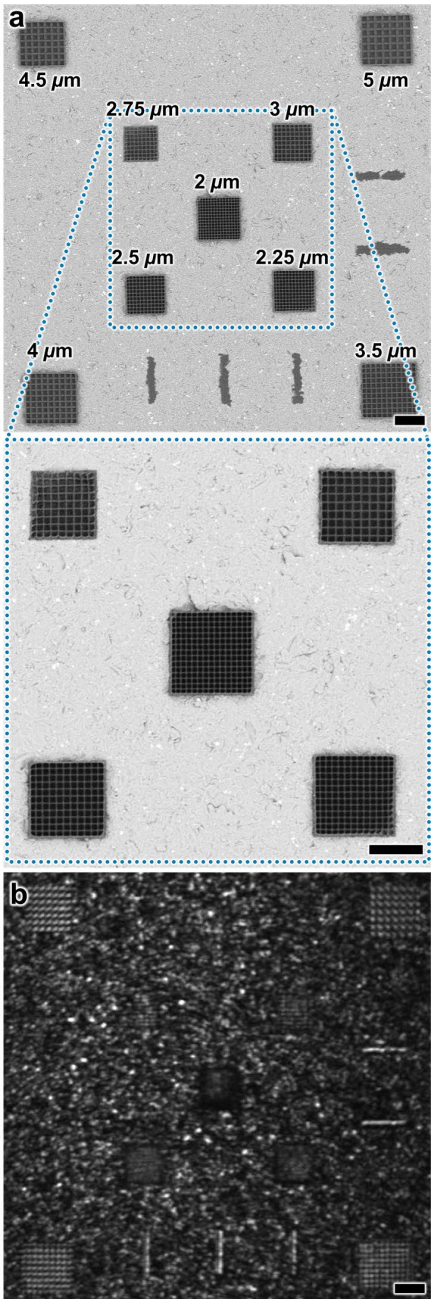

***Figure 3**: Fabrication results. **(a)** SEM micrographs of 2–5 µm triangular-walled microwell arrays. **(b)** A corresponding AOSLO image of the 2–5 µm arrays. Scale bar = 20 µm.*

assembly was removed from the printer, developed using propylene glycol methyl ether acetate (PGMEA) for 20 min, and then IPA for 5 min. The assembly was dried using Nitrogen gas.

Phantom Characterization

Scanning electron microscope (SEM) images of the DLW-based prints were captured using a Phenom XL G2 Benchtop SEM (Thermo Fisher Scientific, Waltham, MA). AOSLO images were captured using an AOSLO system that was custom-built in the FDA laboratory for investigational use on human subjects [18]. For AOSLO imaging, the phantoms were placed at the retinal plane of a model eye, which uses an achromatic glass lens to replicate the focusing properties of a typical human eye. The model eye assembly includes a translation mount for the phantom to bring the printed structures into the center of the AOSLO field of view. Quantitative analysis of AOSLO images was performed with ImageJ (NIH, Bethesda, MD) to determine reflectivity and spatial dimensions *via* established methods [19].

RESULTS AND DISCUSSION

CAM simulations and corresponding micrographs of the DLW-based 3D printing process for a representative microwell array (*i.e.*, the 9 μm center-to-center design) are presented in **Figure 2a** and **2b**, respectively. The entire printing process for each print field (~140×140 μm^2) was completed in less than 15 min. Larger arrays such as the 9 μm array (side length = 99 μm) occupied an entire print field, while arrays with smaller center-to-center distances and side lengths less than 30 μm, such as the 2–3 μm designs, could be included in a single print field, reducing the total print time. Fabrication results revealed effective DLW-based printing fidelity for all the microwell array designs examined despite the non-uniformity of the glass diffuser's rough surface (**Fig. 2c**; **Fig. 3a**).

AOSLO images of the phantom exhibited distinct bright spots in patterns corresponding directly to the microwell arrays (**Fig. 3**)—a critical requirement for imaging characterization. The AOSLO results revealed two key trends. First, the arrays with ≤3 μm center-to-center spacings could not be resolved, and therefore, clearly set a meaningful resolution performance limit for AOSLO (*e.g.*, **Fig. 4a,d**). For example, quantified AOSLO grayscale intensities for the 3 μm design revealed indistinguishable peak-to-valley results (**Fig. 4g**). In contrast, we observed that the larger spacing-associated designs were not only directly visible, but that the imaging conspicuity improved further with increasing center-to-center spacing. For example, the quantified AOSLO peak-to-valley grayscale results increased from 160±25.4 to 190±29.6 (a.u.) for the 5 μm and 9 μm cases, respectively (**Fig. 4**).

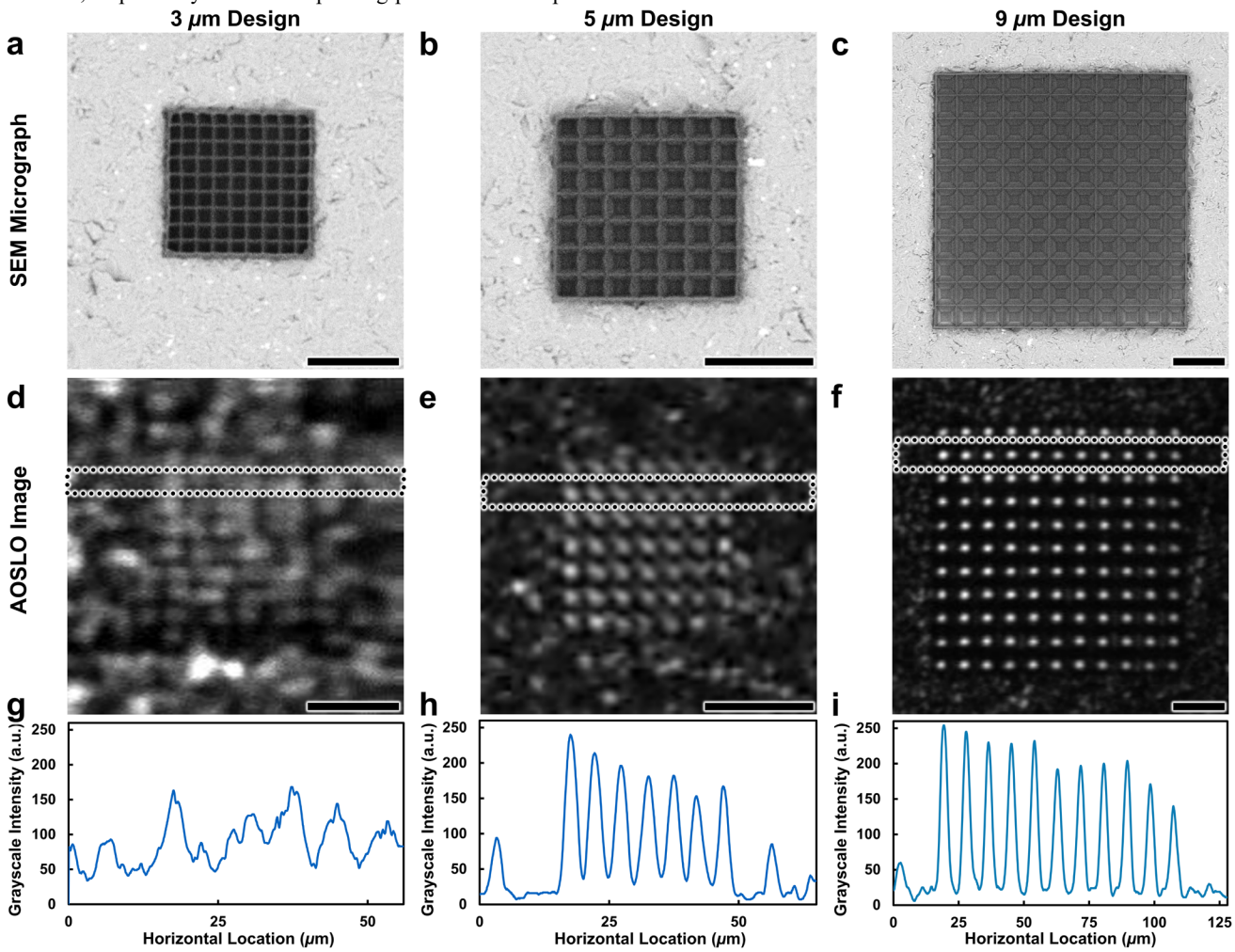

***Figure 4**: Imaging results for the microwell array design. **(a–c)** SEM micrographs, **(d–f)** Corresponding AOSLO images, and **(g–i)** Quantified gray-scale intensities along a representative region of interest of the AOSLO images for microwell arrays with center-to-center designs of: **(a, d, g)** 3 μm, **(b, e, h)** 5 μm, and **(c, f, i)** 9 μm designs. Scale bars = 20 μm.*

CONCLUSIONS

In this work, we investigated a novel strategy for using DLW-based additive manufacturing to 3D print triangular-walled microwell structures directly onto glass diffusers. Previous retinal phantoms from our group required intensive fabrication strategies to achieve an effective phantom including encapsulating gold-coated, micropost structures in PDMS and placing that assembly behind an IPA-filled chamber for index matching within the model eye [11]. Such a complex setup hindered adoption by the AOSLO research community, thus limiting the impact. Later work by our group included a micropost-based system that was limited by irregular reflection patterns from the interstitial space that reduced functionality [12, 19]. Furthermore, previous phantoms used diffuse textures printed on the smooth side of a Si wafer, which led to additional molding strategies and increased fabrication time. In contrast, the fabrication strategy presented here achieved effective photoresist-to-substrate bonding, enabling immediate AOSLO imaging following development. AOSLO imaging demonstrated patterned reflectivity based on varied center-to-center distances. Additional design modifications could further enhance the visibility of the arrays in relation to the adjacent diffuse texture and improve the integrity of the overall structure. Future experiments will investigate phantom-to-phantom repeatability and sources of variation among manufactured microwell arrays, especially for smaller center-to-center distance designs. Overall, these results serve as a fundamental proof of concept of the triangular-walled microwell array phantom as a means to efficiently compare and track AOSLO system performance.

ACKNOWLEDGEMENTS

We greatly appreciate the contributions of Olivia M. Young, Ziteng Wen, Robert Propst, the members of the Bioinspired Advanced Manufacturing (BAM) laboratory and Terrapin Works staff at the University of Maryland, College Park. This research was supported in part by U.S. National Science Foundation (NSF) Award #1943356. Ian Rosenthal was supported by the Oak Ridge Institute for Science and Engineering (ORISE) fellowship program at the FDA.

DISCLAIMER

The mention of commercial products, their sources, or their use in connection with material reported herein is not to be construed as either an actual or implied endorsement of such products by the U.S. Department of Health and Human Services.

REFERENCES

[1] M. Georgiou, A. Kalitzeos, E. J. Patterson, A. Dubra, J. Carroll, and M. Michaelides, “Adaptive optics imaging of inherited retinal diseases,” *British Journal of Ophthalmology*, 102, 8 (2018) pp. 1028–1035.

[2] A. Roorda, and J. L. Duncan, “Adaptive Optics Ophthalmoscopy,” *Annual Review of Vision Science*, 1 (2015) pp. 19-50.

[3] J. Liang, D. R. Williams, and D. T. Miller, "Supernormal vision and high-resolution retinal imaging through adaptive optics," *J. Opt. Soc. Am. A,* 14 (1997) pp. 2884 - 2892.

[4] K. M. Litts, R. F. Cooper, J. L. Duncan, J. Carroll, “Photoreceptor-Based Biomarkers in AOSLO Retinal Imaging,” *Invest. Ophthalmol. Vis. Sci*., 58, 6 (2017) pp. BIO255-BIO267.

[5] L. Yin, B. Masella, D. Dalkara, J. Zhang, G. Flannery, D. V. Schaffer, D. R. Williams, and W. H. Merigan, “Imaging light responses of foveal ganglion cells in the living macaque eye,” *The Journal of Neuroscience: the Official Journal of the Society for Neuroscience*, 34, 19 (2014) pp. 6596–6605.

[6] Z. Popovic, P. Knutsson, J. Thaung, M. Owner-Petersen, and J. Sjöstrand, “Noninvasive imaging of human foveal capillary network using dual-conjugate adaptive optics,” *Investigative Ophthalmology & Visual Science*, 52, 5 (2011) pp. 2649–2655.

[7] D. Scoles, B. P. Higgins, R. F. Cooper, A. M. Dubis, P. Summerfelt, D. V. Weinberg, J. E. Kim, K. E. Stepien, J. Carroll, and A. Dubra, “Microscopic Inner Retinal Hyper-Reflective Phenotypes in Retinal and Neurologic Disease,” *Invest. Ophthalmol. Vis. Sci.,* 55, 7 (2014) pp. 4015-4029.

[8] D. Scoles, Y. N. Sulai, and A. Dubra, “In vivo dark-field imaging of the retinal pigment epithelium cell mosaic. *Biomedical Optics Express*, 4, 9 (2013) pp. 1710–1723.

[9] N. Wynne, J. Carroll, and J. L. Duncan, “Promises and pitfalls of evaluating photoreceptor-based retinal disease with adaptive optics scanning light ophthalmoscopy (AOSLO),” *Prog Retin Eye Res*, 83 (2021) pp. 100920.

[10] H. J. Lee, N. M. Samiudin, T. G. Lee, I. Doh, and S. W. Lee, “Retina phantom for the evaluation of optical coherence tomography angiography based on microfluidic channels,” *Biomed Opt Express*, 10, 11 (2019) pp. 5535–5548.

[11] N. Kedia, Z. Liu, R. D. Sochol, J. Tam, D. X. Hammer, and A. Agrawal, “3-D printed photoreceptor phantoms for evaluating lateral resolution of adaptive optics imaging systems,” *Opt. Lett.,* 44, 7 (2019) pp. 1825–1828.

[12] A. C. Lamont, M. A. Restaino, A. T. Alsharhan, Z. Liu, D. X. Hammer, A. Agrawal, and R. D. Sochol, “Direct Laser Writing of Titanium Dioxide-Laden Retinal Cone Phantoms,” *2020 IEEE 33rd International Conference on Micro Electro Mechanical Systems (MEMS)*, (2020) pp. 1223–1226.

[13] I. Zada, W. Zhang, Y. Li, P. Sun, N. Cai, J. Gu, Q. Liu, H. Su, and D. Zhang, "Angle dependent antireflection property of TiO2 inspired by cicada wings," *Appl. Phys. Lett.* 109, 15 (2016).

[14] V. Hahn, P. Kiefer, T. Frenzel, J. Qu, E. Blasco, C. Barner-Kowollik, and M. Wegener, "Rapid Assembly of Small Materials Building Blocks (Voxels) into Large Functional 3D Metamaterials", *Advanced Functional Materials*, 30, 26 (2020) pp. 1907795.

[15] A.C. Lamont, M. Restaino, M. Kim, and R.D. Sochol, "A facile multi-material direct laser writing strategy", *Lab on a Chip*, 19, 14 (2019) pp. 2340-2345.

[16] A.T. Alsharhan, R. Acevedo, R. Warren, and R.D. Sochol, "3D microfluidics *via* cyclic olefin polymer-based *in situ* direct laser writing", *Lab on a Chip*, 19, 17 (2019) pp. 2799-2810.

[17] A. Agrawal, A. C. Lamont, Z. Liu, R. D. Sochol, and D. X. Hammer, “Engineered Texture Phantom for Measuring Lateral Resolution of Adaptive Optics Ophthalmic Imaging Systems,” in *Imaging and Applied Optics Congress* (2020).

[18] Z. Liu, J. Tam, O. Saeedi, and D. X. Hammer, "Trans-retinal cellular imaging with multimodal adaptive optics," *Biomedical Opt. Express,* 9, 9 (2018) pp. 4246-4262.

[19] C. A. Schneider, W. S. Rasband, and K. W. Eliceiri, “NIH Image to ImageJ: 25 years of image analysis,” *Nature Methods*, 9 (2012) pp. 671-675.

CONTACT

* I. Rosenthal, tel: +1 (301) 405-6928; irosenth@terpmail.umd.edu

EXPLORING MICROSPHERICAL GLASS SHELL RESONATORS FOR VOLATILE ORGANIC COMPOUNDS SENSING

Jiayuan Zhang[1], Vedant Sumaria[1*], and Srinivas Tadigadapa[1]*
[1]Northeastern University, Boston, USA
*These authors contributed equally to this work.

ABSTRACT

We explore the feasibility of a volatile organic compounds (VOC) gas sensor based on an ultra-high quality-factor (Q) whispering-gallery-mode (WGM) microspherical glass (MSG) shell resonator coated with amino terminated poly(2-vinylpyridine). The change in local refractive index caused by polymer absorbing the gas molecules was monitored by the MSG resonator through a shift in its optical resonance frequency. The sensor achieved a sensitivity of 4.91 kHz/ppm to acetone and 21.44 kHz/ppm to ethanol, and the detection of down to 0.375% of ethanol is demonstrated. The limit of detection of the current sensing system is estimated to be 0.09% for ethanol and 0.4% for acetone.

KEYWORDS

Microspherical glass shell, whispering gallery mode resonator, volatile organic compounds gas sensor, microelectromechanical systems

INTRODUCTION

Detection of various volatile organic compounds (VOCs) has been increasingly of interest due to their negative health effects. More than 50 kinds of VOCs have been shown to come from various indoor sources including furniture and cleaning chemicals and have adverse health effects on humans even at low concentrations. The irritation of eye, respiratory system, headache, and nausea have been reported as the consequences of VOC exposure [1]. The ability to sense and identify VOCs at low concentrations, as a consequence, can help evaluate the indoor air quality and aid in the prevention of related health concerns. Due to their numerous applications, they have been developed on thermal, electrochemical, mechanical, and optical detection methods. Even though electrochemical sensors are the most widely used, optical sensors are an attractive alternative because they are immune to electromagnetic noise and their ability to be used in explosive medium.

Whispering gallery mode (WGM) optical resonators have been configured as highly sensitive detectors for various applications. Due to their very high *Q*-factors which results in high resolution and sensitivity, they have been configured as physical sensors such as thermal sensors, microfluidic sensors, and biosensors for the detection of bioanalytes, proteins, and bacteria. WGM resonators have been fabricated in various forms such as microring, microdisk, and microsphere [2]. Recent work has also demonstrated that wafer scale glass blowing technique can be used to form blown-glass microspherical shells configured as optical WGM resonators that can sustain ultrahigh-*Q* WGM resonances [3]. Small changes in the dimensions of the microspherical shell owing to temperature changes or surrounding refractive index or both manifest as large shifts in the resonance frequency of the WGM resonators. Polymers can be used as an absorbing medium to amplify the modification of these properties and to improve performance in the detection of gases and volatile organics.

Detection of acetone vapor realized due to the spectrum shift with refractive index change has been previously demonstrated using self-assembled PMMA-based hemispherical microlasers [4]. In this work, we fabricated microspherical shell glass resonators coated with amino terminated poly(2-vinylpyridine) and characterized the performance of these polymer-coated MSG resonators coupled to tapered optical fiber for detecting VOC vapor. When the sensor is exposed to gas vapor, polymer absorbs the gas molecules which results in a change in the local refractive index. This change results in a change of optical length of the coupled resonance, which can be monitored by the MSG resonator through a shift in its optical resonance frequency. Acetone and ethanol were chosen as the VOC vapor for sensing, and the experiment was done in two different ambient humidity levels to characterize the humidity stability of the sensor.

EXPERIMENT AND RESULTS

Sensor Fabrication

Borosilicate glass microshells are fabricated using chip-scale glass blowing process as shown in Fig. 1. A four-inch silicon wafer was patterned with 250 µm diameter circles and subsequently etched by deep reactive ion etch process to a depth of 250 µm. After etching, Remover PG® and Piranha solution were used to thoroughly clean the surface. The etched silicon wafer was then anodically bonded to a borosilicate glass wafer of 100 µm thickness, and at a positive pressure of 1000 Torr inside the bonded cavity. The bonded wafer was then diced into individual chips. A single chip was placed on a ceramic heater in a vacuum chamber maintained at a pressure of 100 Torr and was heated to 775 °C for 30 seconds, then it was gradually cooled down. During this process, the borosilicate glass was softened, and the large pressure differential created between the sealed cavities and glass blowing ambient pressure of 100 Torr formed near spherical shells.

A thin layer of polymer was then coated onto the microsphere as the gas sensitive agent. Amino terminated poly(2-vinylpyridine) was dissolved in tetrahydrofuran at 0.1 wt% concentration. The solution was placed inside a glass micropipette connected to a

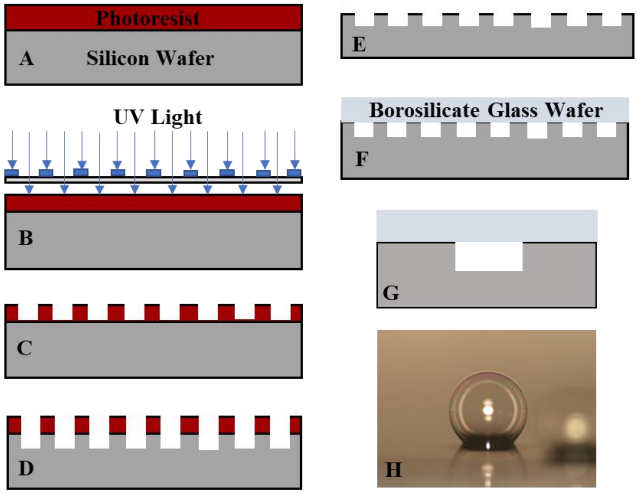

Figure 1: (a-c) Silicon wafer is patterned with circular features. (d-e) Wafer is plasma etched to a depth of 250 µm to define circular pits. (f) Borosilicate glass and the etched silicon wafers anodically bonded. (g-h) Glass microshell is blown at 775 °C in a vacuum oven maintained at a pressure of 100 Torr.

978-1-940470-04-7/HH2022/$25©2022TRF
DOI 10.31438/trf.hh2022.76

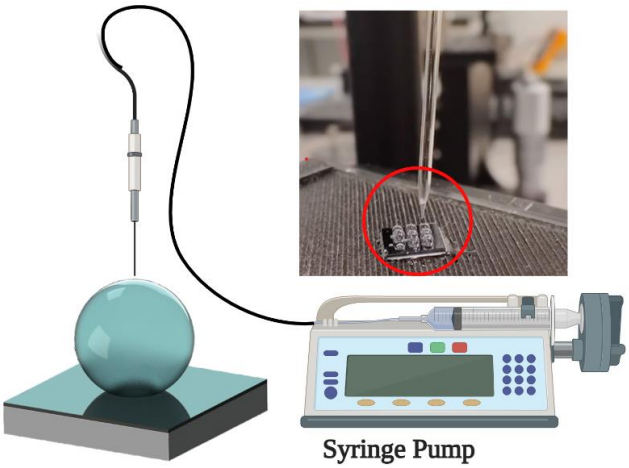

Figure 2: Amino terminated poly(2-vinylpyridine) is coated on the top half of the microspherical shell resonator using the syringe pump and micropipette. Inset: Photo of the micropipette just over the device being tested.

syringe pump as shown in Fig. 2, which drop coated the polymer solution on the outer surface of the top half of the microsphere. It was followed by a heat treatment to evaporate the solvent, leaving a thin polymer film on the surface of the microsphere.

Experimental Setup

The experimental setup for gas sensing is shown in Fig. 3. The device was placed inside a custom designed, 3D-printed testing chamber with a gas inlet. The measurement schematic for tracking the resonance frequency shift of the MSG resonator with the gas flow setup is shown in Fig. 4. Light from a tunable 1550 nm laser (Newport TLB-6728) was used as the source for the excitation of the resonance in the microspherical glass shell. The laser was tuned with a triangular wave to scan the transmission spectrum of the resonator over a 17 nm range. The laser was evanescently coupled to the microspherical glass shell resonator using a tapered optical fiber. The transmitted light intensity from the resonator was measured using a photodiode (Newport 2051-FC). The resonance curve was recorded as the sensor output signal and analyzed for shift in resonance frequency over time.

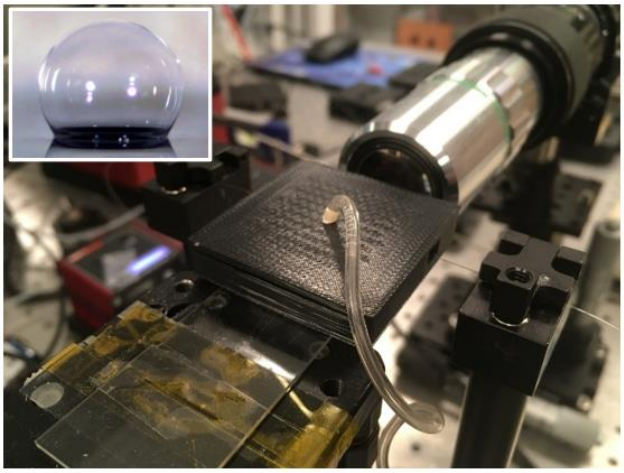

Figure 3: Experimental setup showing the MSG resonator device coupled with tapered optical fiber. The device is placed inside a 3D-printed testing chamber, with gas flowing into the chamber from the inlet. Inset: WGM microsphere before the polymer is deposited.

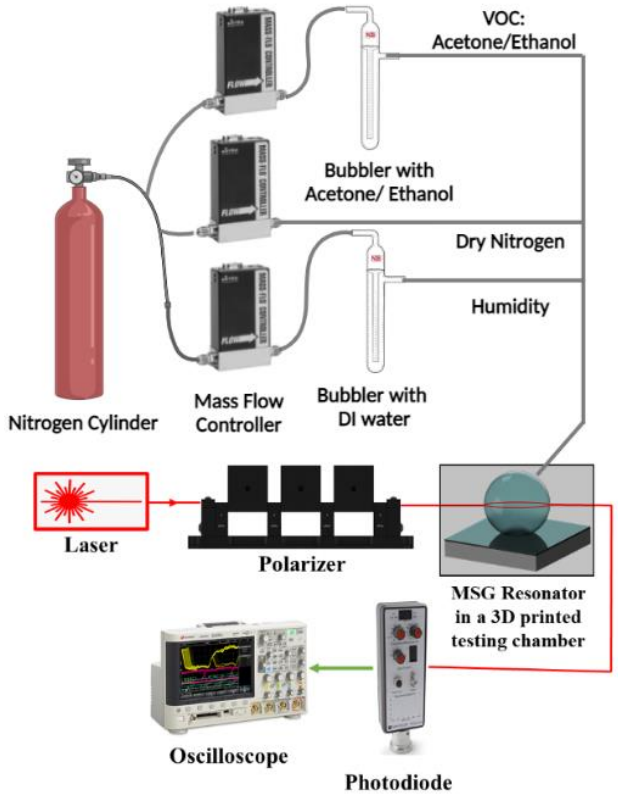

Figure 4: Schematic of the measurement system for tracing the resonance frequency shift of the MSG resonator with the control of concentration of VOC gas being detected using mass flow controller and bubblers.

The fiber tapering was performed by stripping a single mode optical fiber (SMF-28) and cleaning with acetone and isopropyl alcohol. The stripped fiber was clamped between two linear translation stages (Thorlabs MTS50-Z8) and the bare fiber section was placed into the cavity of a ceramic microheater which temperature was slowly increased to 1250 °C for the softening of the silica fiber. After reaching the thermal equilibrium, the translation stages were moved at a constant pulling rate of 40 µm/s while the transmission was monitored through the photodiode. The stages were stopped after about 20 mm of fiber stretching, the fiber was allowed to cool down to room temperature, and it was removed from the heating cavity.

The resonance in the microspherical shell occurs when the coupled light constructively interferes with itself after circulating around the circumference of the microspherical shell for an integer number of times. The condition for the WGM resonance can be describe as the following equation:

$$2\pi n_r r = m\lambda \qquad (1)$$

where r is the radius of the optical path, λ is the wavelength of the light source, n_r is the effective refractive index at the wavelength, and m is the resonance mode number. When the polymer on the microspherical shell absorbs gas molecules, its effective refractive index will be changed, and results in a change in the resonance wavelength. This spectral shift of $\Delta\lambda$ of the resonance wavelengths can be generally described as the following relation:

$$\frac{\Delta\lambda}{\lambda} = \frac{\Delta R}{R} + \frac{\Delta n}{n} \qquad (2)$$

From Eq. (2), there are two mechanisms that could contribute to the spectral shift caused by the absorption of a gas into the polymer. First is due to a change in the effective radius ΔR from polymer swelling and the second is due to the change in the refractive index Δn caused by the formation of polymer-gas blend when the gas is absorbed. Both these phenomena are linked to the concentration of the gas being detected. Among these two, the contribution of change in refractive index is much higher especially for polymers like Amino terminated poly(2-vinylpyridine) due to their high stiffness and amorphous non-crystalline structure.

The gas flowing into the test chamber was controlled by a pair of mass flow controllers which mixed specific amounts of rated VOC vapor with nitrogen to achieve multiple output concentrations of these vapors. VOC vapor used in the test was provided via nitrogen flowing through a bubbler filled with acetone or ethanol the vapor pressure of which can be determined with Antoine equation. The concentration of the vapor at the output of the bubbler under the testing conditions (1 atmosphere pressure, 25 °C temperature) was calculated to be 15% for acetone [5] and 3.75% for ethanol [6]. This vapor was then diluted by mixing with dry nitrogen to achieve the final gas concentration for acetone between 1.5% and 15%, and for ethanol between 0.375% and 3.75%. The total flow rate of the mixed gas was controlled at 200 sccm. The test was performed at two different relative humidity levels at 0% and 37%. To achieve the specific humidity level, dry nitrogen flowing through a bubbler filled with water was used as the humidity source, and the output was mixed with the diluted VOC vapor. Tests were conducted by repeated exposure and recovery of the resonator to the analyte gas, and by changing the VOC vapor concentration between zero and specific concentration points (6 distinct steps between 1.5% and 15% for acetone, and between 0.375% and 3.75% for ethanol) in 5-minute cycles. During the exposure cycles, the shift of a resonance peak was recorded in real time was calculated. The results were analyzed to determine the frequency shift of the resonators when exposed to different species and concentrations of VOC vapors. The same test was also conducted with a microspherical shell resonator without any polymer coating as a reference. The idle state of the resonator was recorded to determine the noise level of resonance frequency.

Results & Discussion

Fig. 5 shows the typical WGM resonance curve of the MSG resonator. The resonance frequency of the resonator was 193.5 THz, corresponding to a wavelength of 1550 nm. After the deposition of the polymer on the microspherical shell, the resonator showed a Q-factor of 827,618, a factor of 10 times reduction from the pristine state in the range of 8.1 million. This reduction is because of increased scattering loss due to the polymer deposition on the surface of the microspherical shell.

Fig. 6 shows the resonance frequency shift during gas testing cycle for acetone vapor exposure at 0% humidity, correlating to the increasing acetone vapor concentrations flowing into the test chamber. The sensor showed an increased frequency shift with increasing VOC vapor concentration. A response time constant of about 100 seconds was experimentally measured for a change in vapor concentration. The calculated time constant could be larger than that of the devices themselves because it includes the time needed for the testing chamber to reach the equilibrium state at gas concentration. The reference resonator without the polymer coating did not show any observable frequency shift during testing, suggesting that the change of refractive index of polymer coating plays an essential role for the detection of the VOC vapors.

The frequency shift was extracted from the frequency-time data and represented as a function of VOC vapor concentration for

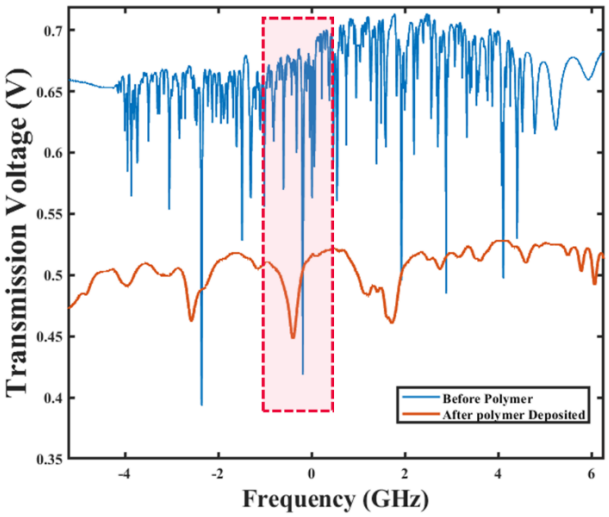

Figure 5: Typical transmission spectrum of the microspherical shell glass resonator used here to perform the gas sensing. Blue: Typical resonance curve of the device with Q-factor in the range of 8.1 million. Red: Resonance curve after polymer is deposited with Q factor of 827,618.

acetone and ethanol under two different humidity levels. The plotted data is shown in Fig. 7. The relationship between VOC vapor concentration and the resonance frequency shift showed a linear dependence in a wide range of concentration for both acetone and ethanol VOC vapors, and at both humidity levels tested. The data points were linear fitted and the sensitivity of the resonator was determined. The result is shown in Table 1. The sensor showed a high sensitivity of 4.91 kHz/ppm to acetone and 21.44 kHz/ppm to ethanol and exhibited about 4 times greater sensitivity to ethanol against acetone, with the selectivity behaving consistently under the two humidity levels under which the tests were performed. A small increase in sensitivity at 37% humidity was observed. This could imply that the presence of water at 37% RH caused the polymer to exhibit a larger refractive index change during the gas exposure compared to dry environment. The noise of the sensor is calculated from its idle state to be 20 MHz, resulting in the limit of detection of 0.09% for ethanol and 0.4% for acetone. The limit of detection is

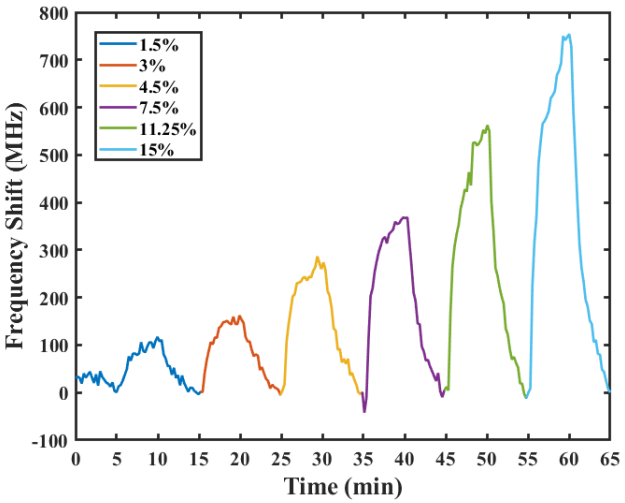

Figure 6: Resonance frequency shift during the acetone vapor exposure at 0% humidity. The concentration of the acetone vapor in this test is varied from 1.5% to 15%.

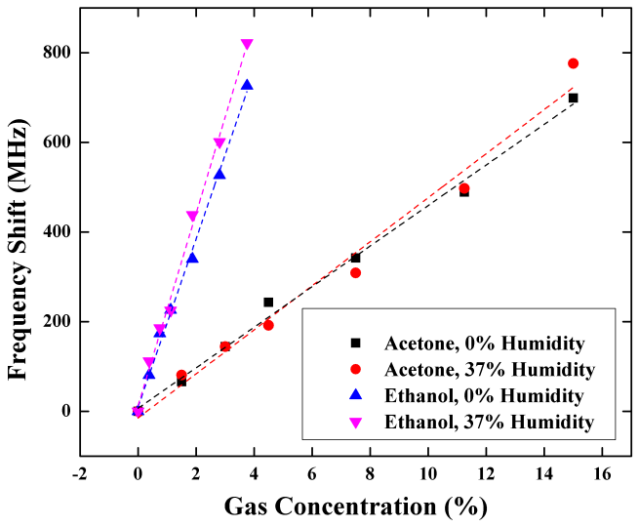

Figure 7: Resonance frequency shift as a function of VOC vapor concentration exposed to the MSG resonator at different relative humidity levels. Dashed lines show linear fit.

Table 1: Sensitivity of the resonator to acetone and ethanol under 0% and 37% humidity levels.

Sensitivity (kHz/ppm)	Acetone	Ethanol
0% Humidity	4.53	18.77
37% Humidity	4.91	21.44

currently limited by the reduced *Q*-factor after polymer coating, which can be improved by developing improved printing methods to reduce scattering loss, and by using the PID controller method for frequency locking. Previous work where similar sensor is used for IR sensing mentions the use of Pound-Drever-Hall (PDH) adaptive locking of the laser frequency at a fixed point on the slope of the resonance curve [7]. The laser was used in combination with a DigiLock 110 from Toptica Photonics. The output of the photodetector was connected to a feedback proportional-integral-derivative (PID) controller, which in turn tunes the voltage-controlled laser frequency and keeps it locked at the same point on the shifted resonance curve upon any physical change to the device. This would significantly reduce the noise arising from random fluctuations in the resonance frequency and thereby significantly improve the signal to noise ratio (SNR).

CONCLUSIONS

We have explored the feasibility of a volatile organic compounds (VOC) gas sensor using an ultrahigh-*Q* whispering gallery mode microspherical glass shell resonator coated with polymer. The change in local refractive index caused by polymer absorbing the gas molecules results in an optical resonance frequency shift in the sensor. The sensor achieved a sensitivity of 4.91 kHz/ppm to acetone and 21.44 kHz/ppm to ethanol, a time constant of 100 seconds, and demonstrated the detection down to 1.5% for acetone and 0.375% for ethanol. The selectivity between ethanol and acetone was observed to be preserved at the two tested humidity levels. The current sensing system achieved a limit of detection of 0.09% for ethanol and 0.4% for acetone. With tailored polymer selection, improved *Q*-factor after the polymer coating, and better testing set-up, polymer-coated whispering gallery mode microspherical shell glass resonators present a huge promise for being used as a general VOC gas sensing platform.

REFERENCES

[1] Bernstein, Jonathan A., et al. "The health effects of nonindustrial indoor air pollution." Journal of Allergy and Clinical Immunology 121.3 (2008): 585-591.

[2] Foreman, Matthew R., Jon D. Swaim, and Frank Vollmer. "Whispering gallery mode sensors." Advances in optics and photonics 7.2 (2015): 168-240.

[3] Zhang, Chenchen, et al. "On-chip glass microspherical shell whispering gallery mode resonators." Scientific reports 7.1 (2017): 1-11.

[4] Ta, Van Duong, et al. "Application of self-assembled hemispherical microlasers as gas sensors." Applied Physics Letters 102.3 (2013): 031107.

[5] Ambrose, D.; Sprake, C.H.S.; Townsend, R., Thermodynamic properties of organic oxygen compounds XXXIII. The vapour pressure of acetone, The Journal of Chemical Thermodynamics, 1974, 6, 7, 693-700.

[6] Kretschmer, Carl B.; Wiebe, Richard., Liquid-Vapor Equilibrium of Ethanol--Toluene Solutions, J. Am. Chem. Soc., 1949, 71, 5, 1793-1797.

[7] Sumaria, Vedant, and Srinivas Tadigadapa. "Whispering-gallery-mode optical microshell resonator infrared detector." *IEEE Sensors Journal* 21.3 (2020): 2634-2641.

CONTACT

*Jiayuan Zhang, zhang.jiayu@northeastern.edu

FLUID FORCES MODULATE CYTOKINE STIMULI FOR PERIPHERAL BLOOD MONONUCLEAR CELL ADHESION TO ENDOTHELIAL CELLS

Prashanth Sundaram[1], *Manjusha Kulkarni*[1], *Emily Bowman*[1], *Janelle Gabriel*[1], *Nicholas Funderburg*[1] and *Shaurya Prakash*[1]

[1]The Ohio State University, Columbus, USA

ABSTRACT

We report using our innovative blood-vessel on chip (BVoC) to manipulate the inflammatory response of endothelial cells (ECs) subjected to simultaneous fluid force and cytokine stimulation. The BVoC presents a microfluidic branching blood vessel analog comprising an endothelial monolayer interfaced with an extracellular matrix (ECM). The BVoC incorporates physiologically valid effects of local fluid dynamics occurring in a blood vessel analog, capturing accurate stagnation pressures at the bifurcation point and shear stress at the branching vessel, in contrast to previous work.

KEYWORDS

Organ-on-chip; blood-vessel-on-chip, inflammation, infectious disease, permeability.

INTRODUCTION

Human immunodeficiency virus (HIV) infection is associated with increased atherosclerotic cardiovascular disease (CVD) risk with the chronic immune activation and inflammation being implicated as a major concern [1, 2]. In particular, plasma levels of interleukin (IL)-6, high-sensitivity C-reactive protein (hs-CRP), D-dimer, and soluble CD14 (sCD14) are independent predictors of mortality, including CVD-related deaths, in people with HIV (PWH). Many "drivers" activate innate immune pathways that result in production of cytokines (TNF, IL-6, IL-1β) that may also contribute to cellular activation and inflammation. These drivers of chronic inflammation likely contribute to altered adhesion molecule expression and migration capabilities of immune cell subsets; thereby promoting atherosclerosis.

Therefore, in this work we investigated using our blood-vessel on chip (BVoC) device to manipulate the inflammatory response of endothelial cells (ECs) subjected to simultaneous fluid force and cytokine stimulation. The BVoC presents a microfluidic branching blood vessel analog comprising an endothelial monolayer interfaced with an extracellular matrix (ECM). The BVoC also incorporates physiologically valid effects of local fluid dynamics occurring in a blood vessel analog, capturing accurate stagnation pressures at the bifurcation point and shear stress at the branching vessel.

To our knowledge, for human aortic endothelial cells (HAECs), this is the first report evaluating changes in peripheral blood mononuclear cell-endothelial cell (PBMC-EC) interaction and PBMC transendothelial migration (TEM) [3] when exposed to simultaneous mechanical and bio-chemical stimuli, critical to cardiovascular disease under a viral insult [4-7]. The adhesion of PBMCs to ECs is critical to the dysregulation of the EC-barrier functions, which directly impacts cardiovascular health. Pro-inflammatory cytokines, tumour necrosis factor-α (TNF-α) and interleukin-1β (IL-1β) disrupt the endothelium and facilitate TEM of monocytes into the arterial intima and induce vascular inflammation [8]. We report an evaluation of the inflammatory response of ECs to physiologically relevant fluid flow and three distinct inflammatory cytokines TNF-α, IL-1β, and lipopolysaccharide (LPS) using our microfluidic device.

MATERIALS AND METHODS

The microfluidic device was fabricated with standard soft lithography of PDMS (polydimethylsiloxane) for a bifurcating channel geometry with a bifurcation point (BP) and two branching vessels (BVs) (Figs. 1A and 1B). Each BV was 500 µm wide x 50 µm deep, separated by a 400 µm wide chamber containing type I rat tail collagen forming the ECM (pH 7.4) [9, 10]. The microchannel was lined with HAECs forming an endothelial barrier (Fig. 1C). In a related study with venous ECs we have reported the protocol to measure endothelial permeability using fluorescent dyes [9]. The same protocol was used here but modified for use with migration of PBMCs. Briefly, HAECs were incubated with 100 ng/mL of LPS or 10 ng/ml of IL-1β or 10 ng/mL of TNF-α, concentrations we have used previously to elicit EC activation, for 24 hours before perfusing carboxyfluorescein succinimidyl ester (CFSE)-labelled PBMCs through the channel. PBMCs were obtained from the fresh blood of healthy male donors. For static control, PBMCs were flushed through the device and incubated for 1 hour at 37˚C. For flow conditions, endothelial growth medium (EGM) containing PBMCs was perfused at 10 µL/min (producing physiologically relevant 38 dyn/cm^2 stagnation pressure and 3 dyn/cm^2 laminar shear stress (LSS)) for 1 hour at 37˚C (Fig. 1D).

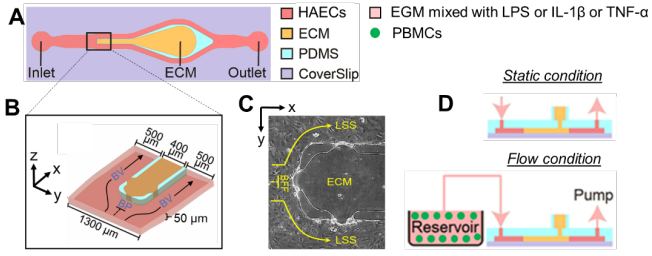

***Figure 1**: (**A**) Schematic of the microfluidic device, depicting the microchannels seeded with HAECs branching around the fibrous ECM. **(B)** Zoomed-in view of the bifurcation region illustrating the apertures at the bifurcation point (BP) and branched vessel (BV). (**C**) Phase-contrast image of HAEC monolayer (Scale bar: 100 µm). (D) Schematic of the experimental setup for "static condition" and "flow condition".*

RESULTS AND DISCUSSION

In a new finding, flow did not influence LPS or TNF-α induced PBMC binding but activated IL-1β for a 2-fold increase in PBMC-EC binding compared to no flow (Fig. 2). PBMC binding correlated to an increased adhesion protein (E-selectin) expression on the EC surface. Increased PBMC binding to ECs might have disrupted the endothelium barrier, initiating PBMC TEM for flow with IL-1β activation (Fig. 3). The binding of PBMCs was more at the BP than the BV for the flow with IL-1β activation suggesting a different mechanism of cell-binding mediated by stagnation pressure as opposed to fluid shear.

978-1-940470-04-7/HH2022/$25©2022TRF
DOI 10.31438/trf.hh2022.77

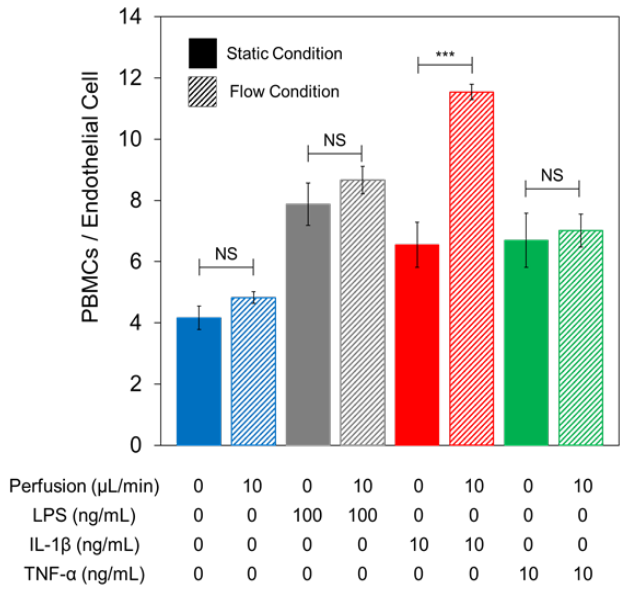

***Figure 2**: Quantitative representation of the number of PBMCs adhering to each endothelial cell for static and 10 µL/min perfusion (flow) condition, both in the absence and presence of LPS (100 ng/ml), IL1-β (10 ng/ml) or TNF-α (10 ng/ml). *** - p<0.001, NS – not significant. Error bars indicate ±SEM (Standard Error of Mean).*

The change in PBMC binding at the BP and BV did not occur for no flow with IL-1β activation. The difference in inflammatory response for IL-1β compared to TNF-α and LPS suggests that IL-1β, which plays a major role in regulating endothelial nitric oxide production, and is one of the major mediators of vasodilation in blood vessels and implicated in cardiovascular health.

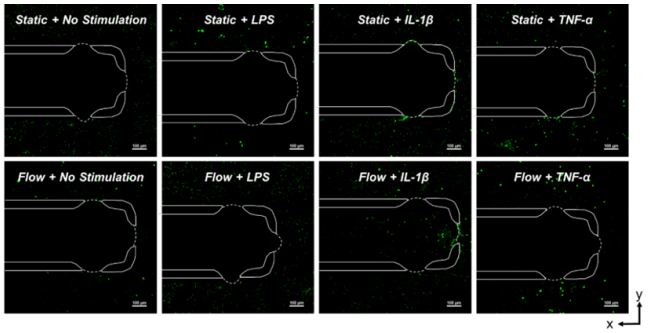

***Figure 3**: Confocal microscopy image showing PBMCs (CFSE tagged, green) transendothelial migration for both static and flow conditions, in the absence and presence of LPS, IL1-β and TNF-α. Scale bars are 100 µm.*

ACKNOWLEDGEMENTS

We acknowledge partial support for this work through the National Institutes of Health (Grant No. R01HL141941), US Army Research Office through grants numbered W911NF-16-0278 and W911-NF-1-0144. The authors acknowledge computational support and research license from the Ohio Supercomputer Center (OSC) and the OSU Nanotech West Cleanroom staff for assistance in fabrication. Images presented in this report were generated using the instruments and services at the Campus Microscopy and Imaging Facility (CMIF), The Ohio State University. This facility is supported in part by grant P30 CA016058, National Cancer Institute, Bethesda, MD. We also acknowledge support from the Ohio State College of Medicine and the Infectious Diseases Institute through their respective seed and bridge grant programs.

REFERENCES

1. A. S. V. Shah, D. Stelzle and K. K. Lee, (2018) " Global Burden of Atherosclerotic Cardiovascular Disease in People Living With HIV" *Circulation*
2. V. A. Triant, H. Lee, C. Hadigan and S. K. Grinspoon, (2007) " Increased acute myocardial infarction rates and cardiovascular risk factors among patients with human immunodeficiency virus disease", *Journal of Clinical Endocrinonology*
3. Cinamon, G. and R. Alon (2003) "A real time in vitro assay for studying leukocyte transendothelial migration under physiological flow conditions." *Journal of Immunological Methods*.
4. Bradfield, F. P., *et al.* (2007) "LPS differentially regulates adhesion and transendothelial migration of human monocytes under static and flow conditions", *International Immunology*.
5. Huang, R.B. and O. Eniola-Adefeso (2012) "Shear stress modulation of IL-1β-induced E-selectin expression in human endothelial cells." *PloS one*.
6. Lee, I., et al. (2010) "Acute myocarditis in dengue hemorrhagic fever: a case report and review of cardiac complications in dengue-affected patients." *International Journal of Infectious Diseases*.
7. Hemkens, G. L. and H. C. Bucher (2014) "HIV infection and cardiovascular disease", *European Heart Journal.*
8. Mamas, M. A., et al. (2008) "Cardiovascular manifestations associated with influenza virus infection." *International Journal of Cardiology*.
9. Akbari, E., *et al.* (2018) "Flow dynamics control endothelial permeability in a microfluidic vessel bifurcation model." *Lab on Chip*.
10. Sundaram, et a. (2021) "Direct current electric field regulates endothelial permeability under physiologically relevant fluid forces in a microfluidic vessel birfucation model.", *Lab on Chip*.

CONTACT

*Shaurya Prakash, tel: +1-614-688-4045; prakash.31@osu.edu

IN VITRO TRI-CULTURE BLOOD-BRAIN BARRIER (BBB) MODEL ENABLING DIRECT INTERCELLULAR CONTACT AT A SUSPENDED LAYER

Seungbeom Noh[*1], *Kenneth L. Monson*[2], *Vladimir Hlady*[3] *and Hanseup Kim*[1]
[1]Electrical and Computer Engineering, University of Utah, Salt Lake City, UT, USA
[2]Mechanical Engineering, University of Utah, UT, USA
[3]Bioengineering, University of Utah, Salt Lake City, UT, USA

ABSTRACT

This paper reports the development of an in vitro tri-culture BBB model that forms suspended BBB layers where direct intercellular connections among BBB cells are established. The in vitro BBB model consists of top and bottom culture chambers and a porous membrane with 30 µm holes, whose hole diameter is 2~3 times larger than the size of cells to allow direct cell-to-cell communication. The porous membrane was coated with hydrogel and a mixture of collagen IV and fibronectin, and the three types of BBB cells of the human brain microvascular endothelial cells, pericytes, and astrocytes were cultured on the membrane. The establishment of the tri-cultured BBB layers was validated by immunostaining. Immunostaining images provided a clear expression of three different identification proteins of the BBB cells confirming the establishment. Then, the successful culture of cells on the large-hole membrane was validated by the measurement of high TEER values of 67 $\Omega \cdot cm^{-2}$ and low permeability coefficient values of 2.9×10^{-7} $cm \cdot s^{-1}$. In summary, the development of the in vitro tri-culture BBB model was successfully delivered.

KEYWORDS

blood-brain-barrier (BBB), in-vitro model, direct cell-to-cell contact, intercellular interaction, SHH signaling pathway, tight-junction, tri-culture, suspended layers

INTRODUCTION

The blood-brain barrier (BBB) is a key structure in preserving homeostasis of the central nervous system (CNS) [1]. It is located between the blood and the brain, is composed of tightly bound cell layers, and provides selective chemical transportation. The BBB helps to prevent undesirable damage and malfunction of the CNS by clearing harmful substances [1]. Meanwhile, the BBB also inhibits drug transport to the brain in some cases. Thus, the BBB has been of critical interest to drug delivery in neuroscience research and the pharmaceutical industry in the past few decades.

Chemical transportation utilizes mainly two pathways through the BBB: the paracellular pathway and the transcellular pathway [1]. The paracellular pathway allows the transportation of hydrophilic chemicals smaller than intercellular tight-junction gaps. The transcellular pathway allows the transportation of lipophilic chemicals absorbed on the blood (luminal) side of the endothelial cells and conveyed to the brain (abluminal) side through the cells.

Interestingly, the expression of the sonic hedgehog (SHH) signaling pathway was reported to determine the tightness of the paracellular pathway [2]. This signaling pathway induces the synthesis of tight junction proteins such as claudin and occludin. However, the pathway becomes more activated when the distance between endothelial cells and astrocytes is small. Thus, the establishment of direct intercellular connection could lead to enhanced BBB integrity. Enhanced BBB integrity was observed by 10% higher trans-endothelial electrical resistance (TEER) values and 40% lower permeability coefficient values at the promoted SHH signaling pathway [3].

Current in vitro models, unfortunately, fail to provide direct intercellular connection. Despite advancements of multi-chamber structure and co-/tri-cultured BBB layers [4-9], membranes with sub-3 µm pore diameters and 10~30 µm thicknesses prevent direct intercellular communication and lower the probability that the signaling proteins of the SHH pathway reach their corresponding receptors. Recently, the development of an in vitro BBB model incorporating a thin silicon nitride (Si_xN_y) membrane was reported [10]. Despite the significantly reduced thickness of the membrane, direct cell-to-cell communication was limited due to the very small 0.5-µm diameter pore size.

To overcome such limitations, a novel in vitro BBB model incorporating larger-than-a-cell-sized holes and a thin hydrogel layer with an already validated polycarbonate membrane was developed. The membrane had 30-µm diameter large holes that allow BBB cells to form layers with an almost-zero distance between them. The hydrogel layer provides an initial extracellular matrix for seeding astrocytes, leads the astrocytes to be connected across the pores in the lateral direction, and is removed before the

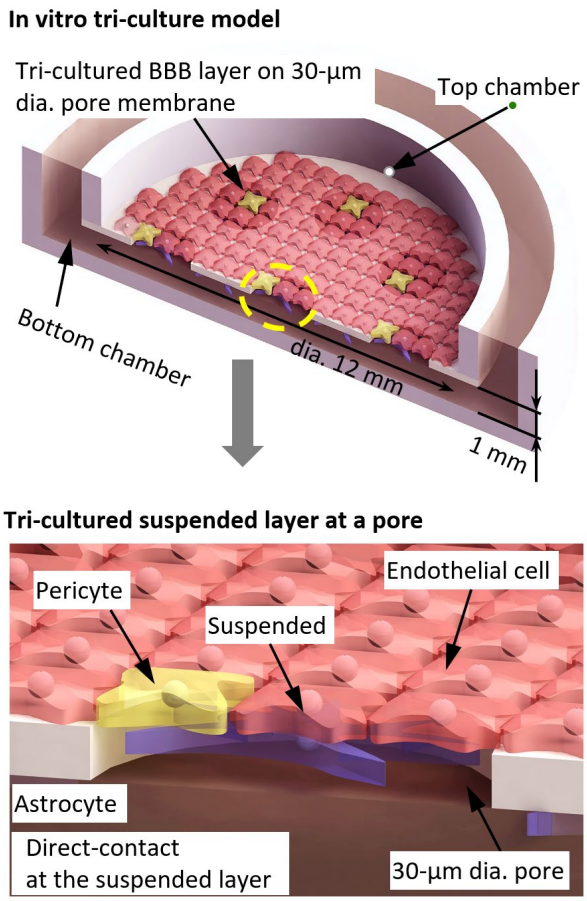

Figure 1. Illustrations of the in vitro tri-culture BBB model at the multi-chamber structure and the detailed suspended cell layers at a pore.

other BBB cells of endothelial cells and pericytes are seeded. Thus, direct cell-to-cell contact between endothelial cells and astrocytes is achieved as shown in Fig.1. Additionally, pericytes are included in this in vitro BBB model to help the proliferation and differentiation of the BBB cells [11].

This paper reports a novel in vitro tri-culture BBB model that is capable of providing suspended cell layers with direct cell-to-cell contact. The fabrication of the in vitro model, tri-culture of BBB cells, and evaluation of the suspended cultured BBB layers and the direct cell-to-cell contact are described.

METHODS

Structure & Fabrication

The tri-culture platform consisted of one porous membrane separating top and bottom chambers. A commercially validated transwell (3413, Corning, NY) was utilized to provide the multi-chamber structure. The existing membrane was replaced with a sheet of porous polycarbonate membrane using adhesive (SILASTIC, Medical Adhesive Silicone, Type A, Dow-Corning, MI) in Fig.2(b). The new polycarbonate membrane had 30-µm diameter pores at 1×10^4 pores·cm^{-2} pore density and 7% porosity (hydrophilic polycarbonate membrane, Sterlitech, WA). The 30-µm diameter pores were larger than the cell sizes of 10~15 µm [1]. The membrane was cut in an 8-mm diameter circle using surgical scissors. The top side of the membrane was then coated with a degradable hydrogel (TrueGel3D, SigmaAldrich) and cured under the pressure of 7.0×10^1 kPa with a 1 kg mass overnight at room temperature.

Spin-Coating Hydrogel Layer

A thin hydrogel layer was spin-coated to form a suspended extracellular matrix on the porous membrane. The hydrogel layer (a) was made by mixing 4 different components of a degradable polymer, cell-degradable solution, buffer solution, and water following the product information [12]. The degradable polymer was mixed with the buffer solution at 300 rpm using a vortex mixer (97043-562, VWR), and the degradable polymer mixture solution was incubated for 1 hour at room temperature. Separately, the cell-degradable solution was diluted with water using the vortex mixer. This cell-degradable solution was incubated for 5 min at room temperature. Then, a final hydrogel solution was prepared by mixing 10 µl culture medium, 36 µl degradable polymer mixture solution, and 4 µl cell-degradable solution. Hydrogel solution (50 µl) was then applied on the top surface of the 30 µm hole membrane on a Si-wafer, and the Si-wafer was spun at 1000 rpm for 40 seconds (WS-400A, Laurell Technologies). The hydrogel-coated membrane was incubated at 37 °C for 20 minutes in Fig.2(b).

Cell culture

Tri-cell culture was performed with human brain microvascular endothelial cells (HBMECs), human brain perivascular cells (pericytes), and human brain astrocytes.

When the cells were fully cultured in a flask at conditions of 37 °C and 5% CO_2 in an incubator (NU-4750, Nuaire), they were seeded into the in vitro tri-culture BBB model. A mixture of mouse collagen type IV (354233, Corning, NY) and human fibronectin (354008, Corning, NY) at a concentration of 100 µg·ml^{-1} in Fig.2(c) was prepared. The 200 µl mixture was applied to the bottom surface of the membrane and left in the incubator at 37 °C for 30 minutes. The astrocytes were seeded to the bottom surface of the top chamber at the concentration of 5.0×10^4 cells·cm^{-2}, and cultured in the incubator for 2 hours in Fig.2(d). The top chamber was flipped and placed into the culture well plate, and the astrocytes were cultured for 3~4 days in Fig.2(e). When the astrocytes were successfully

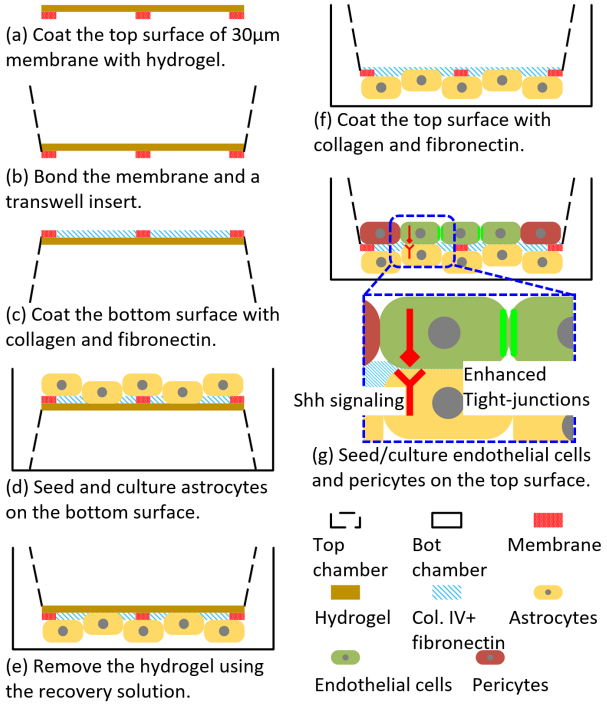

Figure 2. Processes of fabrication, coating, and cell-culture. Top chamber was fabricated with a transwell insert and 30 µm membrane, the coating was performed with biodegradable hydrogel, collagen and fibronectin, and the brain cells were cultured on the suspended layer.

cultured, the hydrogel on the top surface of the membrane was removed by applying a cell recovery solution of the hydrogel product [12]. Cell recovery solution (600-µl) was applied to the top side of the chamber where the hydrogel was present. The culture chamber was incubated at 37 °C for 30 minutes. After the hydrogel layers were removed, the top surface of the membrane was coated with the mixture of collagen type IV and human fibronectin at the same concentration in Fig.2(f). The pre-cultured HBMECs and pericytes were seeded onto the top surface of the membrane at the concentration of 10.0×10^4 cells·cm^{-2} and 1.0×10^4 cells·cm^{-2}, respectively. Finally, the BBB cells were cultured for ≥5 days, and the culture media was changed daily in Fig.2(g).

Suspended Tri-Cultured Cell Layers

The suspended tri-cultured cell layers were validated by optical and immunostaining images and fluidic movement testing. The porous membrane coated with the hydrogel and the mixture of collagen type IV and fibronectin was imaged using a color microscope (EVOS FL Auto, Thermo Fisher). The image was taken before the astrocytes seeding. Immunostaining images were taken with a confocal microscope (FV1000, Olympus), after the cells were successfully cultured. Immunostaining imaging using the confocal microscope proved the presence of identical biomarkers indicating three different cells on the culture membrane. Primary antibodies (abcam, MA) of zonula occludens (ZO-1) for HBMECs, platelet-derived growth factor receptor (PDGFR) beta for pericytes, and glial fibrillary acidic protein (GFAP) for astrocytes were selected as biomarkers, and they were visualized using the secondary antibodies (Thermo Fisher Scientific, MA). The nuclei of the cells were stained with DAPI (Enzo, NY) in phosphate-buffered saline (PBS) for 20 minutes. Immunostaining images showing direct

contact between BBB cells were taken every 1 µm thickness using the confocal microscope. Stacked images (2D and 3D) from the optical and confocal microscopes were then post-processed using ImageJ (version 1.53f51; National Institutes of Health) and analyzed.

Additionally, the successful formation of the suspended cell layers was verified with a measurement of hydraulic flow at the media application of 200 µl to the top chamber and 600 µl to the bottom chamber. After 30 minutes, the height difference between the top and bottom chambers was recorded.

Measurements of TEER and permeability

After cell seeding, cell growth was monitored by real-time TEER values (EVOM^2 epithelial voltmohmeter, WPI), every day from Day 0. TEER values were determined in $\Omega \cdot cm^2$ according to the equation (1), $TEER = (R - R_{blank}) \times A$ (1), where R is the total resistance (Ω), R_{blank} is the background resistance (Ω) on Day 0, and A is the cell culture area (cm^2) [4]. After the TEER values were saturated, permeability coefficients were measured with 100 µM FITC-4k dextran in the tri-culture platform. The amount of permeated compound collected from the bottom chamber was then measured using a spectrometer (495/525 nm, SpectraMax Plus 384 Microplate Reader). The permeability coefficients P were calculated using equation (2), $P = J_s \times A^{-1} \times C_L^{-1}$ (2), where P is the permeability coefficient ($cm \cdot s^{-1}$), J_s is solute flux across the cell layers ($mol \cdot s^{-1}$), A is the membrane area (mm^2), and C_L is the concentration ($mol \cdot m^{-3}$) on the top channel, as previously described and used in [4].

RESULTS

The in vitro tri-culture BBB model with 30-µm diameter pore membrane was successfully fabricated. Successful culture of the suspended tri-culture BBB cell layers was verified, and direct contact between BBB cells were established at the pores of the membrane. These results were validated by imaging and hydrostatic flow testing and were further supported by the measurement of TEER values and permeability coefficients in Fig. 3-6.

Verification of Suspended Tri-Cultured Cell layers

The optical image of the membrane shown in Fig. 3(a) proved the formation of the successfully spin-coated hydrogel layers at the membrane. The observed collagen and fibronectin indicated the suspended layer of the hydrogel. The nuclei-stained image shown in Fig. 3(b) proved the cells were cultured and present on top of the pores. Culture of the BBB cells successfully covered the pores, proven by the result of no fluid movement across the tri-cultured BBB layers in Fig.3(c). Finally, the successful culture of three different cells of HBMEC, pericytes, and astrocytes was validated by the immunostaining image in Fig. 3(d). Identical protein expressions (green: HBMEC [ZO-1], red: pericytes [PDGRF], yellow: astrocytes [GFAP], and blue: nuclei) proved the successful tri-culture across the 30-µm diameter pore membrane. The merged image shows that fully confluent cell layers were established across the suspended cell layers. Thus, Fig. 3 supports the establishment of the suspended tri-cultured cell layers.

Evaluation of Direct Cell-to-Cell Contacts

Direct contact between BBB cells was confirmed via imaging, as shown by the 3D stacked image in Fig. 4. Side views of the reconstructed image show cell connections through the 30-µm pores. The images imply that intercellular connections are unlikely using conventional 20~30 µm thick membranes.

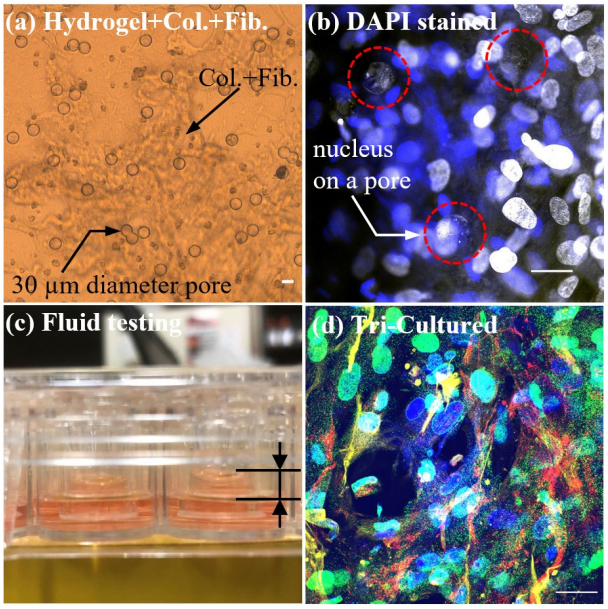

Figure 3. Images proving suspended cell layers and extracellular matrix. (a) optical image after coating with the hydrogel, collagen IV and fibronectin, (b) DAPI stained image showing nucleus existing on pores, (c) recorded photo showing a height difference between the top and bottom chambers after 30 min, and (d) merged image of the three different BBB cells. Scale bar: 30 µm.

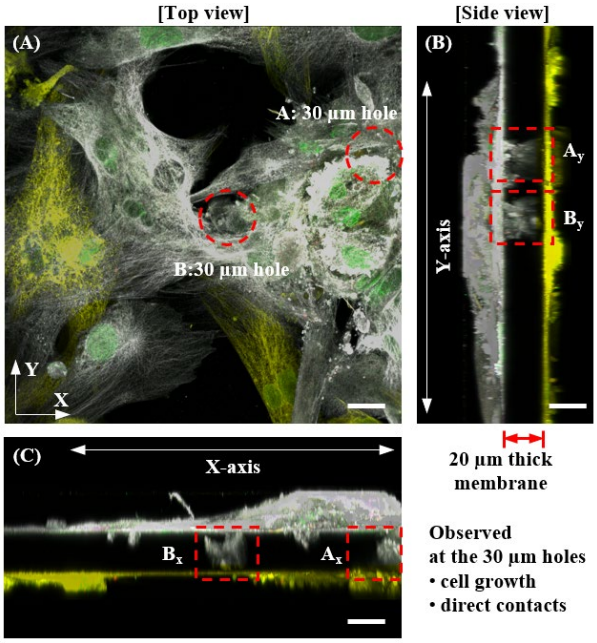

Figure 4. Reconstructed 3D stack images of the BBB cell layers (a) 3D stacked image from the immunostaining images taken every 1 µm, (b) Side-view image along Y-axis, and (c) side-view image along X-axis. Endothelial cells and pericytes are shown as gray, and astrocytes are shown as yellow. Scale bar: 20 µm

Evaluation of TEER and permeability

Higher TEER and lower permeability coefficient values prove the enhanced BBB integrity at the suspended tri-cultured BBB layers in Fig.5. TEER measurement showed the saturated

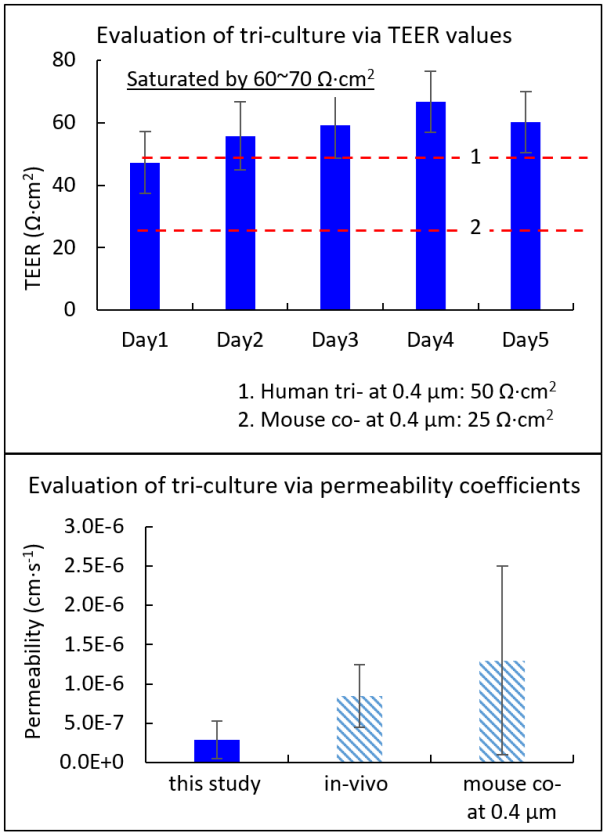

Figure 5: Evaluation of the established tri-culture cell layers via (a) measurement of TEER values for 5 days and (b) measurement of permeability coefficients on day 5.

TEER value of 66 Ω·cm^2 after 5 days of culture, which was 164% higher than the previous measured TEER values of the co-culture cell layers of mouse BBB cells seeded on a conventional membrane [4,13,14]. The tight BBB integrity was also proven with the measured permeability coefficient values, which were 66% and 81% lower than the previously measured in-vivo mouse test and in-vitro mouse co-culture test [14,15]. Thus, it is concluded that there is a strong correlation between the establishment of direct intercellular contact and BBB integrity.

CONCLUSION

This study reported the development of a tri-culture platform that enables building suspended BBB layers by incorporating 30 µm pores and an extracellular matrix consisting of biodegradable hydrogel, collagen IV and fibronectin. The HBMECs, pericytes, and astrocytes were successfully cultured, and direct contact between cells was successfully established. Finally, evaluations of the established BBB layers were performed by optical and immunostaining imaging, and measurement of TEER values and permeability coefficient values. The evaluations indicate that the suspended tri-culture BBB layers would be able to provide an in vitro testing tool of the brain microvascular system that is physiologically and mechanically more representative of the human BBB system.

ACKNOWLEDGEMENTS

This project was performed under generous financial support through the USTAR program funds provided by the State of Utah. Fabrication was performed at the state-of-the-art University of Utah Nano Fabrication Facility located in the Sorenson Molecular Biotechnology Building. The authors thank Prof. Hamid Ghandehari's group and Prof. S. Michael Yu's group (University of Utah, Salt Lake City, UT) for access to spectrometers and microscopes.

REFERENCES

[1]. Arthur J. Vander, and et al., "Human Physiology: The mechanisms of Body Function", 8th edition, McGraw Hill, 2001.

[2]. Gabriela Basile Carballo, and et al., "A highlight on Sonic hedgehog pathway," Cell Communication and Signaling, 2018, 16:11

[3]. Jorge Ivan Alvarez, and et al.,"The Hedgehog Pathway Promotes Blood-Brain Barrier Integrity and CNS Immune Quiescence," Science, 2011, 334, pp.1727-1731

[4]. Ross H. Booth and Hanseup Kim, "Characterization of a microfluidic in vitro model of the blood-brain barrier (µBBB)," Lab Chip, 2012, 12, 1784

[5]. Ross H. Booth, Seungbeom Noh and Hanseup Kim, "A multiple-channel, multiple-assay platform for characterization of full-range shear stress effects on vascular endothelial cells," Lab Chip, 2014, 14, pp.1880-1890

[6]. Ross H. Booth and Hanseup Kim, "Permeability analysis of neuroactive drugs through a dynamic microfluidic in vitro blood-brain-barrier model," the Annals of Biomedical Engineering, Aug. 2014. Published, 11/04/2014.

[7]. Seungbeom Noh and Hanseup Kim, "In-air EIS sensor for in situ and real-time monitoring of in vitro epithelial cells under air-exposure," Lab Chip, 2020, 20, pp.1751-1761.

[8]. Luca Cucullo, and et al.,"Immortalized human brain endothelial cells and flow-based vascular modeling: a marriage of convenience for rational neurovascular studies," J. Cereb. Blood Flow Metab., 2008, 28, 312-28.

[9]. Tae-Eun Park, and et al.,"Hypoxia-enhanced Blood-Brain Barrier Chip recapitulates human barrier function and shuttling of drugs and antibodies," Nature Communications, 2019, 10, 2621.

[10]. Diana Hudecz, and et al.,"U ltrathin Silicon Membranes for in Situ Optical Analysis of Nanoparticle Translocation across a Human Blood−Brain Barrier Model," ACS Nano, 2020, 14:1, 1111-1122.

[11]. Zhangsen Huang, and et al.," Blood-brain barrier integrity in the pathogenesis of Alzheimer's disease," Frontiers in Neuroendocrinology, 2020, 59:100857, pp.1-13.

[12]. Technical Bulletin: TRUE1, TrueGel3D Hydrogel Kits, Sigma-Aldrich.

[13]. Nicole L. Stone and et al, "A Novel Transwell Blood Brain Barrier Model Using Primary Human Cells," Front. Cell. Neurosci., 2019, 13:230

[14]. Guanglei Li and et al., "Permeability of Endothelial and Astrocyte Cocultures: In Vitro Blood–Brain Barrier Models for Drug Delivery Studies," Ann Biomed Eng., 2010, 38(8), pp.2499–2511

[15]. Wei Yuan and et al., "Non-invasive measurement of solute permeability in cerebral microvessels of the rat," Microvascular Research, 2009. 77 , pp.166–173

CONTACT

* Hanseup Kim, tel: +1-801-587-9497; hanseup.kim@utah.edu

IN-SOIL BIODEGRADABLE ZN-AIR BATTERIES

Jingwen Zhang and Mark G. Allen
University of Pennsylvania, Philadelphia, Pennsylvania, USA

ABSTRACT

Increasing interest in data collection for agricultural and environmental sciences has created a need for long-term soil monitoring by wireless sensors. However, implementation of such sub-surface sensors may require on-board power, both for sensor functionality as well as wireless communication. To address this issue, we present Zn-air batteries built from biodegradable materials that can operate on or under the soil. Wax-encapsulated Zn-air electrochemical cells ('batteries') were fabricated based on thin film anodes, catalyst-bearing paper cathodes, and biodegradable gel electrolyte. The batteries provided a stable output voltage of over 1.2 V in soil for a week under relevant sensor discharge conditions.

KEYWORDS

Zinc-air batteries, biodegradable, long-term, in-soil condition

INTRODUCTION

Recent advances in sensor fabrication, wireless communication, and data analysis have led to the establishment and widespread implementation of wireless sensor networks (WSNs). Such networks can be a powerful tool for monitoring large physical areas in a variety of applications, including the natural environment as well as agriculture [1]. The deployment of a variety of subsurface sensors that monitor ambient conditions such as soil moisture, temperature and nutrient level, enable collection of accurate information of the field or farm in real time [2]; such information can be used to drive subsequent agricultural optimizations or interventions in the field.

As a WSN typically operates in a long-term, continuous mode, available energy resources become one of the most crucial challenges. This problem is exacerbated by the need for periodic data collection, node-level or cluster-level data processing, and data communication over the potentially long distances between the sensor nodes and gateways or base stations [1], [3]. Such subsurface sensor networks are often expected to operate without human intervention; however, in many applications, they are expected to be deployed in areas away from convenient access to the established energy grid. Although conventional on-board energy sources could be used to power these sensors, it would be time-consuming and costly to re-collect the sensing systems after the functional lifetime of the sensors has expired, or to replace the energy sources once they are depleted. One solution to this problem is onboard energy sources that can power the subsurface sensors during their functional lifetime, and passively degrade in an environmentally benign fashion after use or exhaustion. Our goal is to develop such long-lifetime, biodegradable, primary energy sources (biodegradable electrochemical cells, or 'biodegradable batteries'), and assess their performance in in-soil conditions.

Selection of the active materials of a conventional battery is mainly based on their performance and electrochemical stability. In contrast, the material requirements for biodegradable batteries are more stringent, considering that not only do the batteries need to exhibit good electrochemical performance and stable output over the operation lifetime, but have the additional constraint of passive degradation into nontoxic products, especially in agricultural settings [4].

Metal-air batteries have attracted significant attention due to their high theoretical energy density and high specific capacity compared to commercial Li-ion batteries. A typical metal-air battery comprises a metal anode and an air cathode (normally comprised of a gas diffusion layer and a catalyst layer) [5]–[7]. The anode and cathode are separated by an electrolyte. The metal is oxidized into metal ions at the anode, while oxygen from the ambient air is absorbed and reduced to hydroxide ions in presence of H_2O at the cathode. In such batteries the oxidant is not stored within the battery volume but instead is extracted from the ambient; this approach enables high energy density, a more compact battery structure, and the potential for reduced environmental impact of the battery (since less material is introduced at the cathode side).

Among the metal-air batteries, Zn-air, Li-air, Al-air and Mg-air have been widely researched [8]. Of this materials set, Mg and Zn are the most popular biodegradable metals previously utilized in transient batteries [4], [9]. Though Mg-air batteries have higher theoretical capacity, their large polarization and high self-corrosion rates make them less favorable for long term applications [10]. Zn-air batteries are a very promising power source for biodegradable sensing systems, due to their high theoretical specific energy density (1084 Wh/kg), abundance of raw materials, safety, low cost, flat discharge voltage, and relatively low corrosion rate [7].

In addition to anode materials, the packaging, electrolyte/separator, and cathode must also be considered. For the package, blends of natural waxes such as those derived from soy and beeswax have been reported as slowly biodegradable hydrophobic encapsulants for soil moisture sensors by Sui et al. [11] ; such waxes protected the sensor for an extended functional lifetime in soil. Simultaneous ecotoxicity tests suggested that these waxes do not hinder the growth of maize. For the separator, the biodegradable and water-soluble polymer poly-(vinyl alcohol) (PVA) can be formed into a hydrogel that functions both as the host of an alkaline electrolyte as well as a separator for Zn-air batteries. The fabrication process for such electrolytes was reported in our previous work [12]. For the cathode, commercially-available Platinum (Pt) loaded air cathodes can be considered, especially for laboratory testing. Ultimately, functional carbon electrodes, including nanostructured carbon and doped carbon, may be lower cost alternatives to Pt-loaded cathodes [13].

Air batteries are typically characterized in air or oxygen [14], [15]. For this application, we will investigate wax-packaged Zn-air batteries buried in soil. Week-long subsurface lifetimes of batteries have been achieved. Preliminary characterization of Pt-free carbon paper cathodes, typically used as a gas diffusion layer for fuel cells, suggests the carbon-based materials can be promising replacements of Pt cathodes for low-power long-term application.

EXPERIMENTAL

Active battery components: For anodes, commercial zinc foils (99.9% pure, 250 μm, Sigma Aldrich) were patterned into disks with strip using an IPG Microsystem IX-200-F green laser (532nm). The disk is 1 cm diameter and comprises the electrochemically active area of the anode, while the strip is utilized for external electrical connection. For air cathodes, commercial Platinum Black paper (4 mg cm^{-2} loading, Fuel Cells Etc.) and carbon paper (Sigracet 22 BB, Fuel Cells Etc.) were purchased and cut into 1 cm diameter discs using a hollow steel punch. Hydrogel electrolyte sheets were fabricated by solution-casting followed by rehydration [2]. 1.5 mg PVA (87-89% hydrolyzed, high molecular weight, Alfa Aesar) was first dissolved in 10 g of deionized water at 85°C. An

978-1-940470-04-7/HH2022/$25©2022TRF
DOI 10.31438/trf.hh2022.79

alkaline solution was prepared by dissolving 1.5 g KOH and 0.64 g K_2CO_3 in 10 g deionized water. After cooling both solutions, the alkaline solution was added to the PVA solution dropwise. The resultant PVA-KOH-K_2CO_3 precursor was then cast onto a glass petri dish, dried in a desiccator, and immersed in saturated KOH-K_2CO_3 solution for more than 2 days. After gel removal from the rehydration solution, discs with a diameter of 1.27 cm were cut from the gel using a second hollow steel punch (this slightly larger gel disc area prevents any short circuit contact between anode and cathode). Gel discs of different mass and thickness were realized by controlling the amount of the precursor used in the gel casting stage.

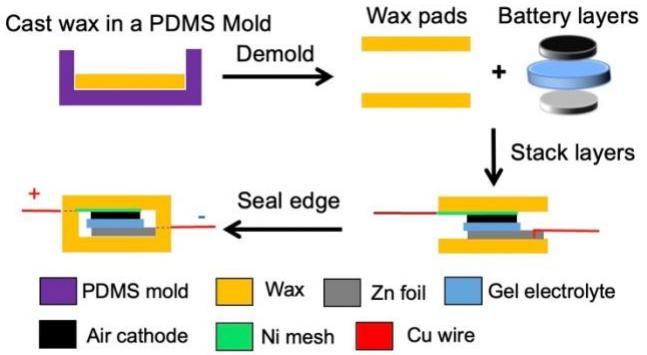

Figure 1: Cross-section of the fabrication process.

Assembly and Packaging: Figure 1 illustrates a cross-section of the wax encapsulation and packaging process. Two types of wax encapsulated batteries, with and without airholes, were fabricated using this method. The preparation of the wax itself is adopted from [11]. Beeswax and soy wax were mixed in a 1:3 mass ratio, melted at 80 °C, and cast in a PDMS mold (10:1 pre-polymer/curing agent, cured at 80 °C). The top and bottom encapsulation pads were demolded after solidification at room temperature. Open airholes were optionally introduced to the top wax pad (the one closest to the cathode side) by using a needle to punch through the pad. The three functional layers of the battery were then sandwiched between the pads, with a thin layer of Ni mesh contacting the cathode side to facilitate testing. Both Ni mesh and anode handle were attached to insulated Cu wires by silver paste for secure external connection. Finally, the four edges of the two pads were manually sealed by melted wax with interconnects enclosed to avoid parasitic leakage current when the battery is discharged in soil.

Reference batteries without packaging were also tested using a clamp board technique. Pairs of acrylic clamp boards with a porous structure in one board were fabricated by CO_2 laser machining and used to immobilize the active battery stack; a pair of screws extending between the boards could be tightened to clamp the active stack together.

Referring to Figure 2, Figure 2(a) shows a schematic of the wax-encapsulated battery, and Figure 2(b) shows the detail of how the nickel mesh structure is attached to the battery cathode. The remaining figures show wax encapsulated batteries with and without air holes, as well as a typical clamp board reference battery.

Test environments: To characterize in-soil performance, the batteries were placed in organic raised bed soil (Harvest Organics, Lowe's) inside 600 mL beakers at a controlled buried depth of 5 cm. Figure 3(a) shows a wax encapsulated battery in a beaker half-filled with soil. After the battery was placed, extra soil was placed on top until the desired depth is reached as shown in Figure 3(b). Copper wires extend from the buried battery to the anodic and cathodic clips of a battery cycler. Batteries of similar packages and gel masses were also tested in the air as references to the in-soil-tested devices.

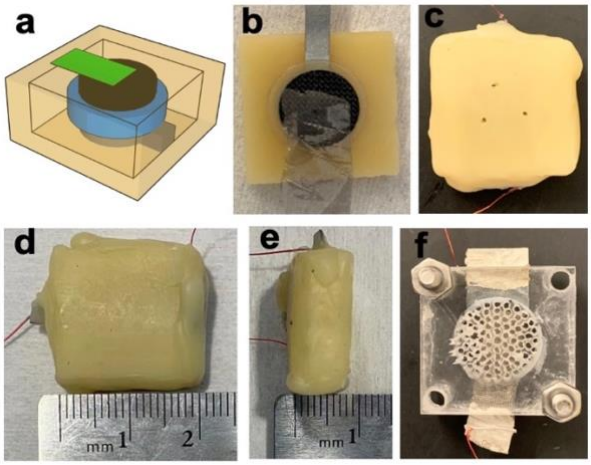

Figure 2: (a) Schematic of wax encapsulated Zn-air battery, (b) top view of a battery on a wax pad, (c), (d) top views of wax encapsulated batteries with and without airholes, (e) side view of a battery with wax package, (f) top view of a clamp board battery.

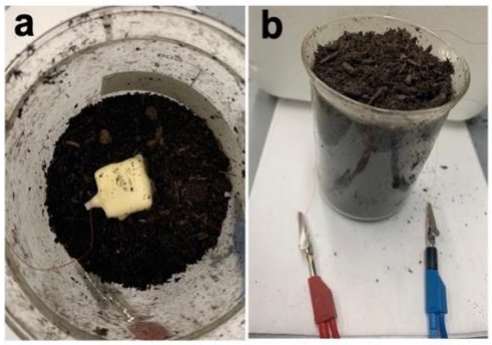

Figure 3: (a) Top view of a battery tested in soil, (b) front view of battery soil test set-up.

Performance characterization: Electrochemical assessment was performed using a BioLogic BCS-805 Ultra-Precision battery cycler. A 10-minute open circuit potential test was first carried out to stabilize the batteries in their respective environments. A current-voltage (I-V) curve to demonstrate the power capability of the battery was then performed through a galvanodynamic test with a scan rate of 5 mA/s from 0 to 100 mA. Battery performance was then characterized by chronopotentiometry testing. Batteries with Pt loaded cathodes were discharged at 30 μA, which is selected based on the power requirements of both MEMS fabricated oxygen sensors as well as RFID chips [16], [17]. A higher discharge current of 1 mA was utilized when characterizing the carbon paper cathodes to understand their catalytic performance in the absence of Pt. A typical 0.9 V cut-off voltage was taken as an endpoint of battery operation.

RESULTS AND DISCUSSION

A notable characteristic of air batteries is that their need to access ambient oxygen typically requires some degree of exposure to the environment. The performance of the battery may therefore be significantly affected by multiple variables in its operating environment. To assess these effects, batteries were characterized in multiple environments (air, 5cm deep in soil) and with multiple degrees of environmental exposure (clamp board, wax package with air holes, wax package with no holes) as shown in Figure 4. In these tests, the gel electrolyte mass was held constant at 38 mg to

eliminate the effect of the amount of gel.

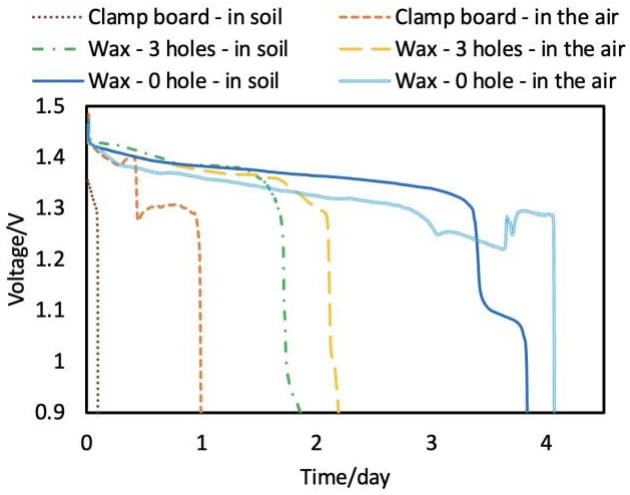

Figure 4: Discharge curves of batteries in various packages in the air and in soil.

The lifetime of the batteries discharged in the air were longer than the ones in soil for all three types of packages. This might be due to the influence of the soil condition. Soil is a porous structure containing solid particles, water and gas [18]. The relative humidity of the soil gas is close to 100% which is much higher than the air [19]. The alkaline electrolyte could absorb more water from the ambient environment when the battery is buried under soil, which could possibly lead to lower concentration of the OH^- in the gel electrolyte. As the solubility of intermediate zincate ion product at the anode side reduces with decreased pH, the zincate ion might reach the supersaturation point earlier and decompose to ZnO, resulting in more rapid passivation of the anode [15].

Another potential mechanism behind the variation of the lifetimes of batteries is carbonation. The OH^- ions in the hydrogel provide the ionic conductivity for the battery. While theoretically no OH^- will be consumed in the overall reaction, CO_2 in the air can diffuse together with O_2 into the battery, and react with the OH^- ions in the alkaline electrolyte to form CO_3^{2-} or HCO_3^-, which have much higher ionic resistivity than OH^- [20]. Since the amount of gel electrolyte is a relatively small 38 mg, the OH^- could be consumed gradually over time (as well as the electrolyte pH falling over time) as the battery discharges. When the concentration of OH^- falls too low, the reduced ionic conductivity can induce a large overpotential, leading to the end of discharge.

Clamp board batteries are the most vulnerable to such environmental variables, since CO_2 and moisture can access the battery not only from the maximally exposed porous structure at the cathode side, but also from side openings. It was thus not surprising to observe that the discharge lifetime of the clamp board batteries was the shortest. Wax-encapsulated batteries with air holes sustained a much longer discharge lifetime, perhaps due in part to the hydrophobic nature of the waxes, which results in extremely low water vapor permeability [21], as well as increased mass transfer limitations between the ambient and the porous cathode.

The wax-encapsulated battery with no air holes provided the longest lifetime both in the air and in soil. This might be due to its minimal exposure to the CO_2 and water vapor in the air and soil gas. However, the question of how these air batteries can function with no nominal air path should be addressed. One possibility is that even though there are no nominal air paths to the ambient, imperfections in sealing result in parasitic air paths sufficient to sustain battery discharge. Another possibility comes from noting that even though the wax has low water vapor permeability, it is permeable to oxygen [21]. The long continuous discharge suggests that even with no nominal air holes, these mechanisms can sustain the low discharge current of 30 μA and fulfill the power requirement of the subsurface sensors.

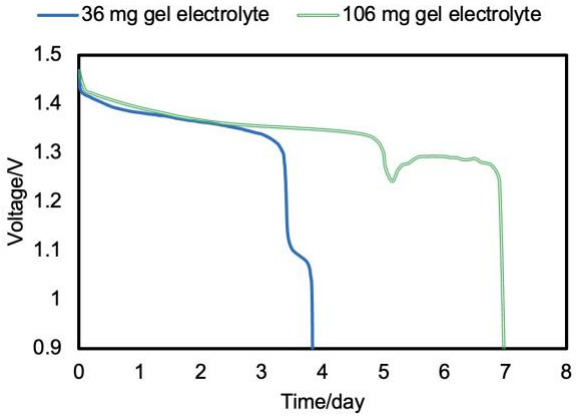

Figure 5: Discharge curves of wax encapsulated batteries (no hole) with different gels in the soil environment.

Since batteries fully encapsulated in wax with no nominal air holes result in superior discharge performance over other packages both in the air and in soil, this geometry was chosen to determine the effect of gel electrolyte mass on battery lifetime. As shown in Figure 5, an increase in the gel mass from 36 mg to 103 mg resulted in an 80% increase in battery discharge lifetime, supporting the hypothesis that the gel electrolyte can limit the performance of the batteries when its mass is low. Remarkably, the fully wax-encapsulated battery with 103 mg gel electrolyte provided a constant output voltage of over 1.2 V for 7 days in soil under a constant 30 μA discharge current.

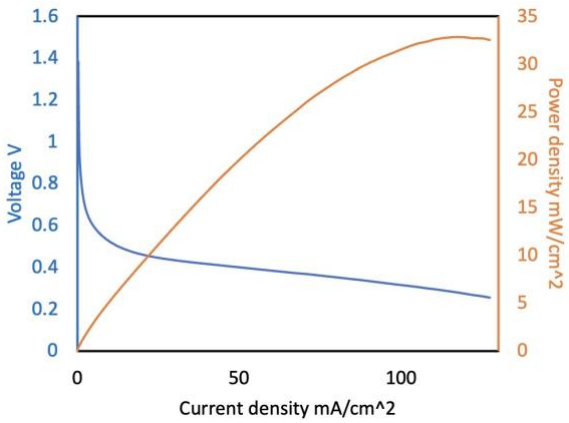

Figure 6: Power curve of the carbon paper cathode with 80 mg of gel electrolyte.

For cost considerations, we have also investigated replacing the air cathode bearing a Pt catalyst with commercial carbon fiber paper. Pt is a traditional oxygen reduction reaction catalyst that has high activity. A concern with replacing Pt with carbon is that the relatively low catalytic activity of carbon would lead to a higher energy barrier for the cathodic reaction and poorer power performance of the air battery [13]. However, it is also noted that in many of these WSN applications, low power output is acceptable.

As an initial test, a carbon-paper cathode material (Sigracet 22 BB) was tested with 80 mg gel electrolyte and clamp boards in air. This cathode material has a bilayer structure that consists of carbon fiber paper support and a carbon micro-porous layer. A galvanodynamic scan of this battery was performed to assess its power output as shown in Figure 6. Benefitting from the high surface area of the microporous layer, the peak power of the carbon paper clamp board battery is 32.9 mW/cm^2, much higher than the tens of μW needed for sensor operation.

Figure 7 shows the discharge profile of the clamp board carbon paper battery. The working voltage of the battery exceeds 1 V under a relatively large discharge current of 1 mA, illustrating that the carbon cathode alone has sufficient catalytic activity for WSN applications at even at higher discharge rates. These results indicate the utility of carbon cathodes in these applications, as well as the potential of Zn-air batteries as biodegradable power sources to sustain long-term operation in subsurface conditions.

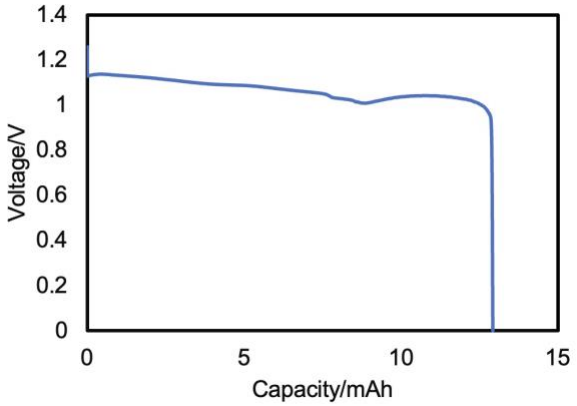

Figure 7: Discharge profile of a battery with a carbon paper cathode at a constant discharge current of 1 mA in air.

CONCLUSIONS

We present the materials and designs of Zn-air batteries with biodegradable package and gel electrolyte. The performance of the batteries with wax and clamp board in the ambient air and in soil environment are characterized by 30 μA constant current discharge. Biowax encapsulation are found to be functional packages both in air and in soil. A wax-encapsulated Zn-air battery with 103 mg gel electrolyte discharged over a week in soil at 5 cm depth. Carbon paper cathodes were also tested and shown to have sufficient catalytic activity for these WSN applications. We believe these results show the potential of Zn-air batteries as biodegradable power sources to sustain long-term operation in subsurface conditions for agricultural applications.

ACKNOWLEDGEMENTS

This material is based upon work primarily supported by the IoT4Ag Engineering Research Center funded by the National Science Foundation (NSF) under NSF Award Number EEC-1941529. This work was also carried out in part at the Singh Center for Nanotechnology, which is supported by the NSF National Nanotechnology Coordinated Infrastructure Program under grant NNCI-2025608.

REFERENCES

[1] P. Corke, T. Wark, R. Jurdak, W. Hu, P. Valencia, and D. Moore, "Environmental wireless sensor networks", *in Proceedings of the IEEE*, 98, 11 (2010).

[2] H. M. Jawad, R. Nordin, S. K. Gharghan, A. M. Jawad, and M. Ismail, "Energy-efficient wireless sensor networks for precision agriculture: A review", *Sensors (Switzerland)*, 17, 8 (2017).

[3] S. Sharma, R. K. Bansal, and S. Bansal, "Issues and challenges in wireless sensor networks", Proceedings - 2013 International Conference on Machine Intelligence Research and Advancement, ICMIRA 2013, 2014.

[4] N. Mittal, A. Ojanguren, M. Niederberger, and E. Lizundia, "Degradation Behavior, Biocompatibility, Electrochemical Performance, and Circularity Potential of Transient Batteries", *Advanced Science*, 8, 12 (2021).

[5] N. Chawla, "Recent advances in air-battery chemistries", *Materials Today Chemistry*, 12 (2019).

[6] V. Caramia and B. Bozzini, "Materials science aspects of zinc-air batteries: A review", *Materials for Renewable and Sustainable Energy*, 3, 2 (2014).

[7] J. S. Lee et al., "Metal-air batteries with high energy density: Li-air versus Zn-air", *Advanced Energy Materials*, 1, 1 (2011).

[8] Md. A. Rahman, X. Wang, and C. Wen, "High Energy Density Metal-Air Batteries: A Review", *Journal of The Electrochemical Society*, 160, 10 (2013).

[9] X. Jia, C. Wang, C. Y. Lee, C. Yu, and G. G. Wallace, "Energy materials for transient power sources", *MRS Bulletin*, 45, 2 (2020).

[10] T. Zhang, Z. Tao, and J. Chen, "Magnesium-air batteries: From principle to application", *Materials Horizons*, 1, 2 (2014).

[11] Y. Sui, M. Atreya, S. Dahal, A. Gopalakrishnan, R. Khosla, and G. L. Whiting, "Controlled Biodegradation of an Additively Fabricated Capacitive Soil Moisture Sensor", *ACS Sustainable Chemistry and Engineering*, 9, 6 (2021).

[12] V. Venkatesh, Q. Yang, J. Zhang, J. Pikul and M. G. Allen, "Fabrication and Characterization of Evaporated ZINC Anodes for Small-Scale ZINC-Air Batteries", 2021 21st International Conference on Solid-State Sensors, Actuators and Microsystems (Transducers), (2021), pp. 1134-1137

[13] Z. L. Wang, D. Xu, J. J. Xu, and X. B. Zhang, "Oxygen electrocatalysts in metal-air batteries: From aqueous to nonaqueous electrolytes", *Chemical Society Reviews*, 43, 22 (2014).

[14] Y. Wei, Y. Shi, Y. Chen, C. Xiao, and S. Ding, "Development of solid electrolytes in Zn-air and Al-air batteries: From material selection to performance improvement strategies", *Journal of Materials Chemistry A*, 9, 8 (2021).

[15] J. Stamm, A. Varzi, A. Latz, and B. Horstmann, "Modeling nucleation and growth of zinc oxide during discharge of primary zinc-air batteries", *Journal of Power Sources*, 360 (2017).

[16] D. She and M. G. Allen, "A micromachined freestanding electrochemical sensor for measuring dissolved oxygen", *Journal of Microelectromechanical Systems*, 28, 3 (2019).

[17] "https://www.nxp.com/docs/en/data-sheet/SL3S1003_1013.pdf."

[18] "https://earthsoils.com/soil-composition/."

[19] "https://www.doctordirt.org/teachingresources/idealsoil."

[20] G. Li et al., "Carbonation effects on the performance of alkaline polymer electrolyte fuel cells", *International Journal of Hydrogen Energy*, 40, 20 (2015).

[21] G. Donhowe and O. Fennema, "Water vapor and oxygen permeability of wax films", *J Am Oil Chem Soc*, 70, 9 (1993).

CONTACT

*J. Zhang, email: zjwen@seas.upenn.edu

SELF-POWERED SWEAT ION SENSOR WITH LONG DURATION ELECTROCHEMICAL POTENTIAL

Jorge A. Rodriguez[1] and Daniela Diaz-Alonso[1]
[1]Center for Engineering and Industrial Development, Mexico

ABSTRACT

The focus of this work lies in the construction of a long-lasting self-powered sweat ion sensor in a galvanic cell configuration of notation Mg(s)|NaCl(aq)|Cu(s), preliminary analysis on expected output of the sensor was obtained using the Nernst equation, then several controlled tests were carried out in the laboratory using different molar concentrations of NaCl in aqueous solution to later carry out tests with human sweat. The results showed that the ion sensor allows the monitoring of electrolyte levels in sweat in the 0.01-0.2 molar range, with a useful life of the electrodes greater than 10 days; the sensor output potential is greater than 1.53 volts when the sensor is in contact with the NaCl electrolyte and greater than 1.46 volts when the electrolyte is human sweat.

KEYWORDS

Electrochemical sensor, ions sweat, electrolyte, self-powered.

INTRODUCTION

The monitoring of ions in sweat is essential to detect imbalances in the human body, such as hypohydration and hyperhydration, due to the variation of sodium and chloride present in sweat. It is also possible to carry out an early screening for cystic fibrosis (CF), which is a genetic condition that affects the cells that produce the mucosa, sweat and gastric juices, when concentrations exceed a value of 0.06 M of chlorine in sweat [1].

The chemical components mostly present in human sweat are sodium and chlorine with molar concentrations of ~10-100 mM/L and ~10-78 mM/L respectively [2]. The main characteristic of sodium and chlorine is that they are charged ions electrically with positive charge and negative charge respectively, and due to this quality it is possible to detect them in aqueous solutions through electrochemical methods, among them, the simplest method is the potentiometric measurement, which requires the use of two metallic electrodes, one of them is the electrode of work and other is the reference electrode, and between them the electrolyte of interest in aqueous solution, its output is an electrical potential called E and measured in volts. The electrochemical potential obtained from the sensor is described through the Nernst equation (equation 1), which relates the process of a chemical oxidation-reduction reaction within an electrochemical cell, using for this, E0 values called standard potential, as well as, the constants of the ideal and Faraday gas and the molar concentrations of the elements that participate in the oxidation and reduction processes in that reaction [3].

$$E = E^0 + (RT/F * \ln [Ox]/[Red]) \quad (1)$$

The electrolytes monitoring of in sweat through the potentiometric method still presents several areas of opportunity aimed at improving: the operating range, the duration of the sensor electrodes, and increasing the output potential. In 2019, a measurement of chlorine in sweat was reported [4], this was carried out through a disposable self-powered patch with a limited output potential of 1.3 V and operation of only a few seconds to detect cystic fibrosis, resulting in only one result positive or negative [4]. On the other hand a sensor for the detection of sodium and potassium in human sweat during exercise was reported in 2020 [5], it was built to deliver a small output potential of 280 mV, making it dependent of external batteries, and their carbon electrodes require a complex chemical manufacturing process. In addition, it is worth mentioning that the works cited above and those currently reported do not exceed electrolyte concentration measurement values above 100 mM/L. This work focuses mainly on solving the problems associated with: increasing the measurement range of molar electrolyte concentrations greater than 100 mM/L, increasing the output electrochemical potential E above 1.3 volts, and improving the sensor timelife, so that it can be part of a continuous sweat electrolyte monitoring system.

MATERIALS AND METHODS

Cell construction

The self-powered sweat ion sensor is built on a Medimart brand flexible absorbent adhesive patch, high purity (99.95%) magnesium tape for the ion sensing electrode, and 24 gauge copper foil (0,022 in) for the reference electrode (purchased from Fisher's Labs) in a galvanic cell configuration as shown in Fig. 1 b, both electrodes have dimensions of 0.15 x 0.31 inches and the separation between them is 0.11 inches. For the laboratory testing stage with NaCl solutions, a cell was built with the mentioned electrodes inside a transparent microcentrifuge tube (Fig. 1 a). For the testing stage with human sweat, the electrodes were attached to the flexible patch using Steren brand double-sided tape parallel to each other so that there were no problems related to the small amounts of sweat secreted by the skin. The electrodes were soldered with strands of 28 AWG gauge flat copper wire to be connected to the instrumentation. It should be noted that two pairs of electrodes were connected in series in order to obtain voltages greater than 3 volts and power supply the instrumentation.

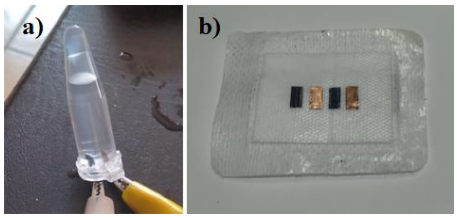

Figure 1: a) Cell for laboratory tests and b) sweat ion sensor in the form of a patch.

Instrumentation and communication

Potential measurements in the laboratory with aqueous NACl solutions were carried out using a Fluke brand digital multimeter, model F15B+ with auto range, measuring only readings related to voltage in volts.

For the measurements in tests with human sweat, a simple instrumentation was carried out on the patch to collect the data from the sensor, it consisted of using the Atmel brand ATtiny85 microcontroller that is capable of operating with a voltage of 1.8 volts, its analog-digital converter to digitize the signal and be able to manipulate it through code with the Arduino IDE application. A Bluetooth BLE module based on the Texas Instruments CC2541 chip was connected to the microcontroller in order to wireless

978-1-940470-04-7/HH2022/$25©2022TRF
DOI 10.31438/trf.hh2022.80

signal transmission (Fig. 2 b), which can operate with a minimum supply voltage of 1.8 volts. The send data can be viewed in an own mobile application designed for android operating system Fig. 2 c.

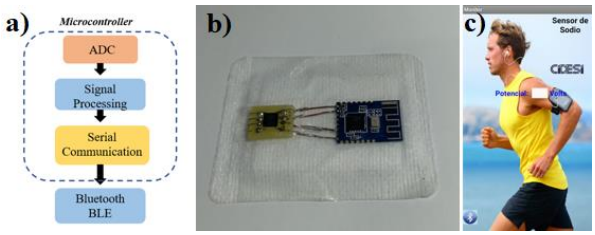

Figure 2: a) Block diagram of the instrumentation, b) microcontroller connected to Bluetooth BLE and c) mobile app.

RESULTS AND DISCUSSION

Initially, mathematical calculations were made with the Nernst equation that showed a range of potentials from 2.78 to 2.84 volts for a molar concentration range of 20 mM/L-160 mM/L Table 1, because these calculations are made taking into account conditions ideal and standard. Subsequently, two stages of tests were carried out with the ion sensor, the results are shown in the following subsections in the form of graphs.

Laboratory tests

Using the cell built especially for these measurements, the results in the Fig. 3 were obtained, which show a cell output potential of 1.53 to 1.6 volts for a molar concentration range of 20 mM/L-160 mM/L. The difference with the results of the mathematical analysis is up to 1.19 volts because the mathematical calculations using the Nernst equation consider standard values obtained with electrodes with large electrode dimensions and standard concentration, pressure and temperature conditions. Regarding the duration of the sensor, measurements were made in the laboratory after 3 weeks after the first tests, which only showed a decrease in potential of 8%.

Table 1: Calculations and measurements of potential with cell: Mg|NaCl|Cu.

[M]	Nernst Equation (V)	Experimental (NaCl) (V)
0.02	2.7794	1.534
0.04	2.7972	1.555
0.06	2.8076	1.571
0.08	2.8156	1.578
0.1	2.8208	1.583
0.12	2.8296	1.591
0.14	2.8364	1.597
0.16	2.8468	1.605

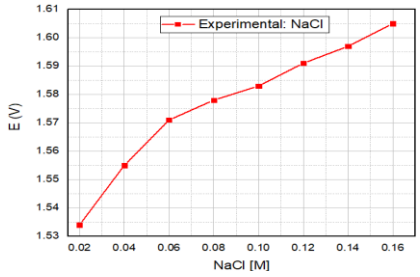

Figure 3: Experimental results with NaCl solutions.

Human sweat tests

Once sensor is able to measure electrolyte concentrations in the range normally found in human sweat (10mM/L-100mM/L), we proceeded to take measurements with a test subject during a period cycling test. After 15 minutes, the results showed stable values of up to 1,468 volts after the first 200 seconds Fig. 4. Although the electrochemical potential was decreased by approximately 1 volt compared to the results of experimental tests in the laboratory, the potential is higher than those of currently reported sensors, and this may be due to the intervention of other factors including sweat and the amount of sweat present during the reaction on the patch.

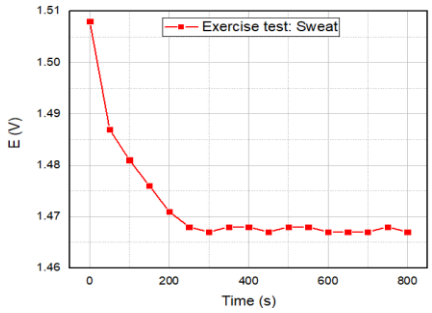

Figure 4: Test results with sweat in an exercise test.

CONCLUSIONS

A simple and low-cost sensor was built that can correctly monitor electrolytes in sweat, obtaining measurement ranges greater than 100 mM/L, electrochemical potentials greater than 1.46 volts, and electrode duration greater than 3 weeks. A more detailed mathematical analysis should be done in future work using Faraday's laws for electrolysis and the Butler-Volmer equation to optimize electrode geometry and cell design with simple fabrication techniques, to obtain optimized results in terms of electrochemical potential and electrolyte measuring range.

ACKNOWLEDGEMENTS

To CIDESI and the National Council of Science and Technology (CONACYT) of Mexico for providing a Ph. D scholarship during the development of this project.

REFERENCES

[1] Lindsay B. Baker, "Physiology of sweat gland function: The roles of sweating and sweat composition in human health", Temperature (Austin, Tex.) vol. 6,3 211-259. (2019).

[2] Jing Xu, Yunsheng Fang, and Jun Chen, "Wearable Biosensors for Non-Invasive Sweat Diagnostics", *Biosensors*, 11, 245, (2021).

[3] Chemistry. An ACS project, Reverté. Barcelona (2005).

[4] Ortega L., Llorella A., Esquivel J. P. and Sabaté N., "Self-powered smart patch for sweat conductivity monitoring", Nature, Microsystems & Nanoengineering (2019).

[5] Paolo Pirovano, Matthew Dorrian et al., "A wearable sensor for the detection of sodium and potassium in human sweat during exercise", Talanta, ElSevier, Volume 219 (2020).

CONTACT

*j.rodriguez@posgrado.cidesi.edu.mx,
daniela.diaz@cidesi.edu.mx

STRETCHABLE GLUCOSE SENSOR VIA CONJUGATED POLYMER CONFORMALLY-COATED CNT ELECTRODES PARTIALLY EMBEDDED IN PDMS

Anthony Palumbo[1], Chenguang Zhao[1], Hongjun Wang[1], Kalle Levon[2], and Eui-Hyeok Yang[2]*
[1]Department of Mechanical Engineering, Stevens Institute of Technology, Hoboken, NJ, USA
[2]New York University Tandon School of Engineering, Brooklyn, NY, USA

ABSTRACT

This paper presents a stretchable glucose sensor composed of dodecylbenzenesulfonate-doped polypyrrole (PPy(DBS))-coated vertically aligned carbon nanotube (VACNT) forests partially embedded in a polydimethylsiloxane (PDMS) substrate. VACNTs are grown via chemical vapor deposition (CVD) and transferred onto partially cured PDMS. A conformal PPy(DBS) layer is electropolymerized on the nanotubes to create PPy(DBS)-coated VACNTs. Next, dip-coating is performed in glucose oxidase (GOx) solution to immobilize GOx with glutaraldehyde (GA) as a crosslinking agent onto the PPy(DBS) surface. The PDMS/CNT/PPy(DBS)/GOx is exposed to varying glucose concentrations to measure its amperometric response. The sensor exhibits a sensitivity of 10 mA cm^{-2} M^{-1}, a linear range of 0.1 mM to 12 mM, and a response time shorter than 5 seconds. Strain is applied to the sensor device, demonstrating its stable sensing function up to 75% strain and with coefficients of determination large than 0.975.

KEYWORDS

Flexible electrode, glucose sensor, electrochemical sensing, carbon nanotubes, polypyrrole

INTRODUCTION

Carbon nanotube (CNT) based electrodes are suitable for diverse biosensing applications owing to their high performance, inherent miniaturization, and low cost [1], [2]. Incorporating sensing materials with flexible and stretchy materials enables sensors to impact a wide range of applications, including electronic skins [3], smart sensor bandages [4], and wearable medical devices [5]. The wearable or skin-attachable flexible sensors can be subjected to various lateral strains via stretching. Therefore, these sensors need to be capable of accommodating various mechanical disturbances such as large bending, twisting, and stretching. Wearable or skin-attachable can be subjected to various lateral strains and need to be capable of accommodating various mechanical disturbances such as large bending, twisting, and stretching. To achieve flexibility, flexible electrodes are often synthesized with elastomeric polymer substrates, including polyimide, polydimethylsiloxane (PDMS), poly (methyl methacrylate) (PMMA), and polyethylene (PE). To achieve conductive transducer functionality, flexible substrates are conventionally deposited with conductive metal thin films, including Au, Ag, and Pt [6]–[8]. Fabrication of these thin metal films on flexible substrates has been demonstrated via established MEMS techniques, such as thermal evaporation, electron beam evaporation, sputtering, and inkjet printing. Upon application of sufficient mechanical deformation, however, metal thin films can lead to crack propagation and/or delamination from the underlying flexible substrate, causing inconsistent readings and premature device failure.

In attempts to bypass these issues, novel strategies are being pursued to combine conductive materials that can undergo strain on par with the capability of their underlying flexible substrates. Owing to their remarkably superior carrier mobility, stability, inherent miniaturization, and outstanding mechanical flexibility, CNTs are promising nanomaterials for flexible or stretchable microelectronics [9]. A highly conductive network is formed from the combined high conductivity of individual nanotubes as observed by forests of vertically aligned CNTs (VACNTs). In contrast, the charge carrier transport is limited by the large intertube electrical resistance caused by the intrinsic charge barriers at tube–tube junctions [10]. For perspective, nanotube film conductivity is reported up to 6000 S cm^{-1}, which is three orders of magnitude lower than the conductivity of a single nanotube [11]. For fabrication of CNT-based flexible electrodes, CNTs are usually deposited or embedded onto flexible or stretchable elastomer polymer substrates such as Polyethylene terephthalate (PET), polycarbonate (PC), or Polydimethylsiloxane (PDMS) [12], [13]. CNT-based flexible electrodes on elastomeric substrates have demonstrated high flexibility, limited only by the cohesive fracture of elastomeric substrates [14]–[16]. We previously demonstrated a flexible electrode design of VACNTs embedded in PDMS as a template that has been extended towards applications of energy storage [17] and pressure sensing [18]. In addition, a conjugated polymer, polypyrrole (PPy), acts as an anti-interference and anti-fouling barrier for glucose sensors [19]–[21]. Due to their synergistic properties, many efforts have been pursued to develop PPy and CNT in glucose sensors; however, current literature does not report their use in high strain applications, such as required by flexible sensors that undergo mechanical deformations in wearable or implantable electronics.

To this end, we adapt the flexible electrode composed of VACNTs embedded in PDMS into a glucose sensor, with PPy(DBS) conformally deposited on individual CNTs as an adherent film with the ease of incorporating glucose oxidase (GOx). We demonstrate a reliable electrochemical performance under strains up to 75% and correlation coefficients greater than 0.976. A wide linear range of 0.1 mM to 12 mM and sensitivity of 10 mA cm^{-2} M^{-1} is achieved, in addition to a response time of shorter than 5 seconds, indicating its potential use for continuous monitoring of physiological fluids with flexible application in wearable sensor applications.

FABRICATION

Figure 1 illustrates the fabrication process of the stretchable platform composed of vertically aligned carbon nanotubes (VACNTs) grown via chemical vapor deposition (CVD) embedded onto suspended polydimethylsiloxane (PDMS).

The PDMS/CNT electrode was reported in our previous work [17], [18]. Atmospheric pressure chemical vapor deposition (APCVD) in a 4-inch diameter quarts tube was pursued to deposit VACNT forests on Si/SiO2, with layers of Al and Fe (5 nm and 3 nm, respectively) deposited via physical vapor deposition (PVD) to serve as a solid catalyst. The furnace temperature was increased from atmosphere to a 750°C growth temperature with Ar gas flow at a gas flow rate of 500 sccm. At 750°C, the temperature was held constant with introduction of H_2 and C_2H_4 gas flows of 60 sccm and 100 sccm, respectively, for 15 minutes. The chamber was then rapidly cooled to ambient temperature with only Ar gas flow, resulting in VACNTs.

The as-grown VACNTs were transferred onto PDMS that was synthesized from 10:1 ratio of base to curing agent (Sylgard 184 Silicone Elastomer, Dow Corning). First, the PDMS was dispensed onto a glass slide and heated on a hot plate at 65°C to achieve a

978-1-940470-04-7/HH2022/$25©2022TRF
DOI 10.31438/trf.hh2022.81

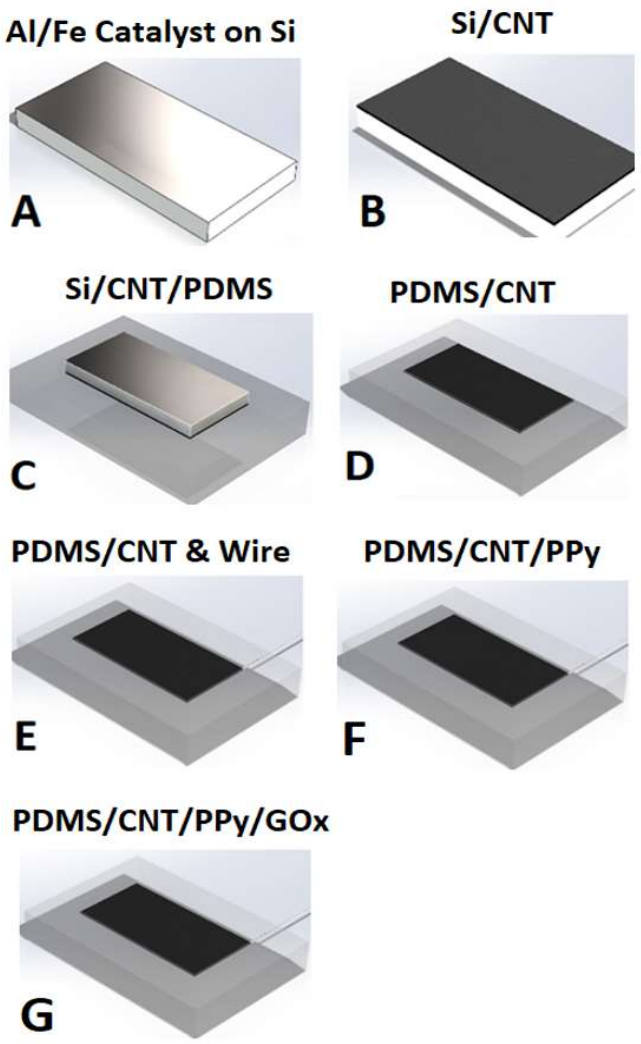

Figure 1: Illustration of the fabrication process: (a) PVD of Al/Fe catalyst onto silicon Si, (b) CVD of CNT forests, (c) CNT transfer onto partially cured PDMS, (d) Si removal after PDMS is fully cured, (e) Wiring from the PDMS/CNT electrode to potentiostat, (f) PPy(DBS) electropolymerization onto CNTs, (g) Electrode dipcoating into solutions of GA and GOx.

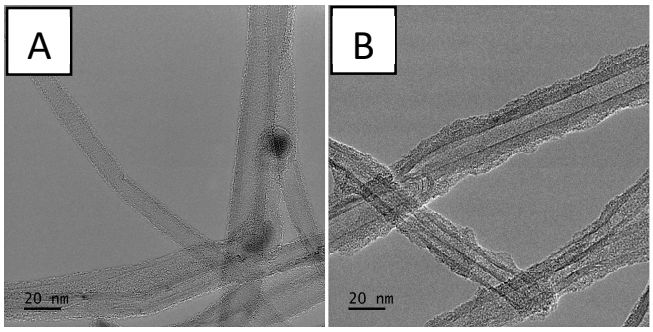

Figure 2: TEM images of: (a) bare CNT, and (b) CNT/PPy(DBS)

partially cured PDMS phase after approximately 30 minutes. The VACNT was placed face down onto the partially cured PDMS surface to fully wet the tips, and the PDMS was left in ambient condition for 12 h to complete the curing process, resulting in VACNT anchored into fully cured PDMS with exposed ends. Due to the strong bonding between CNTs and PDMS, the Si substrate was removed with ease and the exposed CNTs were vertically aligned and interwoven, enabling charge transfer as a flexible conductive electrode.

The PDMS/CNT electrode was conformally coated with PPy(DBS) via electropolymerization, which occurred in a solution consisting of 1 mL pyrrole monomer (Sigma-Aldrich, reagent grade, 98%) and 150 mL of 0.1 M NaDBS (Sigma-Aldrich, technical grade) and the PDMS/CNT acts as the working electrode. An Au-coated SiO_2 substrate was used as the counter electrode, and a saturated calomel electrode (SCE) was used as the reference electrode. Voltage of 0.7 V versus SCE was applied to the working electrolyte to achieve a PPy(DBS) coating with a surface charge density of 50 mC cm^{-2}. The PDMS/CNT/PPy(DBS) was rinsed thoroughly with water and allowed to dry overnight. The conformal PPy(DBS) layers on individual CNTs are shown in Figure 2.

The PDMS/CNT/PPy(DBS) was first dipped in 0.25 wt.% glutaraldehyde (GA) solution as a crosslinking agent for the immobilization of GOx. The dip-coating was achieved in 1.5 hours at room temperature, and then the PDMS/CNT/PPy(DBS) was washed 2-3 times with 0.1 M potassium phosphate buffer. Next, the sample was dipped into a solution of GOx (2 mg/mL) in 0.1 M potassium buffer (pH 7) for 2 hours at 4°C, followed by washing 2-3 times with 0.1 M potassium phosphate buffer.

CHARACTERIZATION

For imaging of CNT and CNT/PPy(DBS), transmission electrode microscopy (TEM) was used. A potentiostat (236A, Princeton Applied Research, Oak Ridge, TN) was used to measure the current response of the sensors with an applied voltage of 0.65 V. Various concentrations of glucose solution were added into a phosphate buffer solution using a syringe for concentration-dependent sensing. Experiments were performed with as-grown PDMS/CNT (without PPy(DBS), PDMS/CNT/PPy(DBS), and PPy(DBS) film coating on flat Au-coated Si/SiO_2. The above procedures were pursued to fabricate each sample, in addition to GA and GOx immobilization via dip coating. Each sample acted as a working electrode with a CNT counter electrode and an Ag/AgCl reference electrode, all inserted into 20 mL of 0.1 M phosphate buffer (pH 7). A constant voltage of 0.65 V was applied and current changes were observed with the addition of glucose solution at intervals of 50 s. For the application of strain, a clamping device was used to apply 15%, 30%, 45%, 60%, and 75% strains. A singled PDMS substrate containing CNT as counter electrode and CNT/PPy(DBS)/GOx as working electrode space apart several mm was used for testing with an Ag/AgCl wire reference electrode. 2 mL of 0.1 M phosphate buffer solution was placed centrally on the

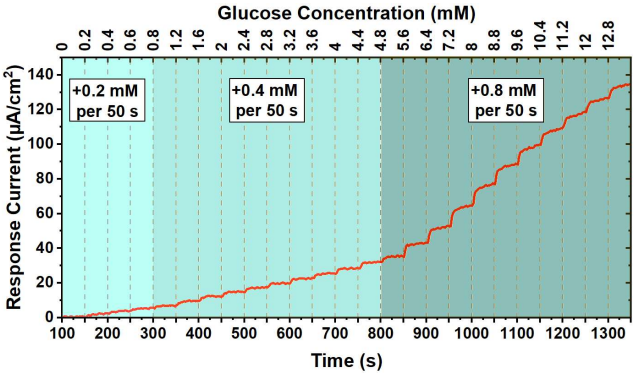

Figure 3: Current response of the fabricated biosensor upon successive addition of glucose at 50 second intervals, without application of strain.

sensor, and successive additions of glucose were added to the solution to observe glucose concentration-dependent current changes.

RESULTS & DISCUSSION

The fabricated electrode was dip-coated into solutions of glutaraldehyde (GA) and glucose oxidase (GOx) to form the glucose-sensitive layer. Alternative sensing can be accomplished such as through the use of immobilization of other enzymes. The biosensor was exposed to iterative concentrations of glucose, and GOx reacts in the presence of glucose, resulting in a concentration-dependent change of measurable current, as shown in Figure 3. The amount of glucose can be determined by measuring the current produced by the following two-step reaction:

$$Glucose + O_2 \xrightarrow{GOx} Gluconic\ acid + H_2O_2 \quad (1)$$

$$H_2O_2 \rightarrow O_2 + 2H^+ + 2e^- \quad (2)$$

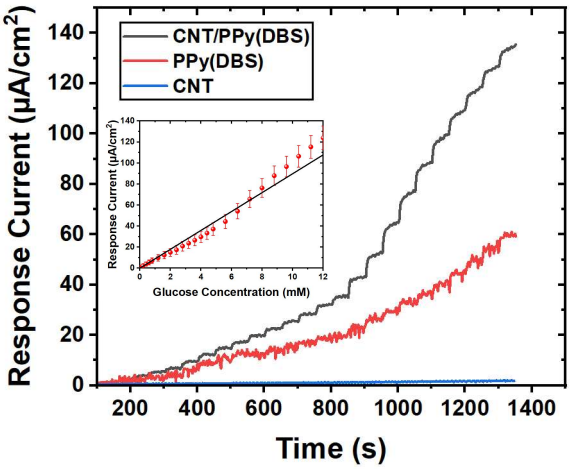

Figure 4: Current response of PPy(DBS)-coated CNTs, PPy(DBS), and CNTs upon successive addition of glucose; inset shows CNT/PPy(DBS) linear calibration curve between the current and the glucose concentration.

Sensitivity of ~10 mA cm^{-2} M^{-1} and a wide linear range WEre observed with glucose concentrations as low as 0.1 mM to 12 mM. The combination of PPy(DBS) coated on CNTs resulted in improved sensing than either material independently with a linear calibration curve between the current and the glucose concentration, as shown in Figure 4. CNTs forests offer high conductivity, commonly ranging from 7 to 14 S cm^{-1} along with the array at 300 K [12], in addition to geometric favorability of high specific surface area. Conformal coating of PPy(DBS) onto individual CNT surfaces results in increased reaction sites, resulting in at least 4x higher sensitivity than observed with independent PPy(DBS) films. The current response upon successive addition of 0.8 mM of glucose under strain shown in Figure 5 demonstrates the use of the sensor for wearable applications which undergo strain. Reliable electrochemical performance under various strains (i.e., stretching up to 75%) was demonstrated with correlation coefficients greater than 0.972, indicating a reliable linear sensing capability of glucose concentrations with strain up to 75%. The response time of shorter than 5 s enables the sensor for continuous monitoring systems [22], [23].

The flexible biosensor can be subjected to various lateral strains via stretching, while providing reliable electrochemical sensing of biomarkers on a patient's skin. We have developed CNT-based sensing electrodes on flexible substrates that exhibit reliable and stable glucose-sensing under stretching up to 75%. Skin-attachable devices for continuous monitoring of patients will enable potential applications for smart sensor bandages, critical wound monitoring, and glucose detection for diabetes.

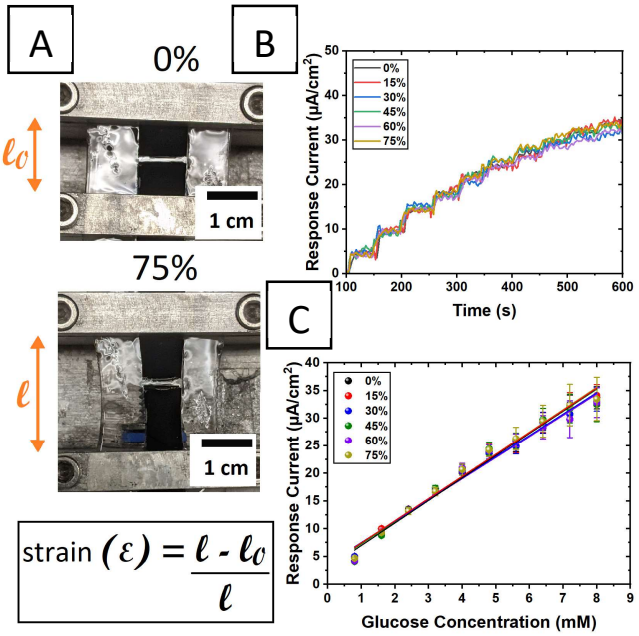

Figure 5: (a) Photographs showing the sensor under 0% and 75% strain, (b) current response upon successive addition of 0.8 mM of glucose, under strain, and (c) linear calibration curves between the current and the glucose concentration

CONCLUSIONS

This paper demonstrates a stretchable glucose sensor composed of PDMS/CNT/PPy(DBS)/GOx. The PDMS substrate enables the application of strain, and VACNTs embedded into the partially cured PDMS allowed the exposed individual CNTs to interconnect, enabling electron transfer as an electrode. Individual CNTs were coated with a conformal coating of PPy(DBS), retaining the high effective surface area of VACNTs forests and greater concentration of reactions sites towards higher sensitivity. The glucose sensor was exposed to iterative glucose concentrations to demonstrate its use as a flexible glucose sensor. A response time of shorter than 5 seconds is observed, enabling the use of this sensor for continuous monitoring. A linear range of 0.1 mM and up to 12 mM is observed with a highly linear response trend and sensitivity of 10 mA cm^{-2} M^{-1}. Applications of strain were introduced to demonstrate the use of this sensor for stretchable sensing applications up to 75% with stable and reliable sensing. Each strain application shown demonstrated a coefficient of determination greater than 0.976. Stretchable biosensors composed of PDMS/CNT/PPy(DBS) can be used for the flexible sensing of alternative electrochemical species, as demonstrated with this proof of concept with glucose oxidase and glucose. The capability of stretchability with electrochemical sensing may ultimately lead to the sensing of biomarkers in a patient's physiological fluids towards potential wearable electronics applications.

ACKNOWLEDGEMENTS

The authors thank Dr. Tsengming (Alex) Chou for his help with SEM/TEM training and guidance. The authors thank Shichen Fu for preparing TEM samples. The authors acknowledge partial support by the Air Force Office of Scientific Research under Grant FA9550-11-10272. This research used microscopy resources, partially funded by the NSF via Grant NSF-DMR-0922522, within the Laboratory for Multiscale Imaging (LMSI) at Stevens Institute of Technology. This work was also partially carried out at the Micro Device Laboratory (MDL) at Stevens Institute of Technology, funded with support from W15QKN-05-D-0011.

REFERENCES

[1] A. J. Bandodkar and J. Wang, "Non-invasive wearable electrochemical sensors: a review," *Trends Biotechnol*, vol. 32, no. 7, pp. 363–371, 2014.

[2] J. R. Windmiller and J. Wang, "Wearable Electrochemical Sensors and Biosensors: A Review," *Electroanalysis*, vol. 25, no. 1, pp. 29–46, 2013, doi: 10.1002/elan.201200349.

[3] Z. Lou *et al.*, "Ultrasensitive and ultraflexible e-skins with dual functionalities for wearable electronics," *Nano Energy*, vol. 38, no. March, pp. 28–35, 2017, doi: 10.1016/j.nanoen.2017.05.024.

[4] H. Derakhshandeh, S. S. Kashaf, F. Aghabaglou, I. O. Ghanavati, and A. Tamayol, "Smart bandages: the future of wound care," *Trends Biotechnol*, vol. 36, no. 12, pp. 1259–1274, 2018.

[5] L. Lu *et al.*, "Wearable health devices in health care: narrative systematic review," *JMIR Mhealth Uhealth*, vol. 8, no. 11, p. e18907, 2020.

[6] H. Kudo, T. Sawada, E. Kazawa, H. Yoshida, Y. Iwasaki, and K. Mitsubayashi, "A flexible and wearable glucose sensor based on functional polymers with Soft-MEMS techniques," *Biosensors and Bioelectronics*, vol. 22, no. 4, pp. 558–562, 2006.

[7] J. J. Mastrototaro, K. W. Johnson, R. J. Morff, D. Lipson, C. C. Andrew, and D. J. Allen, "An electroenzymatic glucose sensor fabricated on a flexible substrate," *Sensors and Actuators B: Chemical*, vol. 5, no. 1–4, pp. 139–144, 1991.

[8] M. A. Abrar, Y. Dong, P. K. Lee, and W. S. Kim, "Bendable electro-chemical lactate sensor printed with silver nano-particles," *Sci Rep*, vol. 6, no. 1, pp. 1–9, 2016.

[9] S. Kumar *et al.*, "Review—Recent Advances in the Development of Carbon Nanotubes Based Flexible Sensors," *Journal of The Electrochemical Society*, vol. 167, no. 4, p. 047506, 2020, doi: 10.1149/1945-7111/ab7331.

[10] W. S. Wong and A. Salleo, *Flexible electronics: materials and applications*, vol. 11. Springer Science & Business Media, 2009.

[11] Z. Wu *et al.*, "Transparent, conductive carbon nanotube films," *Science (1979)*, vol. 305, no. 5688, pp. 1273–1276, 2004.

[12] M. B. Jakubinek *et al.*, "Single-walled carbon nanotube-epoxy composites for structural and conductive aerospace adhesives," *Composites Part B: Engineering*, vol. 69, pp. 87–93, 2015, doi: 10.1016/j.compositesb.2014.09.022.

[13] R. Zhang, A. Palumbo, J. Xu, and E. H. Yang, "CNT-based stretchable supercapacitors," in *Handbook of Nanoengineering, Quantum Sciences and Nanotechnologies*, Francis and Taylor / CRC Press, 2019.

[14] Y. H. Lee *et al.*, "Synthesis of large-area MoS2 atomic layers with chemical vapor deposition," *Adv Mater*, vol. 24, no. 17, pp. 2320–2325, 2012, doi: 10.1002/adma.201104798.

[15] J. Ding *et al.*, "Graphene–vertically aligned carbon nanotube hybrid on PDMS as stretchable electrodes," *Nanotechnology*, vol. 28, p. 465302, 2017, doi: 10.1088/1361-6528/aa8ba9.

[16] R. Xu *et al.*, "Highly conductive, twistable and bendable polypyrrole-carbon nanotube fiber for efficient supercapacitor electrodes," *RSC Advances*, vol. 5, no. 28, pp. 22015–22021, 2015, doi: 10.1039/c5ra01917f.

[17] R. Zhang, K. Yan, A. Palumbo, J. Xu, S. Fu, and E. H. Yang, "A stretchable and bendable all-solid-state pseudocapacitor with dodecylbenzenesulfonate-doped polypyrrole-coated vertically aligned carbon nanotubes partially embedded in PDMS," *Nanotechnology*, vol. 30, no. 9, 2019, doi: 10.1088/1361-6528/aaf135.

[18] R. Zhang *et al.*, "A Flexible Pressure Sensor with Sandwiched Carpets of Vertically Aligned Carbon Nanotubes Partially Embedded in Polydimethylsiloxane Substrates," *IEEE Sensors Journal*, pp. 1–1, 2020, doi: 10.1109/jsen.2020.2999261.

[19] C. Chen, Y. Jiang, and J. Kan, "A noninterference polypyrrole glucose biosensor," *Biosensors and Bioelectronics*, vol. 22, no. 5, pp. 639–643, 2006.

[20] L. Djaouane, B. Nessark, and L. Sibous, "Electrochemical synthesis and surface characterization of (pyrrole+ 2-methylfuran) copolymer," *Journal of Molecular Structure*, vol. 1129, pp. 200–204, 2017.

[21] M. Singh, P. K. Kathuroju, and N. Jampana, "Polypyrrole based amperometric glucose biosensors," *Sensors and Actuators, B: Chemical*, vol. 143, no. 1. pp. 430–443, Dec. 04, 2009. doi: 10.1016/j.snb.2009.09.005.

[22] X. Xuan, H. S. Yoon, and J. Y. Park, "A wearable electrochemical glucose sensor based on simple and low-cost fabrication supported micro-patterned reduced graphene oxide nanocomposite electrode on flexible substrate," *Biosensors and Bioelectronics*, vol. 109, pp. 75–82, 2018.

[23] X. Xue, Z. Qu, Y. Fu, B. Yu, L. Xing, and Y. Zhang, "Self-powered electronic-skin for detecting glucose level in body fluid basing on piezo-enzymatic-reaction coupling process," *Nano Energy*, vol. 26, pp. 148–156, 2016.

TOWARDS SINGLE-CELL PROTEOFORM PROFILING: ON-CHIP ISOELECTRIC FOCUSING IN IMMOBILIZED pH GRADIENT GELS

Gabriela Lomeli[1,2] and Amy E. Herr[1,2,3]*
[1]UC Berkeley-UCSF Graduate Program in Bioengineering, California, USA and
[2]Department of Bioengineering, University of California, Berkeley, California, USA
[3]Chan Zuckerberg Biohub, San Francisco, California, USA

ABSTRACT

Microfluidic tools are an essential capability in understanding cell-to-cell heterogeneity. Similarly, precision microanalytical tools can play an outsize role in measuring molecule-to-molecule heterogeneity, especially as protein post-translational modifications create proteoforms that execute regular and aberrant cellular functions. Although highly related, slight variations in protein charge contribute to proteoform heterogeneity. Electrophoretic methods, including immobilized pH gradient isoelectric focusing (IPG-IEF), provide the resolution to measure subtle protein-to-protein differences. However, conventional IPG-IEF can be low-throughput and requires large starting sample amounts, precluding single-cell analysis. Here, we present the first polydimethylsiloxane (PDMS)-based, immunoprobed, microfluidic IPG-IEF device to our knowledge. We demonstrate separation performance on par with our single-cell IEF device, including resolving analytes differing by only 0.1 pH.

KEYWORDS

Microfluidics, Electrophoresis, Proteoforms, Isoelectric Focusing, Immobilized pH Gradient.

INTRODUCTION

IEF can separate proteoforms arising from post-translational modifications of proteins (Figure 1a) [1,2]. Miniaturization of IEF is necessary for high-throughput analysis of proteoforms with reduced starting sample amounts, as is the case in single-cell studies. Microfluidic IEF has typically been carried out using carrier ampholytes (CAs) [3,4]. In CA-IEF, a mixture of CAs placed between an anolyte and catholyte region arrange themselves into a pH gradient under an applied electric field and then the sample proteins migrate to their isoelectric point, pI, in the gradient. CA-IEF suffers from gradient instability and the pH range cannot be easily engineered [2]. In the current single-cell isoelectric focusing assay, CAs are delivered using a hydrogel lid containing the CA, anolyte, and catholyte regions [3]. Since the CAs are free to diffuse throughout the hydrogel, the delivery lid must be prepared right before the assay is run, which adds a highly time-sensitive step to the assay and limits the throughput of the technique.

Another class of IEF employs IPG gels in which a pH gradient is already established before sample application by incorporating Immobilines into the polyacrylamide (PA) gel. Immobilines are small molecules containing either a carboxyl or tertiary amino group that buffer the gel to a different pH. By creating a gradient in Immobiline concentrations across the gel, a highly tunable pH gradient is created. Tunability is key, since a broad pH range might be desired in a multiplexing study with various proteins, while a narrow pH range increases the minimum resolvable pI difference and can be used to separate proteoforms close in pI. Since the pH gradient is immobilized, drift of protein bands towards the cathode is abolished and the protein band position is reproducible [2,5]. The microfluidic IPG-IEF device presented here is fabricated with a similar robust Immobiline chemistry employed by centimeter-scale IPG strips.

An IPG-IEF microfluidic device was previously reported, but it was fabricated in glass microchannels [6]. Glass microfluidic devices are difficult and expensive to fabricate [4]. Moreover, the sample proteins had to be pre-labeled with dye for detection. To overcome the limitations posed by glass fabrication, the IPG-IEF device presented here is made with PDMS. Additionally, we introduce a photo-active hydrogel overlayed on the IPG hydrogel to covalently immobilize proteins after irradiation with a UV light so that captured proteins can be read out via immunofluorescence.

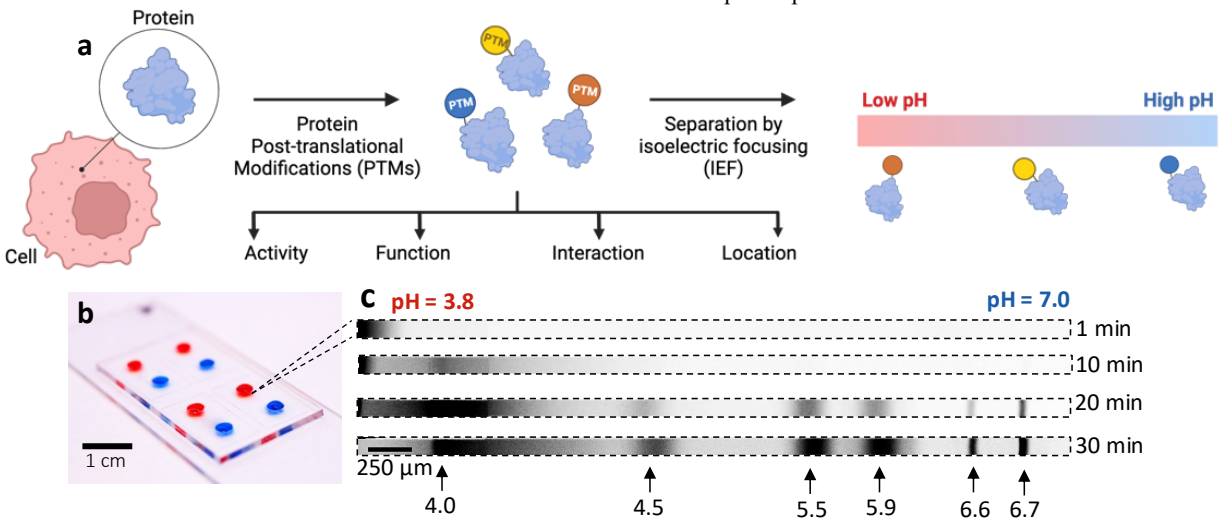

Figure 1: On-chip IPG-IEF enables separation by isoelectric point. (a) IEF can be applied to the analysis of proteoforms. Created with BioRender.com. (b) IPG-IEF device containing food dye-filled single channels. (c) Inverted fluorescent micrographs of IEF-separated pI markers at several time points demonstrates rapid focusing and gradient stability. Representative of n = 3 separations.

978-1-940470-04-7/HH2022/$25©2022TRF
DOI 10.31438/trf.hh2022.82

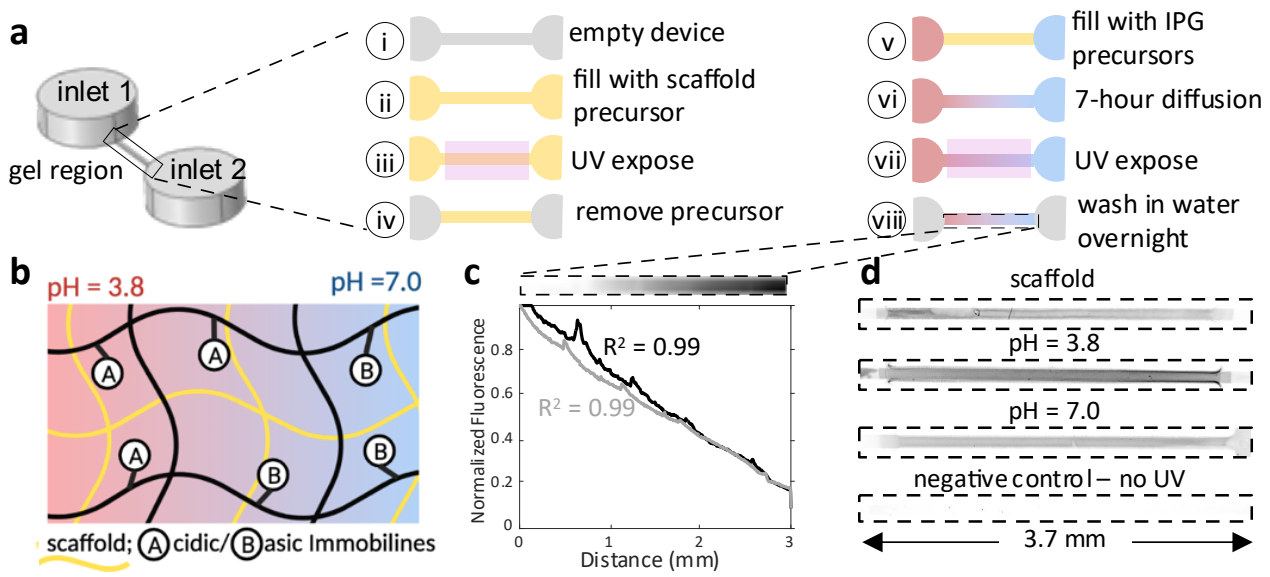

Figure 2: Development of IPG-IEF device. (a) IPG-IEF device fabrication using photopolymerization. b) IPG PA gel is overlayed on scaffold PA gel. Created with BioRender.com. (c) Linearity of gradient monitored with Nile Blue acrylamide dye. Plot shows the intensity profile after 7.5 hours for n = 2 IPG devices. (d) Confirmation of UV polymerization of 3 PA gel precursors individually in microchannels.

RESULTS AND DISCUSSION

Fabrication of IPG-IEF Device

The IPG-IEF device presented here holds 4 separation lanes on a PDMS slab (Figure 1b) and is suitable for 42 of the 9x3 mm footprint lanes. Loaded analytes migrate along the pre-established pH gradient until reaching net zero charge (Figure 1c). Figure 2a details the 2-step photopolymerization of PA gel precursors, which is based on our previous work fabricating stable hydrogel gradients in a PDMS device [7]. Steps i-iv are modified from previous PDMS-based electrophoresis work [8], and steps v-viii were added in the present work to overlay the IPG onto the PA scaffold (Figure 2b). The presence of the scaffold prevents fluid flow and allows the establishment of a linear gradient (Figure 2c). The scaffold also contains a photo-active moiety for in-gel immunoprobing [3]. Next, we confirmed all precursors polymerized in the PDMS channel (Figure 2d). IPG-IEF device fabrication is easy and can be completed in 2 days with ~3 hours of hands-on time.

Performance of IPG-IEF Device

Our IPG-IEF device was designed to separate proteoforms having pI's in the pH range of 3.8 to 7.0. Figure 3a demonstrates separation of 6 pI markers (ranging from 4.0 to 6.7). The intensity profile of all 6 pI markers (Figure 3b) resolves pI markers 6.6 and 6.7, which differ by only 0.1 pH unit. The IPG-IEF device's pH gradient is linear from 4.5 to 6.7 (Figure 3c). A voltage ramp (Figure 4) was utilized to minimize protein precipitation [6]. Critically, the IPG-IEF device performance was comparable to our low-throughput single-cell IEF device capable of differentiating proteoforms differing by a single charge unit (Table 1) [3,9]. The minimum pI difference that can be resolved, Δ(pI)min = 0.20, is a conservative estimate as Δ(pI)min was calculated with pI markers that are 100X smaller than proteins by molecular weight, and therefore have broader peak widths. For context, a single phosphorylation event can cause a pI change of 0.3-0.4 [10].

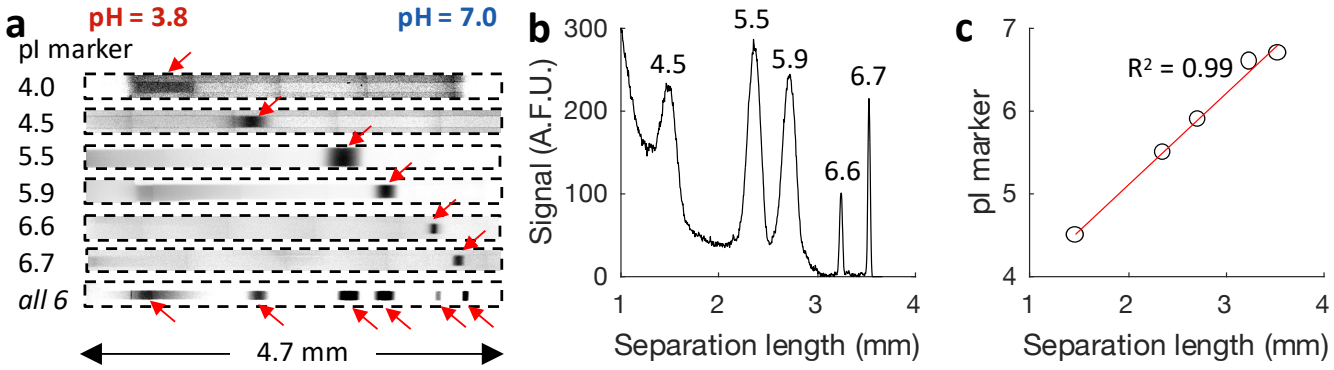

Figure 3: Characterization of pH gradient in IPG device. (a) pI markers were loaded at anode inlet and focused individually to verify identity of each band in the combined "all 6" condition. pI marker 4.0 overlaps with incomplete injection of other pI markers. Brightness and contrast adjusted for each micrograph for better visualization. (b) Intensity plot of "all 6" pI markers after 20 minutes of focusing. (c) Plot shows the position of 5 pI markers in (b) and linearity of pH gradient from pH 4.5 – 6.7. Representative of n = 3 separations.

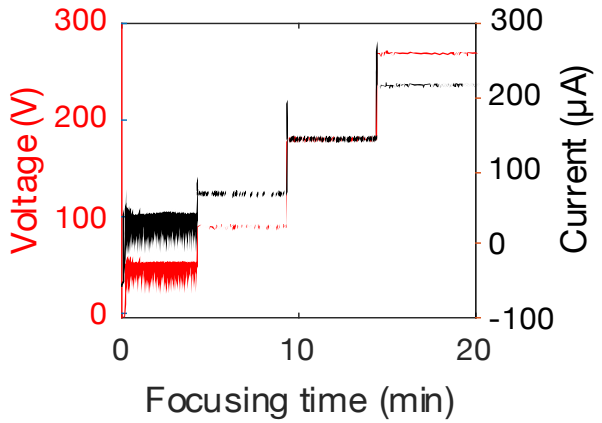

Figure 4: Voltage and current trace under constant voltage conditions. Representative of n = 3 separations.

Immunoprobed Readout of IPG-IEF Device

Finally, we performed IPG-IEF of TurboGFP in our device (Figure 5). To immunoprobe, the PDMS was delaminated from the glass slide and incubated with primary and secondary antibodies. TurboGFP typically has 3 proteoforms in IEF [3,6]. While the proteoforms are not fully resolved, the presence of peak "shoulders" suggests that detecting all 3 proteoforms should be possible with optimization.

CONCLUSION

Answering the National Academy of Engineering's call to "Engineer the Tools of Scientific Discovery," we have developed the first immunoprobed, microfluidic IPG-IEF device in PDMS. In next steps, we will advance to single-cell analysis in an all-in-one microdevice with on-chip lysis, separation, and readout for high-throughput proteoform profiling.

EXPERIMENTAL SECTION

Device Fabrication

The IPG-IEF device was fabricated by standard soft lithography methods. RTV615 PDMS (Momentive) was mixed at a 10:1 ratio, degassed, and poured over a silicon wafer mold of the microchannel features. Each microchannel is 3.5-mm long, 100-µm wide, and 50-µm tall. After the PDMS was cured at 80ºC for 2 hours, a biopsy punch was used to make the 3-mm diameter inlet and outlet holes. To reversibly attach the PDMS to the glass slide substrate, we did not perform plasma bonding.

The next step is to polymerize PA gel in the PDMS channels. Since PA polymerization is oxygen inhibited and PDMS is known to absorb oxygen, the channels are first incubated with 10% benzophenone in acetone for 3 minutes. Benzophenone serves as an oxygen scavenger when exposed to UV [8]. A 6 %T PA gel precursor containing acrylamide/bis-acrylamide (Sigma-Aldrich), the photo-active moiety N-[3-[(3-benzoylphenyl)formamido]propyl] methacrylamide (BPMAC, PharmAgra Laboratories), and VA-086 photoinitator (Wako Chemicals) is then flowed through the channels and photopolymerized with 2 minutes of UV light exposure at 17 mW/cm^2 (Figure 2ai-iv). The inlets were then filled with 6% T PA acidic (pH = 3.8) and basic (pH = 7.0) precursors containing acrylamide/bis-acrylamide, Immobilines (Sigma-Aldrich), and VA-086. The acidic and basic IPG precursor recipes were adapted from previous work [6]. The precursors were allowed to diffuse into the microchannels for 7 hours to establish a linear gradient and then were photopolymerized with 2 minutes of UV light exposure at 17 mW/cm^2 (Figure 2av-viii). The devices were then washed in deionized water overnight and could be stored at 4ºC in deionized water for at least 9 days.

Table 1. Comparison of IPG device with single-cell IEF device[3,7]. Only pI markers with Gaussian profile were used for analysis of IPG device (n = 3; mean ± standard deviation).

	IPG device	single-cell IEF[3,9]
Linearity of pH gradient (R^2)	~0.99	~0.90
$\Delta(pI)_{min}$	0.20 ± 0.0069	0.16 ± 0.02
Peak Capacity	16 ± 2.0	12 ± 5.9
Slope of pH gradient (dpH/dx)	1.18 ± 0.11 mm^{-1}	~0.35 mm^{-1}
Separation length	3.5 mm	9 mm
Focusing time	20 min	~7.5 min
Device can be stored for:	>= 9 days	must be prepared fresh

Gradient Formation and Polymerization Experiments

Nile Blue acrylamide (NB) was used as a proxy for Immobiline chemicals since it has a similar molecular weight and would therefore be expected to diffuse through the PA gels at a similar time scale. For the diffusion experiment in Figure 2c, NB was spiked into the acidic gel precursor at a concentration of 17.4 µM. For the polymerization test experiment in Figure 2d, AlexaFluor-647-labeled donkey anti-rabbit antibody (Invitrogen A-31573) was spiked into the scaffold, acidic, and basic gel precursors at a concentration of 0.01 mg/mL. For the polymerization experiment, the antibody simply served as a large molecular weight dye.

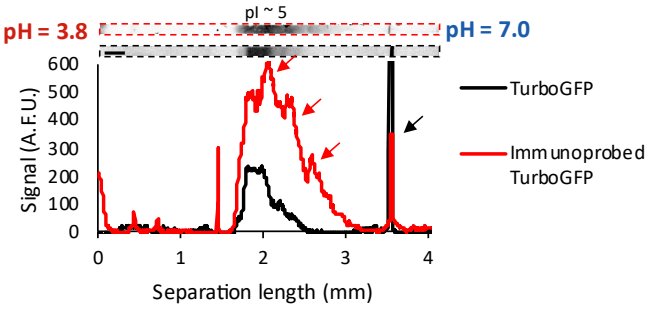

Figure 5: Immunoprobing IPG-IEF device. Inverted fluorescence images and intensity plots of IPG-IEF separated TurboGFP and immunoprobed TurboGFP. Red arrows point to possible TurboGFP proteoforms. Black arrow points to unknown species. Representative of n = 2 separations.

Isoelectric Focusing Experiments

Fluorescent pI markers (Sigma-Aldrich) were used at a concentration ranging from 3.33 µg/mL to 6.67 µg/mL to provide similar band intensities and were diluted in deionized water. The pI marker sample was applied at the anode inlet (near pH = 3.8) and the cathode inlet (near pH = 7.0) remained filled with deionized water. TurboGFP (Evrogen) protein was used at a concentration of 50 nM and applied to the cathode end. For protein experiments, the anode inlet was filled with 1X IEF Anode Buffer and the cathode inlet was filled with 1X IEF Cathode Buffer (Bio-Rad). The inlets were connected to a programmable high voltage power supply, LabSmith HVS448LC 3000V High Voltage Sequencer, with platinum electrodes. An electric field was applied using the following voltage ramp: 50 V/cm for 4 minutes, 100 V/cm for 5 minutes, 200 V/cm for 5 minutes, and 300 V/cm for 6 minutes. For the protein experiments, TurboGFP was immobilized in the IPG gel by irradiation of UV light at 100% intensity for 45 seconds with the Hamamatsu LC8 Spot Light Source.

Immunoprobing

To expose the IPG gels for immunoprobing, the PDMS layer of the IPG-IEF device was gently peeled from the glass slide. Since the PA is covalently bonded to the PDMS and not the glass slide, the PA remains on the PDMS layer. The IPG gels were rinsed in tris-buffered saline with Tween-20 (TBS-T, Cell Signaling Technologies) for 30 minutes and blocked in 2% bovine serum albumin (BSA, Sigma-Aldrich) in TBS-T for 30 minutes. The antibodies used for immunoprobing were primary rabbit anti-tGFP antibody (Pierce PA5-22688) at a concentration of 33 µg/mL and secondary polyclonal antibody AlexaFluor-647-labeled donkey anti-rabbit (Invitrogen A-31573) at a concentration of 67 µg/mL. After primary (2 hour) and secondary (1 hour) antibody incubation steps, the IPG gels were washed in TBS-T for 1 hour. The IPG gels were then rinsed with deionized water briefly and gently dried with a nitrogen stream before fluorescence imaging on an Olympus IX50 inverted epifluorescence microscope.

ACKNOWLEDGEMENTS

This work was funded in part by the National Institutes of Health Grant R01CA203018, National Cancer Institute of the National Institutes of Health, Cancer Moonshot award, Grant Number: 1R33CA225296-01, and the Chan Zuckerberg Biohub to A.E.H. G.L. gratefully acknowledges support from the National Science Foundation Graduate Research Fellowship Program (NSF GRFP). Photolithography was performed in the QB3 Biomolecular Nanotechnology Center. We acknowledge all members of the Herr Lab at UC Berkeley for useful discussions and feedback, and especially Louise Hansen for helping troubleshoot the IPG-IEF device fabrication method.

REFERENCES

[1] L.M. Smith and N.L. Kelleher, "Proteoform: A Single Term Describing Protein Complexity", *Nature Methods*, 10 (2013).

[2] P.G. Righetti, *Immobilized PH Gradients: Theory and Methodology*, Elsevier, 1990.

[3] A.M. Tentori, K.A. Yamauchi, and A.E. Herr, "Detection of Isoforms Differing by a Single Charge Unit in Individual Cells", *Angewandte Chemie International Edition*, 55 (2016).

[4] H. Cui, K. Horiuchi, P. Dutta, and C.F. Ivory, "Isoelectric Focusing in a Poly(Dimethylsiloxane) Microfluidic Chip", *Analytical Chemistry*, 77 (2005).

[5] J.M. Corbett, M.J. Dunn, A. Posch, and A. Görg, "Positional Reproducibility of Protein Spots in Two-Dimensional Polyacrylamide Gel Electrophoresis Using Immobilised PH Gradient Isoelectric Focusing in the First Dimension: An Interlaboratory Comparison", *ELECTROPHORESIS*, 15, 1 (1994).

[6] G.J. Sommer, A.K. Singh, and A.V. Hatch, "On-Chip Isoelectric Focusing Using Photopolymerized Immobilized PH Gradients", *Analytical Chemistry,* 80, 9 (2008).

[7] G. Lomeli and A.E. Herr, "Fabrication of Stable Gradients in a Hydrogel-filled Microfluidic Device", Technical Digest of the 25th International Conference on Miniaturized Systems for Chemistry and Life Sciences (µTAS 2021), Palm Springs, CA, 10/10-14/21.

[8] P. Abdel-Sayed, K.A. Yamauchi, R.E. Gerver, and A.E. Herr, "Fabrication of an Open Microfluidic Device for Immunoblotting", *Analytical Chemistry,* 89, 18 (2017).

[9] S. Jeeawoody, K.A. Yamauchi, A. Su, and A.E. Herr, "Laterally Aggregated Polyacrylamide Gels for Immunoprobed Isoelectric Focusing", *Analytical Chemistry,* 92, 4 (2020).

[10] R.A. O'Neill, A. Bhamidipati, X. Bi, D. Deb-Basu, L. Cahill, J. Ferrante, E. Gentalen, M. Glazer, J. Gossett, K. Hacker, C. Kirby, J. Knittle, R. Loder, C. Mastroieni, M. MacLaren, T. Mills, U. Nguyen, N. Parker, A. Rice, D. Roach, D. Suich, D. Voehringer, K. Voss, J. Yang, T. Yang, and P.B. Vander Horn, "Isoelectric Focusing Technology Quantifies Protein Signaling in 25 Cells", *Proceedings of the National Academy of Sciences*, 103, 44 (2006).

CONTACT

*A.E. Herr, tel: +1-510-666-3396; aeh@berkeley.edu

3D MICROPRINTING OF MULTI-ACTUATOR SOFT ROBOTS ONTO 3D-PRINTED MICROFLUIDIC DEVICES *VIA EX SITU* DIRECT LASER WRITING

Olivia M. Young[1], Chen-Yu Chen[1], Xin Xu[1], William E. Bentley[1], Mark D. Fuge[1], Axel Krieger[2], Paige Mass[3], Joshua P. Kanter[3], Laura Olivieri[3], and Ryan D. Sochol[1]*

[1]University of Maryland, College Park, MD, USA

[2]Johns Hopkins University, Baltimore, MD, USA

[3]Children's National Hospital & George Washington University, Washington DC, USA

ABSTRACT

Soft robots have emerged as powerful alternatives to their rigid counterparts due to inherent advantages including safety for human-robot interactions and adaptability for manipulating delicate objects. Despite recent developments for macroscale multi-actuator soft robots, manufacturing challenges have impeded the miniaturization of such systems due to difficulties in facilitating the macro-to-micro fluidic connections required for controlling soft robots with fluidic actuation schemes. To bypass these barriers, here we introduce a novel "*ex situ* Direct Laser Writing (*es*DLW)"-based hybrid strategy for additively manufacturing mesoscale 3D multi-actuator soft robotic systems directly atop externally accessible microfluidic devices. Specifically, we use two-photon *es*DLW to 3D microprint sophisticated mesoscale multi-actuator soft robotic systems directly on top of—and notably, fluidically sealed to—externally accessible "Digital Light Processing (DLP)"-based 3D-printed microfluidic devices. We interrogated the efficacy of this strategy by loading fluorescently labeled fluids into the *es*DLW-printed soft actuators as well as by performing cyclic burst-pressure experiments. Experimental results revealed uncompromised print-to-microdevice fluidic integrity both qualitatively from an absence of undesired leakage of the fluorescently labeled fluid and quantitatively for 100 cycles of pressure ramping up to 500 kPa inputs. In combination, these results suggest that the presented *es*DLW strategy holds promise as a pathway for scaling fluidically actuated soft robotic systems down to the mesoscale for emerging applications, such as for robot-assisted surgical interventions.

KEYWORDS

Soft Robots, Additive Manufacturing, 3D Printing, Direct Laser Writing, Digital Light Processing

INTRODUCTION

Often taking inspiration from nature, soft robots can be designed to mimic biological systems in the way they move and complete tasks [1,2]. Soft robots are made of compliant materials and have garnered increasing attention due a number of benefits over traditional rigid-bodied robots, particularly in terms of safety for human-robot interactions as well as adaptability for manipulating geometrically complex and/or delicate objects [3,4]. These characteristics make soft robots uniquely well suited for uses in biomedical applications, such as for robot-assisted surgical interventions and as drug delivery vehicles [5,6].

Additive manufacturing (or colloquially, "three-dimensional (3D) printing") has emerged as a robust candidate for soft robot fabrication by providing a pathway to complex, yet advantageous system designs and autonomous, repeatable robot construction [7]. Despite recent developments for macroscale multi-actuator soft robots by our group [8] and others [9-11], manufacturing hurdles have impeded the miniaturization of such systems. One particular challenge for fluidically actuated soft robots is the ability to achieve the macro-to-micro fluidic interfaces that are needed to deliver pneumatic and/or hydraulic inputs into the miniaturized robotic systems [12-14]. Thus, alternative manufacturing strategies that address this issue are in critical demand to enable new classes of mesoscale fluidically actuated soft robotic systems.

Among current additive manufacturing technologies, "Two-Photon Direct Laser Writing (DLW)" offers unparalleled geometric versatility and control with resolutions on the order of 100 nm [15]. Researchers have demonstrated how using DLW to print 3D micro-structures onto macroscale objects can benefit applications in the fields of optics and photonics [16,17] as well as microrobotics [18]. Recently, our group demonstrated such "*ex situ* DLW (*es*DLW)"

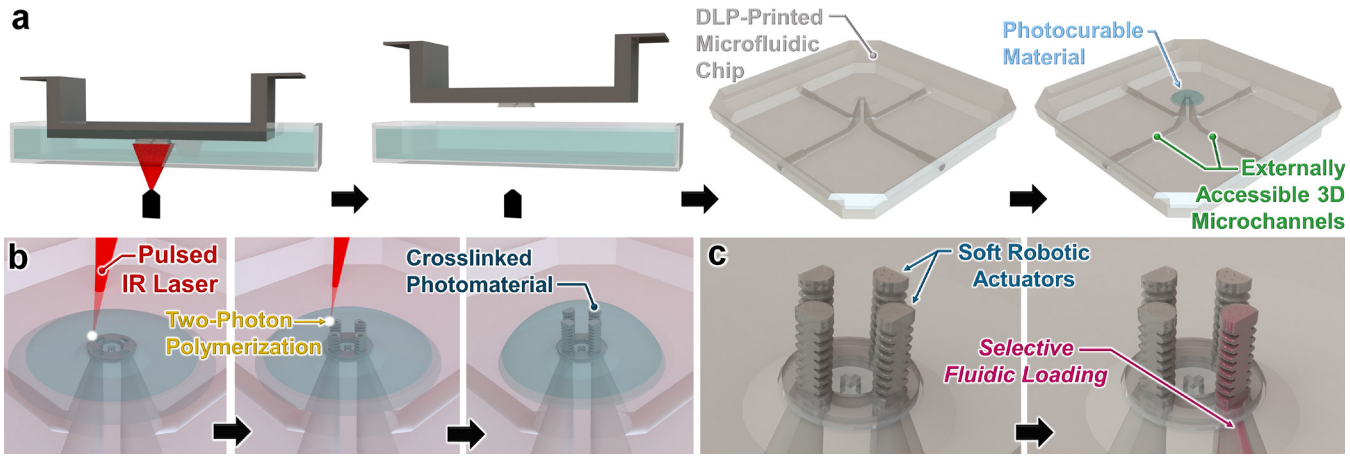

Figure 1: *Conceptual illustrations of the presented strategy for "ex situ Direct Laser Writing (esDLW)"-based 3D microprinting of meso-scale multi-actuator soft robotic systems atop externally accessible "Digital Light Processing (DLP)" 3D-printed microfluidic chips.* ***(a)*** *DLP 3D printing (left) of a microfluidic chip with externally accessible microchannels. Photomaterial is dispensed atop the microchannel ports (right) prior to loading in the DLW 3D printer.* ***(b)*** *The esDLW strategy for 3D microprinting multiple soft actuators directly atop (and fluidically sealed to) the DLP-printed microfluidic chip.* ***(c)*** *After development (to remove uncured photomaterial), input pressures can be applied independently to target actuators and fluids can be infused into and through the actuators for burst-pressure characterizations.*

978-1-940470-04-7/HH2022/$25©2022TRF
DOI 10.31438/trf.hh2022.83

strategies for printing 3D microfluidic technologies atop fluidic tubing [19,20]. Here we explore the potential for extending our *es*DLW approach to overcome the aforementioned challenges to miniaturization by enabling mesoscale multi-actuator soft robotic systems to be 3D microprinted directly onto—and notably, fluidically sealed to—externally accessible microfluidic devices.

CONCEPT

In this work, we introduce a hybrid additive manufacturing strategy for printing mesoscale multi-actuator soft robotic systems onto microfluidic devices (**Fig. 1**). Our approach comprises three primary steps. First, DLP-based 3D printing—a vat photopolymerization approach in which a photocurable material is selectively crosslinked in a layer-by-layer manner—is used to fabricate a microfluidic chip with externally accessible microfluidic channels (**Fig. 1a**). After developing the print to remove any residual DLP-associated photomaterial, a droplet of DLW-compatible photomaterial is dispensed atop the output ports of the microchannels (**Fig. 1a** – *right*). The device is then loaded into a DLW 3D printer, and the multi-actuator soft robot is *es*DLW-printed directly onto the microfluidic chip by scanning a femtosecond pulsed IR laser in a point-by-point, layer-by-layer manner to selectively crosslink the photomaterial in target locations *via* two-photon (or multi-photon) polymerization phenomena (**Fig. 1b**). Importantly, each actuator is printed to align to a distinct, corresponding microchannel output port of the DLP-printed chip. After development, fluids can be loaded *via* the distinct channels of the microfluidic device into desired actuators of the *es*DLW-printed soft robotic system (**Fig. 1c**).

MATERIALS AND METHODS

Digital Light Processing (DLP)-Based 3D Printing of the Microfluidic Chip

The microfluidic device was designed with externally accessible microchannels to allow for facile and targeted fluidic loading into the DLW-printed soft actuators. The microfluidic chips were designed using the computer-aided design (CAD) software, SolidWorks (Dassault Systèmes, France), and printed using the MiiCraft M50 3-D (CADworks3D, Ontario, Canada) DLP printer with the CADworks3D Clear Microfluidics Resin. After the print was completed, the devices were rinsed with isopropyl alcohol (IPA) to remove uncured photoresin from the surface of the device. The devices were then soaked in methanol for 1 min to facilitate clearing of the resin from the interior channels before using pressurized N_2 gas to clean the remaining resin from inside the channels. After removing the residual resin, the devices were UV cured for 10 s and, following a 30 s waiting period, flipped and UV cured for an additional 10 s. The devices were then rinsed with methanol and UV cured for a final 10 s period before being placed in vacuum for 24 hours to remove any residual organic solvents from the chip.

Ex situ Direct Laser Writing (*es*DLW)-Based 3D Microprinting of Multi-Actuator Soft Robotic Systems

The multi-actuator soft robotic systems were designed using the SolidWorks CAD software, exported as an STL file, and then imported into the computer-aided manufacturing (CAM) software, Describe (Nanoscribe GmbH, Karlsruhe, Germany), to generate the DLW laser writing path. The photoresist, IP-Q (Nanoscribe), was dispensed atop the DLP-printed microfluidic chip fully covering the output ports. The device was then loaded into the Nanoscribe Photonic Professional GT2 DLW system in the Dip-in Laser Lithography (DiLL) mode configuration with the 10× objective lens. The multi-actuator soft robotic systems were printed directly atop the DLP-printed microfluidic chips fully aligned to the output ports of the device. To ensure a complete fluidic seal between the microfluidic chip and the soft robotic system, the interface of the top surface of the microfluidic chip was found manually, and the printing process was initiated with approximately 50 μm of overlap between the base of the soft robotic system and the top of the microfluidic chip. Upon completion of the *es*DLW process, the multi-actuator soft robot was developed in propylene glycol methyl ether acetate (PGMEA) for 60 min and rinsed with IPA to remove any uncured photoresist. A vacuum pressure was then applied to each microchannel to remove any remaining uncured photoresist from the actuators. The devices were then dried with N_2 gas.

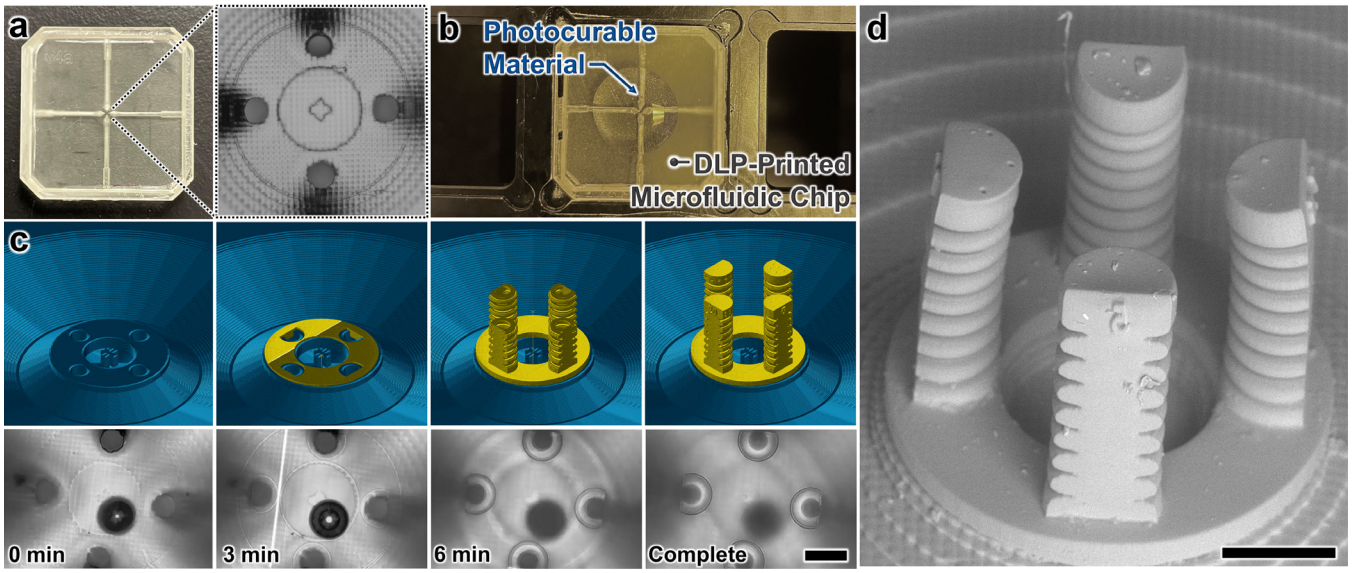

Figure 2: *Fabrication results.* ***(a,b)*** *The DLP-printed microfluidic device* ***(a)*** *before and* ***(b)*** *after dispensing the photomaterial atop the output ports.* ***(c)*** *Computer-aided manufacturing (CAM) simulations (top) and corresponding micrographs of the esDLW process (bottom) for 3D microprinting a multi-actuator soft robotic system directly onto the externally accessible microfluidic device (with each actuator aligned to a distinct, corresponding output port).* ***(d)*** *SEM micrograph of print results. Scale bars = 250 µm.*

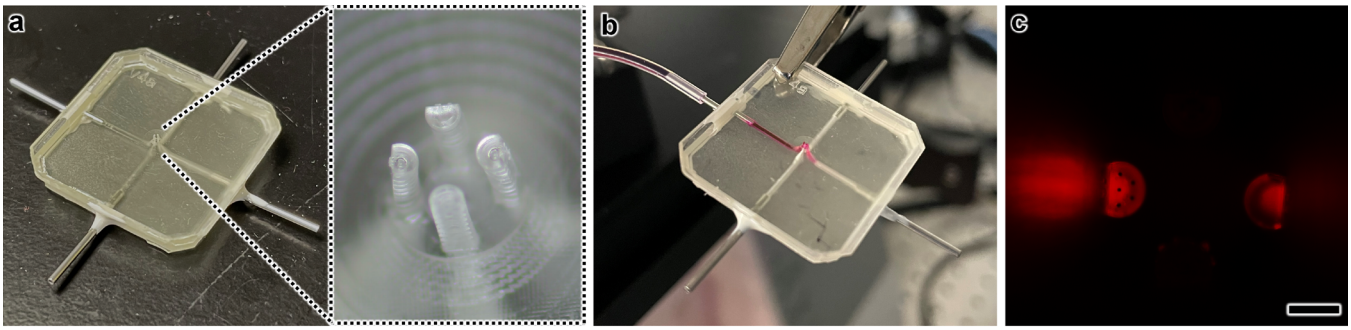

Figure 3: *Fluidic loading experimental results.* ***(a)*** *Images of the multi-actuator soft robotic system on the microfluidic chip prior to fluidic infusion.* ***(b)*** *Fluorescently dyed fluid infused through a channel and up (and out) a soft actuator.* ***(c)*** *Fluorescence micrograph of fluid in the soft actuator. Scale bar = 250 μm.*

Optical Characterization

Scanning electron microscope (SEM) images of fabrication results were obtained using a TM4000 Tabletop SEM (Hitachi, Tokyo, Japan). Brightfield and fluorescence imaging were performed using an inverted fluorescence microscope (Axio Observer.Z1, Zeiss, Germany) connected to a charge-coupled device (CCD) camera (Axiocam 503 Mono, Zeiss). Angled brightfield images were obtained using the Monocular Max 300x microscope objective connected to the Hayer 41MP HD 1080P camera (ShenZhen Hayear Electronics Co. Ltd, China).

Fluidic Experimentation

Fluidic testing was performed using the Fluigent Microfluidic Control System MFCS and OxyGEN software (Fluigent, France). The multi-actuator soft robotic systems were loaded with DI water using fluorinate ethylene propylene fluidic tubing (Cole-Parmer, Vernon Hills, IL) and stainless-steel catheter couplers (20 ga., Instech, Plymouth Meeting, PA). Three separate cyclic burst-pressure experiments were performed corresponding to applied input pressures of approximately 100 kPa, 250 kPa, and 500 kPa for 1.5 s, but then set to 0 kPa for 1.5 s after each pressure increase for all cases. Each set of experiments were performed for n = 100 cycles. For fluorescence imaging, the multi-actuator soft robot was loaded with fluorescently labeled DI water (Rhodamine B, MilliporeSigma, St. Louis, MO) at pressures of 1–3 kPa.

RESULTS AND DISCUSSION

*es*DLW-Based Fabrication

As a preliminary investigation of the efficacy of using *es*DLW to print soft actuators, we fabricated a multi-actuator soft robotic system directly atop DLP-printed microfluidic chips. The chips comprised four externally accessible microchannels with top outlet ports (diameter ≈ 140 μm) and side input ports with diameters of approximately 900 μm to fit 20 ga. stainless steel couplers (**Fig. 2a**). We designed the overall dimensions of the DLP-printed microfluidic device to allow for facile loading into the Nanoscribe DLW 3D printer (**Fig. 2b**). CAM simulations and corresponding micrographs of the *es*DLW process for printing the multi-actuator soft robot directly onto the microfluidic chip are presented in **Figure 2c**. The entire *es*DLW process was completed in less than 8 min. Use of the 10× objective lens during the *es*DLW process allowed the entire multi-actuator soft robot to be printed as a unified system in a single print run (*i.e.*, without any stitching). SEM micrographs of the completed multi-actuator soft robots revealed effective alignment and integration of the multiple soft robotic actuators with each designated fluidic outlet port (**Fig. 2d**). The SEM micrographs also showed no defects or breaks along the interface between the DLP-printed microfluidic chip and the multi-actuator soft robot.

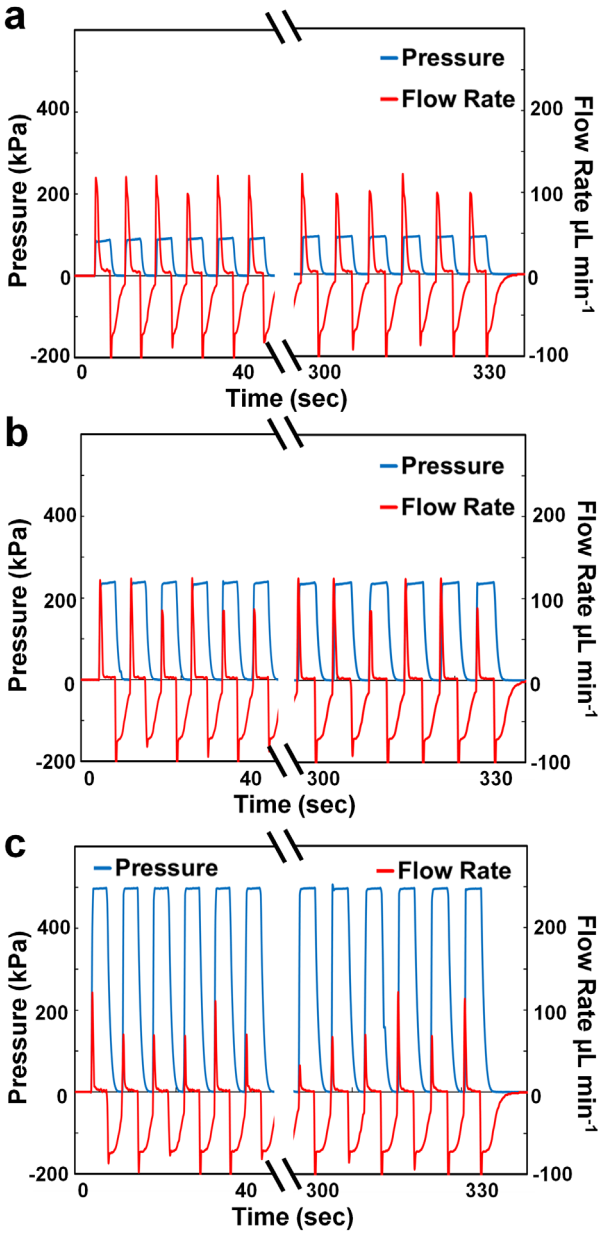

Figure 4: *Experimental results for cyclic burst-pressure testing for n = 100 cycles (per distinct pressure) with fluorescent DI water corresponding to cycles 1–6 and 94–100 for input pressures of:* ***(a)*** *100 kPa;* ***(b)*** *250 kPa; and* ***(c)*** *500 kPa.*

Fluidic Experimentation

As an initial measure of manufacturing efficacy, we performed fluidic loading experiments in which a fluorescently labelled fluid was inputted into the individual actuators to ensure there were no fluid leaks in the microfluidic chip (**Fig. 3a,b**). Fluorescence images of fluidic loading revealed that fluid was restricted to the interior microchannels and the soft actuators (**Fig. 3c**). These results also provided initial evidence supporting effective fluidic sealing between the DLP-printed microfluidic chip and the *es*DLW-printed multi-actuator soft robot system. To more thoroughly interrogate the integrity of this fluidic interface, we performed cyclic burst-pressure experiments for input pressures of 100 kPa, 250 kPa, and 500 kPa (n = 100 cycles for each case). Experimental results for the inputted pressures and corresponding flow rates did not reveal phenomena associated with undesired burst events or fluidic leakage (**Fig. 4**). Specifically, the flow rates consistently returned to 0 μL/min before the input pressure returned to 0 kPa for each pressure cycle for all cycles of all three pressures tested, including for 500 kPa—the upper limit of our experimental setup. Furthermore, we did not observe any significant changes in the flow rate peaks over the course of the experimental runs (**Fig. 4**). In combination, these results suggest that the presented hybrid 3D printing strategy yielded robust fluidic sealing between the DLP-printed microfluidic chip and the *es*DLW-printed soft robotic system, thereby satisfying a key capability for applications that demand high levels of pressurization associated with target soft robotic functionalities.

CONCLUSIONS

In this work, we explored the viability of using *es*DLW to print mesoscale multi-actuator soft robotic systems directly atop DLP-printed externally accessible microfluidic devices. The *es*DLW fabrication and experimental results revealed uncompromised fluidic sealing between the *es*DLW-printed soft actuators and the DLP-printed chip up to 500 kPa for n = 100 cycles. Future efforts should focus on investigating actuation routines for such soft robotic systems as a function of inputted pressures. Although the current study centers on fluidically actuated soft robots, it should be noted that the manufacturing strategy could be extended to a diversity of fields, including for the development of organ-on-a-chip systems. Nonetheless, the mechanical integrity and fluidic loading results demonstrated here can provide a foundation for future soft robotic applications, such as for robot-assisted surgical interventions.

ACKNOWLEDGEMENTS

The authors greatly appreciate the contributions of Bioinspired Advanced Manufacturing (BAM) Laboratory members and Terrapin Works staff at the University of Maryland, College Park. O.Y. is supported by the Clark Doctoral Fellows Program.

REFERENCES

[1] W. Tang, Y. Lin, C. Zhang, Y.L. Liang, J. Wang, W. Wang, *et al.*, "Self-Contained Soft Electrofluidic Actuators", *Science Advances*, 7, 34, (2021).

[2] Z. Li, N.V. Myung, and Y. Yin, "Light-Powered Soft Steam Engines for Self-Adaptive Oscillation and Biomimetic Swimming", *Science Robotics*, 6, 61, (2021)

[3] D. Drotman, S. Jadhav, C. Chan, and M.T. Tolley, "Electronics-Free Pneumatic Circuits for Controlling Soft-Legged Robots", *Science Robotics*, 6, 51 (2021).

[4] W. Huang, J. Xiao, and Z. Xu, "A Variable Structure Pneumatic Soft Robot", *Scientific Reports*, 10, 18778, (2020).

[5] Q. Ze, S. Wu, J. Nishikawa, J. Dai, Y. Sun, S Leanza, *et al*., "Soft Robotic Origami Crawler", *Science Advances*, 8, 13, (2022).

[6] Z. Ren, R. Zhang, R.H. Soon, Z. Liu, W. Hu, P.R. Onck, and M. Sitti, "Soft-Bodied Adaptive Multimodal Locomotion Strategies in Fluid-Filled Confined Spaces", *Science Advances*, 7, 27, (2021).

[7] E.B. Joyee, A.Szmelter, D. Eddinton, and Y. Pan, "3D Printed Biomimetic Soft Robot with Multimodal Locomotion and Multifunctionality", *Soft Robotics*, 9, 1 (2022).

[8] J.D. Hubbard, R. Acevedo, K.M. Edwards, A.T. Alsharhan, Z. Wen, J. Landry, *et al*., "Fully 3D-Printed Soft Robots with Integrated Fluidic Circuitry", *Science Advances*, 7, 29 (2021).

[9] G. Fang, M.C.K. Chow, J.D.L. Ho, Z. He, K. Wang, T.C. Ng, *et al.*, "Soft robotic manipulator for intraoperative MRI-guided transoral laser microsurgery", *Science Robotics*, 6, 57 (2021).

[10] W. Lee, D.J. Preston, M.P. Nemitz, A. Nagarkar, A.K. Mackeith, B. Gorissen, *et al*., "A Buckling-Sheet Ring Oscillator for Electronics-Free Multimodal Locomotion", *Science Robotics*, 7, 63, (2022).

[11] A. Heiden, D. Prennger, JL. Hehner, M. Baumgartner, M. Drack, E. Woritzka, *et al*., "3D Printing of Resilient Biogels for Omnidirectional and Exteroceptive Soft Actuators", *Science Robotics*, 7, 63, (2022).

[12] A.T. Alsharhan, O.M. Young, X. Xu, A.J. Stair, and R.D. Sochol, "Integrated 3D Printed Microfluidic Circuitry and Soft Microrobotic Actuators via *In Situ* Direct Laser Writing", *Journal of Micromechancics and Microengeering*, 31, 4 (2021).

[13] S. Li, R. Zhang, GJ. Zhang, L. Shuai, W. Chang, X. Hu, *et al*., "Microfluidic Manipulation by Spiral Hollow-Fibre Actuators", *Nature Communications*, 13, 1331, (2022).

[14] T. Gopesh, J.H. Wen, D. Santiago-Dieppa, B. Yan, J.S. Pannell, A. Khalessi, A. Norbash, and J. Friend, "Soft Robotic Steerable Microcatheter for the Endovascular Treatment of Cerebral Disorders", *Science Robotics*, 6, 57, (2021).

[15] V. Hahn, P. Kiefer, T. Frenzel, J. Qu, E. Blasco, C. Barner-Kowollik, and M. Wegener, "Rapid Assembly of Small Materials Building Blocks (Voxels) into Large Functional 3D Metamaterials", *Advanced Functional Materials*, 30, 26 (2020).

[16] T. Gissibl, S. Thiele, A. Herkommer, and H. Giessen, "Two-Photon Direct Laser Writing of Ultracompact Multi-lens Objectives", *Nature Photonics*, 10 (2016).

[17] P.-I. Dietrich, M. Blaicher, I. Reuter, M. Billah, T. Hoose, A. Hofmann, *et al*., "In Site 3D Nanoprinting of Free-Form Coupling Elements for Hybrid Photonic Integration", *Nature Photonics*, 12, (2018).

[18] A. Barbot, M. Power, F. Seichepine, and G. Yang, "Liquid Seal for Compact Micropiston Actuation at the Capillary Tip", *Science Advances*, 6, 22, (2020).

[19] R. Acevedo, Z. Wen, I. Rosenthal, E.Z. Freeman, M. Restaino, N. Gonzalez, and R. D. Sochol, "3D Nanoprinted External Microfluidic Structures *via Ex Situ* Direct Laser Writing", 2021 IEEE 34th International Conference on Micro Electro Mechanical Systems (MEMS), Gainesville, FL, 1/25-29/21, IEEE, (2021), pp. 10-13.

[20] Z. Wen, R. Acevedo, K. Rand-Yadin, and R.D. Sochol, "3D Nanoprinted Microinjection Needles *via Ex Situ* Direct Laser Writing", 25th International Conference on Miniaturized Systems for Chemistry and Life Sciences (μTAS), Palm Springs, CA, 10/10-14/21, Chemical and Biological Microsystems Society (2021).

CONTACT

*O.M. Young, tel: +1-301-405-6928; oyoung@umd.edu

A 9.4 GHZ INTRINSICALLY SWITCHABLE LAMB-WAVE RESONATOR USING ATOMIC-LAYER-DEPOSITED FERROELECTRIC HAFNIA-ZIRCONIA

Troy Tharpe and Roozbeh Tabrizian*
Electrical and Computer Engineering Department, University of Florida, Gainesville, Florida, USA

ABSTRACT

This paper reports the first-ever demonstration of a 9.4 GHz Lamb-wave resonator with intrinsic switchability in atomic-layer-deposited (ALD) ferroelectric hafnia-zirconia ($Hf_{0.5}Zr_{0.5}O_2$) films. The resonator is comprised of a 50nm-thick laminated $Hf_{0.5}Zr_{0.5}O_2$ transducer, sandwiched between ~20nm-thick tungsten (W) electrodes. The high resonance frequency is achieved by exciting asymmetric shear-based Lamb-waves, using the rotated polar axis of $Hf_{0.5}Zr_{0.5}O_2$, and with a frequency defined primarily by the transducer thickness. Intrinsic switchability is achieved by nulling the instantaneous polarization of the $Hf_{0.5}Zr_{0.5}O_2$, thanks to the ferroelectric behavior of the film. The resonator prototype demonstrates a quality factor (Q) of 314 and an electromechanical coupling factor (k_t^2) of 0.31% and is intrinsically switched through application of a 10.5V DC. Relying on a standard-CMOS materials and process, along with the very high resonance frequency and the intrinsic switchability, $Hf_{0.5}Zr_{0.5}O_2$ Lamb-wave resonators highlight the promise for creation of CMOS-monolithic frequency references over cm- and mm-wave regimes.

KEYWORDS

Ferroelectric, hafnia-zirconia, Lamb-wave, resonator, intrinsic, switchability, super high frequency.

INTRODUCTION

Micro- and nano-acoustic resonators are vital for creation of chip-scale clocks, frequency references, and spectral processors in modern electronic systems. Q's that are multiple orders of magnitude higher than integrated passives make these resonators superior [1][2]. However, the non-monolithic integration, due to CMOS incompatible fabrication process, and the quality degradation of conventional (*e.g.*, sputtered) piezoelectric films upon miniaturization for frequency scaling, set major barriers for adoption of acoustic resonators in cm- and mm-wave frequency control systems. Further, the exponential increase in wireless traffic volume and corresponding increase in number of frequency bands expose a substantial footprint challenge for current non-monolithic integration approaches.

Despite these inherent drawbacks and challenges, the discovery of ferroelectricity in hafnia [3], along with the first demonstration of ferroelectric hafnia-zirconia as a nanoelectromechanical transducer [4][5][6], augur a promising solution for monolithic integration of high-Q nano-acoustic resonators in advanced semiconductor nodes. Benefiting from the inherent CMOS compatibility and outstanding thickness scalability to sub-5nm [7], ALD ferroelectric hafnia-zirconia films are poised to realize CMOS-monolithic super- and extremely-high frequency nano-acoustic resonators integrated in front- or back-end-of-line (FEOL / BEOL). Here, we demonstrate this potential by presenting the first super-high-frequency ALD hafnia-zirconia resonator, and further demonstrate the intrinsic switchability feature that is enabled by ferroelectricity.

HAFNIA-ZIRCONIA TRANSDUCER

Ferroelectricity, and therefore piezoelectricity within $Hf_{0.5}Zr_{0.5}O_2$ corresponds to the formation of the noncentrosymmetric, polar orthorhombic crystal phase (space group $Pca2_1$) [8][9], stabilized through application of biaxial stress

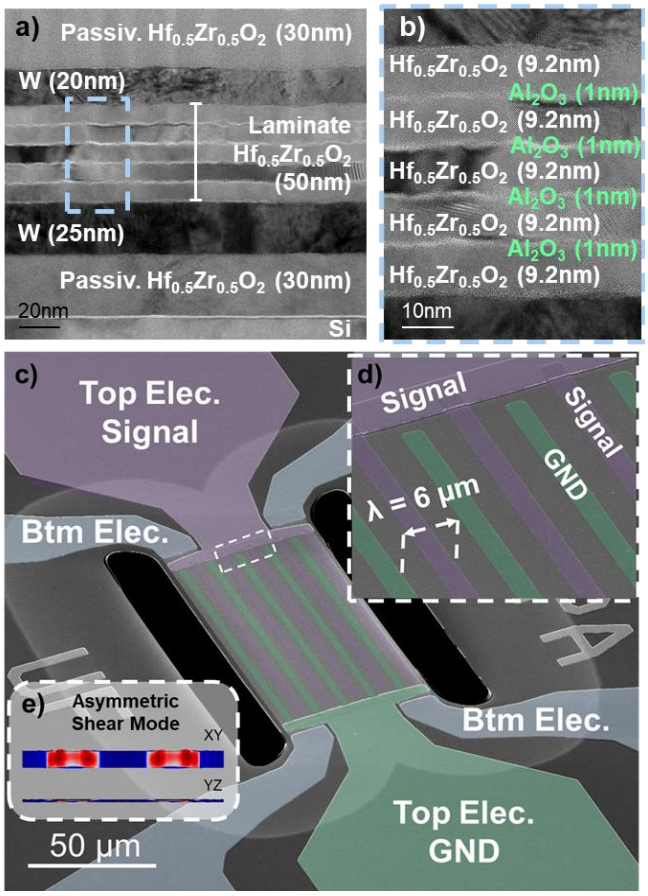

Figure 1. *a) TEM image of the resonant stack with constituent layer material and thickness annotated. b) Small scale TEM image highlighting individual layers of the 50nm, $Hf_{0.5}Zr_{0.5}O_2$ laminate transducer. c) SEM image of a 9.4 GHz intrinsically switchable, $Hf_{0.5}Zr_{0.5}O_2$ Lamb-mode resonator. d) Small-scale SEM highlighting electrode configuration and 6 µm IDT pitch. e) Asymmetric, shear BAW resonance mode.*

[10][11] and limitation of grain size [12]. To provide this environment for ferroelectricity, the 50nm $Hf_{0.5}Zr_{0.5}O_2$ transducer is formed via alternating ALD of 9.2nm $Hf_{0.5}Zr_{0.5}O_2$ and 1nm of Al_2O_3 to limit grain size during crystallization. Crystallization is achieved by rapid thermal anneal (RTA) for 20s in nitrogen ambient, with W electrodes serving as mechanical boundary. Figure 1 (a) depicts a transmission electron microscope (TEM) image of the resonator cross section, while Fig. 1 (b) shows a TEM image highlighting the 50nm, laminate $Hf_{0.5}Zr_{0.5}O_2$ transducer.

Thickness scaling of the $Hf_{0.5}Zr_{0.5}O_2$ transducer to 50nm and beyond is favorable for a larger measurable displacement upon application of electromagnetic field [13]. To verify ferroelectric behavior and electromechanical coupling (post RTA), polarization and displacement hysteresis loops for 20nm W/ 50nm $Hf_{0.5}Zr_{0.5}O_2$/ 25nm W capacitors are measured using a Radiant PiezoMEMS analyzer and NLV laser vibrometer. Figure 2 depicts polarization

978-1-940470-04-7/HH2022/$25©2022TRF
DOI 10.31438/trf.hh2022.84

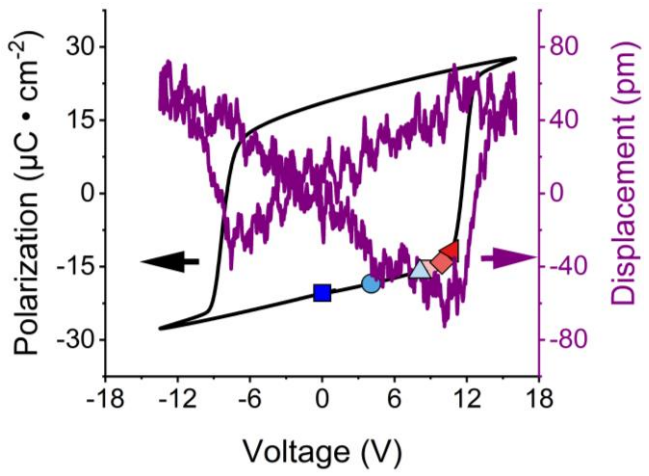

Figure 2. *Polarization and displacement hysteresis loops for a 0.0025 cm² W/ $Hf_{0.5}Zr_{0.5}O_2$/ W capacitor with thickness dimensions noted in Figure 1. d). Highlighted bias voltages correspond to measurement conditions in Figure 4.*

and displacement loops for an unreleased, 0.0025cm² capacitor with cross section identical to fabricated Lamb-wave prototypes, after application of 1,000 cycles of a 15V, 1kHz, square wakeup pulse. Highlighted voltages represent (from left to right) 0V, 4V, 8V, 8.6V, 9.4V, and 10.5V and relate to resonator admittance measurements taken at port 1 subject to corresponding bias.

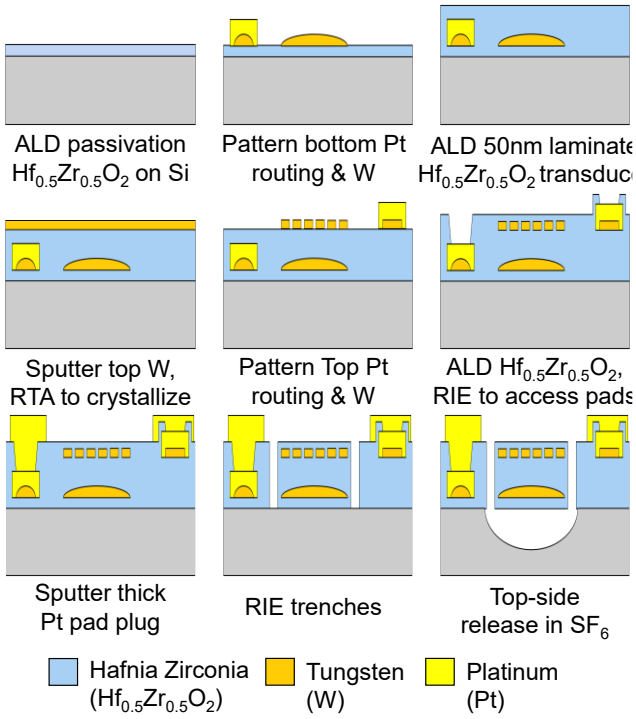

Figure 3. *CMOS-compatible fabrication process to realize $Hf_{0.5}Zr_{0.5}O_2$ Lamb-mode resonators.*

FABRICATION PROCESS

Figure 3 summarizes the nine-step, CMOS compatible fabrication process flow used to realize $Hf_{0.5}Zr_{0.5}O_2$ Lamb-mode resonator prototypes.

Starting with a high resistivity silicon (Si) wafer, 30nm of $Hf_{0.5}Zr_{0.5}O_2$ passivation layer is deposited via ALD using tetrakis(dimethylamido)hafnium(IV) (TDMAH) and tetrakis(dimethylamido)zirconium(IV) (TDMAZ) precursors with a cycle ratio of 1:1. Application of hydrogen and oxygen plasmas at 300W with each monolayer, oxidizes the layer and promotes the formation of orthorhombic phase during subsequent RTA [14][15]. This bottom passivation layer is so named as it protects bottom electrode layers during future release steps. Next 25nm of W is sputtered and patterned using a sulfur hexafluoride (SF_6) and argon reactive ion etch (RIE) recipe to form resonator bottom electrodes, while 150nm of platinum (Pt) is lifted off for bottom routing. Then, the nanolaminate transducer is formed via ALD of 5x 9.2 nm $Hf_{0.5}Zr_{0.5}O_2$ layers, intercalated with 4x 1nm thermal Al_2O_3, using trimethylaluminum (TMA) precursor. Top 20nm W is then sputtered and RTA performed. Subsequently, top device electrodes are pattered using RIE, and top 150nm Pt routing is again lifted off. A symmetric, top 30nm ALD $Hf_{0.5}Zr_{0.5}O_2$ passivation layer is then deposited to again protect the resonant body during release. Access to top and bottom Pt pads are etched using a chlorine (Cl_2), Ar gas chemistry in RIE and thick, 200nm Pt pad plugs are lifted off to form a low resistance resonator contact point. Finally, resonator trenches are defined using a Cl_2 / Ar RIE etch, and the device is released via topside etching of Si using SF_6.

RESONATOR OPERATION MODE

The presented $Hf_{0.5}Zr_{0.5}O_2$, resonators have been primarily designed for excitation of symmetric Lamb modes with predominantly extensional elastic fields. However, due to the unique texturing process of $Hf_{0.5}Zr_{0.5}O_2$ upon annealing and wake-up cycling [16][17], a non-normal (*i.e.*, rotated) polar- / c-axis is achieved that enables excitation of asymmetric modes upon application of electric field across the thickness. In particular, the rotated polar axis enables excitation of an asymmetric Lamb wave with predominant thickness-shear content at 9.4 GHz. Figure 1 (c) depicts a scanning electron microscope (SEM) image of the released resonator prototype. The one-port resonator is configured with one pair of interdigitated transducers (IDTs) connected to a drive signal (highlighted purple), with another IDT pair connected to ground (highlighted green). A floating device bottom electrode (highlighted blue) allows for application of uniform electric field across the thickness of $Hf_{0.5}Zr_{0.5}O_2$ transducer. Considering the rotated polar axis of the film, the vertical electric field enables excitation of both thickness-extensional and thickness-shear waves through the longitudinal piezoelectric coefficient (d_{33}). Figure 1 (d) depicts a small-scale SEM image of the realized Lamb-mode resonator's top electrode, denoting IDT configuration. Figure 1 (e) shows the COMSOL simulated, asymmetric shear mode of excitation, with a polar c-axis tilt of 34º, and frequency primarily defined by transducer thickness.

RESONATOR CHARACTERIZATION

Admittance ($|Y_{11}|$) responses of the presented $Hf_{0.5}Zr_{0.5}O_2$, Lamb-wave resonator are taken using a Keysight N522A vector network analyzer, with a variable DC bias applied to port 1 via bias-Tee network and benchtop DC source. Figure 4 (a) depicts measured $|Y_{11}|$ responses for the resonator presented in Figure 1 (c). Of note, is the coloring and symbology of applied bias voltage, which can be mapped to points denoted on the polarization hysteresis loop displayed in Fig. 2. In the On state (0V DC applied), a Q of 314 and a k_t^2 of 0.31% is measured for the mode at 9.4 GHz. While the Off state corresponds to the application of 10.5V DC, in which the transducer is nearly depolarized, nulling the electromechanical

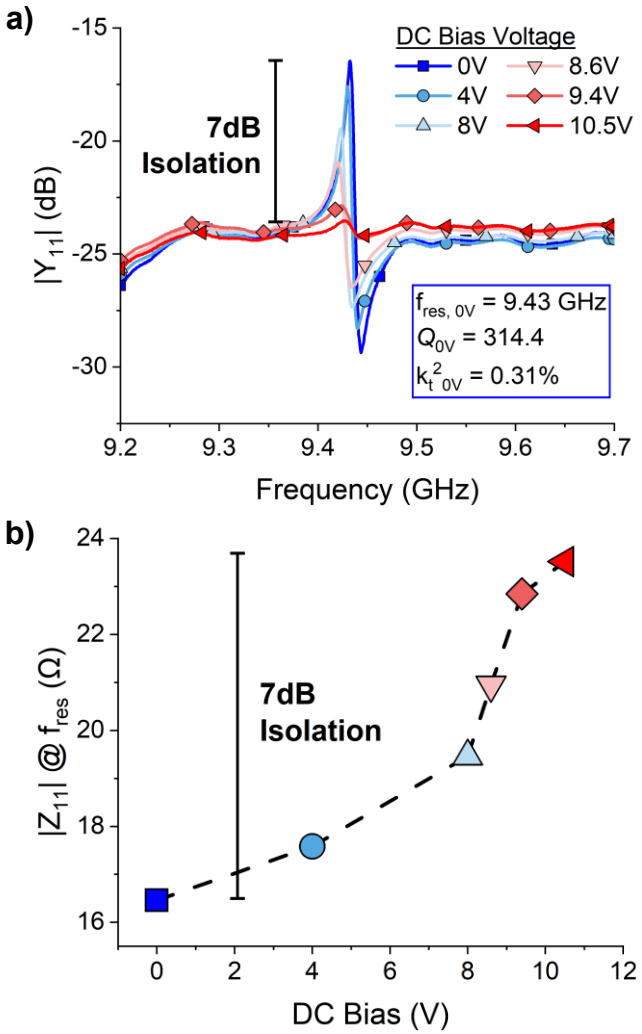

Figure 4. *a) Measured admittance of the device shown in Figure 1. c) taken at varied DC bias. As voltages near coercive and the $Hf_{0.5}Zr_{0.5}O_2$ film depolarizes, the asymmetric, shear, Lamb-mode switches off with 7dB of isolation. b) The magnitude of impedance ($|Z_{11}|$) at resonance for varied DC bias.*

coupling and resulting in ~7dB of on/off isolation. Figure 4. (b) relates bias voltages to impedance values ($|Z_{11}|$).

ELECTROMECHANICAL COUPLING DISCUSSION

The extracted k_t^2 of 0.31% is appreciably smaller than expected for Lamb-mode resonators transduced by $Hf_{0.5}Zr_{0.5}O_2$, owing to $Hf_{0.5}Zr_{0.5}O_2$'s large reported d_{33} coefficient [13]. This lower-than-expected coupling is due to the reversion of polar orthorhombic phase to non-polar monoclinic phase upon resonator release, as first reported elsewhere [18]. With the polar orthorhombic phase of $Hf_{0.5}Zr_{0.5}O_2$ being highly sensitive to stress variations in mechanical boundary condition, it is reasonable to conclude that stress relaxation over the release process results in a lower total percentage of polar orthorhombic phase. This lower percentage of orthorhombic phase in turn decreases k_t^2 as a lower percentage of total transducer volume is polar and therefore capable of electromechanical transduction. Grazing incident x-ray diffraction (GIXRD) can be used to support this, as polar (111) orthorhombic phase for $Hf_{0.5}Zr_{0.5}O_2$ appears at 30.5º 2θ and is discernible from nonpolar monoclinic $(\bar{1}11)$ at 28.5º 2θ and (111) at 31.9º 2θ when indexed according to existing literature [12][19][20].

Figure 5 (a) shows GIXRD scans taken using a Panalytic X'pert Materials Research Diffractometer (MRD) system with xenon proportional detectors for 2θ varied from 28º to 33º, for released and unreleased ferroelectric $Hf_{0.5}Zr_{0.5}O_2$ samples. Note the clear promotion of nonpolar monoclinic phase upon release of $Hf_{0.5}Zr_{0.5}O_2$. Figure 5 (b-c) depicts unit cells for polar orthorhombic and nonpolar monoclinic phases. The lower percentage of polar phase in released films results in diminished ferroelectricity and is a likely cause for the relatively low exhibited k_t^2, representing a need for further investigation.

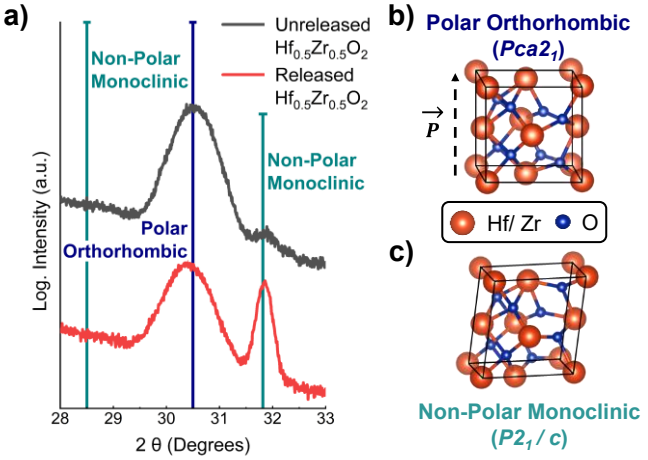

Figure 5. *a) GIXRD scans of released & unreleased, ferroelectric $Hf_{0.5}Zr_{0.5}O_2$ films. Release results in the clear promotion of non-polar, monoclinic phase at 31.8º. b) The polar orthorhombic cell (space group $Pca2_1$) responsible for ferroelectricity in $Hf_{0.5}Zr_{0.5}O_2$. c) The non-polar, monoclinic cell (space group $P2_1/c$).*

CONCLUSION

This work reports the first ever super-high-frequency, ALD hafnia-zirconia resonator, realized via piezoelectric transduction of asymmetric shear-based Lamb-waves at 9.4 GHz. At 0V applied bias, the Lamb-mode resonator achieves a Q of 314.4 and k_t^2 of 0.31%. Additionally, the intrinsic switchability of ferroelectric $Hf_{0.5}Zr_{0.5}O_2$ is demonstrated, with $Hf_{0.5}Zr_{0.5}O_2$ completely depolarizing, and the resonator switching off upon application of 10.5V DC. Comparing on vs off $|Y_{11}|$/ $|Z_{11}|$ yields 7dB of isolation. Further, reasons for lower-than-expected resonator k_t^2 are discussed, with proof found in underlying material morphology.

ACKNOWLEDGEMENTS

This project is supported by DARPA Young Faculty Award program. The authors would like to thank DARPA program manager Dr. Timothy Hancock for his support of this work. The authors would also like to thank the University of Florida Nanoscale Research Facility staff for their great help regarding fabrication and material characterization throughout this project.

REFERENCES

[1] H. Bhugra and G. Piazza, *Piezoelectric MEMS resonators*. Springer, 2017.

[2] D. S. Gardner, G. Schrom, F. Paillet, B. Jamieson, T. Karnik, and S. Borkar, "Review of on-chip inductor

structures with magnetic films," *IEEE Trans. Magn.*, vol. 45, no. 10, pp. 4760–4766, 2009, doi: 10.1109/TMAG.2009.2030590.
[3] T. S. Böscke, J. Müller, D. Bräuhaus, U. Schröder, and U. Böttger, "Ferroelectricity in hafnium oxide thin films," *Appl. Phys. Lett.*, vol. 99, no. 10, 2011, doi: 10.1063/1.3634052.
[4] M. Ghatge, G. Walters, T. Nishida, and R. Tabrizian, "An ultrathin integrated nanoelectromechanical transducer based on hafnium zirconium oxide," *Nat. Electron.*, vol. 2, no. 11, pp. 506–512, 2019, doi: 10.1038/s41928-019-0305-3.
[5] M. Ghatge, G. Walters, T. Nishida, and R. Tabrizian, "A Nano-Mechanical Resonator with 10nm Hafnium-Zirconium Oxide Ferroelectric Transducer," *2018 IEEE Int. Electron Devices Meet.*, pp. 4.6.1-4.6.4, 2019, doi: 10.1109/IEDM.2018.8614633.
[6] M. Ghatge, G. Walters, T. Nishida, and R. Tabrizian, "High-Q UHF and SHF Bulk Acoustic Wave Resonators with Ten-Nanometer Hf0.5Zr0.5O2 Ferroelectric Transducer," *2019 20th Int. Conf. Solid-State Sensors, Actuators Microsystems Eurosensors XXXIII (TRANSDUCERS EUROSENSORS XXXIII)*, pp. 446–449, 2019, doi: 10.1109/TRANSDUCERS.2019.8808308.
[7] J. Lyu, T. Song, I. Fina, and F. Sánchez, "High polarization, endurance and retention in sub-5 nm Hf0.5Zr0.5O2films," *Nanoscale*, vol. 12, no. 20, pp. 11280–11287, 2020, doi: 10.1039/d0nr02204g.
[8] R. Materlik, C. Künneth, and A. Kersch, "The origin of ferroelectricity in Hf 1−x Zr x O 2 : A computational investigation and a surface energy model," *J. Appl. Phys.*, vol. 117, no. 13, p. 134109, Apr. 2015, doi: 10.1063/1.4916707.
[9] R. Batra, T. D. Huan, J. L. Jones, G. Rossetti, and R. Ramprasad, "Factors Favoring Ferroelectricity in Hafnia: A First-Principles Computational Study," *J. Phys. Chem. C*, vol. 121, no. 8, pp. 4139–4145, 2017, doi: 10.1021/acs.jpcc.6b11972.
[10] M. H. Park *et al.*, "Study on the degradation mechanism of the ferroelectric properties of thin Hf0.5Zr0.5O2 films on TiN and Ir electrodes," *Appl. Phys. Lett.*, vol. 105, no. 7, pp. 0–5, 2014, doi: 10.1063/1.4893376.
[11] T. Shiraishi *et al.*, "Impact of mechanical stress on ferroelectricity in (Hf0.5Zr0.5)O2 thin films," *Appl. Phys. Lett.*, vol. 108, no. 26, pp. 0–5, 2016, doi: 10.1063/1.4954942.
[12] H. J. Kim *et al.*, "Grain size engineering for ferroelectric Hf0.5Zr0.5O2 films by an insertion of Al2O3 interlayer," *Appl. Phys. Lett.*, vol. 105, no. 19, pp. 1–6, 2014, doi: 10.1063/1.4902072.
[13] S. Kirbach, K. Kühnel, and W. Weinreich, "Piezoelectric Hafnium Oxide Thin Films for Energy-Harvesting Applications," *Proc. IEEE Conf. Nanotechnol.*, vol. 2018-July, pp. 2018–2021, 2019, doi: 10.1109/NANO.2018.8626275.
[14] T. Tharpe, F. Hakim, and R. Tabrizian, "In-Plane Bulk Acoustic Resonators Using 50nm-Thick Nano-Laminated Ferroelectric Hf0.5Zr0.5O2," *21st Int. Conf. Solid-State Sensors, Actuators Microsystems, TRANSDUCERS 2021*, pp. 313–316, 2021, doi: 10.1109/Transducers50396.2021.9495745.
[15] G. Walters, A. Shekhawat, S. Moghaddam, J. L. Jones, and T. Nishida, "Effect of in situ hydrogen plasma on the ferroelectricity of hafnium zirconium oxide films," *Appl. Phys. Lett.*, vol. 116, no. 3, 2020, doi: 10.1063/1.5135709.
[16] M. Lederer *et al.*, "On the Origin of Wake-Up and Antiferroelectric-Like Behavior in Ferroelectric Hafnium Oxide," *Phys. status solidi - Rapid Res. Lett.*, vol. 15, no. 5, 2021.
[17] P. D. Lomenzo *et al.*, "Harnessing Phase Transitions in Antiferroelectric ZrO2 Using the Size Effect," *Adv. Electron. Mater.*, vol. 2100556, pp. 1–10, 2021, doi: 10.1002/aelm.202100556.
[18] T. Tharpe, X. Zheng, P. X. Feng, and R. Tabrizian, "Resolving Mechanical Properties and Morphology Evolution of Free-Standing Ferroelectric Hf0.5Zr0.5O2," *Adv. Eng. Mater.*, vol. 2101221, pp. 1–9, 2021, doi: 10.1002/adem.202101221.
[19] A. Phys *et al.*, "Compositional and phase dependence of elastic modulus of crystalline and amorphous Hf 1- x Zr x O 2 thin films Compositional and phase dependence of elastic modulus of crystalline and amorphous Hf 1- x Zr x O 2 thin films," vol. 102901, no. February, 2021, doi: 10.1063/5.0044702.
[20] S. Riedel, P. Polakowski, and J. Müller, "A thermally robust and thickness independent ferroelectric phase in laminated hafnium zirconium oxide," vol. 095123, no. June, 2016, doi: 10.1063/1.4964300.

CONTACT

*Troy Tharpe, tel: +1-321-4329557; ttharpe@ufl.edu.

A MICROTIP EQUIPPED BIDIRECTIONAL MICROROBOT FOR NAVIGATING ON AND PENETRATING A LEAF SURFACE

Tony H. Wang, Dea Gyu Kim, Zhijian Hao, and Azadeh Ansari
School of Electrical and Computer Engineering, Georgia Institute of Technology, Atlanta, Georgia, USA

ABSTRACT

This work presents a novel, magnetically actuated, micro-scale robot (with dimensions of 100µm × 112µm × 44µm), equipped with a 43µm long microtip. Under an out-of-plane, sawtooth magnetic wave, the robot undergoes stick-slip motion about its rockers with speeds up to 140µm/s and can travel either forward or backward via introducing a magnetic field offset. When subject to a static, out-of-plane magnetic field, the microrobot upends on its tip and can penetrate leaf tissue, demonstrating selective tip engagement and potential biomedical applications such as drug delivery and DNA extraction.

KEYWORDS

Microrobots, magnetic actuation, microtip, stick-slip motion

INTRODUCTION

Microscale robots (microrobots) show promise for biomedical applications such as drug delivery [1, 2] and microsurgery [3] due to their smaller sizes, less invasive nature, and higher capabilities of maneuvering precisely in narrow and otherwise inaccessible spaces when compared to conventional robots. As the powering provided by on-board batteries becomes insufficient at microscale [4], current methods of microrobot actuation mainly consist of off-board approaches such as magnetic fields, acoustic excitation, electric fields, and optical/thermal heating.

From a biomedical application perspective, magnetic fields are the most attractive approach due to their penetration through tissue, good biocompatibility, and higher steering capabilities. In [1], Lee et al. designed and fabricated a nickel-coated, helical microrobot with a needle to attach onto microtissues for drug delivery. When coated with a biocompatible material such as titanium [2], microrobots could grow stem-cells on their structures and act as transporters. Microrobots with higher remanent magnetic materials, such as neodymium, can penetrate as well as drill through tissue [3] for microsurgical purposes.

Current magnetic setups often utilize multi-axis electromagnetic coils to generate magnetic fields, such as rotational magnetic fields, for motion manipulation. Examples include Helmholtz coils, which enforce uniform magnetic fields, and Maxwell coils, which generate uniform magnetic gradients. While these systems are used extensively in magnetic microrobot literature, their use of multiple in-plane (IP) and out-of-plane (OOP) coils limit the working space of the microrobots to the confines of the electromagnets. This proves disadvantageous if such a setup needs to be placed under a microscope of limited focal length or incorporated around a patient. A more simplistic system, demonstrating the same capabilities as the previous examples, is necessary to advance the range of applications for microrobots.

In this work, we present a microrobot (100µm × 112µm × 44µm) equipped with a 43µm long microtip and capable of bidirectional motion from a single electromagnet. 3D printed via two-photon polymerization (2PP), the microrobot (Figure 1a) consists of a main polymeric body deposited with a nickel thin film and two rocker-like contacts and will henceforth be named the microrocker bot. Under an OOP, static magnetic field within ±1mT provided by the electromagnet, the microrocker bot tilts either forward (with positive offset) or backward (with negative offset) to

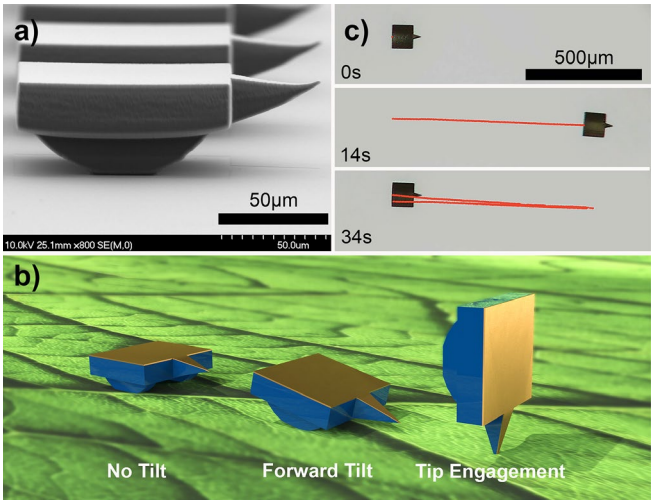

Figure 1: a) Side SEM view of the microrobot. b) A schematic depicting the positional biases of the microrobot from a magnetic offset. The nickel thin film is colored gold while the main body is colored blue. c) Tracked forward and backward motion of the microrobot on glass under a 16Hz oscillating OOP magnetic field.

align its magnetization, biasing its position towards either direction. Outside this range, the microrocker bot completely upends on its front or back for potential tip engagement, demonstrating a new actuation mode (Figure 1b). When the static field is used as a small offset combined with an oscillating magnetic waveform, the robot can travel either forward or backward (Figure 1c) with speeds up to 140µm/s on glass

Additionally, the microrobot could demonstrate bidirectional motion on the biological, rougher surface of a leaf (*Lysimachia nummularia*). When induced with sufficient magnetic field amplitude, the microrocker bot penetrated the leaf surface via upending on its microtip. Such a result provides insights into possible applications for drug delivery and plant DNA extraction.

BACKGROUND

Magnetic actuation

For soft magnetic materials such as nickel, the easy axis of magnetization, defined as the preferred direction for spontaneous magnetization in ferromagnets, lies along their longest dimension if they are geometrically anisotropic [4]. As a result, the nickel thin film's primary magnetization direction will not run along its thickness. Relative to the robot's body, the preferred magnetic orientation of the thin film is front-to-back instead of side-to-side, allowing the robot to pivot about its rockers for forward and backward motion. This can be explained by the different internal stresses present in the front-to-back and side-to-side directions. Due to 3D printing, the top surface of the robot's body consists of raster lines running parallel to the side-to-side direction, which create a higher stress distribution than the front-to-back direction. This will affect the magnetic strain energy density E_s, which is expressed as [5]:

$$E_s = \frac{3}{2}\lambda\sigma \sin^2 \theta_t, \qquad (1)$$

978-1-940470-04-7/HH2022/$25©2022TRF
DOI 10.31438/trf.hh2022.85

where λ is the saturation magnetostriction constant, σ is the film stress, and θ_t is the angle that the raster lines make with the IP direction. Due to the positive tensile stress present in the thin film for both IP directions as well as the negative magnetostriction constant present in nickel, the overall energy density is negative and signifies that the magnetization is decreased by tension. Consequently, the easy axis of magnetization lies in the front-to-back orientation of the robot due to its lower tensile stress.

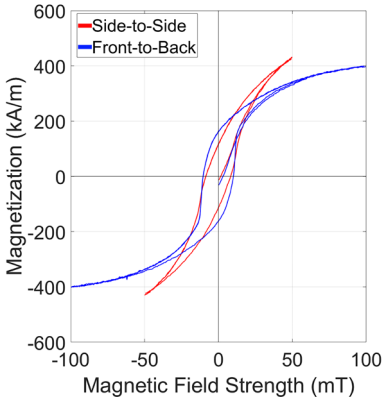

Figure 2: Magnetic hysteresis loop

For characterization, the magnetic properties of the nickel thin film were measured by placing a microrobot inside a vibrating-sample magnetometer. Figure 2 shows the hysteresis loops for two magnetization directions: the robot's front-to-back and side-to-side orientations. The higher coercivity (10.5 > 8.6mT) and retentivity (160 > 115kA/m) values of the front-to-back loop confirms that the easy axis of the nickel thin film lies in that direction. The saturation magnetization of the front-to-back orientation is 400kA/m, which will be used to calculate the maximum force and torque the microtip can exert for penetrating the leaf surface.

Under a magnetic field $\boldsymbol{B}$, the microrocker bot will experience a torque $\boldsymbol{T}$ and force $\boldsymbol{F}$ expressed as:

$$\boldsymbol{T} = V_m \boldsymbol{M} \times \boldsymbol{B} \quad (2)$$

$$\boldsymbol{F} = V_m \boldsymbol{M} \cdot \nabla \boldsymbol{B} \quad (3)$$

where V_m and $\boldsymbol{M}$ are the magnetic material's volume and magnetization vector respectively.

Stick-slip motion

To induce stick-slip motion, a sawtooth waveform is provided from a function generator to the electromagnet for an OOP pulsing magnetic field. The slow ramp and steep decay in a sawtooth wave period correspond to the stick and slip phases respectively, as the instantaneous change in field direction maximizes the robot's rotation during slip phase. For bidirectional motion, a small DC offset can be introduced in the waveform to positionally bias the robot either forward or backward.

Stick-slip motion involves multiple forces and torques that the robot experiences, which primarily include magnetic force and torque, adhesion, drag forces, and kinetic and static friction forces. The OOP magnetic torque during the steep decay of the sawtooth wave causes an increase in angular acceleration as the robot attempts to align its magnetization to the external field. When this acceleration becomes sufficiently high, the rocker's point of contact overcomes the static friction force. Since the robot's angular motion is coupled with its rocker motion, this acceleration allows the robot to enter its slip phase for net motion. For quantitative modeling and simulation of the microrocker bot's stick-slip motion, readers are referred to our previous work [6].

EXPERIMENTAL DESIGN

Fabrication

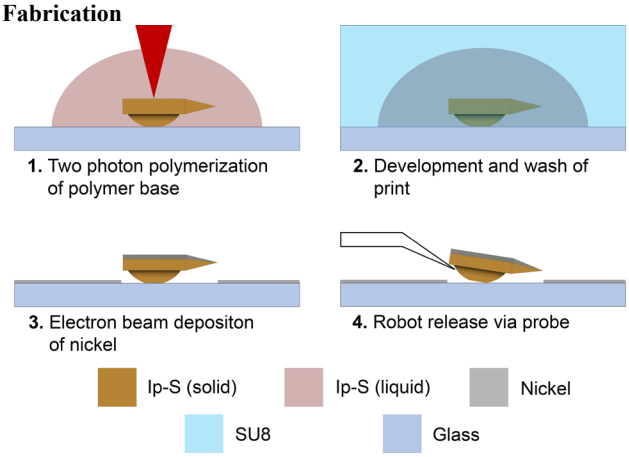

Figure 3: Fabrication process

The microrocker bots were 3D printed via two-photon polymerization on a Nanoscribe Photonic Professional GT printer. Figure 3 details the process. First, a drop of Ip-S photoresin was deposited on an indium tin oxide layered glass slide and loaded into the printer. A 25x objective lens was used for direct laser writing, which serially polymerized the photoresin at the laser's focal point. After the print was finished, the microrobots were developed in SU8 solution for 20 minutes and washed in isopropanol alcohol (IPA) for 2 minutes. For magnetic actuation, the robots were deposited with a 300nm nickel layer through electron beam deposition. Finally, a probe was used to release the microrobots from the surface.

Experimental setup

After release, the robots were transferred to the substrate through a micropipette. While the microrobots could move on the substrate in air, the sample was submerged in water to record more consistent motion and lower adhesion. The sample was then placed on top of 8cm diameter and 9.5mm thick cylindrical electromagnet (Kaka Electronics KK-P25), which was connected to a function generator (Agilent 33220-A). The robots were imaged by a Moticam 1080 camera connected to a top-down microscope (MPI TS150-THZ) and tracked via the DLTdv digitizing tool for video processing [7]. For all experiments, a $10V_{pp}$ sawtooth magnetic waveform with a ±150mV offset was supplied to the electromagnet, which corresponded to an OOP magnetic field amplitude of $3.10mT_{pp}$. and an offset of ±50μT.

RESULTS AND DISCUSSION

Robot speed on glass

To characterize speed, the robot's forward and backward trajectories on a glass slide were recorded from 4Hz to 50Hz in 2Hz increments. As shown in Figure 4, there is a clear speed-frequency variation for forward and backward motions. At lower frequencies, the microrobots oscillate less over a set time, leading to less slip phases and reduced speeds. Meanwhile, at higher frequencies, the faster duty cycles cause higher torsional and translational damping, leading to slower speeds.

Due to the geometric differences between the front and back of the robot, the two plots show significantly different responses to

the applied frequencies. The microrocker bot achieves a peak forward speed of 80µm/s at 12Hz and a peak backward speed of 140µm/s at 20Hz. The robot's front microtip limits forward rocking and consequently the amount of angular acceleration the robot can undergo for forward motion, reducing robot speed.

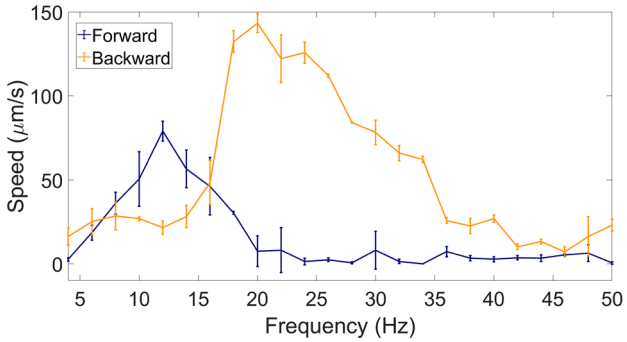

Figure 4: Speed-frequency plot for forward/backward motions. The error bars represent the standard deviation from 3 trials.

The inclusion of a tip additionally explains the different speed-frequency distributions for the two directions. Lower frequencies have longer period cycles and thereby allow the robot to undergo larger displacements. For forward motion, this lower frequency range (8-18Hz) provides a longer response time for the robot to align its magnetization during stick phase, achieving larger displacements and gaining enough angular acceleration during slip phase to overcome the front tip's obstruction to motion. Alternatively, while higher frequencies (20-50Hz) provide faster duty cycles, the lower displacement amplitudes as well as the positional bias from the static magnetic offset cause the tip to become pinned onto the substrate and significantly slow down the robot's speed in comparison to backward motion. This behavior at higher frequencies can be tuned by decreasing the static offset used for forward motion; however, such a change will also bias the neutral position less and change the speed-frequency response. As a result, offset optimization is needed in the future to obtain the best balance between speed and viable frequency range.

Robot motion on a leaf and tip engagement

For mobility on biological surfaces, the microrocker bot was placed on a 2cm diameter leaf and actuated at 12Hz for forward motion and 20Hz for backward motion, corresponding to the peak responses observed in Figure 5. While the robots were able to travel forward and backward, their speeds were reduced with forward and backward speeds reaching 49±6.3µm/s and 54±5.7µm/s respectively from 3 trials. This reduction in speed can be attributed to the uneven and rougher surface of the leaf, which is due to the veins, trichomes, and waxes present [8], and highlights the sensitivity of stick-slip motion to surface inhomogeneities. Faster speeds will require increasing the magnetic field amplitude to induce larger amplitudes for greater angular acceleration.

Additionally, the robot can engage its tip on the leaf surface under a 5mT static field, as the robot has unlimited response time to completely align its magnetization (Figure 5). This result expands upon the static offset control shown in [6] and demonstrates a separate mode from stick-slip motion using a single electromagnet. When upending, the microrobot first rotates about its rockers and then transfers its point of contact to the microtip. As a result, the range of tip engagement can be approximated as 100µm, the distance between the rocker flat edge and microtip, and shows potential applications for precise drug delivery injection.

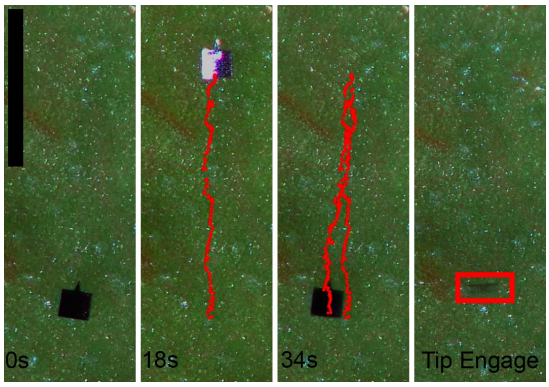

Figure 5: Tracked trajectory of the microrocker bot on a leaf. The tip engagement mode is emphasized due to limited visibility. The black scale bar has a length of 500µm.

Microtip penetration into leaf

To test microtip penetration, a stack of four 2.8cm diameter neodymium magnets was brought underneath the leaf surface for the microrocker bots to engage their tips. The magnetic field strength at the surface of the magnet's center was measured by a Hall effect sensor as 230mT, a value beyond the saturation field strength values (Figure 2) indicated in the hysteresis curve. To calculate the field gradient, the magnetic field amplitudes were measured at varying distances from the magnet's center, and the maximum field gradient was found to be 12T/m. After 5 minutes, the magnet was removed, and the sample was sputtered with 5nm of gold and observed under an SEM.

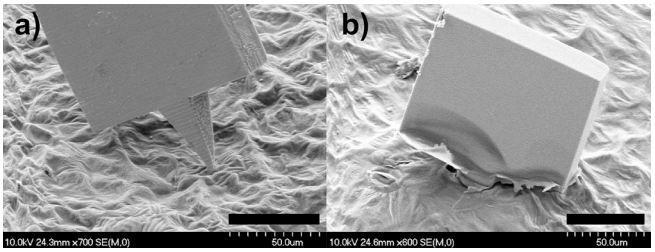

Figure 6: a) 5µm vs. b) full microtip penetration into the leaf. The black scale bar is 500µm in length.

Notably, the SEM photos of the two microrocker bots show very different levels of penetration, with robot 1 (Figure 6a) showing ~4µm of penetration and robot 2 (Figure 6b) showing near complete penetration into the leaf surface. This difference in penetration can be attributed to the different locations of the two robots relative to the magnet's center. While robot 1 was found at the center of the leaf, robot 2 was found at the leaf's edge and consequently experienced magnetic fringing at the magnet's edges. The field strength and gradient at the edge was measured and calculated as 340mT and 24T/m, which caused 150% and 200% increases in torque and force relative to the magnet's center respectively. Since peak force occurs at the critical transition between indentation and penetration of soft solids, additional depth afterwards is more easily achieved due to the lower work of penetration relative to the work of indentation [9]. Despite their variability, these results nonetheless demonstrate that microtip penetration into biological tissue is possible via simply placing a highly magnetic material near the microrocker bots.

Simulation of microtip mechanics

The microtip's mechanical interaction with the leaf surface

was simulated via finite element analysis (FEA) on COMSOL Multiphysics 5.5. Here, the contact between the microtip and leaf substrate was assumed to be quasistatic and frictionless. Based on previous literature characterizing the mechanical properties of leaves [10, 11], the elastic modulus E and Poisson's ratio ν of the leaf were approximated as 2MPa and 0.4 respectively. The microtip itself was modeled as a conical structure with the material properties of Ip-S photoresin (E = 4.6GPa, ν = 0.3) and a flat end diameter of 1.35µm based on SEM images.

For magnetic microrobots, magnetic forces typically have a smaller effect in terms of robot actuation than magnetic torques [4]. Applying the magnetic field and gradient values from the magnet's center as well as the nickel thin film's saturation magnetization to Eq. 3, the magnetic force $\boldsymbol{F_g}$ due to gradient can be calculated as 17nN. To calculate the force $\boldsymbol{F_t}$ applied due to torque $\boldsymbol{T}$, the lever at which $\boldsymbol{T}$ acts upon is the distance vector $\boldsymbol{d}$ between the microtip's edge and the front rocker edge since the robot will initially pivot about its front rocker. At a rotation angle of 20°, the microtip will contact the substrate at a torque of 300µN·µm from Eq. 2. By dividing this torque magnitude by the lever arm length $|\boldsymbol{d}| = \mathbf{100}$µm, $\boldsymbol{F_t}$ can be calculated as 3µN, which is two orders of magnitude higher than $\boldsymbol{F_g}$.

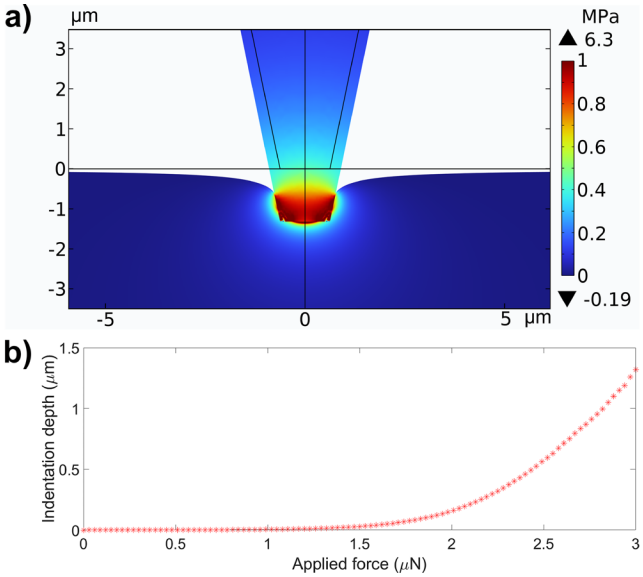

Figure 7: a) Indentation and pressure profile of microtip indentation into leaf. b) Simulated indentation depth vs. force.

Figure 7a shows the maximum pressure exerted by the microtip on the leaf surface. At 6.3MPa, the microtip deforms the leaf surface by 1.3µm. At smaller magnetic forces and torques, the microtip exerts less pressure and cannot deform the mesh, showing a threshold for the applied force. Figure 7b captures this nonlinear relationship between the force and indentation depth. Beyond 1.5µN, the indentation depth notably rises more with increasing forces. At a critical depth [9], the microtip transitions from indentation to penetration when the work of indentation equals to the work of penetration. During penetration, the onset of crack propagation allows microtip to slip into the crack and lowers the required force for penetration as the surrounding tissue relaxes.

CONCLUSION

This work presents a microrobot capable of stick-slip motion via a single electromagnet and mechanical penetration of a biological substrate. This novel method of actuation utilizes a static DC offset in the OOP magnetic field, which biases the robot's position to either travel forward or backward. Additionally, the same motion could be performed on the rougher, more inhomogeneous surface of a leaf, showing proof of concept for traveling on biological substrates to perform drug delivery or DNA extraction by using its microtip for penetration.

Future work will investigate the tip engagement mode of the microrobot as well as coating the microtip with biocompatible materials for potential stem cell delivery. Additionally, motion capabilities will be studied more in dry air environments for more flexibility. Overall, these initial results demonstrate precise steering and tip penetration of an untethered microrobot, opening a wide range of potential biomedical applications.

ACKNOWLEDGEMENTS

This work is supported by the National Science Foundation Graduate Research Fellowship under Grant No. DGE-1650044. The authors thank Prof. Martin Mourigal for magnetic characterization.

REFERENCES

[1] S. Lee, J. Kim, J. Kim, A. K. Hoshiar, J. Park, S. Lee, J. Kim, S. Pané, B. J. Nelson, and H. Choi, "A needle-type microrobot for targeted drug delivery by affixing to a microtissue," Advanced Healthcare Materials, vol. 9, no. 7, 2020.

[2] S. Jeon, S. Kim, S. Ha, S. Lee, E. Kim, S. Y. Kim, S. H. Park, J. H. Jeon, S. W. Kim, C. Moon, B. J. Nelson, J.-young Kim, S.-W. Yu, and H. Choi, "Magnetically actuated microrobots as a platform for Stem Cell Transplantation," Science Robotics, vol. 4, no. 30, 2019.

[3] D. Li, M. Jeong, E. Oren, T. Yu, and T. Qiu, "A helical microrobot with an optimized propeller-shape for propulsion in viscoelastic biological media," Robotics, vol. 8, no. 4, 2019.

[4] E. Diller and M. Sitti, Micro-scale mobile robotics. Foundation and Trends in Robotics, vol. 2, no. 3, 2013.

[5] M. Satō, K. Mukasa, and M. Maeda, "Uniaxial magnetic anisotropy in nickel-iron thin films electrodeposited on scratched surfaces," Japanese Journal of Applied Physics, vol. 8, no. 4, pp. 468–472, 1969.

[6] T.H. Wang, D. Kim, Y. Shi, Z. Hao, and A. Ansari, "Bidirectional microscale rocker robots controlled via neutral position offset", Journal of Micro-Bio Robotics, 2022.

[7] T. L. Hedrick, "Software techniques for two- and three-dimensional kinematic measurements of biological and Biomimetic Systems," Bioinspiration & Biomimetics, vol. 3, no. 3, 2008.

[8] H. Bediaf, R. Sabre, L. Journaux, and F. Cointault, "Comparison of leaf surface roughness analysis methods by sensitivity to noise analysis," Biosystems Engineering, vol. 136, pp. 77–86, 2015.

[9] S. Fregonese and M. Bacca, "Piercing soft solids: A mechanical theory for needle insertion," Journal of the Mechanics and Physics of Solids, vol. 154, 2021.

[10] Y. Onoda, F. Schieving, and N. P. Anten, "A novel method of measuring leaf epidermis and mesophyll stiffness shows the ubiquitous nature of the sandwich structure of leaf laminas in broad-leaved angiosperm species," Journal of Experimental Botany, vol. 66, no. 9, 2015.

[11] W. Zhang, P. Soman, K. Meggs, X. Qu, and S. Chen, "Tuning the Poisson's ratio of biomaterials for investigating cellular response," Advanced Functional Materials, vol. 23, no. 25, 2013.

A SEMI-ANALYTICAL MODELING OF COUPLED PIEZOELECTRIC RESONATORS BASED ON SUPPORT TRANSDUCER TOPOLOGY

Chin-Yu Chang[1], Gayathri Pillai[2], and Sheng-Shian Li[1,3]

[1]Institute of NanoEngineering and MicroSystems, National Tsing Hua University, Hsinchu, Taiwan

[2]Center for Nanoscience and Engineering, Indian Institute of Science, Bengaluru, India

[3]Department of Power Mechanical Engineering, National Tsing Hua University, Hsinchu, Taiwan

ABSTRACT

This work investigates, for the first time, an analytical model of a generic coupled piezoelectric resonator based on support transducer topology. Since a "coupled resonator" consists of multiple length extensional mode (LE) transducer arms and an isochoric bulk mode resonator, we treat each component as a distinct sub-resonator and integrate them into a multiple-port electromechanical circuit based on an array-composite concept. In this work, 2-D finite-element method (FEM) simulations are performed to compensate the uncertainty of analytical solution on the electromechanical coupling coefficient (k_t^2) caused by the elastic modulus mismatch between the single crystal silicon (SCS) passive layer and the aluminum nitride (AlN) transducer. For verification, a TPoS coupled resonator based on AlN-on-Si topology is simulated with the proposed numerical model, showing a motional resistance (R_m) prediction error less than 3.5% and 13.2% as compared with FEM and measurement results, respectively.

KEYWORDS

Support Transducer, Coupled Resonator, TPoS, Analytical Modeling

INTRODUCTION

Microelectromechanical System (MEMS) oscillator has become one of the most popular future timing solutions in the consumer electronic systems [1]. It features with high operating frequency, compact volume, great robustness, and low environmental sensitivity. The quality of the output signal in an oscillator system is represent by frequency stability. Higher quality factor (Q) and lower motional impedance (R_m) from the resonator system can leading to a good frequency stability performance [2]-[4]. Among the existing MEMS technology, capacitive resonators fabricated by single crystal silicon (SCS) have been proofed to enable adequate close to carrier phase noise performance by the high Q-factor [5]. Nonetheless, the large R_m and the demand of high dc-bias voltage for large electrostatic force cause the inconvenience for the sustaining circuit design [6]. Hence, piezoelectric resonator with low R_m from the high electromechanical coupling becomes the better solution for the oscillator system design. However, piezoelectric resonator usually suffers from low Q-factor due to the interfacial material loss from the heterogeneous layer stacking in the piezoelectric resonator. This drawback could be solved by the proposed support transducer topology.

From our previous work, support transducer topology (STT) is a proven technique to enable high Q-factor bulk mode resonator with piezoelectric transduction [7]-[9]. This topology is realized by multiple length extensional (LE) mode resonator and a bulk mode resonator (e.g., Lamé, elliptical mode), as shown in Fig 1. The LE-mode transducer arm driven the bulk mode at the center into desire mode shape efficiently by matching the resonant frequency between resonators. The energy could be conserved inside the resonator system by implementing the high Q bulk mode resonant plate which

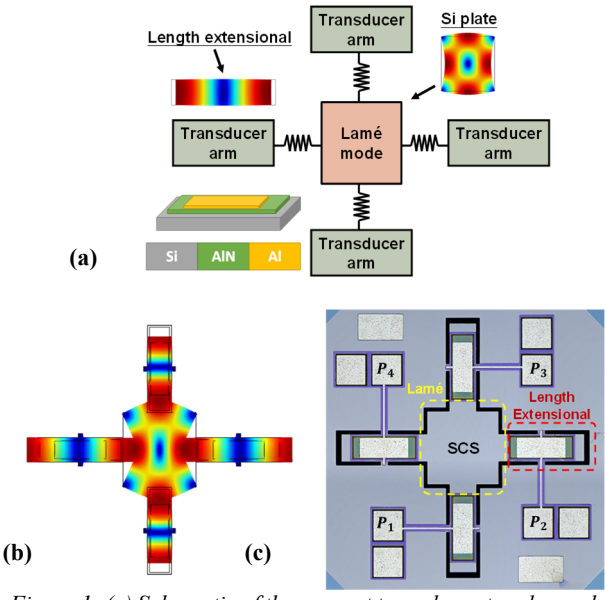

Figure 1: (a) Schematic of the support transducer topology where the transducer arms are placed around the peripheral of the resonator tank, (b) simulated mode shape of the proposed support transducer Lamé mode resonator, and (c) optical image of the fabricated device.

construct by SCS. Previous works has demonstrated that this topology could provide high Q-factor and low R_m for piezoelectric resonator which leading a better close to carrier phase noise performance [10]. Although the theoretical expression of the piezoelectric contour mode resonators has been well studied [11]-[12]. However, the analytical modeling for this unique coupled resonator system has never been reported.

In this work, the support transducer Lamé mode resonator is divided into multiple distinct sub-resonators being integrated into a multiple-port electromechanical circuit based on an array-composite concept. The mismatch of the electromechanical coupling from the theorical calculation is compensated by the use of FEM. The frequency response of the support transducer resonator is successfully predicted by the proposed analytical solution with acceptable error.

ANALYTICAL MODELING

Overview of the analytical model

Fig. 2(a) presents the schematic of the proposed analytical model where each sub-resonator is represented by a series RLC model. The overall system contains the LE-mode resonators which are actuated by piezoelectric effect from the AlN thin-film while the Lamé mode resonant plate is driven by the mechanical vibration of the LE-mode sub-resonators. The outer and inner transformers are used to address the electromechanical coupling from the

978-1-940470-04-7/HH2022/$25©2022TRF
DOI 10.31438/trf.hh2022.86

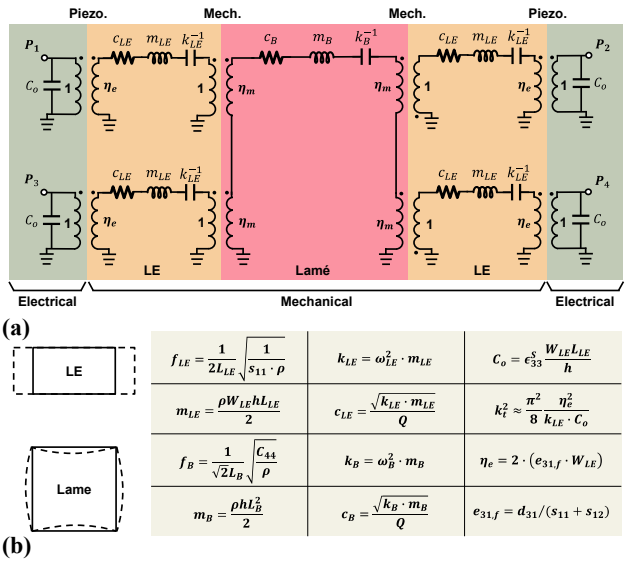

Figure 2: (a) Equivalent circuit model of the proposed support transducer resonator including electromechanical and mechanical coupling. (b) Formulas used to predict the resonant frequency, effective mass, damping, stiffness constant, and coupling factor for LE mode and Lamé mode resonators.

piezoelectric transducer in the LE-mode resonator and the mechanical coupling between different resonators respectively. Fig. 2(b) shows the equations used to calculate the parameters in the proposed analytical model.

For both LE-mode resonator and Lamé mode resonator, the effective mass, damping, and spring constant are derived from Rayleigh method with the mode shape equations. The effective mass for LE-mode (m_{LE}) could be derived by eq. (1) [13]

$$m_{LE} = \frac{\rho W \iint_A [u(x,z)]^2 dxdz}{u_{max}^2} \approx \frac{\rho L_{LE} W_{LE} h}{2} \quad (1)$$

where ρ is the density, h is the thickness, L_{LE} is the length, and W_{LE} is the width of the LE-mode resonator, respectively. $u(x,z)$ and u_{max} are the mode shape equation and the maximum displacement of the length extensional mode resonator, respectively [14]. Note that the approximation for eq. (1) is set with the ideal boundary condition which the lateral dimension is much larger than the thickness dimension, e.g., $L_{LE} \gg h$. The effective mass for the Lamé mode (m_B) resonator is also derive with the similar topology. Eq. (2) express the calculation of the m_B [15]

$$m_B = \frac{\rho h \iint_A [w(x,y)]^2 dxdy}{w_{max}^2} \approx \frac{\rho L_B^2 h}{2} \quad (2)$$

where L_B is the side length of the Lamé mode resonator. $w(x,y)$ and w_{max} are the mode shape equation and the maximum displacement of the Lamé mode resonator, respectively. The effective stiffness and damping constant for both resonators could be derived from the classic second order system as shown in eq. (3) and eq. (4)

$$k_{eff} = \omega_o^2 \cdot m_{eff} \quad (3)$$

Table 1. Parameters used in the proposed model, including device dimensions, thickness configuration, material properties, and modeling parameters.

Device Parameters			**Thickness Configuration**		
LE		Lamé	SCS	AlN	Al
L_{LE}	W_{LE}	L_B	10 μm	0.5 μm	1 μm
214 μm	60 μm	200 μm			
Material Properties					
AlN					
ρ, density	C_{11}^E	C_{12}^E	C_{13}^E	C_{33}^E	ϵ_{33}^S
3300 kg/m^3	410 GPa	149 GPa	99 GPa	389GPa	$9 \cdot \epsilon_0$ F/m
SCS					
ρ, density	C_{11}^E	C_{12}^E	C_{13}^E	C_{33}^E	C_{44}^E
2330 kg/m^3	195 GPa	35 GPa	64 GPa	166 GPa	80 GPa
Modeling Parameters					
LE					
c_{LE}	m_{LE}	k_{LE}	C_0	η_e	
3.458 $\mu N \cdot s/m$	$1.73 \times 10^{-10} kg$	3.164 MN/m	1.02 pf	20.59 $\mu C/m$	
Lame					
c_B	m_B	k_B	η_m		
9.431 $\mu N \cdot s/m$	$4.84 \times 10^{-10} kg$	8.628 MN/m	1		

$$c_{eff} = \frac{\sqrt{k_{eff} \cdot m_{eff}}}{Q} \quad (4)$$

where k_{eff} is the effective stiffness constant, ω_o is the resonant frequency, m_{eff} is the effective mass constant, c_{eff} is the effective damping constant, and Q is the quality factor.

Electromechanical (η_e) and mechanical coupling (η_m)

Electromechanical coupling which enables by the piezoelectric effect could also be express by the numerical calculation. LE-mode piezoelectric resonator is actuated by the vertical electric field and induced the motion at the lateral dimension. This effect is coming from the piezoelectric coefficient (i.e., e_{31}) which represent the coupling between electric field and strain. The electromechanical conversion factor (η_e) is highly depends on the piezoelectric coefficient of the thin-film and the active area which electrode are covered. Eq. (5) shows the numerical expression of η_e

$$\eta_e = 2 \cdot (e_{31,f} \cdot W_{LE}) \quad (5)$$

where $e_{31,f}$ is the transverse piezoelectric coefficient [16], and W_{LE} is the width of the LE-mode resonator. Unlike previous work where the η_e is based on 1-D approach without considering the effect of the material Poisson's ratio [17], plane stress condition is considered in this work to compensate the error from the Poisson's ratio. Eq. (6) shows the calculation of $e_{31,f}$

$$e_{31,f} = \frac{d_{31}}{s_{11} + s_{22}} \quad (6)$$

where d_{31} is the piezoelectric coefficient in strain form, s_{11} and s_{22} are the compliance of the material.

Mechanical coupling (η_m) expresses the energy transfer from the LE-mode resonators to the Lamé mode resonator, which reveals the main idea of the support transducer topology. By connecting LE-mode resonators and a Lamé mode resonator at their maximum velocity location as shown in Fig. 1(a), this ensures almost 100%

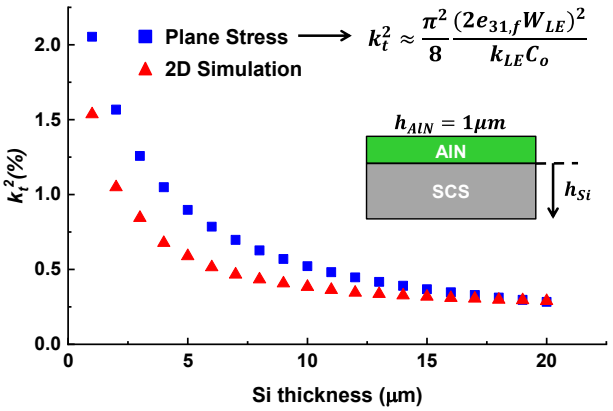

Figure 3: Comparison of the effective electromechanical coupling factor (k_t^2) with fixed h_{AlN} but varied h_{Si} based on plane stress and 2D FEM approach.

energy transfer among constituent resonant tanks. Thus, η_m in this case will be set as value 1 in the model representing no leakage during the energy transfer between resonators. For other devices using the same topology, they might not feature ~100% energy transfer due to the connection points between the transducer arms and the central bulk mode without ideal matching locations.

Table. 1 shows the device dimensions, thickness configuration, material properties, and the modeling parameters used in the analytical modeling. The length and width of the LE-mode resonators are 240μm and 60μm, respectively. The side length of the Lamé mode resonator is 200μm. The device was fabricated with the thickness configuration of 1μm aluminum (Al) serving as electrodes, 0.5μm aluminum nitride (AlN) piezoelectric thin-film, and 10μm Si device layer.

Implementation of Finite Element Method

Despite the electromechanical coupling factor (η_e) considering the Poisson's ratio in the previous section, we found that the numerical calculation based on plane stress condition still has a large error as compared to the FEM result. The error mainly comes from the unwanted out of plane displacement caused by the mismatch of the elastic modulus between the device layer (SCS) and AlN thin film. Previous work has demonstrated the compensation for this non-ideal effect by introducing multiple correction terms into the general equations with the help of FEM [18]. In this work, a 2D FEM simulations are performed to simultaneously correct the error and simplify the compensation process. Fig. 3 shows the comparison of the effective electromechanical conversion factor (k_t^2) with a fixed 1μm AlN thin film but varied thickness of SCS device layer from 1 - 20μm based on the plane stress condition and the FEM approach. The result discloses that a thinner silicon device layer deviates more on the k_t^2 of the piezoelectric contour mode resonator with fixed thickness of AlN thin film. This indicates that the numerical solution for the in-plane mode shape under TPoS configuration might also encounter the same problem.

EXPERIMENTAL RESULT

The proposed support transducer Lamé mode resonator is operated under differential driving and sensing scheme (DIDO) for the practical measurement, the FEM simulation, and the proposed analytical modeling. Fig. 4 shows the comparison of the frequency response between the proposed analytical modeling and the FEM simulation result with a given Q of 6,000. The magnitude and phase response from the equivalent circuit is in good agreement with the

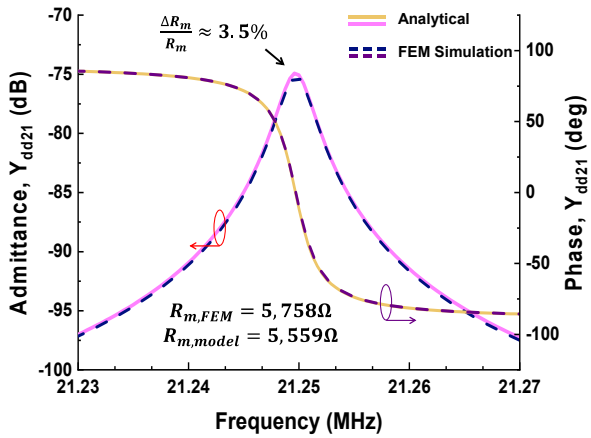

Figure 4: Frequency response from the proposed analytical model and FEM simulation under DIDO condition with a 3.5% error on the prediction of motional resistance.

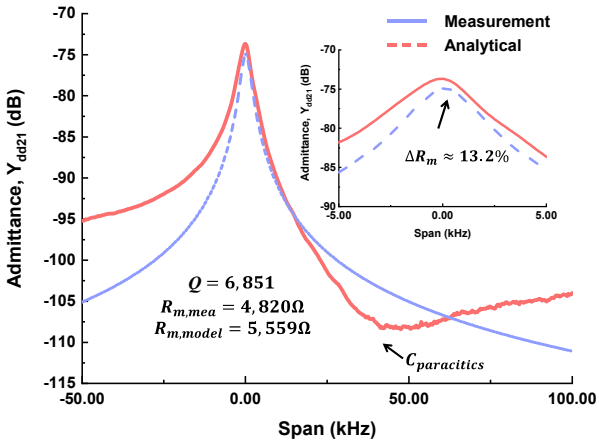

Figure 5: Frequency response of the measurement result and the proposed analytical model showing a 13.2% error on the motional resistance prediction.

FEM results. The motional resistance (R_m) from FEM and analytical model are 5,758Ω and 5,559Ω, respectively. A small difference on R_m of only 3.5% is observed, which confirms the accuracy of the proposed model. These results verify that the proposed analytical modeling can save significant computation time from the FEM in terms of the prediction of the frequency response and motional impedance of the support transducer resonator.

To complete this study, the frequency response of the fabricated device was measured using the network analyzer (Keysight E5071C) with virtual balun to enable DIDO configuration. Fig. 5 shows the comparison of frequency response between the measured admittance and the proposed analytical modeling using the measured Q-factor, 6,851. The Rm from measurement and analytical model are 4,820Ω and 5,559Ω, respectively. A 13.2% on the R_m prediction has been observed from the measurement result. In addition to the error of the motional impedance prediction, the frequency response is not in good agreement between measurement and the modeling.

The discrepancy between the modeling and the measurement might be attributed to the uncertainty in material properties, the asymmetry of the fabricated device, and parasitic capacitance from the experimental setup. For the device design with support transducer topology, there might be certain shift on the resonant

frequency due to the variance from the fabrication process resulting in mismatch on each transducer arm. These frequency mismatches would lead to the leakage during the energy transfer between each sub-system and make the DIDO driving condition not fully cancel out the common mode noise.

CONCLUSION

In this work, an analytical model of the coupled piezoelectric resonator based on support transducer topology has been demonstrated with the comparison among analytical solutions, FEM results, and measurement data. With the help of FEM on the compensation of electromechanical coupling coefficient, the prediction of the motional impedance would only have 3.5% and 13.2% differences as compared to FEM and measurement, respectively. The proposed model can be extended to a reconfigurable mechanism on the analysis of the energy transfer in the coupled resonator system with different bulk mode configurations [19][20].

ACKNOWLEDGEMENTS

This work was supported by MOST 110-2622-E-007-022.

REFERENCES

[1] H. Lee *et al.*, "Low jitter and temperature stable MEMS oscillators," *Proc. IEEE Int. Freq. Control Symp.* (FCS), Baltimore, MD, USA, May 2012.

[2] D. B. Leeson, "A simple model of feedback oscillator noise spectrum," *Proc. IEEE*, vol. 54, no. 2, pp. 329–330, Feb. 1966.

[3] E. Rubiola, The Lesson Effect—Phase Noise in Quasilinear Oscillators. Cambridge, U.K.: Cambridge Univ. Press, Nov. 2008.

[4] A. Hajimiri *et al.*, "A general theory of phase noise in electrical oscillators," *IEEE J. Solid-State Circuits*, vol. 33, no. 2, pp. 179–194, Feb. 1998.

[5] Y.-W. Lin *et al.*, "Low phase noise array-composite micromechanical wine-glass disk oscillator," *Technical Digest, IEEE Int. Electron Devices Mtg.*, Washington, DC, Dec. 5-7, 2005, pp. 287-290.

[6] M.-H. Li *et al.*, "Optimizing the close-to-carrier phase noise of monolithic CMOS-MEMS oscillators using bias-dependent nonlinearity," *Technical Digest, IEEE Int. Electron Devices Mtg.*, San Francisco, CA, USA, Dec. 2014, pp. 22.3.1-22.3.4.

[7] G. Pillai *et al.*, "Exploration and Realization of Novel High-*Q* Bulk Modes Using Support Transducer Topology," *J. Microelectromech. Syst.*, vol. 30, no. 5, pp. 696-702, Jul. 2021.

[8] G. Pillai *et al.*, "Quality factor boosting of Bulk acoustic wave resonator based on a two dimensional array of high *Q* resonant tanks," *Appl. Phys. Lett.*, vol. 116, no. 16, pp. 163502, Apr. 2020.

[9] G. Pillai *et al.*, "Piezoelectric based support transducer design to enable high performance bulk mode resonators," *J. Microelectromech. Syst.*, vol. 28, no. 1, pp. 4-13, Nov. 2018.

[10] H.-T. Jen *et al.*, "High-*Q* support transducer MEMS resonators enabled low phase noise oscillators," *IEEE Trans. Ultrason., Ferroelectr., Freq. Control*, vol. 68, no. 4, pp. 1387-1398, Apr. 2021.

[11] G. Piazza *et al.*, "Piezoelectric aluminum nitride vibrating contour-mode MEMS resonators," *J. Microelectromech. Syst.*, vol. 15, no. 6, pp. 1406-1418, Dec. 2006.

[12] R. Abdolvand *et al.*, "Thin-film piezoelectric-on-silicon resonators for high-frequency reference oscillator applications," *IEEE Trans. Ultrason., Ferroelectr., Freq. Control*, vol. 55, no. 12, pp. 2596-2606, Dec. 2008.

[13] R. Holand, "Contour extensional resonant properties of rectangular piezoelectric plates," *IEEE Trans. Sonics Ultrason.*, vol. 15, no. 2, pp 97-104, Apr. 1968.

[14] G.K. Ho *et al.*, "Piezoelectric-on-Silicon Lateral Bulk Acoustic Wave Micromechanical Resonators," *J. Microelectromech. Syst.*, vol. 17, no. 2, pp. 512-520, Apr. 2008.

[15] J.E.-Y. Lee *et al.*, "Low loss HF band SOI wine glass bulk mode capacitive square-plate resonator," *J. Micromech. Microeng.*, vol. 19, no. 7, pp. 074003, Jun. 2009.

[16] S. Trolier-McKinstry *et al.*, "Thin Film Piezoelectrics for MEMS," *J. Electroceramics*, vol. 12, no. 1, pp. 7-17, Jan. 2004.

[17] V. Kaajakari, *Practical MEMS*, Las Vegas, Small Gear Publishing, 2009, pp. 307-324

[18] T. Cheng *et al.*, "A semi-analytical modeling approach for laterally-vibrating thin-film piezoelectric-on-silicon micromechanical resonators," *J. Micromech. Microeng.*, vol. 25, Oct. 2015.

[19] N. M. Nguyen *et al.*, "Design of piezoelectric MEMS bulk acoustic wave mode-matched gyroscopes based on support transducer," in *Proc. IEEE 34th Int. Conf. Micro Electro Mech. Syst.* (MEMS), Jan. 2021, pp. 338-341.

[20] C.-Y. Chang *et al.*, "Phase Noise Optimization of Piezoelectric Bulk Mode MEMS Oscillators Based on Phase Feedback in Secondary Loop," in *Proc. IEEE 35th Int. Conf. Micro Electro Mech. Syst.* (MEMS), Jan. 2022, pp. 212-215.

CONTACT

*S.-S. Li, tel: +886-3-516-2401; ssli@mx.nthu.edu.tw

AN OUT-OF-PLANE WIDE BANDWIDTH MICRO-G FM ACCELEROMETER WITH DIFFERENTIAL OUTPUT

Seungyong Shin[1], Tanya Chauhan[1], Justin Matthews[1], Haoran Wen[2] and Farrokh Ayazi[1,2]
[1]Georgia Institute of Technology, USA
and [2]StethX Microsystems, USA

ABSTRACT

This paper reports on the design, fabrication, and characterization of a vacuum encapsulated wide bandwidth micro-g out-of-plane accelerometer with differential output utilizing electrostatic frequency modulation. The accelerometer consists of a proof-mass suspended by torsional springs, differential pair of free-free beam (FFB) resonators as transducers, and top-layer polysilicon capacitive electrodes deposited and bridged over TEOS-filled trenches which define the resonators and proof-mass in the device layer of an SOI wafer. The fabricated device measures a scale factor of 41.2Hz/g with a resonator Q of 1800 and a proof-mass Q of 6.7 at 19kHz, which enable low-noise operation in a wide bandwidth. The accelerometer demonstrates high performance with a VRW corresponding to noise density of 5.8μg/√Hz and a bias instability of 23μg, without temperature compensation. The demonstrated performance, while promising, can be further improved by applying temperature compensation techniques to the electronics interface.

KEYWORDS

MEMS, frequency modulation, eFM, accelerometer

INTRODUCTION

The evolution of sensor technology has enabled a large variety of applications that improve the quality of people's daily life. For example, a high-resolution wide-bandwidth Out-of-Plane Accelerometer (OPA) can enable interesting applications such as non-invasive real-time monitoring of mechano-acoustic signals emanating from the heart and lungs, which contain important information about the health of cardiopulmonary system [1].

In order to detect subtle pulmonary signals on the skin, the accelerometer need to have very low noise (<10μg/√Hz) and a wide operational bandwidth (>10kHz). However, for conventional quasi-static capacitive MEMS accelerometers, implementation of these requirements is nontrivial due to design trade-off between noise and bandwidth. In order to overcome this trade-off, large-area submicron-gap out-of-plane capacitive electrodes are needed, which could bring additional challenges in micro-fabrication, such as stiction.

These challenges can be overcome using an electrostatic frequency modulated (eFM) accelerometer, which utilizes smaller electrodes and stiffer structures. Recently, eFM in-plane accelerometers (IPA) with differential readout have shown great potential to meet both bandwidth and noise performance while providing a good linearity and temperature stability [2]. The differential frequency readout scheme provides several important benefits. First, it effectively reduces unwanted frequency shift due to temperature variation. The identical resonators have similar TCFs, and the frequency fluctuation due to temperature variation can be canceled with differential measurement. Second, it suppresses the first order nonlinear effects in gap-closing stiffness modulation mechanism. Furthermore, frequency modulation induced by accelerations orthogonal to the sensing axis mainly results common mode response. Therefore, the differential readout remains unchanged and cross-axis sensitivity can be minimized.

Conventionally, implementation of a differential readout scheme for frequency output OPA utilizing mechanical frequency modulation is difficult due to the 2D nature of common micro-fabrication techniques [3]. However, for eFM OPA using capacitive transduction, differential readout can be achieved in a similar fashion as quasi-static capacitive OPAs [4]. At the same time, the scale factor of eFM OPA has 4th order dependency on the gap size, reducing the transduction area requirement and having significantly lower risks of stiction and pull-in instability than quasi-static capacitive OPAs [5].

Another important specification that needs to be carefully examined is the sensor response time, which is closely related to the system bandwidth. Since the operational bandwidth becomes smaller if the 2nd order proof-mass system is not near critically damped region, it is very important to have a proper damping mechanism for the proof-mass. Resonant accelerometers require high Q resonators to achieve low phase noise; therefore, vacuum packaging is imperative to minimize squeeze film air damping, which can cause the proof-mass to be under-damped and limit the sensor bandwidth [6]. By utilizing submicron gaps [7], this trade-off can be overcome by incorporating dedicated damping electrodes, enabling near-critically-damped proof-mass while maintaining a high resonator Q in vacuum encapsulation.

In this paper, the design, implementation, and characterization of a novel micro-g eFM OPA with differential output and wide open-loop bandwidth (>10kHz) are introduced and its unique design and fabrication process features are described.

OUT OF PLANE ACCELEROMETER DESIGN

The schematic of the eFM OPA is shown in Figure 1, where the device consists of an off-centered proof-mass suspended by torsional spring, two identical free-free beam (FFB) resonators, and top-layer polysilicon capacitive electrodes deposited and bridged over TEOS-filled trenches which define the resonators and proof-mass in the device layer of SOI wafer.

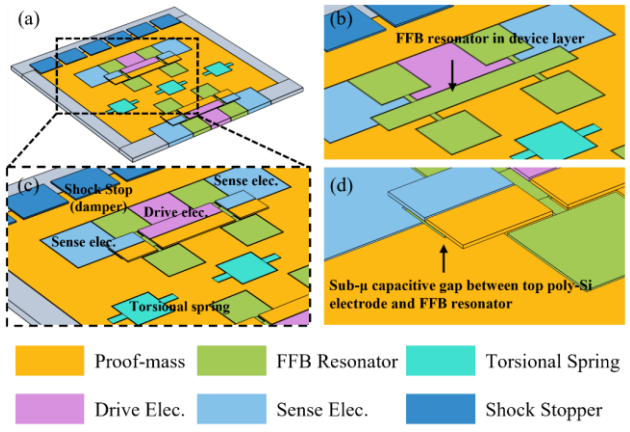

Figure 1: (a) Schematic of the differential readout eFM OPA (b) free-free beam resonator in device layer of SOI wafer which are driven, sensed, and modulated with sub-micron out-of-plane transduction gap (c) zoomed in view of the eFM accelerometer (d) zoomed-in view showing sub-micron out-of-plane gaps and poly-silicon top electrodes.

978-1-940470-04-7/HH2022/$25©2022TRF
DOI 10.31438/trf.hh2022.87

Solid-State Sensors, Actuators, and Microsystems Workshop
Hilton Head Island, South Carolina, June 5-9, 2022

Each resonator is designed to be frequency modulated by electrostatic force (spring softening) resulting from a 200nm capacitive gap between the body of the resonator and movable polysilicon electrodes attached to the proof-mass.

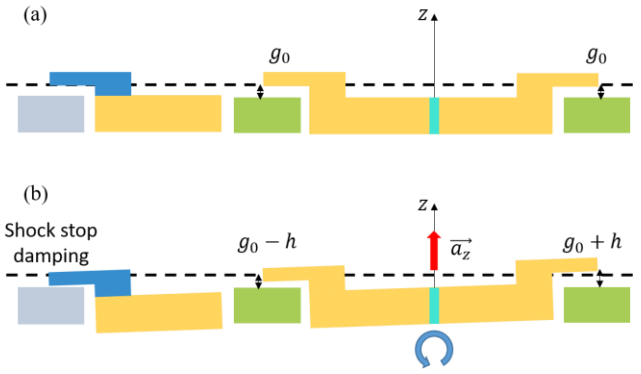

Figure 2: (a) Cross sectional view of the accelerometer. Without external acceleration, two transduction gaps remain unchanged. (b) Tilting motion due to acceleration causes a differential gap change, yielding differential frequency modulation.

As shown in Figure 2, the imbalanced proof-mass creates torque and tilting motion when external acceleration is applied. The generated torque can be expressed as equation 4.1.

$$\tau = M\vec{a} \times \vec{r} = K_\theta \times \theta \tag{1}$$

where M represents effective mass of the proof-mass with respect to the tilting motion, $\vec{r}$ is a vector of center-of-mass from the origin. Since the rotational angle will be very small compared to the dimensions, equivalent z-axis displacement h can be approximated as $d \times tan\theta \approx d\theta$, where d is distance between the anchor to the out-of-plane gap. Such a tilting motion generates differential changes of capacitive gap size as shown in Figure 2(b). When a DC voltage of V_p is applied between the proof-mass and the resonators, the change in the gap results in a change in the electrostatic force and hence the amount of spring softening for each resonator. The differential frequency output of the device is given by:

$$\Delta f_{res} = 2\frac{f_0}{\omega_{proof}^2}\frac{3}{2}\frac{\varepsilon tl}{K_{res}g_0^4}V_p^2 \times \vec{a}_{ext} \tag{2}$$

where f_0 is the unbiased resonant frequency, ω_{proof} is natural frequency of the tilting mode of the proof-mass, and K_{res} represents effective vibrational mode stiffness of the resonator (FFB mode), ε is the permittivity of air, t is thickness of the device, l is length of the transduction area, k_{res} is stiffness of the resonator, g_0 is initial gap size, and V_p is potential difference between the proof-mass and resonator. As shown in equation (2), the scale factor depends inversely on the fourth power of the transduction gap. Therefore, having smaller gap size greatly improves the sensitivity of the eFM accelerometer. For this OPA accelerometer, 200nm of transduction gap, g_0 is implemented using a process similar to the one presented in [7].

Since the nano-scale transduction gap is determined by the thickness of thermally grown sacrificial layer, there is only one capacitive gap size available through the wafer, which makes it difficult for an accelerometer leveraging translational motion of the proof mass to implement shock stop to prevent proof-mass pull-in or mechanical failure under high shock. By leveraging the off-centered teeter-totter structure shown in Figure 2, shock stop can be implemented naturally. Since the longer edge of the proof-mass has always maximum displacement under the tilting motion, the shock stop implemented at the longer side of the proof-mass hits the fixed blocking structure in device layer first under the large external acceleration. Figure 3 shows the designed shock stop structure. It has six stoper structure attached to the fixed outer frame and proof mass alternative manner, which provide shock stopping mechanism for both upward and downward direction.

Additionally, the thin out-of-plane gaps of the shock stopper structure also provide a scalable damping mechanism. With the sub-micron gap, the squeeze film air loss expressed in equation (3) can be engineered to maintain the proof-mass within near critically damped region even in vacuum environment.

$$D_{SFD} = N_e\eta_{eff}l_e\left(\frac{h_e}{g_0}\right)^3 \tag{3}$$

In this equation, N_e stands for number of electrodes, η_{eff} is viscosity of the ambient gas, l_e is electrode length, and h_e is electrode thickness, respectively. The implemented structures are shown in Figure 3. The shock stop structures are attached to the fixed frame and proof-mass alternatively which provide shock stop mechanism in both upward and downward direction which having enough amount of squeezed film air damping.

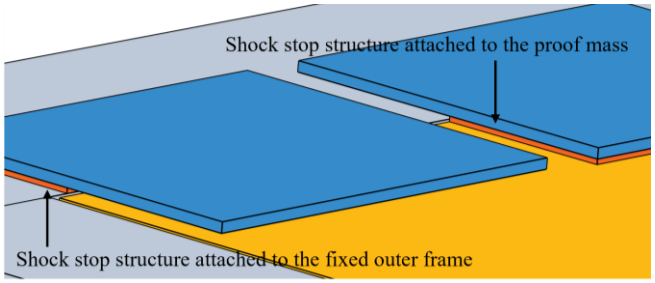

Figure 3: (Exaggerated) Schematic of shock stop structure attached to the fixed outer frame and proof mass alternatively provide shock stops for both upward and downward directions and adequate squeeze film air damping to prevent underdamped response.

The simulated resonant characteristics of the designed proof-mass show unbiased resonant frequency at 21.8kHz with quality factor of 2 corresponding to the squeezed film damping at 10Torr, which means the proof-mass can have near critical damping operation and maintain fast settling time and large operational bandwidth (Fig. 4, 5).

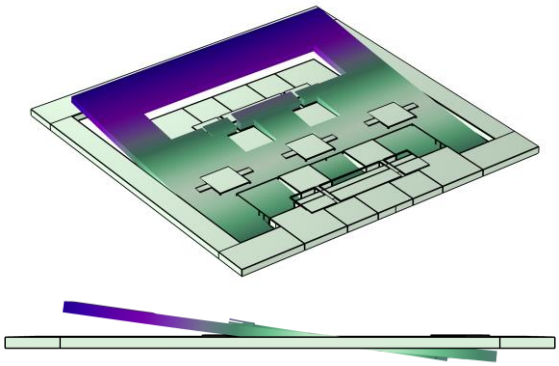

Figure 4: Resonant mode of the proof-mass @ 21.8kHz.

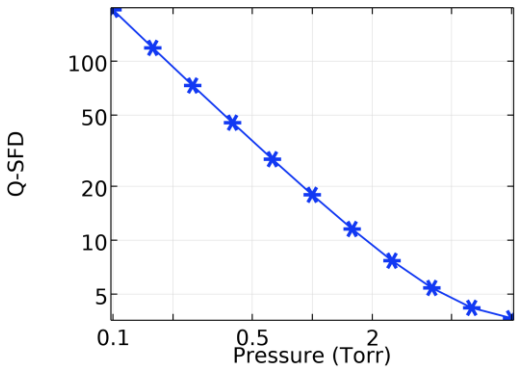

Figure 5: Simulated quality factor corresponding to the squeezed film air damping shows Q of 2 @ 10Torr.

The FFB resonators at 650kHz have low flexure mode stiffness and provides large active transduction area, which enables higher scale factor while having high translational mode stiffness to prevent pull-in instability (Fig. 6).

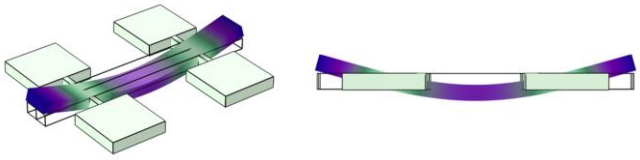

Figure 6: Free-free beam resonator showing un-biased resonant frequency of 650kHz

Moreover, it is possible to design tether and anchor structures in a manner to minimize mechanical coupling loss through the substrate (Q_{ANCHOR}>>1M). The simulated resonator Q due to various mechanisms are summarized in Table 1. Additionally, 200 nm out of plane transduction gap also provide very low motional impedance. The simulation result shows motional impedance of 30.5kΩ for the FFB resonators.

Table 1: Simulated quality factor contributions of the free-free beam resonator.

Resonator Q contribution	
Q_{ANCHOR}	6.2M
Q_{TED}	65.3k
Q_{SFD}@1torr	12.5k
Q_{SFD}@10torr	1.8k

Since the body of the two resonators are electrically isolated from one another, slightly different DC bias voltages can be applied to resonators to provide a second order compensation of the device over temperature in the presence of fabrication imperfections. The differential configuration provides significant benefits by canceling unwanted common mode uncertainties such as temperature coefficient of frequency of the resonators, and the first order nonlinearity in gap-closing frequency modulation. The simulated scale factor nonlinearity is less than 0.5% over ±10g.

EXPERIMENTAL RESULTS

The devices are fabricated on an SOI wafer with 40µm thick device layer and hermetically sealed by Si-Au eutectic wafer bonding targeting 5~10 Torr vacuum level without using a getter. Figure 7 shows colored SEM of a fabricated (un-capped) device.

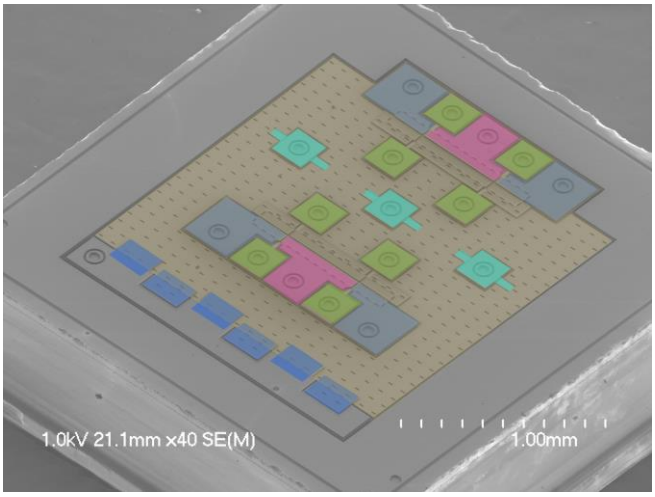

Figure 7: SEM image of a fabricated eFM OPA. The device footprint is 2mm×2mm. (color coding is same as Figure 1)

The fabricated device was interfaced with TIA and measured using vector network analyzer. Figure 8 shows a typical resonant characteristic of a pair of FFB resonators (Q of ~1800 @ 626kHz) with statistical data revealing average resonator Q of 2200 across several capped devices.

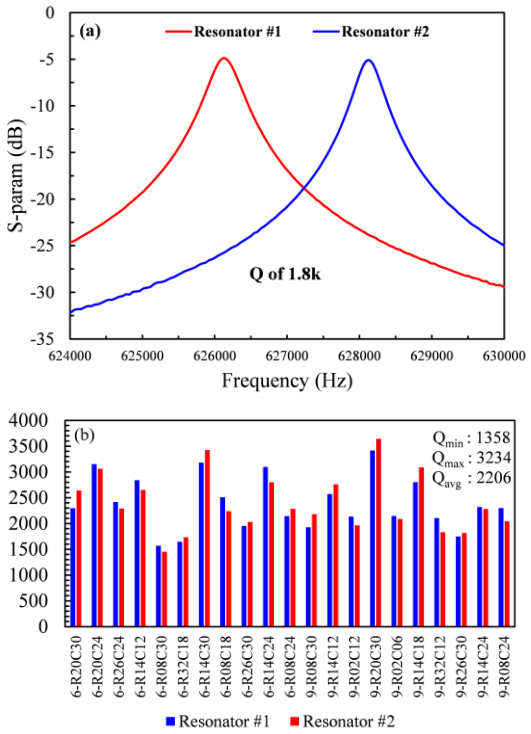

Figure 8: Typical resonant characteristics of proof-mass (a) and differential pair of resonators (b) Statistics of the FFB resonator Q across dies show average Q of ~2,200.

Figure 9 shows measured near critically damped resonant characteristics of the proof-mass (Q of 6.7 @ 19.1kHz). The proof-mass quality factor of 6.3 indicates that system rising time of 18µs and settling time of 0.5ms. A multi-order digital low-pass filter can be applied at the post processing stage to obtain even faster sensor response time.

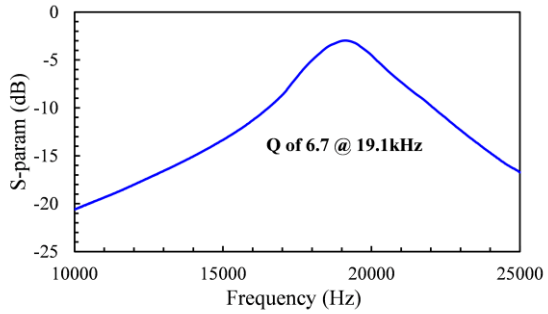

Figure 9: Near critically damped resonant characteristics (Q~6.7 @ 19.1kHz) of proof mass provides wide operational bandwidth.

In order to characterize performance of the accelerometer, a differential pair of two resonators is driven into resonance simultaneously using two independent phase-locked loops (PLL) with discrete TIAs implemented utilizing Zurich Instrument's lock-in amplifier (HF2 LI). The scale factor measurement was done by applying up to ±1g acceleration with 0.2g steps at 10Hz rate using a shaker table. The differential readout (Δf) is calculated with tracked resonant frequencies and the bias is nulled by subtracting the zero-g bias from the beat frequency. The differential readout shows 41.2Hz/g of scale factor (Fig. 10).

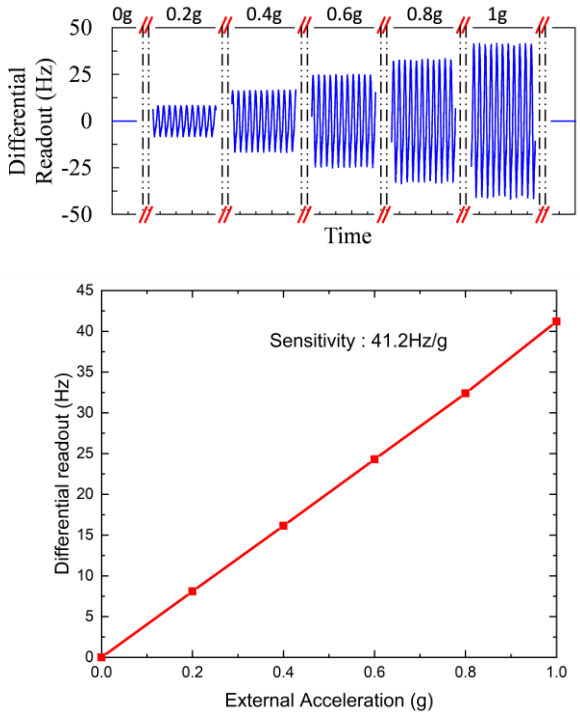

Figure 10: Shaker table measurement shows scale factor of 41.2Hz/g.

The Allan deviation plot of the accelerometer shows a measured velocity random walk corresponding to a noise density of 5.8µg/√Hz and a bias instability of 23µg (Fig. 11). The accelerometer shows excellent noise performance while showing relatively high bias instability starting to increase at short integration time of 0.1s. This is partially due to residual temperature effect of the resonators and partially due to the bias voltage stability. Better frequency stability is expected with proper temperature compensation techniques and more stable DC bias voltage source.

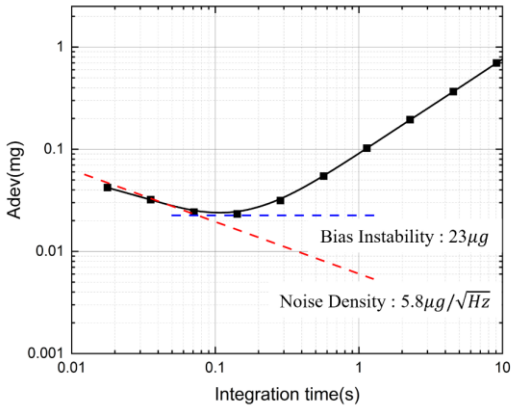

Figure 11: Measured Allan deviation of a prototype eFM OPA.

CONCLUSION

In this paper, the design and implementation of hermetically sealed differential readout out-of-plane eFM accelerometer have been presented and demonstrated its performance. Preliminary results show scale factor of 41.2Hz/g with over 15kHz of near critically damped, Q of 6.7, operational bandwidth. Alan variance analysis shows noise density of 5.8µg/√Hz and BI of 23µg, yielding superior noise and bandwidth performance required for high-end applications. Better frequency stability and measurability is expected with proper temperature compensation techniques.

REFERENCES

[1] Gupta, P., Moghimi, M. J., Jeong, Y., Gupta, D., Inan, O. T., & Ayazi, F. (2020). Precision wearable accelerometer contact microphones for longitudinal monitoring of mechano-acoustic cardiopulmonary signals. NPJ digital medicine, 3(1).

[2] Shin, S., Kwon, H.K., Vukasin, G.D., Kenny, T.W. and Ayazi, F., 2021. A temperature compensated biaxial eFM accelerometer in Epi-seal process. Sensors and Actuators A: Physical, 330, p.112860.

[3] Wang, J., Shang, Y., Chen, J., Sun, Z. and Chen, D., 2012. Micro-machined resonant out-of-plane accelerometer with a differential structure fabricated by silicon-on-insulator–MEMS technology. Micro & Nano Letters, 7(12), pp.1230-1233.

[4] Y. Jeong, A. Daruwalla, H. Wen, and F. Ayazi, "An out-ofplane "hinge-shaped" nano-gap accelerometer with high sensitivity and wide bandwidth," in 2017 19th International Conference on Solid-State Sensors, Actuators and Microsystems (TRANSDUCERS), 2017, pp. 2131-2134.

[5] Daruwalla, A., Wen, H., Gong, M. and Ayazi, F., 2020. High-G and High-Bandwidth Bulk Acoustic Wave (BAW) Accelerometers Using a Metal-Less AlN-HARPSS Process With 95 nm Gaps. IEEE Sensors Letters, 4(8), pp.1-4.

[6] Caspani, A., Comi, C., Corigliano, A., Langfelder, G., Zega, V., & Zerbini, S. (2014). A differential resonant micro accelerometer for out-of-plane measurements. *Procedia Engineering*, 87, 640-643.

[7] Wen, H., Daruwalla, A., Jeong, Y., Gupta, P., Choi, J., Liu, C.S. and Ayazi, F., 2018, April. Wafer-level-packaged HARPSS+ MEMS platform: Integration of robust timing and inertial measurement units (TIMU) on a single chip. In 2018 IEEE/ION position, location and navigation symposium (PLANS) (pp. 261-266).

CONTACT

*S. Shin; sshin312@gatech.edu

DEVELOPMENT OF A SCALABLE SOFT FINGER GRIPPER FOR SOFT ROBOTS

Armin Jamali, Robert Knoerlein, Frank Goldschmidtboeing, and Peter Woias
Department of Microsystems Engineering (IMTEK), University of Freiburg, Germany

ABSTRACT

Soft robotics is vastly drawing attention, especially concerning their unique characteristics. Soft robots could be used to enhance motion as a soft exoskeleton, as soft prosthetics, or function as grippers for lifting objects. A challenge to the fabrication and actuation of conventional Dielectric Elastomer Actuators (DEAs) is that they require a pre-stretch over an external rigid frame. Moreover, the external rigid frame can hardly bend, causing the actuation to be limited to planar. In this research, we characterized a silicone-based elastomer electrically and mechanically as a substitute for conventional elastomers. Then, we developed a fabrication process and implemented a backbone structure to achieve soft and scalable finger grippers capable of lifting and holding arbitrary objects without needing an external frame.

KEYWORDS

Dielectric Elastomer Actuators, Soft Robotics, Soft Grippers, Artificial Muscles, Electroactive Polymers

INTRODUCTION

Soft grippers have the potential to mimic muscles to create artificial hands or to replace rigid body robots [1, 2]. Dielectric elastomer actuators, known as artificial muscles, are a subset of electroactive polymer actuators driven by electrostatic force. In their simplest form, they are made of a thin layer of soft and non-conductive elastomer sandwiched between two compliant layers of electrodes. When the electrodes are connected to a high voltage, and the electric field is applied through the dielectric elastomer, the attraction force between opposite charges results in compression stress, known as the Maxwell stress. As a result of the Maxwell stress, the elastomer contracts in thickness and expands in the area. Concerning the expansion of the area with respect to the changes in the thickness, one can assume a constant volume to a good approximation [3].

$$p = \varepsilon_r \cdot \varepsilon_0 \cdot E^2 \qquad (1)$$

$$S_z = -\frac{p}{Y} = -\left(\frac{\varepsilon_r \cdot \varepsilon_0}{Y}\right)\left(\frac{U}{z}\right)^2 \qquad (2)$$

Here, p is the Maxwell stress, ε_r is the relative permittivity of the elastomer, ε_0 is the vacuum permittivity, z is the thickness of the elastomer, E is the electric field, S_z is the thickness strain, and Y is Young's modulus of the elastomer. Eq. (1) and (2) reflect the mechanical and electrical properties of the elastomer, which mainly affect the performance of the actuator. The equations indicate that, on the one hand, the elastomer must have a relatively low Young's modulus, high relative permittivity, and high electrical breakdown (E_{BD}). On the other hand, the electrodes are only meant to deliver charges; thus, any contribution to the total mechanical resistance is considered a disadvantage. The electrodes must have no thickness and zero mechanical resistance in an ideal case.

On top of the material properties, the design of an effective actuation mechanism is of great importance. DEAs, in their simplest form, perform a planar actuation; therefore, a mechanism is required to translate it to more complex actions like bending or twisting. One example at the application level is a gripping actuator. There are many valuable efforts to design and fabricate a soft gripper. Wang et al. [4] have recently presented a DEA gripping tool with two fingers. They optimized a mechanism to translate the planar actuation into the gripping force. They used the conventional VHB™ 4910 tape from *3M™, Ltd.* for the elastomer and used carbon grease to apply conductive layers. The gripper ultimately managed to apply 100.2 mN gripping force.

In this research, we present an alternative method and a set of materials to overcome some limitations of the performance of a soft gripper. Although showing outstanding actuation qualities, the acrylic VHB™ 4910 tape is highly dependent on a rigid external frame, and its thickness is only defined by the amount of pre-stretch over the frame. This approach limits the application field. A general strategy to gain higher actuation force and motion is to stack the elastomers and electrodes to make multi-stacked or multi-layered actuators. The carbon grease is relatively thick and does not cure well; therefore, it is not the best option for the strategy of multi-stacking. We revised the choice of materials to overcome these barriers, which resulted in a multi-layered, ultra-thin, and compliant actuator. Then, we revised the fabrication process and introduced the backbone structure to produce bending actuators utterly independent from any external frames.

MATERIAL CHARACTERIZATION

VHB™ 4910 is an acrylic adhesive commercially available as double-sided tape. It is available only in viscoelastic form, so one should adjust the thickness by stretching the tape and fixing it to an external rigid frame. The stretched area should not contact other parts; otherwise, it sticks. Then, the carbon grease must be applied to the exposed surfaces, and the following elastomer layers should get stretched in the same way and placed onto the last layer. The method of stretching can cause inaccuracy in achieving the desired thickness, making it difficult to stack the layers accurately. In addition, the tape can mainly function in a straight planar form, and any curvature needs another rigid external support. Thus, one cannot have the tape in a stably curved form.

Considering all the mentioned limitations, we took another approach in this research and implemented a silicone-based elastomer. We mixed the ECOFLEX™ 00-10 with 10% SILICONE THINNER™ from *Smooth-On, Inc.*, and we characterized the elastomer electrically and mechanically. We refer to the compound as Ecoflex10T.

Table 1: Properties of the elastomers

Material	ε_r	E_{BD} ($V\mu m^{-1}$)	Y (kPa)
Ecoflex10T	4.4 @ 20 Hz	22	58
Ecoflex™10	3.5 @ 20 Hz	38	57
VHB™ 4910 [5]	3.2 @ 1 kHz	25	n.a.

As indicated in Table 1, the properties of Ecoflex10T are comparable to VHB™. We also learn from characterization results that adding the thinner to the silicone improves the dielectric constant though decreasing the electrical breakdown strength. Since

978-1-940470-04-7/HH2022/$25©2022TRF
DOI 10.31438/trf.hh2022.88

the ultimate goal of this project is to develop DEAs driven by the lowest possible voltage, we avoid working with very high voltages close to the breakdown voltages. Therefore, the addition of the thinner is favorable. Moreover, uncured Ecoflex10T is liquid; hence, it is suitable for fabrication methods such as molding and spin-coating.

The results of the elastic behavior of cured Ecoflex10T are shown in Figure 1. Accordingly, Young's modulus for very high strains is 58 kPa, while this value for lower strains less than 300% is 14 kPa. For this measurement, Ecoflex10T was molded into standard dog-bone test specimens according to ISO 37:2017-11 [6].

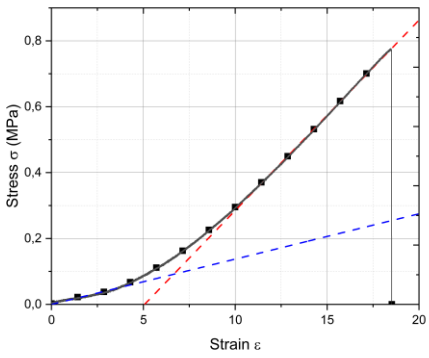

Figure 1: Stress-strain curve of the specimen made of Ecoflex10T, and the linear fits for strains less than 2 and higher than 10.

FABRICATION METHOD

Elastomer

In this research, the spin-coating method was chosen to deposit the elastomer layers one after the other. In this method, the Ecoflex10T was cured in the oven at 85°C right after deposition onto a handling wafer. The amount of the deposited material and the spin-coating parameters would determine the thickness of the cured layer. The elastomer thickness is critical as the Maxwell stress correlates proportionally to the inversed squared of the thickness. In addition, the thickness of the thinnest elastomer determines the maximum allowed voltage to prevent an early-stage breakdown.

Lee, Kim et al. [7] have derived a formula for the spin-coating parameters which control the film thickness. We developed a recipe for every desired film thickness based on this formula. For instance, the rotation speed of 250 rpm for 23 s would result in a thickness of 545 ± 30 µm for 6 grams of Ecoflex10T (with the density of 987 kg.m^{-3} and the viscosity of 6.7 Pa.s). With this repeatable and reproducible method, we obtained layers as thin as 42 µm (Figure 2).

$$h = \frac{h_0}{\sqrt{1+\frac{4\rho\omega^2 h_0^2 t}{3\eta}}} \qquad (3)$$

Here, h_0 describes the initial thickness of the coating material. ρ is the density, η is the viscosity of the liquid, and t represents the duration of spinning [7].

Electrode

As a substitution for the carbon grease, we chose the method of dry-brushing the carbon black powder directly onto the elastomer layer with a soft brush. This method was suggested by H. Shigemune et al. [8]. The deposition of the patterned electrode layer was through a polymethyl methacrylate (PMMA) mask. The pattern was first lasered out using a CO_2 laser (*VersaLaser™, Universal Laser Systems, Inc.*) from the 4-inch PMMA wafer with a 0.5 mm thickness (Figure 3). Then, the mask was placed directly onto the cured layer of elastomer, and with a soft paintbrush, the carbon black powder (*P250, Ensaco®*) was applied to the exposed parts of the Ecoflex10T through the mask. Finally, the remaining carbon black powder was blown away, and the next layer of Ecoflex10T was applied directly onto the electrode layer. It is noteworthy that polymerization of Ecoflex10T is relatively quick (30-minute pot life), so for every elastomer layer, a fresh uncured Ecoflex10T should be prepared.

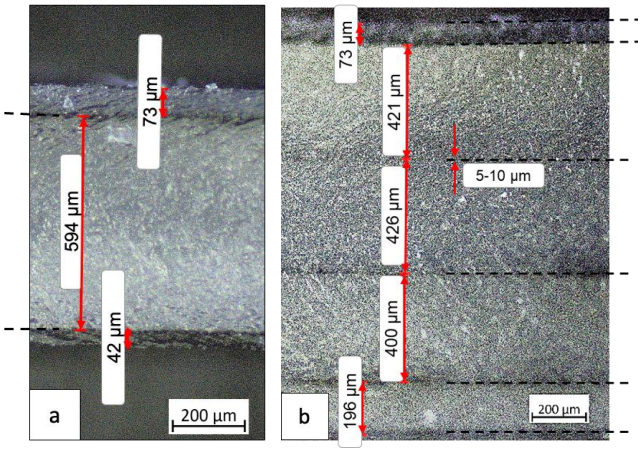

Figure 2: Cross-section view of the actuators under the microscope. The dashed lines indicate the position of the electrode layer with a thickness of less than 10 µm (a) a single layer actuator (b) an actuator with three active layers.

The carbon black powder showed excellent adhesion to the Ecoflex10T, resulting in a uniform and evenly distributed electrode layer. The electrode layer remains conductive even when the actuator is deformed. The final actuator was cut into thin slices for the thickness measurement and observed under the measurement microscope (*Scope.A1, ZEISS*). As indicated in Figure 2, the electrode layer thickness is between 5 µm to 10 µm. The first and the last layer of the actuator are covered with very thin passivation elastomer layers to protect the actuator and the surrounding objects from any unwanted contact. When the layer deposition is over, the actuator is cut out and connected to the contact pins (Figure 3). The thickness and the weight of the actuator are dependent on the number and the thickness of the layers. For comparison, the single layer actuator was 1.46 mm thick and had 1.51 g mass, while a 5-layered actuator was 3.84 mm thick and had 4.57 g mass (Figure 4).

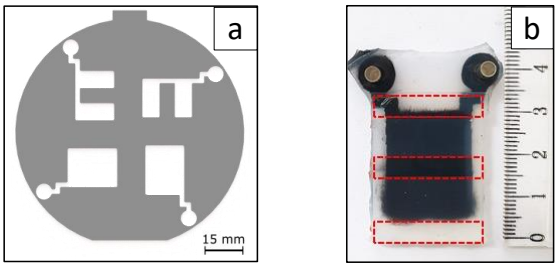

Figure 3: (a) A PMMA mask used for patterning the carbon black powder with a soft brush onto the elastomer (b) The final bending actuator (4 cm × 3 cm) with the full-rectangle design cut out from the wafer. The red dashed lines indicate the position of the transparent PMMA backbone structure.

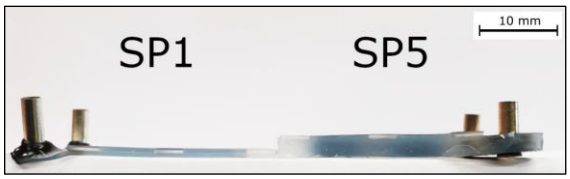

Figure 4: Side view of a single layer (SP1) and a 5-layered (SP5) actuator.

BENDING MECHANISM

When the voltage is applied to the electrodes, the Maxwell stress causes the actuator to shrink thickness. Since the elastomer volume is assumed to remain constant, the actuator surface increases accordingly. A single layer actuator with symmetrical passive layers deforms only in a planar direction as the active area's top and bottom surface expand to the same degree. In case one side, either top or bottom surface, has a higher mechanical resistance, the deformation would be asymmetrical, i.e., the surface with higher resistance would expand less than the other. As a result, the actuator bends towards the stiffer side.

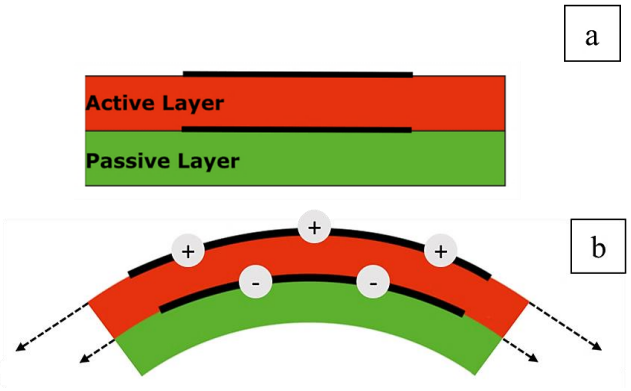

Figure 5: Schematic of the bending mechanism. The area sandwiched between electrode layers is called an active area. As the bottom surface had more resistance due to the thick passive layer, the top surface expands more and bends the actuator.

The mechanism, shown in Figure 5, was the inspiration for the development of bending actuators in this research. Accordingly, we introduced a so-called backbone structure to the last layer. The backbone structure consists of small thin, and rigid parts made of PMMA. As shown in Figure 6, the pieces are placed in the passive layer, increasing the mechanical resistance on that side. The advantage of this mechanism is that the stiffer parts are embedded in the soft actuator, and there is no need for any external support. The bending motion is only possible when the actuator is independent of external rigid frames.

The backbone structure also inhibits the bending in the non-desired direction. Figure 6 illustrates the schematic cross-section of a single layer actuator. The transparent backbone structure in a bending actuator is shown with red dashed lines in Figure 3. All results were achieved with actuators of the same lateral structure but with different numbers of active layers.

Figure 6: Schematic of the cross-section of the bending actuator. (a) the passivation layer (b) PMMA backbones (c) elastomer layer (d) electrode layer (e) active elastomer layer for actuation.

RESULTS

Eventually, the bending actuator was connected to the measurement setup, hanging from the contact pins, and a laser sensor (*scanCONTROL 3002-25/BL, Micro-Epsilon*) was placed in front of the actuator to capture the deflection.

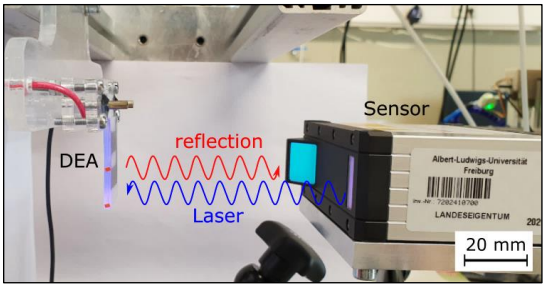

Figure 7: Capturing and measuring the bending line with the laser sensor.

For characterizing the bending actuator, the bending profile was recorded. Figure 8 depicts the maximum bending angle for a 2-layered bending actuator under voltages up to 8 kV.

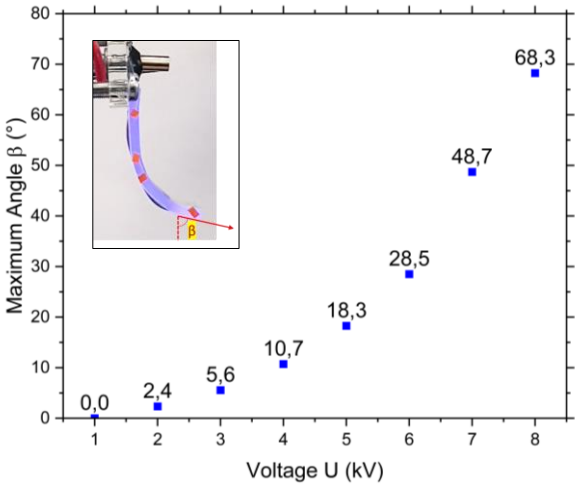

Figure 8: The maximum bending angle (β) for a 2-layered bending actuator.

The soft finger gripper is made of two actuators facing and bending towards each other. The finger gripper can press, hold and lift an object with an arbitrary shape. For the characterization purpose, a basket was designed, and in every measurement step, some incremental weight was added to the basket. The best result was for the fingers with a 5-layered actuator, which held and lifted the weight of 10.29 g (100.9 mN). The setup is shown in Figure 9.

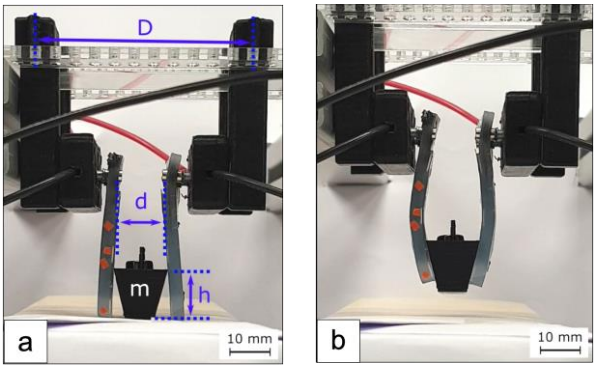

Figure 9: (a) The soft gripper ready for actuation, m_{max}=10.29 g, D = 55 mm, d = 11 mm, h = 14 mm (b) the soft gripper lifting and holding the weight under 8 kV.

CONCLUSION AND OUTLOOK

The key results presented in this paper were the choice of material, the novel actuation mechanism, and the process developed to fabricate the grippers. We deposited the elastomer layers of Ecoflex10T with a spin-coating method and patterned the electrode layers by dry-brushing the carbon black power directly onto the cured elastomer. The thickness of elastomer layers was tunable between 40 µm and 800 µm, and the electrode layer was between 5 µm to 10 µm thick. We also characterized the properties of the elastomer electrically and mechanically (Y = 58 kPa for very high strains and Y = 14 kPa for strains lower than 300%, ε_r = 4.4 @ 20 Hz, and E_{BD} = 22 V.µm^{-1}). This novel fabrication process enables the fabrication of multi-layered bending actuators without external ridged frames.

The bending actuator with two elastomer layers was able to bend up to 68.3°, lifting its weight (W_2 = 22.6 mN), while the 5-layered finger grippers (W_5 = 44.8 mN each) successfully lifted, held, and released the objects up to 100.9 mN. The advantage of this work is the independency from any external frame, scalability, and ease of thickness control for the elastomer layer. This research paves the way for future works for the scientific community to miniaturize the gripper and optimize the backbone structure to realize more complex motions like twisting grippers.

ACKNOWLEDGEMENTS

Funded by the Deutsche Forschungsgemeinschaft (DFG, German Research Foundation) under Germany's Excellence Strategy – EXC-2193/1 – 390951807.

REFERENCES

[1] P. Brochu and Q. Pei, "Advances in dielectric elastomers for actuators and artificial muscles," *Macromolecular rapid communications*, vol. 31, no. 1, pp. 10–36, 2010, doi: 10.1002/marc.200900425.

[2] E. Biddiss and T. Chau, "Dielectric elastomers as actuators for upper limb prosthetics: challenges and opportunities," *Medical engineering & physics*, vol. 30, no. 4, pp. 403–418, 2008, doi: 10.1016/j.medengphy.2007.05.011.

[3] F. Carpi, Ed., *Dielectric elastomers as electromechanical transducers: Fundamentals, materials, devices, models and applications of an emerging electroactive polymer technology*. Amsterdam: Elsevier, 2008.

[4] N. Wang, B. Chen, H. Guo, C. Cui, and X. Zhang, "Design of dielectric elastomer grippers using Bezier curves," *Mechanism and Machine Theory*, vol. 158, p. 104216, 2021, doi: 10.1016/j.mechmachtheory.2020.104216.

[5] N. Thacker, "3M VHB Tape - Specialty Tapes TDS - June 2020," [Online]. Available: https://www.3mdeutschland.de/

[6] ISO 37:2017-11: Rubber, vulcanized or thermoplastic - Determination of tensile stress-strain properties.

[7] U. G. Lee, W.-B. Kim, D. H. Han, and H. S. Chung, "A Modified Equation for Thickness of the Film Fabricated by Spin Coating," *Symmetry*, vol. 11, no. 9, p. 1183, 2019, doi: 10.3390/sym11091183.

[8] H. Shigemune *et al.,* "Dielectric Elastomer Actuators with Carbon Nanotube Electrodes Painted with a Soft Brush," *Actuators*, vol. 7, no. 3, p. 51, 2018, doi: 10.3390/act7030051.

CONTACT

*A. Jamali, tel.: +49-761-203-7508;
armin.jamali@imtek.uni-freiburg.de

ENHANCEMENT OF Q AND K^2 IN $AL_{0.8}SC_{0.2}N$/GAN/SAPPHIRE SURFACE ACOUSTIC WAVE RESONATORS USING SEMICONDUCTOR GROUND CONTACT

Yue Zheng[1], Jialin Wang[1], Mingyo Park[1], Ping Wang[2], Ding Wang[2], Zetian Mi[2] and Azadeh Ansari[1]
[1]Georgia Institute of Technology, Atlanta GA, USA
[2]University of Michigan, Ann Arbor MI 48109, USA

ABSTRACT

This work reports on the super high frequency (SHF) surface acoustic wave (SAW) resonators with bottom ground contact, based on 200 nm-thick epitaxial aluminum scandium nitride ($Al_{0.8}Sc_{0.2}N$) on gallium nitride (GaN)/sapphire with high doped n-GaN as the bottom electrode. $Al_{0.8}Sc_{0.2}N$ epitaxial films are grown on GaN/sapphire template with molecular beam epitaxy (MBE). Interdigital transducers with a pitch size of 0.4 μm are patterned with electron beam lithography (EBL). By taking advantage of a grounded bottom semiconductor contact and the high acoustic velocity of Sezawa modes, a four-time improvement of *Q* value from 172 to 819 is attained at a resonance frequency of 5.792 GHz.

KEYWORDS

Sezawa mode; Aluminum Scandium Nitride; Gallium Nitride; Surface acoustic wave; Molecular Beam Epitaxy; Super High Frequency; Quality factor; Ground Contact.

INTRODUCTION

Surface acoustic wave (SAW) resonators made of piezoelectric materials are well known for offering a low-loss and low-cost solution for RF bandpass filter applications owing to the advantage of high-temperature stability and non-releasing fabrication technique [1], [2]. In order to construct SAW resonators with high quality (*Q*) factor and high electromechanical coupling coefficient (K^2), it is essential to grow a piezoelectric film with an ordered lattice structure and fewer crystallographic defects, particularly when the device is scaled down to target super high frequency (SHF) band required by 5G/6G standards [3]. As a novel piezoelectric material, aluminum scandium nitride ($Al_{1-x}Sc_xN$) deposited by DC magnetron sputtering method can suffer from low growth quality, particularly when the Sc composition is high: abnormally oriented grains can be formed if the $Al_{1-x}Sc_xN$ lattice is mismatched with the growth template [4].

Gallium Nitride (GaN), a wide bandgap piezoelectric material with hexagonal wurtzite structure, is nearly lattice-matched with $Al_{1-x}Sc_xN$ [5]. Besides its applications in piezoelectric transducers, GaN is a versatile material that is promising for on-chip integration of multi-functional III-nitride devices [6]. *In situ* silicon (Si)-doped GaN can serve as a conductive interface [7]. Acoustoelectric amplifiers with DC voltage tuning can be made by harnessing the phonon-electron interaction in unintentionally doped (UID) GaN [8]. With the ability to form two-dimensional electron gas (2DEG), AlGaN/GaN heterostructure is commonly utilized for high mobility electron transistor (HEMT) [9]. With epitaxial $Al_{1-x}Sc_xN$ grown on GaN template, it is possible to leverage the above advantages to control $Al_{1-x}Sc_xN$-based transducers.

In our previous work, we demonstrated ferroelectric polarization switching and fabricated one-port SAW resonators with floating Si-GaN bottom on two separate $Al_{0.8}Sc_{0.2}N$/GaN/sapphire devices [10], [11]. Multiple Sezawa modes operating at 3-6 GHz with moderately high *Q* factor were probed in this structure, offering a multi-band high-frequency solutions to radio frequency (RF) filters. However, to observe both functionalities on the same device, the Si-GaN bottom contact layer needs to be grounded. Therefore, it is necessary to investigate the effect of bottom contact on the performance of the SAW resonator.

The electrostatic boundary conditions of the bottom contact and the normalized thickness (h/λ) of the piezoelectric film both affect the K^2 of SAW modes and lamb-wave (LW) modes due to the change of static capacitance (C_o) and piezoelectric coefficient under different applied electric field [12], [13]. SAW and LW resonators with small h/λ (< 0.5) with grounded bottom electrodes are reported to enhance the K^2 but usually come at a price of increased feedthrough level and degraded *Q* factor [13]–[15]. The impact of metal bottom electrode has been thoroughly investigated in the past; however, the role of a semiconductor ground on resonator performance has not been well understood.

In this work, we report on the first demonstration of two-port $Al_{0.8}Sc_{0.2}N$/GaN/sapphire SAW resonator employing n-type Si-doped GaN as a semiconductor bottom contact. The growth quality of $Al_{1-x}Sc_xN$ is controlled by using (1) GaN as a growth template and (2) molecular beam epitaxy (MBE) to grow textured $Al_{1-x}Sc_xN$ epitaxial thin film. We remove the piezoelectric film under the signal probing region to reduce undesired resonance and parasitic capacitance caused by probing pads. Compared to the SAW resonators with floated bottom contact, the device with grounded bottom contact achieves a boost of *Q* by 376% and a slight improvement of effective mechanical coupling coefficient (k_{eff}^2) for both Rayleigh (R) and Sezawa (S) modes.

DEVICE STRUCTURE AND FABRICATION PROCESS

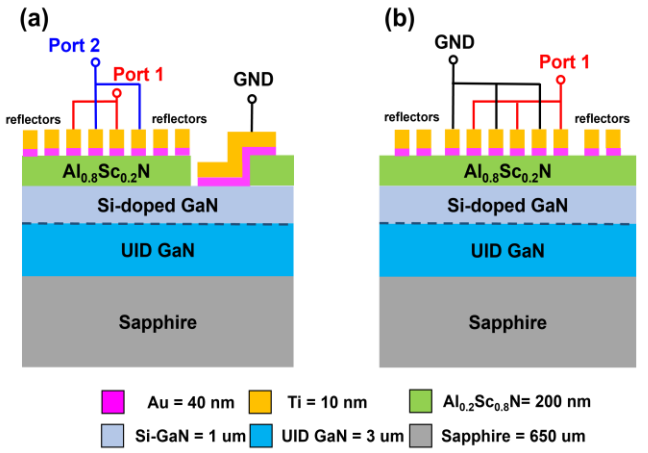

Figure 1: Schematic cross section view of (a) 2-port $Al_{0.8}Sc_{0.2}N$/GaN/Sapphire SAW resonator with grounded GaN contact, and (b) 1-port SAW resonator with floated bottom contact.

We previously reported the fabrication of one-port SAW resonators with 0.4 μm – 0.6 μm pitch sizes and floating Si-GaN bottom contact (Fig. 1(b)). The growth techniques of the $Al_{0.8}Sc_{0.2}N$-on-GaN/sapphire film, the fabrication process of the one-port SAW devices and the RF characterization methods were described in [16] and [10], and hence will not be repeated.

Fig. 2 (a) shows the high-resolution transmission electron

978-1-940470-04-7/HH2022/$25©2022TRF
DOI 10.31438/trf.hh2022.89

microscopy (HRTEM) of the $Al_{0.8}Sc_{0.2}N$/GaN/sapphire film for the fabrication of SAW resonators. The rocking curve (Fig. 2(b)) and the 2theta-omega (2θ/ω) scan (Fig. 2(c)) from X-ray diffraction (XRD) shows a full width at half maximum (FWHM) of 300 arcseconds for the $Al_{0.8}Sc_{0.2}N$ layer.

In this work, we fabricate two-port 0.4 µm-pitched SAW resonators with grounded n-GaN contact (Fig. 1(a)). To access the n-GaN bottom contact (BC), the $Al_{0.8}Sc_{0.2}N$ is etched by inductively coupled plasma (ICP), and conformal Ti/Au coating is subsequently deposited with RF sputtering method. To reduce the high electrical feedthrough level observed in the previous work, we etch the $Al_{0.8}Sc_{0.2}N$ area under the signal probing pads to remove the parasitic capacitance and fill with 200 nm of SiO_2 deposited by electron beam evaporation. Fig. 2(d) shows the scanning electron microscope (SEM) image of the 0.4 µm-pitched two-port SAW resonator, and the inset shows the close-up detail of the interdigital transducer (IDT) structure.

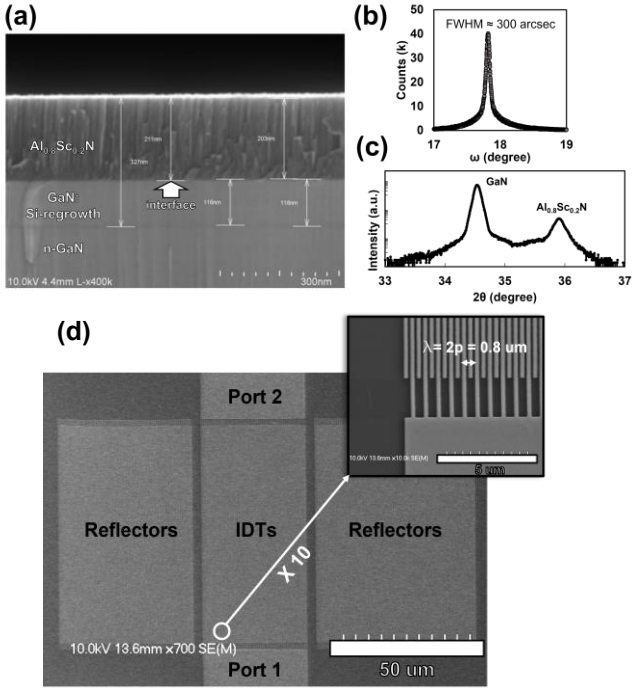

Figure 2. (a) HRTEM image showing the cross-sectional morphology of epitaxial $Al_{0.8}Sc_{0.2}N$ on GaN. (b) Rocking curve and (c) (002) plane XRD 2θ/ω scan of $Al_{0.8}Sc_{0.2}N$/GaN. (d) SEM image of a fabricated 2-port SAW resonator with a 400 nm pitch size. Inset shows the zoomed-in view of the IDT fingers and the bus line.

DEVICE CHARACTERIZATION AND EXPERIMENTAL RESULTS

Characterization of SAW Resonators with Grounded Contact

The frequency response of the SAW devices was measured using Keysight N5224B PNA microwave network analyzer. Fig. 3 illustrates the evaluated tested electromechanical performance of the SAW devices, including floated and grounded BC.

Fig. 3(a) and Fig. 3 (b) present the wideband input admittance (Y_{11}) response and the transfer admittance (Y_{12}) response of the two-port 0.4 µm-pitched SAW resonators with grounded BC. The Y_{11} response from the previous devices (with floated BC) is plotted for comparison. k_{eff}^2 of each mode is determined using [17]:

$$k_{eff}^2 = \frac{\pi^2}{4}(f_p - f_s)\frac{f_s}{f_p^2}, \quad (1)$$

where f_s is the series resonance frequency and f_p is the parallel resonance frequency.

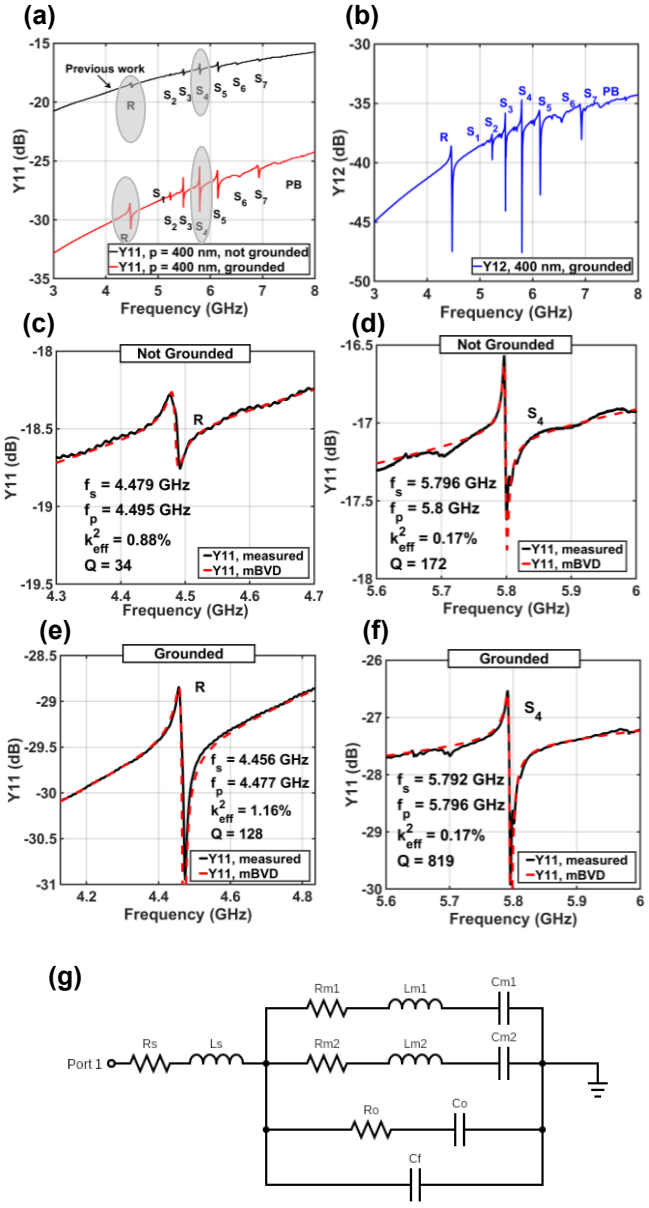

Figure 3. (a) Measured wideband Y_{11} response of the 0.4 µm-pitch $Al_{0.8}Sc_{0.2}N$/GaN/Sapphire SAW resonators with and without grounding the Si-doped GaN surface. (b) Y_{12} response of the resonator with grounded contact. Zoomed-in peak with mBVD fitting of R mode and S_4 mode from the Y_{11} response of SAW resonator (c)-(d) with floated bottom contact and (e)-(f) with grounded contact. (g) Modified Butterworth Van Dyke (mBVD) circuit model for Y_{11} characteristics fitting.

The Bode quality factor (Q_{Bode}) is extracted from S-parameters, according to [18]:

$$Q_{bode}=\omega\times\tau_g(\omega)\frac{|S_{11}|}{(1-|S_{11}|)^2}, \quad (2)$$

where ω is the angular frequency (rad/s) and τ_g is the group delay. The highest Q_{bode} exhibited in the two-port resonator is 819 from the fourth-order Sezawa (S_4) mode at 5.792 GHz. Table 1 compares the measured f_s, f_p, k_{eff}^2 and Q factor of R and S_4 modes with grounded and floated resonator BC.

It can be noticed that the grounded BC has minimal impact on the resonance frequencies. For S_4 mode, a four-time improvement of Q is achieved with grounded BC, showing a Q value of 819 at a resonance frequency of 5.792 GHz. The enhancement of the Q factor could be caused by a shift of the electrical potential profile in GaN layer, as it has been shown that Q can be amplified under the acoustoelectric effect by tuning the potential level in GaN layer [19]. Removal of the piezoelectric film under signal probing pads contribute to the decrease of feedthrough level and may also aid the Q factor enhancement.

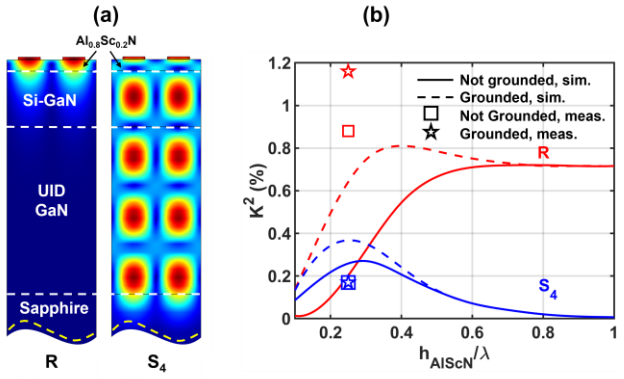

Figure 4. COMSOL simulated (a) 2-D cross-sectional displacement field of Rayleigh (R) mode and fourth-order Sezawa (S_4) mode, and (b) dispersion relations of the electromechanical coupling coefficient (K^2) with respect to the normalized AlScN thickness (h_{AlScN}/λ); marked stars/squares show the measured values for the devices.

In order to study the contribution of bottom ground contact to the electromechanical coupling, finite element modeling (FEM) of the fabricated device is constructed on the scale of one acoustic wavelength (λ) using COMSOL Multiphysics®. The K^2 is assessed by [20]:

$$K^2=2\times\frac{v_{oc}-v_{sc}}{v_{oc}}, \quad (3)$$

where v_{oc} and v_{sc} are the phase velocities when the surface boundary condition of the $Al_{0.8}Sc_{0.2}N$ is open-circuited (free) and short-circuited (grounded) respectively [21]. The relative dielectric permittivity ϵ_r of 13.7 is used for $Al_{0.8}Sc_{0.2}N$ in the simulation [22]. It should be noted that the dielectric property of the thin film is subjected to the residual strain level induced at different growth temperatures, and the actual value ϵ_r of in the AlScN film might be different from the literature value. Fig. 4(a) shows the mode shape of R and S_4 modes of the resonator with 0.4 µm pitch size. Fig. 4(b) compares the dispersion relations of the K^2 of the resonator with grounded and floating electrostatic boundary condition at the AlScN/GaN interface, showing the K^2 enhancement for a normalized thickness (h_{AlScN}/λ) less than 0.6. The K^2 enhancement is due to the improved d_{33} coupling in $Al_{0.8}Sc_{0.2}N$ in the presence of a vertical electric field. It should be noted that the K^2 values of R mode from simulations are smaller than the measured k_{eff}^2 values, which is also reported in [23]. The reason for such underprediction could also be attributed to an overestimation of ϵ_r of $Al_{0.8}Sc_{0.2}N$ at high frequency, as it has been reported that at high frequency, ϵ_r degrades to half of the low-frequency value for aluminum nitride [24].

Table 1. Summary of f, k_{eff}^2 and Q values from the measurements of the 0.4 µm-pitched SAW devices.

Mode	Bottom Contact	f_s (GHz)	f_p (GHz)	k_{eff}^2	Q_{Bode}
R	Not grounded	4.479	4.495	0.88%	34
	grounded	4.456	4.477	1.16%	128
S_4	Not grounded	5.796	5.800	0.17%	172
	grounded	5.792	5.796	0.17%	819

Frequency Response of SAW Resonators with mBVD Model

To further understand the enhancement mechanisms of k_{eff}^2 and Q factor in the resonators with grounded BC, the measured results of R mode and S_4 mode are fitted by the modified Butterworth-Van Dyke (mBVD) circuit model [25]. The model is made of a series RLC circuit (R_m, L_m and C_m) that represents the motional branch of each acoustic resonance and a static capacitance C_0 and a resistance R_0 that model the capacitance between IDT fingers and resistive loss in electrodes (Fig. 3 (g)). An additional feedback capacitance C_f is included to model the UID-GaN film capacitance [26]. R_s and L_s account for the parasitic effect caused by the probing pads to improve impedance matching. The unloaded quality factor Q_m can be extracted using the fitted motional branch circuit component values using:

$$Q_m=\frac{1}{R_m}\sqrt{\frac{L_m}{C_m}}. \quad (4)$$

Fig. 3(c)-(f) show the zoomed-in peaks of R modes and S_4 modes corresponding to each SAW resonator, along with the fitted response using the mBVD model. Table 2 summarizes the mBVD parameters and the evaluated Q_m of R and S_4 modes of the SAW resonators with/without grounding the BC.

Table 2. Summary of the mBVD parameters used to fit the 0.4 µm-pitched SAW devices with/without the grounded BC.

Mode	Bottom Contact	C_o (pF)	C_f (pF)	C_m (fF)	L_m (nH)	R_m (Ω)	Q_m
R	Not grounded	98	5.35	1.22	1029	72	403
	grounded	803	1.22	1.06	1198	74	454
S_4	Not grounded	98	5.35	0.8	941	22	1558
	grounded	803	1.22	0.53	1437	22	2366

CONCLUSION

In this paper, we demonstrate the enhancement of Q and k_{eff}^2 of a multi-mode AlScN/GaN/sapphire SAW resonator with grounded n-GaN contact operating from 3-6 GHz. $Al_{0.8}Sc_{0.2}N$ epitaxial film is grown with the MBE method on a lattice-matched GaN/sapphire template to ensure good film quality. By utilizing the grounded n-

GaN contact and minimizing the parasitic capacitance, the largest enhancement of Q factor occurs in S_4 mode, whose Q value features a four-time improvement from 172 to 819. We verify the role of the grounded bottom contact on K^2 and Q factor with COMSOL FEM and mBVD model. This work demonstrates the versatility of GaN on a single device and facilitates future investigation on DC tuning of the SAW resonator.

REFERENCES

[1] K. Hashimoto, "RF Bulk acoustic wave filters for communications," p. 275, 2009.

[2] Y. Y. Chen, C. M. Lin, and T. T. Wu, "A novel weighted method for wide-band SAW filters using slanted finger interdigital transducers on layered piezoelectric substrates," Proc. - IEEE Ultrason. Symp., vol. 4, pp. 2182–2185, 2005.

[3] A. Bogner, R. Bauder, H.-J. Timme, T. Forster, C. Reccius, R. Weigel, and A. M. Hagelauer, "Enhanced Piezoelectric $Al_{1-x}Sc_xN$ RF-MEMS Resonators for Sub-6 GHz RF-Filter Applications: Design, Fabrication and Characterization," Proc. IEEE Int. Conf. Micro Electro Mech. Syst., pp. 1258–1261, 2020.

[4] C. S. Sandu, F. Parsapour, S. Mertin, V. Pashchenko, R. Matloub, T. LaGrange, B. Heinz, and P. Muralt, "Abnormal Grain Growth in AlScN Thin Films Induced by Complexion Formation at Crystallite Interfaces," Phys. Status Solidi Appl. Mater. Sci., vol. 216, no. 2, Jan. 2019.

[5] P. Wang, D. Wang, N. M. Vu, T. Chiang, J. T. Heron, and Z. Mi, "Fully epitaxial ferroelectric ScAlN grown by molecular beam epitaxy," Appl. Phys. Lett., vol. 118, no. 22, pp. 1–6.

[6] M. Rais-Zadeh, V. J. Gokhale, A. Ansari, M. Faucher, D. Théron, Y. Cordier, and L. Buchaillot, "Gallium nitride as an electromechanical material," J. Microelectromechanical Syst., vol. 23, no. 6, pp. 1252–1271, Dec. 2014.

[7] Y. Arakawa, K. Ueno, H. Imabeppu, A. Kobayashi, J. Ohta, and H. Fujioka, "Electrical properties of Si-doped GaN prepared using pulsed sputtering," Appl. Phys. Lett., vol. 110, no. 4, p. 042103, Jan. 2017.

[8] V. J. Gokhale and M. Rais-Zadeh, "Phonon-Electron Interactions in Piezoelectric Semiconductor Bulk Acoustic Wave Resonators," Sci. Reports 2014 41, vol. 4, no. 1, pp. 1–10, Jul. 2014.

[9] U. K. Mishra, P. Parikh, and Y. F. Wu, "AlGaN/GaN HEMTs - An overview of device operation and applications," Proc. IEEE, vol. 90, no. 6, pp. 1022–1031, 2002.

[10] Y. Zheng, J. Wang, M. Park, P. Wang, D. Wang, Z. Mi, and A. Ansari, "High-Order Sezawa Mode AlScN/GaN/Sapphire Surface Acoustic Wave Resonators," IEEE MEMS, pp. 1046–1049, 2022.

[11] D. Wang, P. Wang, B. Wang, and Z. Mi, "Fully epitaxial ferroelectric ScGaN grown on GaN by molecular beam epitaxy," Appl. Phys. Lett., vol. 119, no. 11, p. 111902, Sep. 2021.

[12] G. Tang, "Investigation on High Performance Surface Acoustic Wave Devices Using ScAlN Thin Films," 2017.

[13] M. Park and A. Ansari, "Epitaxial $Al_{0.77}Sc_{0.23}N$ SAW and Lamb Wave Resonators," IFCS-ISAF 2020 - Jt. Conf. IEEE Int. Freq. Control Symp. IEEE Int. Symp. Appl. Ferroelectr. Proc., Jul. 2020.

[14] A. Qamar, M. Jafari, and M. Rais-Zadeh, "Solidly mounted anti-symmetric lamb-wave delay lines as an alternate to SAW devices," IEEE Electron Device Lett., vol. 39, no. 12, pp. 1916–1919, Dec. 2018.

[15] C. M. Lin, V. Yantchev, J. Zou, Y. Y. Chen, and A. P. Pisano, "Micromachined one-port aluminum nitride lamb wave resonators utilizing the lowest-order symmetric mode," J. Microelectromechanical Syst., vol. 23, no. 1, pp. 78–91, Feb. 2014.

[16] P. Wang, D. A. Laleyan, A. Pandey, Y. Sun, and Z. Mi, "Molecular beam epitaxy and characterization of wurtzite $Sc_xAl_{1-x}N$," Appl. Phys. Lett., vol. 116, no. 15, p. 151903, Apr. 2020.

[17] H. Campanella, "Acoustic wave and electromechanical resonators : concept to key applications," p. 345, 2010.

[18] D. A. Feld, R. Parker, R. Ruby, P. Bradley, and S. Dong, "After 60 years: A new formula for computing quality factor is warranted," in Proceedings - IEEE Ultrasonics Symposium, 2008, pp. 431–436.

[19] V. J. Gokhale, Y. Shim, and M. Rais-Zadeh, "Observation of the acoustoelectric effect in gallium nitride micromechanical bulk acoustic filters," 2010 IEEE Int. Freq. Control Symp. FCS 2010, pp. 524–529, 2010.

[20] K. Yamanouchi and T. Ishii, "High temperature stable acoustic surface wave substrates of $SiO_2/LiNbO_3$ structure with super high coupling," Japanese J. Appl. Physics, Part 1 Regul. Pap. Short Notes Rev. Pap., vol. 41, no. 5 B, pp. 3480–3482, May 2002.

[21] J. Zou, C. M. Lin, A. Gao, and A. P. Pisano, "The multi-mode resonance in AlN lamb wave resonators," J. Microelectromechanical Syst., vol. 27, no. 6, pp. 973–984, Dec. 2018.

[22] G. Wingqvist, F. Tasnádi, A. Zukauskaite, J. Birch, H. Arwin, and L. Hultman, "Increased electromechanical coupling in w-$Sc_xAl_{1-x}N$," Appl. Phys. Lett., vol. 97, no. 11, pp. 95–98, 2010.

[23] Z. Hao, M. Park, D. Kim, A. Clark, R. Dargis, H. Zhu, and A. Ansari, "Single Crystalline ScAlN Surface Acoustic Wave Resonators with Large Figure of Merit ($Q\times k_t^2$)," 2019 IEEE MTT-S International Microwave Symposium (IMS), pp. 786–789, 2019.

[24] A. T. Collins, E. C. Lightowlers, and P. J. Dean, "Lattice Vibration Spectra of Aluminum Nitride," Phys. Rev., vol. 158, no. 3, p. 833, Jun. 1967.

[25] J. D. Larson, P. D. Bradley, S. Wartenberg, and R. C. Ruby, "Modified Butterworth-Van Dyke circuit for FBAR resonators and automated measurement system," Proc. IEEE Ultrason. Symp., vol. 1, pp. 863–868, 2000.

[26] Y. Wang, W. Goh, K. Chai, X. Mu, Y. Hong, P. Kropenlnicki, and M. Je, "Parasitic analysis and π-type Butterworth-Van Dyke model for complementary-metal-oxide-semiconductor Lamb wave resonator with accurate two-port Y-parameter characterizations," Rev. Sci. Instrum., vol. 87, no. 4, p. 045004, Apr. 2016.

CONTACT

*Yue Zheng, Georgia Institute of Technology,
Atlanta, GA 30332; Email: yzheng331@gatech.edu

*Azadeh Ansari, Georgia Institute of Technology,
Atlanta, GA 30332; Email: azadeh.ansari@ece.gatech.edu

GENERATION AND CONTROL OF INTERNAL FLOWS IN A SESSILE DROPLET BY SUBSTRATE OSCILLATION

Tianyi Zhang, Peng Zhou, Terrence Simon, and Tianhong Cui
University of Minnesota, Minneapolis, Minnesota, 55455, USA

ABSTRACT

A simple and low-cost strategy to generate and control internal flows in a sessile droplet for particle and cell agglomeration in droplets is presented. The agglomeration is achieved by structured internal flows within the sessile droplet driven by an oscillating rigid substrate under certain vibration modes. In this work, oscillation of the substrate is experimentally measured, and its corresponding flow patterns are documented. The particles or cells in the sessile droplet are subsequently tracked using the different flow patterns with different flow intensities. The agglomeration capabilities and their dependence on flow characteristics are experimentally verified.

KEYWORDS

Sessile droplet, mode shape, internal flow, particle agglomeration

INTRODUCTION

Using sessile droplets provides a shift from conventional continuous flow techniques such as microfluidic channels, yet offers similar benefits: low sample consumption, high throughput, automation, and, most importantly, flexibility and versatility [1]. As a powerful tool, the use of an internal flow within a sessile droplet has drawn considerable attention in microfluidic applications due to more functionalities, such as mixing [2], cell agglomeration [3], and particle separation [4]. However, it is usually difficult to generate strong circulating flows in small volumes due to low Reynolds numbers [, 5].

Various methods have been developed to generate internal flows in sessile droplets with external energy input. For example, the electrowetting-on-dielectric (EWOD) method uses an alternating electric field to induce droplet oscillation and accompanying flows [6]. Surface acoustic waves (SAW) are actuated on a piezoelectric disk to produce acoustic streaming [7]. Others have used magnetic particles in the droplet to control the flows with an external magnetic field [8]. Low-frequency vertical oscillation of the droplet substrate can also be utilized to cause flows driven by the gas/liquid interfaces vibrating at resonance frequencies [9]. However, these methods have some limitations in their applications, i.e., liquid to be actuated in the sessile droplet must contact special materials (electric conductive, piezoelectric, or magnetic). With vibrating droplets, though no specific materials are required, precise control of droplet volume and driving frequency is required.

In this research, we present a low-cost approach to generating and controlling flows within sessile droplets using an oscillating substrate. The substrate is actuated to give rotational oscillation with a non-uniformly distributed vertical vibrating velocity that induces an internal flow in an attached droplet. Our experiment verifies the correlation between various internal flow patterns and corresponding vibrating velocities distribution of the substrate. The capability for particle and cell agglomeration is verified with experiments.

METHODS

In the present experiment, a sessile droplet with a volume of 100 μL is confined in a recessed retainer 8 mm in diameter and 0.5 mm thick made of polydimethylsiloxane (PDMS). The PDMS pad is cast in a mold using the doctor blade method. Then a biopsy punch is used to make a circular hole on the pad to form the droplet retainer. The retainer is then attached to a glass substrate 0.5 mm thick, which is a rigid, oscillating structure. To enable different mode shapes of the substrate, the glass substrate is attached to the tip of a long polymethyl methacrylate (PMMA) cantilever beam that assumes various vibrational modes when driven at various frequencies.

The experimental setup is schematically shown in Figure 1. With the glass substrate attached at the tip, the PMMA cantilever beam is actuated by an electromagnetic shaker attached near the beam's anchor. Vertical oscillation of the substrate is measured with a Laser Doppler Vibrometer (LDV). The laser beam is focused on the upper surface of the glass substrate and the mode shape of the substrate is recorded by scanning certain areas of the substrate: the rectangles along the length of the cantilever beam, and the circles on the different droplet retainers. The retainer is placed at one of three locations on the substrate indicated in Figure 1 as near, intermediate, and far.

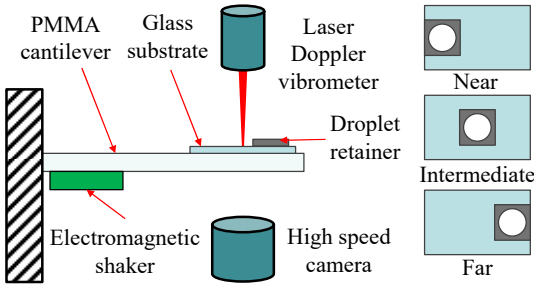

Figure 1: Schematic of the experimental setup (on the left, side view) and three different locations of the droplet retainer (on the right, tip view).

The flow patterns in a sessile droplet are characterized using the particle image velocimetry (PIV) method. The PIV test is done while operating with a 100 μL volume of deionized water containing 15 μm polystyrene (PS) particles. The solution is injected into the retainer to form a droplet and the movement of particles is captured with a high-speed camera located under the glass substrate while the cantilever beam is actuated to vibrate. The particle agglomeration test is conducted using the same PS particle solution while the cell agglomeration experiment uses human pancreatic cancer cells Panc-1 suspension in 1X Phosphate-buffered saline (PBS) pH 7.4 solution.

RESULTS AND DISCUSSION

The frequency response of the entire substrate with three retainers atop it is measured using a frequency chirp signal at frequencies from 0.15 to 2.0 kHz with a voltage of 0.1 V, as shown in Figure 2(a). The magnitude refers to the averaged peak vibrating velocity of each scan point distributed in the scan area. The peaks in frequency response curves correspond to several resonance frequencies of the cantilever beam in different orders of vibrational

978-1-940470-04-7/HH2022/$25©2022TRF
DOI 10.31438/trf.hh2022.90

mode. Note that the peak height at the intermediate retainer at 1.27 kHz is clearly lower than that at the near and far retainers. This is most likely induced by a nodal line (where the vibrating amplitude is zero along the line) crossing the intermediate retainer. This hypothesis is verified by the mode shape results, as shown in Figure 2(a) insert and Figure 2(b), which correspond to the vibrating velocity distributions across the substrate and three droplet retainer positions, respectively. The colors ranging from dark blue to dark red indicate vibrating velocities from 0 to 0.3 mm/s. This frequency, having a nodal line crossing the intermediate retainer (shown as the dark blue area in Figure 2 (b), where zero vibrating amplitude is detected), corresponds to one of the resonance peaks, which enables the substrate to have a seesaw-like rotational oscillation with the nodal line as the axis of rotation.

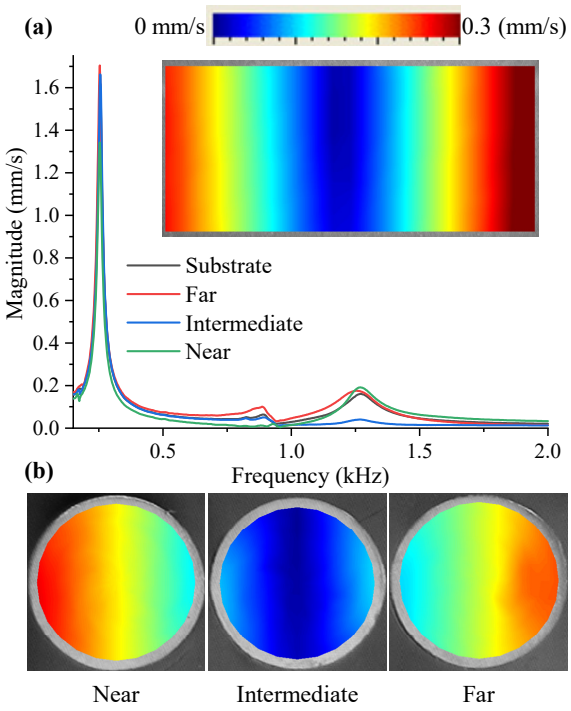

Figure 2: (a) Measured frequency response of the entire glass substrate and each droplet retainer, insert is the peak velocity distribution of the substrate. (b) mode shape of each retainer. The mode shape is obtained at 1.27 kHz.

To have a better vision of vibrating velocity changes with time, the velocity distribution along the diameter of the retainer that is aligned with the cantilever longitudinal direction is measured with the LDV and plotted in Figure 3(a), 3(c), and 3(e), corresponding to the three different droplet retainers. The curves in each plot, ranging from blue to red, indicate various times within half an oscillation cycle. For all the three positions of the retainers, the glass substrate shows an almost rigid plane oscillation in that the velocities measured along the diameter are shown as straight lines. Thus, the movement of the glass substrate is considered a rotational oscillation rather than a flexible vibration. For the far and near retainers, the bottom substrate shows an oblique oscillation where the two ends have different amplitudes. For the intermediate retainer, the substrate shows a rotational oscillation, like a seesaw. Trajectories representing flow directions of the PS particles are calculated with the standard deviation of frames captured by the high-speed camera taken over 0.1 s using ImageJ software. They are shown in Figure 3(b), 3(d), and 3(f), for the three different retainers. Flow directions are distinguished using the original video and are labeled with red arrows. For droplets in the near (Figure 3(b)) and far (Figure 3(d)) retainers, there are two symmetrical vortices, and the flow direction in the center is aligned with the vertical vibrating velocity gradient of the substrate oscillation, from higher to lower velocities. For the intermediate retainer (Figure 3(f)), there is a nodal line where the vibrating velocity is zero and the number of vortices becomes four. Similarly, the flows on the left and right sides aim toward the nodal line and then go along with the line, after gathering in the center.

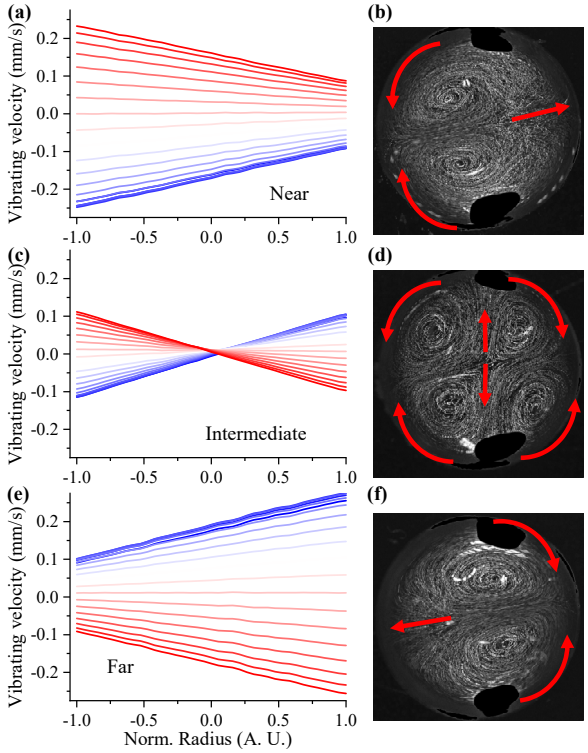

Figure 3: (a), (c), and (e) are measured vibrating velocity distributions along the diameter of the droplet retainer within a half period vibrating at 1.27 kHz. (b), (d), and (f) are flow patterns at different retainers obtained using the same driving frequency. The red arrows indicate the flow direction obtained from the video.

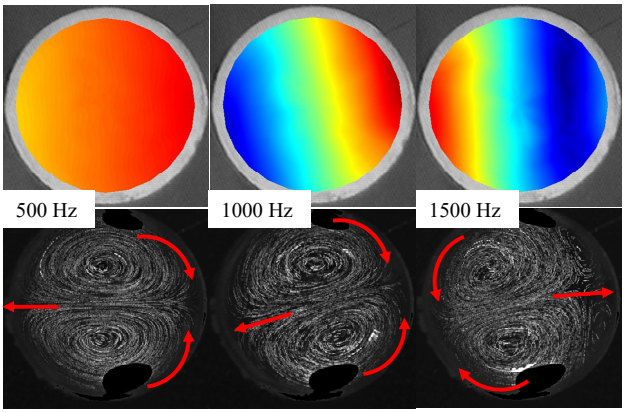

Figure 4: Measured peak velocity distributions of the intermediate droplet retainer (on the top) and flow patterns at different driving frequencies (in the bottom). The red arrows indicate flow direction.

The results in Figure 3 indicate that the internal flow is generated in the sessile droplet once the substrate is actuated into a seesaw-like rotational oscillation. The flow direction will follow the vertical vibrating velocity gradient of the substrate, from higher velocity areas to lower ones. To assess the generality of this phenomenon, the correlations of vertical vibrating velocity gradients with flow patterns are further experimentally described under different driving frequencies using the intermediate droplet retainer, as shown in Figure 4. Regardless of driving frequency, the particle flow direction within the droplet is always in the same direction as that of the vertical vibrational velocity gradient of the oscillating substrate surface. Thereby, this substrate rotational oscillation strategy can provide highly controllable internal flow patterns in a sessile droplet that can potentially be used in various microfluidic applications.

Next, the internal flow in the sessile droplet is utilized for particle and cell agglomeration. A 100 μL deionized water droplet containing 15 μm PS particles is injected into the near, intermediate, and far droplet retainers, successively, and allowed to stand still for 60 s to let gravity drive the particles approaching the bottom. Then the substrate is actuated into rotational oscillation at a driving frequency of 1.27 kHz with a driving voltage of 0.3 V. Meanwhile, the trajectories of PS particles are captured with the high-speed camera located under the substrate. The results are shown in Figure 5, where the three columns correspond to the different retainers. Before oscillation is applied, the particles are uniformly distributed on the bottom of the glass substrate. After the substrate oscillates for 60 s, the particles have accumulated into several regions: for the near and far retainers, the particles are concentrated at two points, as indicated with red circles. These two points are the centers of the two vortices observed in the flow pattern shown in Figure 3(b) and 3(f). For the intermediate retainer, since there exist four vortices (Figure 3(d)), the particle agglomerated pattern shows four gathering points. The particle movement trajectory within 60 s is plotted by calculating the standard deviation of the entire agglomeration process, as shown in the bottom row of Figure 5. It is very clear that PS particles are driven to accumulate in specific locations. By using different flow patterns controlled by substrate rotational oscillation, particles in a sessile droplet can form controlled agglomeration patterns with different numbers of gathering regions.

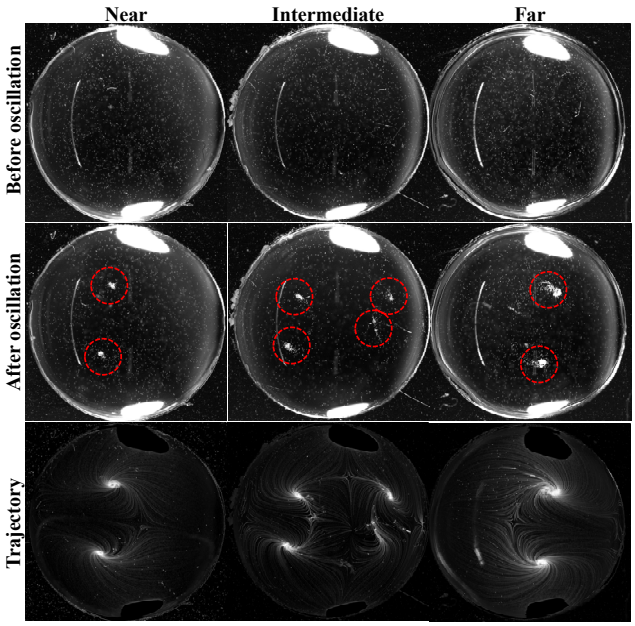

Figure 5: Particle agglomeration results (before and after agglomeration in the first and second row) and moving trajectories (third row) at three different droplet retainers using a driving frequency of 1.27 kHz.

Further, particle agglomeration of different substrate oscillation intensities was recorded. In this case, the substrate was actuated into 1.27 kHz oscillation using different driving voltages, and the far droplet retainer was used. The results are demonstrated

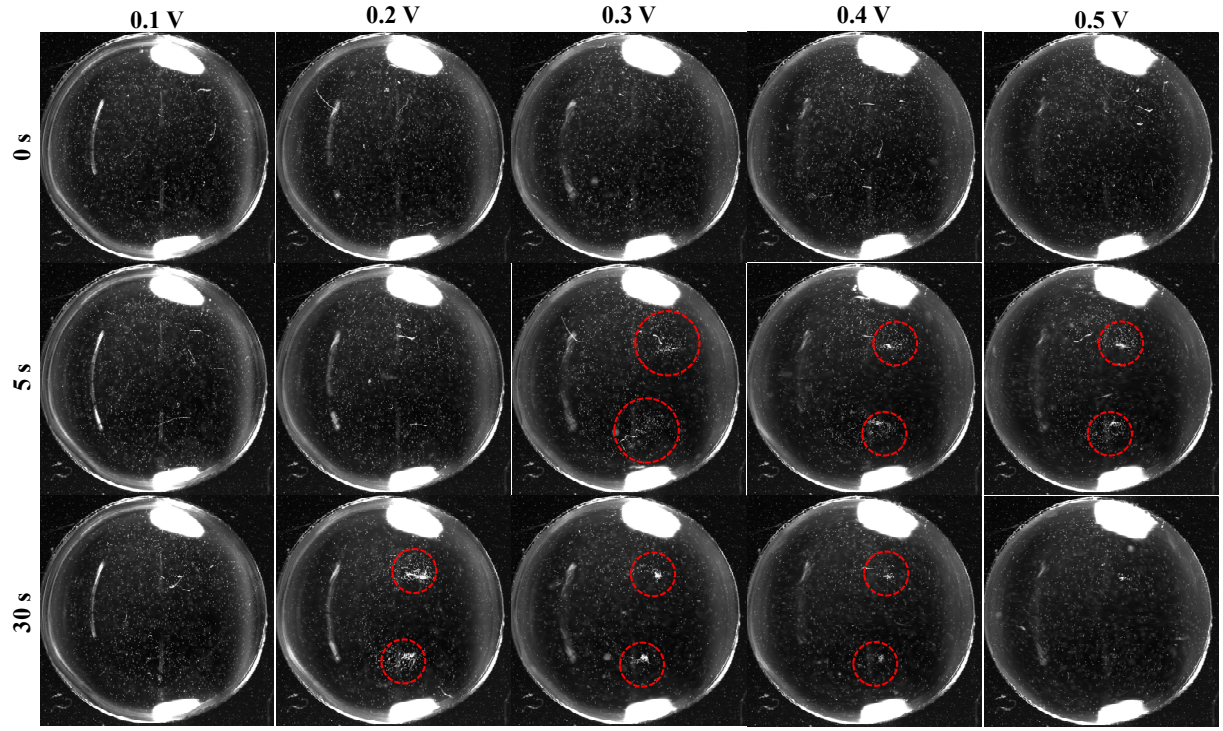

Figure 6: Particle agglomeration results at the far retainer under different driving voltages at a driving frequency of 1.27 kHz.

in Figure 6 in which the five columns correspond to five different driving levels, while the three rows represent various times during substrate oscillation. As the driving voltage increases from 0.1 to 0.5 V, it is observed that the 15 μm PS particles cannot be agglomerated when a low oscillation intensity is used (0.1 V). The distribution of particles is almost unchanged in this driving voltage. Increasing the driving input triggers the particle agglomeration (0.2 V) and the particle accumulation speed and efficiency are enhanced at a higher input level (0.3 V). However, further increasing oscillation intensity (0.4 V) applies an even faster particle gathering speed but induces a smaller number of accumulated particles. This is due to the strong internal flows that tend to redisperse the particles back into the solution. The redispersion becomes obvious when a huge driving voltage (0.5 V) is used. The agglomerated particle can exist for a few seconds and is then quickly redispersed to the solution in this case. The red circles in Figure 6 indicate accumulated particles. The internal flows can not only accumulate particles in sessile droplets but can also break the agglomerated patterns.

Finally, cell agglomeration capability is evaluated using human pancreatic cancer cells (Panc-1 suspension in 1X PBS solution) in the far droplet retainer. The driving frequency and amplitude are 1.27 kHz and 0.3 V, respectively. Optical images of cell suspension at different times are shown in Figure 7. Different from the results in the PS particle agglomeration experiment, the Panc-1 cells turn to form a single line at the location where the two vortices converge (labeled with a red oval). This is most likely to be induced by the size of the cells. Since the cell suspension contains a large number of aggregates that consist of several attached cells, their overall sizes are much larger than that of the 15 μm PS particles. Due to the difference in drag force attributed to the difference in size, the agglomeration pattern of the Panc-1 cell shows different results.

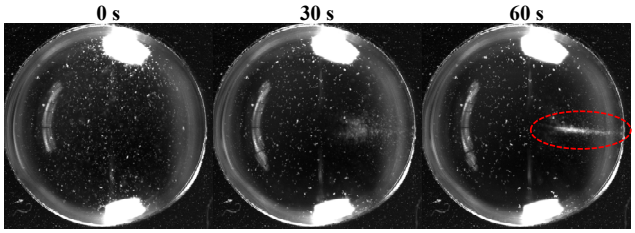

Figure 7: Panc-1 cell agglomeration results at the far droplet retainer with a driving frequency of 1.27 kHz.

CONCLUSION

This paper presents a simple and low-cost strategy to produce and control internal flows in a sessile droplet. This strategy is achieved by actuating a rigid substrate into a rotational oscillation on which a sessile droplet is located. Oscillation with certain vertical vibrating velocity distributions establishes circulation patterns in the sessile droplets. Particle image velocimetry results indicate that the oscillation-induced internal flows form different numbers of symmetrical vortices. Flow patterns are determined by the mode shape of substrate oscillation. The flow direction is the same as the vertical vibrating velocity gradient of the substrate surface. Observations from particle and cell movement also demonstrate that the oscillation-induced internal flows can be employed for particle or cell agglomeration. By adjusting the pattern and intensity of the internal flows, particles can accumulate in different areas and can even be redispersed back to the bulk of the droplet.

ACKNOWLEDGEMENTS

Portions of this work were conducted in the Minnesota Nano Center, which is supported by the National Science Foundation through the National Nano Coordinated Infrastructure Network (NNCI) under Award Number ECCS-2025124. Funding for this project was partially provided by the Minnesota Environment and Natural Resources Trust Fund as recommended by the Legislative-Citizen Commission on Minnesota Resources (LCCMR).

REFERENCES

[1] Garcia-Cordero, Jose L., and Z. Hugh Fan. "Sessile droplets for chemical and biological assays." *Lab on a Chip* 17, no. 13 (2017): 2150-2166.

[2] Frey, Lasse Jannis, David Vorländer, Detlev Rasch, Sven Meinen, Bernhard Müller, Torsten Mayr, Andreas Dietzel, Jan-Hendrik Grosch, and Rainer Krull. "Defining mass transfer in a capillary wave micro-bioreactor for dose-response and other cell-based assays." *Biochemical Engineering Journal* 161 (2020): 107667.

[3] Nam, Hyeono, Hyung Jin Sung, Jinsoo Park, and Jessie S. Jeon. "Manipulation of cancer cells in a sessile droplet via travelling surface acoustic waves." *Lab on a Chip* 22, no. 1 (2022): 47-56.

[4] Wu, Mengxi, Adem Ozcelik, Joseph Rufo, Zeyu Wang, Rui Fang, and Tony Jun Huang. "Acoustofluidic separation of cells and particles." *Microsystems & nanoengineering* 5, no. 1 (2019): 1-18.

[5] Seksinsky, Drue, and Jeffrey S. Marshall. "Droplet Impingement on a Surface at Low Reynolds Numbers." *Journal of Fluids Engineering* 143, no. 2 (2021).

[6] Bansal, Shubhi, and Prosenjit Sen. "Mixing enhancement by degenerate modes in electrically actuated sessile droplets." *Sensors and Actuators B: Chemical* 232 (2016): 318-326.

[7] Shilton, Richie J., Marco Travagliati, Fabio Beltram, and Marco Cecchini. "Nanoliter-droplet acoustic streaming via ultra high frequency surface acoustic waves." *Advanced Materials* 26, no. 29 (2014): 4941-4946.

[8] Chen, Ge, Bing Ji, Yibo Gao, Cong Wang, Jinbo Wu, Bingpu Zhou, and Weijia Wen. "Towards the rapid and efficient mixing on'open-surface'droplet-based microfluidics via magnetic actuation." *Sensors and Actuators B: Chemical* 286 (2019): 181-190.

[9] Frey, Lasse Jannis, David Vorländer, Detlev Rasch, Sven Meinen, Bernhard Müller, Torsten Mayr, Andreas Dietzel, Jan-Hendrik Grosch, and Rainer Krull. "Defining mass transfer in a capillary wave micro-bioreactor for dose-response and other cell-based assays." *Biochemical Engineering Journal* 161 (2020): 107667.

CONTACT

*Tianhong Cui, tel: +1-612-626-1636; cuixx006@umn.edu

IN-SITU ULTRASONIC IMAGING OF PRINTED ELECTRONICS INK DEPOSITION AND CURING

Anuj Baskota[1], Landon Ivy[2], Carlos Ospina[3], Justin Kuo[1], Juneho Hwang[2], Ved Gund[2], Benyamin Davaji[2,4], Peter Doerschuk[2,5], and Amit Lal[1,2]

[1]Geegah Inc., Ithaca, USA. [2]School of Electrical and Computer Engineering, Cornell University, Ithaca, USA. [3]BotFactory Inc, USA. [4]Department of Electrical and Computer Engineering, Northeastern University, Boston, USA. and [5]Meinig School of Biomedical Engineering, Cornell University, Ithaca, USA.

ABSTRACT

We report the first-ever in-situ imaging of 3D-Printed Electronics (PE) ink delivery and drying during the printing using GHz ultrasonic imager. The CMOS integrated GHz ultrasonic technology consists of a 128 x 128-pixel array of Aluminum Nitride transducers that image the surface of the silicon chip with transmit/receive of short ultrasonic pulses. The reflected US pulses measure crucial ink parameters such as ink's acoustic impedance and temperature at a sampling rate of up to 30 frames per second. We demonstrate the observation of ink droplets delivered to a surface, the creation of secondary droplets on the surface, and the time history of the ink curing process. The data at single pixel and images over a collection of images indicates that the GHz imager can be used to provide real-time quantitative feedback on the printing process, thus providing uniform and higher yield PE devices.

KEYWORDS

GHz, ultrasonic imaging, quality control, printed electronics, 3D printing, conductive ink, insulating ink

INTRODUCTION

Printed Electronics (PE) hardware has enabled the rapid development of passive/active circuit components, flexible wearables, diodes, and smart systems with a variety of sensing applications [1]. Over the traditional photolithography fabrication process, PE holds significant advantages in production speed, cost, material usage, flexibility in the substrate choice, and carbon footprint [2]. Although there is a remarkable research and development progress of PE devices, there are still several challenges that have limited its mass manufacturing potential. While printing resolution, uniformity of printed layers, and process stability are a few limitations for PE, one of the major drawbacks is the lack of optimum quality control during the printing process [3].

There are several factors such as ink quality (density, viscosity) and temperature (ink, substrate, and surrounding air) that must be appropriately decided to achieve proper ink adhesion, spread, and drying on the substrate surface [4]. Optical imaging using microscopes has been used for determining film delivery accuracy. Optical imaging generally requires a larger footprint requiring a light source and lensing. Further, optical imaging is only applicable to reflective surfaces, which is difficult for transparent inks. Furthermore, optical imaging also does not allow the imaging of mechanical and thermal properties of the ink. Monitoring the morphology as well as several material properties of ink film deposited on the substrate is necessary to understand the quality of the print. Some imaging modalities such as X-ray and atomic force microscopy have been used to study the printed film morphology and material properties [5,6]. Due to their bulky nature, these techniques are expensive, slow, and almost impossible to carry out real-time in-situ measurements during the print process [7]. Similarly, infrared imaging and thermocouple have been used to measure the real-time temperature of the printing process in additive manufacturing [8]. These techniques have been quite successful for temperature measurement. However, they require complex setup and integration with the printing system. An ideal quality control system for PE should be compact, cheap, and operatable real-time with multi-sensing abilities. This would enable real-time feedback to the users allowing them to be aware of any potential print defects before print completion saving resources and time. This paper demonstrates a unique approach to monitoring the PE process using an ultrasonic imager.

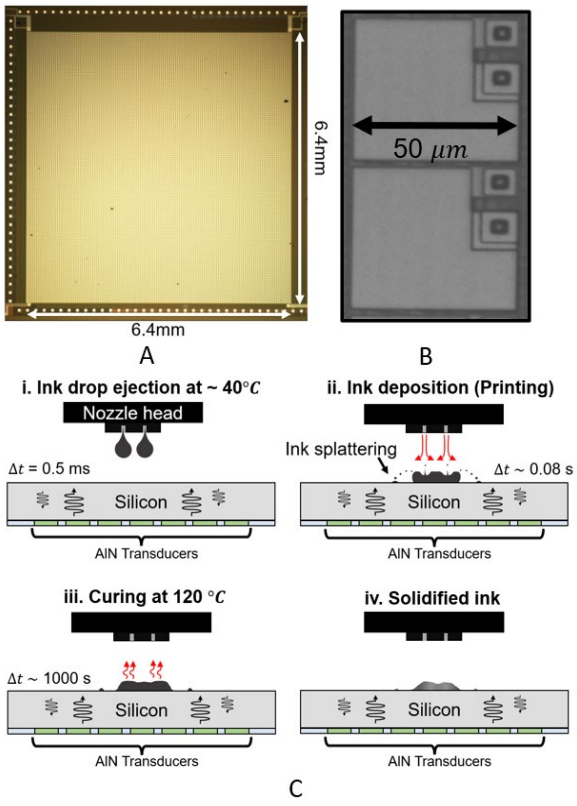

Figure 1. A) Optical image of the 128x128 AlN transducer pixels. B) Micrograph of 2 array pixels (50μm pitch) with integrated T/R circuits. C) Schematic showing ultrasonic imaging of ink printing process i) Ink drop ejection at warm ink temperature (~ 40°C). ii) Ink spreading on the surface causing few micro-drops to splatter. iii) Curing the deposited ink at 120 °C that evaporates the solvent. iv) Solidified ink on the imager surface.

The Geegah imager consists of 128 x 128 transmit/receive pixels with each pixel's pitch being 50 μm (Fig 1A). Each pixel has a 2 μm thick aluminum nitride (AlN) transducer, and most of the necessary circuitry is integrated within using a 130 nm CMOS process (Fig 1B), resulting in a compact, low-cost, low-power chip. The sensing region is the backside of the double-side-polished CMOS substrate with 6.4 x 6.4 mm^2. This optically flat, unobstructed surface without any wirebonds provides a rugged

surface that can be used for printing directly on it. The surface can be cleaned easily using solvent-soaked wipes multiple times without damaging the sensitive CMOS transistors or causing wear on encapsulation around wirebonds. During the ink printing process, high-frequency ultrasonic pulses are launched from these pixels, which then travel through the silicon substrate and are received back by the identical transducers (Fig 1C). The amplitude of these ultrasonic echoes is then used to form an image via the on-chip readout and signal processing circuitry [9]. At GHz frequency, the time taken for a pulse to be transmitted and received by a pixel is approximately 150 ns which enables capturing ink deposition at a very high scanning rate of 10-30 fps for the full 128x128 pixel array.

This ultrasonic (US) GHz imager has few key features that make it a suitable tool for PE quality control. Firstly, the high frequency in the GHz range allows for acquiring high-resolution images as frequency is inversely proportional to the wavelength. When operated at 1.85 GHz, the wavelength is around 4.5 μm in silicon. Secondly, the reflected ultrasonic signal magnitude and phase are used to simultaneously estimate the material's acoustic impedance and temperature data. This integration of multiple sensing modes on the same chip reduces the whole imaging system's power, size, space, and cost. Thirdly, the CMOS-MEMS integration enables additional GPS and RF communication features. This facilitates the users to monitor the print and receive data remotely. Fourthly, ultrasonic waves instead of light allow imaging transparent ink and features that remain hidden/covered during the print, and hence can't be sufficiently detected by optical approaches. Several print defects such as air bubbles and cracks between the substrate (imager surface) and the ink layer is clearly visible using the ultrasonic imager but not necessarily in optical images.

In previous work, we have demonstrated the use of the GHz ultrasonic imager array to sense nematodes [10], and soil parameters[11], based on CMOS integration of piezoelectric AlN transducers. Here, we show the potential of this technology for monitoring and optimization of ink-printing process parameters such as the density, temperature, and distance between the nozzle and the substrate.

METHODS AND EXPERIMENTS

The demonstration of real-time ultrasonic imaging of ink is done using the BotFactory SV2 inkjet printer. This printer utilizes a HP45 cartridge consisting of 300 thermal inkjet nozzles with a firing rate of approximately 2 kHz. A plate inside the nozzle chamber rapidly heats up, boiling the ink causing vapor formation and pressure that pushes the ink towards the extruder. The vapor bubble grows and ruptures that pinches off ink droplet out of the extruder. Due to the surface tension, the excess ink contracts and flows back into the chamber waiting for the next ejection cycle. Conductive ink was used for all the printing experiments in this paper, although results on non-conductive and resistive inks are also possible. This conductive ink consists of a matrix of silver nanoparticles suspended in a solvent. For complete adhesion of the ink on a substrate, thermal curing at a temperature of 120-150 °C is required. This heating causes the solvent to evaporate, leaving behind the silver particles attached to the substrate. The printer has a XYZ step resolution of 10 microns and minimum trace width of 200 µm. The operating temperature of the bed, on which the imager is mounted on, ranges from 25 – 150 °C. Therefore, it is important that the imager can operate at high temperatures.

The GHz imager chip was placed parallel to the printer bed, and Kapton tape was used to secure the PCB with the imager chip in the fixed location to prevent any movements during the printing process (Fig. 2A). A pattern of varying line widths was directly printed on the imager's surface (Fig. 2B). For all experiments, pulse

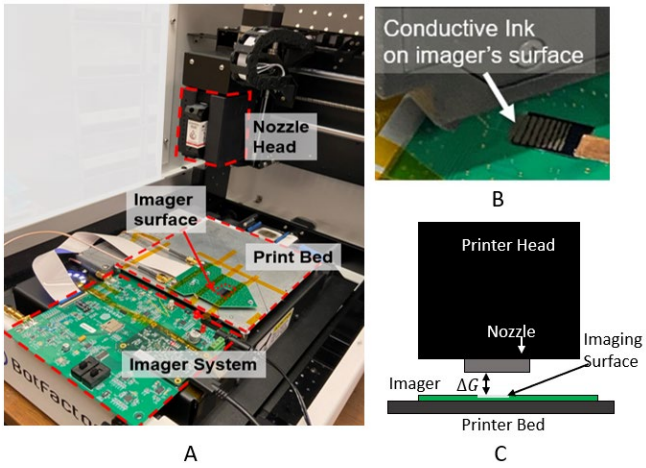

Figure 2.A) Experimental setup of imager chip attached parallel to the SV2 printer's bed. B) Conductive ink deposited on the imager's surface during the print. C) Schematic showing experiment varying gap between nozzle and the imager surface.

frequency used to image the ink was 1.853 GHz, and the sampling rate for the experiments was approximately 5.8 frame per second (fps). The 3D printer's bed temperature was set to 50 °C, whereas the curing was performed at 120 °C. The imager was initially calibrated to measure temperature change of the pixels. This was done by placing the chip inside an environment chamber (Tenny Environmental TJR) and imaging air with 1.853 GHz ultrasound for varying temperatures(-10 to 120 °C). The calibration curve obtained was used to measure the ink printing and curing temperature.

A series of experiments were performed to optimize the distance between the nozzle and substrate. The same line pattern was directly printed on the surface in multiple experiments where only the gap between the imager's surface and the nozzle (**Δ**G) was varied from 4.5 mm to 7.0 mm (Fig 2C). The obtained ultrasonic images were analyzed to quantify the ink splattering and print precision.

RESULTS AND DISCUSSION

The reflected echo from each pixel is received in two modes – in phase (I) and out-of-phase (Q). When imaging with all the pixels, two 128 x 128, 12-bit matrices for I and Q data are generated. These matrices ($\boldsymbol{I_M}$ and $\boldsymbol{Q_M}$) contain the first acoustic echo signal reflected from the backside of the silicon. The background noise is removed from the images by subtracting the measured echo matrices with the air-backed echo ($\boldsymbol{I_B}$ and $\boldsymbol{Q_B}$) thus obtaining the following matrices:

$$\boldsymbol{I_{Image}} = \boldsymbol{I_M} - \boldsymbol{I_B} \quad (1)$$

$$\boldsymbol{Q_{Image}} = \boldsymbol{Q_M} - \boldsymbol{Q_B} \quad (2)$$

The no-echo signal is also sampled after the first echo dies off and before the second echo. The obtained data ($\boldsymbol{I_N}$ and $\boldsymbol{Q_N}$) are used to remove any DC offsets from the images. The two important components of reflected echo are the magnitude and phase. The magnitude represents the intensity of the wave, whereas the phase measures any doppler shift of frequency. Using the I and Q echo/no-echo measurements, magnitude and phase can be calculated as follows:

$$\text{Magnitude} = \sqrt{(\boldsymbol{I_M} - \boldsymbol{I_N})^2 + (\boldsymbol{Q_M} - \boldsymbol{Q_N})^2} \quad (3)$$

$$\text{Phase} = \boldsymbol{\tan^{-1}}\left(\frac{\boldsymbol{I_M} - \boldsymbol{I_N}}{\boldsymbol{Q_M} - \boldsymbol{Q_N}}\right) \quad (4)$$

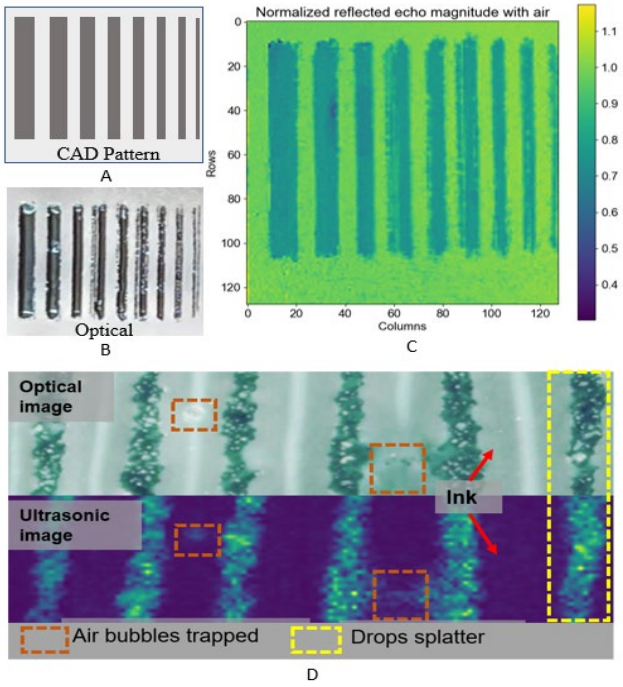

Figure 3.A) CAD pattern (grey area shows ink) for printed conductive ink lines. B) Optical image of the printed conductive ink on the imager surface. C) Ultrasonic image of the same ink patterns. D) Optical and ultrasonic images showing defects in the ink print pattern: air bubbles trapped within ink and tiny drops splattering between the ink lines.

For consistent comparison of the calculated magnitude among different experiments, the magnitude of the measured signal is normalized with the magnitude of baseline using the following relationship:

$$\text{Normalized magnitude} = \frac{\boldsymbol{Magnitude_Measured}}{\boldsymbol{Magnitude_Baseline}} \quad 5)$$

Ultrasonic images of ink printing and curing

The CAD implemented design, optical image, and the magnitude echo of the reflected signal (Fig 3 A,B,C respectively) shows the line patterns deposited on the imager chip. The ultrasonic and optical images (Figure 3 D) reveal print defects such as cracks, trapped air bubbles, and ink splattering on the imager surface. As only a single layer of ink was deposited, the flaws are visible on both imaging modalities. However, ultrasonic imaging would have a significant advantage, especially with transparent ink that is hard to image optically and multi-layered prints where the bottom layer remains hidden due to the top layers.

Temperature Sensing and ink curing

The silicon substrate of the GHz imager makes temperature sensing possible as the change in the speed-of-sound in silicon with temperature manifests as a phase shift in the ultrasonic signal received by the imager pixel transducers [12]. The relationship between the unwrapped phase measured for varying air temperature (-10 to 120 °C) is linear (Fig 4A). Using this calibration curve, the temperature for ink drop deposition was interpolated from 18 pixels (Fig 4B). Here, the temperature can be seen dropping after the liquid delivery as locally heat is removed from the silicon to heat the droplet. The ink can be also seen to spread enabling measurement of spreading in real time. Eventually, the ultrasonically measured temperature slowly returns to the ambient temperature as the ink reaches thermal equilibrium with the substrate. Similarly, the temperature change was recorded from 8 pixels exposed to ink during the curing process (Fig 4C). Although the print bed is measured to be approximately 120° C, the pixel temperature is lower ~ 110 °C due to the rapid heat transfer to the surrounding air and the placement of the imager onto the print surface.

Varying the height between the nozzle and substrate

The distance between the nozzle and substrate affects ink drop breakage properties such as breaking time and rate during ejection, resulting in ink splattering [13]. The reflected echo magnitude

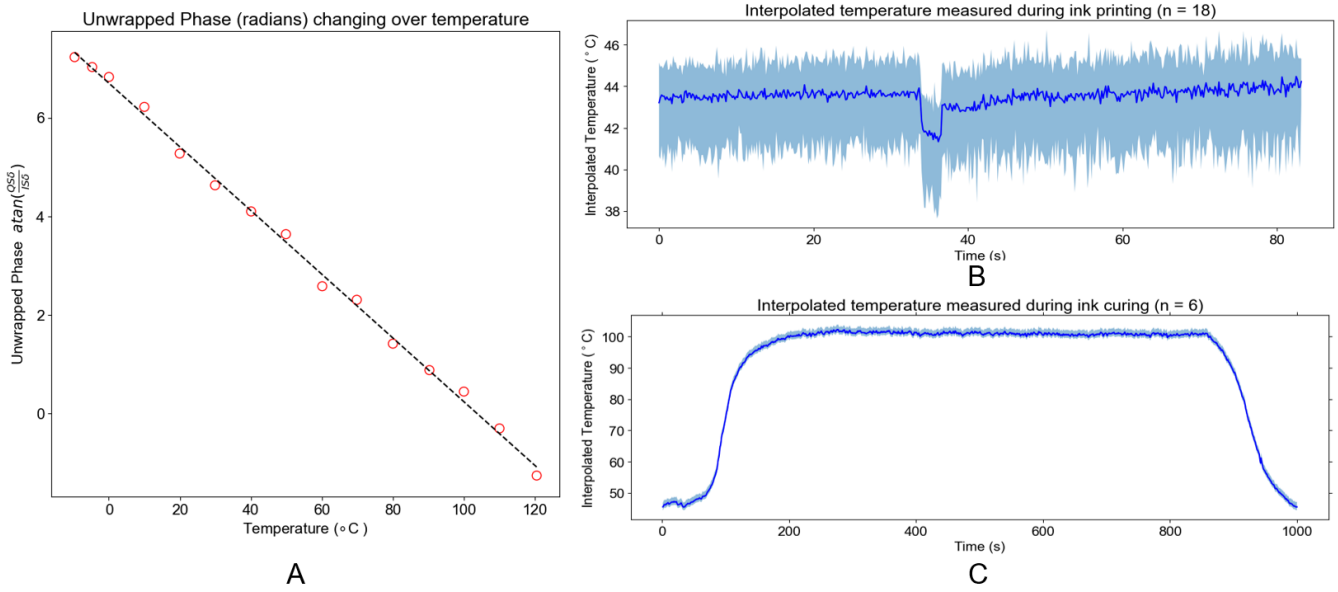

Figure 4. A) Calibration curve showing linear relationship between the calculated unwrapped phase and temperature. B) Interpolated temperature measurement of ink printing. Ink temperature is cooler than the imager surface causes the temperature to drop briefly. C) Interpolated temperature for ink curing. The shadow represents the maximum and minimum values among the measured data.

images (Fig 5A) reveal increasing ink splattering around the printed lines as the gap increases. The splattering was further quantified by plotting the distribution of the signal from all the pixels (Fig 5B). The lower splattering of micro-sized drops results in clear-distinct peaks of signals reflected from air and ink pixels. In contrast, high splattering causes the air gaps to be filled with tiny drops of ink, resulting in broader distribution. This quantification of the ink splattering can optimize the proper height between the nozzle and the substrate to have the least ink splattering.

CONCLUSION

This work demonstrates the GHz ultrasonic imager as a potential tool for quality control in PE manufacturing. Ultrasonically imaging the ink deposition and curing yields crucial data on ink's acoustic impedance and temperature that can be used to predict any anomalies or faults in the prints. In future experiments, the images obtained from the US imager can be correlated with optical images and functional data obtained on FR4/Kapton/Polyimide substrates, using AI/ML approaches to have an automated feedback PE manufacturing process. In addition, different ink types such as resistive and insulating ink will also be imaged to characterize their acoustic properties. This model may help predict ink aging or substrate properties that can be used to provide a sub-optimal print. This capability will specially be useful for printed electronics in adverse environments such as on mobile platforms experiencing temperature, humidity, and vibration variations during the print. The models correlating ultrasonic images to the actual prints may also determine optimum inkjet operating parameters such as distance from the substrate, firing rates of each nozzle, and misfiring nozzles that should not be used in a print. This level of feedback control will enable high yields and greater ink use efficiency, reducing the cost of printed electronics devices. In the future, the imager can be directly integrated with the PE printer for automatic sampling and process optimization of the printing and curing processes.

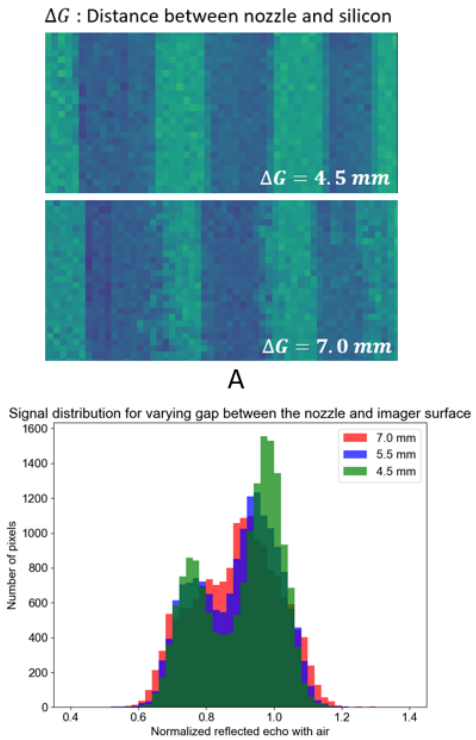

Figure 5. A) Ultrasonic images reveal precise and distorted lines printed for smaller (4.5 mm) and larger gaps (7.0 mm), respectively. B) Distribution of ultrasonic echo amplitude divided into two peaks for varying gap between nozzle and imager surface. A smaller gap causes less splattering, which leads to more distinct peaks.

ACKNOWLEDGEMENTS

This work was performed in part at the Cornell NanoScale Facility, an NNCI member supported by NSF Grant NNCI-2025233. This material is based on research sponsored by Army Research Laboratory under agreement number W911NF-19-2-0345. The U.S. Government is authorized to reproduce and distribute reprints for Government purposes notwithstanding any copyright notation thereon. The views and conclusions contained herein are those of the authors and should not be interpreted as necessarily representing the official policies or endorsements, either expressed or implied, of Army Research Laboratory (ARL) or the U.S. Government.

REFERENCES

[1] S. K. Garlapati et al., "Printed Electronics Based on Inorganic Semiconductors: From Processes and Materials to Devices," Advanced Materials, vol.30, no. 40, p.1707600, Jun. 2018

[2] J. Chang et al., "Challenges of printed electronics on flexible substrates," 2012 IEEE MWSCAS Aug. 2012

[3] M. Mantysalo et al., "Capability of inkjet technology in electronics manufacturing," 2009 59th Electronic Components and Technology Conference, May 2009

[4] Beedasy, V., & Smith, P. J. (2020). Printed Electronics as Prepared by Inkjet Printing. Materials, 13(3), 704

[5]J. Rivnay et al., "Large modulation of carrier transport by grain-boundary molecular packing and microstructure in organic thin films," Nature Materials, vol. 8, no. 12, pp. 952–958, Nov. 2009

[6] R. J. Kline, M. D. McGehee, E. N. Kadnikova, J. Liu, J. M. J. Fréchet, and M. F. Toney, "Dependence of Regioregular Poly(3-hexylthiophene) Film Morphology and Field-Effect Mobility on Molecular Weight," Macromolecules, vol. 38, no. 8, pp. 3312–3319, Apr. 2005

[7] F. Pastorelli, N. Accanto, M. Jørgensen, N. F. van Hulst, and F. C. Krebs, "In situ electrical and thermal monitoring of printed electronics by two-photon mapping," Scientific Reports, vol. 7, no. 1, Jun. 2017

[8] P. K. Rao, J. (Peter) Liu, D. Roberson, Z. (James) Kong, and C. Williams, "Online Real-Time Quality Monitoring in Additive Manufacturing Processes Using Heterogeneous Sensors," Journal of Manufacturing Science and Engineering, vol. 137, no. 6, Sep. 2015

[9] M. Abdelmejeed et al., "Monolithic 180nm CMOS Controlled GHz Ultrasonic Impedance Sensing and Imaging," 2019 IEEE IEDM, Dec. 2019,

[10] J. Kuo et al., "Gigahertz Ultrasonic Imaging of Nematodes in Liquids, Soil, and Air," 2021 IEEE IUS, Sep. 2021

[11] A. Baskota et al., "Gigahertz Ultrasonic Multi-Imaging of Soil Temperature, Morphology, Moisture, and Nematodes," 2022 IEEE MEMS, Jan. 2022

[12] M. Abdelmejeed et al., "A CMOS compatible GHz ultrasonic pulse phase shift-based temperature sensor," 2018 IEEE MEMS, Jan. 2018

[13] J. Park, et al., "Methodology to set up nozzle-to-substrate gap for high resolution electrohydrodynamic jet printing," Applied Physical Letters, vol. 109, no. 13, p. 134104

CONTACT

Anuj Baskota, *anuj@geegah.com

LITHIUM NIOBATE ON SILICON LAMB MODE ACOUSTOELECTRIC WAVEGUIDE WITH 5.5 DB SUSTAINED TERMINAL GAIN

Hakhamanesh Mansoorzare and Reza Abdolvand
University of Central Florida, Orlando, Florida, USA

ABSTRACT

In this work, sustained terminal gain is reported for the first time in micromachined lithium niobate (LN) on silicon (Si) Lamb mode waveguides through acoustoelectric amplification. In such acoustically thin waveguides, the large coupling between the Lamb waves and the drifting electrons in Si gives rise to a very efficient transfer of momentum from electrons to elastic phonons, rendering the waveguide a traveling wave amplifier. In a geometrically optimized waveguide, up to 5.5 dB terminal gain is achieved by dissipating less than 6.5 milliwatts of DC bias power. This is measured for input RF signals up to -20 dBm and gain compression is observed for larger inputs with its characteristic impacted by the DC bias level and the device geometry. Further design improvements are expected to increase the terminal gain, hence, justifying the implementation of micro-acoustic RF amplifiers.

KEYWORDS

Acoustoelectric effect; heterostructure; Lamb wave; lithium niobate; piezoelectric; terminal gain; traveling wave amplifier.

INTRODUCTION

It has been known for decades that transistor-less signal amplification within the acoustic domain can be realized through the acoustoelectric (AE) effect [1]. Once charge carriers at the vicinity of piezoelectrically transduced acoustic waves move faster than the acoustic waves, they could transfer their momentum and amplify the acoustic waves. This phenomenon could be considered an acoustic equivalent to electromagnetic (EM) traveling wave tube amplifiers (TWTA). In a TWTA, a beam of drifting electrons amplifies a slow RF signal that is guided in its proximity within a helix wire or EM resonant cavity [2]. Similarly, in a piezoelectric semiconductor or layered piezoelectric/semiconductor system, drifting electrons could amplify an RF signal that is piezoelectrically transduced into a traveling wave, once they start leading such wave. While originally demonstrated in piezoelectric semiconductors, the acoustic wave amplification required prohibitively large voltages because of the low charge carrier mobility in such materials. Adopting a separate piezoelectric/semiconductor structure allowed for independent optimization of the piezoelectric and semiconductor properties, thus, improving device performance. To efficiently couple the semiconductor with the acoustic waves, surface acoustic waves (SAW) were utilized; for the first time, SAW was excited using a patterned electrode structure that conforms to the SAW wavelength. This led to numerous demonstrations of SAW AE devices comprising piezoelectric substrates and a thin layer of semiconductor that is either deposited or bonded on top of it or held at an infinitesimally small distance from its surface. The former approach allows for a stronger coupling between the charge carriers in semiconductor and SAW, since the evanescent electric field of SAW is confined in the semiconductor rather than being in the air gap. Additionally, the direct film deposition or bonding makes fabrication less complex since the need for nanometer-scale spacers is avoided. However, the deposited or bonded film must be extremely thin for minimizing the mechanical perturbation of SAW. Even with the deposition and bonding processes that are available today, attaining a high carrier mobility in an ultra-thin film remains challenging. Furthermore, the operation frequency of SAW is practically up to ~3 GHz, before surface losses and small features in lithography become limiting. Owing to the recent progress in thin-film deposition and bonding, as well as high piezoelectric couplings provided by lithium niobate (LN), significant improvements in performance of SAW AE devices have been reported [3, 4, 5]. Suspended thin-film LN can support Lamb waves with higher phase velocities compared to SAW, therefore, allowing for higher frequency operation [6]. More importantly, thanks to the large electromechanical coupling of some of these modes and low energy leakage in the suspended structure, this platform has offered superior performance in terms of bandwidth and loss [7]. Therefore, thin-film piezoelectric-on-semiconductor platform has been investigated for realizing AE devices that could enable higher frequency, wider bandwidth, and lower loss compared to traditional SAW counterparts [8, 9, 10]. In this regard, LN on silicon (Si) platform has shown promising performance by leveraging the high coupling of fundamental symmetric (S0) mode; this includes non-reciprocal transmission with more than 30 dB contrast [11] and with more than 33% 6-dB fractional bandwidth [12]. In this work, we aim to explore the potential of this platform in ultimately functioning as a transistor-less amplifier. Through optimization of the device geometry, we present for the first time, up to 5.5 dB sustained terminal gain with no pulsed-operation requirement. This is realized by consuming only a few milliwatts of DC power pumped into the Si layer and for up to -20 dBm continuous wave 613 MHz signal.

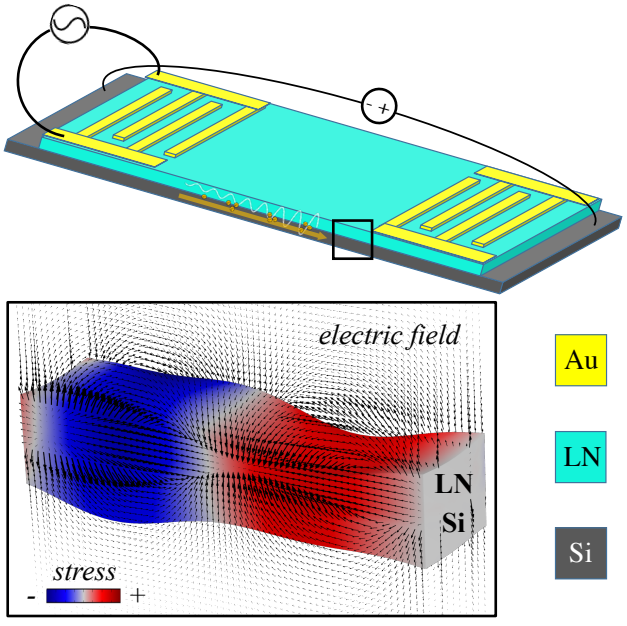

Figure 1: Schematic of suspended LN-on-Si waveguide for AE amplification; the RF signal is amplified by the DC voltage applied to Si. The S0 mode stress and electric field within a wavelength is shown in the inset.

978-1-940470-04-7/HH2022/$25©2022TRF
DOI 10.31438/trf.hh2022.92

METHODS

The fundamental parameter which determines the AE intensity is the coupling between the acoustic waves, S0 mode herein, and the electrons. This is a function of the piezoelectric coupling and the spatial arrangement of the acoustic waves and electrons. Therefore, to attain sufficient signal amplification that not only compensates the losses in the passive LN-on-Si waveguide, but also yields a terminal gain with low DC power budget, the AE coupling must be maximized. This translates into choosing a LN cut/orientation that supports the S0 mode with highest electromechanical coupling and a Si thickness that on one hand does not significantly reduce the electromechanical coupling of the heterostructure and on the other hand provides a sufficient spatial overlap between the drifting electrons and evanescent electric field. Since such evanescent field effectively extends by $1/k_0$ (with k_0 being the acoustic wavenumber), its penetration in Si would be smaller than ~1.6 µm at the acoustic wavelength of this study which is 10 µm. Additionally, to effectively excite the S0 mode, the heterostructure must be acoustically thin. Taking these into consideration, a stack of 1 µm LN on 1 µm Si is chosen for this study. The device schematic as well as the S0 mode stress profile and electric field within a wavelength, simulated by COMSOL, is shown in Fig. 1.

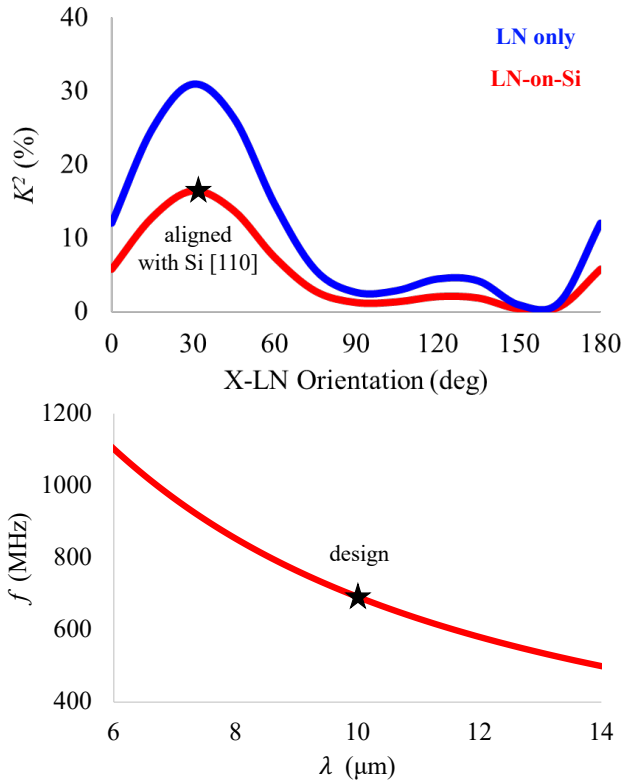

Figure 2: The electromechanical coupling dispersion for 1 µm X-cut LN with/without 1 µm Si for different LN orientations aligned with [110] Si (top). Frequency dispersion for Y30° orientation simulated by COMSOL (bottom).

Among the different cuts of LN, the X-cut LN offers the highest coupling for S0 mode once the acoustic wave propagates in ~30° off Y-axis direction [6]. Fig. 2 shows the electromechanical coupling dispersion of the stack vs. the LN orientation. This is calculated from the S0 phase velocity change because of short/open electrical boundary conditions on LN surface in COMSOL. Note that the addition of Si roughly reduces the electromechanical coupling from 31% to 16% at the optimal orientation. The frequency dispersion of said orientation is also plotted in Fig. 2; from this basic model, the wavelength targeted in this study should result in a passband frequency around ~670 MHz. The estimated electromechanical coupling along with the electrical properties of the stack is used to analytically predict the AE loss/gain from the model presented in [13]. This is shown in Fig. 3; without any external drift field, an AE loss of ~40 dB/mm is expected. Increasing the drift field so that the electron drift velocity reaches the Lamb wave phase velocity, at ~48 V/mm, would eliminate the AE loss, leaving the other less significant sources of loss to become dominant. This comprises the propagation loss in LN, LN-Si interface loss, and transducer electrode loss. Consequently, terminal gain would be possible at a drift field that yields an AE gain which covers all such losses. Limiting the available drift field to ~150 V/mm, up to ~70 dB/mm AE gain is possible. On the other hand, the rest of the loss sources are estimated to be less than 20 dB, which implies a waveguide having a length in the order of 500 µm could provide a 15 dB terminal gain. This, however, ignores the large signal effects and thermal issues that might arise at such high electric field levels.

The drift field is created by applying a voltage across the waveguide using DC contacts to Si outside of the acoustic propagation region. This is an advantage of the Lamb wave platform compared to SAW; in the latter, the semiconductor film and its DC access cause SAW perturbation as they lie within its propagation path. The devices are fabricated in a five-mask process starting with the bonded LN-on-SOI wafer which is provided by NGK Insulators LTD. Interdigital transducers (IDT) made of chromium/gold (25/75 nm) are deposited and patterned via e-beam evaporation and lift-off. Electrical contact points to Si for applying DC voltage are created outside of the waveguide by etching the LN layer. These openings and the RF probe pads are overlaid with another chromium/gold stack. The device boundaries are etched in ICP/RIE using argon (for LN) and DRIE (for Si) with a silicon dioxide mask. The devices are finally released from the backside by etching the Si handle layer and the buried oxide layer in DRIE and buffered oxide etchant, respectively.

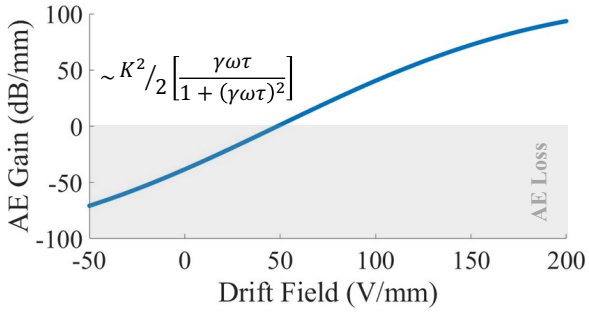

Figure 3: The analytical AE gain as a function of the applied drift field from the simple RC model presented in [13].

RESULTS

The fabricated waveguides have a width of either 150 or 300 µm while their length, being defined as the distance between the two ports IDT, ranges from 400 to 800 µm in 100 µm increments. The measurements are performed using a network analyzer in atmospheric pressure and at room temperature for input signals with -20 dBm power. The transmission response of two 500 µm

long waveguides having different widths is shown in Fig. 4, once biased at 0 V (black) and 125 V (red). The 150 µm wide device shows a maximum insertion loss (IL) improvement of 17.3 dB (going from 31 to 13.7) and the IL of the 300 µm wide waveguide after 39.6 dB AE gain improves from 38.7 to -0.9 dB, thus yielding a 0.9 dB terminal gain. Note that the transmission responses are reported for impedance matched terminations since the IDT impedance is not specifically designed for 50 Ohms. This can be seen from the reflection at the input port of the waveguides once they are terminated with 50 Ohms (Fig 4).

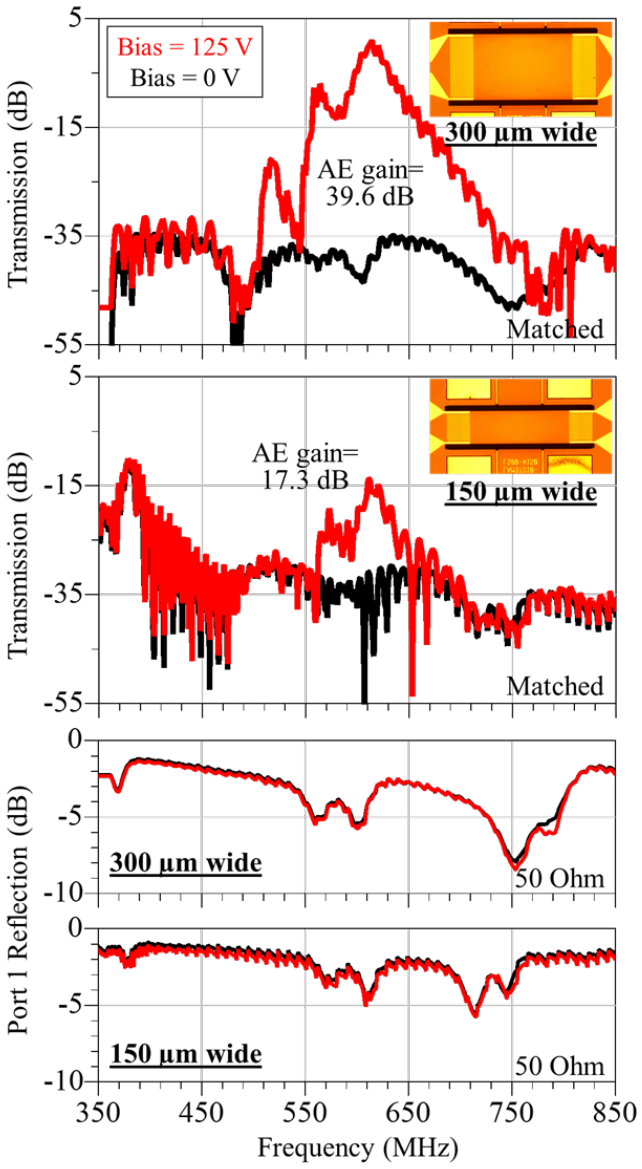

Figure 4: Measured transmission and reflection of waveguides having different widths and same lengths (500 µm) with 125 V bias (red) and no bias (black). The transmissions are reported with matched terminations.

A larger terminal gain is realized in a longer waveguide. This is shown in Fig. 5 for a 600 µm long, 300 µm wide device where the measured transmission responses at few bias points are plotted. By increasing the bias from the lowest to the highest voltage, the IL is improved from 36.8 dB to -5.5 dB, yielding 42.3 dB AE gain and 5.5 dB terminal gain. Keeping the voltage level limited to 125 V, devices with shorter or longer lengths demonstrate lower AE gain, making 600 µm close to the optimal device length. The 5.5 dB measured terminal gain is sustained by a constant DC bias of 125 V and 50 µA – i.e., dissipated power of ~6.25 mW – and is measured for a continuous wave at 613 MHz. As shown in Fig. 5, at this bias, the IL<0 passband has a span of ~30 MHz.

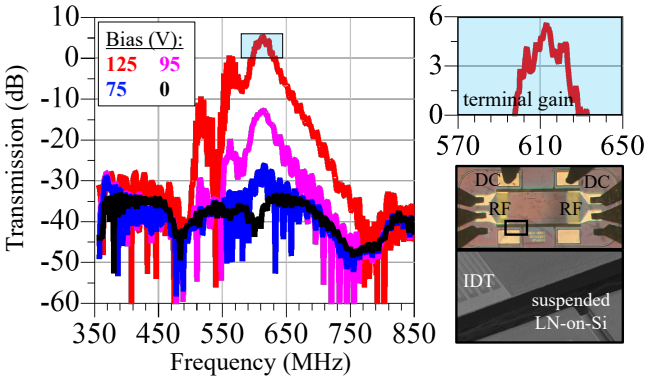

Figure 5: Measured transmission of the waveguide with optimal length (600 µm) showing an AE gain of 42.3 dB which results in 5.5 dB terminal gain with a continuous DC bias of 125V × 50µA.

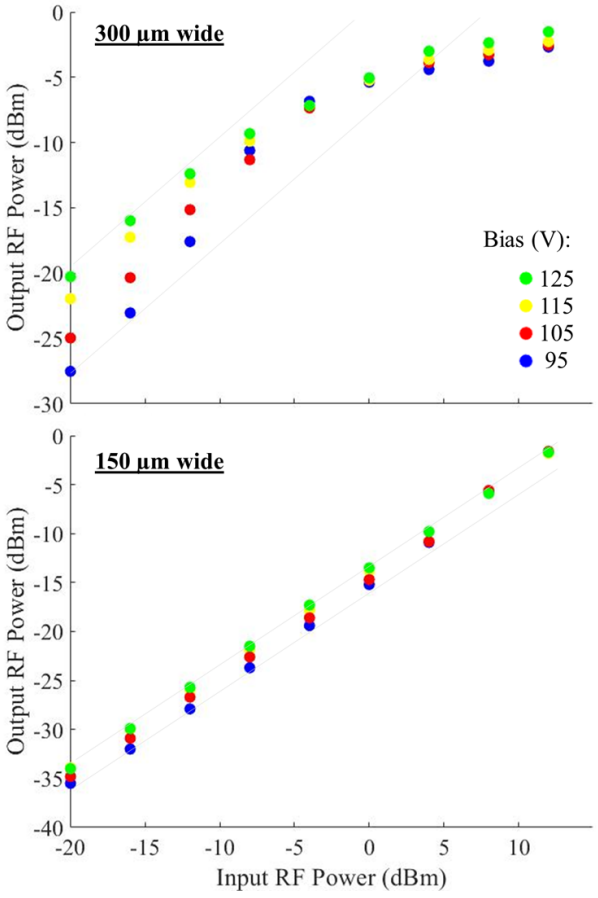

Figure 6: AE gain compression characteristic of waveguides having different widths and same lengths (500 µm). The wider device demonstrates larger gains but more non-linearity.

The measurements so far have been reported for RF input signals at -20 dBm and for larger input signals, the AE gain drops. The gain compression, furthermore, is observed to be affected by the device geometry and the bias level. This is shown in Fig. 6 for the two 500 μm long waveguides of Fig. 4. The input RF power is increased from -20 dBm to +12 dBm while the output power is recorded. The measurements are repeated for several bias levels. Although larger AE gains are measured in the wider device, the AE gain compression starts at lower RF input powers; the narrower device, on the other hand, shows a much more linear gain behavior in the measurement range and across the different bias levels.

CONCLUSIONS

The terminal gain, measured in this work, for continuous waves in micro-acoustic waveguides that are biased with a constant DC voltage, suggests the possibility of implementing more efficient amplifiers with better power handing using Lamb waves in lithium niobate on silicon thin films. Performance improvements are expected by further reducing the silicon thickness and optimizing the electrode design and the fabrication process. Having amplification capabilities in the micro-acoustic domain, where the majority of today's RF signal processing takes place, could lead to single-chip realization of more complex signal processing architectures, and eliminate the need for transistors in some applications.

ACKNOWLEDGEMENTS

This work was supported by the National Science Foundation (NSF) under award 2122670.

REFERENCES

[1] Y. V. Gulyaev and F. S. Hickernell, "Acoustoelectronics: history, present state, and new ideas for a new era," IEEE Ultrasonics Symposium, 2004.

[2] R. Kompfner, "Travelling-wave tubes." Reports on Progress in Physics 15.1, 1952.

[3] S. Ghosh and M. Ricci, "A 3-Port Circulator Based on Non-Reciprocal Acoustoelectric Delay Lines," 2020 Joint Conference of the IEEE International Frequency Control Symposium and International Symposium on Applications of Ferroelectrics (IFCS-ISAF), 2020.

[4] D. C. Malocha, C. Carmichael and A. Weeks, "Acoustoelectric Amplifier With 1.2-dB Insertion Gain Monolithic Graphene Construction and Continuous Wave Operation," in IEEE Trans. on Ultrasonics, Ferroelectrics, and Frequency Control, vol. 67, no. 9, pp. 1960-1963, Sept. 2020.

[5] L. Hackett, et al. "Towards single-chip radiofrequency signal processing via acoustoelectric electron–phonon interactions," Nature communications, vol. 12, no. 1, May 2021.

[6] I. E. Kuznetsova, B. D. Zaitsev, S. G. Joshi and I. A. Borodina, "Investigation of acoustic waves in thin plates of lithium niobate and lithium tantalate", IEEE Trans. Ultrason. Ferroelectr. Freq. Control, vol. 48, no. 1, pp. 322-328, Jan. 2001.

[7] R. Lu, and S. Gong, "RF acoustic microsystems based on suspended lithium niobate thin films: Advances and outlook." Journal of Micromechanics and Microengineering, vol. 31, no. 11, Sept. 2021.

[8] H. Mansoorzare and R. Abdolvand, "Acoustoelectric Amplification in Lateral-Extensional Composite Piezo-Silicon Resonant Cavities," 2019 Joint Conference of the IEEE International Frequency Control Symposium and European Frequency and Time Forum (EFTF/IFC), 2019.

[9] F. Hakim, M. Ramezani, S. Rassay and R. Tabrizian, "Non-Reciprocal Acoustoelectric Amplification in Germanium-Based Lamb Wave Delay Lines," 2019 IEEE International Electron Devices Meeting (IEDM), 2019.

[10] H. Mansoorzare and R. Abdolvand, "Acoustoelectric Non-Reciprocity in Lithium Niobate-on-Silicon Delay Lines," IEEE Electron Device Letters, vol. 41, no. 9, pp. 1444-1447, Jul. 2020.

[11] H. Mansoorzare and R. Abdolvand, "A Thin-Film Piezo-Silicon Acoustoelectric Isolator with More than 30 dB Non-Reciprocal Transmission," IEEE 34th International Conference on Micro Electro Mechanical Systems (MEMS), 2021.

[12] H. Mansoorzare and R. Abdolvand, "Ultra-Wideband Non-Reciprocal Micro-Acoustic Delay Lines with Slanted-Finger Interdigital Transducers," 2022 IEEE 35th International Conference on Micro Electro Mechanical Systems Conference (MEMS), 2022.

[13] R. Adler, "Simple theory of acoustic amplification." IEEE Transactions on Sonics and Ultrasonics 18.3, 1971.

CONTACT

*H. Mansoorzare, tel: +1-352-346-4400; hakha@knights.ucf.edu

MEMS RESONATOR MATCHING NETWORK FOR HIGH-SENSITIVITY SCALN PMUT-BASED ULTRASOUND RECEIVERS

Bernard Herrera Soukup, Pietro Simeoni, Gabriel Giribaldi, Luca Colombo, and Matteo Rinaldi
Northeastern University, USA

ABSTRACT

In this work, we demonstrate the concept of utilizing MEMS Resonator Matching Networks (MRMNs) to increase the sensitivity of an array of piezoelectric micromachined ultrasonic transducers (PMUTs) used in receive mode. The inductive region of the impedance of the MRMNs is set by the center frequency of a MEMS resonator, and it is independent from the resonance frequency of the PMUTs. We use a 20x20 array of 36% doped scandium-aluminum nitride (ScAlN) PMUTs electrically connected in parallel. The array is interfaced with 4 different resonators operating between 400 kHz and 600 kHz, allowing for a significant boost, at arbitrary frequencies, outside of the natural band of the PMUTs in fluid. We report out-of-band gains of up to 10, higher that the quality factor of the PMUTs (Q=3), thus pointing to the possibility of using MRMNs to enable ultrasound receivers with reconfigurable frequency bands.

KEYWORDS

PMUT, Ultrasound, Scandium, MRMN, Reconfigurable

INTRODUCTION

With the unfolding of the vision of the Internet of Things (IoT), the variety of possible computing nodes consistently expands as engineers design them for increasingly specialized functions. A significant subset of these nodes takes advantage of ultrasound for sensing and communication. During the last decade piezoelectric micromachined ultrasound transducers (PMUTs) have drawn significant attention from the research community and have started to see substantial adoption in the commercial realm for applications such as fingerprint authentication, time-of-flight range sensing, imaging, and more [1].

For all these applications, increasing the system sensitivity to incident ultrasound is an important requirement to keep pushing the performance of the computing nodes in terms of size, working range, and power consumption, which will ultimately translate in lower costs and will enable novel applications.

Flexural resonators, such as pMUTs, are characterized by low k_t^2, which means that they have relatively poor conversion capabilities between mechanical and electrical energy. When incident ultrasound bends the pMUT, it generates a voltage across the device electrodes by inducing a charge polarization through the piezoelectric effect. However, the output voltage that can be measured remains limited as most of the incident energy is stored in the transducer's capacitance in the form of reactive power.

The classic approach used to recover the reactive power has been to interface the transducers with inductor-based matching networks (MN). A drawback of this approach is that, at low frequencies, inductors tend to be bulky and are characterized by poor quality factors (Q<10), limiting their efficacy. In recent years, the concept of MEMS Resonator Matching Networks (MRMNs) has been demonstrated in RF wake-up receivers [2], [3]. The inductive region of mechanical resonators is utilized to cancel out the reactance of a capacitive load, while taking advantage of their compact form factor and extremely reduced losses (Q>1000).

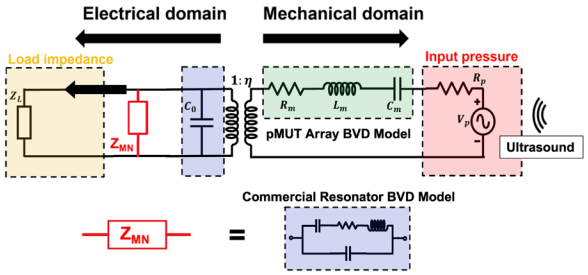

Figure 1: Equivalent circuit of a PMUT-based ultrasound receiver using a mechanical resonator as matching network.

In a first demonstration [4], the same concept was validated with pMUTs, where it was shown that MRMNs can passively amplify the actuation voltage applied on the ultrasound transducers with significantly higher gains than MNs based on inductors. In this work, we propose to use a similar approach in the domain of ultrasound receivers (Fig. 1).

To demonstrate the concept, a 20x20 array of 36% scandium-doped aluminum nitride (ScAlN) pMUTs was fabricated (Fig 2). The PMUTs have a radius of 46 µm, a silicon oxide elastic layer of 1 µm, and a piezoelectric layer of 0.5 µm sandwiched between 200 nm thick electrodes. The array was then interfaced with commercially available resonators to demonstrate their sensitivity-boosting effect.

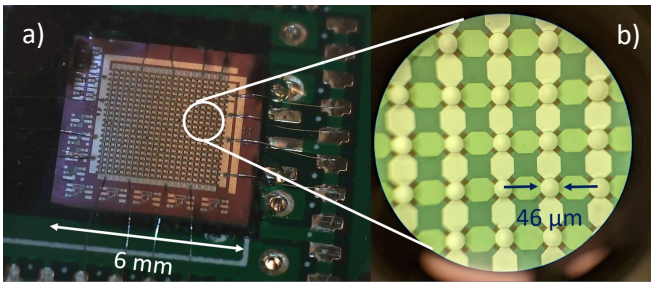

Figure 2. Optical microscope images of the 20x20 $Sc_{0.36}Al_{0.64}N$ PMUT Array. a) Overview of the chip, wire-bonded to a PCB for testing purposes and covered in PDMS for both electrical insulation and mechanical protection. b) Detail of the individual PMUT elements connected in parallel.

METHODOLOGY

The receiving sensitivity of the PMUTs to ultrasound in water was measured by immersing the array in a tank as shown in Fig. 3a. The incident ultrasonic wave was generated through a broadband, commercially available hydrophone (Teledyne TC 4038-4). The actuation frequency was swept over a frequency range between 0 and 2 MHz to extract the standalone array frequency response as shown in Fig. 4. The resonance of the pMUTs was at 700 kHz and showed a peak response of approximately 10 mV with a quality factor (Q) of ~3.

978-1-940470-04-7/HH2022/$25©2022TRF
DOI 10.31438/trf.hh2022.93

Next, the array was interfaced with different MRMNs implemented with commercial resonators (Fig. 3b) with frequencies of operation between 400 and 600 kHz. As shown in Fig. 1, the resonator is connected in parallel to the array electrodes. In this way, when the resonator operates in its inductive region, it will cancel out the reactive impedance introduced by the array's electrical capacitance. The frequency sweep is then repeated to observe how the system's response changes with respect to the standalone array case.

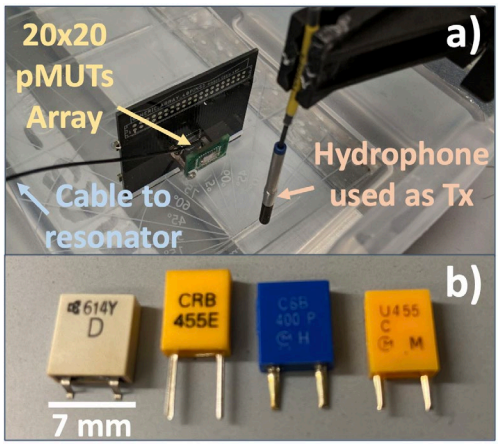

Figure 3. a) Experimental setup used to measure the pMUT array electrical output. b) Commercial resonators used to implement the MRMN.

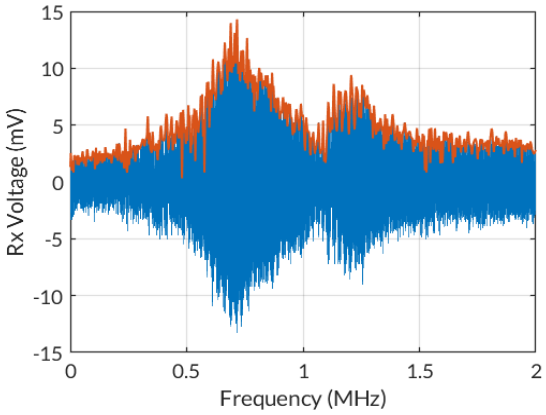

Figure 4. Time-domain frequency sweep pMUT array output voltage and voltage envelope when no MRMN is connected to the transducers.

To verify the voltage gain observed in the frequency sweeps, time-domain, burst measurements were performed for the standalone PMUT array case as well as for each of the PMUT array – MRMN systems. Burst signals, of the same amplitude but with a frequency corresponding to the frequency of maximum gain for each case, were applied to the Tx hydrophone and the Rx voltage on the PMUT array was measured. The number of cycles in the burst was varied in order to allow for the steady state response to be reached, after the particular rise time of each case.

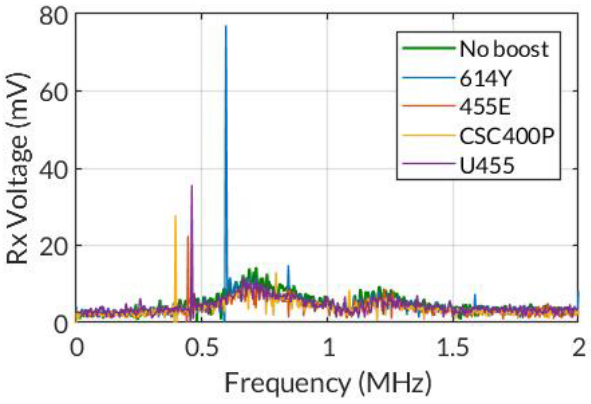

Figure 5. Frequency response of the array when interfaced with the resonators.

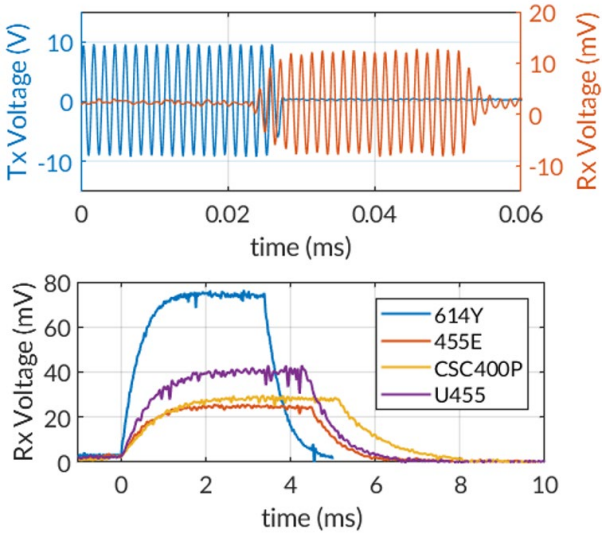

Figure 6. Time-domain, burst response measurements. Top: Standalone PMUT array case. Bottom: Envelope of the PMUT array – MRMN systems' output voltage.

RESULTS

As shown in Fig. 5, each configuration reproduces the response of the standalone PMUTs array, except for a passive sensitivity boost of up to 10 times when the receiver operates in the MRMNs inductive region. The narrow-band, high amplitude peaks are a result of the high quality factor resulting from the addition on the MRMNs.

The time-domain measurements in fig. 6 confirm the measured gains from the frequency sweeps. The different amplitudes of the envelopes in fig. 6 correspond to the different achieved gains, while the varying rise times are a consequence of the different quality factors of each of the resulting PMUT-MRMN systems. The longer rise and fall times observed on the cases with MRMNs, compared to the standalone array, show the trade-off of data rate (bandwidth) for voltage gain from another perspective.

To model the sensitivity boosting mechanism, the admittance response of the mechanical resonators was measured using a Vector Network Analyzer and were then fitted, with modified Butterworth-Van dyke (mBVD) parameters, to reproduce the observed data in circuit simulations performed in Advanced Design System (ADS). The resonators' parameters are shown in Table 1.

The relevant circuit parameters for modeling the PMUT array in the simulation were obtained by using an analytical model that relates the PMUT geometry (radius, thicknesses in the material stack) and material properties (density, piezoelectric coefficient, residual stress) to the equivalent lumped parameters [5]. The static capacitance of the array was obtained from a VNA admittance frequency sweep.

For an individual PMUT the following equivalent circuit parameters in the mechanical domain were extracted: equivalent stiffness of 1560 N/m, equivalent mass of 64×10^{-12} kg, transduction coefficient of 9.4×10^{-6} N/V, and an electrical capacitance of 2 pF. It is important to note that the parameters were calculated including the effect of operation in fluid (mass loading and radiation resistance in water).

Table 1: Equivalent circuit parameters obtained from fitting the mBVD model on VNA Y-parameters measurements taken on the individual resonators.

Model	C_0 [pF]	f_s [kHz]	Q	k_t^2 [%]
614Y	190	587	1590	14.5
455E	277	440	1614	10.7
400P	300	391	3387	6.6
U455	302	455	1826	8.2

ADS simulations, implementing the network shown in fig. 1, show that the expected amplification for all resonators is expected to be approximately 9.3 times the electrical output of the standalone PMUTs array. Fig. 7 shows the experimental gain that was observed on each resonator. It must be noted that, for the calculation of the gain, the amplitude at the peak for the boosted case is divided by the amplitude of the standalone response at that frequency. Therefore, even though the peak amplitude for resonator 614Y is larger than for the others, after dividing for the also larger standalone amplitude at the resonant band of the PMUTs, the gain results in a similar value. The only outlier is resonator 455E that does not closely match the simulation. This could be explained by parasitics from the soldering used when connecting the transducer.

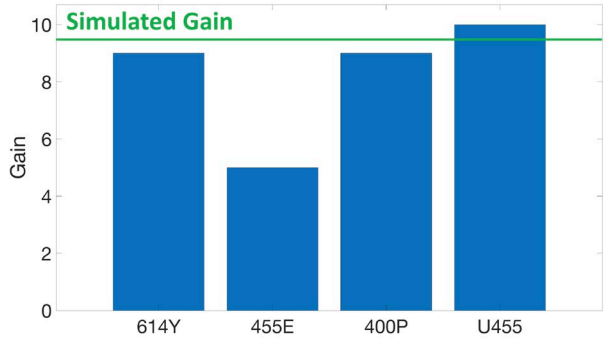

Figure 7. Equivalent circuit simulation gain compared to measured response. All the extracted parameters across different resonators delivered very similar system gain in simulation.

DISCUSSION AND CONCLUSIONS

Based on this analysis, our intuition was confirmed that the high-impedance mechanical branch of the pMUTs plays a negligible role in the matching process, and the optimal matching point between a capacitive load and an MRMN is based on the relative values of the load and resonator capacitances as analytically derived in [3].

This work offers exciting prospects for ultrasonic communication as it shows that the standalone response of the PMUTs does not dominate the receiver sensitivity even when the MRMN is centered out of band. For example, it is theoretically possible to integrate multiple resonators with the PMUT array and design a circuit to multiplex which frequency we desire use to communicate.

The high quality factor of the MRMNs limits the available bandwidth for each frequency. However, in use-cases that involve a large number of sensing nodes that need to transmit small amounts of data, bands of a few kHz are sufficient. We note that a similar switching mechanism could be used to connect a single MRMN to different series resistances to modulate the resonator quality factor. Such mechanism would add an additional degree of freedom to modulate the quality factor of the resonator, thereby trading off sensitivity (range) for bandwidth (data rate). Similarly, if the resonant frequency of the resonator could be tuned, different frequencies of operation could be attained with a single resonator without the need of altering the circuit connections.

ACKNOWLEDGEMENTS

This work was supported by DARPA TUFEN Program contract number HR00112090045. The authors would like to thank the staff of the George J. Kostas Nanoscale Technology and Manufacturing Research Center for assistance in device fabrication.

REFERENCES

[1] J. Jung et. al., "Review of Piezoelectric Micromachined Ultrasonic Transducers and their Applications", Journal of Micromechanics and Microengineering, (2017).

[2] L. Colombo et. al., "High-Figure-of-Merit X-Cut Lithium Niobate MEMS Resonators Operating Around 50 MHz for Large Passive Voltage Amplification in Radio Frequency Applications", IEEE Transactions on Ultrasonics, Ferroelectrics, and Frequency Controls, (2020).

[3] A. Kochar et. al., "Resonant Microelectromechanical Receiver", Journal of Microelectromechanical Systems, (2019).

[4] G. Giribaldi et al., "Matching Network-Boosted 36% ScAlN pMUT Linear Array", IEEE MEMS Conference, (2022) – In-press

[5] P. Simeoni, (2022) pMUTs_Layout_and_Analysis_Tool [Source code] https://github.com/simeonipietro/pMUTs_Layout_and_Analysis_Tool

CONTACT

Bernard Herrera: herrerasoukup.b@northeastern.edu

MODE LOCALIZATION AND TUNABLE OVERLAP IN A CLOSED-CHAIN MICROMECHANICAL RESONATOR ARRAY

Joon Hyong Cho[1,2], Michael A. Cullinan[2] and Jason J. Gorman[1]
[1]National Institute of Standards and Technology, USA
[2]Walker Department of Mechanical Engineering, University of Texas at Austin, USA

ABSTRACT
In this paper, we explore the dynamics of a closed chain of coupled micromechanical resonators, where each resonator is coupled to its two nearest neighbors. The design of a three-resonator array that combines silicon cantilevers with piezoelectric actuation and electrostatic coupling is first introduced. The dynamic behavior of the array is then presented for two voltage schemes for coupling the resonators, demonstrating complex amplitude and frequency dependence that may be useful for sensing applications. Finally, it is shown that analog feedback can induce mode localization in the array and collapse two coupled modes into a single mode, which could provide high sensitivity to external perturbations.

KEYWORDS
Coupled resonators, mode localization, resonator array, piezoelectric.

INTRODUCTION
Coupled micromechanical resonators have received significant attention over the last decade for both their ability to enhance measurement sensitivity in sensors and to demonstrate complex nonlinear behavior that may be useful for both classical and quantum computing [1-12]. Mode localization in coupled resonators has in particular been shown to be a powerful approach for improving the precision of microelectromechanical (MEMS) sensors, where the relative vibration amplitudes between resonators are used to measure external perturbations [1,2]. Sensing examples include accelerometers [3] and mass sensors [4], but mode localization can be used to measure any external signal capable of altering individual resonance frequencies and mode shapes of the coupled resonators.

From a more fundamental perspective, coupled resonators have been used to demonstrate multi-mode avoided crossings, similar to behavior found in atomic systems [5]. Parametric resonance and amplification have also been explored in coupled resonators, resulting in nonlinear frequency conversion and classical dynamics that are analogous to Rabi oscillations found in two-level quantum systems [6]. Finally, coupled nonlinear dynamics have been shown to yield complex bifurcations that can drive oscillations across large arrays including more than 100 resonators [7] and generate phononic frequency combs with fixed frequency spacing around a parametric resonance [8]. Due to this wide range of applications for coupled resonators, there is a continued need to develop new resonator geometries that can better leverage the dynamic behaviors described above.

Many different actuation, sensing, and coupling mechanisms have been used to realize coupled resonator arrays. The combination of electrostatic actuation and capacitive sensing have been the most commonly employed combination [1,3,4], but piezoelectric materials have also been used for actuation and sensing [6,8], often with greater sensitivity. Resonator coupling methods have largely been limited to mechanical coupling, such as a flexural linkage, and electrostatic coupling, which provides continuous tunability. The topology for the majority of coupled resonator arrays has been confined to series connectivity, where each resonator is coupled to the next resonator in a linear chain, with a few exceptions [9-11].

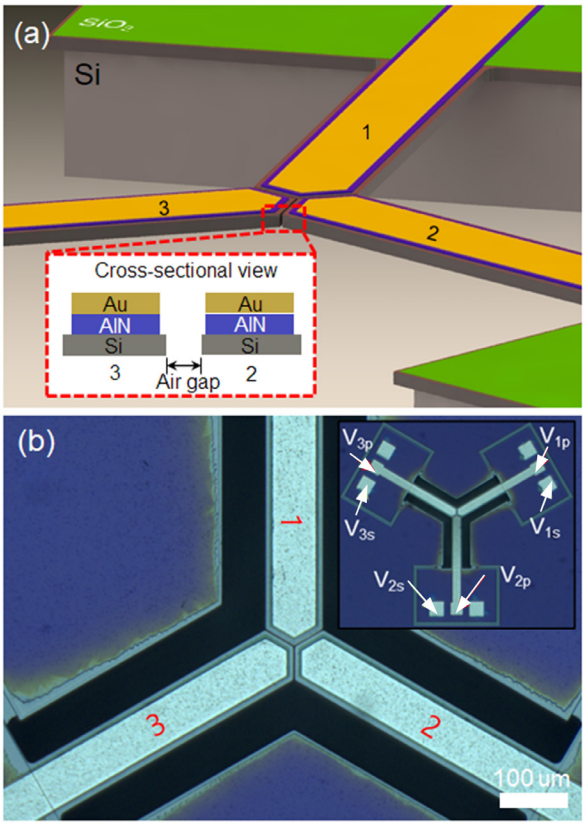

Figure 1: (a) Diagram of a 3-resonator closed-chain array. Inset: Cross-section of device layers. (b) Optical micrograph of a fabricated array. Inset: Electrical connections for the drive and coupling voltages.

Here, we present a new design for resonator arrays that combines piezoelectric actuation and sensing with electrostatic coupling. This results in large vibration amplitudes that are transduced with high sensitivity while also having continuous coupling tunability. In addition, the array is coupled in a closed chain rather than a linear chain, where the last resonator in the chain is coupled back to the first resonator, as described in the next section. As a demonstration of the dynamic behavior of this array, two complementary schemes for tuning the coupling are implemented and the resulting amplitude and resonance frequency behaviors are presented. Finally, feedback control on an individual resonator is shown to be an effective approach for inducing mode localization and may be useful for optimizing the array's sensitivity to external perturbations.

RESONATOR ARRAY DESIGN
The design of the closed-chain coupled resonator array is shown in Fig. 1. The array is composed of three cantilever resonators that are connected to the substrate at the base and coupled to each other at their free ends. The cantilevers have three material layers: a

U.S. Government work not protected by U.S. copyright
DOI 10.31438/trf.hh2022.94

single-crystal silicon layer that is the primary structural element, an aluminum nitride (AlN) layer for piezoelectric actuation and sensing, and a gold layer for electrical contact. A sinusoidal drive voltage with tunable frequency is applied to the gold layer to actuate the cantilever (see Fig. 1b inset, V_{1p}, V_{2p}, and V_{3p}). The tips for all cantilevers come together in the center of the array, where they are separated by a gap in the silicon layer. The coupling between each resonator is controlled by setting the DC voltage on the silicon layer for each resonator, V_{1s}, V_{2s}, and V_{3s}, respectively (see Fig. 1b inset). In general, the electrostatic force between two cantilevers is highly nonlinear with respect to the relative heights of the cantilever tips compared to the substrate plane. However, for small cantilever displacements, the electrostatic force is a linear restoring force that results in a positive increase in stiffness. The combination of the three drive voltages and three coupling voltages provide a number of options for generating unique dynamic behavior. This closed-chain concept has previously been explored theoretically [9] and a closed chain of mechanically coupled tuning fork resonators has been presented previously [10]. However, to our knowledge, resonators with tunable electrostatic coupling in a closed chain has not been demonstrated experimentally to date.

A functional array is shown in Fig. 1b, which was fabricated using the MEMSCAP PiezoMUMPS multi-project wafer process [13]. The silicon layer has the <100> crystal plane oriented out of the plane of the substrate and is 10 µm thick, the AlN layer is 0.5 µm thick, and the electrostatic gap between resonators is 2 µm wide, which is the minimum dimension allowed for the process. Custom fabrication of the array would allow for further optimization of the electrostatic coupling, and the stiffness and resonance frequencies of the resonators.

RESULTS AND DISCUSSION

To demonstrate some of the linear dynamic behaviors attainable with the closed-chain coupled resonator array, we explored two schemes for tuning the electrostatic coupling while driving a single resonator. A homodyne laser interferometer was used to measure the out-of-plane resonator motion in all presented results, where the photodetector voltage is used for resonator amplitude rather than converting to displacement. All measurements were performed under ambient conditions.

In the first coupling scheme, resonator 3 was driven with a sinusoidal (AC) signal, V_{3p}, and was biased with a static DC voltage, V_{3s}, set to 15 V while the electrostatic interactions between the three resonators were tuned with bias voltages V_{1s} and V_{2s} on resonators 1 and 2, respectively (see Fig. 2a). The frequency response of resonator 2 was measured with the interferometer over a frequency range that captures the first three modes of the array and for a range of values for V_{1s} and V_{2s}. A representative frequency response, including amplitude and phase, is shown in Fig. 2b, where the 2nd and 3rd modes are visible. These modes are largely due to resonators 2 and 3, although they are somewhat shifted from those found for the uncoupled resonators. These two resonators should have nearly the same Young's modulus along their length due to their orientation in the silicon layer, resulting in similar resonance frequencies. The 1st mode is only barely detectable near 77 kHz in Fig. 2b. This mode is downshifted from the other two since resonator 1 sits in a different crystal plane.

The amplitudes for modes 2 and 3 for varying V_{1s} and V_{2s} are shown in Figs. 3a and 3c, respectively. Since the array is driven at resonator 3 and measured at resonator 2, only V_{2s} has an effect on amplitude, where it acts like a gain between the input and output signals. However, the electrostatic coupling has a more interesting effect on the resonance frequencies. As V_{1s} changes from positive to negative, the electrostatic coupling increases between resonators

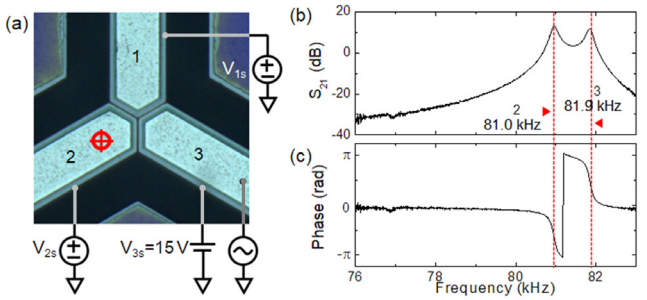

Figure 2: (a) First coupling scheme for the array. Resonator 3 is driven with an AC signal while a 15 V bias voltage is applied to its silicon layer. Varying bias voltages are applied on the silicon layers of resonators 1 and 2. (b) Representative amplitude and c) phase responses measured on resonator 2 with the interferometer (location indicated by the red cross in (a)). V_{1s} = 0 V, V_{2s} = 0 V.

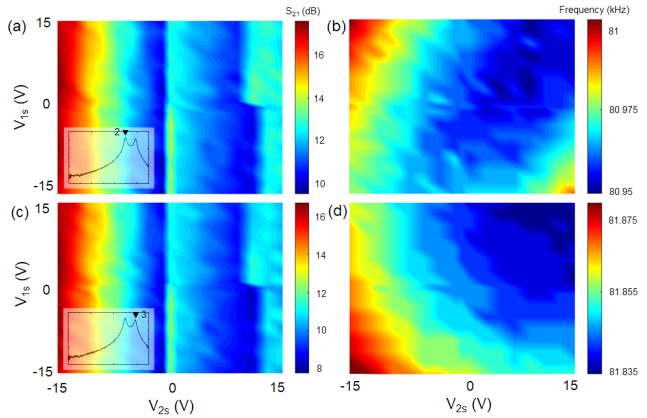

Figure 3: Experimental results for the coupling scheme in Fig. 2. (a) Amplitude and (b) frequency of mode 2. (c) Amplitude and (d) frequency of mode 3. V_{1s} has no effect on amplitude but tunes the frequencies of modes 2 and 3 in opposite directions. V_{2s} tunes both the amplitudes and frequencies for both modes in the same direction. Periodic artifacts in contour maps are computational and not representative of the data.

1 and 3 and decreases between resonators 1 and 2. Therefore, the frequencies for modes 2 and 3 are detuned in opposite directions and are a nonlinear function of the two bias voltages, as indicated by the semi-circular pattern shown in Figs. 3b and 3d. This behavior could provide a useful sensing modality where perturbations of resonator 1 can be transduced by measuring the frequency difference between modes 2 and 3. Examples of measurable perturbations include in-plane motion of resonator 1 and an induced voltage at V_{1s}, similar to voltmeters based on mode localization [14]. Since this is a differential frequency measurement between modes 2 and 3, it may be insensitive to thermal drift in the Young's modulus and coefficient of thermal expansion.

In the second coupling scheme, the coupling between resonators 1 and 2 was set to zero by choosing $V_{1s} = V_{2s}$ while V_{2s} and V_{3s} were varied (see Fig. 4a). A representative frequency response is shown in Fig. 4b, where the 1st mode is more pronounced than in the first scheme. This coupling scheme resulted in more linear behavior for the modal amplitudes and frequencies, as indicated by the linear gradients going from zero voltage to maximum voltage in the contour maps in Fig. 5. While this behavior is not particularly interesting on its own, it does point to the range of behaviors that can be achieved through small changes

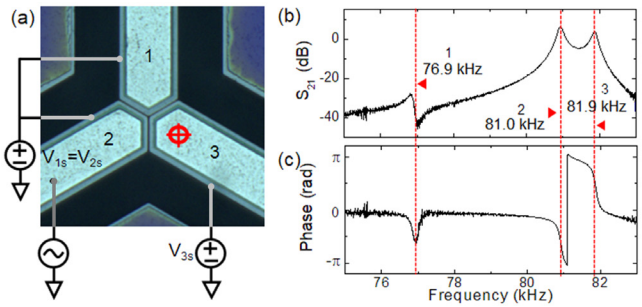

Figure 4: (a) Second coupling scheme for the array. Resonator 2 is driven with an AC signal while the same bias voltage is applied to the silicon layers of resonators 1 and 2. An independent voltage is applied to resonator 3. (b) Representative amplitude and c) phase responses measured on resonator 3 with the interferometer (location indicated by the red cross in (a)). V_{1s} = 0 V, V_{2s} = 0 V.

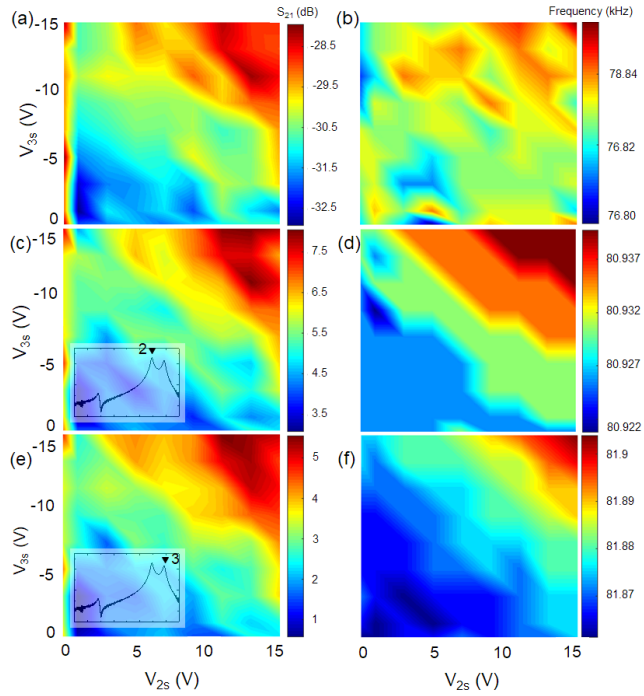

Figure 5: Experimental results for the coupling scheme in Fig. 4. (a,c,e) Amplitude and (b,d,f) frequency for modes 1, 2 and 3, respectively.

to the coupling configuration, as indicated by the dramatic differences in the array dynamics when comparing Figs. 3 and 5. This may be useful for creating mechanical logic gates used in low-bandwidth computation, where the coupling voltages, V_{1s}, V_{2s}, and V_{3s}, would be inputs to the logic gate and the resulting modal amplitude or frequency change would provide the computational output.

Finally, we used the same coupling scheme shown in Fig. 4a to explore the use of feedback control on an individual resonator to induce mode localization. We applied a negative stiffness perturbation to resonator 3, as is often done in mode localization sensors. However, rather than using a passive electromechanical element, such as an electrostatic actuator, analog proportional control was applied, where the interferometer signal was the feedback signal used to reduce the stiffness of the resonator. As seen in Fig. 6, mode 3 is reduced in frequency for increasing proportional gain until modes 2 and 3 collapse into a single mode

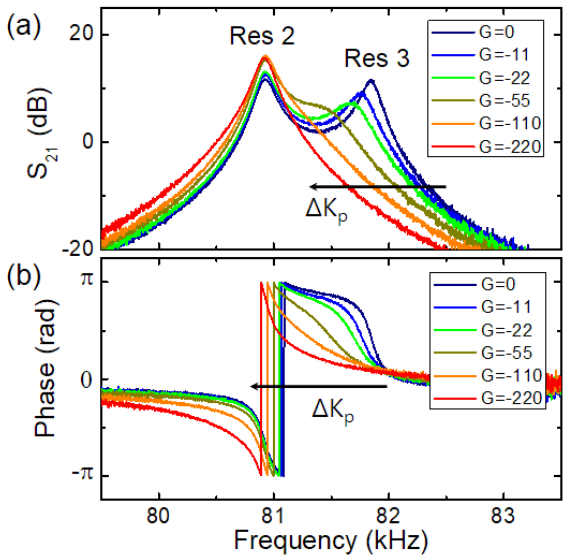

Figure 6: Modal overlap tuning with an analog proportional controller applied to resonator 3. (a) Amplitude and (b) phase of resonator 3 for varying proportional gain, which reduces the resonator stiffness. V_{2s} = 15 V, V_{3s} = -15 V.

that goes through a 2π phase shift on resonance. Similar overlapping modes generated by electrostatic coupling have recently been shown to be highly sensitive to external perturbations by operating in the weak coupling regime [12]. Here, the feedback reduces the stiffness of resonator 3 without changing the coupling between the resonators, thereby causing the modes to overlap. The impact of this feedback approach on the sensitivity of the array to stiffness perturbations on resonator 3 is currently being investigated.

CONCLUSION

A new topology for coupled resonator arrays has been presented that uses a closed chain of piezoelectric cantilevers that are electrostatically coupled at their free ends. Two sets of experiments with different voltage tuning rules for electrostatic coupling show that the dynamic behavior of the array can change dramatically based on the relative coupling forces. Finally, we have demonstrated that feedback control can be used to modify the coupling in the array, which may be useful for optimizing the sensitivity of the array to external perturbations. Future research will focus on expanding these early experiments to better understand the collective dynamics and applying the array to sensing applications.

REFERENCES

[1] P. Thiruvenkatanathan, J. Yan, J. Woodhouse, and A.A. Seshia, "Enhancing Parametric Sensitivity in Electrically Coupled MEMS Resonators," *J. Microelectromech. Sys.* **18**, 1077–1086 (2009).

[2] C. Zhao et al., "A review on coupled MEMS resonators for sensing applications utilizing mode localization," *Sens. Actuators A Phys.* **249**, 93–111 (2016).

[3] Y. Wang et al., "A mass sensor based on 3-DOF mode localized coupled resonator under atmospheric pressure," *Sens. Actuators A Phys.* **279**, 254-262 (2018).

[4] H. Zhang et al., "Mode-localized accelerometer in the nonlinear Duffing regime with 75 ng bias instability and 95 ng/√Hz noise floor," *Microsyst. Nanoeng.* **8**, 17 (2022).

[5] K. Gajo, S. Schüz, and E.M. Weig, "Strong 4-mode coupling of nanomechanical string resonators," *Appl. Phys. Lett.* **111**, 133109 (2017).
[6] H. Okamoto et al., "Coherent phonon manipulation in coupled mechanical resonators," *Nat. Phys.* **9**, 480–484 (2013).
[7] C.B. Wallin et al., "Nondegenerate parametric resonance in large ensembles of coupled micromechanical cantilevers with varying natural frequencies," *Phys. Rev. Lett.* **121**, 264301 (2018).
[8] A. Ganesan, C. Do, and A. Seshia, "Excitation of coupled phononic frequency combs via two-mode parametric three-wave mixing," *Phys. Rev. A 97*, 014302 (2018).
[9] V.B. Chivukula and J.F. Rhoads, "Microelectromechanical bandpass filters based on cyclic coupling architectures," *J. Sound Vib.* **329**, 4313–4332 (2010).
[10] A. Erbes, P. Thiruvenkatanathan, J. Yan, and A. A. Seshia, "Investigating vibration dynamics of cross-coupled MEMS resonators for reduced motional resistance," Transducers & Eurosensors XXVII, Barcelona (2013), pp. 1711–1714.
[11] B. Peng et al., "A sensitivity tunable accelerometer based on series-parallel electromechanically coupled resonators using mode localization," *J. Microelectromech. Sys.* **29**, 3–13 (2020).
[12] H. Zhang et. al, "On weakly coupled resonant MEMS transducers operating in the modal overlap regime," *IEEE Trans. Ultrason. Ferroelectr. Freq Control* **68**, 1448–1457 (2021).
[13] Certain commercial equipment, instruments, or materials are identified in this paper in order to specify the experimental procedure adequately. Such identification is not intended to imply recommendation or endorsement by NIST, nor is it intended to imply that the materials or equipment identified are necessarily the best available for the purpose.
[14] Y. Hao et al., "A micromechanical mode-localized voltmeter," *IEEE Sens. J.* **21**, 4325–4332 (2021).

CONTACT

*J.J. Gorman, tel: +1-301-975-3446; gorman@nist.gov

PHYSICALLY FLEXIBLE MULTI-LAYER LIQUID METAL-BASED BAND-PASS METASURFACE

Arkadeep Mitra[1], Kevin Xu[2], Jun H. Choi[2], and Jeong-Bong Lee[1]*
[1]The University of Texas at Dallas, Richardson, Texas, USA
[2]University at Buffalo, Buffalo, New York, USA

ABSTRACT

A liquid metal-based physically flexible (stretchable, bendable, twistable, and foldable) thickness customized multi-layer second-order band-pass metasurface in the X-band (7 ~ 11.2 GHz) has been designed, fabricated, and characterized. The multi-layer metasurface consists of a liquid metal-based inverter layer in the middle to enable the metasurface extremely thin (total thickness of 4.81 mm, < $\lambda_0/7.5$). Liquid metal has been sprayed into the PDMS replicated patterns by using an airbrush operating at 36 psi. S-parameters of the metasurface sample measured using a WR-90 waveguide setup showed good agreement with simulated results.

KEYWORDS

PDMS, liquid metal, multi-layer, band-pass, flexible, stretchable, bendable, twistable, foldable, metasurface.

INTRODUCTION

Gallium-based liquid metals comprise of binary (e.g., EGaIn) or ternary (e.g., Galinstan) alloys of elements that fall under the zinc group in the periodic table [1]. In presence of oxygen, Galinstan (Ga: 68.5%, In: 21.5%, and Sn: 10%) forms 0.5~3 nm gallium oxide (Ga_2O_3 and Ga_2O) layer [1-2]. The viscoelastic gallium oxide coupled with high conductivities (electrical conductivity: 3.46 x 10^6 S/m at 20° C, thermal conductivity: 16.5 W/m-K at 20° C), low melting point (13.2° C), high boiling point of 1300° C, and low toxicity, when compared to mercury, makes it a favorable alternative [1, 3]. Galinstan when patterned in elastomeric polymers like polydimethylsiloxane (PDMS) (~160% maximum elongation) [4] and Ecoflex (~900% maximum elongation) [5] realizes a myriad range of physically flexible electronics applications ranging from electrocardiogram (ECG) to metasurfaces [3].

Metasurface-based frequency selective surfaces are spatial filters that exist in 1D or 2D as band-pass, band-stop, low-pass, and high-pass [6]. A metasurface comprises of artificially engineered man-made structures that transmit, reflect, or absorb electromagnetic (EM) waves of specific frequency bands [6]. A variety of metasurfaces have been demonstrated such as in spectral filters [7], high impedance surfaces [8], low-profile reflect arrays [9], and absorbers [10]. Metasurfaces are employed in radomes (terrestrial and airborne) [11-12], missiles [11], electromagnetic shielding [11], and Pico cellular wireless communication applications [13].

Liquid metal has been used in PDMS-based metasurfaces. However, previous liquid metal based metasurface works used surface mounting techniques for incorporation of chip resistors which makes it not flexible and/or liquid metal injection through continuous channels which significantly limits design flexibility of the metasurface [14-15]. We have demonstrated a single layer flexible band-stop metasurface using a massive array of discrete patterns of liquid metal which cannot be achievable with previous methods [3, 6]. In this work, we further extend our previous work to demonstrate an extremely thin physically flexible (stretchable, bendable, foldable, and twistable) multi-layer band-pass metasurface operating in the X-band.

DESIGN

The multi-layer metasurface consists of m x n array of modified Jerusalem cross frequency selective surface (FSS) resonator layers at the top and the bottom. Each unit cell of the FSS resonator has 300 µm wide, 4.3 mm long vertical and horizontal dipoles with 1 mm x 2 mm end cap which faces floating patch of the same size (Figure 1a). The top and bottom FSS resonator layers are inductively coupled through a liquid metal inverter layer in the middle with a square aperture (4.3 mm x 4.3 mm) that overlaps the horizontal and vertical dipoles of the resonators (Figure 1b).

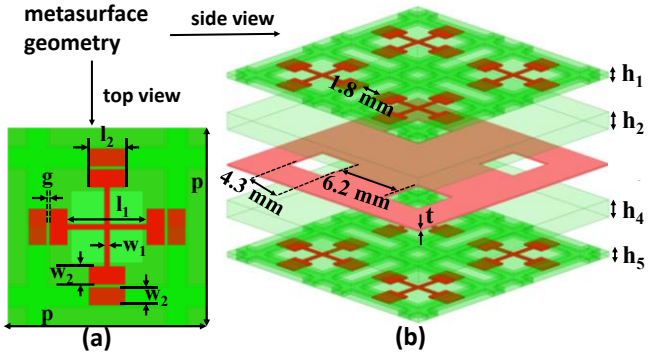

Figure 1. Schematic diagram of the multi-layer band-pass metasurface: (a) Top view of a unit cell: l_2 = 2 mm, l_1 = 4.3 mm, w_1 = 0.3 mm, w_2 = 1 mm, g = 0.2 mm, p = 10.5 mm, (b) 3D view of 2 x 2 cells: t= 0.2 mm, h_1 = 0.7 mm, h_2 = 1.66 mm, h_4 = 1.55 mm, h_5 = 0.7 mm.

The multi-layer metasurface (Figure 1b) have substrate thicknesses of h_1 = 0.7 mm, h_2 = 1.66 mm, t = 0.2 mm, h_4 = 1.55 mm, h_5 = 0.7 mm. The total thickness of the metasurface structure (h = 4.81 mm) is approximately $\lambda_0/7.5$, where λ_0 is the simulated finite array i.e., waveguide wavelength at 8.3 GHz.

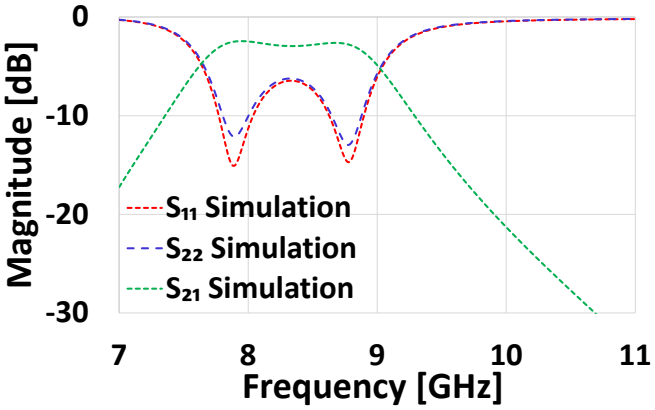

Figure 2. Simulated finite array band-pass metasurface results.

The metasurface comprising of PDMS (relative permittivity ε_r = 2.4 and loss tangent $tan\ \delta$ = 0.02) as the non-conductive and the

978-1-940470-04-7/HH2022/$25©2022TRF
DOI 10.31438/trf.hh2022.95

uniformly thick ($t = 0.2\ mm$) (Figure 1b) liquid metal Galinstan as the conductive media (conductivity $\sigma = 3.46 \times 10^6\ S/m$), has been simulated as a finite array using ANSYS-HFSS (high-frequency structure simulator) which shows broad passing band around 8~9 GHz (Figure 2).

FABRICATION

A 4" inch silicon wafer was patterned with S1813 photoresist and Chromium hard-mask was deposited using e-beam evaporation. Followed by a hard mask deposition and resist lift-off, a plasma etch with C_4F_8 (75 sccm), SF_6 (100 sccm), Ar (30 sccm)

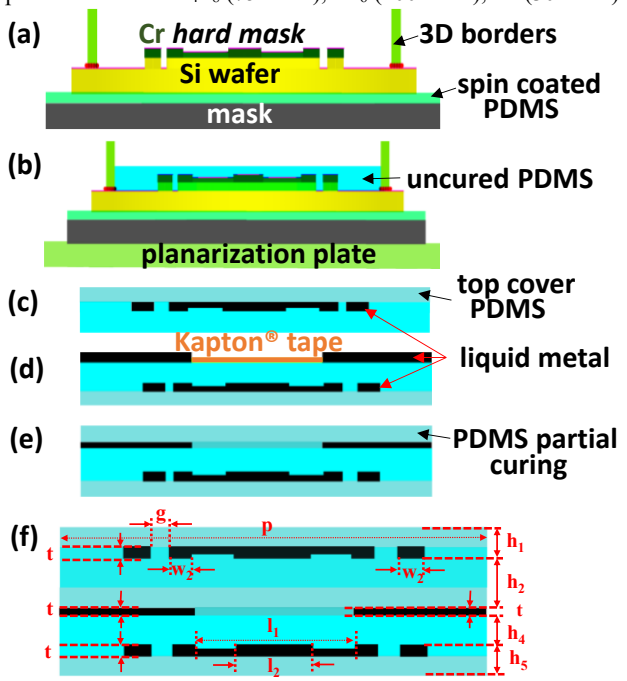

Figure 3. Fabrication sequence: (a) dry-etched Si mold, (b) PDMS replication, (c) top cover PDMS formation for encapsulation, (d) inverter layer liquid metal formation, (e) partially curing PDMS over the inverter layer, (f) top resonator layer aligned/bonded.

for 4 cycles (150 iterations/cycle; total iterations: 552) was done for dry etching of Si as per designed depth ($t = 0.2\ mm$). Teflon was deposited using C_4F_8 (75 sccm) and Ar (30 sccm) as a final step. The patterned Si mold was placed over a glass mask having spin coated uncured Sylgard 184 (Dow Chemical, Midland, MI, USA) 10:1 PDMS. Complete curing was done in a 95° C oven for 16 minutes. Followed by curing, a 3D printed border was placed along the edges of the mold and attached using Devcon epoxy (ITW Performance Polymers, Danvers, MA, USA). Reusability of the Si mold was ensured by these additional steps (Figure 3a).

The Si-mold structure was placed over a planarization plate. Uncured PDMS (10:1) was dispensed through a 1 mL syringe placed vertically centered over the mold and planarization was allowed for 24 hours at room temperature (Figure 3b). Following planarization curing was done on 96° C hotplate for 19 minutes. The cured top layer and bottom layer FSS-PDMS structures were placed over a cleanroom wipe. Galinstan (Changsha Rich Nonferrous Metals Co., Ltd., Hunan, China) mixed with 0.1 ml of 1% NaOH was sprayed into the patterns by using an airbrush (Paasche Airbrush Company, Kenosha, WI, USA) which operated at 36 psi, and was placed ~20 cm over the FSS-PDMS samples. Excess liquid metal outside of patterns were cleaned. A top cover

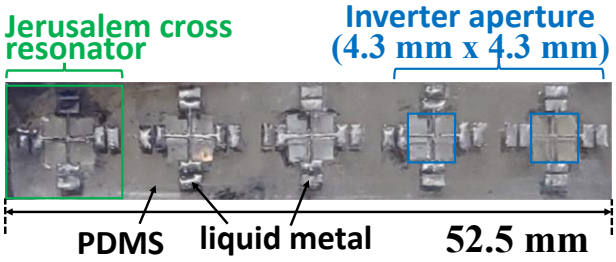

Figure 4. A photomicrograph of 1 x 5 fabricated band-pass metasurface

PDMS was further provided by dispensing through a 1 mL syringe and complete curing was allowed for approximately 48 hours at room temperature (Figure 3c).

The liquid metal patterned bottom FSS layer with protective top cover was flipped over and Kapton® tape (DuPont, Wilmington, DE) windows (4.3 mm x 4.3 mm) (Figure 3d) were placed overlapping the liquid metal patterned horizontal and vertical dipoles of the Jerusalem cross resonators. The Kapton® tape windows were fabricated by placement of four layers of Kapton tape (each layer measuring close to 55 microns) over the PDMS-inverter windows followed by cutting. The PDMS-inverter windows mold was replicated from the dry etched inverter-Si mold. Liquid metal mixed (1 mL) with 0.1 ml of 1% NaOH was sprayed over the collective inverter layer. Following spraying liquid metal planarization was done by placing a glass slide (5.08 cm x 7.62 cm x 0.1 cm) over the liquid metal and applying an external pressure. Following planarization completion, the glass slide was removed, and cleaning was done. For clear demarcation

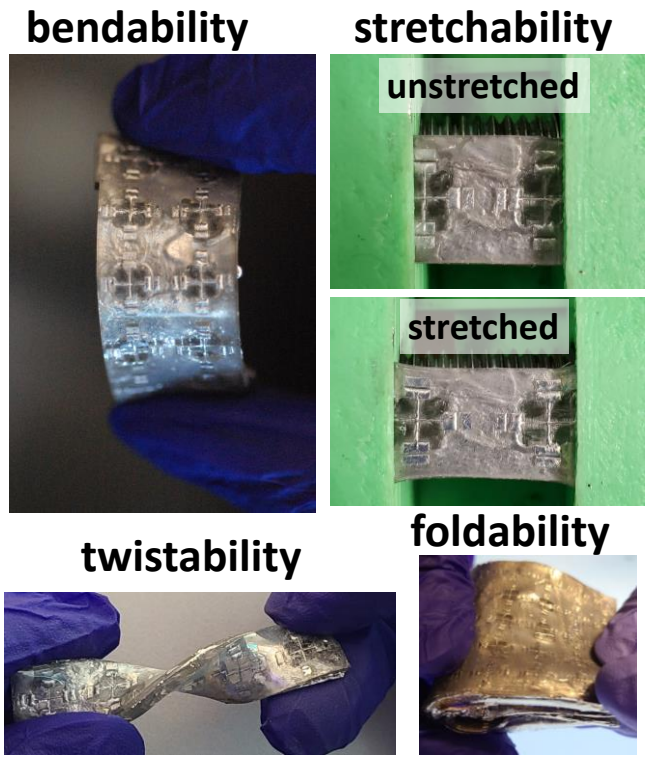

Figure 5. Physical flexibility demonstration of the fabricated metasurface.

of inverter layer window boundary, a very thin NeverWet® (Rust-Oleum Corp., Vernon Hills, IL, USA) layer (4.3 mm x 4.3 mm) was replaced after peeling away the Kapton-tape windows. The NeverWet® [16] skin in-turn was obtained by spraying into the 4.3 mm x 4.3 mm PDMS-inverter windows replicated from the inverter-Si mold. After cleaning and demarcation, the NeverWet® skin was removed. The inverter layer was sealed by dispensing uncured PDMS (10:1) through a 1 mL syringe. Partial curing of the PDMS was allowed for close to 22.5 hours at room temperature (Figure 3e), followed by which the dipoles of the top layer FSS (patterned with liquid metal and provided with protective top cover PDMS, Figure 3c) were aligned with that of the bottom layer FSS before placement on inverter layer. The integrated multi-layer structure ($h = 4.81\ mm$) was cured for another 48 hours at room temperature (Figure 3f). Multiple versions of m x n band-pass metasurfaces were fabricated.

Figure 4 shows a 1 x 5 metasurface. Various versions of the fabricated metasurfaces were repeatedly tested for its bendability, twistability, stretchability, and foldability (Figure 5). No apparent damages on the metasurface were visible after more than 20 cycles of testing, a proof of its physical flexibility.

CHARACTERIZATION

Characterization was done in a waveguide environment (Figure 6) with targeted X-band (7 ~ 11.2 GHz) operation. A 1 x 2 metasurface was cut from the fabricated 1 x 5 metasurface. The metasurface was placed in an inner aperture of limited dimensions (10.16 mm x 22.86 mm), of the sample holder which was in-turn milled from the 6.35 mm thick Arconic MIC 6 cast aluminum sheet. The coaxial adapters acted as the interface between the Keysight N542A PNA-X network analyzer (Keysight Technologies, Santa Rosa, CA, USA) and the WR-90 waveguide (Pasternack, Irvine, CA, USA). Calibrations were performed up to the sample before measuring S-parameters.

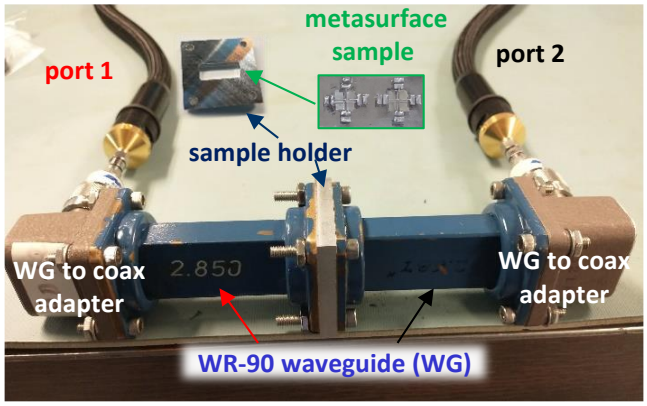

Figure 6. Waveguide characterization setup for the band-pass metasurface sample using WR-90 waveguide.

The measured S-parameters (Figure 7) results for the reflection and transmission of the multi-layer metasurface showed good agreement when compared with the simulation results (Figure 2). The center frequency of the measured and simulated sample was obtained at 8.325 GHz and 8.31 GHz, with a 3-dB fractional bandwidth of 12% and 17% respectively (Figure 7a).

CONCLUSION

In this work we demonstrated fabrication of multiple versions of physically flexible m x n band-pass metasurfaces. Spray coating was used for the discrete as well as continuous patterning of liquid metal in multiple PDMS layers. The waveguide simulation and measurement results showed good agreement.

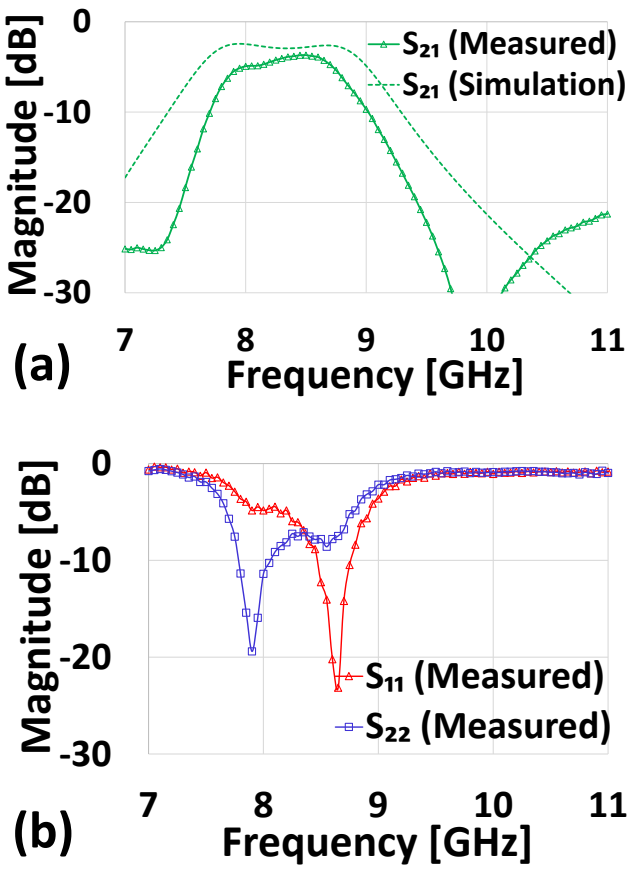

Figure 7. WR-90 waveguide results for band-pass metasurface. (a) Simulated and measured transmission coefficient. (b) Measured reflection coefficients.

We envision this unique, highly resilient physically flexible metasurface to be integrated in field-deployable metasurfaces uniquely suited for communication and military applications such as packable membrane reflectarrays for cargo space limited small satellites, and portable/rollable absorbers for on-demand deployment in stealth blanket operations. In practical applications, freezing point of liquid metal (e.g., at -19° C for Galinstan) [1] must be considered for storage and operation of the flexible metasurface to maintain its physical flexibility. In future works we envision to make the fixed floating patches dynamically tunable.

ACKNOWLEDGEMENTS

This work was supported in part by the United States National Science Foundation grant NSF ECCS-1908779. The authors would also like to acknowledge Dr. Ye Il Choi, Jinwon Jeong and UT Dallas Clean Room staff for their support on this work.

REFERENCES

[1] T. Daeneke, K. Khoshmanesh, N. Mahmood, I.A. de Castro, D. Esrafilzadeh, S. J. Barrow, M.D. Dickey, and K. Kalantar-zadeh, "Liquid metals: fundamentals and applications in chemistry", *Chemical Society Reviews*, 47, 4073 (2018).

[2] D. Kim, P. Thissen, G. Viner, D.-W. Lee, W. Choi, Y.J. Chabal, and J.-B. Lee, "Recovery of nonwetting characteristics by surface modification of gallium-based

liquid metal droplets using hydrochloric acid vapor", *ACS Applied Materials & Interfaces*, 5, 179 (2013).
[3] A. Mitra, K. Xu, S. Babu, J.H. Choi, and J.-B. Lee, "Liquid-Metal-Enabled Flexible Metasurface with Self-Healing Characteristics", *Advanced Materials Interfaces*, 2102141 (2022).
[4] L. Liang, and E. Ruckenstein, "Pervaporation of ethanol-water mixtures through polydimethylsiloxane-polystyrene interpenetrating polymer network supported membranes", *Journal of Membrane Science*, 114, 227 (1996).
[5] J.-B. Chossat, H.-S. Shin, Y.-L. Park, and V. Duchaine, "Soft Tactile Skin Using an Embedded Ionic Liquid and Tomographic Imaging", *Journal of Mechanisms and Robotics*, 7, 021008 (2015).
[6] A. Mitra, K. Xu, S. Babu, J.H. Choi, and J.-B. Lee, "Liquid Metal-Based Flexible Band-Stop Frequency Selective Surface", 2021 IEEE 34th International Conference on Micro Electro Mechanical Systems (MEMS), Gainesville, FL, 1/25-29/22, IEEE, 2021, pp. 953-956.
[7] A.E. Minovich, A.E. Miroshnichenko, A.Y. Bykov, T.V. Murzina, D.N. Neshev, and Y.S. Kivshar, "Functional and nonlinear optical metasurfaces", *Laser & Photonics Reviews*, 9, 195 (2015).
[8] A. Vallecchi, R.J. Langley, and A.G. Schuchinsky, "Metasurfaces With Interleaved Conductors: Phenomenology and Applications to Frequency Selective and High Impedance Surfaces", *IEEE Transactions on Antennas and Propagation*, 64, 599 (2016).
[9] J. Wang, Y. Li, Z.H. Jiang, T. Shi, M.-C. Tang, Z. Zhou, Z.N. Chen, and C.-W. Qiu, "Metantenna: When Metasurface Meets Antenna Again", *IEEE Transactions on Antennas and Propagation*, 68, 1332 (2020).
[10] K. Payne, K. Xu, JH Choi, and JK Lee, "Plasma-Enabled Adaptive Absorber for High-Power Microwave Applications", *IEEE Transactions on Plasma Science*, 46, 934 (2018).
[11] R.S. Anwar, L. Mao, and H. Ning, "Frequency Selective Surfaces: A Review", *Applied Sciences*, 8, 1689 (2018).
[12] E. Ahamed, M.R.I. Faruque, M.F.B. Mansor, and M.T. Islam, "Polarization-dependent tunneled metamaterial structure with enhanced fields properties for X-band application", *Results in Physics*, 15, 102530 (2019).
[13] T.Z. Fadhil, N.A. Murad, M.K.A. Rahim, M.R. Hamid, and L.O. Nur, "A Beam-Split Metasurface Antenna for 5G Applications", *IEEE Access*, 10, 1162 (2021).
[14] S. Ghosh, and S. Lim, "Fluidically reconfigurable multifunctional frequency-selective surface with miniaturization characteristic", *IEEE Transactions on Microwave Theory and Techniques*, 66, 3857 (2018).
[15] H.K. Kim, D. Lee, and S. Lim, "Wireband-Switchable Metamaterial Absorber Using Injected Liquid Metal", *Scientific Reports*, 6, 31823 (2016).
[16] I.D. Joshipura, H.R. Ayers, G.A. Castillo, C. Ladd, C.E. Tabor, J.J. Adams, and M.D. Dickey, "Patterning and Reversible Actuation of Liquid Gallium Alloys by Preventing Adhesion on Rough Surfaces", *ACS Applied Materials & Interfaces*, 10, 44686 (2018).

CONTACT

*Jeong-Bong (JB) Lee, tel: +1-972-658-6750; jblee@utdallas.edu

PIEZORESISTIVE MICRO-PILLAR SENSOR FOR IN-PLANE FORCE SENSING IN BIOLOGICAL APPLICATIONS

Isha Lodhi[1], Durga Gajula[2], Devin K. Brown[1,2], Wilbur A. Lam[2,3,4,5], David R. Myers[3,4,5], and Oliver Brand[1,2]
[1]School of Electrical and Computer Engineering, Georgia Institute of Technology, Atlanta, Georgia, USA
[2]Institute for Electronics and Nanotechnology, Georgia Institute of Technology, Atlanta, Georgia, USA
[3]Wallace H. Coulter Department of Biomedical Engineering, Emory University & Georgia Institute of Technology, Atlanta, Georgia, USA
[4]Department of Pediatrics, Emory University, Atlanta, Georgia, USA
[5]Aflac Cancer and Blood Disorders Center, Children's Healthcare of Atlanta, Atlanta, Georgia, USA

ABSTRACT

This work presents the design, fabrication, and testing of a pillar-based microforce sensor for in-plane force sensing. The novelty of the sensor lies in its design that combines a high aspect ratio SU-8 pillar with 6µm diameter, fabricated on top of a doped silicon piezoresistor with lateral dimensions of 2x2µm or 3x3µm, which acts as the embedded active sensing element. The substrate-embedded sensing element measures the out-of-plane stress created by in-plane (transverse) forces applied to the pillar tip. A force resolution <1 µN is achieved with a lateral device footprint that is at least ten times smaller than previous MEMS force sensors. Moreover, the sensor design based on silicon piezoresistors allows for (integrated) electrical readout and scalable fabrication of sensor arrays for mechanical cell characterization.

KEYWORDS

Piezoresistor, microforce sensor, stress sensing, pillar-based sensor, in-plane force sensing, cell mechanical characterization.

INTRODUCTION

Studies of cell and tissue mechanics have shown that mechanical properties of biological cells and tissue can provide valuable information on biological processes, such as stages of cell differentiation during stem cell growth, or indicate normal or unhealthy functioning of body cells [1-3]. Mechanical characteristics of cells, such as their stiffness or contractile force, can be used as independent biomarkers in clinical diagnosis. For instance, blood platelets apply varying forces on fibrinogen protein dots during clotting processes, and the force that cell populations apply can help diagnose bleeding disorders in patients [3].

As a result, there is interest in technology and equipment that help with mechanical characterization of biological cells, tissues, and processes. Micro/nano-Newton force sensors are an important component of these tools to quantify mechanical force and stress. Considering above applications, MEMS devices are of particular interest because the device dimensions are comparable to the physical dimensions of biological cells themselves (few µm) and high force resolution is achievable. For potential diagnostic applications based on cell mechanical behavior, it is furthermore important to test large cell populations in parallel. Hence, the ability to scale, array and mass fabricate MEMS-based force/stress sensors is of importance.

However, MEMS-based force sensors that report sub-µN force resolution either have a large form factor (~100s µm to mm) or employ fabrication processes that make dense arrays and integration with CMOS circuitry difficult. As an example, Y. Sun et al. reported nano-Newton force resolution using a capacitive comb sensing mechanism using a large sensor design with millimeter dimensions [5]. Although capacitive sensors have advantages over piezoresistors in terms of noise performance and accuracy, their fabrication is generally more challenging in order to minimize and control electrode spacing. In contrast, the sub-µN force sensor designs by T. C. Duc et al. [6] and J. C. Doll et al. [7] utilize micromachined, in-plane cantilevers with embedded piezoresistors for in-plane and/or out-of-plane force sensing. The need for in-plane cantilevers again consumes valuable substrate footprint and the necessary micromachining steps for cantilever release make fabrication of dense sensor arrays challenging. An alternative, pillar-based, two-axis force sensor design demonstrated by J. C. Doll et al. [8] inspired this research. The design features two micromachined clamped-clamped cantilevers in a Swiss cross arrangement with an SU-8 pillar in the center. In-plane forces applied to the pillar bend the cantilever beams and embedded strain gauges transduce the applied force into a resistance change. However, lateral device dimensions are again in the 100s µm range, making dense arrays challenging.

SENSOR DESIGN AND FABRICATION

Sensor Design and Theory of Operation

This work presents a novel design concept for in-plane force sensing using a pillar as a mechanical cantilever structure mounted directly on top of an embedded stress-sensing element. The pillar translates a transverse, in-plane force (F_x) into an out-of-plane stress in the substrate that peaks at the base of the pillar and penetrates the underlying substrate. The novelty of the design lies in integrating doped silicon piezoresistors underneath the pillar base, which allows for a small form factor and simple fabrication process. Moreover, the piezoresistive sensing mechanism allows for device scaling and the fabrication of dense sensor arrays using a process flow that is compatible with CMOS technology.

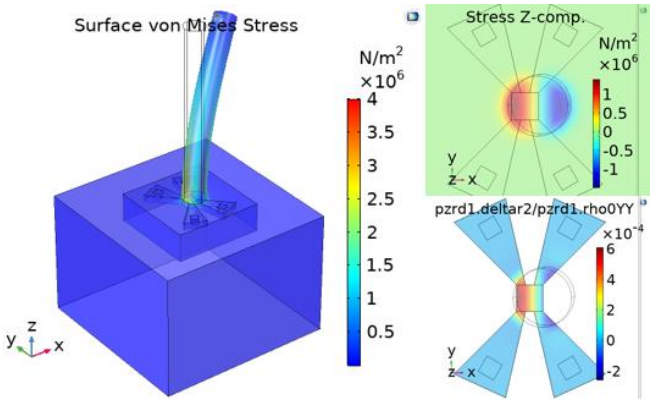

Figure 1: COMSOL FEM simulation of micro-pillar sensor with embedded 3x3µm piezoresistor: (left) von Mises stress upon 0.2µm transverse deflection of SU-8 pillar; (top right) resulting out-of-plane σ_{zz} stress 1µm deep in the plane of the piezoresistor; (bottom right) resulting simulated relative resistivity change $\Delta\rho_{yy}/\rho_0$ in the n-type silicon piezoresistor.

978-1-940470-04-7/HH2022/$25©2022TRF
DOI 10.31438/trf.hh2022.96

Finite element simulations using COMSOL as well as analytical studies were performed to investigate characteristic stress patterns and maximize the sensor output, i.e., the relative resistance change ΔR/R as a function of the applied transverse pillar force/deflection. Figure 1 shows a representative COMSOL simulation where a 0.2µm deflection is applied to the tip of an SU-8 pillar. The transverse pillar deflection creates a characteristic stress distribution in the underlying silicon substrate, with the out-of-plane stress component σ_{zz} approximately twice the magnitude of the in-plane stress components. To harvest the dominant out-of-plane stress component, we use n-doped silicon piezoresistors that have a much larger piezoresistive π_{12} coefficient compared to p-type silicon. Assuming a piezoresistor aligned with the primary flat of a (100) wafer, i.e., aligned in <110> direction, Equation (1) shows the relative resistance change ΔR/R as a function of the in-plane stress components σ_{xx}, σ_{yy} and the out-of-plane stress σ_{zz} [9]. π_{11}, π_{12} and π_{44} are the piezoresistive coefficients and the coordinate axes are aligned with the direction of the piezoresistor.

$$\frac{\Delta R}{R} = \left[\frac{\pi_{11}+\pi_{12}-\pi_{44}}{2}\right]\sigma_{xx} + \left[\frac{\pi_{11}+\pi_{12}+\pi_{44}}{2}\right]\sigma_{yy} + \pi_{12}\sigma_{zz} \qquad (1)$$

The piezoresistors are designed with four electrical contacts for four-point probing and low-noise, Kelvin measurement of the resistance. The contacts are extended out on either end of the sensing element in a "butterfly" design. This design feature and an extended contact geometry allows for access to and probing of the electrical contacts even after pillars are formed on top of the resistor.

Equation (2) highlights the maximum out-of-plane stress generated underneath the pillar as a function of the pillar height L and the pillar radius R. It is noted that the out-of-plane stress changes sign underneath the pillar (see Figure 1) and the piezoresistor must be placed off-center under one-half of the pillar base.

$$\sigma_{zz} = \frac{4}{\pi}\frac{L}{R^3}F_x \qquad (2)$$

Importantly, the z-axis stress due to a transverse force F_x is independent of the material properties of the cantilever/pillar but depends strongly on the aspect ratio of the pillar ($L/2R$) and its radius (R). Scaling the pillar dimensions while keeping the aspect ratio the same increases the maximum stress and, thus, the sensor sensitivity proportional to R^{-2}. In this work, we chose SU-8 photoresist to form the sensor pillars since the negative resist shows favorable structural properties and is easy to process. SU-8 also has the advantage of achieving high-aspect-ratio patterns with good adhesion to the silicon substrate. The pillars are formed off-center on top of the piezoresistors, with the lateral dimension of the resistor covering half the diameter of the pillar. Figure 1 highlights the relative resistivity change in the piezoresistor which has a spatial dependence because of the spatial dependence of σ_{zz}.

Fabrication Process

The fabrication process starts with a p-type (100) silicon wafer. E-beam lithography is used to define narrow (<0.4µm) trenches that outline the lateral piezoresistor edges. These trenches serve to confine the dopants introduced via solid-state diffusion to the piezoresistor body, as well as provide lateral electrical isolation of the piezoresistor from the substrate. Inductive coupled plasma (ICP) etching is used to etch the trenches (~3µm deep), outlining the piezoresistor "butterfly" geometry, using a "nano-Bosch" silicon dry etch process. The trenches are filled with oxide in a thermal oxidation step and the piezoresistor is formed in a furnace using a solid-state phosphorus (n-type) dopant source (pre-deposition step). This is followed by growth of a thermal passivation oxide layer in parallel with dopant drive-in. For formation of the four metal contacts, square openings (1x1 to 2x2µm) are etched in an isotropic wet chemical etching step. This is followed by deposition of the actual metal lines (300nm thick) via sputtering using an AlSi(1%) source. After lift-off of the excess metal, the piezoresistors are tested electrically on a four-point probe station using a semiconductor parameter analyzer (HP4155A) to measure device resistance before pillars are fabricated on top. SU-8 pillars with 6µm diameter and ~55µm height are patterned on top of the working devices using UV maskless lithography. Figure 2 shows step-by-step cross-sections of the fabrication process, along with a top view of the fabricated device prior to, and after, formation of the off-center pillar. Figure 3 shows a SEM micrograph of a fabricated butterfly device before and after SU-8 pillar fabrication.

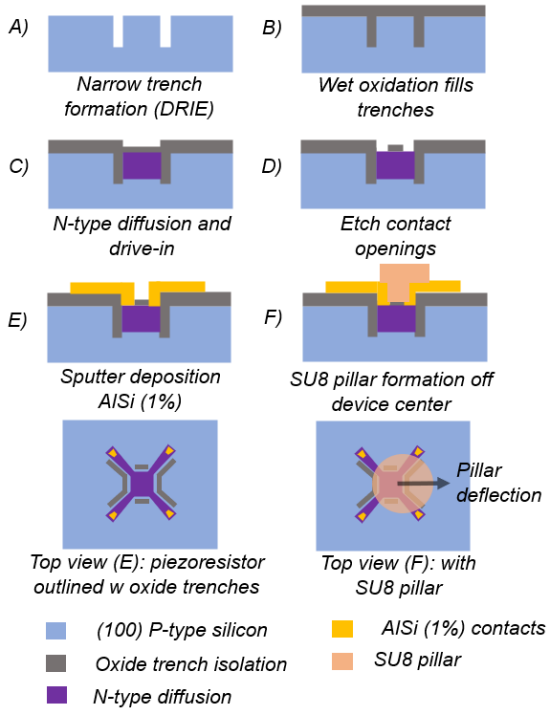

Figure 2: (A-F) Schematic cross-sections of fabrication process with p-type (100) wafer as substrate material; (bottom row) top-view schematics of completed device prior to and after SU-8 pillar fabrication.

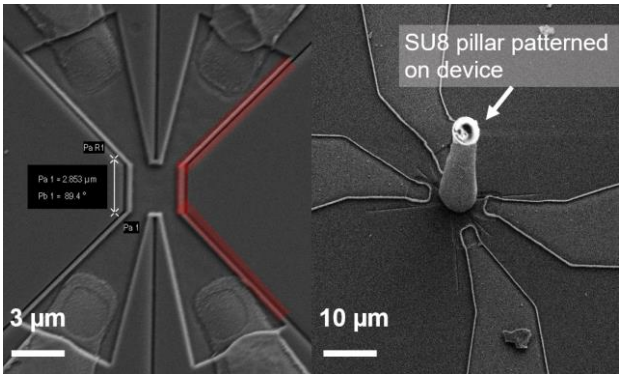

Figure 3: SEM images showing n-doped piezoresistors with extended four-point contacts in a "butterfly" design (left) without and (right) with SU-8 micropillar (5.5µm top diameter; 45µm pillar height). The red line highlights one of the oxide-filled trenches.

MECHANICAL CHARACTERIZATION

Mechanical Test Setup

For mechanical characterization of the micro-pillar sensors, a single-axis transverse displacement is applied to the tip of the SU-8 pillar while the resistance of the embedded piezoresistor is monitored in a four-point Kelvin configuration. The four-point measurement setup uses shielded triax cables and a single-channel source-meter unit (Keithley 2636A) to reduce the electrical noise in the resistance measurement. Controlled transverse deflections in steps of 0.2–0.3µm are applied to the tip of the SU-8 pillars via a stiff tungsten probe (radius 1.2µm) using the test setup schematically shown in Figure 4. The device-under-test is mounted and wire-bonded to a ceramic dual-in-line (DIL) package, which is attached to a printed circuit breakout board that connects with the source-meter unit. The tip of the tungsten probe is first aligned to the tip of the SU-8 pillar using a manual *xyz* micropositioner (MKS Newport 562-XYZ) and a high magnification lens/camera system. Once the tungsten tip is aligned with the pillar tip, a high-resolution, single-axis piezoelectric nanopositioning stage with position control (Physik Instrumente P-611.1S) applies controlled deflections to the pillar tip in *x* direction. The stage has a built-in strain gauge for position sensing and is operated in closed loop in combination with a digital controller to apply small displacements. The entire setup is screw-mounted to an air table with stiff connections improving the mechanical noise floor. During experiments, a housing shields the setup from unwanted air flow in the lab that would introduce measurement noise.

It is important to note that the displacement measured using built-in strain gauge of the single-axis nanopositioning stage is used as a measure of the tip deflection Δx applied to the SU-8 pillar. For this assumption to be correct, the effective spring constant of the mechanical connection between the nanopositioning stage and the tungsten tip has to be much larger than the spring constant of the SU-8 pillar. As shown in Figure 4, we have to consider two main spring constants connected in series, namely the springs associated with tungsten probe (K_{probe}) along with that of the probe holder (K_{holder}). The total spring constant of the setup $K_{setup} = (K_{probe}^{-1} + K_{holder}^{-1})^{-1}$ must be much larger than $K_{SU\text{-}8\ pillar}$.

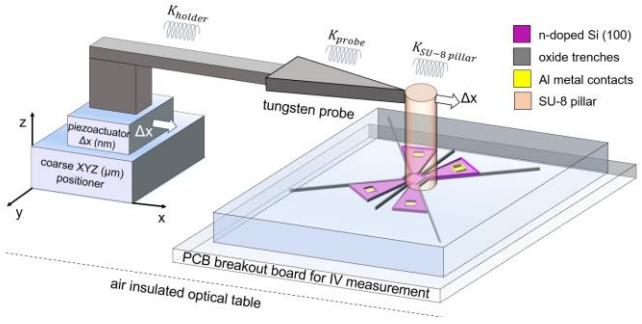

Figure 4: Schematic 3D view of the mechanical testing setup. Cross-roller bearing micromanipulators are used to position a tungsten probe in xyz with respect to the tip of the SU-8 pillar. A high magnification optical system positioned on top of the setup has a live camera to ensure proper probe and pillar alignment. After initial alignment, a closed-loop piezoactuator is used to drive the tungsten probe in sinusoidal waveforms to apply cyclic deflections to the device pillar tip. The device-under-test is wire-bonded to a dual-in-line package which is mounted to a breakout board connected to the source-meter. It is assumed that the Δx measured by the position sensor in the nanopositioning stage is equal to Δx applied to pillar.

Mechanical Characterization Results

Sensor designs of 2x2µm and 3x3µm butterfly piezoresistors with 6µm diameter, and 45-55 µm height SU-8 pillars were mechanically characterized by applying unilateral deflections in the test setup described before. The pillar geometries were kept the same for both piezoresistor dimensions to explore the effect of the piezoresistor dimension on force sensitivity. Figure 5 shows the measured relative resistance change ΔR/R of a 3x3µm piezoresistor as a function of time, while a sinusoidal deflection function with increasing and decreasing amplitude was applied to its pillar tip. The displacement measured by the position sensor embedded in the nanopositioning stage is recorded simultaneously and plotted as a second y-axis in the same graph. The device resistance responds to applied deflection within <0.2s and the measured resistance change closely follows the applied deflection.

Finally, Figure 6 presents the measured ΔR/R for each device as a function of the pillar deflection as well as a comparison with the theoretical sensitivity as simulated using COMSOL. The smaller piezoresistor yields an approx. 20% larger deflection response for the same pillar dimensions because the smaller piezoresistor is better aligned with the high-stress regions at the pillar base. The same behavior is found using COMSOL simulation. The slightly reduced experimental sensitivities compared to the COMSOL simulations are believed to be caused by alignment inaccuracies of the SU-8 pillars on top of the piezoresistors. Simulation studies confirm this dependence of the deflection sensitivity on the pillar lateral alignment to the piezoresistor.

The resulting sensitivity of the pillar-based force sensor to tip deflections, $(\Delta R/R)/\Delta x$, is 0.075%/µm and 0.090%/µm for the 3x3µm and 2x2µm piezoresistor, respectively. To obtain the device sensitivity to in-plane forces F_x applied to the pillar tip, the spring constant of the pillar was simulated using COMSOL, using the pillar dimensions of the actual sensor as obtained by SEM imaging. For the tested devices, the spring constant was simulated as $K_{SU\text{-}8pillar}$ = 8.9 N/m. For the device with 2x2µm piezoresistor, this translates into a force sensitivity, $(\Delta R/R)/F_x$ = 0.01%/µN. Furthermore, the minimum detectable deflection of 0.05µm translates into a force resolution of approximately 0.5µN. As was highlighted before, this force resolution is improved by a factor of 4 if the pillar diameter is reduced by a factor of two while keeping the aspect ratio constant.

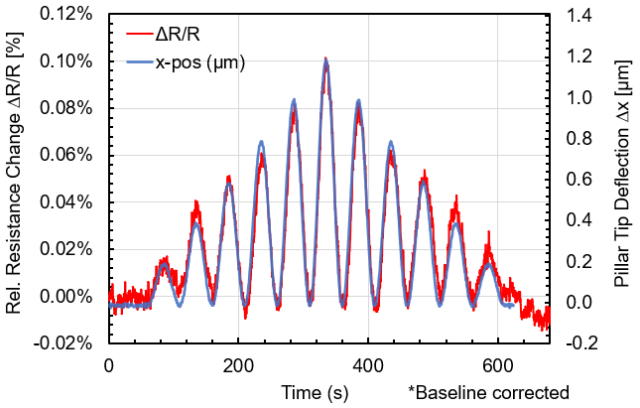

Figure 5: Measured resistance change of a 3x3µm piezoresistor with SU-8 micropillar (6µm diameter, 55µm height) undergoing sinusoidal deflections of increasing/decreasing amplitude applied by a stiff tungsten probe tip mounted to a closed-loop nanopositioner. Displayed are the simultaneously recorded relative resistance change of the piezoresistor (red) and the relative position of the nanopositioner (blue), corresponding to the tip deflection.

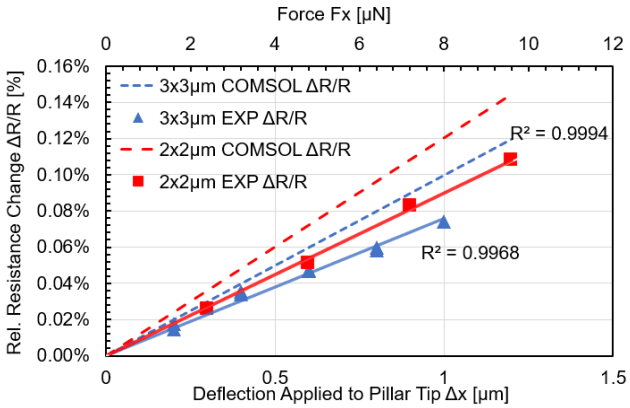

Figure 6: Average (N=3) measured relative resistance change ΔR/R for 2x2µm (red squares) and 3x3µm (blue triangles) butterfly design resistors as a function of the transverse pillar deflection Δx. The solid lines represent linear fits to the experimental data (with R^2 values), while the dashed lines are the results of the COMSOL simulation. The secondary x-axis represents the force applied to the micropillar assuming a pillar spring constant of 8.9N/m, as simulated using COMSOL.

CONCLUSION

Recent research in cell and tissue mechanics has shown that biological tissue and processes have characteristic mechanical properties (e.g., stiffness and single cell contractile forces) that can be used as independent biophysical biomarkers in clinical diagnosis. Thus, there has been a demand for micro/nano-Newton force sensing technology that help in mechanical characterization of tissue and cells as well as biological processes such as cell growth and differentiation. MEMS sensors and silicon-based CMOS fabrication technology are favorable choices to address the pressing need for biomedical lab-on-chip diagnostic and therapeutic devices because these technologies scale down to dimensions that can interface directly with individual cells. Moreover, thanks to well-developed CMOS technology, silicon-based sensing systems can be manufactured at a low-cost in large arrays for potentially testing populations of cells at a time, all alongside CMOS circuitry for single-chip signal processing.

The pillar-based, piezoresistive force sensor presented in this work has the necessary sub-µN force resolution paired with a small lateral form factor that lends itself for arraying. Moreover, the simple device fabrication that does not require micromachining release steps enables straight-forward integration with CMOS technology. Furthermore, analytical and numerical modeling highlight favorable scaling of the force sensor with the force sensitivity expected to increase proportional to R^{-2} while decreasing the pillar radius R and maintaining the pillar aspect ratio. The simple, CMOS compatible, fabrication process allows for arraying of the sensor across a single substrate to potentially form a low-cost, lab-on-chip device for testing large populations of cells.

Future work will focus on scaling down pillar and piezoresistor geometries to move towards nano-Newton force resolution as well as applying the developed sensor technology in biological applications.

ACKNOWLEDGEMENTS

This work has been funded in part by the National Science Foundation under award ECCS-1711259. The work was performed in part at the Georgia Tech Institute for Electronics and Nanotechnology, a member of the National Nanotechnology Coordinated Infrastructure (NNCI), which is supported by the National Science Foundation (ECCS-2025462). The authors would like to thank the staff of Georgia Tech's Institute for Electronics and Nanotechnology for help in device fabrication.

REFERENCES

[1] R. D. González-Cruz, V. C. Fonseca, and E. M. Darling, "Cellular mechanical properties reflect the differentiation potential of adipose-derived mesenchymal stem cells", *Proc. Natl. Acad. Sci.*, 109, E1523-E1529 (2012).

[2] Q. S. Li, G. Y. H. Lee, C. N. Ong, and C. T. Lim, "AFM indentation study of breast cancer cells", *Biochem. Biophys. Res. Commun.*, 374, 609-613 (2008).

[3] D. R. Myers, Y. Qiu, M. E. Fay, M. Tennenbaum, D. Chester, J. Cuadrado, Y. Sakurai, J. Baek, R. Tran, J. C. Ciciliano, B. Ahn, R. G. Mannino, S. T. Bunting, C. Bennett, M. Briones, A. Fernandez-Nieves, M. L. Smith, A. C. Brown, T. Sulchek and W. A. Lam, "Single-platelet nanomechanics measured by high-throughput cytometry," *Nature Materials*, 16, 230-235 (2017).

[4] H. J. Pandya, H. T. Kim, R. Roy, and J. P. Desai, "MEMS based low cost piezoresistive microcantilever force sensor and sensor module," *Material Science in Semiconductor Processing*, 19, 163-173 (2014).

[5] Y. Sun, and B. J. Nelson, "MEMS capacitive force sensors for cellular and flight biomechanics," *Biomedical Materials*, 2, S16-S22 (2007).

[6] T. C. Duc, J. F. Creemer and P. M. Sarro, "Piezoresistive Cantilever for Nano-Newton Sensing in Two Dimensions", 19th IEEE International Conference on Micro-Electro Mechanical Systems, (2006), pp. 586-589.

[7] J. C. Doll, B. C. Petzold, P. Ghale, M. B. Goodman, and B. L. Pruitt, "High frequency force sensing with piezoresistive cantilevers", Int. Solid-State Sensors, Actuators and Microsystems Conf. (Transducers 2009), (2009), pp. 1928-1931.

[8] J. C. Doll, N. Harjee, N. Klejwa, R. Kwon, S. M. Coulthard, B. C. Petzold, M. B. Goodman, and B. L. Pruitt, "SU-8 force sensing pillar arrays for biological measurements," *Lab on a chip*, 9, 1449-1454 (2009).

[9] J. Schwizer, M. Mayer and O. Brand, *Force Sensors for Microelectronic Packaging Applications*, Springer, 2004.

[10] P. Gieschke and O. Paul, "CMOS-integrated sensor chip for in-plane and out-of-plane shear stress", *Procedia Eng.*, 5, 1364-1367 (2010).

[11] A. A. Barlian, W. T. Park, J. R. Mallon, A. J. Rastegar and B. L. Pruitt, "Review: Semiconductor Piezoresistance for Microsystems", *Proceedings of the IEEE*, 97, 513-552 (2009).

CONTACT

*Oliver Brand, tel: +1-404-894-9425, oliver.brand@ece.gatech.edu

ULTRA-LOW NOISE, HIGH-SENSITIVITY MEMS ACCELEROMETER FOR SATELLITE GRAVIMETRY

Inês S. Garcia[1,2], Abdelrahman M. Elhawash[1], Jorge Cabral[2], Tiago Hormigo[3], João T. da Encarnação[4,5], Filipe S. Alves[1,2] and Rosana A. Dias[1]*

[1]International Iberian Nanotechnology Laboratory (INL), 4715-330 Braga, Portugal

[2]ALGORITMI Center, University of Minho, Campus Azurém, 4800-058 Guimarães, Portugal

[3]Spin.Works S.A., Portugal

[4]Delft University of Technology, Netherlands

[5]Center for Space Research, The University of Texas at Austin, USA

ABSTRACT

Satellite gravimetry requires sub-ng acceleration measurement at frequencies below 100mHz. To bring the performance of a MEMS accelerometer closer to this level, one must decrease noise sources and maximize sensitivity (to decrease input-referred electronic noise). Electrostatic pull-in based operation has great potential for high sensitivity since it relies on time transduction. Devices were fabricated with maximized proof mass (170mg over a 13x14mm2 footprint) and tuned damping coefficient (trade-off between noise and sensitivity – pull-in operation requires low Q-factors). Novel stopper designs and caps limit both in-plane and out-of-plane displacements. Devices tested using pull-in voltage-based transduction showed sensitivity of 218 V/g.

KEYWORDS

MEMS accelerometer, pull-in time, gravimetry, ultra-low noise, high-sensitivity

INTRODUCTION

The Earth has been suffering several climatic changes in the past few years that can drastically affect how we live. It is necessary to understand the progress of climatic change and how the various geophysical processes are interconnected, and satellite gravimetry has been shown to be valuable tool over the past few years since it allows to measure mass changes at the Earth's surface. Missions such as CHAMP (DLR), GRACE (DLR / NASA) and GOCE (ESA) have already offered solutions to this challenge, with high development and operational costs [1]. The accelerometer developed for the GRACE-FO mission, on the most sensitive axes, presented a noise spectral density below 0.1nm/s^2/√Hz in the range 10mHz to 1Hz [2]and below 1nm/s^2/√Hz at 0.1mHz.

In order to enable gravimetric missions using miniaturized satellites, geodetic-grade accelerometers with a small size, reduced power consumption and low fabrication costs are required. However, gravimetry and seismology applications require accelerometers with very demanding sensitivity, noise and low frequency specifications, capable of sub-ng acceleration measurements at frequencies below 100mHz.

MEMS devices have reached noise levels of 2.5nm/s^2/√Hz at frequencies below 1Hz [3], while conventional gravimeters can display similar performance even at 10mHz [4]. In electrostatically actuated parallel-plate MEMS structures, the pull-in transition can be explored as a transduction mechanism by applying a voltage higher than the pull-in voltage while measuring the time between the start of the actuation and the pull-in displacement detection [5].

The aim of this work is to develop a geodetic-grade 1-DOF MEMS accelerometer based on pull-in time transduction. A microstructure was therefore designed to maximize the sensitivity limits of this technology and minimize the Brownian noise.

PULL-IN TIME-BASED ACCELEROMETER

Working principle

A pull-in time-based MEMS accelerometer [6] uses electrostatically actuated parallel-plate microstructures that are constantly driven to pull-in. This requires that an actuation voltage higher than the threshold pull-in voltage, V_{PI}, is applied between the parallel-plates. This voltage generates an attraction force between the movable and the anchored plates. The nominal (in case no acceleration is applied) pull-in voltage is determined using (1), here d_0 is the initial distance between the parallel-plates, C_0 the rest capacitance and k the elastic spring constant [6]:

$$V_{PI} = \sqrt{\frac{8}{27}\frac{d_0^2 k}{C_0}} \quad (1)$$

The threshold pull-in voltage also depends on acceleration, according to (2) where m is the proof mass and a is the external acceleration.

$$V_{PI,a} = \sqrt{\frac{8}{27}\frac{(d_0 - ma/k)^2\, k}{C_0}} \quad (2)$$

While the microstructure is actuated to pull-in, a set of sensing electrodes is used to measure (capacitively) the movable mass displacement and this signal is used to detect a chosen displacement threshold corresponding to near full-gap displacement (comprising therefore the full pull-in transition).

Under certain actuation and damping conditions, the pull-in transition shows a highly nonlinear profile of displacement over time, including a plateau at the critical pull-in deflection (1/3 d_0), the so-called meta-stable region. The existence of this region renders the pull-in displacement, and the corresponding pull-in time very sensitive to external accelerations. The pull-in time is measured/counted from the start of the actuation (the moment when a step voltage applied, $V_{STEP}=\alpha V_{PI}$, where $1<\alpha\approx1$) until the proof-mass reaches a displacement well beyond the critical deflection, usually set between 80 and 95% of the full gap. This approach allows very high acceleration resolution since a time measurement is performed instead of a direct transduction of capacitance into acceleration. Moreover, differential measurements are used to improve linearity as well thermal compensation.

The sensitivity of a pull-in time accelerometer, closely related to the metastable region, depends on the actuation voltage (should be just slightly higher than the nominal pull-in voltage) and on the damping conditions – microstructures must present sufficient damping (b) since underdamped or high Q (quality factor) microstructures do not present metastability. The damper design is therefore critical since a trade-off must be met between maximizing sensitivity (b increase) and decreasing thermomechanical noise (b decrease) [6].

978-1-940470-04-7/HH2022/$25©2022TRF
DOI 10.31438/trf.hh2022.97

Designed Structures

In order to maximize acceleration sensitivity, the MEMS design focused on increasing both spring compliance and proof-mass for a maximum footprint of 13mm by 14mm, cf.in Figure 1, while tuning the damping coefficient.

The highly compliant springs have been achieved by exploring fabrication limits (at the limit between manufacturability/yield and compliance maximization), resulting in a design with six folded-springs suspending the large proof-mass (170mg, obtained by leaving a portion of the handle wafer attached to the movable structures).

Since devices with low-quality factors (between 0.5 and 2 – underdamped but near the critically damped condition) are targeted and the proof masses are quite large, it was necessary to increase the number of dampers. The squeeze-film damping is the main damping source, established in gap-changing parallel-plates. Dummy dampers have been previously implemented on the SOI handle wafer [5] but it was found that the damping coefficient achieved per unit of designed area is higher when implemented in the device layer dampers given the higher aspect ratios achievable.

In Table 1, the main design parameters of the intended devices are presented: two different types of devices have been designed, differing in the number of dampers.

Besides the performance specifications, space applications also require that the MEMS structure sustains large accelerations during launch and detachment. For the sake of increasing the robustness of the structures, the designs included both the conventional in-plane mechanical stoppers at 2.9µm (full gap: 3µm) as well as cantilever-like ones at 2.8µm to gradually absorb impact (Figure 1). Additionally, out-of-plane displacement stoppers were implemented by fabricating encapsulation structures.

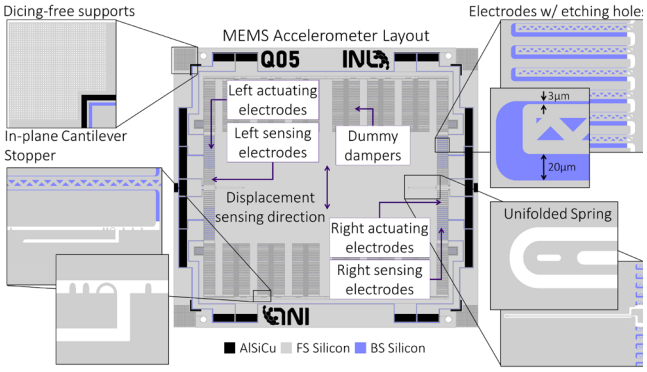

Figure 1. Designed and fabricated MEMS device (total die size: 13mm by 14mm).

Table 1. Microstructure's theoretical design parameters

Parameters	**S1**	**S2**
Mass, m $[mg]$	170	
Resonance Freq., Fn $[Hz]$	21.15	
Spring stiffness, k $[N/m]$	3.00	
Initial gap, d_0 $[\mu m]$	3.00	
Damping coeff., b $[mN.s/m]$	45.2	11.3
Number of dampers	898	224
Quality factor, Q	0.5	2.0
Brownian Noise, a_n $[nm/s^2/\sqrt{Hz}]$	167.80	83.90
Pull-in Voltage, V_{PI} $[V]$	2.38	
Pull-in time sensitivity, $[ms/(um/s^2)]$	1.174	0.014

DEVICE MICROFABRICATION

The accelerometers were fabricated using a three-mask dicing free MEMS process on a 50µm-thick active layer SOI wafer, as presented in [5]. The main fabrication steps are depicted in Figure 2. The fabricated devices are shown in Figure 3.

(a) Wafer preparation: Initially, alignment marks are patterned on the wafer frontside – FS and backside – BS to ensure the alignment between the structures on both sides.
(b) Metal Layer: A thin layer of AlSiCu, 500 nm, is sputtered on the FS and patterned for the electrical contacts.
(c) FS and BS SiO2 layer deposition: A 3 µm layer of silicon dioxide (SiO2) is deposited on both sides of the SOI wafer by plasma-enhanced chemical vapour deposition (PECVD).
(d) FS and BS Hard-mask patterning: The BS and FS oxide layers are then patterned by a reactive ion etching (RIE), to define the hard-masks for the subsequent silicon deep reactive ion etching (DRIE) step.
(e) FS and BS DRIE: The front and back sides are consecutively etched through DRIE, using the buried oxide as etch stop.
(f) Device release: The structures are finally released using hydrogen fluoride (HF) vapor etching.

Two different caps, serving as out-of-plane displacement stoppers, have been fabricated: one for the device bottom part that must accommodate the out-of-plane displacement due to earth gravity (not present in the final application, but necessary to be considered during the device characterization); and, a top side cap that limits the upper device displacement, preventing the collision

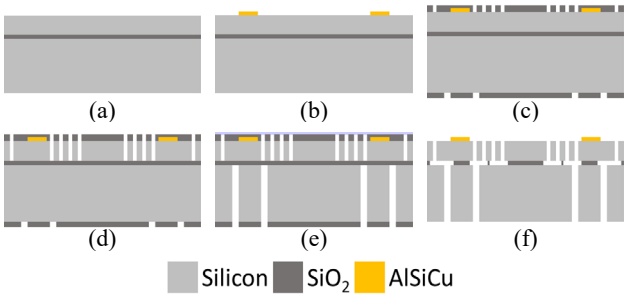

Figure 2: Accelerometer SOI-based fabrication process.

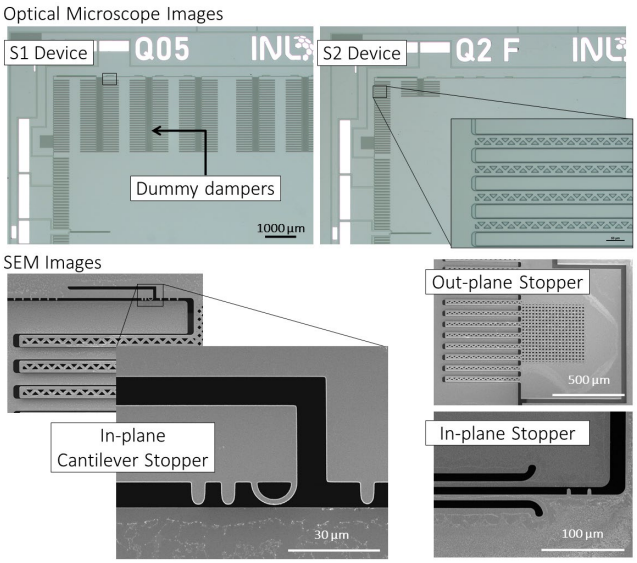

Figure 3. Designed and fabricated MEMS device (total die size: 13mm by 14mm).

of movable mass with the dummy dampers in the device layer. These caps were fabricated using a three-mask standard process on a SSP (Single Side Polished) wafer. The main fabrication steps are presented in Figure 4.

(a) FS and BS SiO2 layer deposition: a 3 µm and 5 µm layer of SiO2 is deposited on the FS and BS of the SSP wafer by PECVD.
(b) FS and BS hard-mask patterning: On the FS, a sequential SiO2 patterning is performed by two different lithography steps and by RIE process to create the multilevel hard-mask.
(c) The BS hard-mask is also patterned by RIE. The FS multilevel mask creates the cavity for the bottom caps and the top stoppers/pillars.
(d) FS 1st DRIE: The front side is initially etched through DRIE to a depth of 19um.
(e) FS hard-mask thinning DRIE: The FS SiO2 hard-mask is thinned by RIE until the thinner level is wholly removed.
(f) FS 2nd DRIE: Then, the front side Si is etched again. So the previously etched areas ended with 20um depth and the top stoppers with 1um.
(g) BS DRIE and cap release: Finally, the caps are etched by the BS through DRIE until the FS is reached and the caps are released from the wafer.

Given the large mass and the highly compliant springs, the resultant out-of-plane displacement is significant (around 10 µm as a result of the Earth's gravity). Therefore, these bottom and top caps are essential to ensure that the device does not get damaged or even break in the handling process and experimental testing. Closed top and bottom caps are also required for MEMS encapsulation.

The fabricated caps limit the out-of-plane displacement of the proof-mas to 20 µm in the negative z/down direction and 1 µm in the positive z/upper direction. This 1 µm limitation is fundamental as it prevents the movable mass (that includes handle layer silicon with a nominal gap of 2um defined but the BOX layer) from colliding with the dummy dampers. The encapsulation scheme and the final device are depicted in Figure 5.

EXPERIMENTAL RESULTS

Experimental Setup

The experimental setup used to evaluate the fabricated microstructures (1) comprises a charge amplifier circuit for capacitive displacement readout (2) and a data acquisition board for the readout voltage acquisition and actuation signal generation, mounted on a high-resolution 6-axis stage from ThorLabs (3), as displayed in Figure 6. The setup is fixed to an anti-vibration table (4) to minimize surrounding vibrations/noise interference.

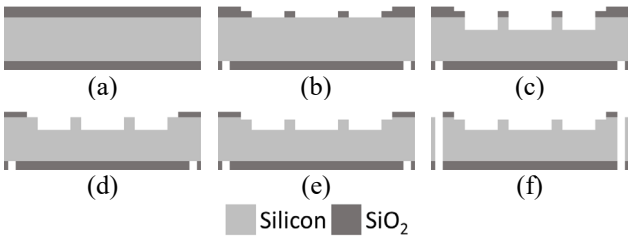

Figure 4. Out-plane stopper cap fabrication process.

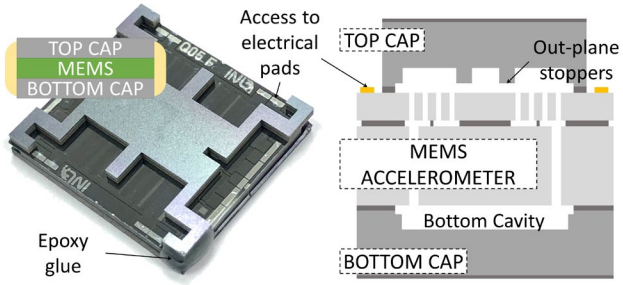

Figure 5. Device encapsulation (top and bottom caps).

Initially, with this high-resolution stage, it is possible to balance the structure to the rest position by correcting the tilt (that results from assembling the MEMS with the caps and its placement in the carrier). The external accelerations are induced in the accelerometer (acc_{ext}) by the tilting of the MEMS structure in the sensing direction, being null when the device is in its rest position and equal to the gravitational acceleration component along the device's sensing axis (acc_g). The proof-mass displacement will affect the gap of the sensing electrodes and with a capacitance to voltage readout circuit it's possible to electrically measure the external acceleration.

In parallel to the microstructure design and fabrication, a low noise electronic readout circuit was also pursued – given the low frequencies targeted, it becomes critical to reduce 1/f noise sources.

Performance Analysis

1) MECHANICAL FEATURES ANALYSIS:

Both devices (S1 and S2) were experimentally characterized for natural frequency (Fn), and quality factor. These features depend directly to the MEMS devices mechanical properties, such as mass, spring constant and damping coefficient, which in turn depend on layout and microfabrication parameters such as over-etch and notch. Both devices were evaluated by SEM inspection. The fabricated devices showed a silicon over-etch smaller than expected on the backside and in the electrodes regions, resulting in a larger proof-mass and a higher damping coefficient (smaller gap in the dampers). The springs' cross-section presented a trapezoidal shape, having a larger width in the device layer top surface and smaller in the near-BOX surface, which should translate to a lower stiffness. This resulted in lower Fn and Q, as depicted in the experimental measurements from Figure 7. Devices parameters extracted from measurements are detailed in Table 2. Furthermore, the nominal pull-in voltage of both devices was also experimentally characterized and is also presented in Figure 7.

2) PULL-IN VOLTAGE SENSITIVITY:

Given the mechanical properties achieved in device S2, this was used to validate pull-in operation. The pull-in voltage was measured for several external accelerations, resulting in the pull-in voltage sensitivity of 218 V/g, presented in Figure 8.

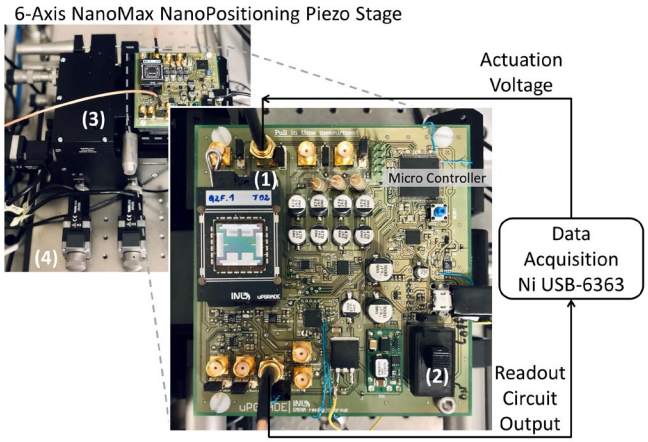

Figure 6. Experimental setup for device characterization.

CONCLUSIONS

A MEMS accelerometer based on pull-in time transduction is presented for geodetic applications. The devices were fabricated through a dicing-free standard SOI-based process, using 50 µm-thick device layer. Furthermore, to ensure the yield of the devices, encapsulation structures were also fabricated. The proposed designs show a large proof-mass (170 mg) with dummy parallel-plates patterned in the device layer to significantly increase the damping coefficient, critical in pull-in-based accelerometers. This approach has been analyzed and implemented using two different designs, differing in the number of dampers and resulting quality factor (device S1 with a theoretical Q factor of 0.5 and S2 with 2). The fabricated devices were experimentally characterized to determine the actual mechanical features and the device behaviour. A silicon over-etch smaller than expected was observed, resulting in smaller electrodes' and dampers' gaps, and a Q-factor of 0.36 and 0.65 were characterized for the devices S1 and S2, respectively. Furthermore, the pull-in voltage of the device S2 was characterized since this was the device that presented the damping coefficient in the desired region, and a pull-in voltage sensitivity of 218 V/g was measured.

The pull-in time sensitivity measurement is currently being pursued since this is a key performance parameter. The high sensitivities expected for these accelerometers may position them as good candidates for the realization of high-performance MEMS geodetic-grade accelerometers. Noise performance and long-term stability are also currently under investigation.

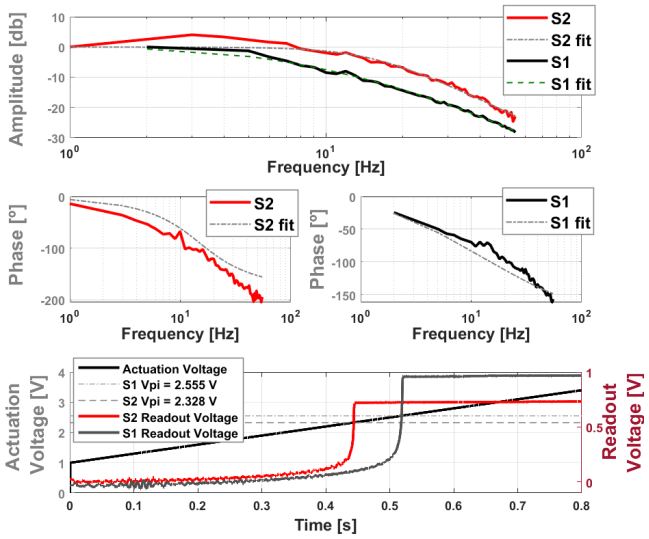

Figure 7: Experimental preliminary characterization of a fabricated S2 device.

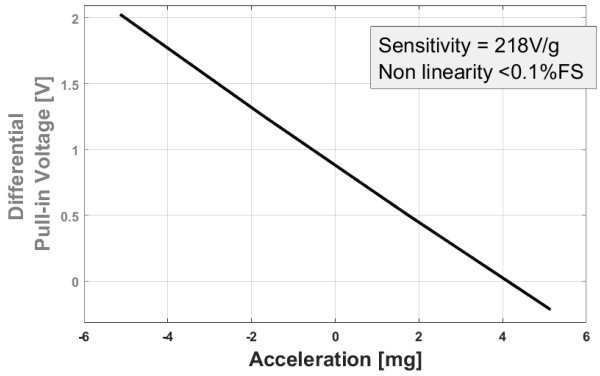

Figure 8: S2 differential pull-in voltage sensitivity, 218 [V/g].

Table 2. Microstructure's experimental parameters

Parameters	**S1**	**S2**
Mass, m $[mg]$	174	177
Resonance Freq., Fn $[Hz]$	11.8	14.9
Spring stiffness, k $[N/m]$	2.64	
Initial gap, $d0$ $[\mu m]$	2.2	
Damping coeff., b $[mN.s/m]$	94.3	24.1
Number of dampers	898	224
Quality factor, Q	0.36	0.65
Pull-in Voltage, V_{PI} $[V]$	2.56	2.33

ACKNOWLEDGMENTS

These developments have been carried out under the project uPGRADE - Miniaturized Prototype for Gravity field Assessment using Distributed Earth-orbiting assets (reference POCI-01-0247-FEDER-045927), co-funded by COMPETE 2020 - Operational Programme for Competitiveness and Internationalization under the PORTUGAL 2020 Partnership Agreement, through the European Regional Development Fund (ERDF), and by the Portuguese Foundation for Science and Technology (FCT) under the UT Austin Portugal Program.

REFERENCES

[1] B. D. Tapley, "GRACE Measurements of Mass Variability in the Earth System," *Science (1979)*, vol. 305, no. 5683, pp. 503–505, 2004, doi: 10.1126/science.1099192.

[2] B. Christophe *et al.*, "A new generation of ultra-sensitive electrostatic accelerometers for GRACE Follow-on and towards the next generation gravity missions," *Acta Astronautica*, vol. 117, no. September 2010, pp. 1–7, 2015, doi: 10.1016/j.actaastro.2015.06.021.

[3] W. T. Pike, I. M. Standley, S. B. Calcutt, and A. G. Mukherjee, "A broad-band silicon microseismometer with 0.25 NG/rtHz performance," in *Proceedings of the IEEE International Conference on Micro Electro Mechanical Systems (MEMS)*, 2018, vol. 2018-January. doi: 10.1109/MEMSYS.2018.8346496.

[4] R. P. Middlemiss, A. Samarelli, D. J. Paul, J. Hough, S. Rowan, and G. D. Hammond, "Measurement of the Earth tides with a MEMS gravimeter," *Nature*, vol. 531, no. 7596, 2016, doi: 10.1038/nature17397.

[5] I. S. Garcia, E. E. Moreira, R. A. Dias, J. Gaspar, F. S. Alves, and L. A. Rocha, "Sub-Micron Mems Accelerometer with Handle-Layer Patterning for Damping Enhancement Using Time Transduction," in *2019 20th International Conference on Solid-State Sensors, Actuators and Microsystems and Eurosensors XXXIII, TRANSDUCERS 2019 and EUROSENSORS XXXIII*, 2019, pp. 2045–2048. doi: 10.1109/TRANSDUCERS.2019.8808247.

[6] R. A. Dias *et al.*, "Real-Time Operation and Characterization of a High-Performance Time-Based Accelerometer," *Journal of Microelectromechanical Systems*, 2015, doi: 10.1109/JMEMS.2015.2487686.

CONTACT

*Rosana A. Dias; rosana.dias@inl.int.

WAFER-LEVEL HIGH-ASPECT-RATIO DEEP REACTIVE ION ETCHING OF 4H-SILICON CARBIDE ON INSULATOR SUBSTRATES

Ardalan Lotfi[1], Michael P. Hardin[1], Zhenming Liu[1], Alex Wood[2], Chris Bolton[2], Kevin Riddell[2]
Huma Ashraf[2], Joanne Carpenter[2], and Farrokh Ayazi[1]
[1]Georgia Institute of Technology, Atlanta, GA, USA
[2]SPTS Technologies – A KLA Company, Ringland Way, Newport NP18 2TA, UK

ABSTRACT

This paper reports on the results of high-aspect-ratio (HAR) Deep Reactive Ion Etching (DRIE) of thick 4H-SiC on Insulator (SiCOI) substrates at wafer-level and outlines the progress and challenges. Different size vertical trenches with high aspect-ratios of 15:1 ~ 20:1 and smooth sidewalls were achieved using electroplated nickel mask on 100mm SiC wafer, and a trench depth uniformity of 2% (±1µm) was measured across the wafer. The transferred recipe on SiCOI substrate was able to reach the buried oxide on all corners of the patterned SiCOI area while it created footing less than 100nm. The trench taper angle was 88.5º with a smooth sidewall, roughness < 120nm, resulting in 4H-SiC bulk acoustic wave resonators with Qs > 2M. These HAR DRIE results at wafer-level are a promising step to enable volume-manufacturing of ultra-high Q SiC resonators, which was previously done at die/small piece level.

KEYWORDS

SiC, SiCOI, DRIE, high-aspect-ratio, ultra-high Q, BAW

INTRODUCTION

Micromechanical resonators have several applications in consumer electronics, robotics, wearable sensors, and inertial navigation. Resonance quality factor is a key performance metric to evaluate the robustness of these micro-electromechanical devices. Although silicon is a well-established material for high-Q resonator applications, monocrystalline SiC promises much smaller intrinsic phononic loss for ultra-high Q applications, potentially 30x smaller than silicon counterparts [1]. Bonded monocrystalline SiCOI substrates allow MEMS device manufacture by providing a layer for release, and are a promising platform for the implementation of ultra-high Q resonators and coriolis gyroscopes owing to SiC's exceptionally high Akhiezer limit (*f·Q=6e14 Hz*) [2].

Silicon carbide is a difficult-to-etch material, and HAR etching of SiC [3-6] is a dirty process due to requiring a hard metal mask such as nickel. The high-aspect-ratio etching of SiC is even more difficult due to the non-volatile etch by-product, i.e. NiC_xF_y, that alters the trench profile by blocking the trench opening, and changes the chamber condition by depositing on the etch chamber sidewall [1, 7]. The passivation growth causes major drift in the trench profile and sidewall surface roughness.

The lack of suitable high-density plasma etching tools with reasonable Mean Time Between Cleans (MTBC) of 100~130 hours at universities, along with the high cost of SiC wafers have hindered the development of HAR DRIE of SiC at wafer level. In addition to the challenge of precisely micromachining SiC [3, 8, 9], other barriers inhibiting the development of SiC MEMS include high material cost and difficult and time-consuming fabrication processes to manufacture SiC-on-Insulator (SiCOI) substrates. The sum of above-mentioned challenges makes the wafer-level implementation and study of thick 4H-SiC capacitive devices challenging and expensive. This paper reports on the progress that has been made in the HAR DRIE of 4H-SiCOI substrate at wafer level using industrial high-density plasma etching tools.

MATERIAL AND METHODS FOR HAR DRIE OF 4H-SIC-ON-INSULATOR

We fabricated 100mm 4H-SiCOI substrates by bonding SiC wafers to silicon handle wafers using SiO_2 TEOS as an intermediate bonding layer, followed by grinding and polishing. The buried oxide thickness was ~3µm and the targeted device layer thickness was 40µm. Several SiC and SiCOI wafers were coated with Cr/Au seed layers, patterned with AZ 9260 PR and nickel electroplated for ~6.5µm, Figure 2. The CD size for the device fabrication at wafer level was 3.5µm, although the nickel mask on these wafers included openings with several dimensions to study the DRIE lagging effect. To preserve samples and reduce development cost, the HAR DRIE recipe development plan included multi-stage transition from bulk SiC wafer piece to SiCOI wafer piece followed by a bulk SiC whole wafer and finally, transferring the recipe to SiCOI whole wafer. The 4H-SiC HAR DRIE recipe was developed at SPTS Technologies, using a Synapse™ module, Figure 2. The Synapse™ uses a doughnut shaped RF source to produce a high-density plasma for the etching of strongly bonded materials such as SiC, with improved mean time between cleans. The details of a typical baseline SiC DRIE recipe are presented elsewhere [10].

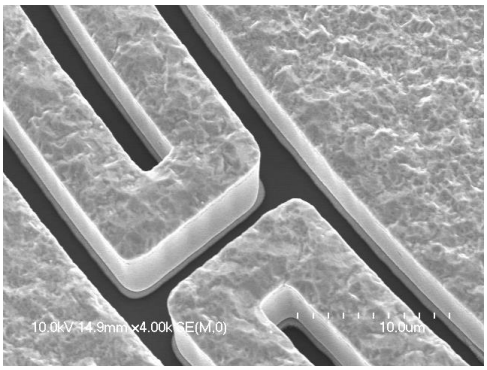

Figure 1: SEM of electroplated nickel mask (6.5 µm). The remaining seed layer on the substrate at the border of Ni mask reveals the sidewall are not completely vertical.

The requirements for the HAR DRIE etching of a 3.5µm CD trench feature in SiC focussed on achieving the 45µm target depth to reach the oxide stop layer while avoiding damage from the process, such as sidewall roughness and notching. To achieve this, development was started in the SPTS Synapse™ module by etching the target feature with a process typically used for 50µm CD through-wafer-via applications. The key modifications to this process that allow clean etching of the trench features were the reduction of pressure, reduction of platen power, and increased gas flows. The alterations to gas flows and platen power increased the etch rate of the feature. In the case of the gas, this allows more chemical etching of the SiC, and for the platen power it is suggested that reduced platen power limits the sputtering of the Ni

978-1-940470-04-7/HH2022/$25©2022TRF
DOI 10.31438/trf.hh2022.98

mask into the feature opening. Transfer of the process to SiCOI wafers was completed to the target depth, with low sidewall roughness and minimal notching on the oxide layer.

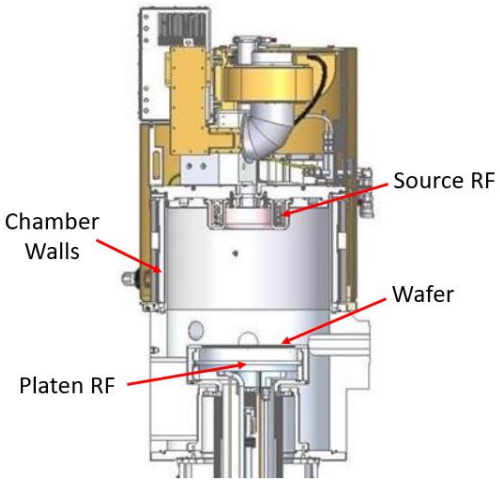

Figure 2: Schematic of the SPTS Technologies Synapse™ module

EXPERIMENT RESULTS

As mentioned above, different mask openings were present in the test pattern to investigate the effect of the mask opening on the etch depth achievable in a fixed time, in this case 65 minutes. The results are summarized in Figure 3. Figure 4 depicts the optical image of the first whole SiCOI wafer etched after the multi-stage recipe transfer from SiC and SiCOI wafer pieces to whole wafers. The cross-sectional SEMs of Figure 5 show the electroplated nickel mask is not vertical at the very top, causing some seed layer to remain due to shadowing effect. However, this has minimal effect on the process. To ensure that the etch recipe reached the buried oxide across SiCOI wafer, 3.6µm CD trench features on SiC wafers were etched to as deep as 57µm with etch rate of 635nm/min and taper angle of 88.5º, Figure 6. The main challenge of etching SiC at wafer level with nickel mask is a knifing effect (illustrated in Figure 7) that occurs due to variations in the thickness of electroplated nickel mask across the wafer. Ni mask recession near the feature edges can create a tapered mask that will exacerbate the issue. It was observed that the addition of an extra 500nm of nickel mask can avoid such damage to the trench opening. In Figure 8, the post-cleaning (using HNO_3) SEM image of HAR DRIE SiCOI sample presented the etch reaching buried oxide at 43µm depth with taper angle of 88.6º, footing < 100nm and sidewall roughness < 120nm. SiCOI wafer-level HAR DRIE resulted in successful fabrication of very high-Q > 2M gyroscopic disk resonators, limited by the thermoelastic damping due to roughness in the trench sidewall, with small as born frequency split, Figure 9. The frequency response of two degenerative modes of BAW disk resonator are shown in Figure 10.

DISCUSSION

The main challenge of transferring SiC DRIE from wafer pieces to the whole wafer is preserving the quality of trench profile while achieving good etch uniformity across the wafer. Lowering the pressure and increasing bias power enhance the etch uniformity; however, it comes at the cost of degrading mask selectivity and increasing sidewall roughness. In the following, several concerns with HAR DRIE of SiCOI are discussed.

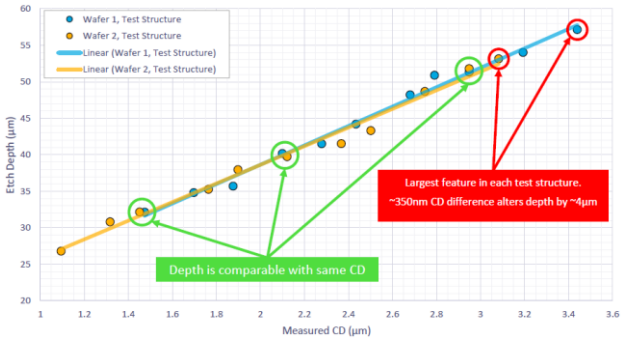

Figure 3: Plot of measured CDs on Ni mask vs etch depth (µm) after 65 minutes DRIE process on whole wafer SiC sample.

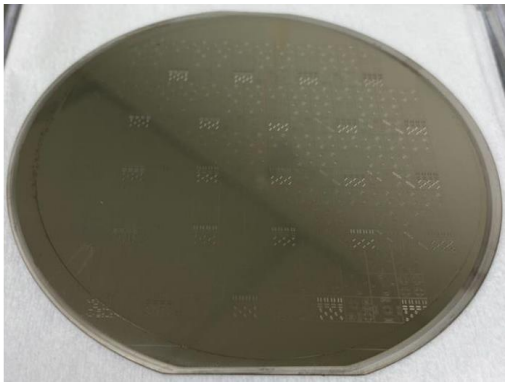

Figure 4: Optical image of a SiCOI substrate after high-aspect-ratio DRIE process using Omega® Synapse™ module.

Ni Mask Erosion and Critical Dimension (CD)

The reduction in mask selectivity can be mitigated by adding to the thickness of electroplated nickel. However, electroplated mask forms around the patterned photoresist, and its verticality depends on the cross-section profile of developed photoresist. Due to the nature of capacitive devices, our design desires a gap width of only a few microns, and 6µm thick electroplated nickel mask is needed to etch 40µm deep into SiC. Realizing such high aspect ratio photoresist with vertical sidewall is a crucial step in the mask preparation process, and therefore optimizing the lithography step prior to the electroplating nickel is a critical task.

It was also observed that achieving a high aspect ratio photoresist with complete vertical walls from bottom to top is a challenging task, since they usually tend to narrow down at the top of the photoresist feature. This feature non-ideality causes the CD to shrink in the case of over-electroplating. It worth noting that the mask thickness variation across the wafer also plays a role in CD variation changes at different location of the wafer based on the same principle.

Mask CD Variations and DRIE Lag Effect

The limits of deep reactive ion etching of high-aspect-ratio trenches into silicon carbide material using nickel mask was studied through various CD sizes, 1µm to 3.4µm, as shown in Figure 3. The lagging effect is pronounced for smaller CD sizes while trench aspect ratio slightly increases. The aspect ratio of 15:1 was achieved for 3.4µm openings while smaller CDs achieved higher aspect ratio of 20:1. The etch depth based on CD size assured that few hundreds of nanometer variations in CD size would not have significant effect on the etch uniformity.

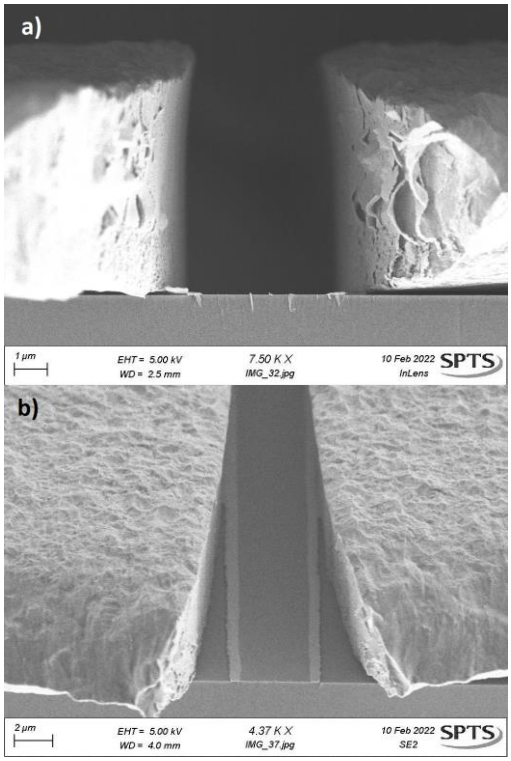

Figure 5: (a) Cross-sectional SEM image of electroplated nickel showing the mask sidewall is not completely vertical. b) Angled view of mask after cleaving which emphasizes the remaining seed layer caused by overhanging nickel during seed layer removal step.

Knifing Effect

As mentioned before, methods used to increase uniformity across a whole wafer reduces mask selectivity during etch processing. It is observed that mask is consumed at the trench opening faster than areas of blanket nickel. The knifing effect happened when trench opening loses the mask protection due to excessive recession of the nickel at the trench opening. The several stages of knifing effect are shown in Figure 7; it was seen this effect caused the passivation to peel off, damaging the trench opening and blocking plasma from the bottom of the trench. Since mask selectivity is calculated based on the mask bulk etch rate, it is not valid for the immediate vicinity of the trench opening. Therefore, it added further complication in defining mask thickness to successfully etch certain depth into SiC without damage to the trench opening while maintain good etch uniformity.

Notching/Footing Effect

In contrast to the knifing effect altering the trench opening at the top, the footing effect occurs at the bottom of the trench where silicon carbide meets underneath insulator layer. A low footing value of < 100nm was achieved on SiCOI wafers. It can be noted that etching SiC uniformly across the wafer is not the only key parameter to keep the footing minimized across the whole SiCOI wafer. The SiCOI device layer total thickness variation (TTV) also plays a crucial role in achieving minimum footing. A low TTV coupled with good uniformity from the etch process results in reduced overetch on the insulator layer, minimizing footing.

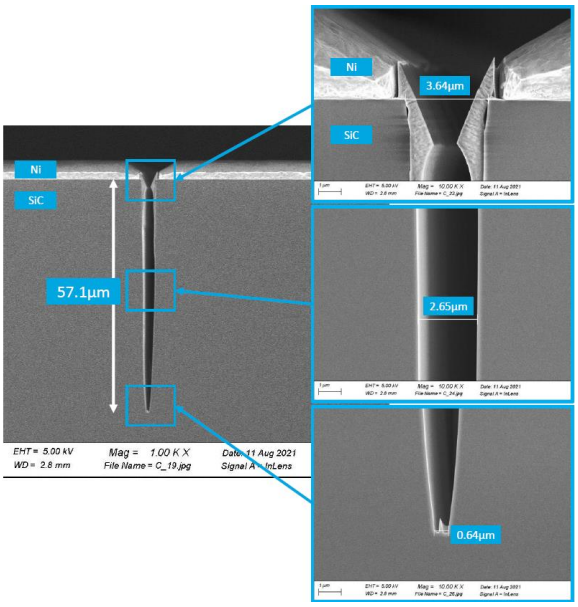

Figure 6: SEM image of HAR DRIE on SiC, it achieved aspect-ratio greater than 15:1 (57:3.6) with Ni mask selectivity of 28:1, 635nm/min etch rate and 88.5° taper angle.

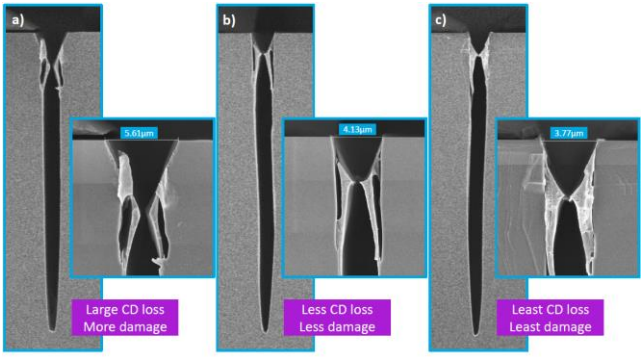

Figure 7: SEM of three different damage profiles caused by the mask thickness variation across the wafer, leading to knifing effect/passivation peel-off.

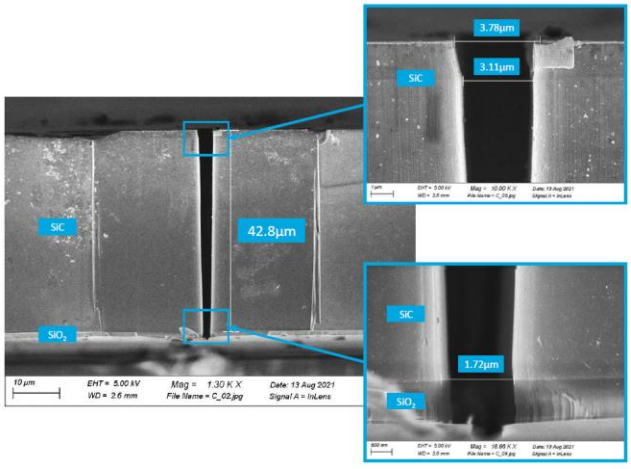

Figure 8: SEM image of HAR DRIE on SiCOI sample after cleaning process. Etch depth was 42.8µm with taper angle of 88.6°, footing < 100nm and sidewall roughness < 120nm.

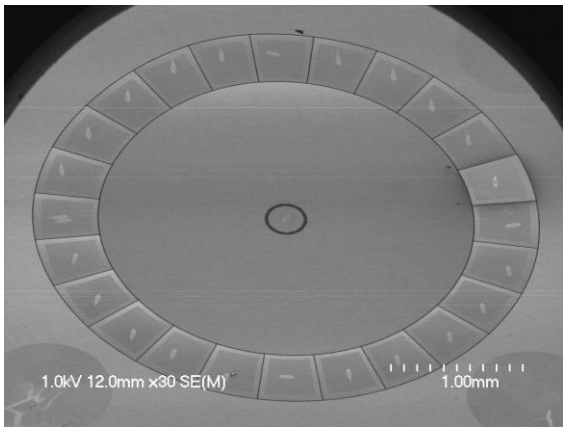

Figure 9: SEM image of a fabricated BAW disk resonator with Q > 2M from the wafer-level HAR DRIE on SiCOI substrate.

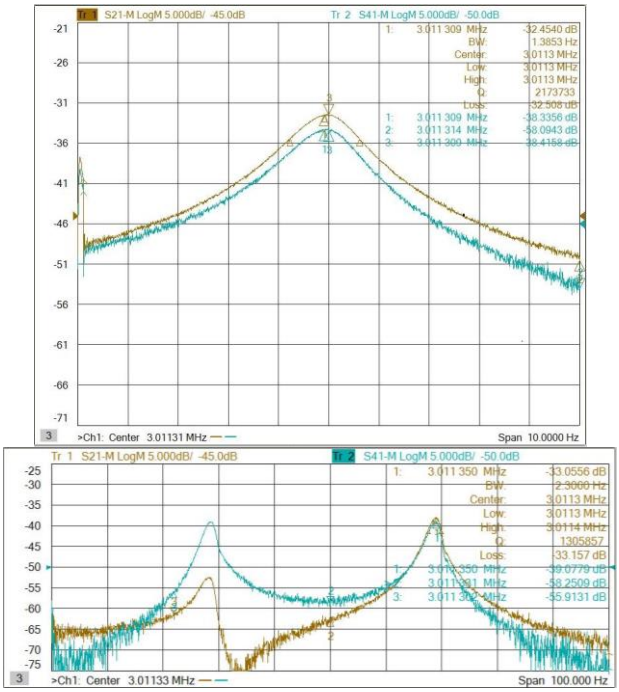

Figure 10: frequency response and Q measurement of the fabricated BAW disk resonator with Q > 2M from the wafer-level HAR DRIE on SiCOI substrate (top). Worst case frequency split of 40Hz measured for a 3MHz m=3 elliptical BAW resonator (~13.5ppm) on the wafer (bottom).

CONCLUSION

For the first time, the results of high-aspect-ratio (HAR) DRIE of thick 4H-SiC on Insulator (SiCOI) at wafer-level were presented. Using 6.5µm electroplated nickel mask, vertical trenches with aspect-ratios of 15:1 ~ 20:1 for CD size of only a few microns were achieved. The trench taper angle was 88.5º with a sidewall roughness less than 120nm, resulting in 4H-SiC bulk acoustic wave resonators with resonance quality factor greater than 2M at 3MHz. Even though the HAR DRIE of SiC faces several challenges consisting excessive mask erosion, mask CD variation and the knifing effect, the presented wafer-level results are a promising step to enable volume-manufacturing of ultra-high-Q monocrystalline SiC resonators.

ACKNOWLEDGEMENTS

This material is based on research sponsored by Army Research Laboratory under agreement number W911NF-19-2-0345. The U.S. Government is authorized to reproduce and distribute reprints for Government purposes notwithstanding any copyright notation thereon. The views and conclusions contained herein are those of the authors and should not be interpreted as necessarily representing the official policies or endorsements, either expressed or implied, of Army Research Laboratory (ARL) or the U.S. Government.

CONTACT

Ardalan Lotfi, alotfi6@gatech.edu
Farrokh Ayazi, ayazi@gatech.edu

REFERENCES

[1] B. Hamelin, J. Yang, and F. Ayazi, "Precision Deep Reactive Ion Etching of Monocrystalline 4H-SiCOI for Bulk Acoustic Wave Resonators with Ultra-Low Dissipation," *Journal of the Electrochemical Society,* vol. 168, no. 1, p. 017512, 2021.

[2] F. Ayazi, L. Sorenson, and R. Tabrizian, "Energy dissipation in micromechanical resonators," in *Micro-and Nanotechnology Sensors, Systems, and Applications III*, 2011, vol. 8031: International Society for Optics and Photonics, p. 803119.

[3] K. M. Dowling, E. H. Ransom, and D. G. Senesky, "Profile evolution of high aspect ratio silicon carbide trenches by inductive coupled plasma etching," *Journal of Microelectromechanical Systems,* vol. 26, no. 1, pp. 135-142, 2016.

[4] L. E. Luna, M. J. Tadjer, T. J. Anderson, E. A. Imhoff, K. D. Hobart, and F. J. Kub, "Dry etching of high aspect ratio 4H-SiC microstructures," *ECS Journal of Solid State Science and Technology,* vol. 6, no. 4, p. P207, 2017.

[5] L. E. Luna, M. J. Tadjer, T. J. Anderson, E. A. Imhoff, K. D. Hobart, and F. J. Kub, "Deep reactive ion etching of 4H-SiC via cyclic SF6/O2 segments," *Journal of Micromechanics and Microengineering,* vol. 27, no. 9, p. 095004, 2017.

[6] K. Racka-Szmidt, B. Stonio, J. Żelazko, M. Filipiak, and M. Sochacki, "A Review: Inductively Coupled Plasma Reactive Ion Etching of Silicon Carbide," *Materials,* vol. 15, no. 1, p. 123, 2021.

[7] B. Hamelin, J. Yang, A. Daruwalla, H. Wen, and F. Ayazi, "Monocrystalline silicon carbide disk resonators on phononic crystals with ultra-low dissipation bulk acoustic wave modes," *Scientific reports,* vol. 9, no. 1, pp. 1-8, 2019.

[8] L. E. Luna, K. D. Hobart, M. J. Tadjer, R. L. Myers-Ward, T. J. Anderson, and F. J. Kub, "SiC wafer bonding and deep reactive ion etching towards high-aspect ratio SiC MEMS fabrication," *ECS Transactions,* vol. 86, no. 5, p. 105, 2018.

[9] J. Yang, B. Hamelin, and F. Ayazi, "Capacitive Lamé Mode Resonators in 65µm-Thick Monocrystalline Silicon Carbide with Q-Factors Exceeding 20 Million," in *2020 IEEE 33rd International Conference on Micro Electro Mechanical Systems (MEMS)*, 2020: IEEE, pp. 226-229.

[10] A. Barker *et al.*, "Advances in back-side via etching of SiC for GaN device applications," in *CS MANTECH Conference*, 2013, pp. 13-16.

ZERO-POWER MULTI-THRESHOLD TEMPERATURE SENSOR BASED ON SHAPE MEMORY ALLOY ANTENNA

Wenxin Zeng, Wei Wang, and Sameer Sonkusale[*]
Department of Electrical and Computer Engineering, Tufts University, USA
Nano Lab, Advanced Technology Laboratory, Tufts University, USA

ABSTRACT

Monitoring critical temperature transition events is essential for perishable goods during transportation. However, conventional sensors require expensive electronics and continuous power sources for their functioning, which makes it impractical for cost and logistical reasons for monitoring a large number of goods. Based on our previous work using shape memory alloy or SMA, we propose a zero-power multi-section SMA-wire-based antenna that can record multiple levels of critical temperature crossing events without any need for peripheral electronic components or batteries. This paper presents details of fabrication and test/validation efforts of the shape memory effect of the conjoined multi-section SMA antenna for the recording of temperature violation events.

KEYWORDS

Antenna, temperature threshold sensor, shape memory alloy, zero-power sensors, near-zero sensors.

INTRODUCTION

With the advent of the era of Internet-of-Things (IoT), there has been a growing need for smart sensors that are low-cost and energy-efficient. In scenarios where a large number of sensors are needed, conventional sensors that consist of electronic memory, controller units, and power supply are quite expensive to deploy at a large scale. The need for a continuous power source is a logistical bottleneck in many applications. Recently, zero-powered sensors have been investigated to address this need. This includes humidity sensors [1,2,3,4], strain sensors [5,6], and tile sensors [7,8]. Other zero-power single-event sensors such as photoswitches [9], package security sensors [10,11], liquid level sensor [12], corrosion sensor [13], and home security sensors [14,15,16] have also been reported, employing different techniques for fabrication. For communication of sensor information, passive Radio-frequency identification (RFID) tags are preferred since it does not need a battery and relies on the backscattering of signal sent by an interrogating reader [17,18].

While the aforementioned sensors may offer zero-power real-time detection, they need peripheral electronic devices to record the sensed information until it is read out by the reader. This data-logging operation is in by itself power-hungry. In some applications, a detailed recording of the whole time is unnecessary, and only some critical events are of interest to the monitoring personnel. For instance, certain goods need to be stored in a certain temperature range, such as chemicals and drugs [19]. Violation in temperature can cause degradation or even adverse effects on these products. Conventional sensors would record the whole temperature history of the goods, while in reality, one is only interested in monitoring whether the temperature threshold was ever crossed. Thus, it will be beneficial to develop a zero-power sensor that can also record those temperature events in by itself for posterity without the need for data logging memory units.

Due to its thermal-mechanical properties, shape memory alloy (SMA) can be used for recording temperature events. It has been used for reconfigurable antenna [20] and temperature sensing [21,22]. In prior work, a battery-free threshold temperature sensor was developed by utilizing the shape change of the SMA as a detector/recorder of events [23]. Relying on the shape memory effect of SMA, the antenna irreversibly changes its configuration from parallel to dipole antenna when the temperature rises above the threshold value. As a result, its radiation profile is altered. The antenna would lock this configuration even after the temperature drops back below the threshold temperature value. This sensor is used to record the temperature violation event without a memory device and power supply, but its usage is limited to monitoring a single threshold level crossing. This article proposes an SMA-based multi-threshold temperature sensor, which can monitor the goods with more detailed historical temperature information and multiple threshold temperature level crossing events. The sensor consists of two SMA sections with different temperature thresholds to provide a more complex shape reconfiguration. This can be scaled up to multiple sections for a more complex temperature monitoring profile.

PRINCIPLE OF SENSOR OPERATION

Properties of Shape Memory Alloy

SMAs are metals that have a memory effect depending on environmental temperature. Most SMAs are alloys made of nickel and titanium. At a low temperature, the SMA is in its martensite state. Atoms are loosely patterned in this state so that the shape of SMA can be easily modified. While at high temperature, the SMA is in the austenite state, where the atoms are tightly arranged, making the whole SMA stiff and rigid [24,25]. When the temperature rises above the threshold, heat is absorbed by the SMA, and the rearranging force between atoms makes the SMA recover to its predefined shape, regardless of its previous deformed shape, which presents the memory effect. As shown in Figure 1, the start and end temperatures for the state-changing from martensite to austenite are A_s and A_f, respectively; the start and end temperatures for the state changing from austenite to martensite are M_s and M_f, respectively [26,27]. Due to the hysteresis, the SMA will keep its shape in austenite form, even if the temperature drops below A_s but above M_s.

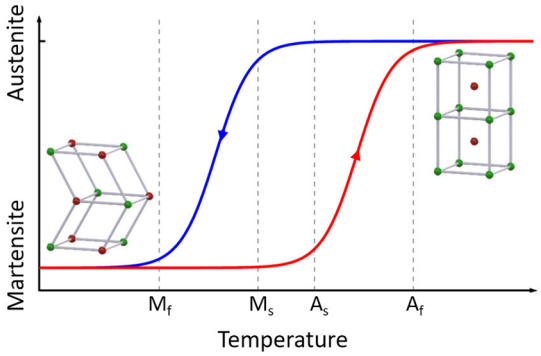

Figure 1: The hysteresis and critical temperature threshold of shape memory alloy. Inserts are Martensite and Austenite crystal structures.

978-1-940470-04-7/HH2022/$25©2022TRF
DOI 10.31438/trf.hh2022.99

Using this shape memory and self-recovery nature of the SMA, an SMA-based antenna is designed for wireless temperature crossing event sensing. To monitor different levels of temperature crossing events, two sections of SMA wire with varying thresholds of temperature are conjoined to form the SMA-based antenna. Each section will recover to its predefined configuration when the temperature exceeds its respective threshold, which leads to different radiation profiles for each crossing event. By sensing and differentiating this radiation information, the key historical temperature information is recorded for posterity and easily recovered.

Sensor Design and Simulation

The sensor is designed as an antenna consisting of two arms that change shape under different temperature conditions, as in Figure 2. Each arm composes one red color section made by a low-temperature threshold SMA of threshold value T_1, and another blue color section fabricated with an SMA with a high-temperature threshold of T_2. The sensor is connected to a tiny PCB board. When the temperature is less than T_1, the whole sensor is in a martensite state and is manually reset to the shape shown in Figure 2(a). When the temperature rises above T_1 but below T_2, the red section recovers its predefined shape forming a straight line, which results in a dipole antenna configuration, as shown in Figure 2(b). This shape reconfiguration (Figure 2(b)) has a different radiation profile than the previous case (Figure 2(a)). Even if the temperature drops back below T_1, the antenna will still hold this dipole antenna configuration. Thus, the temperature crossing event at T_1 is recorded for posterity in the natural shape/state of the SMA antenna. When the temperature further exceeds T_2, which indicates the second temperature crossing event, the blue section recovers to its predefined straight shape, as shown in Figure 2(c). This causes the sensor to form a parallel line configuration. The parallel line antenna has very low radiation since the signals on the two arms cancel each other. Similarly, if the temperature drops below T_2, the antenna will still hold the parallel line shape, thus recording the prior temperature crossing event. By sensing and differentiating the radiation profile in its different configurations, the historical temperature information can be revealed.

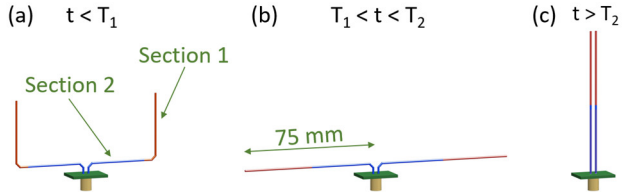

Figure 2: SMA antennas morph into different shapes at different temperature levels. (a) Below the lower threshold, (b) Between two thresholds, and (c) above the second threshold.

In our measurement, the shape variation caused by temperature violation is detected by the reflection coefficient S_{11}. When the temperature exceeds each of these thresholds, the reflection coefficient differs. To quantify the results, S_{11} of the different states of the SMA antenna is simulated. The total length of each multi-section SMA wire is 75 mm, which results in a magnitude peak at 950 MHz in the range of UHF RFID. At a temperature below T_1, the SMA sensor is deformed in a U shape. Under this condition, the impedance of the antenna is 44+5j Ω at 950 MHz. When the temperature is between T_1 and T_2, the antenna switches to a dipole antenna configuration, and the impedance changes to 73+9j Ω. As a result, the minimal magnitude of the return loss S_{11} around 950MHz decreases from 24 dB to 17 dB. When further temperature crossing occurs, the temperature rising above T_2, the SMA wires straighten and form a parallel line antenna. At this point, the impedance of the antenna is 1−29 j Ω. The S_{11} flattens out at 0 dB over the simulated frequency range of 0.7 GHz to 1.2 GHz.

FABRICATION AND CHARACTERIZATION

SMA wires with a diameter of 0.5 mm are used to fabricate the SMA antenna. The thresholds T_1 and T_2 of the two SMA wires are chosen as 30 °C and 50 °C, respectively. The detailed fabrication process of the SMA wire with a specific threshold can be obtained from [28].

To fabricate the multi-section SMA antenna, SMA wires need to be electrically joined together. Soldering is preferred for its robust connection. However, the ordinary soldering process would fail due to the formation of an oxide layer on the surface of the SMA wire [29]. The heat during the soldering greatly accelerates the oxidation process. To eliminate oxidation, phosphoric acid is applied to the polished ends of two SMA wires before soldering [30]. The phosphoric acid wetting on the SMA wires prevents oxidation. Therefore, the two parts can be soldered together. A physically and electrically stable connection is created between the sections of the SMA wire. Afterward, the residue of phosphoric acid and excessive solder is removed for a smooth connection. An antenna is formed by attaching the conjoined multi-section SMA wires to a tiny printed circuit board.

Temperature Response

The temperature response of the sensor is measured by recording the shape of the SMA wire while sweeping the temperature. To ensure that the environment temperature is stable, the fabricated SMA wire is submerged in a water bath, which allows the temperature to be precisely controlled. A thermocouple (RISEPRO) is placed nearby the SMA sensor to detect the environmental temperature. The fabricated multi-section SMA wire is initially cooled at 5 °C in the water bath, and then gradually heated to 60 °C using a hot plate. During the heating process, the shape change of each section is recorded. Initially, both sections are at 0% transition with the manually set shape. When the temperature is above their thresholds, the SMA wires become straight, which leads to a 100% shape transition. Section 1 has a threshold of around 30 °C, and section 2 has a threshold of around 50 °C. In Figure 3, the measured temperature response of Section 1 is depicted as the blue dash line. Its shape starts to change at 28 °C and finishes changing at 32 °C, resulting in a 4 °C transition zone. Similarly, the measured response of section 2, shown as the solid red line, starts to change shape at 48 °C drastically and finishes changing at 53 °C. The transition zone is 5 °C.

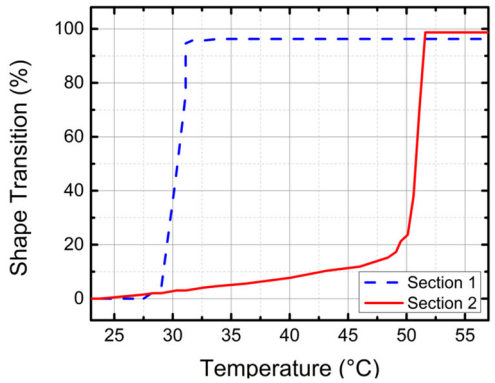

Figure 3: Temperature response of the SMA.

Frequency Response vs. Temperature

The S_{11} of the actual fabricated SMA antenna at different temperatures is characterized by a Vector Network Analyzer (Agilent N5227A). The frequency responses of the SMA antennas are tested under three temperature ranges, which is below 30 °C, between 30 °C and 50 °C, and above 50 °C. The figures of the SMA antennas under different states are shown in Figure 4.

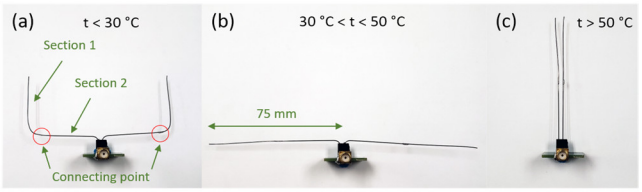

Figure 4: Return loss configured SMA antenna under (a) no temperature violation, t < 30 °C, (b) first degree of temperature violation, 30 °C < t < 50 °C, and (c) second degree of temperature violation, t > 50 °C.

The measured frequency response of the SMA antenna is shown in Figure 5. The return loss configuration is in a U shape state when the temperature is below 30 °C, as shown in Figure 4(a). Similar to the simulation results, the antenna in this state shows the most significant reflection of 30 dB at 950 MHz. When the temperature is between 30 °C and 50 °C, the SMA sensor transforms into a dipole antenna, as shown in Figure 4(b). As a result, the reflection coefficient S_{11} drops to 24 dB at 950 MHz. As the temperature rises above 50 °C, the SMA antenna turns into a parallel antenna, as shown in Figure 4(c), and the S_{11} is less than 3 dB over the 0.7 GHz to 1.2 GHz frequency range.

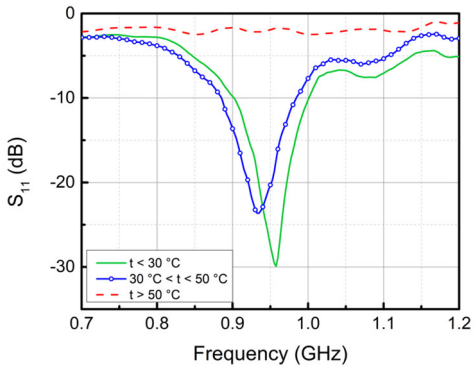

Figure 5: Measured frequency response of the SMA antenna.

DISCUSSION

The SMA antenna presents a transition zone during the sweep of temperature, and the transition is not abrupt. The fabricated multi-section SMA wire will react to two different temperature thresholds. As indicated in Figure 4, the first section will change from the manually set shape to a predefined shape due to the SMA's thermal-mechanical memory effect. The transition-start temperature A_s is 28 °C, and the transition-finish temperature A_f is 32 °C. The 4 °C transition zone indicates a ±2 °C error for the first section at 30 °C. The second section has a higher threshold. Its transition-start temperature is 48 °C, and the transition-finish temperature is 53 °C. The tolerance for the second section is ±3 °C. Such a level of accuracy is suitable for temperature crossing monitoring for routine food and medical-grade products, where the goal is to provide some assurance, and accuracy of temperature sensing is not essential. To achieve more minor transition errors, one needs SMA wires with more rapid change, which can be fabricated by specific techniques and proper material selection [31,32,33]. However, this is not the focus of this paper.

For the proposed multi-section SMA antenna, the radiation response reveals the temperature range that the SMA antenna has experienced. Both simulation and experimental measurement justify that the temperature violation induced shape-change effect can be monitored by the magnitude of the reflection coefficient S_{11} of the antenna. The return loss will be 30 dB when the temperature is below 30 °C. If the temperature ever rises between 30 °C and 50 °C, a 24 dB peak will be detected at 890 MHz in the S_{11}. If the highest temperature the antenna has experienced is above 50 °C, the return loss almost becomes a flat line over the frequency range. Due to the thermal-mechanical memory effect of the SMA wire, any temperature violation will cause the shape of the antenna to change, and the shape is kept (recorded) even after the temperature drops below the thresholds.

CONCLUSION

In this work, a battery-free multi-section SMA-based antenna is presented to monitor dual temperature crossing events. Utilizing the thermo-mechanical memory effect of the SMA wire, the antenna changes its shape in accordance with the phase transition temperatures of the sections of SMA used to make the antenna. The shape change is maintained (recorded) even after the clearance of the temperature crossing event, achieving natural recording of event activity in the shape of the antenna. The return loss of the antenna is used as an electronic indicator of temperature crossing events. The significance of this sensor is that it offers battery-less multiple temperature thresholds sensing and recording, without the need for peripheral electronic components or batter, which provides a low-cost, and logistically easy to use solution for monitoring temperature-sensitive goods.

REFERENCES

[1] P. Sen, S. N. R. Kantareddy, R. Bhattacharyya, S. E. Sarma, and J. E. Siegel, "Low-cost diaper wetness detection using hydrogel-based RFID tags", in IEEE Sensors Journal, 20(6), 3293(2020).

[2] X. Chen, H. He, Z. Khan, L. Sydänheimo, L. Ukkonen, and J. Virkki, "Textile-based batteryless moisture sensor", in IEEE Antennas and Wireless Propagation Letters, 19(1), 198(2020).

[3] V. Vivekananthan, N. R. Alluri, Y. Purusothaman, A. Chandrasekhar, S. Selvarajan, and S.-J. Kim, "Biocompatible collagen nanofibrils: an approach for sustainable energy harvesting and battery-free humidity sensor applications", ACS Appl. Mater. Interfaces, 10, 18650(2018).

[4] H. Guo, J. Chen, L. Tian, Q. Leng, Y. Xi, and C. Hu, "Airflow-induced triboelectric nanogenerator as a self-powered sensor for detecting humidity and airflow rate", ACS Appl. Mater. Interfaces, 6, 17184(2014).

[5] F. Pereira, R. Correia, M. Jordão and N. B. Carvalho, "Chipless strain sensor using phase modulation", 2020 IEEE Wireless Power Transfer Conference (WPTC), 420(2020).

[6] A. Mehmood et al., "Body movement-based controlling through passive RFID integrated into clothing", in IEEE Journal of Radio Frequency Identification, 4(4), 414(2020).

[7] W. Wang, R. Owyeung, Sadeqi, A. Sadeqi, and S. Sonkusale, "Single event recording of temperature and tilt using liquid metal with RFID tags", IEEE Sensor Journal, 20(6), 3249(2020).

[8] Z. Qian, S. Kang, V. Rajaram, et al. "Zero-power infrared digitizers based on plasmonically enhanced micromechanical photoswitches", Nature Nanotech, 12, 969(2017).

[9] B. Rahmadya, X. Chen, S. Takeda, K. Kagoshima, M. Umehira

and W. Kurosaki, “Measurement of a UHF RFID-based battery-less vibration frequency sensitive sensor tag using tilt/vibration switches”, in IEEE Sensors Journal, 20(17), 9901(2020).
[10] W. Wang, A. Sadeqi, and S. Sonkusale, “All-around package security using radio frequency identification threads”, IEEE Sensor, 1(2018).
[11] W. Wang, A. Sadeqi, H. R. Nejad and S. Sonkusale, “Cost-Effective Wireless Sensors for Detection of Package Opening and Tampering”, IEEE Access, 8, 117122(2020).
[12] L. Zhu, N. Alsaab, M. M. -C. Cheng and P. -Y. Chen, “A zero-power ubiquitous wireless liquid-level sensor based on microfluidic-integrated microstrip antenna”, in IEEE Journal of Radio Frequency Identification, 4(3), 265(2020).
[13] K. Bouzaffour, B. Lescop, P. Talbot, F. Gallée and S. Rioual, “Development of an Embedded UHF-RFID Corrosion Sensor for Monitoring Corrosion of Steel in Concrete”, in IEEE Sensors Journal, 21(10), 12306(2021).
[14] C. Asci, W. Wang and S. Sonkusale, “Security monitoring system using magnetically-activated RFID tags”, IEEE SENSORS, Rotterdam, Netherlands, 1(2020).
[15] W. Wang, C. Asci, and S. Sonkusale, “Security monitoring system uses RFID tags”, EDN, (2020), https://www.edn.com/security-monitoring-system-uses-rfid-tags/
[16] W. Wang, C. Asci, W.Zeng, and S. Sonkusale, “Zero-Power Screen Printed Flexible RFID Sensors for Smart Home Journal of Ambient Intelligence and Humanized Computing, in process.
[17] Cook, B.S.; Vyas, R.; Kim, S.; Thai, T.; Le, T.; Traille, A.; Aubert, H.; Tentzeris, M.M. “RFID-based sensors for zero-power autonomous wireless sensor networks”, IEEE Sens, 14, 2419(2014).
[18] Khalid, N.; Mirzavand, R.; Saghlatoon, H.; Honari, M.M.; Mousavi, P. “A three-port zero-power RFID sensor architecture for IoT applications”, IEEE Access, 8, 66888(2020).
[19] K. Biji, C. Ravishankar, C. Mohan, and T. Srinivasa Gopal, “Smart packaging systems for food applications: a review”, J. Food Sci. Technol, 52(10), 6125(2015).
[20] W. Wang, W. Zeng, and S. Sameer, “Tunable radiofrequency antenna using material programming”, unpublished.
[21] W. Wang, W. Zeng, and. Sonkusale, “Battery-free shape-memory alloy antennas for detection and recording of peak temperature activity”, Crystals, 12(1), 86(2022).
[22] W. Wang, C. Asci, W. Zeng, and S. Sonkusael, “Shape memory alloy-based helix antenna for temperature sensing”, unpublished.
[23] W. Wang, W. Zeng, A. Sadeqi, and S. Sonkusale, “Wireless temperature monitoring with shape memory alloy-based antenna”, IEEE Antennas and Wireless Propagation Letters, pp. 313-316, Jan. 2021.
[24] S. Jiang, Y. Zhang, Y. Zhao, “Dynamic recovery and dynamic recrystallization of NiTi shape memory alloy under hot compression deformation”, Transactions of Nonferrous Metals Society of China, 23(1), 140(2013).
[25] A. Nespoli, F. Passaretti, E. Villa, “Phase transition and mechanical damping properties: A DMTA study of NiTiCu shape memory alloys”, Intermetallics, 32, 394(2013).
[26] J. M. Jani, M. Leary, A. Subic, M. A. Gibson, “A review of shape memory alloy research, applications and opportunities”, Materials & Design (1980-2015), 56, 1078(2014).
[27] Y. Liu, J. V. Humbeeck, R. Stalmans, L. Delaey, “Some aspects of the properties of NiTi shape memory alloy”, Journal of Alloys and Compounds, 247(1–2),115(1997).
[28] W. Wang, W. Zeng, W. Ruan, E. Miller, and S. Sonkusale, “Thermo-mechanically trained shape memory alloy for temperature recording with visual readout”, IEEE Sensors Letters, 5, (1), 1(2021).
[29] R. Hahnlen, G. Fox, and M. Dapino, “Ultrasonic soldering of shape memory NiTi to aluminum 2024”, Supplement to the Welding Journal, 1(2012).
[30] N. W Pinto IV, N. L. Johnson, N. P. Irish, M. P. Balogh, D. B Haddad, “Method for soldering shape memory alloys”, U.S. Patent 14/931,056, issued September 26(2017).
[31] I. Mihálcz, “Fundamental characteristics and design method for nickel-titanium shape memory alloy”, Periodica Polytechnica Mechanical Engineering, 45(1), 75(2001).
[32] P. J. S. Buenconsejo, R. Zarnetta, D. König, A. Savan, S. Thienhaus, and A. Ludwig, “A new prototype two-phase (TiNi)–(β-W) SMA system with tailorable thermal hysteresis”, Adv. Funct. Mater., 21, 113(2011).
[33] J. Jiang, L. Cui, Y. Zheng, D. Jiang, Z. Liu, K. Zhao, “Narrow hysteresis behavior of TiNi shape memory alloy constrained by NbTi matrix during incomplete transformation”, Materials Science and Engineering: A, 536, 33(2012).

CONTACT

*Sameer Sonkusale, tel: + 617-627-5113; sameer@ece.tufts.edu

A MODULAR MICROFABRICATION APPROACH WITH MULTI-LAYER MICROPILLAR 3D INTERCONNECTS, UTILIZING DLP 3D PRINTING TOWARDS 3D MICROELECTRODE ARRAYS AND COMPLEX MICROSYSTEMS

Charles M. Didier[1], *Avra Kundu*[1], *and Swaminathan Rajaraman*[1]
[1] University of Central Florida, USA

ABSTRACT

In recent years, 3D printing has enabled multitudes of innovation and advances across scientific disciplines. This statement additionally holds true for the field of *in vitro* biological systems. Resin-based 3D printing (such as Digital Light Processing or DLP 3D Printing) have enabled resolutions of features in the low micrometer-scale, a key for 3D Microelectrode Array (MEA) technology. However, most 3D printed approaches are geared towards monolithic approaches. Here, we demonstrate a modular approach to the microfabrication of 3D MEAs, enabled by *unique micropillar interconnects*, which were fabricated through DLP 3D printing. Conductive silver epoxy and thin film deposition is utilized for a combination packaging approach. The device is subsequently characterized for its print resolution, microelectrode materials and 3D MEA impedance performance.

KEYWORDS

Digital Light Processing (DLP) 3D Printing, 3D MEA, Modular, *In Vitro*, Packaging, Computer Aided Design (CAD).

INTRODUCTION

In vitro systems for biological models are largely *either* customizable or cost-effective. Additionally, the requirement for utilization of 3D microelectrodes-based sensing has been established for more complex microphysiological systems (MPS) research, in areas such as neural and cardiac tissue models **[1]**. With the advent of 3D-printing however, novel strategies have resulted in the ability to balance these requirements, and produce innovative sensor designs to meet biological demand and challenges. The emerging MPS field, is reliant in part by advances in the underlying sensing/stimulation platform technologies. Sensors such as 3D MEAs, can be used to obtain signals from electrogenic cell populations **[2,3]**. Key variable-aspect-ratio interconnect microtowers are integral not only to 3D MEAs (described herein) but additionally for *in vitro* drug dispersal mechanisms **[4]**, magnetically-enhanced micro-robotics **[5]**, and microstructures towards MEMS antennae **[6]**, all of which can be enabled by novel 3D-printing techniques **[7]**. Resin or metal-based 3D-printing methods provide a material canvas onto which other functionalization methods may be incorporated, expanding such non-traditional technologies towards more complex microsystems fabrication.

Previously, our work has demonstrated rapid and cost-effective realization of 3D printed 3D MEAs, along with the methods to ensure their biocompatibility **[8,9]**. Herein, Digital Light Processing (DLP) 3D-printing based microfabrication of defined micropillar 3D through-vias is showcased in modular substrates, as a custom approach for development of an independent and modular 3D MEA. The final fabricated MEA is subsequently characterized for its constituent fabricated components (i.e., resolved positive and negative relief features), as well as for its electrical performance through a full spectrum impedance spectroscopy and microelectrode material definition.

MATERIALS AND METHODS

Solidworks CAD (Dassault Systemes, France) was utilized to design the 3D printed components (**Figures 1-2**), which were fabricated with Pro3dure GR-1 clear resin (Pro3dure, Germany), on

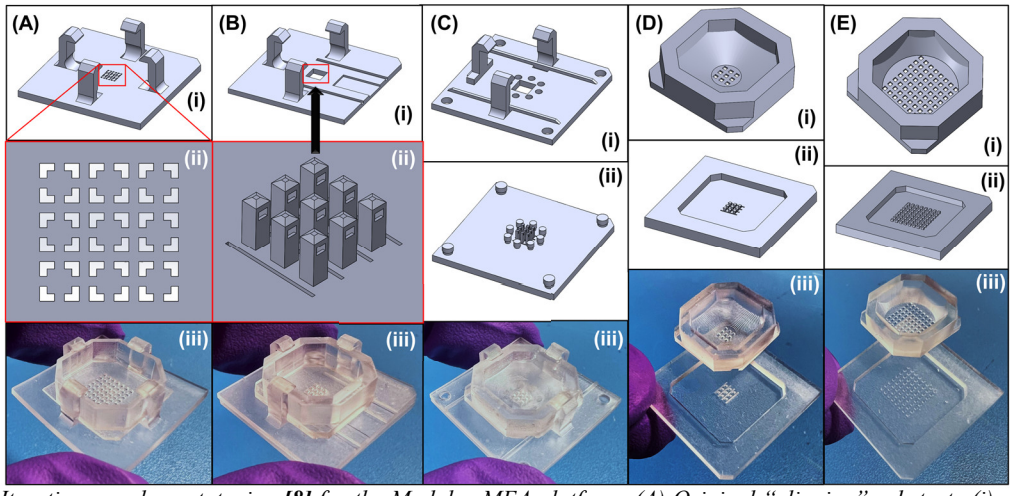

Figure 1 (left): *Iterative sample prototyping **[8]** for the Modular MEA platform. (A) Original "clipping" substrate (i) containing "plus-shaped" vias (ii) for transitioning "plus-shaped" vias from the attached culture well (iii). (B) Next iteration, which added a sliding mechanism for slotting the culture well (i), along with introducing the micropillar 3D interconnects and laser-isolation relief structures in a third layer (ii). The final 3D electrodes (iii) however did not make robust connection with the micropillars. (C) In the next iteration, "raised slide rails" and "snap-button clips" (i) were introduced to better attach the micropillar substrate (ii) once the culture well was in place (iii). (D) In this iteration, **which is detailed fully in this work**, the design was reduced to two components, consisting of the sloped culture well (i) for more directed cell plating, and the recessed micropillar substrate (ii). Once printed (iii), this would allow for a tight-fitting, interchangeable culture well. (E) To demonstrate scalability of the approach in (D), a 64- channel, 8x8 design was additionally prototyped.*

978-1-940470-04-7/HH2022/$25©2022TRF
DOI 10.31438/trf.hh2022.100

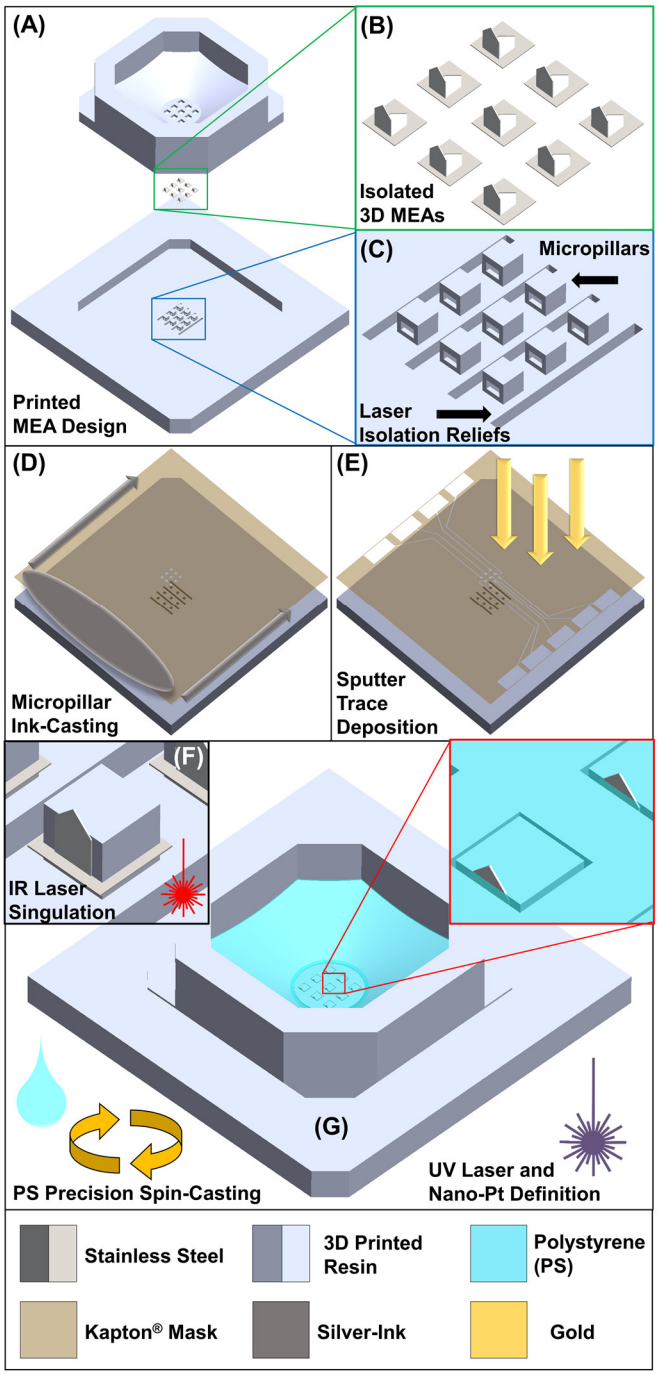

Figure 2: *Modular 3D MEA fabrication schematic (3x3 array). (A) Central components of the MEA platform, including the sloped culture well, the micropillar substrate and the array of SS electrodes between them. (B) Enlarged, isolated SS electrodes. (C) Enlarged schematic of the micropillar substrate, showing the opening of the "inverted-L" vias which would provide silver-ink contact with the micromachined SS electrodes, as well as the laser-isolation reliefs. (D) Illustration of the ink casting process, through the Kapton® mask. (E) Representation of the sputter deposition process through a secondary Kapton® mask after removal of the ink-casting mask. (F) Enlarged schematic which shows the flush connection of the 3D microelectrodes with the micropillar interconnects. (G) Schematic of the assembled and insulated 3D MEA, additionally showing an enlarged schematic of the assembled modular 3D MEA, with the SS electrodes emerging from the partitions in the culture well.*

Asiga MAX X, UV27 DLP 3D-printer at a wavelength of λ=385nm (ASIGA, Australia). Substrate dimensions were defined as: 24mm (length) by 24mm (width) by 2mm (thickness), with a central cut-out of: 16mm (length) by 16mm (width) by 1.3mm (depth). A 3x3 array of micropillars, with dimensions of 400µm (length) by 400µm (width) and 400µm (height), were centrally incorporated with 325µm (length) by 325µm (width) by 1000µm (height), "inverted-L" vias through the micropillars/substrate. Laser-isolation vias (dimensions: 240µm (width) by 3mm (length)) were additionally designed between the rows of micropillars.

The 16mm (length) by 16mm (width) by 8mm (height) interlocking culture well (2mm thick sidewall) was designed in CAD and printed separately, utilizing the same DLP printing. A 3x3 matrix, of 500µm (length) by 500µm (width) openings were incorporated in the culture well, to accommodate the slotting of micropillars and microelectrodes. All prints were subsequently washed in 70% Isopropanol (IPA), and dried before UV-curing to ensure both biocompatibility and proper final print curing **[9,10]**. A modified "Hypo-Rig" assembly (patent-pending **[8,11]**) was similarly designed, printed, and finished, before being fitted with 30G dispensing needles (BSTEAN, USA) for 2D-3D microelectrode transition (**Figure 3A, B**).

3D microelectrodes were IR-laser micromachined (QuickLaze, USA) from 316L stainless-steel (SS) (12.5µm thick) in a 3x3 configuration, with each 2D structure having dimensions of 300µm (width) and 350µm (height) with a 1mm pitch. Horizontal scribe lines between each row of the array were laser defined to allow for full isolation using the integrated laser scribe-vias post-assembly. The SS arrays were subsequently acid-pickled to remove laser debris and other irregularities **[12]**. The array was then aligned and affixed to the back of the culture well, before being transitioned from 2D to 3D utilizing the Hypo-Rig. The culture well / 3D MEA assembly was then aligned and attached to the micropillars on to the base substrate. The micropillars were precisely filled with silver-ink utilizing a UV laser-defined Kapton® (DuPont, USA) shadow mask and then cured at 60°C. To form the contact pads and traces, 30nm of gold was sputtered through a separate Kapton® mask to connect with the bottom sides of the ink-filled vias. A 10µm thick polystyrene insulation was spin-coated inside the assembled culture well and cured at 60°C, before utilizing controlled burst, selective UV-laser micromachining to expose an opening. Nano-porous platinum (N-P Pt.) electroplating was then performed on the laser-exposed electrodes, to increase the functional surface area **[13]**. Full spectrum (100Hz-40MHz) impedance and phase were obtained utilizing the Bode 100 (Omicron Labs, USA), with phosphate buffered saline as the electrolyte and utilizing a Pt anode. Imaging was performed with scanning electron microscopy (SEM; Zeiss, Germany), laser confocal microscopy (Keyence, Japan), and optical modalities (iPhone XS; Apple, USA).

RESULTS AND DISCUSSIONS

Figure 1 illustrates how iterative sample prototyping **[8]** is utilized to quickly change designs during the process development phase. Once an established design is ready to move forward to evaluations, a full microfabrication strategy is designed and deployed (**Figure 2**). "Hypo-Rig" ensures a uniform 2D-3D transition of the SS microelectrodes and the ability to do throughout the array simultaneously (**Figure 3A, B**). The final fabricated device and the laser micromachined array are shown in **Figure 3C, D**.

In-situ impedance characterization was performed during the characterization of the final device, to delineate between "open circuit", SS and N-P Pt. microelectrodes **[14]**. Once electroplating of the microelectrode sites was completed, Energy Dispersive X-ray Spectroscopy (EDS) was performed to confirm the presence and

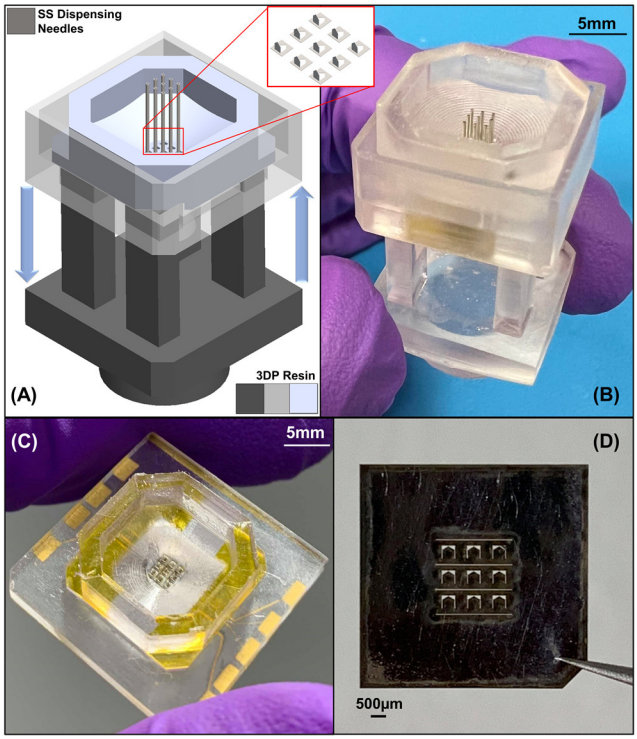

Figure 3: *Schematic and optical images for the custom Hypo-Rig and final Modular 3D MEA. (A) Schematic of the custom Hypo-Rig construct* ***[8,11]****. The enlarged inset details the 2D-3D transition of the microelectrodes. Integrated slots allow for rapid release of the transitioned array. The included release press is designed to fit evenly to provide uniform force distribution when releasing the culture well and transitioned microelectrodes. (B) Optical image showing the fabricated Rig from (A). (C) Optical image of the full fabricated Modular 3D MEA, schematically detailed in* ***Figure 2****. (D) Optical image of a closer view of the precision laser micromachined bulk SS before attachment and 2D-3D transition on the Rig.*

uniformity of the N-P Pt., and impedance scans were obtained again. The 1kHz impedance and phase values of **500 kΩ and -9º** respectively, indicate a suitable microelectrode for biological applications when compared to the initial *in situ* values of 25.0 MΩ, with a phase of -50º (not shown) obtained on SS 3D electrodes by precision laser de-insulation of the microelectrode recording sites. This high impedance was indicative of high oxidation of SS, prior to acid pickling **[12]**. The N-P Pt electroplating is used to enhance 3D microelectrode material electrical performance to an acceptable level **[13, 14]**, as shown in **Figure 4A, B**. A Randles equivalent circuit provided relevant extracted circuit parameters for the N-P Pt. microelectrode and are as follows: solution resistance (R_S) of 180Ω, charge transfer resistance (R_{CT}) of 430Ω, double layer capacitance (C_{DL}) of 4.5pF, and the Warburg coefficient (σ) of 10 x 10^4 $\Omega(s^{-1/2})$, which fall well within reasonable expected values (**Figure 4C**) **[15]**.

From the EDS spectrum obtained for the nano-porous platinum microelectrodes (**Figure 4D**), the presence of Au is expected (due to the sputtering for sample preparation for SEM), and the expected peaks for Pt can be clearly observed, confirming the electroplating of the nano-porous material. The inset in **Figure 4D** shows an SEM image of the N-P Pt. plated microelectrode, illustrating the success of the controlled burst laser ablation of the electrode tip to remove the insulation and the growth of N-P Pt. electrode material. Such a material increases the functional surface area of the microelectrode, without adding to the drawn electrode area, thereby reducing the impedance as demonstrated here.

Combination image analysis was utilized to assess the design to device translation of positive and specifically sensitive negative relief features. While SEM results detailed resolution of positive micropillars, laser confocal imaging allows for precise analysis of negative vias. Optically, the prints match the CAD designs closely (**Figure 5A**). However, under the SEM, it can be observed how curing of the resin during printing may "over-cure" the resin producing rounded corners. If print parameters are not carefully controlled, these errors may propagate throughout the printing process and cause closure of sensitive negative features **[9]**. For SEM imaging (**Figure 5B, C**), top most layers of the micropillars from printing to both illustrate the defined DLP layers, as well as to allow for better analysis of potential internal defects. As may be observed, some via closure is observed, but no major error propagation can be noticed. With respect to the laser confocal analysis (**Figure 5D, E**), the top layers of the micropillar interconnects were removed so that the system could properly interrogate the sensitive negative features of interest. Quantitatively, the values extracted from the laser confocal imaging were all within acceptable margins of error. The foundational ink via width / lengths (forming the base to the micropillars) were designed to be **325µm** and resolved across various prints **at 320.18 +/- 7.13µm**. Laser isolation via width were designed to be **240µm** and resolved to be **231.35 +/- 7.13µm**. The depth of the ink-casting vias was designed at **700µm** which was the depth of the center of the substrate and was measured as **696.15µm +/- 68.66µm**. While the error here is larger, it can be attributed to inconsistencies in the stage under the substrates which would lead to variations in measured depth. Finally, the surface roughness was measured at **1.37 +/- 0.22µm**, which ensures well connected culture well.

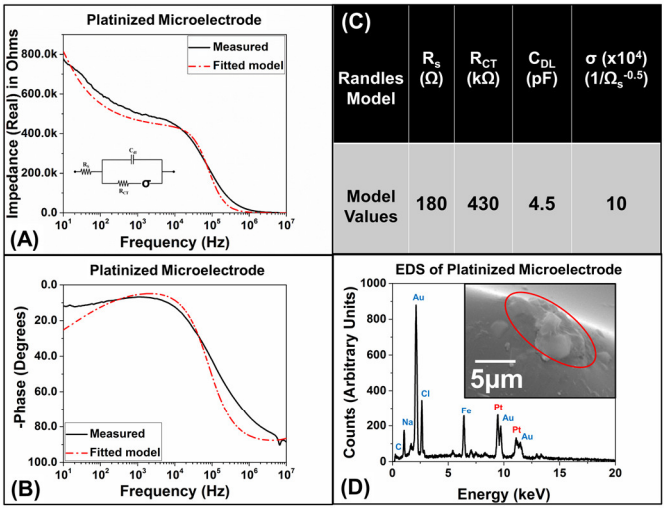

Figure 4: *Microelectrode characterization for the Modular 3D MEA platform. (A-C) Full spectrum (100Hz-40MHz) impedance and phase characterization, with a Randles' equivalent circuit fitting for extracting relevant parameters. Impedance (A) and phase (B) of the nano-porous platinum plated 3D microelectrode recording sites. The 1kHz impedance and phase values of* ***500 kΩ*** *and* ***-9º*** *are well within literature defied values. A custom Randles' circuit is shown as an inset (A), and the resulting fitting is graphed in red. Relevant parameters have been extracted from this model and are detailed in (C). (D) EDS spectrum of the nano-porous platinum microelectrodes.*

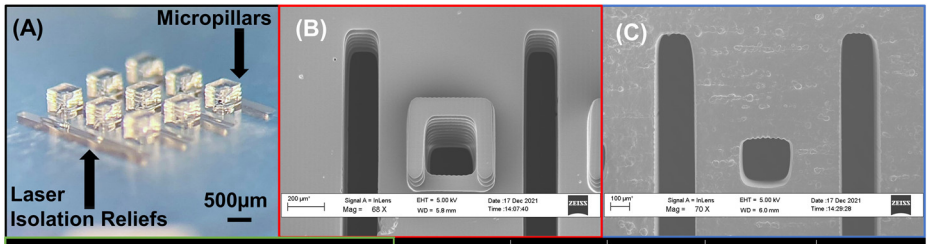

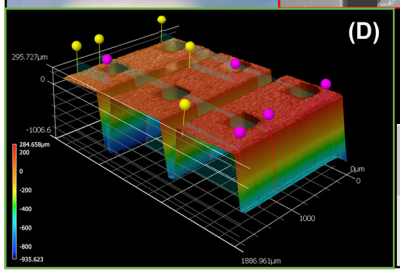

(E)	Ink Via *Width / Length*	Laser Isolation Via *Width*	Substrate Via *Depth* (Under Micropillar)	Surface Roughness
CAD Design Dimensions	325µm	240µm	700µm	N/A
Laser Confocal Dimensions	320.18um +/- 7.13µm	231.35 +/- 7.13µm	*696.15um +/- 68.66µm	1.37µm +/- 0.22µm

Figure 5: *SEM and laser confocal imaging for design to device translation analysis of positive and sensitive negative via features. (A) Enhanced optical image of the micropillar substrate indicating the positive structures as well as the laser isolation reliefs. (B&C) SEM images of the top (B) and bottom (C) of the micropillar substrate. The top of the micropillars in (B) were omitted from this chosen print to illustrate the defined DLP layers. (D) Laser confocal scanning image of a representative section of the micropillar substrate. (E) Quantitative values extracted from the laser confocal imaging from (D), where all values are within acceptable error margins.*

CONCLUSIONS

In this work, we demonstrate a rapidly iterative approach to the development of a modular base for the fabrication of a 3D MEA. We utilized DLP 3D printing, due to its ability to resolve sensitive positive and negative 3D features, and characteristic low surface roughness. The novel micropillar through-via approach described herein enabled a conductive-epoxy casting method to produce higher aspect ratio through-vias, which also served as supports for batch-transitioned 3D electrodes. The final 3D MEA platform was characterized for its design to device translation, utilizing several imaging-based characterization methods. All crucial and sensitive negative relief features were well within reasonable error margins. Additionally, the final fabricated 3D MEA device was characterized for its *in situ* electrical performance, through full spectrum impedance and phase sweeps, both before and after electroplating of nano-porous platinum.

ACKNOWLEDGEMENTS

The authors would like to acknowledge the funding provided through NSF I/UCRC, NIH UG3TR003150 and NIH R43ES029886 grants, as well as through the UCF ORC Doctoral Fellowship (C. M. Didier), and the startup funding of Prof. Rajaraman.

REFERENCES

[1] W. Anderson et al., *"Advances in 3D neuronal microphysiological systems: towards a functional nervous system on a chip,"* In Vitro Cellular & Developmental Biology-Animal, 2021.

[2] J. Choi, et al., *"Recent advances in three-dimensional microelectrode array technologies for in vitro and in vivo cardiac and neuronal interfaces,"* Biosensors and Bioelectronics, 2021.

[3] C. Didier, et al. *"Development of in vitro 2D and 3D microelectrode arrays and their role in advancing biomedical research,"* Journal of Micromechanics and Microengineering, 2020.

[4] U. Robles et al., *"3-D printed structures by microdispensing materials loaded with dielectric and magnetic powders,"* IEEE Transactions on Components, Packaging and Manufacturing Technology, 2018.

[5] G.Shao et al., *"High-resolution 3D printing magnetically-active microstructures using micro-CLIP process,"* Nano-, Bio-, Info-Tech Sensors and 3D Systems III, 2019.

[6] S. F. Shiba et al., *"3D microlithography using an integrated system of 5-mm uv-leds with a tilt-rotational sample holder,"* Micromachines, 2020.

[7] M. Tirado et al., *"Digital light processing (DLP) 3D printing of millimeter-scale high-aspect ratio (HAR) structures exceeding 100: 1,"* 33rd IEEE International Conference on Micro Electro Mechanical Systems (MEMS), 2020.

[8] C. Didier et al., *"Rapid Makerspace Microfabrication and Characterization of 3D Microelectrode Arrays (3D MEAs) for Organ-on-a-Chip Models,"* Journal of Microelectromechanical Systems, 2021.

[9] C. Hart et al., *"Biocompatibility of blank, post-processed and coated 3D printed resin structures with electrogenic cells,"* Biosensors, 2020.

[10] J. Fuh et al., *"Post-cure shrinkage of photo-sensitive material used in laser lithography process,"* Journal of materials processing technology, 1997.

[11] S. Rajaraman et al., *"Fabrication of 3d microelectrodes and use thereof in multi-functional biosystems,"* U.S. Patent Application No. 16/908,666., 2021.

[12] B.S. Covino et al., *"Dissolution behavior of 304 stainless steel in HNO3/HF mixtures,"* Metallurgical Transactions A, 1986.

[13] N. Azim et al., *"Fabrication and characterization of a 3D printed, microelectrodes platform with functionalized electrospun nano-scaffolds and spin coated 3D insulation towards multi-functional biosystems,"* Journal of Microelectromechanical Systems. 2019.

[14] W. Franks et al., *"Impedance characterization and modeling of electrodes for biomedical applications,"* IEEE Transactions on Biomedical Engineering, 2005.

[15] D. Borkholder. *"Cell-based biosensors using microelectrodes,"* Stanford University Thesis, 1999.

CONTACT

*Swaminathan Rajaraman, tel: +1-407-823-4339; Swaminathan.Rajaraman@ucf.edu

CONSTANT PHASE ELEMENT (CPE) MODELING AND ANALYSIS OF MULTI-MATERIAL, MICRO-BULLET SHAPED, HIGH-THROUGHPUT 3D MICROELECTRODES FOR *IN-VITRO* ELECTROPHYSIOLOGICAL APPLICATIONS

Jorge Manrique Castro, and Swaminathan Rajaraman
University of Central Florida, Orlando, Florida, USA

ABSTRACT

***This paper reports for the first time*, modeling, and analysis of Electrochemical Impedance Spectroscopy (EIS) from micro-bullet shaped 3D microelectrodes fabricated in high-throughput array (HT) formats with three different materials [Gold, Biocompatible-Silver Paste and Microelectronic-Silver Paste] in electrode-electrolyte interface. The modeling was based on the Randles' Electrochemical Equivalent Circuit (EEC) with a *Constant Phase Element (CPE) driving element* and impedance data collected from HT-3D Microelectrode Arrays (MEAs) was fitted. *CPE was determined as an excellent adaptative element* for electrical representation in MEA models due to low error per element during fitting process into EEC, and *exceptional matching observed between modeling and experiments* opening new avenues into the understanding of electrochemical interaction of 3D microelectrodes.**

KEYWORDS

3D Microelectrode Arrays (3D MEAs), Modeling, Constant Phase Element (CPE), High-Throughput, Electrochemical Impedance Spectroscopy (EIS).

INTRODUCTION

Electrogenic cell studies are critical for understanding the response of a variety of biological entities under the influence of physicochemical reactions caused by the interaction with their surroundings. This interaction might be caused by drugs, diseases, or environmental conditions **[1]**.

In-vitro studies provide an excellent approach to researchers and laboratories in order to quantify these interactions with functional readouts, and devices equipped with microelectrodes are widely used as means for obtaining electrical signatures from the cultured cells and cellular networks **[2]**. 3D MEAs are being explored as an alternative to the traditional 2D MEAs in *in-vitro* studies in an attempt to improve the spatial and temporal resolution with access provided deeper into the tissue architecture from 3D microelectrode configuration **[3]**. 3D features can be formed using a diversity of materials, each having its inherent physical and chemical properties in addition to a variety of processing methods. Structure of microelectrodes employed into the MEAs is paramount to getting reliable electrical signals (i.e., recording) or providing a charge to the cell/network (i.e., stimulation) **[4]**.

Electrode modeling techniques have been widely investigated by using EECs that provide a fitted response to redox reactions near the electrode surface. Several techniques such as EIS can be applied to record electrical information from MEAs. While 2D MEAs have been modeled using Finite Element Modeling (FEM) **[5]** and other studies have expanded to having theoretical implications for 3D microelectrodes including Method of Images (MoI) **[6]**, there still remains a gap in modeling of 3D microelectrodes due to the non-homogeneity of 3D structures.

3D electrode geometry is key to EIS data which is controlled by various materials and microfabrication processes **[7, 8]**. Electrochemical cells are modeled typically using Randles' EEC **[7]**, widely used in biomedical applications with kinetic and diffusion elements involving electrodes/electrolyte interface for homogeneous and non-homogeneous systems. In order to get the maximum microelectrode selectivity for recording and stimulation in biological settings, a balance between size and impedance is paramount and needs to be considered **[8]**.

Theoretical elements such as Warburg provide a representation of the impedance related to Faradaic processes caused by the diffusion of species. Due to the nature of the microelectrode under analysis, this response might show some tendencies to behave capacitively in the case of a reflective boundary or as a short in the case of transmissive boundary **[9]**. This variability opens up opportunities in terms of adding new elements to electrode modeling, and the CPE presented in this work fits nicely to diffusion

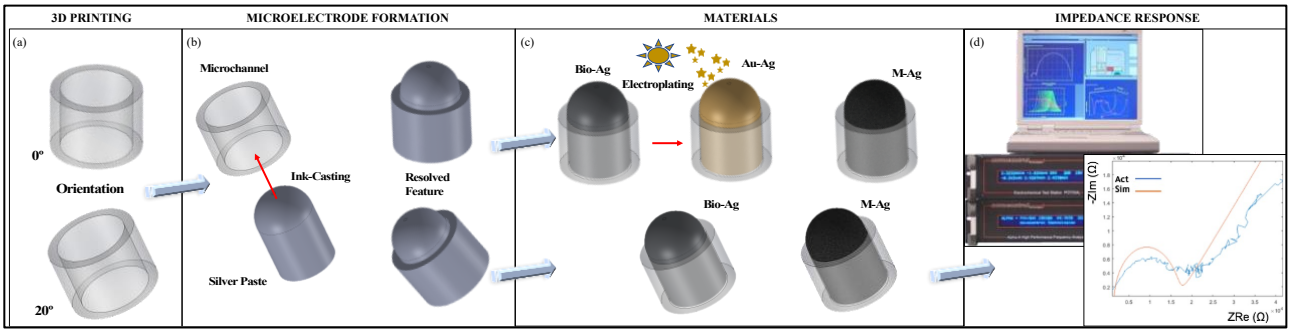

Figure 1: *Schematic process for microelectrodes fabrication and impedance analysis in a sequential fashion. (a): 3D microchannel 3D printed at 0° and 20° with respect to the resin plane using micro-stereolithography. (b): 3D Microelectrode fabrication using an Ink-Casting technique and resolved features for both printing angles after silver paste curing. (c): Materials used to characterize 3D microelectrodes, for 0°, Au-Ag and M-Ag were studied. Au-Ag was fabricated using electroplating atop the Ag paste. On the other hand, for 20°, Bio-Ag and M-Ag were studied. (d): Electrochemical impedance spectroscopy testing showcasing Nyquist and Bode plots responses that were modeled.*

978-1-940470-04-7/HH2022/$25©2022TRF
DOI 10.31438/trf.hh2022.101

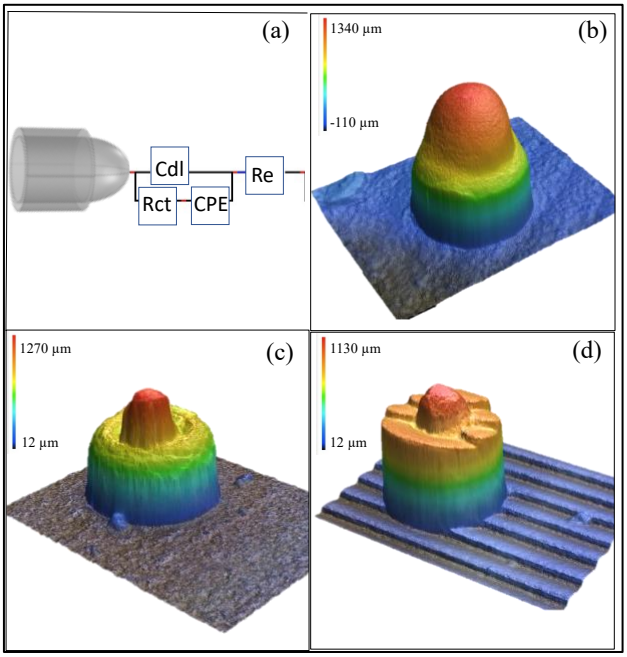

Figure 2: *(a): Randles' EEC model for impedance modeling with Constant Phase Element (CPE [Q, α]). (b-d): Laser confocal microelectrodes characterization for the 3D microelectrodes: (b): Au-Ag at 0º, (c): Bio-Ag at 0º and (d): M-Ag at 20º.*

effects obtained from real measurements due to its versatile theoretical definition.

3D microelectrodes present unique challenges to modeling since 3D electrode geometry is key to EIS data and its response is electrode surface dependent, which is provided by different materials and microfabrication processes. ***CPE is a potential element that is used to fit data for the interpretation of various kinetic and diffusion processes [10] involved in the electrochemistry of in-vitro applications***.

MATERIALS AND METHODS

The detailed microfabrication approach used for these HT-3D MEAs is described in our recently published IEEE JMEMS article **[11]**. Only a brief description of the methods used in this work are detailed below. For more information, the reader is referred to the JMEMS paper. Computer-aided design (CAD) software was employed for the 3D printed microstructures that served as support structure for the microelectrodes. After post processing the 3D printed structures, the microstructures were filled with three different materials and their impedance performance was measured utilizing EIS with a vector analyzer tool. Physical characteristics of the 3D microelectrodes were obtained using 3D surface optical profilometry and Scanning Electron Microscopy (SEM) techniques. Lastly, modeling was performed comparing sets of actual impedance data vs. fitted impedance data, after parameters were extracted from the frequency response of the impedance and phase spectrum.

Microelectrode Design

Multi-well bioplates were designed using CAD software (Solidworks, Dassault Systèmes) with each well containing a variety of microelectrodes. In total, 168 microchannels (7 per well) serving as microelectrode main structure were designed having dimensions of 800 µm height, 1000 µm OD and 800 µm ID. The design included

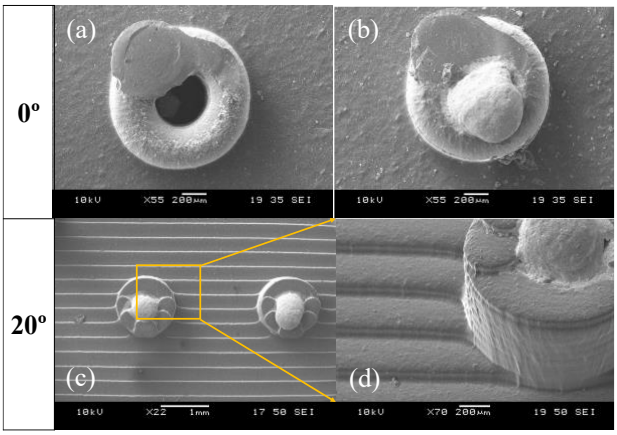

Figure 3: *SEM images of silver-ink cast 3D microelectrodes at 0º and 20º tilt printing angles. Microchannel unfilled in (a) and filled in (b). (c): Top view of MEA. (d): Magnified view of the electrode structure/electrode surface at 180º rotation and 25º tilt in SEM.*

the traces from the back side of the bioplates serving as interface for further electrical characterization with dimensions of 400 µm width by 400 µm depth. The length of these traces was varied depending on the 3D microelectrode and well location.

Microchannel 3D Printing

Microfabrication of electrode microchannels was carried out by using 3D printing (Form 3, Formlabs), based on the working principle of micro-stereolithography (µSLA). Optimization of processes led to our 6/12-well HT-3D MEAs **[12]**, being scaled to the microfabrication of 168 micro-bullet shaped electrodes in a 24-well HT-3D MEA format **[13]**, eliminating short circuits and traces openings in metallization, and reducing mechanical abrasion steps needed to improve surface quality. The microchannels were printed at 0º and 20º tilt angle with opposite orientation with respect to the base plane.

Metallization

Metallization process was performed using an in-house ink-casting technique and three combinations of materials were selected for this research. Ink-casting with Au coated (Gold Plating Solution TSG-250, Transene Company) biocompatible silver paste [Au-Ag], biocompatible silver paste [Bio-Ag] (EP3HTSMED, Masterbond), and microelectronic silver epoxy [M-Ag] (Prima-Solder EG8050, AI Technology) materials were used to ***define 3D microelectrodes at 0º and 20º 3D printing angle*** (**Figure 1**). Au-Ag material was a composite material, whose surface was modified by Au electroplating, using a 50% AC cycle square pulse of amplitude 1 A/cm^2 for 30 s run in a customized LabView executable program. Sulfite gold plating solution (TSG-250, Transene Company) was employed for this electrochemical process.

Optical Characterization

Mechanical structure of the optimized version of the 24-well HT-3D MEAs was analyzed using laser confocal 3D microscopy (VK-X3000, Keyence) and scanning electron microscopy (SEM, JSM-6480, JEOL) to identify microelectrodes/microchannels integrity and surface homogeneity in the metalized electrodes.

Electrical Characterization

Electrochemical impedance spectroscopy was performed using

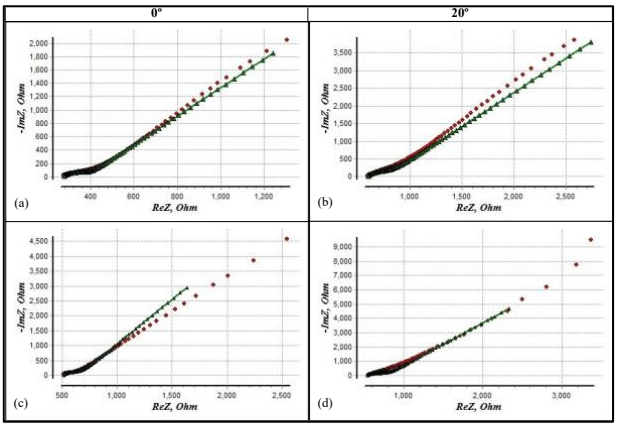

Figure 4: *Nyquist plots for experimental (EIS data) and theoretical (EEC Fitted Model) results implementing EISSA software approach with CPE as driving element of the electrochemical cell. Plots for Au-Ag and Bio-Ag paste-based microelectrodes are shown in (a) and (b) respectively. Plots for M-Ag epoxy-based microelectrodes are depicted in (c) and (d). EISSA experimental data is plotted in red, fitted data in green. Columns provide information about the printing angle used in micro-stereolithography.*

a Vector Network Analyzer (Bode 100, Omicron Lab) utilizing phosphate buffer solution (PBS) as electrolyte and Pt/Ti wire as counter electrode. Electrical modeling involved theoretical fitting of data from EIS and post-processing in the electrophysiologically useful spectrum range (1Hz-10kHz) **[8]** including Nyquist/Bode plots at electrophysiologically-relevant 1kHz **[14]**.

Modeling

Post-processing was performed using ***EIS Spectrum Analyzer (EISSA) software*** **[15]**. Experimental data was compared to Randles' EEC model with the extraction of resistive, capacitive and diffusion parameter (represented by CPE) to obtain the best fitting model based on these electrical parameters.

Table I: *Extracted parameters from the fitted models for the 0° and 20° printing orientation 3D microelectrodes*

Microelectrode 3D printed version	R_e (Ω)	R_{ct} (Ω)	C_{dl} (nF)	CPE [Q] ($\mu\Omega^{-1}.s^{\alpha}$)	CPE [α]
Biocompatible Gold/Silver Paste (Au-Ag)					
0°[a]	278	118	2079	128	0.72
Error (%)	1.8	7.4	8.7	4.0	1.4
20°[b]	598	239	1733	63.8	0.69
Error (%)	1.4	7.5	9.9	3.0	1.5
Microelectronic Silver Epoxy (M-Ag)					
0°	516	200	4500	70.3	0.78
Error (%)	5.6	9.9	9.9	4.5	2.1
20°[b]	543	297	2020	45	0.79
Error (%)	1.3	3.8	7.4	5.5	3.3

[a] *Au electroplated.* [b] *Bottom-side 3D printed orientation.*

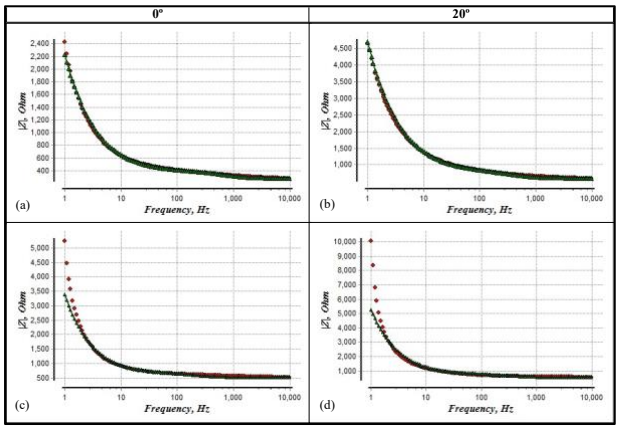

Figure 5: *Bode magnitude plots for experimental (EIS data) and theoretical (EEC Fitted Model) results implementing EISSA software approach with CPE as driving element of the electrochemical cell. Plots for Au-Ag and Bio-Ag paste-based microelectrodes are shown in (a) and (b) respectively. Plots for M-Ag epoxy-based microelectrodes are depicted in (c) and (d). EISSA experimental data is plotted in red, fitted data in green. Columns provide information about the printing angle used in micro-stereolithography.*

RESULTS AND DISCUSSIONS

Modified EEC Randles' model along 3D microelectrode profiles for Au-Ag, Bio-Ag and M-Ag materials are depicted in **Figure 2** and SEM images in **Figure 3**, ***showcasing the micro-bullet shape*** emanating from the microchannel structure, ideal for recording/ stimulation cell studies **[16]**. EIS comparison between the experimental and modeling data using EISSA software are depicted in **Figures 4 and 5**. Real impedance of ***317 Ω was obtained at 1kHz frequency*** for the ***Au-Ag material*** (0° print angle) which is ***exceptionally low for biomedical signaling*** in the electrophysiological range (100Hz to 3kHz) **[5]**. Modeling optimization with CPE found it as suitable diffusion element with ***α ranging from 0.69 to 0.79*** showing a diffusion-capacitive mixed behavior, and ***Q ranging from 45 to 128 $\mu\Omega^{-1}.s^{\alpha}$*** similar to literature reports when used as interface capacitance element **[17]**.

Interesting differences (8% at 0° printing and 13% at 20° printing) for α value in the Au-Ag and Bio-Ag vs M-Ag microelectrodes were found ***clearly depicting the effect of microfabrication and materials on electrode homogeneity*** (surface roughness and porosity). For Au-Ag electrodes, variability in coating thickness due to the electroplated Au is an additional contributor, acting as a surface structure modifier. ***Au-Ag and Bio-Ag microelectrodes presented a more diffusional impedance behavior than M-Ag due to α approaching the ideal value of 0.5*** **[18]**.

Values of the extracted parameters for micro-bullet microelectrodes are summarized in **Table I**. Errors after fitting of R_e, R_{ct}, C_{dl}, Q and α were all estimated to be ***less than 10 %***. These results prove that impedance response and diffusional effects can be modeled for 3D microelectrodes using different materials with high degree of accuracy showing advance in the field for features and functional structures beyond the traditional 2D microelectrodes.

CONCLUSIONS

This investigation demonstrates that materials properties in the conformation of electrode surface for 3D features play an important role in the recording of electrogenic cells for biomedical studies due

to its particular signature when different electrochemical interactions are present.

Electrode modeling driven by CPE elements in the faradaic and non-faradaic processes provided an excellent fitting approach due to its theoretical versatility, where adjustable parameters can lead to a finer matching between the impedance and phase responses to the actual data from microfabricated electrodes.

ACKNOWLEDGEMENTS

This work was supported by the University of Central Florida Research Foundation (UCFRF) funding using the GAP program. The authors would additionally like to acknowledge the Nanoscience Technology Center (NSTC) and UCF Graduate Studies for providing funding to present this research on the Hilton Head MEMS 2022 Workshop. Also, special thanks to Transducer Research Foundation (TRF) for the travel grant provided to JMC as presenting author.

REFERENCES

[1] J. S. Choi, H. J. Lee, S. Rajaraman, and D.-H. Kim, "Recent advances in three-dimensional microelectrode array technologies for in vitro and in vivo cardiac and neuronal interfaces," *Biosensors and Bioelectronics,* vol. 171, p. 112687, 2021/01/01/ 2021, doi: https://doi.org/10.1016/j.bios.2020.112687.

[2] C. M. Didier, A. Kundu, J. M. Castro, C. Hart, and S. Rajaraman, "Compact Micro-Stereolithographic (μSLA) Printed, 3D Microelectrode Arrays (3D MEAS) with Monolithically Defined Positive and Negative Relief Features For in Vitro Cardiac Beat Sensing," in *2022 IEEE 35th International Conference on Micro Electro Mechanical Systems Conference (MEMS)*, 9-13 Jan. 2022 2022, pp. 325-328, doi: 10.1109/MEMS51670.2022.9699662.

[3] F. Santoro *et al.*, "Interfacing Electrogenic Cells with 3D Nanoelectrodes: Position, Shape, and Size Matter," *ACS Nano,* vol. 8, no. 7, pp. 6713-6723, 2014/07/22 2014, doi: 10.1021/nn500393p.

[4] K. D. Wise, A. M. Sodagar, Y. Yao, M. N. Gulari, G. E. Perlin, and K. Najafi, "Microelectrodes, Microelectronics, and Implantable Neural Microsystems," *Proceedings of the IEEE,* vol. 96, no. 7, pp. 1184-1202, 2008, doi: 10.1109/JPROC.2008.922564.

[5] C. Moulin *et al.*, "A New 3-D Finite-Element Model Based on Thin-Film Approximation for Microelectrode Array Recording of Extracellular Action Potential," *IEEE Transactions on Biomedical Engineering,* vol. 55, no. 2, pp. 683-692, 2008, doi: 10.1109/TBME.2007.903522.

[6] T. V. Ness *et al.*, "Modelling and Analysis of Electrical Potentials Recorded in Microelectrode Arrays (MEAs)," *Neuroinformatics,* vol. 13, no. 4, pp. 403-426, 2015/10/01 2015, doi: 10.1007/s12021-015-9265-6.

[7] Z. Wang, A. Murphy, A. O'Riordan, and I. O'Connell, "Equivalent Impedance Models for Electrochemical Nanosensor-Based Integrated System Design," *Sensors,* vol. 21, no. 9, 2021, doi: 10.3390/s21093259.

[8] G. Kovacs, "Introduction to the theory, design, and modeling of thin-film microelectrodes for neural interfaces," *Enabling technologies for cultured neural networks,* 1994.

[9] "Impedance Representation of Bulk-Material and Electrode Processes," in *Impedance Spectroscopy*, 2012, pp. 59-96.

[10] J.-B. Jorcin, M. E. Orazem, N. Pébère, and B. Tribollet, "CPE analysis by local electrochemical impedance spectroscopy," *Electrochimica Acta,* vol. 51, no. 8, pp. 1473-1479, 2006/01/20/ 2006, doi: https://doi.org/10.1016/j.electacta.2005.02.128.

[11] J. M. Castro and S. Rajaraman, "Experimental and Modeling Based Investigations of Process Parameters on a Novel, 3D Printed and Self-Insulated 24-Well, High-Throughput 3D Microelectrode Array Device for Biological Applications," *Journal of Microelectromechanical Systems,* pp. 1-14, 2022, doi: 10.1109/JMEMS.2022.3160663.

[12] A. Kundu, A. Rozman, and S. Rajaraman, "Development of a 3D Printed, Self-Insulated, High-Throughput 3D Microelectrode Array (HT-3DMEA)," *Journal of Microelectromechanical Systems,* vol. 29, no. 5, pp. 1091-1093, 2020, doi: 10.1109/JMEMS.2020.3003644.

[13] J. M. Castro, A. Kundu, A. Rozman, and S. Rajaraman, "Investigation of the Effect of Printing Angle and Device Orientation on Micro-Stereolithographically Printed, and Self-insulated, 24-well, High-Throughput 3D Microelectrode Arrays," in *2021 IEEE Sensors*, 31 Oct.-3 Nov. 2021 2021, pp. 1-4, doi: 10.1109/SENSORS47087.2021.9639637.

[14] Y. H. Kim, A. Y. Kim, G. H. Kim, Y. H. Han, M.-A. Chung, and S.-D. Jung, "Electrochemical and in vitro neuronal recording characteristics of multi-electrode arrays surface-modified with electro-co-deposited gold-platinum nanoparticles," *Biomedical Microdevices,* vol. 18, no. 1, p. 14, 2016/02/01 2016, doi: 10.1007/s10544-016-0044-4.

[15] A. Bondarenko and G. Ragoisha, "Inverse Problem In Potentiodynamic Electrochemical Impedance," in *Progress in Chemometrics Research*, A. L. Pomerantsev Ed. New York: Nova Science Publishers, 2005, pp. 89-102.

[16] C. M. Didier, A. Kundu, D. DeRoo, and S. Rajaraman, "Development of in vitro 2D and 3D microelectrode arrays and their role in advancing biomedical research," *Journal of Micromechanics and Microengineering,* vol. 30, no. 10, p. 103001, 2020/07/21 2020, doi: 10.1088/1361-6439/ab8e91.

[17] W. Franks, I. Schenker, P. Schmutz, and A. Hierlemann, "Impedance characterization and modeling of electrodes for biomedical applications," *IEEE Transactions on Biomedical Engineering,* vol. 52, no. 7, pp. 1295-1302, 2005, doi: 10.1109/TBME.2005.847523.

[18] S. Wang, J. Zhang, O. Gharbi, V. Vivier, M. Gao, and M. E. Orazem, "Electrochemical impedance spectroscopy," *Nature Reviews Methods Primers,* vol. 1, no. 1, p. 41, 2021/06/10 2021, doi: 10.1038/s43586-021-00039-w.

CONTACT

*Swaminathan Rajaraman, tel: +1-407-823-4339; swaminathan.rajaraman@ucf.edu

MECHANICAL SENSING TOWARDS 3D-PRINTED WEARABLES

Sonia F. Roberts[1], *Jack Forman* [2], *Hiroshi Ishii*[2], *and Kristen L. Dorsey**[1,2]
[1]Northeastern University, Boston, USA
[2]Massachusetts Institute of Technology, Cambridge, USA

ABSTRACT

This paper demonstrates the potential of combining two recent technological advances: 1) wearable mechanical sensors and 2) 3D printing processes accessible to a wide range of users. We suggest that compliant, textile-like wearable sensors that are fabricated in easy-to-access processes, like desktop 3D printing, will empower a wide range of users to design, fabricate, and prototype wearable sensors. We characterize the electrical and mechanical properties of a conductive, 3D-printed textile. The electrical and mechanical properties are tunable with the selected print settings, with a gauge factor of greater than 13 in one sensor type.

Keywords – wearable sensor, strain sensor, 3D printing, additive manufacturing

INTRODUCTION

Wearable sensors have been proposed for applications such as human-machine interfaces [1] and health monitoring [2]. Many commercially available wearable devices, such as fitness or step trackers and smart watches, are relatively stiff or contain rigid materials. Researchers have expended significant effort to fabricate sensors embedded in cloth or rubbery materials; many of these fabrication processes require fume hoods or specialized equipment. Some notable exceptions to lab-based fabrication processes include printing conductive ink onto clothing [3] and fibercraft with conductive yarn or thread [4]. While these processes empower users to fabricate wearable sensors at home or in makerspaces, specialized tools may still be required to achieve precise sensor placements and repeatable performance.

Innovations in 3D printing have spurred interest in devices beyond solid forms, including flexible materials [5], 3D printed textiles [6, 7], and 3D printed sensors [8, 9]. A common fabrication approach for 3D printed flexible sensors is to print the conductive layer(s) on top of or embedded within a flexible substrate such as silicone [10]. While these works are major steps towards seamlessly wearable sensors, they require custom fabrication equipment and significant user training or advanced materials for the substrate or conductive layers [2, 11].

This work demonstrates a 3D printing process towards textile-like wearable sensors. In contrast to flexible filament 3D printed sensors, the process uses only commercially available filaments in an unmodified fused deposition modeling (FDM) printer. The resultant material — defeXtiles [12] — is mesh-like, compliant, and its properties are tunable with print settings. To demonstrate defeXtile's applications towards wearable sensors, we characterize its electrical and mechanical responses when printed using conductive PLA.

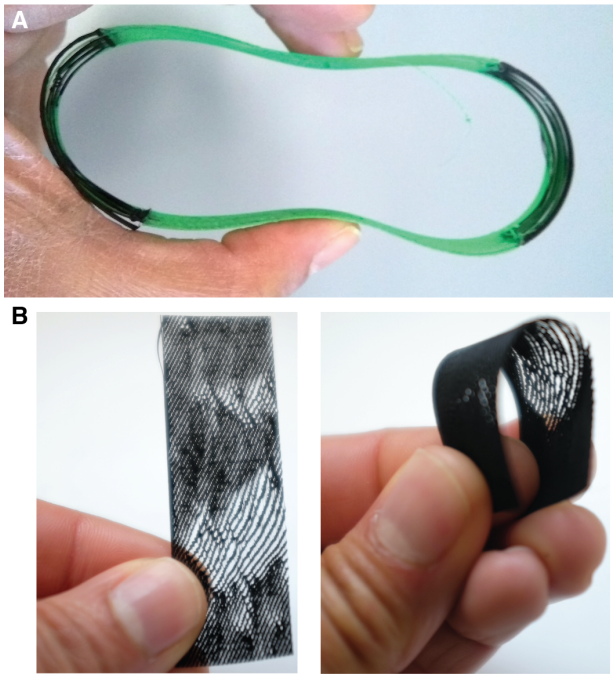

Figure 1: Photographs of defeXtiles samples. (a) A multi-material band with standard PLA (green) and conductive PLA (black). (b) A conductive sample with extrusion multiplier (EM) = 0.4.

DEFEXTILES FABRICATION AND SENSING

Defextiles are fabricated by reducing the extrusion multiplier (i.e., the fraction of material extruded by the print head) in the slicer software during 3D printing. The printed material is a network of thin "threads" between "posts" of larger deposited material. The print's flexibility arises from the mechanical compliance of the threads rather than the use of a flexible filament. In contrast to other flexible prints that print a single layer onto the bed, this approach enables more complex, 3D structures. Fig. 1 is a series of photos with defeXtiles samples. Fabrication process details are available in the Materials and Methods section.

The mechanical properties of the material and thread size are tunable through the extrusion multiplier (EM) and the print head speed settings [6]. Photographs of conductive PLA samples printed with EM of 0.3, 0.4, and 0.5 are presented in Fig. 2 with inset optical micrographs. The sample with an EM of 0.3 has a visible network of posts and threads, while the sample with an EM of 0.5 is almost entirely opaque. The thread diameters are approximately 35 µm and 100 µm for the 0.3 and 0.4

978-1-940470-04-7/HH2022/$25©2022TRF
DOI 10.31438/trf.hh2022.102

Solid-State Sensors, Actuators, and Microsystems Workshop
Hilton Head Island, South Carolina, June 5-9, 2022

EM settings, respectively. The samples with EM of 0.5 have a high enough material extrusion that individual threads are not visible, and the structure similar to a solid print. The thickness of the sample at the posts is approximately 400 µm, which is determined by the nozzle size of the printer.

Using a multi-material 3D printer, both standard and conductive PLA may be deposited to form sensing and structural regions of a print. Due to the brittle nature of the conductive PLA, the extrusion multiplier typically needs to be higher (e.g., EM $>$ 0.3) than for standard PLA (e.g., EM $>$ 0.2) for the print to be successful. Fig. 1a is a photograph of a two-material band of defeXtiles, with standard PLA in green and conductive PLA in black.

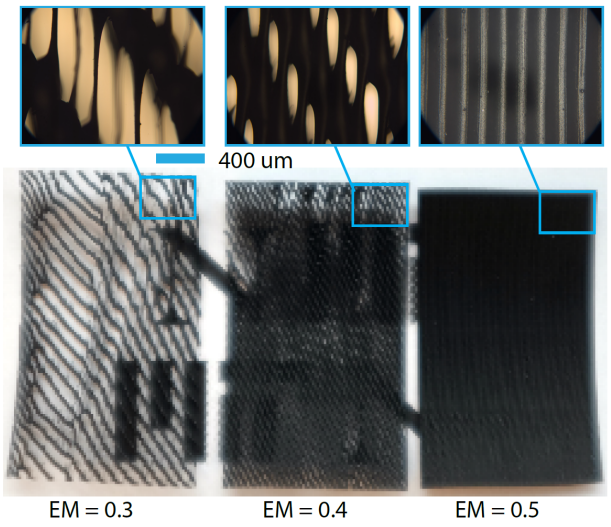

Figure 2: Photographs of conductive PLA defeXtiles samples with varying EM. Insets: Optical micrographs of conductive defeXtiles samples.

Wearable mechanical sensors must simultaneously withstand typical forces experienced during operation while demonstrating high sensitivity. In piezoresistive materials, reversible response to mechanical deformation occurs with changes in 1) the material dimensions; 2) the material conductivity, such as contact between conductive particles in an insulating matrix; or 3) electrical contact between structures.

Resistive approaches, rather than inductive or capacitive, are best suited to defeXtiles because the material has a sheet resistance in the 1 kΩ/sq range. In defeXtiles, similar to many textiles, the material is flexible out of plane but stiff in plane as planar deformation exerts an axial force on the threads. As such, the conductivity of the material under deformation can change in a few ways: the deformation can change the thread geometry, the deformation can cause delamination between printed layers of the material, and the deformation can modify conductivity within the PLA.

RESULTS

The average and standard deviation of sheet resistances for five samples of each EM are displayed in Table 1. The unstressed resistance of a sample ranges with EM. Samples with an EM of 0.3 have the largest sheet resistance, while samples with an EM of 0.5 have the smallest.

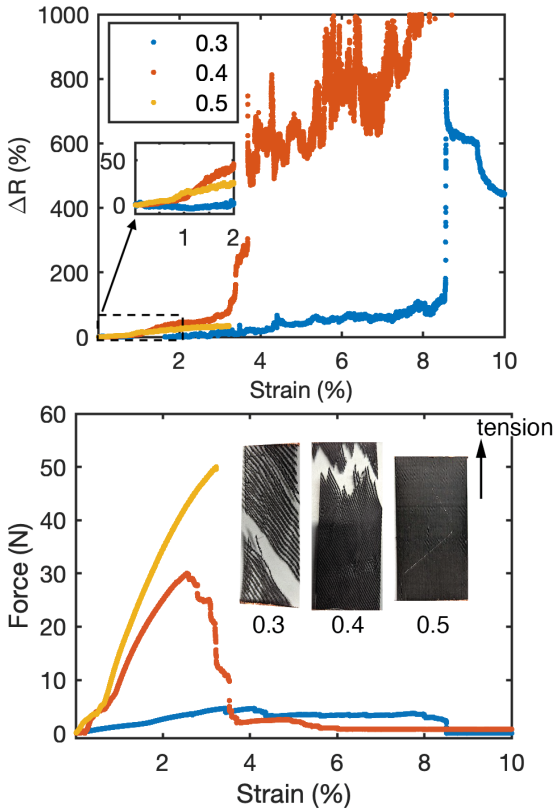

Figure 3: Resistance (top) and force response (bottom) to tension during one cycle of loading to failure. A representative sample of each EM is included.

Fig. 3 illustrates the response of each EM to tension. The 0.5 EM sample had the largest stiffness and was able to tolerate forces of 50 N, at which point the test was stopped. The 0.3 EM sample is most compliant and has the lowest initial sensitivity. Above strains of 1%, the resistance of each sample increases by a percentage of greater than 50 before the samples begin to tear. The force-tension curve illustrates these partial tears (e.g., EM of 0.4 at 2-4% strain), and the samples after the test are shown with the inset photographs. The average and standard deviation in maximum force and tensile gauge factor (GF) (i.e., the ratio of the resistance change to the applied strain) at a tensile strain ε of 1% is presented in Table 1 ($N = 5$).

Fig. 4 is a plot of three representative samples under compression along the length of the sample. The material buckles, mimicking increasing curvature with compression. After test completion, some curvature was observed in the samples, indicating plastic deformation. The resistance of the material in

Table 1: Mechanical and electrical properties with EM (average ± one standard deviation).

Property	0.3	0.4	0.5
Resistance (kΩ/sq)	5±0.34	0.74±0.06	0.44±0.06
Max Tension (N)	3.0±1.0	33.8±6.9	> 50
Tensile GF ($\Delta R/\varepsilon$)	4.0±5.7	11.7±5.2	13.3±5.1
Compressive ΔR (%)	-3.6±1.7	-2.9±1.9	1.3±2.4

the 0.3 and 0.4 EM samples was lower after testing, while the 0.5 EM sample increased slightly in resistance during the test but returned to its initial value when the test was complete. The average resistance change and standard deviation for a compression of 2.4 mm, which corresponds to a curvature of approximately 0.8 cm^{-1}, is shown in Table 1 ($N = 5$).

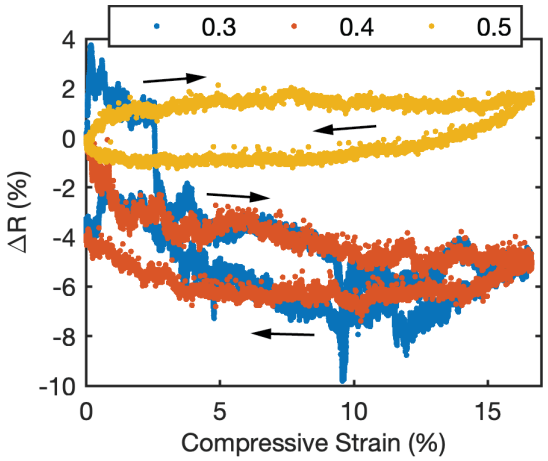

Figure 4: DefeXtiles response to compression and buckling. A representative sample of each EM is included.

DISCUSSION

The mechanical and electrical responses of the defextiles samples vary with EM, and the 0.5 EM samples show the smallest device-to-device variation. In the tensile tests, the resistance increased in all samples, although variations between EM and from sample to sample were present. At small strain, the resistance increase may result from a simultaneous increase in thread length and increase in piezoresistivity of the conductive PLA. If the applied strain were not sufficiently large to cause plastic deformation, the response may be recoverable, enabling the sample to behave as a repeatable mechanical sensor (e.g., strain below 1%).

The largest response to tension occurs when the threads plastically deform or the structure tears, beyond 2% strain. This approach to mechanical sensing is not repeatable due to irreversible changes in the material. However, it does support the use of defeXtiles as conductive layers for signal routing within a wearable device, because the resistance is relatively stable with small deformations. In the 0.3 EM samples, for example, the resistance change is low until the sample begins to tear, because the threads are compliant and can plastically lengthen without large increases in resistance.

In the buckling experiments, the sample with EM of 0.5 showed a small but recoverable change in resistance, while the 0.4 and 0.3 samples showed lower final resistance. The lower final resistance suggests a compressive stress on some part of the material, along with a decrease in piezoresistance. Similarly to the tensile strain experiments, this response might be recoverable at smaller deformation.

When considering sensor design with this material, a tradeoff exists between the mechanical compliance (which is desired for textile-like prints), the sample-to-sample variations (which increase as EM decreases and the post and thread network becomes less ordered), and the electrical properties (higher sensitivity and lower resistance with higher EM). Sensors and conductors may need to be higher EM, while lower EM materials can be used only as an aesthetic or display component, for example to electrically connect LEDs. Using conductive PLA, which is relatively rigid and brittle when compared to other plastic filaments, the defeXtiles fabrication process is best suited to creating conductive, compliant layers or investigating other sensing modalities such as capacitance or layer-to-layer resistance.

CONCLUSIONS AND FUTURE WORK

This paper introduced a 3D-printed conductive textile material and demonstrated the material's applications to conductive wearable sensors. This process makes it possible to fabricate mechanically and electrically tunable materials and multimaterial structures using hobbyist materials and equipment, making it a promising approach for "democratizing" access to wearable mechanical sensors. Additional characterization and fabrication effort is required to design robust structures with both standard and conductive PLA, understand sources of electrical and mechanical variation within the selection of extrusion multiplier, and develop strategies for increasing mechanical robustness while maintaining flexibility. Using materials other than PLA such as flexible filaments or highly conductive filaments may also enable more sophisticated sensor designs, such as capacitive or resistive sensors with the ability to tolerate large deformations. Future work will include demonstrating devices with multiple sensors and presenting practical applications of the sensors to health monitoring and human-machine interfaces.

MATERIALS AND METHODS

A Flash Forge Creator Pro 2 with dual nozzles was used for all prints. Parts were sliced using Simplify3D and printed at a speed of 3600 mm/min as a ring with 20 mm height and 8 cm diameter. Before printing, the global height between nozzle and bed was decreased by 150 µm from the leveling step to allow the material to adhere to the bed. Conductive structures were printed with using ProtoPasta conductive PLA (T = 220 °C, EM = 0.7) and standard PLA structures were printed using Hatchbox PLA (T = 220 °C, EM = 0.4), with a bed temperature set to 40 °C. After printing, the defeXtiles rings were cut into

60 mm × 20 mm strips and annealed by placing into an oven heated to 60 °C which was allowed to cool to room temperature over 3 h. After annealing, the end of each sample was wrapped with copper tape, which served as electrodes. The copper tape was coated with a thin later of hot melt adhesive to provide additional adhesion during mechanical testing and to electrically isolate the samples from the materials testing system.

Resistance during mechanical testing was measured using an NI-6002 USB data acquisition board and voltage divider, and sheet resistance was measured with a benchtop digital multimeter (BK Precision 5492B). Samples were loaded into a materials tester (i-Test 2.5, Mecmesin), gripped with a set of pneumatic grips, and strained at a rate of 2 mm/min for the tension tests and -2 mm/min for the compression tests. Tension tests were terminated when the load reached 50 N or the extension reached 10 mm, while compression tests displaced to -10 mm and returned to 0 mm.

ACKNOWLEDGMENTS

The authors would like to thank Dr. H. Hochsztein for guidance with mechanical test equipment.

References

[1] O. A. Araromi, M. A. Graule, K. L. Dorsey, S. Castellanos, J. R. Foster, W.-H. Hsu, A. E. Passy, J. J. Vlassak, J. C. Weaver, C. J. Walsh, and R. J. Wood, "Ultra-sensitive and resilient compliant strain gauges for soft machines," *Nature*, vol. 587, no. 7833, pp. 219–224, Nov. 2020, number: 7833 Publisher: Nature Publishing Group. [Online]. Available: https://www.nature.com/articles/s41586-020-2892-6

[2] K. Kim, J. Choi, Y. Jeong, I. Cho, M. Kim, S. Kim, Y. Oh, and I. Park, "Highly Sensitive and Wearable Liquid Metal-Based Pressure Sensor for Health Monitoring Applications: Integration of a 3D-Printed Microbump Array with the Microchannel," *Advanced Healthcare Materials*, vol. 8, no. 22, p. 1900978, 2019. [Online]. Available: https://onlinelibrary.wiley.com/doi/abs/10.1002/adhm.201900978

[3] C. Honnet, H. Perner-Wilson, M. Teyssier, B. Fruchard, J. Steimle, A. C. Baptista, and P. Strohmeier, "PolySense: Augmenting Textiles with Electrical Functionality using In-Situ Polymerization," in *Proceedings of the 2020 CHI Conference on Human Factors in Computing Systems*. New York, NY, USA: Association for Computing Machinery, Apr. 2020, pp. 1–13. [Online]. Available: https://doi.org/10.1145/3313831.3376841

[4] Y. Li, X. Miao, L. Niu, G. Jiang, and P. Ma, "Human Motion Recognition of Knitted Flexible Sensor in Walking Cycle," *Sensors*, vol. 20, no. 1, p. 35, Jan. 2020, number: 1 Publisher: Multidisciplinary Digital Publishing Institute. [Online]. Available: https://www.mdpi.com/1424-8220/20/1/35

[5] R. Uysal and J. B. Stubbs, "A New Method of Printing Multi-Material Textiles by Fused Deposition Modelling (FDM)," *TEKSTILEC*, vol. 62, no. 4, pp. 248–257, Nov. 2019. [Online]. Available: http://www.tekstilec.si/wp-content/uploads/2019/11/10.14502Tekstilec2019.62.248-257.pdf

[6] K. L. Dorsey, S. F. Roberts, J. Forman, and H. Ishii, "Analysis of DefeXtiles: a 3D printed textile towards garments and accessories," *Journal of Micromechanics and Microengineering*, vol. 32, no. 3, p. 034005, Feb. 2022, publisher: IOP Publishing. [Online]. Available: https://doi.org/10.1088/1361-6439/ac4fad

[7] J. Forman, M. Dogan, H. Forsythe, and H. Ishii, "DefeXtiles: 3D Printing Quasi-Woven Fabric via Under-Extrusion," in *Proceedings of the 33rd Annual ACM Symposium on User Interface Software and Technology*, 2020. [Online]. Available: https://dl.acm.org/doi/abs/10.1145/3379337.3415876

[8] H. Liu, H. Zhang, W. Han, H. Lin, R. Li, J. Zhu, and W. Huang, "3D Printed Flexible Strain Sensors: From Printing to Devices and Signals," *Advanced Materials*, vol. 33, no. 8, p. 2004782, 2021. [Online]. Available: https://onlinelibrary.wiley.com/doi/abs/10.1002/adma.202004782

[9] H. Nassar, M. Ntagios, W. T. Navaraj, and R. Dahiva, "Multi-Material 3D Printed Bendable Smart Sensing Structures," in *2018 IEEE SENSORS*, Oct. 2018, pp. 1–4, iSSN: 2168-9229.

[10] M. R. Khosravani and T. Reinicke, "3D-printed sensors: Current progress and future challenges," *Sensors and Actuators A: Physical*, vol. 305, p. 111916, Apr. 2020. [Online]. Available: https://www.sciencedirect.com/science/article/pii/S0924424720300868

[11] T. Xiao, C. Qian, R. Yin, K. Wang, Y. Gao, and F. Xuan, "3D Printing of Flexible Strain Sensor Array Based on UV-Curable Multiwalled Carbon Nanotube/Elastomer Composite," *Advanced Materials Technologies*, vol. 6, no. 1, p. 2000745, 2021. [Online]. Available: https://onlinelibrary.wiley.com/doi/abs/10.1002/admt.202000745

[12] J. Forman, M. D. Dogan, H. Forsythe, and H. Ishii, "Defextiles: 3d printing quasi-woven fabric via under-extrusion," in *Proceedings of the 33rd Annual ACM Symposium on User Interface Software and Technology*, 2020, pp. 1222–1233.

CONTACT

*K.L. Dorsey, +1-617-373-2071, k.dorsey@northeastern.edu

MULTIFUNCTIONAL 3D PRINTED $BATIO_3$ PLATONIC SOLIDS PACKAGING FOR IMPLANTABLE MICRODEVICES

Sayemul Islam[1], Sumnoon Ahmed[1], Alanis I. Santiago[1], Michael Domic[1], Jungkwun Kim[2], Seung H. Song[3], and Albert Kim[1]*

[1]Department of Electrical and Computer Engineering, Temple University, Philadelphia, PA, USA
[2]Kansas State University, Manhattan, KS, USA
[3]Sookmyung Women's University, Seoul, Korea

ABSTRACT

In this paper, we present a multifunctional packaging technique for implantable microdevices. The packaging is based on 3D printed bulk piezoelectric barium titanate ($BaTiO_3$) ceramic with unique geometrical shapes (i.e., regular convex polyhedrons; Platonic solid). The $BaTiO_3$ ceramic provides not only a seamless packaging for essential electronics but also a power source for those electronics through ultrasonic powering. Ultrasound has been an attractive powering source for many implantable microdevices. However, most ultrasonic receivers are rectangular or disc, not in ideal form factors; ultrasound is often deflected within the path, and the miniature implants might shift and rotate, resulting in an angular misalignment. Tailoring a three-dimensional polyhedral architecture (i.e., Platonic solid) for an mm-scale ultrasonic receiver can dramatically enhance its omnidirectionality. Utilizing the 3D printing technique, we devised a dodecahedron-shaped $BaTiO_3$ ceramic with the center void space for electronics embodiment. As a proof of concept, an LC (inductor-capacitor pair) resonator is implemented as a representative implantable microdevice. When ultrasound impacts the dodecahedron $BaTiO_3$ ultrasonic receiver, it energizes the embedded LC oscillator, generating resonance radio frequency (RF) waves, which can be detected by an external antenna. The demonstrated device with three combinations of an inductor and a 100-pF capacitor show three unique peaks in the RF spectrum at 2.57, 11.51, and 134.33 MHz, respectively.

KEYWORDS

Piezoelectric; Platonic solids; 3D packaging; implantable microdevice.

INTRODUCTION

Implantable medical devices (IMDs) are useful in monitoring complex physiological information, performing actuation, or drug delivery [1]. Millions of patients have been receiving some form of IMDs each year to improve their quality of life since the placement of the first implantable pacemaker in 1958 [2]. Some examples of implantable medical devices other than cardiac pacemakers are cochlear implants, neurostimulators, drug infusion pumps, implantable insulin pumps, etc. Most of these devices need a continuous source of power for their operation, and most of the time, it is provided using internal batteries. Typical consumption can vary from 30 µW to 10 mW depending on the type of the IMDs [3] However, the use of batteries may not be wise when the implant is considerably small and requires a long-term operation. Therefore, remote powering is considered in many of IMDs.

Among many remote powering technologies, RF or inductive powering is the most well-known. However, the RF powering is prone to high attenuation for deep tissue implants, especially at higher frequencies. The inductive powering also suffers from a short operating range and misalignment issues. As an alternative and promising remote powering method, ultrasound is extensively discussed due to its effective power transfer into deep tissue implants [4]–[8]. Furthermore, ultrasonic powering is less susceptible to directionality, especially the angular misalignment between the transmitter and the receiver transducer. Also, even if IMDs are placed out of optimal location and lose efficiency, some steps can be taken to counter that effect. For example, we previously demonstrated omnidirectional ultrasonic powering for millimeter-scale implantable devices by employing symmetricity of cuboids form factor [9]. Although the transducers typically used in IMDs, usually utilize manufactured lead zirconate titanate (PZT) ceramic, it is possible to make custom 3D printed shapes of piezoelectric transducers that provide a higher degree of symmetricity using lead-free ferroelectric $BaTiO_3$ nanoparticles.

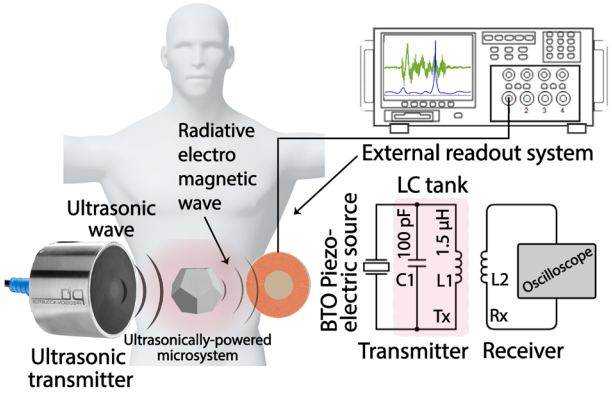

Figure 1: Implantable 3D printed and packaged microdevice sending information through RF radiation by using ultrasonic interrogation.

Here, we present a 3D printed, highly symmetric, piezoelectric transducer as an ultrasonic powering receiver. The transducer also has a small, voided space for carrying small electronics. We previously reported that the ultrasonic powering efficiency and omnidirectionality could be improved when various polyhedral Platonic solids (cube, octahedron, dodecahedron, sphere) are employed as a receiver [10]. Notably, the dodecahedron shape showed a minimal effect on the directionality compared to others. Therefore, we implemented a 3D printed dodecahedron-shaped piezoelectric transducer using $BaTiO_3$ as packaging for an LC resonator. The LC resonator has been utilized in many physiological sensors by employing either a capacitive or inductive sensor [11], [12]. Fig. 1 shows the schematic view of the proposed microdevice. The implanted Platonic solid ultrasonic receiver converts incoming ultrasound from the external transmitter to electrical power for the embedded LC resonator (not shown). The LC resonator then propagates an RF signal in a specific frequency that contains physiological information, picked up wirelessly by a readout system.

978-1-940470-04-7/HH2022/$25©2022TRF
DOI 10.31438/trf.hh2022.103

MATERIALS AND METHODS

Fig. 2 shows the fabrication process. The fabrication methodology was inspired by the recent work of Kim et al. [13]. First, the polyvinylidene difluoride (PVDF; Alfa Aesar, USA) was dissolved in N, N' dimethylformamide (DMF; Thermo Scientific, USA) with a 1:8.8 wt.% ratio while heated in a water bath at 80°C (Fig. 2a). The $BaTiO_3$ nanoparticles (500 nm; US research nanomaterials, USA) were then thoroughly and uniformly mixed (ratio 3.345:1) with the binder solution (PVDF + DMF) for at least 5 minutes using a stirrer (Fig. 2b). The mixture was then loaded into an extrusion syringe pump (10 mL, 600 µm nozzle) and used to 3D print a bespoke form (i.e., dodecahedron with radius = 5.5 mm and a 3.5 mm diameter hole) (Fig. 2c). The 3D printed dodecahedron was then baked in an oven (AT09p7.110 Ai, Across International) for 2 hours at 120°C to evaporate DMF completely (Fig. 2d). Then, the samples were placed in a tube furnace (GSL 1600X, MTI Corporation, USA) for debinding at 650°C for 1 hour, followed by sintering at 1190°C for 3 hours (Fig. 2e). The ramp-up and ramp-down temperature rates were maintained at 5°C/min. After sintering, a conductive electrode layer was created inside the hole and outside using commercially available conductive silver epoxy (8331D, MG Chemicals).

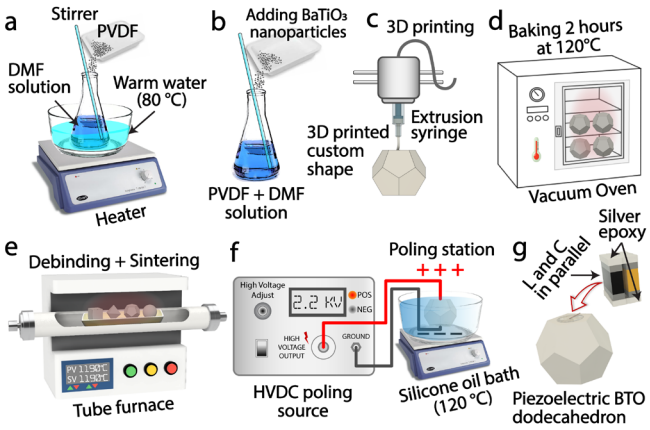

Figure 2: The fabrication process of implantable microdevices.

Since the electric dipoles in bulk $BaTiO_3$ dodecahedron were randomly oriented, they needed to be poled using a high voltage (V_{poling} > 1kV/mm) (Fig. 2f). For the polling process, the samples were placed in a custom-made poling stage which was submerged in silicone oil heated above curie temperature (120°C) [14] and connected to a high voltage DC power supply (230-30R, Spellman, USA) using spring-loaded connectors at the bottom and the top electrodes. They were poled at a high voltage (1 kV/mm) for 1 hour to activate piezoelectricity by aligning randomly oriented electric dipoles. After poling, a pair of an unshielded inductor and a capacitor were soldered into the void space, making contact with the inside electrode (Fig. 2g). The opposite terminal of the LC resonator was then connected to the outer electrode using wire and silver epoxy. Finally, the electrical connections were secured using biocompatible resin (BioMed Clear, Formlabs).

Fig. 3 shows the different states of the $BaTiO_3$ material during the process. Initially, the $BaTiO_3$ was in a dry powdered state. The addition of binder materials (PVDF + DMF) helped to retain the custom shape when molded or 3D printed. Fig. 3(d) shows a scanning electron microscopic (Quanta 450 FEG) image of $BaTiO_3$ before the debinding and sintering process. The particles can be seen attached to each other due to the binding materials. Drying the sample at this state causes the DMF to evaporate and still maintains the shape. After the debinding and the sintering process, the PVDF evaporated out, leaving only $BaTiO_3$ nanoparticles. During the sintering, $BaTiO_3$ particles fused with each other, forming a large and bulk $BaTiO_3$ sample, as shown in Fig. 3(e). The SEM images were taken with an accelerating voltage of 20 kV, spot size 5.5, ETD (Everhart Thornley Detector) with 2500x magnification, and 166 µm horizontal field width view.

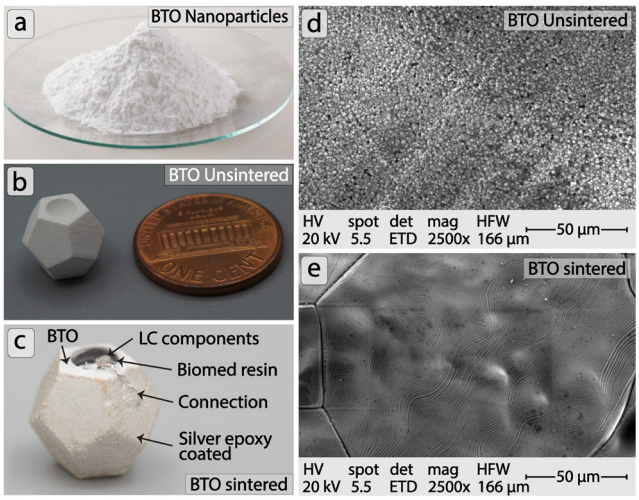

Figure 3: (a) $BaTiO_3$ NPs, (b) sintered $BaTiO_3$, (c) electronics integrated and packaged into the microdevice, (d) SEM pictures of pre-sintered, and (e) sintered $BaTiO_3$ sample.

EXPERIMENT SETUP

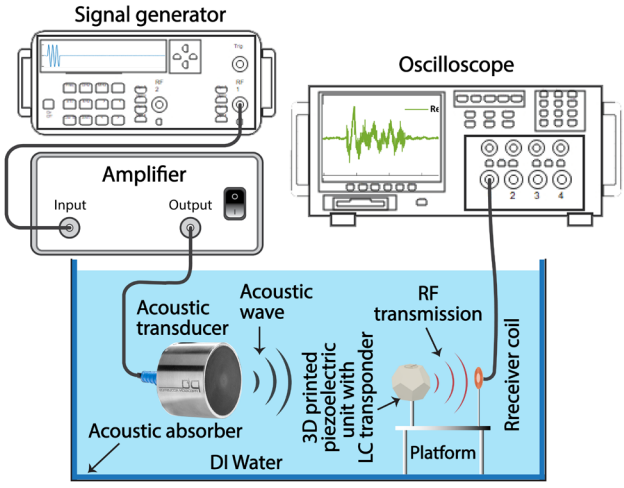

Figure 4: Experiment setup showing the interrogation technique.

The experiment setup is shown in Fig. 4. A water tank (60 × 30 × 40 cm^3) with deionized water was used to mimic the acoustic impedance in the biological environment (acoustic impedance in water is 1.483 MRayls) [15]. Acoustic absorbers were used on the side walls to prevent acoustic reflections and to minimize noise during the experiment. A submersible 60 mm focused acoustic transducer (PA1469, Precision Acoustics Ltd., UK) was used as a transmitter to transmit the acoustic waves to

the dodecahedron $BaTiO_3$ ultrasonic receiver with an LC transponder. The transducer was connected to a signal generator (4065, B&K Precision, USA) via an amplifier (1040L, E&I, USA) and driven using a sinusoidal tone burst (N = 5) of amplitude 200 mV (before 55 dB amplification) and a frequency of 670 kHz at 10 ms interval. The average electric power used by the transmitter was only 4 watts. The microdevice was placed directly in the line of sight with the transmitter at a 7.5 cm distance. A receiver coil (dia = 17.8 mm, width = 0.6 mm, turns = 32, layers = 4) was placed 1 cm away from the microdevice to capture the RF transmission. The receiver coil was connected to an oscilloscope (MSO54, Tektronix, Inc.) for displaying and logging the frequency spectrum. Note that a more user-friendly interface with additional descriptive information on the display can be developed for medical professionals in the future.

RESULTS

A. Ultrasonic response and LC oscillation

The ultrasonic transmitter was excited by the signal generator to transmit energy to the microdevice. As the transmitter started energizing, the burst ultrasonic waves could reach the microdevice and induce an electrical power in response to the piezoelectric $BaTiO_3$ transducer. The input wave is shown in Fig. 5(a) and the corresponding piezoresponse is shown in Fig. 5(b). The piezoresponse energizes the LC circuit, which induces oscillation at its resonance frequency until it is gradually damped out due to the energy dissipation in the circuit. The LC oscillation is shown in Fig. 5(c). It can be observed that the LC oscillation (at its resonance) occurred between each cycle of the burst generated by the $BaTiO_3$ transducer. The LC resonator radiated its signal through the unshielded inductor (acting as an antenna) and can be observed using an external antenna. Repetitive input ultrasound bursts were needed to maintain the oscillation and successful signal capture using the receiver coil.

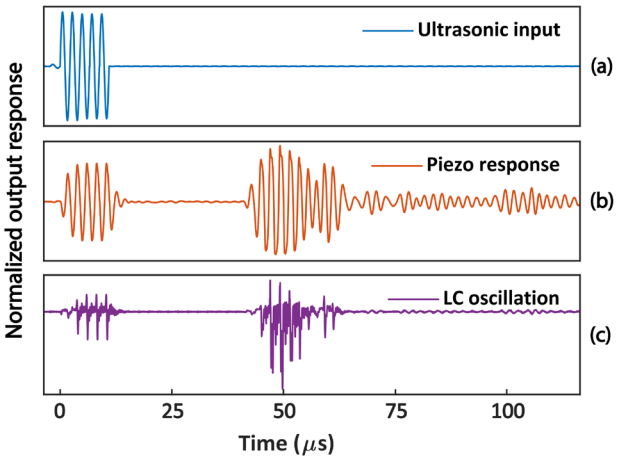

Figure 5: (a) Ultrasonic excitation, (b) piezoelectric response from BTO sample, and (c) oscillation in the LC circuit due to the excitation.

B. Received signal through RF

Three LC resonators with different resonant frequencies were prepared by adjusting inductor values while keeping the capacitor same (C = 100 pF). Three inductor values were 15 nH, 1.5 µH, and 100 µH with corresponding LC resonances at 129.95 MHz, 12.99 MHz, and 1.59 MHz. The transmitted RF signals were observed using the receiver coil on the oscilloscope. The combined frequency spectrum of the wirelessly received signals is shown in Fig. 6. As seen, resonant peaks distinctively appeared as expected with corresponding to the LC resonator circuit combinations. Different inductance values changed the peak location in the spectrum, which demonstrates a good agreement with the calculated resonance values shown in Table 1. The captured waveform carried multiple frequency information: the ultrasonic frequency, ultrasonic bursts frequency, $BaTiO_3$ mechanical resonant frequency, and the LC resonator frequency. To isolate and remove the effect of unwanted signals, we scanned from 1 MHz to 160 MHz in the frequency domain.

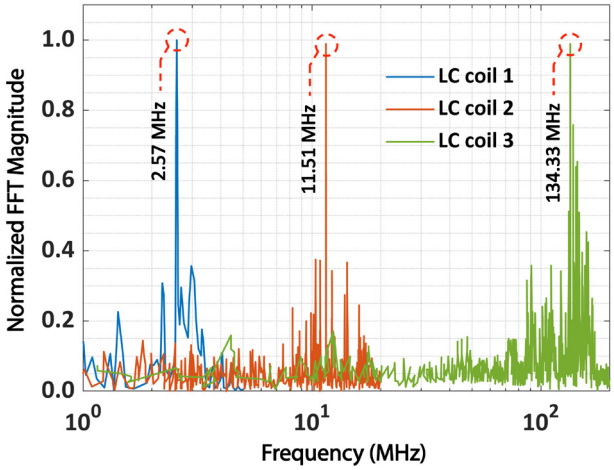

Figure 6: Received RF peaks identified for three different LC combinations.

Table 1: LC tank parameters and corresponding peaks

Parameter	LC type - 1	LC type - 2	LC type - 3
Dimension	L = 1.1 mm W = 1.0 mm	L = 1.1 mm W = 1.0 mm	L = 1.1 mm W = 1.0 mm
Inductance	100 µH	1.5 µH	15 nH
Capacitance	100 pF	100 pF	100 pF
Calculated resonance	1.59 MHz	12.99 MHz	129.95 MHz
Experimental values received	2.57 MHz	11.51 MHz	134.33 MHz

CONCLUSION

The design and fabrication of a multifunctional 3D printed $BaTiO_3$ dodecahedron piezoelectric transducer are demonstrated to be used as packaging for implantable microdevices. As a proof of concept, LC transponders were packaged inside of the transducer. Upon the ultrasonic input, the microdevice could generate and transmit RF signals with peaks indicating the corresponding variable (or sensing) element (inductor in this case). Such multifunctional packaging techniques and advanced miniature electronics are expected to bring numerous biomedical applications in smaller spaces, such as closed-loop sensing and actuation, multi microdevice communication, and enhanced security of the transmitted signal. Therefore, the reported packaging technique shows promising potential in replacing battery-powered or other passive implantable microdevices.

ACKNOWLEDGEMENT

The authors would like to acknowledge Dr. Dmitriy A. Dikin, and Long Zhu from Temple University for their help with the SEM imaging.

Funding: This work was supported by the National Science Foundation (NSF): CAREER award (ECCS-2143723) as well as ECCS-2029077, CNS-2129659, and ECCS-2054567.

CONTACT

For more information, please contact Dr. Albert Kim, email: albertkim@temple.edu; phone: +1 (215) 204-3222.

REFERENCES

[1] W. Khan, E. Muntimadugu, M. Jaffe, and A. J. Domb, "Implantable Medical Devices," in *Focal Controlled Drug Delivery*, 2014, pp. 33–59.

[2] N. M. van Hemel and E. E. van der Wall, "8 October 1958, D Day for the implantable pacemaker," *Neth. Heart J.*, vol. 16, no. 1, pp. 3–4, 2008, [Online]. Available: https://www.ncbi.nlm.nih.gov/pmc/articles/PMC2572009/.

[3] X. Wei and J. Liu, "Power sources and electrical recharging strategies for implantable medical devices," *Front. Energy Power Eng. China*, vol. 2, no. 1, pp. 1–13, 2008, doi: 10.1007/s11708-008-0016-3.

[4] P. J. Larson and B. C. Towe, "Miniature ultrasonically powered wireless nerve cuff stimulator," *2011 5th Int. IEEE/EMBS Conf. Neural Eng. NER 2011*, pp. 265–268, 2011, doi: 10.1109/NER.2011.5910538.

[5] S. Islam and A. Kim, "An ultrasonically powered active stent for endovascular diseases," in *2018 Solid-State Sensors, Actuators and Microsystems Workshop, Hilton Head 2018*, May 2018, no. 18, pp. 228–229, doi: 10.31438/trf.hh2018.64.

[6] A. K. Majumdar, S. Islam, and A. Kim, "An ultrasonically powered implantable micro electrolytic ablation (IMEA) for tumor necrosis," in *2018 Solid-State Sensors, Actuators and Microsystems Workshop, Hilton Head 2018*, May 2018, pp. 100–101, doi: 10.31438/trf.hh2018.29.

[7] A. Kim *et al.*, "An Implantable Ultrasonically-Powered Micro-Light-Source (μLight) for Photodynamic Therapy," *Sci. Rep.*, vol. 9, no. 1, p. 1395, Dec. 2019, doi: 10.1038/s41598-019-38554-2.

[8] R. Campbell *et al.*, "Implantable Cisplatin Synthesis Microdevice for Regional Chemotherapy," *Adv. Healthc. Mater.*, vol. 10, no. 3, p. 2001582, Dec. 2021, doi: 10.1002/adhm.202001582.

[9] S. H. Song, A. Kim, and B. Ziaie, "Omnidirectional Ultrasonic Powering for Millimeter-Scale Implantable Devices," *IEEE Trans. Biomed. Eng.*, vol. 62, no. 11, pp. 2717–2723, Nov. 2015, doi: 10.1109/TBME.2015.2444854.

[10] S. Islam, M. Park, S. H. Song, and A. Kim, "OMNIDIRECTIONAL POLYHEDRAL ULTRASOUND TRANSDUCER FOR POWERING IMPLANTABLE MICRODEVICES," in *2021 21st International Conference on Solid-State Sensors, Actuators and Microsystems (Transducers)*, Jun. 2021, pp. 1404–1407, doi: 10.1109/Transducers50396.2021.9495556.

[11] M. Lei, A. Baldi, E. Nuxoll, R. A. Siegel, and B. Ziaie, "Hydrogel-based microsensors for wireless chemical monitoring," *Biomed. Microdevices*, vol. 11, no. 3, pp. 529–538, Jun. 2009, doi: 10.1007/s10544-008-9168-5.

[12] A. Kim, C. R. Powell, and B. Ziaie, "An implantable pressure sensing system with electromechanical interrogation scheme," *IEEE Trans. Biomed. Eng.*, vol. 61, no. 7, pp. 2209–2217, 2014, doi: 10.1109/TBME.2014.2318023.

[13] H. Kim *et al.*, "Fabrication of bulk piezoelectric and dielectric $BaTiO_3$ ceramics using paste extrusion 3D printing technique," *J. Am. Ceram. Soc.*, vol. 102, no. 6, pp. 3685–3694, Jun. 2019, doi: 10.1111/jace.16242.

[14] A. Ibrahim, M. Meng, and M. Kiani, "A Comprehensive Comparative Study on Inductive and Ultrasonic Wireless Power Transmission to Biomedical Implants," *IEEE Sens. J.*, vol. 18, no. 9, pp. 3813–3826, May 2018, doi: 10.1109/JSEN.2018.2812420.

[15] P. Chen *et al.*, "Acoustic characterization of tissue-mimicking materials for ultrasound perfusion imaging research," *Ultrasound Med. Biol.*, vol. 48, no. 1, pp. 124–142, Jan. 2022, doi: 10.1016/j.ultrasmedbio.2021.09.004.

PAPERTRONICS: FULLY PAPER-INTEGRATED RESISTOR, CAPACITOR, AND TRANSISTOR CIRCUITS

Mya Landers[1], Anwar Elhadad[1], and Seokheun Choi[1,2]*

[1]Bioelectronics & Microsystems Laboratory, Department of Electrical & Computer Engineering, State University of New York at Binghamton (SUNY Binghamton), Binghamton, New York, USA

[2]Center for Research in Advanced Sensing Technologies & Environmental Sustainability, SUNY Binghamton, Binghamton, New York, USA

ABSTRACT

This work presents fabrication techniques for achieving individual electronic components both on the surface and within the fibers of a paper substrate, attaining full integration of paper and functional electronics materials. A process of hydrophobic wax patterning coupled with conductive and semiconductive poly(3,4-ethylenedioxythiophene): poly(styrene sulfonic acid) (PEDOT: PSS)-based ink injection and screen-printing has allowed for the implementation of all-paper-based, tunable resistors, capacitors, and transistors. The characteristics of the paper resistors can be adjusted as desired through finetuning of the PEDOT: PSS-based ink recipe, and the components can be combined in various arrangements to attain paper-based printed circuit boards (PCBs) for a wide range of practical applications. As a first step towards multiple component integration, a simple example circuit design is demonstrated that incorporates the three different components. Furthermore, through the strategic organization of the resistors, transistors, and capacitors and stacking of paper layers, more complex and diverse paper PCBs can be attained while minimizing the perceived surface area of the circuitry, allowing for a compact, pliable, and highly customizable means of fabricating paper-based electronic systems.

KEYWORDS

Papertronics, biodegradable, paper transistors, paper resistors, paper capacitors, paper PCBs

INTRODUCTION

The realization of paper-based electronic technologies has long been an ambition for many research groups, as paper-electronic integration offers to improve upon the disposability, affordability, and sustainability of conventional electronic systems [1-5]. Most of the attempted methods for achieving high-level integration, or bottom-up design, have involved utilizing paper as a substrate material only, while the constituents of individual electronic components have remained distinctly non-paper [6, 7]. Due to the rough, fibrous structure of paper, it often fundamentally interferes with material dispersion and electrical flow as recurrent imperfections within the material interrupt operation [8]. This can limit the precision of paper-made electronic interfaces and reduce the resultant device performance. Therefore, to mitigate this issue, the paper substrate often is first coated in a nonporous priming agent and then sequentially layered with the functional materials to attain the desired electronic component architecture on the "paper" surface [6-8]. Alternatively, paper has also been used in the manufacture of PCBs as well, serving simply as a substrate upon which conductive wires, or traces, are printed followed by adhesion of standard off-shelf surface mountable components [2, 9]. However, neither of these integration methods fully retain the flexibility and ease of disposability implied by the use of paper materials, as the attached electronic materials interfere with device bendability and biodegradability. To tackle this issue, paper must take on a more functional role within paper electronic platforms. Despite this need, a fully integrated paper electronic system has yet to be demonstrated that can take advantage of the paper's 3D structure by utilizing it as a functional material within circuit components as well as a substrate.

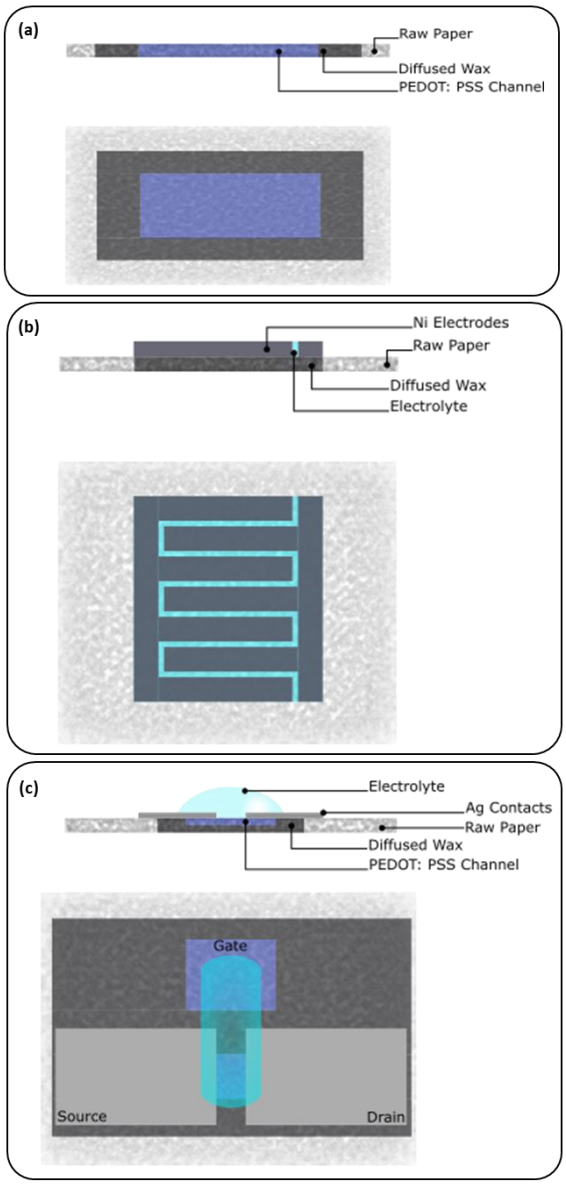

Figure 1: (a) Schematic illustrations of the self-charging power system integrating the MFC and the supercapacitor (back and front view), (b) the MFC inoculated with B. subtilis spores and its operating principle with sweat, and (c) the system applied to human.

978-1-940470-04-7/HH2022/$25©2022TRF
DOI 10.31438/trf.hh2022.104

Herein, our group provided novel approaches to fabrication of paper-based electronic components and PCBs. We successfully designed, assembled, and evaluated three of the most commonly used electronic components on paper: resistors, capacitors, and transistors (Figure 1). These components were achieved through simple, affordable, and rapid fabrication techniques, enabling easy customization and efficient development of paper circuitry for disposable applications.

EXPERIMENTAL PROCEDURE

Materials

Poly(3,4-ethylenedioxythiophene):polystyrene sulfonate (PEDOT:PSS) (Clevios PH1000) was purchased from Heraeus. Dimethyl sulfoxide (DMSO), hydrolyzed polyvinyl alcohol (PVA), and sodium sulfate (Na_2SO_4) were obtained from Sigma-Aldrich. The Whatman Grade 1 filter paper substrate was purchased from VWR. Silver/Silver-Chloride and graphite ink were acquired from Ercon Inc. A nickel conductive spray was purchased from MG Chemicals.

Resistor fabrication

Paper resistors were fabricated by first patterning filter paper with a hydrophobic, wax-printed (Xerox Phaser, ColorQube 8570) boundary with a width of 1 mm and variable length (0.5 cm, 1 cm, 1.5 cm, 3 cm, and 3.5 cm). The wax was diffused throughout the paper fibers via baking at 140°C for 30 s. The paper was then injected with a resistive PEDOT:PSS/DMSO ink. Since DMSO addition enhances the conductivity of PEDOT:PSS, the amount of DMSO in the ink mixture can be manipulated to achieve the desired resistivity [10-12]. Four different ink mixtures were prepared with different ratios of DMSO: 1 wt%, 5 wt%, 10 wt%, and 20 wt%.

Capacitor fabrication

The interdigitated electrolytic capacitor was realized on paper through similar wax-patterning described for the paper resistor. After baking the wax-patterned paper, a mask was laser-cut from copy paper and temporarily pasted onto the filter paper substrate for electrode patterning. The capacitor electrodes were evenly applied via spray coating of a conductive nickel spray. Capacitor electrodes were interdigitated, each with 3 legs of length 10 mm, width 2 mm, and gap 0.75mm.

A gel electrolyte was prepared with PVA and Na_2SO_4. A 75 g/L PVA solution was made by stirring hydrolyzed PVA into distilled water at 85°. As this mixture cooled to room temperature, a 106 g/L Na_2SO_4 solution was separately prepared and mixed thoroughly by sonication for 10 min. The Na_2SO_4 solution was slowly added to the PVA solution at a ratio of 1:2 and stirred until clear. The gel electrolyte was cast over the active region of the interdigitated capacitor electrodes and allowed to set overnight.

Transistor fabrication

A planar, electrolytic p-channel FET was fabricated using a PEDOT:PSS/DMSO semiconductive ink to functionalize a paper channel. Wax was printed onto filter paper to define the transistor channel and gate electrode region. The paper was baked at 140°C for 30 s. The functional inks were prepared by sonicating a mixture of PEDOT: PSS and DMSO for 30 min. A 5% DMSO was introduced to the paper channel and a 10% DMSO ink was applied to the gate. After drying, application of the source and drain electrodes were achieved via screen-printing of the silver/silver-chloride ink. A channel length of 4 mm and a width of 2 mm were chosen for the FET dimensions, resulting in a W/L dimension of 1/2. The PVA/Na_2SO_4 gel electrolyte for the FET was prepared as described for the capacitor electrolyte, and it was applied over the FET's active region and allowed to solidify before use.

Paper PCB fabrication

The three components (resistors, capacitors, and transistors) were designed to be fabricated into a single sheet of paper to facilitate easier and more rapid manufacturing. Since the electronic components share many of the same materials and fabrication processes, these steps can be carried out simultaneously, allowing for an entire paper PCB to be achieved in almost the same amount of time it takes to create just a single component. The only additional step was the screen-printing of conductive graphene ink trace to interconnect the components as desired as per the circuit design. These connections and placements of components on the PCB were adjusted using AutoCAD software, which can be used to design any other variation or custom paper PCB. The order of fabrication for a PCB is as follows: components' wax boundaries are patterned according to the AutoCAD file and heat-diffused in an oven at 140°C, PEDOT:PSS/DMSO inks are applied to the appropriate component regions and allowed to dry, drain and source electrodes are applied to the FET via screen printing and allowed to dry, conductive traces are patterned, and prepared gel electrolyte is cast onto the capacitor and FET.

Measurement procedure

Resistor values were determined via a Lomvum T28B digital multimeter. Capacitor behavior and transistor behavior were monitored and characterized using an Agilent HP Keysight MSOX3054A oscilloscope and an Agilent E3630A DC power supply.

RESULTS AND DISCUSSION

Resistor Characterization

The resistance values of our fabricated paper resistor were measured with the modifications of three distinct variables: the percentage of DMSO used in the ink recipe, the volume of resistive ink applied, and the length of the paper resistor. The trends and effects of these variable manipulations can be obtained from the plots presented (Figure 2). The resistance range of the plots is kept constant for clearer observation of the attainable resistance values for each percent DMSO increment. Data consistency is also represented in the form of error bars with each point placed at the average of 5 resistor samples.

The collected data shows strong correlations between the three variables and paper resistance. As the percentage of DMSO is increased from 1% to 20%, the heightened conductivity of the ink results in much lower resistances in the resulting paper resistors. Resistors fabricated with 1% DMSO inks attained a maximum of about 285 kΩ, whereas 20% DMSO resistors only reached a resistance of about 3.4 kΩ. Therefore, resistive ink recipes with higher concentrations of DMSO can be used to achieve more finetuned low resistance paper resistors and vice versa. Similarly, the length of the paper resistors and volume of ink utilized can be adjusted to further tailor the resistor characteristics since shorter and more saturated paper resistors exhibit lower resistance. In this way, the DMSO concentration, length, and ink volume used for resistor fabrication can be concurrently altered to achieve practically any desired resistance. With the test cases presented here, including DMSO concentrations between 1% and 20%, lengths between 0.5 cm and 3.5 cm, and ink volumes between 2 µL and 20 µL, the range of resistances achieved was from 26 Ω to 280 kΩ. If necessary for the desired circuit, higher resistances could additionally be realized by further decreasing DMSO concentration and ink volume or increasing length. Furthermore, zig-zag resistor designs can be

implemented to reduce their perceived length while still maintaining larger resistance values, allowing for more compact paper PCB designs.

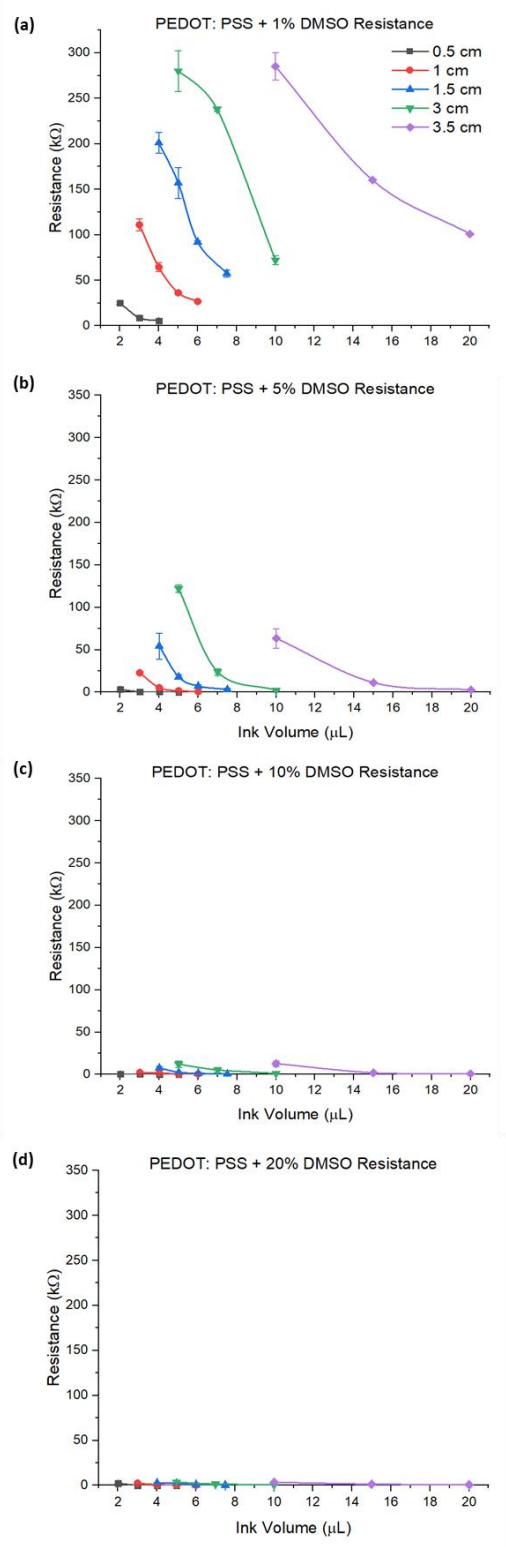

Figure 2: Measured resistance values of fabricated paper resistors at different lengths and applied ink volumes for DMSO percentage at (a) 1%, (b) 5%, (c) 10%, and (d) 20%.

Capacitance characterization

The charging and discharging profiles of the paper-integrated capacitor were measured both with and without the addition of the PVA- Na_2SO_4 gel electrolyte (Figure 3). For the non-electrolytic case, the applied resistance was 200 kΩ with a resulting time constant of 14.2 µs, while the electrolytic case utilized a 100 Ω and exhibited a time constant of 27.14 ns. According to this data, the electrolytic capacitor achieved almost 100 times higher capacitance than it did without the electrolyte, and so the electrolytic capacitor was chosen to be used in subsequent designs.

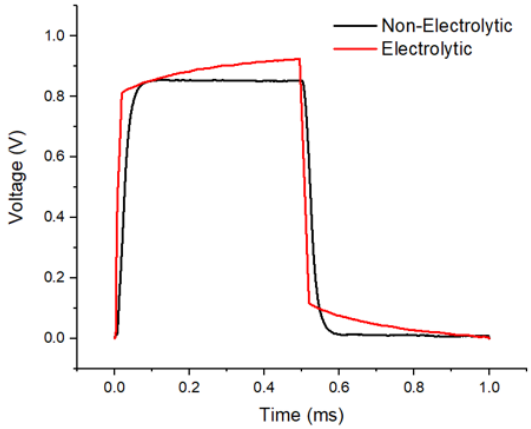

Figure 3: Paper capacitor charge/discharge cycle with and without PVA-Na_2SO_4 electrolyte.

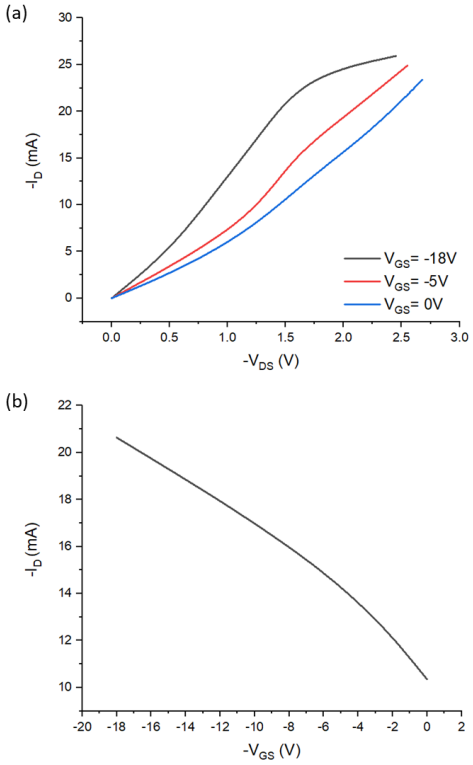

Figure 4: Measured (a) output characteristics and (b) transfer characteristics (V_{DS} = -1.5V) of paper-fabricated FET.

Transistor characterization

The fabricated electrolytic FET was evaluated via its output and transfer characteristic plots (Figure 4). The output characteristic

plot reveals the relationship between the voltage at the drain electrode and the drain current at varying gate biases, whereas the transfer characteristic plot demonstrates the drain current as the gate voltage is modified. The trends exhibited in both plots show that the FET successfully achieves the behavior of a depletion-type p-channel FET [13].

Paper PCBs

Each type of component was used in the design of a paper PCB. The circuit model containing four fully functional paper resistors, a capacitor, and a transistor was fabricated into a single sheet of filter paper, exemplifying the ease in which one could manufacture and customize paper circuitry that requires resistors, capacitors, and transistors. The entire circuit was obtained on a thin sheet of paper and within a small area, occupying a volume of only approximately 0.5 cm^3.

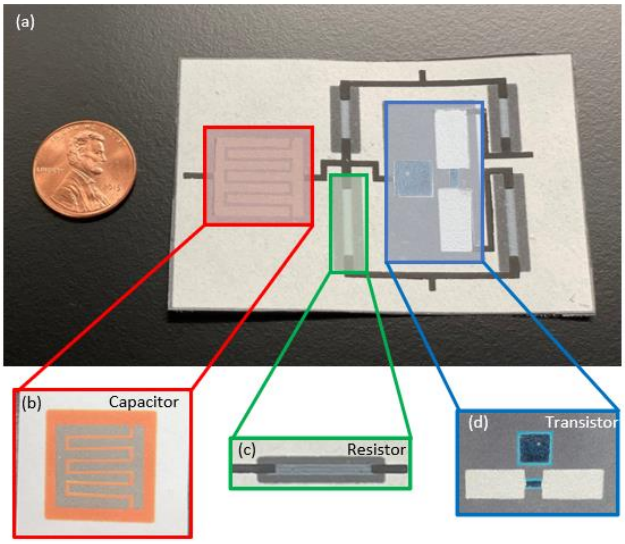

Figure 5: Photographs of (a) example paper printed circuit board (P-PCB) using all paper components, (b) individual paper capacitor, (c) individual paper resistor, and (d) individual paper transistor.

CONCLUSION

In this work, we have successfully demonstrated the capability of achieving functional electronic circuits on paper without significant disruption of the paper's biodegradability and affordability. Employing the presented techniques, users can devise any variation of the resistor, capacitor, and transistor circuits and simultaneously develop the components within a single, compact paper PCB. This capability implies facile integration of electronic circuitry within disposable sensor systems and other short-time use electronic device applications.

ACKNOWLEDGEMENTS

This work was supported mainly by the National Science Foundation (CBET #2100757, ECCS #2020486, and ECCS #1920979).

REFERENCES

[1] D. Tobjörk and R. Österbacka, "Paper electronics," *Advanced Materials*, 23, 1935-1961 (2011).

[2] J. Liu, C. Yang, H. Wu, Z. Lin, Z. Zhang, R. Wang, B. Li, F. Kang, L. Shi and C.P. Wong, "Future paper based printed circuit boards for green electronics: Fabrication and life cycle assessment," *Energy & Environmental Science*, 7, 3674-3682 (2014).

[3] A. Russo, B.Y. Ahn, J.J. Adams, E.B. Duoss, J.T. Bernhard and J.A. Lewis, "Pen-on-paper flexible electronics," *Advanced Materials*, 23, 3426-3430 (2011).

[4] Y. Xu, Q. Fei, M. Page, G. Zhao, Y. Ling, S.B. Stoll, Z. Yan, "Paper-based wearable electronics," *iScience*, 24, 102736, (2021).

[5] Y. Gao and S. Choi, "Stepping Towards Self-powered Papertronics: Integrating Biobatteries into a Single Sheet of Paper," *Advanced Materials Technologies*, 2, 1600194 (2017).

[6] G. Casula, S. Lai, L. Matino, F. Santoro, A. Bonfiglio, P. Cosseddu, "Printed, Low-Voltage All-Organic Transistors and Complementary Circuits on Paper Substrate," *Advanced Electronic Materials*, 6, 1901027 (2020).

[7] J. Costa, A. Wishahi, A. Pouryazdan, "Hand-Drawn Resistors, Capacitors, Diodes, and Circuits for a Pressure Sensor System on Paper," *Advanced Electronic Materials*, 4, 1700600 (2018).

[8] B. Peng, X. Ren, Z. Wang, "High Performance Organic Transistor Active-Matrix Driver Developed on Paper Substrate," *Scientific Repports*, 4, 6430 (2014).

[9] P. Bezuidenhout, S. Smith, T.-H. Joubert, "A Low-Cost Inkjet-Printed Paper-Based Potentiostat," *Applied Sciences*, 8, 968 (2018).

[10] L. Lingstedt, M. Ghittorelli, H. Lu, D. Koutsouras, T. Marszalek, F. Torricelli, N. Craciun, P. Gkoupidenis, P. Blom, "Effect of DMSO Solvent Treatments on the Performance of PEDOT: PSS Based Organic Electrochemical Transistors," *Advanced Electronic Materials*, 5, 1800804 (2019).

[11] M.M. Hamedi, A. Ainla, F. Guder, D.C. Christodouleas, M.T. Fernandez-Abedul, G.M. Whitesides, "Integrating Electronics and Microfluidics on Paper," *Advanced Materials*, 28, 5054-5063 (2016).

[12] Y. Gao and S. Choi, "Merging Electric Bacteria with Paper," *Advanced Materials Technologies*, 3, 1800118 (2018).

[13] P. Ersman, R. Lassnig, J. Strandberg, D. Tu, V. Kashmiri, R. Forchheimer, S. Fabiano, G. Gustafsson, M. Berggren, "All-Printed Large-Scale Integrated Circuits Based on Organic Electrochemical Transistors," *Nature Communications*, 10, 5053 (2019).

CONTACT

*Prof. S. Choi, tel: +1-607-777-5913; sechoi@binghamton.edu

PIEZOELECTRIC PAPER: LARGE-SCALE COMPATIBLE MANUFACTURING PROCESS AND SENSOR DEMONSTRATION

Kanagasubbulakshmi Sankaralingam[1], Ninweh Nina Jeorge[2], Sajana Sumanasinghe[1], Anindya L. Roy[2], Konrad Walus[2] and Boris Stoeber[1,2]*

[1]Department of Mechanical Engineering, [2]Department of Electrical and Computer Engineering
The University of British Columbia, Vancouver, British Columbia, Canada

ABSTRACT

Functionalized paper has been used as a substrate for flexible devices for several years now. However, the methods for preparing such paper substrates are typically too complex for integration with large-scale paper manufacturing processes. Here, we demonstrate a simple process for manufacturing piezoelectric paper that is compatible with the conventional papermaking process. This process utilizes microfibrillated wood pulp to achieve paper with high loading (69 wt%) of piezoelectric $BaTiO_3$ particles (~300 nm diameter) that shows high piezoelectric coefficients up to d_{33} = 15.2 pC/N after corona poling. Such a piezoelectric paper composite is used as a simple accelerometer to demonstrate its utility in inertial sensing applications.

KEYWORDS

Piezoelectric, $BaTiO_3$, Paper based sensors, Accelerometer, Nanomaterials, Large scale, Flexible sensors

INTRODUCTION

Paper based substrates have attracted significant attention in the realm of smart materials and electronics due to a growing desire for environmentally sustainable platforms, potential to exploit the fibrous bulk, and opportunity to incorporate other functional materials within the matrix. In addition, paper presents several other advantages that make it a suitable material to be used in sensing devices. It is easy to manufacture at low cost, it is a dielectric material that can be used in numerous sensing mechanisms, and the porous nature allows it to be used as a paper filter where fluids and particles smaller than the pore size can pass through while larger-sized particles are captured [1], [2].

Many attempts have been made in recent years to improve the physicochemical properties of paper by incorporating nanostructured materials onto wood fiber. For example, carbon nanotubes [3] were added to the matrix of wood pup to fabricate conductive paper as well as titanium dioxide functionalized wood fiber [4] was developed by a hydrolysis method. Likewise, polyelectrolytes attract significant interest in the field of making conductive wood fiber for smart paper applications [5]. Recently, multiple researchers developed paper-based sensing devices that have a wide range of applications in the area of bio and chemical sensing [6].

Integrating nanomaterials within the industrial paper production process has the potential to impart useful electronic properties such as piezoelectricity to conventional paper. In past work, wood pulp-based composites for flexible electronics have been achieved by growing ZnO on wood fibers [7], a complex procedure that is incompatible with standard paper making; another study [8] used an approach to electrostatically bind negatively charged $BaTiO_3$ (BT) onto wood fibers, involving electrostatically coating the wood fiber with a total of 3 layers of anionic and cationic polyelectrolytes poly(diallyldimethyl-ammonium chloride (PDDA) and poly(sodium 4-styrenesulfonate) (PSS), respectively, and the addition of the paper strengthening agent carboxymethylcellulose (CMC). The basic idea of this manufacturing process involves embedding BT into a stable matrix of wood fiber; this can be achieved through fiber functionalization. The fiber functionalization process is realized using a layer-by-layer (LbL) approach, and this results in the creation of a positively charged wood fiber surface. Immersion of thus treated fibers into a BT suspension results in electrostatic binding of the BT nanoparticles directly onto each fiber before using these fibers to make paper. Though this process yields a high BT mass loading of wood fiber, it involves complex steps and is rather time consuming.

Recently the production and potential application of microfibrillated cellulose (MFC) fibers have garnered much attention due to their role in enhancing the tensile strength of the paper-based composite, biodegradability, and renewability. MFC is created by refining wood fibers, a mainly mechanical process that partially separates the cellulose fibrils from the wood fiber matrix. There are reports of various applications of MFC -based materials including composites, scaffolds, electronic materials, and solar cells [9].

In this study, we demonstrate that the use of highly refined MFC wood pulp (up to 300 kWh/t specific refining energy, SRE) facilitates BT binding without requiring the time-consuming steps necessary for unrefined pulp. We believe MFC significantly increases the available surface area for better anchoring of BT particles. We form piezoelectric paper from the functionalized MFC and demonstrate the usefulness of such paper for a sensing application.

FABRICATION OF PIEZOELECTRIC PAPER

Highly refined wood pulp refined at 200 kWh/t and at 300 kWh/t denoted Fiber(200) and Fiber(300), respectively, was obtained from CANFOR Ltd. (British Columbia, Canada) along with unrefined pulp (Fiber(0)). Prior to the functionalization, zeta potential measurements are taken to identify the surface charges of the wood fiber and the BT particles. The measurements on the pristine wood fibers (-23 ± 2.5 mV) and BT particles (-24.7 ± 1 mV) show the necessity of an intermediate layer; hence, the attachment of BT particles onto wood fibers can be enabled through a positive polyelectrolyte interlayer.

In this study, the piezoelectric paper is prepared by functionalizing the wood fiber with the help of cationic polymers to create a uniform positively charged surface to enable the anchoring of 300 nm sized BT particles onto wood fiber. First, an aqueous solution of positively charged PDDA (1 wt % in 0.5 M NaCl) and an aqueous solution of negatively charged PSS (1 wt % in 0.5 M NaCl) are prepared. Here the NaCl serves to avoid coiling up of polyelectrolytes. Different batches of these wet state fibers with a fiber dry weight of 3g per batch are processed in different sequences of steps before forming handsheets according to TAPPI standard T-205. For a 3-layer LbL process as in [8] and shown in Fig. 1 (top) a batch of F(200) fibers is immersed in a PDDA solution (400 mL- for 1 hour), followed by a PSS solution (400 mL- for 1 hour) and again in a PDDA solution (400 mL for 12 hours) to create a positively charged surface on the wood fibers. The wood fibers are then immersed in a BT suspension (1 wt % of BT sonicated in 400 mL of distilled water for 10 minutes) for 12 hours adsorption. Followed this, the functionalized fibers are transferred to

978-1-940470-04-7/HH2022/$25©2022TRF
DOI 10.31438/trf.hh2022.105

400 mL of 5 wt % of CMC dissolved in distilled water and left for 12 hours adsorption under magnetic stirring at 500 RPM.

Other fiber batches undergo much simpler processes employing at most one polyelectrolyte layer as shown in Fig. 1 (bottom). For a single layer process a batch of fibers is immersed in a solution of 1 wt % PDDA dissolved in 0.5 M NaCl (400 mL- for 1 hour). Then the wood fibers are transferred to 1 wt % of BT dispersed in 400 mL of distilled water and left for 12 hours adsorption under magnetic stirring at 500 RPM. In one case, the functionalized fibers are also transferred to 400 mL of 5 wt % of CMC and left for 12 hours adsorption under magnetic stirring at 500 RPM. One batch of refined pulp is also directly immersed in the same BT suspension as above, without prior deposition of a polyelectrolyte. The process using a single polyelectrolyte layer is also applied to non-fibrillated-Fiber(0) pulp to compare the properties of the resulting paper sample with paper based on refined MFC pulp.

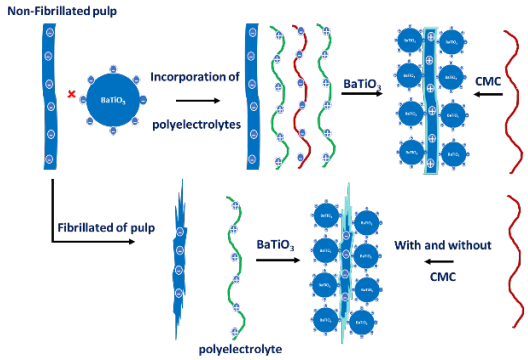

Figure 1: Schematic of a 3-layer LBL process [8] (top) and the simplified fiber functionalization process (bottom)

CHARACTERIZATION AND POLING

The piezoelectric paper is characterized using a scanning electron microscope (SEM) to image the distribution of particles on the fibers, and thermal gravimetric analysis (TGA) allows determining the mass fraction of BT in the paper composite. The paper is subjected to corona poling (Milman Thin Film Systems Pvt. Ltd.) to render it piezoelectric at 122°C (Curie temperature of BT) for 1 hour with a needle voltage of 63 kV and a grid voltage of 25 kV. The piezoelectric coefficients of the hybrid paper samples are measured with a PiezoTest PM300 d_{33} meter (Piezotest Pte. Ltd. Singapore). The piezoelectric paper is characterized by X-ray diffraction (XRD) before and after poling to understand the influence of poling on the tetragonality of the BT lattice structure.

The piezoelectric paper is finally used to construct an accelerometer and this device is characterized by using a sinusoidally driven voice coil actuator (VCA) along with a reference accelerometer (ADXL203EB by Analog Devices). The charge response of the paper-based accelerometer is measured using a Kistler 5015A charge-voltage converter.

RESULTS AND DISCUSSION

Table 1 shows the BT mass fraction and the piezoelectric coefficient of paper samples made according to Fig. 1. The samples with one polymer layer and without CMC show the highest BT loading, and the highest d_{33} value among these samples is achieved for Fiber(300), while the lowest mass loading and d_{33} is achieved for unrefined pulp.. The addition of CMC appears to slightly reduce the BT mass loading while not significantly affecting the piezoelectric properties. The omission of the polyelectrolyte layer does not affect the BT mass loading is a meaningful manner but leads to a significant reduction of the piezoelectric properties of the sample. This shows that MFC eliminates the need for additional functional layers while achieving higher BT loading compared to previous work [8].

Table 1: BT mass loading and piezoelectric coefficient of paper samples; Fiber(SRE) indicates the specific refining energy in kWh/t

Sample	wt% BT	d_{33} [pC/N]
Fiber(0) + PDDA + BT	26	2.0
Fiber(200) + BT	61	4.3
Fiber(200) + PDDA+ BT	64	8.0
Fiber(200) + PDDA +BT+ CMC	53	10.1
Fiber(200) +PDDA +PSS + PDDA +BT +CMC	43	4.7
Fiber(300) + PDDA+ BT	69	15.2

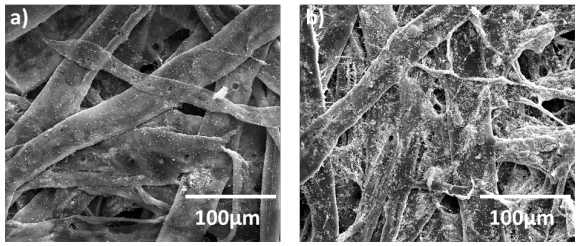

Figure 2: SEM images of a Fiber(0)+PDDA+BT and Fiber(300) + PDDA+ BT paper sample showing a significance difference in the loading of $BaTiO_3$ onto wood fiber.

The SEM images in Fig. 2 clearly elucidate the loading efficiency of MFC over non-fibrillated pulp through its external fibrils which enhances the physical adsorption of particles on the fiber surface. Fig. 3 shows SEM images of the highly loaded piezoelectric paper made from Fiber(300). The BT particles tightly coat the fibrillated wood fibers. The cross section of the fiber matrix also shows that the paper is highly loaded with BT particles.

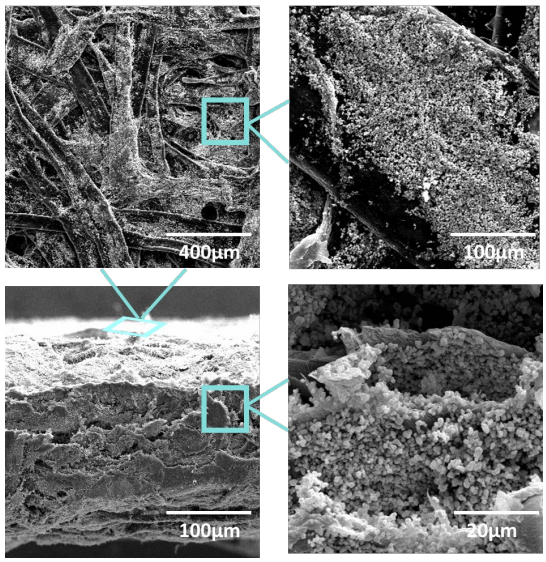

Figure 3: SEM images of a Fiber(300) + PDDA+ BT paper sample showing high loading of $BaTiO_3$ in the wood fiber matrix

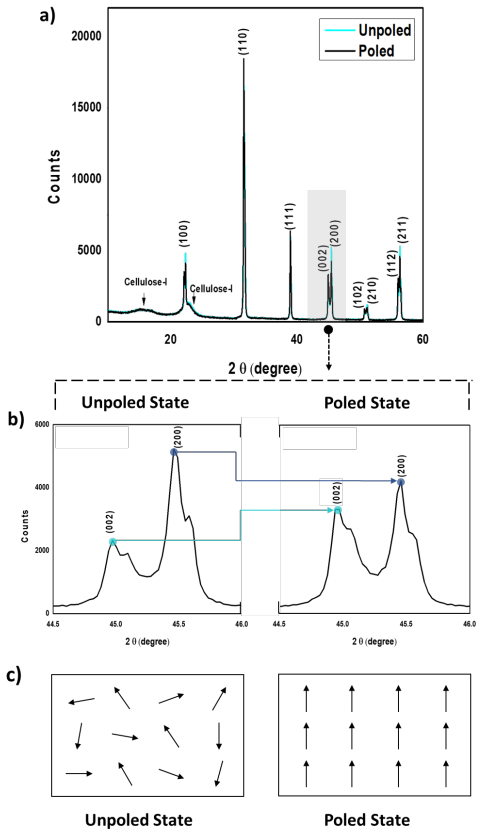

Figure 4: XRD analysis of Fiber(300) + PDDA+ BT piezoelectric paper and influence of poling on domain orientation

XRD characterization allows assessing the effect of poling on domain orientation of BT in the piezoelectric paper. The XRD pattern of the hybrid paper exhibits peaks in the range of 2θ=44.5°-47° corresponding to BT (Fig. 4a) allowing analysis of the structural changes related to corona poling. The peaks at (200) and (002) in both unpoled and poled states suggest that the BT is tetragonal [3]. Tetragonal structures with random orientation show a (200) plane peak intensity twice the intensity of the (002) plane peak. The relative intensity of the (002) plane peak increases by 32.6 % with poling and the relative intensity of the (200) plane peak simultaneously decreases by 18.8 % (shown in Fig.3b); this indicates domain wall reorientation of the ferroelectric domains with the poling process; the domain orientations are schematically depicted in Fig. 3c [10].

DEMONSTRATION OF ACCELEROMETER

The Fiber(300)-based piezoelectric paper is used as a substrate to build an accelerometer to demonstrate its suitability as a substrate for sensing applications. An accelerometer is constructed using the piezoelectric paper by attaching parallel copper electrodes and adding a seismic mass of m = 30 g to one of its sides. This setup is then mounted to a 3D printed cube which is mounted to a VCA as shown in Fig. 5.

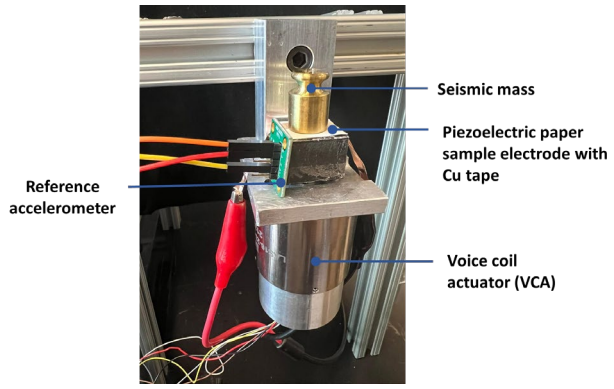

Figure 5: Photograph of an accelerometer set up used in the experiments

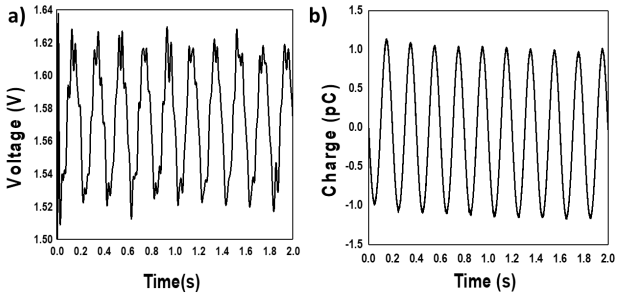

Figure 6: Output signal at 5 Hz from a) commercial reference accelerometer and b) paper accelerometer

The time-dependent output signals of the reference accelerometer and the paper accelerometer for excitation at 5 *Hz* are acquired simultaneously, and they are shown in Fig. 6.

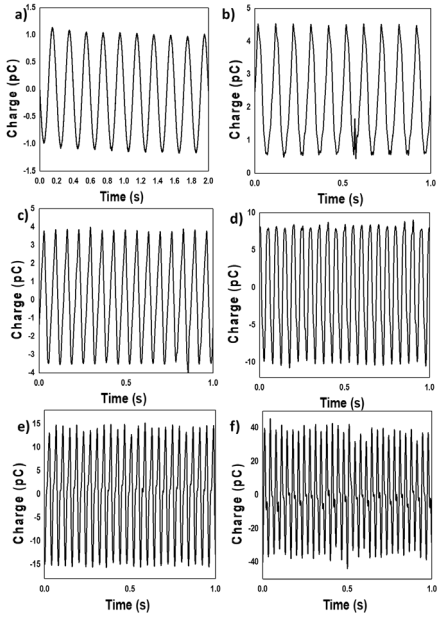

Figure 7: Output signal at different frequencies a) 5 Hz b) 10 Hz c) 15 Hz d) 20 Hz e) 25 Hz f) 30 Hz

To test the frequency response of our paper-based accelerometer, we measured the charge output at frequencies from f = 5 Hz to 30 Hz in 5 Hz intervals. As shown in Fig. 7a-f, the charge output increases with an increase in frequency for a nearly constant displacement amplitude A_d = 1 mm, corresponding to an increasing acceleration amplitude $A_a = A_d (2\pi f)^2$.The sensitivity of the accelerometer $S = A_C / A_a$ (with the charge amplitude A_C) remains approximately constant around 5.82 pC/ms^{-2} in the frequency range; a constant sensitivity is expected as the mechanical resonant frequency of this device most likely occurs above this frequency range. Below resonance, the sensitivity [11]

$A_C/A_a = d_{33} * m$ ---- (1)

allows calculating the piezoelectric coefficient independently to verify consistency. Based on the sensitivity obtained in this frequency range, the d_{33} = 19.7 pC/N is comparable to the value of d_{33} = 15.2 pC/N measured using the d_{33} meter (Table 1).

In addition to the above experiments, one of the Fiber(300)-based paper sample was repeatedly poled for three times at the same poling conditions mentioned in the experimental section to induce the maximum polarization. This yielded the highest piezoelectric coefficient of 32.8 pC/N. However, it decayed to 8 pC/N after 24 hours. Our future work will focus on understanding the mechanisms behind this decay of piezoelectric coefficient in the paper-based composite.

CONCLUSION

We have demonstrated the manufacturing of a piezoelectric paper composite through the electrostatic interaction of polyelectrolyte coated MFC wood pulp with BT nanoparticles. The use of MFC wood pulp enhances the loading of BT nanoparticles on to wood fibers and upon corona poling, yields a piezoelectric coefficient of the composite of up to 32.8 pC/N. As a proof-of-concept demonstration, a piezoelectric paper-based accelerometer was constructed and its time series response at different frequencies was recorded, demonstrating the utility of piezoelectric paper composites for inertial sensing. Our initial experimental results indicate that functionalizing microfibrillated wood fibers with BT nanoparticles is a promising approach to integrate piezoelectric functionality into conventionally manufactured paper and enhance its piezoelectric performance by significantly improving the loading of BT nanoparticles. Such piezoelectric paper composites are expected to open greener avenues for applications in diverse niches such as energy storage, nanogenerators, accelerometers, strain sensing, microfluidic devices, biosensing, tactile sensors and speakers, to name a few.

ACKNOWLEDGEMENTS

The authors thank CANFOR and NSERC for financial support of this work. This research was undertaken, in part, thanks to funding from the Canada Research Chairs program. We also thank Mr. Ben Herring, lab technician for performing the TGA tests for this work at the Shared instrument facility at the Department of Chemistry, University of British Columbia, Canada.

REFERENCES

[1] Mazzeo, Aaron D., Tongfen Liang, Xiyue Zou, Jingjin Xie, Ali Ashraf, Deepti Salvi, Francois Berthiaume, and Ramendra K. Pal. "Paper as a substrate and smart material for electronics, packaging, and robotics." IEEE International Conference on Flexible and Printable Sensors and Systems (2021), pp. 1-3.

[2] Khan, Sherjeel M., Joanna M. Nassar, and Muhammad M. Hussain. "Paper as a substrate and an active material in paper electronics." *ACS Applied Electronic Materials,* 3, 1 (2020).

[3] Anderson, Robin E., Jingwen Guan, Michelle Ricard, Girjesh Dubey, Joseph Su, Gregory Lopinski, Gilles Dorris, Orson Bourne, and Benoit Simard. "Multifunctional single-walled carbon nanotube–cellulose composite paper." *Journal of Materials Chemistry,* 20, 12 (2010).

[4] Marques, Paula AAP, Tito Trindade, and Carlos Pascoal Neto. "Titanium dioxide/cellulose nanocomposites prepared by a controlled hydrolysis method." *Composites Science and Technology,* 66, 7-8 (2006).

[5] Huang, Jianguo, Izumi Ichinose, and Toyoki Kunitake. "Nanocoating of natural cellulose fibers with conjugated polymer: hierarchical polypyrrole composite materials." *Chemical communications,* 13 (2005).

[6] Mirica, Katherine A., Joseph M. Azzarelli, Jonathan G. Weis, Jan M. Schnorr, and Timothy M. Swager. "Rapid prototyping of carbon-based chemiresistive gas sensors on paper." *Proceedings of the National Academy of Sciences,* 110, 35 (2013).

[7] Manekkathodi, Afsal, Ming-Yen Lu, Chun Wen Wang, and Lih-Juann Chen. "Direct growth of aligned zinc oxide nanorods on paper substrates for low-cost flexible electronics." *Advanced materials,* 22, 36 (2010).

[8] Mahadeva, Suresha K., Konrad Walus, and Boris Stoeber. "Piezoelectric paper fabricated via nanostructured barium titanate functionalization of wood cellulose fibers." *ACS applied materials & interfaces,* 6, 10 (2014).

[9] Sharma, Sudhir, Sandeep Sudhakaran Nair, Zhe Zhang, Arthur J. Ragauskas, and Yulin Deng. "Characterization of micro fibrillation process of cellulose and mercerized cellulose pulp." *RSC Advances,* 5, 77 (2015).

[10] Val-Gómez, P., A. Del Campo, F. Rubio-Marcos, J. F. Fernández, and A. Moure. "Poling and depoling influence on the micro-stress states and phase coexistence in KNN-based piezoelectric ceramics." *Journal of the European Ceramic Society,* 39, 4 (2019).

[11] Mahadeva, Suresha K., Konrad Walus, and Boris Stoeber. "Flexible and robust hybrid paper with a large piezoelectric coefficient." *Journal of Materials Chemistry C,* 4, 7 (2016).

CONTACT

*Kanagasubbulakshmi Sankaralingam, tel: +1 -647-540-7524; ksankara@mail.ubc.ca

SCALABLE AND VERSATILE FABRICATION OF OPAL STRUCTURES WITH SLOPE SELF-ASSEMBLY AND CAPILLARY PEELING FOR MICRODEVICES AND SENSORS

Carlos D. Díaz-Marín[1], Diane Li[1], Samantha Cheung[1], Cameron Kilpatrick[2], Rishabh Shetty[1], Geoffrey Vaartstra[1], Ashwin Gopinath[1], and Evelyn N. Wang[1]*
[1]Massachusetts Institute of Technology, Cambridge, Massachusetts, USA
[2]Stanford University, Stanford, California, USA

ABSTRACT

Self-assembly of opals has been extensively studied as a scalable bottom-up fabrication method capable of yielding ordered structures for applications such as optoelectronics, micro thermofluidic devices, and high power density electrodes. However, previous fabrication techniques are limited in the feature sizes achievable, require complex processes and equipment, or are limited in the substrates that can be used. In this work, we combine slope self-assembly with capillary peeling to overcome previous limitations. We demonstrate high-throughput fabrication of ordered opal structures, with a wide range of feature sizes and on previously unachievable substrates. Our experiments show that this approach can yield structures with over 90% crystallinity and that it is compatible with hydrophobic, rough, and curved substrates, therefore enabling new applications for opal structures.

KEYWORDS

Self-assembly, opal, crystal, capillary peeling, transfer, optics, inverse opal, template

INTRODUCTION

Opal structures, consisting of self-assembled, crystalline microsphere arrays, have been extensively studied as a material that due to its order can be used in a wide range of applications including sensing, micro electrochemical devices, lithography masks, optical coatings, and micro thermo-fluidics.[1]–[4] To satisfy the various requirements for these applications, multiple fabrication methods have been developed by leveraging the different types of attractive and repulsive interactions between colloidal particles. However, commonly used methods exhibited limited functionality or suffered from low scalability. For instance, previous methods such as vertical deposition and drop-casting were successful only over a narrow range of sphere sizes and on ultra-smooth, wetting surfaces, were very time-consuming, and suffered from significant crystalline defects.[1], [3], [5], [6]

Here, we demonstrate that by combining slope self-assembly (SSA) with capillary peeling and transfer of the opals we overcome these limitations. We show that this approach is compatible with sphere diameters ranging from 500 nm up to 10 μm. Through modeling, experiments, and image analysis, we develop and validate guidelines for the rational and fast fabrication of opals across this feature size range. Moreover, our method can be used to fabricate opals on previously challenging substrates such as hydrophobic, rough, and curved substrates. Interestingly, we observe that the crystallinity of the opal structures increases with transfer, with values exceeding 90% for opals transferred to the hydrophobic and rough substrates.

The flexibility and scalability of our approach can enable new applications as well as significant enhancement in the performance of applications using opals such as capillary-fed micro thermofluidic devices, micro battery electrodes, and optical sensors.[2], [4], [7]

RESULTS

Figure 1 shows a schematic of our approach combining SSA with capillary peeling and transfer. First, we performed SSA, in which a colloidal solution of polystyrene microspheres suspended in 25% v/v ethanol and 75% v/v DI water was drop cast on an inclined glass slide which was rendered hydrophilic through plasma cleaning (Fig. 1a).[1] As the solvents evaporated, a monolayer array of close-packed spheres was achieved on smooth substrates with a high degree of hydrophilicity (contact angle ~0°). However, SSA on different substrates (e.g., surfaces with higher contact angles, rougher substrates such as mirror-polished copper) suffered from low order of the opal and from delamination of the opal from the substrate. To overcome these substrate-dependent challenges, we used capillary peeling to transfer the ordered opals from the glass slide to another desired substrate. The opal-covered glass slide was slowly dipped vertically into a water reservoir (Fig. 1b) causing the opal film to peel off from the substrate and float at the water-air interface while preserving its ordered shape. Finally, the suspended opal was transferred to a receiving substrate as the substrate was pulled upwards across the water-air interface (Fig 1c).

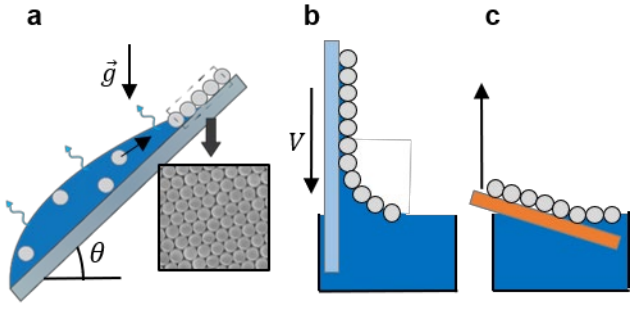

Figure 1: Schematic of our fabrication process. a) An opal is formed through slope self-assembly in which a colloidal solution is drop cast on a hydrophilic glass slide and left to evaporate to the ambient. Capillary and evaporative forces lead to a close packed opal crystal. b) The opal is capillary peeled from the glass slide by dipping it at a slow speed V into a water reservoir. The opal is detached from the substrate and suspended on the water-air interface. c) The floating opal crystal is transferred to a receiving substrate as this substrate passes the water-air interface.

To guide the opal fabrication process, in our previous work we modeled the self-assembly process (Fig. 1a) to extract guidelines for the use of SSA.[1] We demonstrated that for small spheres (diameter below 2 μm), the fraction of substrate that will be covered with spheres scales as

$$Coverage\ fraction \sim \left(\frac{\mu L \dot{m}''_{evap}}{\rho^2 g \sin\theta}\right)^{1/3} \frac{C}{(1-C)D} \qquad (1)$$

where D is the diameter of the opal spheres and C, ρ, and μ are

the colloidal concentration, density, and viscosity of the solution, respectively. $\dot{m}''_{evap}$ is the evaporation rate flux, L is the length of the substrate, θ is the inclination angle of the substrate, and g is the gravitational acceleration.

We validated the scaling of Eq. 1 against experiments where we fabricated opals under different combinations of sphere diameters, temperatures, diameters, and inclination angles. We performed image analysis for these samples to extract the fraction of the substrate covered with opals and plotted it as a function of the parameter $\frac{C}{1-C}\frac{\sin\theta^{-1/3}}{D}$, as suggested by Eq. 1. Our results, shown in Fig. 2 for 500 nm and 2 μm diameter spheres, demonstrate that the opal coverage increases linearly with $\frac{C}{1-C}\frac{\sin\theta^{-1/3}}{D}$, as predicted by Eq. 1. We also observe that with higher temperatures, and therefore higher evaporation rates, this linear increase is faster, further validating our model. More importantly, our results show that the opal coverage can be tuned for the desired sphere size by choosing the appropriate temperature, angle, and concentration providing a path for the fast use of SSA.

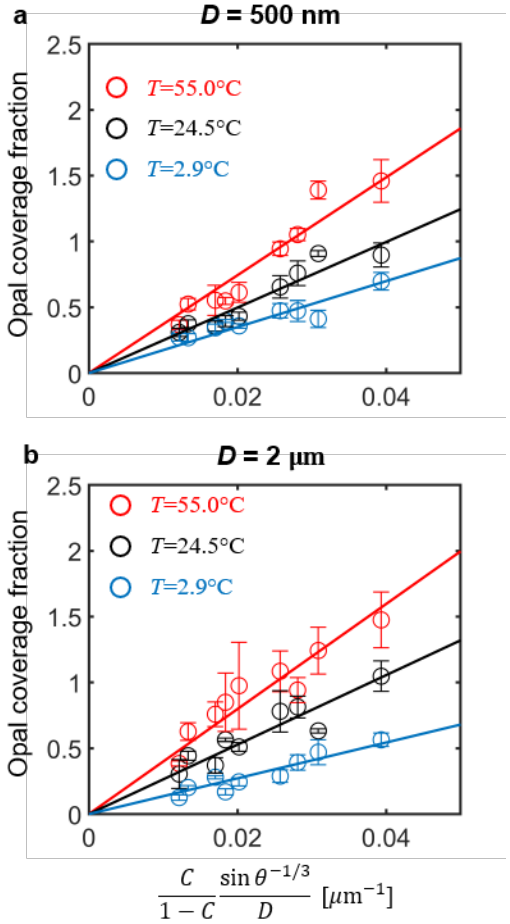

Figure 2: Experimental and modeling results of opal coverage: Experimental results (circles) show the fraction of substrate covered with opals obtained from image processing for (a) 500 nm and (b) 2 μm spheres formed under different angles of inclination θ, temperatures of solvent, and colloidal concentrations C as a function of the parameter $\frac{C}{1-C}\frac{(\sin\theta)^{-1/3}}{D}$*, obtained by our model. Values higher than 1 represent multilayer coverage. Solid lines correspond to the model results given by Eq. 1.*

For larger spheres of 10 μm diameter, capillary forces become more significant[8] and we observed that self-assembly is dominated by strong capillary interparticle attraction which causes spheres to self-assemble starting from the top of the substrate. As a result, assuming no sphere accumulation of spheres at the bottom of the substrate, the coverage fraction scales as

$$Coverage\ fraction \sim \frac{V_0 C}{D A_{sub}} \qquad (2)$$

where V_0 is the volume of solution drop-casted and A_{sub} is the area of the substrate.

Following Eqs. 1 and 2, we were able to fabricate large-scale opal arrays with monolayer coverage for sphere sizes ranging between 500 nm up to 10 μm as shown in Fig. 3. As seen in Fig. 3, we were able to achieve ~1 mm^2 areas of monolayer coverage without a significant presence of double layers or voids. This method can also fabricate larger, centimeter-scale areas. However, these will exhibit small uncovered substrate areas or sphere stacking.

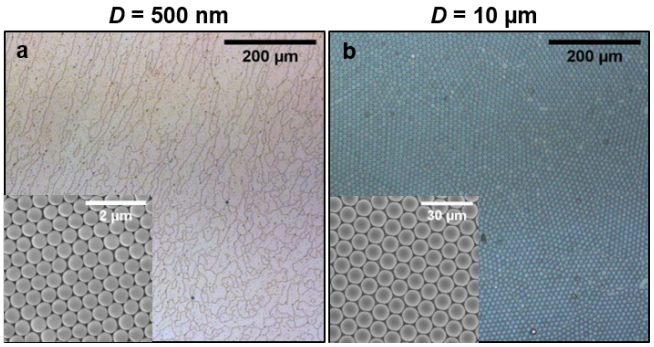

Figure 3: Scanning electron microscopy (SEM) images of the 500 nm and 10 μm sphere samples. Samples were fabricated at room temperature, at a 45° angle, and with polystyrene concentrations of 3.4% v/v and 19.4% v/v, respectively. Opals obtained were ordered and polycrystalline and contained several defects, such as grain boundaries and vacancies.

Our previous results show that slope self-assembly can generate opal structures in a scalable, high-throughput manner (~10 minutes per sample) and with a large range of spheres sizes. However, this method, as is the case for other commonly used colloidal self-assembly methods, is limited to highly wetting and smooth surfaces. This limitation severely restricts the applications where colloidal crystals can be used.

In order to enable the fabrication of opals in rough, nonwetting, and curved substrates, inspired by the capillary transfer of thin films at a liquid-air interface,[9] we capillary peeled the opals from the glass slide by dipping the slide vertically in a water bath at a slow speed (~1 mm/s). During capillary peeling, the spheres detach from the slide and float suspended in the air-water interface preserving their order, as seen in Figure 4. The floating opal can then be transferred to a receiving substrate as this substrate is passed slowly across the air-water interface.

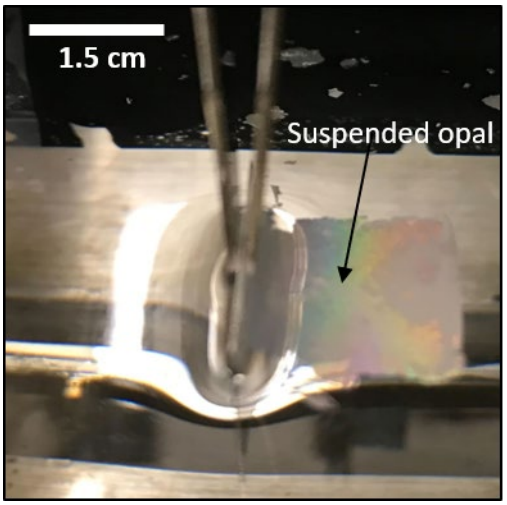

Figure 4: Opal layer floating in the water-air interface after being peeled off from a glass slide. The opal maintains the square shape from the glass slide and the order, as indicated by the visible diffraction, during the capillary transfer process.

This approach enabled transfer of opals to a wide variety of substrates while preserving the order of the sphere arrays. Fig. 5a shows a scanning electron microscope image (SEM) of 10 µm opals that were transferred to a silane coating glass with a contact angle of over 105° while Fig.5b shows an optical image of an opal that was transferred to the outer surface of a copper tube (shown in Fig. 5c). We additionally demonstrated transfer of the opal to the inside of a copper tube (Fig. 5d). We note that in spite of the hydrophobicity of the glass-coated slide and of the limited wetting, roughness, and curvature of the copper tube, the opal maintained good order as seen in Figs. 5a and 5b.

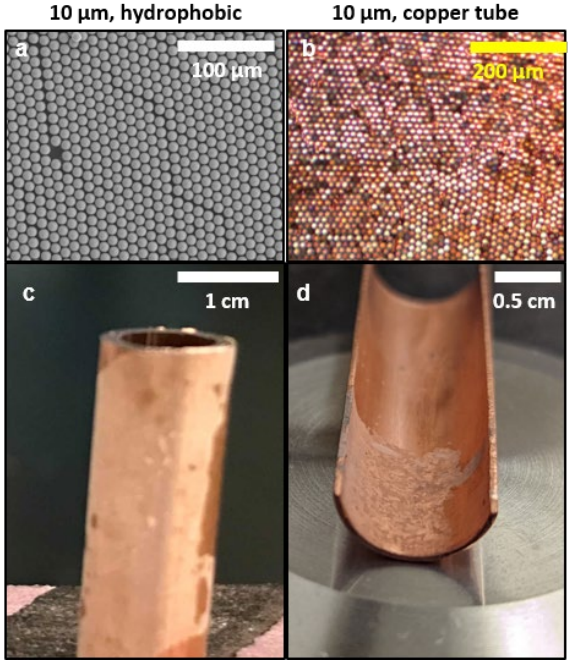

Figure 5: Opals transferred to various substrates. a) Scanning electron microscopy (SEM) image of a 10 µm sphere sample transferred to a silane coated hydrophobic glass slide. b) Optical image of a 10 µm sphere sample transferred to the outside of a copper tube. c) Outside of the copper tube coated with opal structures. d) Inside of a copper tube coated with 10 µm opals.

We further quantified the crystallinity of the opals fabricated with SSA on a glass slide and compared them with the crystallinity of opals transferred to a hydrophobic glass slide and to a mirror-polished flat copper piece. Specifically, we used a Voronoi diagram approach[10] to quantify using SEM images of opals the crystallinity of a sample at five different positions chosen randomly and we repeated this twice for the samples fabricated with SSA and three times for the transferred samples. Figure 6 shows the crystallinity results obtained, where each point corresponds to the average of all the values obtained for a given type of sample.

Our results show that the crystallinity of the samples fabricated on glass by SSA was about 85%, with minor variations as the sphere diameter changed. This value lies within the range of the crystallinity of samples fabricated via vertical deposition with spheres ranging from 100 nm up to 600 nm[10].

Interestingly, we observe that the transferred opals, which were originally fabricated on a glass slide via SSA and then transferred to the desired substrate, exhibit a higher degree of crystallinity than the opals fabricated only using SSA. The crystallinity of samples transferred to the hydrophobic glass and to the copper plate exceeded 90% with small differences across different sphere sizes and similar values regardless of the receiving substrate.

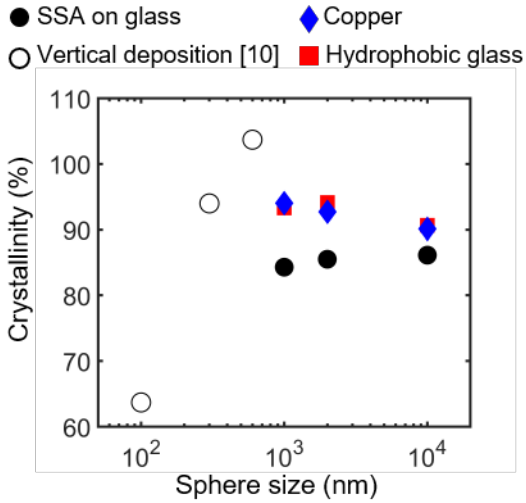

Figure 6: Crystallinity of opals obtained through a Voronoi diagram approach. Vertical deposition yields opals with crystallinities ranging between 60% up to over 100%. In comparison, SSA yields opals with crystallinities of about 85%. Crystallinity increases during transfer reaching values above 90% for a copper substrate and for a hydrophobic glass slide.

We hypothesize that the increase of crystallinity with transfer can be a consequence of forces acting during the transfer process. As the opal is peeled from the substrate the spheres push each other as they move away from the substrate leading to a densification of the opal. This is consistent with previous observations of how a similar transfer of opals can remove void spaces in opals with sub-monolayer coverage.[11] Additionally, the evaporation that accompanies the transfer to the receiving substrate can further enhance close-packing of spheres via capillary forces, leading to an increased crystalline order.

CONCLUSIONS

In this work, we have demonstrated an approach for the fabrication of ordered opal structures in a scalable and high

throughput manner (<30 minutes/sample) over a large range of sphere sizes and on previously unachievable substrates. We investigated the different steps involved in our approach, developing guidelines for the rational and fast use of slope self-assembly for particles with diameters between 500 nm and 10 μm. We observed that our approach can be used to transfer ordered opals to rough, nonwetting, and curved substrates with crystallinities of over 90%, exceeding those of as-fabricated opals. This approach can enable the use of opals in a wide range of previously unattainable applications as well as enhance previously demonstrated performances for opal applications such as micro battery electrodes, optical sensors, and micro thermofluidic devices. Additionally, the insights from this approach can be used to reduce defects and enhance crystallinity of opals via a transfer approach.

ACKNOWLEDGEMENTS

We gratefully acknowledge financial support from the Air Force Office of Scientific Research under Grant No. FA9550-19-1-0392 with Dr. Ali Sayir as program manager, the Office of Energy Efficiency and Renewable Energy under Grant No. DE-EE0009679, and a Professor Amar G. Bose Research Grant. This work made use of the MRSEC Shared Experimental Facilities at MIT, supported by the National Science Foundation under award number DMR1419807.

CONTACT

*C.D. Díaz-Marín, tel: +1-857-472-8139; cddiaz@mit.edu

[1] C. D. Díaz-Marín, R. M. Shetty, S. Cheung, G. Vaartstra, A. Gopinath, and E. N. Wang, "Rational Fabrication of Nano-to-Microsphere Polycrystalline Opals Using Slope Self-Assembly," *Langmuir*, vol. 37, no. 43, (2021)

[2] E. Armstrong and C. O'Dwyer, "Artificial opal photonic crystals and inverse opal structures-fundamentals and applications from optics to energy storage," *J. Mater. Chem. C*, vol. 3, no. 24, (2015)

[3] S. Adera *et al.*, "Enhanced condensation heat transfer using porous silica inverse opal coatings on copper tubes," *Sci. Reports 2021 111*, vol. 11, no. 1, (2021)

[4] J. H. Pikul, H. Gang Zhang, J. Cho, P. V. Braun, and W. P. King, "High-power lithium ion microbatteries from interdigitated three-dimensional bicontinuous nanoporous electrodes," *Nat. Commun.*, vol. 4, no. 1, (2013)

[5] D. J. Norris, E. G. Arlinghaus, L. Meng, R. Heiny, and L. E. Scriven, "Opaline Photonic Crystals: How Does Self-Assembly Work?," *Adv. Mater.*, vol. 16, no. 16 (2004)

[6] B. Perkins-Howard *et al.*, "Surface Wettability Drives the Crystalline Surface Assembly of Monodisperse Spheres in Evaporative Colloidal Lithography," *J. Phys. Chem. C*, vol. 2022, (2021)

[7] G. Vaartstra, L. Zhang, Z. Lu, C. D. Díaz-Marín, J. C. Grossman, and E. N. Wang, "Capillary-fed, thin film evaporation devices," *Journal of Applied Physics*, vol. 128, no. 13. (2020).

[8] N. D. Denkov, O. D. Velev, P. A. Kralchevsky, and I. B. Ivanov, "Mechanism of Formation of Two-Dimensional Crystals from Latex Particles on Substrates," *Langmuir*, vol. 8, no. 12, (1992)

[9] S. Khodaparast, F. Boulogne, C. Poulard, and H. A. Stone, "Water-Based Peeling of Thin Hydrophobic Films," *Phys. Rev. Lett.*, vol. 119, no. 15, (2017)

[10] Y. Suh, Q. Pham, B. Shao, and Y. Won, "The Control of Colloidal Grain Boundaries through Evaporative Vertical Self-Assembly," *Small*, vol. 15, no. 12, (2019)

[11] M. Retsch *et al.*, "Fabrication of Large-Area, Transferable Colloidal Monolayers Utilizing Self-Assembly at the Air/Water Interface," *Macromol. Chem. Phys.*, vol. 210, no. 3–4 (2009)

ULTRA FLEXIBLE MACROPOROUS MICRONEEDLES FOR SUSTAINED DELIVERY OF (2R,6R)-HYDROXYNORKETAMINE

Riddha Das[1,2], Aydin Sadeqi[1,2], Caroline A. Browne[3], Irwin Lucki[3] and Sameer Sonkusale[1,2]*
[1] Department of Electrical and Computer Engineering, Tufts University, USA
[2] Nano Lab, Advanced Technology Laboratory, Tufts University, USA
and [3]Uniformed Services University of Health Sciences, USA

ABSTRACT
Transdermal delivery using microneedles provides an alternative method to locally administer drug molecules with controlled release rate. In this study, our goal was to develop an ultra-flexible macro porous patch with hard microneedles that penetrate the skin. We demonstrated encapsulation of a non-hallucinogenic derivative of a dissociative anesthetic pharmaceutical, which is approved as a therapy for treatment resistant depression. The microneedles are made from biocompatible photo-curable resin. Solid formulation of this drug is encapsulated in the resin, which ensures high drug loading capacity. A flexible substrate is used as the backing to ensure skin conformability. The encapsulated drug molecules are released by diffusion in contact with interstitial fluid. Our findings demonstrate uniform encapsulation of the drug molecules into the resin and sufficient robustness of the microneedles to withstand the skin penetration forces.

KEYWORDS
Microneedle, laser cutting, laser lithography, post-traumatic stress disorder, drug delivery.

INTRODUCTION
Post-traumatic stress disorder (PTSD) is a mental health disorder occurring in susceptible individuals exposed to serious injury and traumatic life events. Despite the widespread availability of therapies to counteract PTSD, current treatments are only marginally effective. Sub-anesthetic doses of ketamine are indicated for the treatment of major depressive disorder. In addition, ketamine is also reported to alleviate chronic pain and PTSD [1]. However, administration of ketamine via intranasal and IV infusion limits its widespread utility due to restricted administration by trained medical practitioners in specialized clinics and status as a scheduled compound. In this work, we report a non-invasive microneedle (MN) transdermal drug delivery device for sustained delivery of ketamine and ketamine's non-hallucinogenic metabolite (2R,6R)-hydroxynorketamine (HNK) to avoid the psychotomimetic side effects and potential abuse liability of ketamine [2].

Existing MNs have issues with reliable penetration (e.g. hydrogel based MN) and/or insufficient drug dosing (e.g. drug coated solid MN) [3,4]. They require expensive cleanroom methods to manufacture and are usually limited in size. Recently, our group developed a cross-over-lines (COL) laser lithography approach to make large area microneedles [5]. It utilizes laser micromachining with user-defined geometric patterns to make high aspect ratio molds. The molds are then used to make ultra-flexible conformal large area microneedle patches. Use of the COL approach enables fabrication over a large area format previously not possible. Another innovation is the direct use of solid drug formulation encapsulated in porous matrix of photocurable resin. We recently demonstrated release of ibuprofen and lidocaine using such macroporous solid hard microneedles (macroPOSH) [6].

DESIGN AND FABRICATION
COL laser lithography was used to make negative polymethyl methacrylate (PMMA) molds [5]. This mold was first duplicated into a super-elastic ecoflex mold. Next, a polymeric mixture solution of photocurable biocompatible dental resin and finely powdered drug (HNK) was cast into the mold and stretched for loading. A flexible substrate such as polyethylene terephthalate (PET) or paper was then applied, and the entire construct was UV cured to realize large area MN patches. The resultant patch exhibited flexible backing with solid cured hard tips. The drug was essentially encapsulated into the porous matrix of the resin and released

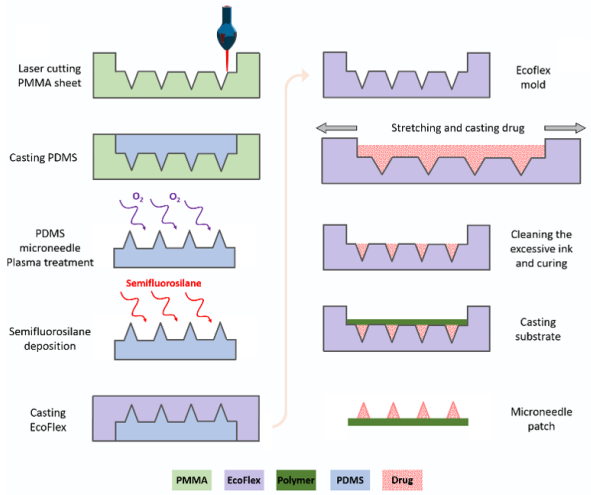

Figure 1: Fabrication of microneedle mold and microneedle patches: CO2 laser cutter was used to fabricate microneedle PMMA mold using the proposed cross-over lines (COL) technique, the PMMA mold was used to fabricate polydimethylsiloxane (PDMS) microneedles mold, which was used to fabricate ecoflex mold. This ecoflex mold was then used to fabricate microneedle patches.

when it came in contact with interstitial fluid. The ability to load drug in powdered form ensures high drug loading capacity in the macroporous solid hard (macroposh) microneedles. Moreover, its hard tips facilitate reliable penetration in all skin types.

978-1-940470-04-7/HH2022/$25©2022TRF
DOI 10.31438/trf.hh2022.107

RESULTS AND DISCUSSION

The microneedle patches were fabricated from HNK encapsulated into dental resin. HNK was grinded to fine powder and was mixed uniformly with the resin solution with the weight ratio of 1:1. The drug solution was then pressed against the mold. The mold was stretched from four sides to ensure maximum penetration of the drug solution. A blade removed the excess drug solution, and the top part of the mold was covered with blank resin solution. The samples were cured using ultraviolet light with wavelength of 405 nm. After a few minutes, the patches get hard enough to be removed from the microneedle molds. The patches were then stored at room temperature. For proof of concept, we made patches of 1x1 cm^2 with 400 microneedles each of base width: 300±30 µm, height: 1500±20 µm, tip: 10±3 µm and resin to drug ratio of 1:1. Scanning Electron Microscopic (SEM) image confirmed the formation of conical microneedles (figure 2a).

Next, HNK release study was performed from the

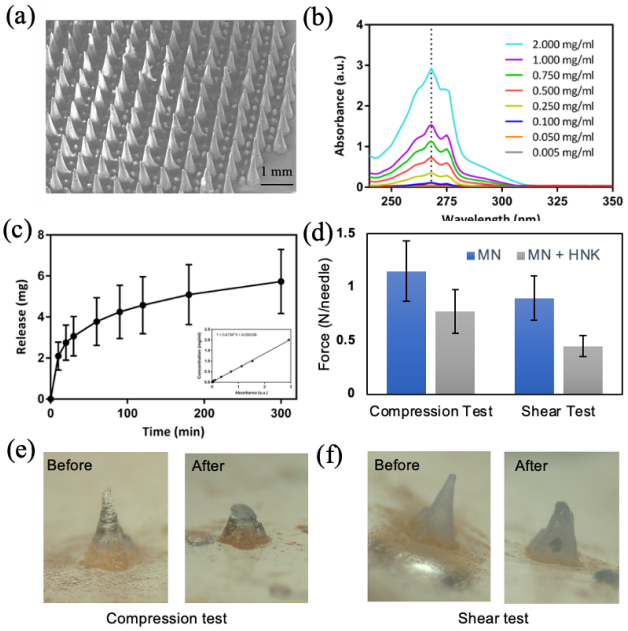

Figure 2: (a) SEM image of microneedle patch (b) Different concentration of HNK measured by UV-vis Spectrophotometer (c) HNK release profile in PBS (inset: Calibration curve of HNK) (d) Comparison of robustness of microneedle patches with and without HNK

microneedle patches in Dulbecco's Phosphate Buffered Saline (PBS). The absorbance was measured between 240 – 350 nm as shown in Figure 2b. We calibrated the HNK solution based on the absorbance amplitude at 268 nm (figure 2c inset). The drug capacity of each microneedle in the patch was estimated to be 18 µg from the release study in buffer solution assuming equal distribution of drug in each microneedle.

The compression and shear tests were performed with an Instron tensile tester (figure 2d). The microneedle without drug started to break down at the force of ~1.1N per needle and ~0.85N per needle on average during compression and shear test respectively. The microneedles with drug started to break down at the force of ~0.75N/needle and ~0.5N/needle

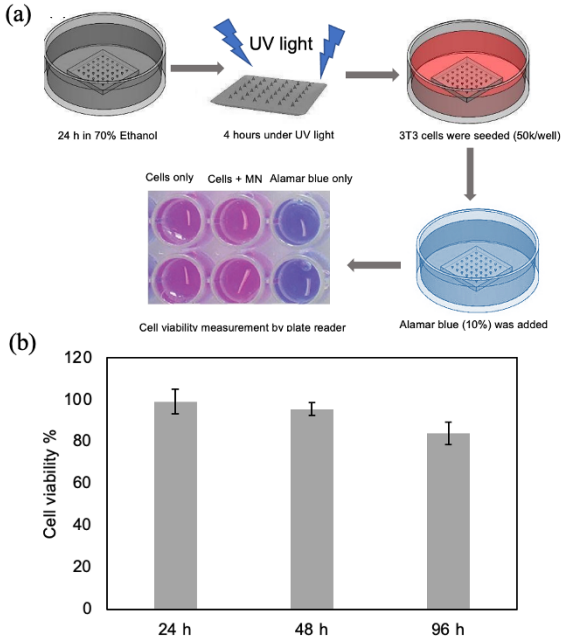

Figure 3: (a) Flow diagram of cell viability measurement experiment with fibroblast 3T3 cells in presence of MN patches (b) cytotoxicity of MN patches

during compression and shear test respectively. Although, there was a significant reduction in robustness after HNK addition, there was an almost ten-fold margin of safety over the force (0.058 N per needle) needed for insertion into skin using microneedles of this geometry.

Cytotoxicity of microneedles was investigated in fibroblast cells (3T3) using a standard protocol. Briefly, the microneedle patches were sterilized by keeping them immersed in 70% ethanol for 24 h in a biosafety cabinet followed by irradiation by UV light for several hours. The sterilized microneedle patches were placed in each of the wells of a 6 well plate. 3T3 cells (50k cells/well) were seeded in all the wells (with and without patches). Alamar blue test was done after 24, 48 and 96 hours at Ex/Em wavelength of 560/590 using a plate reader. The cells in the presence of microneedles grew at a rate similar to the control cells as shown in the Figure 3. Negligible reduction in cell viability was observed even after 96 h. This data demonstrates excellent biocompatibility of the microneedle patches.

To assess the drug capacity and release profile of the microneedle patch, an *in vitro* skin model was developed (Figure 4a). The model was comprised of 10% gelatin in PBS (modeling dermis layer of the skin) covered by a thin layer of parafilm (modeling epidermis layer of the skin). The patch was pressed against the polymer layer with a maximum force not exceeding 20N to achieve penetration. After placing the microneedles patch, the model was placed in an incubator at 37˚C. At different time intervals, the patch was removed and

placed on a fresh *in vitro* set to avoid saturation of the gelatin solution with the release content from the patch. The release content from the patch was qualitatively and quantitatively evaluated for different time intervals.

To evaluate the release content from the patch, the gelatin

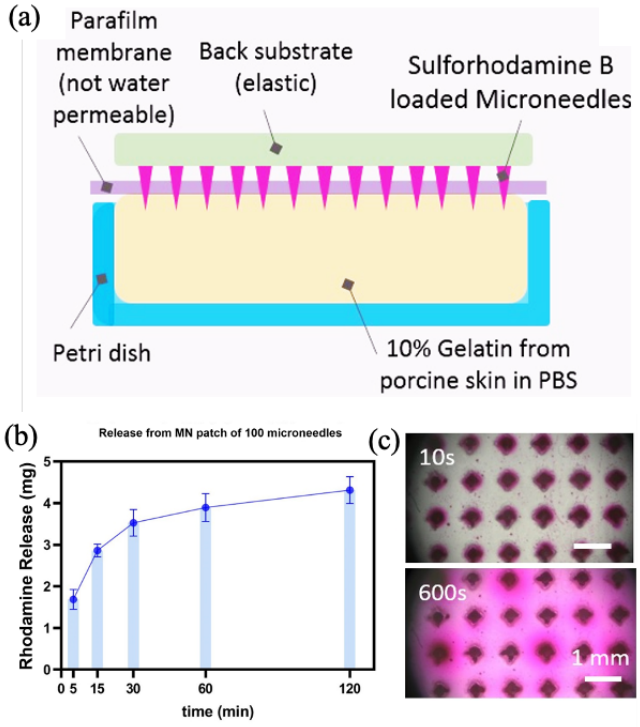

Figure 4. (a) in-vitro skin model (b) quantitative evaluation (c) qualitative evaluation of sulphorhodamine B release profile.

was melted, and the concentration of the released dye was measured using a UV-Vis spectrometer. The dye used in our *in vitro* analysis was sulphorhodamine B. A relatively uniform release pattern was observed from individual microneedles in the patch suggesting uniform fabrication of the needles.

CONCLUSION

In this study, we fabricated HNK loaded macroporous microneedles (MN) patches with ultra-flexible PET sheet backing. The drug is essentially encapsulated into the porous matrix of the resin and released when it comes in contact with interstitial fluid. The ability to load powdered form of a drug ensures high drug loading capacity in the macroporous solid hard (macroposh) microneedles. The ultra flexible backing ensures conformability and its hard tips facilitate reliable penetration in all skin types. According to shear and compression test results of the hard tips, the patches were sufficiently robust to withstand the force during skin penetration. The relatively uniform release profile of the cargo in our *in vitro* skin model confirmed uniform fabrication of each microneedle. MN patches demonstrated excellent biocompatibility in the *in* vitro cytotoxicity experiment. To summarize, we developed a biocompatible ultra flexible transdermal delivery platform for treatment of PTSD using a non-hallucinogenic analog of ketamine, namely HNK. Future studies will involve studying the effects of the extended drug release on behavior in rat models of PTSD symptom clusters.

ACKNOWLEDGEMENTS

The authors would like to acknowledge financial support from TTW program at USUHS under award number HU0001-20-2-0014. The content and conclusions do not necessarily represent the official position or policy of the Uniformed Services University of the Health Sciences, the Department of Defense, or the U.S. Government.

REFERENCES

[1] J. W. Murrough, D. V. Iosifescu, L. C. Chang, R. K. Al Jurdi, C. E. Green, A. M. Perez, S. Iqbal, S. Pillemer, A. Foulkes, A. Shah, D. S. Charney, and S. J. Mathew, "Antidepressant Efficacy of Ketamine in Treatment-Resistant Major Depression: A Two-Site Randomized Controlled Trial", *Am. J. Psychiatry* 170, 1134 (2013).

[2] J. N. Highland, P. Zanos, L. M. Riggs, P. Georgiou, S. M. Clark, P. J. Morris, R. Moaddel, C. J. Thomas, C. A. Zarate, E. F. R. Pereira, and T. D. Gould, "Hydroxynorketamines: Pharmacology and Potential Therapeutic Applications", *Pharmacol. Rev.* 73, 763 (2021).

[3] K. Lee, C. Y. Lee, and H. Jung, "Dissolving microneedles for transdermal drug administration prepared by stepwise controlled drawing of maltose", *Biomaterials* 32, 3134 (2011).

[4] S. F. Lahiji, M. Dangol, and H. A. Jung, "patchless dissolving microneedle delivery system enabling rapid and efficient transdermal drug delivery", *Sci. Rep.* 5, 1 (2015).

[5] H. R. Nejad, A. Sadeqi, G. Kiaee, S. Sonkusale, "Low-Cost and Cleanroom-Free Fabrication of Microneedles", *Microsystems Nanoeng.* 4, 17073 (2018)

[6] A. Sadeqi, G. Kiaee, W. Zeng, H. Rezaei Nejad and S. Sonkusale, "Hard polymeric porous microneedles on stretchable substrate for transdermal drug delivery", *Sci. Rep.* 12, 1853 (2022).

CONTACT

*sameer.sonkusale@tufts.edu

A MOLECULAR IMPRINTED POLYMER (MIP)-BASED NT-PROBNP SENSING ELECTRODE USING LG9 PEPTIDES FOR HEART FAILURE MONITORING

Liang-Kai Wang[1], Chih-Hung Lin[1], Yu-Ting Cheng[1], Hsiao-En Tsai[2] and Chih-Kuo Lee[3]*

[1] Institute of Electronics Engineering, National Yang Ming Chiao Tung University, Hsin-Chu, Taiwan

[2]Department of Internal Medicine, National Taiwan University Hospital Hsin-Chu Branch, Taiwan.

[3]Department of Surgery, National Taiwan University Hospital Hsin-Chu Branch, Taiwan.

ABSTRACT

The abstract presents the first molecular imprinted polymer (MIP)-based N-terminal pro-B-type natriuretic peptide (NT-proBNP) sensing electrode using LG9 peptides as the template molecule for clinical study. The MIP-based sensing electrode is an electrochemical polymerized o-phenylenediamine (o-PD) film, which can accomplish the detection in 25 min., exhibit a sensitivity of $8.24x10^{-1}$ $(ng/mL)^{-1}$ and the limit of detection (LoD) of 14.55 pg/ml in the concentration of NT-proBNP from 0.01 to 1.25 ng/ml. and be reused over than 6 times. As compared to other sensing techniques, the presented electrode exhibits excellent characteristics including high specificity and sensitivity, short testing time, and low cost suitable for ICU applications.

KEYWORDS

Molecular Imprinted Polymer, LG-9, serum test, NT-proBNP.

INTRODUCTION

Recent studies have found the importance of NT-proBNP combined with troponin and lactate assays for decision-making to guide immediate treatment and further diagnosis in patients who might have acute myocardial infarction or myocardial injury caused by other etiologies [1-3]. NT-proBNP test has been identified as an independent risk factor for pulmonologists not only to rule out cardiac dyspnea but also to predict mortality in patients with severe COVID-19, thereby improving individual risk stratification [3]. Although MIP-based sensing technique can exhibit superior characteristics such as high specificity and sensitivity for blood test, the main drawback of this technique is that recognition sites can be easily damaged during the elution process due to agile 3D protein structures and non-cross-linked imprinted film, thereby degrading device performance. Using small or fragmental peptide instead of a full one or protein as the template molecule for the complexity reduction of the electrode fabrication can well resolve the reliability issue [4]. In this work, we develop, characterize, and apply microfabricated MIP-based NT-proBNP sensing electrodes using LG-9 peptides, LQESPRPTG, as the template molecule for serum test. Its high specificity and sensitivity, low limit of detection (LoD) and cost-effective characteristics can improve the diagnostic, therapeutic and prognostic aspects of patients potentially with heart failure syndromes requiring intensive cardiac care.

EXPERIMENTAL

Fig. 1 shows the fabrication flow and measurement set up of the NT-proBNP sensing electrode where electrochemical polymerization of o-PD film is performed using conventional silicon process and linear sweep voltammetry (LSV) measurement is performed via a three-electrode configuration in the potassium ferricyanide solution (Fig. 1 (a) and (b)). Higher current response of the MIP film after the elution process as compared to that of non-imprinted film (NIP) film indicates the LG9 peptides have been successfully embedded in the o-PD film to form a MIP electrode (Fig. 1(c)). The major fabrication processes include 1) Ti (10nm)/Au (30nm) electrode deposition and patterning on a Si_3N_4(800nm) /SiO_2 (500nm) /Si substrate, 2) electrochemical polymerization of o-phenylenediamine film onto the Au electrode in an acetate buffer solution (0.5M, pH 5.2) containing 7.5 mM o-phenylenediamine and 1 µg/ml of LG-9 peptides using cyclic voltammetry from 0 to 1.1V, 3) LG-9 peptide removal in the solution of NaOH/Ethanol. Fig. 2 shows liquid chromatography–mass spectrometry (LC/MS) analyses of the LG9 peptide/PBS and the NT-proBNP solution digested with thermolysin @65°C for 15min. The existence of both signals, i.e., 984.500 and 492.756 representing LG9 peptide molecule with one and two positive charges respectively indicates the protease digestion is effective.

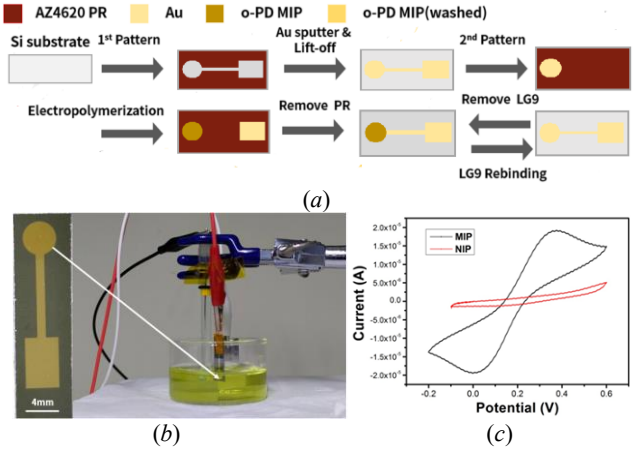

Figure 1: (a) The fabrication processes of the MIP-based Troponin T sensor, (b) Measurement set up: sensor immersion in the blood serum for 10 min (left) and LSV measurement using a three-electrode configuration in the mixture of the 1mM $[Fe(CN)_6]^{3-}$, 1mM $[Fe(CN)_6]^{4-}$ and 0.1M KCl solutions, and (c) I-V response of LSV measurement.

RESULTS AND DISCUSSION

Fig. 3 shows the sensor characterization and blood test results. The sensor electrode exhibits two sensitivity, i.e. $6.36x10^{-2}$ and $8.24x10^{-1}$ in the high (>3 ng/ml)/ low (<1 ng/ml) concentration region, respectively, as shown in Fig. 3(a). The derived LoD for the sensing electrode is based on the following equation [5]:

$$\text{LoD} = 3\sigma/s \quad (1)$$

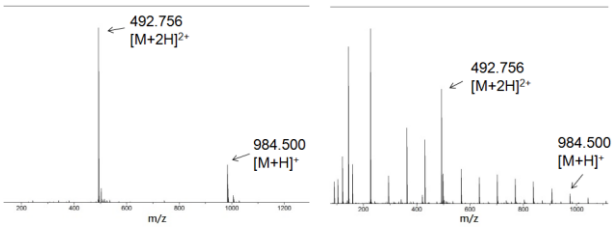

Figure 2. The profile of the LC/MS. (a) LG9 solution, (b) NT-proBNP solution digested with thermolysin for 15min.

978-1-940470-04-7/HH2022/$25©2022TRF
DOI 10.31438/trf.hh2022.108

Table 1. Comparison of NT-proBNP biosensing methods.

	D. Harpaz et al. [6]	University Hospital*	*M. Karimi et al* [7]	**This Work**
Sensor type	SPR	ECLIA*	Electrochemical (Cyclic Voltammetry)	**Electrochemical (LSV)**
Recognition element	Antigen-Antibody	Antibody with ECL	Antigen-Antibody	**MIP**
Testing time	15 min	60 min	70 min	**25 min (15 min+10 min) [5]**
Reusability	One time	One time	One time	**Multiple times**
Measurement Range	127.5 pg/ml	3.59 pg/ml	6 pg/ml	**14.55 pg/ml**
Storage temp./lifetime	4°C/short	4°C/short	4°C/short	**Room temp./Long**
Cost	High	High	Moderate	**Low**

*ElectroChemiLuminescence ImmunoAssay, ECLIA, *https://diagnostics.roche.com/global/en/products/instruments/cobas-e-411.html*

where σ is the standard deviation of the electrode response in the blank solution, and s is the slope of the curve of the sensor output vs. analyte concentration. The LoD was estimated to be ca. 14.55 pg/mL, indicating that the electrode was quite adequate for clinical requirements. Fig. 3(b) and (c) shows the same current response for each NT-proBNP concentration and lower current difference in response to the bovine serum albumin (BSA)/PBS solution indicating the sensor can exhibit excellent reusability and specificity respectively.

Fig. 3(d) shows the correlation of 4 sets of blood test results measured by the MIP sensor and ECLIA methods indicating 94.5% matching in terms of detected NT-proBNP concentration. The detail measurement of the NT-proBNP using the MIP sensor in the serum can be referred to our prior work [5]. The results validate not only the effectiveness of the MIP sensor in comparison with the formal examinations in a tertiary university-affiliated hospital but also the feasibility of the NT-proBNP test for doctors' therapeutic guidance and prognosis assessment. Table I lists the comparison of the present NT-proBNP sensing technologies, among which the MIP-based sensor can exhibit the advantages of high specificity and reusability, short testing times, and cost effective with long storage time [6,7].

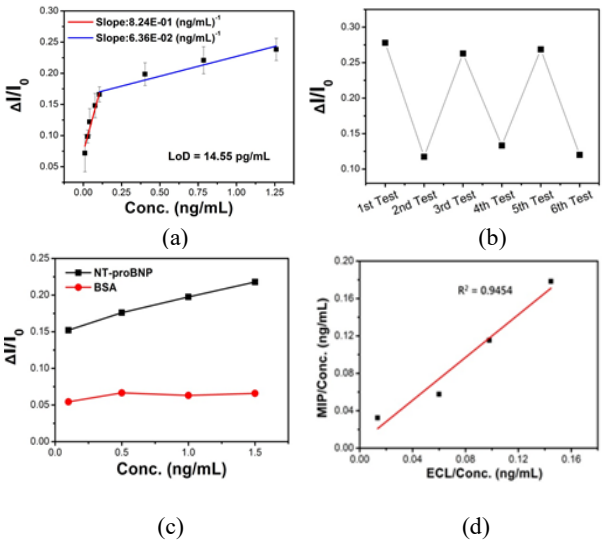

Figure 3: Sensing electrode characterization and blood test results: (a) sensitivity measurement of MIP sensor response, (b) reusability tests: the MIP sensor response immersed repeatedly in the NT-proBNP PBS solutions with different concentrations, i.e. 2 ng/mL and 0.05 *ng/mL, (c) specificity test: the sensor response in the NT-proBNP PBS and BSA/PBS solution, respectively, and (d) statistic correlation of 4 sets of blood test results measured by the MIP sensor and ECLIA methods indicating 94.5% matching in terms of detected NT-proBNP concentration.*

CONCLUSION

A MIP-based NT-proBNP sensing electrode has been successfully developed. The electrode exhibits superior characteristics such as rapid response, good reusability, and high specificity. The clinical blood test results have validated that it is feasible to apply the electrode in clinical applications for detecting heart failure status by monitoring the NT-proBNP concentration accurately.

ACKNOWLEDGEMENTS

This project is funded by the Higher Education Sprout Project by the MOE in Taiwan and in part by MOST 110-2321-B-009-004 and the NTUH Hsin-Chu Branch: 111-HCH001 and 110-HCH080.

REFERENCES

[1] S. Satyan, R. Light, and R. Agarwal, "Relationships of N-terminal pro-B-natriuretic Peptide and Cardiac Troponin T to Left Ventricular Mass and Function and Mortality in Asymptomatic Hemodialysis Patients", Am J Kidney Dis. 50, 1009, (2007).

[2] D. Westermann, J. T. Neumann, N. A. Soerensen, and S. Blankenberg, "High-sensitivity Assays for Troponin in Patients with Cardiac Disease", Nature Reviews Cardiology, 14, 472 (2017).

[3] L. Gao, D. Jiang, X. -S. Wen, X. -C. Cheng, M. Sun, B. He, L.-N. You, P. Lei, X.-W. Tan, S. Qin, G.-Q. Cai, and D.-Y. Zhang, "Prognostic Value of NT-proBNP in Patients with Severe COVID-19", Respir Res., 21, 83, (2020).

[4] A. M. Bossi, P. S. Sharma, L. Montana, G. Zoccatelli, O. Laub, O and R. Levi, "Fingerprint-imprinted Polymer: Rational Selection of Peptide Epitope Templates for the Determination of Proteins by Molecularly Imprinted Polymers", Anal. Chem., 84, 4036, (2012).

[5] Y. T. Lin, L. K. Wang, Y. T. Cheng, C. K. Lee, and H. E. Tsai, "Molecularly Imprinted Polymer/Anodic Aluminum Oxide Nanocomposite Sensing Electrode for Low-Concentration Troponin T Detection for Patient Monitoring Applications." ACS sensors, 6, 2429, (2021).

[6] D. Harpaz, B. Koh, R. C. Seet, I. Abdulhalim, and A. I. Tok, "Functionalized Silicon Dioxide Self-referenced Plasmonic Chip as Point-of-care Biosensor for Stroke Biomarkers NT-proBNP and S100β, Talanta, 212, 120792, (2020).

[7] Y. Zhuo, W. J. Yi, W. B. Lian, R. Yuan, Y. Q. Chai, A. Chen, and C. M. Hu, "Ultrasensitive Electrochemical Strategy for NT-proBNP detection with Gold Nanochains and Horseradish Peroxidase Complex Amplification", Biosens. and Bioelectron., 26, 2188, (2011).

CONTACT

*Yu-Ting Cheng, tel: +886-3-5712121, ytcheng@nycu.edu.tw

HEAVY METAL SENSING IN VEGETABLE AND SOIL SOLUTIONS USING CARBON FIBER ELECTRODE

G M Hasan Ul Banna[1*], *James Siegenthaler*[2], *Romilly Benedict*[3], *Wei Zhang*[3], *and Wen Li*[1,2]
[1]Department of Electrical and Computer Engineering, Michigan State University, East Lansing, MI, USA
[2]Fraunhofer USA Center Midwest, East Lansing, MI, USA
[3]Department of Plant, Soil and Microbial Sciences, Michigan State University, East Lansing, MI, USA

ABSTRACT
This paper reports a non-toxic, eco-friendly, and cost-effective sensing method to detect microgram per liter level of localized heavy metal ions in vegetable plant and agricultural soil solutions using glass encapsulated carbon fiber microelectrode (CFME). As a proof of principle, CFMEs were tested for sensing selected heavy metals in buffer solutions as well as plant and soil solutions using differential pulse anodic stripping voltammetry (DP-ASV). Preliminary results confirm that the CFMEs were able to measure mercury (Hg), lead (Pb), and cadmium (Cd) with a detection limit of 10 µg/L, showcasing good selectivity and sensitivity.

INTRODUCTION
Heavy metal pollution in soils is widespread in the world, resulting from both natural sources and human activities (e.g., mining and smelting, industrial emission, fossil fuel combustion, etc.). Due to their toxicity, bioaccumulation, and environmental persistence, elevated levels of heavy metals in the environment pose major threats to ecosystem health and the safety of food crops grown with contaminated soils and waters. Conventional techniques for heavy metal detection via atomic absorption spectrometry (AAS), inductively coupled plasma atomic emission spectrometry (ICP-AES) or mass spectrometry (ICP-MS) are generally highly sensitive (with part per trillion (ppt) detection limits) and accurate [1,2,3]. However, such methods are not practical for in-situ monitoring due to their vibration sensitivity, calibration requirements, bulkiness, and costly operation. Additionally, they have high power requirements and laborious operation by specifically trained personnel.

Compared to the conventional methods, electrochemical sensors have the advantages of low cost, low power consumption, simplicity, high sensitivity, ease of operation, rapid analysis, portability and applicability for field monitoring of environmental samples. In particular, anodic stripping voltammetry (ASV) has demonstrated the capability to detect heavy metals at sub-part per billion (ppb) level, making it a promising method for field analysis. However, most commonly used electrodes, liquid Hg, are now avoided due to concerns about their toxicity, and solid electrode materials have been explored as alternatives [4]. Among different electrode materials, carbon fiber microelectrodes (CFME) are non-toxic, easy to handle, less expensive, and eco-friendly compared to typical solid metal electrodes such as Bi, Au, and Pt. However, the applications of CFMEs in environmental monitoring have been very limited. In this paper, we demonstrated, for the first time, the use of CFME to detect heavy metals in vegetable plant and soil solutions. This work will lay the foundation to develop new sensing technology for in-situ measurements of heavy metals in environments, e.g., soils, plants, and waters.

METHOD
The CFME was fabricated by inserting an unsized AS4 7.4 µm diameter (Hexcel, Stamford, CT) carbon fiber into a glass capillary. After aspiration, the capillary was pulled on a commercial puller, leaving a tapered seal around the single carbon fiber. The sensing area of the electrode was controlled by the extruded carbon fiber length and cut to ~75 µm from the edge of glass seal as shown in Fig. 1. The other side of the fiber was electrically connected using a conductive graphite adhesive to a wire for electrical connection. To characterize the device's sensing performance, the CFMEs were first tested in a 0.01 M acetate buffer (pH=5.15) solution containing 50 mM NaCl with different concentrations of heavy metals. After that, heavy metal measurements were conducted in plant and soil solutions, which were prepared by extracting fresh cut lettuce leaves and a soil with deionized (DI) water (100 grams in 1 liter each). The extracted plant and soil solutions were further diluted (1:10 vol%) with DI water, and mixed with heavy metal solutions prior to testing with CFMEs. Electrochemical measurements were performed using DP-ASV in a three-electrode mode where the CFME was used as a working electrode (WE), an Ag/AgCl as a reference electrode (RE), and a Pt wire as the counter electrode (CE). DP-ASV parameters are as follows: a plating deposition of -0.7 V for 120 s; and the voltage was ramped to 0.8 V with a frequency of 60 Hz and an amplitude of 40mV with an increment voltage of 2 mV. All the experiments were run in a custom-made Faraday cage.

RESULTS
Using a CFME, measurements were made of Cd, Pb, and Hg in the buffered solutions spiked with 100-1200 µg/L concentrations (Fig. 2). Although the Cd peak at the concentration of below 400 µg/L was not prominent, we observed prominent characteristic peaks for the other two metals, Pb and Hg, at low concentrations even at 10 µg/L range. Distinguishable peaks were observed in the DP-ASV plots obtained from the mixture solution of Cd, Pb, and Hg (Fig. 2d), demonstrating the good selectivity of the CFMEs. Fig. 3 shows DP-ASV plots for 0-1200 µg/L concentrations of Pb and Hg in the simulated plant and soil solutions, where the limit of detection (LOD) was ~400 µg/L for Hg and 200 µg/L for Pb, respectively. The electrode showed good selectivity for Cd, Pb, and Hg at the high concentration of 1200 µg/L (Fig. 4), whereas no strong signals for Cd were detected at low concentrations. The corresponding sensitivity of Cd, Pb, and Hg under different test solutions was summarized in Table 1. While preliminary, these results showed that our fabricated CFMEs are capable of detecting heavy metals in the vegetable plant and soil simulated solutions in the µg/L range. Further investigation is needed to improve the LOD and sensitivity, as well as to fully characterize the electrode's performance in plant and soil environments.

978-1-940470-04-7/HH2022/$25©2022TRF
DOI 10.31438/trf.hh2022.109

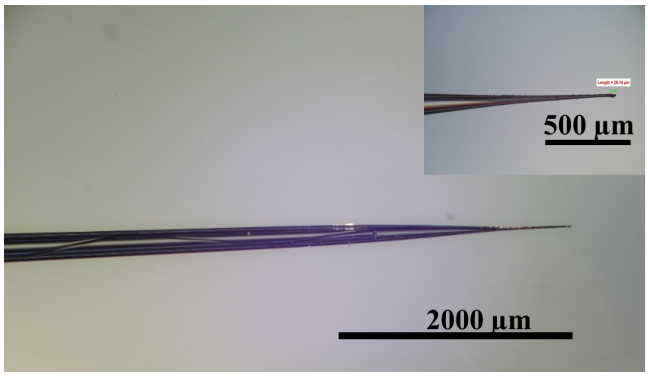

Figure 1: Microscope image of glass encapsulated carbon fiber electrode.

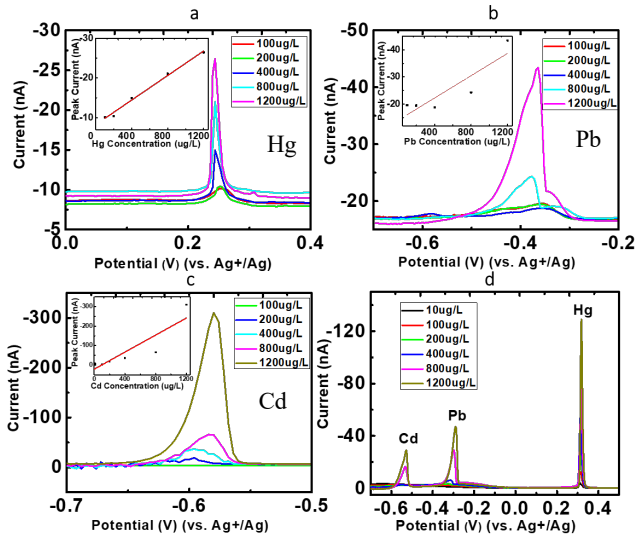

Figure 2: Detection of 100, 200, 400, 800, and 1200 µg/L concentration of (a) Hg, (b) Pb, and (c) Cd in buffer solution (pH=5.15) with CFME as WE. Insets in (a), (b), and (c) illustrate sensitivity of each heavy metal. (d) Detection in the mixture solution of Cd, Pb, Hg, each at 10, 100, 200, 400, 800 and 1200 µg/L concentration.

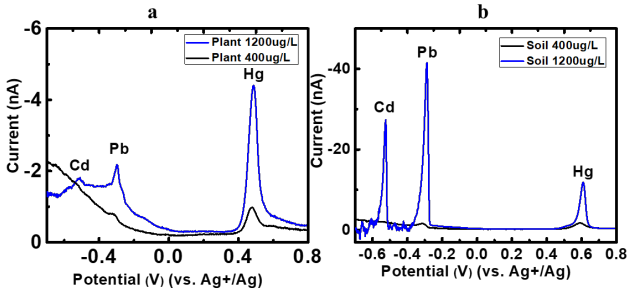

Figure 4: Detection of 400 and 1200 µg/L concentration of mixed Hg, Pd, and Cd in diluted (a) plant solution (pH=6.32) and (b) soil solution (pH=6.13) with CFME as WE.

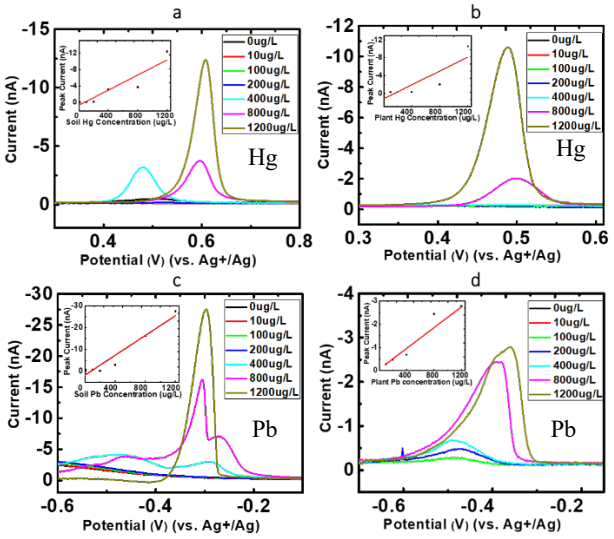

Figure 3: Detection of 0, 10, 100, 200, 400, 800, and 1200 µg/L concentration of Hg and Pb in diluted (a,c) soil solution (pH=6.13) and (b,d) plant solution (pH=6.32) with CFME as WE.

Table 1: Sensitivity of heavy metals in different solutions.

Sensitivity (nA·L/µg)	Buffer	Soil	Plant
Hg	0.01539	0.00913	0.00778
Pb	0.02059	0.02268	0.00225
Cd	0.21874	----------	----------

REFERENCES

[1] K. S. Rao, T. Balaji, T. P. Rao, Y. Babu, and G. Naidu, "Determination of iron, cobalt, nickel, manganese, zinc, copper, cadmium and lead in human hair by inductively coupled plasma-atomic emission spectrometry," Spectrochimica Acta Part B: Atomic Spectroscopy, vol. 57, pp. 1333-1338, (2002).

[2] J. Koelmel and D. Amarasiriwardena, "Imaging of metal bioaccumulation in Hay-scented fern (Dennstaedtia punctilobula) rhizomes growing on contaminated soils by laser ablation ICP-MS," Environmental pollution, vol. 168, pp. 62-70, (2012).

[3] K. Siraj and S. A. Kitte, "Analysis of copper, zinc and lead using atomic absorption spectrophotometer in ground water of Jimma town of Southwestern Ethiopia," International Journal of Chemical and Analytical Science, vol. 4, pp. 201-204, (2013).

[4] Wei Gao, Hnin Y. Y. Nyein, Ziba Shahpar, Hossain M. Fahad, Kevin Chen, Sam Emaminejad, Yuji Gao, Li-Chia Tai, Hiroki Ota, Eric Wu, James Bullock, Yuping Zeng, Der-Hsien Lien, and Ali Javey, "Wearable Microsensor Array for Multiplexed Heavy Metal Monitoring of Body Fluids" ACS Sensors 1 (7), 866-874, (2016)

CONTACT

*Hasan Banna, +1-517-619-4884; bannag@msu.edu

RAPID COST-EFFECTIVE PLOTTER CUT STENCIL MASKS FOR THE DEPOSITION OF ORGANIC AND INORGANIC MATERIALS AND THE CREATION OF A NEW ANTIBIOTIC DIFFUSION TEST FOR MINIMUM LETHAL CONCENTRATION DETECTION

Andre Childs[1], Jorge Pereira[1], Aliyah Baksh[1], Charles M. Didier[1], Edwin Davidson[1], Swadeshmukul Santra[1] and Swaminathan Rajaraman[1]

[1]University of Central Florida, Orlando, Florida, USA

ABSTRACT

The use of plotter cutters in stencil mask prototyping is underutilized but has several advantages over traditional MEMS techniques. In this paper we investigate the use of a conventional plotter cutter as a highly effective benchtop tool for rapid prototyping of stencil masks in the ***sub-100µm range*** and characterize patterned layers of different organic/inorganic materials. Furthermore, a ***diagnostic monitoring application in healthcare and a potential replacement of Standard Kirby-Bauer (KB) Diffusion Antibiotic Resistance Tests*** **[1, 2]** allowing for three times the amount of Antibiotics to be tested within the same nutrient agar petridish are demonstrated.

KEYWORDS

Stencil Mask, Antibiotic Testing, Kirby Bauer, Plotter Cutter, Minimal Inhibitory Concentration

INTRODUCTION

Traditionally MEMS stencils have been largely fabricated using laser micromachining, CNC milling, DRIE, and other photolithographic approaches due to their allowances for great precision and ease of workflow integration. However, with lengthier processing times, high cost and accessibility concerns, these technologies have become much less appealing **[3,4]**. Technologies such as plotter cutters and electronic cutters **[5]** with extreme process optimization could replace older stencil masking technologies. These tools have shown to be more effective in microfluidic and biosensor applications in recent years **[6,7]**. Usage of these stencil masks can be extrapolated to a myriad of applications such as electrode and microenvironment patterning for the manipulation and selective localization of bacterial and eukaryotic cells. Such localization is imperative to the study of cellular behavior such as morphology, response to pharmaceutical drugs in critical disease states such as cancer **[8,9]**. The capabilities demonstrated in this paper showcase how the Silhouette Cameo 4 tool provides precision with a multitude of swift cuts leading to the rapid prototyping of material layers for accurate diagnosis, analysis treatment or acute action. We additionally utilized the stencil masks for varied deposition of organic and inorganic materials such as Cr, Au, SiO_2, gelatin and bacterial patterning and testing using *Escherichia coli*.

MATERIALS AND METHODS

Kapton® Films (75µm thickness) were cut using *Silhouette Cameo 4* plotter in dimensions of 2mm down to 250µm utilizing "Single Line Cut", "Hammer Head" and "Serpentine" designs along with a 2mm design additionally cut for Interdigitated Electrodes fabrication (IDE). Kapton® masks were attached to glass slides, and Cr/Au (50/25 nm) was deposited using E-beam deposition (**Fig. 1**). Separately 10 wt% gelatin was cast through the masks on the glass slides. For bacterial patterning experiments, Kapton® stencils were placed on the surfaces of nutrient agar plates. Cultures of *E. Coli* K-12 bacteria were inoculated within the patterns of the masks, placed

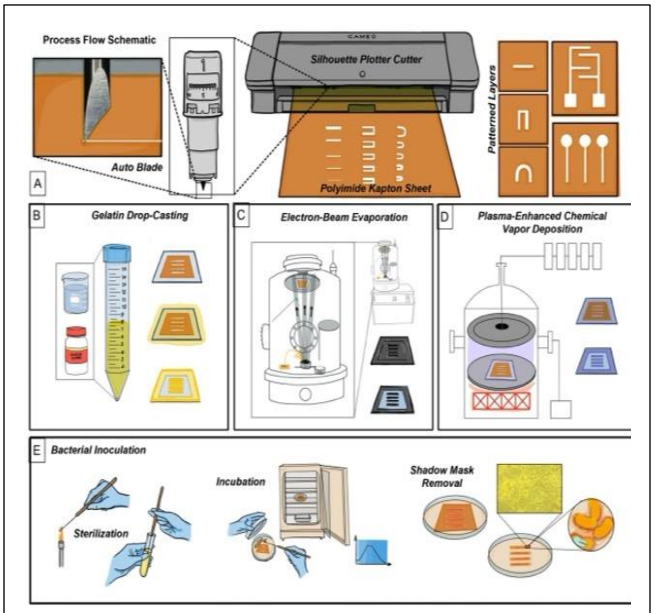

Fig. 1*. Process flow schematic: A) Silhouette Plotter Cutter along with fabricated designs that were evaluated in this study (right). B) Schematic of the casting process for 10 wt % gelatin. C) E-beam evaporation. D) Plasma Enhance Chemical Vapor Deposition (PECVD). E) Culturing of E. Coli K-12.*

in an incubator for 48 hours at 37ºC and removed. Antibiotics Streptomycin Sulfate (5-20µg), Oxytetracycline Hydrochloride (15-60µg) and Kanamycin Sulfate (15-60µg) were utilized in the new diffusion test. Impedance measurements, SEM and Keyence Confocal imaging were used to characterize the stenciled patterns.

RESULTS

The key cutting feature of the plotter cutter is shown in **Fig. 2**. The blade has an ellipsoidal curvature, length of 1400.19µm and a tip of ~ 26µm with a flat surface rather than having a radius of curvature creating a micron-scale flat feature when cutting through materials

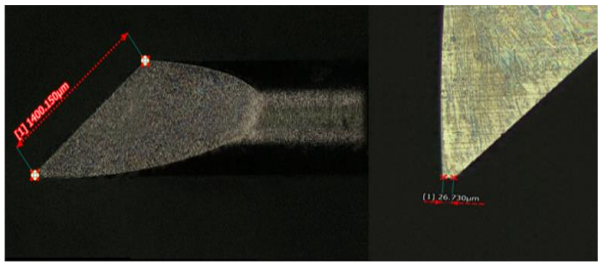

Fig. 2*. Laser confocal scanning images of the AutoBlade from the plotter cutter showcasing ellipsoidal curvature on the left and tip dimensions on the right. The blade characterization helps with assessment of cutting features on specific materials.*

978-1-940470-04-7/HH2022/$25©2022TRF
DOI 10.31438/trf.hh2022.110

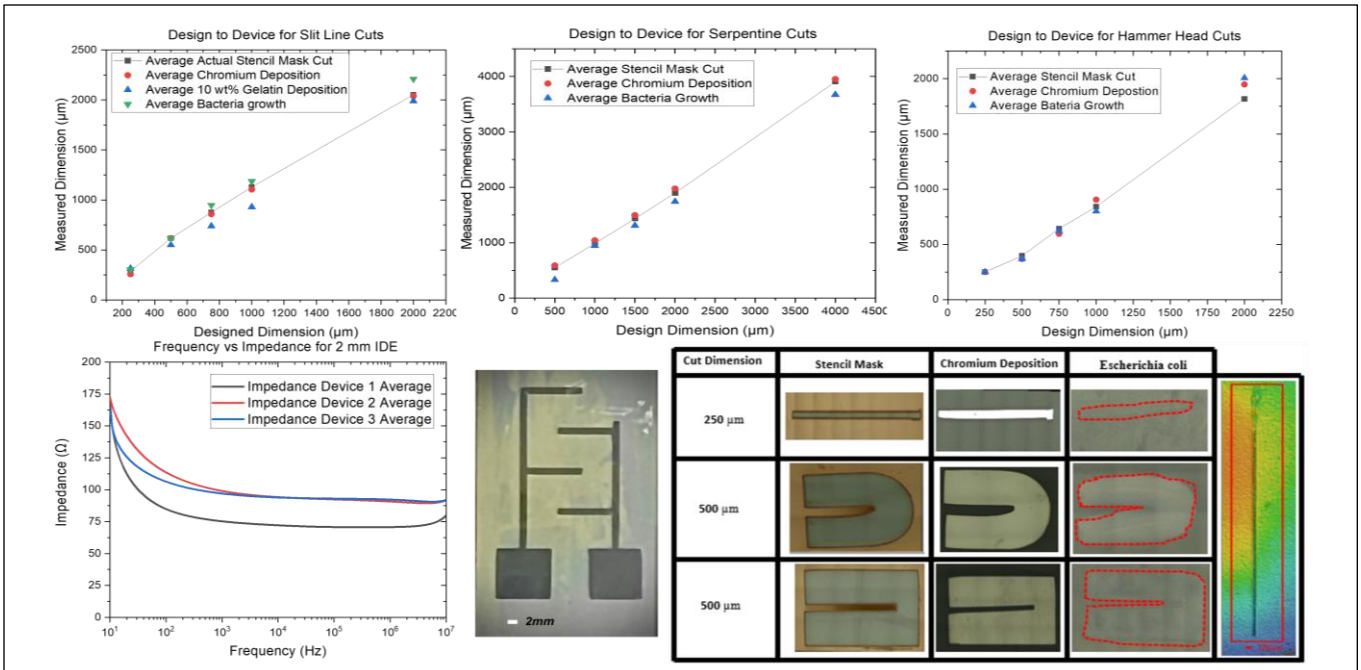

***Fig. 3**. Design to device images and measurement for all stencil mask designs - Slit Line Cuts, Serpentine Cuts, Hammer Head Cuts (Top), along with the impedance characteristics of the 2mm IDE device (Bottom Left). Image of the Cr/Au deposited IDE and the smallest feature size that was micromachined at a sub-100µm cut (Bottom Right).*

analogous to Kapton ®. **Fig. 3** depicts design to device measurement with representative images of patterned features along with the impedance characteristics of the IDE. The design to device followed expected trends of reduced feature sizes producing increased errors with the ***average errors for patterns determined to be 10.46%***. Additionally, an ***optimized sub-100 µm cut*** was demonstrated with the slit line pattern for the first time to our knowledge. The 2mm metal IDE demonstrated ideal microelectrode behavior with an ***1kHz impedance value of 75-100 Ohms*** **(Fig. 3)**.

Further all stencil antibiotic tests showed reduced length measurements of zone of inhibition for all concentrations in the three types of antibiotics used. Average ***zone of inhibition length reductions from 69.4 – 87.5%*** were observed (**Fig. 4**) compared to the standard KB method **[1, 2]**. These suggest increased throughput of KB tests to measurement of minimum inhibitory concentration in a localized fashion to potentially lower limits of detection using our novel diffusion test methodology.

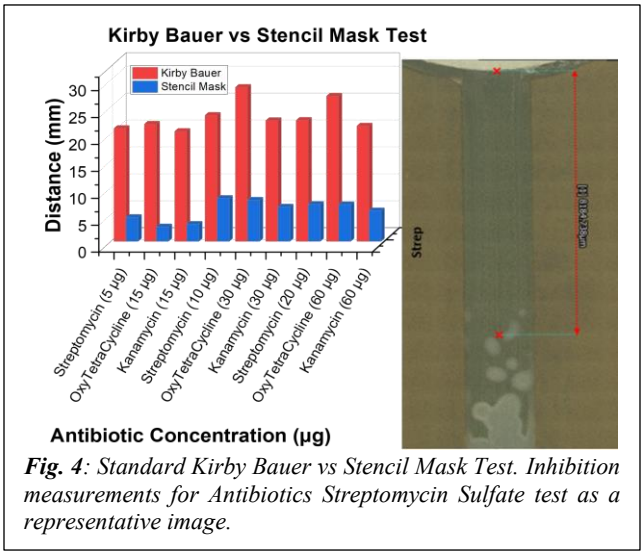

***Fig. 4**: Standard Kirby Bauer vs Stencil Mask Test. Inhibition measurements for Antibiotics Streptomycin Sulfate test as a representative image.*

CONCLUSIONS

Kapton® films (75) µm were best suited for our application as they are thin enough to cut in 1 pass and prevent tearing while cutting. The ***effective parameters*** for cutting through the Kapton® were determined as: ***F=22-26 N; Speed= 1mm/s with fabrication time in seconds***. Design to device measurements showcase an ***average error of 10.46%*** with expected trends with smaller dimensions patterns. Expected IDE impedance performance and a novel diffusion test for minimum lethal concentration detection of bacteria were additionally demonstrated.

ACKNOWLEDGEMENTS

This work is supported by grants from Primordia BioSystems and the Florida High Tech Corridor.

REFERENCES

[1] Hudzicki, J, et al, American Society for Microbiology, 2009
[2] Bonev, B, et al, Antimicrobial Chemotherapy, 2008
[3] Hart, C, et al, Micromachines, 2020
[4] Tsao, C.-W, et al, Micromachines, 2016
[5] Islam, M, et al, Microfluidics and Nanofluidics, 2015
[6] Qamar, A, et al., Micromachines, 2016
[7] A. Kundu, et al., Actuators and Microsystems, 2019
[8] F. Alexander Jr, *et al.,* J. *Phys.: Conf. Ser.* 224 012134, 2010
[9] N. Tandon, et al., Medicine and Biology, 2006.

CONTACT

*Swaminathan Rajaraman, tel: +1-407-823-4339; Swaminathan.Rajaraman@ucf.edu

SCALING EFFECTS OF INKJET MICROFABRICATED 3D GOLD ELECTROCHEMICAL SENSORS FOR AQUEOUS LEAD DETECTION

Annatoma Arif, Bertha J. Chavez, Sheikh D. Hossain, and Robert C. Roberts*
University of Texas at El Paso, USA

ABSTRACT

This paper presents the scaling effects of the microfabricated inkjet printed (IP) gold microelectrochemical sensor (μECS) for aqueous lead detection. The microfabrication of the reported μECS utilizing IP additive manufacturing technology on shape memory polymer (SMP) is introduced for the first time in case of electrochemical sensing applications. The reported microsensor is simple, cost-effective, sensitive, and disposable. The dimension and area of the fabricated μECS is 4.23×4.23×1.52 mm^3 and 2.25 mm^2 respectively. The combination of IP and SMP for microfabrication offers quick maskless fabrication (10 minutes), simple and easy miniaturization (simultaneous curing and shrinking), cost-effectiveness (low sample volume), and high sensitivity (increased effective electrode surface area despite miniaturizing the device).

KEYWORDS

Additive Manufacturing; Inkjet Printing; Micro-electrochemical Sensor; Microfabrication;

INTRODUCTION

Lead (II) contamination causes severe damage to human and children (learning, behavioral, and developmental delay) [1]. Recently, the most adapted and widely used technologies for lead (II) detection are screen printed electrodes (SPE) [2] and lithography [4]. SPE is chosen due to its cost-effectiveness, favorable quality (bulk fabrication), and flexibility in the design [2]. However, this technology fails to provide consistency for batch to batch fabrication/materials and limits materials waste [3]. On the other hand, lithography (etching and lift-off) is extremely time consuming, expensive, and requires cleanroom facility and hazardous materials [4]. Hence, researchers have started focusing on inkjet-printing (IP) additive manufacturing technology for sensor fabrication [5]. This technology ensures high resolution, consistent fabrication quality, and cost-effectiveness. Our group has reported IP macro electrochemical sensor on shape memory polymer (SMP) for the first time for lead (II) detection at Sensors 2021 [6]. The dimension of our previously reported sensor was 13×10×1.52 mm^3 (after curing and shrinking). Currently, we are focusing on microsensor fabrication as it provides simplicity, cost-effectiveness, low fabrication time (macro sensor - 180 minutes and microsensor - 10 minutes), high reproducibility, and fast response time (120 seconds). We are considering IP and SMP for microfabrication as this combination offers quick maskless fabrication (simultaneous curing and shrinking), simple miniaturization (heating the printed sensor/substrate above glass transition temperature and below melting temperature), and high sensitivity (increased effective electrode surface area - miniaturization does not have any impact on effective electrode surface area). The fabrication, characterization, and evaluation of the reported microelectrochemical sensor (μECS) is illustrated in the following sections. Figure 1 represents IP gold (Au) μECS for aqueous lead (II) detection.

FABRICATION

The reported microsensor cell consists of an Au working electrode (WE), Au counter electrode (CE), and silver chloride (AgCl) reference electrode (RE). The pattern for the reported μECS is designed using CAD software (GIMP 2.10.30). We have changed the design compared to our previous sensor [6] because after downscaling (less than 500 μm spacing between electrodes), the electrodes were shorted after shrinking and curing. The pattern is then loaded onto the inkjet printer (DMP-2850). 50 nanometer diameter silver (Ag) nanoparticle conductive ink (ANP-DGP-40-LT-15-C) is used to print the pattern with 10 pL drop-on-demand piezoelectric nozzle. The drop spacing, cartridge temperature, platen temperature, and number of printed layers were investigated for microfabricating the μECSs. After critical investigation, the reported microsensor is fabricated with 20 μm drop spacing, 30°C cartridge temperature, 50°C platen temperature, and single layer of Ag ink. Each Ag IP pattern with dimension of 10.20×10.20×0.52 mm^3 (macro sensor) were placed in a preheated laboratory oven at 180°C for 2 minutes. Patterned Ag μECS is cured and shrunk simultaneously with approximately 58.5% reduction factor [6]. The sintered RE of the μECS cell is chlorinated using 3% sodium hypochlorite solution for 60 seconds. Au WE and CE are obtained with 24K brush gold plating technology. Figure 2 illustrates fabrication processes of the reported microsensor. Finally, scanning electron micrograph (SEM) images were analyzed to characterize the 3D topology of the nanomaterials used for microfabrication.

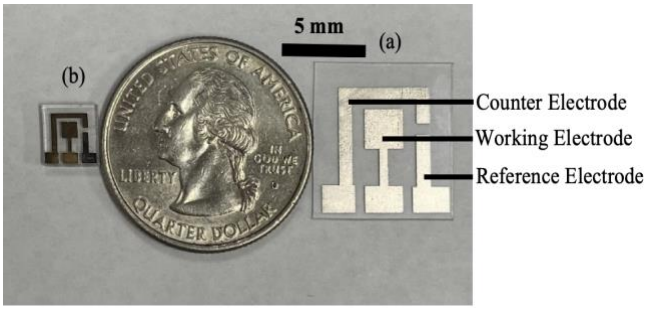

Figure 1: (a) Inkjet printed (IP) silver (Ag) working electrode (WE), counter electrode (CE), reference electrode (RE) (before shrinking and curing) with dimension 10.20×10.20×0.52 mm^3, (b) IP gold (Au) WE, Au CE, and silver chloride (AgCl) RE (after shrinking and curing) with dimension 4.23×4.23×1.52 mm^3.

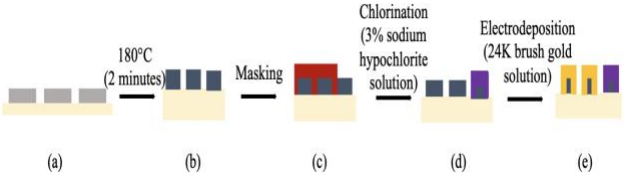

Figure 2: Step by step microfabrication of the gold (Au) inkjet printed (IP) microelectrochemical sensor (μECS) (cross-sectional view): (a) IP silver (Ag) electrodes on shape memory polymer (SMP) - before shrinking and curing (dimension:10.20×10.20×0.52 mm^3 and working electrode area: 19.36 mm^2), (b) IP Ag conductive electrodes on SMP - after curing and shrinking (dimension: 4.23×4.23×1.52 mm^3 and working electrode area: 2.25 mm^2), (c) counter electrode (CE) and working electrode (WE) are covered with masking tape and reference electrode (RE) is exposed for chlorination, (d) silver chloride (AgCl) RE and Ag CE and WE, (e) AgCl RE and Au CE and WE (Au plating immersion technology).

978-1-940470-04-7/HH2022/$25©2022TRF
DOI 10.31438/trf.hh2022.111

RESULTS

The reported µECS is characterized with 3mM lead (II) contaminated aqueous solution (optimized with 0.1 M HCl). Cyclic voltammogram (CV) analysis of the microsensor is performed for optimized aqueous solution with (sample 2) and without (sample 1)

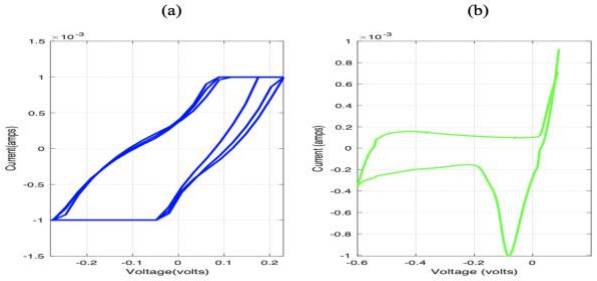

Figure 3: Cyclic Voltammogram (CV) for the microfabricated inkjet printed (IP) gold (a) microsensor and (b) previously reported macro sensor for optimized drinking water without lead (II) ions (0.1 M HCl).

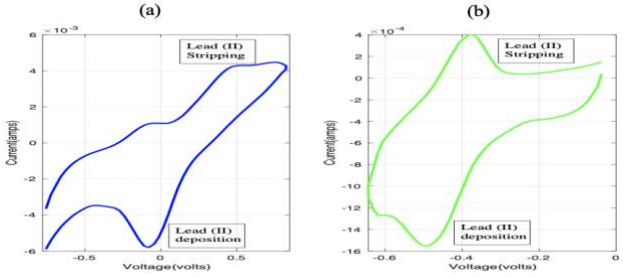

Figure 4: Cyclic Voltammogram (CV) for the microfabricated gold inkjet printed (IP) (a) microsensor and (b) previously reported macro sensor for optimized (0.1 M HCl) drinking water with 3 mM lead (II) ions.

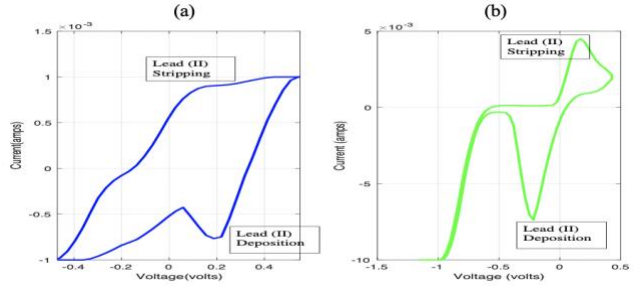

Figure 5: Cyclic Voltammogram (CV) for the fabricated gold inkjet printed (IP) (a) microsensor and (b) previously reported macro sensor for optimized (0.1 M HCl) drinking water with 14.4 µg/L lead (II) ions.

lead (II) ions. Figure 3 and 4 represent the CV graphs for both sample 1 and 2 respectively. It is observed from Figure 3 that there is no indication of lead (II) deposition and stripping in case of lead (II) free aqueous solution. However, a significant pair of peaks i.e. cathodic @ ~ -78.6 mV and anodic @ ~ 470.3 mV are representing lead (II) deposition and stripping respectively in case of 3 mM lead (II) contaminated optimized aqueous solution in Figure 4 (µECS). Figure 5 represents CV analysis of µECS (a) and macro sensor (b) for 14.4 µg/L lead (II) contaminated optimized aqueous solution (according to US Environmental Protection Agency (EPA) the approved lead (II) level in drinking water is 15 µg/L). It is observed that the reported µECS has enough potential to detect lower lead (II) level in the optimized aqueous solution. We have included the CV analysis of our previously reported macro sensor (13×10×1.52 mm^3) alongside the performances of our newly fabricated µECS (4.23×

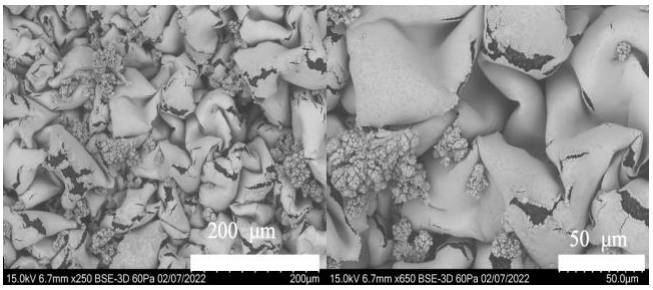

Figure 6: Scanning electron micrograph (SEM) images of the gold inkjet printed microelectrochemical sensor (µECS).

4.23×1.52 mm^3) for each case to understand and analyze the scaling effects in case of microfabrication of the reported microsensor. It is known that electrode surface area is proportional to stripping peak currents for CV analysis. But it is observed that the down scaling of the lateral dimension has bare minimum influence in case of the novel microfabricated µECS as miniaturizing the device using SMP provides increased effective electrode surface area despite reducing the lateral dimension of the electrodes. The twisted, tangled, and squeezed 3D topology shown in the SEM images in Figure 6 supports the claim of increased effective electrode surface area while miniaturization using SMP.

CONCLUSION

The reported IP Au µECS is an effective and efficient microsensor for lead (II) detection in the optimized aqueous solution. The µECS showed consistency and reproducibility in case of 14.4 µg/L lead (II) detection. In comparison to macro sensor, this 3D microsensor has performed potentially promising enough to be considered for further developments and different electrochemical sensing applications. However, the reported analytical results/data exhibits that the proposed additive technology (inkjet printing on SMP) and specific reported parameters for microfabrication has ensured green, direct, and maskless microfabrication of a simple, cost-effective, sensitive, and disposable µECS for lead (II) detection in the optimized aqueous solution.

REFERENCES

[1] D. Stacher, "Screening young children for lead poisoning: guidance for state and local public health officials," *Center for Disease Control and Prevention: Atlanta, GA, USA*, 1997.

[2] S. Laschi, I. Palchetti, and M. Mascini, "Gold-based screen-printed sensor for detection of trace lead," *Sensors and Actuators B: Chemical,* vol. 114, no. 1, pp. 460 – 465, 2006.

[3] Zimmer and Peacock, "Pros and cons of screen printed electrodes," 2020. (accessed on 11 May, 2021).

[4] Y. Kim, X. Ren, J. W. Kim, and H. Noh, "Direct inkjet printing of micro-scale silver electrodes on polydimethylsiloxane (PDMS) microchip," *Journal of Micromechanics and Microengineering,* vol. 24, 2014.

[5] R. C. Roberts, N. C. Tien, and D. Li, "Inkjet printed silver patterning on PDMS to fabricate microelectrodes for microfluidic sensing," *The 13th IEEE Conference on Sensors (Sensors 2014)*, pp. 1100-1103, 2014.

[6] A. Arif, A. M. Contreras, S. D. Hossain, and R.C. Roberts, "Inkjet printed 3D gold electrochemical sensor on shape memory polymer for lead detection," *IEEE Conference on Sensors (Sensors 2021)*, October 29-November 4, 2021.

CONTACT

*A. Arif, tel: +1-915-315-9440; aarif@miners.utep.edu

SMART ELECTROPALATOGRAPHY THIN-FILM FLEXIBLE PRESSURE SENSOR ARRAY FOR LINGUISTIC AND MEDICAL APPLICATIONS

Saeyeong Jeon, Ziqi Jia, Sunghyun Hwang, Suk-il Choi, Jiho Han, and Yong-Kyu Yoon
University of Florida, Gainesville, Florida, USA

ABSTRACT

A thin-film flexible pressure sensor array based smart electropalatography (EPG) device for linguistic and medical applications is presented. This sensor array is designed to monitor the location, pressure, and duration of tongue contact during speech. A 4 x 4 parallel plate capacitive sensing array consisting of silver nanowire (AgNW) electrodes and a polydimethylsiloxane (PDMS) dielectric layer with a thickness of 350 μm is designed, fabricated, and characterized. Top and bottom active shield ground layers are added to mitigate interference use during sensing. This is one of the first flexible pseudo-palates with a total thickness of less than 500 μm, which would significantly reduce the interruption of airflow during speech thus increasing test accuracy, and enhance the comfort of a wearer compared with a commercially available rigid acrylic based pseudo-palate with a thickness of 1 ~ 2 mm.

KEYWORDS

Electropalatography, Capacitive Pressure Sensor, Active Shielding, Pseudo-Palate

INTRODUCTION

Electropalatography (EPG) is a system that can monitor contacts between the tongue and hard palate during articulation and speech and can be utilized to diagnose speech sound disorder and analyze contact patterns. It can be used to improve speech production for people who are suffering from language and communication difficulties [1, 2]. A pseudo-palate is the main component that consists of a palate with an array of electrodes and is used to detect contact patterns between the tongue and the electrodes. Since the first EPG system was developed in the 1970s at Reading University [3], there were several commercially available EPG devices such as SmartPalate system (CompleteSpeech), LinguaGraph (Rose Medical Solution), and WinEPG (Articulate Instruments Ltd) [4].

An artificially duplicated hard palate with an electrode array is inserted into the mouth and mounted between the tongue and the palate. As most commercially available pseudo-palate devices are made with a resistive sensing mechanism, they can only detect the contact locations. The devices often have a thickness of 2 mm or thicker, and thus speech production during the test can be interfered by the device resulting in producing erroneous test data. Moreover, the customized palate devices for production are expensive, and the clinical therapies and the related research are limited in practice.

In this work, a micromachined thin membrane based smart electropalatography device with an active shielded flexible capacitive pressure sensor array is designed, fabricated, and characterized. A schematic of the proposed EPG device attached to the mouth palate is shown in Fig. 1. The capacitive pressure sensor can not only detect the location of the tongue touching the palate but also tell the pressure values and contact time during speech production and articulation. The measurement results can be used as a biomarker for the early detection of tongue movement related diseases such as concussions, Parkinson's disease (PD), and schizophrenia. Furthermore, a thin and flexible palate structure with a PDMS dielectric layer can reduce the interference of tongue movement and increase the comfort of users. Soft lithography with a stencil mask is used for device fabrication. The batch fabrication process makes it manufacturable, and the production cost can be dramatically decreased, letting the device be disposable with sanitization benefits. An active shielding method is widely used for a proximity sensor to mitigate interference and parasitic capacitances [5]. With the active shielding approach, the parasitic capacitance effects resulting from the measurement environment can be effectively eliminated. The system is further configured to have wireless data readout to realize a smart EPG for the internet of things. The active shielded flexible capacitive pressure sensor is directly applicable for linguistic and medical applications.

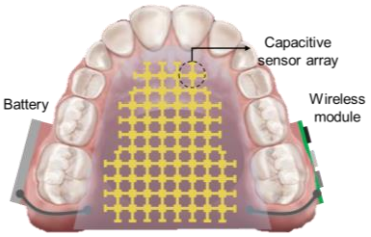

Figure 1: The proposed electropalatography (EPG) device installed on the mouth palate.

FABRICATION

Fig. 2 shows a fabrication process for an active shielded capacitive pressure sensor array. A soft lithography method using soft and flexible PDMS (Sylgard 184 kit, Dow Corning) material is used to micropattern the parallel plate silver nanowire (AgNW 120, ACS Material, LLC) electrodes. First, a silane coated Si wafer is prepared and spin coated with PDMS, where a 10:1 mixture of the prepolymer and the curing agent is used and the AgNW bottom ground layer is spray coated and passivated with a 40 μm thick PDMS layer.

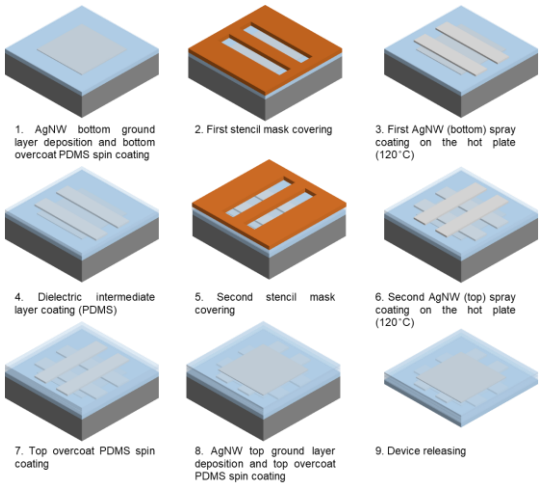

Figure 2: Fabrication process of an active shielding flexible capacitive pressure sensor array.

The first soft lithography is performed with a stencil mask and the

978-1-940470-04-7/HH2022/$25©2022TRF
DOI 10.31438/trf.hh2022.112

bottom AgNW electrodes are spray coated with an airbrush (G222, Master Airbrush) having 0.2 mm nozzle size on a hotplate at 120℃. The intermediate PDMS layer mixed in 50:1 (pre-polymer : curing agent) is spin coated at 300 rpm and the second soft lithography is performed to deposit the top AgNW electrodes with the top overcoating passivation layer. Finally, the top AgNW ground layer is spray coated with the thin PDMS layer and the fabricated device is released from the Si wafer.

MEASUREMENT RESULTS

Fig. 3(a) shows a fabricated 4 x 4 active shielding parallel plate capacitive pressure sensor. The overlapped AgNW electrode area is 4 mm^2 with a pitch between sensors of 1 cm and the PDMS intermediate layer is 350 μm thick. The schematic of the measurement setup is described in Fig. 3(b) and the force gauge (Series 5, Mark-10 Corp.) and LCR meter (E4980A, Agilent, Inc.) are used to apply a constant force of 10 N during the capacitive measurement at 1 MHz with 2 V. The ground layers are connected to the power supply (E3630A, Agilent) with a DC voltage of + 2 V and the inset in Fig. 2(b) shows a unit cell design of the parallel plate capacitive pressure sensor and the simple mechanism of the capacitance changing resulting from the gap changing between the top and bottom electrodes due to the applied force on the sensor.

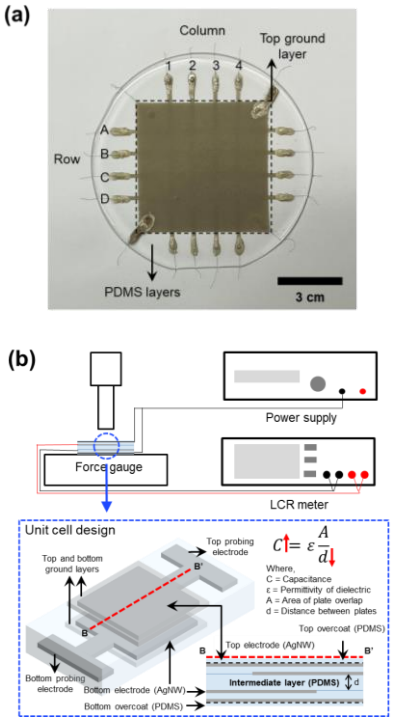

Figure 3: (a) Fabricated 4 x 4 active shielding parallel plate capacitive pressure sensor and (b) measurement setup with the LCR meter, power supply, and the force gauge. (Inset shows a schematic of a unit active shielding capacitive sensor.)

The measurement results of the active shielding case and the non-shielding case are summarized in Fig. 4 left and right, respectively. While reading the capacitance values upon external force to the sensor, one unit sensor (B3) is chosen and monitored without and with active shielding sensors. The non-shielded case shows that all the other sensors are affected by the applied force on the B3 sensor, where ΔC is in the range of 0.82 ~ 1.07 pF, and thus the actual measuring sensor and the neighboring sensors are hardly distinguishable. On the other hand, the active shielding case shows that the parasitic capacitance values are effectively reduced, thus the environmental interference during the measurements can be lowered. The developed active shielding capacitive pressure sensor is well applicable to the smart EPG application.

CONCLUSION

A smart EPG device based on an active shielding flexible capacitive pressure sensor array is successfully fabricated and characterized. A parallel plate flexible capacitive pressure sensor architecture with AgNW electrodes and PDMS intermediate /passivation layers is used. To reduce the parasitic effects during measurement, the active shielding method is applied, and its effectiveness is verified. The fabricated device can be utilized for linguistic and medical applications and contribute to enlarging the research area by not only analyzing the tongue contact patterns but also measuring the tongue pressure during the articulation.

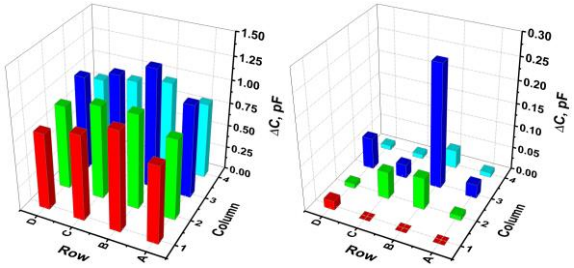

Figure 4: Measurement results of the non-shielded case (Left) and the active shielded case (Right). Sensor B3 is selected, and during the measurement, the parasitic effect is investigated upon the applied force to the sensor. ΔC is the value obtained by subtracting the capacitance values in the non-forced case from the capacitance values in the force applied case in absolute values.

ACKNOWLEDGEMENTS

This research was supported in part by NSF ECCS 2037266. Microfabrication and characterization have been performed at the University of Florida.

REFERENCES

[1] A. A. Wrench, "Advances in EPG palate design", *Advances in Speech Language Pathology,* 9.1, 3-12 (2007).

[2] W. Hardcastle,W. Jones,C. Knight,A. Trudgeon & G. Calder, "New developments in electropalatography: A state-of-the-art report", *Clinical Linguistics & Phonetics*, 3.1, 1-38 (1989).

[3] P. J. Roach, and W. J. Hardcastle, "A computer system for the processing of electropalatographic and other articulatory data", *Proceedings of phonetics symposium, university of essex language centre occasional papers*, p. 17 (1976)

[4] S. M. Zin, S. Z. M. Rasib, F. M. Suhaimi, and M. Mariatti, "The technology of tongue and hard palate contact detection: a review", *Biomedical engineering online*, 20(1), 1-19 (2021).

[5] D. Wang, "FDC1004: Basics of capacitive sensing and applications", *Texas Instruments-App. Report,* 12, 1-12 (2014).

CONTACTS

S. Jeon, tel: +1-352-328-9451; s.jeon@ufl.edu
Z. Jia, tel: +1-352-871-1658; jia.ziqi@ufl.edu
S. Hwang, tel: +1-352-278-8325; sunghyun.hwang@ufl.edu
S. Choi, tel: +1-617-642-9802; sukilchoi@ufl.edu
J. Han, tel: +1-352-871-5727; jihohan@ufl.edu
Y. K. Yoon, tel: +1-716-913-8874; ykyoon@ece.ufl.edu

THEORETICAL AND EXPERIMENTAL VALIDATION ON THE TUNING CAPABILITY OF A PERCOLATION-BASED GAS SENSOR.

Farhan Sadik Sium[1], Shakir ul Khan[1], Seungbeom Noh[1], and Hanseup Kim[1]
[1]Electrical and Computer Engineering, University of Utah, USA

ABSTRACT

This paper reports the theoretical and experimental validation of the tuning capability of a novel sensor based on percolation as the operation principle. To enable the tuning capability, an array of both the commercial and the microfabricated MEMS gas sensors was constructed. The array size and the degrees of freedom (DOF) for current flows within the array were manipulated. Theoretical and experimental results validated (1) that the percolation-based sensor tuning was feasible; (2) that the tuning became more deterministic with increasing array sizes and (3) the tuning threshold became lower with increasing DOF for current movement.

KEYWORDS

Percolation theory, switching tuning, switching uncertainty, gas sensor.

INTRODUCTION

Increasing demands are recently found in an effort to monitor environments through various distributed sensor nodes, and distributed gas sensor nodes have become of some interests in research communities. However, distribution of gas sensors has been mostly impractical with current technology, as conventional gas sensors as well as associated electronics, such as a wireless tethering module, tend to consume significant amounts of power and thus shorten the lifetime down to an impractical level when supported by a battery.

Such a limited lifetime issue of distributed gas sensors was addressed by constructing a normally dormant gas sensor or so-called a near-zero-power gas sensor by some research groups [1-3]. One example was a molecular-bridge mediated gas sensor developed by the authors [5]. The molecular-bridge gas sensor utilized the capture of a target gas as a switch element to allow and disallow current flow to activate the whole sensor node.

However, the previously developed molecular-bridge gas sensor inevitably experienced statistical uncertainty due to non-uniformity of a nanogap size across a wafer as well as random or uncontrolled behaviors of gas molecules entering to the nanogap.

As a method to minimize the device uncertainty, a statistical concept of percolation was previously suggested and validated with limited experimental results with array size variations [4]. However, it lacked a holistic modeling and any expansion to other parameters, failing to provide fundamental understanding on its applicability to device operation.

This paper reports an improved simulation and theoretical modeling of the switching behavior of a percolation-based gas sensor as well as experimental results as a proof.

SIMULATION AND THEORY

A theoretical model for percolation-based sensing was developed through Monte Carlo simulation that computed numerous case probabilities from various design choices. Specifically, the model performed 500 numbers of trials for specific occupancy within a matrix (Fig.1-(A)), and the percolation probability was determined by dividing the total number of percolated cases by the total trial numbers. Whether a matrix was percolated or not was decided by the existence of a spanning cluster of occupied nodes. The developed theoretical model allowed a wide range of input parameters for grid sizes and shapes (or degrees of freedom) to facilitate the prediction and comparison of distinctive designs.

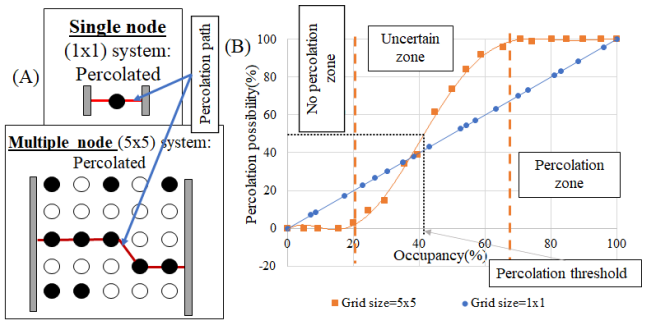

Figure 1: (A) Multiple conductive node system can mimic a single node switching system. Harmonical accord among several nodes result in percolation, depending on forming a conductive path. (B) Simulation results of percolation probability vs. occupancy. The probability could be categorized into three sections: no percolation, uncertainty and percolation zones. The middle zone is the uncertainty-zone that needs to be minimized.

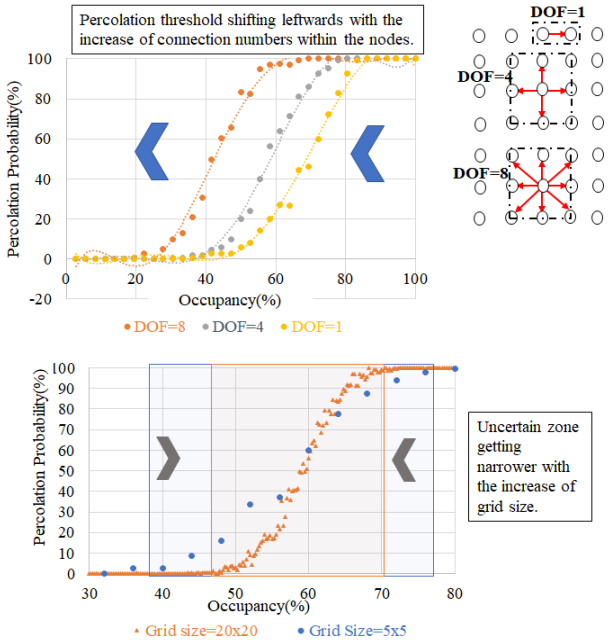

Figure 2: Simulation results of percolation probability vs occupancy depending on (top) degrees of freedom or lattice shapes and (bottom) the array sizes. (Top) As the degrees of freedom (DOF) for current flow through a network of individual stations increase, percolation threshold shifted leftwards or lower. With the increase in grid sizes the system will become more deterministic by shrinking uncertainty zone.

978-1-940470-04-7/HH2022/$25©2022TRF
DOI 10.31438/trf.hh2022.113

The modeling result showed that (1) a percolation characterizing graph was clearly split into three zones: no-percolation, uncertainty, and percolation zones (Fig.1-(B)); that (2) the uncertainty zone was modulated by changing the degrees of freedom (Fig.2-(top)) and the grid sizes (Fig.2-(bottom)). Thus, these modeling results clearly predicted that the percolation behaviors such as reducing uncertainty and modulating the threshold point could be achieved by design choices.

PROOF OF PERCOLATION IN MACRO LEVEL

To verify the modeling results, a macro-level hardware system was established by connecting multiple units of the MQ-3 commercial ethanol sensor (Vendor: Sparkfun) in various DOFs (Fig. 3-(A)). The circuit diagram is shown in Fig. 3-(B). The digital output pin of the sensor module was attached to the gate of the transistor. Thus, each transistor worked as conductive node for percolation. It was plausible to change percolation controlling parameters by simply altering connection among the nodes. (Fig. 3-(B)). The whole sensors were kept inside a shielded gas testing chamber having dimension of 60 x 30 x 40 cm^3. An LED was connected to the end of the circuit output and utilized to verify percolation switching when it was lit up.

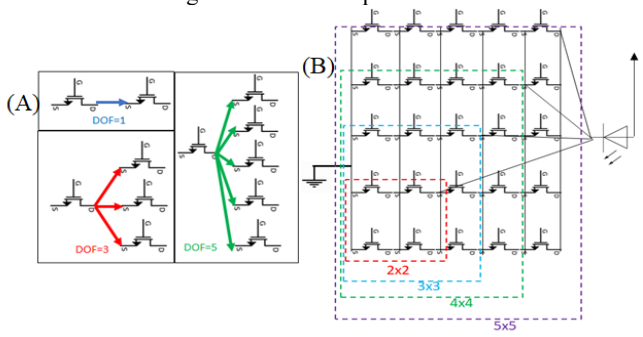

Figure 3. Hardware testing setup diagrams. (A) illustration of variable DOFs realized in multiple units of sensor. (B) circuit diagram for different grid sizes during testing.

(A)

Concentration of Ethanol in the chamber (µg/L)	Grid Size (DOF=5) 1x1	2x2	3x3	4x4	5x5
10	0	0	0	0	0
45	0	0	0	0	0
55	1	0	0	0	0
72	1	1	0	0	0
81	2	3	0	0	0
96	4	3	3	0	0
115	6	7	5	5	0
142	7	10	5	7	0
160	10	10	8	7	7
170	8	11	7	10	10
190	9	11	8	8	11
200	11	12	11	12	11
230	12	12	12	12	12
400	12	12	12	12	12

No. of events where percolation occurred (out of 12)

Uncertain zone Certain zone

(B)

DOF=5(Grid size 5x5) µg/L	No. of events where percolation occurred(out of 12)	DOF=3(Grid size 5x5) µg/L	No. of events where percolation occurred(out of 12)	DOF=1(Grid size 5x5) µg/L	No. of events where percolation occurred(out of 12)
45	0	50	0	60	0
55	0	75	0	78	0
72	0	88	0	95	0
81	2	100	0	110	0
96	4	118	0	124	0
115	6	135	1	145	0
142	7	170	5	178	1
160	10	190	6	198	2
170	11	210	8	219	2
190	12	230	9	237	6
200	12	245	11	254	7
230	12	260	11	267	8
255	12	300	12	320	10
300	12	350	12	365	11
400	12	400	12	410	12

Uncertain zone Certain zone Percolation Threshold

Figure 4. (A) As the grid size increased the uncertainty zone was reduced by 30% (B) With the increase of DOFs for current movement within the gird, the percolation tendency increased from 237µ/L to 115µ/L.

The test result showed a matching result to the model prediction. Figure 4-(A) showed that as the grid size (x-axis) increased from 1x1 to 5x5, the uncertainty zone (orange-colored) gradually reduced from a concentration span of 135 µg/L to that of 40 µg/L by 70.4%. Specifically, the 1x1 or a single sensor switched at any concentrations between 55 and 190 µg/L, while the larger grid sensors of 2x2, 3x3, 4x4 and 5x5 responded to gradually narrower concentrations of between 72 and 190 µg/L, 96 and 200 µg/L, 115 and 190 µg/L, and 160 and 200 µg/L. Figure 4-(B) showed that 5x5 sensor arrays lowered the average threshold points from 237 and 210 to 115 µg/L, as they increased the degrees of freedom from 1 and 3 to 5 dimensions. In other words, they demonstrated switching at a lower concentration when their lattice shapes were more prone to become connected. Based on the results it was evident that uncertainty of switching and switching threshold could be tuned by modulating grid sizes and node connections.

PROOF OF PERCOLATION IN MICRO LEVEL

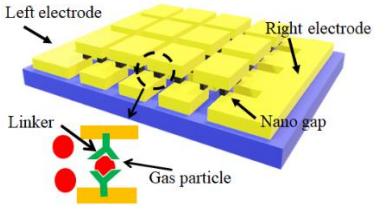

Figure 5: Rhetorical image of the percolation-based gas sensor.

To further verify the modeling prediction on grid sizes vs uncertainties, a micro-level nanogap gas sensor with an array configuration was fabricated based on sacrificial layer removal technique as previously described [3] (Fig.5). This sensor was exposed to a cadaverine gas. The measurement results also confirmed that as the nano-gap array size increased from 1x1 to 36x36, the variance of the amount of gas that is needed for switching gradually decreased from a standard deviation of 15.7 ppm to 2.1 ppm.

CONCLUSION

Both the theoretical and experimental validation on the tuning capability of a percolation-based gas sensor was reported. The theoretical modeling was established based on Monte Carlo Simulation and provided an insightful relationship between switching performance and design parameters. Experimental results confirmed such prediction by theoretical modeling: (1) the tuning of a percolation-based sensor was feasible, (2) the increasing array sizes improved the deterministic character of a switching, and (3) the increasing degrees of freedom lowered the threshold point.

REFERENCES

[1] "Zero-power infrared digitizers based on plasmonically enhanced micromechanical photoswitches", Qian, Z., Kang, S., Rajaram, V., Cassella, C., McGruer, N.E. and Rinaldi, M., Nature nanotechnology, 12(10), pp.969-973, (2017)

[2] "Ultra-low-power chemical sensor node.", Khan, S.H., Jung, Y.J., Hsieh, H.C., Wu, T., Mastrangelo, C.H., Kim, H., Broadbent, S.J. and Looper, R. Proceedings of the GOMAC Tech, (2018).

[3] "Development of a Gas Sensor for Green Leaf Volatile Detection", Khan, S.U.H., Tope, S., Dolpati, R., Kim, K.H., Noh, S., Bulbul, A., Mural, R.V., Banerjee, A., Schnable, J.C., Ji, M. and Mastrangelo, C. IEEE Transducers, pp. 250-253, (2021).

[4] "Statistics-Based Gas Sensor.," Khan, S.U.H., Banerjee, A., Broadbent, S., Bulbul, A., Simmons, M.C., Kim, K.H., Mastrangelo, C.H., Looper, R. and Kim, H., IEEE 32nd International Conference on Micro Electromechanical Systems (MEMS), 137-140, (2019).

[5] "Molecular bridge-mediated ultralow-power gas sensing", Banerjee, A., Khan, S.U.H., Broadbent, S., Bulbul, A., Kim, K.H., Noh, S., Looper, R., Mastrangelo, C.H. and Kim, H., Microsystems & nanoengineering, 7(1), pp.1-11, (2021).

CONTACT

Hanseup Kim; Email: hanseup.kim@utah.edu

A 17.3 GHZ ATOMIC-LAYERED HZO SOLIDLY MOUNTED RESONATOR: TOWARDS CMOS-BEOL MM-WAVE FREQUENCY CONTROL

Troy Tharpe, Shaurya Dabas, Dicheng Mo, and Roozbeh Tabrizian*
Electrical and Computer Engineering Department, University of Florida, Gainesville, Florida, USA

ABSTRACT

This paper reports, for the first time, on a 17.3 GHz hafnia-zirconia (HZO) solidly mounted bulk acoustic wave (BAW) resonator created entirely by atomic layer deposition. CMOS-based ferroelectric, dielectric, and metallic layers with atomically precise thicknesses are stacked to realize a solid-state acoustic cavity with ultra-uniform frequency across the wafer and for back-end-of-line (CMOS-BEOL) integration. The resonator prototype demonstrates a large electromechanical coupling (k_t^2) of 3.62% and a high-quality factor (Q) of 267, setting a new $k_t^2.Q$ record of ~10 at such high operation frequency. Intrinsic switchability is also demonstrated for the resonator, based on exploiting ferroelectric polarization tuning in HZO.

KEYWORDS

Super-high-frequency, CMOS BEOL, solidly mounted resonator, ferroelectric, hafnia-zirconia, intrinsically switchable.

INTRODUCTION

Since demonstration of the resonant gate transistor by Nathanson et. al. in the 1960s [1], monolithic integration of mechanical / acoustic resonators on semiconductor platforms has been vigorously followed. This is primarily driven by the overhead of non-monolithic integration approaches that set fundamental limits on the performance, footprint, and cost of microsystems relying on frequency generation and control.

Having access to high Q and k_t^2 acoustic resonators on standard semiconductor nodes can potentially revolutionize data processing and wireless communication systems by accommodating high-performance local oscillators, clocks, and spectral processors in ultra-miniaturized footprints. Successful demonstrations of CMOS-monolithic resonators include innovative approaches relying on front-end-of-line (FEOL) building blocks (*e.g.*, FinFET) [2] or BEOL metal and dielectric layers [3] to create high-Q resonators. These approaches generally rely on electrostatic transduction, which substantially limit their k_t^2 and make extreme frequency scaling to cm- / mm-wave challenging.

The observation of ferroelectric behavior in hafnia-zirconia ($Hf_{0.5}Zr_{0.5}O_2$ or HZO), and the first demonstration of HZO nano-electro-mechanical transducers [4] have augured the potential for realization of long-coveted CMOS-monolithic high $k_t^2.Q$ acoustic resonators. HZO films, commonly used in amorphous form as high-k dielectric material of advanced CMOS, can be crystallized upon proper application of stress. HZO films deposited by ALD, and stress-engineered by capping electrodes, provide a large remanent polarization and piezoelectric coupling, even upon scaling to sub-5nm. However, the major challenge in using HZO for creation of high $k_t^2.Q$ resonators is the large dependence of its polarization and piezoelectricity on residual stress (also called crystallization stress). As recently demonstrated [5], releasing HZO transducers to create free-standing resonators results in significant degradation of their polarization and piezoelectricity.

In this work, for the first time we demonstrate a solidly mounted resonator (SMR) based on integration of HZO transducer on Bragg acoustic reflectors created from alternating ALD of tungsten (W) and silicon dioxide (SiO_2). This architecture sustains the crystallization-stress, large polarization, and piezoelectricity in HZO facilitating creation of high k_t^2 BAW resonators. Further, the all-ALD fabrication process enables extreme frequency scaling to mm-wave, while benefiting from frequency definition with ultra-high precision, only limited by atomic-level thickness of constituent layers. The CMOS-based materials and processing, and solid-state architecture of the presented resonator makes it perfectly compatible for CMOS-BEOL integration (Fig. 1).

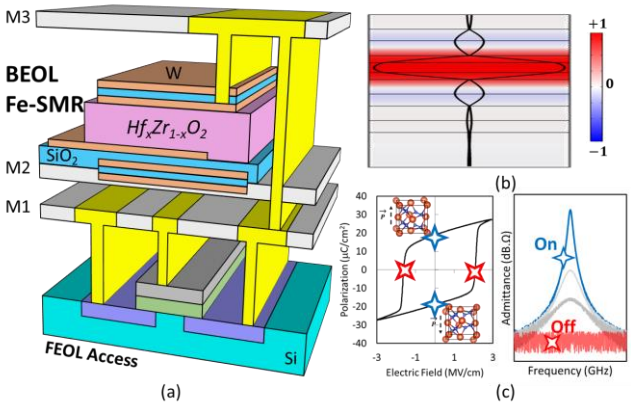

Fig. 1: *(a) Conceptual schematic of atomic-layered HZO SMR integrated on CMOS-BEOL. (b) COMSOL-simulated resonator mode-shape, showing the thickness-extensional stress across the stack. (c) Ferroelectric HZO polarization hysteresis loop and resonator frequency response, highlighting intrinsic switchability.*

CONCEPT

Figure 1 conceptually shows the atomic-layered HZO SMR created by stacking HZO transducer within W/SiO_2 Bragg reflectors. The reflectors not only localize acoustic energy for high-Q operation, but also sustain the crystallization-stress in HZO required for large piezoelectric coupling. Figure 1(b) shows the COMSOL-simulated stress-profile across the resonator stack, highlighting the thickness-mode localization in HZO transducer. Figure 1(c) shows the polarization-hysteresis loop for ferroelectric HZO transducer and conceptual resonator admittance response, highlighting the capability of intrinsic switching by DC-tuning of polarization. This feature is highly desirable for creation of multi-frequency oscillators and multi-band configurable filters.

HAFNIA-ZIRCONIA TRANSDUCER

Transduction of thickness-mode BAW in HZO resonators is achieved via the piezoelectric effect inherent to all ferroelectrics. Upon application of sufficient crystallization stress and limitation of grain size, the polar orthorhombic phase (space group $Pca2_1$) is stabilized. However, due to HZO's inherent polymorphism and acute dependence on residual stress, nonpolar tetragonal and monoclinic phases readily form in the presence of stress nonuniformities. Figure 2 depicts the effect of stress boundary condition on the ferroelectric performance, and therefore orthorhombic composition, of an HZO transducer. Figure 2 (a) shows polarization vs electric field hysteresis measurements for fabricated HZO SMR prototypes, highlighting how a solidly mounted architecture results in a higher remanent polarization and

978-1-940470-04-7/HH2022/$25©2022TRF
DOI 10.31438/trf.hh2022.114

less paraelectric loop slanting, indicative of higher orthorhombic percentage. Figure 2 (b) shows how the higher ferroelectric phase contribution in solidly mounted architectures results in increased displacement vs electric field (*i.e.*, piezoelectric coupling).

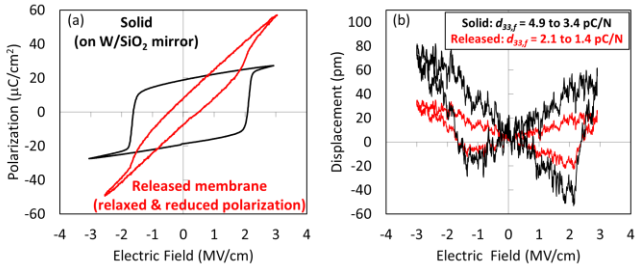

Fig. 2: *(a) Polarization vs electric field and (b) displacement vs electric field hysteresis for solidly mounted W-HZO-W capacitors and released membranes.*

RESONATOR FABRICATION

HZO SMR is fabricated using the process depicted in Fig. 3. First, an acoustic Bragg mirror is formed via four, alternating depositions of 65.5nm ALD W and 81.5nm of ALD SiO_2. Next, 34nm W is ALD and patterned for device bottom electrodes, followed by deposition and patterning of platinum (Pt) routing. The ~50nm thick device transducer, composed of 5, 9nm ALD HZO layers intercalated with 4, 1nm ALD alumina (Al_2O_3) layers is then capped with a symmetric 34nm top W electrode and rapid thermal annealed at 500ºC for 20s in nitrogen ambient. Top electrodes are patterned, and access windows to bottom W electrodes etched, respectively using reactive ion etching. Finally, top Pt is sputtered and lifted off for pads and routing.

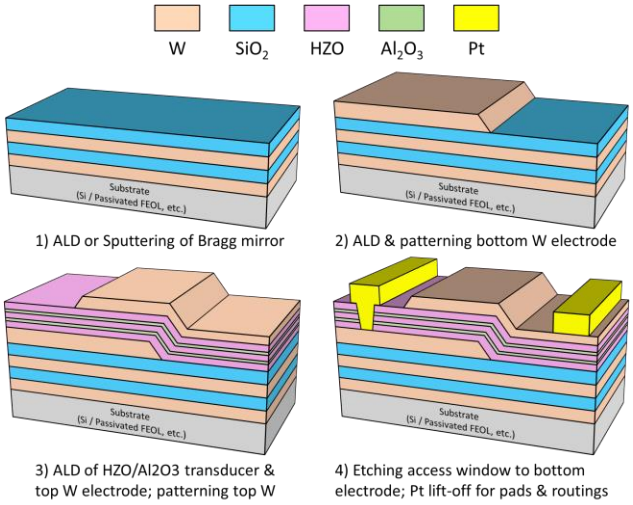

Fig. 3: *Four-step fabrication process for creation of CMOS-BEOL compatible, high k_t^2.Q, HZO transduced, SMR resonators.*

Optical images of the finalized HZO resonator are shown in Fig. 4 (a). Figure 4 (b) depicts a scanning electron microscope (SEM) image of the device active area, highlighting the ~8μm x ~8μm W top electrode used to mitigate lateral wave propagation. Figure 4 (c) shows a cross-sectional SEM image of the HZO nanolaminate transducer atop alternating Bragg-mirror layers. Insets depict a cross sectional transmission electron microscope (XTEM) image of interposed transducer layers with annotated thicknesses and a high-angular dark-field (HAADF) STEM of an orthorhombic grain with measured ~34º c-axis orientation.

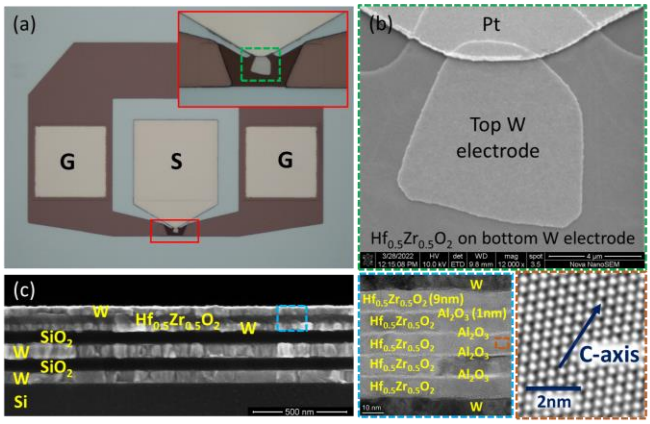

Fig. 4: *(a) Optical image of fabricated HZO SMR BAW resonator. (b) SEM image highlighting device active area. (c) Cross-sectional SEM with constituent layers annotated and inset XTEM of the HZO nanolaminate transducer with further inset depicting HAADF STEM of individual orthorhombic grain.*

RESONATOR CHARACTERIZATION

Figure 5 (a) depicts measured admittance ($|Y_{11}|$) for the HZO SMR at different bias voltages applied using bias-tee. A k_t^2 of 3.62% and Q of 267 is measured at 17.3 GHz. Figure 5 (b) shows the switching trend of admittance as voltages near coercive.

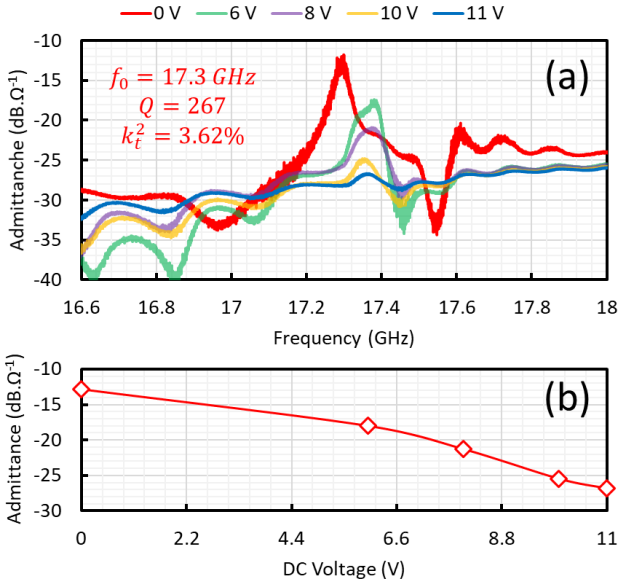

Fig. 5: *(a) Admittance responses for an ~8μm x ~8μm HZO SMR BAW resonator, colored by DC bias voltage. (b) Extracted switching trend of admittance at voltages nearing coercive.*

ACKNOWLEDGEMENTS

This work is supported under the DARPA YFA program.

REFERENCES

[1] H. C. Nathanson, et. al., IEEE TED, vol. 14, no. 3, p. 117.
[2] B. Bahr, et. al., IEEE ISSCC 2018.
[3] M. Li, et. al., IEEE JMEMS, vol. 24, no. 2, p. 360.
[4] M. Ghatge, et. al., IEEE IEDM 2018.
[5] T. Tharpe, et. al., Adv. Eng. Mat, vol. 23, no. 12, 2021.

CONTACT

*Troy Tharpe, tel: +1-321-432-9557; ttharpe@ufl.edu

CO-RESONANT CANTILEVERS FOR MATERIALS RESEARCH AND SENSOR APPLICATIONS

Julia Körner[1*]
[1]Leibniz University Hannover, Germany

ABSTRACT

Employing co-resonant coupling in dynamic-mode cantilever MEMS sensors has the potential for a significant increase in sensitivity while maintaining a reliable oscillation detection. However, the resulting complex interplay between the micro- and nanocantilever has to be carefully considered for application-specific sensor design as it impacts all relevant sensor properties, such as linearity, stability and detectivity. Here, an overview of key parameters, their dependence on the strength of co-resonance and resulting consequences for sensor performance is provided.

KEYWORDS

Cantilever sensor, dynamic-mode, co-resonant coupling, sensitivity, stability, linearity

INTRODUCTION

Dynamic mode cantilever sensors are used in a wide variety of applications, from materials research to mass and gas sensing [1,2]. The persisting challenge is the demand for increased sensitivity while at the same time ensuring reliable and robust oscillation detection. Several innovative ideas are studied for that purpose, for example use of higher order bending modes [3,4] or specifically tailored geometries [5].

Within this scope, we are pursuing an approach of co-resonantly coupled cantilevers [6]. The tremendous potential of this concept has been demonstrated experimentally, e.g. by observing magnetization reversal in Heusler-nanoparticles at room temperature which was not possible with cantilever sensors before [7]. In all experimental studies an increase in measurement signal strength and sensitivity by several orders of magnitude was found compared to a single sensitive microcantilever [8]. Furthermore, we have introduced a novel read-out method based on time-scale observation of sensor beating [9].

Despite its potential, common application of the concept is still limited since the co-resonance induces a multitude of complex interdependencies on sensor properties which had not been fully understood until now. While the theoretical basics can be found in [10,11], we here present very recent extensive experimental studies which allow to validate and verify them. For the first time, this enables comprehensive insights and allows to draw conclusions with regard to practical sensor design. In the following, some key aspects are highlighted.

CREATION OF CO-RESONANT STATE

The sensor concept is based on mechanical coupling of two vastly different oscillators (geometry and material properties), where ideally one is very soft and therefore sensitive to external interactions (i.e. nanocantilever) and the other one ensures reliable oscillation detection (i.e. microcantilever) [6]. Co-resonance is introduced by matching the eigenfrequencies of these two beams, either by appropriate geometric design or by lowering the usually much higher eigenfrequency of the nanocantilever through point mass deposition at its free end. Examples of fabricated sensors are depicted in Fig. 1. While any matching degree is possible, the co-resonance becomes strongly evident for eigenfrequency deviations between micro- and nanocantilever in the range of ±20 %.

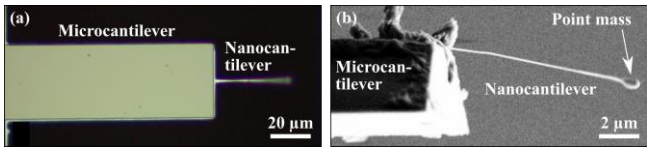

Figure 1: Exemplary co-resonantly coupled sensors: (a) Top view of silicon nitride system with intrinsic eigenfrequency matching (Δf = 1.4 %) by geometry. Dimensions (length (l) x width (w) x thickness (t)): microcantilever = (110 x 40 x 1) µm; nanocantilever = (35 x 1 x 0.1) µm. (b) Side view of silicon microcantilever with carbon nanotube nanocantilever attached by amorphous carbon deposition and eigenfrequency matching by platinum point mass. Dimensions: microcantilever (trapezoidal cross section): l = 105 µm, w_{top} = 15.7 µm, w_{bottom} = 37.2 µm, t = 4.1 µm; nanocantilever (circular cross section): l = 10.7 µm, diameter = 0.1 µm. Please note that only the microcantilever's free end is shown for better visibility.

Table 1: Properties of an experimental co-resonantly coupled sensor made from a silicon microcantilever and a carbon nanotube as depicted in Fig. 1b.

	Microcantilever	*Nanocantilever*
Spring constant	51.6 N/m	0.004 N/m
Quality factor	6540	350
Initial unmatched eigenfreq.	448.32 kHz	1,360 kHz
Adjusted eigenfreq. +10%	Same as initial	493.4 kHz
Adjusted eigenfreq. -1 %	Same as initial	442.4 kHz

CONSEQUENCES FOR SENSOR PERFORMANCE

With reduced eigenfrequency deviation, the amplitude ratio (i.e. amplitude amplification) between the nanocantilever's and microcantilever's free end increases (Fig. 2). While potentially beneficial for some applications, it also means that the nanocantilever can traverse into a non-linear bending regime, chaotic and unstable oscillation and, thus a distorted amplitude response curve (Fig. 3).

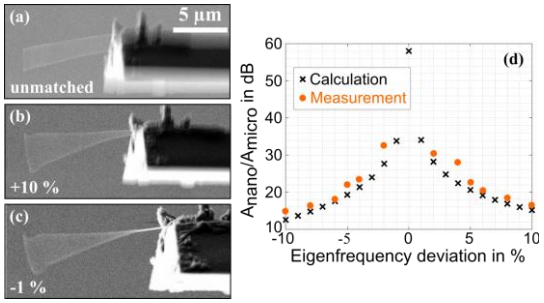

Figure 2: Amplitude amplification for the experimental sensor from Fig. 1b. (a) - (c) Exemplary SEM images of the resulting oscillation envelope for different matching states at an excitation frequency of 448 kHz (+10% means that the nanocantilever's eigenfrequency is 10% above that of the microcantilever). Excitation voltages applied to shaker piezo plate: (a) 200 mV, (b) 50 mV, (c) 20 mV. (d) Measured and calculated amplitude amplification curve based on the initial properties given in Tab. 1. Please note that there is no experimental data available for ±1% and 0% due to undetectable microcantilever amplitude in SEM images.

978-1-940470-04-7/HH2022/$25©2022TRF
DOI 10.31438/trf.hh2022.115

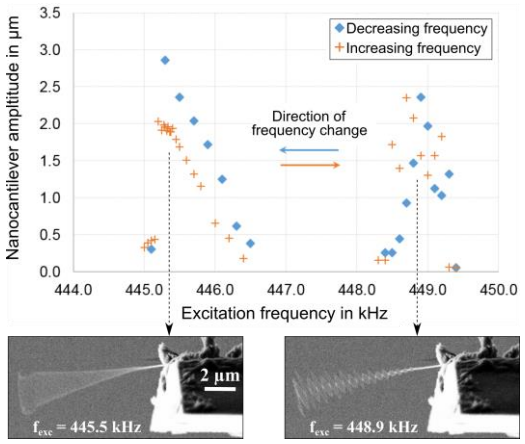

Figure 3: Measured amplitude response curve obtained from SEM images for the experimental sensor with -1% eigenfrequency deviation (properties see Fig. 1b and Tab. 1). The left peak exhibits a Duffing *distortion and the right peak chaotic oscillation behavior of the nanocantilever as visible in the corresponding SEM images.*

Hence, to ensure sensor **stability**, the driving amplitude could be reduced, resulting in a smaller microcantilever amplitude and potentially decreased signal-to-noise ratio. Another solution would be the reduction of eigenfrequency matching, i.e. reduced co-resonant state, but with the drawback of diminished sensitivity.

Sensor **sensitivity** and **detectivity** have an opposing dependency on the degree of eigenfrequency deviation**.** Hence, while sensitivity is large for small deviations, detectivity is reduced [10]. This is due to the fact that the nanocantilever's properties provide a larger fraction of the coupled system's properties for closely matched eigenfrequencies. While beneficial in terms of sensitivity, it can be disadvantageous for detectivity since the nanocantilever often has a (much) lower quality factor than the microcantilever. This results in a significantly smaller quality factor of the measured main resonance peak (Fig. 4). A solution would be to carefully consider material choice for the nanocantilever as well as the conditions under which the sensor is to be used (e.g. vacuum, air, liquid).

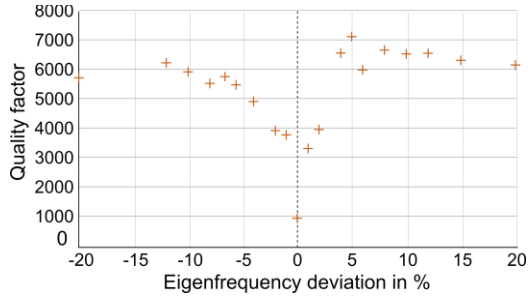

Figure 4: Quality factor of main resonance peak in dependence on eigenfrequency deviation for sensor in Fig. 1b obtained by fitting of measured amplitude response curves with a Lorentzian *peak function.*

SUMMARY

The strength of co-resonance has an impact on many different aspects of the coupled system's behavior and their interplay, and all of them need to be carefully considered and weighted for application-specific sensor design. With the above described new experimental studies, the previous theoretical modelling has been validated and confirmed. Thereby, we enable reliable predictions of sensor performance and derivation of necessary properties to achieve a desired behavior (e.g. sensitivity, amplitude amplification). This provides a practical basis for design of highly sensitive cantilever sensors with reliable oscillation detection which can for example be employed to study properties of novel nanomaterials, previously inaccessible by this technique. Furthermore, since the sensitivity is mainly defined by the nanocantilever properties, the co-resonant concept itself can enable self-sensing/self-actuation on the microcantilever and, hence extend use cases of these types of sensors.

ACKNOWLEDGEMENTS

The reported work is funded by the German Research Foundation DFG (grant number KO5508/3-1). Furthermore, the author would like to thank Christopher F. Reiche for critical review of this manuscript.

REFERENCES

[1] A. Boisen, S. Dohn, S.S. Keller, S. Schmid, and M. Tenje, "Cantilever-like Micromechanical Sensors", *Reports on Progress in Physics*, 74, 036101 (2011).

[2] B. N. Johnson, and R. Mutharasan, "Biosensing Using Dynamic-Mode Cantilever Sensors: A Review", *Biosensors and Bioelectronics*, 32, 1 (2012).

[3] H.-S. Liao, K.-Y. Huang, and C.-S. Chang, "Cantilever-Based Mass Sensor Using High Order Resonances for Liquid Environment", IEEE/ASME International Conference on Advanced Intelligent Mechatronics (AIM), Budapest, Hungary (2011), pp. 652 – 655.

[4] S. An, B. Kim, S. Kwon, G. Moon, M. Lee, and W. Jhe, "Bifurcation-Enhanced Ultrahigh Sensitivity of a Buckled Cantilever", *PNAS*, 115, 2884 (2018).

[5] S. Leahy, and Y. Lai, "A Gap Method for Increasing the Sensitivity of Cantilever Biosensors", *Journal of Applied Physics*, 122, 064502 (2017).

[6] C. F. Reiche, J. Körner, B. Büchner, and T. Mühl, „Introduction of a Co-Resonant Detection Concept for Mechanical Oscillation-based Sensors", *Nanotechnology*, 26, 335501 (2015).

[7] J. Körner, C. F. Reiche, R. Ghunaim, R. Fuge, S. Hampel, B. Büchner, and T. Mühl, „Magnetic Properties of Individual Co_2FeGa Heusler Nanoparticles Studied at Room Temperature by a Highly Sensitive Co-Resonant Cantilever Sensor", *Scientific Reports*, 7, 8881 (2017).

[8] J. Körner, „A highly Sensitive Co-Resonant Cantilever Sensor for Materials Research: Application to Nanomaterial Characterization", *Journal of Materials Research*, 33, 2504 (2018).

[9] G. Bücken, and J. Körner, „Time-Domain Analysis of a Novel Co-Resonant Cantilever MEMS Sensor and Derivation of a New Measurement Concept Based on Beating", *Journal of Microelectromechanical Systems*, 29, 1032 (2020).

[10] J. Körner, „Effective Sensor Properties and Sensitivity Considerations of a Dynamic Co-Resonantly Coupled Cantilever Sensor", *Beilstein Journal of Nanotechnology*, 9, 2546 (2018).

[11] J. Körner, C. F. Reiche, B. Büchner, T. Mühl, and G. Gerlach, „Employing Electro-Mechanical Analogies for Co-Resonantly Coupled Cantilever Sensors", *Journal of Sensors and Sensor Systems*, 5, 242 (2016).

CONTACT

*Julia Körner, Tel: +49-511-762-14041; koerner@geml.uni-hannover.de

FOCUSING OF A RELATIVISTIC ELECTRON BEAM WITH A MICROFABRICATED QUADRUPOLE MAGNET

*Benjamin A Pound, Sophie Crisp, Alexander Ody, Pietro Musumeci, James Rosenzweig, and Robert Candler**
University of California, Los Angeles, California, USA

ABSTRACT

We show in this work the first reported results of relativistic electron beam focusing using a microfabricated device. The application of microfabrication to beam physics responds to a need in the particle accelerator community for miniature, economical components that can be used in a range of diverse applications ranging from nanofabrication to electron beam therapy. Quadrupole magnets, like the device described in this paper, are essential parts of any accelerator. We demonstrate beam focusing of a relativistic (3.2 MeV) electron beam, and further show that vertical steering errors can be corrected by modifying the current in the device instead of re-alignment. We also present magnetic field data that show better than 3% agreement with simulation.

KEYWORDS

Particle accelerator, magnetism, electron optics, quadrupole

INTRODUCTION

Motivation

This work is centered around miniaturizing the magnetic optics used to steer and focus relativistic electron beams. Electron beams are electron currents in free space and are used in medical applications (electron beam therapy, sterilization), nanofabrication, synchrotrons, and many others [1]. The two main components used in electron beam optics are dipole and quadrupole magnets. Whereas traditional optics use mirrors and lenses to steer and focus light, magnetic optics use the Lorentz force to steer and focus electron beams. Dipole magnetic fields feature a homogenous field for steering, whereas quadrupole magnets use quadrupolar fields, which vary linearly in space, for focusing. Electron beams inherently diverge due to space charge effects and non-zero beam emittance, so quadrupoles are needed to periodically refocus the beam. Quadrupoles focus in one transverse dimension and defocus in the other, so several quadrupoles, with fields rotated by 90 degrees, are needed to focus the beam in both dimensions simultaneously.

We present here *the first microfabricated planar quadrupole* (MPQ), whose distinguishing feature is an arbitrarily long magnetic length limited only by wafer size, shown in Fig. 1. The MPQ was inspired by the so-called "Panofsky" style of macro-scale quadrupoles [2]. With more than an order of magnitude reduction in footprint compared to conventional electromagnet quadrupoles, this device is well-suited for integration in upcoming compact electron accelerators.

Quadrupole Mechanism

A quadrupole is characterized by its *transverse gradient*, or the magnetic field gradient produced in the transverse plane, and its *effective magnetic length*, which is the length over which the gradient is maintained. The focusing strength of the quadrupole is dictated by the *integrated gradient*, which is the transverse gradient integrated along the length of the quadrupole. Large-scale conventional quadrupoles produce 1-10 T integrated gradients. Our group previously showed a miniature quadrupole [3] with an integrated gradient of 0.025 T. Photonic crystals have been used to make microscale quadrupoles [4], but can only focus relatively low-energy electron beams (< 35 MeV). The MPQ presented here showed a maximum integrated gradient of 0.044 T. The integrated gradient was limited in this first demonstration by low currents (because of the power supply limits) and a non-optimized geometry. Fixing these issues would improve the integrated gradient by one to two orders of magnitude.

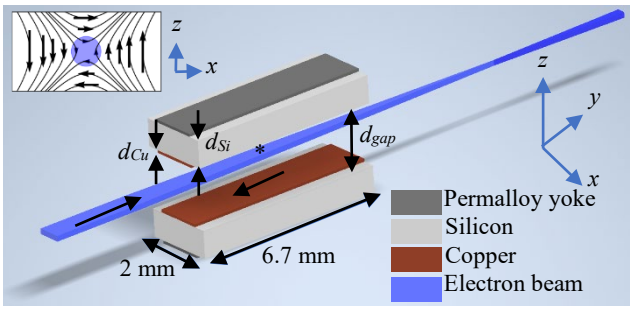

Figure 1: Schematic of one MPQ focusing an electron beam. The current direction is same in both copper sheets (-y direction) as shown by the arrow. The beam direction is also indicated by an arrow in the +y direction. The inset shows the electron beam cross section superimposed on the quadrupole field at the origin ("").*

DESIGN

The MPQs are fabricated by electroplating 2 mm wide, 50 um-thick copper traces on the front and 2 mm wide, 50 um-thick permalloy on the back of a 500 µm-thick silicon wafer (Fig. 2a). The wafer is diced and the MPQs are mounted on PCBs and aluminum fixtures such that the two chips face each other, as shown in Fig. 2b. The MPQ copper carries current (10s A) to generate the magnetic field, and the permalloy guides the magnetic flux to maximize the transverse gradient. The standoff distance between MPQ halves is set with spacers.

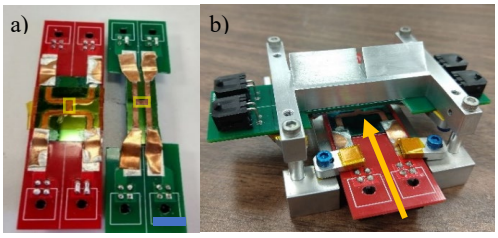

Figure 2: a) MPQ devices, copper side up, mounted on a PCB. Blue scale bar is 1 cm. The active areas from Fig 1 are located at the yellow boxes. b) fully assembled MPQ device with beam direction shown in yellow.

Assuming the length is much greater than other dimensions and the yoke permeability is large and non-saturating, magnetic circuit analysis predicts the gradient of this device to be

$$dB_z/dx = \mu_0 J / (1+d_{gap}/(2d_{Cu}) + d_{Si}/d_{Cu}) \quad (1)$$

where dB_z/dx is the gradient, μ_0 is the permeability of free space, J is the current density in the copper sheets, and d_{gap}, d_{Si}, d_{Cu} are the gap distance between MPQ halves, silicon thickness, and copper sheet thickness respectively (Fig. 1). This scaling law shows that small gaps and small (large) thicknesses for silicon (copper and

978-1-940470-04-7/HH2022/$25©2022TRF
DOI 10.31438/trf.hh2022.116

permalloy) are beneficial to increase the gradient. These considerations informed the design, in tandem with electron beam considerations, fabrication restraints, and simulation.

RESULTS

Hall Probe Magnetic Field Measurement

We first used a Hall probe to map the magnetic field in the MPQ. The gap was set to 5.6 mm to accommodate the Hall probe thickness. We measured dB_z/dx, the transverse gradient, along the y axis, which is the direction the electron beam travels. The experimental results match magnetostatic simulations from RADIA within 3%, which is shown in Fig. 3.

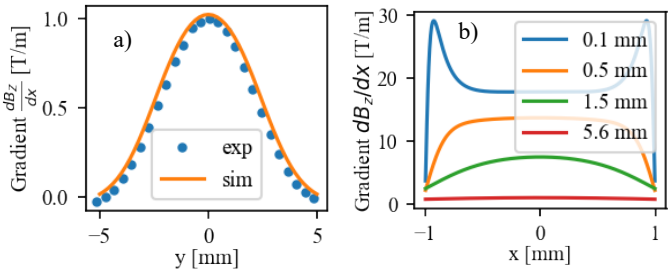

Figure 3: a) Comparison of experimentally measured and simulated gradient (dB_z/dx) along y-axis at $x = z = 0$ at a current of 20 A (2E+8 A/m^2 current density) and 5.6 mm gap. b) RADIA simulations of the transverse gradient (dB_z/dx along the x direction at $y = z = 0$) at different gaps. The gradient becomes larger and more uniform around x=0 with decreasing gap.

Relativistic Electron Beamline Measurements

Focusing of a relativistic electron beam was performed at the UCLA Pegasus beamline [5]. The electron bunch is created in the photoinjector, accelerated to a kinetic energy of 3.2 MeV (relativistic factor γ=7.24), focused by the MPQ, then imaged on a screen 0.5 m downstream. The MPQ gap was set to 1.5 mm. For the first experiment the current in both MPQ halves was the same. The beam was fully focused at a current of 22 A to 335 µm in the x dimension, shown in Fig. 4. As expected, the z beam size continually increased as the current magnitude increased. At 22 A the MPQ magnetic field gradient is around 5 T/m with an integrated gradient of 0.024 T; the integrated gradient at 40 A is 0.044 T, with a focal length of 279 mm.

In addition to beam focusing, the test also revealed a significant beam displacement in the z direction. We found experimentally that the displacement can be compensated and eliminated by using approximately four times more current in the top MPQ half. This effectively superimposes an additional B_x dipole component over the pure quadrupole field which counteracts other sources of vertical deflection. We show the results of both uncompensated and compensated experiments in Fig. 4. The cause of the deflection is still under investigation. We note that in both experiments the x displacement was close to zero, which means that the MPQ was well-centered in the x direction, and the beam over-filled the MPQ aperture, therefore automatically satisfying z alignment.

CONCLUSIONS

We have demonstrated focusing of a relativistic electron beam with a microfabricated device for the first time. We showed that vertical steering errors can be compensated by using different currents in the MPQ top and bottom halves. The measured magnetic field is within 3% of the simulated field. This work is an important step towards microfabricated-enabled accelerator-on-a-chip devices, which could significantly enhance access to relativistic electron beams for research and industrial applications.

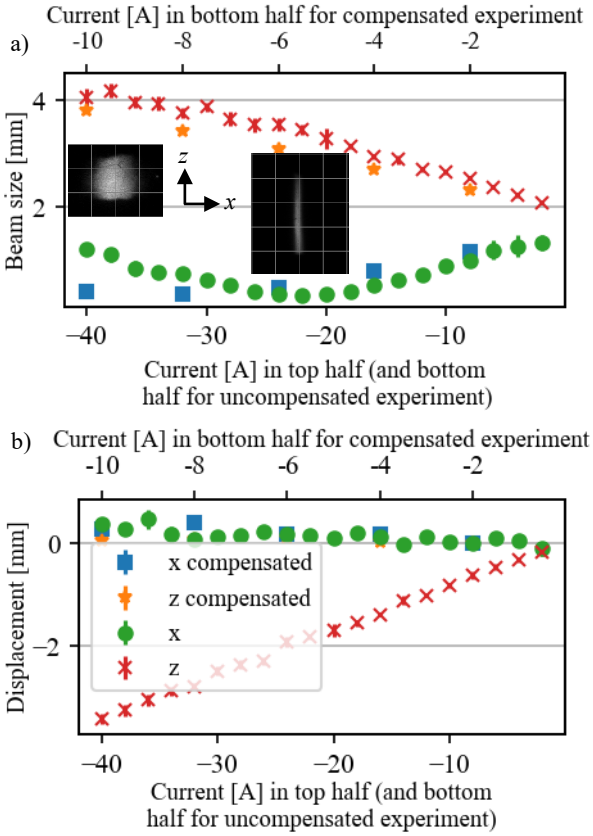

Figure 4: Current compensation preserves beam focusing while mitigating beam shift. Legend in (b) is the same for both plots. a) Beam diameter as a function of current. The current is directed in the -y direction (see Fig. 1). The current in both MPQ halves corresponds to the bottom axis for the uncompensated experiment. For the compensated experiments, the top x-axis shows the current in the bottom half. Images show the unfocused (left) and focused (right) beam. The grid boxes are 1 mm by 1 mm. b) net beam deflection as a function of current with the same axes convention for uncompensated/compensated experiments as (a). Error bars denote one standard deviation of at least five measurements.

REFERENCES

[1] R. W. Hamm and M. E. Hamm, *Industrial Accelerators and Their Applications*. WORLD SCIENTIFIC, 2012.

[2] L. N. Hand and W. K. H. Panofsky, "Magnetic Quadrupole with Rectangular Aperture," *Review of Scientific Instruments*, 30, 10 (1959).

[3] J. Harrison *et al.*, "Fabrication process for thick-film micromachined multi-pole electromagnets," *Journal of Microelectromechanical Systems*, 23, 3 (2014).

[4] D. S. Black, K. J. Leedle, Y. Miao, U. Niedermayer, R. L. Byer, and O. Solgaard, "Laser-Driven Electron Lensing in Silicon Microstructures," *Phys. Rev. Lett.*, 122, 10 (2019).

[5] K. Kabra, S. Li, F. Cropp, T. J. Lane, P. Musumeci, and D. Ratner, "Mapping photocathode quantum efficiency with ghost imaging," *Phys. Rev. Accel. Beams*, 23, 2 (2020).

CONTACT

*R. Candler, rcandler@ucla.edu

INCREASING ELECTRORHEOLOGICAL RESPONSE IN HYDRAULIC ACTUATORS VIA SCALABLE MICROPATTERNED ELECTRODES

Chastity M. Kelly[1], Ashkan Ghanavati[1], Peter G. Kelly[2], and Carol Livermore[1*]*
[1] Northeastern University, Boston, Massachusetts, USA
[2] Markforged, Inc., Watertown, Massachusetts, USA

ABSTRACT

The design, fabrication, and demonstration of an electrorheological valve that operates at reduced electric field are presented. An electrorheological liquid crystal flows between upper and lower electrodes. Applying an electric field aligns the liquid crystal with the field, increasing its apparent viscosity. Valves with conventional flat electrodes and patterned valves with 200 µm high protrusions on the electrodes are compared. The increase in apparent viscosity in patterned valves is about 2.5X greater than in valves with flat electrodes under the same average field. Patterned-electrode valves can potentially control hydraulic actuation of mechanically biomimetic soft robotic organs.

KEYWORDS

Electrorheological fluid, liquid crystal, ER valves, soft robotic

INTRODUCTION

Artificial organs that mimic the complex motions of human systems like the gut will speed the development of implantable and ingestible medical devices [1] by enabling initial testing in a mechanically biomimetic environment without the use of animal models. Although recent advances in soft robotic technology [2] have potential as organ system mimics [3], the size of the required pumps and fluid control valves limits the achievable actuation complexity, making it impractical to accurately mimic the intricate motion of human organ systems. To overcome this challenge, we propose a system of electrically-controlled microvalves based on electrorheological (ER) fluids (Fig. 1) that will be able to precisely control fluid flow from a central source to selectively actuate the small-scale hydraulic actuators, for example to mimic peristalsis. One challenge of such ER microvalves is the large electric field required to operate them, which necessitates some combination of narrow gaps (causing low flow rates) and high voltages. The present work focuses on the potential of a 3D electrode geometry and its resulting electric field concentrations to reduce the average electric fields required to operate the ER valve for future applications in soft robotic systems.

ER fluids display a change in apparent viscosity under the influence of an applied electric field. When integrated into a flow channel with a pair of top/bottom electrodes, these fluids can be used as a valving mechanism to turn flow off and on in hydraulic actuation systems. However, traditional heterogeneous ER fluids contain particles that limit their applicability in microscale systems due to sedimentation and clogging. Homogeneous liquid crystals (LCs) offer a potential solution. The liquid crystal 4-Cyano-4'-pentylbiphenyl (5CB) (Ambeed, Inc.) shows a strong ER response due to its rod-shaped molecules and positive dielectric anisotropy; its viscosity depends on the balance of torques acting on individual liquid crystal molecules [4]. When a strong electric field is applied perpendicular to the flow, the liquid crystals rotate to align with the field, increasing the apparent viscosity (Fig. 1). The use of liquid crystals in microvalves has been demonstrated in [5,6], but these studies used high fields of >1 kV/mm, with typical fields >2.5 kV/mm and some as high as 7 kV/mm [5]. To reduce the required field, the present valve features repeated protrusions on the electrode to locally concentrate electric field and increase applied electric torque. Together with 5CB's nonlinear electric field response, these enhancements can yield higher apparent viscosity at lower applied fields. The approach builds on [7], in which non-straight electrodes bounding the width of a channel concentrated fields to actuate heterogeneous, particulate-based ER fluids. The present work represents the first time that protrusions have enhanced ER fluid actuation in the height direction, where smaller gaps already enable lower voltages to create high fields, as well as the first use of a 3D-patterned electrode geometry in a non-clogging, homogeneous, liquid crystal ER system.

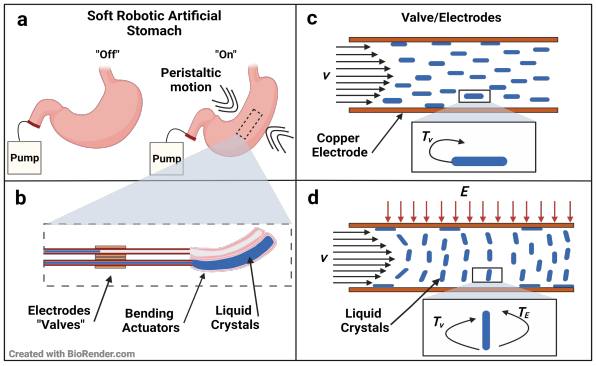

Figure 1: a) Diagram of soft robotic stomach with peristalsis; b) hydraulic actuator filling with LCs; c) fluidic torque aligns LCs with flow for low viscosity ("open" valve); d) electric field rotates LCs perpendicular to flow for high viscosity ("closed" valve).

EXPERIMENTAL

Copper electrodes/valves were 3D printed with a Markforged Metal X™ using a copper-based filament provided by Markforged, Inc., which is composed of copper powder and a polymer/wax binder. After printing, the wax is removed in a boiling Opteon SF-79 solvent bath, creating a semi-porous structure in the part that allows the remaining binder to be thermally debound in a sintering furnace. After sintering, the electrode is fully dense and only pure copper remains. Tape-cut polyimide sidewalls (142 µm, McMaster-Carr) complete the channels, set channel height together with any 3D patterning, and electrically insulate the electrodes. The patterned electrode features protrusions of approximately 200 µm height and 356 µm length separated by 356 µm spaces in the flow direction (Fig. 2). Each electrode plate also includes inlets, outlets, and holes for mechanical alignment pins that ensure correct registration of the two plates. The inter-electrode gap for the flat-electrode device is 426 µm based on the tape height. The effective gap between the electrodes for the patterned-electrode device reflects both its 284 µm tape thickness and the geometry of the 3D-printed protrusions and is confirmed through flow measurements.

The zero-voltage flow resistance and effective height of the patterned valve (with protrusions) are measured by connecting the patterned valve and the flat valve (without protrusions) in parallel to a syringe pump and weighing exiting flows with balances (Fig. 3a). The effective resistance of the patterned valve is calculated from the known resistances and measured flows. The effective

978-1-940470-04-7/HH2022/$25©2022TRF
DOI 10.31438/trf.hh2022.117

height of the patterned valve is determined using the Poiseuille equation for flow in a rectangular channel. Because the flow's utilization of the available channel volume depends on flow rate, the measurement is repeated at different flow rates (Fig. 3b). At low flow rates, the measured resistance and effective height depend less on flow rate. The effective height of the channel at nearly full channel utilization is 525 μm, within the experimental uncertainty of its 484 μm nominal height given nonidealities in the printed protrusions. The inter-electrode gap is taken to be 525 μm, and the effective height is interpolated to determine the zero-voltage resistance of the patterned valve at each flow rate.

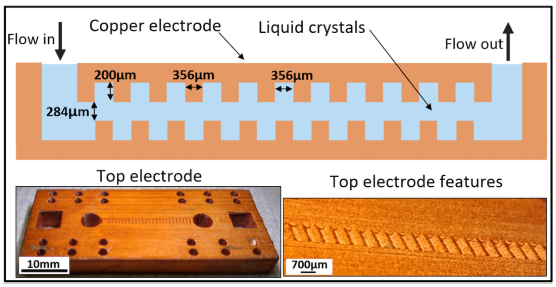

Figure 2: a) Schematic diagram of patterned electrodes; b) photograph of the top electrode; c) zoomed-in photograph of locally protrusions (fabricated as grooves) on the top electrode.

The patterned valve's effectiveness under applied electric fields from 0.2 kV/mm to 1.9 kV/mm is determined by monitoring exiting flow rates from the two parallel valves while applying the field across just the patterned valve (Fig. 3a). The flow circuit is analyzed to extract the patterned valve's resistance under electric field, and apparent viscosity is determined from measured resistance using the Poisseuille equation. The flat valve's effectiveness under electric field is determined similarly, by applying the field across the flat valve. The applied voltages are scaled by channel height to ensure equal electric fields.

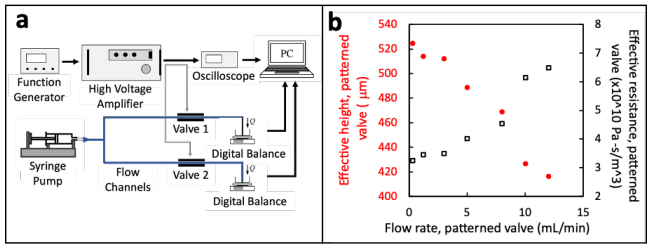

Figure 3: a) Diagram of experiment; b) Effective height (red) and resistance (black) vs. patterned valve flow rate.

RESULTS AND DISCUSSION

Fig. 4 plots the apparent viscosity vs. applied electric field for the patterned and flat valves for flow rates of 0.6 mL/min and 1.2 mL/min. The apparent viscosity of the patterned valve saturates at a field of less than 0.6 kV/mm, comparing favorably with the typically >2.5 kV/mm used in prior work [5,6]. The saturation value of apparent viscosity in the patterned valve is approximately 0.10 Pa-s, equal to 4.3X the liquid crystal's zero-field viscosity of 0.0234 Pa-s and similar to [4]. In contrast, the flat valve's maximum apparent viscosity is 0.060 Pa-s, just 2.6X the zero-field viscosity. Furthermore, the flat valve's maximum apparent viscosity is first observed at an electric field of 1.9 kV/mm, more than 3X greater than the saturation field of the patterned valve, and even then the flat valve's viscosity shows no evidence of saturation. Above 0.5 kV/mm, the valve with the 3D-patterned electrode yields on average 2.5X larger apparent viscosity than in the valve with the flat electrode; the difference is attributed to electric field concentrations at the corners of the protrusions and the nonlinear ER response of 5CB to electric field.

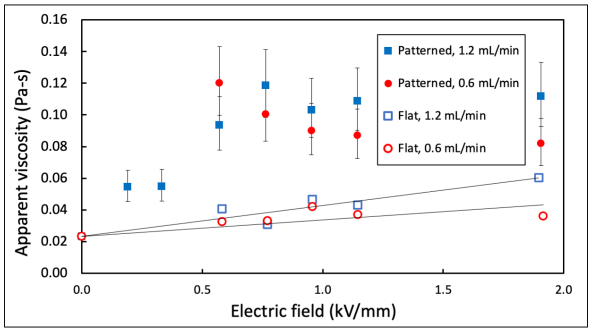

Figure 4: Apparent viscosity vs. field for patterned and flat valves at 0.6 (red) and 1.2 mL/min (blue). Lines are guides to the eye.

The patterned valve's height is the primary source of experimental uncertainty. If its height were larger than measured, the results would overestimate the field in the patterned valve and underestimate its performance relative to the flat valve. On the other hand, if the height of the patterned valve were smaller, the results would overstate the performance of the patterned valve. The effects of a ±30 μm height variation are captured in the error bars for the patterned valve. These experimental results suggest that in the future, ER valves with field-concentrating, 3D-patterned electrodes can be suitable for providing compact, integrated control of soft robotic actuation of organ system mimics for the testing and development of new medical devices.

REFERENCES

[1] K. Kalantar-zadeh, N. Ha, J.Z. Ou, and K.J. Berean, "Ingestible Sensors", *ACS Sens.*, 2, 468−483 (2017).

[2] J. Walker, T. Zidek, C. Harbel, S. Yoon, F. Sterling Strickland, S. Kumar, and M. Shin, "Soft Robotics: A Review of Recent Developments of Pneumatic Soft Actuators", *Actuators*, 9, 3 (2020).

[3] Y. Dang, Y. Liu, R. Hashem, D. Bhattacharya, J. Allen, M. Stommel, L.K. Cheng, and W. Xu, *Soft Robot.*, 3, 273-283 (2021).

[4] K. Negita, "Electrorheological effect in the nematic phase of 4-n-pentyl-48-cyanobiphenyl", *J. Chem. Phys.*, 105, 7837 (1996).

[5] T. Miyoshi, K. Yoshida, J. Kim, S.I. Eom, and S. Yokota, "An MEMS-based multiple electro-rheological bending actuator system with an alternating pressure source", *Sensors and Actuators A*, 245, 68–75 (2016).

[6] M. De Volder, K. Yoshida, S. Yokota, and D. Reynaerts, "The use of liquid crystals as electrorheological fluids in microsystems: model and measurements", *J. Micromech. Microeng.*, 16, 612 (2006).

[7] X. Huo and G. Yossifon, "Significant enhancement of the electrorheological effect by non-straight electrode geometry", *Soft Matter*, 15, 6455 (2019).

CONTACT

*C. Livermore, tel: +1-617-373-4922; c.livermore@neu.edu

AUTOMOTIVE MEMS ACCELEROMETER DESIGN VERIFICATION USING NONLINEAR COMPACT MODELING

Shaikh MD R. Tousif[1]*, Brian Van Dyk*[2]*, Aaron Geisberger*[1]
[1]NXP Semiconductors Inc., Chandler, Arizona, USA
[2]Coventor, Inc., A Lam Research Company, Fremont, California, USA

ABSTRACT

A design methodology for the verification of an automotive high-g MEMS capacitive accelerometer using a non-linear compact model in *CoventorMP® MEMS+®* is reported. The design vehicle is a lateral accelerometer surrounded by a flexible stop frame from NXP Semiconductor Inc. The coupled multi-physics compact model accurately predicts the transient, dynamic response of the system to shock stimuli within practical simulation times enabling more efficient design iterations to reduce dynamic contact forces, therefore improving device reliability. By employing compact models to represent the transducer and flexible lateral overload stoppers, this methodology enables comprehensive design exploration that is intractable with standard Finite Element (FE) approaches.

KEYWORDS

Dynamic modeling, flexible contact modeling

INTRODUCTION

Standard FE models, especially those that incorporate multiple physical domains, consist of detailed representations with large numbers of degrees of freedom (DoF) to achieve a high level of confidence in the accuracy of the models. Accordingly, a common practice in the MEMS industry is to rely on Reduced Order Models (ROMs) to decrease the number of DoF to accelerate design decisions by reducing the time required to perform simulations. Although several approaches [1] include some mechanical nonlinearities [2,3], these ROMs often neglect nonlinear characteristics critical for MEMS inertial sensor design, including electrostatic spring softening effects associated with electromechanical coupling or contact forces.

The methodology presented here employs a nonlinear compact model which allows for the accuracy inherent to a detailed standard FE model but with a significant reduction in the number of DoF by taking advantage of specialized MEMS+® components [4,5]. Compact modeling is a common technique employed by circuit engineers to generate models that are sufficiently simple to be incorporated and tractable in simulation environments but are also sufficiently accurate to render the outcome of the simulators useful to engineers [6]. The use of compact models which incorporate all coupled multi-physical nonlinearities essential to the design of the accelerometer and surrounding frame, including electrostatic softening and contact, enable capturing the complete system behavior without the uncertainty associated with generating ROMs or the intractable simulation requirements of a detailed FEM approach.

MODELING

The capacitive accelerometer is shown in Fig. 1. The flexible model is built using nonlinear Timoshenko and Bernoulli beam components available in the MEMS+® library and captures all relevant mechanical nonlinearities in the springs and proof-mass. The gap-closing sense and self-test electrodes are capable of modeling sense capacitance change, contact and squeeze-film damping. The surrounding frame acts as a flexible motion stop and is included in the design, as illustrated in Fig. 2. The ability to model transducer and enclosure interaction enabled by the compact modeling approach of MEMS+® represents a critical engineering requirement for MEMS designers.

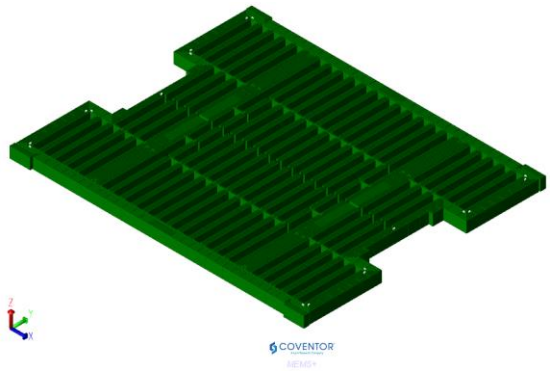

Figure 1: Lateral accelerometer and flexible stop frame design from NXP modeled in MEMS+®

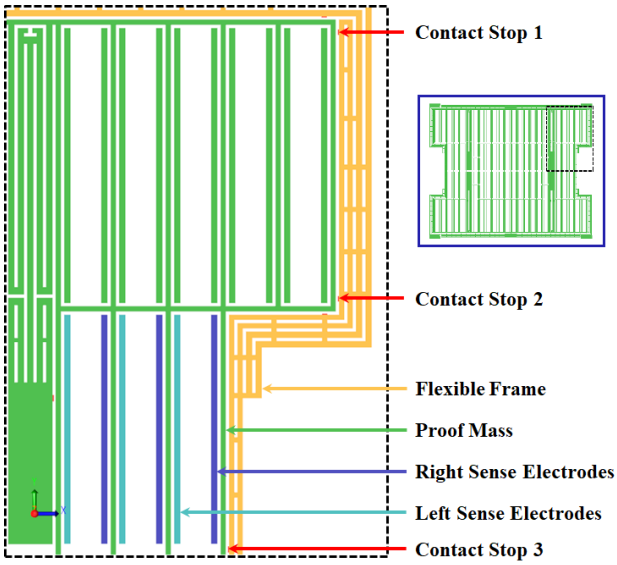

Figure 2: Zoomed view of accelerometer and stop frame, highlighted by functional group

SIMULATION RESULTS

A parametric study varying both Critical Dimension (CD) affecting the width of the spring elements to model etch loss and proof-mass thickness shows good correlation with measured capacitance data for static low and high bias conditions. In addition, the dynamic behavior of the device was well predicted by the compact modeling approach of MEMS+®. Transient analyses computing the response of the accelerometer and surrounding stop frame are practical, requiring on the order of a few minutes for each simulation. Dynamic impact forces on the flexible stops resulting from sinusoidal shock signals of peak magnitudes $25e^3$ g's, $50e^3$ g's and $75e^3$ g's are extracted, as depicted in Fig. 3.

978-1-940470-04-7/HH2022/$25©2022TRF
DOI 10.31438/trf.hh2022.118

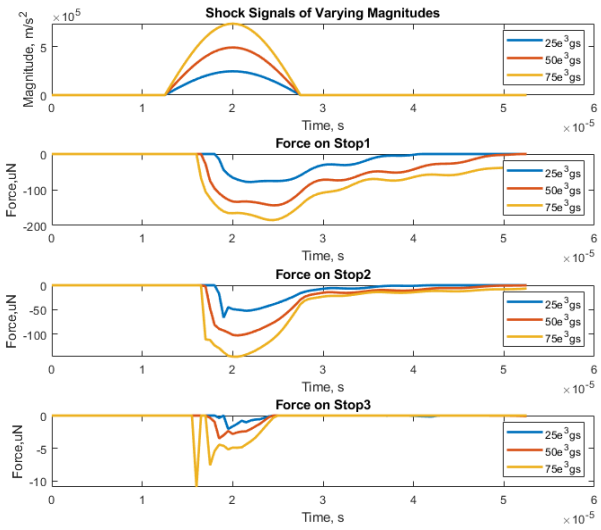

Figure 3: Impact force on the stoppers for $25e^3$ g's, $50e^3$ g's and $75e^3$ g's shocks

Furthermore, the model is easily transferred to CoventorWare®, the complementary standard FE solver within the CoventorMP® suite. Using CoventorWare®, a static stress analysis subjecting the frame to the maximum contact force extracted from the transient shock simulations indicated slight displacement of the frame with no risk of failure, Fig. 4.

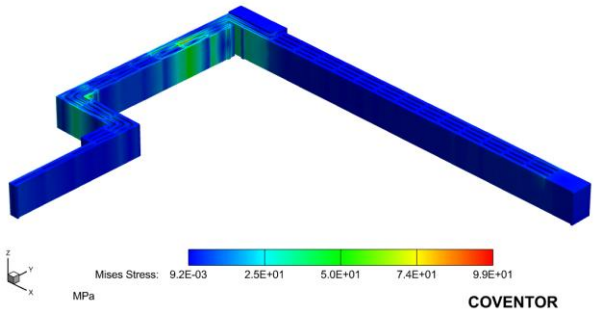

Figure 4: CoventorWare® result showing maximum stress on the frame for $75e^3$ g's is within yield strength of silicon

REFERENCES

[1] L. Feng, P. Benner, J. Korvik, "System-Level Modeling of MEMS by Means of Model Order Reduction (Mathematical Approximation) – Mathematical Background", in System-level Modeling of MEMS, WILEY-VCH Verlag GmbH & Co. KGaA, 2013, pp. 53-93.

[2] M. Dorwarth, S. Kehrberg, R. Maul, R. Eid, F. Lang, B. Schmidt and J. Mehner, "Nonlinear Model Order Reduction for high Q MEMS gyroscopes," in 11th International Mutli-Conference on Systems, Signals and Devices, 2014, pp. 1-4.

[3] T. Mähne, K. Kehr, A. Franke, J. Hauer and B. Schmidt, "Creating Virtual Prototypes of Complex Micro-Electro-Mechanical Transducers Using Reduced-Order Modeling and VHDL-AMS," in Proc. of the 8th International Forum on Specification and Design Languages, 2005.

[4] A. Parent, A. Krust, G. Lorenz, I. Favorskiy and T. Piirainen, "Efficient nonlinear Simulink models of MEMS gyroscopes generated with a novel model order reduction method", IEEE Proceedings, June 2015.

[5] 5. G. Lorenz and G. Schröpfer, "3D Parametric-Library-Based MEMS/IC Design," in System-level Modeling of MEMS, WILEY-VCH Verlag GmbH & Co.KGaA, 2013, pp. 407-424.

[6] Gennady Gildenblat (Editor). *Compact Modeling: Principles, Techniques and Applications.* Springer, 2010.

EXPLORE MEMS SWITCH FOR HIGH POWER AC/DC APPLICATIONS

Xu Zhu, Jim Terazawa, Chris Nassar, Michael Comstock and Chris F. Keimel
Menlo Microsystems Inc., Irvine, CA, USA

ABSTRACT

In this work, MEMS switch technology for high power AC/DC application is demonstrated for the first time. To achieve high current handling capability, a 3D hybrid integration architecture is adopted to guarantee the uniform current distribution across the massive switch array. The test results demonstrate the switch on state resistance is comparable to traditional relay and the switch itself is capable of handling 10A current with reasonable temperature rise inside the device.

KEYWORDS

AC/DC switch, distributed design, 3D hybrid integration.

INTRODUCTION

Over past decades, MEMS ohmic contact switch technology has been transferred from academic research to commercialized products[1,2]. Majority effort has been focused on RF and Microwave applications[3]. In this work, a MEMS switch array device for high power AC/DC application is demonstrated for the first time.

Bulky mechanical relays are widely used in power systems for control. Semiconductor devices require a large die to achieve low "ON" resistance comparable to mechanical relay. Tiny MEMS switch inheriting the merit of metal ohmic contact presents a new solution. To achieve at least 10A operation current and to minimize the power loss of the switch device itself through heat generation, an array of MEMS switches in parallel is the obvious approach. Due to material conductivity limitations of both mechanical structures and contacts, a couple hundred switch elements are needed. Although this takes the total contact resistance down to the single digit milliohms of a traditional bulky mechanical relay, it brings a challenge of connecting all switches together while keeping the similar total resistance under the constraint of a typical wafer process with achievable interconnection thickness and width. The heat dissipation is in the range of Watt; therefore, the thermal rise during the operation must be considered in the design phase.

DESIGN OF CHIP AND MODULE

To address aforementioned challenges, a distributed switch design with hybrid integration scheme is explored. Leveraging Through-Glass-Via (TGV) technology[4,5], arrays of highly electrically and thermally conductive Cu vias are placed adjacent to MEMS switch elements as shown in Figure 1(a) and (b). The short and wide connection from TGVs to MEMS switches cuts on-chip interconnect resistance to negligible level. All these TGVs will be connected together outside the chip, *e.g.* inside the product module or on a PCB where the metal thickness could be ~10× more than of a wafer process. Moreover, the positive and negative terminals can connect to different conducting planes of a multi-layer substrate, resulting in low electrical resistance and an effective thermal dissipation path, as an example in Figure 2.

Figure 1 (a) shows the top view of a 5×5mm hermetically sealed switch device. There are 440 switches inside the sealed cavity. These switches adopt the classical MEMS cantilever structure as in Figure 3: a big movable actuation electrode attaching to two cantilever beams, and two contact bumps at the end of the plate. The fixed electrode sits on wafer surface with a gap to top electrode around 1.1μm. The target actuation voltage is ~50V. Two MEMS switches are placed in series back-to-back with shared anchors. The purpose of this design is to achieve better off-state isolation. One implementation of the power switch is to have MEMS switches placed column by column such that the current comes into device from "+" TGV terminals, passes through switches horizontally and flows out through the "-" TGV terminals. To reduce the wafer probing complexity, TGVs in each column can be tight together on the device top surface forming "+" and "-" bar. Multiple solder ball arrays will be placed on these bars to maintain parallel electrical and thermal conducting path from switches under the cap wafer to the external substrate as shown in Figure 2.

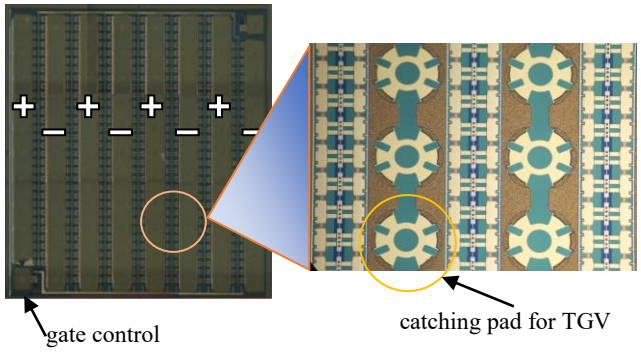

Figure 1. MEMS power switch die.
(a) Top view full hermetic sealed 5×5mm die.
(b) Zoom view onto the underlying device wafer.

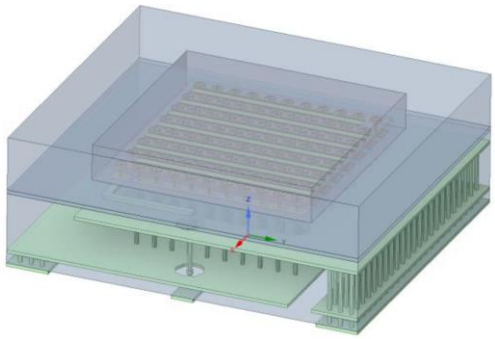

Figure 2. Prototype package design to be implemented in 4 layers laminate whereas layer 2 and 3 will be dedicated to the positive and negative electrode exclusively. The external positive and negative terminals are formed on the bottom of the module.

With such a design architecture, the total resistance of the device can be approximated using the formula below. The factor 4 related to resistance contribution from TVG are due to two factors: (1) a pair of TGV is required to form current conducting path into and out of the chip as in Figure 1Figure 3(a); (2) each TVG functions input/output post for MEMS switches on both of its sides, as show in Figure 1 (b). Trace resistance contribution can be neglected. More accurate number can be obtained from commercial FEM software.

$$R_{total} = R_{TGV}/num_of_TVG \times 4 + R_{contact}/num_of_beams$$

978-1-940470-04-7/HH2022/$25©2022TRF
DOI 10.31438/trf.hh2022.119

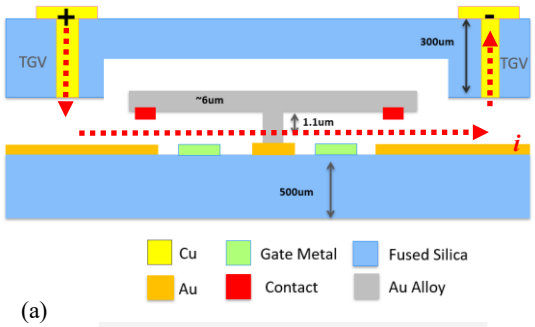

(a)

(b)

Figure 3. Illustration of device structure and current flow into and out of the encapsulated MEMS switch. Red dash line indicates the current flow path.

(a) Cross section of metal MEMS switch which will be sealed by a cap wafer

(b) Perspective view of single cantilever switch element.

Characterization Setup and Test Results

The device characterization is conducted on a 200mm hermetic, bonded wafer on a Cascade Elite 300 wafer probe station, Figure 4. A Keithley 2651A, capable of sourcing 20A current DC and 50A pulse, captures device resistance at different input current levels. An IR camera from Optris is used to record device temperature. The probe card is designed with 4-pt Kelvin capability to measure resistance of adjacent pairs of columns and multiple force probes per column. Contact resistance ~20mOhm and property on/off switch have been achieved throughout majority of test sites on the first wafer lot. This demonstrates the design with more than 400 switch elements per device are practical in the commercial foundry.

(a)

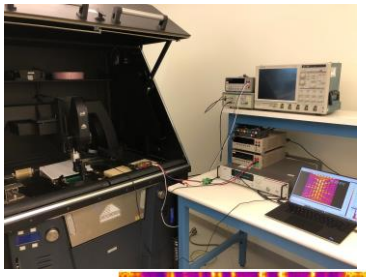

(b)

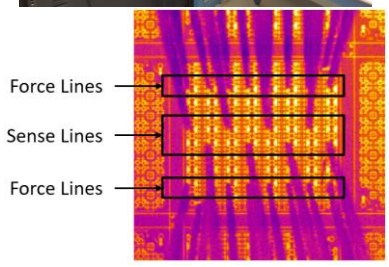

Figure 4. High Power MEMS switch characterization setup.

(a) Cascade wafer probe system with IR camera monitoring the device temperature.

(b) Probe card design with multiple 4-pt Kelvin to achieve evenly current distribution.

In high current tests, all probes in the probe card are configures as +/- force lines; the Keithley's output is ramped from 0A to 10A then back to 0A. Up to 14A was evaluated. By post postprocessing, the temperature measured by the IR camera are categorized as three regions: tungsten probe needles which touching down vertical bars, the vertical bar (RDL) and glass where underneath are switch elements. The hottest spot on the glass surface is ~124°C at 10A and average surface temperature is ~80°C as in Figure 5.

The resistance remains stable value over the range of testing current as in Figure 6 whereases semiconductor switch contact resistance typically doubles or triples its value.

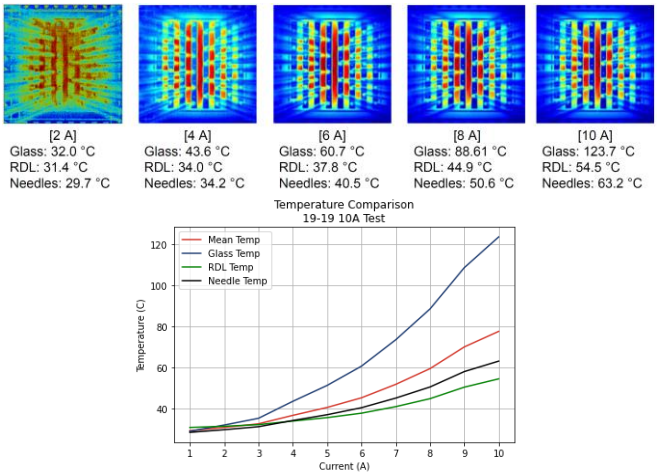

Figure 5. IR image of the switch under 2-10A test current. Three temperate readings are reported: hottest point on transparent glass regions, on metal bar (RDL) strips and the probe needles. IR camera temperature range is set to auto scale therefore the color map.

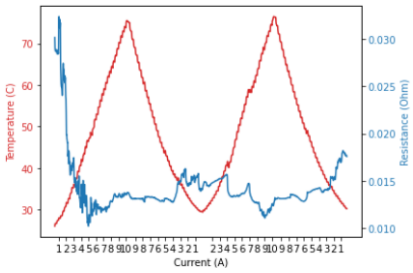

Figure 6. The contact remains stable when current ramp between 1A to 10A. The contact resistance drop during the initial ramp is caused by the self-heating therefore self-probe tip cleaning.

ACKNOWLEGE

Special thanks to Matt Strohmayer and Max de Feijter for their help on device characterization and preparation for testing.

REFERENCES

[1] https://www.analog.com/en/product-category/mems-switches.html.

[2] https://menlomicro.com/products/rf

[3] G. M. Rebeize, "RF MEMS Theory, Design and Technology", *Weiley 2003*.

[4] US patent 11,171,094

[5] US patent 11,148,935

CONTACT

*Xu Zhu, tel: +1-412-606-1937; xu.zhu@menlomicro.com

HYDROGEN GETTERS FOR MICROELECTRONICS PACKAGING RELIABILITY IMPROVEMENT

Hua Xia[*], *Jeffrey Vriens, and David DeWire*
Hermetic Solutions Group LLC, Trevose, PA 19053, USA

ABSTRACT

The microstructures and hydrogen absorption responses from accumulative roll milled (ARM) Pd foils are studied with x-ray diffraction, manometry, and residual gas analysis measurements for the design and fabrication of a passive hydrogen getter that can be embedded into an electronic sensing device for effectively scavenging outgassed hydrogen gas from package materials. The engineered ARM Pd foil has demonstrated its hydrogen sorption capacity from 5% to 10% with a sorption rate of 40 to 5 ppm/min, which are about 2 to 3 orders higher than conventional outgassing rates of glass, polymer, epoxy, ceramic, and metallic package materials.

KEYWORDS

Hydrogen outgassing, nanocrystalline microstructures, hydrogen getter, sensing device reliability.

INTRODUCTION

Most of hermetically sealed electronic sensing devices and actuators are sensitive to outgassed H_2, O_2, H_2O, CO_2, CH_4, HCs and VOCs that are often a primary factor leading to performance drift in frequency, amplitude, and reliability [1]. For example, an inertial angular rate measurement based Coriolis vibratory gyroscope sensor may suffers vacuum instability due to the outgassing from its components because such a sensor contains various potential outgassing materials like quartz glass as a sensing element, Kovar alloy for housing, glass to metal pins for electrical contacts, and Indium solder for bonding. The outgassed hydroxyl (OH) may be a source moisture or corrosion. Another example is associated with Lithium-ion batteries storage systems, specifically in electrical drive vehicles, that the outgassing of toxic chemical vapors such as hydrogen fluoride, hydrogen sulfides, and carbon dioxide is potential hazardous. One exception is polyethylene film based MEMS nuclear radiation sensor or dosimeter that is based on the radiation induced H_2 outgas driven membrane deflection [2].

Since any hermetically sealed packages are an integration of glass, polymer, epoxy, ceramics and metallic materials, the entrapped gasses could be released from these materials into the package, especially under elevated operating temperature. For example, a polymer/epoxy dominated package may outgas 10% (100,000 ppmv) hydrogen gas during its 20 year operating lifetime. For most electronic sensing devices, hydrogen outgas is especially regarded as undesirable contaminant [3] that may cause sensing device erosion [4], despite of limited use as sensing mechanism in nuclear radiation sensor. It is recognized that a mitigation method by implementing a pre-bake out process before package sealing could eliminate some of "early infant mortality" type failures. However, it is also recognized that a installing a passive hydrogen getter element inside an electronic sensing device could effectively control outgassing quantity and improve sensing device reliability.

Palladium (Pd) has high solubility for hydrogen in the bulk. When Pd is exposed to molecular hydrogen, is dissociated into atomic hydrogen, which is characterized by a high dissociation rate. Because hydrogen atoms diffuse easily through a Pd, the metal is rapidly converted into palladium-hydride. The bulk Pd material has nominal particle sizes from a few microns to a few ten microns. The hydrides PdH(x) form after H atoms are diffused into Pd face-centered cubic lattice structure. At α-phase of PdH($x \leq 0.02$) the Pd lattice expands slightly, from 388.9 pm to 389.5 pm. β-phase appears when $x>0.02$, with a lattice constant of 402.5 pm. Both phases coexist until a composition of PdH($x \leq 0.58$) when the α-phase disappears.

Most hydrogen sensors have typically used nanoscale Pd film as a sensing material for hydrogen gas detection, but the maximum concentration is usually limited to ~5% (50,000 ppmv) due to undesirable H_2 induced embrittlement and slowed response rate [5]. The increased hydride formation not only causes highly elastic strains in the film but also reduces bulk Pd material's ductility and mechanical strength. While using Pd as H_2 gettering material it is desirable to have more than 10% (100,000 ppmv) H_2 sorption capacity while maintaining desirable mechanical ductility and strength. To enable conventional bulk Pd material as a desirable gettering material with high sorption capacity, a nano-crystallite-rich Pd foil microstructural material is developed by a so-called accumulative mill rolling process to effectively enhance not only sorption capacity but also mitigate mechanical deterioration.

EXPERIMENTS AND RESUTLS

Initial bulk Pd sheet material is processed by accumulative mill rolling process that can reduce initial ¼" thickness as a foil with a thickness ranging from 50μm to 150μm by compressional mechanical pressure. Meanwhile, the microstructures of the bulk Pd material has been modified by increased nano-scaled grains. As shown in Fig.1 that the Pd foil has its dominated diffraction peaks by Pd (111), Pd (200), Pd (220) and P (311), observed by x-ray diffraction measurement taken from a typical accumulative processed 100μm-thick foil sample. Meanwhile, nano-crystallite formation of Pd grains has been demonstrated by broadening peak around $2\theta \approx 46^o$, as indicated by dashed red curve. By calculating integrated area ratio from the broadening area and full integrated area from x-ray diffraction pattern, the estimate volume ratio of nano-crystallites is close to about 30%. If this broadened background is only due to particle sizes reduced by the AMR process, the estimated particle sizes are 20~30 nm.

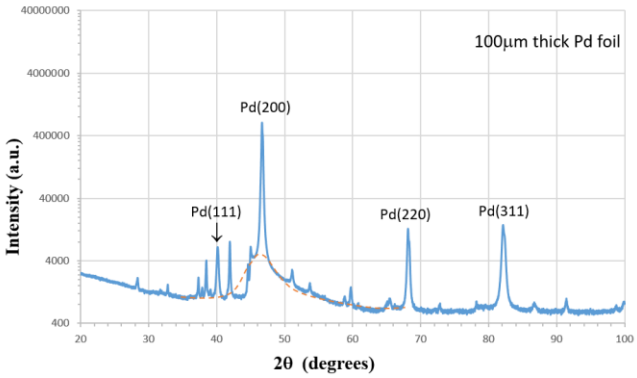

Figure 1: X-ray diffraction patterns of Pd foil sample where the diffraction peaks and the small peaks may imply multi-phase microstructures. The broadened peak around Pd (200) has been attributed to the formation of the nanocrystalline microstructures.

978-1-940470-04-7/HH2022/$25©2022TRF
DOI 10.31438/trf.hh2022.120

The sorption responses of the ARM Pd foil material to hydrogen gas absorption have been characterized by a combined manometric measurement by observing testing chamber hydrogen gas absorption induced pressure variation and residual gas analysis (RGA). Figure 2 has shown a manometry measurement from a typical 1" squared Pd foil with thickness of 0.004" (100μm) that gives the dynamic pressure response amplitude as a function of time, where the testing chamber temperature is also monitored simultaneously. To know exact how much H_2 gas is absorbed by the Pd foil, the gas composition in the testing chamber is taken out and analyzed by a mass spectroscopic instrument for residual gas analysis (RGA).

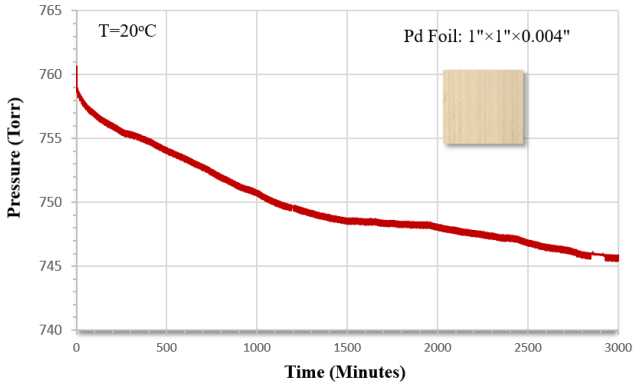

Figure 2: Manometry measured pressure amplitude variation in a 1-liter testing chamber from a typical foil sample.

As a hydrogen getter it is desirable to high sorption capacity, which is determined by the maximum hydride formation PdH(x). For ARM processed Pd foil its sorption capacity is also dependent upon the sizes and thickness of the foil. Figure 3 is a typical H_2 gas sorption response as a function of time, which has demonstrated 2.3 torr-liter/cm^2 sorption capacity within 3000 min (50h) and 1.71% (17,100 ppmv) hydrogen gas has been absorbed by the Pd foil. Theoretically, this Pd foil could absorb about 5.6% (56,000 ppmv) hydrogen. For most of electronic sensing devices and packages, the predicted outgassed hydrogen is normally between 1% and 3% during 20 year's operation. On the other hand, a 0.006"-thick AMR Pd foil could have its maximum H_2 uptake capacity up to 10% (100,000 ppmv), which could be used for high outgassing polymer or epoxy material dominated electronic sensing devices and packages. Hydrogen sorption rate is another critic response parameter for any getters to be used as an effective

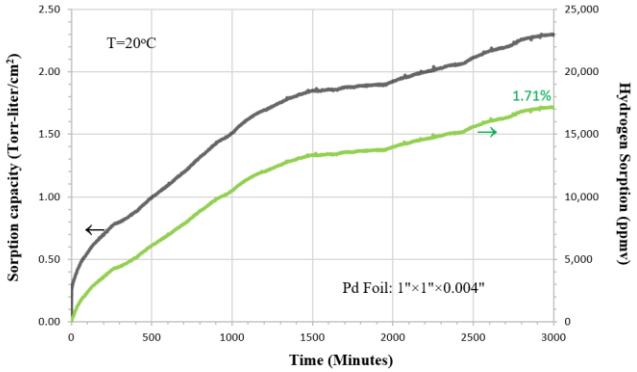

Figure 3: Measured H_2 absorption capacity (black curve) and actually hydrogen sorption quantity (green curve) from a typical 0.004" (100μm)-thick 1" squared Pd foil during 3000min (50h) measurements under 760 torr/20°C STP conditions.

absorber to remove outgassed H_2 from any sensing devices. Figure 4 shows that the observed H_2 sorption rate can change from initial ~40 ppm/min down to ~5 ppm/min, which is 2 to 3 orders quicker than outgassing rates of most polymer and epoxy materials.

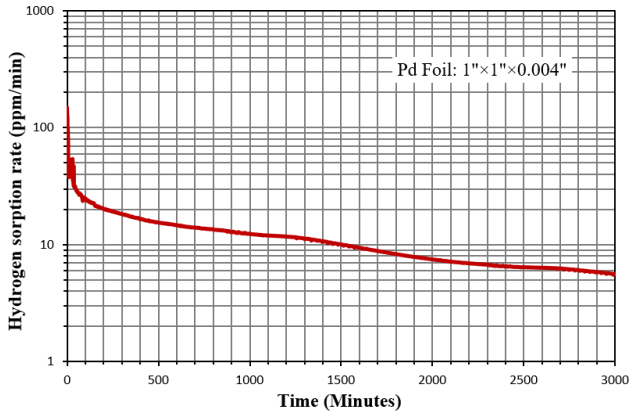

Figure 4: Measured H_2 absorption rate from a typical 0.004" (100μm)-thick Pd foil, from manometry and RGA measurements.

For practical sensing device application, a Pd foil could be cut in any kind of form factor even down to 50μ×50μm size for a space constrained sensing device. Besides, these H_2 getters can be installed in sensing devices either by heat spot welding or by using NASA specified low-outgassing adhesive materials, which have been tested based on MIL-STD-883 standard. It is concluded that the accumulative mill rolling process could be a practical engineering solution for enabling a conventional bulk Pd metal material as a desirable passive H_2 getter for scavenging outgassed H_2 from any electronic sensing devices and packages for ensuring operating reliability during its 10-20 years lifetime.

ACKNOWLEDGEMENTS

We appreciate Y. Maswadeh at EAG Laboratories for the material analyses, J. T. Rossiter and D. Rossiter at Oneida Research Service for their RGA testing services.

REFERENCES

[1] D. Ragle and S. Kayali, "Hydrogen effects on GaAs microwave semiconductors", Final Report on *IEEE 1997 GaAs Reliability Workshop Proceedings*.

[2] D. Kumar, J. Philippe, S. Charlot, S. Assié, A. Lecestre, A. Ferrand, H. Aubert, and P. Pons, "Polyethylene Outgassing Study for MEMS Nuclear Radiation Sensor", *Eurosensors Conference*, *Proceedings* **2018**, *2*(13), 718 (2018).

[3] D. Gortat, M. Sparkes, S. Fairchild, P. Murray, M. Cahay, T. Back, G. Gruen, N. Lockwood, W. O'Neill, "Laser stimulated grain growth in 304 stainless steel anodes for reduced hydrogen outgassing", Proc. SPIE. 10083, Fiber Lasers XIV: Technology and Systems 2017.

[4] I. Darmadi, F. Anggoro, A. Nugroho, and C. Landhammer, "High-performance nanostructured Palladium-based hydrogen sensors current limitations and strategies for their mitigation", *ACS Sensors*, 5, 3306 (2020).

[5] Z. Zhao, M. A. Carpenter, D. Welch, H. Xia, "All-optical hydrogen sensor based on a high alloy content Palladium thin film", *Sensors and Actuators B*, 113, 532 (2006).

CONTACT

*Hua Xia, tel: +1-509-881-5420; hxia@hermeticsolutions.com

Author Index

Scroll to the title and select a **Blue** link to open a paper. After viewing the paper, use the bookmarks to the left to return to the beginning of the Author Index.

A

Abdolvand, Reza 199, 222, 368
Acosta, Victor 107
Agrawal, Anant 296
Ahmed, Sumnoon 415
Akhkandi, Parvin 199
Aksyuk, Vladimir A. 35
Alban, Eduardo 199
Allen, Mark G. 310
Alsaedi, Mossab K. 158
Alter, Anne L. 187
Alves, Filipe S. 391
Amnache, Amrid 258
Ansari, Azadeh 56, 340, 356
Archdeacon, Michael T. 5
Arif, Annatoma 440
Asci, Cihan 96
Ashraf, Huma 395
Ashton, Randolph 262
Assylbekova, Meruyert 48
Ayazi, Farrokh 75, 348, 395

B

Bahl, Gaurav 108
Baksh, Aliyah 146, 262, 438
Balog, Nicole 154
Baltazar, Francisco 272
Banerjee, Aishwaryadev 13
Banna, G M Hasan Ul 436
Barahona, Jeffrey 292
Barekatain, Matin 43, 226
Baskota, Anuj 364
Beardslee, Luke A. 81, 100, 165, 286
Bedair, Sarah S. 191
Benedict, Romilly 436
Bentley, William E. 332

Bergbreiter, Sarah 23, 110
Berthiaume, Francois 122
Blauvelt, David 272
Bogie, Kath M. 250
Bolton, Chris 395
Borbash, Vivian 286
Bosak, Alexander 262
Botasini, Santiago 81
Bousse, Nicholas E. 108, 187
Bowman, Emily 304
Brand, Oliver 165, 387
Brown, Devin K. 387
Browne, Caroline A. 431
Bruno, Dylan 191
Bulbul, Ashrafuzzaman 13, 138

C

Cabral, Jorge 391
Campbell, Rebecca 134, 266
Candler, Robert 450
Carlton, Brent 199
Carpenter, Joanne 395
Carr, William N. 280
Carter, Gavin 292
Cepeda-Torres, Omar S. 146
Chand, Rakesh 210
Chang, Chin-Yu 344
Chapin, Ashley A. 270
Chauhan, Tanya 348
Chavez, Bertha J. 440
Chen, Chen-Yu 332
Chen, Shangyi 67
Chen, Yung-Hsiang 210
Cheng, Junce 242
Cheng, Xuanbing 274
Cheng, Yu-Ting 434
Cheung, Samantha 427
Childs, Andre 438
Cho, Joon Hyong 379
Cho, Sung Kwon 206
Choi, Gihoon 130
Choi, Jun H. 383

Choi, Seokheun 85, 118, 282, 288, 419
Choi, Suk-il 442
Chong Rodriguez, Alicia 21
Chong, Hao 250
Choudhary, Chandrashekhar 5
Chui, Benjamin 272
Colombo, Luca 48, 376
Colton, Adira 27, 161, 254
Comstock, Michael 456
Conrad, Luca 179
Cornils, Lasse 179
Coskun, M. Bulut 63
Crisp, Sophie 450
Cui, Jiarui 9
Cui, Tianhong 360
Cullinan, Michael A. 379

D

da Encarnação, João T. 391
Dabas, Shaurya 175, 446
Dalpati, Rana 13
Das, Riddha 158, 431
Davaji, Benyamin 31, 183, 364
Davidson, Edwin 438
Del-Rio-Ruiz, Ruben 96
DeRoo, David 17
DeWire, David 458
Dhagat, Pallavi 39
Dias, Rosana A. 391
Diaz-Alonso, Daniela 318
Díaz-Marín, Carlos D. 427
Dickie, Matthew 63
Didier, Charles M. 146, 262, 403, 438
Doerschuk, Peter 183, 364
Domic, Michael 415
Dorsey, Kristen L. 411
Downey, Brian P. 39

E

El-Gamal, Mourad N. 214
Elhadad, Anwar 282, 419
Elhawash, Abdelrahman M. 391

Elsayed, Mohannad Y. 214
Emaminejad, Sam 274

F

Field, Leslie 47
Figueroa, Jose L. 195
Forman, Jack 411
Forman, Sarah 274
Fox, David 262
Fréchette, Luc G. 258
Freitas Orrico, Julia 146, 262
Frez, Cliff 63
Fuge, Mark D. 332
Fuller, Sawyer B. 79
Funderburg, Nicholas 304
Furness, John B. 114

G

Gabrielle, Janelle 304
Gajula, Durga 387
Galanko Klemash, Mary E. 191
Gao, Yang 288
Garcia-O'Donnell, Lucas 296
Garcia, Inês S. 391
Geisberger, Aaron 454
Gerach, Timo 179
Ghalichechian, Nima 67
Ghanam, Muhannad 179
Ghanavati, Ashkan 452
Ghodssi, Reza 81, 100, 270, 286
Gill, John 63
Giribaldi, Gabriel 48, 376
Gokhale, Vikrant J. 39
Goldschmidtboeing, Frank 179, 352
Gond-Charton, Paul 258
Gong, Yan 173
Gopalakrishnan, Sarath 320, 372
Gopinath, Ashwin 427
Gorman, Jason J. 379
Gratuze, Mathieu 278
Guan, Weihua 150, 9
Gund, Ved 71, 183, 364

H

Hager, Eiko, ... 179
Hakim, Faysal 52
Hall, Harris J. 195
Hammer, Daniel X. 296
Han, Jiho 442
Han, Jinjing 270
Haniff, Tariq 272
Hao, Zhijian 340
Hardin, Michael P. 75, 395
Hart, Cacie 234
Hasan, Rabiul 138
Hatasaka, Bryan 13
Heckman, Emily M. 195
Herberholz, Jens 270
Herr, Amy E. 126, 328
Higgins, Nicholas 272
Hlady, Vladimir 306
Ho, Tawen 270
Ho, Yens 210
Hong, Vu 108
Hormigo, Tiago 391
Hossain, Nafize I. 142
Hossain, Sheikh Dobir D. 284, 440
Hsu, Tzu-Hsuan 210
Hu, Tony Y. 93
Huang, Yan-Ming 210
Hudson, Trevor 89
Huusari, Timo 199
Hwang, Juneho 364
Hwang, Sunghyun 280, 442
Hyuck Ahn, Chae 108

I

Ishii, Hiroshi 411
Islam, Sayemul 415
Ivy, Landon 71, 183, 364
Iyer, Nisha 262

J

Jaklin, Jan 179
Jamali, Armin 352

Jander, Albrecht 39
Janowski, Miroslaw 27
Javanmard, Mehdi 122
Jeon, Saeyeong 442
Jeorge, Ninweh Nina 423
Ji, Mingyue 13
Jia, Ziqi 246, 442
Jiang, Jiaxin 5
Judy, Jack W. 246
Jung-Kubiak, Cecile 63

K

Kadian, Sachin 104, 238
Kanter, Joshua P. 332
Karkhanis, Mohit 13
Katzer, D. Scott 39
Keimel, Chris F. 456
Kelly, Chastity M. 452
Kelly, Peter G. 452
Kenny, Thomas W. 108, 187
Kerkes, Tristan 5
Kermani, Hamideh 222
Kessler, Marc 179
Khan, Shakir-ul Haque 13, 444
Kiebala, Tobias M. 191
Kilpatrick, Cameron 427
Kim, Albert 134, 266, 415
Kim, Dea Gyu 340
Kim, Eun Sok 43, 226, 230
Kim, Hanseup 13, 138, 306, 444
Kim, Jungkwun “JK” 134, 266, 415
Kim, Kyeongheon 13
Kim, Sukjun 23, 110
Knoerlein, Robert 352
Körner, Julia 448
Krieger, Axel 332
Krishnakumar, Akshay 314
Kshirsagar, Aneesh 9
Kubicek, Regan 23, 110
Kulkarni, Manjusha 304
Kumar, Suneel 122
Kundu, Avra 403

Kundu, Somnath 199
Kuo, Justin 31, 364
Kurd, Nasser 199

L

Lal, Amit 31, 71, 183, 364
Lam, Wilbur A. 387
Landers, Mya 419
Lee, Chih-Kuo 434
Lee, Hyowon 114
Lee, Jaehoon 43, 230
Lee, Jeong-Bong 383
Leong, Ethan 202
Levon, Kalle 324
Levy, Joshua A. 81, 100, 286
Li Sip, Yuen Yee 262
Li, Diane 427
Li, Ming-Huang 210
Li, Sheng-Shian 344
Li, Tao 5
Li, Wen 173, 436
Li, Wenbo 206
Li, Yuankai 266
Liang, Yajie 27
Light, Yooli K. 130
Lim, Jongcheon 114
Lin, Chia-Ying 5
Lin, Chih-Hung 434
Lin, Shuyu 274
Liu, Hai 226
Liu, Tianyi 9, 150
Liu, Tingyi Leo 242
Liu, Yang 126
Liu, Zhenming 75, 395
Liu, Zhuolin 296
Livermore, Carol 452
Lobaton, Edgar 292
Lodhi, Isha 387
Lohani, Bhushan 284
Lomeli, Gabriela 328
Lopez, Daniel 35
Lotfi, Ardalan 75, 395

Lucki, Irwin 431
Luo, Hao 199
Lust, Mark C. 67

M

Mack, Shawn 39
Majd, Yasaman 199, 222
Majerus, Steve J.A. 250
Maldonado, Jesus 122
Mangadu, Betty 130
Manrique Castro, Jorge 17, 146, 407
Mansoorzare, Hakhamanesh 368
Mass, Paige 332
Mastrangelo, Carlos 13, 138
Matthews, Justin 348
Mazzeo, Aaron 122
McCants, Carl E. 60
McComb, J. Gordon 89
McDaniel, Sean A. 195
Meagher, Robert J. 130
Meng, Ellis 89
Mercader, Anthony 206
Meyer, David J. 39
Mi, Zetian 356
Michetti, Giuseppe 218
Miller, James M.L. 108
Miller, Jr., Francis J. 292
Mishra, Rupesh Kumar 314
Mitra, Arkadeep 383
Mix, Jason 199
Mo, Dicheng 169, 175, 446
Monson, Kenneth L. 306
Moore, Michael J. 262
Moyer, Jarrett 272
Mural, Ravi V. 13
Musumeci, Pietro 450
Myers, David R. 387
Myong, Elliot 89

N

Nabki, Frédéric 278
Nassar, Chris 456

Nejati, Sina 104, 154, 320
Ng, Eldwin J. 108
Ngoh, Brian 296
Ni, Di 71, 183
Niroui, Farnaz 112
Noh, Seungbeom 13, 138, 306, 444

O

Ody, Alexander 450
Oishi, Peter 272
Olivieri, Laura 332
Ospina, Carlos 183, 364
Ouchen, Fahima 195
Owyeung, Rachel 96

P

Palumbo, Anthony 324
Park, Mingyo 56, 356
Park, Won Min 266
Pavlidis, Spyridon 292
Pelz, Uwe 179
Pena-Flores, Norma 270
Pereira, Jorge 438
Perez-Morelo, Diego J. 35
Pillai, Gayathri 344
Piranej, Selma 17
Pirro, Michele 48
Politza, Anthony J. 150
Pollard, Kevin 262
Populin, Luis C. 114
Poree, Lawrence 1
Pound, Benjamin A 450
Pradeep, Yelehanka 210
Prakash, Shaurya 304

R

Rafiee, Zahra 85, 118
Rahimi, Rahim 104, 154, 238, 314, 320, 372
Rahiminejad, Sofia 63
Rais-Zadeh, Mina 63
Rajaraman, Swaminathan 17, 146, 234, 262, 403, 407, 438
Rassay, Sushant 169, 175

Razaulla, Talha 161
Rezaei Nejad, Hojatollah 158
Rezaie, Maryam 85, 118
Richardson, Hayley 292
Riddell, Kevin 395
Rinaldi, Matteo 31, 48, 218, 376
Rivera, Ulisses Alberto Heredia 314
Roberts, Robert Chris C. 284, 440
Roberts, Sonia F. 411
Rodríguez, Jorge A. 318
Romming, Niklas 179
Rosenthal, Ian 296
Rosenzweig, James 450
Roussos, Jason A. 39
Roy, Akash 226
Roy, Anindya L. 423
Roy, Shuvo 272
Rudy, Ryan 191
Rustogi, Paritosh 246

S

Saberi, Mohammadreza 179
Sadeghian Esfahani, Kianoush 43
Sadeqi, Aydin 431
Sagi, H. Claude 5
Salaita, Khalid 17
Sankaralingam, Kanagasubbulakshmi 423
Santiago, Alanis I. 134, 415
Santra, Swadeshmukul 438
Sarker, Sunandita 27
Sartipi, Mina 34.1
Satterthwaite, Peter F. 112
Schnable, James C. 13
Scholten, Kee 89
Schwartz, Steven A. 165
Sedaghat, Sotoudeh 154
Selvamani, Vidhya 104, 238
Sengupta, Kaushik 122
Shah, Piyush J. 195
Shahraini, Sarah 199
Shamsian, Olya Noruz 118
Sharma, Atul 158

Shetty, Rishabh 427
Shevade, Abhijit 63
Shin, Seungyong 348
Shinde,Uttunga 179
Siegenthaler, James 436
Simeoni, Pietro 376
Simon, Terrence 360
Singh, Navpreet 214
Sium, Farhan Sadik 444
Smith, Rosemary 276
Sochol, Ryan D. 27, 161, 254, 296, 332
Sommerhage, Frank 17, 234
Song, Seung H. 415
Sonkusale, Sameer 96, 158, 399, 431
Soukup, Bernard Herrera 376
Starke, Thomas 284
Starman, LaVern 195
Stine, Justin M. 81, 270, 286
Stoeber, Boris 423
Straker, Michael A. 100, 286
Sumanasinghe, Sajana 423
Sumaria, Vedant 276, 300
Sundaram, Prashanth 304
Sureshkumar, Krithika 5

T

Tabassum, Shawana 142
Tabrizian, Roozbeh 52, 169, 175, 336, 446
Tadigadapa, Srinivas 276, 300
Tan, Jun Ying 134, 266
Tang, Yongkui 43, 226
Tang, Zifan 9
Terazawa, Jim 456
Tharpe, Troy 336, 446
Thorpe, Ryan 122
Toda, Risaku 63
Tope, Sayali 13
Torres, David 195
Tousif, Shaikh Md Rubayiat 454
Tran, Steven 138
Tsai, Hsiao-En 434
Tseng, Victor Farm-Guoo 191

V

Vaartstra, Geoffrey 427
Van Dyk, Brian 454
Velez, Camilo 202
Vidana Morales, Ruth 199
Vriens, Jeffery 458
Vukasin, Gabrielle D. 187

W

Waimin, Jose 372
Walczak, Piotr 27
Walus, Konrad 423
Wanf, Liang-Kai 434
Wang, Ding 356
Wang, Evelyn N. 427
Wang, Hongjun 324
Wang, Jialin 356
Wang, Mingkang 35
Wang, Ping 356
Wang, Tony H. 340
Wang, Wei 399
Wang, Xuechun 89
Ward, Matthew P. 114
Warren, Roseanne 161
Wen, Haoran 348
Wen, Ziteng 27
Widmer, Giovanni 96
Woias, Peter 179, 352
Wood, Alex 395
Wu, Guan-Lin 210

X

Xia, Hua 458
Xiang, Liu 173
Xie, Pengfei 122
Xu, Kevin 383
Xu, Xin 27, 254, 332

Y

Yang, Eui-Hyeok 324
Yang, Yushi 108
Yoon, Yong-Kyu YK 246, 280, 442

Young, Olivia M. 161, 254, 332

Z

Zaeeri, Amin 314
Zang, Ling 13
Zareei, Amin 238
Zeng, Wenxin 399
Zhai, Lei 262
Zhang, Jiayuan 300
Zhang, Jingwen 310
Zhang, Tianyi 360
Zhang, Wei 436
Zhao, Chenguang 324
Zhao, Jianing 108
Zheng, Yue 56, 356
Zhou, Peng 360
Zhu, Chengjie 122
Zhu, Jialun 274
Zhu, Weikun 112
Zhu, Xu 456
Zorman, Christian A. 250

TRF – Hilton Head Memories

by Joseph M. Giachino

I read the Hilton Head notice announcing the awards in honor of Denice Denton, Wen Ko and Mark Shannon and it made me realize how rapidly time has passed. In my judgment the honors are well deserved and long overdue. I knew Wen and Denice very well and only knew of Mark by reputation. A sobering thought for me is that Mark was born the year I entered college.

This notice made me realize that most of the people now attending the Hilton Head Workshop have little knowledge how or why the workshop came about. So here is my take on the three why's of the workshop. Why a workshop? Why Hilton Head? Why TRF? These are the recollections of a very senior citizen.

WHY A WORKSHOP

A conference called TRANDUCERS was established in the 1970s. This conference was the place to present work concerning solid-state sensors, and later, actuators. The idea was that the conference should be held every two years in a different geographic area (Europe, Asia, Americas). This meant that the Americas would only host this meeting every six years. While at that time the field was small, a meeting every six years seemed inadequate to meet the community's needs in the Americas. Steve Senturia attempted to get a Gordon Conference on Microsensors to fill the void, but the application was turned down. That news was met with a determination to "do it ourselves."

Ken Wise initiated a meeting to address the best way to fill this void. To my recollection, the big meeting to discuss what to do was held in Michigan and the people present were:

Ken Wise – University of Michigan
Wen Ko – Case Western Reserve University
Dave Eddy – General Motors
Ben Hocker – Honeywell
Tom Poteat – Bell Labs
Steve Senturia – Massachusetts Institute of Technology
Joe Giachino – Ford

I am sure I left some out so check with Ken and Ben. I know Scott Chang–General Motors was supporting the Transaction printing.

The result reached at this meeting was that there should be a North America meeting every two years, in the even years when there was no Americas TRANSDUCERS meeting.

The format of the meeting was fashioned after the Gordon Conferences. There is a limit on the attendees, and in theory participants are invited to attend. The workshop concept led the group to limit attendees to persons based in North and South America. The format was to have only one session, with all in attendance, each day—rather than parallel sessions. Lunches that would allow people to talk and exchange ideas were included in the program. There was a free afternoon to allow participants time to explore.

The meeting also included a "rump" session, where refreshments were served and a very free flow of comments was encouraged. Several rump session comments have stuck in my memory

over the years: “Single crystal bigots” and “I agree with Professor Senturia.” I do not know whether any of our current Hilton Head Workshop attendees have any idea as to what these quotes refer!

WHY HILTON HEAD

The group decided the workshop would work best in a resort-type location with a casual, laid-back atmosphere to encourage people to informally interact. There were many suggestions for the venue including Mackinac Island, Mich., and Sandusky, Ohio.

Tom Poteat suggested Hilton Head, S.C. None of the other attendees knew of Hilton Head. Tom had grown up in the area and filled us in on the history and status. Hilton Head is a barrier island and in the early days was a place locals took their pigs to spend the winter. The pigs could forage for food, and they could not leave the island. I do not know how much of that is fact and how much is folklore. In the 1960s, developers began turning the island into an upscale resort community. The group was concerned about how accessible the island was to people coming from around the country. Tom let us know that the island was easily reached from Savannah and that there was even a small airport on the island, with shuttle service, if one did not want to drive.

What made the group decide on Hilton Head? Note that members of the group all had been previously involved in conference management and understood the effort involved in the tasks required for a successful meeting. So, when Tom said “If you select Hilton Head, I will be the local arrangements chair,” the group selected Hilton Head. After the first workshop, the suggestion was made that, like many IEEE meetings, the location should alternate between east coast and west coast. The suggestion was made that the meeting be held in Monterey, California. The group agreed that was a good location and the question was asked, “Who would like to be local arrangements chair for Monterey”? As there were no volunteers, thus was born the Hilton Head Workshop.

WHY TRF

The original plan was to have the IEEE Electron Device Society (EDS) sponsor the workshop, and the first two workshops indeed were sponsored by EDS. Note that this workshop was valuable to EDS because the profit from the year’s first workshop made EDS conferences profitable for that year.

The workshop committee had contacted the European and Asian groups concerning limiting attendance to the Americas. No group objected; in fact, the Europeans started EUORSENSORS based on the model of limiting attendance to Europeans. The EDS professional staff had no objection as all parties were in concert. However, an EDS member in a position of authority did object. This member was adamant that IEEE meetings had to be open to any and all IEEE members. It was further stated that if the workshop did not abide by these rules, there would be no IEEE support.

The workshop committee wanted to continue the successful workshop formula. As this could not be done under the auspicious of the IEEE, the Transducer Research Foundation (TRF) became the sponsor.

Wen Ko had, prior to the IEEE sponsorship of the first workshop, established TRF as an Ohio nonprofit. This was done as the model for this type of workshop was new and the committee

was not certain that EDS would approve of the concept. The committee wanted IEEE financial and technical (archiving, administrative) support to better serve the sensor community. When IEEE did not support our efforts, the TRF Board went out on its own.

Before we hired Katharine Cline's firm (Preferred Meeting Management, Inc.) in 1999, we ran the workshop by ourselves. This included a website, printing the proceedings, administration and all the mundane items that need to be done. Here are some examples that come to mind:

The TRF Board agreed that if there was any shortfall in revenue, the Board as individuals would make up the difference. To the relief of all, this has never been necessary.

The proceedings from the early meetings were printed by General Motors and delivered to Hilton Head by Dave Eddy. The one exception is when Dave was injured in an accident, and he had Mike Putty deliver the proceedings.

Tom Poteat negotiated with the hotel and had one keg of beer donated to the rump session. We worked with the hotel to allow us to buy our own wine, and it was served at the banquet and rump session. The hotel only charged a corkage fee, which reduced the expense.

We sold extra proceedings for cash—no credit cards or digital wallets, just plain money. To reduce the risk of having loose cash around, the monies were used to buy the wine.

Creating a Community

From the outset, the Workshop was devoted to creating a community of co-workers, including students. The founders take considerable pride in how that original intent has matured to the point where presentations by students, especially at our poster session, are many of the highlights of our program. As a "networking" event, the Hilton Head Workshop cannot be beat. It is the best!